

AD-A130 811

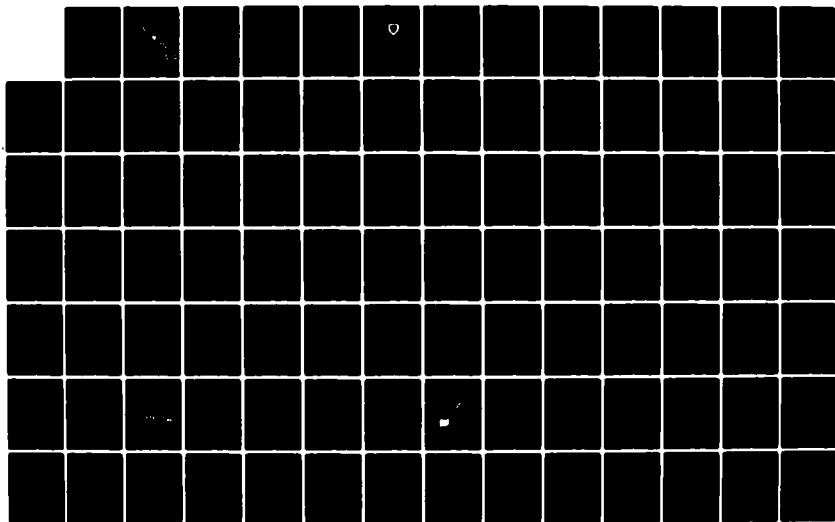
PROCEEDINGS OF THE SYMPOSIUM ON FREQUENCY CONTROL (36TH  
ANNUAL) 2-4 JUNE 1..(U) ARMY ELECTRONICS RESEARCH AND  
DEVELOPMENT COMMAND FORT MONMOUTH E PAIGE ET AL. 1982

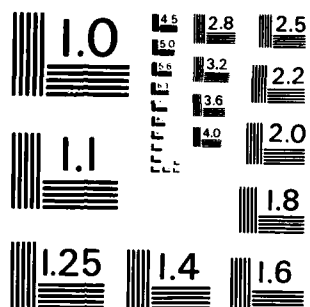
1/9

UNCLASSIFIED

F/G 20/14

NL



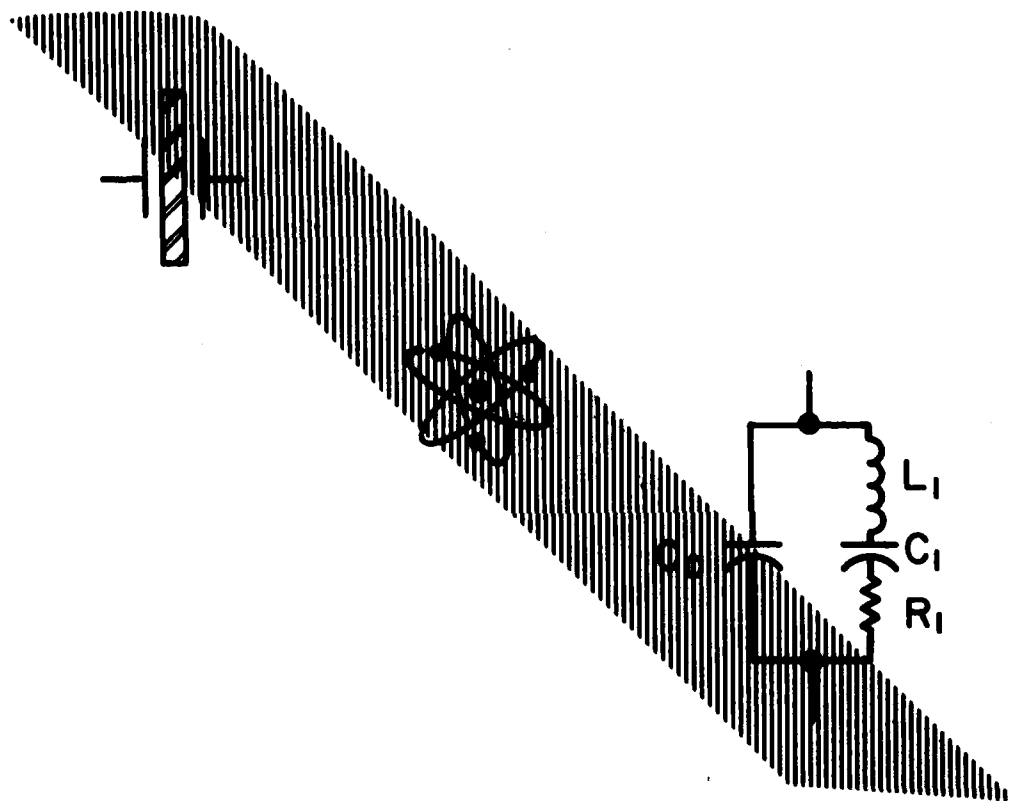


MICROCOPY RESOLUTION TEST CHART  
NATIONAL BUREAU OF STANDARDS-1963-A

PROCEEDINGS  
OF THE  
36TH ANNUAL SYMPOSIUM ON FREQUENCY CONTROL  
1982

AD A130811

DTIC FILE COPY



2-4 JUNE 1982

DTIC  
ELECT

MAR 25 1983

S E

U.S. ARMY ELECTRONICS RESEARCH AND  
DEVELOPMENT COMMAND

88 03 25 006

This document has been approved  
for public release and sale; its  
distribution is unlimited.

(1)

## COMPONENT PART NOTICE

THIS PAPER IS A COMPONENT PART OF THE FOLLOWING COMPILATION REPORT:

(TITLE): Proceedings of Symposium on Frequency Control (36th Annual) 1982, 2-4 Jun 1982

(SOURCE): U.S. Army Electronics Research and Development Command, Fort Monmouth, NJ.  
Electronics Technology and Devices Lab.

TO ORDER THE COMPLETE COMPILATION REPORT USE AD-A130 811.

THE COMPONENT PART IS PROVIDED HERE TO ALLOW USERS ACCESS TO INDIVIDUALLY AUTHORED SECTIONS OF PROCEEDINGS, ANNALS, SYMPOSIA, ETC. HOWEVER, THE COMPONENT SHOULD BE CONSIDERED WITHIN THE CONTEXT OF THE OVERALL COMPILATION REPORT AND NOT AS A STAND-ALONE TECHNICAL REPORT.

THE FOLLOWING COMPONENT PART NUMBERS COMPRISE THE COMPILATION REPORT:

AD#:	TITLE:
AD-P001 501	The Design of Partially Controlled Quartz Crystal Resonators.
AD-P001 502	Effect of Transverse Force on the Thickness-Shear Resonance Frequencies in Rectangular, Doubly-Rotated Crystal Plates.
AD-P001 503	Recent Results with the Air Force Hydrothermal Facility.
AD-P001 504	Growth and Characterisation of High Purity Quartz.
AD-P001 505	Radiation Effects in Synthetic and High Purity Synthetic Quartz: Some Recent Infrared Electron Spin Resonance and Acoustic Loss Results.
AD-P001 506	The Influence of Crystal Growth Rate and Electrodiffusion (Sweep or Point Defects in a Quartz.
AD-P001 507	A Comparison of Quartz Crystals Grown from Fused Silica and from Crystalline Nutrient.
AD-P001 508	A Method of Adjusting Resonant Frequency and Frequency-Temperature Coefficients of Miniaturized GT Cut Quartz Resonators.
AD-P001 509	Electroelastic Effects and Impurity Relaxation in Quartz Resonators.
AD-P001 510	DC Plasma Anodization of Quartz Resonators.
AD-P001 511	Characterization of Alkali Impurities in Quartz.
AD-P001 512	The Elastic, Dielectric and Piezoelectric Constants of Berlinite.
AD-P001 513	Thermal Frequency Behavior in Contoured Quartz Crystal Plates Induced by Direct Irradiation of Laser Beam.
AD-P001 514	Thermal Hysteresis of AT + SC-Cut Quartz Crystal Resonators; Automated Measurement Method and Results.
AD-P001 515	Elastic Constants of Quartz and Their Temperature Coefficients.
AD-P001 516	Turnover Temperatures for Doubly Rotated Quartz.
AD-P001 517	SC-Cut Resonators for Temperature Compensated Oscillators.

DTIC

AUG 4 1983

A

This document has been approved for public release and sale; its distribution is unlimited.

# COMPONENT PART NOTICE (CON'T)

AD#:	TITLE:
AD-P001 518	Photoluminescence from Worked Surface Layers and Frequency Instability of Quartz Resonators.
AD-P001 519	Growth Tunnels in Quartz Crystals.
AD-P001 520	Vibration Compensation of the SEETALK Rubidium Oscillator.
AD-P001 521	Amplitude-Frequency Effect of SC-Cut Quartz Trapped Energy Resonators.
AD-P001 522	Further Development in SC Cut Crystal Resonator Technology.
AD-P001 523	The Effect of Blank Geometry on the Acceleration Sensitivity of AT & SC-Cut Quartz Resonators.
AD-P001 524	"Atomic Clocks": Preview of an Exhibit at the Smithsonian.
AD-P001 525	A Squarewave F. M. Servo System with Digital Signal Processing for Cesium Frequency Standards.
AD-P001 526	Performance Characteristics of Cesium Beam Tube Electron Multipliers.
AD-P001 527	A Cesium Beam Frequency Standard with Microprocessor Control.
AD-P001 528	Experimental Results of the Light-Weight Hydrogen Maser Development Program.
AD-P001 529	Characteristics of Oscillating Compact Hydrogen Masers.
AD-P001 530	The Development of a Magnetically Enhanced Hydrogen Gas Dissociator.
AD-P001 531	Preliminary Measurements on EFOS 1 H Maser.
AD-P001 532	The Torsional Tuning Fork as a Temperature Sensor.
AD-P001 533	Inertial Guidance and Underwater Sound Detection Using SAW Sensors.
AD-P001 534	A Surface Acoustic Wave Gas Detector.
AD-P001 535	Pressure and Temperature Measurements with SAW Sensors.
AD-P001 536	New Quartz Resonators with Precision Frequency Linearity over a Wide Temperature Range.
AD-P001 537	New Method for the Measurement of Quartz Crystal Resonator Parameters.
AD-P001 538	An Instrument for Automated Measurement of the Angles of Cut of Doubly Rotated Quartz Crystals.
AD-P001 539	Performance of an Automated High Accuracy Phase Measurement System.
AD-P001 540	A Frequency Domain Reflectometer for Quartz Resonator Investigations.
AD-P001 541	Frequency Stabilization of a lGaAs Lasers.
AD-P001 542	Frequency Stability and Control Characteristics of (GaAl)As Semiconductor Lasers.
AD-P001 543	Short-Term Frequency Stability and Systematic Effects on the Rubidium 87 Maser Oscillator Frequency.
AD-P001 544	On the Lightshift and Buffer Gas Shift in Passive Rubidium Frequency Standards.
AD-P001 545	Spectral Characteristics of Single Mode GaAlAs Semiconductor Lasers.

COMPONENT PART NOTICE (Cont'd)

AD#:	TITLE:
AD-P001 546	The U.S. Navy's Standardized Precise Time and Time Interval (PTTI) Platform Distribution System (PDS).
AD-P001 547	Optimal Time and Frequency Transfer Using GPS Signals.
AD-P001 548	Intermediate Bandwidth Quartz Crystal Filters - A Simple Approach to Predistortion.
AD-P001 549	Developments in Low Loss, Low Ripple SAW Filters.
AD-P001 550	Multipole SAW Resonator Filters.
AD-P001 551	Recent Advances in UHF Crystal Filters.
AD-P001 552	Magnetostatic Wave Multi-Channel Filters.
AD-P001 553	Application of SAW Convolvers and Correlators.
AD-P001 554	Ultrareproducible SAW Resonator Production.
AD-P001 555	Development of Precision SAW Oscillators for Military Applications.
AD-P001 556	Effects of RIE Tuning on the Electrical and Temperature Characteristics of Quartz SAW Resonators.
AD-P001 557	Frequency Fine Tuning of Reliable SAW Transducers Using Anodization Technique.
AD-P001 558	A Digitally Compensated Hybrid Crystal Oscillator.
AD-P001 559	Theoretical and Practical Effects of the Resonator Specifications and Characteristics upon Precision Crystal Oscillator Design and Performance.
AD-P001 560	Reducing SAW Oscillator Temperature Sensitivity with Digital Compensation.
AD-P001 561	Update on the Tactical Miniature Crystal Oscillator Program.
AD-P001 562	Argos System Quartz Device Performance and Orbital Data.
AD-P001 563	Computer Aided Design and Assembly of Oscillators.
AD-P001 564	Improved Ring-Supported Resonators.
AD-P001 565	Aluminum Nitride Thin Film and Composite Bulk Wave Resonators.
AD-P001 566	SAW and SSBW Propagation in Indium Phosphide.
AD-P001 567	Unwanted Responses in Quartz Low Frequency X-Cut Bars.
AD-P001 568	Progress in the Development of Miniature Thin Film BAW Resonator and Filter Technology.
AD-P001 569	Development and Technology of Piezoelectric Bulk Wave Resonators and Transducers.
AD-P001 570	Temperature Compensated Crystal Oscillator Panel Discussion.
AD-P001 571	Methods of Temperature Compensation.
AD-P001 572	Dual Mode Digitally Temperature Compensated Crystal Oscillator
AD-P001 573	A Temperature Compensated SC Cut Quartz Crystal Oscillator.

A

PROCEEDINGS  
of the  
THIRTY-SIXTH ANNUAL FREQUENCY CONTROL SYMPOSIUM  
1982  
Sponsored By



U.S. ARMY ELECTRONICS RESEARCH AND DEVELOPMENT COMMAND

Major General Emmett Paige, Jr.  
Commanding

ELECTRONICS TECHNOLOGY AND DEVICES LABORATORY

Dr. C.G. Thornton  
Director

All rights reserved  
Printed in U.S.A.

None of the papers contained in the Proceedings may be reproduced in whole or in part, except for the customary brief abstract, without permission of the author, and without due credit to the Symposium.

2-4 June 1982  
Marriott Hotel  
Philadelphia, Pennsylvania

Accession For	
NTIS GRA&I	<input checked="" type="checkbox"/>
DTIC TAB	<input type="checkbox"/>
Unannounced	<input type="checkbox"/>
Justification	<i>file</i>
By _____	
Distribution/	
Availability Codes	
Dist	Avail and/or Special
A	



# THIRTY-SIXTH ANNUAL FREQUENCY CONTROL SYMPOSIUM

Sponsored By

U.S. ARMY ELECTRONICS RESEARCH AND DEVELOPMENT COMMAND  
ELECTRONICS TECHNOLOGY AND DEVICES LABORATORY

Fort Monmouth, New Jersey

2-4 June 1982

Marriott Hotel

Philadelphia, Pennsylvania

## TECHNICAL PROGRAM COMMITTEE

Executive Chairman ..... Mr. V. G. Gelinovatch

Technical Chairman ..... Dr. Arthur Ballato

U.S. Army Electronics Technology and Devices Laboratory

Mr. E. J. Alexander  
Bell Laboratories

Dr. D. R. Koehler  
Sandia Laboratories

Mr. M. Bloch  
Frequency Electronics, Inc.

Mr. J. A. Kusters  
Hewlett-Packard

\* Mr. A. Chi  
NASA/Goddard Space Flight Center

Mr. T. Lukaszek  
U.S. Army, ERADCOM

Dr. L. Claiborne  
Texas Instruments

Dr. T. Meeker  
Bell Laboratories

Mr. L. Conlee  
Motorola

Dr. T. E. Parker  
Raytheon

Dr. L. S. Cutler  
Hewlett-Packard

Mr. S. Schodowski  
U.S. Army, ERADCOM

Mr. M. Frerking  
Collins Radio Company

Dr. S. Stein  
National Bureau of Standards

Dr. E. Hafner  
U.S. Army, ERADCOM (retired)

Dr. W. J. Tanski  
Schlumberger Research

Dr. H. Hellwig  
Frequency & Time Systems, Inc.

Dr. J. Vig  
U.S. Army, ERADCOM

Dr. W. H. Horton  
Piezo Technology, Inc.

Dr. G. M. R. Winkler  
U.S. Naval Observatory

Mr. D. Kemper  
Quartztek, Inc.

Dr. N. Yannoni  
RADC/Air Force

\* Deceased

## TECHNICAL SESSION CHAIRMEN

### CRYSTAL RESONATOR THEORY

E. P. EerNisse, Quartex, Inc.

### FUNDAMENTAL STUDIES OF QUARTZ

D. R. Koehler, Sandia Laboratories

### QUARTZ RESONATOR STUDIES

E. Hafner, U.S. Army ERADCOM (retired)

### MATERIAL CONSTANTS & SC RESONATORS - I

D. R. Kinloch, Sawyer Research Products, Inc.

### SC RESONATORS - II; THE CRYSTAL SURFACE

R. C. Smythe, Piezo Technology, Inc.

### ATOMIC CLOCKS-OVERVIEW, CESIUM STANDARDS

L. S. Cutler, Hewlett Packard Laboratories

### HYDROGEN MASERS

H. Hellwig, Frequency and Time Systems, Inc.

### ACOUSTIC SENSORS

W. J. Tanski, Schlumberger - Doll Research Center

### MEASUREMENTS

W. H. Horton, Piezo Technology, Inc.

### LASER DIODES & OPTICAL PUMPING

S. R. Stein, National Bureau of Standards

### FREQUENCY & TIME DISTRIBUTION

G. M. R. Winkler, U.S. Naval Observatory

### SURFACE, BULK, AND MSW FILTERS

D. Reifel, Motorola, Inc.

### FABRICATION & APPLICATIONS OF SAWs

L. Claiborne, Texas Instruments

### OSCILLATORS

M. Bloch, Frequency Electronics, Inc.

### NOVEL MATERIALS AND RESONATORS

T. R. Meeker, Bell Laboratories

### PANEL DISCUSSION- "Temperature Compensated Crystal Oscillators"

Panel Chairman: D. W. Newell, Northern Illinois University

### SEMINAR - "Piezoelectric Resonators"

T. R. Meeker, Bell Laboratories, Inc., and  
A. W. Warner, Frequency Electronics, Inc.

## TABLE OF CONTENTS

<b>Opening Remarks</b>	
- Dr. E. A. Gerber, (retired), U.S. Army Electronics Research and Development Command Electronics Technology and Devices Laboratory .....	1
<b>Crystal Resonator Theory</b>	
<b>Third Overtone Quartz Resonator</b>	
- R. D. Mindlin .....	3
<b>The Design of Partially Controlled Quartz Crystal Resonators</b>	
- R. C. Peach, The General Electric Co., Ltd. ....	22
<b>Effect of Transverse Force on the Thickness-Shear Resonance Frequencies in Rectangular, Doubly-Rotated Crystal Plates</b>	
- P. C. Y. Lee and C. S. Lam, Princeton University .....	29
<b>An Analysis of Contoured SC-Cut Quartz Crystal Resonators</b>	
- H. F. Tiersten and D. S. Stevens, Rensselaer Polytechnic Institute .....	37
<b>Temperature Induced Frequency Changes in Electroded Contoured SC-Cut Quartz Crystal Resonators</b>	
- D. S. Stevens and H. F. Tiersten, Rensselaer Polytechnic Institute .....	46
<b>Fundamental Studies of Quartz</b>	
<b>Recent Results with the Air Force Hydrothermal Facility</b>	
- A. F. Armington, J. J. Larkin, J. J. O'Connor and J. A. Horrigan, RADC .....	55
<b>Growth and Characterisation of High Purity Quartz</b>	
- D. F. Croxall, I. R. A. Christie, J. M. Holt, B. J. Isherwood and A. G. Todd, The General Electric Co., Ltd. ....	62
<b>Radiation Effects in Synthetic and High Purity Synthetic Quartz: Some Recent Infrared Electron Spin Resonance and Acoustic Loss Results</b>	
- S. P. Doherty, S. E. Morris, D. C. Andrews and D. F. Croxall, The General Electric Co., Ltd. ....	66
<b>The Influence of Crystal Growth Rate and Electrodiffusion (Sweeping) on Point Defects in <math>\alpha</math>-Quartz</b>	
- J. J. Martin, L. E. Halliburton, R. B. Bossoli, Oklahoma State University and A. F. Armington, RADC .....	77
<b>A Comparison of Quartz Crystals Grown from Fused Silica and from Crystalline Nutrient</b>	
- R. J. Baughman, Sandia National Laboratories .....	82
<b>Quartz Resonator Studies</b>	
<b>A Method of Adjusting Resonant Frequency and Frequency-Temperature Coefficients of Miniaturized GT Cut Quartz Resonators</b>	
- O. Ochiai, A. Kudo, A. Nakajima and H. Kawashima, Daini Seikosha Co., Ltd. ....	90
<b>Electroelastic Effects and Impurity Relaxation in Quartz Resonators</b>	
- R. Brendel and J. J. Gagnepain, C. N. R. S. ....	97
<b>DC Plasma Anodization of Quartz Resonators</b>	
- C. W. Shanley and L. N. Dworsky, Motorola, Inc. ....	108
<b>Characterization of Alkali Impurities in Quartz</b>	
- F. Euler, H. Lipson, A. Kahan and A. F. Armington, RADC .....	115
<b>Material Constants &amp; SC Resonators - I</b>	
<b>The Elastic, Dielectric and Piezoelectric Constants of Berlinite</b>	
- D. S. Bailey, W. Soluch, D. L. Lee, J. F. Vetelino and J. C. Andle, University of Maine and B. Chai, Allied Corporation .....	124

## TABLE OF CONTENTS (Continued)

Thermal Frequency Behavior in Contoured Quartz Crystal Plates Induced by Direct Irradiation of Laser Beam - N. Oura, N. Kuramochi, J. Nakamura and T. Ogawa, Tokyo Institute of Technology . . . . .	133
Thermal Hysteresis of AT + SC-Cut Quartz Crystal Resonators; Automated Measurement Method and Results - H. J. Förster, Siemens AG . . . . .	140
Elastic Constants of Quartz and Their Temperature Coefficients - A. Kahan, RADC . . . . .	159
Turnover Temperatures for Doubly Rotated Quartz - A. Kahan, RADC . . . . .	170
SC-Cut Resonators for Temperature Compensated Oscillators - J. R. Vig, R. L. Filler and J. A. Kosinski, USAERADCOM . . . . .	181
<b>SC Resonators - II; The Crystal Surface</b>	
Photoluminescence from Worked Surface Layers and Frequency Instability of Quartz Resonators - A. Halperin, S. Katz and M. Ronen, The Hebrew University of Jerusalem . . . . .	187
Growth Tunnels in Quartz Crystals - S. Katz, A. Halperin and M. Schieber, The Hebrew University of Jerusalem . . . . .	193
Vibration Compensation of the SEEKTALK Rubidium Oscillator - C. Colson, EFRATOM California, Inc. . . . .	197
Amplitude-Frequency Effect of SC-Cut Quartz Trapped Energy Resonators - R. Bourquin, D. Nassour and D. Hauden, ENSMM . . . . .	200
Further Development in SC Cut Crystal Resonator Technology - A. Warner, B. Goldfrank and J. Tsacfas, Frequency Electronics Inc. . . . .	208
The Effect of Blank Geometry on the Acceleration Sensitivity of AT & SC-Cut Quartz Resonators - R. L. Filler, J. A. Kosinski and J. R. Vig, USAERADCOM . . . . .	215
<b>Atomic Clocks - Overview; Cesium Standards</b>	
"Atomic Clocks": Preview of an Exhibit at the Smithsonian - P. Forman, Smithsonian Institution . . . . .	220
A Squarewave F. M. Servo System with Digital Signal Processing for Cesium Frequency Standards - Y. Nakadan and Y. Koga, National Research Laboratory of Metrology . . . . .	223
Performance Characteristics of Cesium Beam Tube Electron Multipliers - E. R. Straka, Hewlett-Packard . . . . .	230
A Cesium Beam Frequency Standard with Microprocessor Control - R. Michael Garvey, Frequency and Time Systems, Inc. . . . .	236
<b>Hydrogen Masers</b>	
Experimental Results of the Light-Weight Hydrogen Maser Development Program - H. E. Peters, Sigma Tau Standards Corporation . . . . .	240
Characteristics of Oscillating Compact Hydrogen Masers - H. T. M. Wang, Hughes Research Laboratories . . . . .	249

## TABLE OF CONTENTS (Continued)

The Development of a Magnetically Enhanced Hydrogen Gas Dissociator - L. Maleki, Jet Propulsion Laboratory .....	255
Preliminary Measurements on EFOS 1 H Maser - G. Busca, F. Addor, F. Hadorn, G. Nicolas, L. Prost, H. Brandenberger, P. Thomann, Asulab S.A., and L. Johnson, Oscilloquartz, S.A. ....	260
<b>Acoustic Sensors</b>	
The Torsional Tuning Fork as a Temperature Sensor - R. J. Dinger, Asulab S.A. ....	265
Inertial Guidance and Underwater Sound Detection Using SAW Sensors - E. J. Staples, J. Wise and A. P. Andrews, Rockwell International .....	270
A Surface Acoustic Wave Gas Detector - A. Bryant, M. Poirier, D. L. Lee and J. F. Vetelino, University of Maine. ....	276
Pressure and Temperature Measurements with SAW Sensors - D. Hauden, S. Rousseau, G. Jalliet and R. Coquerel, C. N. R. S. ....	284
New Quartz Resonators with Precision Frequency Linearity over a Wide Temperature Range - M. Nakazawa, H. Ito, A. Usui, Shinshu University and A. Ballato and T. Lukaszek, USAERADCOM. ....	290
<b>Measurements</b>	
New Method for the Measurement of Quartz Crystal Resonator Parameters - R. C. Peach, A. J. Dyer, A. J. Byrne and S. P. Doherty, The General Electric Co., Ltd. ....	297
An Instrument for Automated Measurement of the Angles of Cut of Doubly Rotated Quartz Crystals - J. L. Chambers, Advanced Research and Applications Corporation. ....	302
Performance of an Automated High Accuracy Phase Measurement System - S. Stein, D. Glaze, J. Levine, J. Gray, D. Hilliard, D. Howe, NBS and L. Erb, ERBTEC Engineering Inc. ....	314
A Frequency Domain Reflectometer for Quartz Resonator Investigations - C. S. Stone, Brightline Corporation and O. J. Baltzer, Tracor, Inc. ....	321
<b>Laser Diodes &amp; Optical Pumping</b>	
Frequency Stabilization of AlGaAs Lasers - M. Ohtsu, H. Tsuchida and T. Tako, Tokyo Institute of Technology .....	327
Frequency Stability and Control Characteristics of (GaAl)As Semiconductor Lasers - A. Mooradian and D. Welford, Lincoln Laboratory, MIT .....	338
Short-Term Frequency Stability and Systematic Effects on the Rubidium 87 Maser Oscillator Frequency - M. Têtu, P. Tremblay, D. Bonnier and J. Vanier, Université Laval. ....	340
On the Lightshift and Buffer Gas Shift in Passive Rubidium Frequency Standards - J. Vanier, R. Kinski, P. Paulin, J. Y. Savard, M. Têtu and N. Cyr, Université Laval .....	348
Spectral Characteristics of Single Mode GaAlAs Semiconductor Lasers - R. O. Miles, NRL. ....	355
Ultra-Stable Laser Clock - R. L. Facklam, Wright-Patterson AFB, Ohio .....	361

## TABLE OF CONTENTS (Continued)

A Laser Atomic Beam Standard - C. C. Leiby, Jr., R. H. Picard, RADC, J. E. Thomas, P. R. Hemmer and S. Ezekiel, MIT .....	370
<b>Frequency &amp; Time Distribution</b>	
Vibration and Acceleration-Induced Timing Errors of Clocks and Clock Systems - F. L. Walls, National Bureau of Standards .....	371
The U.S. Navy's Standardized Precise Time and Time Interval (PTTI) Platform Distribution System (PDS) - R. T. Allen, Naval Electronic Systems Command .....	372
Optimal Time and Frequency Transfer Using GPS Signals - D. W. Allan and J. A. Barnes, NBS .....	378
Test Results of the STI GPS Time Transfer Receiver - D. L. Hall, HRB Singer, Inc. and K. Putkovich, U.S. Naval Observatory .....	388
<b>Surface, Bulk, and MSW Filters</b>	
Intermediate Bandwidth Quartz Crystal Filters - A Simple Approach to Predistortion - R. C. Peach, A. J. Dyer, A. J. Byrne and E. Read, The General Electric Co., Ltd. and J. K. Stevenson Polytechnic of the South Bank .....	389
Developments in Low Loss, Low Ripple SAW Filters - K. H. Yen, K. F. Lau, R. B. Stokes, A. M. Kong and R. S. Kagiwada, TRW .....	396
Multipole SAW Resonator Filters - W. J. Tanski, Sperry Research Center .....	400
Recent Advances in UHF Crystal Filters - B. d'Albaret and P. Siffert, CEPE .....	405
Magnetostatic Wave Multi-Channel Filters - J. D. Adam, Westinghouse .....	419
<b>Fabrication &amp; Applications of SAWs</b>	
Application of SAW Convolvers and Correlators - H. Gautier, Thomson-CSF .....	428
Ultrareproducible SAW Resonator Production - W. E. Bulst and E. Willibald, Siemens, A.G. ....	442
Development of Precision SAW Oscillators for Military Applications - T. E. Parker, Raytheon Co. ....	453
Effects of RIE Tuning on the Electrical and Temperature Characteristics of Quartz SAW Resonators C. Kotecki, Motorola, Inc. ....	459
Frequency Fine Tuning of Reliable SAW Transducers Using Anodization Technique - F. Y. Cho, T. B. Chatham and R. Ponce de Leon, Motorola, Inc. ....	470
<b>Oscillators</b>	
A Digitally Compensated Hybrid Crystal Oscillator - G. B. Pollard, Hughes Aircraft Company .....	474

## TABLE OF CONTENTS (Continued)

Theoretical and Practical Effects of the Resonator Specifications and Characteristics upon Precision Crystal Oscillator Design and Performance - B. Parzen, Frequency Electronics Inc. ....	480
Reducing SAW Oscillator Temperature Sensitivity with Digital Compensation - A. J. Slobodnik, Jr., R. D. Colvin, G. A. Roberts, J. H. Silva, RADC .....	486
Update on the Tactical Miniature Crystal Oscillator Program - H. W. Jackson, The Bendix Corporation .....	492
Argos System Quartz Device Performance and Orbital Data - M. Geesen, EMD; M. Brunet, CNES; M. Meirs, A. Strauss, J. Ho and M. Rosenfeld, Frequency Electronics Inc. ....	499
Computer Aided Design and Assembly of Oscillators - T. M. Hall, Bell Laboratories, Inc. ....	507
<b>Novel Materials and Resonators</b>	
Improved Ring Supported Resonators - M. Nakazawa, H. Ito, Shinshu University, T. Lukaszek and A. Ballato, USAERADCOM .....	513
Aluminum Nitride Thin Film and Composite Bulk Wave Resonators - K. M. Lakin, J. S. Wang and A. R. Landin, Ames Laboratory .....	517
SAW and SSBW Propagation in Indium Phosphide - J. Henaff and M. Feldmann, CNET .....	525
Unwanted Responses in Quartz Low Frequency X-Cut Bars - J. F. Werner, The General Electric Co., Ltd., H. W. Edwards and M. Smith, Salford Electrical Instruments Ltd. ....	529
Progress in the Development of Miniature Thin Film BAW Resonator and Filter Technology - T. W. Grudkowski, J. F. Black, G. W. Drake, and D. E. Cullen, United Technologies Research Center .....	537
<b>Seminar</b>	
Development and Technology of Piezoelectric Bulk Wave Resonators and Transducers - T. R. Meeker, Bell Telephone Laboratories, Inc. ....	549
<b>Panel Discussion</b>	
Temperature Compensated Crystal Oscillator Panel Discussion - D. E. Newell, Northern Illinois University .....	562
Methods of Temperature Compensation - M. E. Frerking, Collins Telecommunications Products Division, Rockwell International Corp. ....	564
Dual Mode Digitally Temperature Compensated Crystal Oscillator - R. Rubach, Midland Ross Corporation/NEL Unit .....	571
A Temperature Compensated SC Cut Quartz Crystal Oscillator - E. K. Miguel, Northern Illinois University .....	576
AUTHOR INDEX .....	586
SPECIFICATIONS AND STANDARDS GERMANE TO FREQUENCY CONTROL .....	587

*Memorandum for the*  
*Commander*  
**36th Annual Frequency Control Symposium - 1982**

**OPENING REMARKS**

**DR. E. A. GERBER**  
(retired)

**US ARMY ELECTRONICS RESEARCH AND DEVELOPMENT COMMAND**  
**FT. MONMOUTH, NJ 07703**

On behalf of the United States Army Electronics Research and Development Command, parent command of the sponsoring Electronics Technology and Devices Laboratory, I take great pleasure in welcoming you all here and formally open the 36th Annual Frequency Control Symposium. I am speaking here for Major General Emmett Paige, Jr., the Commanding General of the Electronics Research and Development Command and for Dr. Clairence Thornton, Director of the Electronics Technology and Devices Laboratory. Both gentlemen are attending an important conference in Washington and regret very much that they cannot be with us today.

I would like to extend a special welcome to our friends from other countries. It is always exciting to realize how much the common interest in a field of science and technology is uniting people across distances and political boundaries.

It gives me great satisfaction personally to again be able to attend this annual event. I only missed the Symposium of 1959 of all the 36 conferences. But please do not draw the wrong conclusion as to my expertise in our field. When you are moved into management, away from personal research, you don't have the opportunity to remain in contact with the activities in specific technical topics and you will be surprised how fast technology moves forward without you. But when I finally retired, I was able to return at some degree to my favored hobby, frequency control. I was amazed how far you have progressed in controlling all the disturbing influences of time, design and environment on our frequency control devices.

At this occasion, I cannot resist the temptation to look back at the birth of our conferences. It happened in 1947 when the first symposium was held in a conference room of the former Squire Signal Laboratory. The purpose of this first meeting was to review progress on the various contracts to assist the military in future program planning. The next three symposia were expanded and moved to Gibbs Hall. After that they were moved to Asbury Park in 1951 and stayed there until the first meeting in Atlantic City in 1960, the fourteenth symposium.

I remember too well, by today's standards, all the frequency control devices available in 1947 were totally inadequate. The holders leaked, high frequency crystal units aged or drifted badly and they had high resistance at low drive levels. There was considerable variation of resistance with temperature and many of them had unwanted modes which caused off-frequency operation of the equipment.

It is beneficial once in a while to look back in order to be proud and happy on the tremendous progress which has been achieved in crystals. A similar statement is valid for our atomic standards considering how much we have gained in accuracy and ease of operation together with a tremendous reduction in size specifically when we remember the first eight-foot Cesium beam giant. But now enough of the past. Let us begin to look at today's progress in our field and get some glimpse of new advances the future may bring for frequency control.

In this regard, I wish all of you an interesting, profitable and enjoyable meeting.

Thank you.

### THIRD OVERTONE QUARTZ RESONATOR

R.D. Mindlin  
89 Deer Hill Drive, Ridgefield, CT 06877, U.S.A.

ABSTRACT - The Lee-Nikodem equations of motion of elastic plates are solved for the case of vibrations of an AT-cut quartz strip, with free faces and edges, at frequencies up to and including the third harmonic thickness-shear overtone.

#### 1. Introduction

About 30 years ago, A.W. Warner [1] developed a high precision crystal-plate resonator utilizing the third harmonic overtone of thickness-shear vibration, i.e. a mode involving a thickness-shear motion with three nodes across the thickness of the plate rather than the one node of the fundamental thickness-shear mode. At about the same time, equations were developed which extended the classical (Lagrange-Germain-Cauchy) range of frequencies to include that of the fundamental thickness-shear mode; but it was not until much later that Lee and Nikodem [2,3] formulated equations suitable for studying vibrations at frequencies of the harmonic overtone modes of thickness-shear.

In the present paper, the Lee-Nikodem third-order equations are solved for a case of rotated-Y-cut quartz plates with free faces and a pair of parallel, free edges. The results of computations for the AT-cut plate

are presented for vibrations in the neighborhood of the frequency of the fundamental thickness-shear mode and in the neighborhood of the third harmonic overtone. The differences between the two exhibit some of the reasons for the higher stability of the latter.

## 2. Lee-Nikodem Equations

To obtain two-dimensional equations of motion of plates from the three-dimensional equations of linear elasticity, Lee and Nikodem start with an expansion of the three-dimensional, rectangular components of displacement,  $u_j$ ,  $j=1,2,3$ , in series of trigonometric functions of the thickness-coordinate,  $x_2$ , of the plate:

$$u_j = \sum_{n=0}^{\infty} u_j^{(n)} \cos n\beta, \quad (1)$$

where the  $u_j^{(n)}$  are independent of  $x_2$  and

$$\beta = \pi(1 - x_2/b)/2 \quad (2)$$

in which  $b$  is the half-thickness of the plate. The functions  $\cos n\beta$  give the shapes of the simple thickness-modes of an infinite, isotropic plate with free faces at  $x_2 = \pm b$ .

The expression (1), for the  $u_j$ , is substituted in the variational equation of motion [4]:

$$\int_V (T_{ij,i} - \rho \ddot{u}_j) \delta u_j dV = 0 \quad (3)$$

where the  $T_{ij}$  are the components of stress,  $\rho$  is the mass density and  $V$  is the volume. The integration is performed over the thickness of the plate and leads to stress-equations of motion of order  $n$ ; which are, omitting the terms accounting for surface tractions,

$$T_{ij}^{(n)} - (n\pi/2b) T_{2j}^{(n)} = e_n \rho \ddot{u}_j^{(n)}, \quad (4)$$

where

$$T_{ij}^{(n)} = b^{-1} \int_{-b}^b T_{ij} \cos n\beta \, dx_2, \quad \bar{T}_{ij}^{(n)} = b^{-1} \int_{-b}^b T_{ij} \sin n\beta \, dx_2, \quad (5)$$

and  $e_n = 2$  for  $n=0$  and  $e_n = 1$  for  $n > 0$ . (Corrections of [3] by a factor of 2, for  $n=0$ , were kindly supplied by Professor Lee).

The three-dimensional strain-displacement relations,

$$S_{ij} = (u_{j,i} + u_{i,j})/2, \quad (6)$$

become, with (1),

$$S_{ij} = \sum_{n=0}^{\infty} (S_{ij}^{(n)} \cos n\beta + \bar{S}_{ij}^{(n)} \sin n\beta), \quad (7)$$

where

$$s_{ij}^{(n)} = (u_{j,i}^{(n)} + u_{i,j}^{(n)})/2, \quad \xi_{ij}^{(n)} = n\pi(\delta_{2i}u_j^{(n)} + \delta_{2j}u_i^{(n)})/4b \quad (8)$$

and  $\delta_{ij}$  is the Kronecker delta.

The three-dimensional stress-strain relations,

$$T_{ij} = c_{ijkl}S_{kl}, \quad i,j,k,l=1,2,3 \quad \text{or} \quad T_p = c_{pq}S_q, \quad p,q=1\dots 6, \quad (9)$$

become, from (5) and (6),

$$T_{ij}^{(n)} = c_{ijkl}(e_n S_{kl}^{(n)} + \sum_{m=1}^{\infty} A_{mn} \xi_{kl}^{(m)}), \quad \tau_{ij}^{(n)} = c_{ijkl}(\xi_{kl}^{(n)} + \sum_{m=1}^{\infty} A_{nm} S_{kl}^{(m)}), \quad (10)$$

where

$$A_{mn} = 0, \quad m+n \text{ even}; \quad 4m/(m^2 - n^2)\pi, \quad m+n \text{ odd}. \quad (11)$$

The components of stress (10) are derivable from a strain energy density,  $U$ , according to

$$T_{ij}^{(n)} = \partial U / \partial S_{ij}^{(n)}, \quad \tau_{ij}^{(n)} = \partial U / \partial \xi_{ij}^{(n)} \quad (12)$$

where

$$2U = c_{ijkl} \sum_{n=0}^{\infty} [e_n S_{ij}^{(n)} S_{kl}^{(n)} + \xi_{ij}^{(n)} \xi_{kl}^{(n)} + \sum_{m=0}^{\infty} (A_{mn} S_{ij}^{(n)} \xi_{kl}^{(m)} + A_{nm} \xi_{ij}^{(n)} S_{kl}^{(m)})] \quad (13)$$

### 3. Reduction to a Special Case

The example to be studied is one of steady vibrations at frequencies high enough to include the third harmonic overtone of the thickness-shear family of modes of an AT-cut quartz plate bounded by free faces at  $x_2 = \pm b$  and free edges at  $x_1 = \pm a$ . The modes are to be straight-crested along  $x_3$  and antisymmetric with respect to both  $x_1$  and  $x_2$ . Thus, we take, of (1), only

$$\begin{aligned} u_1 &= (u_1^{(1)} \cos \beta + u_1^{(3)} \cos 3\beta) e^{i\omega t}, \\ u_2 &= (u_2^{(0)} + u_2^{(2)} \cos 2\beta) e^{i\omega t}, \\ u_3 &= (u_3^{(0)} + u_3^{(2)} \cos 2\beta) e^{i\omega t}, \end{aligned} \quad (14)$$

in which the  $u_j^{(n)}$  depend only on  $x_1$ . The second term in  $u_1$  accommodates the third harmonic overtone thickness-shear mode.

What remain of the stress-equations of motion (4) are

$$\begin{aligned} T_{12,1}^{(0)} + 2\rho\omega^2 u_2^{(0)} &= 0, & T_{13,1}^{(0)} + 2\rho\omega^2 u_3^{(0)} &= 0, \\ T_{11,1}^{(1)} - (\pi/2b)T_{21}^{(1)} + \rho\omega^2 u_1^{(1)} &= 0, & T_{12,1}^{(2)} - (\pi/b)T_{22}^{(2)} + \rho\omega^2 u_2^{(2)} &= 0, \\ T_{13}^{(2)} - (\pi/b)T_{23}^{(2)} + \rho\omega^2 u_3^{(2)} &= 0, & T_{11,1}^{(3)} - (3\pi/2b)T_{21}^{(3)} + \rho\omega^2 u_1^{(3)} &= 0. \end{aligned} \quad (15)$$

and the only non-zero components of strain are, from (8) and (14),

$$\begin{aligned}
S_5^{(0)} &= u_{3,1}^{(0)}, & S_6^{(0)} &= u_{2,1}^{(0)}, \\
S_1^{(1)} &= u_{1,1}^{(1)}, & S_6^{(1)} &= (\pi/2b)u_1^{(1)}, \\
S_5^{(2)} &= u_{3,1}^{(2)}, & S_6^{(2)} &= u_{2,1}^{(2)}, \\
S_2^{(2)} &= (\pi/b)u_2^{(2)}, & S_4^{(2)} &= (\pi/b)u_3^{(2)}, \\
S_1^{(3)} &= u_{1,1}^{(3)}, & S_6^{(3)} &= (3\pi/2b)u_1^{(3)}.
\end{aligned} \tag{16}$$

Nine constants of elasticity, referred to axes in and normal to the plane of the plate (with  $x_1$  an axis of two-fold symmetry of the elastic properties of quartz), enter into the present example. As computed by A. Ballato [5] from R. Bechmann's [6] principal constants, they are (in  $\text{N/m}^2 \times 10^{-9}$ ):

$$\begin{aligned}
c_{11} &= 86.74 & c_{12} &= -8.260543013 & c_{55} &= 68.80698505 \\
c_{22} &= 129.7663387 & c_{24} &= 5.700423178 & c_{66} &= 29.01301496 \\
c_{44} &= 38.61152627 & c_{14} &= -3.654869573 & c_{56} &= 2.533571817
\end{aligned}$$

Of the remaining twelve constants, four ( $c_{13}, c_{23}, c_{33}, c_{43}$ ) do not enter into the present example, as the modes are independent of  $x_3$ ; and the others ( $c_{15}, c_{25}, c_{35}, c_{45}, c_{16}, c_{26}, c_{36}, c_{46}$ ) are zero for the rotated-Y-cuts of quartz.

Lee and Nikodem introduce a low frequency correction factor  $k_1$  and a high frequency correction factor  $k_2$ . The former appears as a factor of  $A_{10}$  in the strain energy density appropriate to the present example:

$$\begin{aligned}
2U = & 2(c_{55}S_5^{(0)}S_5^{(0)} + c_{66}S_6^{(0)}S_6^{(0)} + 2c_{56}S_5^{(0)}S_6^{(0)}) + c_{11}S_1^{(1)}S_1^{(1)} \\
& + c_{55}S_5^{(2)}S_5^{(2)} + c_{66}S_6^{(2)}S_6^{(2)} + 2c_{56}S_5^{(2)}S_6^{(2)} + c_{11}S_1^{(3)}S_1^{(3)} \\
& + c_{22}S_2^{(2)}S_2^{(2)} + c_{44}S_4^{(2)}S_4^{(2)} + 2c_{24}S_2^{(2)}S_4^{(2)} + c_{66}S_6^{(1)}S_6^{(1)} + c_{66}S_6^{(3)}S_6^{(3)} \\
& + 2k_1A_{10}(c_{66}S_6^{(0)} + c_{56}S_5^{(0)})S_6^{(1)} + 2A_{12}(c_{66}S_6^{(2)} + c_{56}S_5^{(2)})S_6^{(1)} \\
& + 2A_{21}(c_{12}S_2^{(2)} + c_{14}S_4^{(2)})S_1^{(1)} + 2A_{23}(c_{12}S_2^{(2)} + c_{14}S_4^{(2)})S_1^{(3)} \\
& + 2A_{30}(c_{66}S_6^{(0)} + c_{56}S_5^{(0)})S_6^{(3)} + 2A_{32}(c_{66}S_6^{(2)} + c_{56}S_5^{(2)})S_6^{(3)} ,
\end{aligned} \tag{17}$$

where

$$\begin{aligned}
A_{10} &= 4/\pi , & A_{12} &= -4/3\pi , & A_{21} &= 8/3\pi , \\
A_{23} &= -8/5\pi , & A_{30} &= 4/3\pi , & A_{32} &= 12/5\pi .
\end{aligned} \tag{18}$$

The correction factor  $k_2$ , in the present example, is inserted as a divisor of the term  $2\rho\omega^2u_2^{(0)}$  in the first of (15).

Adjusted values of  $k_1$  and  $k_2$ , as supplied by Professor Lee, are

$$k_1^2 = \pi^2/8 , \quad k_2^2 = 0.901. \tag{19}$$

From (12), (17) and (16), the surviving stress-displacement relations are

$$\begin{aligned}
T_{13}^{(0)} &= 2[c_{55}u_{3,1}^{(0)} + c_{56}(u_{2,1}^{(0)} + k_1 b^{-1}u_1^{(1)} + b^{-1}u_1^{(3)})], \\
T_{12}^{(0)} &= 2[c_{56}u_{3,1}^{(0)} + c_{66}(u_{2,1}^{(0)} + k_1 b^{-1}u_1^{(1)} + b^{-1}u_1^{(3)})], \\
T_{11}^{(1)} &= c_{11}u_{1,1}^{(1)} + (8/3b)(c_{12}u_2^{(2)} + c_{14}u_3^{(2)}), \\
T_{13}^{(2)} &= c_{55}u_{3,1}^{(2)} + c_{56}[u_{2,1}^{(2)} - (2/3b)u_1^{(1)} + (18/5b)u_1^{(3)}], \\
T_{12}^{(2)} &= c_{56}u_{3,1}^{(2)} + c_{66}[u_{2,1}^{(2)} - (2/3b)u_1^{(1)} + (18/5b)u_1^{(3)}], \\
T_{11}^{(3)} &= c_{11}u_{1,1}^{(3)} + (8/5b)(c_{12}u_2^{(2)} + c_{14}u_3^{(2)}), \\
T_{12}^{(1)} &= (4k_1/\pi)(c_{56}u_{3,1}^{(0)} + c_{66}u_{2,1}^{(0)}) + (\pi/2b)c_{66}u_1^{(1)} - (4/3\pi)(c_{56}u_{3,1}^{(2)} + c_{66}u_{2,1}^{(2)}), \\
T_{22}^{(2)} &= (8/\pi)c_{12}(u_{1,1}^{(1)}/3 - u_{1,1}^{(3)}/5) + (\pi/b)(c_{22}u_2^{(2)} + c_{24}u_3^{(2)}), \\
T_{23}^{(1)} &= (8/\pi)c_{14}(u_{1,1}^{(1)}/3 - u_{1,1}^{(3)}/5) + (\pi/b)(c_{24}u_2^{(2)} + c_{44}u_3^{(2)}), \\
T_{12}^{(3)} &= (4/3\pi)(c_{56}u_{3,1}^{(0)} + c_{66}u_{2,1}^{(0)}) + (12/5\pi)(c_{56}u_{3,1}^{(2)} + c_{66}u_{2,1}^{(2)}) + (3\pi/2b)c_{66}u_1^{(3)}.
\end{aligned} \tag{20}$$

The displacement equations of motion, to be solved, are obtained by substituting the stress-displacement relations (20) into the stress-equations of motion (15) -- with  $k_2$  inserted in the first of (15), as mentioned previously.

Finally, the edge conditions are

$$T_{13}^{(0)} = T_{12}^{(0)} = T_{11}^{(1)} = T_{13}^{(2)} = T_{12}^{(2)} = T_{11}^{(3)} = 0 \quad \text{on} \quad x_1 = \pm a. \tag{21}$$

#### 4. Dispersion Relation

In (14) we take, omitting the factor  $e^{i\omega t}$ ,

$$\begin{aligned} u_2^{(0)} &= A_2^{(0)} \sin \xi x_1, & u_2^{(2)} &= A_2^{(2)} \sin \xi x_1, \\ u_3^{(0)} &= A_3^{(0)} \sin \xi x_1, & u_3^{(2)} &= A_3^{(2)} \sin \xi x_1, \\ u_1^{(1)} &= A_1^{(1)} \cos \xi x_1, & u_1^{(3)} &= A_1^{(3)} \cos \xi x_1 \end{aligned} \quad (22)$$

and substitute first in (20) and the result in (15) to produce a set of six simultaneous, homogeneous, linear algebraic equations in the six amplitudes  $A_j^{(n)}$  of (22):

$$\begin{aligned} a_{11}A_2^{(0)} + a_{12}A_3^{(0)} + a_{13}A_1^{(1)} + 0 + 0 + a_{16}A_1^{(3)} &= 0 \\ a_{12}A_2^{(0)} + a_{22}A_3^{(0)} + a_{23}A_1^{(1)} + 0 + 0 + a_{26}A_1^{(3)} &= 0 \\ a_{13}A_2^{(0)} + a_{23}A_3^{(0)} + a_{33}A_1^{(1)} + a_{34}A_2^{(2)} + a_{35}A_3^{(2)} + 0 &= 0 \\ 0 + 0 + a_{34}A_1^{(1)} + a_{44}A_2^{(2)} + a_{45}A_3^{(2)} + a_{46}A_1^{(3)} &= 0 \\ 0 + 0 + a_{35}A_1^{(1)} + a_{45}A_2^{(2)} + a_{55}A_3^{(2)} + a_{56}A_1^{(3)} &= 0 \\ a_{16}A_2^{(0)} + a_{26}A_3^{(0)} + 0 + a_{46}A_2^{(2)} + a_{56}A_3^{(2)} + a_{66}A_1^{(3)} &= 0 \end{aligned} \quad (23)$$

The coefficients  $a_{pq}$ , made dimensionless and real by some manipulations of the equations, are

$$\begin{aligned}
a_{11} &= 2(z^2 - \Omega^2/k_2), \quad a_{12} = 2\bar{c}_{56}z^2, \quad a_{13} = 4k_1z^2/\pi, \quad a_{16} = 4z^2/\pi, \\
a_{22} &= 2(\bar{c}_{55}z^2 - \Omega^2), \quad a_{23} = 4k_1\bar{c}_{56}z^2/\pi, \quad a_{26} = 4\bar{c}_{56}z^2/\pi, \\
a_{33} &= (\bar{c}_{11}z^2 + 1 - \Omega^2)z^2, \quad a_{34} = -4(1 + 4\bar{c}_{12})z^2/3\pi, \quad a_{35} = 4(4\bar{c}_{14} - \bar{c}_{56})z^2/3\pi, \\
a_{44} &= z^2 + 4\bar{c}_{22} - \Omega^2, \quad a_{45} = 4\bar{c}_{24} + \bar{c}_{56}z^2, \quad a_{46} = 4(9 + 4\bar{c}_{12})z^2/5\pi, \\
a_{55} &= \bar{c}_{55}z^2 + 4\bar{c}_{44} - \Omega^2, \quad a_{56} = 4(4\bar{c}_{14} + 9\bar{c}_{56})z^2/5\pi, \\
a_{66} &= (\bar{c}_{11}z^2 + 9 - \Omega^2)z^2,
\end{aligned} \tag{24}$$

where

$$z = 2\xi b/\pi, \quad \Omega = \omega/\bar{\omega}, \quad \bar{\omega}^2 = \pi^2 c_{66}/4\rho b^2, \quad \bar{c}_{pq} = c_{pq}/c_{66};$$

i.e.  $z$  is the ratio of the thickness of the plate to the half-wave-length along the plate and  $\Omega$  is the ratio of the frequency to that of the fundamental thickness-shear mode of the infinite plate.

The determinant of the coefficients of the  $A_j^{(n)}$ , set equal to zero:

$$|a_{pq}| = 0, \tag{25}$$

in which  $a_{14} = a_{15} = a_{24} = a_{25} = a_{36} = 0$ ,  $a_{pq} = a_{qp}$ , produces the dispersion relation  $\Omega$  vs.  $z$ : a sextic, algebraic equation in  $z^2$ . The equation is the same as (43) of [3] except for the factors 2 in  $a_{11}$ ,  $a_{12}$ ,  $a_{22}$  as already noted above in connection with (4). Also, here, all the elements  $a_{pq}$  are real as a result of multiplication of the third and sixth rows and columns by  $z$ .

The six branches of the dispersion relation, computed on the HP-85 micro-computer, are illustrated in Fig. 1. The characters of the branches are indicated by their identifying symbols:

- F = Flexure
- FS = Face-shear
- $1_1$  = 1<sup>st</sup> Thickness-shear (in  $x_1$ -direction)
- $2_3$  = 2<sup>nd</sup> Thickness-shear (in  $x_3$ -direction)
- $3_1$  = 3<sup>rd</sup> (Harmonic) Thickness-shear (in  $x_1$ -direction)
- $2_2$  = 2<sup>nd</sup> Thickness-stretch (in  $x_2$ -direction)

The subscripts in the symbols  $1_1$ ,  $2_3$ ,  $3_1$ ,  $2_2$  designate the direction of displacement (or predominant displacement) at  $z=0$ , whereas the numbers themselves give the number of nodes between  $x_2 = \pm b$ . Thus: in  $2_3$  the displacement at  $z=0$  is predominantly in the direction of  $x_3$  with two nodes across the thickness of the plate. Note that the roots  $z$  for branches F and FS are real for all  $\Omega$ , but the roots for the remaining four branches may be real or imaginary, depending on the frequency. If imaginary, the variation of displacement along  $x_1$  is exponential or hyperbolic rather than trigonometric.

The zigzags in the curves in Fig. 1 result from the spacing of dots on the cathode ray tube display of the HP-85. The figure is the HP-85's hard copy of the CRT display. The roots  $z$  were actually computed to an accuracy of  $10^{-9}$  -- a precision required for their subsequent use in solving (34) and (37). Intervals of 0.02 in  $\Omega$  were employed for Fig. 1, resulting in a computation time, for the range  $0 < \Omega < 4$ , of about 6 hours or about 18 seconds

per root. The secant iterative method was used, with starting values given by the following approximate formulas, followed by increments of  $10^{-6}$  in  $z_n^2$ :

$$\left. \begin{array}{l} F : z_1^2 \\ 1_1 : z_3^2 \end{array} \right\} = 6.42258(1+G)\Omega^2[1 \pm (1+K)^{\frac{1}{2}}]/\pi^2, \quad (26)$$

$$G = \pi^2/12(\bar{c}_{11} - \bar{c}_{12}^2/\bar{c}_{22}), \quad K = 4G(\Omega^{-2} - 1)/(1+G)^2 \quad (27)$$

$$FS : z_2^2 = 0.44119 \Omega^2 \quad (28)$$

$$z_3 : z_4^2 = \begin{cases} 2.229(\Omega^2/\Omega_4^2 - 1), & \Omega < \Omega_4, \\ 0.42395(\Omega^2/\Omega_4^2 - 1), & \Omega > \Omega_4, \end{cases} \quad (29)$$

$$z_2 : z_6^2 = 16(\Omega^2/\Omega_6^2 - 1), \quad \Omega > \Omega_6, \quad (30)$$

$$\Omega_4^2, \Omega_6^2 = 2\{\bar{c}_{22} + \bar{c}_{44} \mp [(\bar{c}_{22} - \bar{c}_{44})^2 + 4\bar{c}_{24}^2]^{\frac{1}{2}}\} \quad (31)$$

$$3_1 : z_5^2 = \begin{cases} 0.33799(\Omega^2 - 9), & \Omega < 3, \\ 0.40651(\Omega^2 - 9), & \Omega > 3. \end{cases} \quad (32)$$

These trial roots match closely or exactly the roots of the sextic at  $z=0$  and at  $\Omega=0,3$  (except  $z_6$  at  $\Omega=3$ ) resulting in trial values adequate for convergence of the iteration for all  $0 < \Omega < 4$ .

## 5. Frequency Spectrum

For each of the roots  $z_n^2$  of (25), five amplitude ratios, say

$$A_2^{(0)}/A_1^{(1)} = \alpha_{1n}, A_3^{(0)}/A_1^{(1)} = \alpha_{2n}, A_2^{(2)}/A_1^{(1)} = \alpha_{3n}, A_3^{(2)}/A_1^{(1)} = \alpha_{4n}, A_1^{(3)}/A_1^{(1)} = \alpha_{5n}, \quad (33)$$

may be found from five of the six equations (23). Thus, with the third of (23) omitted, we may write

$$\begin{aligned} a_{11}(z_n^{\alpha_{1n}}) + a_{12}(z_n^{\alpha_{2n}}) + 0 + 0 + a_{16}\alpha_{5n} &= -a_{13} \\ a_{12}(z_n^{\alpha_{1n}}) + a_{22}(z_n^{\alpha_{2n}}) + 0 + 0 + a_{26}\alpha_{5n} &= -a_{23} \\ 0 + 0 + a_{44}(z_n^{\alpha_{3n}}) + a_{45}(z_n^{\alpha_{4n}}) + a_{46}\alpha_{5n} &= -a_{34}, \quad (34) \\ 0 + 0 + a_{45}(z_n^{\alpha_{3n}}) + a_{55}(z_n^{\alpha_{4n}}) + a_{56}\alpha_{5n} &= -a_{35} \\ a_{16}(z_n^{\alpha_{1n}}) + a_{26}(z_n^{\alpha_{2n}}) + a_{46}(z_n^{\alpha_{3n}}) + a_{56}(z_n^{\alpha_{4n}}) + a_{66}\alpha_{5n} &= 0. \end{aligned}$$

This form is chosen because the  $z_n^{\alpha_{1n}}, z_n^{\alpha_{2n}}, z_n^{\alpha_{3n}}, z_n^{\alpha_{4n}}$  and  $\alpha_{5n}$  are real for all  $\Omega$ , as are also the  $a_{pq}$  -- as arranged previously.

With the six  $z_n$  from (25) and the thirty  $\alpha_{pn}$  determined from (34), we may now write, in place of (22):

$$\begin{aligned}
u_2^{(0)} &= \sum_{n=1}^6 A_n \alpha_{1n} \sin \xi_n x_1, & u_3^{(0)} &= \sum_{n=1}^6 A_n \alpha_{2n} \sin \xi_n x_1, \\
u_1^{(1)} &= \sum_{n=1}^6 A_n \cos \xi_n x_1, & u_2^{(2)} &= \sum_{n=1}^6 A_n \alpha_{3n} \sin \xi_n x_1, \\
u_3^{(2)} &= \sum_{n=1}^6 A_n \alpha_{4n} \sin \xi_n x_1, & u_1^{(3)} &= \sum_{n=1}^6 A_n \alpha_{5n} \cos \xi_n x_1.
\end{aligned} \quad (35)$$

Upon substituting the displacements (35) in the formulas (20) for the stresses and the results in the edge conditions (21), we have the six equations:

$$\sum_{n=1}^6 A_n b_{mn} = 0, \quad m=1 \dots 6, \quad (36)$$

where

$$\begin{aligned}
b_{1n} &= (\bar{c}_{56} z_n \alpha_{1n} + \bar{c}_{55} z_n \alpha_{2n} + 2k_1 \bar{c}_{56}/\pi + 2\bar{c}_{56} \alpha_{5n}/\pi) \hat{z}_n^\ell, \\
b_{2n} &= (z_n \alpha_{1n} + \bar{c}_{56} z_n \alpha_{2n} + 2k_1/\pi + 2\alpha_{5n}/\pi) \cos \hat{z}_n^\ell, \\
b_{3n} &= (-\bar{c}_{11} z_n^2 + 16z_n \alpha_{3n}/3 + 16\bar{c}_{14} z_n \alpha_{4n}/3) \hat{z}_n^{-1} \sin \hat{z}_n^\ell, \\
b_{4n} &= (-4\bar{c}_{56}/3\pi + \bar{c}_{56} z_n \alpha_{3n} + \bar{c}_{55} z_n \alpha_{4n} + 36\bar{c}_{56} \alpha_{5n}/5\pi) \cos \hat{z}_n^\ell, \\
b_{5n} &= (-4/3\pi + z_n \alpha_{3n} + \bar{c}_{56} z_n \alpha_{4n} + 36\alpha_{5n}/5\pi) \cos \hat{z}_n^\ell, \\
b_{6n} &= (16\bar{c}_{12} z_n \alpha_{3n}/5\pi + 16\bar{c}_{14} z_n \alpha_{4n}/5\pi + \bar{c}_{11} z_n^2 \alpha_{5n}) \hat{z}_n^{-1} \sin \hat{z}_n^\ell,
\end{aligned}$$

in which  $\hat{z}_n = \pi z_n/2 = \xi_n b$ ,  $\ell = a/b$  and the  $b_{mn}$  are real for all  $\Omega$ .

The roots  $\ell$  of the equation obtained by setting the  $6 \times 6$  determinant of the coefficients of the  $A_n$ , in (36), equal to zero:

$$|b_{mn}| = 0, \quad (37)$$

produce the data for plotting a frequency spectrum  $\Omega$  vs.  $a/b$ .

The results of computations in the two ranges:

$$0.99 < \Omega < 1.01, \quad 16 < a/b < 24$$

and

$$2.995 < \Omega < 3.005, \quad 18 < a/b < 22$$

are illustrated in Figs. 2 and 3. To construct these figures, the six roots  $z_n$  of the sextic (25) were first computed for a given  $\Omega$ . Then the five linear equations (34) were solved for the  $\alpha_{pn}$  for each of the six  $z_n$  and the resulting combinations of  $\alpha_{pn}$  and  $z_n$  substituted in the transcendental equation (37), after which the range of  $\ell (= a/b)$  was traversed in steps of 0.1 for Fig. 2 and 0.025 for Fig. 3 and the value of  $|b_{mn}|$  computed at each step. A change of sign of  $|b_{mn}|$  indicated a straddled root  $\ell$  which was then determined to  $10^{-3}$  by successive linear interpolations. The process was then repeated at intervals of  $\Omega$  of  $5 \times 10^{-5}$ . Figs. 2 and 3 required about 58 and 49 hours of computation, respectively, on the HP-85.

In Fig. 2:

F22...30 are overtones of flexure

FS11...15 are overtones of face-shear

1<sub>1</sub> is the 1<sup>st</sup> thickness-shear (fundamental).

In Fig. 3:

- F62...74 are overtones of flexure
- FS37...41 are overtones of face-shear
- $1_1 33...35$  are anharmonic overtones of the  $1^{\text{st}}$  (fundamental) thickness-shear
- $2_3 23...27$  are anharmonic overtones of the  $2^{\text{nd}}$  transverse thickness-shear
- $3_1 1$  is the  $3^{\text{rd}}$  harmonic thickness-shear overtone.

The numbers following the symbols F, FS,  $1_1$ ,  $2_3$  and  $3_1$  designate both the order of the overtone and the approximate number of half-wave-lengths between  $x_1 = \pm a$ .

Fig. 2 illustrates the well known phenomenon of strong coupling of the  $1^{\text{st}}$  thickness-shear fundamental with flexure overtones and weak coupling with face-shear overtones. Fig. 3 shows that the  $3^{\text{rd}}$  harmonic thickness-shear mode has moderately strong coupling with flexure overtones and weak coupling with face-shear overtones and, in addition, weak coupling with transverse thickness-shear overtones. As for the interaction of the  $3^{\text{rd}}$  harmonic thickness-shear overtone with the anharmonic overtones of the fundamental thickness shear, the coupling is moderately strong at small  $a/b$  (thick plates and low-order anharmonic overtones) and diminishes as  $a/b$  increases (thin plates and increasing order of anharmonic overtones).

Finally, the minimum absolute values of the slopes of the segments  $1_1 1$  are much larger than those of  $3_1 1$ . For large  $a/b$ , the ratio of those slopes is approximated by the ratio of the curvatures of branches  $3_1$  and  $1_1$  at  $z=0$  in Fig. 1. The exact values of those curvatures, in the three-dimensional theory, were given by Ekstein [7, Eq. 56]:

$$\kappa_n = \left[ \frac{d^2 \Omega}{dz^2} \right]_{z=0} = k + C \cot(n\pi/2 \, c_2^{\frac{1}{2}}) + D \cot(n\pi/2 \, c_3^{\frac{1}{2}}),$$

where

$$k = (\bar{c}_{11} + A + B), \quad n = 1, 3, 5, \dots,$$

$$A = [(1 + \bar{c}_{12}) \cos \theta + (\bar{c}_{14} + \bar{c}_{56}) \sin \theta]^2 / (1 - c_2),$$

$$B = [(\bar{c}_{14} + \bar{c}_{56}) \cos \theta - (1 + \bar{c}_{12}) \sin \theta]^2 / (1 - c_3),$$

$$C = 4[(c_2 + \bar{c}_{12}) \cos \theta + (c_2 \bar{c}_{56} + \bar{c}_{14})]^2 / n^2 \pi \, c_2^{\frac{1}{2}} (1 - c_2)^2,$$

$$D = 4[(c_3 + \bar{c}_{12}) \sin \theta - (c_3 \bar{c}_{56} + \bar{c}_{14})]^2 / n^2 \pi \, c_3^{\frac{1}{2}} (1 - c_3)^2,$$

$$c_2, c_3 = \{\bar{c}_{22} + \bar{c}_{44} \pm [(\bar{c}_{22} - \bar{c}_{44})^2 + 4\bar{c}_{24}^2]^{\frac{1}{2}}\} / 2,$$

$$\tan \theta = \bar{c}_{24} / (c_2 - \bar{c}_{44}).$$

For the present case, the curvature ratio  $k_1/k_3$  is 4.7 and that is the ratio of the slopes.

The large ratio of slopes and the absence, at large  $a/b$ , of strong coupling with all overtones except those of flexure (which, at such high overtones, have very small amplitudes) are important contributors to the high stability of third harmonic overtone resonators.

ACKNOWLEDGEMENT - This work was sponsored by the Department of the Navy, Office of Naval Research, Structural Mechanics Program, Contract N00014-80-C-0559.

#### REFERENCES

- [1] A.W. Warner, "High Frequency Crystal Units for Primary Frequency Standards," Proc. I.R.E. 40, 1030-1033 (1952).
- [2] P.C.Y. Lee and Z. Nikodem, "An Approximate Theory for High-Frequency Vibrations of Elastic Plates," Int. J. Solids Structures, 8, 581-612 (1972).
- [3] Z. Nikodem and P.C.Y. Lee, "Approximate Theory of Vibrations of Crystal Plates at High Frequencies," Int. J. Solids Structures, 10, 177-196 (1974).
- [4] A.E.H. Love, A Treatise on the Mathematical Theory of Elasticity, Cambridge, 4th Edition, 1927, p. 166.
- [5] A. Ballato, private communication.
- [6] R. Bechmann, "Elastic and Piezoelectric Constants of Alpha-Quartz," Phys. Rev., 110, 1060-1061 (1950).
- [7] H. Ekstein, "High Frequency Vibrations of Thin Crystal Plates," Phys. Rev., 68, 11-23 (1945).

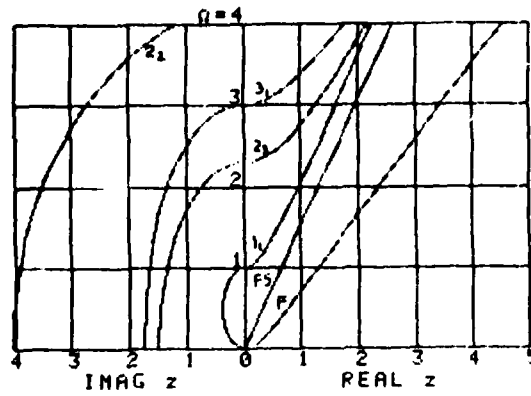


Figure 1.

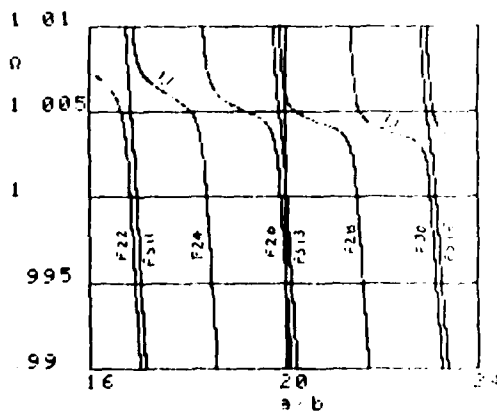


Figure 2.

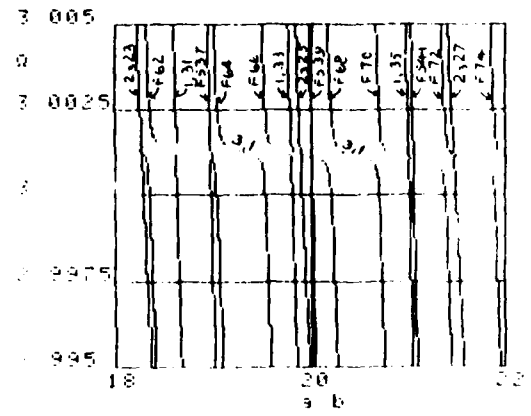


Figure 3

# THE DESIGN OF PARTIALLY CONTROLLED QUARTZ CRYSTAL RESONATORS\*

R C Peach

The General Electric Company, p.l.c., Hirst Research Centre,  
Wembley, HA9 7PF, England

## Abstract

Partially contoured crystal resonators using only an edge bevel are frequently used for high Q AT-cut devices in the lower frequency ranges. Treatments have been proposed in the past for uniformly contoured crystals neglecting electrode mass loading<sup>2</sup>, but a convincing theory for the case of a flat crystal blank with only an edge bevel and a non-negligible plateback has proved much more difficult.

This paper follows previous workers in reducing the problem to two dimensional form by a rigorous deduction of the dispersion relations for waveguided modes in each region, accurate to second order in the transverse wave numbers, corresponding to a normal thickness shear mode at cut-off. The procedure, familiar from quantum mechanics, of using the harmonic oscillator functions as a basis, and deducing the eigensolutions in terms of this basis by a perturbation approach has been adopted. This method takes care of boundary matching problems automatically, but it does require the evaluation of a number of numerical integrations over the basis functions; this is however very easily accomplished by modern computers.

Key words : Contoured crystal resonator, Acoustic waveguide.

## 1. Introduction

For high Q crystals with frequencies of a few MHz, the use of a spherical edge bevel to confine the energy has long been popular. However despite work on the problems of fully contoured crystals<sup>1,2</sup> and crystals with a partial cylindrical contour<sup>3</sup>, most design data for the general case of a partial spherical contour has remained entirely empirical.

At first sight the problem is a formidable one; a realistic finite element analysis of such a three dimensional structure would be an enormous

undertaking, and the complexities of the geometry make a semi-analytic approach scarcely more attractive. Tiersten and Smythel<sup>2</sup> used an equation for a uniform bevel, whose solutions may be expressed in terms of Hermite polynomials, if the condition that they vanish at  $\pm\infty$  is imposed. In general this equation may be solved with parabolic cylinder functions, and these were used by Vangheluwe<sup>3</sup> for the case of the partial cylindrical contour. This general approach of seeking a solution in each region, and constructing the function by matching across the boundaries, is still feasible for the two dimensional case of a spherical bevel if the material is isotropic in the plane. Using circular polar coordinates the modes for a uniform bevel are expressible in terms of associated Laguerre polynomials, and in the general case solutions may be constructed with Bessel functions in the flat region, and with confluent hypergeometric (or alternatively Whittaker functions)<sup>4</sup> in the bevel region. However when anisotropy is introduced the problem becomes vastly more complex and there does not appear to be any reasonable way of solving the equations directly in terms of known functions. For this reason a somewhat different approach is adopted, which requires more numerical analysis but completely resolves the above difficulties with the analytic approach.

Following previous workers it is assumed that the solution may be constructed using a single family of waveguided plate modes. For AT-cut quartz this would be the thickness shear-thickness twist family which corresponds to a pure shear wave at cut-off. Analysing the properties and dispersion relations for the particular set of waveguide modes, for both an infinite fully electroded and an infinite unelectroded plate, provides approximate equations for the behaviour of the resonator mode in each of the different regions, and is the starting point for the method presented here. However, the basic plate mode analysis for this paper is not performed by approximate analytic methods, but uses

\*This work was done in support of Salford Electrical Instruments Ltd, Times Mill, Heywood, England

a fully general computer programme which can analyse with equal ease, any family of modes, in any piezoelectric material, with any metal overlay. Having deduced the basic parameters of the system, the eigenvalue problem involving differential operators is replaced by an equivalent algebraic eigenvalue problem using an expansion in terms of the complete set of basis functions provided by the uniform bevel equation. This procedure involves the evaluation of a certain set of two dimensional integrals, but the special properties of the basis functions make this comparatively easy. In addition variations in resonator geometry may be accommodated by this technique at no additional expense. To solve the eigenvalue problem the set of basis functions used is truncated at finite order, but for low order modes this produces a negligible error, and the solutions thus found are necessarily continuous across all boundaries no matter how complicated the geometry.

To summarize, the basic assumptions of the theory are:

- (a) The solution may be constructed from just one family of waveguided modes.
- (b) The equations of motion in each region may be deduced from an analysis of the corresponding infinite plate geometry, and the final solution may be constructed by matching the functions and their first derivatives across all boundaries.
- (c) The bevel is assumed to confine the energy sufficiently that the finite crystal size may be ignored.
- (d) The equation for the bevel region may be deduced on the basis that the variation in thickness is 'slow'.

Within the constraints of these assumptions no significant error is produced in constructing the solution, and a wide range of geometrical variations may be accommodated without difficulty.

## 2. General plate mode analysis

The method for analysing plate modes is fairly well known, especially in connection with the study of surface acoustic wave devices, but in view of its fundamental importance a brief description is given here.

The most general structure which we must consider consists of an arbitrary piezoelectric layer with arbitrary metal layers on either side (Fig 1). The complete solution will be formed by a superposition of partial waves, which, loosely speaking, will consist of three acoustic waves, one longitudinal and two shear, propagating upwards, and three similar waves propagating downwards, in each layer. In addition there will be two partial waves in the piezoelectric layer to account for the predominantly electrostatic disturbances. Therefore if a coordinate system is established with Z axis normal to the plate, then to satisfy boundary conditions we may assume that all twenty partial waves have a common

$$A = \exp[i(k_1x + k_2y - \omega t)] \quad (1)$$

dependence with respect to x and y coordinates. So choosing fixed but arbitrary values for  $k_1$ ,  $k_2$  and  $\omega$  the equations of motion in each region may be used to deduce the z dependence of each partial wave. For example if we assume a dependence

$$\exp[i(k_1x + k_2y + k_3z - \omega t)] \quad (2)$$

for the three displacement components  $u_i$ , and the potential  $\phi$ , in the piezoelectric, then the equations of motion become

$$\begin{aligned} c_{ijkl}u_{k,j}k_j + e_{kij}\phi_{,k}k_k &= \omega^2\rho u_i \\ -e_{ijk}u_{k,j}k_j + \epsilon_{ijk}\phi_{,k}k_k &= 0 \end{aligned} \quad (3)$$

As  $k_1, k_2$  and  $\omega$  are fixed a solution of this set of homogeneous equations will provide eight possible values for  $k_3$  (in general complex), corresponding to the eight partial waves in the piezoelectric. In each of the metal layers a simpler set of equations apply and there will be six possible roots. For these partial waves to form a solution certain boundary conditions must be satisfied; the normal stress components must vanish at the outer boundaries, and displacement and normal stress components must be continuous across the inner boundaries. In addition we impose the electrical condition that both metal layers are at zero potential as it will suffice to deduce the short circuit frequencies of the final resonator. The boundary conditions therefore give a  $20 \times 20$  homogeneous set of equations for the partial wave amplitudes, and the condition for a solution is given by the vanishing of the  $20 \times 20$  determinant of coefficients. It is most unlikely that the initial choice of  $k_1, k_2$  and  $\omega$  will furnish a solution, and so keeping  $k_1$  and  $k_2$  fixed  $\omega$  is varied in a computer search routine until a zero value of the determinant is located. By repeating this procedure for a range of values of  $k_1$  and  $k_2$  it is possible to map out the dispersion relationship, and of course all possible information about the mode amplitudes is readily available.

For small values of  $k_1$  and  $k_2$ , and a suitable choice of x and y axes, the dispersion relation may be written as

$$ak_1^2 + bk_2^2 = (\omega^2 - \omega_0^2) \quad (4)$$

For the purpose of this work the 'a' and 'b' coefficients have been deduced by computing the mode frequencies for a suitable range of small values of  $k_1$  and  $k_2$ , and then performing a least squares fit of Eq (4).

For the free piezoelectric plate the problem is exactly similar but is much less complicated as only eight partial waves are involved.

## 3. The general formulation

Having established the parameters of the waveguide modes it is possible to write down the approximate equations in each region for the structure shown in Figure 2. If the dispersion relation in the electrode region is given by

$$a_1 k_1^2 + b_1 k_2^2 = (\omega^2 - \omega_1^2) \quad (5)$$

and we suppose that this relation is also valid below cut-off, then we may use the equivalent differential equation for the mode amplitude

$$a_1 \frac{\partial^2 A}{\partial x^2} + b_1 \frac{\partial^2 A}{\partial y^2} - \omega_1^2 A = -\omega^2 A \quad (6)$$

In the flat unelectroded region

$$a_2 \frac{\partial^2 A}{\partial x^2} + b_2 \frac{\partial^2 A}{\partial y^2} - \omega_2^2 A = \omega^2 A \quad (7)$$

and in the bevel region

$$a_2 \frac{\partial^2 A}{\partial x^2} + b_2 \frac{\partial^2 A}{\partial y^2} - (\alpha + R(x^2 + y^2))A = -\omega^2 A \quad (8)$$

where  $x = \frac{r}{\omega_2} (1 - r^2/Rh)$  and  $R = \frac{r^2}{\omega_2/Rh}$  where  $R$  is the bevel radius. Eq (8) has been deduced by assuming that the rate of variation of thickness is 'slow' compared to the characteristic rate of variation of the mode amplitude, and choosing  $\alpha$  and  $R$  to ensure continuity between Eqs (7) and (8), and to match the first order variation of frequency with thickness at the bevel edge. It must be realized however that it is very difficult to give a precise criterion for the validity of such an assumption.

If we now seek separable solutions of Eq (8) in the form

$$A(x, y) = X(x) Y(y)$$

then the equations become

$$a_2 \frac{\partial^2 X}{\partial x^2} - \frac{\omega_2^2 x^2}{Rh} X = -\lambda X \quad (9)$$

$$b_2 \frac{\partial^2 Y}{\partial y^2} - \frac{\omega_2^2 y^2}{Rh} Y = -\mu Y \quad (10)$$

$$\text{where } \mu + \lambda = \omega^2 - \omega_2^2 (1 - r^2/Rh) \quad (11)$$

If the condition that  $X \rightarrow 0$  as  $x \rightarrow \pm\infty$  is imposed then solutions can exist only for certain values of  $\lambda$

$$X = e^{-\frac{1}{2}\lambda x^2} H_m(x')$$

$$\text{where } x' = \left( \frac{2}{Rh a_2} \right)^{1/2} x \text{ and } \frac{\lambda}{\omega_2} \left( \frac{Rh}{a_2} \right)^{1/2} = 2m + 1 \quad (m \text{ integral})$$

$$\text{and similarly for } y$$

$$Y = e^{-\frac{1}{2}\mu y^2} H_n(y')$$

$$\text{where } y' = \left( \frac{2}{Rh b_2} \right)^{1/2} y \quad \dots = (2n+1) \cdot 2 \left( \frac{b_2}{Rh} \right)^{1/2} \quad (13)$$

The Hermite polynomials may be defined by

$$H_0(x) = 1, \quad H_1(x) = 2x \quad (14)$$

and the recurrence relation

$$H_{n+1} = 2xH_n(x) - 2nH_{n-1}(x) \quad (15)$$

in addition repeated use of the recurrence relation is the ideal computer method for evaluation of these functions. Although these functions are of course not solutions of our present problem they do have a number of extremely useful properties. The differential equations (9) and (10) are self-adjoint and with the chosen boundary conditions satisfy the requirements of Sturm-Liouville theory, their solutions therefore form a complete orthonormal set. Specifically if we define

$$\psi_n(x') = (2^n n! \sqrt{\pi})^{-1/2} H_n(x') e^{-\frac{1}{2}x'^2}, \text{ then an arbitrary function } A(x', y') \text{ defined over the whole } x'-y' \text{ plane may be written}^5$$

$$A(x', y') = \sum_{m=0}^{\infty} \sum_{n=0}^{\infty} c_{mn} \psi_m(x') \psi_n(y')$$

where

$$c_{mn} = \int_{-\infty}^{\infty} \int_{-\infty}^{\infty} A(x', y') \psi_m(x') \psi_n(y') dx' dy' \quad (16)$$

This is analogous to a Fourier series expansion, and we will transform the problem, so that instead of solving for  $A(x, y)$  directly, we deduce its components,  $c_{mn}$ , in terms of the chosen set of basis functions. To illustrate the method of transformation we will introduce a more compact notation (originally due to Dirac)<sup>6</sup>,  $\psi_m(x') \psi_n(y')$   $\rightarrow$  where each value of index  $p$  corresponds to a specific pair of indices  $m$  and  $n$ . We will also define

$$H \equiv -a_2 \frac{\partial^2}{\partial x^2} - b_2 \frac{\partial^2}{\partial y^2} + (\alpha + R(x^2 + y^2)) \quad (17)$$

for all  $x$  and  $y$

$$V = V_1 + V_2 \text{ where}$$

$$V_1 = \omega_2^2 - \alpha - R(x^2 + y^2) = \frac{\omega_2^2}{Rh} (r^2 - (x^2 + y^2)) \quad (18)$$

in the flat region,  $V_1 = 0$  elsewhere

$$V_2 = (a_2 - a_1) \frac{x^2}{2x^2} + (b_2 - b_1) \frac{y^2}{2y^2} - \frac{\omega_2^2}{2} + \frac{\omega_1^2}{2}$$

in the electroded region,  $V_2 = 0$  elsewhere.

The fundamental equation for the problem may now be written symbolically as

$$(H + V)|A\rangle = \omega^2|A\rangle \quad (20)$$

and the set of basis functions are defined by

$$|p\rangle = \sum_p |p\rangle \quad (21)$$

Using the expression (14),  $|A\rangle = \sum_p c_p |p\rangle$ , and substituting into (18) we obtain:

$$\sum_p c_p (H + V)|p\rangle = \omega^2 \sum_p c_p |p\rangle$$

$$\sum_p c_p (\omega_p^2 + V)|p\rangle = \omega^2 \sum_p c_p |p\rangle \quad (22)$$

and so using the orthogonality relationship  $\langle q|p\rangle = \delta_{pq}$

$$\sum_p (\omega_p^2 \delta_{pq} + \langle q|V|p\rangle) c_p = \omega^2 c_q \quad (23)$$

where  $\langle q|V|p\rangle$  is a symbolic way of denoting the double integral

$$\langle q|V|p\rangle = \iint \psi_m(x') \psi_n(y') \cdot V \cdot \psi_m(x') \psi_n(y') dx' dy'$$

with  $q = m', n'$ ,  $p = m, n$  (24)

Equation (23) is a matrix (infinite) problem exactly equivalent to the original formulation in terms of differential equations. The procedure is to truncate the matrix at a finite order and solve the eigenvalue problem for  $\omega$  and  $c_p$  using a standard computer routine. It is intuitively reasonable that for the low order modes which have a small dependence on the higher order basis functions the error in this method will be small; a more precise statement will be given in the next section.

The obvious disadvantage of this technique is the need to evaluate the double integrals of Eq (24), but due to the special properties of the functions  $\psi_n(x')$  this is not as much of a problem as might first appear. The indefinite integral over one of the coordinates,  $x'$  say, may be deduced by simple analytic means, for example

$$\int_a^a H_n(x') H_m(x') e^{-x'^2} dx' =$$

$$- \frac{2e^{-a^2}}{(m-n)} [m H_n(a) H_{m-1}(a) - n H_{n-1}(a) H_m(a)] \quad (25)$$

$m \neq n$

the case  $m = n$  is a bit more complicated but an explicit formula can be constructed by successive integration by parts.

Integrals of the form

$$\int_a^a H_n(x') H_m(x') x'^2 e^{-x'^2} dx' \text{ and}$$

$$\int_a^a H_n(x') e^{-\frac{1}{2}x'^2} \frac{d^2}{dx'^2} (H_n(x') e^{-\frac{1}{2}x'^2}) dx'$$

are readily reduced to integrals of the type given in Eq (23). With this method the evaluation of Eq (22) reduces to a finite integral of a continuous function of  $y'$ , which is very easily evaluated by a standard numerical quadrature routine.

Having accepted the need to evaluate a number of integrals, a great many difficulties are resolved, the boundary matching problems which were so troublesome originally are now taken care of automatically, and variations of the basic resonator geometry presented here may be introduced with no fundamental increase in complexity.

#### 4 The nature of the approximation

The proposed method takes the exact Eq (23) and truncates the system at a finite order,  $N$  say, and then by solving for the eigenvalues and eigenvectors of the resulting matrix provides approximations for  $N$  resonator modes. It is important to have some indication of the nature of this approximation, and some way of gauging the probable error. First we must note that the matrix of coefficients  $\langle q|V|p\rangle$  is not necessarily Hermitian (or symmetric in this case as all functions are real), due to the presence of terms in  $x^2/x^2$  and  $x^2/y^2$  in  $V_2$ . However calculation shows that  $a_2$  and  $a_1$ , and  $b_2$  and  $b_1$ , are virtually identical, so we may neglect the asymmetric terms with negligible error, and it is assumed that this is done for the purposes of this paper.

A variational method is often used to approximate resonator modes. This consists of taking a trial function containing a number of adjustable parameters, and attempting to determine these parameters by minimising an expression which is known to have a minimum for the true solution. For this problem the formula

$$\frac{\langle A|H+V|A\rangle}{\langle A|A\rangle} \quad (26)$$

(26) will be minimized when  $|A\rangle$  is the lowest frequency mode. If we construct the trial function by a finite superposition of the basis functions  $|p\rangle$ , and minimize Eq (26) by varying the coefficients, then it is easily shown that the resulting approximation is exactly the same as that obtained from the smallest eigenvalue of Eq (23) with the same finite set of basis functions. A generalization of this result may be stated by the following theorem:

#### Theorem

The true eigenfrequency of any mode is a lower bound on any approximation to that frequency which may be obtained using a truncated form of Eq (23).

A proof of this result, which is not trivial, would be beyond the scope of this paper. The theorem tells us that if we enlarge the set of basis functions used, the frequency estimates we obtain will be lower, but still larger than the true values. So in practical terms if using more basis functions produces a negligible reduction in estimated frequency, then the error is almost certainly minimal, and this criterion is used to

assess accuracy. The method can therefore be regarded as a type of variational approach which provides a simultaneous estimate of  $N$  mutually orthogonal modes.

If the matrix is not Hermitian (symmetric) then the theorem could be violated, and in general it is difficult to make a precise statement.

#### Practical results and comparison with experiment

Initially this method has been used for various crystal designs on AT-cut quartz. Due to the symmetrical form of the geometry with respect to the  $x$  and  $y$  axes, the modes naturally divide into four classes, even in  $x$  and  $y$ , odd in  $x$  or  $y$ , and odd in both  $x$  and  $y$ . For modes symmetric in  $x$  and  $y$ , which give the largest amplitude responses, only basis functions which are also symmetric in  $x$  and  $y$  need be considered, and a similar rule holds for the other sets of modes. For all the following calculations a set of 36 basis functions has been used.

Unfortunately detailed experimental data for the more sensitive parameters, such as the relative frequencies of the modes as functions of bevel and flat radii, is not yet readily available. For this reason all old and not entirely reliable data has been employed<sup>7</sup>. Two designs with the following parameters have been analysed.

1	Frequency	7.3 MHz
	Radius of edge bevel on each side	135 mm
	Radius of flat	2-3.5 mm
	Radius of electrode	1.5 mm
	Plateback (nominal)	50 kHz
2	Frequency	4.3 MHz
	Radius of edge bevel on each side	72 mm
	Radius of flat	3-4.5 mm
	Radius of electrode	2.5 mm
	Plateback (nominal)	50 kHz

For the first of these designs the waveguide analysis programme gave parameters

$$\begin{aligned} a_1 &= 0.406 \times 10^8 \\ b_1 &= 0.260 \times 10^8 \\ a_2 &= 0.407 \times 10^8 \\ b_2 &= 0.276 \times 10^8 \end{aligned}$$

and for the second

$$\begin{aligned} a_1 &= 0.404 \times 10^8 \\ b_1 &= 0.258 \times 10^8 \end{aligned}$$

with  $a_2$  and  $b_2$  being unaltered. Figures 3-7 show graphical representations of the first three symmetric and first two antisymmetric modes for design 1 with a 2.5 mm radius flat; the mode amplitude is plotted as a function of the transverse coordinates  $x$  being the 'X' crystallographic axis. The dotted circle represents the boundary of the bevel, and it can be clearly seen that for higher order modes a considerable amount of energy is contained in the bevel region. Figures 8 and 9 show plots of the theoretical ratio of spurious mode to fundamental mode frequency for each of the two designs, with a

range of values of flat radius. The three curves on each graph represent the first three fully symmetric spurious modes, and the experimental values are also shown. This is a very sensitive test of the theory, and it is seen that although there is qualitative agreement, there is still a considerable discrepancy in absolute values. The parameters in Eq (8), describing the contoured region, are not based on any very firm theoretical foundation, particularly for a sharp bevel. Agreement with experiment can be considerably improved by a more empirical choice, but until more and better data is available no firm rule can be given.

Using the methods already described in this paper values for the motional parameters, such as the inductance, can also be deduced. The waveguide analysis programmes can evaluate the charge density induced on the electrodes by each Fourier component of the mode amplitude. For the set of basis functions chosen, Fourier transform techniques are trivial, and the charge density may therefore be expressed as a function in  $XY$  space, and integrated over the electrode area by a combination of analytic and numerical techniques as before. This information combined with the total mode energy is sufficient to determine the motional inductance.

#### 5 Conclusions

This paper describes a technique for the analysis of general contoured crystal resonators on any material. It has a high degree of flexibility, for instance the case of a contoured crystal with a different edge bevel can be easily accommodated, and within the basic assumptions of the model it is quite rigorous. The method is characterized by a higher degree of reliance on numerical techniques than has been usual in the past with semi-analytic treatments, but it is still a relatively trivial problem for modern computers. Comparison with experimental results, such as they are, indicates that some modification to the parameters of the theory is required, but it has not yet been possible to draw firm conclusions on this point.

#### 6 References

- 1 Tiersten H F and Snythe R C 'An analysis of overtone modes in contoured crystal resonators' Proc 31st Annual Frequency Control Symposium pp 44-47 1977
- 2 Tiersten H F and Snythe R C 'An analysis of contoured crystal resonators operating in overtones of coupled thickness shear and thickness twist' J Acoust Soc Am : 65 6 pp 1455-1460 1979
- 3 Vangheluwe D C L 'The frequency and motional capacitance of partial contoured crystal resonators' : Proc 34th Ann Freq Control Symposium, pp 412-413 1980
- 4 Abramowitz and Stegun : Handbook of Mathematical Functions Dover 1964
- 5 Arfken G 'Mathematical Methods for Physicists' 2nd Ed : Academic Press 1970
- 6 Dirac P A M 'Principles of quantum mechanics' 4th ed, Oxford University Press 1959
- 7 Hirst Research Centre Reports : 12,294, 1955 and 12,776W, 1957.

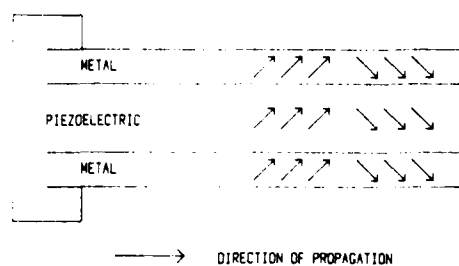


Figure 1. Waveguide Geometry for Analysis of Modes by Superposition of Partial Waves

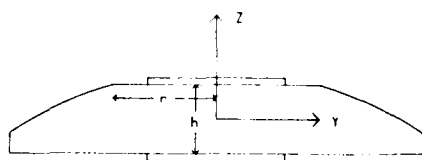


Figure 2. Idealized Bevelled Crystal Geometry

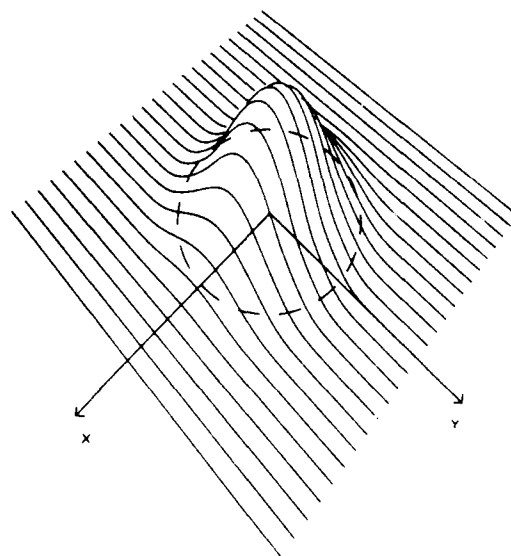


Figure 4. First Symmetric Spurious Mode

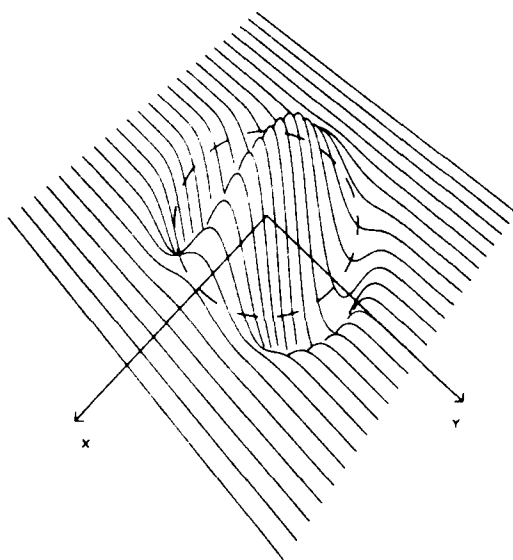


Figure 3. Fundamental Mode

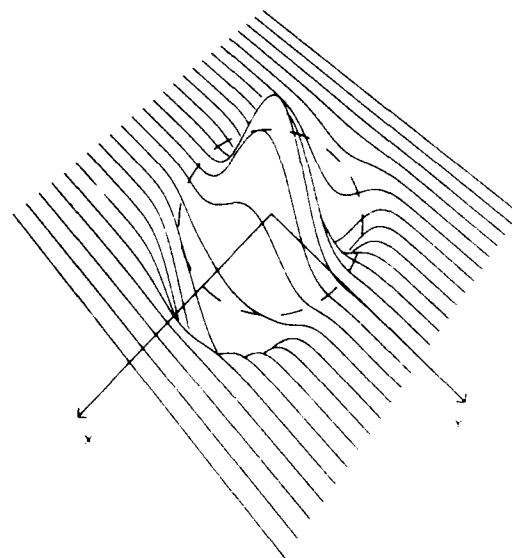


Figure 5. Second Symmetric Spurious Mode

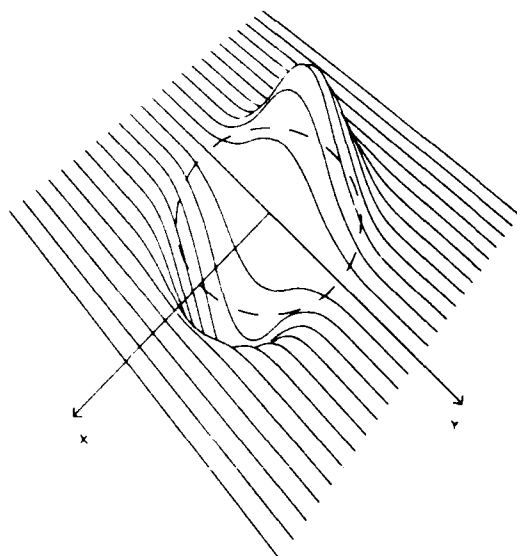


Figure 6. Second Asymmetric Spurious Mode

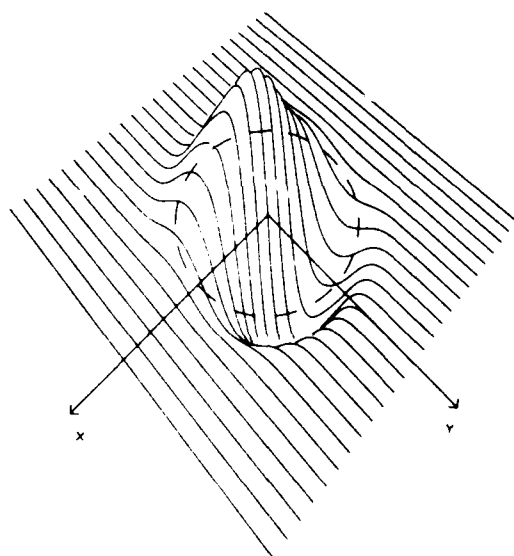


Figure 7. First Asymmetric Spurious Mode

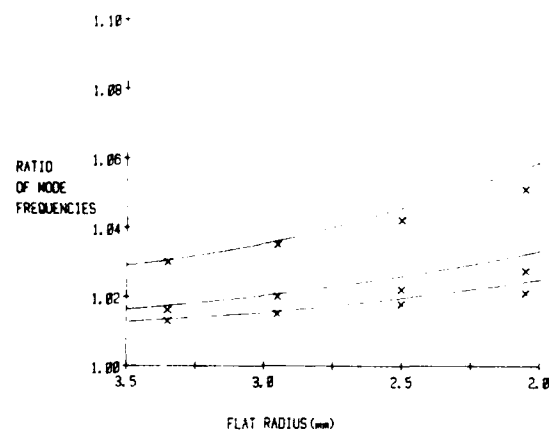


Figure 8. Spurious Modes for Crystal Design 1

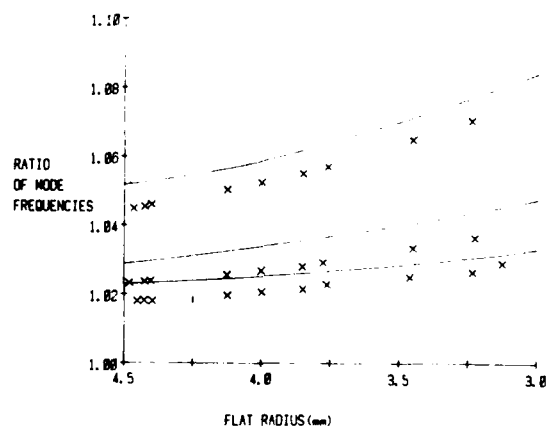


Figure 9. Spurious Modes for Crystal Design 2

AD P001502

EFFECT OF TRANSVERSE FORCE ON THE THICKNESS-SHEAR RESONANCE  
FREQUENCIES IN RECTANGULAR, DOUBLY-ROTATED CRYSTAL PLATESP.C.Y. Lee and J.S. Lam  
Department of Civil Engineering  
Princeton University  
Princeton, N.J. 08544Summary

The effect of initial stresses, owing to the transverse loading, on the changes in the thickness-shear resonance frequencies in rectangular, doubly-rotated crystal plates has been studied. The plate is clamped along one of its edges and is subject to a transverse load uniformly distributed along the opposite, parallel edge. The remaining pair of edges are free of traction.

A system of one-dimensional equations is derived from Mindlin's two-dimensional first-order equations for crystal plates. The governing equations for the first six displacement components symmetric to the  $x_1x_3$  plane of the plate are employed to obtain the approximate two-dimensional fields of displacement, strain and stress. These initial stress and displacement components are thus dependent on the magnitude of the load, the dimensions and orientations of the plate. They are computed and plotted along the  $x_1$  and  $x_3$  axes of SC-cut plate for various values of azimuth angle  $\alpha$ .

By taking the initial fields of stress and displacement at the center of the electrodes (also the center of the plate) as the average values and by neglecting the coupling of the incremental thickness-shear mode of vibration with other modes, an explicit formula is obtained for predicting the force-sensitivity of the resonator. The thickness-shear frequency changes are predicted for both AT and SC cuts and are compared with previously predicted values by Lee, Wang and Markenscoff and with experimental values of Hinkins, Barcus and Perry, and those by Fletcher and Douglas.

Thickness-shear Vibration under initial stresses

Let a rectangular plate, which has a length  $2a$ , thickness  $2b$ , and width  $2c$ , be referred to the rectangular coordinate system  $(x_1, x_2, x_3)$  and its middle plane be coincident with the  $x_1x_3$  plane as shown in Figure 1. The azimuth angle  $\alpha$  is the angle between the  $x_1$  axis of the plate and the  $x_1'$  axis of the crystal. For instance, in a rotated Y-cut plate, we may choose the diagonal axis of quartz as the  $x_1'$  axis. Referred to the  $x_1$  system, the stress equation of motion for the incremental thickness-shear vibration is,

$$\begin{aligned} & \frac{\partial}{\partial x_1} \left[ (1 + v_{1,1}^{(0)}) t_1^{(1)} + v_{1,3}^{(0)} t_5^{(1)} \right] \\ & + \frac{\partial}{\partial x_3} \left[ (1 + v_{1,1}^{(0)}) t_5^{(1)} + v_{1,3}^{(0)} t_3^{(1)} \right] \\ & = \frac{\partial}{\partial x_1} \left[ (1 + v_{1,1}^{(0)}) t_6^{(0)} + v_{1,3}^{(0)} t_4^{(0)} \right] = \frac{2}{3} b^3 u_1^{(1)}, \quad (1) \end{aligned}$$

the incremental stress-strain relations

$$\begin{aligned} t_1^{(0)} &= 2b(c_{11} + c_{11k} E_k^{(0)}) \frac{\partial}{\partial x_1} \left( \frac{u_1^{(0)}}{b} \right) \\ &+ \frac{2}{3} b^3 c_{11} + c_{11k} E_k^{(0)} \frac{\partial}{\partial x_1} \left( \frac{u_1^{(0)}}{b} \right), \\ t_1^{(1)} &= \frac{2}{3} b^3 c_{11} E_k^{(1)} \frac{\partial}{\partial x_1} \left( \frac{u_1^{(1)}}{b} \right) \\ &+ \frac{2}{3} b^3 (c_{11} + c_{11k} E_k^{(0)}) \frac{\partial}{\partial x_1} \left( \frac{u_1^{(1)}}{b} \right), \quad (2) \end{aligned}$$

and the incremental strain-displacement relations

$$\begin{aligned} \epsilon_1^{(0)} &= (1 + v_{1,1}^{(0)}) u_{1,1}^{(0)} + \frac{1}{2} v_{2,1}^{(0)} u_{2,1}^{(0)}, \text{ etc.} \\ \epsilon_1^{(1)} &= v_{1,1}^{(0)} u_{1,1}^{(1)} + (1 + v_{1,1}^{(0)}) u_{1,1}^{(1)}, \text{ etc.} \end{aligned} \quad (3)$$

where

$$\begin{aligned} \kappa_{(1)} &= \sqrt{12} \quad , \quad \text{when } i = 2, 4, 6. \\ &= 1 \quad \quad \quad i = 1, 3, 5. \end{aligned}$$

In obtaining (1) from Eq. (3), we have neglected the coupling of  $u_1^{(1)}$  with other incremental vibrational modes and let  $t_1^{(0)} = t_2^{(0)} = t_3^{(0)} = 0$  for they contribute mainly to thickness-stretch deformations. It may be seen that the initial displacement gradients  $E_k^{(0)}$  and initial strain  $E_k^{(0)}$  are coupled to the incremental displacement  $u_1^{(1)}$ , stress  $t_1^{(1)}$  and strain  $\epsilon_1^{(1)}$  in all three equations (1)-(3). In order to employ these equations to predict frequency changes, we need to obtain initial stresses, strains and displacements first.

### Initial Stresses and Displacements

We assume initial fields of stress and displacement are governed by Mindlin's two-dimensional first-order equations for crystal plates<sup>2</sup> as given below.

Stress equations of motion

$$\tau_{ij,i}^{(0)} = 2b \ddot{u}_j^{(0)} \quad i, j = 1, 2, 3. \quad (4)$$

$$\tau_{ab,a}^{(0)} - \tau_{2b}^{(0)} = \frac{2}{3} b^3 \ddot{u}_b^{(1)} \quad a, b = 1, 3.$$

Stress-strain relations

$$\tau_p^{(0)} = 2b \bar{c}_{pq} E_q^{(0)} \quad p, q = 1, 3, 4, 5, 6. \quad (5)$$

$$\tau_p^{(1)} = \frac{2b^3}{3} \gamma_{pq} E_q^{(1)} \quad p, q = 1, 3, 5.$$

Strain-displacement relations

$$E_1^{(0)} = u_{1,1}^{(0)}, \quad E_1^{(1)} = u_{1,1}^{(1)},$$

$$E_3^{(0)} = u_{3,3}^{(0)}, \quad E_3^{(1)} = u_{3,3}^{(1)}, \quad (6)$$

$$E_4^{(0)} = u_{2,3}^{(0)} + u_{3,2}^{(0)}, \quad E_5^{(1)} = u_{3,1}^{(1)} + u_{1,3}^{(1)}.$$

$$E_5^{(0)} = u_{1,3}^{(0)} + u_{3,1}^{(0)},$$

$$E_6^{(0)} = u_{2,1}^{(0)} + u_{1,2}^{(0)}.$$

It is extremely difficult to solve these coupled eqns (4)-(6). In a previous paper<sup>1</sup>, an approximate method was developed for obtaining two-dimensional solutions from Cauchy's flexural theory of crystal plates, and the result was shown to be close to those by other analytical and numerical methods.

In the next section, in a similar manner, we are going to derive a system of one-dimensional equations to replace eqs (4)-(6).

### One-dimensional Equations

In order to replace approximately the two-dimensional equations, we expand displacement in a series of trigonometrical functions as follows.<sup>4,5</sup>

$$u_j^{(0)}(x_1, x_3, t) = \int_{-\infty}^{\infty} v_j^{(n)}(x_1, t) \cos \frac{n\pi}{2} \left(1 - \frac{x_3}{c}\right) dx_3$$

$$u_b^{(1)}(x_1, x_3, t) = \int_{-\infty}^{\infty} v_b^{(n)}(x_1, t) \cos \frac{n\pi}{2} \left(1 - \frac{x_3}{c}\right) dx_3$$

By substituting (7) into (4)-(6) and integrating by parts over  $x_3 = -c$  to  $x_3 = +c$ , we obtain the one-dimensional stress equations of motion

$$\sigma_{1j,1}^{(n)} - \frac{n\pi}{2c} \bar{\tau}_{3j}^{(n)} = 2b \rho (1 + \delta_{n0}) \ddot{v}_j^{(n)}, \quad j=1, 2, 3,$$

$$\tau_{1b,1}^{(n)} - \frac{n\pi}{2c} \bar{\tau}_{3b}^{(n)} - \sigma_{2b}^{(n)} = \frac{2b^3}{3} \rho (1 + \delta_{n0}) \ddot{v}_b^{(n)}, \quad b=1, 3$$

where  $\bar{x} = \frac{x_3}{c}$  and

$$\tau_{1j}^{(n)} = \int_{-1}^1 \tau_{1j}^{(0)} \cos \frac{n\pi}{2} (1 - \bar{x}_3) d\bar{x}_3,$$

$$\bar{\tau}_{1j}^{(n)} = \int_{-1}^1 \tau_{1j}^{(0)} \sin \frac{n\pi}{2} (1 - \bar{x}_3) d\bar{x}_3,$$

$$\tau_{1b}^{(n)} = \int_{-1}^1 \tau_{1b}^{(1)} \cos \frac{n\pi}{2} (1 - \bar{x}_3) d\bar{x}_3,$$

$$\bar{\tau}_{1b}^{(n)} = \int_{-1}^1 \tau_{1b}^{(1)} \sin \frac{n\pi}{2} (1 - \bar{x}_3) d\bar{x}_3.$$

The one-dimensional stress-displacement relations can be obtained by inserting (7) into (5) and then, in turn, into (9).

In eqs. (7), we choose to retain the first six displacement components symmetric with respect to the  $x_1 x_3$  plane of the plate, i.e.

$$u_1^{(0)} = v_1^{(0)},$$

$$u_2^{(0)} = v_2^{(0)} - v_2^{(2)} \cos \frac{\pi}{2} \bar{x}_3,$$

$$u_3^{(0)} = v_3^{(1)} \sin \frac{\pi}{2} \bar{x}_3,$$

$$u_1^{(1)} = v_1^{(0)},$$

$$u_4^{(1)} = v_4^{(1)} \sin \frac{\pi}{2} \bar{x}_3.$$

The displacement equations of motion governing these six displacement components are

$$\bar{c}_{11} v_{1,11}^{(0)} + \bar{c}_{16} K_1 (v_{2,11}^{(0)} + \psi_{1,1}^{(0)}) + \frac{1}{c} \bar{c}_{13} v_{3,1}^{(1)} = \rho \ddot{v}_1^{(0)},$$

$$\bar{c}_{66} K_1^2 (v_{2,11}^{(0)} + \psi_{1,1}^{(0)}) + \bar{c}_{61} K_1 v_{1,11}^{(0)} + \frac{1}{c} \bar{c}_{63} K_1 v_{3,1}^{(1)} = \rho \ddot{v}_2^{(0)},$$

$$\bar{c}_{66} K_1^2 v_{2,11}^{(2)} - \left( \frac{2}{3c} \bar{c}_{63} K_1 + \frac{8}{3c} \bar{c}_{45} K_3 \right) v_{3,1}^{(1)} - \frac{8}{3c} \bar{c}_{44} K_3^2 v_3^{(1)} - \frac{\pi^2}{c} \bar{c}_{44} K_3^2 v_2^{(2)} = \rho \ddot{v}_2^{(2)},$$

$$\bar{c}_{55} v_{3,11}^{(1)} + \bar{c}_{54} K_3 \psi_{3,1}^{(1)} + \left( \frac{8}{3c} \bar{c}_{54} K_3 + \frac{2}{3c} \bar{c}_{36} K_1 \right) v_{2,1}^{(2)} - \frac{2}{c} \bar{c}_{31} v_{1,1}^{(0)} - \frac{2}{c} \bar{c}_{36} K_1 (v_{2,1}^{(0)} + \psi_{1,1}^{(0)}) - \frac{\pi^2}{4c^2} \bar{c}_{33} v_3^{(1)} = \rho \ddot{v}_3^{(1)},$$

$$\gamma_{11} v_{1,11}^{(0)} + \frac{1}{c} \gamma_{13} \psi_{3,1}^{(1)} - \frac{3}{b^2} \bar{c}_{61} K_1 v_{1,1}^{(0)} \quad (11)$$

$$- \frac{3}{b^2} \bar{c}_{66} K_1^2 (v_{2,1}^{(0)} + \psi_{1,1}^{(0)})$$

$$- \frac{3}{b^2 c} \bar{c}_{63} K_1 v_3^{(1)} = \rho \ddot{v}_1^{(0)},$$

$$\gamma_{55} \psi_{3,11}^{(1)} - \frac{2}{c} \gamma_{13} \psi_{1,1}^{(0)} - \frac{3}{b^2} \bar{c}_{45} K_3 v_{3,1}^{(1)} - \frac{8}{b^2} \bar{c}_{44} K_3^2 v_2^{(2)}$$

$$- \left( \frac{\pi^2}{4c^2} \gamma_{33} + \frac{3}{b^2} \bar{c}_{44} K_3^2 \right) v_3^{(1)} = \rho \ddot{v}_3^{(1)}.$$

#### Form of the Solutions

For static problems, we set the acceleration terms of displacements in (11) to zero. By assuming displacements in exponential form  $e^{\lambda x_1}$  and inserting them into (11), we have the characteristic equation in the following form

$$t_1^6 + t_2^6 + t_3^6 + t_4^6 + t_5^6 + t_6^6 = 0, \quad (12)$$

where

$$t_i = (\bar{c}_{ij} \gamma_{ij} / \rho c^2)^{1/6}, \quad i=1, \dots, 6.$$

Let  $t_1, t_2, \dots, t_6$  be the six non-zero roots of (12) and  $r = \lambda/c$ . Then the solution of (11) has the form

$$v_1^{(0)} = \sum_{p=1}^6 A_p e^{\lambda_p r \bar{x}_1} + \sum_{p=7}^{12} A_p \bar{x}_1^{(12-p)},$$

$$v_2^{(0)} = \sum_{p=1}^6 B_p e^{\lambda_p r \bar{x}_1} + \sum_{p=7}^{12} B_p \bar{x}_1^{(12-p)},$$

$$v_2^{(2)} \dots$$

$$v_3^{(1)} \dots \quad (13)$$

$$v_1^{(0)} = \frac{1}{c} \sum_{p=1}^6 E_p e^{\lambda_p r \bar{x}_1} + \frac{1}{c} \sum_{p=7}^{12} E_p \bar{x}_1^{(12-p)},$$

$$v_3^{(1)} \dots$$

In (13), the sixth order polynomials in  $\bar{x}_1$  correspond to the six repeated zero roots of (12). The amplitude ratios among  $A_p, B_p, \dots, E_p, p=1, 2, \dots, 12$  can be obtained by substituting (13) into (11). Therefore we have only twelve unknown amplitudes, say  $A_p$ .

#### Boundary Conditions

For a plate clamped at  $x_1 = -a$  and subject to a uniform load  $q'$  (force per unit length) at  $x_1 = +a$  as shown in Fig. 1, we have the boundary conditions

$$v_1^{(0)} = v_2^{(0)} = v_2^{(2)} = v_3^{(1)} = v_1^{(0)} = \psi_3^{(1)} = 0 \quad \text{at } \bar{x}_1 \equiv \frac{x_1}{a} = -1,$$

$$\sigma_1^{(0)} = \sigma_6^{(2)} = \sigma_5^{(1)} = \tau_1^{(0)} = \tau_5^{(1)} = 0,$$

$$\sigma_6^{(0)} = 2q' \quad \text{at } \bar{x}_1 = +1. \quad (14)$$

By the stress-displacement relations, the second set of stress boundary conditions of (14) can be expressed as below.

$$v_{1,1}^{(0)} + K_1 \hat{C}_{16} (v_{2,1}^{(0)} + v_1^{(0)}) + \frac{1}{c} \hat{C}_{13} v_3^{(1)} = 0,$$

$$K_1^2 \hat{C}_{66} v_{2,1}^{(2)} - \frac{2}{3c} K_1 \hat{C}_{63} v_3^{(1)} = 0,$$

$$K_3^2 \hat{C}_{54} (v_3^{(1)} + \frac{8}{3c} v_2^{(2)}) + \hat{C}_{55} v_{3,1}^{(1)} = 0,$$

$$v_{1,1}^{(0)} + \frac{1}{c} \hat{C}_{13} v_3^{(1)} = 0, \quad (15)$$

$$v_{3,1}^{(1)} = 0,$$

$$K_1 \hat{C}_{16} v_{1,1}^{(0)} + K_1^2 \hat{C}_{66} (v_{2,1}^{(0)} + v_1^{(0)}) + K_1 \hat{C}_{36} v_3^{(1)} = \frac{q'}{2b\hat{C}_{11}}.$$

where

$$\hat{C}_{pq} = \bar{C}_{pq} / \bar{C}_{11}, \quad \hat{C}_{pq} = \bar{C}_{pq} / \bar{C}_{11}.$$

Eqs.(14) provide the twelve conditions for solving the twelve unknown amplitudes  $A_i$ .

#### Variations of Initial Stresses and Displacements

A rectangular SC-cut quartz plate with  $a/c = 1.75$ , shown in Fig. 1, is chosen for the study.

For a given edge shear intensity  $q'$ , the amplitudes  $A_i$  can be computed from (14) and displacement components from (13). Then the two-dimensional displacements and stresses can be obtained from (10) and (16) respectively, with  $\lambda$  regarded as a parameter.

For the visualization of their two dimensional variations in the plate, some of the stress and displacement components are computed and plotted along the  $x_1$  and  $x_3$  axes in dimensionless quantities and for various values of  $\lambda$ , as shown in Figs.2-7.

#### Force Sensitivity

By taking the initial fields of stress and displacement at the center of the plate (also the center of the electrodes) as the average values and by neglecting the coupling of the incremental thickness-shear mode of vibration with other modes, an explicit formula is obtained from (1)

$$\begin{aligned} \hat{C}_{11} v_{1,1}^{(0)} + \frac{\hat{C}_{16} k^2}{2\hat{C}_{66}} (v_{2,1}^{(0)} + v_1^{(0)}) + \frac{\hat{C}_{13}^2}{\hat{C}_{66}} (C_{16k} E_{k,1}^{(1)} + C_{56k} E_{k,3}^{(1)}) \\ k=1,2,\dots,6. \end{aligned} \quad (16)$$

Eq. (16) has identical form as that given in Ref.6. However, in the present paper, the initial strains  $E_k^{(n)}$  are computed from the two-dimensional theory and  $k$  ranges from 1 to 6 for doubly-rotated cuts.

The changes of thickness-shear resonance frequencies  $f/f_0$  are computed as a function of the azimuth angle  $\theta$ , for both AT and SC cuts of quartz plate.

In Fig. 8, the presently predicted values of  $f/f_0$  are compared with our previously predicted values<sup>6</sup> and with the experimental values by Miggins, Barcus and Perry. Figs. 9 and 10 give the comparison of predicted  $f/f_0$  with measured values by Fletcher and Douglas<sup>8</sup> for AT and SC cuts, respectively.

It may be seen from Figs. 8-10 that Eq.(16) predicts the locations of zero and maximum of  $f/f_0$  as a function of  $\theta$  quite well and has also identified the predominant factors contributing to the force sensitivity of the resonators.

In order to take into account of the spatial variations of the initial stresses and the coupling of the thickness-shear with other modes, like extension and flexure, for more accurate predictions, a perturbation method should be employed as the next step.

#### References

1. P.C.Y. Lee, Y.S. Wang, and X. Markenscoff, J. Acous. Soc. Am. **57**, 95-105 (1975).
2. R.D. Mindlin, "An Introduction to the Mathematical Theory of Vibrations of Elastic Plates," U.S. Army Signal Corps Engineering Laboratories, Fort Monmouth, N.J. 1955.
3. P.C.Y. Lee and S.L. Lam, Proc. 35th Ann. Freq. Cont. Symp. 193-204 (1981).
4. P.C.Y. Lee and Z. Nikodem, Int. J. Solids Structures, **8**, 581-612 (1972).
5. Z. Nikodem and P.C.Y. Lee, Int. J. Solids Structures, **11**, 177-196 (1974).
6. P.C.Y. Lee, Y.S. Wang and X. Markenscoff, J. Acous. Soc. Am., **59**, 90-96 (1976).
7. C.R. Miggins, L.C. Barcus, and R.W. Perry, Repts. 1-20, Lowell Tech. Inst. Found. (1961-1966).
8. E.D. Fletcher and A.J. Douglas, Proc. 33rd Ann. Freq. Cont. Symp. 346-350 (1979).

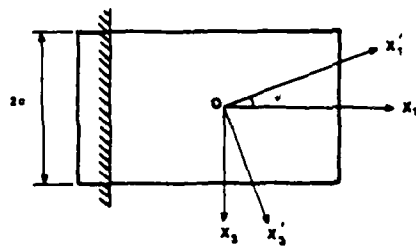
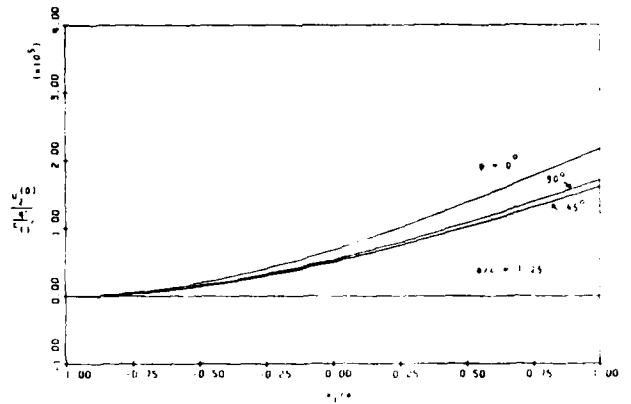
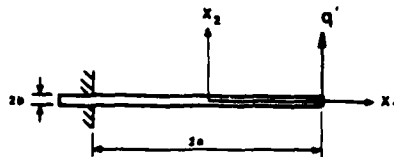
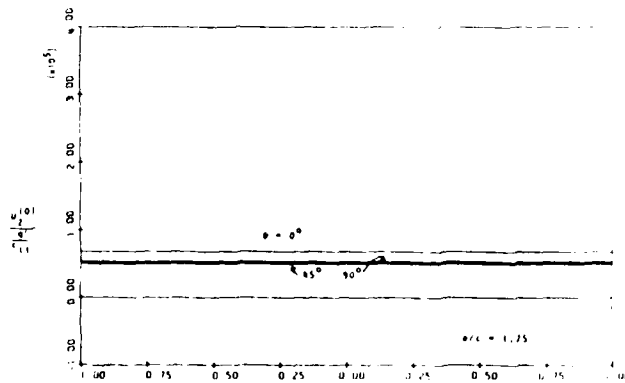


Fig. 1 A rectangular cantilever plate referred to  $x_1$  coordinate system,  $x_1'$  referred to axes of crystal symmetry, and  $\theta$  the azimuth angle.



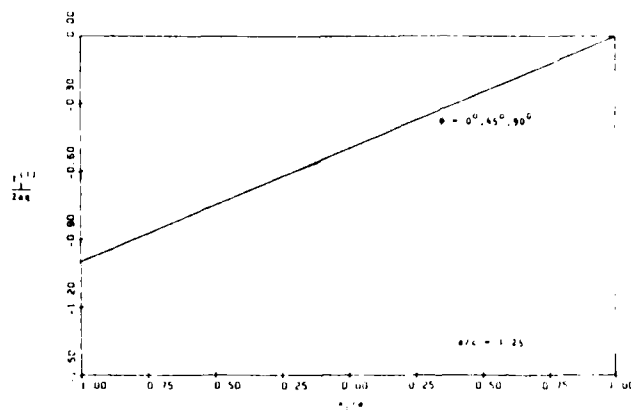
$u_2^{(0)}$  ALONG  $x_1$ -AXIS

Fig. 2 Displacement  $u_2^{(0)}$  along the  $x_1$  axis of a rectangular SC-cut of quartz plate ( $r = a/c = 1.25$ ).



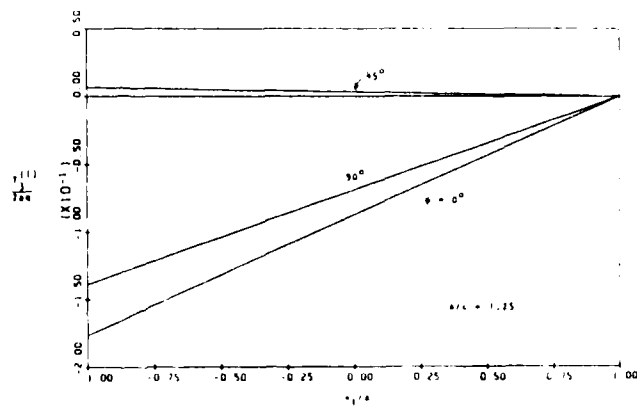
$u_2^{(0)}$  ALONG  $x_3$ -AXIS

Fig. 3 Displacement  $u_2^{(0)}$  along the  $x_3$  axis of the plate.



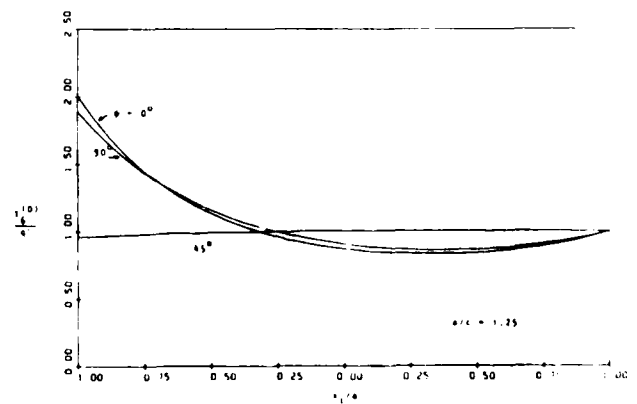
T11 ALONG X1-AXIS

Fig. 4 Bending couple  $T_1^{(1)}$  along the  $x_1$  axis of the plate.



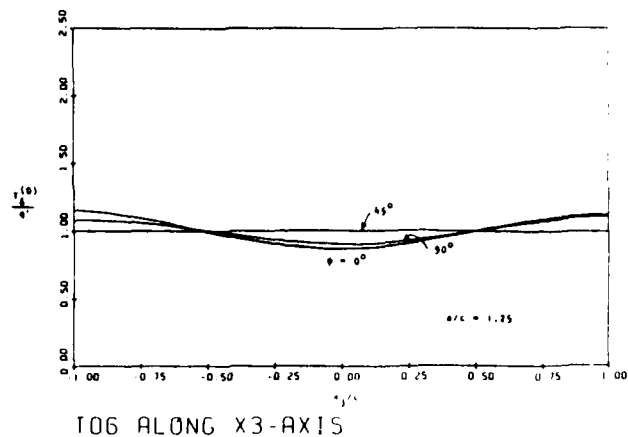
T13 ALONG X1-AXIS

Fig. 5 Bending couple  $T_3^{(1)}$  along the  $x_1$  axis of the plate.



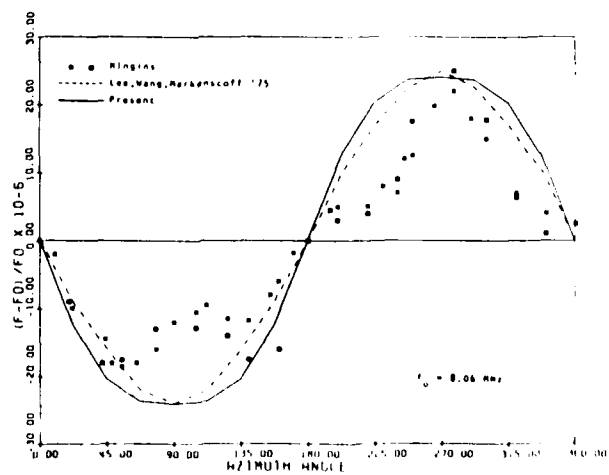
T06 ALONG X1-AXIS

Fig. 6 Transverse shear  $T_6^{(0)}$  along the  $x_1$  axis of the plate.



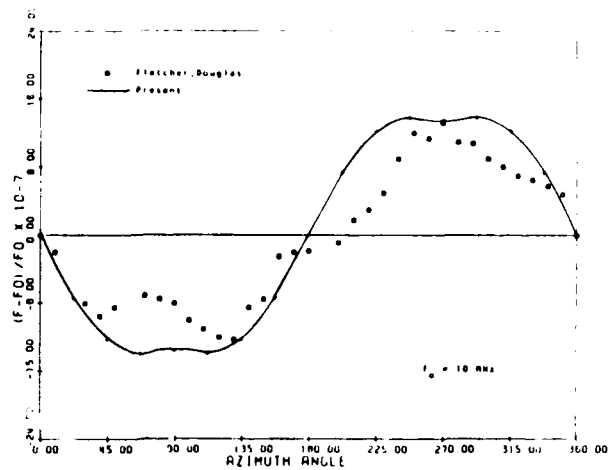
T06 ALONG X3-AXIS

Fig. 7 Transverse shear  $T_6^{(0)}$  along the  $x_3$  axis of the plate.



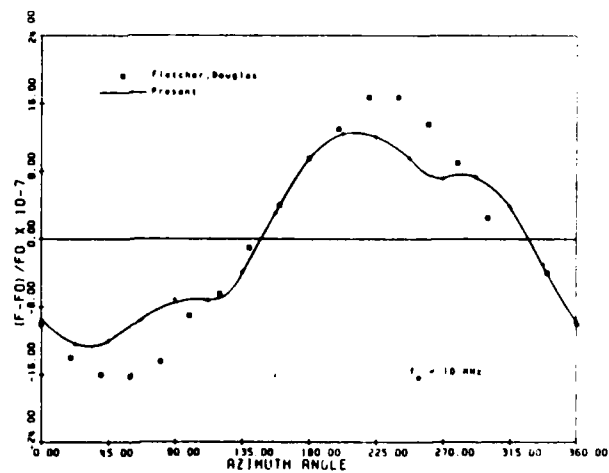
FREQUENCY SHIFT AT CUT

Fig. 8 Frequency changes as a function of azimuth angle  $\psi$ , for AT-cut plate.



FREQUENCY SHIFT AT-CUT

Fig. 9  $\Delta f/f_0$  vs  $\psi$  for an AT-cut plate.



FREQUENCY SHIFT SC-CUT

Fig. 10  $\Delta f/f_0$  vs  $\psi$  for an SC-cut plate.

## AN ANALYSIS OF CONTOURED SC-CUT QUARTZ CRYSTAL RESONATORS

H.F. Tiersten and D.S. Stevens

Department of Mechanical Engineering,  
Aeronautical Engineering & Mechanics  
Rensselaer Polytechnic Institute, Troy, New York 12181

Abstract

A previous treatment of SC-cut quartz trapped energy resonators is extended to the case of plates with slowly varying thickness. As in the earlier treatment, the approximate equations are referred to rotated coordinate axes obtained from the eigenvector triad of the pure thickness solution for the SC-cut. The approximate dispersion equation describing the mode shape along the surface of the SC-cut, which was used in the recent treatment of the trapped energy resonator, is extended to include the influence of certain relatively large transformed elastic constants that were neglected in the earlier work. The extended equation is considerably more accurate than the earlier one. A scalar differential equation describing the mode shapes along the surface of the contoured SC-cut for the family associated with each odd harmonic is obtained from the extended dispersion equation for the flat plate. The scalar equation is applied in the analysis of contoured SC-cut quartz crystal resonators, and an approximate lumped parameter representation of the admittance, which is valid in the vicinity of a resonance, is obtained. The analysis holds for the fundamental and odd harmonic and anharmonic overtone thickness modes of interest.

1. Introduction

Previous analytical work on contoured crystal resonators holds only for rotated Y-cuts of quartz. In recent years the doubly-rotated SC-cut<sup>1,2</sup> has given every indication of possessing significant technological advantages<sup>3,4</sup> over the AT-cut. On account of the additional anisotropy of the SC-cut, the existing analytical treatment of contoured resonators does not hold.

In a recent analysis<sup>5</sup> of SC-cut quartz trapped energy resonators with rectangular electrodes certain transformed elastic constants were neglected, which are not that small. In this work the earlier treatment<sup>5</sup> is extended to include the influence of the transformed elastic constants that are not that small and were neglected in the earlier work. As in the earlier treatment<sup>5</sup> the analysis proceeds by decomposing the mechanical displacement vector along the orthogonal eigenvector triad of the pure thickness solution and transforming the independent spatial variables to a Cartesian coordinate system containing the plate

normal and the component in the plane of the plate of the large thickness eigen-displacement of interest. Since the piezoelectric coupling is small in quartz and we are interested in obtaining the dispersion relations in the vicinity of the thickness-frequencies of interest for small wavenumbers along the plate, only the thickness-dependence of all electrical variables is included in the treatment. The resulting system of transformed differential equations and boundary conditions on the major surfaces of the plate are employed in the determination of the asymptotic dispersion relation in the vicinity of each thickness-frequency of interest using a generalization of a procedure used in the case of rotated Y-cut quartz<sup>6,7</sup>. The corrected asymptotic dispersion relation for the flat plate is considerably more accurate than the earlier one<sup>5</sup>. The dispersion equation enables us to construct the differential equation that describes the mode shape along the surface of the flat plate. The resulting single scalar equation may readily be generalized to be applicable to the description of the mode shape along the surface of the contoured SC-cut since the thickness is slowly varying. Since the influence of the contouring on the trapping is much greater than the influence of the electrode<sup>8</sup>, the edge of the electrode is ignored in the determination of the eigensolutions. Since the mode is sharply confined to the vicinity of the center of the contoured plate, the edge of the plate is ignored in the analysis.

An inhomogeneous differential equation is obtained for each harmonic thickness mode of interest for the case of a driving voltage applied across surface electrodes. The differential equation obtained depends on the order of the odd harmonic. The resulting system of equations is applied in the analysis of the forced vibrations of a plano-convex contoured SC-cut quartz crystal resonator and a lumped parameter representation of the admittance is obtained. Some numerical results are presented.

2. Transformation of Equations

As in the earlier treatment<sup>5</sup> the stress equations of motion and charge equation of electrostatics may be written in the form

$$\hat{T}_{mn,m} = \hat{\rho} \hat{u}_n, \quad D_{m,m} = 0, \quad (2.1)$$

The linear piezoelectric constitutive equations are given by

$$\hat{T}_{mn} = \hat{c}_{mnrs} \hat{u}_{r,s} + \hat{e}_{rmn} \hat{\varphi}, \quad (2.2)$$

$$D_m = \hat{e}_{mrs} \hat{u}_{r,s} - \hat{c}_{mn} \hat{\varphi}, \quad (2.3)$$

The notation is conventional<sup>1</sup> and carets have been introduced over the mechanical variables and the elastic and piezoelectric constants because we are going to transform from the Cartesian coordinate system presently being employed to a combination of two very special Cartesian coordinate systems that facilitate the analysis. Moreover, in the original coordinate system we consistently use the tensor indices  $m, n, r, s$ . The substitution of (2.2) and (2.3) in (2.1) yields

$$\hat{c}_{mnrs} \hat{u}_{r,sm} + \hat{e}_{rmn} \hat{\varphi},_{rm} = \hat{c} \ddot{\hat{u}}_n, \quad (2.4)$$

$$\hat{e}_{mrs} \hat{u}_{r,sm} - \hat{c}_{mn} \hat{\varphi},_{nm} = 0, \quad (2.5)$$

which are the differential equations of linear piezoelectricity.

The coordinate axes are oriented with  $\hat{x}_2$  normal to the major surfaces of the plate, which are at  $\hat{x}_2 = \pm h$ , and  $\hat{x}_1$  directed along the axis of second rotation of the doubly-rotated quartz plate. Since in the modes of interest the spatial rate of variation of the dependent variables in the plane of the plate is much less than in the thickness direction and the piezoelectric coupling is small, we can ignore the  $\hat{x}_2$  dependence of  $\hat{\varphi}$  and  $D_v$  and of any variable in the expression for  $D_v$ , and in place of Eqs. (2.3) and (2.5), respectively, write

$$D_2 = \hat{c}_{2r2} \hat{u}_{r,2} - \hat{e}_{22} \hat{\varphi},_2, \quad (2.6)$$

$$\hat{e}_{2r2} \hat{u}_{r,22} - \hat{e}_{22} \hat{\varphi},_{22} = 0, \quad (2.7)$$

and we have introduced the convention that the subscripts  $u, v, w$  take the values 1 and 3, but skip 2. Moreover, it is advantageous for us to write (2.2) and (2.4), respectively, in the forms

$$\hat{T}_{mn} = \hat{c}_{mnr2} \hat{u}_{r,2} + \hat{e}_{2mn} \hat{\varphi},_2 + \hat{c}_{vnm} \hat{u}_{r,v}, \quad (2.8)$$

$$\hat{c}_{2nr2} \hat{u}_{r,22} + \hat{e}_{22n} \hat{\varphi},_{22} + (\hat{c}_{2rnv} + \hat{c}_{2nrv}) \hat{u}_{r,2v} + \hat{c}_{vnrv} \hat{u}_{r,wv} = \hat{c} \ddot{\hat{u}}_n, \quad (2.9)$$

since we are interested in modes in the vicinity of the frequencies of thickness vibration. Substituting from (2.7) into (2.9), we obtain

$$\hat{c}_{2nr2} \hat{u}_{r,22} + (\hat{c}_{2rnv} + \hat{c}_{2nrv}) \hat{u}_{r,2v} + \hat{c}_{vnrv} \hat{u}_{r,wv} = \hat{c} \ddot{\hat{u}}_n, \quad (2.10)$$

where

$$\hat{c}_{2nr2} = \hat{c}_{2nr2} + \frac{\hat{e}_{22n} \hat{e}_{22r}}{\hat{c}_{22}} \quad (2.11)$$

are the usual piezoelectrically stiffened elastic constants.

For thickness vibrations only  $\hat{x}_2$ -dependence is considered and (2.10) takes the form

$$\hat{c}_{2nr2} \hat{u}_{r,22} = \hat{c} \ddot{\hat{u}}_n. \quad (2.12)$$

In the case of the unelectroded plate the antisymmetric thickness vibration solution can be written in the form

$$\hat{u}_r = A_r \sin \gamma x_2 e^{i\omega t}, \quad (2.13)$$

which satisfies (2.12) provided

$$(\hat{c}_{2nr2} - \bar{c} \delta_{nr}) A_r = 0, \quad (2.14)$$

where

$$\bar{c} = \hat{c} \omega^2 / \gamma^2. \quad (2.15)$$

For a nontrivial solution the determinant of the coefficients of  $A_r$  in (2.14) must vanish, i.e.,

$$|\hat{c}_{2nr2} - \bar{c} \delta_{nr}| = 0, \quad (2.16)$$

which yields a cubic equation in  $\bar{c}$ . Since the  $\hat{c}_{2nr2}$  constitute a symmetric, positive-definite matrix<sup>11</sup>, Eq. (2.16) yields three real, positive roots<sup>12</sup>  $\bar{c}^{(i)}$  ( $i=1,2,3$ ), which yield mutually orthogonal eigenvectors  $A_r^{(i)}$  when substituted in (2.14), and we may write

$$A_r^{(i)} A_r^{(j)} = N_{(i)}^2 \delta_{ij}, \quad (2.17)$$

where the  $N_{(i)}$  are the normalization factors. If we normalize the  $A_r^{(i)}$  thus

$$q_r^{(i)} = A_r^{(i)} / N_{(i)}, \quad (2.18)$$

and write the  $q_r^{(i)}$  as a  $3 \times 3$  orthogonal transformation matrix  $Q_{ir}$ , from (2.17) we have the orthogonality relations

$$Q_{ir} Q_{jr} = \delta_{ij}, \quad (2.19)$$

and, of course, the other orthogonality relations

$$Q_{ir} Q_{is} = \delta_{rs}, \quad (2.20)$$

hold.

We may now transform the components of the vector  $\hat{u}_r$  in the original coordinate system to the components  $u_i$  in the thickness solution eigenvector coordinate system and vice-versa, thus

$$u_i = Q_{ir} \hat{u}_r, \quad \hat{u}_r = Q_{ir} u_i. \quad (2.21)$$

A schematic diagram showing the original coordinate system along with the eigenvector coordinate system is shown in Fig. 1. For a pure thickness solution for an unelectroded plate, one of the thickness eigen-displacements, say  $u_1$ , exists and the other two vanish identically. Moreover, for a mode of vibration in the vicinity of the thickness solution for which  $u_1$  exists, although  $u_2$  and  $u_3$  exist they are one or more orders of magnitude

smaller than  $u_1$ . This is the reason there is a significant advantage in decomposing the mechanical displacement along the eigenvector triad of the pure thickness solution when describing this type of mode.

Clearly, the independent variables  $x_2$  must be referred to a Cartesian coordinate system containing the axis  $\hat{x}_2$ , which is normal to the major surfaces of the plate, and two orthogonal axes in the plane of the plate. Of all the orthogonal coordinate systems in the plane of the plate, one is particularly well suited for the description of modes of vibration in the vicinity of the pure thickness solution  $u_1$ , when, as is the case in this work, it is dominantly a thickness-shear displacement, as shown in Fig.1. That coordinate system contains the axis formed by the projection of the  $u_1$ -eigen-displacement direction on the plane of the plate as shown in Fig.2. From (2.21)<sub>2</sub> the angle  $\theta$  is given by

$$\theta = \tan^{-1}(-Q_{13}/Q_{11}). \quad (2.22)$$

and the planar rotation matrix  $R_{av}$  is given by

$$R_{av} = \begin{pmatrix} \cos \theta & -\sin \theta \\ \sin \theta & \cos \theta \end{pmatrix}, \quad (2.23)$$

where we have introduced the convention that the subscripts a, b, c, d take the values 1 and 3 but skip 2. Clearly, the planar coordinates  $x_a$  and  $\hat{x}_v$  are related by

$$x_a = R_{av} \hat{x}_v, \quad \hat{x}_v = R_{av}^T x_a, \quad (2.24)$$

the first of which yields

$$\partial/\partial \hat{x}_v = R_{av} \partial/\partial x_a. \quad (2.25)$$

Transforming (2.10) with  $Q_{ij}$ , substituting from (2.21)<sub>2</sub> for  $\hat{u}_v$  and  $\hat{u}_n$  and (2.25) for the partial derivatives with respect to  $\hat{x}_v$  and  $\hat{x}_n$  and employing (2.14) with (2.18) and (2.19), we obtain

$$\begin{aligned} \bar{c}_{j,22}^{(j)} u_{j,22} + (c_{aij2} + c_{ajiz}) u_{i,2a} \\ + c_{ajib} u_{i,ab} = \bar{c}_{ij}^{(j)}, \end{aligned} \quad (2.26)$$

where

$$\begin{aligned} c_{aij2} &= Q_{jn} Q_{ir} R_{av} \bar{c}_{vnr2}, \\ c_{ajib} &= R_{av} Q_{jn} Q_{ir} R_{bw} \bar{c}_{vnrw}. \end{aligned} \quad (2.27)$$

In the case of the thickness vibrations of the electroded plate with shorted electrodes the three solutions of the differential equations are coupled<sup>3-5</sup> in the transcendental frequency equation. However, since the piezoelectric coupling is small in quartz and the three  $\bar{c}_{ij}^{(j)}$  are sufficiently widely separated, the transcendental frequency equation approximately uncouples and we effectively have three independent transcendental frequency equations<sup>1</sup>, one for each thickness eigen-displacement  $u_i$ . Consequently, (2.26) is a useful form for the treatment of modes of vibration in the vicinity of the pure thickness solution  $u_1$  for the electroded as well as the unelectroded plate.

For the electroded plate with shorted electrodes the electrical boundary condition is

$$\varphi = 0 \quad \text{at} \quad x_2 = \pm h. \quad (2.28)$$

Substituting from (2.21)<sub>2</sub> into (2.7), integrating and satisfying (2.28), we obtain

$$\varphi = (e_{22j}/\epsilon_{22}) u_j + C x_2, \quad (2.29)$$

where

$$e_{22j} = Q_{jr} \hat{e}_{22r}, \quad C = -(e_{22j}/\epsilon_{22}) u_j (h)/h. \quad (2.30)$$

In the case of the unelectroded plate because of the reasoning leading to (2.6) we can neglect the electric field outside the plate<sup>1</sup> and the electrical boundary condition becomes

$$D_2 = 0 \quad \text{at} \quad x_2 = \pm h. \quad (2.31)$$

Hence, from (2.31) with (2.6), for the unelectroded plate, we obtain

$$\varphi = (e_{22j}/\epsilon_{22}) u_j, \quad (2.32)$$

which is the same as (2.29) but with  $C=0$ .

The traction boundary conditions on the major surfaces of the plate employ the constitutive equations in (2.8) with  $m=2$ . Transforming (2.8) for  $m=2$  with  $Q_{ij}$ , substituting from (2.21)<sub>2</sub>, (2.25), (2.29), (2.30)<sub>1</sub>, and (2.11) and employing (2.14) with (2.18) and (2.19) and (2.27)<sub>1</sub>, we obtain

$$T_{2j} = \bar{c}_{ij}^{(j)} u_{j,2} + c_{22j} C + c_{aij2} u_{i,a}, \quad (2.33)$$

which holds for the electroded plate and for the unelectroded plate provided  $C=0$ . As noted in the Introduction the traction continuity conditions along the surfaces separating the electroded from the unelectroded regions and at the free edges of the plate are not needed in this work.

### 3. Dispersion Equations

Although in this work we are primarily interested in the dispersion equation in the electroded region of the plate, we obtain the dispersion equation for the unelectroded region because the treatment is somewhat simpler and it has been shown<sup>1</sup> that the dispersion equation for the electroded plate may readily be inferred from that for the unelectroded plate. The differential equations expressed in terms of the thickness eigen-displacements in the transformed coordinate system are given in (2.26). The boundary conditions on the major surfaces of the unelectroded plate are

$$T_{2j} = 0 \quad \text{at} \quad x_2 = \pm h. \quad (3.1)$$

where the constitutive equations for  $T_{ij}$  expressed in the same way are given in (2.33) with  $C=0$ . Since we are interested in the solution for plate waves in the vicinity of the thickness frequencies for the thickness eigen-displacement  $u_1$  with wave, or decay, numbers in the plane of the plate that are much smaller than the thickness wavenumbers, a large number of terms in (2.26) and (2.33) are

negligible, independent of the values of the associated transformed elastic coefficients<sup>11</sup>. In addition, among the other terms a number of the transformed elastic constants are very small and can be neglected, specifically  $c_{11}$ ,  $c_{17}$ ,  $c_{88}$ ,  $c_{99}$ ,  $c_{77}$ ,  $c_{81}$ ,  $c_{91}$ ,  $c_{14}$ ,  $c_{15}$ ,  $c_{16}$ ,  $c_{18}$  and  $c_{72}$ . As a consequence of the foregoing the differential equations (2.26) and constitutive equations (2.33) with  $C = 0$ , reduce to the considerably simpler forms

$$\begin{aligned} c_{11} u_{1,11} + 2c_{16} u_{1,12} + (c_{12} + c_{66}) u_{2,12} + c_{58} u_{1,33} \\ + (c_{36} + c_{57}) u_{3,23} + \bar{c}^{(1)} u_{1,22} = \rho \ddot{u}_1, \\ \bar{c}^{(2)} u_{2,22} + (c_{12} + c_{66}) u_{1,12} = \rho \ddot{u}_2, \\ \bar{c}^{(3)} u_{3,22} + (c_{36} + c_{57}) u_{1,23} = \rho \ddot{u}_3, \quad (3.2) \\ T_{21} = \bar{c}^{(1)} u_{1,2} + c_{66} u_{2,1} + c_{16} u_{1,1} + c_{36} u_{3,3}, \\ T_{22} = \bar{c}^{(2)} u_{2,2} + c_{12} u_{1,1}, \\ T_{23} = \bar{c}^{(3)} u_{3,2} + c_{57} u_{1,3}. \quad (3.3) \end{aligned}$$

We must now obtain asymptotic solutions to (3.2) and (3.1) with (3.3) in the vicinity of odd  $u_1$  thickness frequencies for small wavenumbers along the plate. Note that both  $u_1$  and  $u_2$  and  $u_3$  are coupled directly in (3.2) and (3.3) but that  $u_2$  and  $u_3$  are not. This is the essential reason that we are ultimately able to obtain a relatively simple useful description. Since solutions decaying in both directions along the plate are somewhat simpler than those exhibiting trigonometric behavior in one or both directions and the dispersion equations for trigonometric behavior may readily be obtained<sup>12</sup> from those for decaying behavior, we consider the decaying solutions. Accordingly, as a solution of (3.2) consider

$$\begin{aligned} u_1 &= (A \sin \pi x_2 + B \cos \pi x_2) e^{-\xi x_1} e^{-\nu x_3} e^{i \omega t}, \\ u_2 &= (C \sin \pi x_2 + D \cos \pi x_2) e^{-\xi x_1} e^{-\nu x_3} e^{i \omega t}, \\ u_3 &= (E \sin \pi x_2 + F \cos \pi x_2) e^{-\xi x_1} e^{-\nu x_3} e^{i \omega t}, \quad (3.4) \end{aligned}$$

which satisfies (3.2) provided a system of six homogeneous linear algebraic equations in A, B, C, D, E and F are satisfied and which are too lengthy to present here<sup>11</sup>.

In earlier work<sup>10</sup> on a simpler problem of this nature the asymptotic dispersion relation was obtained starting with the pure thickness solution of interest. However, in the situation under consideration here the thickness coupling appearing in (3.4) is caused by the term containing  $c_{16}$  in (3.2)<sub>1</sub>, which vanishes in the case of the pure thickness solution. Since in this instance the thickness terms in each of (3.4) are uncoupled, the asymptotic dispersion relation cannot be obtained starting with the pure thickness solution of interest. Nevertheless, the asymptotic dispersion relation may be obtained by starting with a solution

varying with  $x_1$ , i.e., containing  $\xi$ , and including the complete effect of the  $c_{16}$  terms in (3.2)<sub>1</sub> and (3.3)<sub>1</sub>, i.e., including the term linear in  $\xi$  in the coefficients of A and B in the resulting algebraic equations in the starting form<sup>11</sup>. This starting solution for the  $u_1$  term is equivalent to the solution for thickness-twist waves in rotated Y-cut quartz plates obtained by Mindlin<sup>13</sup>. Thus, in consideration of the foregoing and following the procedure used in Refs. 8 and 9, to lowest order in  $\xi$  and  $\nu$  for large A and B, we obtain

$$\pi_{\pm}^{(1)} = \frac{n\pi}{2h} \pm i \xi c_{16} / \bar{c}^{(1)}, \quad B_{\pm}^{(1)} = \pm i A_{\pm}^{(1)}, \quad (3.5)$$

$$C_{\pm}^{(1)} = \mp \frac{i r_1 \xi A_{\pm}^{(1)}}{\pi_{\pm}^{(1)}}, \quad D_{\pm}^{(1)} = \frac{r_1 \xi A_{\pm}^{(1)}}{\pi_{\pm}^{(1)}}, \quad (3.6)$$

$$E_{\pm}^{(1)} = \mp \frac{i r_3 \nu A_{\pm}^{(1)}}{\pi_{\pm}^{(1)}}, \quad F_{\pm}^{(1)} = \frac{r_3 \nu A_{\pm}^{(1)}}{\pi_{\pm}^{(1)}},$$

where

$$r_2 = \frac{c_{12} + c_{66}}{\bar{c}^{(1)} - \bar{c}^{(2)}}, \quad r_3 = \frac{c_{36} + c_{45}}{\bar{c}^{(1)} - \bar{c}^{(3)}}, \quad (3.7)$$

$$\begin{aligned} \pi_2 &= \kappa_2 \frac{n\pi}{2h}, \quad \pi_3 = \kappa_3 \frac{n\pi}{2h}, \\ \kappa_2 &= \sqrt{\frac{\bar{c}^{(1)}}{\bar{c}^{(2)}}}, \quad \kappa_3 = \sqrt{\frac{\bar{c}^{(1)}}{\bar{c}^{(3)}}}. \quad (3.8) \end{aligned}$$

Similarly, for large C and D and large E and F, respectively, we obtain

$$\begin{aligned} D_{\pm}^{(2)} &= \pm i C_{\pm}^{(2)}, \quad A_{\pm}^{(2)} = \pm \frac{i r_2 \xi}{2} C_{\pm}^{(2)}, \\ B_{\pm}^{(2)} &= -\frac{r_2 \xi}{2} C_{\pm}^{(2)}, \quad E_{\pm}^{(2)} = F_{\pm}^{(2)} = 0, \quad (3.9) \end{aligned}$$

$$\begin{aligned} F_{\pm}^{(3)} &= \pm i E_{\pm}^{(3)}, \quad A_{\pm}^{(3)} = \pm \frac{i r_3 \nu}{3} E_{\pm}^{(3)}, \\ B_{\pm}^{(3)} &= -\frac{r_3 \nu}{3} E_{\pm}^{(3)}, \quad C_{\pm}^{(3)} = D_{\pm}^{(3)} = 0, \quad (3.10) \end{aligned}$$

in which the amplitudes that have been shown to vanish are of order higher than linear in  $\xi$  or  $\nu$  and, hence, turn out to be negligible to order  $\xi^2$  and  $\nu^2$ .

In order to satisfy the boundary conditions in (3.1) with (3.3), we take a sum of the six asymptotic solutions of the differential equations in the form

$$\begin{aligned} u_1 &= [A_+^{(1)} (\sin \pi_1^+ x_2 + i \cos \pi_1^+ x_2) \\ &+ A_-^{(1)} (\sin \pi_1^- x_2 - i \cos \pi_1^- x_2) \\ &+ \frac{i r_2 \xi}{2} C_+^{(2)} (\sin \pi_2^+ x_2 + i \cos \pi_2^+ x_2) \end{aligned}$$

$$\begin{aligned}
& - \frac{ir_2 \bar{\epsilon}}{2} C_-^{(2)} (\sin \bar{\epsilon} x_2 - i \cos \bar{\epsilon} x_2) \\
& + \frac{ir_3 v}{3} E_+^{(3)} (\sin \bar{\epsilon} x_2 + i \cos \bar{\epsilon} x_2) \\
& - \frac{ir_3 v}{3} E_-^{(3)} (\sin \bar{\epsilon} x_2 - i \cos \bar{\epsilon} x_2) \Big] e^{-\bar{\epsilon} x_1} e^{-v x_3}, \\
u_2 = & \left[ - \frac{ir_2 \bar{\epsilon}}{1} A_+^{(1)} (\sin \bar{\epsilon} x_2 + i \cos \bar{\epsilon} x_2) \right. \\
& + \frac{ir_2 \bar{\epsilon}}{1} A_-^{(1)} (\sin \bar{\epsilon} x_2 - i \cos \bar{\epsilon} x_2) \\
& + C_+^{(2)} (\sin \bar{\epsilon} x_2 + i \cos \bar{\epsilon} x_2) \\
& \left. + C_-^{(2)} (\sin \bar{\epsilon} x_2 - i \cos \bar{\epsilon} x_2) \right] e^{-\bar{\epsilon} x_1} e^{-v x_3}, \\
u_3 = & \left[ - \frac{ir_3 v}{1} A_+^{(1)} (\sin \bar{\epsilon} x_2 + i \cos \bar{\epsilon} x_2) \right. \\
& + \frac{ir_3 v}{1} A_-^{(1)} (\sin \bar{\epsilon} x_2 - i \cos \bar{\epsilon} x_2) \\
& + E_+^{(3)} (\sin \bar{\epsilon} x_2 + i \cos \bar{\epsilon} x_2) \\
& \left. + E_-^{(3)} (\sin \bar{\epsilon} x_2 - i \cos \bar{\epsilon} x_2) \right] e^{-\bar{\epsilon} x_1} e^{-v x_3}, \quad (3.11)
\end{aligned}$$

which satisfies Eqs. (3.1) with (3.3) provided a system of six homogeneous linear algebraic equations in  $A_+^{(1)}$ ,  $A_-^{(1)}$ ,  $C_+^{(2)}$ ,  $C_-^{(2)}$ ,  $E_+^{(3)}$  and  $E_-^{(3)}$  are satisfied and which are too lengthy to present here<sup>11</sup>. Since we are interested in modes in the vicinity of the thickness solution for large  $A_+^{(1)}$  and  $A_-^{(1)}$  for which  $\bar{\epsilon}_1$  is very near the expression given in (3.5)<sub>1</sub>, we take

$$\bar{\epsilon}_1 = \frac{n\pi}{2} + i \frac{c_{16}}{\bar{\epsilon}(1)} \bar{\epsilon} h + \alpha_n, \quad n=1,3,5 \dots, \quad (3.12)$$

where  $\alpha_n$  is small, and substitute from (3.12) into the vanishing determinant obtained<sup>12</sup> from the aforementioned six equations obtained from the boundary conditions (3.1) with (3.3), and expand<sup>13</sup> the trigonometric functions and the determinant to obtain

$$\begin{aligned}
\alpha_n = & - \frac{\bar{\epsilon}^2 4h^2 (r_2 \bar{\epsilon}^{(1)} - c_{66}) (r_2 \bar{\epsilon}^{(1)} + c_{12})}{\bar{\epsilon}(1) \bar{\epsilon}(2) n^2} \cot \kappa_2 \frac{n\pi}{2} \\
& - \frac{\bar{\epsilon}^2 4h^2 (r_3 \bar{\epsilon}^{(3)} - c_{36}) (r_3 \bar{\epsilon}^{(3)} + c_{45})}{\bar{\epsilon}(1) \bar{\epsilon}(3) n^2} \cot \kappa_3 \frac{n\pi}{2}, \quad (3.13)
\end{aligned}$$

to order  $\bar{\epsilon}$  and  $v$ . Moreover, from the six homogeneous linear algebraic equations, we obtain

$$\begin{aligned}
A_-^{(1)} &= A_+^{(1)}, \quad C_-^{(2)} = -C_+^{(2)} \\
&= \frac{i(-1)^{\frac{n+1}{2}} \bar{\epsilon} (r_2 \bar{\epsilon}^{(2)} + c_{12})}{\bar{\epsilon}^{(2)} n^2 \sin \bar{\epsilon} h} A_+^{(1)}, \\
E_-^{(3)} &= -E_+^{(3)} = \frac{i(-1)^{\frac{n+1}{2}} v (r_3 \bar{\epsilon}^{(3)} + c_{45})}{\bar{\epsilon}^{(3)} n^3 \sin \bar{\epsilon} h} A_+^{(1)}. \quad (3.14)
\end{aligned}$$

Now, substituting from Eqs. (3.5)<sub>1</sub>, (3.6), (3.8) - (3.10), (3.12) and (3.13) into either of the two algebraic equations obtained from (3.2)<sub>1</sub> for either  $\bar{\epsilon}_1$  or  $\bar{\epsilon}_2$ , for nonzero  $A_+^{(1)}$  and  $A_-^{(1)}$  we obtain

$$M_n \bar{\epsilon}^2 + P_n v^2 - \frac{n^2 \bar{\epsilon}^{(1)}}{4h^2} + c_{11}^2 = 0, \quad (3.15)$$

where

$$\begin{aligned}
M_n = & c_{11} + \frac{2c_{16}}{\bar{\epsilon}(1)} + r_2 (c_{12} + c_{66}) \\
& + \frac{4(r_2 \bar{\epsilon}^{(2)} + c_{12}) (r_2 \bar{\epsilon}^{(1)} - c_{66})}{n^2 \bar{\epsilon}^{(2)} n^2} \cot \kappa_2 \frac{n\pi}{2}, \quad (3.16)
\end{aligned}$$

$$\begin{aligned}
P_n = & c_{58} + r_3 (c_{36} + c_{45}) \\
& + \frac{4(r_3 \bar{\epsilon}^{(3)} + c_{45}) (r_3 \bar{\epsilon}^{(1)} - c_{36})}{n^2 \bar{\epsilon}^{(3)} n^3} \cot \kappa_3 \frac{n\pi}{2}. \quad (3.17)
\end{aligned}$$

Furthermore, it can be shown<sup>11</sup> that all the equations are satisfied to second order in  $\bar{\epsilon}$  and  $v$ , but not to third order. The dominant algebraic equations for the  $\bar{\epsilon}_1$  and  $\bar{\epsilon}_2$  solutions, respectively, do not yield any conditions to second order in  $\bar{\epsilon}$  or  $v$ , but turn out<sup>11</sup> to be of third order in  $\bar{\epsilon}$  or  $v$ .

Equation (3.15) is the asymptotic dispersion relation for decaying solutions in  $x_1$  and  $x_3$  for the unelectroded plate. Hence, past experience<sup>14</sup> indicates that for trigonometric solutions in  $x_1$  and  $x_3$  for the electroded plate the asymptotic dispersion equations are given by

$$M_n \bar{\epsilon}^2 + P_n v^2 + \frac{n^2 \bar{\epsilon}^{(1)}}{4h^2} - c_{11}^2 = 0, \quad (3.18)$$

where

$$\begin{aligned}
c^{(1)} &= \bar{\epsilon}^{(1)} \left( 1 - \frac{\pi k_{26}}{n^2 \bar{\epsilon}^{(2)}} - 2\hat{R} \right), \\
k_{26}^2 &= \frac{c_{26}^2}{\bar{\epsilon}(1) c_{22}^2}, \quad \hat{R} = \frac{2c_{16} h'}{c_{11} h}, \quad (3.19)
\end{aligned}$$

and  $\rho'$  and  $2h'$  denote the mass density and thickness of the electrodes, respectively.

The manner of derivation of (3.15) reveals that for (3.18) for each  $n$  we must have the homogeneous equation

$$\left( M_n \frac{\partial^2}{\partial x_1^2} + P_n \frac{\partial^2}{\partial x_3^2} + \frac{n^2 - 2c(1)}{4h^2} - \omega^2 \right) u_1^n = 0, \quad (3.20)$$

where  $u_1^n$  is the asymptotic solution function for the  $u_1$ -displacement for the  $n$ th odd harmonic, which is very accurately given by

$$u_1^n = 2A_+^{(1)} \sin \frac{n\pi x_2}{2h} \cos \pi x_1 \cos \pi x_3 e^{i\omega t}, \quad (3.21)$$

for small  $\xi$  and  $\eta$ . Consequently, it is clear that the homogeneous differential equation governing the mode shapes along the surface for  $u_1^n$  may be written in the form

$$M_n \frac{\partial^2 u_1^n}{\partial x_1^2} + P_n \frac{\partial^2 u_1^n}{\partial x_3^2} - \frac{n^2 - 2c(1)}{4h^2} u_1^n - \omega^2 u_1^n = 0, \quad (3.22)$$

since the substitution of (3.21) in (3.22) yields (3.18). When a driving voltage is applied across the surface electrodes it can be shown<sup>11</sup> that a transformation of the inhomogeneous terms from the boundary conditions into the differential equations causes the equation obtained from (3.2)<sub>1</sub> to be inhomogeneous. Now, the homogeneous form of the inhomogeneous equation obtained from (3.2)<sub>1</sub> is the equation from which the dispersion relation (3.18) is ultimately obtained and all other equations are homogeneous as in the case of the eigensolutions<sup>11</sup> leading to (3.18). Since in an expansion in an infinite sum of the eigensolutions of the associated homogeneous problem for the electroded plate with shorted electrodes the equations that remain homogeneous in the inhomogeneous problem are satisfied termwise and the homogeneous form of the inhomogeneous equation yields (3.18), the inhomogeneous differential equation may ultimately be written in the form

$$\sum_{n=1,3,5}^{\infty} \left[ M_n \frac{\partial^2 u_1^n}{\partial x_1^2} + P_n \frac{\partial^2 u_1^n}{\partial x_3^2} - \frac{n^2 - 2c(1)}{4h^2} u_1^n - \omega^2 u_1^n \right] = 2 \frac{e_{26} V x_2}{c(1) 2h} e^{i\omega t}, \quad (3.23)$$

where  $V$  is the driving voltage and

$$u_1^n = \sum_{n=1,3,5}^{\infty} u_1^n, \quad c(1) = \bar{c}(1) (1 - k_{26}^2). \quad (3.24)$$

Utilizing the orthogonality of  $\sin n\pi x_2/2h$  in the interval  $-h$  to  $h$ , from (3.23) we obtain

$$M_n \frac{\partial^2 u_1^n}{\partial x_1^2} + P_n \frac{\partial^2 u_1^n}{\partial x_3^2} - \frac{n^2 - 2c(1)}{4h^2} u_1^n - \omega^2 u_1^n = 2 \frac{e_{26} V x_2}{c(1) 2h} e^{i\omega t}, \quad (3.25)$$

where

$$u_1^n = \tilde{u}_1^n(x_1, x_3, t) \sin \frac{n\pi x_2}{2h}. \quad (3.26)$$

Equation (3.25) is the inhomogeneous differential equation in  $x_1$ ,  $x_3$  and  $t$  governing the system of anharmonic modes associated with the  $n$ th odd harmonic thickness mode for a driving voltage  $V$  applied across the surface electrodes. It can be shown<sup>11</sup> that when (3.25) is applicable the approximate edge conditions to be satisfied at a junction between an electroded and an unelectroded region of an SC-cut quartz plate are the continuity of

$$\tilde{u}_1^n \text{ and } \partial \tilde{u}_1^n / \partial n, \quad (3.27)$$

where  $n$  in  $\partial/\partial n$  represents the normal to the junction.

#### 4. Contoured Resonator

A schematic diagram of a plano-convex resonator is shown in Fig.3. It has been shown that the slowly varying thickness of a spherically contoured resonator can be represented in the form<sup>12</sup>

$$2h = 2h_0 (1 - (x_1^2 + x_3^2)/4Rh_0), \quad (4.1)$$

the substitution of which in (3.25) and expansion to first order in  $x_1^2 + x_3^2$  yields

$$M_n \frac{\partial^2 u_1^n}{\partial x_1^2} + P_n \frac{\partial^2 u_1^n}{\partial x_3^2} - \frac{n^2 - 2c(1)}{4h_0^2} \left[ 1 + \frac{(x_1^2 + x_3^2)}{2Rh_0} \right] u_1^n + \omega^2 u_1^n = 2 \frac{e_{26} V x_2}{c(1) 2h} e^{i\omega t}, \quad (4.2)$$

where

$$\tilde{u}_1^n = u_1^n(x_1, x_3) e^{i\omega t}. \quad (4.3)$$

Equation (4.2) is the inhomogeneous differential equation for the anharmonic family of the  $n$ th odd harmonic of the SC-cut quartz plano-convex resonator. It has been shown that the eigensolutions of the associated homogeneous problem, i.e., of (4.2) with  $V=0$ , can be written in the form<sup>12</sup>

$$u_{nmp} = e^{-\frac{\alpha_n}{2} \frac{x_1^2}{2}} H_m(\sqrt{\frac{\alpha_n}{2}} x_1) e^{-\frac{\beta_n}{2} \frac{x_3^2}{2}} H_p(\sqrt{\frac{\beta_n}{2}} x_3), \quad (4.4)$$

where  $H_m$  and  $H_p$  are Hermite polynomials and

$$\alpha_n^2 = \frac{n^2 - 2c(1)}{8Rh_0^3 M_n}, \quad \beta_n^2 = \frac{n^2 - 2c(1)}{8Rh_0^3 P_n}. \quad (4.5)$$

The eigenfrequencies  $\omega$ , obtained from the solution (4.4) are given by

$$u_{nmp}^2 = \frac{n^2 - 2\epsilon_c(1)}{4h_0^2} \left[ 1 + \frac{1}{n^2} \left( \frac{2h_0}{R} \right)^{1/2} \left( \sqrt{\frac{M_n}{\epsilon_c(1)}} (2m+1) + \sqrt{\frac{P_n}{\epsilon_c(1)}} (2p+1) \right) \right], \quad (4.5)$$

where

$$n = 1, 3, 5, \dots, \quad m, p = 0, 2, 4, \dots \quad (4.7)$$

As noted in the Introduction, since the mode is sharply confined to the vicinity of the center of the plate, the edge of the electrode and, of course, the edge of the plate are both ignored in the treatment used in obtaining the solution presented here.

We now write the steady-state solution of (4.2) as a sum of eigensolutions (4.4), thus

$$u^n = \sum_{m,p} H_{nmp}^{nmp} u_{nmp}. \quad (4.8)$$

Substituting from (4.8) into (4.2) and employing the homogeneous form of (4.2) for each eigensolution, we obtain

$$\sum_{m,p} H_{nmp}^{nmp} (u^2 - u_{nmp}^2) u_{nmp} = u^2 (-1)^{\frac{n-1}{2}} \frac{e_{26} 4V}{c(1) n^2 - 2}, \quad (4.9)$$

from which with the aid of the orthogonality of the  $u_{nmp}$ , we obtain

$$H_{nmp}^{nmp} = \frac{(-1)^{\frac{n-1}{2}} e_{26} 4V}{c(1) n^2 - 2 L_{nmp} [1 - (u^2/x^2)]}, \quad (4.10)$$

where

$$L_{nmp} = \frac{2^m m! 2^p p!}{\epsilon_n \epsilon_n}, \quad \epsilon_{nmp} = 4F_{1nm} F_{3np}, \quad (4.11)$$

and

$$F_{1nm} = \int_0^1 e^{-x_1^2/n^2} H_m(\sqrt{x_1/n}) dx_1, \quad (4.12)$$

$$F_{3np} = \int_0^1 e^{-x_3^2/n^2} H_p(\sqrt{x_3/n}) dx_3.$$

Since the mode is sharply confined to the center of the contoured resonator, in obtaining (4.10) from (4.9) we have replaced the circular electrode of radius  $R$  by the circumscribed square of lengths  $2\hat{x}_1 = 2\hat{x}_3 = 2\hat{x}$  in order to simplify the integrals and obtain (4.12). Thus, we now have the series representation of the steady-state solution for the linear forced vibrations of the contoured resonator. The representation is given by (4.8) with (4.10) - (4.12), (4.4), (4.3), (3.26), (3.24) and (2.29) with (2.30), all in the absence of the term that results from the transformation of

the driving voltage. In the vicinity of a resonance, say the NMPth, one term in the sums in (4.8) with (4.3) and (3.24), dominates and the others are negligible. Thus, from (4.8), (4.3), (3.24), and (2.29), in the vicinity of said resonance the steady-state solution may be written

$$u_1 = H_{NMP}^{NMP} \sin \frac{N^2 x_2}{2h} u_{NMP} e^{i\omega t} - \frac{e_{26} V x_2}{c(1) 2h} e^{i\omega t},$$

$$\phi = \frac{V x_2}{2h} e^{i\omega t} + \frac{e_{26}}{\epsilon_{22}} H_{NMP}^{NMP} u_{NMP} \left( \sin \frac{N^2 x_2}{2h} - (-1)^{\frac{N-1}{2}} \frac{x_2}{h} \right) e^{i\omega t}, \quad (4.13)$$

where we have taken the liberty of introducing the terms resulting from the transformation of the driving voltage, which have heretofore been omitted, and, as usual,  $u_{NMP}$  in (4.13) is to be replaced by

$$u_{NMP} = u_{NMP} + i u_{NMP} / 2Q_{NMP}, \quad (4.14)$$

in which  $Q_{NMP}$  is the unloaded quality factor of the SC-cut contoured resonator in the NMPth mode. The admittance  $Y_{NMP}$  of this SC-cut contoured resonator operating in the NMPth mode is obtained by first substituting from (4.13) into

$$D_2 = e_{26} u_{1,2} - e_{22} \phi_{,2}, \quad (4.15)$$

which is obtained by substituting from (2.21) into (2.6), employing (2.30), and ignoring  $u_2$  and  $\phi_2$ , which are negligible for modes in the vicinity of the  $u_1$ -thickness mode, and then substituting from (4.15) into

$$I = - \int_{\hat{A}_c} \hat{D}_2 dx_1 dx_3, \quad (4.16)$$

with the result

$$Y_{NMP} = \frac{I}{V} = \frac{i\omega \epsilon_{22}}{2h_0} (1 + \hat{k}_{26}^2) \hat{A}_c + \frac{i\omega \epsilon_{22} \hat{k}_{26}^2 4V}{[(\epsilon_{NMP}^2 - 1) N^2 - 2] L_{NMP} h_0}, \quad (4.17)$$

where

$$\hat{k}_{26}^2 = e_{26}^2 / \epsilon_{22} \epsilon_c(1), \quad \hat{A}_c = A_c (1 + \epsilon_{26}^2 / \epsilon_{22} \epsilon_c(1)), \quad (4.18)$$

and in obtaining the second term in (4.17) we have again replaced the circular electrode by the circumscribed square to perform the integrations. The quantities  $\epsilon_c$  and  $\hat{A}_c$ , defined by

$$\epsilon_c = \frac{A_c \epsilon_{22} (1 + \hat{k}_{26}^2)}{2h_0}, \quad \hat{A}_c = \frac{4\epsilon_{22} \hat{k}_{26}^2 4V}{N^2 - 2 L_{NMP} h_0}, \quad (4.19)$$

are called the static and motional capacitances, respectively.

Equation (4.6) has been employed in the calculation of some resonant frequencies of two plano-convex resonators. One resonator has a nominal fundamental frequency of 5 MHz, which corresponds to a plate thickness  $2h_1 = 1.3595$  mm, and a radius of curvature  $R = 5$  cm, and the other resonator has a nominal fundamental frequency of 10 MHz, for which  $2h_2 = 1.1707$  mm, and a radius of curvature  $R = 10$  cm. For each resonator calculations were performed for both very thickness electrodes and 2000-Å thick gold electrodes 4 mm in diameter and the results are given in Tables I and II. We believe that the calculations are accurate because of the accuracy obtained in the case of AT-cut quartz. The static capacitances of each resonator have been calculated from Eq. (4.19), and have the values

$$C_0^1 = 1.7 \text{ pf}; \quad C_0^{10} = 3.75 \text{ pf}. \quad (4.20)$$

The resonant capacitances have been calculated from Eq. (4.19) for some of the modes of each resonator and the results are given in Table III.

#### Acknowledgement

This work was supported in part by the Army Research Office under Contract No. DAAG 29-79-C-0088 and the National Science Foundation under Grant No. MEA-115340.

#### References

1. H.F. Tiersten and R.C. Smythe, "An Analysis of Contoured Crystal Resonators Operating in Overtones of Coupled Thickness Shear and Thickness Twist," *J. Acoust. Soc. Am.*, **65**, 1455 (1979).
2. E.P. Eer Nisse, "Quartz Resonator Frequency Shifts Arising from Electrode Stress," *Proceedings of the 19th Annual Symposium on Frequency Control*, U.S. Army Electronics Command, Fort Monmouth, New Jersey, 1 (1975).
3. A. Ballato, E.P. Eer Nisse and T.J. Lukaszek, "Experimental Verification of Stress Compensation in the SC-Cut," *1978 Ultrasonics Symposium Proceedings*, IEEE Cat. No. CH 1344-1SU, Institute of Electrical and Electronics Engineers, New York, 148 (1978).
4. A. Ballato, "Doubly Rotated Thickness Mode Plate Vibrators," in *Physical Acoustics*, edited by W.E. Mason and R.N. Thurston (Academic, New York, 1977), Vol. XIII, Sec. V.A.2.
5. R.L. Fuller and J.R. Vig, "The Acceleration and Warpage Characteristics of Four-Point-Mounted SC- and AT-Cut Resonators," *Proceedings of the 38th Annual Symposium on Frequency Control*, U.S. Army Electronics Research and Development Command, Fort Monmouth, New Jersey, 110 (1981).
6. L.F. Stevens and H.F. Tiersten, "An Analysis of SC-Cut Quartz Trapped Energy Resonators with Rectangular Electrodes," *Proceedings of the 38th Annual Symposium on Frequency Control*, U.S. Army Electronics Research and Development Command, Fort Monmouth, New Jersey, 205 (1981).
7. Normal coordinates have been used in this manner before in the determination of the dispersion relations at the cut-off frequencies for propagation along the diagonal axis in a monoclinic crystal plate by R.K. Kaul and R.D. Mindlin, "Vibrations of an Infinite, Monoclinic Crystal Plate at High Frequencies and Long Wavelengths," *J. Acoust. Soc. Am.*, **34**, 1895 (1962).
8. H.F. Tiersten, "Analysis of Intermodulation in Thickness-Shear and Trapped Energy Resonators," *J. Acoust. Soc. Am.*, **57**, 667 (1975).
9. H.F. Tiersten, "Analysis of Trapped Energy Resonators Operating in Overtones of Coupled Thickness Shear and Thickness Twist," *J. Acoust. Soc. Am.*, **59**, 879 (1976).
10. H.F. Tiersten, *Linear Piezoelectric Plate Vibrations* (Plenum, New York, 1969), Chap. 7, Sec. 1.
11. For more detail see H.F. Tiersten and D.S. Stevens "An Analysis of Harmonic and Anharmonic Modes in Contoured SC-Cut Quartz Crystal Resonators," to be issued as a technical report, Rensselaer Polytechnic Institute, Troy, New York.
12. W.L. Ferrar, *Algebra* (Oxford, London, 1941), Chap. XII, Sec. 2.2.
13. Ref. 10, Chap. 9, Sec. 2.
14. H.F. Tiersten, "Electromechanical Coupling Factors and Fundamental Material Constants of Thickness Vibrating Piezoelectric Plates," *Ultrasonics*, **8**, 19 (1970).
15. Ref. 4, Sec. III.
16. R.D. Mindlin, "Thickness-Twist Vibrations of an Infinite Monoclinic Crystal Plate," *Intern. J. Solids and Structures*, **1**, 141 (1965).
17. Equations (2.14) and (2.19) of Ref. 1 are written incorrectly in that the sum appearing in (3.23) of this work has been omitted. The remainder of Ref. 1 is correct since the sum on  $n$  properly appears from Eq. (3.11) on in the forced vibration analysis.
18. C.J. Wilson, "Vibration Modes of AT-Cut Convex Quartz Resonators," *J. Phys.*, **D7**, 2449 (1974).
19. P.M. Morse and H. Feshbach, *Methods of Theoretical Physics* (McGraw-Hill, New York, 1953), p. 756.

TABLE I

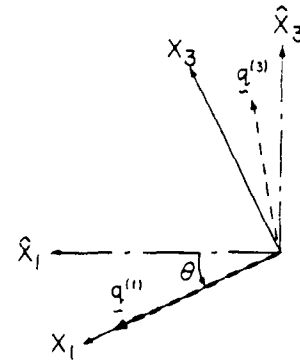
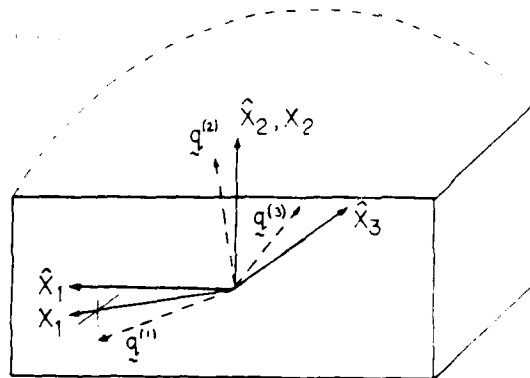
Mode NMP	$\hat{R} = 0$ Freq (kHz)	$\hat{R} = 0.00811$ Freq (kHz)
100	5142.2	5101.4
102	5371.0	5330.1
120	5476.2	5435.3
122	5691.5	5650.4
300	15133.8	15011.6
500	25150.9	24947.2

TABLE II

Mode NMP	$\hat{R} = 0$ Freq (kHz)	$\hat{R} = 0.0162$ Freq (kHz)
100	10196.5	10032.8
102	10524.7	10360.8
120	10676.9	10512.9
122	10990.7	10826.2
300	30181.2	29690.6
500	50200.7	49383.2

TABLE III

Mode NMP	$\hat{R} = 0$ $C_1^5$ (fF)	$\hat{R} = 0$ $C_1^{10}$ (fF)	$\hat{R} = 0.0162$ $C_1^{10}$ (fF)
100	2.39	2.11	2.14
102	.50	1.04	1.05
120	.16	.94	.94
122	.03	.46	.46
300	.10	.07	.07
500	.02	.02	.02

Figure 2. Plan View Showing the Original Coordinate System, the Transformed Coordinate System in the Plane of the Plate and the Projections of the Thickness Solution Eigen Displacements  $u_1$  and  $u_3$  on the Plane of the PlateFigure 1. Schematic Diagram Showing the Original Coordinate System, the Thickness Solution Eigen-Displacement Coordinate System and the Projection of the Eigen Displacement  $u_1$  on the Plane of the Plate

Plano - Convex Resonator

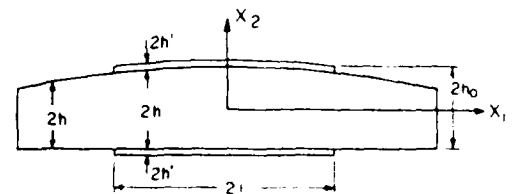


Figure 3. Schematic Diagram Showing a Plano Convex Resonator

## TEMPERATURE INDUCED FREQUENCY CHANGES IN ELECTRODED CONTOURED SC-CUT QUARTZ CRYSTAL RESONATORS

D.S. Stevens and H.F. Tiersten

Department of Mechanical Engineering,  
Aeronautical Engineering & Mechanics  
Rensselaer Polytechnic Institute, Troy, New York 12181

Abstract

A system of approximate plate equations for the determination of thermal stresses in electroded piezoelectric plates is applied to contoured SC-cut quartz crystal resonators. The changes in resonant frequency resulting from the thermally induced biasing stresses and strains are determined from the equation for the perturbation of the eigenfrequency of the piezoelectric solution due to a bias using the modal solutions for the contoured SC-cut quartz crystal resonator. The influence of the electrode size is included in the treatment in addition to the contouring. To this end the very important temperature derivative of the piezoelectric constant for the thickness-mode of interest in SC-cut quartz plates is evaluated from measurement. The changes in resonant frequency with temperature are calculated for the fundamental and some of the odd harmonic overtones which were obtained in the recent analysis of the contoured SC-cut.

1. Introduction

The equation for the perturbation in eigenfrequency of the piezoelectric solution due to a bias has been obtained<sup>1</sup>. The change in resonant frequency due to any bias may readily be found from the perturbation equation if the bias and unbiased mode shape are known. In addition, a system of approximate plate equations for the determination of thermal stresses in thin anisotropic plates coated with large much thinner films has been derived<sup>2</sup> from the static form of Mindlin's plate equations<sup>3-5</sup>. Furthermore, an analysis of contoured SC-cut quartz crystal resonators has been performed<sup>6</sup> and the mode shapes and resonant frequencies have been determined.

In this paper an improved version of the thermally induced biasing three-dimensional displacement field resulting from the solution of the approximate static thermoelastic plate equations<sup>2</sup> is employed in the equation for the perturbation in eigenfrequency<sup>1</sup>, along with the solution for the modes in contoured SC-cut quartz plates<sup>6</sup> and the temperature derivatives of the fundamental elastic constants of quartz<sup>7</sup>, in the calculation of the temperature dependence of the resonant frequencies of contoured SC-cut quartz resonators. However, in order to include the very important influence of the temperature dependence<sup>8</sup> of the motional

capacitive effect of the electrodes on the resonant frequencies, the temperature derivative of the piezoelectric constant for the thickness mode of interest in SC-cut quartz is first evaluated from measurement<sup>9</sup>. Calculated changes in resonant frequency with temperature are presented for the fundamental and some of the odd harmonic overtone thickness-modes of the contoured SC-cut quartz crystal resonator. The calculations clearly reveal the influence of both the contouring and the electrode size on the temperature dependence of the resonant frequency.

2. Perturbation Equations

The equation for the perturbation in eigenfrequency<sup>1</sup> mentioned in the Introduction may be written in the form

$$\dot{\omega}_\mu = H_\mu / 2\omega_\mu, \quad \omega = \omega_\mu - \Delta_\mu, \quad (2.1)$$

where  $\omega_\mu$  and  $\omega$  are the unperturbed and perturbed eigenfrequencies, respectively, and

$$H_\mu = - \int_V [\tilde{K}_{LV}^n g_{V,L}^\mu + \tilde{f}_{L,L}^n] dv, \quad (2.2)$$

and  $V$  is the undeformed volume of the piezoelectric plate at the reference temperature  $T_0$ . In (2.2)  $g_V^\mu$  and  $f_L^\mu$  denote the normalized mechanical displacement vector and electric potential, respectively, of the  $\mu$ th eigensolution, and are defined by

$$g_V^\mu = \frac{u_V^\mu}{N_\mu}, \quad f_L^\mu = \frac{\phi_L^\mu}{N_\mu}, \quad N_\mu^2 = \int_V \rho u_V^\mu u_V^\mu dv, \quad (2.3)$$

where  $u_V^\mu$  and  $\phi_L^\mu$  are the mechanical displacement and electric potential, respectively, which satisfy the equations of linear piezoelectricity

$$\begin{aligned} \tilde{K}_{LV}^f &= \tilde{\epsilon}_{LV} u_{V,M} + e_{MLV} \tilde{\phi}_{L,M}, \\ \tilde{f}_L^f &= e_{LMV} u_{V,M} - \tilde{\epsilon}_{LM} \tilde{\phi}_{L,M}, \end{aligned} \quad (2.4)$$

$$\tilde{K}_{LV,L}^f = \rho \ddot{u}_V, \quad \tilde{f}_{L,L}^f = 0, \quad (2.5)$$

subject to the appropriate boundary conditions. The quantities  $\tilde{\epsilon}_{LV}$ ,  $e_{MLV}$  and  $e_{LMV}$  denote the

second-order elastic, piezoelectric and dielectric constants, respectively, and  $\rho$  denotes the mass density. Equations (2.4) are the linear piezoelectric constitutive relations and (2.5) are the stress equations of motion and charge equation of electrostatics, respectively. The upper cycle notation for many dynamic variables and the capital Latin and lower case Greek index notation is being employed for consistency with Ref.1 as is the remainder of the notation in this section. The variables  $\hat{x}_Y$  and  $\hat{x}_L$  in (2.2) denote the portion of the Piola-Kirchhoff stress tensor and reference electric displacement vector, respectively, resulting from the biasing state and a change in the fundamental material constants in the presence of the  $q_Y$  and  $\hat{f}_L$ , and are given by

$$\begin{aligned}\hat{x}_{LV}^n &= (\hat{c}_{LV\alpha\beta} + \Delta c_{LV\alpha\beta}) g_{\alpha,M}^{\mu} + (\hat{e}_{MLV} + \Delta e_{MLV}) \hat{f}_M^{\mu}, \\ \hat{x}_L^n &= (\hat{e}_{LMV} + \Delta e_{LMV}) g_{Y,M}^{\mu} + (\hat{e}_{LM} + \Delta e_{LM}) \hat{f}_M^{\mu},\end{aligned}\quad (2.6)$$

where  $\hat{c}_{LV\alpha\beta}$ ,  $\hat{e}_{MLV}$ , and  $\hat{e}_{LM}$  are effective constants that depend on the biasing state and  $\Delta c_{LV\alpha\beta}$ ,  $\Delta e_{MLV}$  and  $\Delta e_{LM}$  denote small changes in the fundamental elastic, piezoelectric and dielectric constants, respectively, due to a change in temperature.

When nonlinearities due to biasing deformation only are included, we have

$$\begin{aligned}\hat{c}_{LM} &= b_{LMCD} E_{CD}^1 - 2e_{LM} E_{LM}^1, \\ \hat{e}_{LMV} &= -k_{LMVBC} E_{BC}^1 + e_{LMK} w_{Y,K}, \\ \hat{c}_{LV\alpha\beta} &= T_{LV\alpha\beta}^1 + c_{LV\alpha\beta} E_{AB}^1 + c_{LV\alpha\beta} w_{Y,K} \\ &\quad + c_{LV\alpha\beta} w_{Y,K},\end{aligned}\quad (2.7)$$

where for a thermoelastic biasing state and relatively small changes in temperature  $T$  from the reference temperature  $T_0$ ,

$$\begin{aligned}T_{LM}^1 &= c_{LMKN} E_{KN}^1 - v_{LM} (T - T_0), \\ E_{KN}^1 &= \frac{1}{2} (w_{K,N} + w_{N,K}),\end{aligned}\quad (2.8)$$

$c_{LV\alpha\beta}$ ,  $b_{LM}$  and  $k_{LMVBC}$  denote the third-order elastic constants, the electrostrictive constants and the first-order electroelastic constants, respectively,  $e_{LM}$  denotes the permeability of free-space,  $w_Y$  denotes the static biasing displacement field, and  $v_{LM}$  denotes the thermoelastic coupling coefficients. Thus, in this description the present position  $y$  is related to the reference position  $X$  by

$$y(X_L, t) = X_L + w(X_L, t) + u(X_L, t). \quad (2.9)$$

### 3. Temperature Induced Biasing State

A schematic diagram of the contoured plate along with the associated coordinate system is

shown in Fig.1. It has been shown that referred to the coordinate system in Fig.1 the static purely extensional thermoelastic plate equations for the plated crystal plate may be written in the form

$$v_{AB,A}^{(0)} = 0, \quad v_{AB,A}^{(2)} = 0, \quad (3.1)$$

where  $A, B, C, D$  take the values 1 and 3 and skip 2 and  $v_{AB}^{(0)}$  and  $v_{AB}^{(2)}$  are the zero and second order plate stress resultants, respectively, for the electroded crystal plate. For homogeneous temperature states and identical electrodes on the upper and lower surfaces the extensional constitutive equations may be written in the form

$$\begin{aligned}v_{AB}^{(0)} &= 2h \left( v_{ABCD} + \frac{2h'}{h} v_{ABCD}' \right) E_{CD}^{(0)} + 2h \left( \frac{1}{3} v_{ABCD} + \frac{2h'}{h} v_{ABCD}' \right) E_{CD}^{(2)} - 2h \left( \hat{e}_{AB} + \frac{2h'}{h} v_{AB}^{*'} \right) (T - T_0), \\ v_{AB}^{(2)} &= \frac{2}{3} h^3 \left( v_{ABCD} + \frac{6h'}{h} v_{ABCD}' \right) E_{CD}^{(0)} + \frac{2}{5} h^5 v_{ABCD} + \frac{10h'}{h} v_{ABCD}' E_{CD}^{(2)} - \frac{2}{3} h^3 \left( \hat{e}_{AB} + \frac{6h'}{h} v_{AB}^{*'} \right) (T - T_0),\end{aligned}\quad (3.2)$$

where

$$v_R^{*'} = v_R' - v_{2R}' c_{2R}' / c_{22}', \quad (3.3)$$

in the compressed notation and we have introduced the usual compressed matrix notation for tensor indices according to the scheme

$$R, S = 1, 3, 5; \quad W, V = 2, 4, 6, \quad (3.4)$$

and

$$v_{RS} = c_{RS} - c_{RW} c_{WV}^{-1} c_{VS}, \quad \hat{e}_R = v_R - c_{RW} c_{WV}^{-1} v_V. \quad (3.5)$$

The  $v_{AB}$  are Voigt's anisotropic plate elastic constants and the  $\hat{e}_A$  are the associated anisotropic plate thermoelastic constants. For the case of anisotropic extension considered here the three-dimensional strains  $E_L$ , which are needed in the perturbation equation, are related to the plate strains by

$$E_{KL} = \frac{1}{2} (w_{K,L} + w_{L,K}) = E_{KL}^{(0)} + x_{KL}^2 E_{KL}^{(2)}. \quad (3.6)$$

The plate strains  $E_{AB}^{(n)}$  ( $n=0,2$ ), which occur in (3.2), are given by

$$E_{AB}^{(n)} = \frac{1}{2} (w_{A,B}^{(n)} + w_{B,A}^{(n)}), \quad (3.7)$$

and the remaining plate strains, which are needed in (3.6) as well, may be obtained from

$$\begin{aligned}E_W^{(0)} &= -c_{WV}^{-1} c_{VS} E_S^{(0)} + c_{WV}^{-1} v_V (T - T_0), \\ E_W^{(2)} &= -c_{WV}^{-1} c_{VS} E_S^{(2)}.\end{aligned}\quad (3.8)$$

The foregoing has been for the electroded portion of the plate. In the unelectroded portion the situation is somewhat simpler and we have the ordinary stress equations of equilibrium

$$T_{ML,M}^1 = 0, \quad (3.9)$$

along with the constitutive equations (2.8)<sub>1</sub>. Since the outside edges of the plate are traction free along with the unelectroded major surfaces, we have

$$\hat{N}_M T_{ML}^1 = 0, \quad (3.10)$$

on all unelectroded surfaces, where  $\hat{N}_M$  denotes the unit normal to all unelectroded surfaces of the plate at  $T=T_0$ . From (3.9) and (3.10) we have

$$T_{ML}^1 = 0, \quad (3.11)$$

for the unelectroded portion of the plate. Since the thermoelastic coupling constants  $v_{ML}$  are related to the coefficients  $\alpha_{JK}$  by the usual relation

$$v_{ML} = c_{MLJK} \alpha_{JK}, \quad (3.12)$$

from (2.8)<sub>1</sub>, (3.11) and (3.12), we have

$$E_{JK}^1 = \alpha_{JK} (T - T_0), \quad (3.13)$$

in the unelectroded region.

By virtue of (3.11), along the edges of the electroded region of the plate, we have

$$N_A v_{AB}^{(0)} = 0, \quad N_A v_{AB}^{(2)} = 0, \quad (3.14)$$

where  $N_A$  denotes the outwardly directed unit normal to the edge of the electrode at  $T=T_0$ . The solution satisfying (3.14) and (3.1) takes the form

$$v_{AB}^{(0)} = 0, \quad v_{AB}^{(2)} = 0. \quad (3.15)$$

This solution is unique to within static homogeneous plate rotations of zero and second order. Substituting from (3.2) into (3.15), we obtain

$$\begin{aligned} \left( v_{RS} + \frac{2h'}{h} v_{RS}' \right) E_S^{(0)} + h \left( \frac{2}{3} v_{RS} + \frac{2h'}{h} v_{RS}' \right) E_S^{(2)} \\ = \left( \bar{s}_R + \frac{2h'}{h} v_R^{*'} \right) (T - T_0), \\ \left( v_{RS} + \frac{6h'}{h} v_{RS}' \right) E_S^{(0)} + h \left( \frac{2}{5} v_{RS} + \frac{6h'}{h} v_{RS}' \right) E_S^{(2)} \\ = \left( \bar{s}_R + \frac{6h'}{h} v_R^{*'} \right) (T - T_0). \end{aligned} \quad (3.16)$$

Equations (3.16) constitute six inhomogeneous linear equations which may readily be solved for the six plate strains  $E_{ij}^{(0)}$  and  $E_{ij}^{(2)}$ . When  $E_{ij}^{(0)}$  and  $E_{ij}^{(2)}$  have been determined from (3.16),  $E_{ij}^{(1)}$  and  $E_{ij}^{(3)}$  are readily determined from (3.8). Then the three-dimensional biasing strain can be obtained from (3.6), which is for anisotropic extension. There is no flexure because the resonator has identical electrodes and is subject to a homogeneous temperature change  $(T - T_0)$ .

We now note that since the equations of equilibrium for the plate stress resultants, (3.1), are satisfied trivially, only the homogeneous plate strains  $E_{ij}^{(1)}$  and  $E_{ij}^{(3)}$  can be determined from (3.16) and (3.8), which yield  $E_{ij}^{(1)}$  from (3.6), but Eqs. (2.6) and (2.7) reveal that the biasing three-dimensional displacement gradients  $w_{i,j}$  are required in order to evaluate the perturbation integral  $H_1$  in (2.2). Whenever only plate strains  $E_{ij}^{(1)}$  are determined from the plate equations, the associated plate rotations  $\psi_{ij}^{(1)}$  are determined by requiring consistency with the three-dimensional rotation gradient-strain gradient relations

$$\psi_{KL,M} = E_{ML,K} - E_{MK,L}, \quad (3.17)$$

where

$$\psi_{KL} = \frac{1}{2} (w_{L,K} - w_{K,L}), \quad \psi_{KL}^{(n)} = \frac{1}{2} [w_{L,K}^{(n)} - w_{K,L}^{(n)}] + (n+1) \left( \frac{1}{2} w_L^{(n+1)} - \frac{1}{2} w_K^{(n+1)} \right). \quad (3.18)$$

Then the three-dimensional displacement gradients in the electroded region are given by

$$\begin{aligned} w_{A,B} = E_{AB}^{(0)} + X_2^2 E_{AB}^{(2)}, \quad w_{2,A} = E_{2A}^{(0)} \\ w_{A,2} = E_{2A}^{(0)} + 2X_2^2 E_{2A}^{(2)}, \quad w_{2,2} = E_{22}^{(0)} + X_2^2 E_{22}^{(2)}, \end{aligned} \quad (3.19)$$

which with (3.16), (3.8), (2.7)<sub>3</sub> and (2.8) yields  $\hat{c}_{ijvw}$  in the electroded region as a known linear function of  $(T - T_0)$ . In the unelectroded region the homogeneous strain state is given by (3.13) and the static homogeneous (global) infinitesimal rigid rotation is arbitrary<sup>4</sup>. In fact, the change in frequency due to a homogeneous infinitesimal rigid rotation has been shown to vanish<sup>5</sup>. Consequently, we may select the homogeneous infinitesimal rigid rotation to take any value that is convenient and in particular to vanish, and we have

$$\psi_{KL}^1 = \frac{1}{2} (w_{L,K} - w_{K,L}) = 0, \quad (3.20)$$

which with (2.8)<sub>2</sub> and (3.13) yields

$$w_{J,K} = \psi_{JK} (T - T_0). \quad (3.21)$$

The substitution of (3.13), (3.21) and (3.11) in (2.7)<sub>3</sub> yields  $\hat{c}_{ijvw}$  as a known linear function of  $(T - T_0)$  in the unelectroded region.

#### 4. Eigenmodes in Contoured Resonators and the Equivalent Trapped Energy Mode

It has been shown that the eigensolutions for contoured SC-cut quartz resonators, referred to coordinate axes obtained from the eigenvector triad of the pure thickness solution for the SC-cut, can be written in the form

$$u_{lnmp} = \sin \frac{n\pi X_2}{2h} u_{nmp} e^{i l \pi n p t}, \quad (4.1)$$

where the  $X_2$ -axis is shown in Fig.1 and  $u_1$  is in the direction of the thickness eigendisplacement of interest<sup>6</sup> and

$$u_{nmp} = A_{nmp} e^{-\alpha_n \frac{x_1^2}{2}} H_m(\sqrt{\alpha_n} x_1) e^{-\beta_n \frac{x_3^2}{2}} H_p(\sqrt{\beta_n} x_3), \quad (4.2)$$

and along with  $u_1$  we have

$$\varphi = \frac{\epsilon_{26}}{\epsilon_{22}} u_{nmp} \left( \sin \frac{n\pi x_2}{2h} - (-1)^{\frac{n-1}{2}} \frac{x_2}{h} \right) e^{i\omega_{nmp} t}, \quad (4.3)$$

where for the modes of interest<sup>6</sup>

$$n=1,3,5, \dots; m,p=0,2,4, \dots. \quad (4.4)$$

In (4.2)  $H_m$  and  $H_p$  are Hermite polynomials and

$$\alpha_n^2 = \frac{n^2 \pi^2 \epsilon_{26}^2 (1)}{8 R h_o^3 M_n}, \quad \beta_n^2 = \frac{n^2 \pi^2 \epsilon_{26}^2 (1)}{8 R h_o^3 P_n}, \quad (4.5)$$

where

$$M_n = c_{11} + \frac{2c_{16}^2}{\bar{\epsilon}(1)} + r_2(c_{12} + c_{66}) + \frac{4(r_2 \bar{\epsilon}(2) + c_{12})(r_2 \bar{\epsilon}(1) - c_{66})}{n\pi \bar{\epsilon}(2) \kappa_2} \cot \kappa_2 \frac{n\pi}{2},$$

$$P_n = c_{55} + r_3(c_{36} + c_{45}) + \frac{4(r_3 \bar{\epsilon}(3) + c_{45})(r_3 \bar{\epsilon}(1) - c_{36})}{n\pi \bar{\epsilon}(3) \kappa_3} \cot \kappa_3 \frac{n\pi}{2}, \quad (4.6)$$

and

$$\kappa_2 = \sqrt{\frac{\bar{\epsilon}(1)}{\bar{\epsilon}(2)}}, \quad \kappa_3 = \sqrt{\frac{\bar{\epsilon}(1)}{\bar{\epsilon}(3)}}, \quad r_2 = \frac{c_{12} + c_{66}}{\bar{\epsilon}(1) - \bar{\epsilon}(2)},$$

$$r_3 = \frac{c_{36} + c_{45}}{\bar{\epsilon}(1) - \bar{\epsilon}(3)}. \quad (4.7)$$

In Eqs. (4.3) - (4.9) the material constants are the transformed constants discussed in Ref.6 and the  $\bar{\epsilon}(i)$  ( $i=1,2,3$ ) are the eigenvalues for the piezoelectrically stiffened plane waves for the thickness direction of the SC-cut<sup>6</sup>. The eigenfrequencies for this eigensolution are given by

$$\omega_{nmp}^2 = \frac{n^2 \pi^2 \epsilon_{26}^2 (1)}{4 h_o^2 \rho} \left[ 1 + \frac{1}{n\pi} \sqrt{\frac{2h_o}{R}} \left( \sqrt{\frac{M_n}{\bar{\epsilon}(1)}} (2m+1) + \sqrt{\frac{P_n}{\bar{\epsilon}(1)}} (2p+1) \right) \right], \quad (4.8)$$

where

$$\bar{\epsilon}(1) = \bar{\epsilon}(1) / \left( 1 - \frac{8k_{26}^2}{n^2 \pi^2} - 2R \right),$$

$$k_{26}^2 = \frac{\epsilon_{26}^2}{\bar{\epsilon}(1) \epsilon_{22}}, \quad R = \frac{2c_{16}^2}{c_{11} c_{22}}, \quad (4.9)$$

and  $c$  and  $c'$  are the mass densities of the quartz and electrodes, respectively.

In addition to  $u_{1nmp}$  given in (4.1) there are both  $u_{2nmp}$  and  $u_{3nmp}$ , which are an order of magnitude smaller than  $u_{1nmp}$ , but are required in this work because the SC-cut is thermally compensated for the pure thickness mode of interest. However, since the  $u_2$ - and  $u_3$ -displacement fields accompanying the larger  $u_1$ -displacement field are known only for the electroded and unelectroded flat plate<sup>6,7,8</sup>, we fit the Gaussian mode shape given in (4.1) and (4.2) for the contoured resonator to a trapped energy mode<sup>9</sup> in a flat plate in accordance with the diagram shown in Fig.2. Since the Gaussian mode shape is sharply confined to the vicinity of the center of the contoured resonator, we replace the circular electrode by the circumscribed square for convenience in performing the perturbation integrals (2.2). Furthermore, for the same reasons we take the flat plate to have the thickness  $2h_o$  in the central region and the thicknesses  $2h_1$  and  $2h_3$  of the contoured resonator at the lines of inflection of the Gaussian mode shape in the  $X_1$ - and  $X_3$ -directions, respectively, which are given by

$$2h_1 = 2h_o (1 - a_1^2/4Rh_o), \quad 2h_3 = 2h_o (1 - a_3^2/4Rh_o). \quad (4.10)$$

The equivalent trapped energy mode is fitted to the Gaussian by matching the Gaussian at the center of the plate and requiring the volumes under the Gaussian mode shape and the equivalent trapped energy mode to be separately the same under the inner rectangular region defined by the lines of inflection of the Gaussian mode shape in the two directions and the outer regions. This is a reasonable procedure for our purposes because such a function can match the Gaussian quite well, we integrate over the mode shape in the perturbation integral (2.2) and the analysis in Sec.3 shows that the thermally induced biasing state consists of two essentially homogeneous states.

Since the equivalent trapped energy mode is to be determined by matching to the known Gaussian mode shape in accordance with the foregoing procedure, the dispersion relations are not needed and only the continuity of the mechanical displacement  $u_1$  need be imposed at the line of inflection in each direction. The solution functions for the trapped energy eigen modes have been shown to be of the form

$$\bar{u}_1 = \bar{B} \sin \frac{n\pi x_2}{2h} \cos \bar{\epsilon}_1 x_1 \cos \bar{\epsilon}_3 x_3,$$

$$S_1 = \bar{B}^S \sin \frac{n\pi x_2}{2h} e^{-\bar{\epsilon}_1^S (x_1 - a_1)} \cos \bar{\epsilon}_3 x_3,$$

$$u_1^T = B^T \sin \frac{n\pi X_2}{2h} \cos \bar{\xi} X_1 e^{-\nu^T(X_3-a_3)},$$

$$u_1^C = B^C \sin \frac{n\pi X_2}{2h} e^{-\bar{\xi}^S(X_1-a_1)} e^{-\nu^T(X_3-a_3)}. \quad (4.11)$$

In accordance with the matching procedure outlined, we take

$$\bar{B} = A_{nmp}, \quad (4.12)$$

and obtain  $\bar{\xi}$  and  $\bar{\nu}$  from the relation

$$\int_0^{a_1} e^{-\bar{\nu} X_1} H_m(\sqrt{\frac{\bar{\nu}}{2}} X_1) dX_1 = \int_0^{a_3} e^{-\bar{\nu} X_3} H_p(\sqrt{\frac{\bar{\nu}}{2}} X_3) dX_3$$

$$= \int_0^{a_1} \cos \bar{\xi} X_1 dX_1 = \int_0^{a_3} \cos \bar{\nu} X_3 dX_3, \quad (4.13)$$

from which, by separately equating the product integrals, we obtain the transcendental equations

$$\frac{\sin \bar{\xi} a_1}{\bar{\xi} a_1} = \frac{-}{\sqrt{2\bar{\nu} a_1}} \operatorname{erf}\left(\sqrt{\frac{\bar{\nu}}{2}} a_1\right),$$

$$\frac{\sin \bar{\nu} a_3}{\bar{\nu} a_3} = \frac{-}{\sqrt{2\bar{\xi} a_3}} \operatorname{erf}\left(\sqrt{\frac{\bar{\xi}}{2}} a_3\right), \quad (4.14)$$

for the fundamental and harmonic overtones. The one root of each of (4.14) determines the values of  $\bar{\xi}$  and  $\bar{\nu}$  for the equivalent trapped mode. Equation (4.13), and, of course, (4.14) are for the harmonic modes only, for which  $H_1 = H_2 = 1$ .

Since the equivalent trapped energy mode is continuous at the junctions, the relations between the amplitudes in the different regions are

$$B^S = \bar{B} \cos \bar{\xi} a_1, \quad B^T = \bar{B} \cos \bar{\nu} a_3,$$

$$B^C = \bar{B} \cos \bar{\xi} a_1 \cos \bar{\nu} a_3. \quad (4.15)$$

which with (4.12) gives all amplitudes of the equivalent trapped energy mode in terms of the amplitude of the Gaussian mode shape. By following a procedure similar to the one employed in the treatment of the central region, for  $H_1 = H_2 = 1$ , we obtain

$$\bar{\xi}^S = \frac{\cos \bar{\xi} a_1}{\int_0^{a_1} e^{-\bar{\nu} X_1} H_m(\sqrt{\frac{\bar{\nu}}{2}} X_1) dX_1}, \quad \bar{\nu}^T = \frac{\cos \bar{\nu} a_3}{\int_0^{a_3} e^{-\bar{\xi} X_3} H_p(\sqrt{\frac{\bar{\xi}}{2}} X_3) dX_3}.$$

$$(4.16)$$

We now have the  $u_1$ -displacement field for the equivalent trapped energy mode.

As noted earlier in addition to the  $u_1$  ( $\bar{u}_1$ ) displacement field there are accompanying  $u_2$  ( $\bar{u}_2$ ) and  $u_3$  ( $\bar{u}_3$ ) displacement fields, and to the same order in  $\bar{\xi}$  ( $\bar{\nu}$ ) there are accompanying corrections to the  $u_1$  ( $\bar{u}_1$ ) displacement fields, which are given by

$$\bar{u}_1 = \bar{B} \left( 1 + \frac{c_{16}}{\bar{c}(1)} \bar{\xi} X_2 \right) \sin \frac{n\pi X_2}{2h} \cos \bar{\xi} X_1 \cos \bar{\nu} X_3,$$

$$\bar{u}_2 = \left[ \frac{r_2 \bar{\xi} 2h}{n\pi} \bar{B} \cos \frac{n\pi X_2}{2h} + \bar{C} \cos \frac{\kappa_2 n\pi X_2}{2h} \right] \sin \bar{\xi} X_1 \cos \bar{\nu} X_3,$$

$$\bar{u}_3 = \left[ \frac{r_3 \bar{\nu} 2h}{n\pi} \bar{B} \cos \frac{n\pi X_2}{2h} + \bar{E} \cos \frac{\kappa_3 n\pi X_2}{2h} \right] \cos \bar{\xi} X_1 \sin \bar{\nu} X_3, \quad (4.17)$$

where

$$\bar{C} = (-1)^{\frac{n+1}{2}} \frac{(r_2 \bar{c}(2) + c_{12}) \bar{\xi} 2h \bar{B}}{\bar{c}(2) \kappa_2 n\pi \sin \kappa_2 n\pi/2},$$

$$\bar{E} = (-1)^{\frac{n+1}{2}} \frac{(r_3 \bar{c}(3) + c_{45}) \bar{\nu} 2h \bar{B}}{\bar{c}(3) \kappa_3 n\pi \sin \kappa_3 n\pi/2}, \quad (4.18)$$

and

$$u_1^S = B^S \left( 1 + \frac{c_{16}}{\bar{c}(1)} \bar{\xi} X_2 \right) \sin \frac{n\pi X_2}{2h} e^{-\bar{\xi}^S(X_1-a_1)} \cos \bar{\nu} X_3,$$

$$u_2^S = \left[ \frac{r_2 \bar{\xi}^S 2h}{n\pi} B^S \cos \frac{n\pi X_2}{2h} + C^S \cos \frac{\kappa_2 n\pi X_2}{2h} \right] \cdot e^{-\bar{\xi}^S(X_1-a_1)} \cos \bar{\nu} X_3,$$

$$u_3^S = \left[ \frac{r_3 \bar{\nu}^S 2h}{n\pi} B^S \cos \frac{n\pi X_2}{2h} + E^S \cos \frac{\kappa_3 n\pi X_2}{2h} \right] \cdot e^{-\bar{\xi}^S(X_1-a_1)} \sin \bar{\nu} X_3, \quad (4.19)$$

where

$$C^S = (-1)^{\frac{n+1}{2}} \frac{(r_2 \bar{c}(2) + c_{12}) \bar{\xi}^S 2h B^S}{\bar{c}(2) \kappa_2 n\pi \sin \kappa_2 n\pi/2},$$

$$E^S = (-1)^{\frac{n+1}{2}} \frac{(r_3 \bar{c}(3) + c_{45}) \bar{\nu}^S 2h B^S}{\bar{c}(3) \kappa_3 n\pi \sin \kappa_3 n\pi/2}, \quad (4.20)$$

with similar expressions<sup>11</sup> for  $u_2^T$  and  $u_3^C$ . As noted earlier in this section this solution is referred to the eigenvector triad of the pure thickness solution for the SC-cut<sup>11</sup>. For purposes of calculation of the temperature dependence of the resonant frequency it is advisable<sup>11</sup> to transform back to the original conventional coordinate axes for the SC-cut, thus

$$\tilde{u}_i = Q_{2i} u_i, \quad (4.21)$$

where  $\tilde{u}_i$  denotes the components of the mechanical displacement in the original coordinate system for the SC-cut and  $Q_{2i}$  denotes the transformation from that system to the eigenvector triad.

## 5. Temperature Dependence of Resonant Frequency

The change in the resonant frequency with temperature of any electroded contoured SC-cut quartz plate resulting from the thermally induced biasing may now be determined from (2.1) and (2.2) with (2.6) and (2.7). However, Eq. (2.2) cannot be used for calculation as it appears because the temperature derivatives of the complete piezoelectric and dielectric tensors are not presently known, nor are all the fundamental coefficients appearing in (2.7) known. Nevertheless, since the piezoelectric coupling and wavenumbers along the plate are both small, the temperature dependence of only the transformed thickness piezoelectric and dielectric constants  $e_{26}$  and  $\epsilon_{22}$  need be retained in  $H_L$ . Moreover, since  $(1/e_{26})de_{26}/dT \gg (1/\epsilon_{22})d\epsilon_{22}/dT$ , we ignore  $(1/\epsilon_{22})d\epsilon_{22}/dT$ . Furthermore  $(1/e_{26})de_{26}/dT$  can and should be excluded from wave terms in  $H_L$  because the existing temperature derivatives of the fundamental elastic constants of quartz effectively contain the small influence of the temperature dependence of the piezoelectric and dielectric constants, which results from the piezoelectric stiffening of the waves. In addition, we ignore the  $\partial e_{ij}/\partial T$  since they are not known. Then the  $(1/e_{26})de_{26}/dT$  that we retain is not fundamental but effective<sup>11</sup>. In view of the foregoing, the general electroelastic perturbation integral in (2.2) with (2.6) and (2.7) may be written in the reduced form<sup>12</sup>

$$H_L = - \frac{1}{V} \int_V (\hat{c}_{LVM_0} + \Delta \hat{c}_{LVM_0}) \tilde{g}_{1,M}^L \tilde{g}_{V,L}^L - \frac{2c_{26}^2}{\epsilon_{22}} \frac{1}{c_{26}} g_{1,2}^{(u)} \frac{g_1^{(h)}(h)}{h} \Big] dV, \quad (5.1)$$

where

$$L = (T - T_0)d/dT. \quad (5.2)$$

In (5.1) the first term under the integral sign is decomposed in the original conventional coordinate system for the SC-cut because the  $\hat{c}_{LVM_0}$  and  $\Delta \hat{c}_{LVM_0}$  are known in that coordinate system, while the second term is decomposed along the eigenvector trial of the pure thickness solution<sup>13</sup>. From (5.1) for the geometry shown in Fig. 2, we obtain

$$H_L = -4 \int_{-h}^h dx_2 \left[ \int_0^{\frac{1}{2}} dx_1 \left( \int_0^{\frac{1}{2}} (\bar{C} + \bar{C}) dx_3 + \int_{\frac{1}{2}}^{\frac{3}{2}} \bar{C} dx_3 \right) + \int_0^{\frac{1}{2}} dx_1 \left( \int_0^{\frac{1}{2}} \bar{S} dx_3 + \int_{\frac{1}{2}}^{\frac{3}{2}} \bar{C} dx_3 \right) \right], \quad (5.3)$$

where

$$\bar{C} = (\hat{c}_{LVM_0} + \Delta \hat{c}_{LVM_0}) \tilde{g}_{1,M}^L \tilde{g}_{V,L}^L, \quad \bar{S} = -2 \frac{c_{26}^2}{\epsilon_{22}} \frac{1}{c_{26}} g_{1,2}^{(u)} \frac{g_1^{(h)}(h)}{h}. \quad (5.4)$$

The  $\tilde{g}_{1,M}^L$  in (5.4) are known as linear expressions in  $(T - T_0)$  from the analyses in Sec. 3 and the change in the elastic constants with temperature

$\Delta \hat{c}_{LVM_0}$  are given by

$$\Delta \hat{c}_{LVM_0} = (dc_{LVM_0}/dT)(T - T_0), \quad (5.5)$$

where the  $dc_{LVM_0}/dT$  are obtained from the first temperature derivatives of the fundamental elastic constants of quartz  $dc_{LVM_0}/dT$  referred to the principal axes by the tensor transformation relation

$$\frac{d}{dT} \hat{c}_{LVM_0} = a_{LD}^a a_{VE}^a a_{MF}^a a_{NG}^a \frac{d}{dT} \hat{c}_{2DEFG}, \quad (5.6)$$

where the  $a_{ij}$  are the matrix of direction cosines for the transformation from the principal axes to the coordinate system containing the axes referred to the electroded plate. When the conventional IEEE notation<sup>14</sup> for doubly-rotated plates is written in the form  $(Y, X, W, I)C, S$ , where  $v = 0$ , the rotation angles  $\psi$  and  $\theta$  are the first two Euler angles, and for the SC-cut,  $\psi = -34.184^\circ$ ,  $\theta = 21.93^\circ$ , from which the  $a_{ij}$  can be determined<sup>15</sup>. Clearly, the transformation relations for the second and third order elastic, piezoelectric and dielectric constants, and coefficients of linear expansion may be written in the respective forms

$$\begin{aligned} \hat{c}_{KLMN} &= a_{KD}^a a_{LE}^a a_{MF}^a a_{NG}^a \hat{c}_{2DEFG}, \\ \hat{c}_{KLMNAB} &= a_{KD}^a a_{LE}^a a_{MF}^a a_{NG}^a a_{AH}^a a_{BI}^a \hat{c}_{3DEFGHI}, \\ \hat{c}_{KLM} &= a_{KD}^a a_{LE}^a a_{MF}^a \hat{c}_{DEF}, \\ \hat{c}_{KL} &= a_{KD}^a a_{LE}^a \hat{c}_{MN}, \quad \hat{c}_{KL} = a_{KM}^a a_{LN}^a \hat{c}_{KN}, \end{aligned} \quad (5.7)$$

where the tensor quantities with the upper cycle are referred to the principal axes of the crystal.

Before the temperature dependence of the resonant frequency of a contoured SC-cut quartz resonator can be calculated, the temperature dependence of  $c_{26}$  must be estimated from experimental data. This estimate has been made using data<sup>16</sup> on the temperature dependence of the resonant frequencies of both the fundamental and fifth harmonic overtone trapped energy modes in SC-cut quartz plates with rectangular electrodes. From the data provided by Lukaszek<sup>16</sup> and the analysis we obtain the estimate<sup>17</sup>

$$(1/c_{26})dc_{26}/dT = -4.6 \times 10^{-4} \text{ K}^{-1}. \quad (5.8)$$

Calculations have been performed using the known values of the second order elastic, piezoelectric and dielectric constants of quartz<sup>18</sup>, the third order elastic<sup>19</sup> and thermoelastic<sup>20</sup> constants of quartz and the recently obtained first temperature derivatives of the fundamental elastic constants of quartz along with the estimate in (5.8). The results of the calculations are presented in Figs. 3-7. Figure 3 shows the calculated change in frequency with temperature of the SC-cut ( $\psi = -34.184^\circ$ ,  $\theta = 21.93^\circ$ ) as a function of the radius of curvature for the first, third and fifth harmonics for a nominal fundamental frequency of

5 MHz, which corresponds to a plate thickness  $2h = .3595$  mm. An electrode diameter  $2r$  of 4 mm is assumed unless otherwise noted. The results are independent of the thickness of the electrode because the influence of the electrode thickness is about two orders of magnitude smaller than the scale shown in the figure. Note that the curves are asymptotic to values determined by the electrode size for the partially electroded flat plate as  $R$  becomes large. Figure 4 shows the same type of information as Fig. 3, but for an SC-cut with a nominal fundamental frequency of 10 MHz, which corresponds to a plate thickness  $2h = .179$  mm. Note that in both Figs. 3 and 4 the slope of the change in frequency with temperature as a function of radius of curvature is much less for the fundamental mode than for the overtones in the vicinity of the AT-cut, and that the slope is much shallower for the overtone modes than for the fundamental mode. The change in frequency due to the presence of 2000 Å thick gold electrodes<sup>2,3</sup> for which the actual changes are shown in Fig. 4. Since a portion of the aging rate is a result of the relaxation of residual stress in the electrodes, the change in frequency shown in Fig. 5 is the portion of the actual change in the frequency that contributes to the aging rate. Note that the change in frequency with temperature due to the electrodes shown in Fig. 5 is about two orders of magnitude smaller than the actual change shown in Fig. 4. Figure 5 shows that the change in frequency with temperature resulting from the electrodes for the SC-cut is about one-tenth of that for the AT-cut, thereby substantiating the fact that the SC-cut will have much better aging characteristics than the SC-cut. Figure 6 shows the change in frequency with temperature vs. the  $L/h$  ratio for a plane-convex SC-cut resonator with a center thickness  $2h = .3595$  mm, a radius of curvature  $R = 5$  cm. Figure 6 clearly shows that the change in frequency with temperature is a rather significant function of the electrode configuration for small  $L/h$  ratios and is asymptotic to different values for each harmonic of the fully electroded contoured resonator at different  $L/h$  ratios. Note that the overtones are asymptotic to their fully electroded values at much lower  $L/h$  ratios than the fundamental. This is a result of the fact that the harmonics are much more sharply confined to the center of the plate than the fundamental. Finally Fig. 7 shows scissored plates at the rotation angle  $\theta$  for a fixed angle  $\theta = 21.1^\circ$  for the zero temperature cut as a function of the value of curvature  $R$  for the first, third and fifth harmonics for the two different values of  $L/h$  considered here.

#### Acknowledgments

We wish to thank A. Ballato and T.J. Lukaszek of the U.S. Army Electronics Technology and Devices Laboratory for kindly providing the data used in the estimation of electrode aging.

This work was supported in part by the Army Research Office under Contract No. DAAG 29-79-C-0088 and the National Science Foundation under Grant No. MEA 8115349.

#### References

1. H.F. Tiersten, "Perturbation Theory for Linear Electroelastic Equations for Small Fields Superposed on a Bias," *J. Acoust. Soc. Am.*, **64**, 832 (1978).
2. H.F. Tiersten and B.K. Sinha, "Temperature Dependence of the Resonant Frequency of Electroded Doubly-Rotated Quartz Thickness-Mode Resonators," *J. Appl. Phys.*, **50**, 4038 (1979).
3. R.D. Mindlin, "An Introduction to the Mathematical Theory of the Vibration of Elastic Plates," U.S. Army Signal Corps Eng. Lab., Fort Monmouth, New Jersey (1955). Signal Corps Contract DA-36-03956-56772.
4. R.D. Mindlin, "High Frequency Vibrations of Crystal Plates," *Quart. Appl. Math.*, **19**, 51 (1961).
5. H.F. Tiersten, *Linear Piezoelectric Plate Vibrations* (Plenum, New York, 1969), Chap. 13.
6. H.F. Tiersten and D.S. Stevens, "An Analysis of Contoured SC-Cut Quartz Crystal Resonators," *Proceedings of the 36th Annual Symposium on Frequency Control*, U.S. Army Electronics Research and Development Command, Fort Monmouth, New Jersey (1982), previous paper.
7. B.K. Sinha and H.F. Tiersten, "First Temperature Derivatives of the Fundamental Elastic Constants of Quartz," *J. Appl. Phys.*, **50**, 2732 (1979).
8. M. Onoe, "Relationship Between Temperature Behavior of Resonant and Antiresonant Frequencies and Electromechanical Coupling Factors of Piezoelectric Resonators," *Proc. IEEE*, **57**, 702 (1969).
9. A. Ballato, "Apparent Orientation Shifts of Mass-Loaded Plate Vibrators," *Proc. IEEE*, **64**, 1449 (1976).
10. T.J. Lukaszek, private communication.
11. For more detail see D.S. Stevens and H.F. Tiersten, "Temperature Dependence of the Resonant Frequency of Electroded Contoured SC-Cut Quartz Crystal Resonators," to be issued as a technical report, Rensselaer Polytechnic Institute, Troy, New York.
12. D.S. Stevens and H.F. Tiersten, "Temperature Dependence of Electroded Contoured AT-Cut Quartz Crystal Resonators," Rensselaer Polytechnic Institute, Troy, New York.
13. The expressions for the  $n$ th order plate rotations are obtained by substituting from the thickness expansion for the mechanical displacement field into the expression for the three-dimensional small local rotation and proceeding exactly as in the determination of the  $n$ th order plate strains obtained in Ref. 3.
14. A.E.H. Love, *A Treatise on the Mathematical Theory of Elasticity*, 4th ed. (Cambridge University Press, Cambridge, 1926) also (Dover, New York, 1944) Secs. 15 and 11c.
15. H.F. Tiersten, "Analysis of Trapped Energy Resonators Operating in Overtones of Coupled Thickness-Shear and Thickness-Twist," *J. Acoust. Soc. Am.*, **59**, 879 (1976).
16. IEEE Standard on Piezoelectricity - IEEE Std. 176 - 1978.

17. This transformation determines what we have referred to as the original conventional coordinate system for the SC-cut.
18. R. Bechmann, "Elastic and Piezoelectric Constants of Alpha-Quartz," Phys. Rev., 110, 1060 (1958).
19. R.N. Thurston, H.J. McSkimin and P. Andreatch, Jr., "Third Order Elastic Constants of Quartz," J. Appl. Phys., 37, 267 (1966).
20. F. Kohlrausch, Lehrbuch der prakt. Physik, 16. Aufl. 5, 158 (1930). Constants employed in Ref. 21.
21. R. Bechmann, A.D. Ballato and T.J. Lukaszek, "Higher Order Temperature Coefficients of the Elastic Stiffnesses and Compliances of Alpha-Quartz," Proc. IRE, 50, 1812 (1962).
22. In this work the SC-cut has been defined as the zero temperature cut for pure thickness vibrations of the fully electroded flat plate for the thickness mode of interest, i.e., the temperature dependence of the motional capacitive effect has been included in the definition.
23. The change in frequency due to the presence of the electrodes is obtained by subtracting the calculated change without the electrodes from the calculated change with the electrodes.

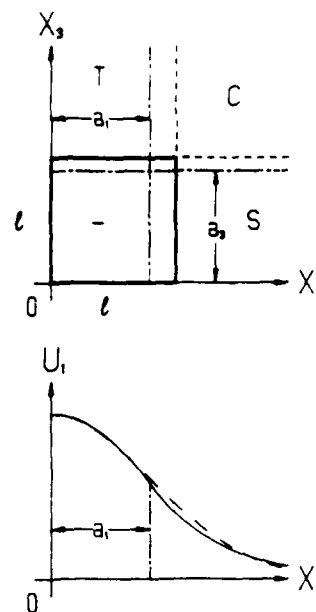


Figure 2. Diagram of One Quadrant of the Equivalent Trapped Energy Resonator Showing the Gaussian Mode Shape for the Contoured Resonator and the Equivalent Trapped Energy Mode Shape

#### Plano - Convex Resonator

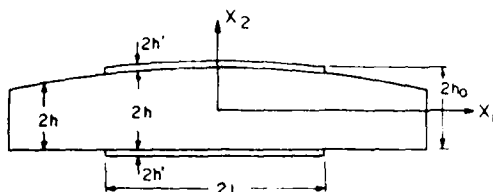


Figure 1. Schematic Diagram of the Plano Convex Resonator

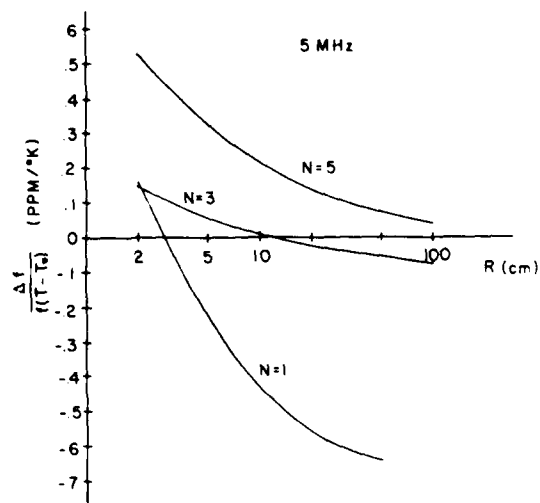


Figure 3. Relative Change in the Resonant Frequency per  $^{\circ}\text{K}$  for a Plano-Convex SC-Cut Quartz Resonator as a Function of the Radius of Curvature for the Three Lowest Harmonic Modes. The nominal Fundamental Plate Frequency is 5 MHz.

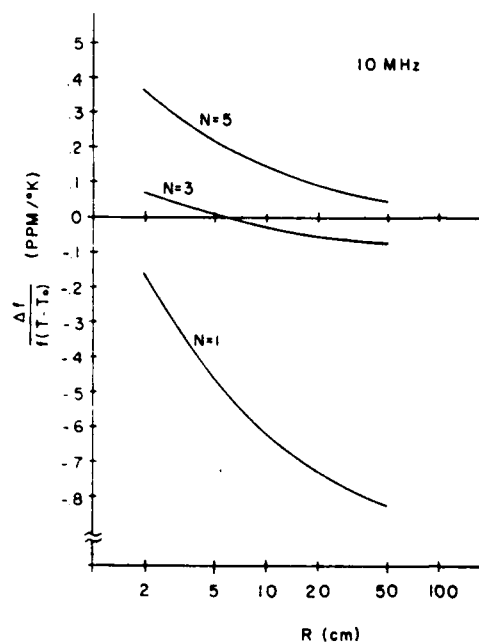


Figure 4. Relative Change in the Resonant Frequency per  $^{\circ}\text{K}$  for a Plano-Convex SC-Cut Quartz Resonator as a Function of the Radius of Curvature for the Three Lowest Harmonic Modes. The Nominal Fundamental Plate Frequency is 10 MHz.

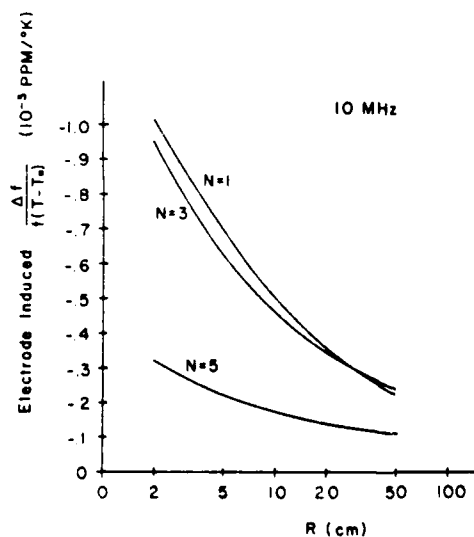


Figure 5. Relative Change in the Resonant Frequency per  $^{\circ}\text{K}$  due to 2000 Å Thick Gold Electrodes for a Plano-Convex SC Cut Quartz Resonator with a Nominal Fundamental Plate Frequency of 10 MHz as a Function of the Radius of Curvature for the Lowest Three Harmonic Modes.

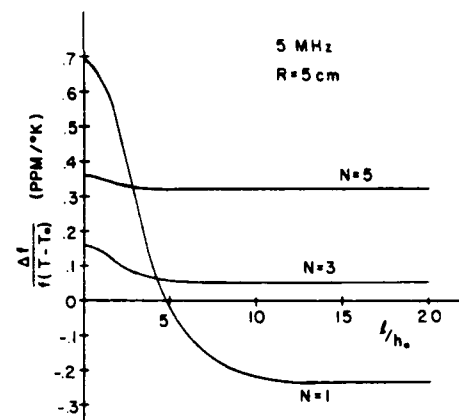


Figure 6. Relative Change in the Resonant Frequency per  $^{\circ}\text{K}$  for the Three Lowest Harmonic Modes as a Function of the  $l/h_0$  Ratio for a Plano-Convex SC-Cut Quartz Resonator with a Nominal Fundamental Plate Frequency of 10 MHz,  $R=5$  cm and 2000 Å Thick Gold Electrodes.

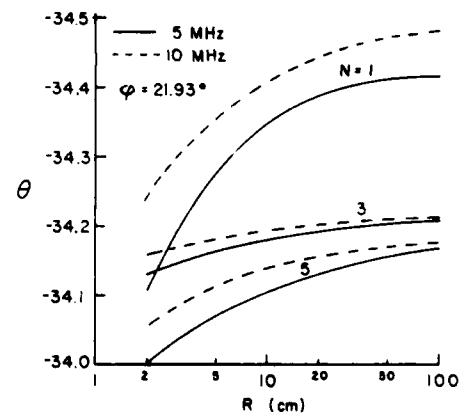


Figure 7. Rotation Angle  $\theta$  for the Zero Temperature Coefficient of Frequency SC-Cut for a Fixed Value of  $\varphi = 21.93^{\circ}$  as a Function of the Radius of Curvature  $R$  for Some Harmonic Modes for Plates with Nominal Fundamental Frequencies of Both 5 and 10 MHz.

## RECENT RESULTS WITH THE AIR FORCE HYDROTHERMAL FACILITY

A.F. Armington, J.J. Larkin, J.J. O'Connor and J.A. Horrigan

Rome Air Development Center  
Solid State Sciences Division  
Hanscom AFB, MA 01731SUMMARY

Using low growth rates and high purity nutrient, high purity quartz can be produced without the use of a liner. The most promising synthetic seed material found thus far is from the X growth area of the crystal. The Q of the X seed crystals appears to be over 2 million.

INTRODUCTION

The hydrothermal system at RADC has been in operation for about two years. During this time the primary emphasis has been on the growth of high purity quartz with a minimum number of defects based on the assumption that a high purity defect free material may have superior characteristics for frequency and time applications. The initial emphasis has been on the production of crystals with low aluminum concentration. In this phase it was determined that quartz crystals with an aluminum concentration of about a part per million could be reproducibly grown using high purity nutrient in silver lined autoclaves, about three times less aluminum than in unlined autoclaves. This study has been with hydroxide mineralizer with growth rates between ten and forty mils per day. More recently, we have been studying the effects of defects on the seed on dislocation density. We have also been continuing work on the purity of synthetic quartz.

PURIFICATION

As stated in the paper we gave last year<sup>1</sup>, we can routinely produce synthetic quartz with an aluminum content of approximately one part per million (atomic). Two methods of analysis are used, atomic absorption and electron spin resonance. The results of a comparison between these methods is shown on Figure 1. All of these results were obtained for crystals grown in silver liners and only those crystals which were relatively pure in terms of aluminum are shown here. The difference between the two methods is usually within a part per million, as shown on the third line of the Figure. Since EPR measures only substitutional aluminum while atomic absorption measures total aluminum, it appears that essentially all the aluminum is substitutionally bound in the lattice. Otherwise the atomic absorption

values would be significantly higher than the EPR results. We are also trying to compare the "oxine" method for aluminum with these results. This method is used in Japan for aluminum.

We have also continued our study on the use of noble metal liners. Because of mechanical problems with platinum liners we have concentrated on silver during this time. Figure 2 shows a comparison between a number of runs in silver liners compared to several unlined runs. These results are by atomic absorption since we are interested in other elements aside from aluminum. The arithmetic average of the most pertinent impurities is shown near the bottom of the Figure. Two pieces of information can be derived from the Figure. First, the amount of aluminum is about three times greater in the case of the unlined runs than in the silver lined runs. What we believe is the source of this impurity will be discussed shortly. The second conclusion from the analytical results is the low impurity concentration of the other elements determined. With the possible exception of lithium in the unlined run, most elements aside from aluminum are present in only small amounts. The source of the lithium is not due only to lithium hydroxide addition to the mineralizer since it was also added to the runs in the silver liner. We did expect a higher iron concentration in the unlined runs, but it is not indicated by the data.

We had previously performed some measurements on the metals exposed to the mineralizer during the run using EDAX which is at best a semiquantitative tool. Several materials were analyzed using atomic absorption. It was found that the holder material, used to support the seed and baffle, contained about 400 ppm of aluminum. We replaced this holder with a holder formed from silver. The aluminum results are shown in Figure 3 where they are compared with the average value for lined and unlined runs. Since the purity in this case is comparable to that of lined runs, it appears that the use of a silver liner does not improve the aluminum purity. In small autoclaves it is useful however, since it is easier to clean the liner than the unlined autoclaves. We are also analyzing the "liquid moly", used as a lubricant in the autoclaves, but this analysis has not been obtained.

In our previous paper at this conference<sup>1</sup>, we reported a significant rate of transport of silver when we grew crystals using carbonate in a silver liner. We felt that this might be partly due to oxygen in the system since we had made no attempt to eliminate oxygen during the run. We therefore tried a run using high purity silicon added to the charge to scavenge the oxygen from the system. After the run there were no needles of silver in the autoclave which had been observed in the other carbonate runs. The crystal however, cleaved easily along the seed indicating a high degree of strain. The silver concentration in the crystal was quite low however as is shown in Figure 4.

In an attempt to scavenge or neutralize the aluminum, we added a small amount of phosphoric acid to one experiment. The premise in this case was that the phosphate might help complex aluminum in the solution or might alter the aluminum in the growing crystal since the phosphate might help make the defect electrically neutral, thus lowering the concentration of Group one impurities in the crystal. The results shown in Figure 5 indicate both a higher aluminum and sodium concentration. Thus, the addition of phosphate was detrimental to the crystal. EPR results indicated that all the aluminum present was in defects of the same type as produced in normal quartz runs.

We reported last year that crystals grown from high purity sand contained large amounts of aluminum, the source of which was unknown. Since then, as previously mentioned, we have found a significant aluminum content in the baffle holder material. This is not the only source however. In Figure 6, we show the previous results using the purified sand, with a 0.1 % sodium hydroxide mineralizer. We also performed a run using ground cultured quartz as the nutrient with all other run conditions the same. There is a considerable decrease in the aluminum content of the resulting crystal which would not be the case if all the aluminum was coming from the holder which was the same in both experiments. Thus, some of the aluminum in the crystal must come from the sand. In this pure sand there are numerous grain boundaries, which contain feldspar (aluminum silicates), this would be more soluble than quartz and preferentially dissolve during a run<sup>2</sup>. It is suspected that this is the source of additional aluminum. The low concentration of hydroxide used in this run however, does seem detrimental to the quality of the crystal. The last line on the Figure gives the value of the analysis for a run at 0.5 N NaOH. The aluminum content is lower by an order of magnitude.

The effect of seasoning a silver liner by performing a series of runs in the same liner has also been investigated. The results are shown in Figure 7 for a liner used in a series of 0.5 N NaOH runs. It appears that the first run produces a crystal of higher aluminum concentration and possibly the first three runs are more contaminated. After that there does not seem to be

any significant change in the aluminum concentration. We have also experimented with the effect of growth rate on aluminum impurity in the crystal. The results for a series of unlined runs are shown on Figure 8. In this case we took the atomic absorption values. From this Figure, it can be seen that the lowest aluminum concentration for our experimental conditions is produced at a low growth rate, below twenty to twenty-five mils per day. The open circle at a growth rate below ten mils per day is the experiment using a silver holder rather than the impure holder used in the other runs shown on the Figure.

#### IMPERFECTIONS

Efforts are underway to reduce the number of dislocations in the grown crystal by reducing the number of defects in the seed. This has been done by using select natural crystals<sup>3</sup>, but it would be more economical if a technique could be found using synthetic material. We have tried several techniques including etching and sweeping of the seed as well as the use of seeds fabricated from the X growth area. Dislocations in this area do not propagate in the Z direction but in a direction at a low angle to the Z face. Thus dislocations from these seeds might propagate away from the growing direction and out of the crystal. Sweeping the seed, either in air or moderate vacuum, did not decrease the dislocation density. In this case we intentionally used a poor quality seed since a decrease in dislocations would be more easily observed. The top two topographs in Figure 9 show the results for the samples swept in air and vacuum. The topographs of crystals grown from unswept seeds are similar. We have not improved the dislocation density as yet by etching the seed, but these studies are continuing. As might be expected, the use of a Z face seed culled from the X growth area did result in a lower dislocation density in the crystal. The bottom topograph on the figure shows the low dislocation material produced from an X growth seed. This is somewhat misleading since the whole crystal is not shown and there were some dislocations produced by the cutting of the seed. The analytical results for a sample grown from this type seed are shown in Figure 10, where they are compared with the average impurity on silver lined runs. The material is at least as pure as material grown from other seeds. This result must be regarded as preliminary however, since it is based on a single analysis. A semiquantitative measurement of the optical  $Q$  indicates a value of  $Q$  equal to 2.3 million. Preliminary etching studies on the X seed crystals indicate a lower value for the dislocation density. A Z seed crystal in the same autoclave had an average density of 54 to 57 channels per square cm, while the X seed crystal density was 17 to 23 per square cm. The average value includes the crystal over the seed area with saw damage, which increased the dislocation density. In areas away from this damage, the density was about 3 per square centimeter. These studies are being continued and we will report on this more extensively when we have obtained a larger number of samples.

# REFERENCES

1. A.F. Armington, J.J. Larkin, J.J. O'Connor, and J.A. Horrigan, Proceedings of the 35th Annual Frequency and Control Symposium, Philadelphia, May 27, 1981, EIA, Washington, P. 297.
2. J.J. Martin, L.E. Halliburton and R.B. Bussoii, IBID, p. 317.
3. Baldwin Sawyer, private communication.
4. R.L. Barnes, P.E. Freeland, R.A. Laudise and J.R. Patel, J. Cryst. Growth, 43 (1978) 676.

AA	1.3	1.3	0.9	0.7	13*	15	2	3	2	0	5*
EPR	0.7	0.9	7.1	12.4	0.9	18.4 12.4	3.3	1.0	1.3	3.3	1.1
AA-EPR	0.6	0.4	-0.2	11.7	12.1	-1.4 +2.6	-1.3	1.2	0.7	2.3	3.9

\* PARTS PER MILLION ATOMIC IN SILVER LINER

+ PLATINUM LINER

Figure 1. Comparison of Analytical Techniques

SILVER LINER					NO LINER						
Al	Fe	Li	Na	K	Al	Fe	Li	Na	K		
1.3	1.7	6.3	0.0	<0.5	0.0	2.7	9.4	1.7	0.7		
0.7	1.7	5.2	<0.5	<0.5	10	0.5	14	3			
5.4	2.2	1	1.3	<1	10		10	2.8	2.6		
2	1	<0.5	<0.5	4	0.0						
3	0.9	<0.5	<0.5	4	11.6						
2	0.0	<0.5	0.0	1	4.0						
2	0.5	<0.5	<0.5	4	9.0						
0	2	1	2.4	2.4	5						
5	27	0.5	11	0.5							
AVE.	2.0	1.3	1.2	1.5	1.2	AVE.	0	1.5	0	2.5	1.1
ALUMINUM AVERAGE DEVIATION -1.2					ALUMINUM AVERAGE DEVIATION -2.0						

\* PARTS PER MILLION ATOMIC

Figure 2. Comparison on Silver Lined and Unlined Runs

# EFFECT OF SILVER HOLDER ON ALUMINUM CONCENTRATION

ALUMINUM (PARTS PER MILLION ATOMIC)

SILVER LINER (AVERAGE)

2.9

UNLINED (AVERAGE)

8

SILVER HOLDER

1.9

Figure 3. Results using Silver Holder

## CARBONATE RUNS IN SILVER LINERS

	AL	FE	LI	NA	K	AG
STANDARD	10	--	7	42	--	18
WITH SILICON	9	0.9	3	28	0.5	0.5

Figure 4. Effect of Silicon Addition to Carbonate Run

# EFFECT OF PHOSPHORIC ACID ON PURITY (PARTS PER MILLION ATOMIC)

	Al	Fe	Li	Na	K	Al (EPR)
PREVIOUS RUN	5.4	2.2	1	1.3	<1	0.8
PHOSPHATE RUN (AA)	17	4	5	5	<0.5	0.9

Figure 5. Effect of Phosphate Addition to Mineralizer

### IMPURITIES\* IN QUARTZ GROWN IN 0.1 N NaOH

SAMPLE	GROWTH RATE*	Al	Fe	Na	Li	K
PURIFIED SAND		15	0.26	3.1	0.75	1.5
CULTURED QUARTZ		16	<0.5	2	5	<0.5
CRYSTAL SAND NUTRIENT	10	388 453	6.4	3.6	100	<1
CRYSTAL CULTURED NUTRIENT 0.1 N NaOH	10	68	-	-	-	-
CRYSTAL CULTURED NUTRIENT 0.5 N NaOH	25	6.9	2.7	9.4	1.7	0.7

\* PPMA

+ MILS/DAY

Figure 6. Runs at Low Hydroxide Concentration

### EFFECT OF SEASONING ON ALUMINUM CONCENTRATION

NUMBER OF RUNS IN LINER	1	2	3	4	5	6
ALUMINUM BY AA	15	13	17	5.4	1	5
ALUMINUM BY EPR	16.4	0.9	0.8	1.7	0.7	3.3

CONCENTRATIONS IN PPMA

Figure 7. Effect of Liner Seasoning on Aluminum Content

# GROWTH RATE VS ALUMINUM CONCENTRATION (PPMA)

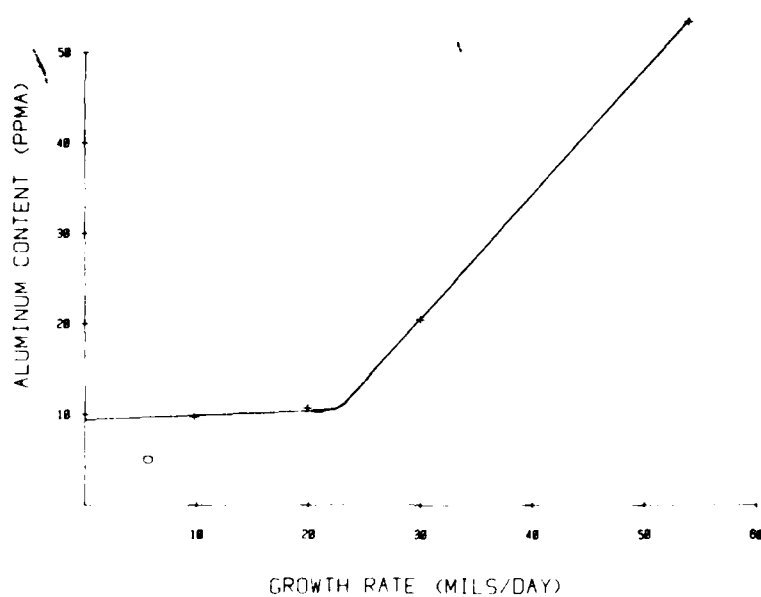


Figure 8. Growth Rate versus Aluminum Concentration



Figure 9. Topographs of Swept Seeds and X Area Seeds

PURITY OF CRYSTALS WITH X-GROWTH SEEDS (AA-PPMA)

	Al	Fe	Li	Na	K
Z SEED	2.9	1.3	1.2	1.5	1.2
X SEED	5 (1.1)*	-	0.5	11	0.6

\* Al by EPR

Figure 10. Purity of Material Grown from X-Area Seed



## GROWTH AND CHARACTERISATION OF HIGH PURITY QUARTZ

D F Croxall, I R A Christie, J M Holt, B J Isherwood and A G Todd

The General Electric Company, p.l.c., Hirst Research Centre  
Wembley, HA9 7PP, England

AD P001504

### Abstract

Quartz crystals have been grown which have a purity and crystalline perfection significantly in advance of any quartz that is produced commercially today.

The crystals produced were approximately 50 mm x 50 mm in area and were 30 mm thick in the growth direction. The total metal ion concentration was less than 1 ppm, with an aluminium content of less than 0.1 ppm. The crystalline perfection is demonstrated by a dislocation density of  $<10$  lines per  $\text{cm}^2$ .

### 1 Introduction

Recently, a requirement has arisen for synthetic quartz of a quality superior to that currently available commercially. This high quality quartz is needed for several purposes. For example it allows the role of the material in the variability in performance of piezoelectric devices to be determined. It is also essential for the development of high frequency high stability devices especially those required to be stable under high fluxes of ionising radiation. It was in response to these needs that the present work was undertaken. The two aspects of quartz crystal growth that have received attention have been that of reducing the metal ion impurities in the crystals to a minimum and that of reducing the dislocation density to a very low level. The growth of quartz with a very low level of dislocations has been reported<sup>1</sup> but this low defect level has not been realised in crystals of high purity.

## 2 Growth procedure

### 2.1 Autoclaves

The autoclaves used were of 63 mm bore and 300 mm in length. The internal surfaces were coated with gold by electrodeposition to prevent contamination of the growth solution. Baffles and seed supports were either of platinum or gold plated silver.

### 2.2 Nutrient

Most of the impurities in synthetic quartz are transferred to the crystal from the nutrient which usually consists of crushed natural quartz. To avoid contamination by this mechanism, high purity fused silica was used as the source of the nutrient. The direct use of silica in its glassy state is not possible since its solubility in the growth solution is much higher than that of  $\alpha$ -quartz. Consequently very rapid deposition of quartz occurs during the initial growth period resulting in a highly strained layer next to the seed. To overcome this problem, the silica nutrient was converted to  $\alpha$ -quartz by heating in the autoclave for 24 hours under normal operating conditions. After conversion of the silica, the seeds were inserted into the autoclave and a normal growth run was carried out.

### 2.3 Growth solution and conditions

High purity sodium hydroxide (Aristar grade, BDH Ltd) and double deionised water were used to make up the growth solution.

A concentration of 0.1 M sodium hydroxide was used for the conversion of the silica nutrient in order to prevent excessive spontaneous nucleation on the autoclave walls. A 1.25 M solution concentration was used for growth of crystals.

The conditions for growth were as follows:

Base temperature	400°C
Temperature gradient	45°C
Pressure	1,500 atmospheres

A relatively low pressure was employed due to a pressure limitation on the autoclaves.

### 2.4 Seeds

Since the essence of producing crystals with a very low dislocation density is the use of low dislocation density seeds, particular care was taken in the present work over seed selection and preparation.

A number of high quality natural quartz crystals were cut into 1 mm thick plates of basal orientation. These plates were examined by transmission X-ray topography to select areas of very low dislocation density and these areas were used for seeds. The seed surfaces were prepared by Syton polishing, followed by a brief etch in 40% HF solution. X-ray topography was used to ensure all cutting damage had been removed from the seed surfaces.

In some cases second generation high purity crystals were grown on seed plates cut from first generation high purity crystals.

### 3 Assessment

#### 3.1 Purity

Samples of several crystals were submitted for examination by mass spectrometry with levels of aluminium and iron also determined by atomic absorption techniques. The results from a typical crystal are compared below with an analysis of the silica from which the crystal was grown.

#### Mass spectroscopy results

All figures are ppm weight.

Element	Starting silica	Crystal (LHPQ 20)
Zn	0.3	<0.02
Cu	0.07	<0.01
Fe	1.5	<0.08
Mn	0.01	<0.005
Al	3	<0.05
Ge	0.2	n.d. <0.005
Au	n.d. <0.005	0.01
Pt	n.d. <0.005	0.01

The following elements were not detected above the indicated maximum instrument sensitivity levels in either silica or crystal:

Ca <0.1 ppm	K <0.3 ppm
W <0.05 "	Na <0.5 "
Sn <0.03 "	
Ba, Sb, Cr	<0.01 "
V, Ag, Co, Ni	<0.005 "

The results obtained by atomic absorption techniques were as indicated below:

Silica	Crystal (LHPQ 20)
Fe 2.0 ppm	0.05 ppm
Al 0.5 ppm	0.03 ppm

#### 3.2 Infra-red examination

Recent research has suggested<sup>2</sup> that there is a direct correlation between radiation hardness and aluminium content. An assessment of the level of substitutional Al present in the crystals was made, by the measurement of infra-red absorption at

770K, of the Al-OH centres formed on irradiation.

Typical values of aluminium content deduced from these measurements are as follows:

Crystal	Al level
LHPQ 9	0.020 ppm
LHPQ 13	0.005 ppm
LHPQ 17	0.052 ppm
LHPQ 20	not detectable

An assessment of the mechanical 'Q' of the quartz was made, by measurement of the room temperature infra-red absorption at 3500 and 3410 cm<sup>-1</sup>, and the following results were obtained.

Sample	Growth rate mm/side/day	MQ 3500 cm <sup>-1</sup>	MQ 3410 cm <sup>-1</sup>
LHPQ 7	0.35	2.3 x 10 <sup>6</sup>	2.4 x 10 <sup>6</sup>
LHPQ 9	0.28	2.5 x 10 <sup>6</sup>	2.7 x 10 <sup>6</sup>
LHPQ 17	0.27	2.1 x 10 <sup>6</sup>	1.9 x 10 <sup>6</sup>
LHPQ 20	0.16	2.6 x 10 <sup>6</sup>	3.2 x 10 <sup>6</sup>

#### Structural evaluation

Sections were cut through the seed and overgrowth of several of the crystals and examined by transmission X-ray topography. Figure 1 shows a MoK $\alpha$  1120 topograph of a 1 mm thick <1010> slice from a typical crystal. The topograph clearly demonstrates that the dislocation density is at a very low level. All of the dislocations can be shown to be of the edge type<sup>3</sup> and to have originated at the seed-overgrowth interface or to have propagated from the seed. Those dislocations which in Figure 1 give the appearance of initiating in the overgrowth can be shown to have entered the slice from the adjacent parts of the crystal. No evidence of dislocation generation at inclusions has been recorded. The seed plates were selected to contain very few dislocations but are rendered visible in the topograph by virtue of the contrast from growth striations, from precipitates and to a lesser extent from the lattice parameter mismatch with the overgrowth as a consequence of the higher impurity content of the natural crystal.

When a seed was cut from one of the pure crystals, the contrast between the seed and the overgrowth disappeared as illustrated in Figure 2.

A further feature of the X-ray topographs of the pure crystals is the absence of growth sector boundary contrast. This may be attributed to a low level of segregated impurity elements in the 'X' growth sectors leading to a minimal amount of lattice mismatch strain at the sector boundaries. In Figure 3, a topograph of a slice of commercial quartz, the boundaries between the Z and X growth sectors are prominent contrast features. Figure 4 is a topograph of a slice from a pure quartz crystal. The seed used for the growth of this particular crystal was commercial synthetic quartz

and therefore the dislocation content of the 'Z' growth sector is relatively high. However, the growth sector boundaries are poorly defined particularly between the Z and fast X. It will be noted that the fast 'X' growth sector itself lacks growth striation contrast and the only dislocations present originate from the edge of the seed plate.

#### Discussion

The present work has produced single crystal quartz with some unique features which make it of interest both in terms of practical use and as a vehicle for further study of  $\alpha$ -quartz.

A major practical incentive for the growth of the crystals was the provision of quartz for the construction of very stable piezoelectric devices. The purity levels that were achieved were indeed sufficient to endow devices made from the crystals with a degree of radiation hardness, as reported in another paper presented at this Conference<sup>4</sup>. The relation between purity, defect content and stability of piezoelectric performance in the absence of ionising radiation is less well defined but in critical situations where frequency stability is of paramount importance the use of pure quartz is most desirable.

One interesting possibility which arises as a consequence of the high purity of the crystals is that growth zone boundaries may not be as damaging to piezoelectric performance as they are at normal impurity levels. The indications are that, in the absence of significant impurity segregation, these regions are relatively strain free and therefore the inclusion of part of such a boundary in a wafer would not necessarily degrade piezoelectric performance. In a similar vein, the seed-overgrowth interfaces in the high purity crystals grown on high purity seed plates were also virtually featureless on X-ray topographical inspection and it is conceivable that wafers cut to include part of the seed plate would perform in an acceptable manner.

The very low dislocation content of the crystals may also have repercussions in terms of the mechanical behaviour of the quartz during wafer preparation. In the fabrication of high frequency bulk wave devices, wafers which are of the order of

50  $\mu$ m thick must undergo various stages of polishing and handling which result in breakage at a significant level. It would be anticipated that pure, low defect content crystals would have some advantage in respect of their response to such mechanical operations since the number and severity of the stress raises in the crystal should be reduced. Difficulties due to 'punch through' of thin wafers on etching are also likely to be reduced due to the absence of dislocation 'bundles' running through the thickness of the wafer.

In the sphere of research, the purity of the crystals combined with their perfection, will allow some of the intrinsic properties of  $\alpha$ -quartz to be studied. For example, such parameters as lattice constants and elastic constants are influenced in a complex way by the presence of impurities and therefore a high purity material is needed to establish their intrinsic values. The intentional doping of the pure crystals with single impurity elements also becomes possible and therefore the effect of individual impurities on growth mechanisms and on physical properties can be resolved. Some insight into the interaction of impurity induced strain and dislocation structure has already been obtained from the study of topographs and the greatly simplified pattern of defects in the pure crystals is likely to prove a fruitful field for future work.

#### Acknowledgment

This work has been carried out with the support of Procurement Executive, Ministry of Defence, sponsored by DCVD.

#### References

- 1 Barnes et al, Journal of Crystal Growth, 43, (1978), 676-686
- 2 Halliburton, Markes and Martin, Proc 34th Ann Freq Con Symp, Ft Monmouth, May 1980
- 3 Lang, A R and Miuscov, V F, J Appl Phys 38, (1967), 3477
- 4 Doherty, S P, Morris, S E, Andrews, D C and Croxall, D F, Proc 36th Ann Freq Con Symp.



Figure 1.  $11\bar{2}0$  Topograph of  $\langle 10\bar{1}0 \rangle$  Slice of High Purity Quartz Grown on a Natural Seed



Figure 2.  $11\bar{2}0$  Topograph of  $\langle 10\bar{1}0 \rangle$  Slice of High Purity Quartz Grown on a High Purity Seed



Figure 3.  $11\bar{2}0$  Topograph of  $\langle 10\bar{1}0 \rangle$  Slice of Commercial Quartz



Figure 4.  $11\bar{2}0$  Topograph of  $\langle 10\bar{1}0 \rangle$  Slice of High Purity Quartz Grown on a Commercial Quartz Seed

RADIATION EFFECTS IN SYNTHETIC AND HIGH PURITY SYNTHETIC QUARTZ : SOME RECENT  
INFRARED, ELECTRON SPIN RESONANCE AND ACOUSTIC LOSS RESULTS

S P Doherty, S E Morris, D C Andrews and D F Croxall

The General Electric Company, p.l.c., Hirst Research Centre,  
Wembley, HA9 7PP, England

AD P001505

Abstract

Radiation effects in synthetic and high purity synthetic quartz are examined in a research programme at the GEC Hirst Research Centre, Wembley England. Low temperature infrared absorption, electron spin resonance (ESR) and variable temperature acoustic loss/crystal parameter measurement are used in a study of radiation induced defects in quartz and their interaction with device properties with the goal of developing radiation hardened quartz crystals.

Infrared absorption

Five grades of quartz (one natural, three ordinary and one high purity synthetic) were examined in a study of the effects of irradiation and sweeping on their low temperature infrared absorption. Six additional samples of high purity quartz were also examined as received (at room temperature and 77 K) and following irradiation. The aims of this work included:

- (i) measurement of the (substitutional) Al-OH<sup>-</sup> content following irradiation in natural, synthetic and high purity quartz and comparison with the total aluminium content as determined by atomic absorption and mass spectroscopy.
- (ii) measurement of the ratio of Al-OH<sup>-</sup> to Al-hole centre formation following irradiation.
- (iii) examination of the effects of irradiation and sweeping on the individual OH<sup>-</sup> and Al-OH<sup>-</sup> bands.
- (iv) examination of the Al-OH<sup>-</sup> content of different growth regions in high purity quartz.
- (v) investigation of the relationship between OH<sup>-</sup> content, estimated mechanical Q and growth rate in high purity quartz.

The synthetic quartz samples were Z slices, approximately 13 x 13 x 4 mm. The natural specimen was considerably thinner due to its much greater impurity content (approximately 65 ppm Al). The samples included an experimental Salford Electrical Instruments<sup>1</sup> (SEI) specimen (about 15 years old), a slow grown synthetic Russian (RUS) specimen, a

specimen from a small demonstration bar (DEM) of synthetic material and a specimen of high purity synthetic quartz (LHPQ 13), grown at the Hirst Research Centre. The samples were chosen to give a wide range of OH<sup>-</sup> and Al-OH<sup>-</sup> centre concentrations for comparison under the different treatments. The infrared measurements were made at 77 K in an evacuated cryostat with IR vitreosil windows using a Nicolet 7199C Fourier Transform Infrared Spectrometer. A background spectrum of an evacuated cryostat without a sample present was always subtracted from the measured spectrum.

The various (as yet unassigned) OH<sup>-</sup> bands occur in quartz at nominally 3580, 3437, 3400 and 3348 cm<sup>-1</sup> 2-8. The Al-OH<sup>-</sup> bands occur at nominally 3367 and 3306 cm<sup>-1</sup>. Additional bands occur on either side of the 3580 cm<sup>-1</sup> band and these are included in the overall estimation of the '3580' cm<sup>-1</sup> band as shown in the figures. The 3580 cm<sup>-1</sup> band itself is split into three overlapping bands following irradiation in high purity quartz.

The OH<sup>-</sup> and Al-OH<sup>-</sup> centre concentrations have been determined from the area under the absorption peaks using the relationship proposed by Kats<sup>2</sup>. Using the area is more accurate than measuring the peak height and assuming a peak width and shape factor.

$$N_H = 2.16 \times 10^{16} H_{\text{cm}} \text{ cm}^{-3} \quad (1)$$

(assuming gaussian shape and  $p = 0.43$ )

working backwards,

$$N_H = 2.03 \times 10^{16} \times \frac{\text{Area under peak}}{\text{thickness in cm}} \text{ cm}^{-3} \quad (2)$$

$$\text{and } 1 \text{ ppm (Si)} = 2.657 \times 10^{16} \text{ cm}^{-3} \quad (3)$$

Figure 1 shows the 77 K infrared absorption spectrum of Russian synthetic quartz before and after x-irradiation. Figure 2 shows a comparison between the Russian and high purity (LHPQ 20) synthetic quartz as received. (The absorbance scales are different but the plots have been scaled on the heights of the intrinsic bands to provide a valid comparison).

The overall behaviour of the Al-OH<sup>+</sup> (sum of 3367 and 3306 cm<sup>-1</sup>), other OH<sup>+</sup> (sum of '3580', 3437, 3400 and 3348 cm<sup>-1</sup>) and total OH<sup>+</sup> (sum of Al-OH<sup>+</sup> and other OH<sup>+</sup>) centres as a function of treatment is shown in Figure 3. The measurements were made as received, following x-irradiation (85 kV, 35 mA, half an hour) then following sweeping (in air, 24 hours, 500V, 550°C) and finally following re-irradiation. The major results are:

- (i) the Al-OH<sup>+</sup> centre clearly grows at the expense of the other OH<sup>+</sup> centres, but the total OH<sup>+</sup> content grows at each step indicating a source of hydrogen within the crystal.
- (ii) the Al-OH<sup>+</sup> centre decreases upon sweeping which is not expected on the basis of the currently understood model<sup>6-9</sup>, unless the sweeping was incomplete.
- (iii) the high purity material has an infinitesimal Al-OH<sup>+</sup> content (0.005 ppm) and a very low OH<sup>+</sup> content (1.124 ppm).

Figure 4 shows the individual OH<sup>+</sup> band concentrations as a function of treatment and illustrates the growth of the bands at '3580' cm<sup>-1</sup> at each step in high purity material. Figure 5 examines the inter OH<sup>+</sup> band ratios as a function of treatment and highlights the relative growth of the '3580' cm<sup>-1</sup> bands and relative decline of the 3437 cm<sup>-1</sup> band in high purity material following irradiation. This is the opposite behaviour to that exhibited by ordinary synthetic quartz.

Six high purity quartz specimens were examined in total (LHPQ 7(1), 9(1), 13(1), 17(1), 17(2), 17(3) and 20(1)). LHPQ 7(1) and 9(1) were initially irradiated to determine the aluminium content (see Table 1). LHPQ 13(1) formed part of the comparative irradiation and sweeping study. LHPQ 17(1), (2) and (3) were cut from the Z, Fast X and Minor R growth regions respectively and were examined to determine the aluminium content in the different growth zones. LHPQ 20(1) was a very low growth rate specimen (0.16 mm/side/day). The 77K infrared absorption spectra for LHPQ 13(1) and 20(1) as received and following irradiation are shown in Figures 7 and 8 respectively.

The effects of irradiation on the individual OH<sup>+</sup> bands in high purity quartz are demonstrated in Figures 9 and 10. The '3580' cm<sup>-1</sup> band increases following irradiation due to the growth of the associated side peaks and the splitting into three of the principal 3580 cm<sup>-1</sup> peak. The other bands are suppressed upon irradiation.

Figure 11 illustrates the relationship between growth rate and OH<sup>+</sup> content and growth rate and estimated mechanical Q (after Brice<sup>10</sup>). The results are shown in Table 2. Additional data will be added to these graphs in future to cover <0.1 to >0.5 mm/side/day. With the exception of LHPQ 13(1) (0.34 mm/side/day) which appears to have an unusually high Q, the OH<sup>+</sup> content appears to decrease and the mechanical Q increase as the growth rate is reduced.

Table 1 - Impurity content of infrared quartz samples

Sample	Atomic absorption		Infrared	
	Al (ppm)	Fe (ppm)	Al-OH (ppm)*	OH <sup>+</sup> (ppm)
SEI	11.2	0.55	8.43	-
DEM	9.3	0.10	12.44	8.58
RUS	9.1	0.10	5.12	3.73
Natural	65	4	34.28	-
LHPQ 7	-	-	0.018	-
LHPQ 9	0.2*	0.4*	0.020	-
LHPQ 13	0.01	<0.02	0.005	1.124
LHPQ 17(1) Z	-	-	0.052	1.775
LHPQ 17(2) Fast X	-	-	0.017	0.767
LHPQ 17(3) Minor R	-	-	0.002	1.347
LHPQ 20	0.03	<0.05	not detectable	0.274

\* Atomic absorption results should be regarded as being too high, + Following first irradiation

The impurity content of the quartz used in this study is indicated in Table 1. Atomic absorption analysis was performed on the actual IR specimens (at HRC) and is compared with the infrared derived results. With the exception of the result for the demonstration quartz (for which the Al-OH<sup>+</sup> content was larger than the total Al content) the results are in agreement. From these figures it is possible to infer the Al-OH<sup>+</sup> to Al-hole ratio following the first irradiation (SEI 3.04:1, RUS 1.29:1, Natural 1.12:1). The 3367 : 3306 cm<sup>-1</sup> Al-OH band ratios are illustrated in Figure 6.

The conclusions of this infrared study are that high purity synthetic quartz grown at the Hirst Research Centre is an essentially aluminium free (<0.05 ppm), low OH<sup>+</sup> content (<1.5 ppm) and high Q (>2 x 10<sup>6</sup>) material. Its behaviour under irradiation has distinct differences to that of ordinary synthetic quartz due to the absence of substitutional Al centres.

Table 2 - OH<sup>-</sup> content, mechanical Q and growth rate for high purity quartz

Material	OH <sup>-</sup> content (ppm)	Estimated Q (millions)		Growth rate (mm/side/day)
		3500 cm <sup>-1</sup>	3410 cm <sup>-1</sup>	
LHPQ 7(1)	-			0.35
LHPQ 9(1)	-			0.28
LHPQ 13(1)	1.124	3.38	4.41	0.34
LHPQ 17(1)	1.075	2.10	1.91	0.27
LHPQ 17(2)	0.767			0.27
LHPQ 17(3)	1.347			0.27
LHPQ 20(1)	0.279	2.62	3.18	0.16

However the questions that this study leaves unanswered include:

- (i) what is the identity of the OH<sup>-</sup> type centres that give rise to the 3580, 3437, 3400 and 3348 cm<sup>-1</sup> bands.
- (ii) where do the hydrogen ions from these sites go to in high purity quartz following irradiation (they don't go to Al sites to form Al-OH<sup>-</sup> centres as in ordinary synthetic material).
- (iii) what is the source of the additional hydrogen that appears following irradiation in ordinary synthetic quartz.
- (iv) what is the relationship between growth rate, OH<sup>-</sup> content and mechanical Q
- (v) what is the ratio of Al-hole to Al-OH<sup>-</sup> centre formation in high purity quartz and how does this compare with ordinary unswept/swept synthetic quartz.

#### Electron spin resonance

Preliminary ESR measurements at the Clarendon Laboratory, Oxford on the same natural, SEI synthetic and high purity synthetic (LHPQ 7 and 9) quartz have attempted to compare the two aluminium hole centre concentrations in each. Following room temperature x-irradiation the samples were placed in a double sample cavity and the ESR spectra recorded at a frequency of 9.583 GHz at 35 K with the field along the C axis. The natural to SEI hole centre ratio was found to be about 5.6:1, in good agreement with the atomic absorption (5.80:1) and infrared (4.07:1) results. Measurements on high purity sample LHPQ 9 indicated an Al-hole centre concentration of about 0.04 ppm with a S/N ratio of 2:1.

#### Acoustic loss, Q<sup>-1</sup>

Preliminary acoustic loss (Q<sup>-1</sup>) measurements as a function of temperature from 77 K to 300 K are reported for a Russian synthetic and high purity synthetic quartz resonator. 5 MHz 5th overtone AT-cut plano-convex glass encapsulated resonators were fabricated by SEI from Russian and high purity (LHPQ 7) synthetic quartz. The results were obtained using a new acoustic loss/crystal parameter measurement system which has been developed to allow automated measurement of crystal resonators in the frequency range 300 kHz to 1.3 GHz as a function of temperature (initially from 77 K to 300 K).

The measurement system, which forms in effect a programmable network analyser, consists of a Rohde and Schwarz ZPV vector analyser (with 300 kHz - 2 GHz 50 ohm plug-in E3) with accompanying ZPV-Z5 s parameter test set, HP 3335 millihertz synthesiser (200 Hz - 80 MHz) (and Adret 7100 synthesiser 300 kHz - 1.3 GHz), HP 9826 desktop computer/controller, Lake Shore Cryogenics DRC-84C cryogenic temperature controller and Oxford Instruments CF-100 (3.6 K - 500 K) flow cryostat and accessories. Two 50 ohm coaxial leads run into the cryostat which maintain a 50 ohm environment down to the interchangeable crystal mount on the cold finger. The signal leads are connected to the crystal mounting through SMA connectors which allows calibration of the cables essentially to the pins of the device using open circuit, short circuit and matched load calibration components.

Preliminary measurements were made using a direct transmission technique with the resonator connected in series. The acoustic loss was obtained from the ±45° and zero phase points using

$$Q = \frac{f}{df} (2R_0 + R) / R \quad (4)$$

where  $f$  is the zero phase frequency  
 $df$  is the frequency difference between + and -45 degrees  
 $R_0$  is the characteristic impedance (50 ohms)  
 $R$  is the impedance of the crystal at zero phase

Future measurements will be made using the new crystal measurement technique reported elsewhere in these proceedings<sup>11</sup> with full error correction.

Figures 12 and 13 show the as received acoustic loss and (300 K normalised) frequency temperature characteristics of the Russian synthetic resonator. Figures 14 and 15 show the as received acoustic loss and (300 K normalised) frequency temperature characteristics of the high purity synthetic resonator. The overall response of the high purity resonator is very good with an essentially constant Q of  $2 \times 10^6$  over the entire temperature range. This reflects strongly on the overall quality of the material.

The Russian and high purity synthetic resonators form part of a study to look at the radiation induced frequency offset in precision natural, synthetic and high purity resonators which will be cumulatively irradiated to 1 MRad. The acoustic loss for each of the resonators will be measured after each irradiation along with the radiation induced frequency offset.

#### Radiation induced frequency offset

Ten two resonator narrowband 20 MHz bipole crystal filter packages (in which one resonator was fabricated from natural and the other from high purity (LHPQ 6) synthetic quartz) were irradiated to a total dose of 1 MRad (gamma and some neutrons) in a spent nuclear fuel store. Two packages were used as controls. The radiation induced frequency offset was obtained by measuring the frequency for a number of days prior to irradiation and then monitoring the post irradiation recovery.

The fractional frequency shifts between the last day pre-irradiation and the first day post irradiation are shown in Table 3. As each pair of resonators was in the same package, both received the same dose.

The results in Table 3 clearly show the difference between the radiation induced frequency offset in the natural and high purity resonators. Two control resonator pairs (#3,4 and #27,28) give a measure of the uncertainties in the results. All the natural resonators show large negative frequency offsets ranging from -1.83 to -15.37 ppm. The high purity resonators by comparison show mainly positive frequency offsets of about an order of magnitude smaller, -0.125 to +0.315 ppm. The

offsets for high purity resonators #8,16 and 30 are anomalously high and indicate oscillation on an adjacent response. The resonators were of a bipole type with only one side excited and as such did not have as distinct a central response as the 5 MHz 5th OT AT-cut precision resonators. In addition resonators 8 and 25 showed high series resistances when measured on arrival. The second column shows the offsets on the 22nd day post-irradiation and indicate the magnitude of the post irradiation annealing. Again the changes in the high purity resonators appear to be about an order of magnitude smaller than those in the natural resonators.

Figures 16 and 17 show the fractional frequency shift as a function of time before and after 1 MRad of irradiation for resonators 1 and 2. Figures 18 and 19 show the same information for resonators 11 and 12.

Work is currently in progress to repeat these measurements on a series of precision glass encapsulated 5 MHz 5th OT AT-cut plano convex resonators which have been fabricated from natural, synthetic and high purity synthetic quartz. These measurements will be made for a series of dose rates up to 1 MRad and should enable a much more accurate determination of the dose dependent frequency offset to be made for high purity resonators.

#### Conclusions

Infrared, ESR, acoustic loss and radiation induced frequency offset on natural, synthetic and high purity quartz have shown significant improvements in material quality and device response when using very high purity synthetic quartz grown at

Table 3 - Post irradiation frequency offset for natural and high purity synthetic quartz resonators following 1 MRad total dose

Resonator	Day 0		Day 22	
	Natural	Synthetic	Natural	Synthetic
1,2	- 5.92	- 0.125	- 5.76	-0.080
3,4	+ 0.605	- 0.125	+ 0.490	-0.080
5,6	-15.37	+ 0.210	-13.53	+0.355
7,8	- 7.48	-31.6	- 6.91	- 4.73
9,10	- 4.11	+ 0.190	- 3.93	+ 0.135
11,12	- 1.93	- 0.340	- 1.97	- 0.270
13,14	- 9.61	+ 0.575	- 8.68	+ 0.405
15,16	- 8.10	- 5.20	- 7.68	- 5.10
17,18	-10.86	+ 0.315	-10.00	+ 0.265
25,26	- 9.96	-	- 9.20	-
27,28	+ 0.370	+ 0.175	+ 0.195	0.055
29,30	-13.32	+88.74	-12.77	+ 83.69

Notes 1 Resonators 3,4 and 27,28 were controls

2 Resonators 8 and 25 had unusually high resistances when measured as received

the GEC Hirst Research Centre. This material appears to be a very promising candidate for the fabrication of radiation hardened quartz devices and further research is in hand to qualify the preliminary results presented here.

In addition, current research indicates that there are still considerable gaps in our understanding of the mechanism and steps involved in both sweeping and the interaction of radiation with quartz which need to be resolved in order to fully solve the radiation hardness problem.

#### Acknowledgements

The authors are grateful to Mr A Hargreaves of SEI for fabricating the 20 MHz and 5 MHz resonators used in this study.

Part of this work has been carried out with the support of Procurement Executive, Ministry of Defence, sponsored by DCVD.

#### References

- 1 Salford Electrical Instruments Ltd., Times Mill, Heywood, Lancs, England

- 2 Kats A, Philips Res Rep 17, 133, (1962)
- 3 Brown R N and Kahan A, J Phys Chem Solids, 36, 467, (1975)
- 4 Lipson H G, Euler F and Armington A F, Proc of the 32nd Annual Symposium on Frequency Control, 11, (1978)
- 5 Lipson H G, Kahan A, Brown R N and Euler F K, Proc of the 35th Annual Symposium on Frequency Control, 329, (1981)
- 6 Sibley W A, Martin J J, Wintersgil M C and Brown J D, J App Phys, 50, 5449, (1979)
- 7 Martin J J, Doherty S P, Halliburton L E, Markes M, Koumvakalis N, Sibley W A, Brown R N, and Armington A, Proc of the 33rd Annual Symposium on Frequency Control, 134, (1979)
- 8 Doherty S P, Martin J J, Armington A F and Brown R N, J App Phys, 51, 4164, (1980)
- 9 Halliburton L E, Koumvakalis N, Markes M E, and Martin J J, J App Phys, 52, 3565, (1981)
- 10 Brice J C and Cole A M, Proc of the 32nd Annual Symposium on Frequency Control, 1, (1978)
- 11 Peach R C, Dyer A J, Byrne A J and Doherty S P, Proc of the 36th Annual Symposium on Frequency Control

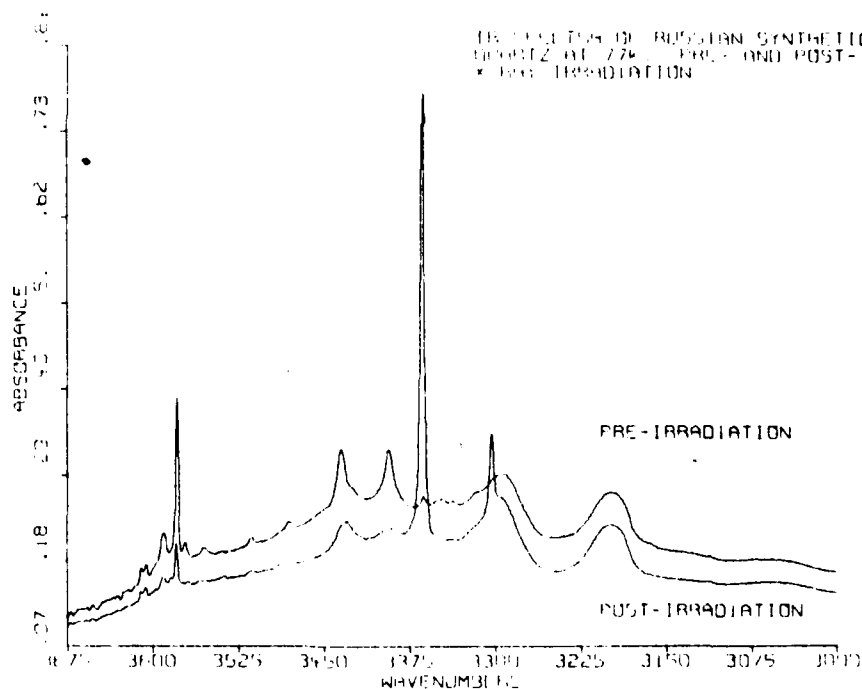


Figure 1 77K Infrared Absorption Spectrum of Russian Synthetic Quartz Before and After Irradiation

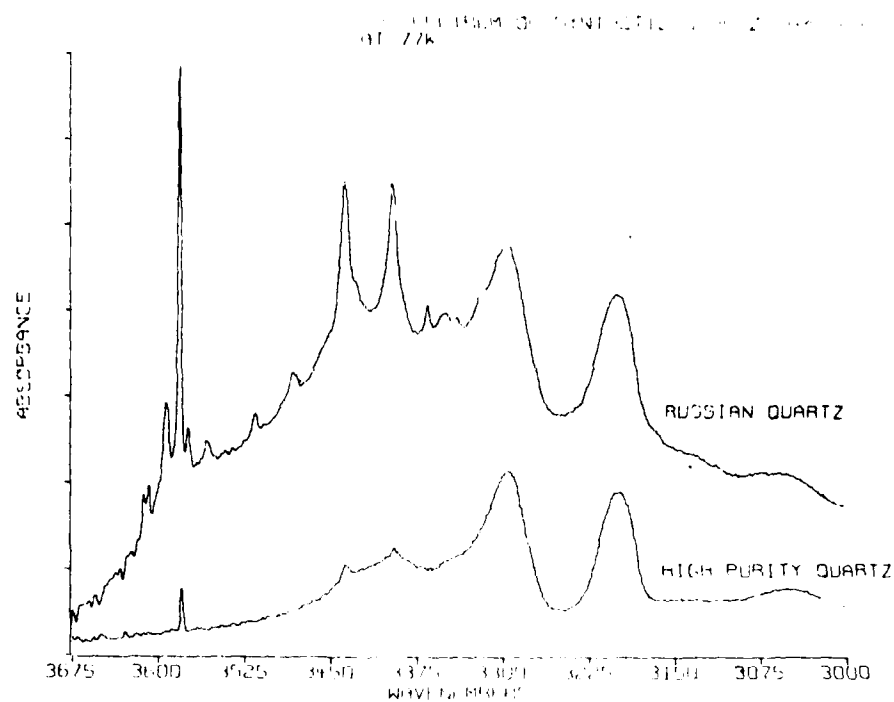


Figure 2. Comparison of 77K Infrared Absorption Spectra of Russian and High Purity Synthetic Quartz as Received

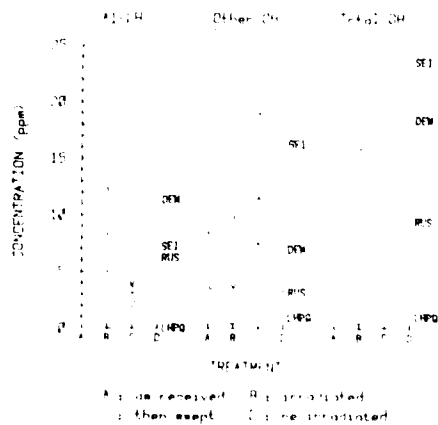


Figure 3. A1 OH, OH and Total OH Centre Concentrations Shown as a Function of Treatment

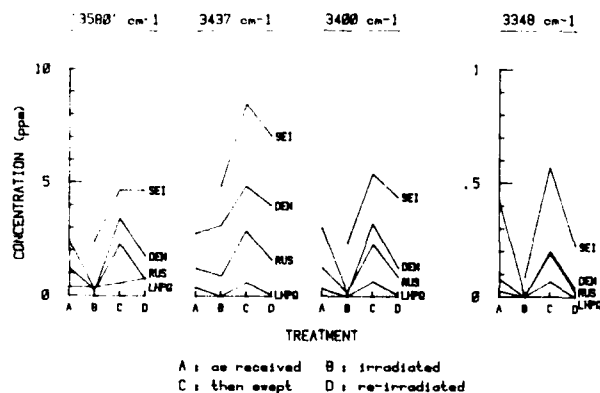


Figure 4. Individual OH Band Concentrations shown as a Function of Treatment

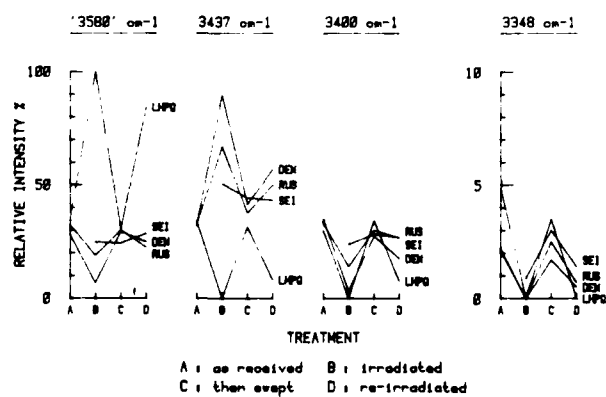


Figure 5. Individual OH Band Ratios as a Percentage of the Total Other OH Shown as a Function of Treatment

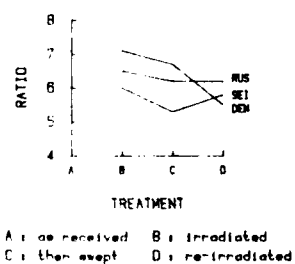


Figure 6. 3367  $\text{cm}^{-1}$ ; 3306  $\text{cm}^{-1}$  A1-OH Band Ratios Shown as a Function of Treatment

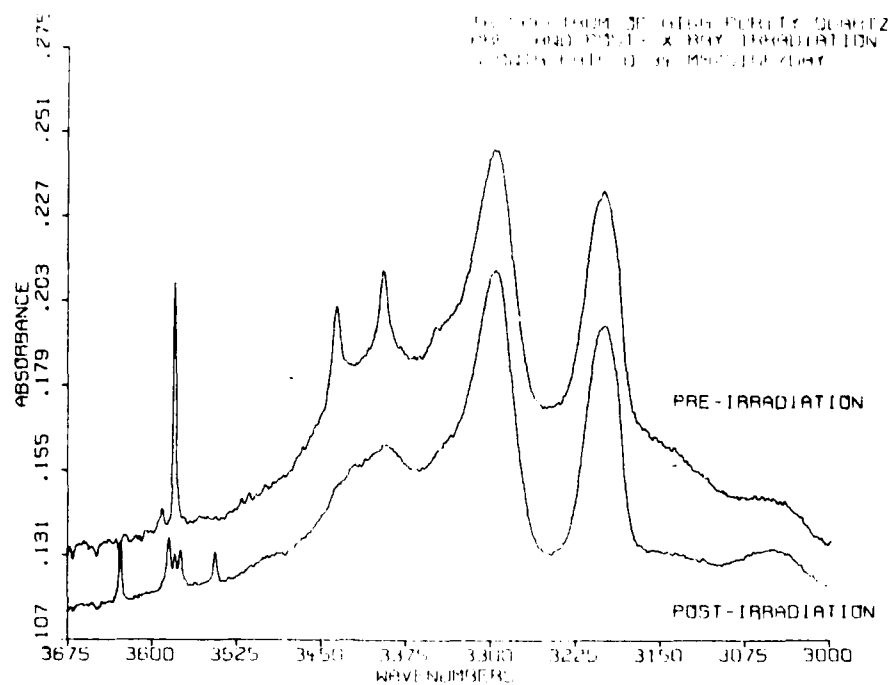


Figure 7. 77K Infrared Absorption Spectrum of High Purity Quartz LHPQ 13(1) as Received and Following Irradiation

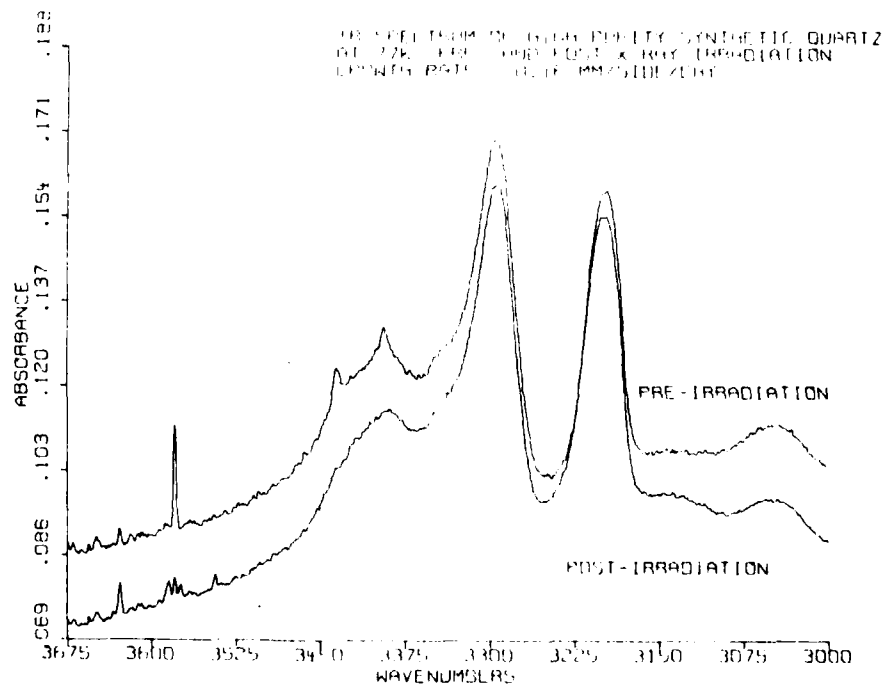


Figure 8. 77K Infrared Absorption Spectrum of High Purity Quartz LHPQ 20(1) as Received and Following Irradiation

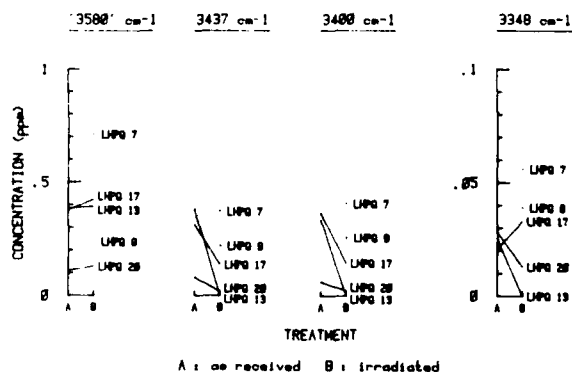


Figure 9. Individual High Purity OH Band Concentrations Shown as a Function of Treatment

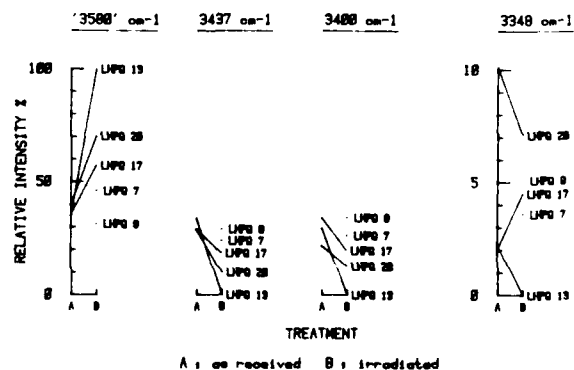


Figure 10. High Purity OH Band Concentrations as a Percentage of the Total Other OH Shown as a Function of Treatment

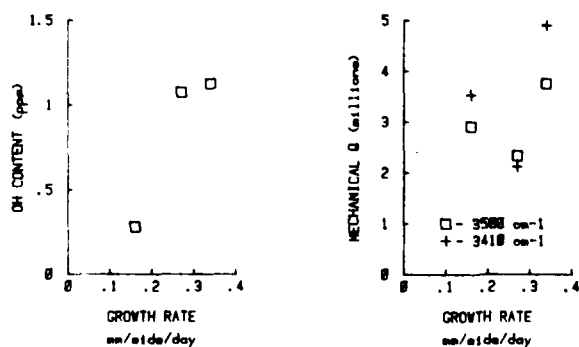


Figure 11. OH Content and Mechanical Q for High Purity Quartz Shown as a Function of Growth Rate

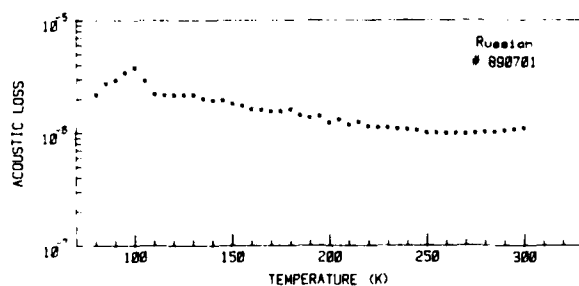


Figure 12. Acoustic Loss as a Function of Temperature for 5 MHz 5th Overtone AT-Cut Russian Quartz Resonator as Received

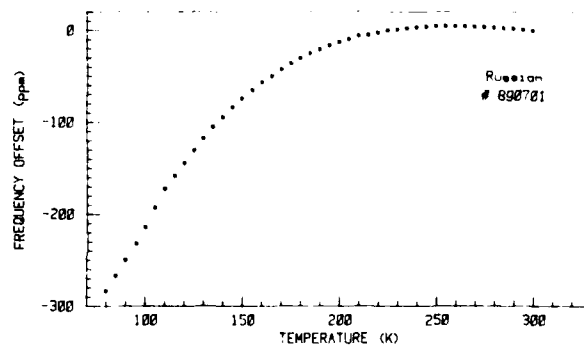


Figure 13. Frequency-Temperature Characteristic (normalized to 300K) for 5 MHz 5th Overtone AT-Cut Russian Quartz Resonator as Received

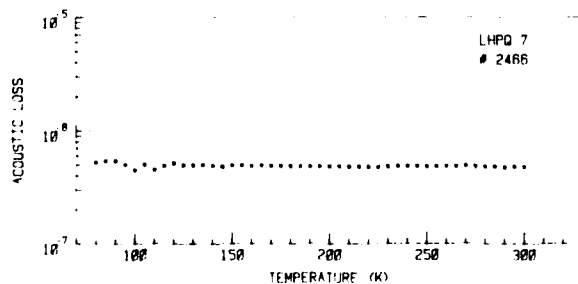


Figure 14. Acoustic Loss as a Function of Temperature for 5 MHz 5th Overtone AT-Cut High Purity Quartz Resonator as Received

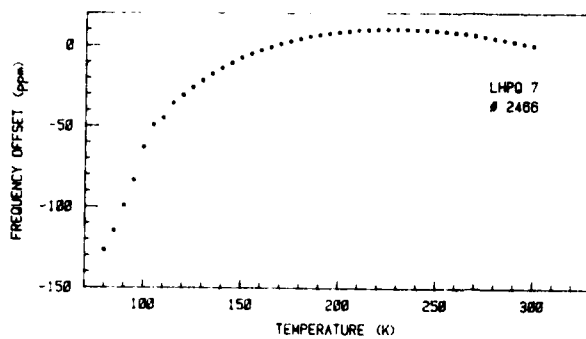


Figure 15. Frequency-Temperature Characteristic (Normalized to 300K) for 5MHz 5th Overtone AT-Cut High Purity Quartz Resonator as Received

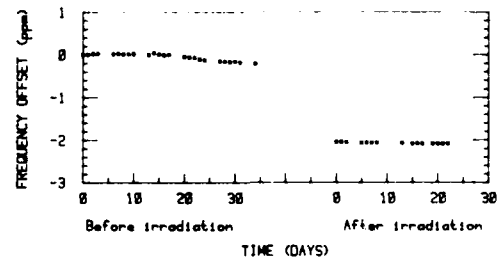


Figure 18. Fractional Frequency Shift as a Function of Time Before and After Irradiation for 20 MHz 3rd Overtone AT-Cut Natural Resonator No. 11

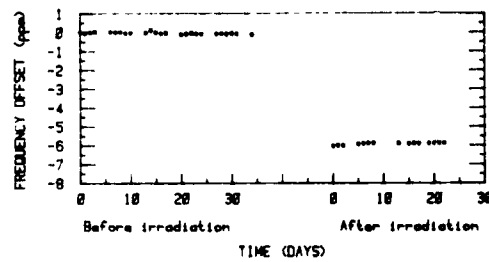


Figure 16. Fractional Frequency Shift as a Function of Time Before and After 1 MRad Irradiation for 20 MHz 3rd Overtone AT-Cut Natural Resonator No. 1

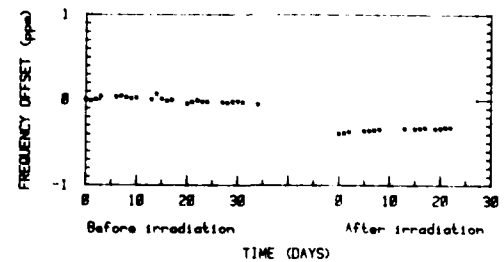


Figure 19. Fractional Frequency Shift as a Function of Time Before and After Irradiation for 20 MHz 3rd Overtone AT-Cut High Purity Resonator No. 12

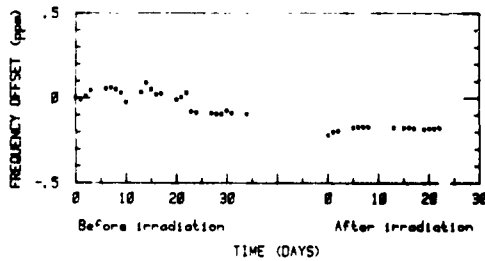


Figure 17. Fractional Frequency Shift as a Function of Time Before and After 1 MRad Irradiation for 20 MHz 3rd Overtone AT-Cut High Purity Resonator No. 2

AD P001506

THE INFLUENCE OF CRYSTAL GROWTH RATE AND  
ELECTRODIFFUSION (SWEEPING) ON POINT DEFECTS IN  $\alpha$ -QUARTZ\*

J. J. Martin, L. E. Halliburton, and R. B. Bossoli  
Oklahoma State University, Stillwater, Oklahoma 74078

and

A. F. Armington  
Rome Air Development Center, Hanscom AFB, Massachusetts 01731

Summary

As-grown quartz exhibits OH-related infrared absorption bands at 3585, 3437, and 3400  $\text{cm}^{-1}$  when examined at 77 K. We have investigated the strengths of these bands in a series of quartz crystals grown at different rates in the Air Force Hydrothermal Facility at Hanscom AFB. Growth rates were varied from 0.3 to 1.4 mm/day. All three infrared bands listed above were small for crystal growth rates below 0.3 mm/day. However, their strengths increase nearly linearly with growth rates above this value. The industry standard for determining the "Q value" of quartz is to measure the room temperature infrared absorption at or near 3500  $\text{cm}^{-1}$ . Our results indicate that slow growth results in a reduction of the OH<sup>-</sup> bands in this region and should correspond to higher Q material.

Electrodiffusion (sweeping) is a post-growth treatment which allows selective removal of interstitial ions from quartz and the technique has been commercially developed as a means of increasing the material's radiation hardness. In order to better understand this phenomenon, we have systematically investigated the various aspects of sweeping. Our results were obtained under a variety of conditions and include both alkali and proton sweeping. All quartz contains  $\text{Al}^{3+}$  ions substituting for  $\text{Si}^{4+}$  ions, with the necessary charge compensation provided by interstitial alkali ( $\text{Li}^+$  and  $\text{Na}^+$ ) ions or protons ( $\text{H}^+$ ). These interstitial ions can be released from their trapping sites by radiation or by thermal activation and then they can migrate through the crystal along the relatively large Z-axis channels. Protons from the surrounding air or hydrogen atmosphere can be brought into the crystal at the anode while alkali ions are removed at the cathode. When one alkali is to replace another alkali, the appropriate alkali salt is deposited at the anode and a vacuum surrounds the crystal. The sweeping is done in the 480 to 490°C range and the electric fields vary from greater than 3000 volts/cm for protons to less than 20 volts/cm for alkalis.

Introduction

As-grown synthetic alpha-quartz contains a variety of point defects.<sup>1,2</sup> These defects fall into two general categories: (1) substitutional aluminum ions with their associated interstitial alkali ion and (2) OH<sup>-</sup> molecules trapped adjacent to unidentified defects in the lattice. The concentration

of both types of defects increases with increased crystal growth rate, and both have been shown to play a direct role in the performance of crystal resonators. For example, early internal friction studies by Jones and Brown<sup>3</sup> showed that both the  $\text{Al-Na}^+$  center loss peak near 50 K and the room temperature acoustic loss of 5MHz 5th overtone AT-cut crystals increased with the rate at which the original stone was grown. In the case of hydrogen, Dodd and Fraser<sup>4</sup> and Sawyer<sup>5</sup> have shown that the mechanical Q of a crystal is related to the OH<sup>-</sup> content of the quartz. This result has led to the routine use of infrared optical absorption as a method of predicting the Q of a quartz stone. The optical Q is usually determined by comparing the room temperature absorption coefficient at 3500  $\text{cm}^{-1}$  with that at 3800  $\text{cm}^{-1}$ . In high quality quartz, this is basically a measurement of the intensity of the temperature-broadened OH<sup>-</sup> bands at 3437  $\text{cm}^{-1}$  and 3400  $\text{cm}^{-1}$ .

Interstitial alkali ions and protons are trapped by substitutional aluminum ions and, quite possibly, by other defects. When thermally liberated from their traps, they can diffuse along the large Z-axis channels. This diffusion is responsible for the increasing acoustic loss observed at high temperatures<sup>6,7,8</sup> and for the annealing behavior of radiation-induced defects. A technologically important result occurs when an electric field applied parallel to the Z axis is used to force these interstitial ions out of the sample and replace them with others. King,<sup>9</sup> making use of this characteristic, was among the first to develop the electrodiffusion (sweeping) process as a method for changing the concentration of specific interstitial cations. During his extensive infrared study, Katz<sup>10</sup> used this process to "sweep" hydrogen and alkali ions into and out of the quartz. Fraser<sup>11</sup> described the basic technology for the selective sweeping of alkalis and Kreft<sup>12</sup> has shown that holes can be swept into quartz if the process is carried out in vacuum at temperatures above the phase transition. Brown, O'Connor and Armington<sup>13</sup> have investigated alkali sweeping and the use of an inert gas atmosphere. A number of studies have shown that the radiation hardness of oscillators is significantly enhanced if electrodiffusion is used to replace the alkalis in quartz with protons.<sup>14-16</sup> Recently, Jain and Nowick<sup>17</sup> have investigated ionic conductivity in both synthetic and natural quartz.

Electrodiffusion is closely related to ionic conductivity in quartz. The main difference is that

in electrodiffusion specific ions (protons or an alkali) are brought into the sample and exchanged for the monovalent ions initially present. Electrical conduction in quartz is mainly ionic and one-dimensional. The conductivity is governed by the motion of these monovalent ions along the Z-axis channels. In as-grown quartz, alkali ions are interstitially trapped next to the substitutional aluminum and are thermally released as the temperature increases. If only one alkali species, say  $\text{Na}^+$ , is present the conductivity can be described as

$$\sigma = nev \quad (1)$$

where  $n$  is the number of monovalent ions released from the traps,  $e$  is the fundamental charge, and  $v$  is their mobility. When the ions are almost completely associated with the aluminum we expect that

$$n \sim \exp(-E_A/2kT) \quad (2)$$

where  $E_A$  is the energy of association. The mobility is also thermally activated with

$$v = \frac{ed^2}{kT} \nu \exp(-E_m/kT) \quad (3)$$

where  $d$  is the jump distance,  $\nu$  the jump frequency, and  $E_m$  is the activation energy for the interstitial migration.<sup>18</sup> Equations (2) and (3), when combined with Eq. (1), suggest that the conductivity can be described by

$$\sigma T = A \exp(-E/kT) \quad (4)$$

where

$$E = E_m + \frac{1}{2}E_A \quad (5)$$

Thus, a plot of  $\log(\sigma T)$  versus  $T^{-1}$  should yield a straight line. Jain and Nowick<sup>17</sup> observed such behavior and found activation energies near 1.4 and 1.0 eV for synthetic and natural quartz, respectively. The problem of electrodiffusion is somewhat more complicated since several species of ions are being transported, each of which will have different mobilities and different association energies, and since ions are moving into and out of the sample. However, the basic process is expected to be thermally activated and governed, at least to the first approximation, by Eqs. (4) and (5).

A systematic study of the electrodiffusion process in quartz is presently underway at Oklahoma State University. We are carrying out this study using  $\text{H}_2$ ,  $\text{D}_2$ , and vacuum atmospheres. The process for alkalis is being investigated by using salt-film electrodes as the source of the alkali ions. Measurements of the ionic currents are being made as functions of time, temperature, and applied electric field.

#### Experimental Procedure

The series of quartz stones used in our growth rate study were grown at rates ranging from 0.3 mm/day to 1.4 mm/day at the Air Force Hydrothermal Facility.<sup>19,20</sup> The nutrient was synthetic quartz and the seeds were  $\text{O}^\circ$  plates. Sodium hydroxide with a small quantity of lithium hydroxide was used as the mineralizer for all runs except one where sodium carbonate was used. The autoclave was three inches in diameter. Optical samples having typical dimensions of  $10 \times 10 \times 3 \text{ mm}^3$  for the X, Y, and Z

directions, respectively, were cut from the z-growth region of each stone. A Beckman 4240 infrared spectrophotometer was used for the optical absorption measurements. A Dewar containing liquid nitrogen maintained the sample near 80 K during the measurements. Since Z-plate samples were used, the electric vector of the incident light was always perpendicular to the Z axis. The samples were run in the as-grown condition and then were re-run after receiving an intense room temperature irradiation. This irradiation converted the aluminum-alkali centers into  $\text{Al}^-\text{OH}^-$  and  $\text{Al}^-\text{hole}$  centers. The latter infrared scan revealed the infrared-active  $\text{Al}^-\text{OH}^-$  centers and allowed us to estimate the aluminum content of each sample.

The electrodiffusion studies were carried out on samples cut from unswept lumbered bars of z-growth material. These were purchased from Sawyer Research Products and included Electronic Grade, Premium Q, and Super Premium Q quartz. The actual sweeping samples were polished Z plates 3 mm thick and 15 mm x 17 mm in the X and Y directions. Such samples are a convenient size for use in the sweeping apparatus and for subsequent infrared evaluations. Plano-convex AT-cut resonator blanks of the Warner design are directly swept when acoustic loss measurements are used for evaluation.

The sweeping system consisted of a vitreous silica jacket evacuated with a diffusion pump and heated by an external clamshell furnace. This system allows us to electrodiffuse quartz either in a controlled atmosphere or in a vacuum of  $5 \times 10^{-6}$  Torr or better. The quartz plate is usually mounted between graphite clamps and the sample temperature is measured by a thermocouple attached to the bottom clamp. A variable DC power supply is used to establish the electric field with typical fields being 15 V/cm for alkali sweeps and 3000 V/cm or greater for hydrogen sweeps.

The sweeping procedure begins by vapor depositing gold electrodes on the two sample faces. If Li, Na, or K is to be swept into a crystal, the appropriate salt is first vapor deposited on one side and is then followed by a gold electrode. The electrodiffusion is carried out in the desired atmosphere at a temperature between 480 and 490°C. A  $\text{H}_2$  atmosphere is used for hydrogen sweeping, whereas all alkali sweeping is done in vacuum. (The graphite clamps are baked-out before each alkali sweep.) The sample current is recorded as a function of time using a digital multimeter and a laboratory computer. Hydrogen sweeps are continued until the current becomes steady, which takes approximately 24 hours. Alkali sweeps are continued until a sufficient number of positive ions have been transported; this usually takes less than two hours. When the sweep is complete the furnace is slowly programmed down in temperature while the sample current and temperature are continually recorded. These latter data give the effective ionic conductivity as a function of temperature for the specific process.

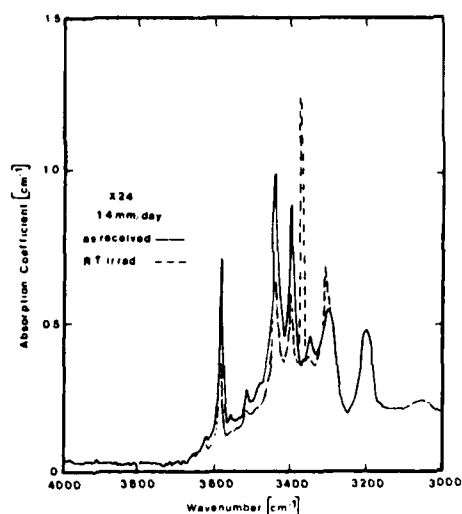


Fig. 1. The solid curve shows the infrared absorption spectrum for a fast-growth sample. The 3585, 3437, and 3400  $\text{cm}^{-1}$   $\text{OH}^-$  bands are large. The dashed curve shows that a room-temperature irradiation reduces these  $\text{OH}^-$  bands and produces the 3367 and 3306  $\text{cm}^{-1}$   $\text{Al-OH}^-$  bands.

#### Results and Discussion

##### Growth Rate Study

The infrared absorption at liquid nitrogen temperature of a z-growth sample cut from a stone grown at 1.4 mm/day is shown by the solid line in Fig. 1. This spectrum is similar to that reported by Sibley et al.<sup>2</sup> for Sawyer Electronic Grade material. The dashed line in Fig. 1 shows the effect of a room temperature irradiation on the sample. Such an irradiation removes alkali ions from the aluminum sites and removes protons from the defects responsible for the absorption bands at 3585  $\text{cm}^{-1}$ , 3437  $\text{cm}^{-1}$ , and 3400  $\text{cm}^{-1}$ . The protons are transferred to the aluminum site and form  $\text{Al-OH}^-$  centers which give rise to the 3367  $\text{cm}^{-1}$  and 3306  $\text{cm}^{-1}$  bands. Some  $\text{Al}^-$  hole centers also are created by the room-temperature irradiation.

Figure 2 shows the peak absorption coefficients for the 3585  $\text{cm}^{-1}$  and 3400  $\text{cm}^{-1}$   $\text{OH}^-$  bands as a function of crystal growth rate. Both bands increase rapidly for growth rates faster than 0.7 mm/day. Although not plotted in Fig. 2, the 3437  $\text{cm}^{-1}$  band shows similar behavior. The infrared absorption spectrum for the two slowest grown samples are very similar to that observed by Sibley et al.<sup>2</sup> for Sawyer Premium Q grade material. Figure 3 shows that the aluminum content, as measured by the height of the 3367  $\text{cm}^{-1}$   $\text{Al-OH}^-$  band produced by a room-temperature irradiation, also increases with growth rate. The ESR test<sup>21</sup> for aluminum concentration was run on the slowest and fastest grown samples. They showed approximately 1 ppm and 12 ppm aluminum, respectively.

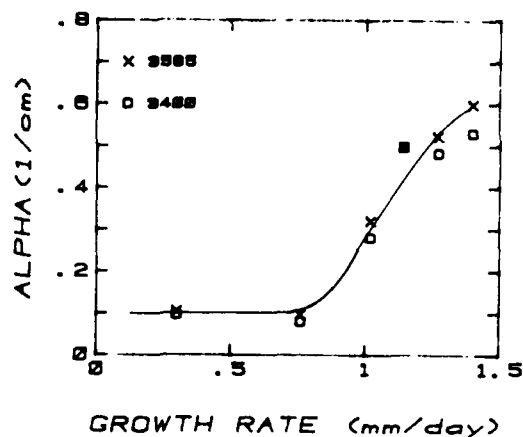


Fig. 2. The heights of the 3585 and 3400  $\text{cm}^{-1}$   $\text{OH}^-$ -related bands are shown as a function of growth rate. The 3437  $\text{cm}^{-1}$  band follows the same curve.

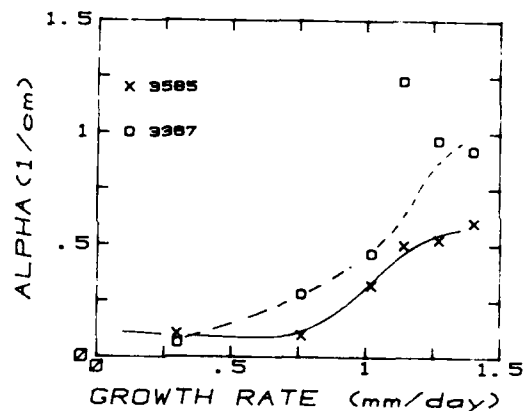


Fig. 3. The 3585  $\text{OH}^-$  defect band and the 3367  $\text{cm}^{-1}$   $\text{Al-OH}^-$  band are shown as a function of the growth rate.

##### Electrodiffusion Study

The current-versus-time curves obtained by sweeping  $\text{H}^+$  and  $\text{Na}^+$  into Z-plate samples from Premium Q grade bar PQ-B are shown in Fig. 4. Similar curves were obtained for samples from Electronic Grade bar EG-B and Super Premium Q bar SP-A. The curves are characterized by an initial decrease which we believe is caused by the replacement of  $\text{Li}^+$  ions with protons or  $\text{Na}^+$  ions. When  $\text{Li}^+$  is swept into previously unswept samples, the initial decrease of the current is much smaller than that shown in Fig. 4. The steady current observed after the initial decrease (i.e., at later times) apparently represents the continuous motion of one species through the sample. The alkali sweeps are usually terminated after 30 to 120 minutes in order to prevent depletion of the source film of alkali

salt. The curves shown in Fig. 4 were obtained with applied fields of 4000 V/cm for the hydrogen and 17 V/cm for the sodium runs, respectively. Similar low fields of 10 to 20 V/cm give comparable currents when sweeping  $\text{Li}^+$  and  $\text{K}^+$ . It appears that hydrogen, which is the ion used in commercial sweeping, is much less mobile than the alkalis.

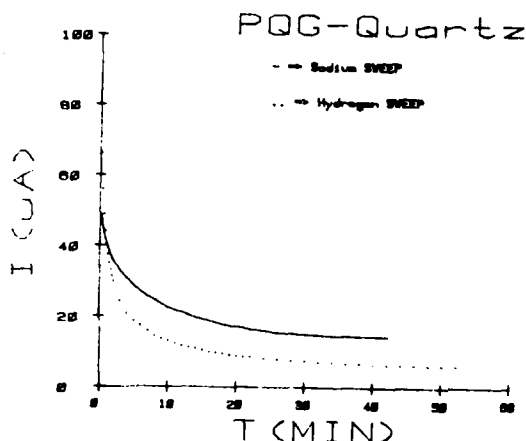


Fig. 4. The current-versus-time for the electrodiffusion of sodium and hydrogen in Premium Q grade samples PQ-GN and PQ-GH are shown.

Infrared scans at liquid nitrogen temperatures were made as a routine characterization of samples after sweeping. No changes in the infrared spectra were found as a result of alkali sweeps using  $\text{Li}^+$ ,  $\text{Na}^+$ , and  $\text{K}^+$ . When hydrogen was swept into the crystals, the 3367 and 3306  $\text{cm}^{-1}$   $\text{Al}-\text{OH}^-$  infrared bands were produced, as expected. This shows that the alkali ion initially charge compensating the aluminum was replaced by a proton.

Since we were unable to observe any significant difference between  $\text{Na}^+$ ,  $\text{Li}^+$ , or  $\text{K}^+$  swept samples with either infrared or electron spin resonance techniques, we investigated the acoustic loss spectra from a series of 5MHz 5th overtone AT-cut resonator blanks fabricated from Premium Q material (bar PQ-E). Earlier reports by Martin et al.<sup>22,23</sup> have shown that the as-grown blanks have a small loss peak at 55 K due to the  $\text{Al}-\text{Na}^+$  center. When the blanks were swept with hydrogen, deuterium, or lithium, this  $\text{Al}-\text{Na}^+$  loss peak was removed and no new peaks were introduced.

Figure 5 compares the acoustic loss,  $Q^{-1}$ , spectra of unswept,  $\text{Li}^+$ -swept, and  $\text{Na}^+$ -swept resonator blanks. The unswept blank shows a small  $\text{Al}-\text{Na}^+$  loss peak at 55 K with a height,  $\Delta Q^{-1}$ , of approximately  $0.5 \times 10^{-6}$ . No such peak was found in the  $\text{Li}^+$ -swept blank, while the  $\text{Na}^+$ -swept blank showed a very large 55 K peak with  $\Delta Q^{-1} = 2 \times 10^{-4}$ , as shown in Fig. 5. Since this bar contains 10 to 15 ppm aluminum<sup>1</sup>, we conclude that the concentration, C, of  $\text{Al}-\text{Na}^+$  centers is given by

$$C = [5(\pm 20\%) \times 10^4] \Delta Q^{-1} \quad (6)$$

where C is the concentration in ppm and  $\Delta Q^{-1}$  is the height of the  $\text{Al}-\text{Na}^+$  center loss peak at 55 K. Thus, the unswept blank probably contains about 0.3 ppm  $\text{Al}-\text{Na}^+$  centers; the remaining 10 to 15 ppm of aluminum must be compensated by  $\text{Li}^+$ . Since the mineralizer used in growing Premium Q quartz is predominantly  $\text{Na}_2\text{CO}_3$ , the essentially total exclusion of  $\text{Na}^+$  from the aluminum sites by the addition of the small amount of  $\text{Li}_2\text{CO}_3$  to the growth solution is remarkable. Since the unswept and  $\text{Li}^+$ -swept blanks both contain 10-15 ppm  $\text{Al}-\text{Li}^+$  centers, we believe that the  $\text{Al}-\text{Li}^+$  center does not couple to the AT-cut thickness shear mode. An additional, much smaller, loss peak related to the  $\text{Al}-\text{Na}^+$  center was observed at approximately 135 K in the AT-cut blank that had been  $\text{Na}^+$  swept. Park and Nowick<sup>24</sup> observed two sodium-related peaks in their dielectric loss measurements.

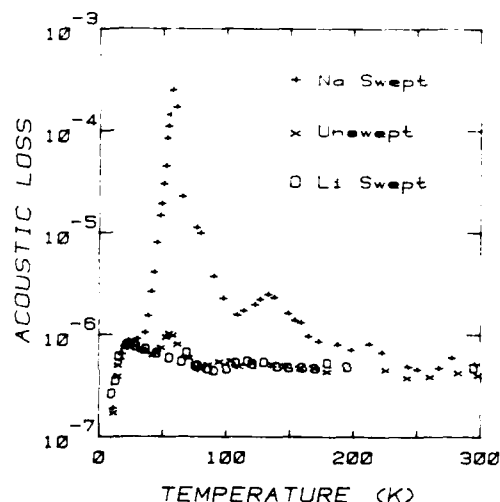


Fig. 5. The acoustic loss-versus-temperature spectrum for unswept,  $\text{Li}^+$ -swept, and  $\text{Na}^+$ -swept 5MHz 5th overtone AT-cut resonator blanks all fabricated from bar PQ-E are shown. The peak at 55 K is due to the  $\text{Al}-\text{Na}^+$  center.

When the current reaches a steady value during a sweeping run we believe that one species of ion is brought into the sample at the positive electrode, transported through the sample, and removed at the negative electrode. Therefore, only one species is involved in the conduction process and the conductivity should be described by Eqs. 1 through 5. Figure 6 shows a plot of  $\log \sigma T$  versus  $1000/T$  for a sodium sweep and a hydrogen sweep on previously unswept samples taken from bar PQ-G. Both curves show the expected straight line behavior. The apparent conductivity in the hydrogen sweep is much less than that for the sodium sweep. Activation energies of 1.2 and 1.9 eV were found for the sodium and hydrogen sweeps, respectively. Our value of 1.2 eV for the sodium case is slightly less than 1.3 to 1.4 eV found by Jain and Nowick<sup>17</sup> in their ionic conductivity studies of synthetic

quartz. We have observed activation energies ranging between 0.95 and 1.2 eV for lithium and sodium electrodiffusion in a number of Electronic Grade and Premium Q samples. Our values of the activation energy for hydrogen sweeping vary between 1.8 and 1.9 eV. In interpreting these numbers, it is important to remember that the observed activation energy in ionic conductivity depends upon both the migration energy and upon the association energy of the traps, and other factors may also be involved since ions are brought into and out-of the sample.

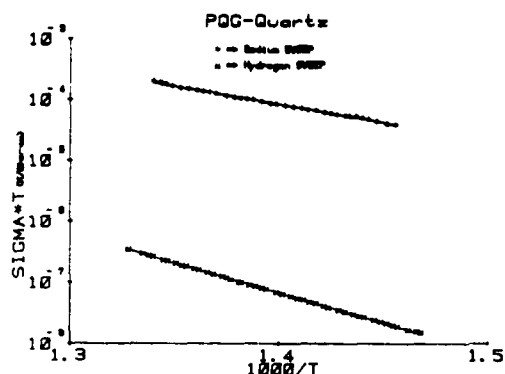


Fig. 6. The apparent ionic conductivity is plotted as  $\log(\sigma T)$  versus  $1000/T$  for sodium and hydrogen electrodiffusion runs on samples from bar PQ-G.

#### Conclusions

Both the  $\text{OH}^-$ -related defects which give rise to infrared bands at 3585, 3437, and  $3400 \text{ cm}^{-1}$  and the aluminum content increase with the growth rate of a quartz stone. Therefore, the slowest growth should yield the highest quality material. Since all quartz contains some aluminum, electrodiffusion to replace the alkali with hydrogen will improve its performance. Alkali ions can be swept into as-grown quartz using the appropriate salt as a source and a vacuum atmosphere. Also, it has been shown that  $\text{Na}^+$  and  $\text{Li}^+$  ions can be interchanged. Hydrogen can be swept in using either a  $\text{H}_2$  or an air atmosphere and the electrodiffusion of protons requires a much larger applied electric field than is needed for alkalis. Both hydrogen and alkali electrodiffusion have been shown to be thermally activated processes and activation energies have been measured.

#### Acknowledgement

This work was supported in part by U.S. Air Force Contract F19628-80-C-0086, RADC, Hanscom AFB, MA 01731.

#### References

1. L. E. Halliburton, N. Koumvakalis, M. E. Marques and J. J. Martin, *J. Appl. Phys.* **52**, 3565 (1981).
2. W. A. Sibley, J. J. Martin, M. C. Wintersgill and J. D. Brown, *J. Appl. Phys.* **50**, 5449 (1979).
3. C. K. Jones and C. S. Brown, *Proc. Phys. Soc.* **79**, 930 (1962).
4. D. M. Dodd and D. B. Fraser, *J. Phys. Chem. Solids* **26**, 673 (1965).
5. B. Sawyer, *IEEE Trans. Sonics Ultrason.* **SU-19**, 41 (1972).
6. D. B. Fraser, In *Physical Acoustics*, W. P. Mason, ed Vol. V, pp. 54-110, Academic Press, N.Y. (1968).
7. D. R. Koshler, *Proc. of the 35th Ann. Freq. Control Symposium, USAERADCOM, Ft. Monmouth, N. J.*, p. 322, May (1981).
8. H. G. Lipson, A. Kahan, R. N. Brown and F. K. Euler, *Proc. 35th Ann. Freq. Control Symposium USAERADCOM, Ft. Monmouth N. J.*, p. 329, May (1981).
9. J. C. King, *Bell Syst. Techn. J.* **38**, 573 (1959).
10. A. Kats, *Phillips Res. Rpts* **17**, 133 (1962).
11. D. B. Fraser, *J. Appl. Phys.* **35**, 2913 (1964).
12. Gerda B. Kreft, *Rad. Effects* **26**, 249 (1975).
13. R. N. Brown, J. J. O'Conner and A. F. Armington, *Mat. Res. Bull.* **15**, 1063 (1980).
14. T. M. Flanagan and T. F. Wrobel, *IEEE Trans. Nucl. Sci.* **NS-16**, 130, (Dec. 1969).
15. P. Pellegrini, F. Euler, A. Kahan, J. M. Flanagan and T. F. Wrobel, *IEEE Trans. Nucl. Sci.* **NS-25**, 1267 (1978).
16. J. C. King and H. H. Sanders, *IEEE Trans. Nuc. Sci.*, **NS-19**, 23 (1972).
17. H. Jain and A. S. Nowick, *J. Appl. Phys.* **53**, 477 (1982).
18. A. B. Lidiard, *Hand. d. Physik* **20**, 246 (1957).
19. A. F. Armington, J. J. Larkin, J. J. O'Conner, and J. A. Horrigan, *Proc. 35th Ann. Freq. Control Symposium, USAERADCOM, Ft. Monmouth, N. J.*, p. 297, (1981).
20. The growth rate for quartz is defined as the increase in thickness of the stone, including both sides, per unit time in the direction perpendicular to the seed plate.
21. M. E. Marques and L. E. Halliburton, *J. Appl. Phys.* **50**, 8172 (1979).
22. J. J. Martin and S. P. Doherty, *Proc. 34th Ann. Freq. Control Symposium, USAERADCOM, Ft. Monmouth, N. J.*, p. 81, (1980).
23. J. J. Martin, L. E. Halliburton, and R. B. Bossoli, *Proc. 35th Ann. Freq. Control Symposium, USAERADCOM, Ft. Monmouth, N. J.*, p. 317, (1981).
24. D. S. Park and A. S. Nowick, *Phys. Stat. Sol.* (a) **26**, 617 (1974).

\*Copies of the proceedings are available from the Electronics Industries Association, 2001 Eye Street, NW, Washington D.C. 20006

A COMPARISON OF QUARTZ CRYSTALS GROWN FROM FUSED SILICA  
AND FROM CRYSTALLINE NUTRIENT\*

R. J. Baughman

Sandia National Laboratories  
Albuquerque, New Mexico 87185

Summary

Synthetic quartz crystals are traditionally grown from a crystalline nutrient. Most of the present crystal growth is from natural quartz nutrient imported from Brazil. This material is handpicked for quality but does have limited purity levels. The raw material may or may not contain levels of impurities that are detrimental to the intended purpose of the grown crystal. Impurity concentration and species of natural lascus are not uniform or consistent even when produced from the same source of supply.

This work reports a comparison of crystals grown in 1978 from a fused silica nutrient and crystalline nutrient in a new autoclave to those recently grown in the same aged autoclave. Several crystal characteristics will be discussed.

Introduction

The growth of synthetic single crystal quartz has evolved to giant proportions with the increase in our technological way of life. Hundreds of thousands of pounds of quartz crystals are used by the communications (including CB radio), telephony, electronic watch, and frequency and time standards industries. The demands of these technologies for synthetic quartz crystals have pushed commercial sources beyond present capacities, both with respect to quantity of crystals grown and the need for ever increasing quality. Most of the present synthetic material is grown from natural crystalline quartz nutrient imported from Brazil. This material is handpicked for quality but does have limited purity levels. This single-source-of-supply

situation causes some concern in the industry. There are deposits of crystalline quartz materials available elsewhere, but they are limited.

With vast supplies of amorphous silica available on this continent, it would be advantageous if these materials could be used to grow synthetic quartz crystals. Very high purity fused silica is now being produced from these sources of supply and is readily available. Efforts to grow usable high quality quartz crystals from an amorphous nutrient have not been successful.<sup>1-4</sup>

Attempts to grow quartz single crystals using a SiO<sub>2</sub> glass (amorphous) nutrient is not a recent endeavor. In 1946, both Nacken<sup>2</sup> and the Woosters<sup>3</sup> proposed the growth of quartz crystals using amorphous silica as nutrient because of its very high solubility in alkaline solutions. Both were unsuccessful. Walker<sup>4</sup> abandoned the method in 1947. The most recently reported growth from this nutrient came from E. D. Kolk et al<sup>1</sup> in 1976. This work was directed at finding new sources of nutrient materials and covered both crystalline and amorphous materials. Regarding the amorphous materials, they reported that the quality was poor with grown specimens exhibiting many cracks.

The high solubility of fused silica in caustic solution originally attracted workers to this nutrient and subsequently turns out to be one of the major problems to its successful utilization. This high solubility can allow massive transport of silicate materials, resulting in uncontrollable deposition of nutrient on the seed crystals as well as being responsible for significant spurious nucleation and growth. To compound the problem, fused silica undergoes a transformation from the amorphous phase to a crystalline phase early in the crystal growth procedure. This transformation is responsible for continually changing the material transport rate due to the large difference in solubility<sup>4</sup> of the two separate SiO<sub>2</sub> phases.

\*This work performed at Sandia National Laboratories supported by the U. S. Department of Energy under contract number DE-AC04-76-DP00789.

AD P001507

These growth problems have now been overcome and several characteristics of crystals grown directly from a fused silica nutrient are reported.

### Infrared Absorption

The quartz crystal samples were 10 x 10 x 1 mm in dimension and were cut parallel to the AT orientation. The samples grown from a crystalline nutrient (Sawyer Premium Q) are labeled 1-11-3. Those grown from a fused silica nutrient (Suprasil-2) in a virgin autoclave are labeled 1-24-3, and those grown from fused silica nutrient in an aged autoclave are labeled 1-16-3. The quartz seed material was from Western Electric Company and is labeled WE.

Near-infrared-visible spectra of the above quartz samples was obtained on a Cary 14 UV-vis-nir double grating spectrophotometer. Standard light sources and detectors were employed. The spectra were taken with an air reference and were subsequently digitized and normalized for baseline variations and plotted on the expanded scale as shown.

Figure 1 shows absorption data in the near-infrared visible region from 4,000 to 10,000  $\text{cm}^{-1}$ . This figure compares crystals grown from a fused silica nutrient (1-16-3) with crystals grown from Sawyer Premium Q grade nutrient (1-11-3). A spectrum of Western Electric seed crystal stock is also included. Absorption in this region yields little analytical information other than identifying broad general absorption zones and impurity bands. Combination bands at the upper 4000 and 6000  $\text{cm}^{-1}$  region are attributed to  $\text{OH}^-$  bending and stretching. The band at  $\sim 5500 \text{ cm}^{-1}$  is probably due to inclusion of molecular water. This figure does show that the crystals grown from fused silica contains less  $\text{OH}^-$  and molecular water than those grown from a crystalline nutrient. All are higher quality than the seed plate material from Western Electric.

Figure 2 compares the absorption of fused silica grown quartz produced in a virgin autoclave (1-24-3) with that grown in an aged autoclave (1-16-3). The general  $\text{OH}^-$  bond and stretching absorptions are present while the molecular water band at 5500  $\text{cm}^{-1}$  is notably absent in both curves.

The FT-IR data were taken with a Nicolet 7199 Fourier transform infrared spectrometer equipped with a liquid nitrogen cooled  $\text{HgCdTe}$  detector. The

spectra were taken at a 2  $\text{cm}^{-1}$  resolution with 256 interferograms coadded for greater signal-to-noise ratios. Both room temperature and 93K spectra were obtained while the spectrometer was purged with  $\text{N}_2$ . The low temperature data were obtained using a Beckman Model VLT-2 liquid nitrogen cryostat.

Infrared absorption spectra for crystals 1-16-3 are presented in Figure 3. These spectra represent data observed at room temperature and at 93K. Although limited information can be extracted from these broad range curves, they do indicate areas of further interest. The area of major interest, 3000 to 3700  $\text{cm}^{-1}$  is further amplified in Figures 4, 5, and 6.

A comparison of IR absorption at room temperature and at 93K for crystals 1-16-3 is presented in Figure 4. Lattice mode overtone absorptions at 3200 and 3300  $\text{cm}^{-1}$  are broad and do not sharpen with decreases in temperature. Those bands that do sharpen with decreased temperature are associated with  $\text{OH}^-$  stretching vibrations.

Many of the absorption peaks have been identified in work published by Katz<sup>5</sup>. The band at 3400  $\text{cm}^{-1}$  is attributed to  $\text{OH}^-$  in the vicinity of  $\text{Li}^+$  while the band at 3581  $\text{cm}^{-1}$  is due to  $\text{OH}^-$  near  $\text{K}^+$ . Lipson et al<sup>6</sup> identified bands at 3348 and 3487  $\text{cm}^{-1}$  as being associated with  $\text{OH}^-$ .

In Figure 5, the 93K spectra are presented for crystal 1-16-3 and the crystal grown from Sawyer Premium Q nutrient (1-11-3). It is seen that the spectra are nearly identical for each absorption band. Verification of this similarity is confirmed by a direct subtraction of the 1-16-3 spectra from that of the 1-11-3 sample. This difference spectrum is presented as the lower curve of Figure 5. This curve indicates that the impurity levels of these two crystal samples are the same order of magnitude.

Infrared spectra for Western Electric seed plate crystals are compared to 1-16-3 in Figure 6. There are noticeable differences in these bands. The Western Electric material shows bands at 3306 and 3367  $\text{cm}^{-1}$  that are identified by Katz<sup>5</sup> as being  $\text{OH}^-$  near  $\text{Al}^{+3}$  that have no alkali metal ions in the vicinity. Two bands, 3470 and 3590  $\text{cm}^{-1}$ , occur in the Western Electric sample that are absent in all other tested crystals.

### Conductivity Measurements

Thin disks of single crystal quartz cut normal to the AT orientation were sandwiched between evaporated Al electrodes and mounted on an Al support. The sample is mounted in a vacuum chamber to avoid spurious signals due to air ions. The electrodes are attached to 50 ohm coaxial cables, so that the bias can appear on one center conductor and the signal on the other, with the whole system shielded. The current due to charge carriers created in the bulk of the crystal by an x-ray pulse was monitored by a Keithley 602 electrometer and digitized on a Nicolet Signal Averager. The dose to the sample from the Febetron 706, 600 keV pulsed electron beam x-ray source is calibrated with CaF<sub>2</sub> thermoluminescent dosimeters (TLD) and monitored on each shot with a photodiode responding to pilot B scintillator. This work is described in more detail in the work by R. C. Hughes.<sup>7</sup>

Figure 7 shows the potential well for a Na<sup>+</sup> ion which is compensating an Al substitutional. Ionizing radiation causes the formation of electron-hole pairs which can diffuse through the quartz lattice. Many holes will find one of these sites and become bound to it (the A center). The alkali ion is now free to diffuse down the c-axis channel. These ions give rise to a large delayed radiation-induced current (DRIC), which can be monitored after a radiation pulse. There is a rough correlation between the hardness of a quartz resonator and the magnitude of the DRIC: the higher the DRIC the worse the performance of an oscillator made from that quartz sample.

The DRIC from sample 1-16-3 following a 3 nanosecond x-ray pulse is shown in Figure 8. The magnitude of the signal and its time dependent decay are similar to unswept natural z-cut quartz which we have studied and indicates the presence of a few parts per million Al with alkali compensating ions. It is expected that quartz grown with smaller amounts of substantial Al impurity will show a much smaller DRIC and will probably make harder quartz resonators.

### Analytical Results

The results of chemical analyses are tabulated in Table I. The materials are divided among three categories: liquid reagents, solid reagents, and silicon-rich materials. Two of the liquid reagents (the distilled water samples)

were analyzed by inductively-coupled plasma optical emission spectrometry. Because of its high sodium content, the caustic solution could be more sensitively analyzed by flameless atomic absorption spectrometry. The liquid reagents were analyzed by the comparison of synthetic standards to the neat reagents or by the standard addition of known amounts of sought for elements to the reagents. Thus, sample handling was minimized and sensitivity was maximized. A report of "less-than-or-equal-to" indicates that instrumental factors or laboratory contamination limited the sensitivity of the analytical technique.

The solid reagents were dissolved in distilled water, sometimes with the aid of ultrapure mineral acids, and analyzed by flameless atomic absorption or inductively-coupled plasma optical emission spectrometry.

Known amounts of the analytes were added to aliquots of the dissolved reagents in order to obtain analytical curves. Concentrations of analytes obtained in solution were converted to concentrations in terms of micrograms of analyte per gram of solid reagent and are thus reported.

The silicon-rich materials (suprasil, alpha quartz, and the autoclave residue) were analyzed by (thermal) neutron activation and wet analysis.

Except for etching the exterior of the samples to remove contamination, no sample treatment was required for neutron activation. The samples were irradiated for 12 minutes. Longer irradiation times would reduce the detection limits for long-lived isotopes (e.g., of Fe, Ni, Cr, and Ag) by a factor of 10 or more. Results obtained by neutron activation analysis are indicated by an asterisk in the accompanying table. For the remaining elements, the samples were dissolved in ultrapure hydrofluoric acid, which was subsequently fumed off in ultrapure sulfuric acid. The resulting solutions were analyzed by flameless atomic absorption or inductively-coupled plasma optical emission spectrometry for lithium, iron, and (for the autoclave residue) potassium, and aluminum. Aluminum in the suprasil and the alpha quartz was analyzed by the fluorescence of its 8-hydroxy quinolate complex. The aluminum values reported are the excess over laboratory contamination corresponding to approximately 0.8 microgram aluminum per gram of sample.

### Conclusion

Although no special procedures to enhance crystal purity levels were undertaken, it is evident from the infrared, DRIC, and analytical data that crystals grown from a fused silica nutrient are equal in quality to the best commercially available quartz crystals. Crystals grown from Sawyer Premium Q nutrient provides the best available source of raw material for the growth of synthetic quartz. Crystals grown from this nutrient did not exceed the quality of the fused silica produced crystals. It is shown that crystals produced in a virgin autoclave do contain more impurities than those produced from an aged autoclave. This data indicates that further efforts to reduce the exposure of the autoclave body to the caustic growth solution would be advantageous.

### Acknowledgements

The author would like to express his appreciation to D. S. Ginley, David M. Haaland, R. C. Hughes, and D. R. Tallant of Sandia National Laboratories, Albuquerque, NM for extremely helpful discussions and technical assistance.

### References

1. E. D. Kolb, K. Nassau, R. A. Landise, E. E. Simpson, and K. M. Kroupa, J. Cryst. Grow., Vol 36, p 93 (1976).
2. R. Nacken, "Report on Research-Contract for Synthesis of Oscillator Crystals," Captured German Report RDRDC/13/18, Feb. 28, 1946; also Office of Technical Services Reports PB-6498, "Artificial Quartz Crystals, 1945," PB-18,748; and PB-28,897, "Report on Investigations in European Theater, January 1946, with Special Reference to German ERSATZ Quartz Program," Department of Commerce, Washington, DC.
3. Nora Wooster and W. A. Wooster, Nature, Vol. 157, p 157 (1946).
4. A. C. Walker, Am. Ceram. Soc. Meeting, Pittsburg, PA, April 29 (1952).
5. A. Katz, Phillips Research Reports, Vol. 17, p 133 (1962).
6. H. C. Lipson, F. Euler, and A. F. Armington, Proceedings of the "32nd Annual Symposium on Frequency Control," p 11 (1973).
7. R. C. Hughes, Radiation Effects, Vol. 26, p 225 (1975)

### NEAR-INFRARED ABSORBANCE DATA FOR HYDROTHERMAL QUARTZ GROWTH

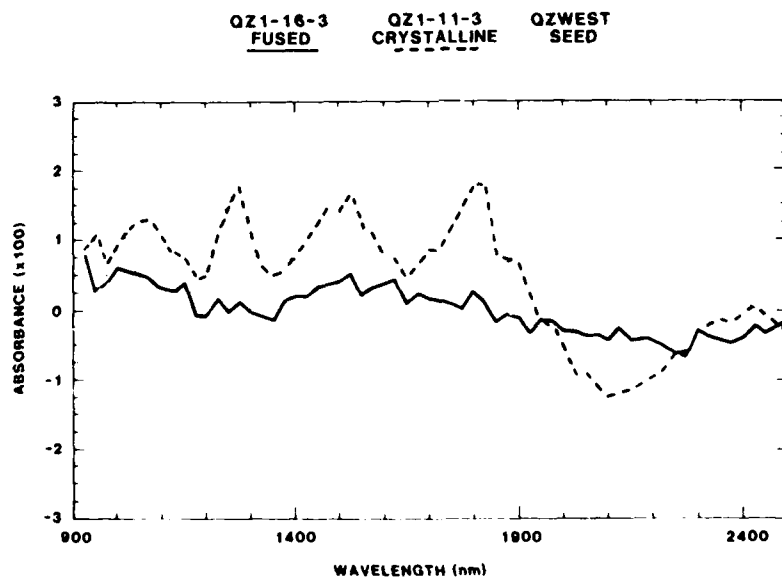


Figure 1. IR Spectra for Quartz Crystals Grown from a Fused Silica Nutrient and a Crystalline Nutrient Compared to Western Electric Seed Crystal

AD-A130 811

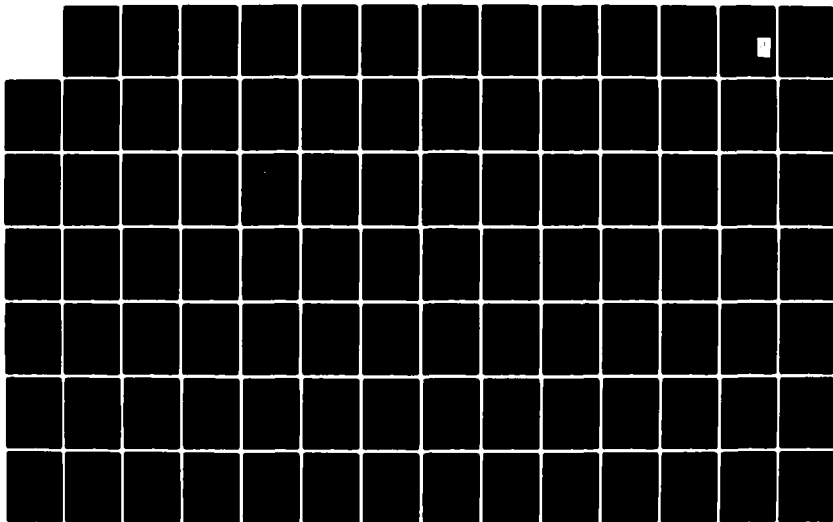
PROCEEDINGS OF THE SYMPOSIUM ON FREQUENCY CONTROL (36TH  
ANNUAL) 2-4 JUNE 1..(U) ARMY ELECTRONICS RESEARCH AND  
DEVELOPMENT COMMAND FORT MONMOUTH. E PAIGE ET AL. 1982

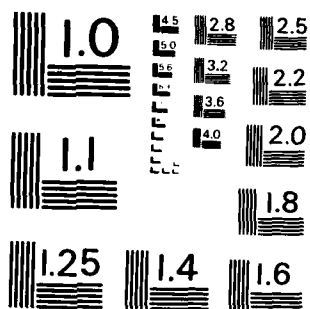
F/G 20/14

NL

2/8

UNCLASSIFIED





MICROCOPY RESOLUTION TEST CHART  
NATIONAL BUREAU OF STANDARDS-1963-A

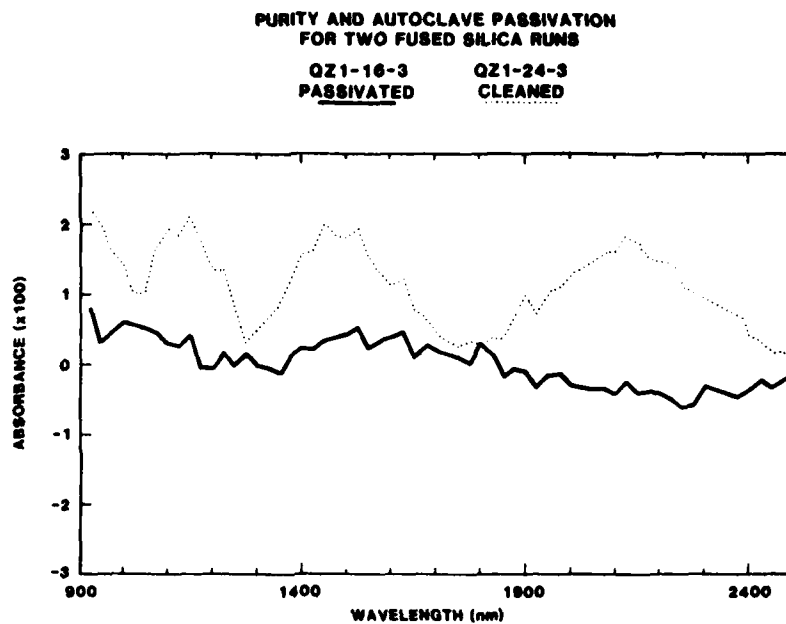


Figure 2. IR Spectra for Quartz Crystals Grown from a Virgin Autoclave Compared to Those Grown in an Aged Autoclave

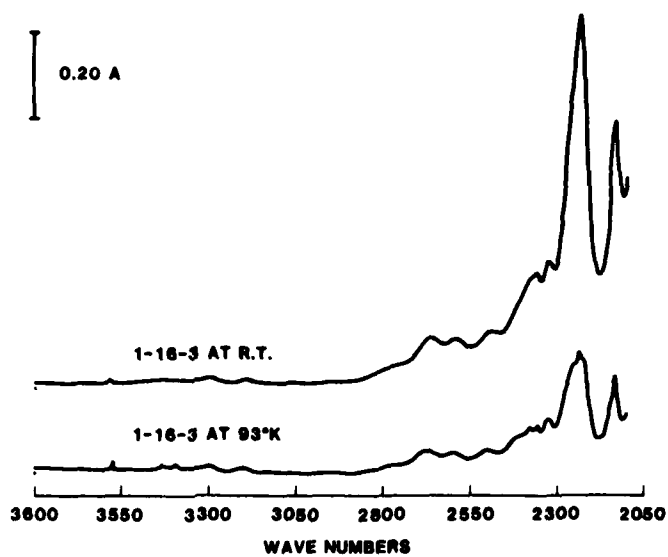


Figure 3. Broad Range IR Spectra at Room Temperature and 93 K for Quartz Crystal 1-16-3 Grown from Fused Silica Nutrient

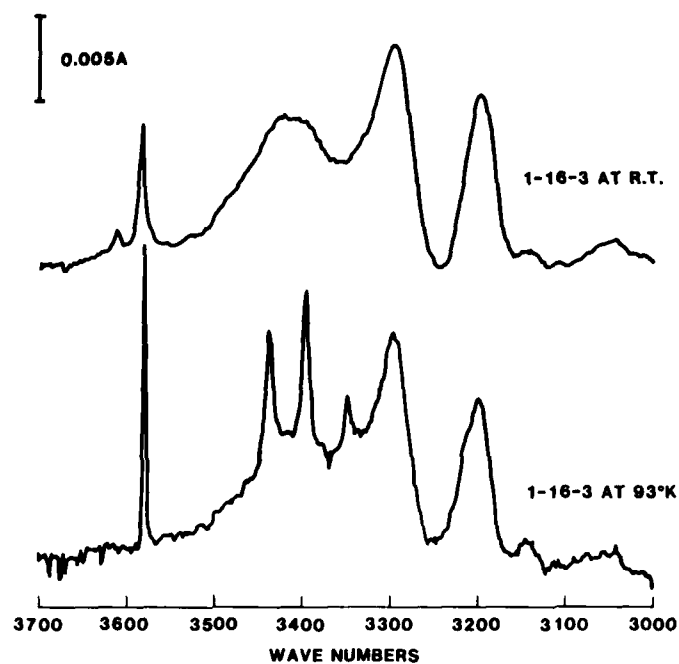


Figure 4. Spectra Comparing Quartz 1-16-3 at Room Temperature and 93 K

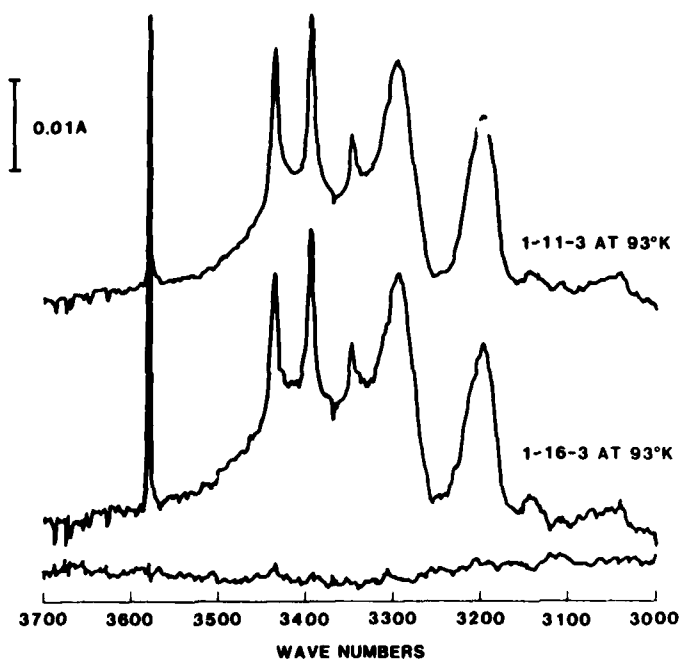


Figure 5. Spectra at 93 K Comparing Quartz 1-16-3 with Quartz Grown from Crystalline Nutrient

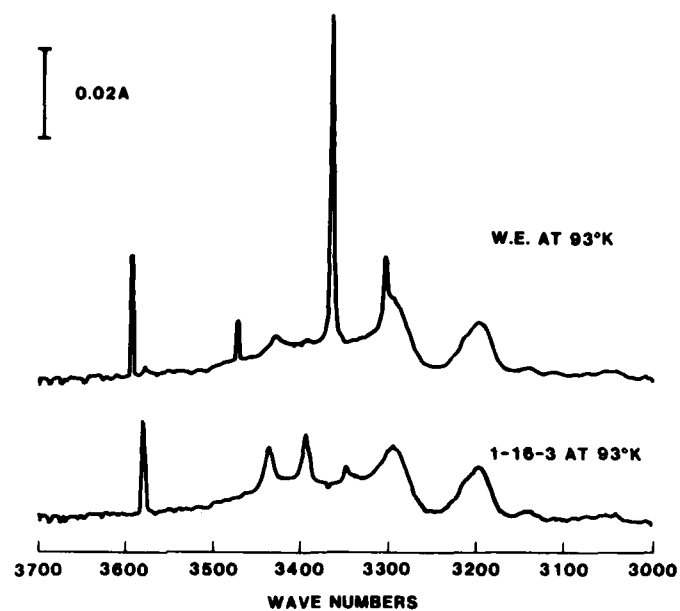


Figure 6. Spectra at 93 K Comparing Quartz 1-16-3 with Western Electric Seed Crystal

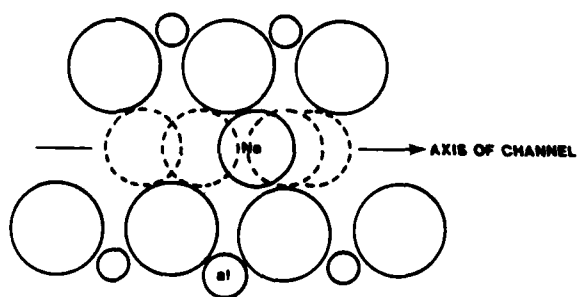


Figure 7. Substitutional  $Al^{3+}$  ion with Interstitial  $Na^{+}$  Ion as Charge Compensation

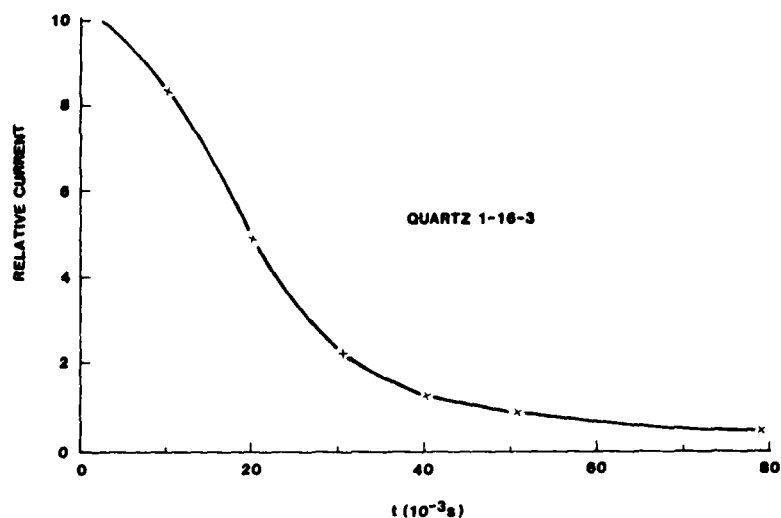


Figure 8. Delayed Radiation-Induced Current (DRIC) for Crystal 1-16-3

TABLE I  
SILICON-RICH MATERIALS  
CONCENTRATIONS IN MICROGRAMS/gram (SOLID)

	Li	Na	K	Al	Fe	Mn	Ni	Cr	Ag
SUPRASIL-2	<0.1	0.18 ± 0.02*	<0.8*	0.5 ± 0.3	0.3 ± 0.2	<0.001*	<2*	<1*	<1*
ALPHA-QUARTZ	0.05 ± .02	1.1 ± .2*	<0.6*	0 ± .2	<0.35	<0.002*	<2*	<2*	<1*
AUTOCLAVE RESIDUE	105, 107, 171	3000 ± 500*	19, 5, 16	5.3, 2.5, 5.2	40, 72, 417 90 ± 20* <150	1.3 ± 0.3*	<5*	1.1 ± 0.5*	44, 76, 110, 268*

\*ANALYZED BY NEUTRON ACTIVATION

LIQUID REAGENTS  
CONCENTRATION IN PARTS-PER-BILLION

	Li	Na	K	Al	Fe	Se	Ni	Cr	Mn
DISTILLED WATER (CONLEY)	<2	<5	<100	20 ± 10	<20	<500	NR	NR	NR
DISTILLED WATER (BAUGHMAN)	<2	<5	<100	20 ± 10	<20	<500	NR	NR	NR
CAUSTIC SOLUTION	NR	NR	NR	55 ± 10	150 ± 20	NR	11 ± 2	19 ± 4	5 ± 1

SOLID REAGENTS  
CONCENTRATION IN MICROGRAMS/gram

	Fe	Al	K	Cr
LITHIUM CARBONATE	15 ± 3	13 ± 3	NR	2.2 ± 0.4
SODIUM HYDROXIDE	11 ± 2	1.5 ± 0.5	4.4 ± 0.5	NR
LITHIUM NITRATE	0.7 ± 0.3	<0.05	25 ± 10	NR

A Method of Adjusting Resonant Frequency and Frequency-Temperature Coefficients of Miniaturized GT Cut Quartz Resonators

O. Ochiai, A. Kudo, A. Nakajima and H. Kawashima

Daini Seikosha Co., Ltd.

Takatsukashinden, Matsudo-shi, Chiba, Japan

AD P001508

Summary

The new type miniaturized GT cut quartz crystal resonator developed by us consists of a vibrational portion and two supporting portions incorporated into one-body by a photolithographic process. It is highly shock resistant and has excellent frequency temperature characteristics over a wide temperature range. It is, however, impossible to avoid a distribution of resonant frequency of a principal vibration caused by that of dimensions and a distribution of frequency temperature characteristics caused by that of a dimensional ratio in resonator production. We have been developing a method of adjusting the resonant frequency of the principal vibration and frequency temperature coefficients of the miniaturized GT cut quartz crystal resonator. Consequently, by eliminating weights disposed on a plurality of positions of a vibrational portion or by adding weights on a plurality of positions of a vibrational portion, we have established a method of adjusting the resonant frequency of the principal vibration and the frequency temperature coefficients.

Introduction

In recent years, with the introduction of the quartz crystal resonator to wrist watches, the time accuracy has greatly improved. However, since most quartz resonators that are used nowadays in wrist watches are flexural resonators of a tuning fork type of +5°X cut, an error of 5 to 20 seconds a month occurs. Therefore, wrist watches of greater accuracy are required in industrial field. Various methods to upgrade accuracy have been experienced with.

In order to realize high accuracy wrist watches having an error of less than a few seconds a year, we have been developing a GT cut quartz resonator with excellent frequency temperature characteristics. The conventional rectangular plane GT cut quartz resonator is well-known for its excellent frequency temperature characteristics and has a frequency deviation of less than one to two ppm in a temperature range of 100 degree centigrade as a result of the coupling of two extensional vibration modes dependent of the width and length dimension of the resonator.

Using a finite element method we analyzed a form of resonator and adopted a photolithographic process in production, to develop a miniaturized GT cut quartz resonator having a new plane form, with a stronger shock resistance, and equipped with excellent frequency temperature characteristics. We made a report on this resonator at the 34th symposium.

In addition, we have also been developing a method of absorbing a distribution of resonant frequency and frequency temperature coefficients caused in production by adding weights on a vibrational portion or eliminating weights disposed on a vibrational portion so as to put this miniaturized GT cut quartz resonator to practical use.

Discussion

Fig. 1 shows a cutting angle of a GT cut plate. After the plate is polished to the desired thickness, a quartz resonator with a shape like that shown in Fig. 2 is formed by a photolithographic process, wherein an approximately square vibrational portion is connected to supporting portions at the center of both width sides, thus forming one body. Fig. 3(a) shows a mode chart of a width extensional vibration of a principal vibration, and Fig. 3(b) also shows a mode chart of a length extensional vibration that is coupled with the width extensional vibration. A solid line indicates a static condition, and a wave line also indicates a vibrational condition.

Frequency and Frequency Adjustment

A GT cut quartz resonator with excellent frequency temperature characteristics can be obtained as a result of a coupling between the width extensional vibration of the principal vibration and the length extensional vibration of the sub-vibration. We call frequency  $f_W$  of the width extensional vibration mode the principal vibration frequency and frequency  $f_L$  of the length extensional vibration mode the sub-vibration frequency. A frequency equation of a GT cut quartz resonator having a simple rectangular shape can be expressed as follows in accordance with Mr. Nakazawa's findings.

$$f = \frac{1}{2W} \sqrt{\frac{P_{11}}{\rho}} \sqrt{\frac{1}{2} [1 + K_1 R^2 \pm \sqrt{(1 - K_1 R^2)^2 + 4 K_2^2 R^2}]} \quad \dots\dots\dots (1)$$

where, W : a dimension of width  
R : the width to length ratio  
ρ : density

$$K_1 = P_{33}/P_{11}, \quad K_2 = P_{13}/P_{11}$$

$$\begin{bmatrix} P_{11} & P_{13} & P_{15} \\ P_{13} & P_{33} & P_{35} \\ P_{15} & P_{35} & P_{55} \end{bmatrix} = \begin{bmatrix} S_{11} & S_{13} & S_{15} \\ S_{13} & S_{33} & S_{35} \\ S_{15} & S_{35} & S_{55} \end{bmatrix}^{-1}$$

$S_{ij}$  : elastic compliance

With respect to the new type GT cut quartz resonator developed by us, additional articles of a dimensional ratio and so on are needed on account of the two end supports as compared with the conventional type. And after the addition, the theoretical relationship among the various factors and frequency is in agreement with the experimental results. The resonant frequency  $f_W$  of the principal vibration is very dependent on the width dimension W and furthermore, is determined by a cutting angle and a dimensional ratio. It is impossible to avoid a distribution of these factors during production of the width dimension results in a large distribution of the resonant frequency  $f_W$  of the principal vibration. As a method to reduce the distribution of the resonant frequency  $f_W$  of the principal vibration and to adjust the resonant frequency  $f_W$  efficiently and accurately, we thought out an adjusting method by adding or subtracting weights on the vibrational portion. As to the position of weights they can be disposed on end portions of the length side, in the vicinity of the nodal point of the length side mode, and in the vicinity of corners of the vibrational portion, in which a distortion of the width vibration is very small, and the amplitude of the vibration is large.

#### Adjustment of F-T Characteristics

The GT cut quartz resonator has excellent cubic curve frequency-temperature characteristics as a result of the coupling of the principal vibration  $f_W$  and the sub-vibration  $f_L$ . The factors determining this coupling condition are the cut angle and the dimensional ratio R. In particular, since the dimensional ratio R is the main factor contributing to the frequency temperature characteristics, a distribution of the dimensional ratio in production can cause a distribution of frequency temperature characteristics.

Since the resonant frequency  $f_W$  of the principal vibration is dependent upon the width dimension W and also, the resonant frequency  $f_L$  of the sub-vibration is dependent upon the length dimension L, to change the dimensional ratio R is equivalent to changing the frequency difference of  $f_W$  and  $f_L$ .

The frequency temperature characteristics are dependent upon the coupling condition of two modes of the principal vibration  $f_W$  and the sub-vibration  $f_L$ , the coupling intensity can be determined by mutual vibration efficiency and each value of the resonant frequencies, that is to say, the frequency difference of two vibration modes. Therefore, in order to represent the frequency difference thereof, we defined the normalized frequency  $\delta$  as follows:

$$\delta = \frac{f_W - f_L}{f_W} \times 100 \quad (\%) \quad \dots\dots\dots (2)$$

$\delta$  is a function of the dimensional ratio R and cut angle, the optimum  $\delta$  is to all intents and purposes determined by the dimensional ratio.

From these results, we estimated that it might be possible to adjust frequency temperature coefficients by changing the normalized frequency  $\delta$ , in other words, by changing either of the resonant frequencies of the two vibration modes or both resonant frequencies thereof. We thought that it would be possible to adjust frequency temperature coefficients in the same way as with resonant frequency adjustment. In case of adjusting the resonant frequency and frequency temperature coefficients, it is of great importance to find out whether it is possible to adjust the resonant frequency and frequency temperature coefficients independently, namely,

- (1) if it is possible to adjust frequency temperature coefficients without changing the resonant frequency  $f_W$  of the principal vibration.
- (2) if it is possible to adjust the resonant frequency  $f_W$  without changing the frequency temperature coefficients.

Therefore, the key point to development may be if the positions of weights satisfy either of the above-mentioned methods.

#### Experimental Results

In order to determine the optimum position of weights for an adjustment of the resonant frequency and frequency temperature coefficients, we actually manufactured resonators, and conducted an experiment. The consequent results are explained as follows.

### Frequency Adjustment

After thorough investigation of the vibration modes of the width side and the length side shown in Fig. 3, we conducted an experiment on the positions of three kinds of weights as shown in Fig. 4. Of three kinds of weights  $W_M$ ,  $C_M$ ,  $L_M$ , the weights  $W_M$  are positioned on the end portions of the length side in the vicinity of a nodal line AA' of the length side vibration, the weights  $C_M$  are positioned on each corner, and the weights  $L_M$  are positioned on the end portions of the width side in the vicinity of a nodal line BB' of the width side vibration.

Fig. 5 shows a change in the resonant frequency when the weights  $W_M$ ,  $L_M$ ,  $C_M$  are respectively eliminated. The eliminated quantity of weights is represented by area thereof. Since the frequencies  $f_W$ ,  $f_L$  to eliminated quantity of weights changes almost in a straight line whichever weights are eliminated, it is very easy to adjust frequencies  $f_W$ ,  $f_L$ .

Fig. 6 shows a  $\delta$  change to eliminated quantity of weights when eliminating each of the weights  $W_M$ ,  $L_M$ ,  $C_M$ .  $\delta$  before the adjustment is zero.

Fig. 7 shows the relationship between the normalized frequency  $\delta$  and the first and second temperature coefficients  $\alpha$ ,  $\beta$  when eliminating each of the weights  $W_M$ ,  $L_M$ ,  $C_M$ . There is a firm relationship between  $\delta$  and  $\alpha$ ,  $\beta$ , which can be seen as almost in a straight line. However, the quantity of change of  $\alpha$ ,  $\beta$  caused by that of  $\delta$  differs according to the position of the weights. This is the reason why the magnitude of distortion differs according to the position of each weights.

Fig. 8(a) shows the relationship between quantity of a change of  $\delta$  and that of the principal vibration  $f_W$  when eliminating the weight  $C_M$ . As shown in this figure, there is a close relationship between the quantity of the change of  $\delta$  and that of  $f_W$  when eliminating the weights. Fig. 8(b) shows measurement values of  $\alpha$ ,  $\beta$  to the quantity of the change of  $f_W$ , as will be apparent from this figure,  $\alpha$  and  $\beta$  change in a straight line as the  $f_W$  changes. This shows the case of the weight  $C_M$  and also in the case of the weights  $W_M$ ,  $L_M$ , there is a close relationship between the quantity of the change of  $f_W$  and  $\alpha$ ,  $\beta$ .

Fig. 9 shows a rate of the frequency change when eliminating weights along the length side. The lower graph shows the rate of the change of principal vibration  $f_W$  and the sub-vibration  $f_L$  when eliminating the constant quantity of weights in the vicinity of the black circles shown in the upper figure. We suppose the rate of frequency change to be 1 at zero position. A solid line shows the measurement of the principal vibration  $f_W$  and a dotted line shows that of the sub-vibration  $f_L$ .

Fig. 10 shows quantity of a change of the first and second order temperature coefficients  $\alpha$ ,  $\beta$ , versus a change of 10% of the principal vibration  $f_W$  when eliminating each of the weights shown in Fig. 9. As will be apparent from this graph, when eliminating the weights in the vicinity of the center of the length side, the quantity of the change of both  $\alpha$ ,  $\beta$  shifts to positive values, on the other hand, when eliminating the weights in the vicinity of the corners, they shift to negative values. From these results, when eliminating the

weights in the vicinity of the middle between the center of the length side and the corner, even if the resonant frequency of the principal vibration  $f_W$  changes, the quantity of the change of  $\alpha$ ,  $\beta$  is zero, namely, frequency temperature characteristics do not change. From Fig. 10, it will be understood that, according to frequency temperature characteristics, after adjusting the frequency temperature coefficients by an elimination of the weights in the vicinity of the center of the length side or the weights in the vicinity of the corners, it is possible to adjust the principal vibration  $f_W$  without changing the frequency temperature characteristics. Therefore we can say the relationship between frequency and temperature coefficients, in case of eliminating weights has been explained, but, inversely it is needless to say it is also possible to adjust them in case of adding weights. In this case, the relationship between the change of frequency and  $\alpha$ ,  $\beta$  becomes inverse at a plus or minus sign, when compared with the method for eliminating weights.

Fig. 11 is an example of frequency temperature characteristics obtained after adjusting frequency temperature coefficients and resonant frequency. Wave lines are examples of resonator frequency temperature characteristics obtained after a photolithographic process, and solid lines show frequency temperature characteristics obtained after adjustment of resonator frequency temperature coefficients.

Photo 1 shows an oscillator including a resonator, which has a length of 3.5 mm, a width of 1.6 mm, and a thickness of 0.05 mm, developed by us. The main characteristics of this design are summarized as follows:

- |                          |                           |
|--------------------------|---------------------------|
| (1) frequency            | 2.097152 MHz              |
| (2) series resistance    | 80 $\Omega$               |
| (3) motional capacitance | 5.5 x 10 <sup>-3</sup> PF |
| (4) quality factor       | 174 x 10 <sup>3</sup>     |
| (5) shunt capacitance    | 2.4 PF                    |

### Conclusion

We have basically confirmed it is entirely possible to adjust frequency temperature coefficients and the resonant frequency of the principal vibration  $f_W$  without changing frequency temperature characteristics in the same way by eliminating weights placed on a vibrational portion or by adding weights on a vibrational portion.

Therefore, as a consequence we can say that it is possible to manufacture GT cut quartz resonators in miniaturized form with excellent frequency temperature characteristics. In the near future, we expect to see a miniaturized GT cut quartz resonator used not only for wrist watches, but also for consumer products requiring high accuracy.

### Acknowledgement

The authors would like to thank Messers. Kubota, Ando, Watanabe, Kai, Iwama, and Mrs. Ohki for their help and encouragement, and in particular, to thank Mr. Osawa and many other people for their help in the experimental work leading to the realization of the GT cut quartz resonator.

### References

1. H. Kawashima, H. Sato, and O. Ochiai  
"New Frequency Temperature Characteristics of Miniaturized GT Cut Quartz Resonators", proc. 34th AFCS pp131-139, 1980
2. H. Kawashima, O. Ochiai and H. Sato  
"Miniaturized GT Cut Quartz Resonator", EM Symposium, Japan, 1981
3. M. Nakazawa  
"Analysis on the GT Quartz Crystal Vibrator", IEE Japan, US76-6, pp7-12, 1976

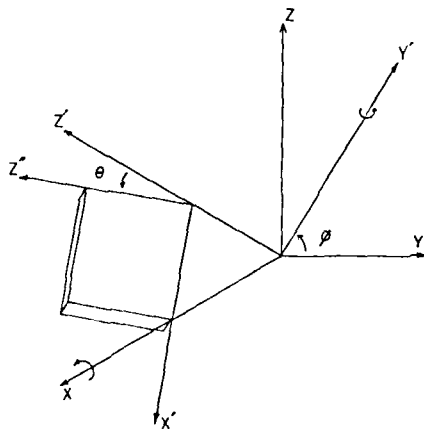


Fig. 1 An orientation of cut of GT plate

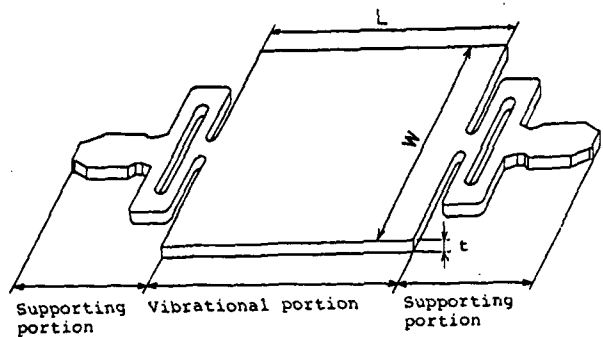


Fig. 2 A concrete shape of a GT-cut quartz resonator

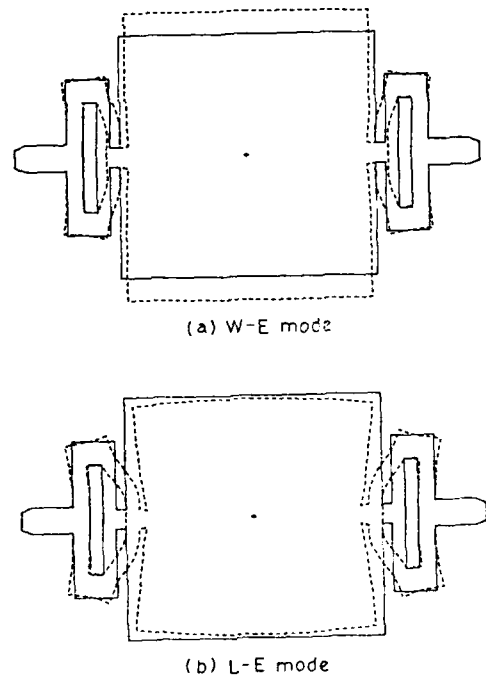


Fig. 3 Displacements of W-E mode and L-E mode

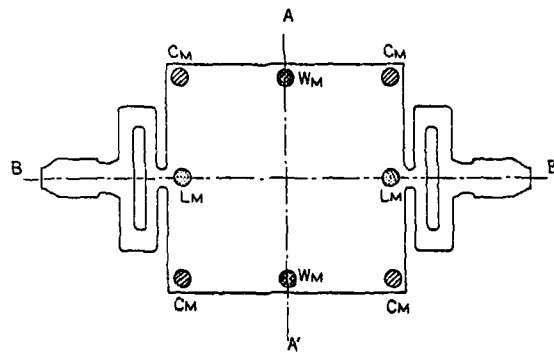


Fig. 4 Each position of weights

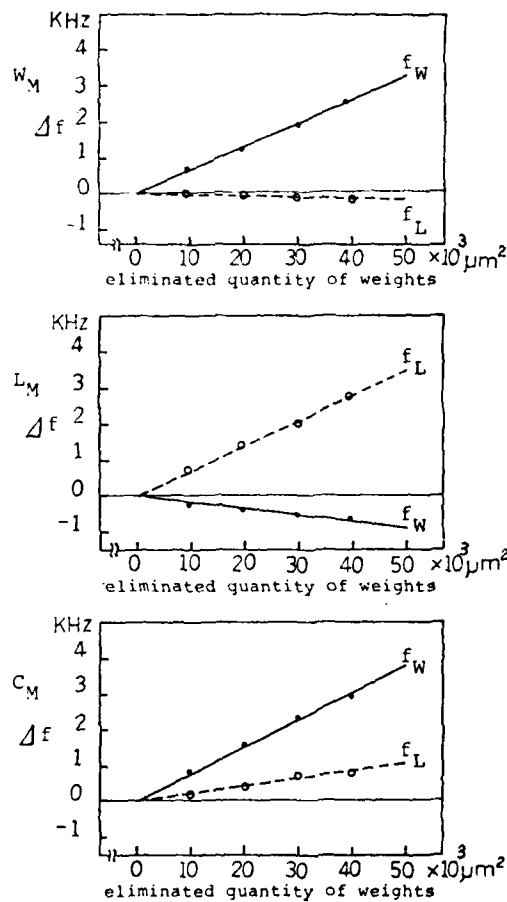


Fig. 5 A change of resonant frequency to eliminated quantity of weights

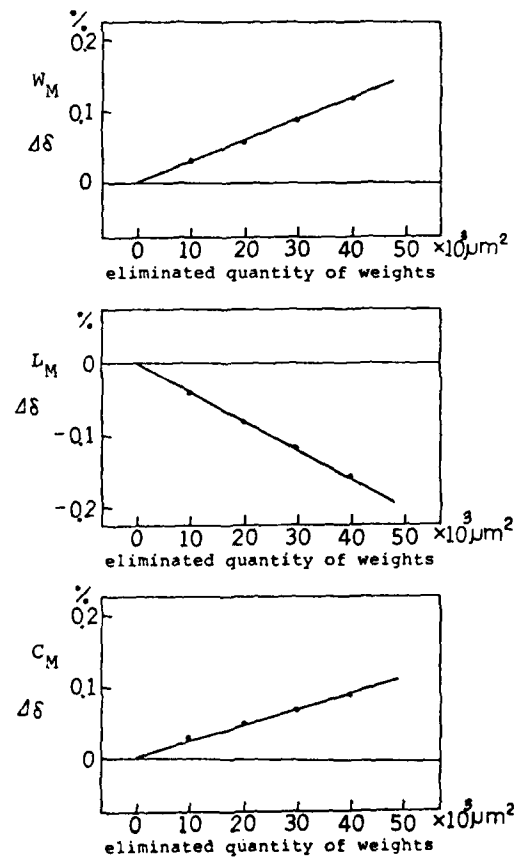


Fig. 6 A change of normalized frequency to eliminated quantity of weights

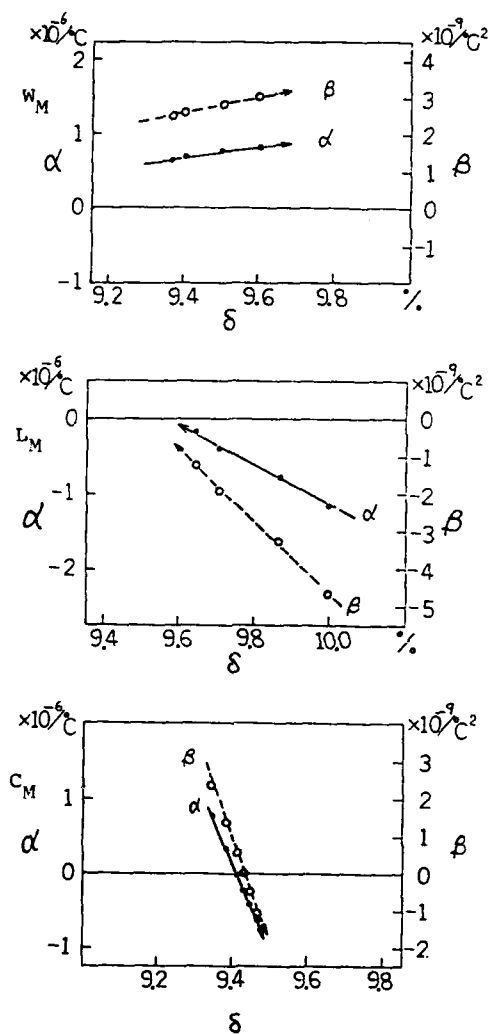


Fig. 7 Relationship between the normalized frequency  $\delta$  and the first and second temperature coefficients  $\alpha, \beta$

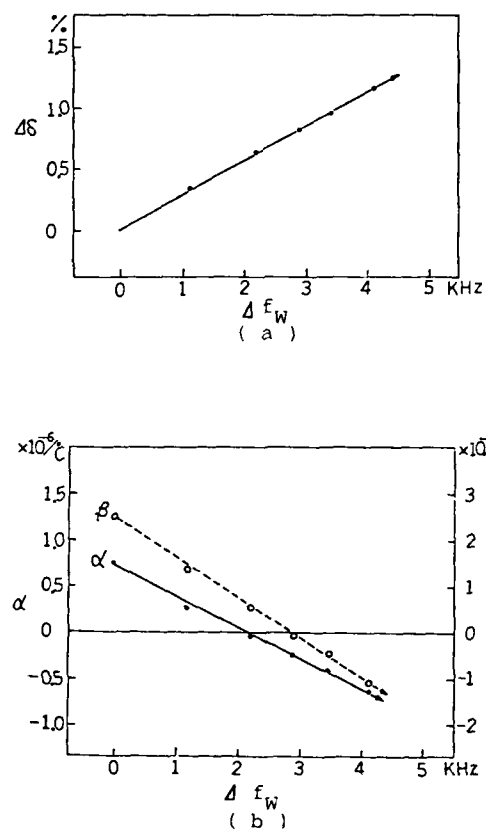


Fig. 8 Relationship between  $f_W$  and  $\Delta\delta$ , and between  $f_W$  and  $\alpha, \beta$

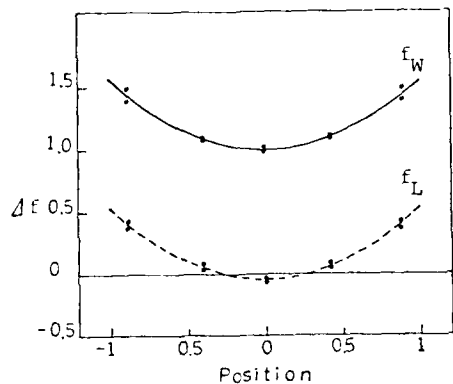
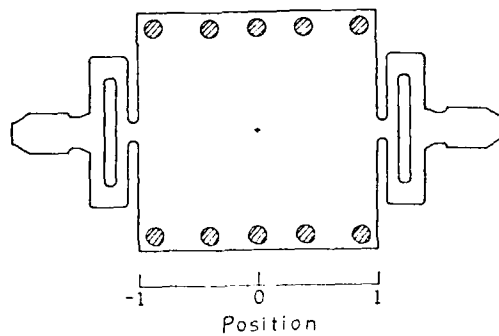


Fig. 9 A rate of a change between  $f_W$  and  $f_L$  when eliminating weights

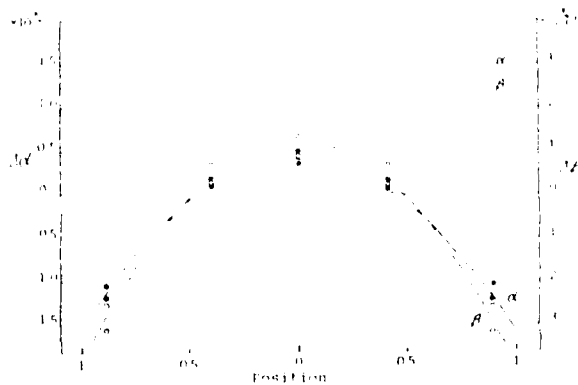


Fig. 10 A rate of  $\alpha, \beta$ , when eliminating weights of the length side

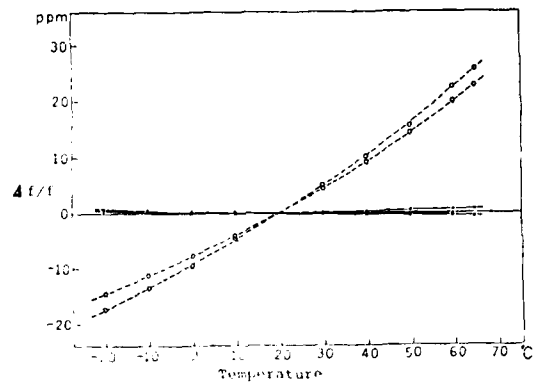


Fig. 11 F-T characteristics obtained after adjustment of frequency-temperature coefficients

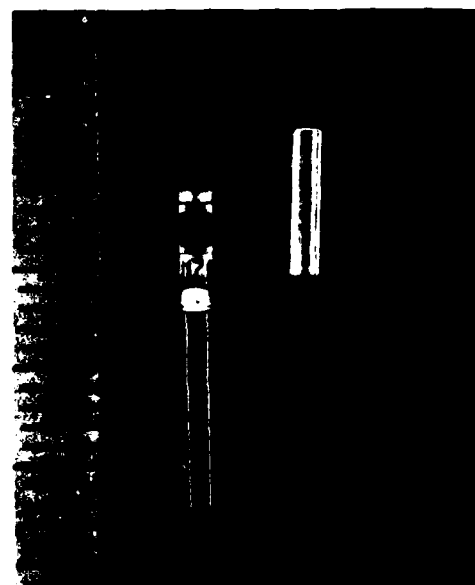


Photo 1 shows an oscillator

ELECTROELASTIC EFFECTS AND IMPURITY RELAXATION  
IN QUARTZ RESONATORS

R. Brendel, J.J. Gagnepain

Laboratoire de Physique et Métrologie des Oscillateurs du C.N.R.S.,  
associé à l'Université de Franche-Comté-Besançon  
32, avenue de l'Observatoire - 25000 Besançon - FranceSummary

The application of an electric DC field on a quartz crystal resonator induces a fast variation of the resonance frequency followed by a slow quasiexponential decay typical of ionic impurity relaxation (J. Kusters, FCS 1970). The frequency variation under the DC field was interpreted in terms of an electroelastic effect corresponding to a change of the elastic constants through nonlinear piezoelectricity (K. Bruska, FCS 1970).

Starting from general rotationally invariant nonlinear electroelastic equations for small fields superposed on a bias (J.C. Baumhauer, H.F. Tiersten, JASA 54, 4, 1975) and using the experimental data on the electroelastic effect available in the literature, the values of the independent components of the material electroelastic tensor are obtained.

Then this tensor is used to calculate the frequency shift of a resonator submitted to a DC voltage superposed on the vibration. The slow decay of the resonance frequency can be studied by means of a model of ionic impurity diffusion introduced in the electroelastic equations. It is shown how the steady state frequency shift at constant DC voltage can be related to the impurity concentration.

The measurement of the relaxation time constant also offers a possibility of identifying the nature of the impurities (Na<sup>+</sup>, K<sup>+</sup>, Li<sup>+</sup>). But because of the lack of knowledge in the quartz crystal lattice characteristics (deformation potential, etc.), a precalculation will be necessary to make more comparisons and discussions on the basis of the same impurity relaxation behavior at low temperature.

Introduction

Impurities are a source of frequency and phase shifts in quartz resonators. When exposed to microwave radiation, S. Gagnepain et al. have observed at low temperature, the relaxation of the impurities and the corresponding frequency shift and the results of this relaxation.

These impurities can be characterized by different methods, e.g. infrared spectroscopy, magnetic resonance, acoustic losses and conductivity measurements, etc... Another method is proposed which could have the advantage of being more simply carried out. This method is based on the diffusion of the impurities under a DC field, the frequency shift coming from the nonlinear electroelastic effect is used as a probe to point out the impurity relaxation. In principle the nature and the concentration of impurity can respectively be deduced from the relaxation time (or the related activation energy) and the relaxation amplitude. But such an approach needs a model of both frequency/DC field effect and impurity diffusion process. But the first part involves the third order electroelastic constants which are to be entirely determined, and this was the first task of this study.

General electroelastic equations

The material coefficients are the independent coefficients appearing in the scalar state function used to express the constitutive equations of electroelasticity. Different forms are possible for this state function according to the thermodynamic variables used. The most convenient form for the present problem is the linear potential or stored energy per unit mass  $\phi_0(\epsilon_{ij}, E_i)$  expressed in terms of the strain tensor  $\epsilon_{ij}$  and the electric field  $E_i$  referred to the initial reference state.

$$\begin{aligned} \phi_0 = & \frac{1}{2} C_{ijkl} \epsilon_{ij} \epsilon_{kl} + \frac{1}{6} C_{ijklm} \epsilon_{ij} \epsilon_{kl} \epsilon_{lm} + \frac{1}{24} C_{ijklmn} \epsilon_{ij} \epsilon_{kl} \epsilon_{lm} \epsilon_{mn} \\ & + \frac{1}{6} e_{ijk} E_i \epsilon_{jk} + \frac{1}{24} e_{ijklm} E_i \epsilon_{jk} \epsilon_{lm} + \frac{1}{24} e_{ijklmn} E_i \epsilon_{jk} \epsilon_{lm} \epsilon_{mn} \\ & + \frac{1}{2} \epsilon_{ijk} E_i E_j E_k + \frac{1}{24} \epsilon_{ijklm} E_i E_j E_k E_l E_m + \dots \end{aligned}$$

$\epsilon_{ij}$  is the mass per unit volume of the material,  $\rho_0$ ,  $C_{ijkl}$ ,  $C_{ijklm}$ ,  $C_{ijklmn}$  are the second, third, fourth, fifth, sixth order piezoelectric coefficients,  $e_{ijk}$ ,  $e_{ijklm}$ ,  $e_{ijklmn}$  are the second, third, fourth, fifth, sixth order piezoelectric coefficients,  $\epsilon_{ijk}$  is the third order piezoelectric coefficient,  $\epsilon_{ijklm}$  is the fourth order piezoelectric coefficient,  $\epsilon_{ijklmn}$  is the fifth order piezoelectric coefficient,  $\epsilon_{ijklmn}$  is the sixth order piezoelectric coefficient.

Motion and charge equations expressed with the reference or natural coordinates  $a_i$  have the following form:

$$c_{11} = \frac{1}{2} \frac{a_1}{a_2} \quad (2)$$

$$\frac{\partial \alpha_i}{\partial \alpha_i} \quad (3)$$

When dealing with small fields superposed on a plane it is convenient to split all quantities into static and dynamic parts.

$$\frac{\partial F}{\partial a_1} = 0 \quad (\text{because there is no acceleration for the static bias}) \quad (4)$$

$$\frac{\bar{g}_i}{\bar{g}_1} \quad (15)$$

$$E_{\text{eff}} = \frac{E_0}{2} \quad (6)$$

$$\begin{aligned} F_{1,1} &= A_{1,1} k k \frac{\frac{\partial \psi}{\partial t}}{\frac{\partial \psi}{\partial t}} + A_{1,2} \frac{\frac{\partial \psi}{\partial t}}{\frac{\partial \psi}{\partial t}} \\ \frac{\partial \psi}{\partial t} &= A_{1,1} k k \frac{\frac{\partial \psi}{\partial t}}{\frac{\partial \psi}{\partial t}} + A_{1,2} \frac{\frac{\partial \psi}{\partial t}}{\frac{\partial \psi}{\partial t}} \end{aligned} \quad (19)$$
$$A_{ijk} = C_{ijk} + \frac{1}{2} \delta_{ij} \delta_{ik}$$

$$\hat{A}_{ijk} = e_{ijk} + \hat{\sigma}_{ijk}$$

$$A_{12} = -\hat{c}_{12} - \hat{c}_{13}$$

$$10kl = 10lmm\delta k + 10nl\delta mk + 10nl\delta m + 10klmm$$

$$+ \left( e_{\text{max}}^{\text{A}} + e_{\text{min}}^{\text{A}} \right) \frac{\bar{z}_4}{z_4}$$

$$\frac{\partial \eta}{\partial t} = -\frac{1}{n} \left( \frac{\partial n}{\partial t} + \frac{\partial n}{\partial x} v_x + \frac{\partial n}{\partial y} v_y + \frac{\partial n}{\partial z} v_z \right)$$

$$= \frac{1}{2} \left( e^{i k x} \frac{\partial}{\partial x} - e^{-i k x} \frac{\partial}{\partial x} \right) \frac{1}{3a} = \frac{1}{3a} \frac{\partial}{\partial x}$$

$$+ \frac{1}{2} e^{-\epsilon_0} \ln(k + \epsilon_0) - \frac{1}{2} \ln(k - \epsilon_0) + \frac{1}{2} \ln(k + \epsilon_0) - \frac{1}{2} \ln(k - \epsilon_0) = \frac{1}{2} \ln(k + \epsilon_0) - \frac{1}{2} \ln(k - \epsilon_0)$$

$$\hat{\epsilon}_{ik} = [\epsilon_{ikmn} + \epsilon_0 (\delta_{ik} \delta_{mn} - \delta_{in} \delta_{km} - \delta_{im} \delta_{kn} + \delta_{km} \delta_{in})] \frac{\partial u_n}{\partial x_m}$$

$$= \epsilon_{ijk} \frac{\partial \bar{a}}{\partial a_n}$$

Frequency shift of the plate  
submitted to 20 field

98

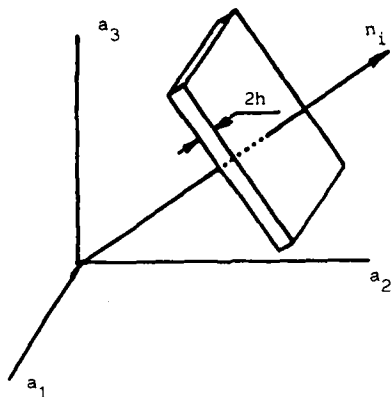


Fig. 1 : Plate resonator

The unperturbed mechanical displacement and electric potential of each mode can be written

$$u_j^0 = \tilde{u}_j^0 e^{j\omega_0 t} \quad (14)$$

$$\phi^0 = \tilde{\phi}^0 e^{j\omega_0 t} \quad (15)$$

where the eigenfrequency  $\omega_0$  is related to the eigenvelocity  $V_0$  by

$$\omega_0 = (2p + 1) \frac{\pi V_0}{2h} \quad (16)$$

The eigenvalue and eigenvector of the mode will be denoted

$$\lambda = \omega_0 V_0^2 \quad (17)$$

and  $\tilde{u}_j$  respectively.

The frequency shift of the resonator submitted to a static bias defined by the difference between perturbed and unperturbed frequencies

$$\Delta\omega = \omega - \omega_0 \quad (18)$$

can be obtained from the perturbation relations<sup>7</sup> in which second order terms are neglected

$$\begin{aligned} \omega_0 \Delta\omega + \frac{1}{2} \frac{\partial^2 \omega_0}{\partial a_k \partial a_l} \tilde{u}_j^0 \tilde{u}_j^0 dV_0^0 = \\ \frac{1}{2} \frac{\partial^2 \omega_0}{\partial a_k \partial a_l} \frac{\partial \tilde{u}_j^0}{\partial a_k} \frac{\partial \tilde{u}_j^0}{\partial a_l} + 2\tilde{e}_{kjl} \frac{\partial \tilde{u}_j^0}{\partial a_k} \frac{\partial \tilde{\phi}^0}{\partial a_l} \\ - \tilde{e}_{kjl} \frac{\partial^2 \tilde{\phi}^0}{\partial a_k \partial a_l} dV_0^0 \end{aligned} \quad (19)$$

where  $V_0^0$  is the effective volume of the underformed crystal.

The determination of the perturbing terms  $C_{ijkl}$  ... will be somewhat simpler if it is performed by using a set of coordinates bound to the plate. Let  $a'_i$  be the natural coordinates in such axes with  $a'_1$  normal to the plane of the plate (see Fig. 2).

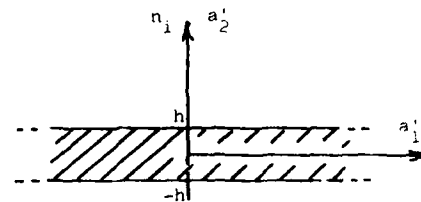


Fig. 2 : Plate axes

All the other terms expressed with respect to these axes will be consistently denoted with the same "prime". Let  $p_{ij}$  be the transformation matrix

$$a'_i = p_{ij} a_j \quad (20)$$

The normal  $n_i$  is along  $a'_2$  so

$$n_i = p_{2i} \quad (21)$$

The expression of the frequency shift does not depend on the chosen set of axes and because of the infinite extent of the plate in the directions  $a'_1$  and  $a'_2$ , displacements and potential do not depend upon these variables. In the plate axes, the integration over the entire volume of the crystal reduces to integration with respect to  $a'_1$  between  $-h$  and  $+h$ . By using equations (13) and after some transformations it is possible to express the frequency shift as a function of the material coefficients given in the rectangular crystallographic set of axes and the biasing static displacements and potential gradients given with respect to the plate axes

$$\frac{\Delta\omega}{\omega_0} = \frac{1}{2\lambda h} \int_{-h}^{+h} \left( \tilde{C}_m \frac{\partial \tilde{u}_m^0}{\partial a'_2} + \tilde{D} \frac{\partial \tilde{\phi}^0}{\partial a'_2} \right) \cos^2 \frac{\omega_0 a'_2}{V} da'_2 \quad (22)$$

where :

$$\begin{aligned} \tilde{C}_m = n_j \tilde{C}_{ijk} (p_{mk} + 2p_{mn} \tilde{u}_n^0 \tilde{e}_{kln} + \tilde{e}_{jln} p_{mn} \tilde{e}_{kl} \tilde{u}_n^0 \\ + 2p_{mn} \tilde{u}_j^0 \tilde{e}_{lmn} \tilde{e}_{kl} + \tilde{e}_{jln} p_{mn} \tilde{e}_{kl} \tilde{u}_n^0) \\ + p_{11}^2 (\tilde{e}_{11} p_{mn} - \tilde{e}_{1n} \delta_{m1}) \end{aligned} \quad (23)$$

$$\tilde{D} = n_j \tilde{e}_{jkl} + \tilde{e}_{jkl} \tilde{e}_{l1} \tilde{e}_{1k} - 2p_{1n} \tilde{e}_{ln} - \tilde{e}_{1n} p_{11} \tilde{e}_{1k} + p_{11}^2 \quad (24)$$

$$r_i = \frac{Y_i \epsilon_i}{\epsilon_i} \quad (25)$$

$$r_{ijk} = C_{ijkl} n_i n_j n_k \quad (26)$$

$$r_{ij} = C_{klij} n_i n_j n_k \quad (27)$$

$$r_{ijk} = C_{ijkl} n_i n_j n_k \quad (28)$$

$$r_{ijkln} = C_{ijklmn} n_i n_j n_k n_l n_m \quad (29)$$

$$r_{ijk} = C_{mijkl} n_i n_j n_k n_m \quad (30)$$

$$r_{ijk} = C_{iklmn} n_i n_j n_k n_l n_m \quad (31)$$

$$r_{ijk} = C_{iklm} n_i n_j n_k n_l n_m \quad (32)$$

The relation between frequency shift and applied DC field needs the static displacements and potential gradients (see Eq.(22)). The static strain is small enough so the gradients can be obtained from the linear equations of piezoelectricity applied to the infinite plate of Fig. 2 whose faces are traction free and submitted to a static potential difference

$$\bar{\phi}'(-h) = 0 \quad \text{and} \quad \bar{\phi}'(+h) = \bar{\phi}'_0 \quad (33)$$

Then, the static displacements and potential gradients take the following form

$$\frac{\partial u'_m}{\partial a'_2} = -\sigma'_m \frac{\partial \bar{\phi}'}{\partial a'_2} \quad (34)$$

$$\frac{\partial \bar{\phi}'}{\partial a'_2} = \frac{\bar{\phi}'_0}{2h} = -\bar{E} \quad (35)$$

are the components of the matrix  $\Delta'^{-1}$ ,  $\Gamma'$  where  $\Delta'^{-1}$  is the inverse of the matrix

$$\Delta' = \begin{bmatrix} C'_{66} & C'_{26} & C'_{46} \\ C'_{26} & C'_{22} & C'_{24} \\ C'_{46} & C'_{24} & C'_{44} \end{bmatrix} \quad (36)$$

and

$$\Gamma' = \begin{bmatrix} C'_{26} \\ C'_{46} \\ C'_{24} \end{bmatrix}$$

and  $\bar{E}$  is the applied static electric field.

Substituting equation (34) into (22) yields

$$\frac{\Delta\omega}{\omega_0} = \frac{1}{2\lambda h} (\hat{D} - \sigma'_m \hat{C}_m) \int \frac{\partial \bar{\phi}'}{\partial a'_2} \cos^2 \frac{\omega_0 a'_2}{V} da'_2 \quad (37)$$

This equation holds when the strain does not notably affect the distribution of the potential in the crystal if the electromechanical coupling factor is small. When the static field is homogeneous, replacing the potential gradient by its value (35) gives the so called electroelastic (or polarizing<sup>3,11</sup>) effect

$$\left(\frac{\Delta\omega}{\omega_0}\right) = \frac{1}{2\lambda} (\sigma'_m \hat{C}_m - \hat{D}) \quad (38)$$

#### Determination of the electroelastic coefficients from the measurement of the electroelastic effect

$\hat{D}$  and  $\hat{C}_m$  previously defined contain the linear and nonlinear material coefficients among which electroelastic and electrostrictive coefficients are unknown. The electrostrictive coefficients will no longer be considered here because they appear to have a negligible contribution to the electroelastic effect. This assumption is supported by the fact that electrostriction is an even function of the applied electric field which induces a frequency shift whose sign does not depend on the positive or negative direction of the applied field, while the odd electroelastic effect does depend on it; as a consequence, frequency shift must show some difference when inverting the direction of the field if electrostrictive effect is involved. But experiments do not show such a difference<sup>3</sup>. Electrostriction is a quadratic function of the applied electric field, and the plot of frequency vs. electric field could show a parabolic curvature. Indeed no appreciable departure from the straight line<sup>3,5,11,12</sup> is observed. As a consequence attempts to obtain electrostrictive coefficients from the measurements of the electroelastic effect have not led to consistent results.

Finally the third order dielectric permittivity whose numerical value were obtained by other methods<sup>13</sup> appears to have no practical importance in the electroelastic effect.

Solving equation (38) for the unknown electroelastic coefficients  $e_{ijk\ell mn}$  gives relations of the form

$$F_{ijk\ell m} e_{ijk\ell m} = 2\lambda \left(\frac{\Delta\omega}{\omega_0}\right) H - S \quad (39)$$

where

$$F_{ijk\ell m} = n_i n_j n_k (2r_{\ell} \sigma_{\ell} - \ell_{\ell}) \ell_m \quad (40)$$

$$\sigma_{\ell} = p_{k\ell} \sigma'_k \quad (41)$$

S is the sum of five terms

$$S = M + N + P + Q + R \quad (42)$$

where

$$M = \sigma_i n_j \Gamma_{jk} (\delta_{ik} + 2\epsilon_i \epsilon_k) \quad (43)$$

(2nd order elastic constants)

$$N = \sigma_i \Gamma_{ijk} \epsilon_j \epsilon_k \quad (44)$$

(3rd order elastic constants)

$$P = \gamma_i n_i (2r \sigma_j \epsilon_j - 1) \quad (45)$$

(2nd order piezoelectric constants)

$$Q = r \epsilon_o (\sigma_2^2 r - 2n_i \epsilon_i) \quad (46)$$

(2nd order permittivity)

$$R = -r^2 \kappa \quad (47)$$

(3rd order permittivity)

Because electroelastic constants are material coefficients they obey the material symmetry of the crystal. When using matrix notation it is well known today there are 8 independent electroelastic constants among the 23 non zero constants for quartz.

Using the experimental measurements of the electroelastic effect available in the literature<sup>1,2,3,4,5,6,7,8,9,10</sup> equations corresponding to various cuts and vibration modes were solved to determine the 8 independent electroelastic coefficients.

$e_{111}$	- 2.86	+ 0.13
$e_{113}$	- 21.24	+ 2
$e_{113}$	63.56	+ 6
$e_{122}$	3.54	+ 1.6
$e_{124}$	6.49	+ 0.8
$e_{134}$	88.32	+ 8.1
$e_{144}$	- 1.41	+ 0.64
$e_{155}$	43.66	+ 4.3

Table I  
Independent material electroelastic coefficients for right hand quartz  
(unit:  $\text{C/m}^2$  at 20°C)

By using a least squares method, the results of Table I were obtained with a mean squared error of about 7%. The given uncertainty were calculated assuming an experimental error of  $\pm 5\%$  on the electroelastic effect measurement. Calculations were carried out for right hand quartz at 20°C following the IEEE Standard 176 for plates orientation<sup>14</sup>. Note that the relative uncertainty is less than 10% except for  $e_{122}$  and  $e_{144}$  because these two coefficients could have played a minor role in the cuts which were used.

As a verification and in order to compare the present results with previous ones given by Hruska<sup>15</sup>, the electroelastic effect  $(\Delta\omega/\omega) E_H$  was plotted using the calculated electroelastic coefficients of Table I in equation (38) for cuts (yxwL)<sup>16</sup> and for the three modes of vibration (Fig. 3)<sup>16</sup>. The shape and magnitude of the curves thus obtained are very close to those published by Hruska<sup>15</sup> using his own coefficients and relations. This comparison shows that the phenomenological coefficients and relations stated by Kusters<sup>3</sup> and Hruska<sup>5</sup> give the right magnitude of the electroelastic effect even if they cannot be used without care for evaluating other phenomena where electroelastic coefficients are involved<sup>2,16</sup>. In fact, in these phenomenological coefficients the electroelastic part and the nonlinear elastic part are not separated. This can be also observed in Table II where the contributions of the different coefficients are separately given (see Eqs. (43)-(47)).

mode	C	E	A
$(\frac{\Delta\omega}{\omega}) E_H$ $10^{-12} \text{ m/V}$	5.31	- 0.17	- 0.81
M	- 1.1	- 0.47	- 0.9
A	- 0.5	0.27	0.27
P	- 0.63	- 0.47	- 0.17
W	- 0.29	-	- 0.11
R	- 0.007	-	-
electroelastic constants	0.64	-	- 0.11

Table II  
Contribution of different coefficients to the electroelastic effect for cut (yxwL)<sup>16</sup>  
(see Eqs. (43)-(47) for explanation of the terms  
M, P, W, R)

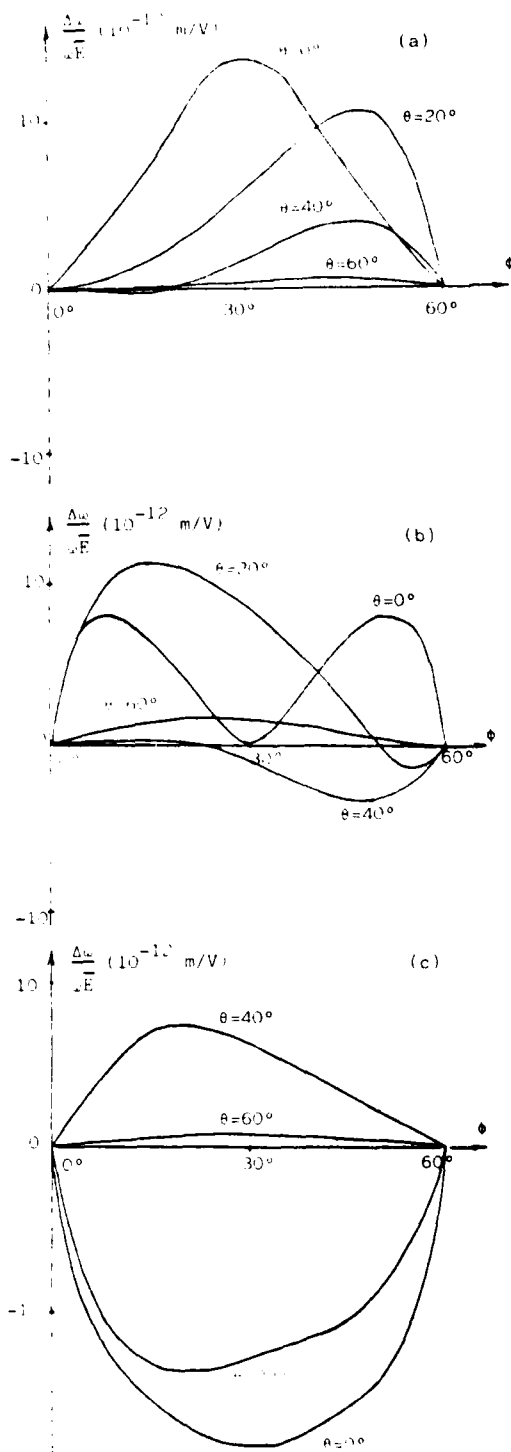


Fig. 1. Electrostatic effect for plates  
 (a) A mode; (b) B mode; (c) C mode

### Impurity diffusion in quartz

The most common interpretation of the ionic conductivity in quartz assumes that some  $\text{Si}^{4+}$  atoms are replaced by  $\text{Al}^{3+}$  associated with a monovalent cation ( $\text{Na}^+$ ,  $\text{Li}^+$ ,  $\text{K}^+$ , ...) achieving charge neutrality in the crystal. When submitted to a DC field, cations diffuse in the crystal towards the negatively polarized electrode leaving behind them uniformly distributed negative charges. Only one kind of impurity is diffusing. In a one-dimensional crystal, as considered here, moreover it is assumed that impurities can neither enter nor leave the crystal (blocking electrodes). So the net total charge of the crystal is always zero. For convenience the calculations are performed using a set of axes bounded to the crystal denoting for simplicity  $x$  the axis normal to the plate (instead of  $0a_2$  previously used).

Assuming an uniform initial impurity concentration  $n_0$  the steady state, reached when the impurities are in the new equilibrium positions under the DC field, is described by the following equations

$$\frac{pE}{U_T} - \frac{dp}{dx} = 0 \quad (48)$$

$$\frac{dE}{dx} = \frac{p - n_0}{\epsilon} e \quad (49)$$

$$E = - \frac{d\phi}{dx} \quad (50)$$

$$U_T = \frac{D}{\mu} = \frac{k_B T}{e} \quad (51)$$

with the following boundary conditions

$$\phi(-h) = 0, \quad \phi(+h) = \phi_0 \quad (52)$$

$$\int_{-h}^{+h} p dx = 2 h n_0 \quad (53)$$

where  $p(x)$  is the local concentration of the moving cations,  $E(x)$  and  $\phi(x)$  the local electric field and potential,  $e$  is the electron charge,  $\epsilon$  the permittivity of the crystal in the  $x$ -direction,  $U_T$  the thermodynamical potential defining the Einstein's relation (51) between diffusion constant  $D$  and mobility  $\mu$ . Eq. (48) expresses there is no ionic current in the steady state and Eq. (49) is Gauss's law. By using the above relations it can be shown that the potential  $\phi(x)$  is solution of a nonlinear second order differential equation

$$\frac{d^2\phi}{dx^2} = \frac{n_0 e}{\epsilon} - p(-h) \frac{e}{\epsilon} \exp \left( - \frac{\phi(x)}{U_T} \right) \quad (54)$$

If the thermodynamical potential  $U_T$  ( $U_T = 26$  mV at 300K) is much smaller than the applied DC potential (typically  $\phi_0 = 500$  V) Eq. (54) reduces to

$$\frac{d^2\phi}{dx^2} = \frac{n_0 e}{\epsilon} \left[ 1 - \frac{\phi_0}{U_T} \exp \left( - \frac{\phi(x)}{U_T} \right) \right] \quad (55)$$

It is possible to obtain an approximate solution for the steady state potential when the following condition occurs

$$\frac{\phi_0}{n_0} > \frac{\epsilon}{8eh^2} \quad (56)$$

This condition, which approximately corresponds to  $n > 10^{18}$  impurities/m<sup>3</sup> for  $\phi_0 = 500$  V and  $2h = 0,6$  mm is almost already fulfilled in practical cases. In such a case the total charge concentration  $\rho(x) = (p(x) - n)e$ , the electric field  $E(x)$  and the potential  $\phi(x)$  have the shapes showed on Fig. 4 a,b,c respectively. Then it appears that the crystal can be shared into three zones (see Table III), zones I and III practically present uniform charge concentration corresponding to linearly varying electric field and quadratic variation of potential. Zone II, where charge concentration and electric field both are close to zero, corresponds to a uniform potential.

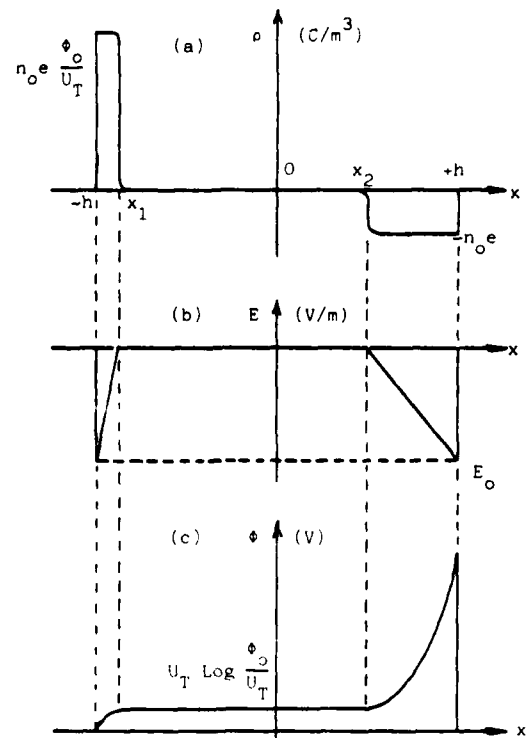


Fig. 4 : a) Charge concentration  
b) Electric field c) Potential

	Zone I	Zone II	Zone III
limits	$-h < x < x_1 = -h + \sqrt{\frac{2\epsilon U_T^2}{n_0 e \phi_0}}$	$x_1 < x < x_2 = h - \sqrt{\frac{2\epsilon \phi_0}{n_0 e}}$	$x_2 < x < +h$
charge	$\rho^{(1)} = n_0 e \frac{\phi_0}{U_T}$	$\rho^{(2)} = 0$	$\rho^{(3)} = -n_0 e$
electric field	$E^{(1)} = \frac{n_0 e \phi_0}{\epsilon U_T} (x+h) + E_0$	$E^{(2)} = 0$ $E_0 = -\sqrt{\frac{2n_0 e \phi_0}{\epsilon}}$	$E^{(3)} = \frac{n_0 e}{\epsilon} (h-x) + E_0$
potential	$\phi^{(1)} = -\frac{n_0 e \phi_0}{2\epsilon U_T} (x+h)^2 - E_0 (x+h)$	$\phi^{(2)} = U_T \log \frac{\phi_0}{U_T}$	$\phi^{(3)} = \phi_0 + \frac{n_0 e}{2\epsilon} (h-x)^2 + E_0 (h-x)$

Table III  
Charge concentration, electric field and potential distribution for a crystal of thickness  $2h$  submitted to a potential difference  $\phi_0$  after the steady state is reached when  $\phi_0 \gg U_T$  and  $\phi_0 n_0 \epsilon > 8eh^2 U_T$  (see Fig. 4)

### Steady state frequency shift

Because the electromechanical coupling factor is small in quartz, one can consider that at least in first approximation, the repartition of potential does not depend on the modification of the strain due to diffusion. In such a case equations (35), (37) and (38) with the notation of preceding section enable to express the frequency shift under the following form

$$\frac{\Delta\omega}{\omega_0}(t) = \frac{\omega_0}{\omega_0} \left( \frac{\Delta\omega}{\omega_0} \right)_H - h \int_{-h}^{+h} \frac{\partial\phi(x,t)}{\partial x} \cos^2 \frac{\omega_0 x}{V} dx \quad (57)$$

where  $(\Delta\omega/\omega_0)_H$  would be the initial frequency shift when there is no diffusion and  $\partial\phi(x,t)/\partial x$  is the potential gradient during diffusion process. Fig. 5 shows the observed quasi-exponential frequency shift.

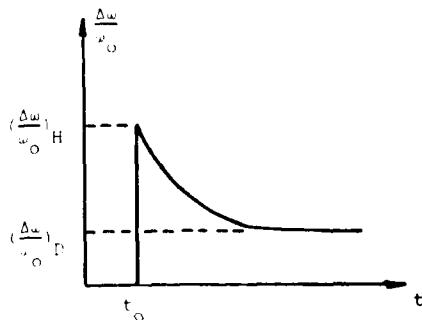


Fig. 5

Frequency shift of a resonator submitted to a DC electric field at time  $t_0$

$(\Delta\omega/\omega_0)_H$  : initial frequency shift due to the electroelastic effect

$(\Delta\omega/\omega_0)_a$  : frequency shift after diffusion corresponding to the steady state

The frequency shift can be obtained when the local electric field is known either numerically in the general case or analytically with the approximate steady state solution summarized in Table III from which the following result is obtained:

$$\frac{\Delta\omega}{\omega_0} = \frac{\pi^2 \phi_0}{8 h^2 \omega_0} \left( \frac{\Delta\omega}{\omega_0} \right)_H \quad (58)$$

Fig. 6 presents the steady state frequency shift as a function of the impurity concentration  $n_0$ . This curve shows how the impurity concentration can be determined from the amplitude of the relaxation of the electroelastic effect.

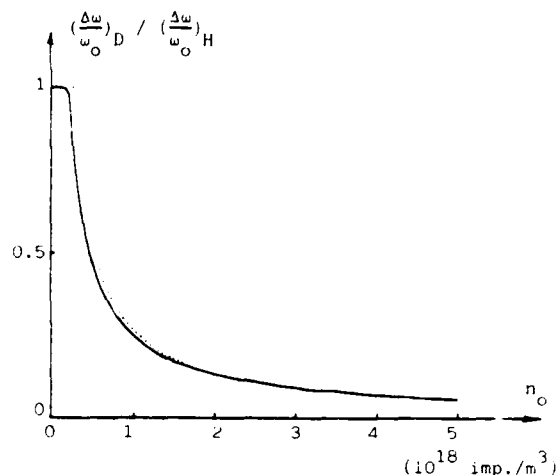


Fig. 6

Frequency shift after the steady state of diffusion is reached :  $(\Delta\omega/\omega_0)_a$  referred to the frequency shift without diffusion :  $(\Delta\omega/\omega_0)_H$ . Solid line corresponds to the numerical solution obtained by solving Eq. (55) by relaxation method and then using the result to carry out the integral of Eq. (57). Dotted line corresponds to the approximate solution (58).

The method will be most sensitive when the impurity content is in the range of  $10^{17}$  to  $10^{18}$  impurities/ $m^3$ . However values obtained by other methods typically indicate impurity concentration of the order of magnitude of one to ten ppm Si for cationic monovalent impurities ; that is about  $10^{22}$  to  $10^{23}$  impurities/ $m^3$ . This fact is easily explained if it is remembered that only a small part of the impurities are ionized at room temperature, furthermore the ionized impurity concentration must increase with temperature following an Arrhenius' law

$$n_0 = N_0 e^{-\frac{W_a}{k_B T}} \quad (59)$$

where  $W_a$  is the ionization energy and  $N$  a constant depending on the concentration of Al substitutionals.

So the strong influence of temperature on the concentration appears when the frequency shift after steady state diffusion is plotted as a function of the temperature. Experiments performed between 30°C and 100°C indeed shows a variation (Fig. 7) with a shape very similar to the theoretical curve (Fig. 6).

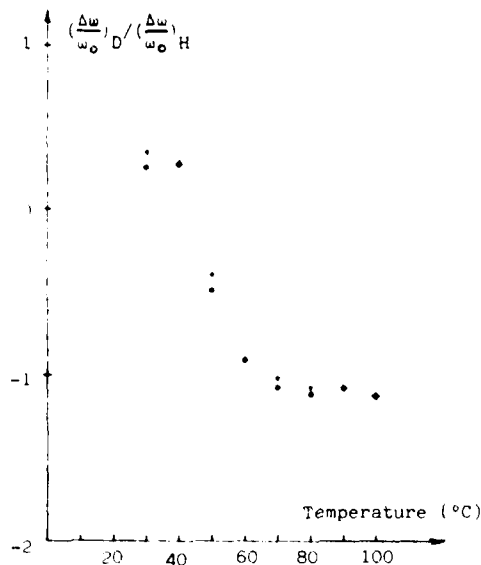


Fig. 7  
Experimental frequency shift as a function of temperature (FC cut). See Fig. 6 for definition of the vertical scale. Crosses and circles correspond to opposite orientations of the applied DC field

Because this latter curve is obtained from a one-dimensional model of diffusion it does not present frequency shifts  $(\Delta\omega/\omega_0)_D$  which after diffusion can have a magnitude greater than the initial frequency shift  $(\Delta\omega/\omega_0)_H$  as it appears on the experimental plot. Even if direct quantitative comparison is difficult between experiment and theory it still shows this experimental method used together with a more refined diffusion model can be a very simple and fruitful tool for the analysis of impurities in quartz and their incidence on the stability of quartz oscillators. As an example, an estimation of the activation energy  $W_a$  from the curve of Fig. 7 gives an approximate value of  $W_a \approx 1$  eV which can be compared to the binding energies already known from ionic conductivity measurements.

The second step in this study will be the calculation of the transient diffusion process, in order to evaluate the impurity relaxation time, characteristic of the impurity type. However such a calculation needs the knowledge of the deformation potentials and potential wells of the crystal structure.

These characteristics are not known for quartz, but some partial informations can be also obtained from low temperature measurements.

#### Impurity relaxation at low temperature

The impurity atom can occupy two equilibrium positions in a double well potential, when trapped by the  $Al^{3+}$  atom. (In fact more than two positions can occur). The ion can jump from one site to the other one and cross over the potential barrier by thermal activation. Such a model was proposed by Stevels<sup>21</sup>. Similar models of resonant absorption and relaxation absorption in amorphous solids were also built up. They are based on the assumption of an asymmetrical two-level system with broad distribution of the energy splitting. A review can be found in ref. 22. The same model can be transposed to quartz crystal.

The origin of the relaxation of the impurity lies in its coupling to elastic strains through the deformation potential. The two states of the impurity are shifted in energy relative to each other, and therefore the equilibrium is disturbed. Then a relaxation process takes place to restore equilibrium. There is a feedback to the elastic wave which induces dispersion (velocity shift when the feedback is in phase) and absorption (attenuation of the wave when the feedback is out of phase<sup>23</sup>). For a resonator they lead to frequency shift and finite Q-factor. The last one can be written

$$\frac{1}{Q} = \frac{n D^2}{4 \rho v^2 k_B T} \frac{-t}{1 + t^2}$$

where  $n$  is the number of impurities per unit volume,  $\rho$  the specific mass of the crystal,  $v$  the sound wave velocity,  $k_B$  the Boltzmann constant,  $T$  the absolute temperature,  $t$  the wave angular frequency and  $D$  the deformation potential introduced by the relation

$$E' = E + D\epsilon$$

which shows how the elastic strain  $\epsilon$  affects the energy difference  $E$  between the two states of the impurity. Indeed the main difficulty is in the determination of  $D$ , which is not known.

$\tau$  is the relaxation time of the impurity system in the case of transitions by thermal activation, it can be shown that  $\tau$  is related to temperature by an Arrhenian type relation

$$\tau = \tau_0 \exp \left( \frac{W_a}{k_B T} \right)$$

where  $W_a$  is the activation energy of the process, corresponding to the potential barrier height (Fig. 8).

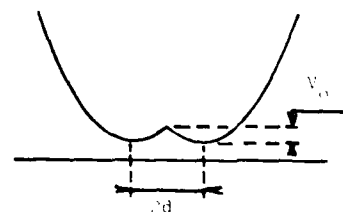


Fig. 8 : Double well potential

The double well is approximated by two parabolic curves with minima separated by a distance  $2d$ .

The calculation of the eigenfrequencies of the quantum mechanical harmonic oscillator gives  $\tau_0$ .

$$\tau_0 = \pi \sqrt{\frac{md}{2V_0}} \quad (63)$$

where  $m$  is the mass of the impurity.

As for  $V_0$ , the distance  $2d$  between the two well bottoms is also unknown.

$V_0$  and  $d$  depend on the characteristics of the lattice and of the defect ( $Al^{3+}$  + alkaline ion). It is related to the previous parameters but also to the wave structure, i.e. to the components of the sound wave amplitude, to the propagation direction and the velocity.

The acoustic losses ( $1/Q$ ) were measured on the B and C modes of three SC and FC doubly rotated cut resonators. The results are shown on Fig. 9a, b and c. Two peaks can be observed. The peak at 20K is due to the interaction of the sound wave phonons with the thermal phonons of the crystal lattice. The second peak, at 50K, is attributed to  $Na^+$  impurities. It can be observed that the B mode exhibits a lower peak than the C mode. For each resonator this shows how in the same crystal with the same impurity content and the same propagation direction the peak intensity is modified when changing the wave polarization because this difference cannot be explained only by the ratio of the velocity. But the temperature  $T_m$  of the peak maximum remains constant as expected from the relation

$$k_B T_m = - \frac{V_0}{\ln(\omega \tau_0)}$$

which does not include the deformation potential  $\epsilon$ .

Reduction of these data enable to evaluate the relaxation time  $\tau_0 = 2.5 \cdot 10^{-12}$  s (which can be compared with Stevels's value  $\tau_0 = 2 \cdot 10^{-13}$  s), the potential barrier height  $V_0 = 0.040$  eV (0.055 eV by Stevels) and the distance between the two wells  $2d = 8 \text{ \AA}$ .

#### Conclusion

The diffusion of impurities under an applied DC field could be used for characterizing the impurity content of quartz crystal, as shown by this analysis. However the lack of knowledge of the lattice and defect characteristics, essentially the deformation potentials and potential wells, do not allow to obtain the absolute impurity concentration, but relative evaluations can be made with respect to a crystal with a known impu-

rity content. On the other hand this method, combined with low temperature measurements, can lead to the determination of those lattice potentials, and therefore to a better knowledge of quartz crystal. This is not only interesting for the fundamental point of view, but also for the practical one of quartz resonator sensitivity to ionizing radiations.

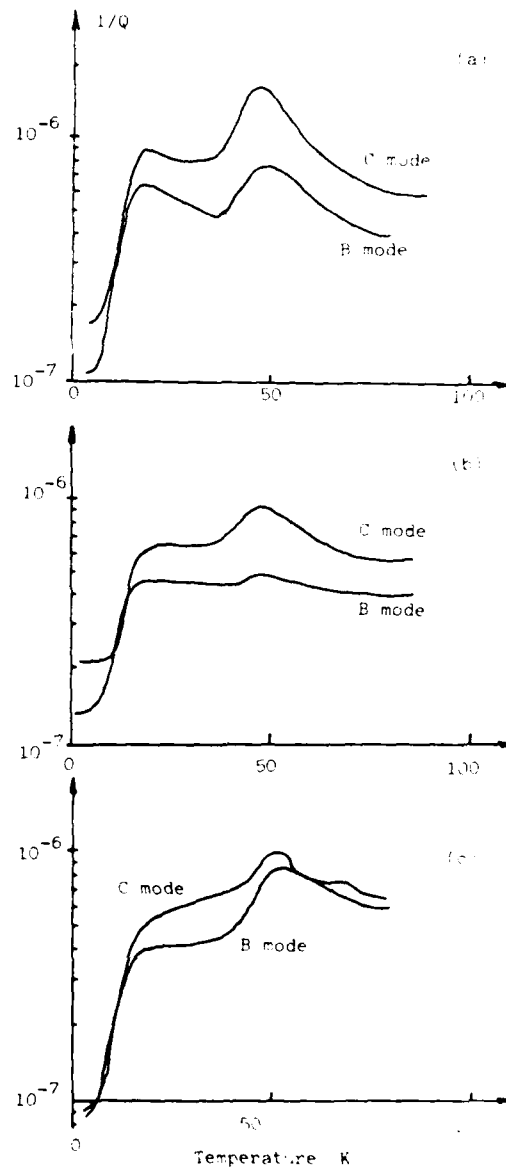


Fig. 9 : Low temperature acoustic losses for the two shear modes

- a) FC cut # 24b
- b) FC cut # 24c
- c) SC cut # 20c

### Acknowledgements

This work was supported in part by the U.S. Air Force under Grant n° AFOSR-81-0191.

The authors also are grateful to J. Gros Lambert, C. Paulin and G. Robichon for providing the data at low temperatures, and to Dr. Kusters for his numerical data of the electroelastic effect.

### References

1. J.C. Baumhauer, H.F. Tiersten, "Nonlinear electroelastic equations for small fields superposed on a bias", J. Acoust. Soc. Am., 54, n° 4, 1018, (1973).
2. A.I. Korobov, V.E. Lyamov, "Nonlinear piezoelectric coefficients of  $\text{LiNbO}_3$ ", Sov. Phys. Solid State, 17, n° 5, 932, (1975) and reference therein. The sign of coefficient  $e_{nijk}$  differs from reference 1.
3. J.A. Kusters, "The effect of static electric field on the elastic constants of  $\alpha$ -quartz", Proc. of the 24th A.F.C.S., 46, (1970).
4. K. Hruska, "Polarizing effect with piezoelectric plates and second order effects", IEEE Trans. S.U., 18, n° 1, 1, (1971).
5. K. Hruska, "The electroelastic tensor and other second order phenomena in quasilinear interpretation of the polarizing effect with thickness vibrations of  $\alpha$ -quartz plates", Proc. of the 31st A.F.C.S., 159, (1977).
6. K. Hruska, "Second order phenomena in  $\alpha$ -quartz and the polarizing effect with plates of orientation  $(xz)$ ", IEEE Trans. S.U., 25, n° 4, 198, (1978).
7. H.F. Tiersten, "Perturbation theory for linear electroelastic equations for small fields superposed on a bias", J. Acoust. Soc. Am., 64, n° 3, 81, (1978).
8. H.F. Tiersten, "Linear piezoelectric plate vibrations", N.Y. Plenum Press (1969).
9. K. Hruska, A. Khogali, "Polarizing effect with  $\alpha$ -quartz rods and the electroelastic tensor", IEEE Trans. S.U., 18, n° 3, 171, (1971).
10. K. Hruska, "On the linear polarizing effect with  $\alpha$ -quartz AT plates", IEEE Trans. SU-28, n° 2, 198, (1981).
11. K. Hruska, "The influence of an electric field on the frequency of piezoelectric cuts", Czech. J. Phys., B11, 150, (1961).
12. D. Hammond, C. Adams, L. Cutler, "Precision crystal units", Proc. of the 17th A.F.C.S., 215, (1961).
13. R. Besson, J.J. Gagnepain, "Détermination des coefficients non linéaires de polarisation électrique du quartz", C.R. Acad. Sc. Paris, B274, 225, (1972).
14. IRE Standards on Piezoelectric Crystals, IRE Standard 176.
15. K. Hruska, "Polarizing effect with doubly rotated  $\alpha$ -quartz plates vibrating in thickness", IEEE Trans. SU-25, n° 6, 390, (1978).
16. A.K. Ganguly, K.L. Davis, "Nonlinear interactions in degenerate surface acoustic wave elastic convolvers", J. Appl. Phys., 51, n° 2, 920, (1980).
17. J.A. Weil, "The aluminum centers in  $\alpha$ -quartz", Rad. effects, 26, 261, (1975) and numerous references therein. Also proc. of the 27th A.F.C.S., 153, (1973).
18. R.A. Poll, S.L. Ridgway, "Effects of pulsed ionizing radiation on some selected quartz oscillator crystals", IEEE Trans. NS-13, n° 6, 130, (1966).
19. N.F. Mott, R.N. Gurney, "Electronic processes in ionic crystals", Oxford (1948), chapter II.
20. R.C. Hughes, "Electronic and ionic charge carriers in irradiated single crystal and fused quartz", Rad. Effect, 26, 225, (1975).
21. J.M. Stevels, "The dielectric properties of quartz crystals and fused silica in relation with their imperfections", Proc. of the International School of Physics Enrico Fermi, (1963).
22. S. Hunklinger, W. Arnold, "Ultrasonic properties of glasses at low temperatures", Physical Acoustics, W.P. Mason, R.N. Thurston Editors, vol. XII, Academic Press, (1976).
23. J. Jackle, L. Piché, W. Arnold, S. Hunklinger, "Elastic effects of structural relaxation in glasses at low temperature", Journal of Non-Crystalline Solids, 20, (1976).
24. H.J. Maris, "Interaction of sound waves with thermal phonons in dielectric crystals", Physical Acoustics, W.P. Mason, R.N. Thurston Editors, vol. VIII, Academic Press, (1971).
25. D.B. Fraser, "Impurities and anelasticity in crystalline quartz", Physical Acoustics, W.P. Mason, R.N. Thurston Editors, vol. V, Academic Press, (1968).
26. J. VERHOOGEN, "Ionic diffusion and electrical conductivity in quartz", Am. Miner., 37, 637, (1952).

DC PLASMA ANODIZATION OF QUARTZ RESONATORS

C.W. SHANLEY AND L.N. DWORSKY

MOTOROLA, INC.

AD P001510

ABSTRACT

A technique for final tuning AT-quartz resonators having aluminum electrodes by means of a low energy DC oxygen plasma is described.<sup>1</sup> Compared to other techniques, this method is clean, dry, protective, selective, and does not significantly heat the crystal.

In this process a small volume of oxygen plasma is generated in a plasma "gun" by a DC potential. A positive bias on the crystal electrode placed near the plasma causes the electrode to be anodized. The oxide layer increases the mass of the electrode and thereby lowers its frequency. Unbiased electrodes are not affected by the process, so monolithic filters may be tuned.

1

INTRODUCTION

Aluminum is generally used to form electrodes on VHF quartz crystals, chiefly because of its low density. This permits the deposition of relatively thick electrodes having good electrical characteristics, but without excessive mass loading. Additional advantages include low cost, good adhesion to quartz and an acoustic impedance close to that of quartz.

One problem often associated with aluminum electrodes is the gradual growth of an oxide layer which can cause aging. This oxide growth begins immediately after the formation of the electrode and continues until a thickness of around 50Å is reached. The resulting mass increase of the electrode causes a frequency decrease of the resonator.

A solution to the aging problem is to induce oxide growth well beyond any which would occur under ordinary conditions. In 1976 Bottom<sup>2</sup> described a method of adjusting the frequency of

resonators with aluminum electrodes by anodizing them in a liquid bath. Later Ang<sup>3</sup> showed how this technique has been applied in a manufacturing environment. One disadvantage of the described technique is the necessity of removing the crystal from the bath and carefully drying it before each frequency measurement.

Reche<sup>4</sup> reported on the anodization of electrodes in an RF generated oxygen plasma. This eliminated the necessity of drying the crystal prior to measuring its frequency. One difficulty was that the crystal was heated to a high temperature (160°C) by the plasma, causing temperature induced frequency shifts.

When used for final frequency adjustment, both liquid and RF anodization have the advantage over shadow masking techniques of providing uniform deposition of a protective oxide coating on the electrode.

DC PLASMA ANODIZATION

The primary mechanism of oxide formation during anodization appears to be the movement of positive aluminum ions through the oxide to the oxide-oxygen interface. There they combine with negative oxygen ions to form aluminum oxide. After the formation of the initial oxide, an electric field of proper polarity is required across the oxide to promote aluminum ion migration.

Figure 1 is a representation of the glow produced in a DC cold cathode discharge. The plasma density is greatest in the visible glow regions of the negative glow and the positive column.

Most plasma anodization experiments described in the literature do not use the simple geometry of Figure 1. Various anode and cathode geometries can expand, contract, or even eliminate some of the regions shown in Figure 1. Further complications arise from the fact that the operating pressure can also affect the

size and distribution of the different regions.

Miles and Smith<sup>5</sup> observed the highest rates of anodization at two pressures near 50 microns and 1 torr, where the sample was believed to be in the negative glow and positive column, respectively. Most of the data in the literature has been taken at the lower pressure in the negative glow.<sup>6</sup> In these cases the oxide growth rate follows a near logarithmic growth rate, where the oxide thickness increases with the logarithm of the time.

In many cases<sup>6</sup> oxide growth has been observed to be limited by sputtering. Oxygen ions striking the anodized surface may sputter off the oxide at a rate close to the anodization rate, thereby limiting growth. Conversely, material may be sputtered from the anode or cathode and deposited on the crystal, thereby enhancing the apparent anodization rate.

#### EXPERIMENTAL PROCEDURE

For the experiments described here, a small plasma "gun" was constructed (Figure 2). The gun is approximately 1.4 cm in diameter and 2.3 cm in length, and made of aluminum. The exterior is hard coat anodized to prevent a glow from being established on the outside of the gun. The anode and cathode are separated by an aluminum oxide insulator. A stainless steel screen was inserted to provide a uniform, porous cathode surface. The back of the gun is ported to allow fresh neutral oxygen into the gun chamber.

The crystal to be anodized is placed approximately 5 mm from the end of the plasma gun. This crystal is then outside the region of the visible glow of the plasma, where heating of the crystal by the plasma is minimal. It is also far enough away from the gun that no sputtered anode material is deposited on the electrode.

When sufficient voltage is applied at the proper pressure, a glow discharge is established between the cathode screen and the anode ring. The various regions shown in Figure 1 are not discernable in the small anode-cathode gap, but the area around the anode ring glows in a way characteristic of the positive column. The visible glow is contained within the gun.

A positive bias voltage is applied to the electrode to be anodized. This induces a field across the existing oxide which helps the transport of aluminum ions. In addition, negative oxygen

ions are attracted from the plasma to the electrode surface. RF measurements are made by turning off the plasma and measuring the reflection coefficient ( $S_{11}$ ) of the electrode. The RF switching is performed by PIN diodes. The process is controlled by a Hewlett-Packard 9825 calculator, interfaced to a small Motorola 6800 microprocessor system which handles timing and switching functions. The process of turning off the plasma, making the frequency measurement, calculating the current rate, and re-establishing the plasma requires less than three seconds.

Experiments were conducted in two different vacuum chambers. The first had only a roughing pump. The chamber was rough pumped to 600-800 microns and back-filled to operating pressure (approximately 2 torr). Later experiments were done in a system with both a roughing pump and cryogenic pump (Cryotorr-8 from CTI Cryogenics). In these later experiments the system was rough pumped to around 1 torr and cryopumped to better than  $10^{-4}$  torr before backfilling.

#### RESULTS

##### RATES

Crystals ranging from 3rd overtone 30 MHz crystals to 5th overtone 175 MHz crystals have been tuned using this technique. A typical anodization run is shown in Figure 3. Since the subject of interest is the frequency change as a function of time, it is not sufficient to monitor oxide growth. As the oxide grows, it consumes some of the aluminum in the electrode. The curve here expresses the anodization process by the equivalent plateback in angstroms of aluminum. In this way, the scale may be translated to the frequency change for any crystal. For reference a scale showing the equivalent frequency change for a 5th overtone 100 MHz resonator is also shown.

The data shown in Figure 3 was taken at an oxygen pressure of 2.2 torr, and a bias voltage on the electrode of 30 VDC. The voltage applied to the plasma gun was -600 V, and the current observed was 0.5 ma. The power dissipation in the plasma was thus slightly less than a third of a watt. The curve resembles a simple exponential, but is in reality more complex. Figure 4 shows the same data plotted logarithmically. Region I has almost twice the slope of region II.

Such a change in slope indicates a change in the rate controlling step of a physical process. This is seen, for example, in diffusion experiments, where the rate change may indicate a change from

grain boundary diffusion to bulk diffusion. Both processes are simultaneously happening, but each dominates the net phenomena under different circumstances.

Possible limitations to the rate at which the oxide can form include aluminum availability, crystal cleanliness, oxygen availability, sputtering, and the kinetics of the reaction forming  $\text{Al}_2\text{O}_3$ . The oxygen reaches the crystal at a constant rate, which is determined by the pressure and is the same in regions I and II. Similarly, the reaction forming  $\text{Al}_2\text{O}_3$  proceeds at the same rates in regions I and II, if both aluminum and oxygen are present. On the other hand, aluminum availability would be greater in region I, since in region II the oxide will have grown to a thickness sufficient to impede the aluminum flow.

The oxygen ions are attracted to the crystal electrodes by a low bias voltage. Unbiased electrodes do not changes in frequency, indicating that no material is sputtered onto or off of the surface. It follows that sputtering is not likely to be the rate determining step in either region. The kinetics of  $\text{Al}_2\text{O}_3$  formation are not likely to be slow enough to limit the rate. It is probable, therefore, that the arrival of oxygen at the electrode may be the slowest and hence the rate limiting step in region I. In region II, the oxide is thicker, causing the electric field across it to be reduced. In this case, the arrival of aluminum at the oxide/oxygen interface may be the rate limiting step.

Figure 5 shows the logarithmic anodization rate (equivalent angstroms of aluminum divided by the log of the time) as a function of bias voltage on the electrode. Data from the slopes in region I and region II are shown. The scatter in the data may be due to the different frequency crystals used or to small amounts of contamination. Pump oil, inadequate cleaning, or other contaminants will adversely affect the anodization rate by reducing the aluminum surface available for anodization.

Region I shows a variation in rate with different bias voltages, whereas region II remains relatively constant. If region I is oxygen limited, it might be expected that higher bias voltages would attract more oxygen ions and thereby increase the rate. Instead there is an apparent decrease in anodization rate with bias voltage. The bias voltage may be disturbing the distribution of the plasma and thereby affecting the observed rate.

In region II the oxide has increased in thickness, causing the electric field across it to be reduced. The higher the bias voltage, the later the breakpoint between regions I and II will occur. Region II behavior corresponds to a particular electric field level and is therefore independent of voltage, as observed.

#### EFFECT OF PRESSURE

As mentioned previously, the glow discharge is strongly affected by pressure and by the anode and cathode geometry. For the gun geometry described here, the highest rates were obtained for an oxygen pressure of 2.2 torr. At pressures greater than 2.4 torr, the plasma would not reliably ignite. At pressures lower than about 1.4 torr, the plasma was weak and would often be extinguished.

For pressures near 2.2 torr, however, the slope of region I should be influenced by the pressure. Figure 6 shows data from a resonator run at 1.8 torr and 15 volts bias. The oxygen concentration is less at this pressure than in the case of the previous curves, and the rate in region I has been reduced to the rate of region II. This is consistent with the hypothesis that near the normal operating conditions, oxygen availability is the rate controlling step in region I.

#### MONOLITHIC FILTERS

Several monolithic crystal filters have been tuned using this technique. A crystal is placed near the plasma gun as previously described. The frequency of each resonator is measured prior to anodization. The resonator not being measured must be tuned out by some convenient method so as not to affect the measurement. Each electrode may then be anodized for the appropriate amount of time. The tuning process continues in an iterative fashion until both electrodes are at the desired frequency. If one electrode finishes before the other, the bias potential is removed from it.

Experiments have shown that unbiased (floating) electrodes adjacent to biased electrodes do not change in frequency. Although they might be expected to suffer from some sputtering, none has been detected to within the experimental accuracy ( $\pm 200$  Hz), even after one hour of exposure to the plasma. A strong negative charge, measured to be around -60V, is induced by the plasma on the floating electrode and prevents anodization or sputtering.

The chief disadvantage to this technique of final tuning crystal filters is the limited tuning range available.

The electrodes must be well defined and have an accurate amount of plateback. However, the tuning range may be doubled if the ground electrodes of the filter are also anodized.

#### AGING

Crystals with aluminum electrodes often age downward in frequency due to long term growth of the aluminum oxide layer. The anodization process produces an oxide layer far in excess of normal oxidation. Anodized devices are more resistant to subsequent oxide growth than standard aluminum devices, and should therefore show less aging. This was confirmed by Bottom<sup>2</sup> for the case of liquid anodization.

Figure 7 shows the average frequency shift for 19 crystals aged at 120°C for 500 hours. The crystals were 155 MHz, 5th overtone devices. At the end of 500 hours the crystals had an average frequency shift of -3.5 PPM, with a standard deviation of 2.1 PPM. Only 2 of the 19 devices failed to be within 5 parts per million of their initial frequency.

#### SUMMARY

A method of tuning aluminum resonators on quartz crystals has been described. The technique uses a low energy DC oxygen plasma to transform some of the aluminum forming the resonator into aluminum oxide, thereby increasing the resonator mass and lowering its frequency. Both oscillators and monolithic crystal filters may be tuned.

The technique is clean and dry, and does not significantly heat the crystal. Since the amount of oxide which can be produced in a reasonable amount of time is limited, the method is most useful for high overtone, high frequency devices where the frequency change with thickness is large.

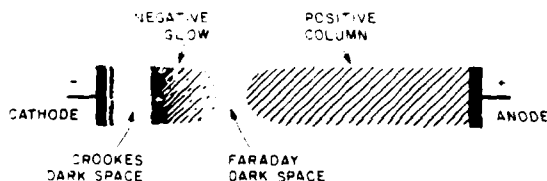


Figure 1. Typical DC Glow Discharge

#### REFERENCES

1. Patent #4,232,239; Dworsky, Whalin, and Glotzbach, Motorola, Inc. (1980).
2. Bottom, Virgil E., "A Novel Method for Adjusting the Frequency of Aluminum Plated Quartz Crystal Resonators," Proceedings of the 30th Annual Symposium on Frequency Control, 1976.
3. Ang, Dick, "A Microprocessor Assisted Anodizing Apparatus for Frequency Adjustment," Proceedings of the 33rd Annual Symposium on Frequency Control, 1979.
4. Reche, J.J.H., "Frequency Tuning of Quartz Resonators by Plasma Anodization," Proceedings of the 32nd Annual Symposium on Frequency Control, 1978.
5. Miles, J.L., and Smith, P.H., "The Formation of Metal Oxide Films Using Gaseous and Solid Electrolytes," Journal of the Electrochemical Society, V.110, No. 12, 1963, pp. 1240-1245.
6. O'Hanlon, John F., "Plasma Anodization of Metals and Semiconductors," Journal of Vacuum Science and Technology, V. 7, No. 2, 1969, pp. 330-338.

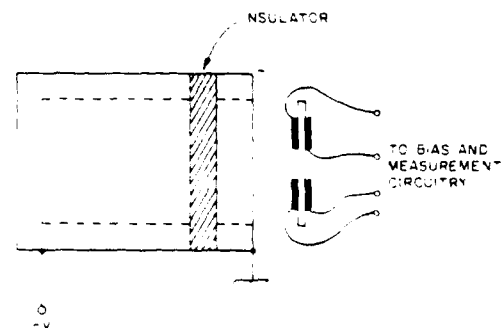


Figure 2. Schematic Representation of Anodization "Gun" and Crystal

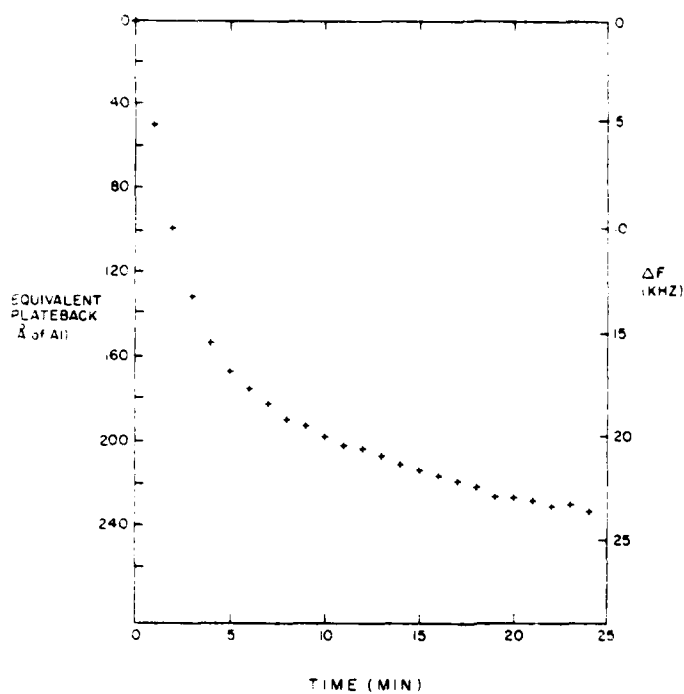


Figure 3. Anodization as a Function of Time. The Right Hand Axis Shows the Equivalent Frequency Change for a 100 MHz 5th Overtone Resonator

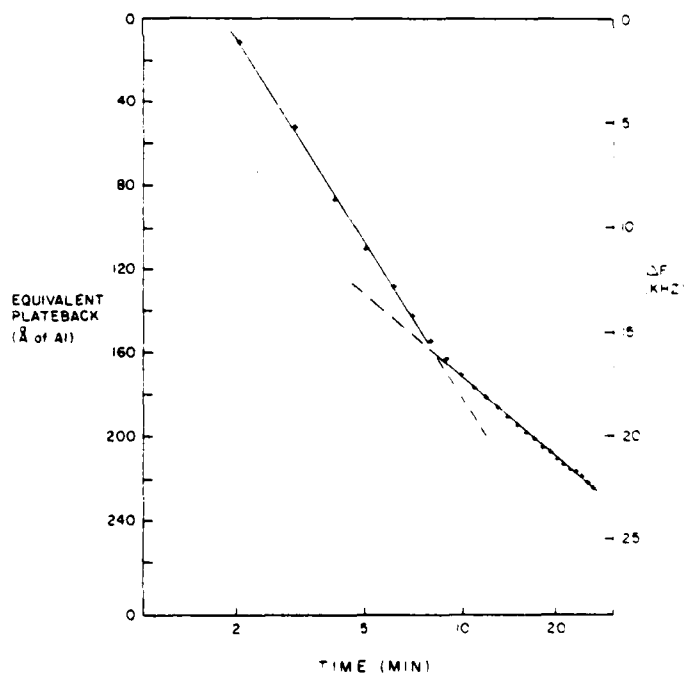


Figure 4. Same Data as Figure 3, Plotted as a Function of the Log of the Time. Region I has the Higher Slope.

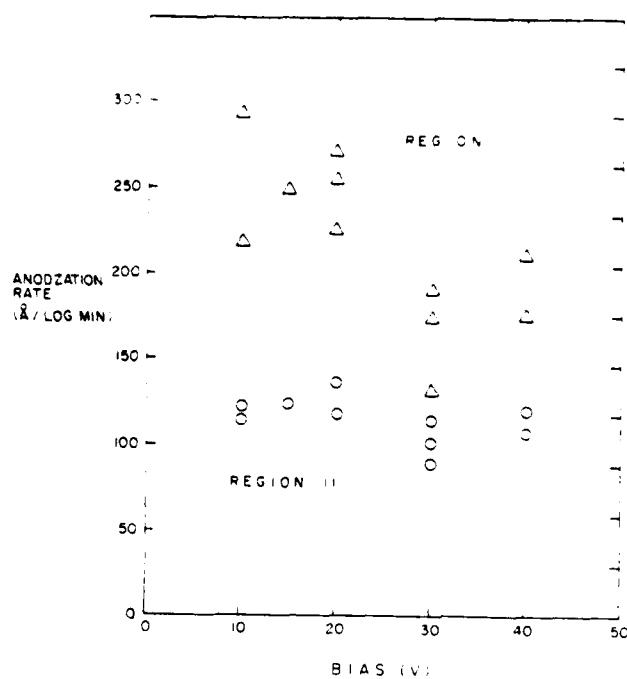


Figure 5. Anodization Rate as a Function of Bias Voltage. Data From Region I are Shown as Triangles; Data from Region II as Circles.

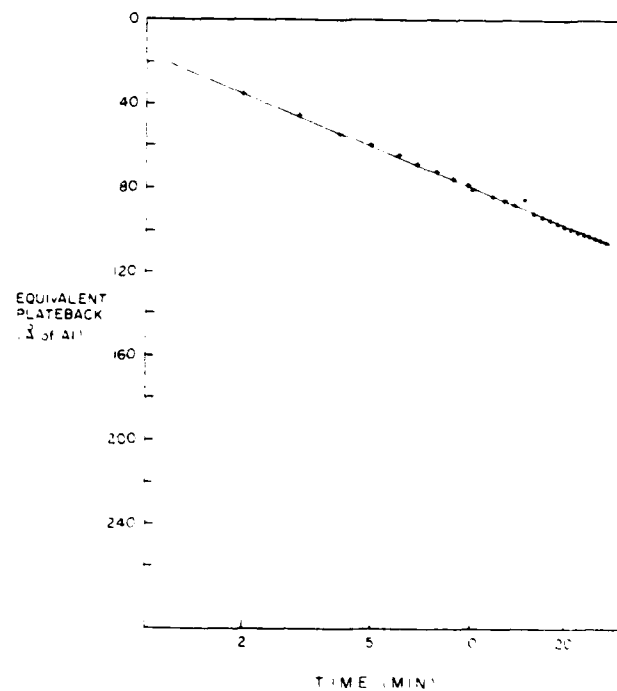


Figure 6. Anodization as a Function of Time for a Pressure of 1.8 Torr.

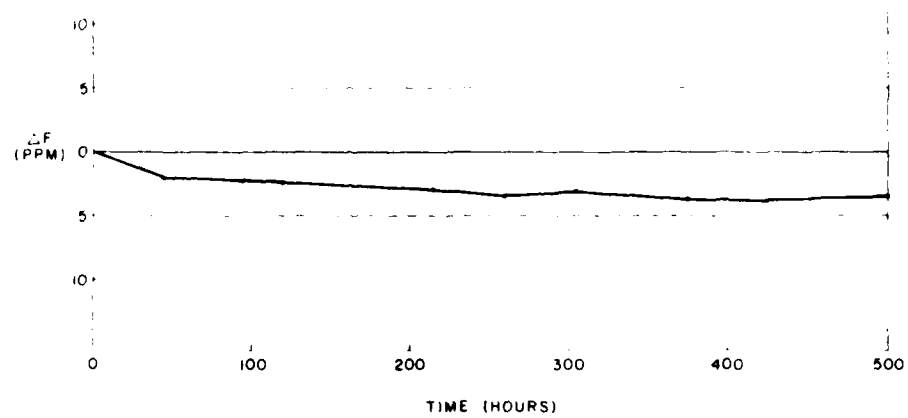


Figure 7. Average Frequency Change as a Function of Time for 19 Devices Aged at 120°C.

## CHARACTERIZATION OF ALKALI IMPURITIES IN QUARTZ

Ferdinand Euler, Herbert G. Lipson, Alfred Kahan and Alton F. Armington

Solid State Sciences Division  
Rome Air Development Center  
Hanscom AFB, MA 01731

AD P001511

Summary

We report acoustic loss measurements from room temperature to above 500°C on resonator disks fabricated from high-grade as-grown and swept synthetic quartz, containing both  $\text{Li}^+$  and  $\text{Na}^+$  alkali impurities. As-grown quartz disks showed an exponential rise of acoustic loss  $Q^{-1}$  with temperature  $T$ , starting above 200°C. Swept samples show the onset of a rise above 400°C and show high-temperature losses which increase irreversibly with time and are tentatively attributed to the presence of residual alkali. Loss peaks above 300°C were found in the swept disks. Some of these disappear after exposure to temperatures above 400°C.

The movement of alkali ions  $M^+$  during air and vacuum sweeping has been characterized in terms of the strength of  $\text{Al-OH}^-$  and as-grown  $\text{OH}^-$  defect center infrared bands. We measured the strength of these bands after relatively short periods of sweeping, ranging from 3 to 24 hours, as well as their distribution between the anode and cathode. The alkali ion replacement with  $\text{H}^+$  proceeds from the anode to the cathode and is affected by the as-grown  $\text{OH}^-$  distribution. Depletion of as-grown  $\text{OH}^-$  was found after vacuum sweeping. The alkali ion movement is substantially slower for vacuum as compared to air sweeping and also for  $\text{Na}^+$  vs  $\text{Li}^+$  impurities.

**Key words.** Quartz Material, Impurities, Sweeping, Infrared Spectroscopy, Resonators,  $Q$ -Measurements, Acoustic Losses.

Introduction

This paper reports improved methods for characterizing as-grown and swept quartz with

low impurity and defect concentrations. Two characterization techniques are utilized in our laboratory, (1) high temperature  $Q$ -measurements of quartz resonators and resonator disks and (2) low temperature infrared spectroscopy of impurity bands.<sup>1</sup> Both techniques deal with the detection of interstitial impurity ions that serve as charge compensators for substitutional aluminum ions  $\text{Al}^{3+}$  located in silicon sites.

The migration of alkali ions such as  $\text{Na}^+$  and  $\text{Li}^+$  give rise to exponentially increasing<sup>2</sup> acoustic losses  $Q^{-1}$  with temperature  $T$ . In as-grown quartz the details of the loss curves depend on the alkali ion activation energies, concentrations and the nature of the defect sites involved. In swept quartz, with most of the alkali ions removed and replaced by hydrogen, forming the  $\text{Al-OH}^-$  defect, the exponential  $Q^{-1}(T)$  rise was reduced by a large factor. Our previous measurements<sup>1</sup>, performed on enclosed resonators up to 350°C confirmed these results. We have extended these measurements to temperatures above 500°C using quartz disks placed in an evacuable ceramic holder and report data for swept and unswept Premium- $Q$  (grown with lithium additive) and High- $Q$  quartz (grown without lithium).

In the sweeping process the replacement of alkali ions with hydrogen at aluminum sites leads to intensity changes of the infrared impurity bands. It was previously found<sup>1</sup> that in the initial stages of sweeping the growth of infrared bands associated with the  $\text{Al-OH}^-$  defect (measured with the beam along the sweeping axis) occurs immediately in air and after longer sweeping time in vacuum. The as-grown  $\text{OH}^-$  bands remain unchanged with air sweeping but deplete with vacuum sweeping. In order to find how the  $\text{Al-OH}^-$  formation proceeds along the sweeping axis, our measurements were modified and extended to determine the spatial distribution of  $\text{Al-OH}^-$  and as-grown  $\text{OH}^-$  defects between anode and

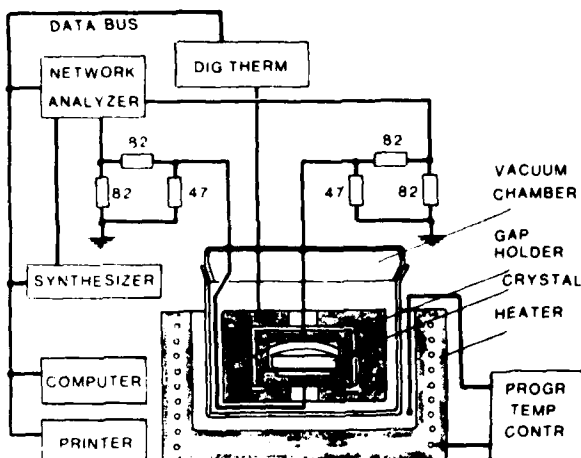


Figure 1. Automated Q-measurement system for quartz resonator disks. Resistor values given in ohms.

cathode after short periods of sweeping, ranging from 3 to 24 hours.

Changes in the OH<sup>-</sup> bands after sweeping have been the subject of many investigations<sup>3-6</sup>, but only limited data exist on the spatial distribution of band strength between anode and cathode. Krefft reported<sup>7</sup> this type of variation in terms of room temperature spectra for natural quartz with high impurity content, swept at 700°C. A significant result of this investigation was that after sweeping in vacuum, OH<sup>-</sup> bands at 3610 and 3484 cm<sup>-1</sup>, designated as thermally unstable,<sup>3</sup> were depleted while those at 3311 and 3378 cm<sup>-1</sup> became stronger, with the largest change occurring close to the anode. Assignment of these bands to specific defect centers is complicated by the  $\alpha$  to  $\beta$  transition undergone by the crystal and the large line width of the room temperature bands.

We have utilized low temperature spectroscopy, with its inherent higher sensitivity for detecting small changes in absorption coefficient, to measure defect concentration changes in synthetic quartz with low impurity concentration after sweeping at temperatures below the  $\alpha$  to  $\beta$  transition. We report infrared data on the distribution of Al-OH<sup>-</sup> and as-grown OH<sup>-</sup> defects between the anode and cathode for Premium-Q and High-Q synthetic quartz swept in air and vacuum. The effect of uniform and non-uniform initial OH<sup>-</sup> distribution across the crystal, aluminum concentration, and differences between quartz containing lithium and sodium impurities on the sweeping process are discussed.

#### Acoustic Losses In Resonator Disks

##### Experimental Procedures

A block diagram of the experimental setup is shown in Fig. 1. The resonator disk, of plano-con-

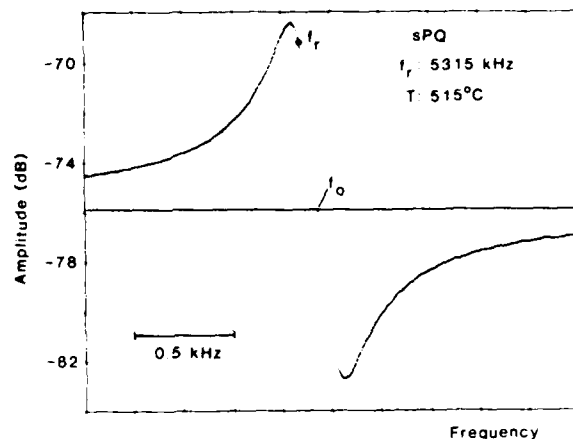


Figure 2. Resonance curve of swept Premium-Q disk sPQ. The horizontal line at -75.9 dB relates to the off-resonance impedance  $Z_0 = 26.7 \text{ k}\Omega$ , for the parallel capacitance  $C_0 = 1.12 \text{ pF}$  of the crystal. Series resonance at  $f_r$ . Center frequency  $f_0$ . Calculated via equation (1):  $R_1 = 14.0 \text{ k}\Omega$ .

vex shape, is placed in a two-part ceramic gap holder<sup>2,8</sup> and supported on a narrow rim on the bottom surface. The gap of the holder is wide enough to avoid contact with the crystal, at any temperature up to 550°C. The gap spacing can be varied by means of adjustable gold-plated Kovar electrodes. The two-part ceramic holder is mounted in a stainless steel enclosure to which a chromel-alumel thermocouple is attached. This assembly is enclosed in a Vycor vacuum chamber. The electrodes are connected to a network analyzer through a modified  $\Pi$  network. A programmable synthesizer provides the stepwise variable frequency. A data bus connects these components to a desktop computer and printer for automatic data recording.

For the present study, all but one of the disks have been taken from enclosed resonators previously measured up to 350°C. The plated electrodes were removed from the disks by aqua regia, followed by washing with distilled water and drying in hot air. This procedure yields resonance resistance values less than twice those of the enclosed resonators. All disks are 5 MHz 5th overtone plano-convex or bi-convex AT-cut and are listed in Table I.

A programmable temperature controller provides linear ramps with adjustable rates between 0.1 and 1.9 °C/min. Usually, the crystal was heated from room temperature to 250°C with 0.2 °C/min and above 250°C with 0.1 °C/min. The temperature interval between data points is generally less than 1°C.

The controlling computer program calls for repetitive frequency sweeping through the series resonance in 100 steps, with 1 or 100 msec per step. It selects appropriate starting frequencies and step widths, and determines series resonance frequency  $f_r$ . The resonance resistance  $R_1$  is calculated

Table I. Identification of Disks and Resonators.

Sweeping Status	Quartz Material	Autoclave* Run No.	Crystal No.	Aluminum** ppm (at.)	Designations Disk Resonator	Data Shown in Figure No. This Paper	Ref. 1
unswept	High-Q	E42-21	19	10.1	HQ (a) -	3	-
					- T-1107	-	3
	Premium-Q	D14-45	39	$1 \pm 0.4$	PQ G-7	3	2
air swept*	High-Q	E42-21	18	6.1	sHQ3 U-1973	3	3
					sHQ5 U-1975	3	
	Premium-Q	D14-45	10	-	sPQ N-171	2,4	2
vacuum swept†	Premium-Q	D14-45	E	<0.4	vs3 M-3	5,6	
					vs5 M-5	5	2

\* Sawyer Research Products, Inc.

† T.J. Young, Sandia Laboratories

\*\*ESR data from L.E. Halliburton, Oklahoma State University  
(a) unplated blank T-11

ted from maximum amplitude  $A_m$  with a calibration function  $R(A)$  derived from replacing the crystal with a series of resistors. For high  $R_1$  values,  $A_m$  is associated with a complex impedance  $Z_m$  and

$$R_1 = Z_m / [1 - (Z_m/Z_0)^2] \quad (1)$$

with an off-resonance impedance

$$Z_0 = 1 / (2 \pi f_r C_0) \quad (2)$$

$C_0$  is the parallel capacitance of the crystal equivalent circuit. For each data point the off-resonance amplitude  $A_0$  is measured  $\pm 10$  kHz from the center frequency  $f_0$ , and  $Z_0$  is calculated from the average  $A_0$ . The positions of  $f_0$  and  $f_r$  are shown for a typical resonance curve in Fig. 2.

### Results

Figure 3 shows  $R_1(T)$  of unswept and swept crystals. The curves were plotted as  $\log(R_1 T)$  vs  $1000/T$ . This should result in straight lines if the exponentially rising loss function  $R_1(T)$  is due to thermally activated motion<sup>9</sup> of interstitial impurity ions, e.g.  $Va^+$  in HQ and  $Li^+$  in PQ. The unswept samples show an exponential rise between 200 and 500°C. Repeated temperature cycling showed that, up to at least 480°C,  $R_1(T)$  is reversible with these 2 samples. Above 500°C,  $R_1(T)$  rises very steeply and the crystals exhibit signs of permanent degradation. Subsequent temperature cycling of PQ shows  $R_1(T)$  curves 30 to 100% above the previous values, and these exhibit narrow peaks at irregular intervals. This degradation is corroborated by the appearance of spurious modes in resonance curves at various temperatures. With HQ, the degradation was much more severe. After

returning from 505°C, the 5th overtone resonance was undetectable while the 3rd overtone showed highly unstable  $R_1$  values in excess of 0.5M $\Omega$ . After removal from the holder, the two disks showed scratches and chipping in the center region of the major surfaces.

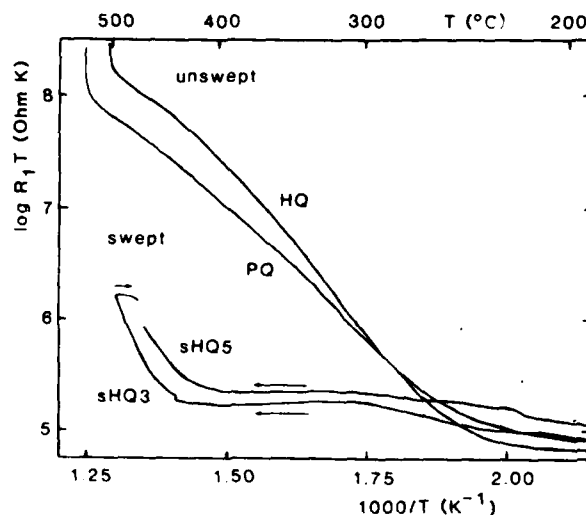


Figure 3. Function  $\log(R_1 T)$  vs  $1000/T$  for unswept disks HQ and PQ and for swept disks sHQ3 and sHQ5. Arrows indicate the direction of temperature change.

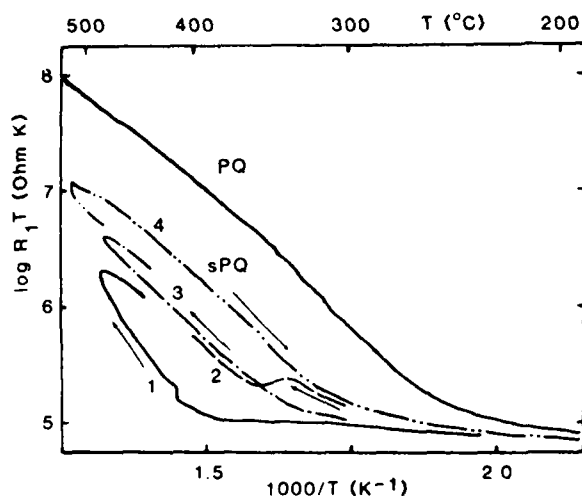


Figure 4. Function  $\log(R_1T)$  vs  $1000/T$  for air swept Premium-Q disk sPQ and unswept disk PQ. Runs 1 - 4 numbered in chronological sequence.

The lower two curves in Fig. 3 and all curves in Figures 4 and 5 relate to swept disks. In the sweeping process, the alkali ions are removed from the material and the exponential rise of  $R_1(T)$  should be absent. Up to approximately 400°C, this is indeed shown by our data. Above this temperature, however, all samples display substantial increases of resistance. This increase is temperature as well as time dependent. This phenomenon was extensively studied with crystal sPQ, shown in Figure 4. The levels of  $R_1(T)$  increase with each successive run. The curves show two instances of vertical rise, occurring at 418°C in run 1 and at 515°C in run 4, implying that  $R_1$  increases with time at constant temperatures. In both cases the temperature was maintained for 2 to 3 hours and  $R_1$  as function of time followed a saturation curve with estimated time constants between 2 and 3 hours.

Fig. 5 shows that, for vacuum swept crystals, the rise of  $R_1(T)$  above 400°C is more than twice as steep as with air swept quartz. With vacuum swept quartz this portion of  $R_1(T)$  is unstable and the resonance splits into numerous interfering modes as shown in Fig. 6. After return to room temperature, crystals vs3 and vs5 showed  $R_1$  values of 30,000 and 2200  $\Omega$ , respectively. Upon inspection, the two major surfaces showed a multitude of scratches in the center. Etching with diluted HF increased the depth of these scratches but did not reveal any macrotwinning.

Peaks of  $R_1(T)$  were observed in most swept crystals, near 330°C with the sHQ crystals and at the same temperature with sPQ, and near 400°C with vs3. The peaks of sPQ and vs3 disappeared after further heating above 400°C.

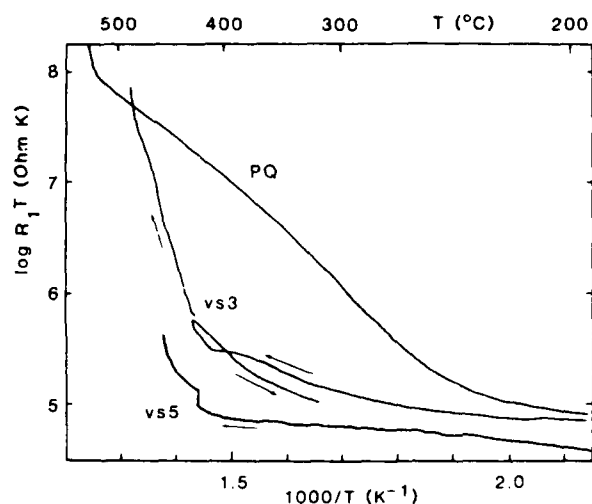


Figure 5. Function  $\log(R_1T)$  vs  $1000/T$  for vacuum swept Premium-Q disks vs3 and vs5, with curve for unswept disk PQ added for comparison.

#### Discussion

Observation of the resonance linewidth at various temperatures indicates that the motional inductance and capacitance values of the crystals show only small changes with  $T$ . Thus,  $R_1$  can, in first approximation, be considered proportional to the acoustic losses  $Q^{-1}$ . The latter, in turn, have been attributed to thermally activated ion motion<sup>2,8</sup> and may be considered proportional to the ionic conductivity  $\sigma$ . Recently, Jain and Nowick<sup>9</sup> showed that  $\sigma$  is proportional either to  $T^{-1} \exp[-(E_A + E_m)/kT]$

or to  $T^{-1} \exp[-(E_A/2 + E_m)/kT]$ , with the activation energies  $E_A$  for dissociation of  $Al-M^+$  and  $E_m$  for motion of  $M^+$  along the crystal channels, ( $M^+$  stands for interstitial metal ions, e.g.  $Na^+$  or  $Li^+$ ). The higher exponent, involving  $E_A + E_m$ , implies additional pairing sites (traps) for  $M^+$  besides  $Al-M^+$ . Our unswept quartz data show some curvature in  $\log(R_1T)$  vs  $1/T$ . If interpreted as an intermediate case with comparable activated  $M^+$  and trap concentrations in the 300 to 500°C temperature range, comparison with calculated  $\sigma T$  vs  $1/T$  curves yields  $E_A = 1.2 \pm 0.2$  eV,  $E_m = 0.2 \pm 0.1$  eV. The concentrations of additional  $M^+$  traps are estimated to be  $10^{-5}$  to  $10^{-4}$  of the total  $M^+$  content.

An alternate explanation for the observed curvatures is a peak between 350 and 400°C superimposed on the straight lines. Peaks near these temperatures have been observed on unswept as well as swept quartz and were attributed to dielectric relaxation of defect centers. Activation energies derived from the slope of the straight

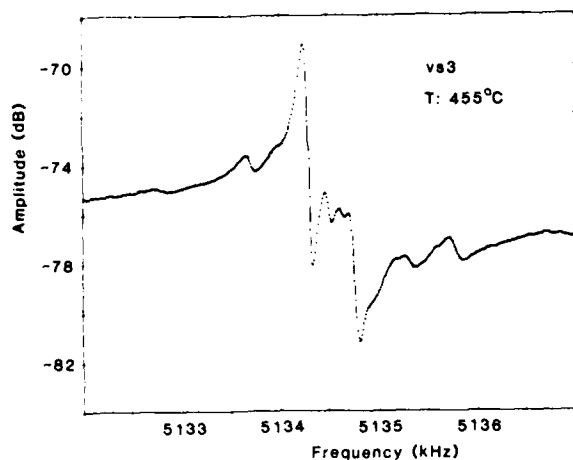


Figure 6. Multimode resonance curve for vacuum swept disk vs3.

lines are approximately 0.85 eV for PQ and 1 eV for HQ. These values are in line with literature data, e.g. the value 0.7 eV observed by King and Fraser<sup>2,8</sup> for natural quartz and 0.72, 0.77, and 0.92 eV found by Fraser<sup>10</sup> for  $\text{Li}^+$ ,  $\text{Na}^+$  and  $\text{K}^+$  swept into natural quartz. Jain and Nowick's<sup>9</sup> conductivity measurements yielded 0.82 eV for natural and 1.36 eV for synthetic quartz.

With our swept crystals, the observed permanent increase of the rising portion of  $R_1(T)$  may relate to sweeping or any one of the procedures involved in the resonator fabrication. The curve pertaining to run 4 of sPQ, in Fig. 4, is remarkably parallel to that of the unswept PQ, alluding to the presence of residual lithium impurity. Its location about one order of magnitude below PQ would then imply that as much as 10% of the original alkali content remained in the crystal after sweeping, possibly stuck in channels interrupted or clogged by defects. These alkali ions then diffused above 400°C into regular  $\text{Al-M}^+$  positions from which they can be activated.

In our vacuum swept crystals, this behavior is masked by permanent degradation. Degradation characterized by steeply rising unstable  $R_1$  values, multimode resonance curves, high room temperature resistance and visible surface damage was found with our unswept and vacuum swept crystals but not with those swept in air, even after exposures to temperatures exceeding 500°C. Measurements on more samples are required before one can interpret this behavior.

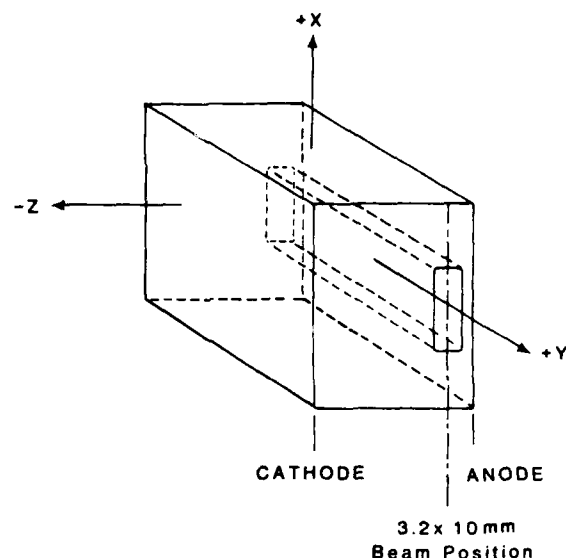


Figure 7. Example of aperture position for scanning along the Z-axis between cathode and anode with the beam in Y-direction.

#### Sweeping Monitored By Low Temperature

#### Infrared Spectroscopy

#### Experimental Procedures

The Premium-Q and High-Q quartz samples used in these investigations were grown at Sawyer Research Products (SARP) by the same process, except that for Premium-Q lithium salt was added to the mineralizer. The aluminum impurity content as determined from electron spin resonance varied from 5 to 8 ppm for High-Q and from 0.6 to 1.3 ppm for Premium-Q. The materials were obtained as unswept bars which were cut and polished into rectangular sections, with parallel x, y, and z faces, approximately 1.5 x 1.8 x 2.0 cm in size. The experimental procedures for both air and vacuum sweeping are described in previous publications.<sup>5,11</sup> For these short-term sweeping experiments, the samples were clamped between platinum foils with the +Z face at the anode and the -Z face at the cathode.

The infrared transmissions of the samples were measured between 3100 - 3700  $\text{cm}^{-1}$  at 85K with a Digilab FTS-14 Fourier Spectrophotometer at a resolution of 2  $\text{cm}^{-1}$  using unpolarized radiation with E Z or E Y. The full beam of the spectrometer was focused through the crystal for measurements in the direction of sweeping (E Z). In addition, the crystal was scanned normal to the

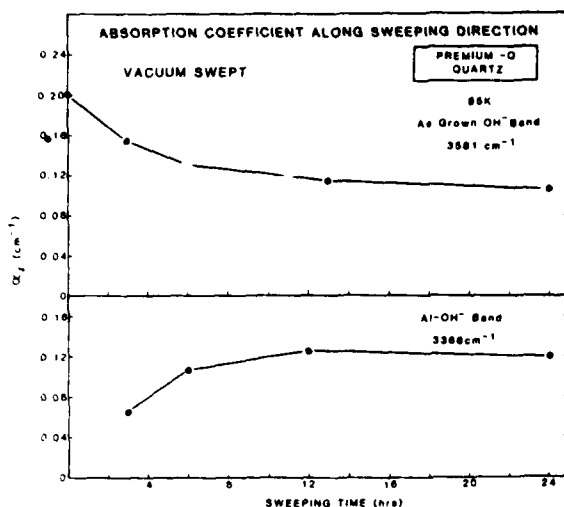


Figure 8. Absorption coefficient  $\alpha_z$ ,  $E \perp Z$ , as function of sweeping time, for vacuum swept Premium-Q quartz.

direction of sweeping ( $E \parallel Y$ ) by moving a  $3.2 \times 10$  mm aperture along the +Y face between the anode and cathode as shown in Figure 7.

#### Experimental Results

Figure 8 shows absorption coefficient values  $\alpha_z$  measured along the sweeping direction for the 3366 cm<sup>-1</sup> Al-OH<sup>-</sup> band and 3581 cm<sup>-1</sup> as-grown OH<sup>-</sup> band for Premium-Q quartz vacuum swept for periods of 3 to 24 hours. Unswept Premium-Q and High-Q quartz has four bands associated with OH<sup>-</sup> vibrations with peaks at 3348, 3396, 3438 and 3581 cm<sup>-1</sup>. The 3581 cm<sup>-1</sup> band has a strong narrow peak with an easily determined background absorption while the others require subtraction of the Si-O lattice vibration contribution. For this reason we have chosen the 3581 cm<sup>-1</sup> band to monitor changes in as-grown OH<sup>-</sup>. 3366 cm<sup>-1</sup> absorption, not present in the unswept sample, appears after the first 3 hour sweeping period accompanied by a strong decrease in 3581 cm<sup>-1</sup> absorption. After this initial sweeping period, 3366 cm<sup>-1</sup> band strength increases and 3581 cm<sup>-1</sup> band strength decreases more gradually with essentially no change observed after 12 hours.

Figure 9 shows absorption coefficient values  $\alpha_y$  measured normal to the sweeping direction for Premium-Q quartz before and after sweeping in air for 3 hours. These values were determined from the designated transmissions measured through the  $3.2 \times 10$  mm aperture centered at Z-axis positions between the anode and cathode.

As indicated by the unswept data, this crystal has a very small increase in as-grown OH<sup>-</sup> concentration between the anode and the center, and a

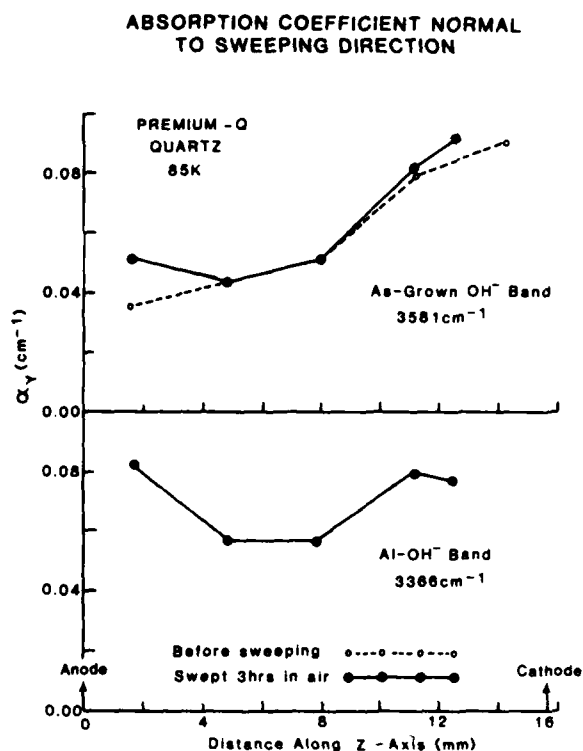


Figure 9. Absorption coefficient  $\alpha_y$ , for 3581 and 3366 cm<sup>-1</sup> bands as function of position between anode and cathode, before and after sweeping Premium-Q quartz 3 hours in air.

much more pronounced increase between the center and the cathode. The only significant changes in the 3581 cm<sup>-1</sup> absorption after 3 hours of sweeping are small increases close to the anode and the cathode. After sweeping, 3366 cm<sup>-1</sup> absorption is strongest close to the anode, decreases toward the center of the crystal and then increases toward the cathode. The increase in Al-OH<sup>-</sup> absorption tends to follow the as-grown OH<sup>-</sup> distribution.

Figure 10 shows the 3366 cm<sup>-1</sup> Al-OH<sup>-</sup> and 3581 cm<sup>-1</sup> as-grown OH<sup>-</sup> band behavior for Premium-Q samples swept in air and vacuum for progressive short time periods. Both these samples and that of Figure 9 were adjacent crystals cut from the same bar and had approximately the same initial OH<sup>-</sup> distribution. The 3 hour air sweeping produces an Al-OH<sup>-</sup> distribution similar to that shown in Figure 9. An additional 3 hour air sweeping increases the overall Al-OH<sup>-</sup>, and the resulting curve follows the pattern of the as-grown OH<sup>-</sup> distribution.

With vacuum sweeping, the Al-OH<sup>-</sup> distribution is considerably different from that observed for air sweeping especially during the initial stages. A 3 hour sweeping produces Al-OH<sup>-</sup> close to the anode with a sharp decrease toward the center of

# ABSORPTION COEFFICIENT NORMAL TO SWEEPING DIRECTION

PREMIUM-Q  
QUARTZ  
85K

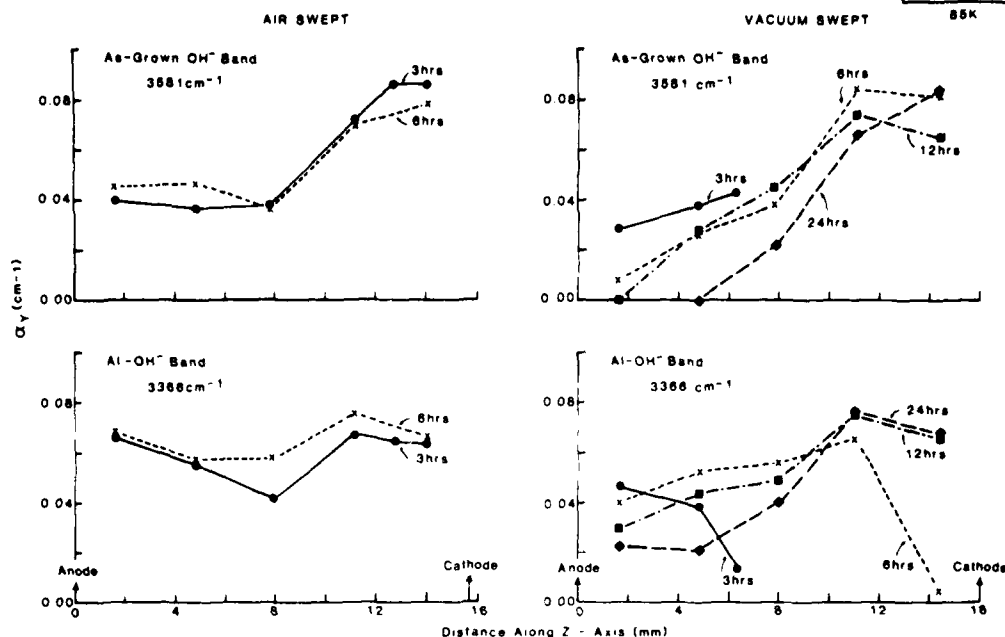


Figure 10. Absorption coefficient  $\alpha_y$ , for 3581 and 3366  $\text{cm}^{-1}$  bands as function of position between anode and cathode after air or vacuum sweeping Premium-Q quartz for the indicated time periods.

the crystal. An additional 3 hours increases the overall absorption, but a sharp decrease is still observed close to the cathode. With further sweeping, the Al-OH<sup>-</sup> band strength is reduced near the anode and increases toward the cathode.

An even more striking difference between air and vacuum sweeping is observed for the as-grown OH<sup>-</sup> band. As-grown OH<sup>-</sup> is reduced near the anode during the initial 3 hour sweeping and totally depleted after 12 hours. This depletion region moves toward the center of the crystal after 24 hours, but the OH<sup>-</sup> concentration in the vicinity of the cathode is essentially unaffected.

The results of a similar study for High-Q quartz, containing Na<sup>+</sup> are shown in Figure 11. The High-Q aluminum content was approximately seven times larger than that of the Premium-Q. The as-grown OH<sup>-</sup> absorption strength in an unswept sample is in the same general range as that of the Premium-Q, and shows a gradual variation across the crystal,  $(0.060 - 0.040 \text{ cm}^{-1})$ , between the anode and cathode.

After 3 hours of air sweeping, a strong Al-OH<sup>-</sup> band is observed with a band strength approximately six times larger than that of the Premium-Q, very close to the aluminum ratio of the samples. This band is concentrated close to the anode, decreasing to zero only 4 mm away. Sweeping times of 6 and 12 hours increase the total band strength and move

the Al-OH<sup>-</sup> distribution further through the crystal toward the cathode, but at a much slower rate than with the Premium-Q crystal. After the 12 hour sweeping period the Al-OH<sup>-</sup> distribution approaches that of the as-grown OH<sup>-</sup>. Similar to the Premium-Q, the High-Q shows little change in as-grown OH<sup>-</sup> distribution with increasing sweeping time.

Six hours of vacuum sweeping introduces a very small Al-OH<sup>-</sup> band and little change in the as-grown OH<sup>-</sup> band. Sweeping for an additional 6 hours produces a relatively strong Al-OH<sup>-</sup> band close to the anode which decreases sharply toward the crystal center. In contrast the as-grown OH<sup>-</sup> is depleted at the anode and rises sharply toward the center. These features observed for High-Q quartz are in general agreement with those found for Premium-Q. With both air and vacuum sweeping, the replacement of the alkali ions with H<sup>+</sup> proceeds along the anode-cathode axis at a slower rate than in Premium-Q.

## Discussion

These experimental results lead to the following conclusions about the sweeping process and the inherent differences between air and vacuum sweeping. The replacement of alkali ions with H<sup>+</sup> begins at the anode and proceeds toward the cathode as sweeping progresses. Increased Al-OH<sup>-</sup> formation is found in regions of the crystal with stronger as-grown OH<sup>-</sup> concentration. This relationship

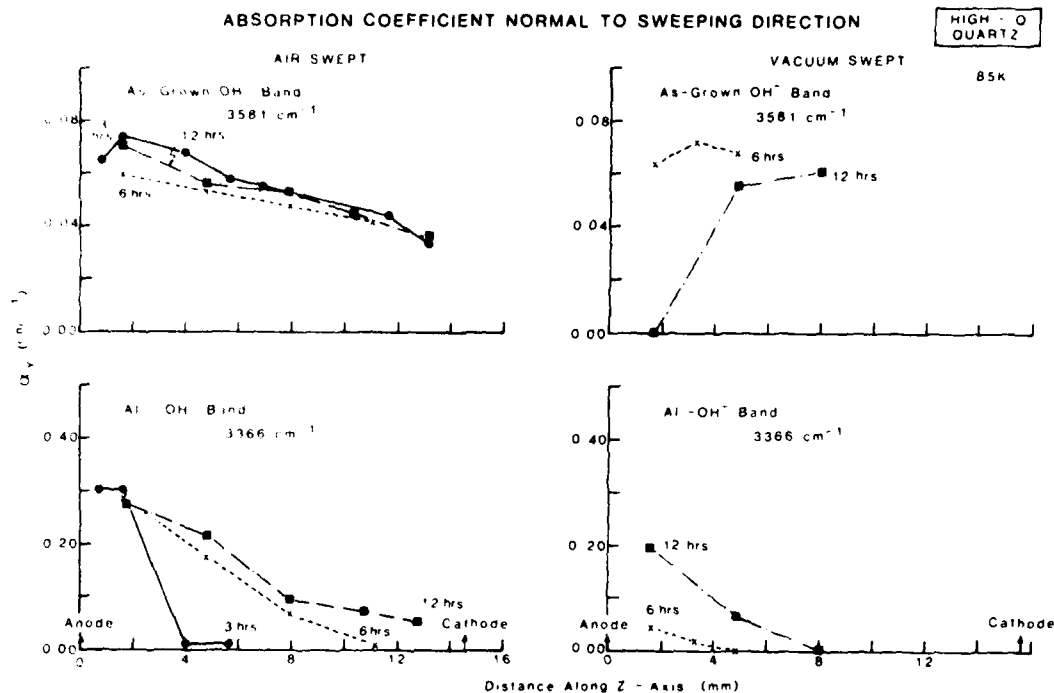


Figure 11. Absorption coefficient  $\alpha_y$  for 3581 and 3366  $\text{cm}^{-1}$  bands as function of position between anode and cathode after air or vacuum sweeping High-Q quartz for the indicated time periods.

might be evidence that with air sweeping, hydrogen for the  $\text{Al-OH}^-$  defects may initially be supplied from the as-grown  $\text{OH}^-$  and subsequently replaced from electrolysis of water in the air ambient. A sharp rise in the  $\text{Al-OH}^-$  band in a specific region of the crystal can also result from a localized increase in aluminum concentration. With vacuum sweeping, a strong depletion of as-grown  $\text{OH}^-$  occurs near the anode and advances toward the cathode, indicating that these  $\text{OH}^-$  ions are the source of hydrogen for the alkali replacement process. Owing to a more limited hydrogen supply, vacuum sweeping forms  $\text{Al-OH}^-$  at slower rate than air sweeping. This means that longer time periods are required to sweep a sample in vacuum. The slower  $\text{Al-OH}^-$  formation in High-Q as compared to Premium-Q is attributed to the difference in diffusion rates of Na and Li ions.<sup>12</sup> The progressive depletion of both  $\text{Al-OH}^-$  and as-grown  $\text{OH}^-$  between the anode and crystal center observed in Premium-Q with increasing vacuum sweeping time may indicate re-diffusion of alkali to the  $\text{Al}^{3+}$  sites when the crystal is still at high temperature with no electric field. Another possibility is the formation of aluminum-hole centers.

#### Conclusions

1. The high-temperature acoustic loss spectrum shows that the effects of sweeping are partially reversed by heating above 400°C. This reversal saturates and the exponential loss curve paral-

els that found in unswept quartz. The additional loss is contributed by residual alkali ions not removed by the sweeping process due to defective channels.

2. Alkali ion replacement with hydrogen depends on the initial  $\text{OH}^-$  concentration and distribution in the crystal both for air and vacuum sweeping.

3. Vacuum sweeping, where no hydrogen is supplied by the ambient, involves the dissociation of as-grown  $\text{OH}^-$  defects and proceeds at a slower rate than air sweeping.

#### Acknowledgement

The authors wish to thank Mr. John J. O'Connor for sweeping several of the crystals. They also recognize with thanks the capable and creative assistance of Mr. Paul A. Ligor in assembling, testing, and operating the instrumentation.

#### References

1. H. G. Lipson, A. Kahan, R. N. Brown, and F. Euler, Proc. 35th Annual Symposium on Frequency Control (ASFC), 329 (1931).
2. J. C. King and D. B. Fraser, Proc. 15th ASFC, 2 (1961); J. C. King, Proc. IEE London, B109, Suppl. 22, 1 (1962).

3. A. Kats, Philips Res. Repts. 17, 133 (1962)
4. D. M. Dodd and D. B. Fraser, J. Phys. Chem. Solids 26, 673 (1965)
5. H. G. Lipson, F. Euler, and A. F. Armington, Proc. 32nd ASFC, 11 (1978)
6. L. E. Halliburton, M. E. Markes, and J. J. Martin, Proc 34th ASFC, 1 (1980)
7. G. B. Krefft, Radiation Effects, 26, 249 (1975)
8. D. B. Fraser, Physical Acoustics, Vol. 5, W. P. Mason, ed., Academic Press, New York, (1968), 59.
9. H. Jain and A. S. Nowick, J. Appl. Phys., 53(1) 477 (1982)
10. D. B. Fraser, J. Appl. Phys., 35, 2913 (1964)
11. F. Euler, H. G. Lipson, and P. A. Ligor, Proc. 34th ASFC, 72 (1980)
12. J. Verhoogen, Amer. Mineralogist 37, 637 (1952)

THE ELASTIC, DIELECTRIC AND PIEZOELECTRIC CONSTANTS OF BERLINITE\*

D. S. Bailey, W. Soluch,† D. L. Lee, J. F. Vetelino and J. Andle  
Department of Electrical Engineering and Laboratory for Surface  
Science and Technology, University of Maine, Orono, Maine 04469

B. H. T. Chai  
Allied Corporation, Corporate Headquarters  
Morristown, New Jersey 07960

Summary

The elastic, piezoelectric and dielectric constants of berlinite ( $\alpha$ - $\text{AlPO}_4$ ) are presented. The berlinite samples were obtained from the Allied Corporation and grown by one of the authors (BHTC). The elastic constants were measured using the pulse echo overlap method. The piezoelectric constants were obtained from the measurement of the resonance and antiresonance frequencies of stiffened shear modes for several Y and  $\pm 45^\circ$  rotated Y-cut plates. The relative dielectric constants were measured using capacitive techniques from the X and Z-cut plates at 2 MHz. The measured elastic constants are in reasonable agreement with the results of Chang and Barsch<sup>1</sup>. The results for the piezoelectric constants,  $e_{11}$  and  $e_{14}$ , were found to be smaller in magnitude than the values reported by Chang and Barsch<sup>1</sup>. The measured values of the relative dielectric constants,  $\epsilon_{11}$  and  $\epsilon_{33}$ , were approximately equal to 4.8.

In order to further validate the experimentally determined material constants of berlinite, the surface acoustic wave (SAW) velocity and a measure of the SAW piezoelectric coupling,  $\Delta v/v$ , were calculated and compared to experimental results for several crystallographic orientations. The values of the calculated SAW velocity and  $\Delta v/v$  were found to be in good agreement with experimental results. The values of  $\Delta v/v$  predicted using the material constants reported by Chang and Barsch<sup>1</sup> were found to be significantly larger than the present theoretical and experimental results. It may therefore be concluded that the actual piezoelectric coupling in berlinite is not as high as that predicted using the Chang and Barsch data<sup>1</sup> for  $e_{11}$  and  $e_{14}$ .

Introduction

In the last decade several approaches have been proposed<sup>2</sup>, to achieve a combination of temperature stability and reasonable piezoelectric coupling in microwave acoustic devices superior to that obtained using quartz. One of the most promising approaches in terms of device simplicity involves the use of a single substrate which can include single crystals, ceramics and mixed crystals.

Several single crystals have been proposed

\*Work supported by the Allied Corporation, Morristown, New Jersey.

†Visiting Professor on leave from the Tele and Radio Research Inst., Ratuszowa 11, 03-450 Warsaw, Poland.

as possible alternatives to quartz. These include lithium tantalate, berlinite, sulfosalt materials, paratellurite,  $\beta$ -eucryptite, lead potassium niobate, lithium tetraborate, tellurium vanadate and promastite. Over the last five years the material which has demonstrated the most promise is berlinite. Exciting preliminary theoretical and experimental results for surface acoustic wave (SAW) and bulk wave properties in berlinite in the late 1970's motivated several research groups to initiate berlinite crystal growing programs.

To date, the highest quality berlinite samples available have been grown at the Allied Corporation. Preliminary results on studies of bulk and SAW properties of Allied grown berlinite have been very encouraging. As a consequence, a study involving the experimental determination of the elastic, dielectric and piezoelectric constants at 25°C and a theoretical and experimental study of the SAW properties of berlinite have been performed. Using the experimentally determined material constants, the SAW velocity and piezoelectric coupling ( $\Delta v/v$ ) were theoretically predicted for a large number of orientations. Several berlinite devices were fabricated and the SAW properties were experimentally determined and compared to the theoretical results.

Material Constants of Berlinite

Berlinite exhibits trigonal symmetry (class  $D_{3d}$ ) and has six independent elastic constants  $c_{11}^E$ ,  $c_{33}^E$ ,  $c_{44}^E$ ,  $c_{66}^E$ ,  $c_{13}^E$  and  $c_{14}^E$ , two dielectric constants,  $\epsilon_{11}$  and  $\epsilon_{33}$ , and two piezoelectric constants,  $e_{11}$  and  $e_{14}$ .

Elastic Constants

The zero-field elastic constants can be determined by measurements of the bulk acoustic wave velocities for a sufficient number of distinct propagation and polarization directions. For each of the particular directions, the acoustic wave velocity,  $v$ , can be expressed as,

$$v = \frac{\bar{c}}{\rho} \quad (1)$$

where

$\bar{c}$  = effective elastic constant for the particular direction

and

$\rho$  = mass density.

AD P001512

Since there are six independent elastic constants in berlinite the effective elastic constant should be measured for at least six different bulk acoustic modes. The analytical expressions for the 14 elastic constants used in the present study are listed in Table I.

By relating the acoustic wave velocity to the crystal length,  $l$ , and the corresponding propagation delay time,  $t$ , one obtains from (1),

$$\bar{c} = \frac{c_{ij}^2}{t^2} \quad (2)$$

The six elastic constants were deduced by measuring the bulk wave velocities of modes 2,3,7-10, 12 and 13 described in Table I. None of these eight modes contain piezoelectric or dielectric constants and are referred to as unstiffened modes. The bulk wave velocities were measured using a Panametrics Ultrasonic Time Intervalometer system 5054. This system makes use of the pulse overlap method described by McKimmon.<sup>4</sup>

The round trip bulk wave transit times for a number of crystal samples on each of the eight different orientations given in Table I were measured and the associated bulk wave velocities were obtained from equations 1 and 2. Since there are eight equations relating bulk wave velocities to  $c_{ij}$  and only six independent elastic constants, some of the equations were solved directly and the others were solved using a minimization technique. In particular this involved the minimization of the following function,

$$\sum_{n=1}^8 \sum_{m=1}^M \left( \bar{c}_{nm}^{\text{exp}} - \bar{c}_{nm}^{\text{th}} \right)^2 W_{nm} \quad (3)$$

where

$\bar{c}_{nm}^{\text{exp}}$  = The measured effective elastic constant for mode,  $n$ , and sample,  $m$ .

$\bar{c}_{nm}^{\text{th}}$  = The effective elastic constant for mode,  $n$ , expressed in terms of the  $c_{ij}$ 's from Table I.

$W_{nm}$  = A weighting factor chosen by the user based on confidence in a particular mode and sample, as determined by crystal sample misalignment.

$M_n$  = Number of available samples of mode,  $n$ .

and

$n$  = The unstiffened mode number.

The function given in equation (3) was minimized using an  $n$  dimensional search program.

#### Dielectric Constants

The two dielectric constants,  $\epsilon_{11}^S$  and  $\epsilon_{33}^S$ , can be evaluated from measurements of the capacitance of thin plates cut perpendicular to the X and Z axis, respectively. If the measurements are made at a frequency lower than the lowest resonance

frequency, the dielectric constants at constant stress,  $\epsilon_{11}^T$  and  $\epsilon_{33}^T$ , are determined. If the measurements are made above the fundamental resonance frequency, then the dielectric constants at constant strain,  $\epsilon_{11}^S$  and  $\epsilon_{33}^S$ , are determined. The relationship between the dielectric constants measured at the two above conditions is given for berlinite as follows,

$$\epsilon_{11}^T - \epsilon_{11}^S = 2d_{11} e_{11} + d_{14} e_{14},$$

and

$$\epsilon_{33}^T - \epsilon_{33}^S = 0. \quad (4)$$

The dielectric constant,  $\epsilon_{ij}^T$ , can be measured with better accuracy than  $\epsilon_{ij}^S$ , primarily due to the lower frequency used in these measurements. For this reason it is recommended that  $\epsilon_{ij}^T$  be measured directly and that  $\epsilon_{ij}^S$  be calculated from equation (4) once the piezoelectric constants are known.

If the fringing capacitance at the edge of the electrodes is neglected, the capacitance of a parallel-plate capacitor below the fundamental resonance frequency is given by,

$$C = \frac{\bar{\epsilon}^T A}{T} \quad (5)$$

where

$\bar{\epsilon}^T$  = effective dielectric constant under constant stress,

$A$  = electrode area

and

$T$  = plate thickness.

The measured value of the capacitance per unit area,  $(C/A)$ , is always greater than the value of capacitance per unit area of the plate with infinite electrodes,  $(C/A)_\infty$ . This is due primarily to fringing capacitance.

Consider the parallel-plate capacitor shown in Figure 1. One electrode completely covers one side of the plate while the other side is covered with a circular spot of area less than that of the plate.<sup>5</sup> It is reasonable to assume that the fringing capacitance is proportional to the circumference of the circular electrode. The measured capacitance,  $C_m$ , is then given by,

$$C_m = (C/A)_\infty \pi r^2 + a 2\pi r, \quad (6)$$

where

$r$  = radius of the circular electrode,

and

$a$  = constant.

Dividing both sides of equation (6) by  $A = \pi r^2$  one obtains,

$$(C/A)_m = (C/A)_\infty + \frac{2}{r} \quad (7)$$

From equation (7) one may expect that the graph of  $(C/A)$  as a function of the reciprocal of the radius will be a straight line. If  $(C/A)_m$  is measured for several different values of  $r$ , then  $(C/A)_\infty$  can be evaluated by extrapolating to  $r = \infty$ . The dielectric constant will then be determined from the expression,

$$\epsilon^T = (C/A)_\infty T. \quad (8)$$

In the case of berlinite, the above measurements are performed for the X and Z cut plates respectively in order to determine the dielectric constants,  $\epsilon_{11}^T$  and  $\epsilon_{33}^T$ .

#### Piezoelectric Constants

The two piezoelectric constants,  $e_{11}$  and  $e_{14}$ , can be determined from the measured frequency response of the vibrating plate shown in Figure 2. If a lossless piezoelectric plate vibrates in a pure thickness mode, then the input impedance of this plate as a function of frequency can be written as follows<sup>3</sup>

$$Z(f) = \frac{1}{j2\pi f C_0} \left[ 1 - k^2 \frac{\tan \frac{\pi f}{2 f_a}}{\frac{\pi f}{2 f_a}} \right], \quad (9)$$

where

$C_0$  = plate capacitance,

$k$  = effective electromechanical coupling factor

and

$f_a$  = frequency at which  $Z = \infty$  or antiresonance frequency.

The term,  $k^2$ , can be expressed as follows,

$$k^2 = \frac{\bar{e}^2}{\bar{c} \bar{\epsilon}^S}, \quad (10)$$

where

$\bar{e}$  = effective piezoelectric constant

and

$\bar{\epsilon}^S$  = effective dielectric constant at constant strain.

For the resonance condition,  $Z(fr) = 0$ , the relation between  $k$ ,  $f_a$  and the resonance frequency,  $f_r$ , can be written from equation (9) as follows,

$$k^2 = \frac{2 \frac{f_r}{f_a} \tan \frac{\pi f_r}{2 f_a}}{\frac{f_r}{f_a}}. \quad (11)$$

For the stiffened modes, 1, 6, 11 and 14 defined in Table II, the effective elastic constant can be written making use of relation (10) as

$$\bar{c} = \frac{c}{1-k^2}, \quad (12)$$

where  $c$  is the effective unstiffened elastic constant which is related to  $\bar{c}$  as follows,

$$c = \bar{c} [e_{ij}^T]^2 = 0. \quad (13)$$

From equations (10) and (12) the following expression results for  $\bar{e}$ ,

$$\bar{e} = \frac{k^2}{1-k^2} \bar{\epsilon}^S. \quad (14)$$

The effective unstiffened elastic, dielectric and piezoelectric constants for modes 1, 6, 11 and 14 are summarized in Table II. The two unknown piezoelectric constants,  $e_{11}$  and  $e_{14}$ , can be determined from at least two modes presented in Table II. One of these modes must depend on the piezoelectric constant,  $e_{14}$ . For example, if modes 6 and 11 are chosen, then from equation (14) one obtains for modes 6 and 11 the following relations for the piezoelectric constants,

$$e_{11} = \left[ \frac{k_{11}^2}{1-k_{11}^2} c_{66} \epsilon_{11}^S \right]^{1/2} \quad (15)$$

and

$$e_{11} + e_{14} =$$

$$\left[ \frac{k_{26}^2}{1-k_{26}^2} (c_{44} + c_{66} + 2c_{14}) (\epsilon_{11}^S + \epsilon_{33}^S) \right]^{1/2}, \quad (16)$$

where the sign of  $e_{11}$  must be positive.<sup>3</sup>

Substituting  $e_{11}$  from equation (15) into equation (16) one obtains,

$$e_{14} = \frac{k_{26}^2}{\sqrt{1-k_{26}^2}} (c_{44} + c_{66} + 2c_{14}) (\epsilon_{11}^S + \epsilon_{33}^S) - \frac{k_{11}^2}{\sqrt{1-k_{11}^2}} c_{66} \epsilon_{11}^S. \quad (17)$$

Since  $\epsilon_{11}^S \sim \epsilon_{11}^T$  for weakly coupling materials, the dielectric constants at constant stress rather than constant strain are used in the above expressions to a good approximation.

In order to experimentally determine  $k_{11}$  and  $k_{26}$  one must account for losses which occur in the actual vibrating plate or resonator. These losses exist due to internal losses such as dielectric, piezoelectric and elastic losses and external damping caused by metal electrodes, electrical contacts and mechanical mounting. These losses can be represented by a series resistance,  $r$ , in the electrical equivalent circuit for the resonator shown in Figure 3. When this circuit is connected as the bridging element of a pi network having a resistance,  $R$ , in each leg, the transfer function between the input voltages,  $v_1$  and  $v_2$ , can be expressed as follows,

$$v_2/v_1 = S_{12} = \left[ \frac{F^2 + (r\omega C_0)^2}{(\frac{r}{k} + F)^2 + (\frac{1-F}{\omega C_0 R} + r\omega C_0)^2} \right]^{-1/2}, \quad (18)$$

where

$$F = \frac{f}{f_r} \frac{\tan \frac{\pi}{2} \frac{f}{f_a}}{\tan \frac{\pi}{2} \frac{f}{f_a}}.$$

When  $r=0$ , the measured frequencies of maximum and minimum transmission are  $f_r$  and  $f_a$  respectively. This corresponds to  $Z=0$  and  $Z=\infty$  respectively. However due to the finite internal resistance,  $r$ , the measured frequencies of maximum and minimum transmission,  $f_1$  and  $f_2$ , will not be exactly equal to  $f_r$  and  $f_a$  respectively. Therefore the capacitance,  $C_0$ , and the resistance,  $r$ , are measured by means of a bridge, and then, from the measured  $f_1$  and  $f_2$  frequencies, the values of  $f_r$  and  $f_a$  can be evaluated. This is done by numerically solving the following two equations,

$$\left. \frac{d S_{12}}{df} \right|_{f=f_1} = 0 \quad (19)$$

and

$$\left. \frac{d S_{12}}{df} \right|_{f=f_2} = 0. \quad (20)$$

Once  $f_r$  and  $f_a$  are determined from equations (19) and (20),  $k^2 a$  is obtained from equation (11).  $e_{11}$  and  $e_{14}$  are then deduced from equations (15) and (17).

#### The SAW Properties of Berlinite

In order to determine the validity of the measured elastic, dielectric and piezoelectric constants, the SAW velocity,  $v$ , and coupling,  $v/v_1$ , were theoretically predicted for several crystal orientations and compared to experiment. The delay line used in making the measurements was designed with a large aperture, to minimize the effects of non-zero power flow angle, and with few fingers and wide center to center separation in order to minimize the effects of transducer metallization. The devices consisted of 25 unsplit finger pair transducers having finger width of 10  $\mu$ m, an aperture of 2mm and roughly a unity stripe to gap ratio. Transducer center to center separation was 6mm and the aluminum electrodes were 1500  $\text{\AA}$  thick.

The SAW velocity was obtained by measurement of the center frequency for the transducer passband and from knowledge of the finger periodicity. The coupling was measured using two techniques, standard conductance measurements using an R bridge and the phase change method. The latter technique measures the change in delay line phase and corresponding velocity shift when a metal layer is evaporated in situ on the crystal surface between the electrodes.

#### Results and Discussion

##### Elastic Constants

Measurements of the effective elastic constants for the unstiffened modes listed in Table I were performed at room temperature on a number of berlinite cubes using the procedure outlined earlier. Two types of cubes were supplied, those having face normals parallel to all three crystallographic axes (XYZ cubes) and those having one pair of face normals parallel to the crystal X-axis with the other two pairs rotated by  $\pm 45^\circ$  with respect to the Y and Z axis ( $\pm 45^\circ$  cubes). All crystal samples were nominally 0.3" on a side and had opposing faces which were extremely parallel as a result of a double-face polishing technique. Information on orientation accuracy supplied by X-ray data from Allied indicated that the X, Y and Z polished faces were generally aligned to within a few tenths of a degree. A few samples, however, had angular misalignments of nearly one degree. No information was supplied on the  $\pm 45^\circ$  cubes; however, one such crystal was subsequently sent to Mann Laboratories in Cambridge, Massachusetts for X-ray measurements in order to determine the magnitude of the orientation misalignment of both the  $\pm 45^\circ$  faces. It was determined to be only about 15 minutes in rotation about the X-crystallographic axis and slightly less than one degree out of the Y-Z crystal plane.

Suitability of any given sample face for measurement was determined by its orientation accuracy as well as the sensitivity of the effective elastic constant modes associated with this face to misalignment. It was found that, in general, a  $1^\circ$  angular misalignment in a face normal resulted in nominally a 1% error in effective elastic constant. One exception was found to be the X-face for which sensitivity to orientation error was more than an order of magnitude smaller.

Effective elastic constants at room temperature for modes associated with suitable faces were then obtained experimentally as outlined earlier. Effective elastic constant values obtained for any sample, which were found to be widely scattered from values for other samples of the same mode, were omitted from the least square fit procedure.

In performing the least squares fit for the elastic constants,  $c_{11}$ , a unity weighting factor was chosen for all modes with the exception of the unstiffened X-face modes,  $n=1$  and  $n=3$ . Because of the significantly lower sensitivity to crystal misalignment associated with these faces, a weighting factor of 10 was chosen. This, in effect, forces these two effective elastic constants to obey nearly exactly the functional relationship with respect to the elastic constants indicated in Table I. In the limit of an infinite weighting factor, the functional relationship becomes an identity. One further modification to the fitting procedure was to fix the value of  $c_{11}$  as determined by measurements of the stiffened X-face longitudinal mode  $n=1$  and measurements of  $c_{11}$  and  $c_{14}$ . This choice was also motivated by the insensitivity of the X-face modes to misalignment error.

In performing the fit, an initial guess for the elastic constants,  $c_{11}$ , was provided based upon experimental measurements of the effective elastic constants for six unstiffened modes

( $n=2, 3, 7, 8, 9, 10$ ). The values obtained for the effective elastic constant for each mode,  $n$ , were averaged over all  $M$  samples. The resultant six equations were then solved for the six independent elastic constants which were then used as the initial guess for the fitting routine. Table III indicates the room temperature values of the elastic constants obtained as a result of the least squares fit as well as a comparison with measured values of Chang and Barsch.<sup>1</sup> Also indicated is an estimate of the error associated with each constant. This estimate is based upon the spread between the initial guess for  $c_{ij}$  and the final fitted value. In the limit of no experimental error, initial and final values become identical.

A further check of the validity of the obtained room temperature data set is found by comparing the effective elastic constants for each mode,  $n$ , generated by this set with average experimental values. Table IV shows this comparison and includes as an independent check of the data set a comparison for a number of stiffened modes as well. The effective elastic constants for these modes required, additionally, the inclusion of the measured room temperature piezoelectric and dielectric constants. All deviations are well within experimental error.

#### Dielectric Constants

Four X and four Z-cut berlinite plates of a thickness  $T = (0.566 \pm 0.003 \text{ mm})$  and an area of about  $1 \text{ cm}^2$  were used for dielectric constant measurements. The well polished surfaces were plated with a  $0.1 \mu\text{m}$  thick aluminum layer in a vacuum system equipped with an electron gun evaporator. Each of these samples was then attached to the stainless steel support by means of a silver paste.

The circular top electrodes were fabricated by standard photolithographic technology. The diameters of the top electrodes used were approximately equal to 8.9, 7.8, 5.8 and 4.5 millimeters respectively with an accuracy of about  $\pm .005 \text{ mm}$ .

The capacitance of each sample was measured by means of the HP250B RX meter at a frequency of 1 MHz. The accuracy of the capacitance measurement was estimated to be about  $\pm 0.01 \text{ pf}$ .

From extrapolation to infinite diameter, the value obtained for  $(C/A)_{\infty}$  was  $7.45 \text{ pF/cm}^2$  for the X and Z-cut samples. Data appropriate to a Z-cut sample is shown in Figure 4.

It is estimated from equation (7) and taking measurement errors in account that,

$$\frac{\epsilon_{11}^T}{\epsilon_0} - \frac{\epsilon_{33}^T}{\epsilon_0} = 4.8 \pm .2$$

The X-cut samples were also measured at a frequency of 15 MHz. From these measurements it was estimated that  $\frac{\epsilon_{11}^T}{\epsilon_0} = 4.7$ .

The berlinite dielectric constant,  $\epsilon_{11}^T$  and  $\epsilon_{33}^T$ , have been measured by many authors.<sup>6-9</sup> However,

the measurement procedures were not well defined and the results were sample dependent. The published values of the relative dielectric constant,  $\epsilon_{11}^T/\epsilon_0$ , ranged from 6.05 to 4.55 and,  $\epsilon_{33}^T/\epsilon_0$ , ranged from 6.03 to 4.39. The differences in these results may be attributed to crystal defects, water and fringing capacitance. Crystal defects such as bubbles and inclusions have a strong influence on the dielectric constant. Water having a relatively large dielectric constant of 80 may have the most significant effect on the dielectric constant of berlinite. Due to defects and water, relaxation peaks were observed in the loss tangent and step-like kinks in the dielectric constant as a function of temperature.<sup>7,8</sup> In these cases, the dielectric constant has a strong frequency dependence. Therefore, the larger measured values of the berlinite dielectric constant were probably received for samples with a significant water content.

In the present work, good reproducibility of the measured dielectric constant from sample to sample was obtained. Also changes in the dielectric constant with frequency were small. This indicates that the berlinite crystals studied in the present work were of high quality and with low water content.

Finally, if fringing capacitance is excluded, the dielectric constant will be larger than expected. As described earlier, the fringing capacitance has been accounted for in the present work.

#### Piezoelectric Constants

The piezoelectric constants of both berlinite and quartz were determined. The reason for examining the latter, for which the piezoelectric constants are well known, was to insure that the experimental procedure was accurate. Three Y-cuts, three  $-45^\circ$  Y-rotated cuts and one  $+45^\circ$  Y-rotated cut of berlinite were studied. The resonance and anti-resonance frequencies,  $f_r$  and  $f_a$ , for the Y-cut and  $+45^\circ$  Y-rotated cuts were determined as discussed earlier. The results were averaged and the associated electromechanical coupling coefficients,  $k_{11}$  and  $k_{36}$ , were then determined from equation (11). Finally, equations (15) and (17) were used to obtain  $e_{11}$  and  $e_{14}$ .

The values obtained for the piezoelectric constants for berlinite are summarized in Table V and compared to experimental results obtained by other workers. Also given in Table V is a comparison between the experimentally determined piezoelectric constants of quartz and values given by Bechmann.<sup>10</sup> In the case of quartz, the agreement between the present results and those of Bechmann is excellent, thereby insuring the validity of the present experimental approach.

In the case of  $e_{11}$  and  $e_{14}$  for berlinite, the present results are much smaller than those reported by Chang and Barsch.<sup>1</sup> This is not unexpected since the pulse measurement technique used in the Chang and Barsch work is very inaccurate when the electromechanical coupling is small. In this case the measurement error is comparable to the piezoelectric stiffening term.

From the known values of the  $e_{11}$ ,  $e_{14}$  and  $c_{11}$  constants,  $d_{11}$  and  $d_{14}$  were evaluated. An examination of the values for  $d_{11}$  in Table V reveals that the values of the present study are, in all cases, lower than those obtained in previous studies. Since Mason's measurements<sup>6</sup> were performed on old, poor quality berlinite crystals, the existing differences, therefore, might be justified. The berlinite crystals used by Kolb et al<sup>9</sup> were also not of high quality since they received a large scattering in the  $d_{14}$ ,  $e_{11}$  and  $e_{33}$  constants. They also received too large a value for the  $d_{11}$  constant for quartz. Therefore, their results are suspect. Uchino and Cross<sup>11</sup> received good agreement for the  $d_{11}$  constant of quartz, but they studied old berlinite crystals. Finally, both Kolb et al<sup>9</sup> and Uchino and Cross<sup>11</sup> used methods which were not accepted by IEEE Standard of Piezoelectricity for piezoelectric constant determination.

#### SAW Velocity and $\Delta v/v$

The berlinite samples used for the SAW velocity determination were typically 1cm long in the propagation direction with a thickness about 1mm. Alignment accuracy in the propagation direction was estimated to be  $\pm 1^\circ$ . The SAW velocity for several orientations was determined as described earlier. The results of the measurements are presented in Table VI and compared to a theoretical calculation based on the material constants given earlier.

An estimated error in SAW velocity measurements of  $\pm 20$  m/sec is based upon accuracy with which transducer finger periodicity and center frequency could be measured.

The agreement between theory and experiment is within  $\pm 15$  m/sec for all cuts studied except the  $71.5^\circ$  Z-axis cylinder cut. The fact that the crystals may be misoriented by at least  $.5^\circ$  and that the transducer alignment is accurate within  $\pm 1^\circ$  might explain in part the discrepancy of 46 m/sec in this cut.

The  $\Delta v/v$  parameter was determined using the conductance and phase methods for several orientations. In the conductance method, the input conductance,  $G$ , and capacitance,  $C$ , of the two interdigital transducers in each orientation were measured by means of the HP250B RX meter. From these measurements, the known central frequencies,  $f_0$ , the number of finger pairs,  $N$ , and the effective dielectric constant,  $\epsilon^T$ , and the  $\Delta v/v$  parameters were evaluated. The results presented in Table VII are the average of the measurements on each transducer. Due to the poor quality of the interdigital transducer fingers (partial fingers, narrow fingers) and due to the input conductance and capacitance measurement errors, the accuracy of the  $\Delta v/v$  determination using the conductance method was about  $\pm 20\%$ .

The  $\Delta v/v$  parameter was also measured by means of the phase method in a vacuum system for three orientations listed in Table VII. The error in the  $\Delta v/v$  measurement is estimated to be about  $\pm 4\%$ . The agreement for the  $\Delta v/v$  parameter received from the two methods is very good.

The measured  $\Delta v/v$  parameters are also compared with values calculated using our material constant and the material constants of Chang and Barsch in Table VII. The values of  $\Delta v/v$  determined using the material constants measured in the present study are in much better agreement with experiment than the  $\Delta v/v$  values predicted using the material constants of Chang and Barsch.<sup>1</sup> This seems to indicate that the present values of  $e_{11}$  and  $e_{14}$  are more reliable than the values reported by Chang and Barsch. Possible discrepancies between the present theory and experiment may be attributed to sample orientation errors and small errors in  $e_{11}$  and  $e_{14}$ .

#### Summary and Conclusions

Berlinite crystals grown by the Allied Corporation have been evaluated both experimentally and theoretically to determine their potential for microwave acoustic applications. The room temperature values of the elastic, dielectric and piezoelectric constants have been obtained and yield good predictions of SAW velocity and electromechanical coupling measured experimentally on a number of delay line orientations. The repeatability of the measured constants from sample to sample indicates the high quality and uniformity of the Allied grown material. The electromechanical coupling of berlinite was found to be significantly lower than that reported by Chang and Barsch<sup>1</sup> but still almost three times that of ST-cut quartz for temperature compensated orientations.

#### References

1. Z. P. Chang and G. R. Barsch, "Elastic constants and thermal expansion of berlinite," IEEE Trans., Vol. SU-23, 127 (1976).
2. J. E. Vetolino, "Methods for temperature compensation in SAW devices," Proc. Nat. Elec. Conf., Vol. 35, 340 (1981).
3. IEEE Standard on Piezoelectricity, 23 (1978).
4. H. J. McSkimin, "Pulse superposition method for measuring ultrasonic wave velocities in solids," J. Acoust. Soc. Am., Vol. 33, 42 (1961).
5. V. E. Bottom, "Dielectric constants of quartz," J. Appl. Phys., Vol. 43, 1493 (1972).
6. W. P. Mason, "Piezoelectric crystals and their applications to ultrasonics," 208 (1950) Van Nostrand, New York.
7. G. R. Barsch and K. E. Spear, "Temperature compensated piezoelectric oxide materials," Tech. Report 30 (1979), Penn State Univ.
8. G. R. Barsch and K. E. Spear, "Single crystal substrates for surface acoustic wave devices," Tech. Report, 25 (1982), Penn State Univ.
9. E. D. Kolb, A. M. Glass, R. L. Rosenberg, J. C. Grenier, and R. A. Laudise, "Dielectric and piezoelectric properties of aluminum phosphate," IEEE Ultra. Symposium Proc., 332 (1981).
10. R. Bechmann, "Elastic and piezoelectric constants of Alpha-quartz," Phys. Review, Vol. 110, 1060 (1958).
11. K. Uchino and L. E. Cross, "A high-sensitivity AC dilatometer for the direct measurement

of piezoelectricity and electrostriction," 33rd  
Freq. Control Symposium, 110 (1979).

Table I. Effective elastic constants,  $\bar{c}$ , of berlinite.  
 $Y'/\pm 45^\circ$  designates a  $\pm 45^\circ$  rotated Y-cut sample.

No.	Direction of Propagation	Mode	
1	X	L	$c_{11} + e_{11}^2/c_{11}$
2	X	FS	$(c_{66} + c_{44})/2 + [(c_{66} - c_{44})^2 + 4c_{14}^2]^{1/2}/2$
3	X	SS	$(c_{66} + c_{44})/2 - [(c_{66} - c_{44})^2 + 4c_{14}^2]^{1/2}/2$
4	Y	QL	$(c_{44} + c_{11})/2 + [(c_{44} - c_{11})^2 + 4c_{14}^2]^{1/2}/2$
5	Y	QS	$(c_{44} + c_{11})/2 - [(c_{44} - c_{11})^2 + 4c_{14}^2]^{1/2}/2$
6	Y	S	$c_{66} + e_{11}^2/c_{11}$
7	Z	L	$c_{33}$
8	Z	S	$c_{44}$
9	$Y'/+45^\circ$	QL	$(c_{11} + c_{33} + 2c_{44} - 2c_{14})/4 + [(c_{11} - c_{33} - 2c_{14})^2/4 + (c_{44} + c_{13} - c_{14})^2]^{1/2}/2$
10	$Y'/+45^\circ$	QS	$(c_{11} + c_{33} + 2c_{44} - 2c_{14})/4 - [(c_{11} - c_{33} - 2c_{14})^2/4 + (c_{44} + c_{13} - c_{14})^2]^{1/2}/2$
11	$Y'/+45^\circ$	S	$(c_{44} + c_{66} + 2c_{14})/2 + (e_{26}^2/c_{22}^2)$
12	$Y'/-45^\circ$	QL	$(c_{11} + c_{33} + 2c_{44} + 2c_{14})/4 + [(c_{11} - c_{33} + 2c_{14})^2/4 + (c_{44} + c_{13} + c_{14})^2]^{1/2}/2$
13	$Y'/-45^\circ$	QS	$(c_{11} + c_{33} + 2c_{44} + 2c_{14})/4 - [(c_{11} - c_{33} + 2c_{14})^2/4 + (c_{44} + c_{13} + c_{14})^2]^{1/2}/2$
14	$Y'/-45^\circ$	S	$(c_{44} + c_{66} - 2c_{14})/2 + (e_{26}^2/c_{22}^2)$

$e_{26}^2 = -(e_{11} + e_{14})/2$   
 $e_{26}^2 = -(e_{11} - e_{14})/2$   
 $c_{22}^S = (c_{11}^S + c_{33}^S)/2$

L = Longitudinal  
FS = Fast Shear  
SS = Slow Shear  
S = Shear

QL = Quasi - Longitudinal  
QS = Quasi - Shear  
 $c_{ij}^E = c_{ij}^E$   
 $c_{ij}^S = c_{ij}^S$

Table II. Effective unstiffened elastic constants and effective dielectric and piezoelectric constants for modes 1, 6, 11, and 14 in berlinite.

No.	Direction of Propagation	Mode	$\bar{c}$	$\bar{\epsilon}^S$	$\bar{e}$
1	X	L	$c_{11}$	$c_{11}^S$	$e_{11}$
6	Y	S	$c_{66}$	$c_{11}^S$	$e_{11}$
11	$Y'/+45$	S	$(c_{44} + c_{66} + 2c_{14})/2$	$(c_{11}^S + c_{33}^S)/2$	$-(e_{11} + e_{14})/2$
14	$Y'/-45$	S	$(c_{44} + c_{66} - 2c_{14})/2$	$(c_{11}^S + c_{33}^S)/2$	$-(e_{11} - e_{14})/2$

Table III. Comparison of present results for room temperature elastic constants (in  $10^{11}$  N/m<sup>2</sup>) with corresponding data of Chang and Barsch<sup>1</sup>.

$c_{ij}^E$	Present Work	Chang and Barsch
$c_{11}$	$.6931 \pm .002$	$.6401 \pm .007$
$c_{12}$	$.1051 \pm .014$	$.0724 \pm .013$
$c_{13}$	$.1348 \pm .007$	$.0957 \pm .026$
$c_{14}$	$-.1299 \pm .002$	$-.1722 \pm .003$
$c_{33}$	$.8662 \pm .002$	$.8576 \pm .003$
$c_{44}$	$.4302 \pm .002$	$.4317 \pm .003$
$c_{66}$	$.2940 \pm .005$	$.2236 \pm .006$

Figure 1. Parallel-plate capacitor viewed from the top and the side.

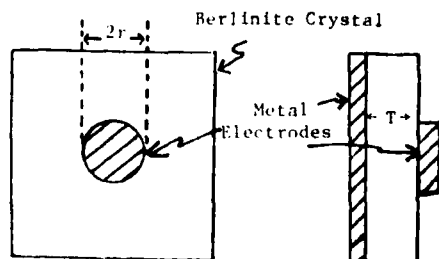


Figure 2. Geometry of a vibrating berlinite plate.

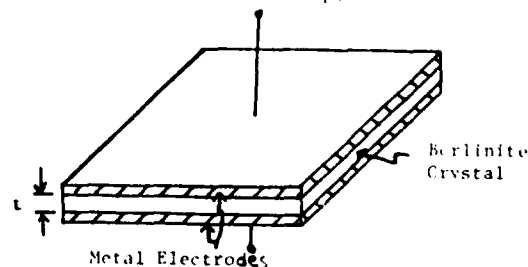


Table IV. Comparison of average experimental and computed values for effective elastic constants (in  $10^{11}$  N/m<sup>2</sup>).

A. Modes Used in Least Square Fit				
n	Mode	$\frac{1}{H_n} \sum_{n=1}^N \frac{H_n}{C_n} \exp$	$\frac{1}{C_n}$	Percent Difference
1	XL	.6976 ± .0015	.6977	.015
2	XFS	.5065 ± .0005	.5088	-.05
3	XSS	.2156 ± .0002	.2155	.05
7	XL	.8863 ± .003	.8862	.01
8	XS	.4324 ± .003	.4302	-.50
9	+45 QL	1.0247 ± .005	1.0228	.19
10	+45 QS	.3278 ± .003	.3270	.24
12	-45 QL	.7878 ± .004	.7908	-.38
13	-45 QS	.2991 ± .002	.2997	-.20
B. Modes Used as an Independent Check				
4	YQL	.7412 ± .005	.7464	.70
5	YQS	.3804 ± .006	.3769	.93
6	YS	.2995 ± .001	.2966	.30
11	+45 S	.2350 ± .002	.2339	.50
14	-45 S	.4915 ± .002	.4928	.26

Figure 3. Equivalent electrical circuit of a resonator where  $Z_r(f)$  is the impedance of the lossy piezoelectric plate and,

$$X_s = \frac{1}{\omega C_0} \left( 1 - \frac{\frac{\pi}{2} \frac{f}{fa}}{k^2 \tan \frac{\pi}{2} \frac{f}{fa}} \right).$$

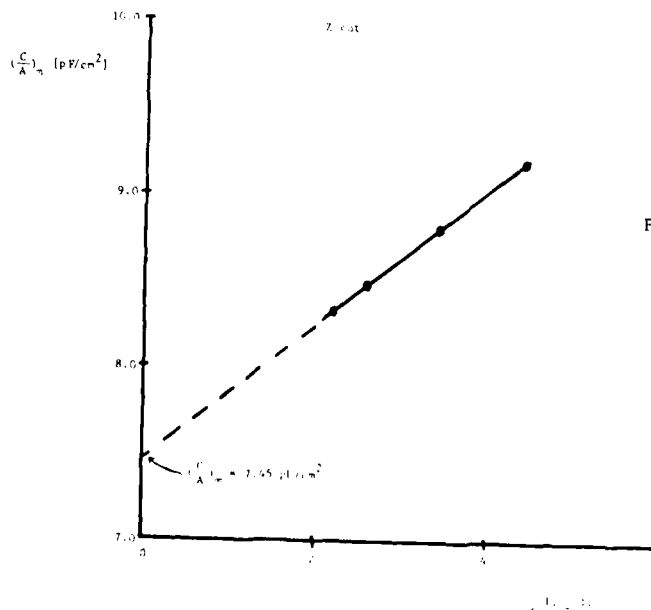
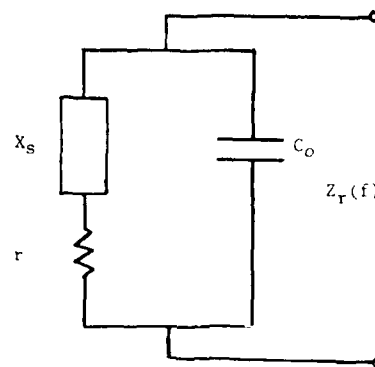


Figure 4. Variation of  $(C/A)_0$  for Z-cut berli-nite as a function<sup>m</sup> of the inverse electrode radius. Dots - experimental data; solid line - curve fit to experimental data; dashed line - extrapolation to infinite radius.

Table V. Room temperature piezoelectric constants,  $e_{ij}$  and  $d_{ij}$ , of berlinite and quartz.

$e_{ij}$ [Coul/m <sup>2</sup> ] $d_{ij} \times 10^{-12}$ [m/V]	Berlinite					Quartz			
	Present Study	Chang, Barsch [1]	Mason [2]	Kolb et al. [3]	Uchino Cross [11]	Present Study	Bechmann [10]	Uchino Cross [11]	Kolb et al. [3]
$e_{11}$	0.14	0.30	—	—	—	0.16	0.17	—	—
$e_{14}$	0.02	-0.13	—	—	—	-0.04	-0.04	—	—
$d_{11}$	2.87 <sup>a</sup>	5.30 <sup>b</sup>	3.33	3.52	3.98	—	2.31	2.27	2.80
$d_{14}$	2.20 <sup>a</sup>	0.03 <sup>b</sup>	1.55	—	—	—	0.73	—	—

<sup>a</sup>) Calculated from the  $e_{11}$ ,  $e_{14}$  and  $c_{ij}$  determined in the present study.

<sup>b</sup>) Calculated from the  $e_{11}$ ,  $e_{14}$  and  $c_{ij}$  determined by Chang and Barsch [1].

Table VI. Measured center frequency and associated SAW velocity for different orientations in berlinite.

	Euler Angles			Center Frequency $f_c$ [MHz]	SAW velocity	
	$\phi$	$\theta$	$\psi$		Exp [m/sec]	Theory [m/sec]
-30.4° X-Boule	0	-80.4°	0	69.92	2744	2752
-46.6° X-Boule	0	-46.6°	0	68.05	2749	2763
19.1° X-Cut	90°	90°	19.1°	68.75	2777	2776
71.5° Z-Cylinder	71.5°	90°	0	70.07	2831	2785
Doubly Rotated A°	13.2°	90°	-11.5°	68.40	2763	2777
Doubly Rotated B°	10.3°	90°	-15.5°	68.85	2781	2788

Table VII. Comparison of the experimentally measured values of  $\Delta v/v$  as determined by the conductance method and the phase method with theoretical values based on material constants determined by Chang and Barsch.<sup>1</sup>

Orientation	$\frac{\Delta v}{v} \times 10^{-2}$			
	Conductance Method	Phase Method	Theory <sup>a</sup>	Theory <sup>b</sup>
- 80.4° X -Boule	0.10	0.10	0.105	0.230
- 46.6° X -Boule	0.06	—	0.068	0.157
19.1° X-Cut	0.13	0.13	0.100	0.271
71.5° Z-Cylinder	0.14	0.15	0.116	0.266
Doubly Rotated A°	0.13	—	0.111	0.269
Doubly Rotated B°	0.13	—	0.113	0.252

<sup>a</sup>Theory utilizing material constants determined in the present study.

<sup>b</sup>Theory utilizing material constants determined by Chang and Barsch [1].

THERMAL FREQUENCY BEHAVIOR IN CONTOURED QUARTZ CRYSTAL PLATES  
INDUCED BY DIRECT IRRADIATION OF LASER BEAM

Nobunori Oura, Naimu Kuramochi, Junichi Nakamura, and Takashi Ogawa

Research Laboratory of Precision Machinery and Electronics,  
Tokyo Institute of Technology,  
4259, Nagatsuta, Midori-ku, Yokohama 227, Japan

Summary

The oscillation frequency behavior of the quartz crystal plates is observed, while a laser beam as a kind of probe is irradiating different points of their principal surfaces. Such frequency behavior is characteristic to the respective angle of cut and is independent of the geometry and type of the electrode or support.

There are three kinds of region on an AT-cut plate which show different types of thermal frequency behavior. The amounts of the frequency shifts in IT-cut and SC-cut plates are about 1/5 to 1/10 times those in AT-cut plate for the same irradiation power of the laser.

The results suggest a possibility of compensation for the thermal frequency transient of a crystal unit by optimizing the electrode configuration and the reflectivity of the electrodes for the infrared rays.

Introduction

The oscillating frequency of an oven-controlled crystal oscillator shows an excursion not anticipated from the static temperature-frequency characteristics of the crystal units, when the oven-temperature was subjected to a small change.<sup>1</sup> This phenomenon is known as the thermal-shock. The cause of the thermal shock is mainly stress due to nonuniform temperature distribution in the quartz crystal plate with a temperature change. To obtain a resonator immune to a temperature change, a new cut of quartz crystal was devised.<sup>2</sup>

The thermal frequency transient is usually observed as a whole by producing the abrupt change in temperature of the oven in which the crystal resonator was placed. This approach is not sufficient for the analysis of the mechanism of the thermal shock in a plate of a finite size.

As an approach to analyze the mechanism of the thermal shock in a crystal plate of a finite size, a laser beam was employed in our study as a small heat source to cause a thermal-stress in the plate. Using a laser beam, Gagnepain measured the frequency variations due to thermal gradient in a 10-MHz AT-cut plate.<sup>3</sup>

We utilized a laser beam as a kind of probe to cause the thermal frequency behavior of the plate as well as the electrical probe method<sup>4</sup> in the study of vibrational modes. We irradiated different points of the principal surfaces of AT-cut, IT-cut and SC-cut plates excited by a gap-type holder or evaporated electrodes.

Experimental

1. Frequency transient measuring system

The measuring system is shown in Fig.1, in which a quartz resonator and an active circuit compose an oscillator under test. A specimen plate is directly irradiated by a laser beam of He-Ne laser with 3.1 mW, whose beam diameter is 1.2 mm. The specimen plates were operated at room temperature. The exciting current was less than 1.0 mA. The output frequencies from both oscillators, the reference and the oscillator under test, are mixed. The lower sideband frequency is outputed on a printer and/or a recorder.

2. Thermal frequency behavior of AT-cut plate

The specimens used are 5th overtone 5-MHz plano-convex AT-cut plates with maximum thickness of 1.68 mm, diameter of 15 mm, radius of curvature of 120 mm, and Q of  $2.3 \times 10^4$  in vacuum. The specimens with positive or negative frequency temperature coefficient were prepared. A gap-type holder was also used to eliminate the effect of the evaporated electrodes and the supporting on the frequency behavior.

As shown in Fig.2, the holder is composed of an upper electrode and lower electrode made of brass, and a glass spacer. On the lower electrode, three small paper shims of 30  $\mu$ m, on which the specimen plate is placed, are set. Holes of 1 mm in diameter are drilled in the upper electrode, through which a laser beam irradiates the specimen. Two kinds of the upper electrode were made as shown in Fig.3. The gap between the upper electrode and the specimen is about 50  $\mu$ m. The polar coordinates as shown in Fig.4 is used to indicate the points on the specimen surface on which the beam is irradiated.

When the specimen is irradiated directly, a frequency change of the order of 0.01 Hz at 5-MHz took place, as shown in Fig.5. As is seen from the figure, the signal to noise ratio is inferior. Therefore, a black line is drawn on the surface along the irradiating points for the higher absorption of the beam. As shown in Fig.6, about 50 times frequency excursion was obtained for the same irradiation power without any substantial change in the frequency behavior.

The types of the frequency behavior are divided into three types, (a), (b), and (c) as shown in the right-hand side of Fig.7. Type (a) shows a positive frequency excursion at the time when laser beam is irradiated. Type (b) shows a negative frequency excursion and type (c) shows spikes at the beginning and the end of the irradiation. A region on the plate, which shows type (a) frequency behavior, is named region I, the region showing type (b) is named region II, and the region showing type (c) is named region III.

The region I has the shape of an ellipse, whose major axis is 0.7D and minor axis, 0.5D, where D is a diameter of the specimen. The shape of the region I roughly corresponds to that of the dominant displacement region of the thickness-shear fundamental vibrational mode.<sup>5</sup> The types of the frequency behavior do not depend on the frequency-temperature coefficient of the specimen, that is, whether it is positive or negative. The maximum frequency excursions along diameters are shown in Fig.8. In this case, only the frequency excursion in the region III is estimated as the excursion settled down after the spikes. The crossovers on the axis of abscissa compose the borderline between the region I and II.

The frequency behavior of specimens excited with evaporated electrodes are shown in Figs.9 and 10. Upon measuring the frequency excursion on the point D, the specimen is dotted with black ink. The types of the behavior is similar to that in Fig. 6. This result means that the behavior is characteristic to plano-convex AT-cut plate and independent of the type and configuration of electrode and supporting.

The values of the frequency excursion to the radiation power were measured by attenuating the intensity of the beam with neutral density filters. As shown in Fig.11, the frequency excursions are proportional to the irradiated power ( $P < 3.5 \text{ mW}$ ) and the proportionality holds independent of the regions.

### 3. Thermal frequency behavior of IT-cut plate and SC-cut plate

The IT-cut specimen used is ; 5th overtone 5 MHz plano-convex plate, 15 mm in diameter, maximum thickness of 1.794 mm, radius of curvature of 120 mm, and Q of  $1.96 \times 10^6$  in vacuum with Cr-Au evaporated electrodes. In this case, the specimen was glued to supporting wires of a holder like the HC/60 with conductive cement and irradiated.

Since the temperature coefficient of the specimen at room temperature is  $5 \times 10^{-7}/^\circ\text{C}$  and the frequency excursion of IT-cut plate due to thermal stress is smaller than that of AT-cut, the static frequency temperature characteristics are dominant in comparison with the dynamic ones. Figure 12 shows the frequency excursions of the IT-cut plate.

The steep negative excursion with irradiation at the wave front in Fig.12 is due to the thermal shock. The positive slope following the thermal shock is due to the static characteristics. The amount of the excursion due to the thermal shock is about 1/5 times that of the AT-cut plate. A two-dimensional map of the frequency behavior type of IT-cut plate induced by thermal stress is shown in Fig.13. The shape of the region I is a circle with a radius of 0.5D, where D is a diameter of the specimen. The region III, which was observed in AT-cut plate, was not able to be found.

The SC-cut specimen is; 3rd overtone 8 MHz plano-convex plate, 14.019 mm in diameter, maximum thickness of 0.664 mm, radius of curvature of 178 mm, and Q of  $1.12 \times 10^6$  in vacuum with Cr-Au evaporated electrodes. The frequency excursions of the specimen are shown in Fig.14. Note that excursion C and D are measured with black dot on the surface. The distinct frequency behavior such as in AT-cut and IT-cut plate was not found.

### 4. Time constants of the frequency excursion

To measure the time constants of the frequency transient, the frequency excursion of the AT-cut specimen was recorded on a strip chart shown in Fig.15 by increasing the driving speed of the chart. After a few seconds of irradiation, the frequency excursion settled down. The frequency excursion in the region I and II seems to be exponential. Therefore, both two excursions may be written as Eq.(1).

$$\Delta f = \Delta F \{1 - \exp(-t/\tau)\}, \quad (1)$$

where  $\Delta F$  is the stationary frequency excursion,  $t$  is elapsed time, and  $\tau$  is time constant. By trial computation, it turned out that the excursion in the region I has one time constant, while the excursion in the region II has two constants. The excursion in the region II may be expressed by

$$\Delta f = \Delta F_1 \{1 - \exp(-t/\tau_1)\} + \Delta F_2 \{1 - \exp(-t/\tau_2)\}. \quad (2)$$

The excursions expressed by Eqs.(1) and (2) are shown in Fig.16. The excursion in the region III is assumed to be expressed by superposition of Eqs.(1) and (2) as follows.

$$\Delta f = \Delta F \{1 - \exp(-t/\tau)\} + \Delta F_1 \{1 - \exp(-t/\tau_1)\} + \Delta F_2 \{1 - \exp(-t/\tau_2)\}, \quad (3)$$

where  $\Delta F_2$  is 10 to 20 % of  $\Delta F_1$  and  $\tau_2$  is larger than  $\tau_1$ .  $\tau_1$  has little influence on the excursion and was neglected. A result is shown in Fig.17. A good agreement is obtained between the calculated and the experimental.

### Discussion

Noguchi showed that the thermal shock is caused mainly by thermal radiation onto the crystal plate rather than the thermal conduction from the supporting to the plate.<sup>6</sup> Therefore, the overall frequency excursion of a crystal plate, that is, thermal shock is considered due to integration of excursions on every point on the principal surfaces.

Warner showed that a circular plano-convex AT-cut plate excited with parallel field gives rise to a positive frequency excursion, when the plate is subjected an abrupt increase in temperature.<sup>1</sup> On the other hand, as is well known, the plate with key-hole electrodes shows a negative excursion.

These exclusive phenomena in AT-cut plate can be explained from our study; When the plate is irradiated by the infrared rays with a wavelength greater than 3  $\mu\text{m}$ , the evaporated electrode, for example Au or Ag, reflects almost all of the rays and the naked part of the plate absorbs almost the rays. In Warner's experiment, the central part of the plate is a naked circle, which absorbs the infrared rays, whereas the peripheral part of the plate, which is evaporated, reflects the rays. Therefore when the plate is irradiated, a positive frequency excursion occurs as a whole. In the case of a plate with key-hole electrodes, the central part of the plate is not evaporated. Therefore the temperature increase in the peripheral part causes a negative frequency excursion.

These facts suggest that the thermal shock of AT-cut plate can be compensated to a certain extent by optimizing the configuration of the exciting electrodes.

There must be an optimum electrode configuration for every cut and mode of crystal plate from the viewpoint of thermal shock. Some proposals for electrode configuration with less thermal shock are shown in Fig.18. Annular electrode was proposed by Ianouchevsky to improve the frequency aging.<sup>7</sup> Yakuwa and others measured the frequency transient of an AT-cut plate with annular electrodes.<sup>8</sup> They could not compensate the thermal shock, since the map of frequency behavior of the plate was not yet known. We will recommend annular electrodes from the viewpoint of thermal shock. A point of the design is to make the integration of frequency excursions over naked part of the plate vanish.

The proportionality relation between the laser power and the frequency excursion is available for fast response laser powermeter. Because the frequency excursion is not due to the static frequency temperature characteristics but due to thermal stress in the plate.

### Conclusion

The thermal frequency behavior of AT-, IT-, and SC-cut plano-convex plates was observed by irradiation of a He-Ne laser beam on the plates. There exist on AT-cut plate three kinds of region, each of which shows different type of frequency excursion, when the plate is irradiated. The frequency excursion is proportional to the irradiating beam power ( $P < 3.5 \text{ mW}$ ) on the plate. The results suggest a possibility of compensation for thermal shock of a crystal unit by optimizing the configuration and material of electrodes.

### Acknowledgement

The authors wish to thank Professor Emeritus of Tokyo Institute of Technology H.Fukuyo, Professors T. Musha and T.Tako, and Dr. Y. Teramachi for their fruitful discussion and extend their thanks to Dr.J.Otomo of Nihon Dempa Kogyo Co., Ltd. and Dr. S.Nonaka of Nippon Electric Co., Ltd. They also wish to thank Mr.T.Hayashi and Mr.S.Tachi for their help in the experiment.

### References

- (1) A.W.Warner, "Use of Parallel-Field Excitation in the Design of Quartz Crystal Units," Proc. 17th AFCS (1963)p.248.
- (2) J.A.Kusters, "The SC Cut Crystal - An Overview," Proc. 1981 Ultrasonic Symposium (IEEE, 1981)p.402.
- (3) J.J. Gagnepain, "Fundamental Noise Studies of Quartz Crystal Resonators," Proc. 30th AFCS (1976) p.84.
- (4) I.Koga, H.Fukuyo, and J.E.Rhodes, "Modes of Vibration of Quartz Crystal Resonators Investigated by Means of the Probe Method," Proc. 13th AFCS (1959)p.54.
- (5) K.Iijima, Y.Tsuzuki, Y.Hirose, and M.Akiyama, "Laser Interferometric Measurement of the Vibration Displacements of a Plano-Convex AT-Cut Quartz Crystal Resonator," Proc. 30th AFCS (1976) p.65.
- (6) Y.Noguchi, Doctoral Thesis, Tokyo Institute of Technology, Tokyo, Japan, 1982 (In Japanese).
- (7) W.Ianouchevsky, "High Q Crystal Units," Proc. 17th AFCS (1963)p.233.
- (8) K.Yakuwa et al., "Quartz Crystal Unit for Fast Warm-Up Oscillator," Paper of Technical Group on Component Parts and Materials, (IECE of Japan) CPM70-11(1970) (In Japanese)

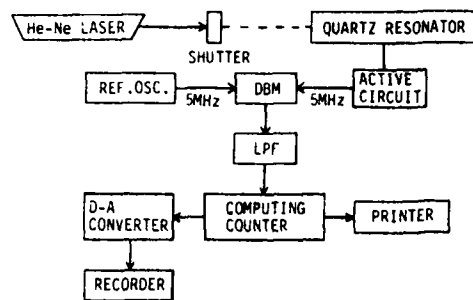


Fig.1 Block diagram of the frequency-transient measuring system.

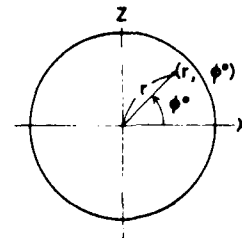


Fig.4 The polar coordinates indicating the point on the specimen surface on which the beam is irradiated.

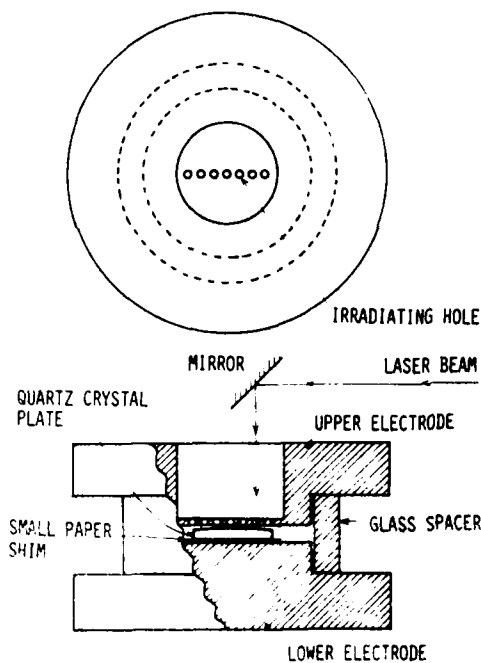


Fig.2 Gap-type holder.

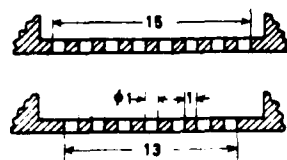


Fig.3 Two kinds of the upper electrode having different arrangement of irradiating holes.

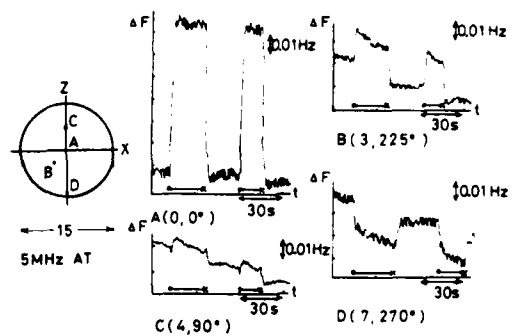


Fig.5 The frequency excursion of a 5-MHz AT-cut plate. A, B, C, and D are the irradiating points. The marks  $\rightarrow$  show the irradiating periods.

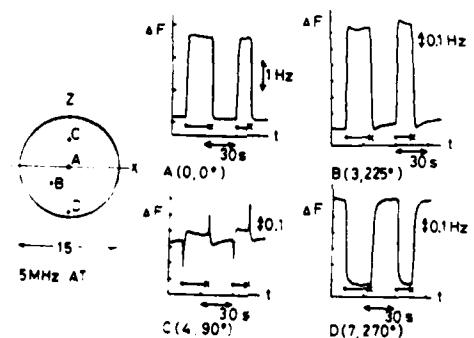


Fig.6 The frequency excursion of the 5-MHz AT-cut plate having a black line on the surface for the higher absorption of the beam.

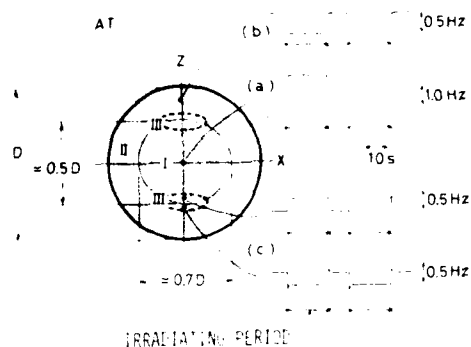


Fig. 7 Two-dimensional map of the frequency behavior type of AT-cut plate.

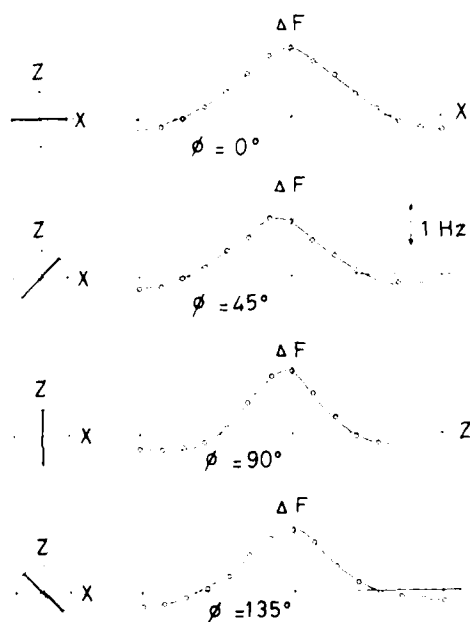


Fig. 8 The maximum frequency excursions along diameters with black line.

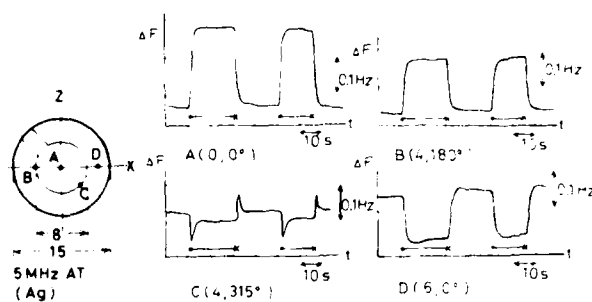


Fig. 9 The frequency behavior of a 5-MHz AT-cut plate excited with evaporated Ag electrode.

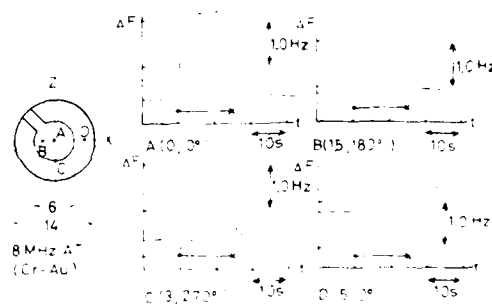


Fig. 10 The frequency behavior of an 8-MHz AT-cut plate excited with evaporated Cr-Au electrode.

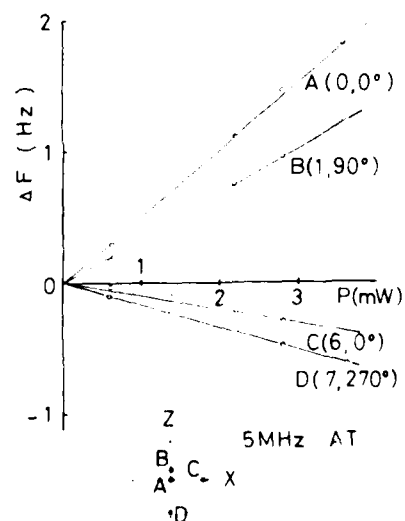


Fig. 11 The frequency excursion vs. irradiating power.

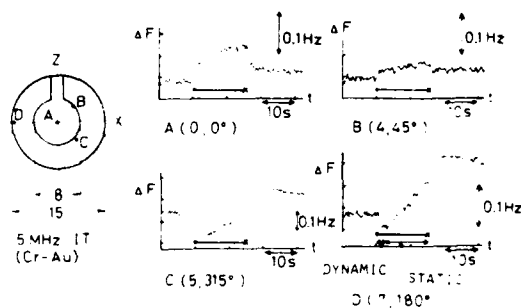


Fig. 12 The frequency excursion of a 5-MHz IT-cut plate.

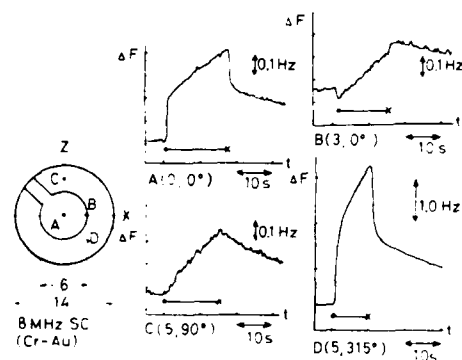


Fig. 14 The frequency excursion of an 8-MHz SC-cut plate.

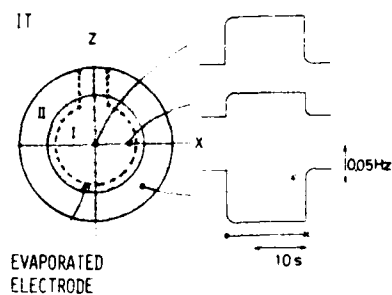


Fig. 13 Two dimensional map of the frequency behavior type of IT-cut plate.

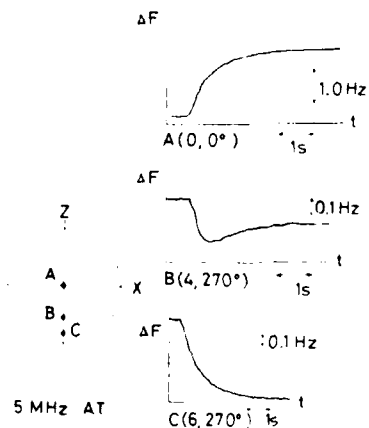


Fig. 15 The frequency transient behavior of an AT-cut plate at the earlier time of the irradiation.

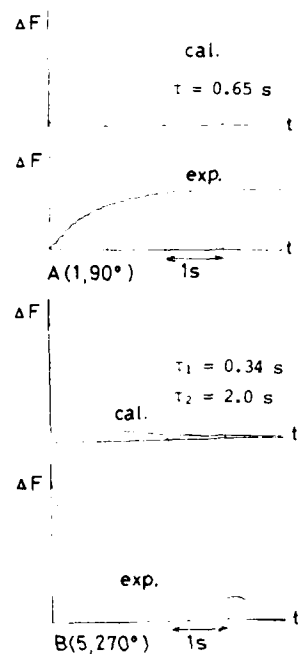


Fig.16 Simulations of the frequency transient behavior of an AT-cut plate on the region I (point A) and the region II (point B).

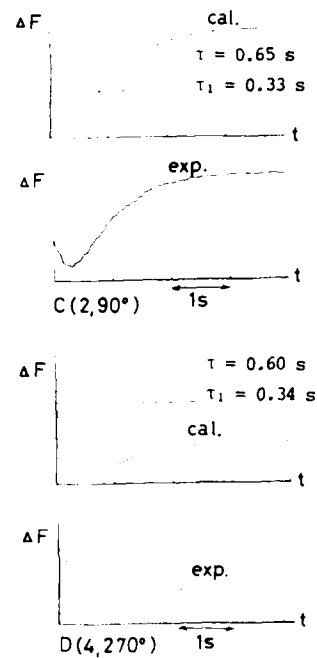


Fig.17 Simulations of the frequency transient behavior of an AT-cut plate on the region III.

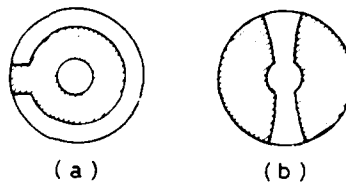


Fig.18 Proposals for electrode configurations with less thermal shock.

AD P001514

# Thermal Hysteresis of AT + SC-Cut Quartz Crystal Resonators

## Automated Measurement Method and Results

Hans-Joachim Forster, Siemens AG,  
Hofmannstraße 51, 8000 München 79, West Germany

### Summary

It is the intention of this paper to demonstrate the temperature compensation limits of precision quartz crystal resonators mounted in the traditional HC-21/J glass enclosure. A computer-controlled hysteresis measurement station was set up to measure the thermal hysteresis (thermal retrace) of the resonator, which restricts attainable compensation accuracy. The station was used to take measurements of various crystals from 3 German manufacturers. When compared with the AT-cut specimens, the SC-cut crystals displayed no real advantages.

The frequency stability attainable with digitally temperature-compensated quartz crystal oscillators is limited to around  $\Delta f/f = \pm 1 \cdot 10^{-7}$  solely by the thermal hysteresis of the crystal resonators. If the inaccuracy of the temperature sensor used for compensation, together with the resolution error in the digitalization are taken into account, an attainable frequency stability of  $\Delta f/f = \pm 2 \cdot 10^{-7}$  can be assumed for series production without a high rejection rate. This value is practically independent of the operating temperature range.

### Introduction

Digital temperature compensation of quartz crystal resonators offers the following significant advantages:

1. Extremely low power consumption through the use of CMOS technology.
2. Immediate operational readiness after switch-on.
3. Higher accuracy than with analog temperature compensation.
4. Simple, computer-controlled adjustment in a single temperature cycle.

The frequency stability attainable is however principally limited by the hysteresis phenomenon of the crystal resonator to be compensated. For this reason it is essential that the designer of digitally compensated crystal oscillators is aware of the recurrent accuracy of the frequency-temperature curve.

A computer-controlled measuring station was set up for the purpose of measuring the specimens both economically and in a reproducible manner. Once the desired temperature limits, step width (static measurement) and number of loops have been entered manually, all measurements are made fully automatically.

### Test System

The versatile temperature test system is shown in Fig. 1.

The measuring station is made up primarily of standard, commercially available interface-bus compatible devices in accordance with the IEEE 488 standard (Hewlett-Packard interface bus). For any devices which are not directly HP-IB compatible, interface converters must be used, e.g. from the HP-IB to the V24 serial interface. The controller used is an HP 9621 desk-top computer. Programming language is HPL (Hewlett-Packard language).

The temperature test chamber can be equipped with several measurement fixtures. Measurements are made using computer-controlled check switches. The data logger can scan up to 20 temperature check points. The two VHF switches enable up to 12 frequency check points to be switched to the frequency measuring system. The data logger has an integrated timer which can take over time control of the measuring station.

Fig. 2 shows the basic construction of the measurement fixture.

The measurement chamber takes the form of a thick-walled aluminium chamber containing both the oscillator and resonator, the latter also having excellent thermal contact with the temperature precision resistor. Measurements are taken using an "original oscillator", in other words, with an oscillating circuit which is also used later on in the oscillator to be compensated. To keep the influence of the circuit on the crystal frequency to a minimum, the pulling device (capacitive diode) is short-circuited while the hysteresis is being measured.

Measurements were carried out using two different oscillator circuits which are depicted in Figs. 3 and 4.

The oscillator stage with transistor T1 in common-collector connection is a Colpitts circuit in which the crystal takes the place of the circuit inductance. Capacitors C1 and C2 can be chosen relatively large even without using a transistor with a particularly steep characteristic. The effective load capacitance of the quartz crystal is given in the first approximation by series capacitances C1 and C2.

The inductor connected in shunt with capacitor C2 prevents the harmonic-mode crystal from starting to oscillate at the fundamental, because the inductor bypasses the inductor L1 and the capacitance C2 acts capacitively only for the second harmonic.

Oscillator circuit A is a self-limiting circuit, whereas circuit B has an additional AGC. At the start of oscillation, transistor T1 operates at its peak emitter-current and therefore at maximum transconductance. Once the voltage at the collector of transistor T2 reaches a certain value, diode D becomes conductive and draws control current from transistor T2, causing the transconductance of transistor T1 to be reduced. Circuit B is ideally suited for setting different crystal currents.

#### Accuracy of Measurement and Reproducibility

The accuracy of the frequency measurement is  $1 \times 10^{-9}$  for a measuring time of one second. The counter and the synthesizer used for frequency generation are fed by an atomic standard frequency generator.

The main problem is the reproducibility of the temperature measurement. Absolute accuracy is uninteresting. The temperature measuring device, which works with Pt 100 platinum precision resistors, offers resolution to  $0.01^\circ\text{C}$ . Since the temperature of the room in which the measuring station is located is maintained at the correct level by an air-conditioning unit, reproducibility of the temperature measurement in the order of  $0.01^\circ\text{C}$  within the maximum measurement period of one week can be assumed.

With standard AT-cut crystals, the maximum slope of the frequency temperature curve is about  $1 \times 10^{-6}/^\circ\text{C}$ . This gives a reproducibility of the temperature setup for hysteresis measurement in excess of  $\pm 1 \times 10^{-3}$ .

#### Measurement Error Caused by Temperature Ripple of the Environmental Chamber

The temperature of the test chamber is regulated not by continuous but by two-position discontinuous control. The highest ripple occurs at a temperature setting of  $+5^\circ\text{C}$ . The maximum ripple is  $0.1^\circ\text{C}$  peak to peak for a period duration of some 9 minutes. The maximum transconductance is in this case  $0.5 \times 10^{-3} \text{ } \Omega/\text{sec}$ .

If the value of  $1 \times 10^{-6} \text{ sec}/^\circ\text{C}$  is set for the dynamic temperature coefficient  $\tilde{A}$  (see 2

and 3), a worst-case error of approx.  $5 \times 10^{-3}$  is obtained at an oven temperature of  $55^\circ\text{C}$ . If the time between frequency and temperature measurement is short (several seconds), the mean measurement error attributable to the temperature ripple of the test chamber will be in the region of  $(1...2) \times 10^{-3}$ .

#### Test Technique

To eliminate measurement errors caused by the dynamic temperature coefficient, measurements are made statically. In this case the difference between the check points is about  $5^\circ\text{C}$ . Measurement of the next point is not effected until sufficient thermal balance has been restored. This leads to pauses of 15 to 45 minutes between each measurement. Around a week is needed to measure 5 temperature loops between, say,  $-40$  and  $+90^\circ\text{C}$ .

It is practically impossible to achieve exactly the same reference temperature for the frequency comparison, given the increases and decreases in temperature. The use of the desk-top computer, however, together with the spline interpolation, makes it relatively easy to switch over to standardized temperatures for frequency comparison. Spline interpolation is used whenever given points for a graphic representation have to be interconnected by as smooth a curve as possible. The term "spline function" is so called because, in its third degree, it describes the behavior of a flexible curved rule (spline) of the kind used by draughtsmen to draw smooth curves. Each section of the curve between the check points is therefore a part of a third degree polynomial. Given "n" check points, four coefficients have to be determined for each of (n-1) polynomials. To ensure the curves flow smoothly, the coefficients are selected in such a way that the first and second derivatives to the edges agree. The curve is then visually "kink-free".

With the separation of the temperature check points at  $5^\circ\text{C}$ , interpolation accuracy is about  $1 \times 10^{-3}$ .

#### Measurement Results

Measurements were taken of many quartz crystals from three German manufacturers. Only 10-MHz crystals working in third overtone mode and with enclosure type HC-27/U were tested. The following figures show several chosen typical measurement results. Three temperature cycles were made for each type, each cycle consisting of an up run and a down run. With nearly all the test specimens it is striking that quite large hysteresis values are obtained in the first cycle. The reproducibility of the second and third cycles is in general excellent. Up to the first up run, the difference between the individual up runs and down runs is extremely small, namely  $\pm 1 \times 10^{-3}$ . In the first up run a "calming phase" evidently sets in.

It is striking that the quartz crystals of each manufacturer demonstrate a somewhat typical hysteresis curve which could be described as the manufacturer's "trademark". The logical conclusion

of this is that it should therefore be possible to reduce the hysteresis by taking certain action. It cannot, nor should it be the purpose of this paper to establish guidelines for the manufacture of low-hysteresis quartz crystals. Only the measurement results of precision quartz crystals from standard production are presented.

It should also be noted that the quartz crystals examined were intended for use in temperature-stabilized quartz oscillators where the hysteresis behavior plays only a subordinate role.

Since the hysteresis curves cannot provide as with any information about possible changes in frequency between individual temperature cycles, a further type of representation was chosen which shows the recurrent accuracy of the frequency for given reference temperatures after each run. Here the turnover temperatures are especially suitable, since in these cases the hysteresis measurement errors are extremely small.

#### Results with AT-Cut Crystals From Company "1"

Fig. 5 shows the typical frequency temperature curve of the quartz crystals examined, as well as the typical values of the equivalent electrical circuit diagram and details of the mechanical design.

With an effective oscillator-circuit load capacity of 120 pf the separation to the series resonant frequency of the crystal is still only  $12 \times 10^{-6}$ , i.e. the influence of the circuit on the crystal frequency is comparatively small.

The thermal hysteresis of quartz crystal 1 (Fig. 6) is at some hundred-millionths ( $10^{-8}$ ) also relatively low. Fig. 7 illustrates the good reproducibility between individual up and down runs, with the first up run already mentioned being the exception. The recurrent accuracy of the frequency (Fig. 8) can also be considered as good.

Quartz crystal 2 (Fig. 9) exhibits hysteresis values of up to  $\pm 1 \times 10^{-7}$ . The recurrent accuracy of the reference temperatures, i.e. lower turnover temperature, inflection temperature and upper turnover temperature is however excellent (Fig. 10).

The hysteresis values of quartz crystal 3 shown in Fig. 11 are similar to those of crystal 2; with crystal 3, however, the hysteresis is particularly high at the turnover temperatures. The recurrent accuracy after three temperature cycles is good (Fig. 12).

As has already been mentioned, two different oscillator circuits were used to do the measurements. Fig. 13 shows the results of crystal 1 with circuits A and B. The differences in the results can be attributed to variations in the crystal current in the temperature range measured. Circuit A allows different temperature-stabilized crystal currents to be adjusted. The results with crystal 1 with crystal currents of 0.2 - 5 mA can be seen in Fig. 14. It can be seen, albeit not distinctly,

that the hysteresis tends to increase with small crystal currents.

Fig. 15 provides us with an interesting result. Besides showing the good recurrent accuracy of frequency of crystal 1 at the reference temperature of  $+25^{\circ}\text{C}$ , it also reveals that the hysteresis is even greater for cycles between  $+20$  and  $+30^{\circ}\text{C}$  than between  $+10$  and  $+40^{\circ}\text{C}$ .

#### Results with AT-Cut Crystals From Company "2"

The typical electrical and mechanical characteristics are shown in Fig. 16. The motional inductance is somewhat higher than it was in the crystals of company "1", with the result that the influence of the circuit on the crystal frequency is even smaller. In this case silver electrodes were used instead of gold electrodes.

Fig. 17 shows the typical hysteresis curve of these crystals. The results obtained with other samples from company "2" were equally as bad. It was however surprising to note the good compliance between the individual up runs (apart from the first up run) and the individual down runs. No further measurements or evaluations were made with these crystals and they were not given further consideration.

#### Results With AT-Cut Crystals From Company "3"

The electrical characteristics are similar to those of crystals from company "2". Here, as with company "1", gold electrodes were also used (see Fig. 18). The hysteresis of crystal 1 reaches a value up to  $\pm 1 \times 10^{-7}$  and the recurrent accuracy of the frequency for the turnover temperatures and the inflection temperature is also very good (Figs. 19 and 20). The values of other samples from company "3" were of the same standard.

Crystal 2 is mounted inside a nitrogen-filled cold-welded metal enclosure. Compared with crystal 1, which was mounted in a glass vacuum package, temperature cycles 2 and 3 reveal relatively good hysteresis values and good reproducibility. Only the first cycle showed fairly large deviations. The recurrent accuracy of the frequency is not very good (Figs. 21 and 22).

Crystal 3 is mounted inside a helium-filled cold-welded metal enclosure. Its behavior is similar to that of crystal 2 in the nitrogen-filled enclosure with the exception of cycle 1 which in this case has particularly bad values (Figs. 23 and 24).

#### Results with SC-Cut Crystals From Company "3"

Fig. 25 shows the typical frequency temperature curve of the crystals in a TO-3 cold-welded enclosure, as well as the typical values of the equivalent electrical circuit diagram and details of the mechanical design. With an effective oscillator-circuit load capacitance of 120 pf the separation to the series resonant frequency of the crystal is still only  $1 \times 10^{-6}$ , i.e. the influence of the circuit on the crystal frequency

is very small.

Figs. 26 and 27 illustrate the hysteresis measurement values of two sample crystals. Apart from the first temperature cycle, hysteresis values of only some hundred-millionths ( $10^{-8}$ ) were obtained above  $+20^{\circ}\text{C}$ . The recurrent accuracy of the frequency at  $20^{\circ}\text{C}$  is shown in Fig. 31. The values are no better than those of the AT-cut crystals.

We were also able to examine SC-cut crystals from company "3" in the HC-27/U all-glass enclosure. The typical characteristics are given in Fig. 28. The frequency temperature curve in the upper temperature range (Figs. 29 and 30) is not as flat as that of the TO-3 samples. The results of the hysteresis measurements reveal no real advantages over those of the AT-cut crystals. The recurrent accuracy of the frequency (Fig. 31) is also no better.

#### Conclusion

The values of the SC-cut crystals measured were not vastly superior to those of the AT-cut specimens. Compared with the AT-cut specimens, the SC-cut crystals have a lower pulling sensitivity thanks to their relatively high motional inductance and the correspondingly high compensation requirement (synthesizer instead of capacitive diode) which, when taken into account, would tend to suggest that these expensive crystals, which were originally designed for high stability ( $10^{-8}$ ... $10^{-9}$ ) temperature-stabilized quartz crystal oscillators, are not particularly suitable for digital temperature compensation.

The frequency stability attainable with digitally temperature-compensated quartz crystal oscillators is limited to around

$$\Delta f/f = \pm 1 \cdot 10^{-7}$$

solely by the thermal hysteresis of the crystal resonators. If the inaccuracy of the temperature sensor used for compensation together with the resolution error in the digitalization are taken into account, an attainable frequency stability of

$$\Delta f/f = \pm 2 \cdot 10^{-7}$$

can be assumed for series production without a high rejection rate. This value is practically independent of the operating temperature range.

#### Bibliography

1. Renard, A.M., Barnhill, K., Raytheon Company, "Digital Temperature Compensation of Crystal Oscillators", Proceedings of the 35th Annual Symposium on Frequency Control sponsored by the US Army Electronics Command, p. 445, 1931
2. Marianneau, G., Gagnepain, J.J., Laboratoire de Physique et Metrologie des Oscillateurs, "Digital Temperature Control for Ultrastable Quartz Oscillators", Proceedings of the 34th Annual Symposium on Frequency Control sponsored by the US Army Electronics Command, 1930
3. Tneobald, G., Marianneau, G., Pretot, R., Gagnepain, J.J., Laboratoire de Physique et Metrologie des Oscillateurs, "Dynamic Thermal Behavior of Quartz Resonators", Proceedings of the 33rd Annual Symposium on Frequency Control sponsored by the US Army Electronics Command, p. 239, 1979
4. Frerking, M.E., Rockwell International, "Crystal Oscillator Design and Temperature Compensation", Van Nostrand Reinhold Company, 1978. ISBN: 0-442-22459-1
5. Onoe, M., Yamagishi, I., Nariai, H., Institute of Industrial Science, University of Tokyo, "Temperature Compensation of Crystal Oscillator by Microcomputer", Proceedings of the 32nd Annual Symposium on Frequency Control sponsored by the US Army Electronics Command, p. 398, 1973
6. Ballato, A., USAERADCOM, "Frequency-Temperature - Load Capacitance Behavior of Resonators for TCXO Application", IEEE Trans Sonics and Ultrasonics, Vol SU-25, No.4, p. 190, July 1978
7. Ballato, A., Vig, J.R., USAERADCOM, "Static and Dynamic Frequency - Temperature Behavior of Singly and Doubly-Rotated, Oven-Controlled Quartz Resonators", Proceedings of the 32nd Annual Symposium on Frequency Control sponsored by the US Army Electronics Command, p. 180, 1973
8. Scott, P.J., Motorola Communications Group, "Design Considerations for a Digitally Temperature Compensated Crystal Oscillator", Proceedings of the 31st Annual Symposium on Frequency Control sponsored by the US Army Electronics Command, p. 407, 1977
9. Lipoff, S.J., Little, A.D., Cambridge, Massachusetts, "Design of Voltage Controlled Crystal Oscillators", Proceedings of the 30th Annual Symposium on Frequency Control sponsored by the US Army Electronics Command, p. 301, 1976
10. Mroch, A.B., Hykes, G.R., Collins Radio Group, Rockwell International, "A Miniature High Stability TCXO Using Digital Compensation", Proceedings of the 30th Annual Symposium on Frequency Control sponsored by the US Army Electronics Command, p. 292, 1976
11. Forster, H.J., Siemens AG, "Temperature Compensated Crystal Oscillators for 2 kHz to 60 MHz", Siemens Review 1975 No. 12, p. 545
12. Fujita, S., Uchida, H., Nippon Electronic Company, "An Analysis of Frequency Stability for TCXO", Proceedings of the 28th Annual Symposium on Frequency Control sponsored by the US Army Electronics Command, p. 294, 1975

13. Besson, R., "Phenomene d'hysteresis dans la deformation piezoelectrique du quartz", C.R. Acad. De. Paris, p. 279 (20 decembre 1971)
14. Hammond, D.L., Adams, C.A., Benjaminson, A., Hewlett-Packard Company, "Hysteresis Effects in Quartz Resonators", Proceedings of the 22nd Annual Symposium on Frequency Control sponsored by the US Army Electronics Command, p. 55, 1968
15. Ralston and Wilf, "Mathematical Methods for Digital Computers", Volume II, (New York, John Wiley and Sons, Inc., 1967, p. 156)
16. T.N.E. Grenville, "Theory and Applications of Spline Functions", (New York, Academic Press, 1969)

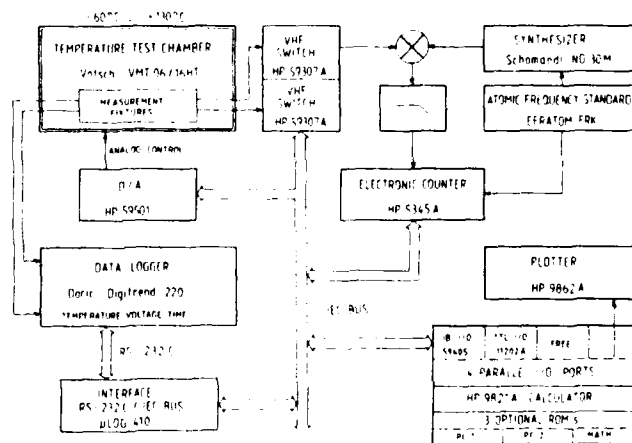


Figure 1. Versatile Temperature Test System

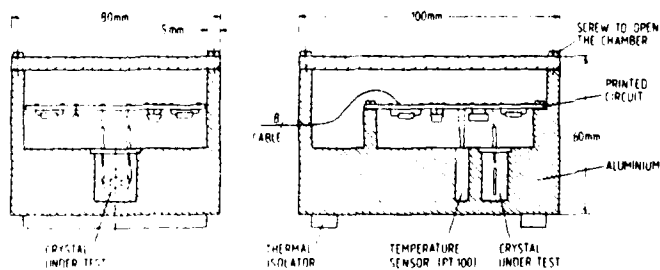


Figure 2. Measurement Fixture



Figure 3. Oscillator Circuit A

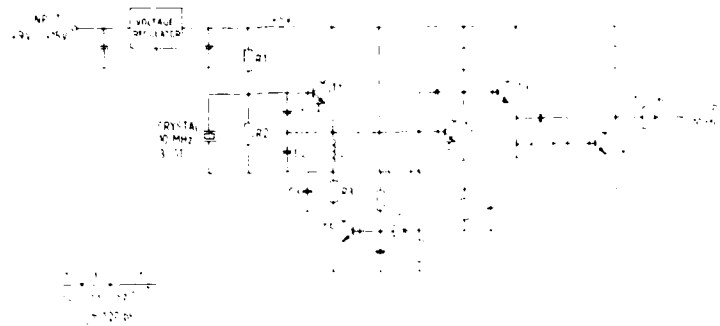


Figure 4. Oscillator Circuit B

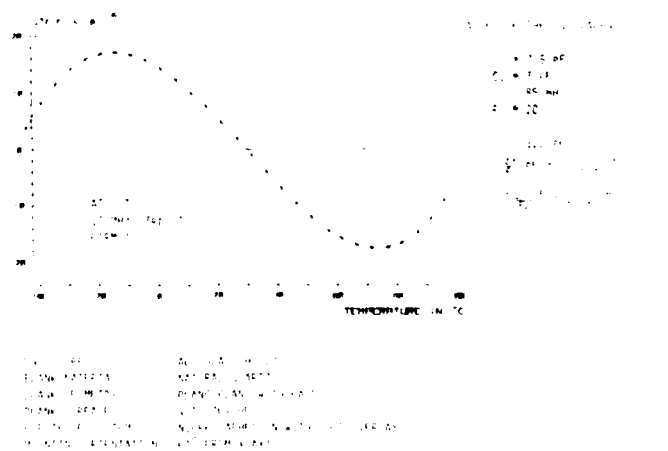


Figure 5. AT Cut 10 MHz 3rd OT Firm 1

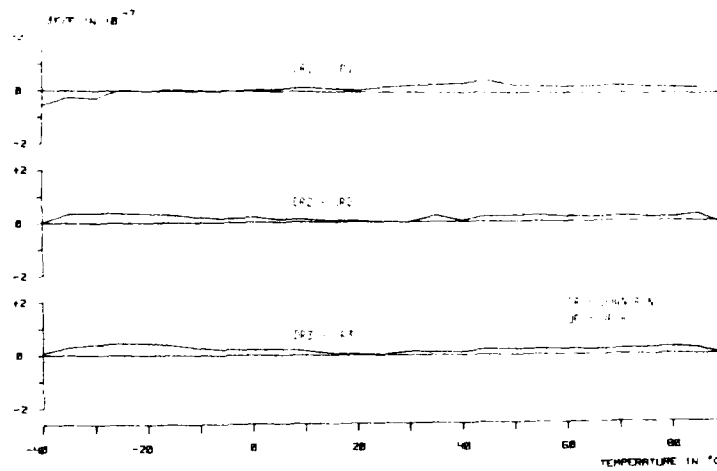


Figure 6. AT-Cut Crystal Firm 1, No. 1  
Oscillator Circuit A, Crystal Current 3 mA

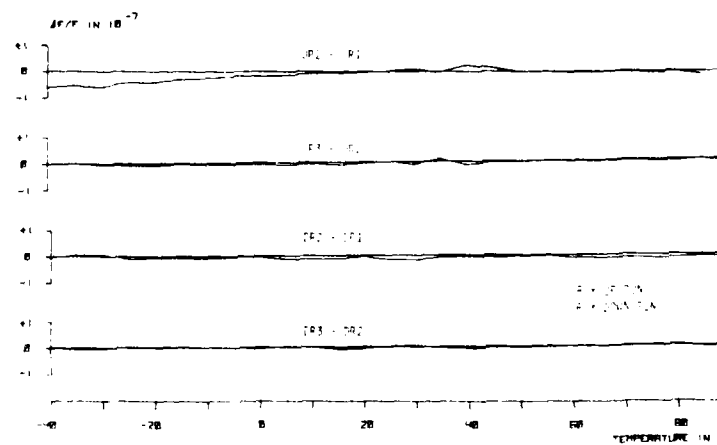


Figure 7. AT-Cut Crystal Firm 1, No. 1  
Oscillator Circuit A, Crystal Current 3 mA

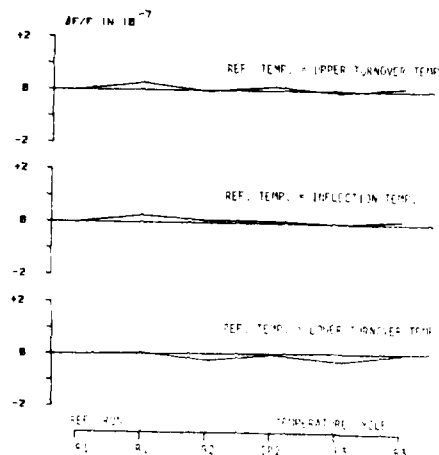


Figure 8. AT-Cut Crystal Firm 1, No. 1  
Oscillator Circuit A, Crystal Current 3 mA

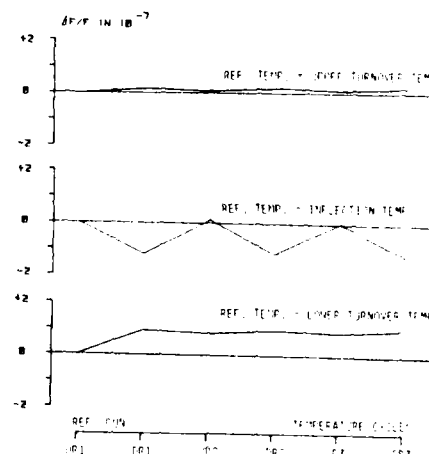


Figure 10. AT-Cut Crystal Firm 1, No. 2  
Oscillator Circuit A, Crystal Current 3 mA

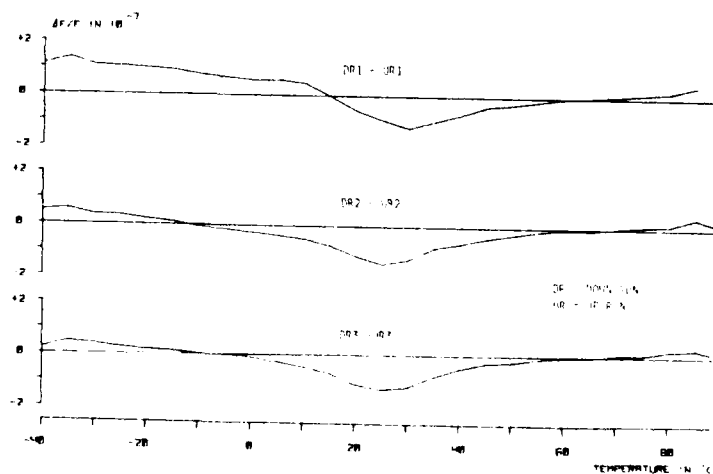


Figure 9. AT-Cut Crystal Firm 1, No. 2  
Oscillator Circuit A, Crystal Current 3 mA

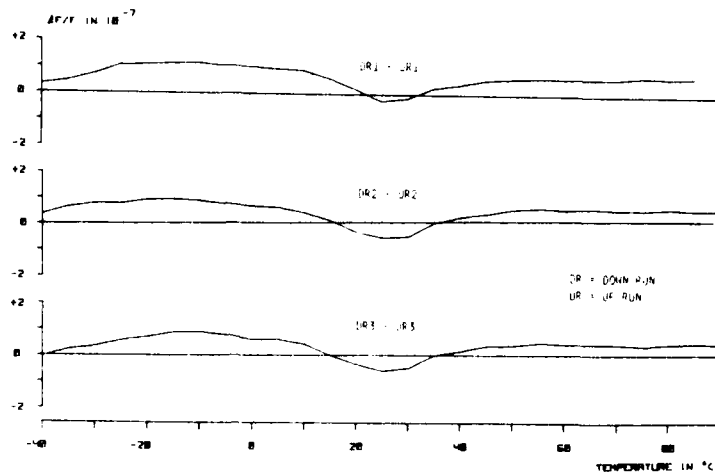


Figure 11. AT-Cut Crystal Firm 1, No. 3  
Oscillator Circuit A, Crystal Current 3 mA

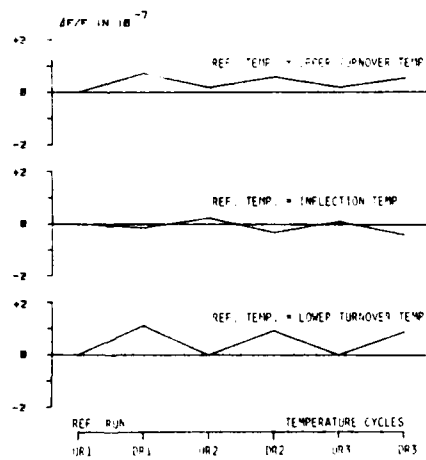


Figure 12. AT-Cut Crystal Firm 1, No. 3  
Oscillator Circuit A, Crystal Current 3 mA

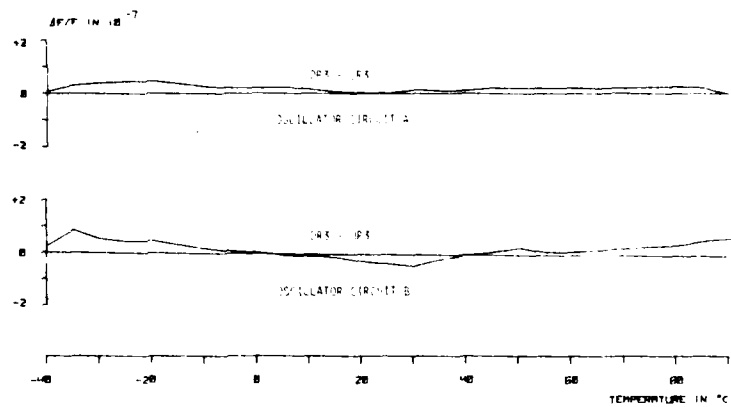


Figure 13. AT-Cut Crystal Firm 1, No. 1  
Crystal Current 3 mA

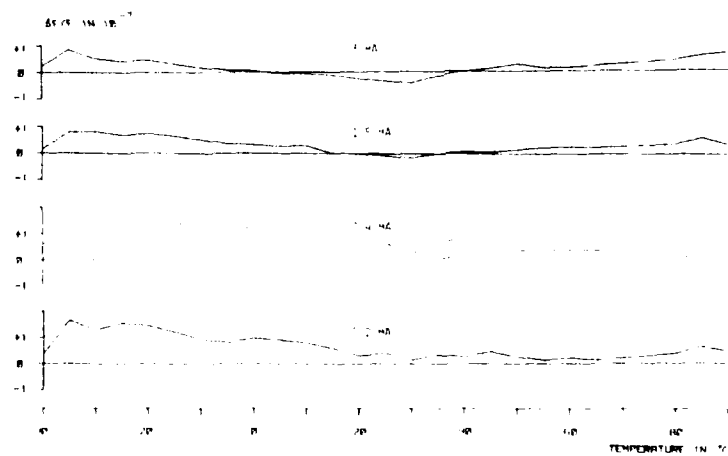


Figure 14. AT-Cut Crystal Firm 1, No. 1  
Oscillator Circuit B

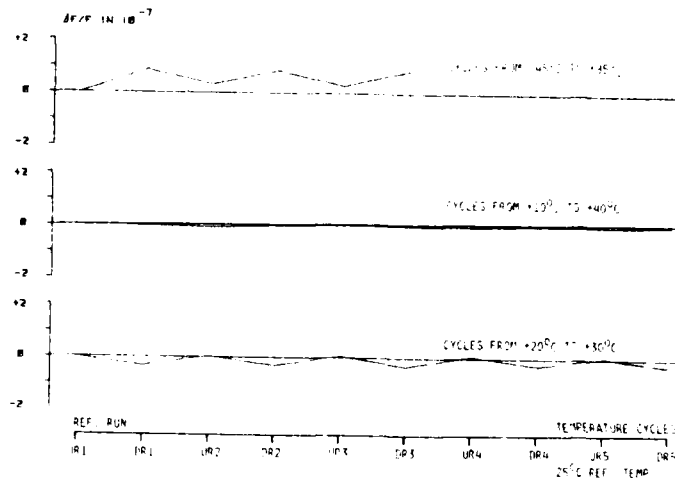


Figure 15. AT-Cut Crystal Firm 1, No. 1  
Oscillator Circuit B, Crystal Current 0.4 mA

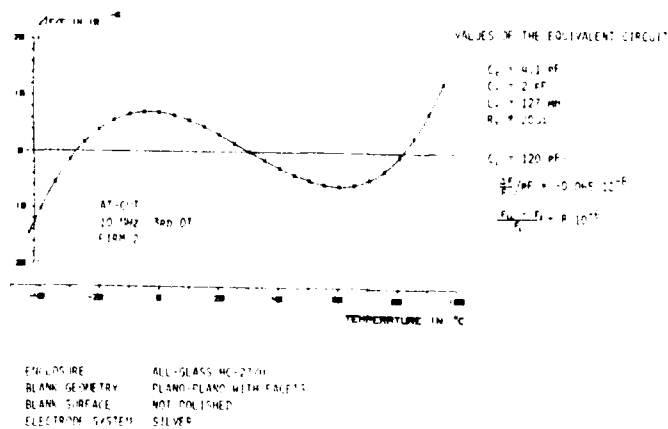


Figure 16. AT-Cut 10 MHz 3rd OT Firm 2

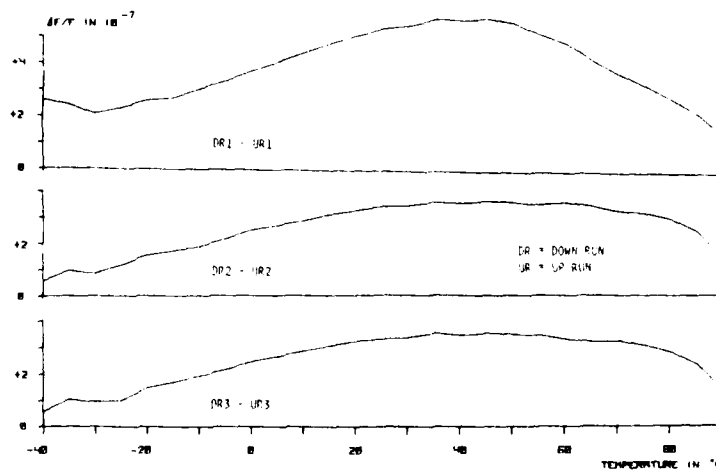
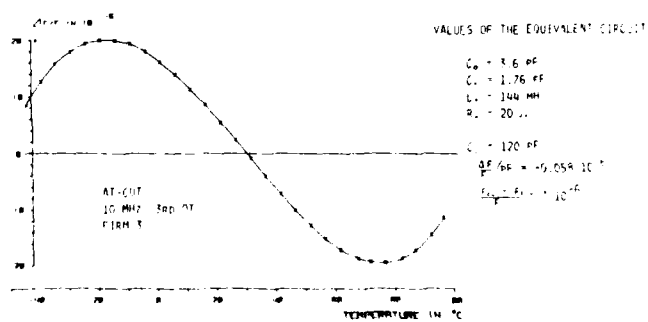


Figure 17. AT-Cut Crystal Firm 2, No. 1  
Oscillator Circuit A, Crystal Current 3 mA



ENCLOSURE: ALUMINUM HOUSING  
BLANK MATERIAL: NATURAL QUARTZ  
BLANK GEOMETRY: PLANO-PLANO WITH FACETS  
BLANK SURFACE: NOT POLISHED  
ELECTRODE SYSTEM: VOLS

Figure 18. AT-Cut 10 MHz 3rd OT Firm 3

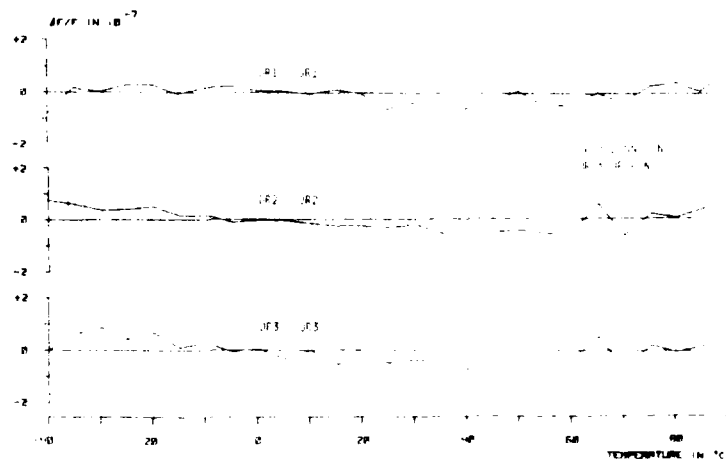


Figure 19. AT-Cut Crystal Firm 3 No. 1  
Oscillator Circuit B, Crystal Current 1.5 mA

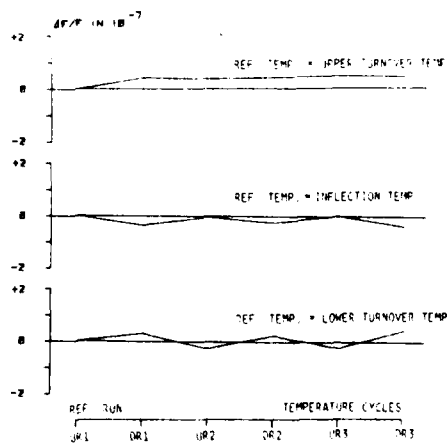


Figure 20. AT-Cut Crystal Firm 3 No. 1  
Oscillator Circuit B, Crystal Current 1.5 mA

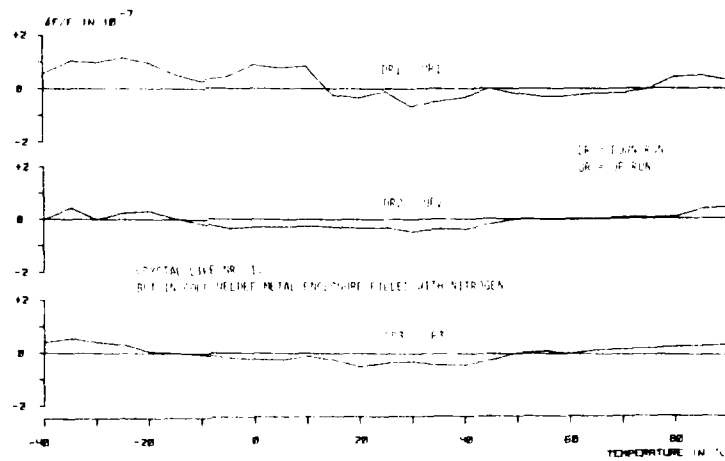


Figure 21. AT-Cut Crystal Firm 3 No. 2  
Oscillator Circuit A, Crystal Current 3 mA

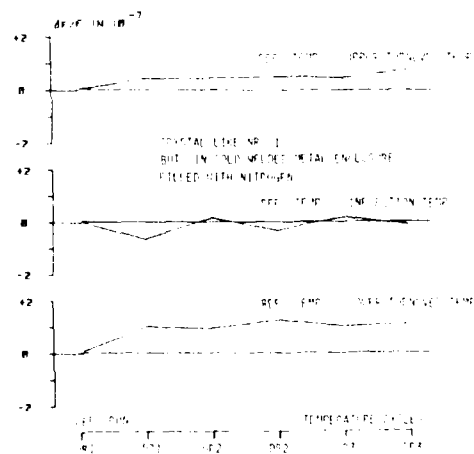


Figure 22. AT Cut Crystal Firm 3, No. 3  
Oscillator Circuit A, Crystal Current 3 mA

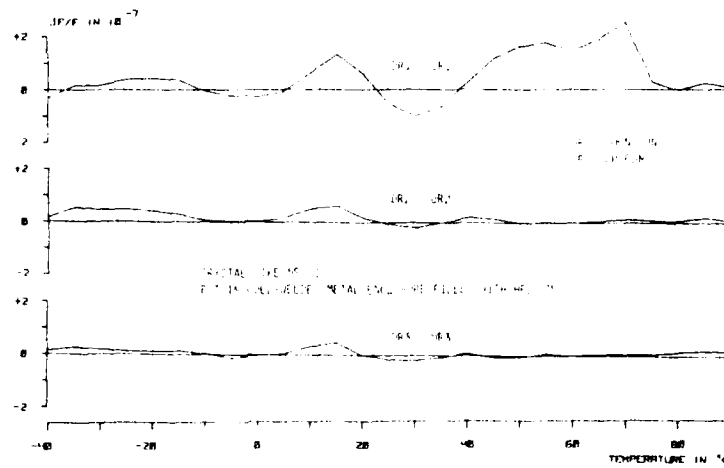


Figure 23. AT-Cut Crystal Firm 3 No. 3  
Oscillator Circuit A, Crystal Current 3 mA

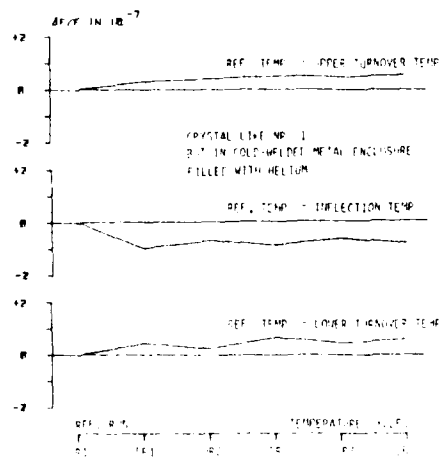
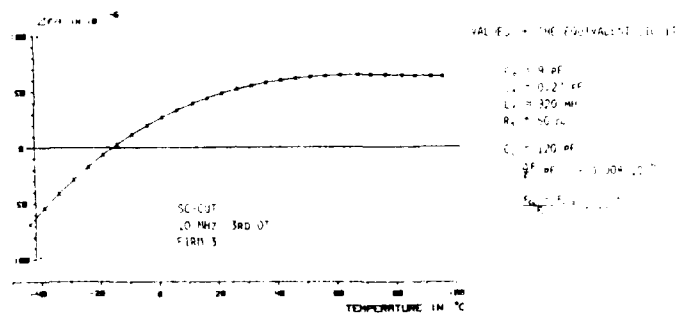


Figure 24. AT-Cut Crystal Firm 3 No. 3  
Oscillator Circuit A, Crystal Current 3 mA



ENCLOSURE METAL CAN, WELDED TO-3  
 BLANK MATERIAL NATURAL QUARTZ  
 BLANK SURFACE POLISHED  
 ELECTRODE SYSTEM WAFER

Figure 25. SC-Cut 10 MHz 3rd OT Firm 3

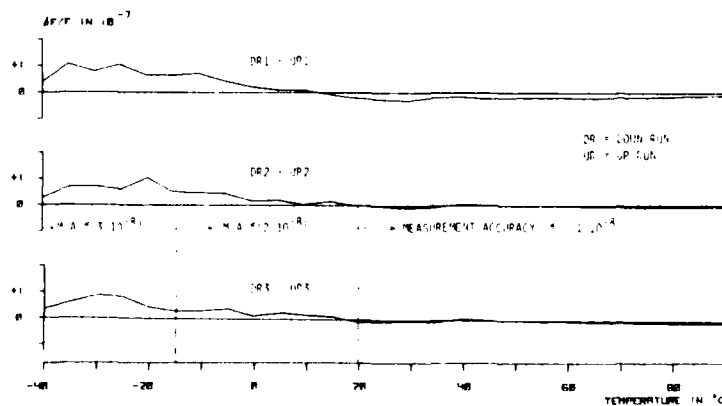


Figure 26. SC-Cut Crystal Firm 3 No. 1  
 Oscillator Circuit A, Crystal Current 2 mA

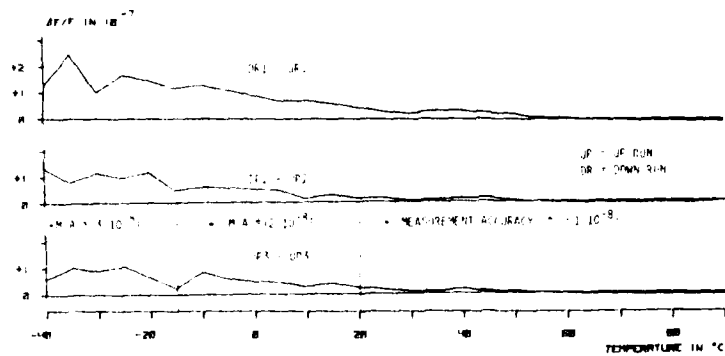
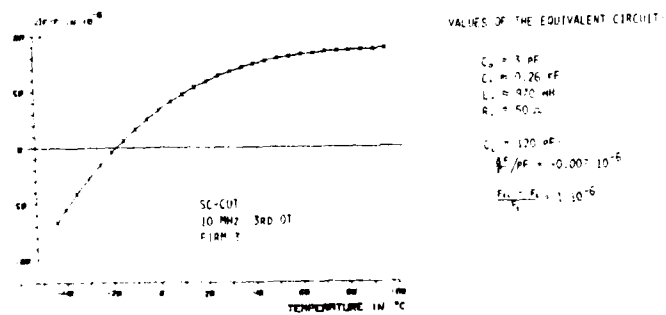


Figure 27. SC-Cut Crystal Firm 3 No. 2  
Oscillator Circuit A, Crystal Current 2 mA



OSCILLATOR: ALL-GLASS HORIZONTAL  
GLASS MATERIAL: NATURAL QUARTZ  
GLASS SURFACE: POLISHED  
ELECTRONIC SYSTEM: 100K

Figure 28. SC-Cut MHz 3rd OT Firm 3

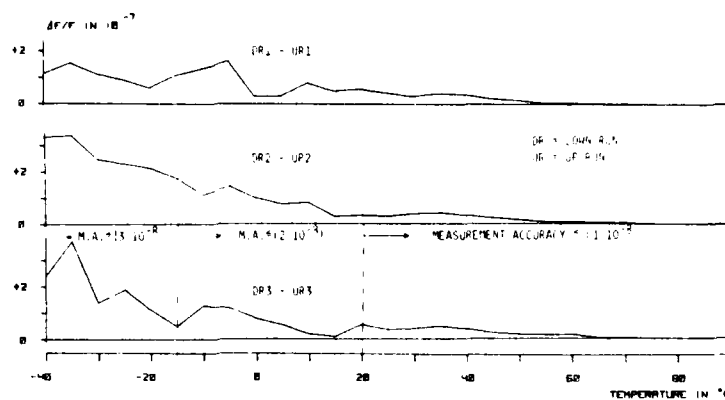


Figure 29. SC-Cut Crystal Firm 3 No. 3  
Oscillator Circuit A, Crystal Current 2 mA

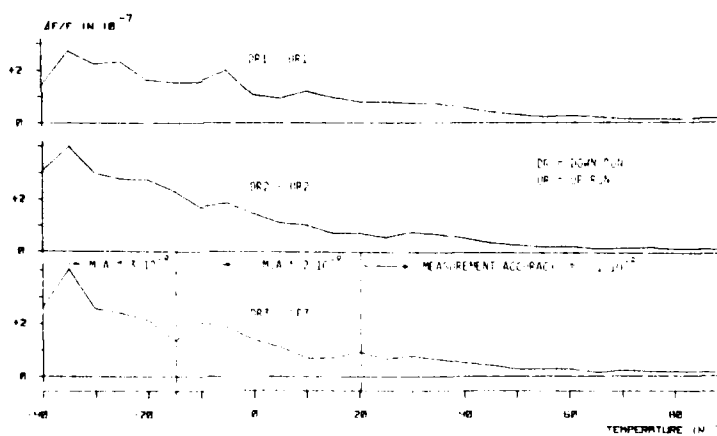


Figure 30. SC-Cut Crystal Firm 3 No. 4  
Oscillator Circuit A, Crystal Current 2 mA

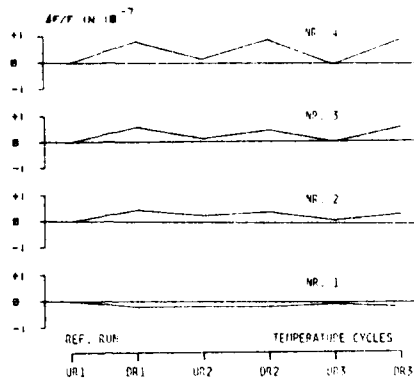


Figure 31. SC-Cut Crystal Firm 3 No. 1 to 4, 20 °C Ref. Temp.  
Oscillator Circuit A, Crystal Current 2 mA



## ELASTIC CONSTANTS OF QUARTZ AND THEIR TEMPERATURE COEFFICIENTS

Alfred Kahan

Solid State Sciences Division  
Rome Air Development Center  
Hanscom Air Force Base, MA 01731

AD P001515

Summary

The frequency and temperature dependencies of singly and doubly rotated crystal cuts are determined by the elastic, piezoelectric, and dielectric constants of the material and their temperature coefficients. We have subjected the data set from which the currently derived accepted values of these constants are derived to a least square analysis. We find extensive differences between currently listed constants and the least square derived values. The major differences occur in the elastic constants  $c_{13}$  and  $c_{33}$ . We derive a new set of temperature coefficients of elastic constants based on a data set of 100-120 experimental data points. These computations point out the need to redetermine these constants on a geometrically consistent sample set, and on a statistically significant number of doubly rotated disks and resonators.

**Key Words** Quartz, Material Properties, Elastic Constants, Crystal Resonators, Frequency Standards

Introduction

The critical performance characteristics of a crystal resonator device, frequency, electromechanical coupling, and temperature sensitivity, are determined by the elastic, piezoelectric, and dielectric constants of the material and their temperature coefficients. In this investigation we consider the influence of the material coefficients on the thickness vibrations of crystallographically doubly rotated quartz. The simplest mathematical formalism, a vibrating infinite plate with appropriate boundary conditions, relates the measured frequencies, and their temperature dependencies, to the material constants and their temperature coefficients. The set of four coupled differential equations yields a set of linear equations for the displacement and results in three eigenvalues for the phase velocities. The general formulation of this approach is outlined, for example, in Tiersten.<sup>1</sup>

For an arbitrary doubly rotated quartz cut, the vibration frequencies are determined by ten independent fundamental material constants: six elastic, two piezoelectric, and two dielectric. In turn, the vibration frequencies can be used, in conjunction with the mathematical formalism, to derive numerical values for the material proper-

ties. The derived material values are mathematical formalism dependent, and they may differ from the intrinsic constants.

For highly symmetric crystal orientations, the cubic equation for the frequency eigenvalues can be factored, and the number of material constants involved in determining the vibration frequencies are drastically reduced. In some cases the resulting frequency depends on a single elastic constant. These directions, designated as the uncoupled mode orientations, are the ones utilized most often for the experimental determination of the elastic constants.

The experimental determination of the elastic constants of quartz and their temperature coefficients has occupied many investigators over long periods of time. Cady<sup>2</sup> reviews several approaches and lists corresponding numerical values. This work is a corrected reprint of the classic treatise published on the subject of piezoelectricity in 1946, and the listed values are the ones accepted in 1946. Currently, the most widely accepted elastic constant values are the ones determined by McSkimin<sup>3</sup>, and independently by Bechmann, Ballato, and Lukaszek.<sup>4</sup> [This reference is hereafter abbreviated as BBL(1962)]. The most widely accepted values for the temperature coefficients of the elastic constants are again given by BBL(1962). The elastic constants are in general agreement with previous investigations, but the BBL(1962) derived temperature coefficients contain several novel determinations.

We have applied a least square analysis to the BBL(1962) data set and we find major discrepancies between the listed values and the least square fit derived constants. This raises serious questions with respect to the validity of the material values, and their applicability to crystallographically doubly rotated piezoelectrically excited resonators.

Thickness Vibrations of Quartz

Figure 1 depicts the plate geometry and crystallographic coordinate system used in this investigation.  $x_1$  and  $x_3$  are in the plane of the plate, and the phase velocity propagates along  $x_2$ , normal to the plate. The position of the plate is described by angles  $(\psi, \theta)$ , where  $\psi$  and  $\theta$  are rotations around the  $z$ - and  $x$ -axis, respectively.

Tiersten<sup>1</sup> has formulated the general mathematical equations for anisotropic, piezoelectric, infinite plate vibrating in the thickness mode, with a forcing alternating voltage and vanishing mechanical stresses at the plate surfaces  $x_2 = \pm h$ . Based on this formulation, we have developed explicit mathematical expressions for the frequencies of doubly rotated quartz. These equations are derived in Reference 5 and are summarized in this Section.

The solution of the linear differential equations yields a cubic algebraic equation for the three eigenvalues  $\Gamma$ ,

$$\Gamma^3 + A_2 \Gamma^2 + A_1 \Gamma + A_0 = 0 \quad (1)$$

The three real eigenvalues  $\Gamma^1$ ,  $l = 1, 2, 3$ , designate the three modes of vibrations. These are related to the phase velocity  $v^1$  and density  $\rho$ , by

$$\Gamma^1 = \rho (v^1)^2 \quad (2)$$

The coefficients of the cubic equation are defined in terms of the "stiffened" elastic constants  $\Gamma_{pq}$

$$A_2 = -(\Gamma_{22} + \Gamma_{44} + \Gamma_{66}) \quad (3)$$

$$A_1 = (\Gamma_{22} \Gamma_{44} - \Gamma_{24}^2) + (\Gamma_{22} \Gamma_{66} - \Gamma_{26}^2) + (\Gamma_{44} \Gamma_{66} - \Gamma_{46}^2) \quad (4)$$

$$A_0 = \Gamma_{22} \Gamma_{44} \Gamma_{66} - 2 \Gamma_{24} \Gamma_{26} \Gamma_{46} - \Gamma_{22} \Gamma_{44} \Gamma_{66} - 2 \Gamma_{24} \Gamma_{26} \Gamma_{46} \quad (5)$$

Table I lists for any arbitrary rotation angles  $\phi$  and  $\theta$ , the appropriate "stiffened" elastic constants in terms of the 6 fundamental elastic constants  $c_{pq}$ , 2 piezoelectric constants  $e_{ip}$ , and 2 dielectric constants  $\epsilon_{ij}$ . The angular range extends over  $0 < \phi < 60^\circ$  and  $0 < \theta < 90^\circ$ .

The calculation of the electromechanical coupling factor includes both the eigenvalues and the eigenvectors. Other eigenvector dependent field quantities include, stress, strain, electric displacement, and power density. Explicit formulas for the field quantities in terms of the eigenvectors are given by Slobodnik, Delmonico, and Conway.<sup>6</sup> A particular set of eigenvectors which avoids most of the computational difficulties encountered with degeneracies is given by

$$\beta^1 = (s^1)^{-1/2} \begin{Bmatrix} A_3^1 \\ A_4^1 \\ A_5^1 \end{Bmatrix} \quad (6)$$

where

$$A_3^1 = (\Gamma_{22} - \Gamma_{26} - \Gamma^1) (\Gamma_{44} - \Gamma_{46} - \Gamma^1) - (\Gamma_{24} - \Gamma_{26}) (\Gamma_{24} - \Gamma_{46}) \quad (7)$$

$$A_4^1 = (\Gamma_{44} - \Gamma_{24} - \Gamma^1) (\Gamma_{66} - \Gamma_{26} - \Gamma^1) - (\Gamma_{46} - \Gamma_{24}) (\Gamma_{46} - \Gamma_{26}) \quad (8)$$

Table I. Rotated and Crystal Axes Referred Material Constants for Quartz

$$\begin{aligned} \Gamma_{22} &= [c_{11} + (e_{11}^2/\epsilon) \sin^2 \phi] \cos^4 \theta + c_{33} \sin^4 \theta \\ &\quad + (c_{13}/2 + c_{44}) \sin^2 2\theta - 2c_{14} \sin 2\theta \cos^2 \theta \cos 3\phi \\ \Gamma_{44} &= c_{44} \cos^2 2\theta + (1/2)c_{14} \sin 4\theta \cos 3\phi \\ &\quad + (1/4)[c_{11} + (e_{11}^2/\epsilon) \sin^2 \phi - 2c_{13} + c_{33}] \sin^2 2\theta \\ \Gamma_{66} &= [c_{66} + (e_{11}^2/\epsilon) \cos^2 3\phi] \cos^2 \theta + (c_{44} + e_{14}^2/\epsilon) \sin^2 \theta \\ &\quad + (c_{14} + e_{11}e_{14}/\epsilon) \sin 2\theta \cos 3\phi \\ \Gamma_{24} &= \cos \theta \{ \sin \theta [-c_{11} + (e_{11}^2/\epsilon) \sin^2 \phi] \cos^2 \theta \\ &\quad + (c_{13} + 2c_{44}) \cos 2\theta + c_{33} \sin^2 \theta \} \\ &\quad - c_{14} \cos 3\phi \cos 3\theta \\ \Gamma_{26} &= -\sin 3\phi \cos^2 \theta [(3c_{14} + e_{11}e_{14}/\epsilon) \sin \theta \\ &\quad + (e_{11}^2/\epsilon) \cos 3\phi \cos \theta] \\ \Gamma_{46} &= \sin 3\phi \cos \theta [(3\sin^2 \theta - 1)c_{14} + (e_{11}e_{14}/\epsilon) \sin^2 \theta \\ &\quad + (1/2)(e_{11}^2/\epsilon) \cos 3\phi \sin 2\theta] \end{aligned}$$

$$\text{where } \epsilon = \epsilon_{11} + \epsilon_{33} \tan^2 \theta$$

$$e'_{22} = e_{11} \cos^2 \theta + e_{33} \sin^2 \theta$$

$$e'_{22} = e_{11} \sin 3\phi \cos^3 \theta$$

$$e'_{24} = -e_{11} \sin 3\phi \sin \theta \cos^2 \theta$$

$$e'_{26} = -\cos \theta (e_{11} \cos 3\phi \cos \theta + e_{14} \sin \theta)$$

$$A_5^1 = (\Gamma_{66} - \Gamma_{46} - \Gamma^1) (\Gamma_{22} - \Gamma_{24} - \Gamma^1) - (\Gamma_{26} - \Gamma_{46}) (\Gamma_{26} - \Gamma_{24}) \quad (9)$$

and the normalization length is

$$s^1 = (A_3^1)^2 + (A_4^1)^2 + (A_5^1)^2 \quad (10)$$

For a particular eigenvalue  $\Gamma^1$ , the electromechanical coupling factor becomes

$$k^1 = (e_{26}^1 A_3^1 + e_{22}^1 A_4^1 + e_{24}^1 A_5^1) / (\epsilon_{22}^1 \Gamma^1 s^1)^{1/2} \quad (11)$$

Explicit expressions for the rotated piezoelectric and dielectric constants are also listed in Table I.

In the single mode excitation approximation, the short-circuit resonance frequency equation becomes uncoupled, and the  $l$ th mode  $m$ th overtone eigenfrequency, after neglecting higher order terms, becomes

$$\omega_m^1 = 2\pi f_m^1 = (1/2h) m\pi v^1 [1 - 4(k^1)^2/m^2\pi^2] \quad (12)$$

We note that even for single mode excitation and linear approximation, the overtone frequencies are not harmonic integral multiples of the fundamental, but are modified by the electromechanical coupling factor.

For quartz, the maximum value of  $k$  is approximately 0.15, and the  $(1-4k^2/m^2\pi^2)$  term becomes 0.992. Consequently, for all practical purposes we can neglect this correction and introduce a zeroth order approximation for the  $l$ th mode frequency, as

$$2hf_m = mv/2 = (m/2)(\Gamma/\rho)^{1/2} \quad (13)$$

where  $2hf_m$  is the frequency-thickness constant. This frequency relationship, usually designated as the antiresonance frequency, is the one used to develop expressions for the temperature coefficients.

#### Static Frequency-Temperature Characteristics

In a series of experiments, Bechmann, Ballato, and Lukaszek<sup>4,7,8</sup> have evaluated the static frequency as a function of temperature characteristics of quartz resonators in the temperature range of -200 to +200 °C. They have shown that the behavior can be modeled well by a cubic equation in the form

$$\Delta f/f_0 = (f-f_0)/f_0 = \sum_{n=1}^3 T_n(f)(T-T_0)^n \quad (14)$$

where  $T_n(f)$  is the temperature coefficient of frequency,  $T$  the variable temperature, and  $f_0$  the frequency at reference temperature  $T_0$ . In most applications, the series is expanded around reference temperature  $T_0 = 25$  °C.

The task is to develop equations relating the 1st, 2nd, and 3rd order temperature coefficients of frequency to the fundamental material constants and their temperature coefficients. The resulting equations are lengthy, but straightforward. The detailed derivations, and explicit algebraic expressions for these quantities, are given in Reference 9. For given  $(\phi, \theta)$ ,  $c_{pq}$ , and  $T_n(c_{pq})$ , one successively calculates  $T_n(\Gamma_{pq})$ ,  $T_n(\Lambda_m)$ ,  $T_n(\Gamma)$ ,  $T_n(\rho)$ ,  $T_n(h)$ , and  $T_n(f)$ . Alternately, using the same mathematical formalism and a data fitting program, one can derive the temperature coefficients of the elastic constants,  $T_n(c_{pq})$ , from sets of  $T_n(f)$ .

#### Uncoupled Mode Vibrations

The eigenvalue equation, Eq. (1), can also be written as

$$\begin{aligned} &(\Gamma_{22} - \Gamma)(\Gamma_{44} - \Gamma)(\Gamma_{66} - \Gamma) \\ &- \Gamma_{46}(\Gamma_{22} - \Gamma) - \Gamma_{26}(\Gamma_{44} - \Gamma) \\ &- \Gamma_{24}(\Gamma_{66} - \Gamma) - 2\Gamma_{24}\Gamma_{26}\Gamma_{46} = 0 \end{aligned} \quad (15)$$

When any two of the three off-diagonal matrix elements  $\Gamma_{24}$ ,  $\Gamma_{26}$ , and  $\Gamma_{46}$ , vanish, the equation factors into a linear and quadratic term in  $\Gamma$ . The  $(\phi, \theta)$  combinations that satisfy  $\Gamma_{pq} = 0$ , can be evaluated from the expressions given in

Table I. Figure 2 is a plot of these solutions using the material constants given in BBL(1962). In Figure 2, the overlapping curves at  $\phi = 0$  and  $60^\circ$  and at  $\theta = 90^\circ$  are displaced for clarity.

We note that  $\Gamma_{24} = 0$  is satisfied by  $(\phi, \theta)^\circ$ , that is for any  $\phi$  at  $\theta = 90^\circ$ . It is also satisfied by a continuous function between  $\phi = 0$  and  $60^\circ$ , with end points  $(0, 40.8)^\circ$  and  $(60, 72.4)^\circ$ , and by a third branch continuous between  $(30, 0)^\circ$  and  $(60, 17.7)^\circ$ .

$\Gamma_{26} = 0$  is satisfied by any  $\theta$  at  $\phi = 0$  and  $60^\circ$ , and for any  $\phi$  at  $\theta = 90^\circ$ , that is,  $(0, \theta)^\circ$ ,  $(60, \theta)^\circ$ , and  $(\phi, 90)^\circ$ . In addition, the bracketed term of  $\Gamma_{26}$  yields a slowly varying function, symmetric around  $(30, 0)^\circ$  and increasing to  $\theta = 0.8^\circ$  at  $\phi = 0$  and  $60^\circ$ . The deviation from  $(\phi, 0)^\circ$  is due to small contribution of the piezoelectric constants.

$\Gamma_{46} = 0$  has solutions  $(0, \theta)^\circ$ ,  $(60, \theta)^\circ$ , and  $(\phi, 90)^\circ$ . The bracketed term yields a continuous function between  $(0, 35.48)^\circ$  and  $(60, 34.94)^\circ$ . The small variations in  $\theta$  are again due to piezoelectric effects. If we neglect piezoelectric effects we obtain  $(\phi, 35.26)^\circ$ , which is exactly the AT-cut angle. It is uncertain whether this is a pure coincidence, or is a contributing factor in determining the position of the AT-cut.

The overlap, or intersection, of two or three solutions of  $\Gamma_{pq} = 0$  gives the uncoupled modes of vibration. From the diagram depicted in Figure 2, these directions are given by  $(0, \theta)^\circ$ ,  $(60, \theta)^\circ$ ,  $(\phi, 90)^\circ$ , and  $(30, 0)^\circ$ . One of the problems associated with the preferred directions is that the piezoelectrically "stiffened" elastic constant may no longer be "stiffened", has no piezoelectric coupling, and it can not be excited by piezoelectric means. An inspection of Table I shows that for  $\Gamma_{22}$ ,  $\Gamma_{44}$ , and  $\Gamma_{24}$ , the piezoelectric constant is multiplied by a  $\sin^2\phi$  factor, which vanishes both at  $\phi = 0$  and  $60^\circ$ . Thus at  $(0, \theta)^\circ$  and  $(60, \theta)^\circ$  two of the modes are piezoelectrically inactive, and at  $(\phi, 90)^\circ$  none of the modes can be excited by an alternating voltage applied to the electrodes.

McSkimin<sup>3</sup> has evaluated the elastic constants from ultrasonic excitation. He selected  $(0, 0)^\circ$ ,  $(0, 90)^\circ$ , and  $(30, 0)^\circ$ . At these points, the three modes of vibrations reduce to the values listed in Table II. The choice of  $(0, 90)^\circ$  is not unique. Any  $(\phi, 90)^\circ$  will give a doubly degenerate  $\Gamma^{(1)} = \Gamma^{(2)} = c_{44}$  and  $\Gamma^{(3)} = c_{33}$ . Similarly,  $(0, 0)^\circ$  and  $(60, 0)^\circ$  yield identical values. From the angular orientation chosen by McSkimin one can evaluate  $c_{11}/c_{11}$  and all elastic constants except  $c_{13}$ . The determination of  $c_{13}$  involves four other elastic constants, and, depending on accumulation or cancellation of experimental errors, may be the least accurate. By the same token,  $c_{33}$  and  $c_{44}$  should be very accurate. For  $c_{13}$  McSkimin chose  $(0, 45)^\circ$ , at which point

$$\begin{aligned} c_{13} = & (c_{14} - c_{44}) \\ & + [(2\Gamma - (c_{33} + c_{44}))/2\Gamma - (c_{11} - 2c_{14} + c_{44})]^{1/2} \end{aligned} \quad (16)$$

Table II. Eigenvalues  $\Gamma^{(1)}$  for Highly Symmetric  $(\phi, \theta)$  Orientations

$(\phi, \theta)$	$\Gamma^{(1)}; \Gamma^{(2)}$	$\Gamma^{(3)}$
$(0,0)$ and $(60,0)$	$(1/2) \{ (c_{11} + c_{44}) \pm [(c_{11} - c_{44})^2 + 4c_{14}^2]^{1/2} \}$	$c_{66} + e_{11}^2/\epsilon_{11}$
$(\phi, 90)$	$c_{44}$	$c_{33}$
$(30,0)$	$(1/2) \{ (c_{44} + c_{66}) \pm [(c_{44} - c_{66})^2 + 4c_{14}^2]^{1/2} \}$	$c_{11} + e_{11}^2/\epsilon_{11}$

but any other angular orientation will result in similar complexity.

If one is restricted to determine the material parameters from piezoelectric excitation, for example, from frequencies derived from resonators or disks in dielectric gap holders, the key equation determining the angular cuts is

$$\begin{aligned} \Gamma^{(3)}(0, \theta); \Gamma^{(3)}(60, \theta) = \\ (c_{66} + e_{11}^2/\epsilon) \cos^2 \theta + (c_{44} + e_{14}^2/\epsilon) \sin^2 \theta \\ \pm (c_{14} + e_{11}e_{14}/\epsilon) \sin 2\theta \end{aligned} \quad (17)$$

where the plus sign applies to  $\phi = 0$ , and the minus sign to  $\phi = 60^\circ$ . The proper selection of  $\theta$  at  $\phi = 0$  and  $60^\circ$  will yield  $c_{14}$ ,  $c_{44}$ ,  $c_{66}$ , the piezoelectric, and the dielectric constants. It is especially important to have identical  $\theta$ -angle cuts for both  $\phi = 0$  and  $60^\circ$ . This allows simplifications in terms of  $\Gamma^{(3)}(0, \theta) \pm \Gamma^{(3)}(60, \theta)$ . As before,  $c_{11}$  is determined from  $(30,0)^\circ$ , but neither  $c_{13}$  nor  $c_{33}$  are accessible to uncoupled mode piezoelectric excitation.

#### Experimental Values of Elastic Constants

The most widely accepted  $c_{pq}$  values are the ones derived by McSkimin<sup>3</sup>, and independently by BBL (1962) and these are in general agreement with previous investigations. McSkimin applied ultrasonic excitation to bulk crystals along the uncoupled directions, whereas BBL(1962) utilized piezoelectric excitation and doubly rotated crystal disks in a resonator configuration. Both investigators used the same mathematical description to relate experimental wave velocities to  $c_{pq}$ . Table III, under the heading "Observed", lists the experimental data set of both investigations, and Table IV lists the derived elastic coefficients. The differences between the McSkimin and BBL derived values are small, and either set can be used equally well to calculate appropriate quantities of interest.

Table III, under the heading "BBL(1962)", lists three sets of calculated values. The first column is taken from BBL(1962) and the second column, listed under "This Work I", is calculated in this investigation, using the BBL(1962) derived constants. The slight differences in values

are due to the fact that the BBL calculations use a "semi-stiffened" elastic constant,

$$\Gamma_{pq} = (c_{pq} + e_{2p}e_{2q}/\epsilon_{22})'$$

rather than the rigorous definition

$$\Gamma_{pq} = c_{pq}' + e_{2p}e_{2q}'/\epsilon_{22}'$$

McSkimin<sup>10</sup> et. al. have applied a least square minimization fit to the experimental data, and the derived  $c_{pq}$  values in Table IV are the result of this analysis. They minimized the variance

$$\sigma^2 = (1/m) \sum_{i=1}^m G_i (Z_{\text{exp}} - Z_{\text{cal}})_i^2 \quad (18)$$

where  $Z$  stands either for the elastic constants or the respective temperature coefficients, and the summation is over the number of experimental points  $m$ . The weighing factor  $G_i$  can be taken either as  $G_i = 1$  or as  $G_i = 1/Z_{\text{exp}}^2$ . If the experimental points are equally reliable on an absolute basis, then  $G_i = 1$  is the appropriate choice. In case the experimental points are equally valid on a percentage basis, then one chooses  $G_i = 1/Z_{\text{exp}}^2$ . For this data set, the differences between the two approaches are insignificant, but for consistency with the least square fit for the temperature coefficients, where one is forced to choose  $G_i = 1$ , we also select  $G_i = 1$  for the elastic constants.

The variances for the various calculations are listed at the bottom of Table III. The experimental and calculated velocity values listed in Table III are rounded off to the nearest integer, whereas the computations were carried out to the appropriate number of decimal places. Hence, there are small differences between the listed variances, and ones computed based on listed velocities. The close agreement between experimental and calculated velocities for the McSkimin data, as reflected in  $\sigma^2 = 0.5$ , is not surprising. McSkimin used 10 of the 11 test points to derive 6  $c_{pq}$  values and  $e_{11}^2/\epsilon_{11}$ , and one does expect a close fit. It is more questionable whether 7 fitting parameters and 10 data points constitute a statistically significant set, especially, if these points are chosen along the uncoupled directions.

The variances of the BBL data set, using the BBL(1962) derived material constants, is listed in Table III as  $\sigma^2 = 7186$ . BBL(1962) have not performed a least square analysis to their 14 point data set, and from their publication it is unclear how the listed  $c_{pq}$  values were derived. We have subjected the BBL data set to a least square minimization routine, and the results of the best fit to the experimental data, are listed in Table III under "This Work II" and in Table IV under "This Work". We note that the least square fit analysis reduces the initial  $\sigma^2 = 7186$  to  $\sigma^2 = 2198$ , with corresponding differences in  $c_{pq}$ . The major  $c_{pq}$  changes occur in  $c_{13}$  and  $c_{33}$ , the two constants not accessible to uncoupled mode piezoelectric excitation.

Table III. Measured and Calculated Velocities For Doubly Rotated Quartz Orientations

Orientation Angles $\varphi$ $\theta$		Mode	Velocity Data (m/sec)					
			BBL (1962)				McSkimin, Ref. 3	
			Obs.	Calculated		Obs.	Calc.	
BBL	This Work	I		II				
0	0	a(Y)					6006	6005
0	0	b(Y)					4323	4322
0	0	c(Y)	3892	3914	3915	3901	3918	3917
0	35°15'	c(AT)	3320	3320	3322	3246		
0	45	a					7121	7021
0	45	b					3981	3981
0	45	c					3427	3427
0	90	a					6319	6319
0	90	b,c					4687	4688
20	34°20'	c(IT)	3386	3566	3551	3467		
30	0	a(X)	5690	5746	5746	5643	5749	5749
30	0	b(X)					5114	5114
30	0	c(X)					3298	3298
30	10	a	5780	5960	5956	5830		
30	30	b	4096	4100	4097	4104		
45	34.5	c(RT)	4080	4094	4080	4117		
45	35	b	4416	4540	4533	4417		
47.5	33	c	4202	4176	4162	4205		
50	32	c	4212	4240	4223	4271		
50	33	c	4316	4200	4183	4228		
50	38	b	4694	4776	4767	4684		
55	47	b	5038	5030	5021	5004		
60	49°13'	b(BT)	5080	5060	5072	5089		
Number of test points			14				11	
Least Square Fit Variance			7570    7186    2198				0.5	

Table IV. Elastic Constants of Quartz

pq	Elastic Constants $c_{pq}$ in units of $10^9$ N/m <sup>2</sup>		
	McSkimin	BBL (1962) data	This Work
11	86.80	86.74	83.53
13	11.91	11.91	- 0.88
14	-18.04	-17.91	-18.88
33	105.75	107.2	77.60
44	58.20	57.94	57.32
66	39.88	39.88	39.58

The large differences in  $c_{33}$  is disturbing. This constant, as indicated in Table II, is the easiest to determine by non-piezoelectric means from  $(\varphi, \theta)$  and it should be the most accurate. Yet, it shows the largest variation when computed from an arbitrary, crystallographically doubly rotated, piezoelectrically excited resonator set. At the same time,  $c_{44}$ , computed by the same technique from  $(\varphi, 90)$ , does agree very well.

We performed several computational efforts trying to improve the BBL(1962) data fit. One included the assumption that one of the 14 test points is inaccurate. We systematically neglected one test point at a time and re-fitted the data. There were some improvements, but none of them dramatic. The best initial 13 point data fit is ob-

tained by omitting  $(30, 0)^\circ$ , with the variance reduced to  $\sigma^2 = 5363$ , and the best final fit is obtained by neglecting the AT-cut  $(0, 35.25)^\circ$ , with  $\sigma^2 = 1360$ . However, the AT-cut is exactly the point that BBL(1962) assumes to be in perfect coincidence. Another supposition was that BBL(1962) has mislabeled one of the modes. The mode assignment of each test point was changed, one at the time, and the data re-fitted. In all cases the initial  $\sigma^2 = 7186$  value increased, confirming the accuracy of the BBL(1962) mode assignment.

There is another BBL data set<sup>7</sup>, designated as BBL(1961), consisting of 17 rotations with 47 test points. Some test points of the two sets are identical, and some are listed in BBL(1962) with slightly different  $\varphi$ -angles. Also, all  $(\varphi, \theta)$  combinations of this data set are given as integers, without any error bars, a highly unrealistic situation. Nevertheless, we have performed a least square minimization of the 47 test points and the initial  $\sigma^2 = 5840$  can be reduced to  $\sigma^2 = 2903$ , the same order of magnitude as the BBL(1962) data fit. The  $c_{pq}$  values for this fit, in units of  $10^9$  N/m<sup>2</sup>, are:  $c_{11} = 86.3$ ,  $c_{13} = 6.8$ ,  $c_{14} = -17.1$ ,  $c_{33} = 90.3$ ,  $c_{44} = 66.0$ , and  $c_{66} = 32.2$ .

We are confronted with two issues: (1) the validity of the BBL(1962) determined  $c_{pq}$  owing to the large variance associated with the data set,

and (2) that the number of points, 14, used to derive the least square fit  $c_{pq}$  set in this investigation, are still statistically insignificant. Consequently, despite the reduced variance, there is no assurance that this  $c_{pq}$  set gives a more realistic prediction of the frequencies of doubly rotated cuts. The BBL(1962)  $c_{pq}$  values, confirmed by independent measurements by McSkimin, are in general agreement with previous data accumulated by many investigators over the last 50-70 years. However, all previous investigations utilized uncoupled mode orientations, and, to the best of our knowledge, BBL(1962) was the first group trying to derive  $c_{pq}$  from widely rotated ( $\phi, \theta$ ) cuts. Thus, despite all the reservations, one is forced, at the present time, to retain and accept BBL(1962), or McSkimin,  $c_{pq}$  values. In this context, the least square fit derived  $c_{pq}$ , listed in Table IV, can be regarded as an indication that despite all previous work on this subject, it is essential that new experimental investigations be conducted to determine the intrinsic elastic constants of quartz.

#### Temperature Coefficients of the Elastic Constants

##### BBL(1962)

BBL(1962) derived the temperature coefficients of the elastic constants,  $T_n(c_{pq})$ , from a set of 23-24 crystallographically doubly rotated resonators. The coefficients were obtained by fitting the frequency-temperature curves in the -200 to +200 °C range by the cubic  $T_n(f)(T-T_0)^n$  relationship. The values derived from this data set is listed in Table V as BBL(1962). The mathematical formalism used by BBL to relate  $T_n(c_{pq})$  to  $T_n(f)$ , with the exception of a slight variation in the  $T_n(\rho)$  term, is the same as used in this investigation. The differences involve small contributions of cross terms in  $T_2(\rho)$  and  $T_3(\rho)$ , and are discussed in Reference 9. However, the methodology used by BBL(1962) to derive the six  $T_n(c_{pq})$  from the 23 experimental points is unclear. It seems, that rather than using all 23 points to compute the six values, they have utilized selected data points to derive specific values and have neglected the statistical influence of the other data points.

We have applied a least square fit analysis to the BBL(1962) data set, and the results are listed in Table V under the heading "BBL(1962) L.S.F.". The corresponding variances, Eq. (18), are listed in Table VI. We note that the largest variations in  $T_1(c_{pq})$  occur in  $T_1(c_{13})$ , and  $T_1(c_{33})$ , and that the variances are reduced from  $8.9 \times 10^{-12}/^\circ\text{C}^2$  to  $2.4 \times 10^{-12}/^\circ\text{C}^2$ . Similar order of magnitude variance reductions occur for the higher order temperature coefficients.

For all temperature coefficient calculations we used the BBL(1962)  $c_{pq}$  values listed in Table IV. The 14 data points used by BBL to derive  $c_{pq}$  are part of the 24 points utilized for the temperature coefficients. The frequency data for the additional 10 points are not listed, and they could not be included to re-determine  $c_{pq}$  from a consistent

Table V. Temperature Coefficients of Elastic Constants

	$T_1(c_{pq})$ $10^{-6}/^\circ\text{C}$	$T_2(c_{pq})$ $10^{-12}/^\circ\text{C}^2$	$T_3(c_{pq})$ $10^{-18}/^\circ\text{C}^3$
pq = 11			
BBL(1962)	-48.5	-107	-70
BBL(1962) L.S.F.	-43.0	-109	-64.8
BBL(1963) L.S.F.	-35.6	-117	-100
Adams et. al.	-49.6	-107	-74
pq = 13			
BBL(1962)	-550	-1150	-750
BBL(1962) L.S.F.	-669	-971	393
BBL(1963) L.S.F.	-612	-900	45.4
Adams et. al.	-651	-1021	-240
pq = 14			
BBL(1962)	101	-48	-590
BBL(1962) L.S.F.	94.8	0.54	-400
BBL(1963) L.S.F.	93.2	-46.6	-612
Adams et. al.	89	-19	-521
pq = 33			
BBL(1962)	-160	-275	-250
BBL(1962) L.S.F.	-218	-147	283
BBL(1963) L.S.F.	-205	-100	254
Adams et. al.	-192	-162	67
pq = 44			
BBL(1962)	-177	-216	-216
BBL(1962) L.S.F.	-179	-303	-480
BBL(1963) L.S.F.	-184	-273	-247
Adams et. al.	-172	-261	-194
pq = 66			
BBL(1962)	178	118	21
BBL(1962) L.S.F.	176	219	324
BBL(1963) L.S.F.	180	172	25.4
Adams et. al.	167	164	29

Table VI. Least Square Fit Variances For  $T_n(f)$  Data Sets

	$\sigma^2$ [ $T_1(f)$ ] $10^{-12}/^\circ\text{C}^2$	$\sigma^2$ [ $T_2(f)$ ] $10^{-18}/^\circ\text{C}^4$	$\sigma^2$ [ $T_3(f)$ ] $10^{-24}/^\circ\text{C}^6$
BBL(1962) Data Set			
Number of test points	24	23	23
BBL(1962) $T_n(c_{pq})$	8.9	37	367
BBL(1962) L.S.F. $T_n(c_{pq})$	2.4	11	97
BBL(1963) Data Set			
Number of test points	113	106	99
BBL(1962) $T_n(c_{pq})$	20.7	75	771
BBL(1963) L.S.F. $T_n(c_{pq})$	9.2	33	506

set of data points. For consistency, the BBL(1962)  $T_2(c_{pq})$  values are based on BBL(1962)  $T_1(c_{pq})$ , and BBL(1962) Least Square Fit  $T_2(c_{pq})$  are based on BBL(1962) Least Square Fit  $T_1(c_{pq})$ . Similar considerations apply to  $T_3(c_{pq})$ .

Our major concern regarding  $T_n(c_{pq})$  based on this data set relates to the fact that the computation of the first, second, and third order temperature coefficients involve a knowledge of the elastic constants, and that the higher order coefficients also depend on the values of the lower order coefficients. Errors are accumulative, and  $c_{pq}$  inaccuracies are reflected in all temperature coefficients. Similarly,  $T_1(c_{pq})$  errors invalidate  $T_2(c_{pq})$  results, and these in turn affect  $T_n(c_{pq})$ . The BBL(1962) derived temperature coefficients are claimed to be more accurate than ones determined by previous investigators, and are often in sharp disagreement with previous results. The problems associated with the BBL(1962) data set regarding agreement with accepted  $c_{pq}$  values, raises more serious questions with respect the BBL(1962) derived temperature coefficients.

#### BBL (1963)

Subsequent to BBL(1962), Bechmann, Ballato, and Lukaszek have published a report<sup>8</sup>, hereafter abbreviated as BBL(1963), with extensive  $T_n(f)$  data. They have measured the frequency-temperature characteristics of 100-120 doubly rotated cuts, and have tabulated the corresponding  $T_n(f)$  coefficients. This set consists of a wide range of  $(\phi, \theta)$  and data on all three vibration modes. BBL(1962) data is a subset of BBL(1963). An unfortunate omission is frequency-thickness constants for this data set. A knowledge of this data would enable one to calculate  $c_{pq}$  values from a statistically significant number of doubly rotated crystal resonators.

In BBL(1963), the authors use their BBL(1962) derived  $T_n(c_{pq})$  values and calculate  $T_n(f)$  for each data point. However, they have not used this new data set as a check on the original values, or to derive a new set of  $T_n(c_{pq})$ . We have performed a least square analysis fit to BBL(1963), and the results of these computations, a new set of  $T_n(c_{pq})$ , are listed in Table V as "BBL(1963) L.S.F.". The corresponding variances are listed in Table VI. We also list the variances for this data set based on the original BBL(1962) parameters. Increasing the number of experimental points from 23-24 to 100-113 increases the variances by a factor of two. This is expected, as the BBL(1962) data is a subset of BBL(1963). A judicious choice of 20-25 points from this data may indeed give very low variances, and in the limit, a choice of six points would give zero deviation. The least square fit to the smaller data set reduced the variances by factors of 3 to 4, but for the larger data set the errors were reduced by factors of 2 only.

We are confronted with two data sets, and three  $T_n(c_{pq})$  sets. Is there a rational choice, and from a fundamental point of view, does it really make any difference which set is selected?

The purpose of the data analysis is to obtain in a concise form, in conjunction with a mathematical formalism, the parameters required to calculate and predict the frequency as a function of temperature characteristics of a resonator. The intention is not to provide a vehicle for a virtuoso performance in curve fitting or least square analysis.

It does not make too much sense to select "BBL(1962) Least Square Fit" as the working set. BBL(1962) is a subset of BBL(1963) points, selected by some unknown methodology, or simply by the availability data at that time period. There is no indication whatsoever that  $T_n(f)$  values of the reduced data set are more accurate or are better defined in terms of  $(\phi, \theta)$ . Similarly, the BBL(1962) set was derived by BBL from a minimum number of individual experimental points, for example,  $T_n(c_{11})$  from (30,0),  $T_n(c_{66})$  from (0,0), and the statistical evidence of the remaining points was ignored. Parameters based on such a narrow data base may not give realistic predictions for arbitrary doubly rotated crystal cuts.

The resonators tested for the BBL(1963) report contained different crystal configurations, square, rectangular, and circular, were supplied by several manufacturers using different geometries and fabrication processes, and were tested at different overtones and operating procedures. It then represents a broad realistic cross-section of a large variety of resonators, and their numbers and angular distributions were large enough to qualify them as a statistically significant set. All three BBL  $T_n(c_{pq})$  sets give similar results, but among these sets the preferred selection is "BBL(1963) Least Square Fit."

#### Adams et. al. Data Set

Adams, Enslow, Kusters, and Ward<sup>11</sup> also published a set of temperature coefficients, and for reference purposes these are also listed in Table V. It is claimed that this set is superior to BBL(1962). However, in their paper Adams et. al. do not state the number of points in the data set, the angular distribution  $(\phi, \theta)$  of the cuts, or the least square fit variances of  $T_n(f)$ . In addition, they have used the BBL(1962)  $c_{pq}$  values to calculate  $T_n(c_{pq})$ . The only experimental comparison shown is variation around the AT-cut. The authors' contention, that their data set has smaller variances with their  $T_n(c_{pq})$  than with BBL(1962) is obvious and selfevident. Indeed, the Adams et. al.  $T_n(c_{pq})$  may be far superior to BBL(1963) Least Square Fit in predicting the general behavior of doubly rotated cuts.

#### Locl of $T_n(f) = 0$ .

Most  $(\phi, \theta)$  orientations of practical interest for high stability oscillator applications lie along the locl of the zeros of the first order temperature coefficients of frequency,  $T_1(f) = 0$ . These orientations include the temperature compensated cuts, for example, AT, IT, FC, SC, RT, or BT. The temperature sensitivity of frequency is greatly reduced by minimizing the linear contributions of

$T_1(f)$ . Similarly, the linear coefficient cut, the LC-cut, is given by the intersection of  $T_2(f) = T_3(f) = 0$ . For the LC-cut, the only variation is due to  $T_1(f)$ , and this cut has been extensively applied as a thermometer<sup>12</sup>.

The loci of  $T_1(f) = 0$  for the b- and c-modes of vibrations have been initially published in BBL(1961) and they have been reproduced by Ballato and his coworkers during the last 20 years in many of their publications. Figure 3 shows the corrected version of these curves. The correction applies in the range of  $\phi = 45-55^\circ$ . BBL(1961) shows only one cross over between the b- and c-modes, whereas calculations carried out with smaller  $\phi$ -angle intervals also detects the intersection between  $\phi = 49-50^\circ$ .

Figure 4 shows the loci of  $T_1(f) = 0$  based on the newly determined BBL(1963) L.S.F. parameters. There is close agreement with BBL(1962) for the major b-mode, and for the major c-mode at  $\phi < 40^\circ$ . The major c-mode shows a continuous  $\theta \sim 35^\circ$  for  $0^\circ \leq \phi \leq 60^\circ$ , rather than the drop in  $\theta$ -values above  $\phi = 45^\circ$ . The shape of the major b-mode is essentially unchanged, and the b- and c-mode cross overs occur close to the BBL(1962) based calculations.  $T_1(f) = 0$  also shows an additional minor c-mode branch between  $\phi = 50-60^\circ$ . Figure 5 shows the corresponding electromechanical coupling factor along  $T_1(f) = 0$ . Accurate experimental data in the  $\phi > 40^\circ$  region would be very helpful in clarifying the proper values for  $c_{pq}$  and  $T_n(c_{pq})$ .

The LC-cut can also serve as a good example in comparing the BBL(1962) and BBL(1963) L.S.F. parameters. Figure 6 shows  $T_2(f) = T_3(f) = 0$  as a function of  $(\phi, \theta)$  calculated for both sets. We note that these quantities are sensitive functions of the material constants. The intersection based on BBL(1962) is at  $(7.97, 12.02)^\circ$ , and for BBL(1963) L.S.F. at  $(13.69, 8.75)^\circ$ . Calculations carried out by Hammond et. al. place the LC-cut at  $(8.44, 13.0)^\circ$ . The experimentally determined value is  $(11.17, 9.39)^\circ$ , and in Figure 6 it is plotted as the LC experimental point. The reasons for the discrepancy for BBL(1962) based computations are unclear. Figure 6 also shows the Adams et. al. based calculations locating the LC-cut at  $(12.64, 9.72)^\circ$ , the closest agreement with the experimental point.

#### Discussion

The knowledge of the elastic constants of quartz and their temperature coefficients are imperative in describing the frequency and the temperature response of the resonator device. We find serious discrepancies in the original analysis of the BBL(1962) data set, and this raises issues regarding the applicability of currently accepted  $c_{pq}$  and  $T_n(c_{pq})$  values to crystallographically doubly rotated cuts. There are several possibilities which may account for this configurations. Strictly speaking, the derived material constants are not necessarily the intrinsic values and their applicability to other situations need to be estab-

lished. Geometrical factors may influence results, and sets of values derived from one configuration and experimental procedures may not automatically be applied to other modes of operation. Adams et. al.<sup>11</sup> also caution that their  $T_n(c_{pq})$  data is "exactly applicable to crystals having the same physical characteristics as the ones in this study; i.e. same diameter, thickness, contour, etc." BBL(1963) also list a collection of factors which influence the temperature-frequency behavior of the resonator.

McSkimin experiments were carried out on 0.5 cubic inch quartz samples, whereas BBL obtained the material from several sources, had large thickness to diameter ratio variations, and included plano-plano, beveled at the edges, and plano-convex geometries. Sample set divergencies extended to support structure, electrode size, air gap holder and resonator enclosure, drive level, and operations at different overtones, all of which affect the measured frequencies. In addition, BBL samples may also reflect differences in fabrication processes rather than intrinsic properties of the material.

Another possibility relates to the fact that we are trying to apply the theoretical formulation of an infinite plate to a finite electroded disk. This is very simplistic approach, it works well when symmetries cancel a large number of terms, but it does not describe the realities of doubly rotated disks.

Recent discussions with A. Ballato tends to support the argument that for the BBL sample set they lacked an accurate knowledge of  $(\phi, \theta)$ . The oriented plates and finished resonators were acquired from outside sources, and there was no independent check on  $(\phi, \theta)$ . It is then not too surprising that this mixture of geometrical configurations and experimental procedures yield large variances, and deviation with predicted results can always be attributed to these factors.

This investigation points out the need for the experimental redetermination of the elastic constants of quartz and their temperature coefficients on a geometrically consistent sample sets, on a statistically significant number of doubly rotated crystals, bulk and disk configurations, air gap and resonator enclosures, and piezoelectric and other means of excitations. It also calls for detailed documentation of sample and experimental procedures. A new experimental investigation will also afford the opportunity to evaluate novel factors, discovered during the last twenty years, which influence resonator behavior.

#### References

1. H.F. Tiersten, Linear Piezoelectric Plate Vibrations, Plenum Press, pp. 88-93 (1969)
2. W.G. Cady, Piezoelectricity, Dover Publications, Volume I, pp. 134-157 (1964)

3. H.J. McSkimin, "Measurement of the 25 °C Zero-Field Elastic Moduli of Quartz by High Frequency Plane-Wave Propagation". J. Acc. Soc. Amer., 34, 1271-4(1962)
4. R. Bechmann, A.D. Ballato, and T.J. Lukaszek, "Higher-Order Temperature Coefficients of the Elastic Stiffnesses and Compliances of  $\alpha$ -Quartz" Proc. IRE, 50, 1812-1822(1962)
5. A. Kahan, "Elastic Constants of Quartz", RADC TR-82-117, May 1982
6. A.J. Slobodnik, R.T. Delmonico, and E.D. Conway, "Microwave Acoustic Handbook", Vol. 3, "Bulk Wave Velocities", RADC-TR-80-188, 1980
7. R. Bechmann, A.D. Ballato, and T.J. Lukaszek, "Frequency-Temperature Behavior of Thickness Modes of Doubly-Rotated Quartz Plates", 15th Annual Symposium on Frequency Control, 22(1961)
8. R. Bechmann, A.D. Ballato, and T.J. Lukaszek, "Higher-Order Temperature Coefficients of the Elastic Stiffnesses and Compliances of  $\alpha$ -Quartz" USAELRDL TR 2261, Sep 1963
9. A. Kahan, "Temperature Coefficients of Elastic Constants of Quartz", RADC-TR-82-(to be published)
10. H.J. McSkimin, P. Andreatch, and R.N. Thurston, "Elastic Moduli of Quartz versus Hydrostatic Pressure at 25 °C and -195.8 °C, J. App. Phys., 36, 1624-1632(1965)
11. C.A. Adams, G.M. Enslow, J.A. Kusters, and R.W. Ward, "Selected Topics in Quartz Crystal Research", 24th Annual Symposium on Frequency Control, 55-63(1970)
12. D.L. Hammond, C.A. Adams, and P. Schmidt, "A Linear Quartz-Crystal, Temperature-Sensing Element", ISA Trans., 4, 349-354(1965)

## SINGLY AND DOUBLY ROTATED CRYSTAL PLATES

### COORDINATE SYSTEM

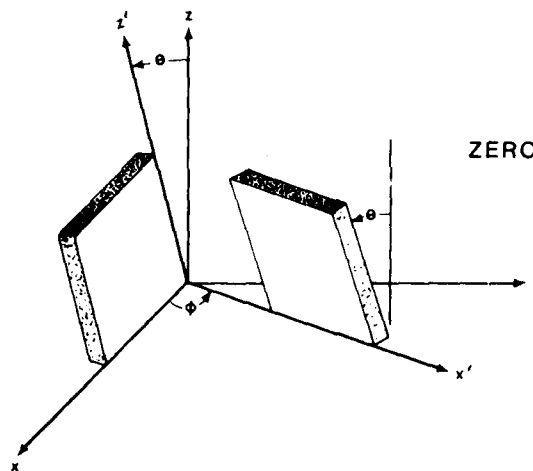


Figure 1. Coordinate System for Doubly Rotated Crystal Plate

### ZEROS OF OFF-DIAGONAL $\Gamma_{pq}$ ELEMENTS

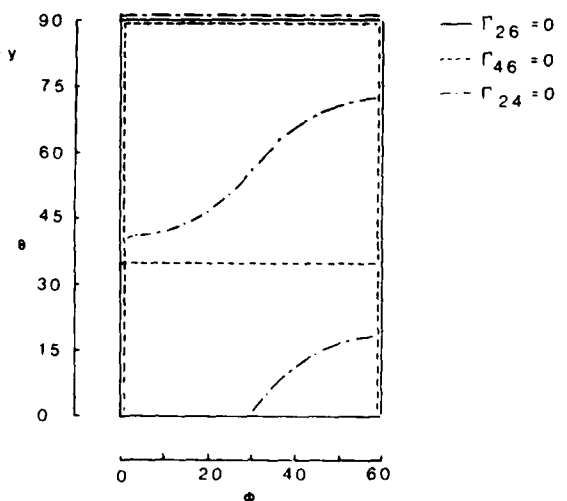


Figure 2. Zero Values of Off-Diagonal Piezoelectrically "Stiffened" Elastic Constants

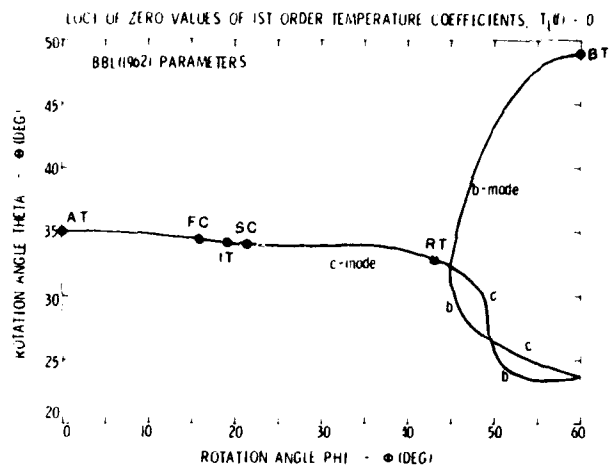


Figure 3. Loci of Zero Values of First Order Temperature Coefficients of Frequency Based on Material Constants of Bechmann, Ballato, and Lukaszek, Reference 4

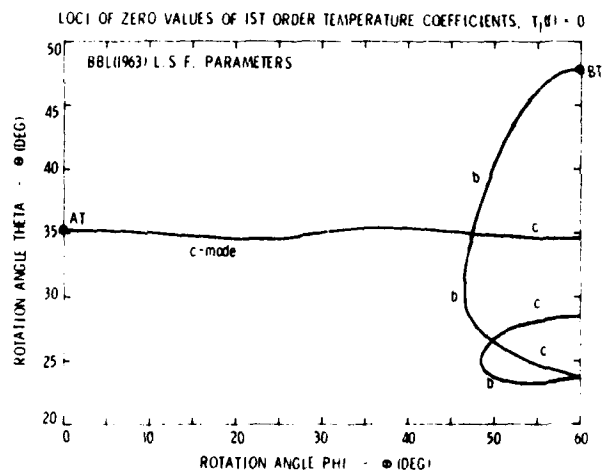


Figure 4. Loci of  $T_1(f) = 0$ , Based on BBL(1963) L.S.F. Temperature Coefficients

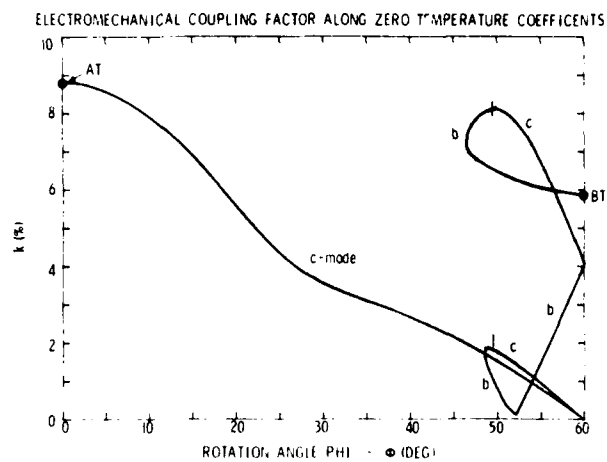


Figure 5. Electromechanical Coupling Factor Along  $T_1(f) = 0$  for the BBL(1963) L.S.F. Based Calculations

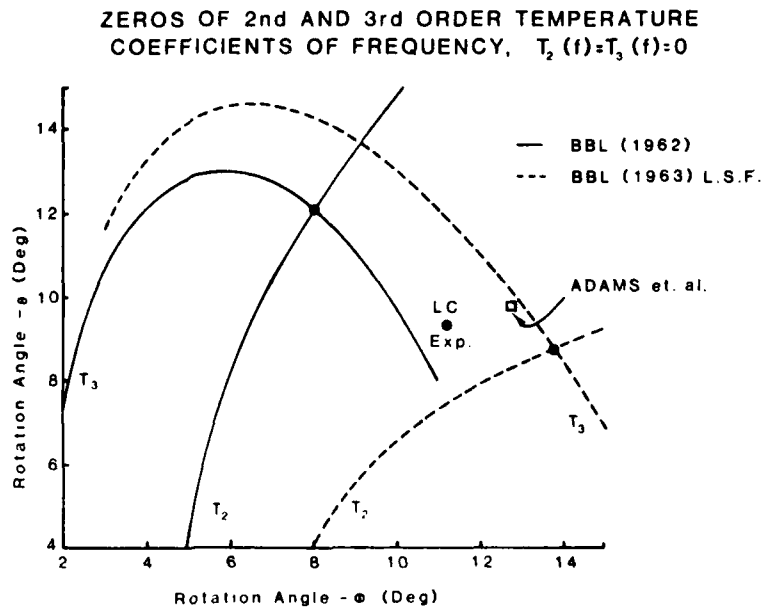


Figure 6. Loci of  $T_2(f) = T_3(f) = 0$  in the Vicinity of the LC Cut

## TURNOVER TEMPERATURES FOR DOUBLY ROTATED QUARTZ

Alfred Kahan

Solid State Sciences Division  
 Rome Air Development Center  
 Hanscom Air Force Base, MA 01731

Summary

The turnover temperatures,  $T_{TO}$ , of quartz plates vibrating in the thickness mode are calculated for doubly rotated orientations in the temperature range of  $-200$  to  $+200$  °C. In addition to the standard cuts of interest situated along the loci of zero values of the first order temperature coefficients of frequency, we find another family of doubly rotated quartz orientations, vibrating in c-mode resonance, with  $T_{TO}$  values  $70$  °C and above. The significance of these orientations are that for the same  $T_{TO}$  they are considerably less sensitive to crystallographic orientation than currently utilized singly or doubly rotated cuts. For  $T_{TO} = 90$  °C, the static frequency as a function of temperature coefficients of these orientations are between the AT-cut and BT-cuts, and they become less sensitive to temperature with increasing  $T_{TO}$ .

Key Words Quartz, Crystal Resonators, Frequency Standards

Introduction

The most important performance parameter of a crystal oscillator is the static frequency as a function of temperature,  $f(T)$ , characteristic of the device. In the temperature range of interest to this investigation,  $-200$  to  $+200$  °C,  $f(T)$  is described by a cubic equation with coefficients  $T_1(f)$ ,  $T_2(f)$ , and  $T_3(f)$ . The frequency coefficients  $T_n(f)$ , are determined by the temperature coefficients of the elastic, piezoelectric, and dielectric constants, and by the expansion coefficients of the material used in fabricating the resonator element. Single crystal  $\alpha$ -quartz is the most commonly used material for piezoelectric resonators, owing to its superior mechanical, physical, and chemical properties. Quartz belongs to the trigonal crystal system, and material properties are crystal orientation dependent. Certain orientations exist which have considerably smaller  $f(T)$  sensitivity than other directions. Typical examples include the standard AT- and BT-cuts.

The normalized frequency offsets as a function of temperature may exhibit a maximum and a minimum. These positions are designated as the turnover temperatures,  $T_{TO}$ . For high stability applications, the resonator device is enclosed in a precisely controlled oven and maintained at  $T_{TO}$ . Most mili-

tary applications specify upper environmental temperatures in the  $60$  to  $100$  °C range. The crystal orientation is selected to locate  $T_{TO}$  several degrees above the highest anticipated environmental temperature. Owing to  $T_{TO}$  sensitivity to crystallographic orientation, narrow angular tolerances, in order of minutes or seconds or arc, have to be maintained throughout the resonator fabrication process. Both requirements, precise oven control and crystal orientation, affect considerably oscillator costs. The singly rotated AT- and BT-cut crystals are the most widely used orientations for high stability applications. The novel doubly rotated SC-cut orientation has considerably smaller temperature coefficient of frequency than the AT-cut.<sup>1</sup> However, this order of magnitude improvement in performance is at the expense of an order of magnitude reduction in allowable crystal orientation tolerances.

Quartz plates support three modes of transverse vibrations, usually designated as the a-, b-, and c-modes. The AT- and SC-cuts are c-mode vibrations, whereas the BT-cut belongs to the b-mode branch. Technically, all three cuts are defined by orientations which yield zero values for the first order temperature coefficients of frequency,  $T_1(f) = 0$ . Other cuts situated along the  $T_1(f) = 0$  locus include the IT-, FC-, and RT-cuts. This topic has been reviewed extensively by Ballato.<sup>2</sup> The attraction of cuts along  $T_1(f) = 0$  is due to the fact that, compared to other modes or orientations, the normalized frequency offsets are slowly varying functions of temperature. For these cuts only 2nd and 3rd order coefficients,  $T_2(f)$  and  $T_3(f)$ , contribute to frequency offsets.

Resonator performance parameters of interest include the position of  $T_{TO}$ , and the magnitude of the frequency variation around  $T_{TO}$ . These parameters are determined by all three temperature coefficients of frequency, and not only by  $T_1(f)$  alone. A judicious selection of angular orientations which properly balance  $T_1(f)$ ,  $T_2(f)$ , and  $T_3(f)$ , may result, compared to currently preferred cuts, in improved performance or trade-offs, for example, relaxation of crystallographic angular tolerances. Consequently, for the three transverse vibrations of quartz, we have computed  $T_{TO}$  for all angular orientations. The results of these calculations are the subject of this investigation.

AD P001516

### Coordinate System

Quartz orientations of interest to transverse mode piezoelectric resonator applications are rotations around the crystallographic z-axis and/or x-axis. Figure 1 illustrates the coordinate system used to describe the various crystal orientations and cuts. The initial position of the plate is that of a Y-cut, thickness direction normal to the y-axis. The position of the rotated plate is described by  $(\phi, \theta)$ , where  $\phi$  and  $\theta$  are rotations around the z- and x-axis, respectively.

Owing to crystal symmetries applicable to quartz, all rotations can be mapped into

$$0 \leq \phi \leq 60^\circ \quad \text{and} \quad 0 \leq \theta \leq 90^\circ$$

In this nomenclature, the approximate values of the AT-, SC-, and BT-cuts are  $(0, 35)^\circ$ ,  $(22, 34)^\circ$ , and  $(60, 49)^\circ$ , respectively. Another commonly used mapping region is

$$0 \leq \phi \leq 30^\circ \quad \text{and} \quad -90 \leq \theta \leq 90^\circ$$

The two descriptions are related by the transformations

$$\phi + 60 = \phi' \quad \text{and} \quad \theta + 90 = \theta'$$

In this nomenclature, the BT-cut becomes  $(0, -49)^\circ$ , and, for example, the combination  $(40^\circ 54', 16^\circ 34')$  transforms to  $(19^\circ 06', -16^\circ 34')$ .

### Static Frequency - Temperature Characteristics

In a series of experiments, Bechmann, Ballato, and Lukaszek<sup>3,4</sup> have evaluated the static frequency as a function of temperature behavior of quartz resonators in the temperature range of -200 to +200 °C. They have shown that the normalized frequency offsets are described well by a cubic equation in the form

$$\Delta f/f_0 = (f - f_0)/f_0 = \sum_{n=1}^3 T_n(f)(T - T_0)^n \quad (1)$$

where  $T_n(f)$  are the temperature coefficients of frequency,  $T$  the variable temperature, and  $f_0$  the frequency at reference temperature  $T_0$ . In most applications, the series is expanded around reference temperature  $T_0 = 25^\circ\text{C}$ .

$T_n(f)$  are calculated from the six fundamental elastic, two dielectric, and two piezoelectric constants, and their temperature coefficients. The most commonly used mathematical formalism relating  $T_n(f)$  to the material coefficients, an infinite plate with the proper boundary conditions, is discussed and reviewed by many investigators, for example, Ballato.<sup>2</sup> Reference 5 discusses the validity of currently accepted material constant values, and lists four alternate sets of temperature coefficients. For our purposes, the specific set used to calculate  $T_{to}$ , and to illustrate  $f(T)$  behavior, is not critical. All sets give similar results, but specific values will depend on the particular

choice for the material constants. The exception is the crystal region between  $\phi = 50$ - $60^\circ$ , where results are highly sensitive to assumed material temperature coefficients.

The general shape of the normalized frequency offsets as a function of temperature are described in many publications. Figure 2 shows the characteristics for  $\phi = 0$ , for  $\theta$ -angles near the AT-cut. This figure is included for illustration purposes only. We note that Eq. (1) defines one real root at  $T = T_0 = 25^\circ\text{C}$ . The frequency-temperature curves may have two additional real roots, and a maximum and a minimum. This will occur if  $[T_2(f)]^2 > 4T_1(f)T_3(f)$ . The maximum and minimum positions, designated as the turnover temperatures, are located at

$$T_{to} - T_0 = \{-T_2(f) \pm [(T_2(f))^2 - 3T_1(f)T_3(f)]^{1/2}\} / 3T_3(f) \quad (2)$$

At these positions, as illustrated in Figure 1, the normalized frequency offset is a slowly varying function of temperature, and, in a controlled environment, one is able to obtain high stability operation.  $T_{to}$  shifts to higher temperatures with increasing  $\theta$  and for any  $T_{to}$ ,  $\theta$  is uniquely defined. Figures 3 and 4 show, for  $T_{to} = 90^\circ\text{C}$ , the sensitivities of  $\Delta f/f_0$  to small changes in  $\theta$ , for the AT- and BT-cuts, respectively. BT-cut sensitivities are approximately one-half that of the AT-cut.

Most resonators of practical interest for high stability operation are situated along the loci of the zeros of the 1st order temperature coefficients of frequency,  $T_1(f) = 0$ . These include the AT-cut ( $\phi = 0^\circ$ ), IT-cut, FC-cut, SC-cut, ( $\phi \sim 23^\circ$ ), RT-cut, and BT-cut ( $\phi = 60^\circ$ ). The specific parameters for these cuts are reviewed by Ballato.<sup>2</sup> A corrected curve of the  $T_1(f) = 0$  locus is given in Reference 5. The steepness of the frequency-temperature curve near  $T_{to}$  will depend on both  $\phi$  and  $\theta$ , and on the proximity to the inflection temperature  $T_i$ , given by  $T_i - T_0 = -T_2(f)/3T_3(f)$ .

### Turnover Temperatures

Figures 5a, 5b, and 5c show the turnover temperatures as a function of  $(\phi, \theta)$  in the temperature range of -200 to +200 °C. The horizontal lines through these curves indicate the position of the inflection temperature. At  $\phi = 0$  only the c-mode has turnover temperatures, and  $T_{to}$  shifts drastically with  $\theta$ . The steep  $T_{to}$  slope for the c-mode branch is maintained at all  $\phi$ -angles. This branch is usually referred to as the family of AT-cut crystals. Figure 6 shows more detailed curves of  $T_{to}$  along the  $T_1(f) = 0$  locus. The inflection temperature increases with  $\phi$ , and at  $\phi = 22^\circ$ ,  $T_i \sim 90^\circ\text{C}$ . For optimum frequency-temperature operations, i.e. very small normalized frequency offsets as a function of temperature, one ideally selects a doubly rotated cut with  $T_{to} = T_i$ . However, by definition, the curves are steepest at  $T_i$ , and the slightest deviation in angular orientation results in drastic  $T_{to}$  variations. This is also illustra-

ted in Figure 7. We cross-plot the  $(\phi, \theta)$  positions for specific  $T_{to}$  between 60 and 100 °C. Near  $\phi = 0$ , the turnover temperatures are comparatively speaking well separated, but owing to the rise in  $T_1$  with increasing  $\phi$ , they coalesce in the  $\phi = 16$  to 20° region. The flat  $\theta$ -value region around  $\phi \sim 25^\circ$  indicates that, from an angular sensitivity point of view, it is desirable to shift the SC-cut to higher  $\phi$ -values.

The curves in Figures 6 and 7 are calculated based on BBL(1963) L.S.F. temperature coefficient values.<sup>5</sup> We obtain very similar shapes with Adams et. al. derived coefficients,<sup>6</sup> but there are differences in the absolute  $\theta$ -values. For example, for  $T_{to} = 80$  °C, using BBL(1963) L.S.F. coefficients,  $\theta$  decreases from 35.5° at  $\phi = 0^\circ$  to 34.15° at the  $\phi \sim 25^\circ$  minimum, whereas with Adams et. al. based calculations  $\theta$  decreases from 35.2 at  $\phi = 0$  to  $\theta = 33.0^\circ$  at the  $\phi \sim 27^\circ$  minimum. The  $\theta$ -values at the  $\phi \sim 36^\circ$  maximum are  $\theta \sim 34.9^\circ$  for BBL(1963) L.S.F. and  $\theta \sim 33.85^\circ$  for Adams et. al. Experimental SC-cut  $T_{to}$  values lie between the values predicted by the two sets.

For  $\phi$ -values between 50-60°, the b- and c-modes interchange, and the type of behavior exhibited by the c-mode for  $\phi < 50^\circ$  is shown by the b-mode for  $\phi > 50^\circ$ . However, the inflection temperature is around -100 °C, and the b-mode does not have an equivalent SC-cut for 25 °C and above.

#### AK-cut Crystals

A closer examination of Figures 5a, 5b, and 5c indicates that for c-mode vibrations, starting at  $\phi \sim 30^\circ$ ,  $T_{to}$  is a multi-valued function. The same  $T_{to}$  can be obtained from several  $\theta$ -angle orientations. For example, for  $\phi = 35^\circ$  and  $T_{to} = 80$  °C, in addition to usual  $\theta \sim 35^\circ$ , we note a plateau at  $\theta = 25 - 27^\circ$ . This branch is first detected at  $\phi = 30^\circ$  with the minimum  $T_{to} = 160$  °C, dips at  $\phi = 35$  and 40° to a  $T_{to}$  minimum of  $\sim 80$  °C, increases at  $\phi = 45^\circ$  to  $T_{to} \sim 110$  °C, and disappears at  $\phi = 50^\circ$  and above. Figure 8 shows detailed curves for this c-mode branch, based on BBL(1963) L.S.F. coefficients. Figure 9 shows the same branch based on Adams et. al. determined temperature coefficients. The steep lines on the right hand side in Figure 9 are the  $T_1(f) = 0$  family. In Figure 8 we omit the AT-cut related vertical lines for clarity. We arbitrarily designate this new family of cuts as the AK-cut.

We note that the AK-cuts yield turnover temperatures in the regions of interest to high stability oscillator applications. Instead of the steep slopes characteristic of the AT-cuts, the AK-cuts show considerably less sensitivity to crystallographic orientations. Figure 10 shows the loci for  $T_{to} = 75 - 120$  °C as a function of  $(\phi, \theta)$ , for BBL(1963) L.S.F. based computations. The lowest  $T_{to}$  is  $\sim 75^\circ$ C, and for each  $\phi$  and  $T_{to}$ , we have a choice of two  $\theta$ -values. For Adams et. al. based calculations, the lowest  $T_{to}$  is  $\sim 55^\circ$ C, and similar type of elliptic curves. The higher the  $T_{to}$ , the wider the angular range.

For the AK-cut crystals, we have approximately a 6° wide  $\phi$ -angle and 4° wide  $\theta$ -angle region where  $T_{to}$  values are between 75 and 80 °C. This angular range allows complete relaxation of tolerances in fabrication, with corresponding cost reduction. The wide choice of  $(\phi, \theta)$  for the same  $T_{to}$ , also allows optimization in terms of b-mode to c-mode separation, selection of strong electromechanical coupling factors, and design for slowly varying  $f(T)$ .

Figure 11 shows for the AK-cut,  $T_{to} = 90^\circ$ C, the sensitivity of  $\Delta f/f_0$  to changes in the  $\theta$ -angle. This is to be compared with the AT- and BT-cut, shown in Figures 3 and 4, respectively. Instead of minutes of arc deviations characteristic of AT- and BT-cuts, for the AK-cut  $\Delta\theta$  are given in terms of degrees. The curves indicate that AK-cut insensitivities to angular orientations are, approximately, a factor of 50 greater than for the AT-cut.

Figure 12 shows the normalized frequency offsets,  $T_{to} = 90$ , for the AT-, BT-, and AK-cuts. The AK-cut has a positive curvature, similar to the BT-cut, and its frequency coefficient is approximately twice that of the AT-cut, but is smaller than the BT-cut. The particular  $(\phi, \theta)$  combination chosen for this illustration is not critical; all  $T_{to} = 90$  °C  $(\phi, \theta)$  combinations have very similar  $f(T)$  curves. For the AT- and BT-cuts, the curvatures of  $f(T)$  increase with  $T_{to}$ . Figure 13 shows  $\Delta f/f_0$  for the three cuts at  $T_{to} = 200$  °C. We show two representative AK-cuts, and both have considerably smaller curvatures than comparable AT- or BT-cuts. For high temperature applications, the AK-cut is preferable, even from a performance point of view.

#### Other Doubly Rotated Cuts

Figures 5a, 5b, and 5c indicate that in addition to the AK-cut, there are other  $(\phi, \theta)$  combinations which show plateaus or small slopes for particular  $T_{to}$ . For example, the a-mode, between  $\phi = 35-60^\circ$ , exhibits flat  $T_{to}$  between -120 and -80 °C, and it is useful, for high stability low temperature applications.

For  $\phi$  between 50 and 60°, the c-mode also exhibits another branch, with  $T_{to}$  plateaus between 60 and 100 °C. We have not investigated this region in detail. Results are very sensitive to small changes in assumed material constants, and are also affected by the closeness of the b- and c-mode crossover. This limitation is also manifested at  $\phi = 50-55^\circ$  and  $\theta = 20-25^\circ$ , where  $T_{to}$  undergoes wild gyrations. For this crystal region, one can not have any confidence that computations predict realistically  $T_{to}$  values or  $f(T)$ .

#### Experimental Verification

The existence of the AK-cut family has been verified experimentally. Several  $(\phi, \theta)$  orientations were fabricated in 10 MHz, 3rd overtone, resonator configuration.<sup>7</sup> Figure 14 shows four experimental turnover temperatures. For ease of fabrication, the initial  $(\phi, \theta)$  combinations were selected for

their proximity to x-ray planes. We find that at  $(30, 24.44)^\circ$ ,  $T_{to} = 173^\circ\text{C}$ ; for  $(36.0, 24.44)^\circ$ ,  $T_{to} = 87^\circ\text{C}$ ; for  $(36.58, 28.45)^\circ$ ,  $T_{to} = 77^\circ\text{C}$ ; and for  $(46.1, 23.58)^\circ$ ,  $T_{to} = 112^\circ\text{C}$ .  $Q$ -values are  $\sim 1.5 \times 10^6$ , in line with 10 MHz, 3rd overtone, resonators.  $f(T)$  values also agree well with computations. Considering the uncertainties in the material constants, and the simplified mathematical formalism of these computations, the general agreement with predicted results are indeed very surprising.

#### References

1. J.A. Kusters, C.A. Adams, H. Yoshida, and J.G. Leach, "TTC's - Further Developmental Results", 31st Annual Frequency Control Symposium, 3-7(1977).
2. A. Ballato, "Doubly Rotated Thickness Mode Plate Vibrators", *Physical Acoustics*, vol. XIII, W. P. Mason, and R. N. Thurston, editors, Academic Press, pp. 151-181(1977).
3. R. Bechmann, A.D. Ballato, and T.J. Lukaszek, "Higher-Order Temperature Coefficients of the Elastic Stiffnesses and Compliances of Alpha-Quartz", *Proc. of the IRE*, 50, 1812-1822(1962).
4. R. Bechmann, A.D. Ballato, and T.J. Lukaszek, "Higher Order Temperature Coefficients of the Elastic Stiffnesses and Compliances of Alpha-Quartz", USAELRDL TR-2261, Sept 1963.
5. A. Kahan, "Elastic Constants of Quartz and Their Temperature Coefficients", 36th Annual Frequency Control Symposium, 1982.
6. C.A. Adams, G.M. Enslow, J.A. Kusters, and R.W. Ward, "Selected Topics in Quartz Crystal Research", 24th Annual Frequency Control Symposium, 55-63(1970).
7. The resonators were fabricated to our specifications at, and purchased from, Frequency Electronics, Inc. We would like to thank J. Tsacilas for orienting and cutting the plates, and B. Goldfrank for fabrication and for initial measurements. We would also like to express appreciation to Ferdinand Euler for performing the experimental evaluations.

SINGLY AND DOUBLY ROTATED CRYSTAL PLATES  
COORDINATE SYSTEM

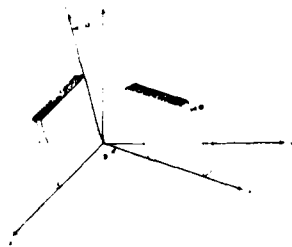


Figure 1. Coordinate System for Doubly Rotated Crystal Plate

FREQUENCY - TEMPERATURE CHARACTERISTICS OF AT-CUT ( $\theta = 0$ ) RESONATORS

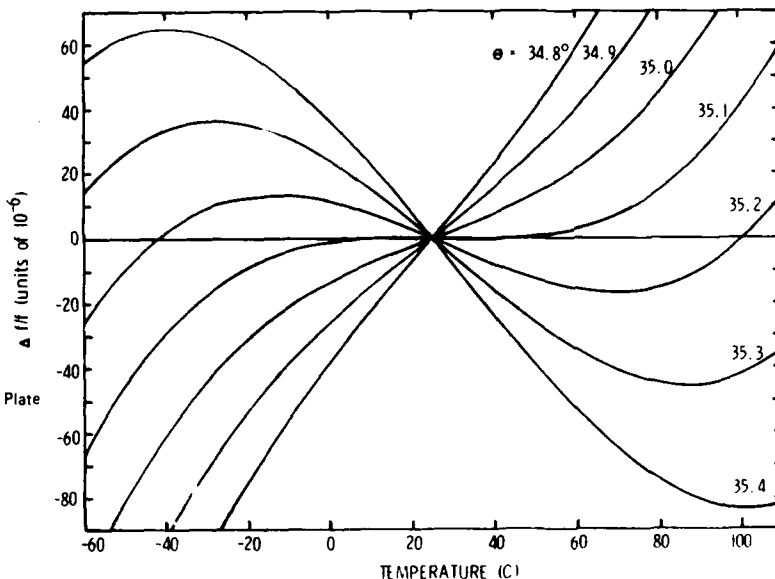


Figure 2. Normalized Frequency Offset as a Function of Temperature for AT-Cut plate ( $0, \sim 35^\circ$ ).

# FREQUENCY-TEMPERATURE-ANGLE CHARACTERISTICS

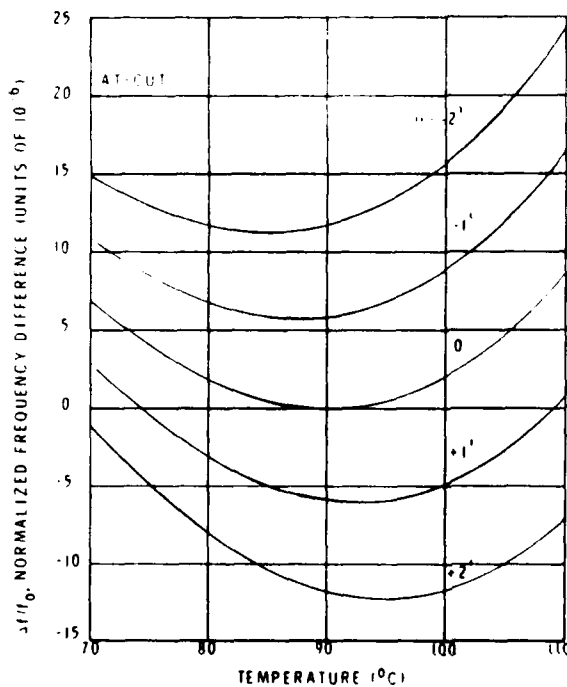


Figure 3. Sensitivity of Normalized Frequency Offset to Small Angular Variations for an AT-Cut Plate,  $(0, \sim 35)^{\circ}$ , Oriented for  $90^{\circ}\text{C}$  Turnover Temperature.

# FREQUENCY-TEMPERATURE-ANGLE CHARACTERISTICS

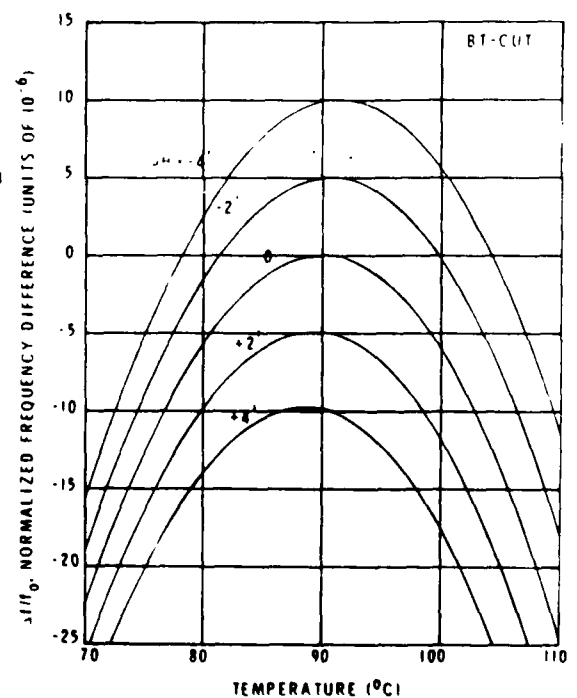


Figure 4. Sensitivity of Normalized Frequency Offset to Small Angular Variations for a BT-Cut Plate,  $(60, \sim 49)^{\circ}$ , Oriented for  $90^{\circ}\text{C}$  Turnover Temperature.

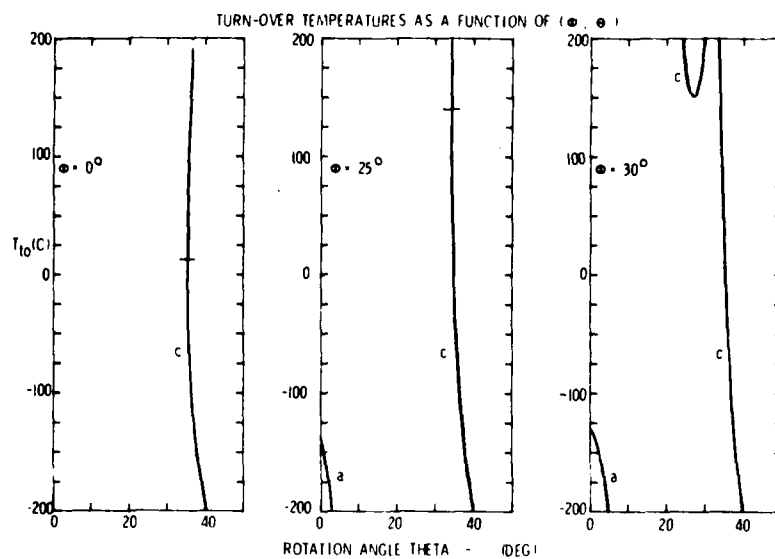


Figure 5a. Turnover Temperatures for Crystallographically Doubly Rotated Quartz,  $\phi = 0, 25$ , and  $30^\circ$ .

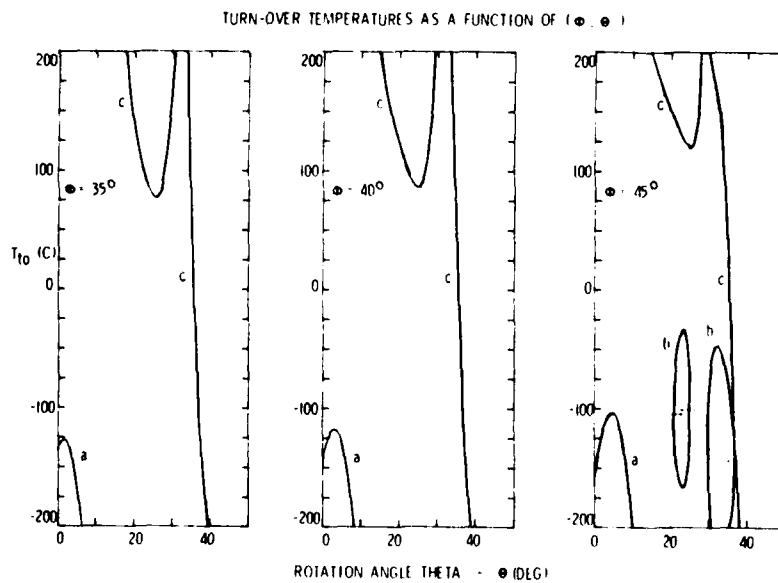


Figure 5b. Turnover Temperatures for Crystallographically Doubly Rotated Quartz,  $\phi = 35, 40$ , and  $45^\circ$ .

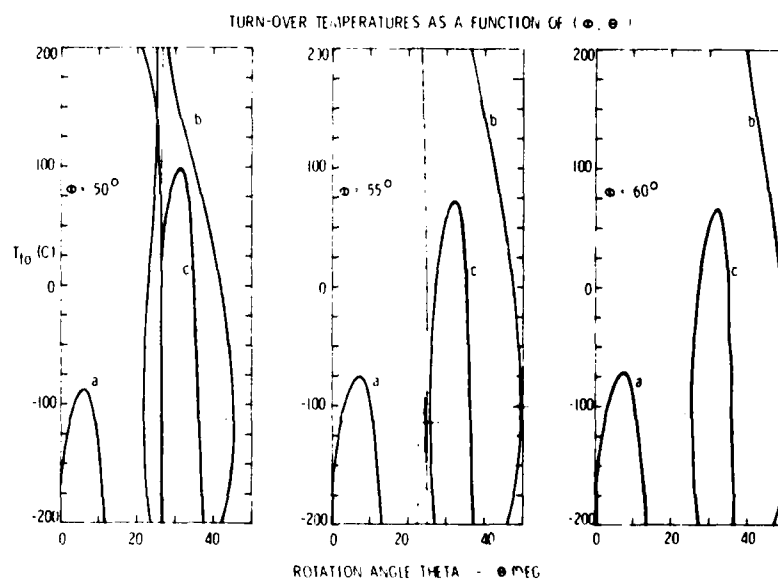


Figure 5c. Turnover Temperatures for Crystallographically Doubly Rotated Quartz,  $\phi = 50, 55$ , and  $60^\circ$ .

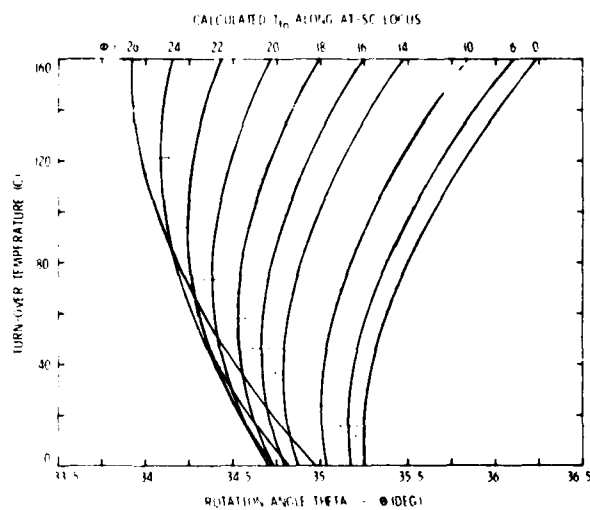


Figure 6. Turnover Temperatures Along  $T_1(f) = 0$  locus,  $\phi = 0 - 26^\circ$ . The Horizontal Lines Indicate the Position of the Inflection Temperatures.

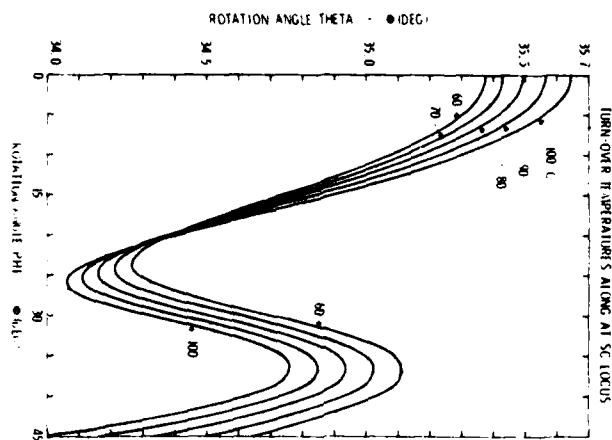


Figure 7. Constant Turnover Temperatures,  $T_{to} = 60 - 100^{\circ}\text{C}$ , as a Function of  $(\phi, \theta)$  for AT-Cut Family

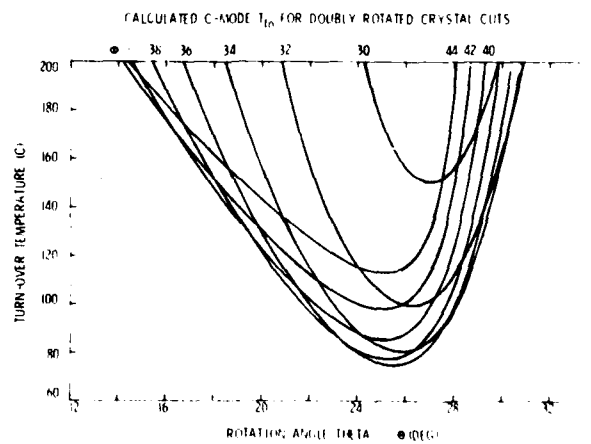


Figure 8. Turnover Temperatures for AK-Cut Crystals,  $\phi = 30 - 44^{\circ}$ . Calculations Based on BBL(1963) L.S.F. Coefficients

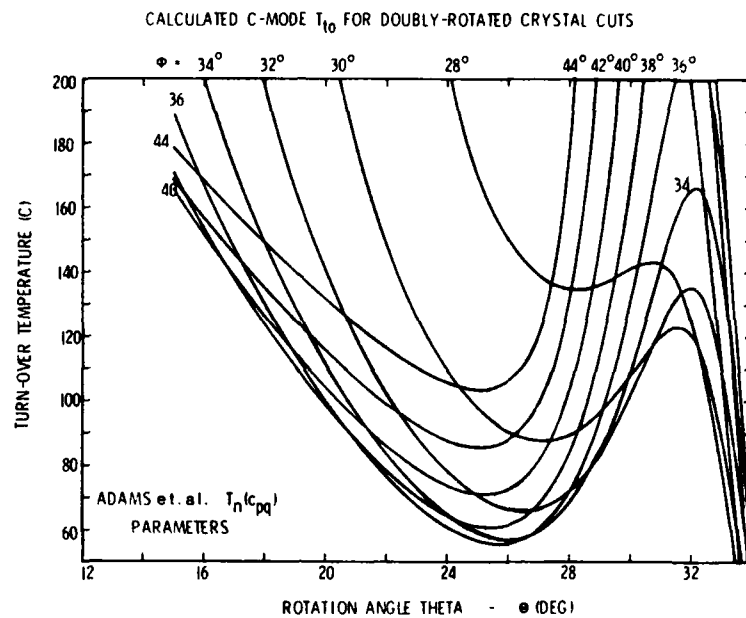


Figure 9. Turnover Temperatures for AK-Cut Crystal,  $\phi = 28-44^\circ$ . Calculations Based on Adams et al. coefficients, Ref. 6. Curves for  $\theta > 32^\circ$  are part of the AT-Cut Family.

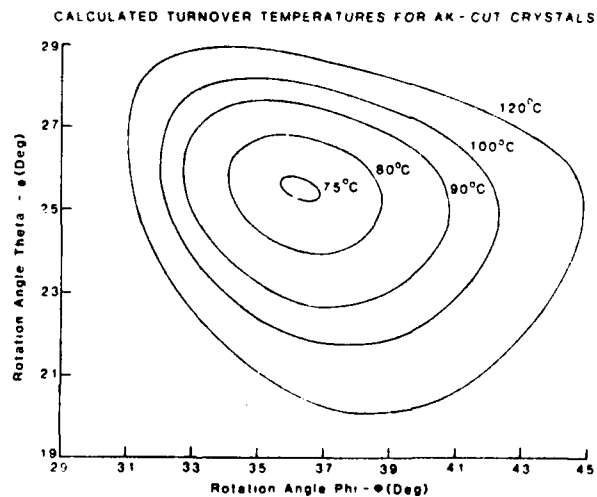


Figure 10. Constant Turnover Temperatures,  $T_{10} = 75-120^\circ\text{C}$ , for AK-Cut Plates, BBL(1963) L.S.F. coefficients.

# FREQUENCY-TEMPERATURE-ANGLE CHARACTERISTICS

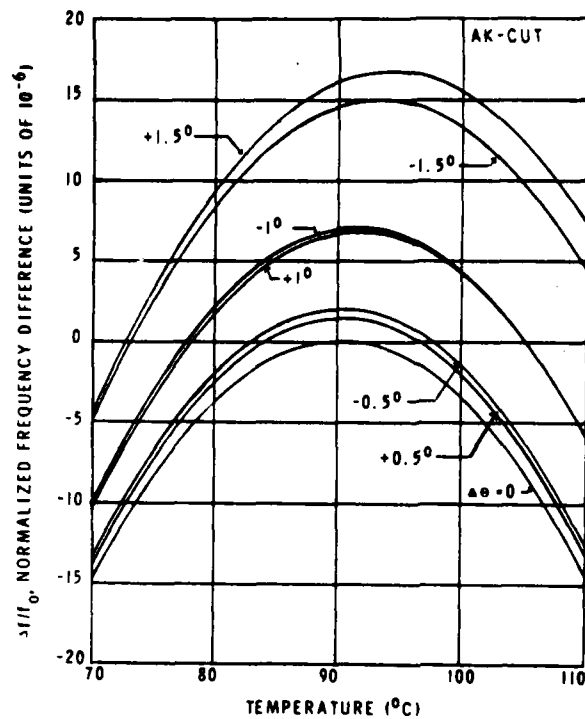


Figure 11. Sensitivity of Normalized Frequency Offsets to Angular Variations for AK-Cut Plate, Oriented for  $T_{10} = 90^{\circ}\text{C}$ .

# FREQUENCY-TEMPERATURE CHARACTERISTICS

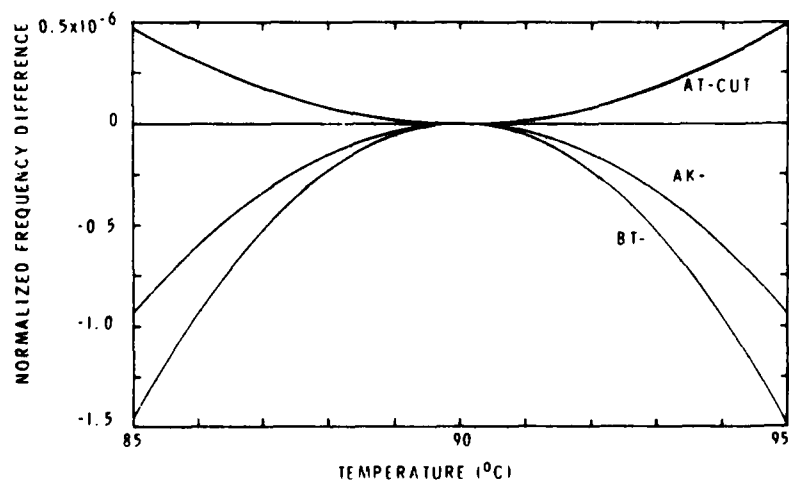


Figure 12. Comparison of Normalized Frequency Offsets as a Function of Temperature for AT-, BT-, and AK-Cut Plates Oriented for  $T_{10} = 90^{\circ}\text{C}$ .

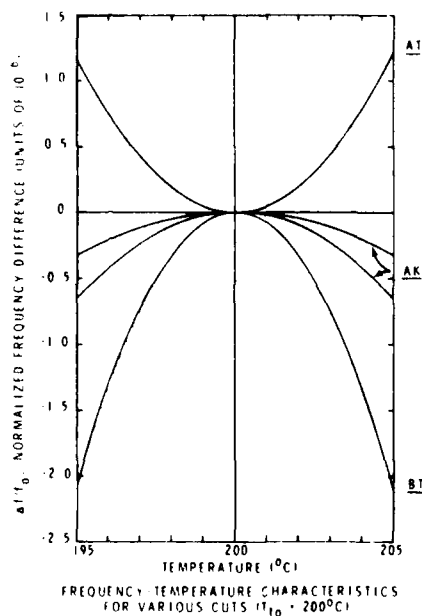


Figure 13. Comparison of Normalized Frequency Offsets as a Function of Temperature for AT-, BT-, and AK-Cut Plates Oriented for  $T_{10} = 200^{\circ}\text{C}$ .

#### CALCULATED TURNOVER TEMPERATURES FOR AK-CUT CRYSTALS

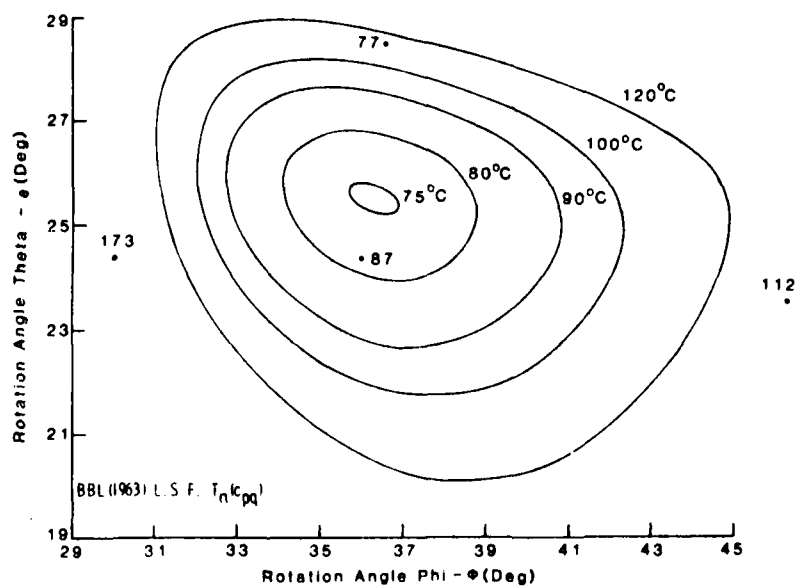


Figure 14. Comparison of Calculated and Experimental Data Measured on 10 MHz, 3rd Overtone AK-Cut Crystal Resonators.  $T_{10}$  Values are Indicated Next to the Experimental Points, Plotted as Dots.

## SC-CUT RESONATORS FOR TEMPERATURE COMPENSATED OSCILLATORS

John R. Vig, Raymond L. Filler and John A. Kosinski

US Army Electronics Technology and Devices Laboratory (ERADCOM)  
Fort Monmouth, New Jersey 07703Abstract

The frequency - temperature vs. angle-of-cut characteristics have been determined for SC-cut TCXO resonators. The  $\theta$ -values were such that the lower turnover temperatures ranged from +100°C to -70°C. From the frequency vs. temperature (f vs T) characteristics of these resonators, the optimum angles of cut, minimum frequency deviations and maximum f vs. T slopes have been determined for various temperature ranges (i.e., -40°C to +75°C, -54°C to +85°C and 0°C to +60°C). It has been found that the angle-of-cut tolerances are easy to achieve with conventional cutting equipment.

The initial hysteresis results indicate that SC-cut resonators may permit a significant improvement in the stabilities achievable with TCXO's.

Key Words: Quartz, quartz crystal, quartz resonator, AT-cut, SC-cut, quartz oscillator, crystal oscillator, hysteresis, thermal hysteresis, frequency vs. temperature, activity dip, thermal shock.

Introduction

In the introduction to a Frequency Control Symposium paper in 1973, the authors state that temperature compensated crystal oscillators (TCXO's) with "...stabilities of  $\pm 5$  pp 10<sup>7</sup> from -40°C to +75°C have been a commercial realization for about a decade." A recent survey of TCXO manufacturers has indicated that, over the same temperature range, the state-of-the-art in commercially available TCXO's is still  $\pm 5$  pp 10<sup>7</sup>; i.e., the state-of-the-art of TCXO's has been on a plateau for the past 20 years.

The main reasons for this lack of progress are thermal hysteresis in the normally used AT-cut crystal units, and the small circuit component tolerances that are required in order to compensate to better than  $\pm 5$  pp 10<sup>7</sup>.

The motivations for the studies reported in this paper are: 1. there is a need for better than  $\pm 5$  pp 10<sup>7</sup> TCXO's and clocks, 2. SC-cut resonators operated in dual mode oscillators have been shown to have the potential for  $\pm 1$  pp 10<sup>8</sup> compensation, 3. lower hysteresis may possibly be achievable with SC-cut resonators because some

stress relief effects that can lead to hysteresis are absent in such resonators, 4. rapid calibration runs are possible due to the thermal transient compensated nature of SC-cut resonators, 5. SC-cut resonators exhibit a very low incidence of activity dips in the c-mode, 6. as is shown below, the angle of cut tolerances are relatively easy to achieve in SC-cut TCXO resonators, and 7. the availability of low cost, low power microcomputers promises the realization of high stability SC-cut TCXO's and clocks at a reasonable cost.

Frequency vs. Temperature vs. Angle-of-Cut Characteristics

In order to define the optimum angles of cut for SC-cut TCXO resonators, groups of 5 MHz fundamental mode and 5 MHz 3rd overtone SC-cut resonators, with widely varying  $\theta$ -angles, were fabricated and evaluated. All of the resonators were plano-convex. The fundamental mode blanks were made with a 1.5 diopter contour, and the 3rd overtone blanks with a 4.0 diopter contour. The blank diameters were 14 mm.

The blanks used in these experiments were cut to the nominal angles specified by the authors and were X-ray sorted into one minute  $\theta$ -angle groupings by the vendor. The  $\theta$ -angles were held constant at 21°56' and 34°01', the angle from the reference  $\theta$ -angle, was varied in 20 minute increments up to 120 minutes. (The reference  $\theta$ -angles are the  $\theta$ -angles for which the slope of the frequency vs. temperature curves are zero at the inflection temperature; e.g., this angle is 33°39' for 5 MHz fundamental mode resonators and is 34°01' for 5 MHz 3rd overtone resonators.<sup>4</sup>) The angles of cut given below are believed to be accurate to better than  $\pm 10'$  in  $\theta$  and  $\pm 2'$  in  $\theta$ . While such loose tolerances would be unacceptable for oven controlled SC-cut oscillator applications, as will be shown below, such tolerances should be adequate for most SC-cut TCXO applications.

The frequency vs. temperature characteristic of a typical SC-cut TCXO resonator is shown in Figure 1. In a typical temperature range of interest, such as -40°C to +75°C, the characteristic is as shown in Figure 2.

To optimize resonators for conventional TCXO applications, a primary goal is often to minimize

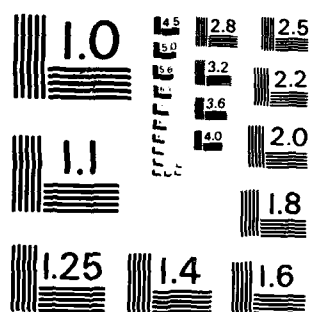
AD P001517

UNCLASSIFIED

3/8

F/G 20/14

NL



MICROCOPY RESOLUTION TEST CHART  
NATIONAL BUREAU OF STANDARDS-1963-A

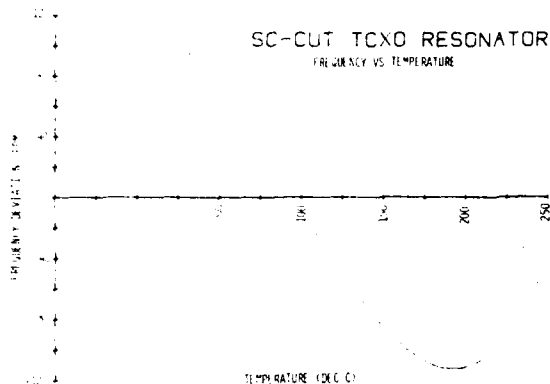


Figure 1 - Frequency vs. Temperature Characteristic of SC-Cut TCXO Resonator Over A Wide Temperature Range

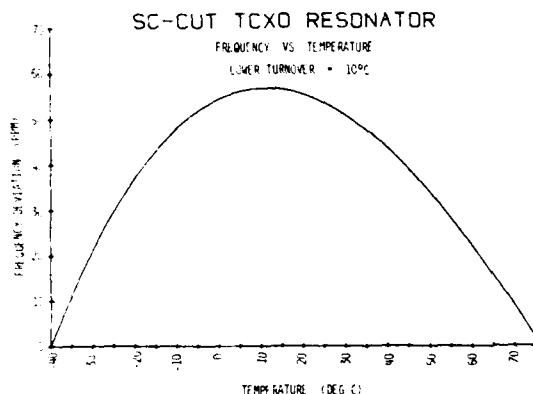


Figure 2 - Frequency vs. Temperature Characteristic of SC-Cut TCXO Resonator

the frequency excursion over the temperature range. A significant future application of SC-cut TCXO resonators is likely to be in microcomputer compensated clock oscillators wherein the frequency vs. temperature characteristic of the resonator is stored in a memory and, based on the resonator's temperature, the clock is advanced or retarded, as required, to keep accurate time. In such an application, where the frequency is not "pulled", a primary goal is to minimize the clock errors due to thermometry errors, i.e., to minimize the maximum frequency vs. temperature slope over the temperature range.

The frequency vs. temperature data for over 200 resonators ranging from  $\Delta\theta = 0'$  to  $\Delta\theta = 120'$  were analyzed to determine: 1. the minimum frequency excursions over various temperature ranges, 2. the minimum frequency vs. temperature slopes at the temperature range extremes, 3. the lower turnover temperature vs.  $\Delta\theta$  characteristics, and 4. the "angle sensitivities" of the frequency excursions and of the frequency vs. temperature slopes.

TEMPERATURE RANGE (°C)	APPROXIMATE $\Delta\theta$	SLOPE AT RANGE LIMITS	LOWER TURNOVER	FREQUENCY EXCURSION	AT-CUT DIFFERENCE
-40 TO 75	41'	1.5 ppm/°C	25°C	15 ppm	15 ppm
"	32'	"	"	"	"
-54 TO 85	48'	1.4 ppm/°C	12°C	15 ppm	24 ppm
"	31'	"	"	"	"
0 TO 60	24'	1.5 ppm/°C	25°C	15 ppm	15 ppm
"	21'	"	"	"	"

Table I - Optimized TCXO Resonator Properties

Table I shows a summary of the optimized properties of SC-cut TCXO resonators for three temperature ranges: 1.  $-40^{\circ}\text{C}$  to  $+75^{\circ}\text{C}$ , 2.  $-54^{\circ}\text{C}$  to  $+85^{\circ}\text{C}$  and 3.  $0^{\circ}\text{C}$  to  $60^{\circ}\text{C}$ . For each temperature range, the first lines show the minimized slopes at the temperature range limits and the corresponding lower turnover temperatures. The second lines show the minimized frequency excursions between the turnover temperature and the temperature range limits (i.e., the differences between the minimum and maximum frequencies), and both the corresponding lower turnover temperature and the frequency excursion for an AT-cut resonator that is optimized for the same temperature range. The approximate  $\Delta\theta$ 's for the optimum resonators are also shown.

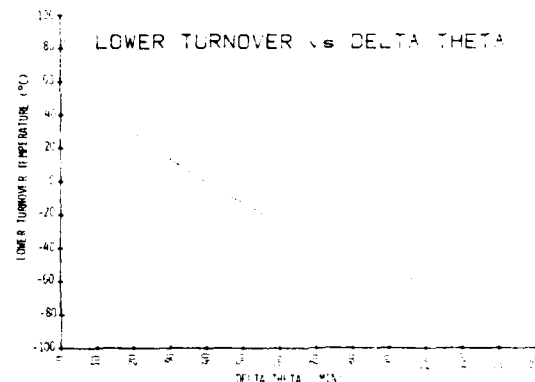


Figure 3 - Lower Turnover Temperature vs.  $\Delta\theta$

Figure 3 shows the relationship between the lower turnover temperature and  $\Delta\theta$  for  $\Delta\theta$  up to  $120'$ . A section of this curve for the  $-10^{\circ}\text{C}$  to  $+20^{\circ}\text{C}$  turnover temperature range that is of interest for many TCXO applications is shown magnified in Figure 4. Since the slope of this curve is about  $1.4^{\circ}\text{C}$  per minute change in  $\theta$ , it is clear that SC-cut TCXO resonators are relatively insensitive to cutting errors.

Further evidence for the relative insensitivity to cutting errors is presented in Figure 5 in which the sensitivities of the maximum frequency excursion (left scale) and of the maximum slope of the frequency vs. temperature curve

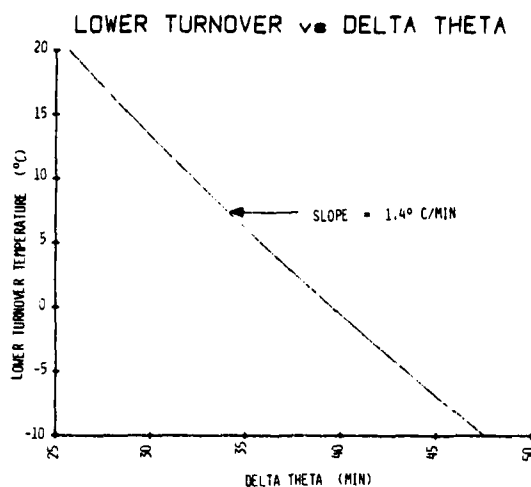


Figure 4 - Lower Turnover Temperature vs.  $\Delta\theta$

(right scale) is shown as a function of  $\Delta\theta$  (top scale) and as a function of the lower turnover temperature (bottom scale) for the  $-40^{\circ}\text{C}$  to  $+75^{\circ}\text{C}$  temperature range. From these curves one can see that, for example, if one makes a three minute cutting error in  $\theta$ , the maximum slope increases from 1.9 ppm per  $^{\circ}\text{C}$  to 2.1 ppm per  $^{\circ}\text{C}$  and the frequency excursion increases from 56 ppm to about 66 ppm; i.e., both quantities increase by less than 20%. Since cutting to  $\pm 3'$  in  $\theta$  (and  $\pm 10'$  in  $\phi$ ) is within the state-of-the-art, for many potential applications, SC-cut TCXO resonator blanks should be as easy or easier to cut to the proper angles as AT-cut blanks that are made to comparable frequency vs. temperature characteristic tolerances.

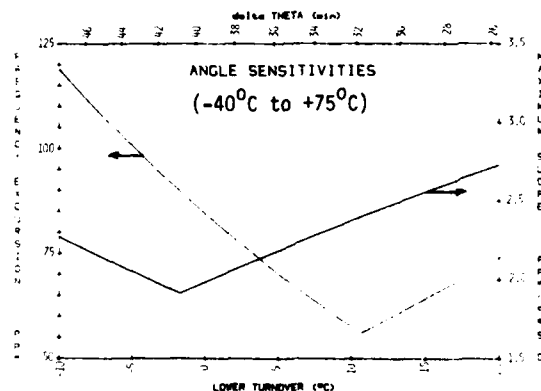


Figure 5 - Sensitivities to Cutting Errors

#### Thermal Transient Characteristic

The warmup characteristics of four-point-mounted ceramic flatpack enclosed SC-cut resonators with turnover temperatures near  $100^{\circ}\text{C}$  have been reported previously.<sup>5</sup> The measurements had been made by monitoring the resonator frequency while immersing the resonator in ice water, and

after thermal equilibrium had been reached, rapidly transferring the resonator into boiling water.

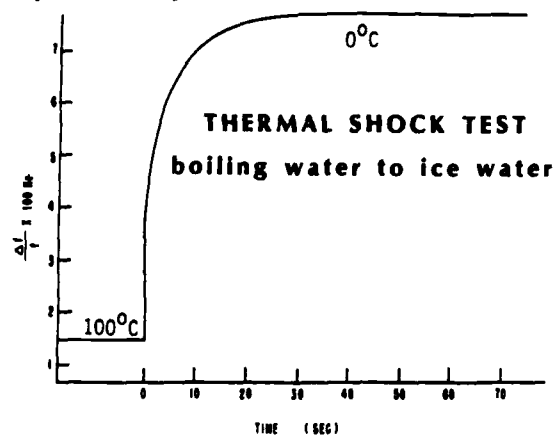


Figure 6 - Thermal Shock Response of SC-Cut TCXO Resonator

This experiment was repeated with a group of ten SC-cut TCXO resonators with turnover temperatures near  $0^{\circ}\text{C}$ . The resonators were immersed into boiling water first, then into ice water. The result for a typical test is shown in Figure 6. As expected, the thermal transient compensation was not affected by the fact that the  $\theta$ -angles were approximately  $40'$  higher for these resonators than for the resonators that had the turnover temperatures near  $100^{\circ}\text{C}$ . For all ten TCXO resonators, the frequency overshoot during the thermal shock was less than 1 ppm. The average overshoot was less than  $5 \times 10^{-7}$ , and the average thermal time constant was 10 seconds.

#### Activity Dip Incidence

Nearly all designs of SC-cut resonators that have been investigated have exhibited an extremely low incidence of activity dips in the c-mode. However, the initial frequency vs. temperature results for the b-modes of the same overtones as the c-modes have indicated a high incidence of activity dips. When the b-modes' frequency vs. temperature characteristics were measured at the same 1.5 ma drive current as was used to measure the c-modes, each of ten resonators measured exhibited more than one large activity dip. When some of the measurements were repeated with drive currents as low as 0.1 ma, the activity dips diminished but did not disappear. The b-mode's frequency vs. temperature characteristics need to be studied further.

#### Thermal Hysteresis

A major limitation on the frequency accuracies achievable with TCXO's is the non-repeatability of the resonator's frequency vs. temperature characteristic, i.e., thermal hysteresis. Figure 7 shows an example of a resonator that exhibits a relatively poor 1 ppm thermal hysteresis at the lower turnover temperature.



### Initial Hysteresis Results

Each resonator was measured in a minimum of two "good" oscillators. Only the largest of the hysteresis values measured for each resonator-oscillator combination is reported. (The results obtained with one of the oscillators is omitted since this oscillator consistently produced poor results. An example of the data obtained with this unit is plotted in Figure 9. It is obviously a defective circuit; it was obviously contributing significantly to the hysteresis.)

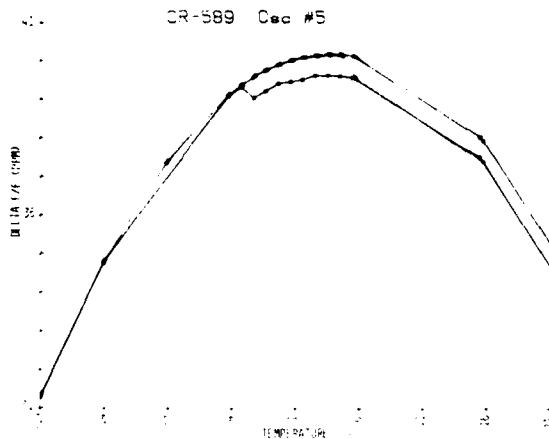


Figure 9 - "Thermal Hysteresis" with Defective Oscillator

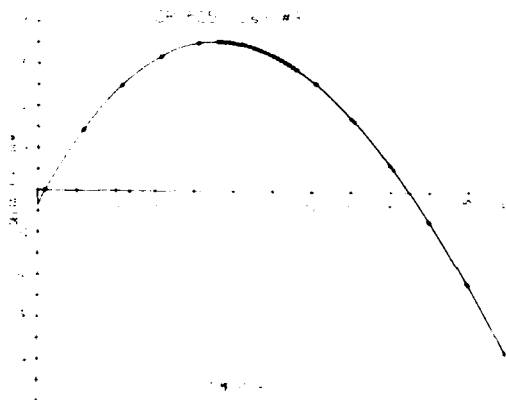


Figure 10 - Hysteresis Result for "Good" SC-Cut Unit

The results plotted for a typical SC-cut hysteresis run is shown in Figure 10. For the SC-cut units especially, there was not enough separation among the four curves of a run for one to be able to determine hysteresis from the plotted data. The numbers reported below were calculated from the least-squares fit to the data.

The results for the initial units evaluated are shown in Table II. The "worst hysteresis" column shows the worst result for the worst unit

RESONATOR TYPE	LTP RANGE	AVERAGE DEVIATION AT LTP	WORST HYSTERESIS AT LTP	NO. OF UNITS
SC-FUNDAMENTAL (YCB25)	1°C to 35°C	$1.5 \times 10^{-8}$	$5.0 \times 10^{-8}$	4
SC 3RD OVERTONE (YCB25)	-30°C to 30°C	$7.5 \times 10^{-9}$	$1.7 \times 10^{-8}$	1
SC-FUNDAMENTAL (SCAD2)	7-9°C to 77°C	$5.4 \times 10^{-8}$	$8.5 \times 10^{-8}$	1
AT-FUNDAMENTAL	-150°C	$4.0 \times 10^{-7}$	$8.2 \times 10^{-7}$	1
AT 3RD OVERTONE	-160°C	$1.7 \times 10^{-7}$	$5.2 \times 10^{-7}$	1

Table II - Initial Hysteresis Results

in each group. For each run the values of the lower turnover frequencies obtained during the second, third and fourth passes through the lower turnover point were compared with the value obtained during the initial "calibration" pass, and the average of the absolute values of the deviations was calculated. The "average deviation" column of Table II shows the average of all average deviations, for each resonator type.

The worst of the nine SC-cut units exhibited a hysteresis of  $8.5 \times 10^{-8}$ . The hysteresis of the two similarly fabricated ceramic flatpack enclosed AT-cut units were about an order of magnitude worse than the worst SC-cut units.

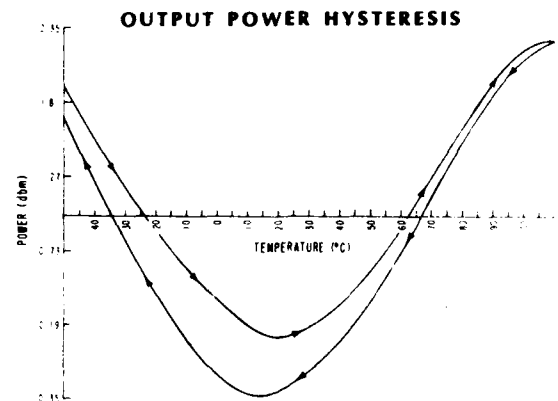


Figure 11 - Hysteresis in Oscillator Power Output

The use of oscillators for the initial measurements of hysteresis was chosen due to availability, not because it is the best method. During each hysteresis run, in addition to measuring frequency and temperature, the oscillator power outputs were also monitored. Invariably, the power output vs. temperature exhibited hysteresis. A typical power vs. temperature hysteresis curve is shown in Figure 11. Since the oscillator circuitry contributed to the measurement results a finite but unknown amount,

the results in Table II represent upper limits on the resonators' contributions to the measured hysteresis. These preliminary hysteresis results for SC-cut resonators are therefore encouraging.

#### Summary and Conclusions

The frequency - temperature characteristics vs. angle-of-cut have been determined for SC-cut TCXO resonators. For many potential applications, the angle-of-cut tolerances are easy to achieve with conventional cutting equipment.

The minimum frequency excursion over a given temperature range is significantly higher for SC-cut resonators than for AT-cut resonators. Since SC-cut resonators' motional capacitance is approximately one third that of AT-cut resonators of the same overtone, it is significantly more difficult to compensate SC-cut resonators with conventional analog compensation techniques. However, overtone SC-cut TCXO resonators in dual mode oscillators (using a b-mode or some other temperature sensitive mode for thermometry) promise to provide very high accuracy clock oscillators through "external" compensation techniques.

The preliminary hysteresis results are encouraging. The results indicate that SC-cut resonators may permit a significant improvement in the stabilities achievable with TCXO's. This is especially true for clock applications. Before a substantial improvement in TCXO stabilities can be realized, the following will need to be resolved:

1. The term "hysteresis" will have to be defined in such a manner that its measured value will be indicative of the worst case frequency vs. temperature non-repeatability in actual use. The required temperature cycles, dwell times, rates of change of temperatures, etc. will need to be included in the definition.

2. Measurement methods will need to be established that can measure a resonator's hysteresis without having the measurement equipment contribute significantly to the results. (The reflectometer technique described by Stone and Baltzer<sup>8</sup> is a promising alternative.)

3. Oscillator circuits and circuit components will need to be carefully selected in order to minimize the oscillator circuits' contribution to hysteresis.

4. To minimize thermometry related frequency errors, dual mode oscillators which utilize modes that are not subject to significant activity dips or hysteresis effects will need to be developed.

#### Acknowledgements

The authors wish to thank M. Washington for fabricating most of the resonators used in these experiments, R. Brandmayr and M. Spaight for their assistance in preparing the resonator blanks, and E. Simon and R. Williams for performing some of the frequency vs. temperature

measurements. Thanks are also due J. Keres, T. Snowden and the resonator development group at GEND for their assistance with fabricating the resonators used in the hysteresis experiments.

#### References

1. G.E. Buroker and M.E. Frenking, "A Digitally Compensated TCXO," Proc. 27th Annual Symposium on Frequency Control, pp 191-198, 1973
2. J.A. Kusters and J.G. Leach, "Dual Mode Operation of Temperature and Stress Compensated Crystals," Proc. 32nd Annual Symposium on Frequency Control, pp 389-397, 1978
3. Sawyer Crystal Systems, Conroe, Texas
4. R.W. Ward, "Design of High Performance SC-Resonators" Proc. 35th Annual Symposium on Frequency Control, pp 99-103, 1981.
5. R.L. Filler and J.R. Vig, "The Acceleration and Warmup Characteristics of Four-Point-Mounted SC and AT-cut Resonators," Proc. 35th Annual Symposium on Frequency Control, pp 110-116, 1981
6. E.P. EerNisse, "Calculations on the Stress Compensated (SC-cut) Quartz Resonator," Proc. 30th Annual Symposium on Frequency Control, pp 8-11, 1976
7. B. Parzen, Design of Crystal and Other Harmonic Oscillators, John Wiley and Sons, Inc. Publishers, New York, to be published in late 1982.
8. C.S. Stone and O.J. Baltzer, "A Frequency Domain Reflectometer for Quartz Resonator Investigations," elsewhere in these Proceedings.

PHOTOLUMINESCENCE FROM WORKED SURFACE LAYERS AND  
FREQUENCY INSTABILITY OF QUARTZ RESONATORS

A. Halperin, S. Katz and M. Ronen

Racah Institute of Physics  
The Hebrew University of Jerusalem  
Israel

Summary

The disturbed surface layers produced by polishing and lapping affect considerably the frequency stability of quartz resonators. The present work describes the use of photoluminescence (PL) emitted from these layers for understanding the nature of the frequency instability. Experiments included measurements after successive etchings, thermal treatments and ultrasonic cleaning. The effects on the PL were compared to those on the resonator frequency. Our results support strongly the contamination mechanism for the frequency instability due to the worked layer in quartz resonators. It seems that vapors (including water) adsorbed in the cracks and grooves of the disturbed layers play an important role in the frequency instability due to the worked layers.

Key words: Quartz, Resonators, Worked Layers, Photoluminescence, Frequency Instability, Adsorption, Etching, Thermal Release.

Introduction

The disturbed surface layers produced by lapping and polishing in the process of preparation of quartz resonators are known to affect considerably the quality and the frequency stability of the resonators. The thickness of the worked layers and with it the frequency instability are known to go up with the coarseness of the polishing powders and with the polishing pressure<sup>1,2</sup>. Two mechanisms were suggested to explain the frequency drift due to the worked layers. The first assumes that the drift is due to the strain in the surface layers produced during the polishing<sup>1,3,4</sup>. The frequency instability then results from the gradual release of the stress produced by the processing<sup>1</sup>. By the second mechanism the frequency instability is attributed to the release of embedded abrasives or contaminants from the cracks in the worked surface layers.

In the present work we have observed under certain conditions photoluminescence (PL) excited by UV light. This PL was found to originate from the worked surface layers and depended on the coarseness of the grinding in a way similar to that of the frequency instability. Similarities in

behavior between the two effects were observed also in other treatments, e.g. in the elimination of the effects by thermal annealing. The PL produced in the worked layers served thus as a tool helping to clarify the nature of the mechanism causing the frequency instability due to the disturbed layers. The results will be shown to support strongly the contamination mechanism as the main cause for the frequency instability due to the worked layers in quartz resonators.

Experimental

The crystals used in the present work were natural and synthetic quartz in AT and BT cuts. They were lapped with carborundum powders of various meshes (220-3000#). Diamond powder pastes were used for polishing to nearly optical flatness. The crystals were etched by a 48% hydrofluoric acid solution. PL and excitation spectra were recorded using a Cary 14 spectrophotometer. For the excitation spectra the crystals were placed in the sample holder cell of the Cary. A combination of mica and perspex filters placed between the crystal and the photomultiplier of the Cary blocked almost completely the UV exciting light from reaching the detector.

For measuring the emission spectra the sample replaced the visible light source of the Cary and was excited by light from a high pressure Xenon arc lamp or a Mercury arc lamp through a double monochromator (0.25 meter Jarrell-Ash Double Monochromator). The emission spectrum was then dispersed and recorded by the Cary 14 spectrophotometer.

The resonator frequencies were measured in a transmission method set-up which included a XUD Rohde and Schwarz Decade Frequency Synthesizer and Exciter, a RQZ Crystal Measuring Head and a USVH Selective Microvoltmeter. The resonators were placed in a home-built holder with a variable air gap between electrodes set by accurate micrometer screws and kept at a constant temperature ( $\pm 0.1^\circ$ ) during the measurements. The resonator frequencies were also recorded using a crystal controlled oscillator and a 5245L Hewlett-Packard Electronic Counter connected to a 581A Hewlett-Packard Digital-Analog Converter and a chart recorder. The later set-up was used especially for long term frequency measurements. Thermal treatments were

AD P001518

performed by keeping the crystals in a test tube placed in a furnace for about 15 minutes at every stabilized temperature.

### Results

Figure 1 shows the excitation spectrum and Figure 2 gives the emission spectrum of the PL excited by UV light. The excitation maxima appear near 230nm and 260nm. The emission shows a maximum near 420nm and a tail towards longer wavelengths. The intensity of the PL as well as the ratio of the emissions excited in the two bands at 230 and 260nm varied with the conditions of lapping and polishing of the crystal surfaces. The PL could be eliminated almost completely by ultrasonic cleaning in distilled water or in acetone. This shows that the PL is not intrinsic to the quartz and seems to be associated with contaminants. It is shown below that the PL is limited to the worked layers and thus measurement of the PL can provide information on these layers.

In the first series of experiments we have measured the PL after successive short etching periods. Figure 3 gives the intensity of the PL as function of etching time for crystals lapped with various grinding powders. Curve a of Figure 3 was obtained after grinding with coarse (220#) carborundum, Curve b was obtained after grinding with a finer powder (1400#) and Curve c gives the results obtained with nearly optically polished surfaces. It is evident that the intensity of the PL and the total etching time needed for its elimination go down with the fineness of the grinding. In all the curves there is a rise in the PL at comparatively short etching times. The PL then decreases sharply to a lower value from which a further gradual decrease in it takes place. The PL disappears completely when the worked layer is entirely etched away. While the total etching time needed for full elimination of the PL was many hours with the very rough surfaces (Curve a), it is much shorter in Curve b and very short in Curve c (nearly optical polishing). The results thus show clearly that the PL is limited to the worked layers.

Figure 4a shows again the effect of the etching on the PL for a crystal with rough surfaces (220#). This time the etching was stopped several times and the crystal was left standing in ambient room atmosphere, each time for nearly 20 hours. The standing time for itself affected only slightly the PL (usually there was a small increase). However, when resuming the etching there was a considerable increase in the PL, similar to that obtained in the beginning but weaker. This effect of standing could be repeated many times with the intensities going down in successive sets of experiments until the worked layer was completely etched. Curve b of Figure 4 shows the reduction in crystal thickness by the etching. The PL versus etching time shown in Figure 3 can be in a way related to the curves of frequency shift versus etching time reported by Fukuyo and Oura<sup>2</sup> a matter which will be discussed below.

Figure 5a shows the effect of annealing at various temperatures upon the PL of the worked layer. The PL was measured each time after cooling back to room temperature. It is seen to decrease strongly below 200°C. The cancellation of the PL by annealing can be analysed by thermo-analytical methods. Curve b in Figure 5 gives the temperature derivative of the PL ( $-dI/dT$ ). It peaks at about 160°C. Keeping the thermally treated crystal for some time (e.g. one day) in ambient atmosphere at room temperature caused some re-appearance of the PL, which indicated that vapors from the atmosphere play a role in the centers causing the PL. This was also supported by the following experiment: Two quartz crystals were lapped (with 220# carborundum). One of the crystals was left at room temperature and the other was kept at about 20° above room temperature. The PL intensity of both crystals was measured every day during a week. The results are shown in Figure 6, in which Curve a gives the PL of the crystal kept at 20° above room temperature and Curve b gives that of the one kept at room temperature. It can be seen that while the PL of the first crystal decreased with standing time, that of the latter one increased with time. This fits the hypothesis of vapors from the atmosphere participating in the process.

Some measurements were also performed on the effects of grinding processes and thermal treatment on the quartz resonator frequency. Figure 7a shows the frequency drift versus time for a crystal lapped with 600# carborundum. Soon after lapping the crystal was dried for one minute at about 70°C after which it was placed between the electrodes and kept at constant temperature (a few degrees above room temperature) when the recording of the frequency started. The frequency is seen to rise in a way similar to that described by Oura et al<sup>1</sup>. We have also confirmed the results described in Ref. 1 by which the frequency drift is smaller when lapping with finer abrasive powder and goes down practically to zero with nearly optically polished surfaces.

Figure 7b gives the frequency drift with time for a crystal lapped in a way similar to that used for Figure 7a but annealed for 20 minutes at 350°C and cooled back to room-temperature before recording the frequency. The frequency decreased now during the first few hours after which it increased very slightly with time. It should be noted that the initial decrease in frequency observed in Curve 7b was much smaller in other similar experiments.

Curve a in Figure 8 shows the frequency drift of an AT cut resonator lapped with 600# carborundum to a frequency of about 4014 KHz. The annealing was performed in a way similar to that described for Figure 5 and the frequency measurements were carried out as for Figure 7. We note that though the frequency rise starts at about 100°C, the main rise occurs near 280°C. Curve 8b gives the same as 8a but after fine lapping and polishing of the same crystal to 4082 KHz when most of the original worked layer was removed. The

frequency drift is now much smaller as expected. Curve 8c gives the temperature derivative of Curve 8a ( $\Delta f/\Delta T$ ). It exhibits a peak at about 280°C and a long tail towards lower temperatures. In spite of the analogous behavior between the PL and the frequency during the thermal treatment (compare Figures 5 and 8), there is a distinct difference between the two effects. While the peak of  $-\Delta L/\Delta T$  occurs below 200°C that for  $\Delta f/\Delta T$  appears near 300°C.

#### Discussion

The PL was shown to decrease gradually with etching time and it came down to zero intensity when the disturbed layer was completely etched away. This proves that it originates in the disturbed layer. It was also shown in the present work that the PL depended strongly on the roughness of the worked layer and was affected by etching. At short etching times the luminescence increased and gave a complex maximum. The exact nature of the process causing this increase in PL is not clear. It seems, however, that it involves the adsorption of some components from the hydrofluoric acid solution at the rough surfaces of the worked layers. Fukuyo and Oura<sup>2</sup> have observed an abrupt decrease in frequency of quartz resonators after short etching times, an effect which could be eliminated by preheating to 520°C. This is in a way similar to the effect of the increase in PL in our experiments and so it may also be related with adsorption at the crystal surfaces. Quantitatively the two effects differed from each other. While the frequency decrease observed in Ref. 2 was limited to the removal of very thin layers (of the order of a small fraction of a micron) the increase in PL in our experiments lasted (in roughly polished crystals) until more than one micron was removed from each face by etching (see Figure 4). This behavior should be attributed partly to differences in the roughness of the polished crystal faces and partly to the characteristics of the two effects: while the PL depends on the availability of the rough worked layer, the frequency will turn to go up with the removal of material from the surfaces, which starts after very short etching times. Thus only in the very initial stage of etching it may be possible to observe a decrease in frequency due to adsorption.

Our thermal treatment experiments both on the PL (Figure 5) and frequency shift (Figure 8) support strongly the contamination model. Both the effects fit well the shape of thermogravimetric curves in which the reduction in mass is plotted as function of temperature. For the analysis of such curves it is convenient to take the temperature derivatives when conventional methods common in thermally stimulated processes, e.g. thermoluminescence, can be used<sup>5</sup>. The derivatives are given in Figures 5b and 8c for the PL and the frequency shift respectively. For the PL we obtained an activation energy of 0.72 eV using the initial rise method<sup>6</sup> and a value of 0.8 eV assuming first order kinetics and using the peak shape method<sup>6</sup>. The results obtained from the frequency shift were different. We note that

Curve 8c shows a long tail on its low temperature side down to about 100°C. The initial rise method gave for this tail an activation energy of about 0.4 eV, while from the shape of the main peak at 280°C we obtained values near to 2 eV. In spite of the relatively high inaccuracy in the derivative curves resulting from the scattering of the experimental points (especially in Curve 8c) the difference between the thermal stability of the PL and that of the frequency shift is real. The discrepancy may have resulted from differences in the origin of the two measured effects. Because of the high scattering of the light at the rough surfaces of the crystals the PL reaching the detector was limited to a very thin surface layer of about 1 micron. The thermal activation energy measured from Curve 5b should therefore be related to the release of contaminants from these shallow surface layers. For the frequency shifts, however, the release of contaminants from the whole thickness of the worked layers had an effect. The effective layer depth in this case was a few microns and hence the higher peak temperature and higher activation energy.

It has been mentioned above that prolonged ultrasonic cleaning of the crystals in water as well as in other solvents eliminated almost completely the PL. Similarly, such cleaning resulted in an appreciable increase in the frequency of roughly polished resonators. This frequency increase was under certain conditions by more than one percent of the resonator frequency. This can be accounted for by assuming that during the rough polishing the grooves and cracks in the worked layer are filled up with the ground quartz powder mixed with some abrasive and probably also other contaminants. It is known<sup>7</sup> that quartz powder adsorbs strongly water vapor. More than that, the release of the adsorbed water from the quartz powder was shown<sup>7</sup> to take place over a wide temperature range up to about 600°C. The exact thermal behavior will depend on the roughness of the powder particles and on the depth of the layers. We suggest that the thermal elimination of the PL and the frequency drift with temperature result from the release of vapors from the powder filled cracks of the worked layer. The temperature at which the main release of the vapors occurs will then depend on the roughness and depth of the worked layers.

#### Acknowledgement

We acknowledge with thanks a grant by A.D. Bergmann Foundation which helped to carry out this research.

#### References

1. N. Oura et al. IEEE Trans. on Instrumentation and Measurement, **1 M - 30** (1981) 139.
2. H. Fukuyo and N. Oura, Proc. of the 30th Ann. Freq. Control Symp., (1976) 254.

3. Y. Sekiguchi and H. Funakubo, *Journal of Materials Science* 15, (1980) 3066.
4. E. Fukushima and H. Nimura, *J. Phys. Soc. Japan* 16, (1961) 928.
5. See: R. Chen and Y. Kirsh, "Analysis of thermally stimulated processes" *International Series on the Science of the Solid State*, Vol. 15, 1981, Ch. 4.
6. A. Halperin et al., *Physical Review* 117, (1960) 416. See also: Chap. 6 of Ref. 5.
7. G.J. Moore and H.E. Rose, *Journal of Thermal Analysis* 15, (1979) 37.

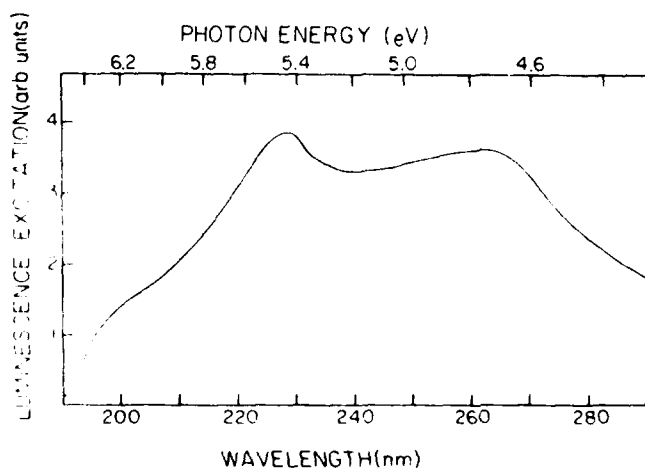


Figure 1. Excitation Spectrum for the PL Originating in the Worked Layer of Quartz Plates

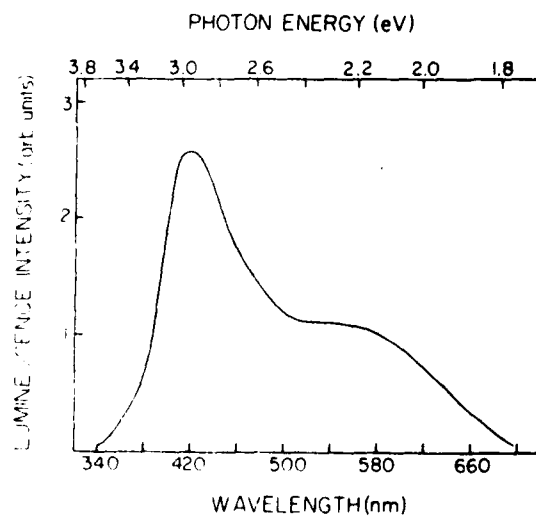


Figure 2. Emission Spectrum of the PL Excited by UV Light

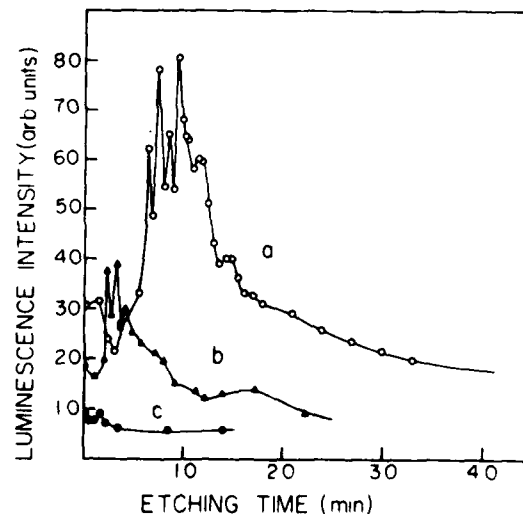


Figure 3. The Effect of Etching Time on the PL for Crystals Lapped with Various Grinding Powders

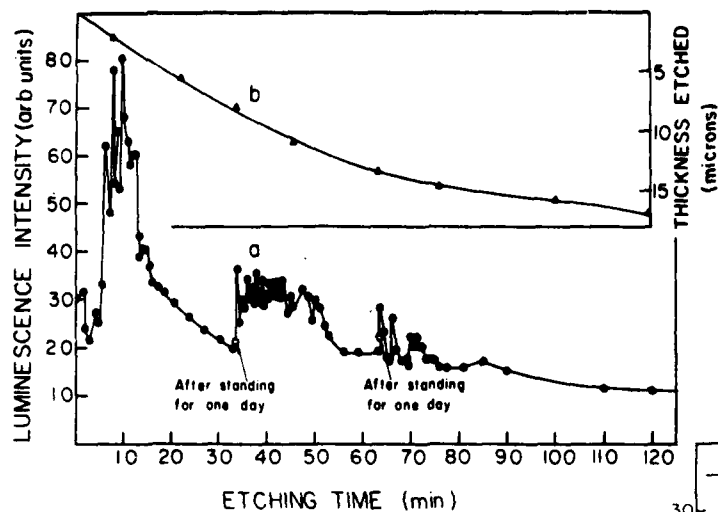


Figure 4. The Effect of Standing in Ambient Atmosphere on the PL of a Roughly Polished (220 #) Quartz Crystal (Curve a). Curve b Gives the Thickness Etched Away.

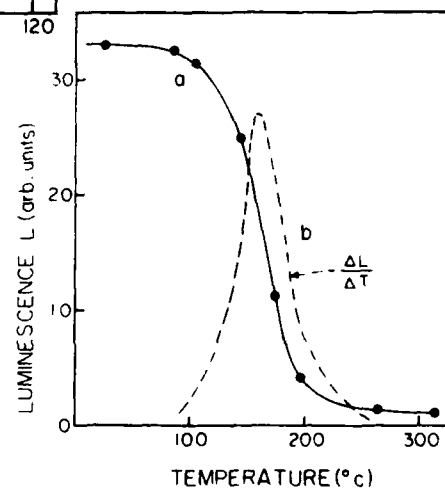


Figure 5. The Effect of Heating to Various Temperatures on the PL of the Worked Layer (Curve a). Curve b Gives the Temperature Derivative of the PL Intensity ( $-\Delta L / \Delta T$ ).

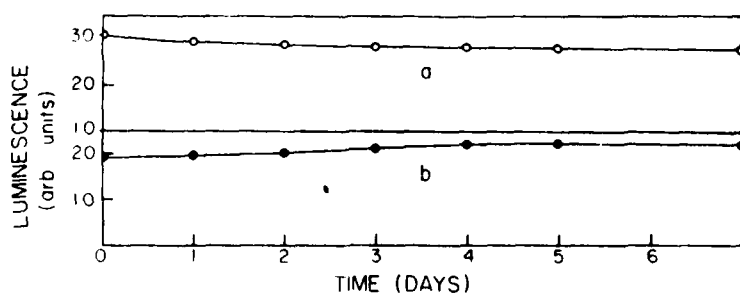


Figure 6. The Dependence on Standing Time of the PL of a Crystal Kept at 20° Above Room Temperature (Curve a) and That of One Kept at Room Temperature (Curve b).

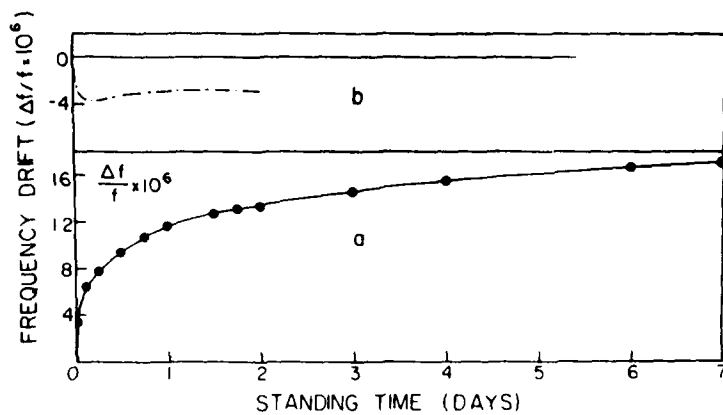


Figure 7. The Frequency Drift Versus Standing Time for a Crystal Lapped with 600 #Carborundum (Curve a) and for One Lapped as for Curve a But Preheated at 350°C (Curve b).

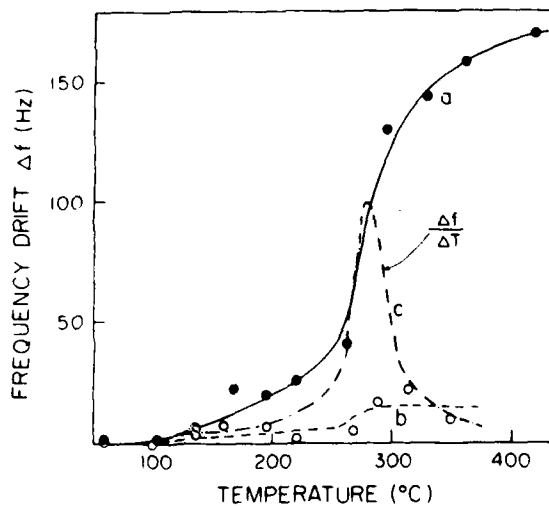


Figure 8. The Frequency Drift of an AT-Cut Quartz Resonator. a - After Lapping with 600 #Carborundum, b - The Same Crystal as in a But After Fine Polishing Which Removed Most of the Worked Layer. Curve c Gives the Temperature Derivative of Curve a ( $\Delta f / \Delta T$ ).

# GROWTH TUNNELS IN QUARTZ CRYSTALS

S. Katz and A. Halperin  
Racah Institute of Physics  
Hebrew University of Jerusalem, Israel

and

M. Schieber  
School of Applied Science and Technology,  
Hebrew University, Jerusalem, Israel

## Summary

Tunnels observed in unetched quartz crystals showing a multitude of orientations in the crystal are described. They varied from a fraction of a micron up to about 2 microns in their diameters, and penetrated a few millimeters into the crystal. The diameter was constant along the whole length of a given tunnel.

It is suggested that these tunnels as well as tunnels in quartz in general, were formed during the growth of the crystal. By this assumption etching only broadens existing tunnels, and so makes them observable optically.

**Key-words:** Quartz, Growth, Tunnels, Microscopic Observations, Edge Illumination.

## Introduction

Defects having the shape of tunnels affect considerably the quality and frequency stability of quartz resonators. It is therefore important to understand their origin. Tunnels have been observed in natural and synthetic quartz by several investigators<sup>1-5</sup>. Nielsen and Foster<sup>1</sup> have observed deep etch tubes, ribbon-like in shape, in synthetic and natural quartz. They hesitated to state that the structure and characteristics of the tunnels can be ascribed to a dislocation. Another model suggested by these authors involved non-uniform incorporation of impurities in the crystal during its growth. In an additional model they suggested that the tubes were formed by etching of impurities precipitated along dislocation lines. This, they say, would account for the great depth of penetration and small cross section of the observed etch tubes. Iwasaki<sup>2</sup> has observed tunnels in synthetic quartz only after prolonged etching in hydrofluoric acid. He concluded accordingly that the defects were formed by etching, and suggested that vapors of the acid penetrating along dislocation lines produce the tunnels. Ser et al<sup>3</sup> studied natural quartz. They stressed that by optical microscopy the tunnels are observable only after etching, and suggested that the tunnels were formed along dislocation lines decorated by impurities. The etching then removes these impurities. The tunnels observed by Ser et al<sup>3</sup> showed wide variations in orientation in the crystal and usually started at inclusions in the crystal. They have also observed some line defects that showed

a higher contrast in x-ray topography than that of dislocation lines and concluded that the defects were narrow tunnels not observable optically. In the present work we report on tunnels observed optically in crystals that have not been etched chemically. We suggest that tunnels in general may have been formed during the growth process, and not by chemical etching which only broadens the existing tunnels in crystals to dimensions which make them observable optically.

## Experimental

The experiments were carried out on commercial synthetic AT-cut crystals. The sawn crystal plates were polished using various meshes of silicon carbide powders (1000#-3000#). The crystals were studied using an optical projection microscope (Vickers). The tunnels were observed either by transmission or by edge illumination of the crystal. In the latter case the crystal had to be rotated and at a given orientation the reflection from the tunnels became brilliant.

## Results

Figure 1 is an optical micrograph (x 110) obtained by light transmitted through the crystal. It shows many tunnels which vary widely in crystal orientation. About a dozen of different orientations can be seen in the plane of the crystal plate, and additional orientations are obtained from the different angles of penetration into the crystal plate. The diameter of a given tunnel was constant along its whole length. Some of the tunnels are barely visible and they seem to be only a fraction of a micron in diameter. Those giving the stronger contrast are 1-2 microns in diameter. Practically all the tunnels penetrate through the whole thickness of the plates which was 300-500 microns. In Fig. 1 the density of the tubes is of the order of  $10^4 \text{ cm}^{-2}$ . The tunnels generally had the shape of straight lines. Figure 2 (also x 110) was obtained by edge illumination. The tunnels are well focused at the crystal surface under examination and get out of focus on penetration into the bulk of the crystal, which gives them an appearance of comets. One notices that the angle of penetration in relation to the crystal surface is not the same for all the tunnels. This is clearer in Fig. 3 taken at a higher magnification (x 330), which also shows bundles of tunnels. It is interesting that

AD P001519

in the reflection photographs (Figures 2 and 3), the orientation at which the reflection from the tunnels flashed up was the same for all the tunnels in spite of the wide variation in orientations. This suggests that the walls of the tunnels are not parallel to the main direction of the tunnel but are rather built of segments with preferred crystal orientations. The flash-up of the tunnels is then obtained by near-specular reflections from these segment facets. Figure 4 (x 110) is a transmission photograph of another synthetic crystal. In this case the crystal has been etched during the process of manufacture as a resonator. This time the density of tunnels is quite high and they show a wide variation in contrast. Some of the tunnels are a few microns in diameter while others are barely visible optically. In this crystal the tunnels are all parallel to each other.

#### Discussion and Conclusions

Existing models for tunnels in quartz assume that they were formed by etching along regular dislocations or along impurity decorated ones.

A few difficulties arise in these models:

- 1) It is difficult to accept that the acid or even its vapors can etch the crystal a few millimeters deep along a dislocation line of atomic dimensions in cross section.
- 2) It is improbable that dislocation lines will have so many orientations in quartz crystals (see Figures 1-3) all advancing in straight lines.
- 3) Etching along dislocation lines should necessarily start near the crystal surfaces. It should then advance more into the bulk of the crystal near the surface compared to that deeper along the tunnel. The cross section should then come down with the depth of penetration. Our observations, however, showed that the cross-section of the tunnels was constant along their whole length.

To overcome the latter difficulty it has been assumed<sup>2</sup> that the strain energy associated with the presence of impurities at a dislocation line results in faster etching along the dislocation compared to that in the rest of the crystal. Even so, one should still expect the cross-section to go down with the depth of penetration, at least for comparatively short etching times.

In the present work we have observed tunnels in crystals seen after slicing, without chemical etching. These tunnels were certainly formed during the growth of the crystal. In order to remove the difficulties stated above we suggest that tunnels in general are formed during the crystal growth. It seems that the "growth-tunnels" are usually too narrow to be observed optically. Etching, then, broadens them to make them observable optically.

The growth hypothesis removes or at least removes the above stated difficulties. Most tunnels have been observed to start at inclusions<sup>3</sup> or at the seed boundary. Such defects should inhibit the advance of the growth front when a tunnel is initiated. The orientation of the tunnels is

then determined by the direction of the growth front. If this is the case tunnels originating at neighboring points in the crystal should not vary much in orientation. This was indeed observed in the present work for bundles of tunnels (see Figure 3). The orientation along a given tunnel can by this hypothesis change with the direction of advance of the growth front. Nielsen et al<sup>1</sup> have indeed reported that tunnels showed "a strong tendency to follow the direction of growth".

The observation of tunnels in unetched crystals supports strongly our "growth hypothesis". One can still argue that the tunnels in unetched crystals are "etch tunnels" formed during the cooling-down of the autoclave. This hypothesis, however, leaves the difficulties stated above unsolved, which makes the growth hypothesis more preferable.

A growth hypothesis has been suggested by Nielsen et al<sup>1</sup> for tunnels starting at the seed. These authors suggested that the NaOH solution used in hydrothermal growth may etch tubes in the quartz seed before growth begins. The disturbance causing etch tubes then remains and is propagated as the crystal grows. We thus only extend the growth hypothesis to include tunnels originating at other defects, e.g. at inclusions in the crystal.

Vig et al reported<sup>5</sup> that swept and especially vacuum-swept crystals produce far fewer tunnels by etching. These observations show that sweeping increases the resistance to etching in the tunnels. In connection with this it is worth noting that the rate of etching in quartz is believed to depend strongly on the number of tetrahedral coordination sites at the etched surface<sup>6</sup>. This model has been used to explain the differences by more than a factor of one hundred in the etching rate of quartz, depending on the orientation of the attacked surface. If so, the sweeping may affect internal surfaces in the tunnels in a way that the tetrahedral coordination sites enabling an easy attack are eliminated.

#### Acknowledgement

We acknowledge with thanks a grant by the A.D. Bergmann Foundation.

#### References

1. J.W. Nielsen and F.G. Foster, *The American Mineralogist*, **45** (1960) 299.
2. F. Iwasaki, *J. Crystal Growth*, **39** (1977) 291.
3. A. Ser et al., *J. Appl. Crystallography*, **13** (1980) 50.
4. J.F. Balascio and M.S. Lias, *Proc. of the 34th Ann. Freq. Control Symp.* (1980) 65.
5. J.R. Vig et al., *Proc. of the 31st Ann. Freq. Control Symp.*, (1977) 131. See also references 22 to 30 of this paper.
6. F.M. Ernster, *J. Phys. Chem. Solids*, **13** (1960) 347.



Figure 1. A Transmission Micrograph (x 110) of an Unetched AT-Cut Synthetic Quartz Plate

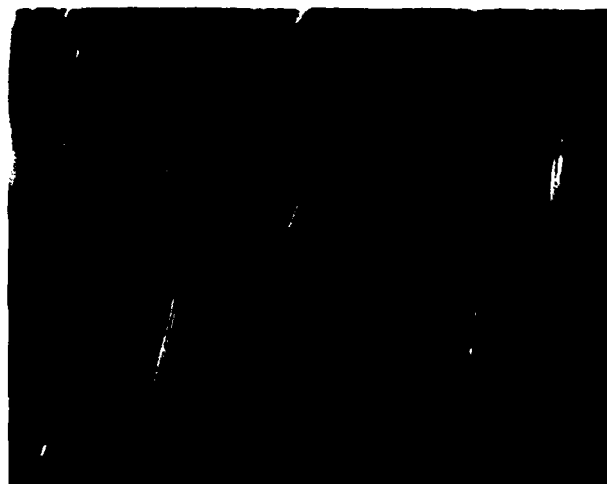


Figure 2. A Micrograph (x 110) Showing the Tunnels as Observed by Edge Illumination. The Same Crystal as in Figure 1.

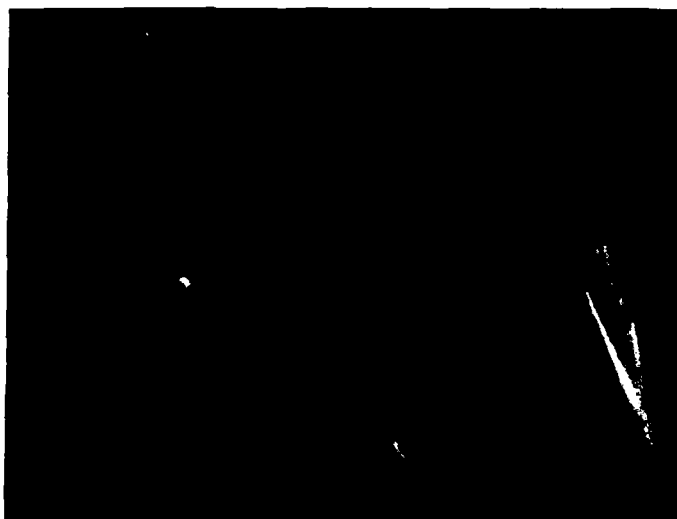


Figure 3. The Same as Figure 2 but at a Higher Magnification (x 330)

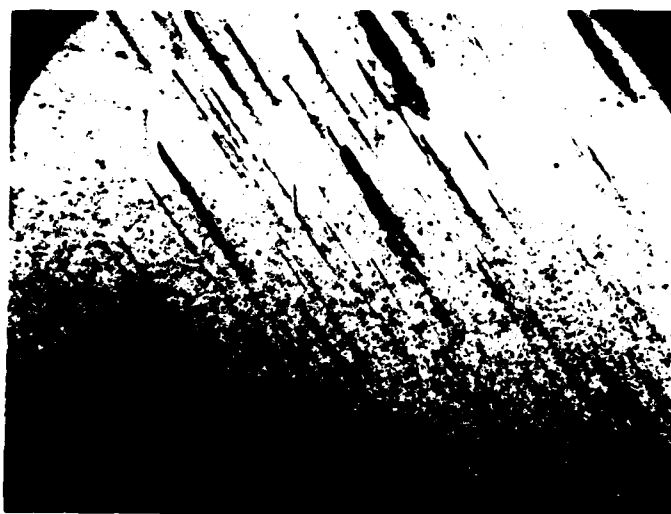


Figure 4. A Transmission Micrograph (x 110) of an AT-Cut Synthetic Quartz Plate Etched During the Process of Manufacture as a Resonator

# VIBRATION COMPENSATION OF THE SEEKTALK RUBIDIUM OSCILLATOR

Carl Colson

Efratom  
Irvine, California

## Summary

In the past, atomic oscillators have not been designed to operate in the presence of severe vibration. In recent years some have been designed to allow some vibration but now they are being called on to accommodate sinusoidal vibration up to 14 "g's" peak and random vibration spectra up to 0.5g<sup>2</sup>/Hz or more. These levels perhaps required only survival a few years ago, but are now the operating environment of atomic oscillators.

Efforts to improve the acceleration-susceptibility of the rubidium oscillator have been successful in the rubidium portion, but vibration-induced sidebands in the quartz-crystal oscillator cause a great deal of difficulty when multiplied to 6.8 GHz to interrogate the rubidium. Of course, the quartz oscillator frequency is also the output available to the user who has similar difficulties in multiplying to UHF or microwave.

Approaches to alleviate the difficulty include (a) "non-crystal" oscillator, (b) less sensitive quartz crystals, (c) accelerometer compensation schemes and (d) combinations of these. This paper concentrates on accelerometer compensation of the vibration and acceleration sensitivity of the crystal. Considerable reference is made to the research done by Dr. R. L. Filler<sup>1,2</sup> and V. R. Rosati<sup>2</sup>. It is our plan to combine the government research effort with Efratom's developmental capability to produce a miniature rubidium oscillator suitable for operation as a precise atomic oscillator in the severe Seektalk vibration environment.

## Introduction

The Seektalk Oscillator vibration requirements can be translated to a phase-noise plot<sup>1</sup> as shown in Figure 1. It is evident that a 20 to 30 dB reduction is required in order to keep the phase-noise spectrum to a reasonable level when crystals having a 1 to 3 ppb/g sensitivity are used. The reduction scheme is shown in block diagram form in Figure 2<sup>2</sup>. It should be emphasized that for the compensation to be correct, the accelerometer and amplifier must subtract the acceleration effects by supplying

the proper magnitude and phase, there perhaps being a tendency to overlook phase at first. To appreciate the part phase plays, one may assign a single pole within the compensation bandwidth of the accelerometer and see that the phase lag causes lack of compensation even more rapidly than does decrease in gain. Also, mechanical alignment of the sensitive axes of the crystal and accelerometer (Figure 3) is critical if an order of magnitude or more compensation in all axes is to be achieved. The sensitive-axis error is related to the cosine of the mismatch angle, but the cross axis sensitivity to the sine. This means that for instance a 6° misalignment alone would cause a cross axis response of one-tenth the uncompensated on-axis response.

## Requirements

### Crystal

The crystal should be an SC-Cut for high sensitivity to applied voltage. It appears that a fundamental resonator has a high sensitivity (7 ppb/v)<sup>2</sup> with third and fifth overtones having progressively less voltage sensitivity (3 and 1.8 ppb/v respectively). We would assume from this that voltage sensitivity is dependent on electric field strength rather than applied voltage. The "lesser" doubly-rotated cuts (FC, IT) are less voltage sensitive, as to be expected if the voltage sensitivity is caused by applying the electric field along a particular crystal axis. The crystal should have a low acceleration sensitivity for two reasons; the correction will only be an order of magnitude or so, and the correcting voltage should be within limits that are reasonable such as  $\pm 10$  volts rather than say  $\pm 100$  volts. In the example of Figure 2, with an acceleration sensitivity of 3 ppb/g and a voltage sensitivity of 3 ppb/g, a  $\pm 10$ g correction requires  $\pm 10$ V.

### Oscillator

The oscillator itself should obviously be designed to accommodate the large low-frequency voltage swings at the crystal terminals. The oscillating stage input should certainly see no more than a few millivolts at its input. The tuning diode should certainly not cause even a

AD P001520

fraction of a part per billion frequency change in response to the compensating voltages. For instance, if the tuning diode had an average sensitivity of  $5 \times 10^{-8}/V$ , it should have a few millivolts or less impressed across it as a result of the compensation voltage. Otherwise, both of these would create sidebands of their own at the vibration frequency.

#### Accelerometer

Suitable accelerometers fall into two major categories; piezoelectric and piezoresistive. Relative merits of the two are tabulated in Table 1. In general, the piezoelectric accelerometer with a charge amplifier has been used in precise instrumentation for many years and is well-developed. The piezoresistive type is more attractive for circuit simplicity, size, weight, price and dc response. With dc response, the compensation may be accomplished in the earth's field without the capital equipment and man hours involved in alignment by vibrating in all axes. Accurate response below about 5 Hz is not operationally required with the rubidium oscillator since the servo loop has a bandwidth exceeding this. Substantial effort is being directed toward choosing the optimum piezoresistive accelerometer, but an excellent sub miniature piezoelectric device is still very much in contention.

#### Amplifier

In general the amplifier signal must bring the accelerometer signal up to about 1 v/g with a minimum bandwidth of about 30 times the highest frequency to be compensated. This could mean a gain of perhaps 250 with a bandwidth of more than 40 kHz, so an amplifier with a gain bandwidth product of 10 MHz or more would be in order. The operational gain adjusts of course to match the g-sensitivity of the crystal.

A bridge amplifier for a piezoresistive accelerometer must be adjustable over a wide range, since a dc offset of several "g's" is common in accelerometers having a suitable resonant frequency.

A charge amplifier has minimum offset adjustment considerations, but in order to have a low frequency corner of a few tenths hertz, it requires very high resistances. The same is true if the accelerometer is operated as a voltage source. For instance the sensitivity of small accelerometers runs about 3 pc/g. For 1 mv/g sensitivity, the capacitance would be 3 nf and then for a 0.5 hertz corner frequency the resistor would be 100 megohms.

#### Results

Tests so far have been quite general to identify surprises such as oscillator circuit sensitivity to compensating voltage, behaviour of accelerometers, practicality of aligning the accelerometer axis with the g-sensitive vector of the crystal etc.

The reduction in sensitivity has been 15 dB in most cases (3 ppb/g to 0.5 ppb/g), that is, most axes and most frequencies up to about 500 Hz.

The g-sensitive vector of the crystal seems to shift a bit (several degrees) as the unit is vibrated in two or three axes. Crystals tested so far have been in HC-40 holders with three point epoxy mounts. We will be interested to see if this was an isolated case or if the vector stabilizes after being vibrated several times.

#### Credits

This paper describes work in progress on an Air Force contract. (Seektalk Program Office, ESD).

#### References

- 1) Filler, Raymond "The Effect of Vibration on Quartz Crystal Resonators" DELET-TR-80-10 (U.S. Army Electronics Research and Development Command) May, 1980.
- 2) Rosati, Vincent R & Filler "Reduction of the Effects of Vibration on SC-Cut Quartz Crystal Oscillators" Proc. 35th Annual Frequency Control Symposium May, 1981.

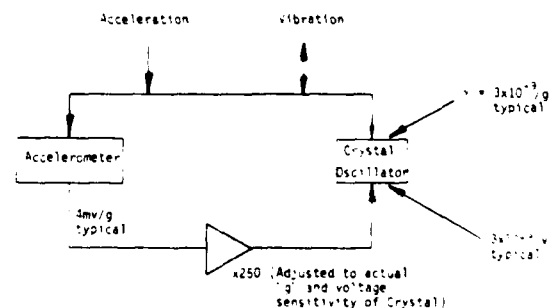
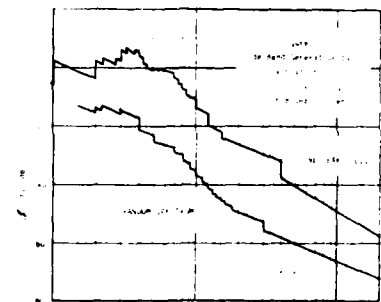


Figure 2 Block Diagram of Vibration-Compensation Scheme

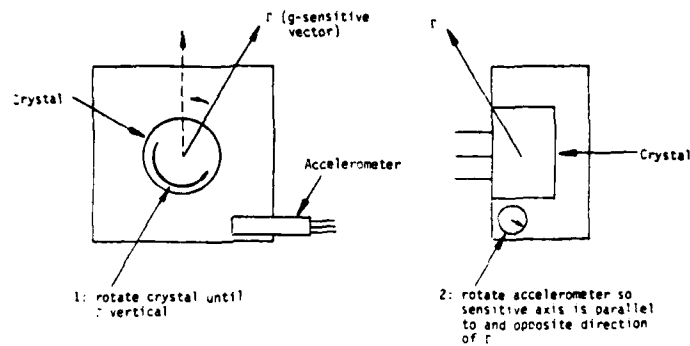


Figure 3: Procedure for aligning sensitive axes of crystal and accelerometer.

Table 1

Comparison of Piezoelectric and Piezoresistive Accelerometers.  
In order of supposed importance for this application.

	<u>Piezoelectric</u>	<u>Piezoresistive</u>
Output Impedance	High (hundreds of picofarads)	Low (hundreds of ohms)
Resonant Frequency	Tens of Kiloherztz	Few Kiloherztz
Sensitivity	1-5 mv/g	.5-4 mv/g
RF Field Susceptibility	Sensitive	Less sensitive
Transverse sensitivity	< 3%	< 3%
DC Response	None, 1-10 Hz minimum depending on charge amplifier	Yes
Cost	High - \$400.	Less High - \$300.
Complexity in use	Charge amplifier	Zero adjustment
Size, Weight	$10 \times 10^{-3} \text{ in}^3$ , 2.5 gram	$2 \times 10^{-3} \text{ in}^3$ , 1 gram
Accuracy	$\pm .5 \text{ dB}$ over frequency	$\pm .5 \text{ dB}$ over frequency
Temperature Sensitivity	Negligible when mounted on crystal oven	

AMPLITUDE FREQUENCY EFFECT  
OF SC-CUT QUARTZ TRAPPED ENERGY RESONATORS

R. Bourquin, D. Nassour, L. Bauder

Ecole Nationale Supérieure de Mécanique et des Microtechniques  
La Bouloie, Route de Gray, 25030 BESANCON, FRANCE.

Abstract

An approximate tridimensional analysis of an SC-cut quartz trapped energy resonator vibrating in quasi thickness shear mode is made for the C-mode. Three displacement components are calculated in an axis reference system where the C-mode has just two components none zero. It is chosen such that displacement directions are close to that one of SC-cut propagation direction in infinite medium. Then, a simplified analysis enables to obtain two coupled equations to calculate  $u_1$  and  $u_2$  - components of the displacement. A third equation couples together three displacement components.

If we consider that  $u_1$  and  $u_2$  are as external force terms acting on  $u_3$ , it is possible to resolve the third equation and to obtain  $u_3$  which is decomposed along its eigenvectors.

Amplitude-Frequency (A.F.) effect due to non linearities of the crystal is calculated with results of previous analysis by using perturbation technique. A relation of A.F. effect is given as a function of the applied power and the curvature radius.

Comparison between theoretical and experimental values of resonance frequencies of SC-cut quartz resonators vibrating in the vicinity of overtones and anharmonic modes of C-mode is made at 5 MHz ( $3^{rd}$  and  $5^{th}$  overtone). Numerical value of fourth order coefficients is obtained from experimental results of A.F. effect.

1. Introduction

Presently, analytical calculation of Amplitude-Frequency effect (A.F. effect) in thickness shear mode resonators has been made only in the case of nonlinear resonance in rotated Y-Cut Quartz plate<sup>1-3</sup>. Gagnepain and Lall presented experimental results about A-F behaviour of plano-convex energy trapped resonators built from doubly rotated quartz crystal cuts. Analytical model of energy trapped resonators are presented<sup>5-7</sup>, but only in the case of single rotated cuts. A SC-Cut Quartz crystal resonator has some advantages compared to AT-Cut resonators as a weak stress sensitivity. For this cut, the three modes A, B, C are piezoelectrically excited.

In this paper, only the case of the C-mode of resonance will be considered. An approximation will be made by considering that the resonator thickness is slowly changed with the coordinates of the surface. Then mechanical displacement keeps a direction very close to this one of the C-mode and electrical variables are only depending on resonator thickness. To determinate A.F. effect we can describe the resonator by linear equations with homogeneous boundary conditions. The axis reference system is chosen such as mechanical displacement of the C-mode has just two components  $u_1$  and  $u_2$  different of zero. Displacement  $u_3$  which is practically the B-mode, is obtained by considering that  $u_1$  and  $u_2$  are driving terms. The determination of mechanical displacement components and electrical potential enables to calculate the A.F. effect due to the nonlinear terms in stress and electrical displacement relations by using a perturbation method.

2. Mechanical displacement

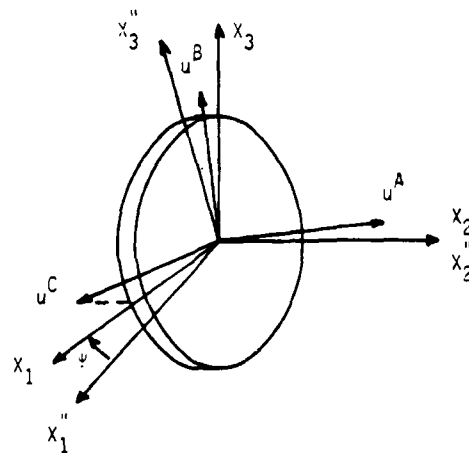


Fig. 1

AD P001521

The figure 1 shows the axis reference system used. System  $(X''_1, X''_2, X''_3)$  axis is the usual axis system obtained from crystallographic axis after two rotations ( $\theta = 22^\circ 20'$  and  $\phi = 34^\circ 6'$ ) which defines the SC-Cut where  $X''_2$  axis is the normal to the plate surface. Every mechanical displacement vectors which are eigenvectors for plane waves propagating in  $X''_2$  direction, have defined components. In the case of the SC-Cut, the C-mode which present a zero temperature coefficient of the first order of the resonance frequency, is corresponding to a displacement vector  $u_1$ . Its components are  $u_1$  (0.956, -0.241 and 0.166). Because we are considering just the quasi thickness shear mode in  $u_1$ -direction, the  $(X_1, X_2, X_3)$  axis system obtained from the previous axis by rotation  $\gamma$  around  $X''_2$ , can be used advantageously. The angle  $\gamma$  is given by the relation

$$\gamma = \tan^{-1} (u_3^C / u_1^C) = 9^\circ 53' \quad (2.1)$$

In this new axis system, displacement vectors of the three modes have the following components

$$u_1^A = (0.2402, 0.9683, 0.0687)$$

$$u_2^B = (-0.0167, -0.067, 0.997)$$

$$u_3^C = (0.9704, -0.2415, 0)$$

We can see that the B-mode corresponds practically to the displacement in the  $X_2$  direction.

#### Infinite thin plate vibrating in the C-mode

If we consider a thin plate vibrating in the C-mode which has infinite dimensions following  $X_1$  and  $X_3$  axis and a thickness equal to  $2h_0$  ( $X_2$ -axis), the mechanical displacement  $u_1$  and the electrical potential  $\phi$  are only depending on  $x_2$ -coordinate. Moreover the component  $u_3$  is null for the C-mode in the selected axis system. Equilibrium equations are written following the form

$$C_{55} u_{1,22} + C_{26} u_{2,22} + C_{26} u_{2,22} = 0 \quad (2.2)$$

$$C_{22} u_{2,22} + C_{26} u_{1,22} + C_{22} u_{2,22} = 0 \quad (2.3)$$

$$C_{26} u_{1,22} + C_{22} u_{2,22} + C_{22} u_{2,22} = 0 \quad (2.4)$$

The relation (2.4) is the Poisson's equation. Elastic, dielectric and piezoelectric constants are calculated in the new axis system  $(X_1, X_2, X_3)$ .  $u_1$  and  $u_2$  which are the displacement components of the C-mode can be written

$$u_1 = A_1 u^C; \quad u_2 = A_2 u^C \quad (2.5)$$

with

$$A_1^2 + A_2^2 = 1 \quad (2.6)$$

and we put

$$A_1 = A; \quad A_2 = B \quad (2.7)$$

By using the relation (2.5) in equation (2.2) - (2.4), a new relation is found

$$C_{55} A^2 + C_{26} A B + C_{26} A B = 0 \quad (2.8)$$

where the effective mechanical coefficient is equal to

$$C = C_{55} A^2 + C_{26} A B + C_{26} A B \quad (2.9)$$

$C_{ij}$  are the stiffened elastic constants

$$C_{ij} = C_{ij} + (e_{21} e_{2j}) / e_{22} \quad (2.10)$$

The boundary conditions associated to the equation system (2.2 - 2.4) are given by

$$C_{26} u_{1,2} + C_{22} u_{2,2} - C_{22} u_{2,2} = 0 \quad (2.11)$$

$$C_{26} u_{1,2} + C_{22} u_{2,2} + C_{22} u_{2,2} = 0 \quad (2.12)$$

$$C_{55} u_{1,2} + C_{26} u_{2,2} + C_{26} u_{2,2} = 0 \quad (2.13)$$

If we suppose a sinusoidal dependance of the potential and the mechanical displacement as  $(\exp(j\omega t))$ , the solutions of the equations systems (2.8, 2.11 - 2.13) taking into account the values of  $u_1$  and  $u_2$  (2.5), leads to the displacement vector  $u^C$  and the resonance frequencies  $\omega_n$

$$u^C = A \sin \frac{n\pi x_2}{2h_0} \quad (2.14)$$

and

$$\omega_n = \frac{n\pi}{2h_0} \sqrt{\frac{C}{\rho}} \quad (2.15)$$

#### Flano-convex resonator vibrating in the C-mode

Calculation of the displacement components  $u_1$  and  $u_2$ . The resonator is represented on the figure 2. The curvature radius  $R$  is large enough in order that the thickness  $2h(x_1, x_3)$  could be considered as slowly variable between the center and the edge of the disk. Then the mechanical displacement is mainly function of the thickness  $x_2$  and only at the second order of the coordinates  $x_1$  and  $x_3$  in the plate.

Because the small value of the electromechanical coupling in Quartz-crystal, the potential  $\phi$  and the electrical displacement  $D_2$  are only depending on  $x_2$ . By taking into account the amplitude of magnitude of the elastic coefficients, equilibrium equation are written for  $u_1$  and  $u_2$  following the form :

$$C_{55} u_{1,22} + C_{56} u_{1,22} + C_{55} u_{1,33} + C_{16} u_{2,11} + C_{26} u_{2,22} + C_{45} u_{2,33} + C_{26} u_{2,22} = 0 \quad (2.16)$$

$$\begin{aligned} \omega_0^2 \ddot{u}_2 = & C_{66} u_{2,11} + C_{22} u_{2,22} + C_{44} u_{2,33} + C_{16} u_{1,11} \\ & + C_{26} u_{1,22} + C_{45} u_{1,33} + e_{22} \ddot{\phi}_{,22} \end{aligned} \quad (2.17)$$

At this system the Poisson's equation (2.4) is joint. Both equations which do not take into account every elastic coefficients, are good enough to determinate the mechanical displacement in order to calculate the A.F. effect. Moreover, the component  $u_3$  is considered as a correcting term of  $u_1$  and  $u_2$  and it will be calculate later.

$u_1$  and  $u_2$  are given by the relation (2.5) and the sum  $\alpha_1 \ddot{u}_1 + \alpha_2 \ddot{u}_2$  is calculated from relations (2.16), (2.17), (2.6) and (2.7). It can be written :

$$\omega_0^2 \ddot{u}^C = \ddot{C}_{11} u^C_{,11} + \Gamma u^C_{,22} + \ddot{C}_{55} u^C_{,33} \quad (2.18)$$

where

$$\ddot{C}_{11} = \frac{1}{1+k^2} (C_{11} + 2k C_{16} + k^2 C_{66}) \quad (2.19)$$

$$\ddot{C}_{55} = \frac{1}{1+k^2} (C_{55} + 2k C_{45} + k^2 C_{44}) \quad (2.20)$$

A sinusoidal time dependance of the mechanical displacement  $u^C$  follows the form :

$$u^C = \ddot{u}^C(x_1, x_3) \sin Lx_2 \exp(j\omega t) \quad (2.21)$$

If the curvature radius is large compare to the thickness  $2h_0$ , the thickness  $2h(x_1, x_3)$  at a given point in the plane  $(X_1, X_3)$  has an approximate value like :

$$\frac{1}{4h^2} = \frac{1}{4h_0^2} \left[ 1 + \frac{x_1^2 + x_3^2}{2Rh_0} \right] \quad (2.22)$$

and the following equation takes the place of the relation (2.18)

$$\ddot{C}_{11} \ddot{u}^C_{,11} + \ddot{C}_{55} \ddot{u}^C_{,33} + \left[ \omega_0^2 - \frac{n^2 \pi^2 \Gamma}{4h_0^2} \left( 1 + \frac{x_1^2 + x_3^2}{2Rh_0} \right) \right] \ddot{u}^C = 0 \quad (2.23)$$

It is similar than this one proposed for AT-Cut plano-convex resonator<sup>5,6</sup> and  $u^C$  is the same mechanical displacement than for the AT-Cut. With the homogeneous boundary conditions (2.11) - (2.13), displacement  $u^C$  is written :

$$\begin{aligned} \ddot{u}^C_{nmp} = & A_{nmp} \exp\left(-\frac{\alpha_n x_1^2 + \beta_n x_3^2}{2}\right) H_m(x_1 \sqrt{2\alpha_n}) \\ & \times H_p(x_3 \sqrt{2\beta_n}) \sin Lx_2 \end{aligned} \quad (2.24)$$

where  $H_m$  and  $H_p$  are Hermite's polynomials of order  $m$  and  $p$  and  $\alpha_n$ ,  $\beta_n$ ,  $C_n$  are constants such as

$$\alpha_n = \frac{n\pi}{(8h_0^3 R)^{1/2}} (\Gamma/\ddot{C}_{11})^{1/2} \quad (2.25)$$

$$\beta_n = \frac{n\pi}{(8h_0^3 R)^{1/2}} (\Gamma/\ddot{C}_{55})^{1/2} \quad (2.26)$$

Resonance frequencies for overtones ( $m = p = 0$ ) and for anharmonics ( $m$  and  $p \neq 0$ ) of C-mode are given by

$$\begin{aligned} \omega_{nmp} = & \frac{n\pi}{2h_0} (\Gamma/\omega_0)^{1/2} \left[ 1 + \frac{1}{n\pi} \left( \frac{2h_0}{R} \right)^{1/2} \left[ (2m+1) \left( \frac{\ddot{C}_{11}}{\Gamma} \right)^{1/2} \right. \right. \\ & \left. \left. + (2p+1) \left( \frac{\ddot{C}_{55}}{\Gamma} \right)^{1/2} \right] \right]^{1/2} \end{aligned} \quad (2.27)$$

Calculated and experimental values of resonance frequencies of a SC-Cut resonator at 5 MHz on fifth overtone are summarized and compared in the table I. The curvature radius is equal to 150 mm and the thickness at the center is 1.821 mm. Table II shows the results corresponding to a SC-Cut resonator at 5 MHz on third overtone having a curvature radius of 300 mm and a thickness of 1.092 mm. Both resonators have a diameter of 15 mm. The first one has metallized electrodes on its faces and the second one is a R.V.A. electrodeless resonator. The approximate solution found shows a good agreement between theoretical and measured values, mainly for smallest index  $n$ ,  $m$  and  $p$ . For large index, approximations made to obtain the relation (2.27) are less and less realistic because the vibration is localized at the resonator center and it depends stronger on the coordinates  $x_1$  and  $x_3$  when  $m$  and  $p$  are increasing.

The amplitude  $A_{nmp}$  can be calculated as a function of the excitation power  $P$  applied to the resonator. For quasi thickness shear vibration, only the dependence of  $u_1$  and  $u_2$  versus  $x_2$  has to be considered and by introducing the viscosity coefficients  $\eta_{ij}$  of  $C_{66}$ ,  $C_{22}$  and  $C_{26}$ , the dissipated power can be written

$$\begin{aligned} P = & \int_{V_0} \ddot{u}^2_{nmp} \left[ (\eta_{66} + k \eta_{26}) (u_{1,2})^2 \right. \\ & \left. + (\eta_{22} + \frac{1}{k} \eta_{26}) (u_{2,2})^2 \right] dV_0 \end{aligned} \quad (2.28)$$

where  $V_0$  is the total resonator volume.

In the case of an energy trapped resonator, the amplitude of the mechanical displacement is very weak at its edge and the integration can be performed on  $x_1$  and  $x_3$  varying from  $-\infty$  to  $+\infty$ . By using (2.24) (2.5) and (2.7) the vibration amplitude is deduced from (2.28) for the overtones (n<sup>o</sup>)

$$A_{n00} = \frac{2h_0(\alpha_n B_n)^{\frac{1}{2}} P^{\frac{1}{2}}}{n\pi \omega_{n00}(\pi n_c h_0)^{\frac{1}{2}}} \quad (2.29)$$

where the effective viscosity coefficients  $\eta_c$  of the C-mode is given by

$$\eta_c = (\eta_{66} + 2k\eta_{26} + k^2\eta_{22})/(1+k^2) \quad (2.30)$$

$u_3$  displacement: As stated above, the mechanical displacement of the B-mode for the SC-Cut is quite along the  $X_3$  axis of the used coordinate system. Thus the components  $u_3$  must be obtained from the third equation of motion. In account of the orders of magnitude for the elastic coefficients and since the partial derivatives of  $u_1$  and  $u_2$  with respect to the thickness  $x_2$  are one order of magnitude higher than those ones calculated with respect to  $x_1$  and  $x_3$ ,  $u_3$  is governing by the following equation, which couples together  $u_3$  with  $u_1$  and  $u_2$

$$\begin{aligned} \rho_3 \ddot{u}_3 = & C_{55}u_{3,11} + C_{44}u_{3,22} + C_{33}u_{3,33} + C_{46}u_{1,22} \\ & + C_{24}u_{2,22} + (C_{13} + C_{55})u_{1,13} + e_{24}\ddot{z}_{,22} \end{aligned} \quad (2.31)$$

If the driving frequency is very near a resonant frequency of the C-mode,  $u_3$  is smaller than  $u_c$  and we can use in (2.31) the expression of the partial derivatives of  $u_1$  and  $u_2$  calculated from (2.24) and (2.25), which was obtained in the case of pure C-mode. The solution of this equation is written following the form

$$u_3 = g(x_1, x_3) \sin L x_2 \exp(j\omega t) \quad (2.32)$$

By substituting in (2.31), employing (2.24), (2.25), (2.4) and (2.22) (the thickness is still slowly varying) the unknown function  $g$  must satisfy the equation

$$\begin{aligned} C_{55}g_{,11} + C_{33}g_{,33} + \left[ \rho_3 \omega^2 - \frac{n^2 C_{44}}{4h_0^2} \left( 1 + \frac{x_1^2 + x_3^2}{2R h_0} \right) \right] g = \\ \frac{A_{n00}}{(1+k^2)^{\frac{1}{2}}} \left[ (C_{46} + kC_{24}) L^2 + (C_{13} + C_{55}) \alpha_n^3 n x_1 x_3 \right] \\ \times \exp\left(-\frac{n^2 x_1^2 + R n^2 x_3^2}{2}\right) \end{aligned} \quad (2.33)$$

which is valid only for the noo modes and where  $C_{24}$  and  $C_{46}$  are stiffened elastic coefficients. To resolve the equation (2.33) we expand the function  $g(x_1, x_3)$  on the set of eigensolutions of the homogeneous equation associated with (2.33), which are

$$\begin{aligned} g_{nrq} = & \frac{(\epsilon_n \eta_n)^{\frac{1}{4}}}{\sqrt{n!q!}} H_r(x_1 \sqrt{2\epsilon_n}) H_q(\sqrt{2\eta_n}) \\ & \times \exp\left(-\frac{\epsilon_n x_1^2 + \eta_n x_3^2}{2}\right) \end{aligned} \quad (2.34)$$

and the corresponding eigenfrequencies are

$$\begin{aligned} \omega_{nrq} = & \frac{n\pi}{2h_0} \left( \frac{C_{44}}{C_{55}} \right)^{\frac{1}{2}} \left[ 1 + \frac{1}{n!} \left( \frac{2h_0}{R} \right)^{\frac{1}{2}} \left[ (2r+1) \left( \frac{C_{55}}{C_{44}} \right)^{\frac{1}{2}} \right. \right. \\ & \left. \left. + (2q+1) \left( \frac{C_{33}}{C_{44}} \right)^{\frac{1}{2}} \right] \right]^{\frac{1}{2}} \end{aligned} \quad (2.35)$$

where

$$\epsilon_n = \frac{n\pi}{(8Rh_0)^{\frac{1}{2}}} \left( \frac{C_{44}}{C_{55}} \right)^{\frac{1}{2}} ; \eta_n = \frac{n\pi}{(8Rh_0)^{\frac{1}{2}}} \left( \frac{C_{44}}{C_{33}} \right)^{\frac{1}{2}} \quad (2.36)$$

and by using Green's function<sup>9</sup>, we obtain

$$\begin{aligned} g(x_1, x_3) = & \frac{A_{n00}}{(1+k^2)^{\frac{1}{2}}} \frac{(\epsilon_n \eta_n)^{\frac{1}{4}}}{\sqrt{n!}} \\ & \times \left[ (C_{46} + kC_{24}) L^2 \frac{g_{nrq}(x_1, x_3)}{\rho_3(\omega^2 - \omega_{nrq}^2)} \frac{C_r^1 C_q^3}{\sqrt{r!q!}} \right. \\ & \left. + (C_{13} + C_{55}) \alpha_n^3 n \sum_{r,q} \frac{g_{nrq}(x_1, x_3)}{\rho_3(\omega^2 - \omega_{nrq}^2)} \frac{Q_r^1 Q_q^3}{\sqrt{r!q!}} \right] \end{aligned} \quad (2.37)$$

where

$$\begin{aligned} C_r^1 = & \int_{-\infty}^{\infty} H_r(x_1 \sqrt{2\epsilon_n}) \exp\left(-\frac{\alpha_n + \epsilon_n}{2} x_1^2\right) dx_1 \\ C_q^3 = & \int_{-\infty}^{\infty} H_q(x_3 \sqrt{2\eta_n}) \exp\left(-\frac{\beta_n + \eta_n}{2} x_3^2\right) dx_3 \\ Q_r^1 = & \int_{-\infty}^{\infty} x_1 H_r(x_1 \sqrt{2\epsilon_n}) \exp\left(-\frac{\alpha_n + \epsilon_n}{2} x_1^2\right) dx_1 \\ Q_q^3 = & \int_{-\infty}^{\infty} x_3 H_q(x_3 \sqrt{2\eta_n}) \exp\left(-\frac{\beta_n + \eta_n}{2} x_3^2\right) dx_3 \end{aligned} \quad (2.38)$$

In these expressions, as in (2.28), the integration is performed for  $x_1$  and  $x_3$  varying from  $-\infty$  to  $+\infty$ .  $\omega_{nrq}$  are the frequency given by (2.35). The driving frequency is very close to the noo mode's eigenfrequency (eq. 2.27). According to the parity of the Hermite's polynomials, every integrals  $C_1^r$  and  $C_3^q$  are null for odd values of  $r$  and  $q$ . For the same reason  $Q_1^r$  and  $Q_3^q$  are null alike if  $r$  and  $q$  are even. By using expressions of the Hermite's polynomials, we can now write (2.37) as an expansion as respect to  $x_1$  and  $x_3$ . For the two first terms, the result is

$$g(x_1, x_3) = \frac{A_{noo}}{\pi(1+k^2)^{\frac{1}{2}}} (g_0 + g_1 x_1 + \dots) \exp\left(-\frac{\epsilon_n x_1^2 + \eta_n x_3^2}{2}\right) \quad (2.40)$$

$$g_0 = (\overline{C_{46}} + k\overline{C_{24}}) L^2 (\epsilon_n \eta_n)^{\frac{1}{2}} \kappa_0 \quad (2.41)$$

$$g_1 = 2(c_{13} + c_{55}) \alpha_n \beta_n \epsilon_n \eta_n \kappa_1$$

$\kappa_0$  and  $\kappa_1$  are series whose the first terms are

$$\begin{aligned} \kappa_0 &= \frac{C_{00}^1 C_{00}^3}{\lambda_{00}} - \frac{C_{00}^1 C_{00}^3}{2\lambda_{02}} - \frac{C_{20}^1 C_{00}^3}{2\lambda_{20}} + \frac{C_{00}^1 C_{04}^3}{8\lambda_{04}} + \frac{C_{22}^1 C_{00}^3}{4\lambda_{22}} + \frac{C_{40}^1 C_{00}^3}{8\lambda_{40}} + \dots \\ \kappa_1 &= \frac{Q_{11}^1 Q_{11}^3}{\lambda_{11}} - \frac{Q_{13}^1 Q_{13}^3}{2\lambda_{13}} - \frac{Q_{31}^1 Q_{31}^3}{2\lambda_{31}} + \frac{3Q_{33}^1 Q_{33}^3}{4\lambda_{33}} + \frac{Q_{51}^1 Q_{51}^3}{8\lambda_{51}} + \frac{Q_{15}^1 Q_{15}^3}{8\lambda_{15}} + \dots \end{aligned} \quad (2.42)$$

where the following notation is introduced

$$\lambda_{nrq} = \frac{1}{\rho_0 (\omega^2 - \omega_{nrq}^2)} \quad (2.43)$$

The two first terms was calculated for a third overtones, 5 MHz resonator with the sizes of the B.V.A. resonator and maximal values found are  $-1.5 \cdot 10^{-5}$  A<sub>noo</sub> at  $(x_1 = x_3 = 0)$  for the first and  $-0.015$  A<sub>noo</sub> at  $(x_1 = \frac{1}{2} L, x_3 = \frac{1}{2} L)$  for the second one. Thus the first term is negligible compare to the second one and the  $u_3$  displacement can be accurately given by

$$u_3 = \frac{2A_{noo}}{\pi(1+k^2)^{\frac{1}{2}}} (c_{13} + c_{55}) \alpha_n \beta_n \epsilon_n \eta_n \kappa_1 x_1 x_3 \exp\left(-\frac{\epsilon_n x_1^2 + \eta_n x_3^2}{2}\right) \sin Lx_2 \exp(j\omega t) \quad (2.44)$$

which is analogous to the  $u_{310}$  displacement for the case of single-rotated AT-Cut.

### 3. Amplitude-Frequency effect in SC-Cut Quartz

If nonlinear terms are taken into account in Maxwell-Piola's stress tensor and material electric displacement vector, the equilibrium state equations could be written in general forms

$$P_{LM,L}^{\lambda} + P_{LM,L}^n + \rho_0 \omega^2 u_M = 0 \quad (3.1)$$

$$D_{L,L}^{\lambda} + D_{L,L}^n = 0 \quad (3.2)$$

$P_{LM}^{\lambda}$  and  $P_{LM}^n$  are respectively the linear and nonlinear parts of the total Piola's tensor (mechanical and electrical terms),  $D_L^{\lambda}$  and  $D_L^n$  the linear and nonlinear parts of material electric displacement. These quantities are expressed in material coordinates system<sup>11</sup> and  $\rho_0$  is the specific mass. The corresponding boundary conditions are

$$N_L (P_{LM}^{\lambda} + P_{LM}^n) = T_M \quad (3.3)$$

where  $N_L$  represent the components of the unitary vector normal to the surface and  $T_M$  the applied force per unit reference area. By using the perturbation theory<sup>12,13</sup>, the difference between the eigenfrequency  $\omega_n$  of the  $n$ th eigensolution can be obtained in the case of linear problem and the actual resonant frequency  $\omega$ , determined by the equations (3.1) - (3.3). By introducing the normalized eigenfunctions

$$g_L^Y = \frac{u_L^Y}{N(Y)}, \quad f^Y = \frac{\phi^Y}{N(Y)} \quad (3.4)$$

where  $N(Y)$  is the normalizing factor so that

$$N^2(Y) \delta_{YB} = \int_{V_0} \rho_0 u_M^Y u_M^B dV_0 \quad (3.5)$$

The integration is performed on the volume  $V_0$  of the resonator. With the above defined notations, the frequency variation is equal to

$$\omega_Y - \omega = R_Y / 2N(Y) \omega_Y^2 \quad (3.6)$$

with

$$\begin{aligned} R_Y &= \int_{S_0} (T_M g_M^Y + N_L D_L^Y f) dS_0 \\ &- \int_{V_0} (P_{LM}^n g_M^Y + D_L^n f) dV_0 \end{aligned} \quad (3.7)$$

In this expression, the integral on the surface  $S_0$  of the resonator gives the frequency shift due to nonhomogeneous boundary conditions. If only linear terms in  $u_L$  and  $\phi_L$  occurs, i.e. if  $T_M$  is a linear function of this variables, the frequency perturbation is not depending on the vibration amplitude. Then, the amplitude-frequency effect is described only by the integral on the volume in which nonlinear terms  $P_{LM}^n$  and  $D_L^n$  appear. The relative variation between the li-

near and nonlinear resonance frequencies is given by

$$\frac{\omega - \omega_Y}{\omega_Y} = - \frac{\int_V (P_{LM}^n g_{ML}^Y + D_L^n f_{LY}^Y) dV_0}{2N(Y) \omega_Y} \quad (3.8)$$

For the SC-Cut resonator vibrating in noo-mode, we shown previously that the displacement  $u_3$  is smaller than  $u_1$  and  $u_2$ . Furthermore, the derivatives of  $u_1$  and  $u_2$  with respect to  $x_1$  or  $x_3$  and the electrical potential  $\phi$  is assumed as having a thickness dependence. Thus, only  $P_{21}^n = P_6^n$ ,  $P_{22}^n = P_2^n$  and  $D_2^n$  occur in (3.8). These quantities may be written as functions of  $u_{1,2}$  and  $\phi_2$ . Since the ratio  $k$  between  $u_1$  and  $u_2$  is smaller than unity in practice case, we can neglect terms of power order for  $k$  greater than unity. In the coordinates system used here, all material coefficients are none zero. From the published values<sup>1,14</sup> of the third and fourth order coefficients, we have only retained mechanical terms as cubic terms in  $P_2^n$  and  $P_6^n$ .

$$P_2^n = \left[ \frac{1}{2} C_{22} + \frac{1}{2} C_{266} + k(C_{26} + C_{226}) \right] (u_{1,2})^2 + \frac{1}{2} (\epsilon_0 - e_{22,2}) (\phi_2)^2 - \left[ (e_{2,26} - k e_{22} + k e_{2,22}) u_{1,2} \phi_2 + \left[ \frac{1}{2} C_{226} + \frac{1}{6} C_{2666} + \frac{1}{2} k (C_{22} + C_{222} + C_{266} + C_{2266}) \right] (u_{1,2})^3 \right] \quad (3.9)$$

$$P_6^n = \left[ \frac{3}{2} C_{26} + \frac{1}{2} C_{666} + k(C_{22} + C_{266}) \right] (u_{1,2})^2 - \frac{1}{2} e_{22,6} (\phi_2)^2 + (e_{22} - e_{2,66} - k e_{2,26}) u_{1,2} \phi_2 + \left[ \frac{1}{2} C_{22} + C_{266} + \frac{1}{6} C_{6666} + \frac{1}{2} k (3 C_{226} + C_{2666}) \right] (u_{1,2})^3 \quad (3.10)$$

$$D_2^n = \frac{1}{2} (e_{22} - e_{2,66} - k e_{2,26}) (u_{1,2})^2 - \left[ e_{22,6} + k (e_{22,2} - \epsilon_0) \right] u_{1,2} \phi_2 + \frac{1}{2} k_{222} (\phi_2)^2 \quad (3.11)$$

where we used (2.5) and (2.7). In piezoelectric coefficients the dot shares the part of electrical (first) and the part of mechanical subscripts. Since for the unperturbed problem we consider homogeneous boundary conditions, the electrical potential which appears in the above expressions is, from relation (2.4), such as

$$\phi_2 = \lambda u_{1,2} \quad (3.12)$$

$$\lambda = \frac{e_{26} + k e_{22}}{e_{22}} \quad (3.13)$$

The mechanical displacement is obtained from (2.24) for noo-modes

$$u_{noo}^c = A_{noo} \sin Lx_2 \exp\left(-\frac{\alpha_n x_1^2 + \beta_n x_3^2}{2}\right) \quad (3.14)$$

By using (3.8), (3.4) and (3.5), the relative frequency shift corresponding to the A-F effect is found

$$\frac{\Delta f}{f_{noo}} = \frac{\frac{3}{n^2} \frac{1}{4}}{36 \pi^2 h_0^2 f_{noo}^3 (\dot{C}_{11} \dot{C}_{55})^{\frac{1}{8}} \dot{C}_2^{\frac{1}{2}}} \left[ \frac{3}{2} C_{26} + \frac{1}{2} C_{666} + \frac{3}{2} k (C_{22} + C_{266}) + \frac{3}{2} \lambda (e_{22} - e_{2,66} - \frac{5}{3} k e_{2,26}) - \frac{3 \lambda^2}{2} (e_{22,6} + k (e_{22,2} - \epsilon_0)) + \frac{1}{2} k_{222} \right] \frac{1}{R^{\frac{1}{2}}} + \frac{\frac{3 n^3}{9} \frac{1}{R^{\frac{1}{2}}}}{2048 \sqrt{2} \pi^2 h_0^2 f_{noo}^4 \rho_0 \eta_c (\dot{C}_{11} \dot{C}_{55})^{\frac{1}{4}}} \left[ \frac{1}{2} C_{22} + C_{266} + \frac{1}{6} C_{6666} + 2 k (C_{226} + \frac{1}{3} C_{2666}) \right] \frac{P}{R^{\frac{1}{2}}} \quad (3.15)$$

In this expression, we can see that anisochronism for SC-Cut is the sum of a term proportional to the square root of the applied power and of a term proportional to the power. In the case of single rotated cut Quartz resonator the first term is null because the coefficients which appear in this one are null. Moreover, every coefficients of the third order are not known and actually, it is not possible to calculate those which are used in our reference axis-system. Values of constants are the following

$$\begin{aligned}
C_{22} &= 11.533 \cdot 10^{10} \text{ N/m}^2 \\
C_{26} &= 2.026 \cdot 10^{10} \text{ N/m}^2 \\
C_{226} &= 1.10 \cdot 10^{10} \text{ N/m}^2 \\
C_{266} &= 7.9 \cdot 10^{10} \text{ N/m}^2 \\
C_{666} &= 3.2 \cdot 10^{10} \text{ N/m}^2 \\
e_{22} &= 0.089 \text{ C/m}^2 \\
e_{26} &= -0.037 \text{ C/m}^2 \\
\epsilon_{22} &= 39.779 \cdot 10^{-12} \text{ F/m} \\
\text{and } k &= -0.24\%
\end{aligned}$$

In the case of B.V.A. resonator, attenuation constants are respectively

$$\gamma_n = 3.1 \cdot 10^5 \text{ m}^{-2} \text{ and } \beta_n = 3.62 \cdot 10^5 \text{ m}^{-2}$$

Numerically, the part of the relation (3.15) proportional to the applied power  $P$  has a preponderant value for power greater than  $100 \mu\text{W}$ .

From measurements performed with such a resonator having a  $Q$  factor equal to  $2.3 \cdot 10^6$  and an A-F effect of  $3.3 \text{ Hz/mW}$ , elastic constants of the fourth order are calculated in an axis system and are equal to

$$\frac{1}{6} C_{6666} + \frac{2}{3} k C_{2666} = 2.17 \cdot 10^{11} \text{ N/m}^2 \quad (3.16)$$

By taking into account just elastic constants in the term proportional to  $P^2$  in the relation (3.15), the frequency shift due to the A-F effect can be written for a B.V.A. resonator

$$\Delta f = 65 P^{1/2} + 3300 P \quad (3.17)$$

where  $\Delta f$  is in Hertz and  $P$  in Watts.

For a weak power, smaller than  $100 \mu\text{W}$ , a SC-Cut quartz resonator can present an A-F effect nonlinear in power (Fig. 3), but as every coefficients appearing in the relation (3.15) are not known, the first term of (3.17) is only an estimation.

The analytical treatment used here in the case of the C-mode can be extended to the other modes A and B. The increase of the A-F effect when the radius of curvature decrease is due to the augmentation of the local density energy. The fourth order elastic coefficients of Quartz crystal can be reached by measuring the A-F effects for resonators having different cristallographic orientations and by using the theoretical model presented here.

#### References

1. R. Besson, J.J. Gagnepain, Physical Acoustics, Vol. XI, p. 245288. (Academic Press, New York, 1975)
2. H.F. Tiersten, "Analysis of nonlinear resonance in thickness-shear and trapped energy resonators" J. Acoust. Soc. Am. **59**, 866 (1976)

3. J.J. Gagnepain, "Non linear properties of quartz crystal and quartz resonators, a review" Proceedings of the 35<sup>th</sup> Annual Symposium on Frequency Control, US Army Command, Fort Monmouth, New Jersey, 1, (1981)

4. J.J. Gagnepain, J.C. Ponçot, C. Peugeot, "Amplitude-Frequency behaviour of doubly rotated Quartz resonators" Proceedings of the 31<sup>st</sup> Annual Symposium on Frequency Control, US Army Command, Fort Monmouth, New Jersey, 17 (1977)

5. C.J. Wilson, "Vibrations modes of AT-Cut convex Quartz resonators", J. of Phys., D, App. Phys. **7**, 2449 (1974)

6. H.F. Tiersten, R.C. Smyte, "An analysis of overtone modes in contoured crystal resonators" Proceedings of the 31<sup>st</sup> Annual Symposium on Frequency Control, US Army Command, Fort Monmouth, New Jersey 44, (1977)

7. R.J. Besson, B.M. Dulmet, D.P. Gillet, "Analysis of the influence of some parameters in Quartz bulk resonator" I.E.E.E. Ultrasonics Symposium, New Jersey, 1978.

8. E.P. Eer Nisse, "Quartz resonator frequency shift arising from electrodes stress" Proceedings of the 29<sup>th</sup> Annual on Frequency Control, US Army Command, Fort Monmouth, New Jersey, 1, (1975)

9. J. Mathews, R.L. Walker, "Mathematical methods of physics" (Benjamin, New York, 1965) Chap. 9.

10. K. Iijima, Y. Tsuzuki, Y. Hirose, M. Akiyama, "Laser interferometric measurement of the vibration displacements of a plano-convex AT-Cut Quartz crystal resonator" Proceedings of the 30<sup>th</sup> Annual Symposium on Frequency Control, Fort Monmouth, New Jersey, 65 (1976).

11. H.F. Tiersten, "Nonlinear electroelastic equations cubic in the small field variables", J. Acoust. Soc. Am. **57**, 660 (1975).

12. P.M. Morse, H. Feshbach, "Methods of theoretical physics" (Mc Graw-Hill, New York (1953).

13. H.F. Tiersten, B.K. Sinha, "A perturbation analysis of the attenuation and dispersion of surface waves" J. App. Phys. **49**, 1, 87 (1978).

14. C.K. Hruska, "Second order phenomena in quartz and the polarising effect with plates of orientation (XZ/)" I.E.E.E., SU-25, 4, 198 (1978)

15. R.N. Thurston, J.M. Mc Skimin, P. Andreatch, "Third order elastic coefficients of quartz". J. App. Phys. **37**, 1, 267 (1965).

16. J.P. Valentin, C.P. Guérin, R.J. Besson, "Indirect amplitude frequency effect in resonators working on two frequency" Proceedings of the 35<sup>th</sup> Annual Frequency Control Symposium, US Army Electronics research and Development Command, Fort Monmouth, New Jersey (1981).

17. M. Planat, work carried along L.P.M.O. Resonator Private communication.

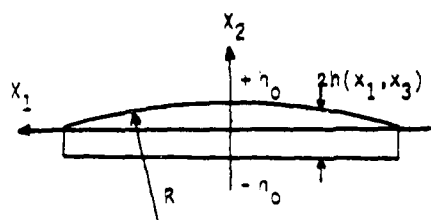


FIG 2 PLANO-CONVEX RESONATOR

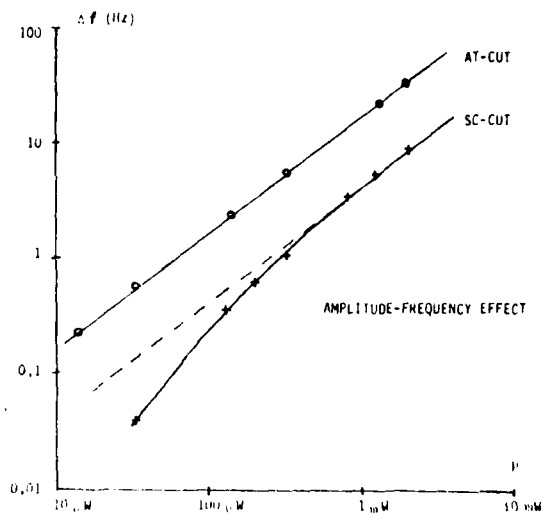


FIG 3 A-F EFFECT

TABLE I

$n m p$	$f$ MHz calculated	$f$ MHz measured
3 0 0	3.019	3.015
3 0 2	3.108	3.105
3 2 0	3.123	3.122
5 0 0	5.000	5.000
5 0 2	5.090	5.092
5 2 0	5.104	5.100
5 0 4	5.173	5.172
5 2 2	5.192	5.187
5 4 0	5.207	5.200
7 0 0	6.990	6.984
7 0 2	7.070	7.082
7 2 0	7.085	7.110
7 0 4	7.139	7.192
7 2 2	7.174	7.207
7 4 0	7.189	7.236

TABLE II

$n m p$	$f$ MHz calculated	$f$ MHz measured
3 0 0	5.000	4.9999
3 0 2	5.082	5.0888
3 2 0	5.096	5.0959
3 0 4	5.163	5.1783
3 2 2	5.176	5.1848
3 4 0	5.190	5.1939
3 0 6	5.242	5.268
3 2 4	5.255	5.278
3 4 2	5.269	5.293
3 6 0	5.282	
5 0 0	8.302	8.3085
5 0 2	8.386	8.4038
5 2 0	8.400	8.4108
5 0 4	8.468	8.4946
5 2 2	8.481	8.5018
5 4 0	8.495	8.5115
5 0 6	8.549	8.5817
5 2 4	8.562	8.5889
5 4 2	8.576	8.5989
5 6 0	8.589	8.6104
7 0 0	11.607	11.6164
7 0 2	11.689	11.7114
7 2 0	11.703	11.7411
7 0 4	11.772	11.8094
7 2 2	11.796	11.8169
7 4 0	11.799	11.8691

## FURTHER DEVELOPMENT IN SC CUT CRYSTAL RESONATOR TECHNOLOGY

A. W. Warner, B. Goldfrank and J. Tsacilas

Frequency Electronics, Inc.  
Mitchel Field, New York

AD P001522

This is probably our last paper in a series of papers on the development of a vibration resistant crystal unit, in particular, an SC cut crystal unit with a 1% magnitude of the acceleration sensitivity vector. In previous talks, in addition to design data, we have discussed the fabrication and measurement of doubly oriented and triply oriented SC blanks with special emphasis on the use of X-ray to measure precisely the orientation angles, and on test methods to determine a reasonable amount of time, the acceleration coefficients.

It may be well to review briefly those developments that have proved to be most helpful. The first figure shows the angular tolerances necessary to maintain a reasonable spread in turn-over temperature, both for the SC angle of  $\theta = 21.95^\circ$  and FEI's modified angle of  $\theta = 23.75^\circ$ . Comparing the two angles, at a nominal operating temperature of  $90^\circ\text{C}$ , we go from an impossible  $\pm 9$  seconds of arc to a difficult  $\pm 30$  seconds. Even at  $75^\circ\text{C}$  operating temperature, the tolerances are  $\pm 30$  seconds and  $\pm 1$  minute. In addition to requiring a very flat surface, some sophisticated X-ray orientation measurements are called for. FEI has developed an X-ray goniometer using the 22.3 plane, whose normal lies in the X-2 plane at  $34^\circ 17'$  from X. (The AT cut uses a similar plane whose normal is in the Y-Z plane). The second figure shows the big advantage in using the 22.3 plane, that is, only one angle measurement is needed to determine turn-over temperature. The cracked line gives the combinations of  $\theta$  and  $\phi$  angles which will produce the same turn-over temperature. The line marked  $\theta'$  is the X-ray reading which corresponds to the same turn-over temperature for various  $\theta$  angles. In the area of interest,  $\theta = 22^\circ$  to  $24^\circ$ ,  $\theta'$  is nearly invariant. Figure 3 is a blow up of this region.  $\theta'$  of  $22^\circ$  is shown here as  $8^\circ$  ( $30^\circ - 22^\circ$ ). Figure 4 shows an array of  $\theta'$  angles for various turn-over temperature for one crystal unit design. A change in overtone or contour width, of course, shift the pattern slightly up or down.

A second area of helpful improvements is that of acceleration sensitivity measurements. As acceleration coefficients approach  $10^{-10}$  per g, evaluation in a reasonable time becomes very difficult. At first we used a vibration table and looked at sidebands presented in 33rd Avid proceedings, 1979. The coefficients so

measured represented not only the acceleration sensitivity but also resonance effects, non-linear effects, noise isolation from gages, and drift. The equipment was expensive and the test time was about 4 hours. The alternative to this is the 2g turn-over test, i.e., 1g up vs. 1g down. With the crystal mounted in its oven oscillator and stabilized for one hour, five successive frequencies are measured at 5 second intervals, re-oriented by  $180^\circ$ , and five more readings taken. By repeating this procedure three times, the true acceleration sensitivity for this one orientation can usually be ascertained, even in the presence of drift and noise. Both easy and difficult measurements are shown in Figure 5. If measurements are taken at three mutually perpendicular directions, the worst case vector can be calculated.

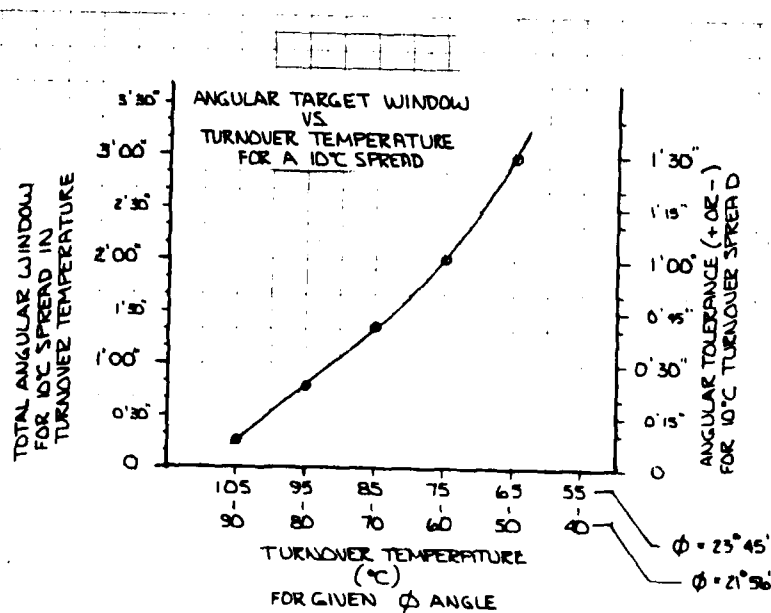
A third useful development is the use of a triangular shaped gold strip for thermo-compression bonding, a method licensed by Western Electric. The ribbon is shown in Figure 6. The use of a gold to gold bond can lower both the pressure and temperature necessary to weld, and a smaller, better defined spot can usually be obtained. The triangular shape provides a cleaning action as the gold moves out from the apex during compression. Both horizontal and vertical stripes have been used. Figure 7 shows a completed bond and Figure 8 shows the typical pull-off patterns when tested to destruction.

Crystal units using both the gold strip ribbons, and the more conventional aluminum lead ribbons have been made using both the  $21.95^\circ$  angle and the  $23.75^\circ$  angle. We have observed that the magnitude of the acceleration sensitivity vector for the successful designs were somewhat better when the  $23.75^\circ$  angle was used. The reasons for this are not clear, but it motivated an experiment using an even larger angle. A group of 17 crystal units were made using horizontal and vertical gold stripe ribbons, bonded at three points  $90^\circ$  apart. Three aberrant units were removed from the series, and the remaining had magnitudes of the acceleration sensitivity vector averaging  $1.5 \times 10^{-10}$  g, with a standard deviation of  $2.1 \times 10^{-10}$  g. Units that were between  $1$  and  $3 \times 10^{-10}$  g. The units were less sensitive to mounting variation than the previous groups.

The group of 14 crystal units is too small to be significant, but nevertheless, tests were made to assess the penalty of using a  $\phi$  angle of  $3^\circ$  from optimum for stress compensation. Figure 9 shows the effect of a thermal gradient of  $0.75^\circ\text{C}$  per minute, on frequency at the three  $\phi$  angles used. There is definitely a penalty in using the  $25^\circ$  angle. Figure 10 shows frequency vs. amplitude of vibration (crystal current). Figure 11 shows the inflection temperature, where the advantage lies with the larger angle. The impedance of a  $25^\circ \phi$  is 20% higher than for a  $21.95^\circ \phi$ , making adjustment to frequency more difficult.

We have performed cutting experiments on pre-angled bars, where the  $\phi$  angle is built in. This permits AT type cutting of blanks. The spread of angles was only  $\pm 1.5'$ . Cutting at a double angle is 3 times worse where the saw blade enters at an edge.

In conclusion, I would like to point out that with single angle X-ray techniques, pre-angled bars, and if frequency adjustment is done at a temperature near turn-over temperature, then the manufacture of the vastly superior SC cut is really comparable to that of the AT cut.



EG 44-82

Figure 1. Angular Target Window

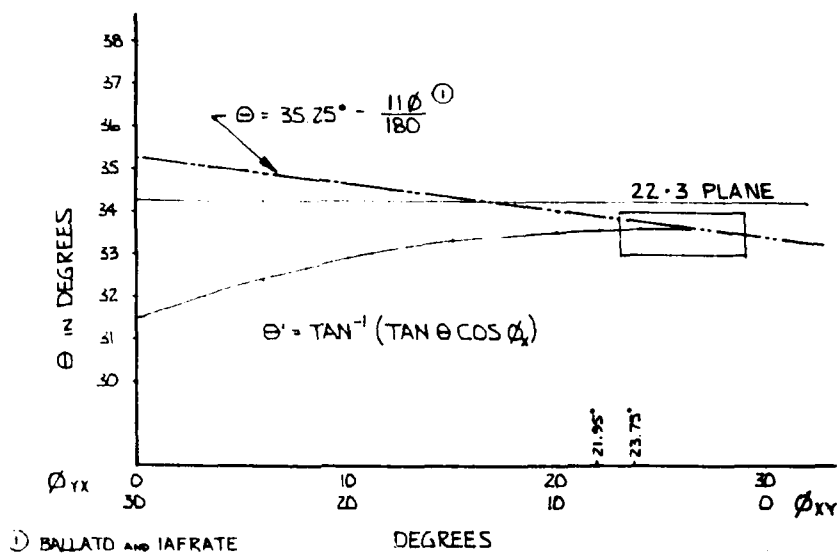


Figure 2. Theta ( $\theta$ ) vs. Phi ( $\phi$ )

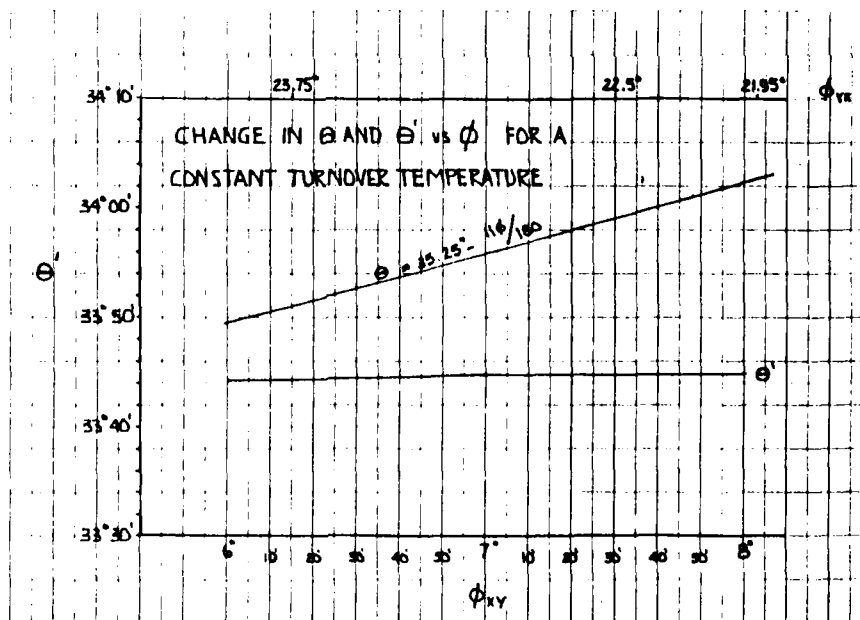


Figure 3. Blow Up of Figure 2

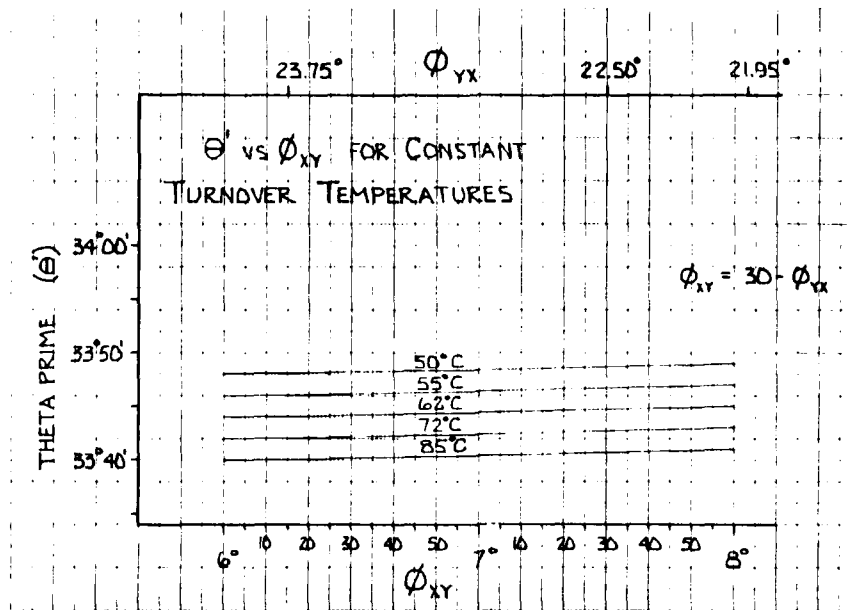


Figure 4.  $\Theta'$  vs.  $\Phi_{XY}$  for Constant Turnover Temperatures

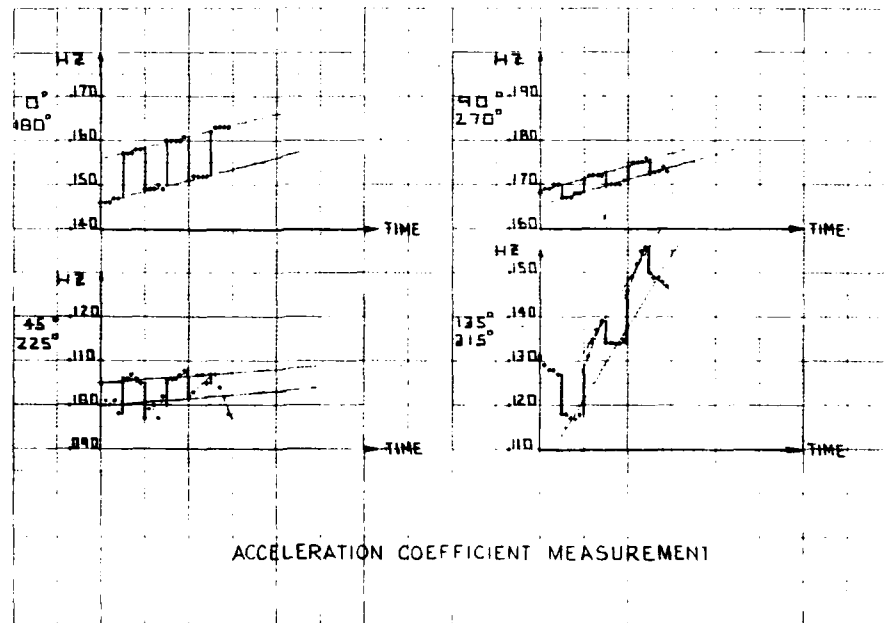
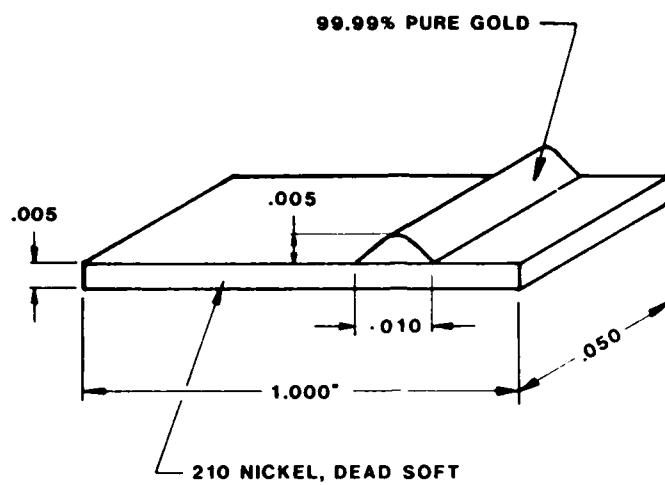


Figure 5. Typical Measurement Data



#### NICKEL-GOLD RIBBON FOR THERMAL-COMPRESSION BONDING

Figure 6. Gold Stripe

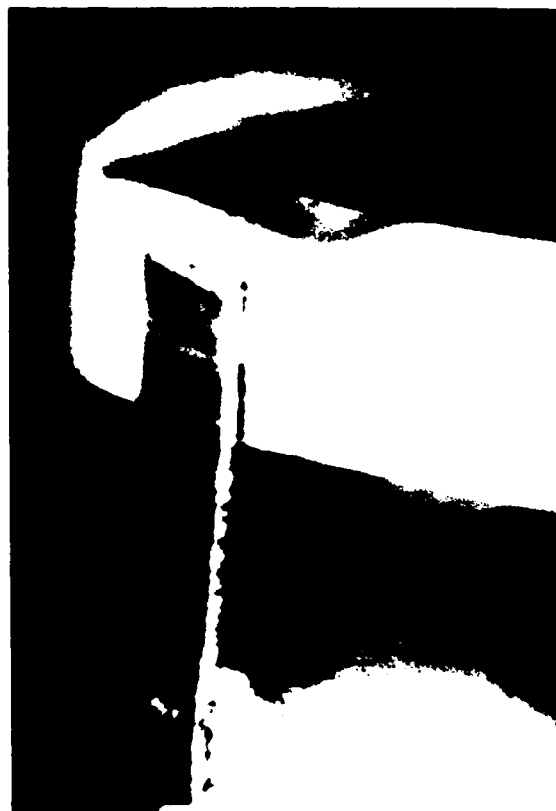


Figure 7. Typical Gold Horizontal Thermocompression Bond

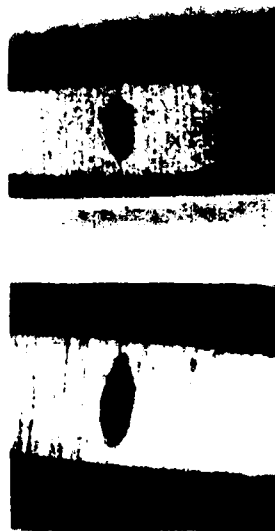


Figure 8. Pull Off Patterns for Vertical Thermocompression Bonds

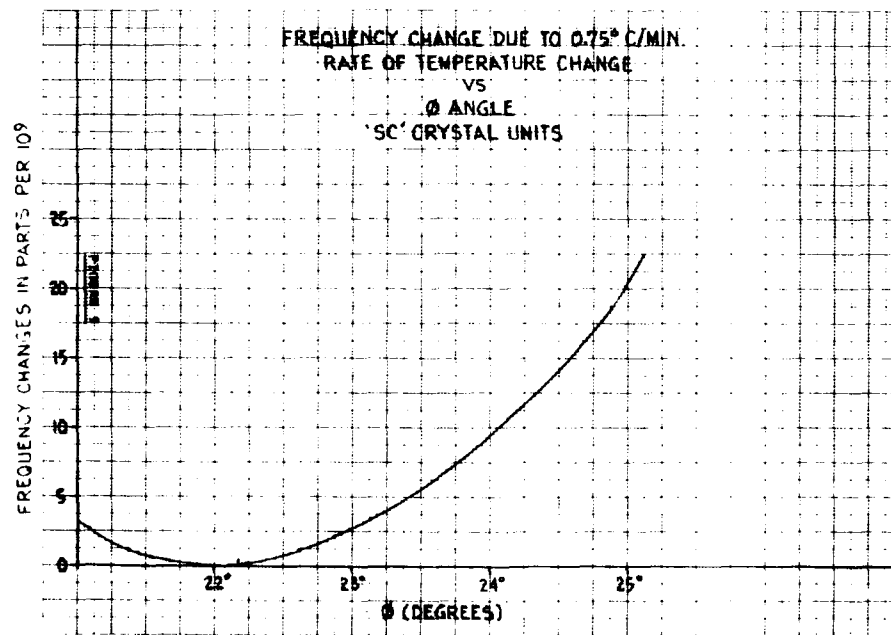


Figure 9. Thermal Gradient

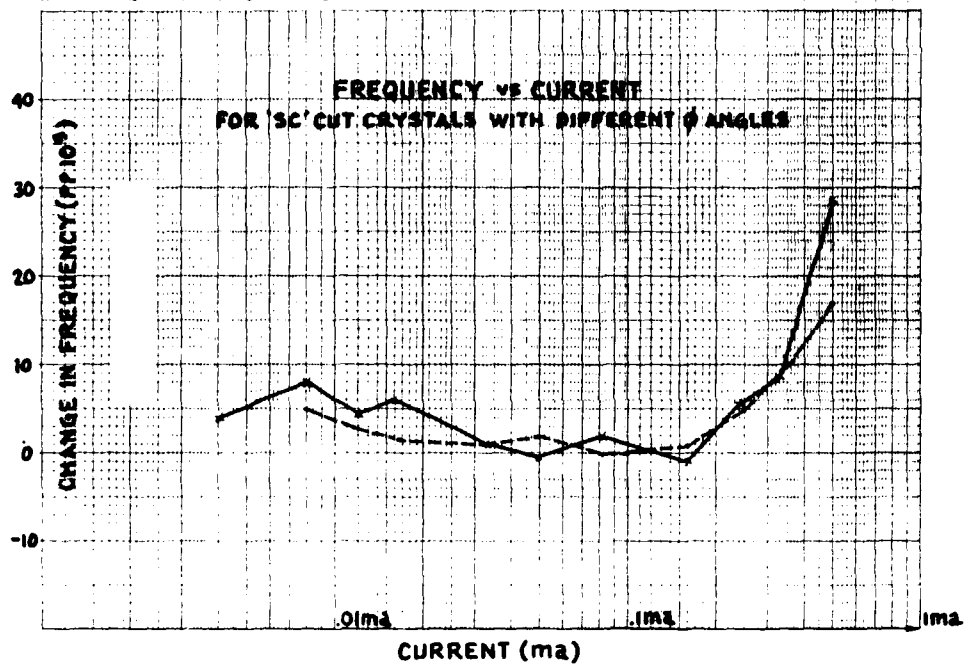


Figure 10. Frequency VS. Amplitude

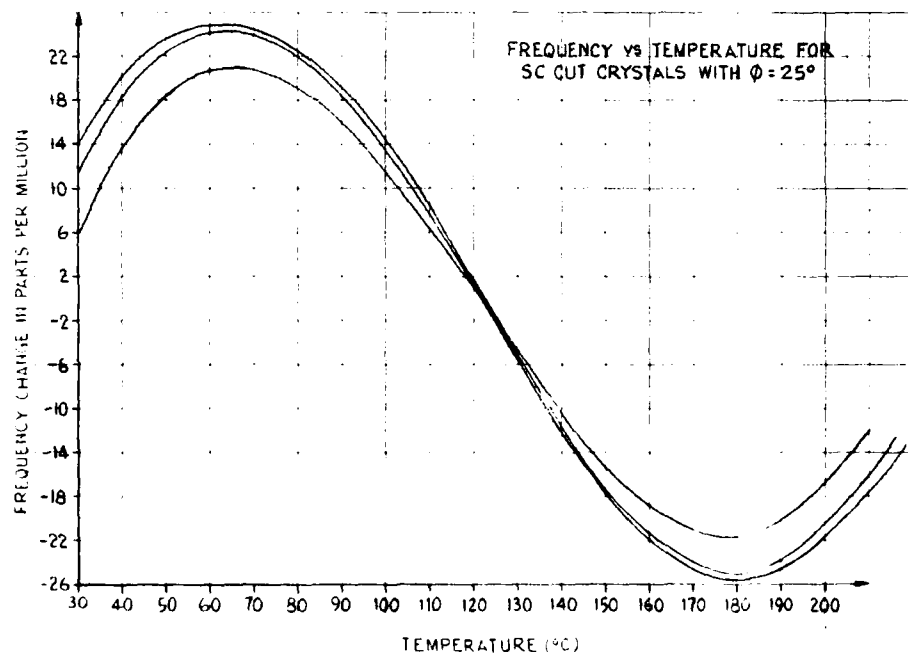


Figure 11. Temperature Curve for 'SC' Cut Crystal with  $\phi = 25^\circ$

## THE EFFECT OF BLANK GEOMETRY ON THE ACCELERATION SENSITIVITY OF AT &amp; SC-CUT QUARTZ RESONATORS

Raymond L. Filler, John A. Kosinski and John R. Vig

US Army Electronics Technology & Devices Laboratory (ERADCOM)  
Fort Monmouth, New Jersey 07703Abstract

The acceleration-sensitivity of AT-cut resonators has a marked dependance on blank curvature. As the plate contour becomes flatter, the acceleration sensitivity coefficient decreases approximately linearly with diopter value. Four types of AT-cut resonators were studied: 5 MHz fundamental mode, 5 MHz third-overtone, 10 MHz third-overtone, and 20 MHz fundamental mode. Biconvex units of a given contour have been found not to have a substantially lower acceleration sensitivity than plano-convex units of the same contour.

No relationship has been observed between blank curvature and acceleration sensitivity for SC-cut resonators. A large number of fundamental mode and third overtone AT and SC-cut designs have been evaluated. To date, the acceleration sensitivities of the best AT-cut designs are no worse than that of the best SC-cut designs.

**Key words:** Quartz, quartz crystal, quartz resonator, quartz oscillator, crystal oscillator, SC-cut, AT-cut, acceleration, vibration, phase noise, frequency control.

Introduction

As evidenced by the large number of papers presented in recent years on the acceleration sensitivity of frequency standards<sup>1-19</sup>, there is considerable interest in this subject. The state of the art is such that currently available devices cannot provide the degree of spectral purity required by some modern communications, navigation and radar systems.<sup>20,21</sup> Some precision timing applications also require immunity from the frequency offset effects of acceleration.<sup>11,19</sup>

As part of a development program on high precision ceramic flatpack enclosed quartz crystal resonators, both SC-cut and AT-cut, the effects of blank geometry on various resonator performance parameters have been investigated. The effects of blank contour on some resonator parameters have been reported previously.<sup>22-25</sup> In this paper, the effect of blank contour on the acceleration sensitivity is reported.

Resonator Configuration

The experiments were performed on resonators enclosed in ceramic flatpacks. The details of the fabrication of such resonators have been reported previously.<sup>15, 26-33</sup> The enclosures are available in two sizes. The larger of the two is used to house the 5 MHz and 10 MHz resonators described below. The smaller package is used for the 20 MHz fundamental mode devices.

The 5 MHz and 10 MHz quartz blanks were 14 mm diameter, and were bonded to four 1.5 mm wide molybdenum ribbon "1" clips with silver filled polyimide adhesive.<sup>32</sup> Two clip heights, 0.7 mm and 1.1 mm, and two clip thicknesses, 25  $\mu$ m and 18  $\mu$ m, were investigated. The clips were spaced 90° apart on the perimeter of the blank, two on the XX' axis and two on the ZZ' axis.

The 20 MHz quartz blanks were 6.4 mm diameter. The dimensions of the clips were 0.75 mm wide x 0.7 mm high x 25  $\mu$ m thick. The clips were spaced 90° apart, 45° from the ZZ' axis.

Acceleration Sensitivity Measurement System

The resonators were connected to appropriate oscillator circuits and the acceleration sensitivities were determined from the response of the oscillators to sinusoidal vibration.<sup>11</sup> The use of this technique minimizes temperature stability requirements and allows a search for mechanical resonances in the resonator mounting structure. The oscillators were potted in beeswax to eliminate contributions to the acceleration sensitivity from relative motions of oscillator components. The sidebands which appear are caused by frequency modulation of the resonator operating frequency (known as the carrier). The relative magnitude of the power in the first sideband to the power in the carrier is denoted by  $\mathcal{L}$ .<sup>11</sup>  $\mathcal{L}$  is related to the acceleration sensitivity,  $\gamma$ , of the resonator by

$$\gamma = \frac{2f_v}{aF_0} \cdot 10^{\mathcal{L}/20} \quad (1)$$

where:  $f_v$  = vibration frequency in Hz  
 $F_0$  = resonator operating frequency in Hz  
 $a$  = acceleration level in g's  
 $\mathcal{L}$  = sideband/carrier ratio in decibels

The value of  $\gamma$  was determined for several vibration frequencies in order to be certain that

AD P001523

mechanical resonances in the oscillator or resonator are absent.

The acceleration sensitivity has been shown to have the properties of a vector<sup>6</sup>, i.e., it has magnitude and direction. The magnitude is obtained by measuring the acceleration sensitivity in three mutually perpendicular directions, and taking the square root of the sum of the squares of the three measured values. The units are fractional frequency deviation per g, where g is the magnitude of the earth's gravitational acceleration at sea level.

The fact that the magnitude of the vector,  $S$ , is reported below is very important, especially when comparisons are made with previously reported results. Some have, in the past, reported  $S$  along one arbitrary direction, for example, along a major axis of the enclosure. The selected axis is usually, but not always, the worst of the three major axes of the enclosure. Such an arbitrarily selected axis is not, in general, the worst case condition for a given resonator. The value reported by us is the worst case acceleration sensitivity for each unit.

### Results

Acceleration sensitivity as a function of contour has been investigated for: 1. 5 MHz fundamental mode AT-cut resonators, 2. 5 MHz 3rd overtone AT-cut resonators, 3. 10 MHz 3rd overtone AT-cut resonators, and 4. 5 MHz fundamental mode SC-cut resonators. For the 20 MHz AT-cut units, only plano-plano blank geometry was studied.

#### 5 MHz Fundamental Mode AT-cut Resonators

The results for the 5 MHz, fundamental mode AT-cut resonators are shown in Figure 1. These results are an extension of the data presented last year.<sup>15</sup> The resonators were mounted on 0.7 mm x 25  $\mu$ m x 1.5 mm clips. The horizontal axis in Figure 1 is the contour in units of diopter. Biconvex geometry was chosen for all of the low contour units to ensure that the Q's would be sufficient for proper oscillator operation. The minimum value of the acceleration sensitivity measured was  $5.7 \times 10^{-10}$ /g for a 1.37 diopter, biconvex design. This is a factor of 22 improvement over the 2.87 diopter, plano-convex design. As a reference point, the commonly quoted value for the acceleration sensitivity of AT-cut quartz resonators and the specification for the best commercially available "off-the-shelf" oscillator is  $2 \times 10^{-9}$ /g.

#### 5 MHz 3rd Overtone AT-cut Resonators

The 5 MHz 3rd overtone AT-cut units displayed a similar dependence on contour. Several dozen of these devices were fabricated, some with plano-convex designs and some with biconvex designs. The results for these units are given in Figure 2. In spite of the large scatter at each contour value, it appears that there is a dependence of the acceleration sensitivity on contour. The

minimum sensitivity measured was  $3.8 \times 10^{-10}$ /g for a 2.0 diopter, biconvex unit. The solid line is a least-squares fit to a quadratic function of the average acceleration sensitivity at each contour. No physical significance is attributed to the function selected. The fact that the curve crosses zero at zero contour is wishful thinking on the part of the authors. The equation of the curve is:

$$S \times 10^{10}/g = 0.35 D^2 + 1.9 D \quad (2)$$

Three different clip dimensions are included in Figure 2, as follows: 1. 0.7 mm x 25  $\mu$ m x 1.5 mm ("short"); 2. 1.1 mm x 25  $\mu$ m x 1.5 mm ("normal"); and 3. 1.1 mm x 18  $\mu$ m x 1.5 mm ("thin"). There was no discernable differences among the (limited number of) "short" and "thin" clips and the "normal" clips.

#### 10 MHz 3rd Overtone AT-cut Resonators

The most convincing evidence for the contour dependence hypothesis was obtained from the results for the 10 MHz 3rd overtone AT-cut units. In all, 82 resonators were measured. The results are shown in Figure 3. As in the previous figure, both biconvex and plano-convex units are shown. The three clip structures, "normal", "short", and "thin", made no discernable difference and are omitted for clarity. The smoothness of the transition from plano-convex to biconvex suggests that the contour dependence is a function of the contour only and not of the symmetry of the blank geometry. The lowest acceleration sensitivity obtained to date for these 10 MHz devices is  $3.2 \times 10^{-10}$ /g. The solid curve is again a quadratic function that was arbitrarily chosen to cross zero at zero contour. The equation of the curve is

$$S \times 10^{10}/g = 3.3 D^2 + 11.0 \quad (3)$$

#### Acceleration Sensitivity Vector Direction

The behavior of the direction of the acceleration sensitivity vector as a function of contour for AT-cut resonators shows that the magnitude of the component in the plane of the blank does not vary systematically with contour. All of the systematic variation is in the component normal to the crystal blank.

#### 20 MHz Fundamental Mode AT-Cut Resonators

The only plano-plano devices available for comparison, to date, were nominally plano-plano, 20 MHz fundamental mode units. These were of the highly shock resistant type which have been described previously.<sup>32</sup> The minimum acceleration sensitivity for this group of devices was  $2.4 \times 10^{-10}$ /g although 80% of the units tested had an acceleration sensitivity of 8 to  $9 \times 10^{-10}$ /g. The blanks used in these units had been lapped "flat" with a 1  $\mu$ m aluminum oxide abrasive, then etched to frequency. Such a surface finishing process generally results in blanks that are slightly biconvex, however, the blank curvatures were not measured. These resonators were intended

for a TCXO application and were not designed for minimum vibration sensitivity. The clips, for example, were designed to withstand a 20,000 g shock.

#### 5 MHz Fundamental Mode SC-cut Resonators

The contour dependence experiment was repeated for 5 MHz fundamental mode SC-cut resonators. Two clip sizes were used, "normal" and "short". In addition, since an SC-cut blank is inherently asymmetrical in the thickness direction, the effect of the side that is contoured was also investigated. (One face of an SC-blank develops a positive charge upon compression, the other face develops a negative charge. In contrast, a true AT-cut blank does not develop a charge on either face upon compression.) For some of the units the positive on compression side was contoured, and for some of the units the negative on compression side was contoured. The results are shown in Fig 4. There was no observable dependence of  $|\ddot{x}|$  on either the contour or the side that was contoured.

#### Q and Activity Dip Incidence vs. Contour

The process of using a large radius of curvature contour for reducing the acceleration sensitivity of AT-cut resonators is useful only if it does not degrade other important resonator parameters. Two important parameters are the Q and the incidence of activity dips. For 10 MHz 3rd overtone units, for example, maximum Q's in excess of 1 million were measured for all diopter values between 0.5 diopter (biconvex) and 2.0 diopter (plano-convex), with the spread of values being comparable over the entire range. No systematic dependence of activity dip incidence on contour was observed.

#### Conclusions

Previous discussions on improving acceleration sensitivity were based upon the symmetry of the mounting structure,<sup>10,34</sup> and on precise location of the mounting points.<sup>5,13</sup> The mounting structure used for the above experiments, being only on one side of the blank, is quite asymmetrical. Even so, an acceleration sensitivity of  $3.2 \times 10^{-10}/g$  has been observed, which is comparable to the best SC-cut performance reported previously. The mounting orientation's average deviation from XX'/ZZ' for the 10 MHz resonators was  $1.8^\circ$ ; the deviations ranged from  $0^\circ$  to  $15^\circ$ . No correlation was observed between acceleration sensitivity and the actual mounting orientations even at the lower diopeters, where the normal-to-the-blank component of the acceleration sensitivity vector was not dominant.

According to the above described results, a substantial improvement in the acceleration sensitivity of AT-cut resonators can be achieved by selecting the blank contour to be as flat as possible.

Although blank contour has now been identified as a significant parameter that can be used

to reduce the acceleration sensitivity of AT-cut resonators, the parameter(s) that cause the scatter among otherwise "identical" units is yet to be identified.

#### Acknowledgements

The authors wish to thank J. Keres, T. Snowden and the resonator development group at GEND for their assistance in fabricating the resonators used in these experiments. Thanks are also due to W. Washington, R. Brandmayr, J. Gualtieri and H. Spaight of ERADCOM for their assistance in preparing the resonators blanks.

#### References

1. W.J. Spencer and W.L. Smith, "Precision Crystal Frequency Standards," Proc. 15 ASFC\*, pp 139-155 (1961), AD 265455
2. G.F. Johnson, "Vibration Characteristics of Crystal Oscillators," Proc 21st ASFC\*, pp 287-293 (1967), AD 659792
3. M. Valdois, J. Besson and J.J. Gagnepain, "Influence of Environment Conditions on a Quartz Resonator," Proc 28th ASFC\*, pp 19-32, (1974), AD A011113
4. P.C.Y. Lee and K.M. Wu, "Effects of Acceleration on the Resonance Frequency of Crystal Plates," Proc 30th ASFC\*, pp 1-7 (1976), AD A046089
5. P.C.Y. Lee and K.M. Wu "The Influence of Support Configuration on the Acceleration Sensitivity of Quartz Resonator Plates," Proc 31st ASFC\*, pp 29-34 (1977), AD A088221
6. J.M. Przyjemski, "Improvement in System Performance Using a Crystal Oscillator Compensated for Acceleration," Proc 32nd ASFC\*, pp 426-431 (1978)
7. A. Warner, B. Goldfrank, M. Meirs and M. Rosenfeld, "Low 'g' Sensitivity Crystal Units and Their Testing," Proc 33rd ASFC\*, pp 306-310 (1979)
8. T.J. Lukaszek and A. Ballato, "Resonators for Severe Environments," Proc 33rd ASFC\*, pp. 311-321 (1979)
9. A. Ballato, "Resonators Compensated for Acceleration Fields," Proc 33rd ASFC\*, pp 322-336, (1979)
10. R. Besson, J.J. Gagnepain, D. Janiaud and M. Valdois, "Design of a Bulk Wave Quartz Resonator Insensitive to Accelerations," Proc 33rd ASFC\*, pp 337-345 (1979)
11. R.L. Filler, "The Effect of Vibration on Frequency Standards and Clocks," Proc 35th ASFC\*, pp 31-39 (1981)

12. M. Nakazawa, T. Lukaszek and A. Ballato, "Force- and Acceleration-Frequency Effects in Grooved and Ring-Supported Resonators," Proc 35th ASFC\*, pp 71-91 (1981)
13. B. Goldfrank, J. Ho and A. Warner, "Update of SC-Cut Crystal Resonator Technology," Proc 35th ASFC\*, pp 92-98 (1981)
14. R.W. Ward, "Design of High Performance SC Resonators," Proc 35th ASFC\*, pp 99-103 (1981)
15. R.L. Filler and J.R. Vig, "The Acceleration and Warm-up Characteristics of Four-Point-Mounted SC and AT-Cut Resonators," Proc 35th ASFC\*, pp 110-116 (1981)
16. V.J. Rosati and R.L. Filler, "Reduction of the Effects of Vibration on SC-Cut Quartz Crystal Oscillators," Proc 35th ASFC\*, pp 117-121 (1981)
17. A.W. Warner, B. Goldfrank and J. Tsacalis, "Further Development in SC-Cut Resonator Technology," these proceedings, (1982)
18. C. Colson, "Vibration Compensation of the SEETALK Rubidium Oscillator," these proceedings, (1982)
19. F.L. Walls, "Vibration and Acceleration Induced Timing Errors of Atomic Clocks and Clock Systems," these proceedings, (1982)
20. J. Moses, "Navstar Global Positioning System Oscillator Requirements for the GPS Manpack," Proc 30th ASFC\*, pp 390-400 (1976), AD A046089
21. R.J. Kulpinski, "Minimum Methods for Synchronization of Airborne Clocks," Proc 30th ASFC\*, pp 401-413 (1976), AD A046089
22. R.E. Bennett, editor, "Quartz Resonator Handbook," Department of the Army (1960) AD 251289
23. R.L. Filler and J.R. Vig, "Fundamental Mode SC-Cut Resonators," Proc 34th ASFC\*, pp 187-193 (1980)
24. J.R. Vig, W. Washington and R.L. Filler, "Adjusting the Frequency vs. Temperature Characteristic of SC-Cut Resonators by Contouring," Proc 35th ASFC\*, pp 104-109 (1981)
25. J.A. Kusters, C.A. Adams and H. Yoshida, "ITC's - Further Developmental Results," Proc 31st ASFC\*, pp 3-7 (1977), AD A088221
26. J.R. Vig and E. Hafner, "Packaging Precision Quartz Crystal Resonators," Technical Report ECOM-1143, US Army Electronics Command, Fort Monmouth, NJ, (July 1973), AD 763215
27. P.D. Wilcox, G.S. Snow, E. Hafner and J.R. Vig, "A New Ceramic Flatpack for Quartz Resonators," Proc 29th ASFC\*, pp 202-219 (1975), AD A017466
28. R.D. Peters, "Ceramic Flatpack Enclosures for Precision Quartz Crystal Units," Proc 30th ASFC\*, pp 224-231 (1976), AD A046089
29. J.R. Vig, J.W. LeBus and R.L. Filler, "Chemically Polished Quartz," Proc. 31st ASFC\*, pp 131-143 (1977) AD A088221
30. J.R. Vig, R.J. Brandmayr and R.L. Filler, "Etching Studies on Singly and Doubly Rotated Quartz Plates," Proc. 33rd ASFC\*, pp. 351-358 (1979)
31. J.R. Vig, "UV/Ozone Cleaning of Surfaces: A Review," In Surface Contamination: Genesis, Detection and Control, K.L. Mittal, ed., Vol 1, pp 235-254, Plenum Press, New York, 1979
32. R.L. Filler, J.M. Frank, R.D. Peters and J.R. Vig, "Polyimide Bonded Resonators," Proc. 32nd ASFC\*, pp 290-298 (1978)
33. R.L. Filler, L.J. Keres, T.M. Snowden and J.R. Vig, "Ceramic Flatpack Enclosed SC and AT-Cut Resonators," 1980 Ultrasonics Symposium Proceedings, IEEE, (1980)
34. D.L. Hammond, "Precision Quartz Resonators," Proc 15th ASFC\*, pp 125-138 (1961), AD 265455

\*ASFC-Annual Symposium on Frequency Control, copies available from:

1956 - 1977:  
National Technical Information Service  
Sill Building  
5285 Port Royal Road  
Springfield, VA 22161

1978 - 1981:  
Electronic Industries Association  
2001 Eye Street  
Washington, DC 20006

# 5MHz fund AT

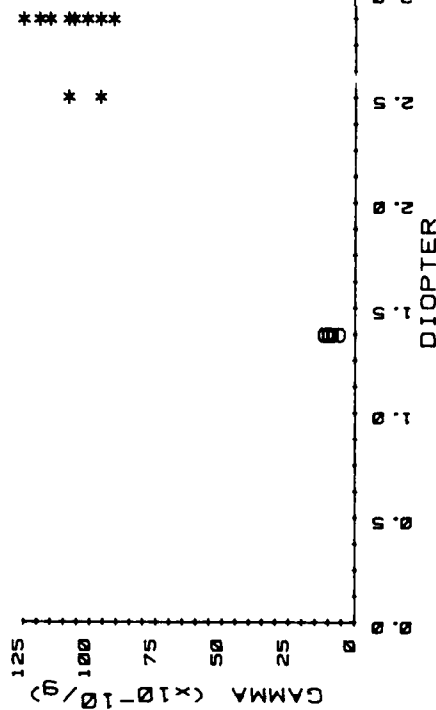


FIGURE 1 - ACCELERATION SENSITIVITY VS. CONTOUR FOR 5MHz, FUNDAMENTAL MODE, AT-CUT RESONATORS. \* - PLANO-CONVEX, O - BICONVEX

# 5MHz 3rd O/T AT

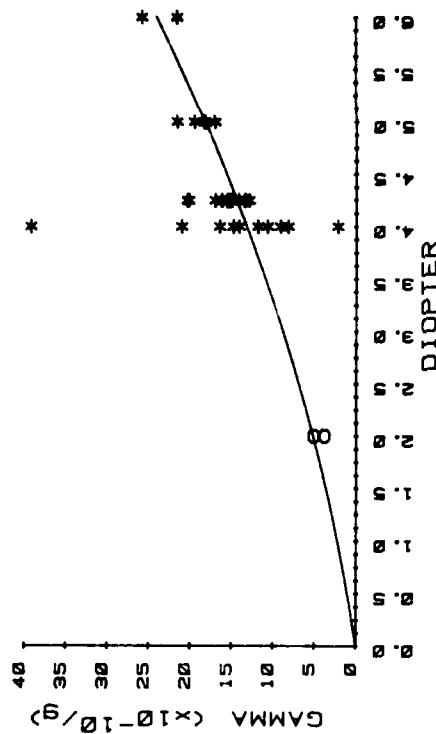


FIGURE 2 - ACCELERATION SENSITIVITY VS. CONTOUR FOR 5MHz, THIRD OVERTONE, AT-CUT RESONATORS. \* - PLANO-CONVEX, O - BICONVEX

# 10MHz 3rd O/T AT

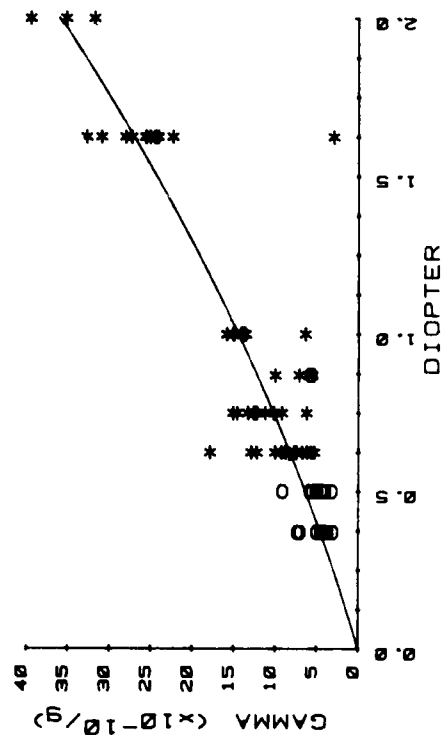


FIGURE 3 - ACCELERATION SENSITIVITY VS. CONTOUR FOR 10MHz, THIRD OVERTONE, AT-CUT RESONATORS. \* - PLANO-CONVEX, O - BICONVEX

# 5MHz fund SC

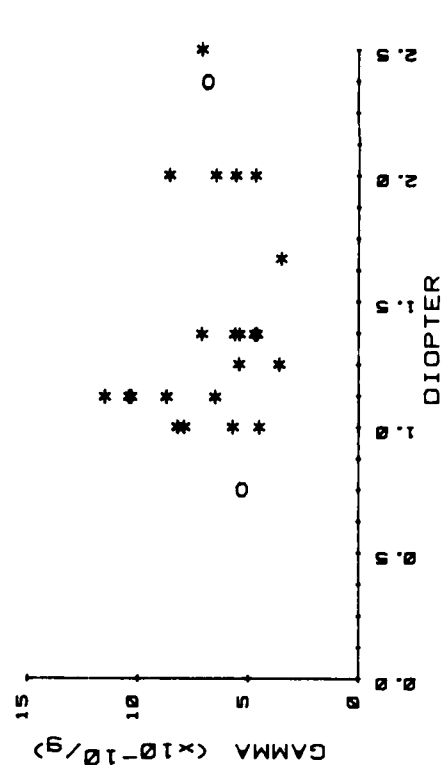


FIGURE 4 - ACCELERATION SENSITIVITY VS. CONTOUR FOR 5MHz, FUNDAMENTAL MODE, SC-CUT RESONATORS. \* - PLANO-CONVEX, O - BICONVEX

## "ATOMIC CLOCKS"

PREVIEW OF AN EXHIBIT AT THE SMITHSONIAN

Paul Forman  
Smithsonian Institution  
Washington, D.C. 20560

### Orientation

Early in December of this year the Smithsonian's National Museum of American History (formerly...of History and Technology) will open an exhibit on the historical development of atomic frequency and time standards. "Atomic Clocks" will occupy about 100m<sup>2</sup> behind the exhibit "Atom Smashers...Fifty Years." Intended as a long-term temporary exhibit, "Atomic Clocks" will remain for several years.

The idea, conceptual structure, and collection of objects and illustrations for this exhibit is due chiefly to Dr. Geiger, who worked on this project for more than two years from 1979 through 1981. It was given that the exhibit would be historical, for that is characteristic of this museum, in presenting the history of science and technology, rather than current science and technology, we are able to engage and inform not merely the lay visitor but also the scientist and engineer, and most effectively those most knowledgeable about the field in question.

The viewer is introduced in the first section of the exhibit to the concept of a time standard and to measures of the goodness of clocks. The second section traces microwave technique through World War II to the first atomic clock, the NBS ammonia absorption device. There follow three sections dealing respectively with atomic beam clocks, optically pumped vapor cell clocks, and masers. In each of these three cases we seek to show how ideas in the minds of physicists engaged in basic research became commercially manufactured instruments offered for sale off the shelf. In the sixth and final section, devoted to applications of atomic clocks, we will seek to bring the exhibit up to date.

### Exhibition

#### 1. Goodness of Clocks and Standards of Time

Having defined the figures of merit "accuracy" and "stability," which throughout the exhibit we use as the measures of the goodness of clocks, we turn to the notion of a time standard. A 19th century transit instrument from Vassar College Observatory symbolizes the fact that for centuries, indeed until the middle of the 20th century, the rotation of the earth was the standard of time. A 19th century transit instrument from Vassar College Observatory symbolizes the fact that for centuries, indeed until the middle of the 20th century, the rotation of the earth was the standard of time.

watch are presented as eminently useful for dividing the day, but by their nature unsuitable as standards--universal, independent of past history, and largely independent of present conditions. James Clerk Maxwell's Treatise on Electricity and Magnetism (1873) is open to that passage where, with sardonic wit, he suggests that the wavelength of a spectral line, unlike the definition of the meter, "would be independent of any changes in the dimensions of the earth and should be adopted by those who expect their writings to be more permanent than that body." In the second edition of their Elements of Natural Philosophy (1879) Wm. Thomson (Lord Kelvin) and P.G. Tait went further to suggest that the vibrations of sodium or hydrogen atoms would provide an absolute standard of time. But how to count them?

#### 2. Microwaves and the First Atomic Clock

We quickly trace the development of microwaves from laboratory curiosity to laboratory technology between the early 1930s and the mid-1940s. The first of these termini is represented by a magnetostatic oscillator tube constructed by C.E. Cleeton as a graduate student of N.H. Williams at the University of Michigan in 1933. With it Cleeton produced microwaves in the centimeter range and observed the inversion transition of the ammonia molecule. A couple klystrons, vintage 1945, stand for the transformation of every aspect of the production and manipulation of microwaves which occurred during the Second World War. Finally the time was ripe for proposals by R.V. Pound, Wm. V. Smith, and others for "Frequency Stabilization of Microwave Oscillators by Spectrum Lines."

These advances led the National Bureau of Standards to launch a program to develop atomic clocks. Their efforts focused first upon the most direct approach, locking a quartz oscillator to the inversion transition absorption line of ammonia. Early in 1949 the NBS announced success. But with a stability of only  $10^{-8}$  the ammonia absorption clock was a disappointment.

#### 3. Atomic Beams: The Most Accurate Clock

The viewer is led gradually up to the full complexity of the atomic beam clock, a technique which was developed by R.V. Pound and H.G. Debye in 1948. The viewer is led gradually up to the full complexity of the atomic beam clock, a technique which was developed by R.V. Pound and H.G. Debye in 1948.

AD P001524

Dunoyer's demonstration of sodium beams in 1911, to Stern and Gerlach's experiment in the early 1920s, and then to the "Molecular Beam Resonance Method" of Rabi & Co. in the late 1930s. The final step, Ramsey's "New Molecular Beam Resonance Method," is represented also by a pair of separated field coils, circa 1949, among the earliest used by Ramsey.

It was another former member of Rabi's pre-war group who put together the first atomic-beam clock, and--what was of considerably greater significance--put it together as a prototype for a manufactured device. Jerrold Zacharias first persuaded his graduate students at MIT to the project, and then, when at the end of 1954 their device began to work, persuaded the National Company in Malden, Mass. to undertake engineering development and marketing. The exhibit includes the MIT prototype, the National prototype (1955), and the National Company's "Atomichron," NC 1001, serial number 101 (i.e., nr 1), the first atomic clock to come off a "production line." The Atomichron's specified stability was  $10^{-9}$ , but under laboratory conditions  $10^{-10}$ . Its price tag read \$30k, which, as they were 1956 dollars, is ten times what, say, an HP-5061A costs today.

Needless to say, the latter sum is still significant. We are therefore much indebted to the Hewlett-Packard Foundation for contributing an operable 5061A to our exhibit. We look to the Naval Observatory to set it accurately for us.

Having distinguished atomic-beam clocks as the most accurate, we conclude the section of the exhibit devoted to them with a photographic review of cesium-beam atomic clocks as national and international time standards. We range from NPL Cs I flanked by Essen and Parry in the Teddington Laboratory (1955), through the several NBS cesium clocks, to the PTB Cs 1 and the NRC Cs VI standards.

#### 4. "Pumped" Atoms: The Smallest and Cheapest Atomic Clock

The "Atomichron" did not persuade everyone that cesium beams were the wave of the future. Although it worked impressively well, it was frightfully expensive, and seemed to hold little promise of being made compact, light, sturdy, and simple to operate. By contrast, the approach represented by the original NBS ammonia clock--the absorption of microwaves in a gas or vapor cell--promised all these characteristics, and relative cheapness as well, if only it could be made to work well. But to get an absorption line out of a vapor cell that was strong enough and narrow enough to lock onto, new ideas were needed: optical pumping, collision narrowing, and optical detection of microwave resonance. Once again we resort to original publications (of Kastler, Dicke, Bitter, Dehmelt), photographs and illustrations to introduce these ideas.

In 1954 Robert Dicke, well aware of these ideas and their bearing on this problem, launched a program to develop an atomic frequency standard based upon microwave absorption in an alkali-vapor

cell--but now, with optical pumping, detecting microwave emission. This work, in collaboration with Thomas Carver, is represented by the heart of their apparatus, a silver-plated micro-wave cavity, slotted to admit the pumping light.

The last trick needed to make the vapor cell work was discovered by Hans Dehmelt late in 1956. We display the pretty little bulb in which he found that microwave resonance caused a marked drop in the intensity of the pumping light transmitted through the vapor. Nothing could be simpler.

Several different laboratories followed up this observation, even to the point of a commercial product. In our exhibit, however, we tell only the story of research and development at Varian Associates, to whom Dehmelt had assigned his patent. The notebooks of Earle Bell and Arnold Bloom record the crucial steps toward their "Atomic Stabilized Frequency Source." The exhibit includes a preproduction prototype (1960) and an early production model (1961) of Varian's V-4700A rubidium vapor frequency standard. A Tracor Model 304D is exploded and sectioned so that the visitor can get some "insight" into these devices, and an early Efratom standard points the way toward miniaturization.

#### 5. The Maser: The Most Stable Clock.

Once more we return to the early 1950s, for there too are the origins of the third principal type of atomic clock, the maser. First conceived by Charles Townes on a park bench in Washington on a spring morning in 1951, it was three years before he and his students had one working, and nearly four before Columbia called a news conference. By then--January 1955--a second maser had been constructed and with it their relative stability determined ( $10^{10}$ ). We exhibit a composite apparatus, including ammonia source, state-selector, and microwave cavity, assembled from relics donated by Townes in years past to the Smithsonian and to the Franklin Institute.

The ammonia maser demonstrated brilliantly the principle of amplification by stimulated emission. But it had its problems--practical ones, such as pumping all that ammonia, and theoretical ones, such as the doppler shift and short residence time of the ammonia molecules in the microwave cavity. Both Ramsey and Zacharias, anticipating that an atomic-beam maser would give a  $10^5$  improvement, spent years on the problem before Ramsey and Kleppner found the answer in atomic hydrogen and a paraffin-lined storage bulb (1960). In 1979, starting from a pile of junk in a corner of Ramsey's laboratory, all the main components of the original hydrogen maser were located here and there at Harvard and elsewhere, and assembled for display in this exhibit. (Fig. 1-3.)

Although Ramsey et al claimed far too much in ascribing a stability of  $10^{-15}$  to their first H-maser, they were certainly right about the potential of the device. Their publication immediately drew the attention of Varian's East Coast research

arm, Bomac Laboratories in nearby Beverly. Soon they were actively involved in the design of a commercial model. We exhibit the earliest surviving of these H-10 masers, as Varian called them. It was the last of their preproduction prototypes, delivered to the Naval Research Laboratory in the spring of 1964, and donated to the Smithsonian last year.

The exhibit will include one further section on the uses to which atomic clocks are currently and increasingly put. We omit to describe it here, however, because our work is not yet complete, and because when we leave the ground of history there is nothing we could say that would be new to you.

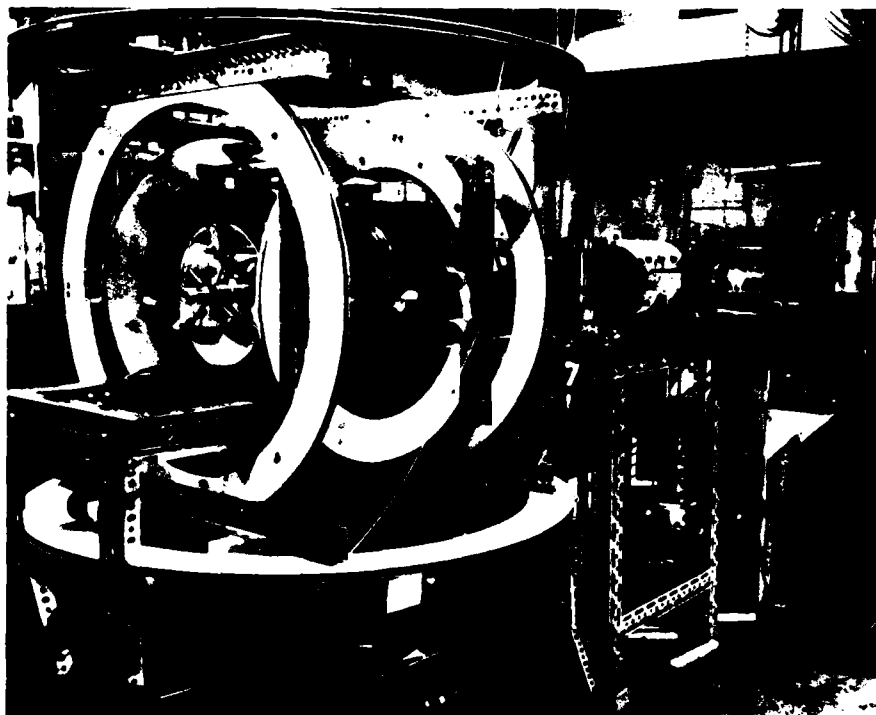


Fig.1 Original atomic hydrogen maser in N. F. Ramsey's laboratory, November 1960



Fig.2 Remains of H-maser, November 1979

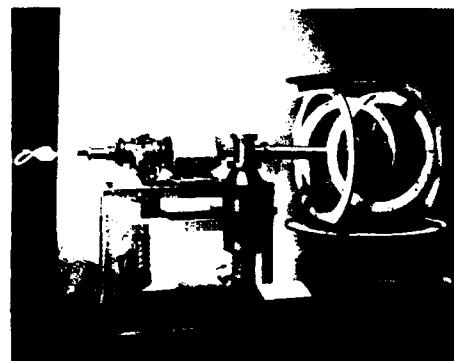


Fig.3 H-maser restored, 1980

This paper is a condensation of the oral presentation illustrated by circa 120 slides of objects, photographs and drawings to be included in the exhibition.

A SQUAREWAVE F.M. SERVO SYSTEM WITH A DIGITAL SIGNAL PROCESSING  
FOR CESIUM FREQUENCY STANDARDS

Y. Nakadan and Y. Koga

National Research Laboratory of Metrology  
Tsukuba Science City, Ibaraki, Japan

Summary

This paper describes a servo system with a digital signal processing which has been applied to a cesium frequency standard recently.

In contrast to the former servo system which adopted an analogue lock-in system with 2 Hz frequency modulation, the new system has various advantages such as a good linearity of modulation and demodulation, little dc offset of signal processing and easy compensations for optimum control. Some experiments at other laboratories show that the linear dc drift of output signal can be removed by a signal processing with the second order differences.

In this paper, the experimental results and its theoretical analyses on the servo system which takes higher order differences into the calculation for processing, are presented.

The results show that it seems to be quite effective for the improvement of the frequency stability.

Introduction

The cesium beam frequency standard NRLM-II<sup>1)</sup> of the National Research Laboratory of Metrology of Japan was constructed in 1975. During 1977 and 1978, the preliminary evaluation of accuracy was made<sup>2)</sup>, and the work has been directed toward improvement of its accuracy.

One of the factor of the largest errors in the accuracy evaluation was the uncertainty of frequency shifts due to known changes in the modulation width. The amount of error was estimated as  $4.5 \cdot 10^{-11}$ . The system used for the excitation of the cesium resonance in the NRLM-II is a single control loop system which consists of two voltage controlled crystal oscillators (5 MHz VCX01 and 5.00688 MHz VCX02) and a commercial frequency synthesizer (12.63 MHz). The microwave signal for excitation is produced by multiplying the output of VCX02. The

VCX02 is continuously phase locked to the VCX01.

The uncertainty of the frequency shift was caused by switching transients in the beam signal due to the square wave modulation and by nonlinearity on frequency characteristics phase lock loop of the VCX02. So, in order to remove the effect of the transients in the beam signal and to get the error signal of the servo system by taking difference of averaged beam signals which correspond to frequencies separated from the vicinity of the center of the Ramsey line by 50 Hz, a digital signal processing system using a personal computer, a voltage to frequency converter and an electronic counter is introduced instead of a conventional lock-in amplifier.

There have been some experiments on digital servo systems<sup>3)-5)</sup>. One is a system which utilized the calculation of the first difference by using a time interval counter and others use an up and down counter with counting sequence in order to eliminate the linear dc drift of the background noise.

This paper describes a digital filtering system which calculates higher order differences in software to remove higher order disturbances of the background noise.

Principle of the Servo System

A square wave frequency modulation servo system with a digital processing for cesium frequency standard is shown in Figure 1. The time sequence diagram and waveforms of the designation index are shown in Figure 2. Square wave frequency modulation is operated by the remote switching apparatus attached to the synthesizer with 4s in the modulation period and 100 Hz in the modulation width. The synthesizer output signal is fed to a phase sensitive detector (P.S.D.). The error signal is applied to VCX02 in such a way that phase difference is reduced to zero. Therefore, 9192 MHz is also modulated with 4s in the modulation after an ① in Figure 2. The detector output

AD P001525

Voltage which is shown ② in Figure 1 is converted into frequency and is counted by an electronic counter after an opportune time delay. In Figure 2, the measuring sections of the electronic counter and the output of the digital analog converter are shown as ③ and ④ respectively.

#### Analysis of the Digital Servo System

Figure 3 shows the block diagram of the digital servo system of Figure 1. The parameters of the system are as follows:

- $f_0$  resonance frequency of cesium atom, 9192 MHz
- $f_1$  self-sufficient frequency of VCX01
- $f_2$  controlled output frequency of VCX01, 1 MHz
- $E_1$  detection sensitivity of Ramsey signal including an electrometer amplifier, V/Hz
- $K_2$  voltage to frequency conversion gain, Hz/V
- $K_3$  frequency to digit conversion gain of electronic counter, 1/Hz
- $K_4$  gain depending on calculation
- $E_2$  digital to analog conversion gain, V
- $K_5$  voltage to frequency conversion gain, Hz/V
- $N$  multiplication factor of a frequency multiplier
- $G(s)$  transfer function depending on a calculation formula
- $T$  modulation period, s

The open loop transfer function can be written as

$$F(s) = K \frac{1 - e^{-sT}}{s} \cdot \frac{g(s)}{s} \quad \dots (1)$$

where

$$K = K_1 \cdot K_2 \cdot K_3 \cdot K_4 \cdot K_5 \cdot K_0 \cdot N \cdot \frac{1}{T} \quad \dots (2)$$

$\frac{1 - e^{-sT}}{s}$  is the open loop transfer function sampling by an electronic counter and digital servo hold.

#### Calculation formula to obtain

##### Transfer Function $g(s)$

The error signal is obtained as a difference of two signals corresponding to the frequencies  $f_A$ ,  $f_B$  as shown in Figure 2.

This is equivalent to computing the first order difference, and it is insufficient to the rejection of the higher order drift of background beam intensity or operational amplifier. In order to remove such a drift, it is necessary to take the difference of higher order.

Now, as VCX01 is controlled to Ramsey resonance line,  $E_A$  is nearly equal to  $E_B$ .

The first order difference,  $\Delta x_{2n}$ , is

$$\Delta x_{2n} = x_{2n-1} - x_{2n} = K_2(E_{An} - E_{Bn}) \quad \dots (3)$$

where  $x_{2n-1}$  and  $x_{2n}$  are the  $2n-1$ -th and  $2n$ -th input data from the electronic counter.

We extend this idea to the difference of higher order, the second order difference is

$$\Delta^2 x_{2n} = \Delta^2 x_{2n} = x_{2n-2} - 2x_{2n-1} + x_{2n} \quad \dots (4)$$

and the  $m$ -th order difference is

$$\Delta^m x_{2n} = \Delta^m x_{2n} = \sum_{r=0}^m (-1)^r \binom{m}{r} x_{2n-m+r} \quad \dots (5)$$

$$\text{where } \binom{m}{r} = \frac{m!}{r!(m-r)!} \quad \dots (6)$$

$\binom{m}{r}$  is the binomial coefficient.

Now, if we apply the signal of any frequency  $e^{j\omega t}$  to  $x_{2n}$  of the first difference of (3),

$$\begin{aligned} \Delta e^{j\omega t} &= e^{j\omega(t-T)} - e^{j\omega t} \\ &= je^{-j\omega T/2} (2\sin\omega T/2) e^{j\omega t} \quad \dots (7) \end{aligned}$$

This equation shows a band pass filter of center frequency,

$$f = \frac{1}{2T} \quad (0 \leq \omega T \leq \pi) \quad \dots (8)$$

The difference of  $m$ -th order is

$$\Delta^m (e^{j\omega t}) = \binom{m}{j} e^{-jm\omega T/2} (2\sin\omega T/2)^m e^{j\omega t} \quad \dots (9)$$

An indicial response of this formula is obtained by a step frequency change of VCX01. The error signal of  $n$ -th period,  $y(nT)$ , is

$$\begin{aligned} Y(nT) &= x_{2n-1} - x_{2n} \\ &= K_2(E_{An} - E_{Bn}) \quad (10) \end{aligned}$$

From the equation (4) of the second difference

$$\begin{aligned} \Delta y(nT) &= y(nT-T) - y(nT) \\ &= (1 - e^{-sT}) y(nT), \quad (11) \end{aligned}$$

and then the  $i$ -th order difference (5) can

be written

$$\begin{aligned}\Delta^i y(nT) &= \Delta[\Delta^{i-1}] [y(nT)] \\ &= \sum_{r=0}^i \binom{i}{r} y(nT - (i-r)T) \\ &= (1+e^{-sT})^i y(nT) \quad \dots (12)\end{aligned}$$

$\Delta^i y(nT)$  is also given by a binomial forms,

$$\binom{i}{r} = \frac{i!}{r!(i-r)!} \quad \text{and } i=m-1. \quad \dots (13)$$

It is understood that  $m$  resistors must be set aside for buffer storage in order to execute (12).

The magnitude of Equation (12) becomes

$$(1+e^{-sT})^i = (2\cos T/2)^i e^{-jiT/2} \quad \dots (14)$$

which lead to the structure shown in Figure 4.  $(2\cos T/2)^i$  is a low pass filter which has weighting coefficients of a binomial form and is called a cosine window<sup>11</sup>.

The difference  $y(nT)$  is given by

$$y(nT) = K_4 \frac{1-e^{-2sT}}{s} \quad \dots (15)$$

Then, the transfer function,  $g(s)$ , is written from (12) and (15) as

$$\begin{aligned}g(s) &= \frac{1-e^{-2sT}}{s} (1+e^{-sT})^{m-1} \\ &= \frac{1-e^{-sT}}{s} (1+e^{-sT})^m \quad \dots (16)\end{aligned}$$

### Integration

Simple first order difference equation acts as an integrator,

$$u(nT) = u(nT-T) + y(nT) \quad \dots (17)$$

where  $u(nT)$  and  $y(nT)$  are the  $n$ -th input and output data of stored resistors. The  $z$  transform of this equation is

$$U(z) = (1-z^{-1})^{-1} Y(z) \quad \dots (18)$$

This is one of the recursive digital filter<sup>12</sup>, shown in Figure 5.

The Laplace transform of (18) is

$$U(s) = \frac{1}{Ts} \quad \dots (19)$$

Therefore, from equations (1), (16) and (19), the Laplace transforms of an over all transfer function is written by

$$G(s) = \left( \frac{1-e^{-sT}}{s} \right) (1+e^{-sT})^m \frac{1}{s} \quad \dots (20)$$

Taking the  $z$  transform, this equation is written as

$$G(z) = (1-z^{-1})^{-1} (1+z^{-1})^m \quad \dots (21)$$

### Experimental Result and Analyses

The values of the parameters of the actual instruments are as follows,  $K_1 = 4.0 \times 10^{-7}$  V/Hz,  $K_2 = 10^{-7}$  Hz/V,  $K_3 = 10^{-7}$  Hz,  $K_4 = 50$  (2nd difference),  $K_5 = 10^{-7}$  V, including ATT.  $10^{-7}$ ,  $K_6 = 6.6 \times 10^{-7}$  Hz/V,  $T = 1838$ ,  $T = 4s$ , then  $K = 6 \times 10^{-7}$ .

The detector consists of a potentiometer and an operational amplifier with  $10^4$  ohm input impedance, current to voltage conversion resistor. This voltage is still more amplified 30 dB gain, and then is converted to frequency by a voltage to frequency converter of 10 volts to 1 MHz.

The electronic counter has a display of 8 digits in decade step for gate time of 3.3s. Measuring frequencies are adjusted at about 500 kHz by shifting the output level of the operational amplifier, because of removing the noise of quantization.

Two voltage controlled crystal oscillators generate the 2.5 and 2.5034 MHz signals. In free running, their temperature coefficients are  $1 \times 10^{-6}$  /°C. The aging rates of long term are less than  $5 \times 10^{-6}$  per day, and for 1s, the short term frequency stabilities are characterized by  $2.2 \times 10^{-11}$ . The flat regions called "flicker floor" are observed at  $2 \times 10^{-11}$  in averaging times greater than a second.

The frequency stabilities of the two oscillators are 2.5 MHz and 2.5034 MHz, and the signals are sent to the detector. The signals are converted to voltage by the potentiometer, and then amplified by the operational amplifier. The signals are converted to frequency by the voltage to frequency converter, and then the frequency is measured by the electronic counter.

The results of the experiment are shown in Figure 6. The storage resistors are used for the digital filter, but it is not shown in this paper with the results of the experiment.

For input ranging from 1 to 10, the digital filter is used for the output ranging from 1 to 10.

Figure 6 shows the relative frequency stability between NRLM-II by using the digital filter and an HP design clock with a high performance time. They appear to have been influenced mainly the limitation of frequency stability imposed by the HP design clock rather than that of the standard itself. In order to estimate the frequency stability of NRLM-II, the measurements were taken for various beam intensities. The result shows the relative frequency stability was not affected at a beam intensity of half value of normal operation.

The influence caused by switching transients of square wave frequency modulation was simply removed by means of the digital processing of resonance signal as shown in Figure 7.

#### Analysis in the Frequency Domain

From the form of the transfer function as given by Equation (20), the magnitude and phase angle becomes to

$$|G(j\omega)| = \left[ \frac{\sin \pi T/2}{\pi T/2} \right]^2 \cdot [2 |\cos \pi T/2|]^m \cdot \frac{1}{\omega T} \quad \dots (22)$$

$$\angle G(j\omega) = -(2+m) \cdot T/2 - \pi/2. \quad \dots (23)$$

The normalized logarithm of magnitude and phase angle diagrams without an integrator are shown in Figure 8. As the log magnitude and phase diagrams are obtained, the stability characteristics can be simply determined from the point on plot of the transfer function at which the magnitude is unity  $[G(j\omega)=0\text{dB}]$  and the phase angle is  $180^\circ$ . The stability characteristics is then given by  $-(2+m) \cdot T/2 - \pi/2 = -\pi$  which is obtained from (23) letting in (22).

$$K \cdot G(j\omega) \frac{1}{(2+m)T} = 1 \quad \dots (24)$$

then,

$$K = \frac{1}{\omega T} \cdot \frac{1}{(2+m)} \left[ \frac{\sin \pi/2(2+m)}{\pi/2(2+m)} \right]^2 \cdot [2^m |\cos \pi/2(2+m)|^m]. \quad \dots (25)$$

#### Analysis in the z Transform Domain

The source of disturbance signals in the digital servo loop are signal detection noise,  $d$ , such as atomic beam noise, offset and drift of the operational amplifier, the quantization noise of digital signal processing,  $q$ , and offset and drift of the VCXOl,  $o$ .

The function of changes of the VCXOl output frequency  $f_1$ ,  $\Delta f_1$ , is given by

$$\Delta f_1 = \frac{1}{1+KG(z)} \left\{ \frac{KG(z)}{NK_1} \cdot d(z) + K_0 \cdot q(z) + o(z) \right\} \quad \dots (26)$$

where  $KG(z) = K(1-z^{-1})^{-1}(1+z^{-1})^m$ . Now, we consider the effect of disturbance signals  $d$ ,  $q$  and  $o$  separately.

#### The Effect of $d$

In general, the z transform of disturbance can be written

$$d(z) = (1-z^{-1})^{-p} \quad \dots (27)$$

Then, if the transfer function  $G(z)$  to disturbance  $d(z)$  has  $(1-z^{-1})^m$  as the basic element,  $m=p$ , the effect of disturbance  $d(z)$  is negligible. Taking the z transform of Equation (5),

$$\Delta^m x_n = (1 - z^{-1})^m. \quad \dots (28)$$

We explained at Equation (9) the action of the filter as previously stated. For the disturbance of the actual instrument, it would be effective enough to take 3 or 4 for  $m$ .

#### The Effect of the Quantization error $q$

The quantization error depends on mainly the digital to analog converter which produces an error of  $1.3 \cdot 10^{-11}$  in terms of normalized frequency error for a sampling time of 4s. On the other hand, errors from the voltage to frequency converter and the electronic counter are less than  $2 \cdot 10^{-11}$ .

#### The Effect of oscillator disturbance $o$

For the offset input,  $o_0(t)$ ,  $\Delta f_1$  is zero.

But, if the  $o_0(t)$  is drift input,

$$\mathcal{L}\{o_0(t)\} = \frac{Tz}{(z-1)^2} 2\pi \Delta f_0 \quad \dots (30)$$

the error transform  $\Delta f_1$  is as

$$\Delta f_1 = \lim_{z \rightarrow 1} \frac{z-1}{z} \cdot \frac{1}{1+KG(z)} \left\{ \frac{Tz}{(z-1)^2} 2\pi \Delta f_0 \right\} = \frac{T}{K'} 2\pi \Delta f_0 \quad (31)$$

where  $K' = \frac{T}{2^m}$ .

The final value of  $\Delta f_1$  has the residual error  $\frac{T}{K'} 2\pi \Delta f_0$ . As  $K'$  includes  $1/T$ , steady-state error increases in proportion to  $T$ . The offset of the controlled actual instruments becomes  $1.5 \cdot 10^{-11}$  from that the aging rates of the VCXOl are less than  $5 \cdot 10^{-11}$ /day.

Analysis of this system shows that the influence of drift or aging of electrometer is removed by taking the higher order difference into the calculation.

If we use longer  $T$  in period, noise can be more decreased by averaging. However, steady-state error caused by drift of the VCXOl increases in proportion to  $T$ , then it is necessary to choose the optimum  $T$ .

#### Conclusion

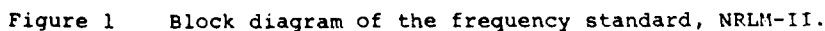
Analyses of this system show that the calculation of m-th order difference

Then, it is effective to the rejection of

1. the higher order disturbances including the drift of background noise,
2. the white noise and sudden large noise,
3. the influence caused by switching transients of square wave frequency modulation.

1. our system can take higher order difference in calculation against the second order difference of another systems,
2. control signals are able to obtained from D/A converter respond to every new period.

- 1) Y. Koga, Y. Nakadan and J. Yoda: Oyo Buturi 45 (1976) pp. 735 [in Japanese].
- 2) Y. Koga, Y. Nakadan and J. Yoda, "The cesium beam frequency standard NRLM-II," Journal de Physique, Colloque C8, Supplément au n°12, Tome 42, Décembre 1981, pp. c8-247.
- 3) D.A. Howe and H.F. Salazar, "A digital 5.00688 MHz synthesizer and squarewave fm servo system for cesium standards, in Proceedings 29th Annu. Symp. Frequency Control, 1974, pp. 363-372.
- 4) M. Jardino, M. Desaintfuscien, R. Barillet, J. Viennet, P. Petit, and C. Audoin, "Frequency stability of a mercury ion frequency standard," Appl. Phys., vol. 24, pp. 107-112, 1981.
- 5) M. Kobayashi, K. Nakagiri, S. Urabe, M. Shibuki and Y. Saburi, "Design of and preliminary results on a cesium-beam standard at the Radio Research Laboratories," IEEE Trans Instrum. Meas., vol. IM-27, pp. 343-348. Dec. 1978.
- 6) R.W. Hamming, "Digital filters," Prentice-Hall Inc., Englewood Cliffs, N.J., 1977.
- 7) B. Gold and C. M. Rader, "Digital processing of signals," McGraw-Hill, Inc., 1969.



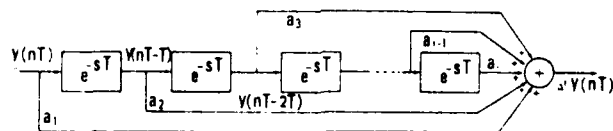
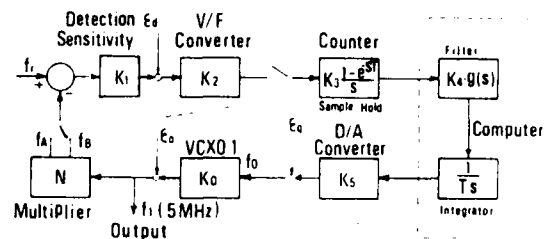
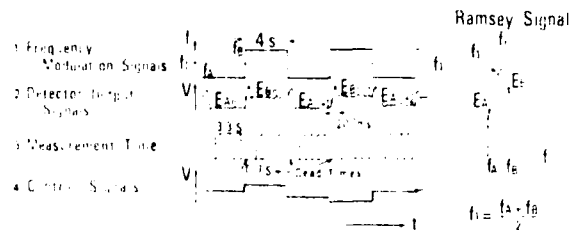


Figure 4 Non-recursive filter of i-th order difference.

Figure 5 Digital integrator.

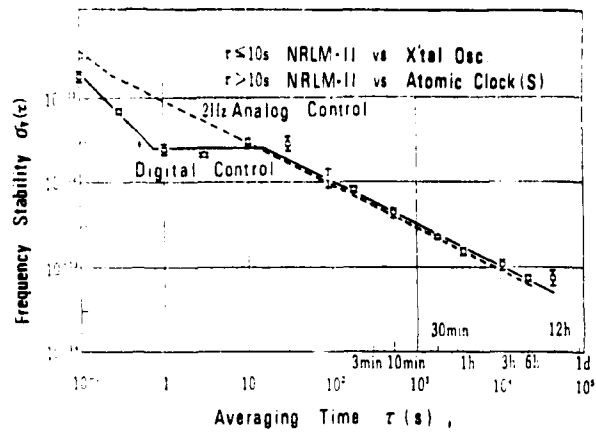


Figure 6 Relative frequency stability measured with respect to the HP cesium clock and crystal oscillator.

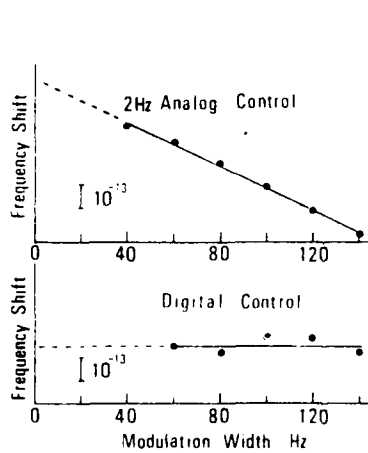


Figure 7 Frequency shift due to modulation width.

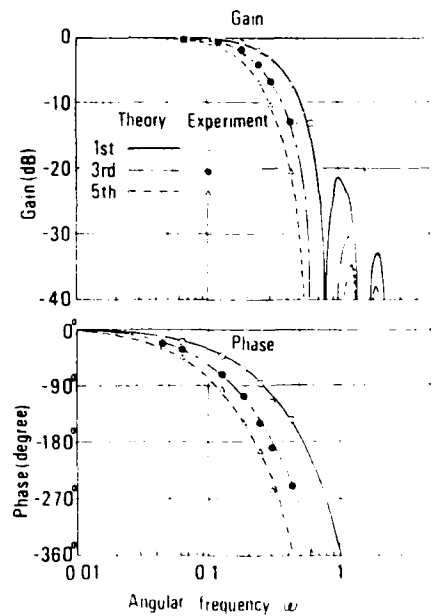
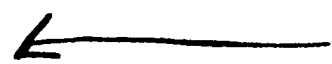


Figure 8 Normalized magnitude and phase angle diagrams without an integrator.



# PERFORMANCE CHARACTERISTICS OF CESIUM BEAM TUBE ELECTRON MULTIPLIERS

Emil R. Straka

Hewlett-Packard  
Santa Clara Instrument Division  
Santa Clara, California

AD P001526

## Summary

A demountable test system is used to determine operating characteristics of electron multipliers which will be used in cesium beam tubes. Tests are performed using an electron input signal. Multiplier gain and dynode secondary electron emission coefficients are calculated from these test data.

Environmental effects of air exposure and vacuum bake are also determined.

## Objective

This work was undertaken as part of a continuing program to develop improved methods for assuring quality in the manufacture of cesium beam tubes.

## Background

### Device Description

The electron multiplier is used as a linear signal amplifier and is located within the vacuum envelope of the CBT. The multiplier design uses a "box and grid" type of dynode (Figure 1). Each dynode consists of a grid and a housing which is lined with a silver-magnesium alloy. The grid is at the input aperture of each dynode. The output aperture is totally open. The alloy is processed in a manner similar to that described by Wargo, Haxby and Shepherd (1) in order to establish a surface with proper secondary emitting characteristics.

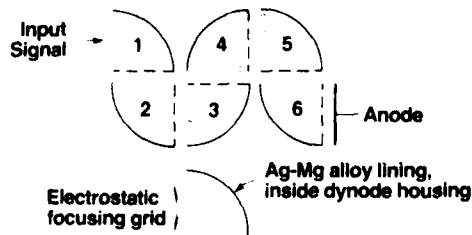


Figure 1. Schematic arrangement of the box and grid multiplier and a single dynode.

## Theory of Operation

The input signal consists of a cesium ion beam which is accelerated to the first dynode by some potential difference ( $-V_1$ ) measured with respect to the ionizer. The secondary electrons which are produced at the first dynode are then accelerated to dynode 2 by a potential difference ( $+V_2$ ) measured with respect to dynode 1. The electron current continues to be amplified as it proceeds on to subsequent dynodes until the fully amplified signal is collected at the anode. The inter-dynode potential differences are very nearly the same in our multiplier design so that  $V_2 = V_1 = V_3 = \dots$  etc. However,  $|V_2| \ll |V_1|$ . Since each dynode acts as an amplifier, the net gain  $G_N$  of a multiplier with  $N$  dynodes may be described in terms of the emission coefficients ( $\bar{c}$ ) of the dynodes and the ion-electron conversion efficiency ( $\eta_1$ ) of the first dynode. Then

$$G_N(V) = \eta_1 \bar{c}_1 \bar{c}_2 \dots \bar{c}_N \quad (1)$$

where  $\eta_1 = \eta_1(-V_1)$   
 $\bar{c}_N = \bar{c}_N(V_N)$

The subscripts refer to each dynode number. If we arrange that all inter-dynode voltages are equal and that secondary electron emission coefficients are equal, equation (1) becomes

$$G_N(V) = [\eta_1(-V_1)] [\bar{c}(V_1)]^{N-1} \quad (2)$$

## Electron Multiplier Operating Characteristics

### Test Apparatus

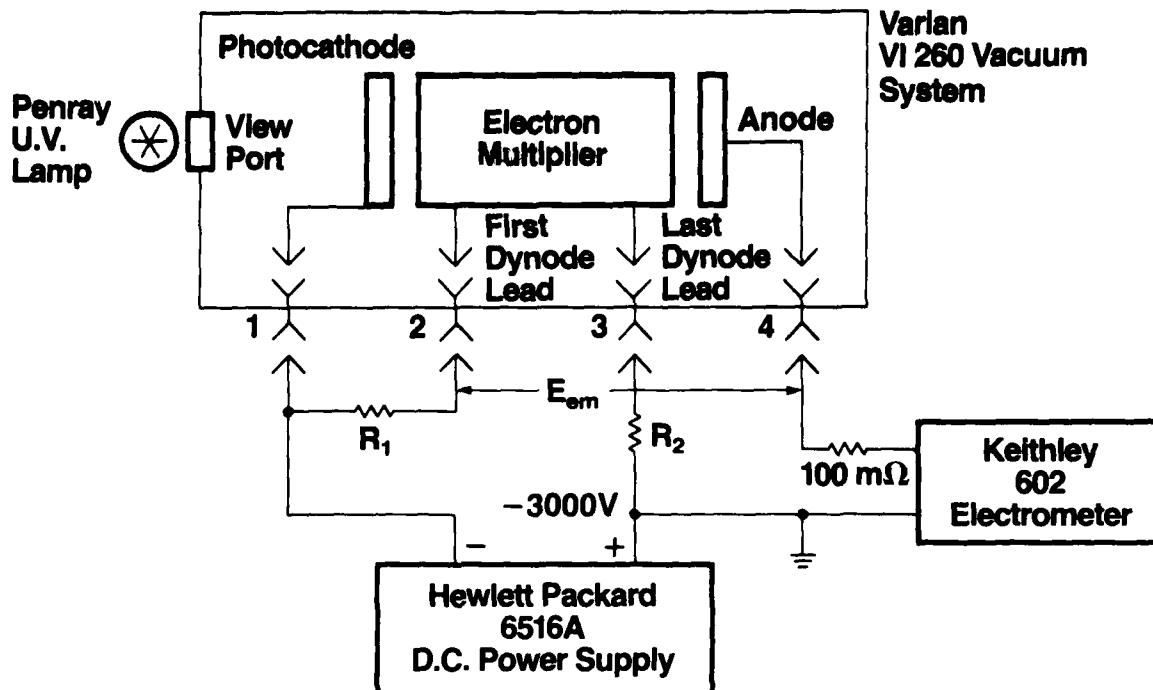


Figure 2. Schematic representation of the electron multiplier test setup. The voltage applied to the multiplier and anode is  $E_{em}$ . Output current measurements are obtained with this configuration.

The test apparatus employs an electron input signal rather than cesium ions for reasons that are quite obvious:

- 1) Once a multiplier is cesiated it cannot be opened to atmosphere without destroying the secondary emitting properties of at least the first dynode. Consequently, the performance would be badly degraded and the multiplier would no longer be useful.
  - 2) Cesium source isolation is needed when the system is open to atmosphere. This requires a more complex arrangement.
  - 3) Cesium of the test chamber can lead to system maintenance problems over long time periods.
- And finally,
- 4) Since we are really interested in getting a measure of  $\delta$ , an electron source is quite appropriate, reliable and easy to maintain.

$R_1$  is chosen so that the cathode to first dynode voltage is the same as the inter-dynode

voltage.  $R_2$  is chosen to match the circuitry of the frequency standard. 100MΩ is used at the electrometer input only for protection of the electrometer from inadvertent current spikes. The proximity focused transmission photocathode is an aluminum film on a disk of fused silica. The sapphire view port transmits U.V. radiation to the cathode which, in turn, ejects photoelectrons. U.V. filters are used to vary the input signal level. Signal levels of up to  $10^{-10}$ A. can be achieved. Input signals down to about  $5 \times 10^{-14}$ A. can be achieved albeit the measurements may be somewhat tedious.

Figure 2 shows the arrangement for making output current measurements. Input current measurements are performed after removing  $R_1$  and  $R_2$  and relocating the electrometer input lead from feedthrough 4 to feedthrough 2.

### Experimental Results

**General.** The determination of multiplier gain characteristics is accomplished solely by means of input current - output current - multiplier voltage ( $E_{em}$ ) relationships.

Figure 3 is an example of a set of current transfer characteristics curves.

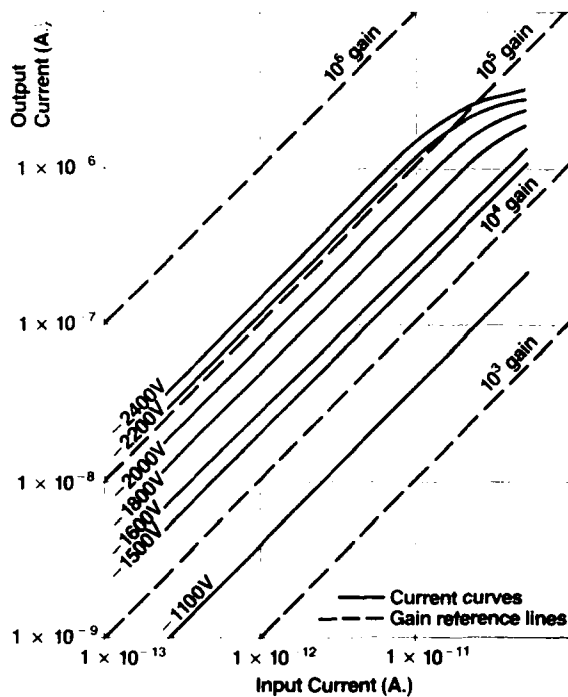


Figure 3. Current transfer characteristics curves for a 6 dynode multiplier. Multiplier voltage ( $E_{em}$ ) is expressed as 1st dynode potential relative to the multiplier anode.

For all values of  $E_{em}$  shown in Figure 3, each output current curve has at least one region of linear response over some input signal range. However as we would expect, as the multiplier becomes saturated, we see that linearity degrades. We may safely say that this specific multiplier will operate in an unsaturated mode for all  $E_{em} = -2400V$  if the output current does not exceed  $1\mu A$ .

Another way of looking at the multiplier characteristics is to plot log multiplier gain as a function of  $E_{em}$  for various input levels. Figure 4 shows such a curve. Multiplier gain at a given  $E_{em}$  is defined as the output current at that voltage divided by the input current. Since we have said that this multiplier will be unsaturated if the output current lies below the upper limit of about  $1\mu A$ , then the following relationships between gain and saturation can be used for this particular multiplier:

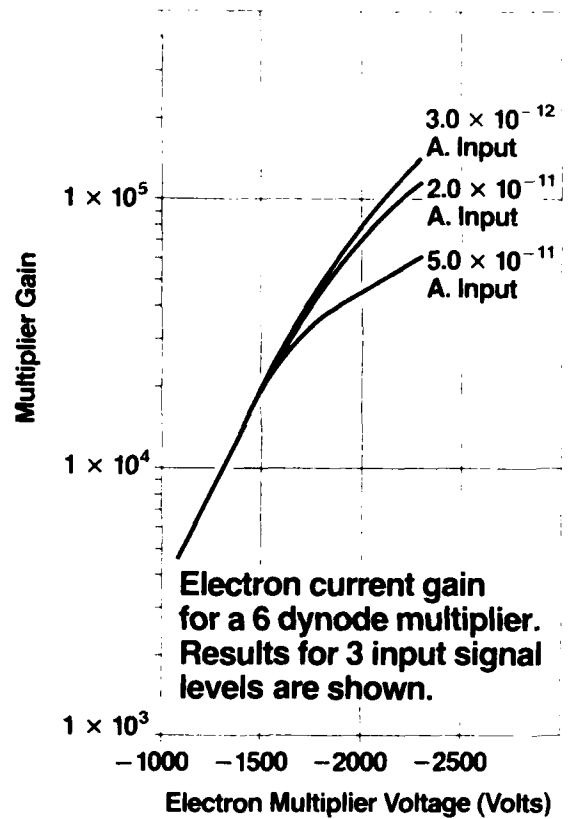


Figure 4. Multiplier gain as a function of multiplier voltage.

If the input signal level is then gain saturation occurs at and above gains of

- |                              |                   |
|------------------------------|-------------------|
| 1. $7.1 \times 10^{-12} A$ . | $1.4 \times 10^5$ |
| 2. $2.0 \times 10^{-11} A$ . | $5.0 \times 10^4$ |
| 3. $5.0 \times 10^{-11} A$ . | $2.0 \times 10^4$ |

Hence in the range  $E_{em} = 0$  to  $-2400V$  where the input signal is  $7.1 \times 10^{-12} A$  or less, an unsaturated curve is shown in Figure 4 as the  $3.0 \times 10^{-12} A$  input curve. For higher input levels, saturation begins as the respective curve begins to break away from the unsaturated curve as  $E_{em}$  increases. Figure 4 shows that saturation begins at about  $2.3 \times 10^4$  gain when the input is  $5.0 \times 10^{-11} A$ , and at about  $5.0 \times 10^4$  gain when the input is  $2.0 \times 10^{-11} A$ .

These data can be useful in monitoring process consistency if one measures gain of multipliers which always have the same number of dynodes. However when comparing multipliers which have different numbers of dynodes, it is more convenient to get a measure of single dynode performance. We begin by arranging that all

dynodes in the multiplier have very nearly the same secondary electron yield. We also choose an input signal level which assures us that we avoid gain saturation for the entire range of  $E_{em}$ . Then if the ion-electron conversion efficiency ( $\eta_{ie}$ ) is replaced by the secondary electron emission coefficient  $\delta(V)$ , equation (2), becomes

$$\delta(V) = \text{Log} \left[ \frac{\text{Log } G(V)}{N} \right] \quad (3)$$

where  $\delta(V)$  is the calculated mean secondary electron emission ratio,  
 $G(V)$  is the gain calculated from output and input current measurements  
 $(V)$  is the inter-dynode voltage  
 $N$  is the number of dynodes in the multiplier.

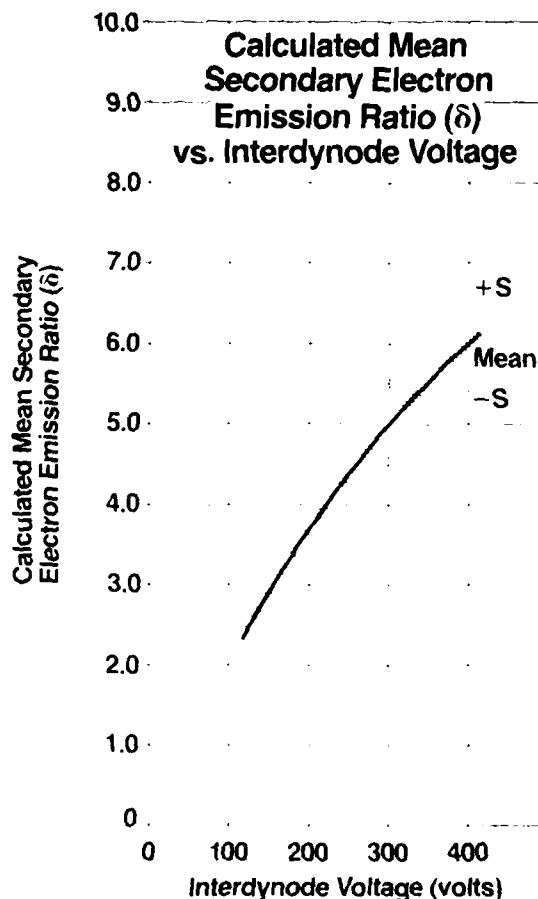


Figure 5. Secondary electron emission ratio as a function of inter-dynode voltage: evaluation of 26 process lots. The width of the band is two standard deviations.

Figure 5 shows the calculated mean secondary electron ratio as a function of inter-dynode voltage. This curve is based upon test results from 26 separate dynode lots processed in the Hewlett-Packard cesium beam production line. We prefer to use the single dynode performance to monitor process uniformity since the number of dynodes in the multiplier does not complicate comparisons of several multiplier types.

**Environmental: Air Exposure.** This topic seems to take on renewed interest every so often since low levels of CBT beam signal have frequently been blamed on multiplier processing and handling during fabrication. Since we qualify batches of multipliers prior to installing them in tubes, it was appropriate to seek a more complete picture by determining the effect on multipliers when exposed to air for a variety of time intervals.

This work was accomplished by exposing the test multiplier to room air which was typically at 70°F and had a nominal relative humidity of 40%. 45 minutes elapsed between the time the dynodes left the dynode processor and the assembled multiplier was first pumped down in the test chamber. Consequently, the exposure interval range is .75 hours to 33.8 hours.

#### Air exposure effect on electron multiplier gain.

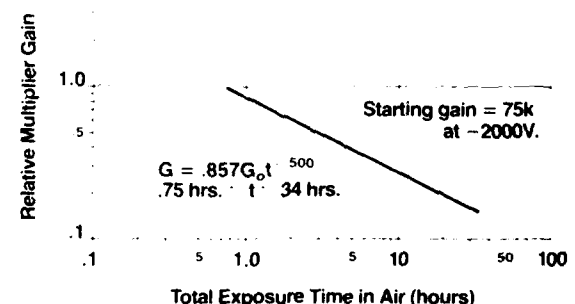


Figure 6. Gain degradation caused by exposure to room air, 70°F, 40% nominal relative humidity.  $G_0$  is original gain.  $t$  is time of exposure.

Figure 6 shows that the gain has  $t^{-1/2}$  dependence where  $t$  is exposure time. Note that multiplier gain could be expected to degrade 50% after 3 hours exposure to room air. Proper storage and handling conditions obviously play a major role in maintaining multiplier quality.

Environmental: Tube Exhaust Bake. Also of considerable interest is the effect that tube bake has upon multiplier gain.

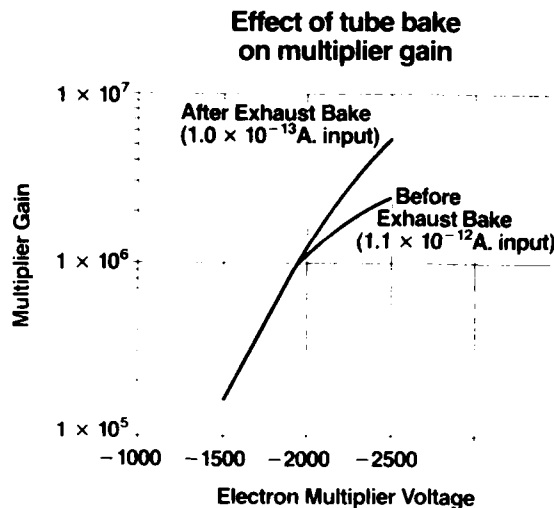


Figure 7. Calculated gain curves before and after tube bake. The unsaturated portions of the curves show excellent agreement thus indicating no gain degradation.

Figure 7 shows the vacuum bake did not degrade the performance of this multiplier. The difference in the two curves is due only to the fact that this 9-dynode multiplier saturates easily and too high an input signal level was used in the first test. The unsaturated section of the before-bake curve perfectly matches the same portion of the after-bake curve. Our conclusion is that the multiplier is very compatible with the tube exhaust bake.

**Development Process Results.** Having established a reliable method for evaluating dynode performance and then gathering statistics on the production process we have undertaken efforts to develop improved dynodes. Dynodes which exhibit higher gain and greater long term stability will allow us to operate multipliers at lower voltages thereby extending first dynode lifetime. Figure 8 shows the improved performance of recent development dynodes. The comparison is made against the mean of 26 production process runs, presented earlier in Figure 5 and against one of the higher quality production runs. At 200 volts we observe  $\bar{\delta} = 5.9$  for the development process,  $\bar{\delta} = 5.0$  for the better production run and  $\bar{\delta} = 4.4$  for the mean of the production runs. If we were to use these improved dynodes in 6 dynode multipliers and operate at -1500V, the respective electron current gains would be  $42 \times 10^4$ ,  $16 \times 10^4$  and  $7.3 \times 10^4$ . We have neglected the fact that in the cesium tube we must consider the

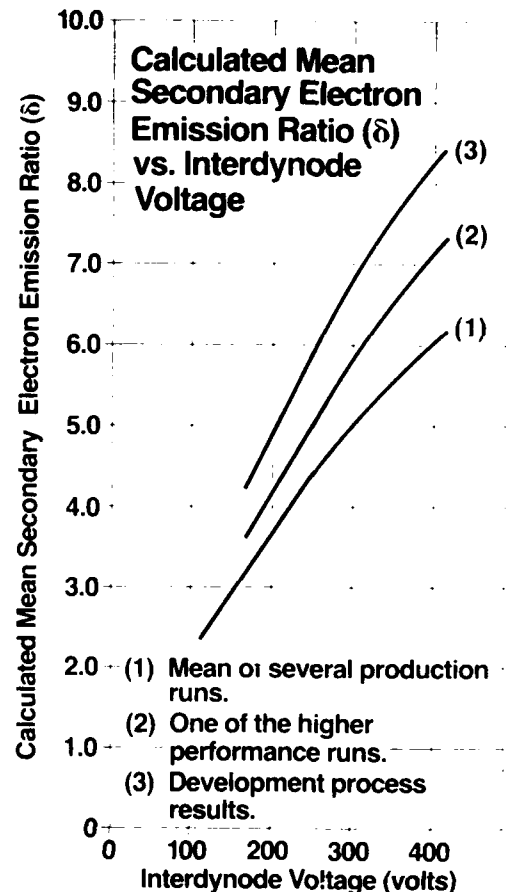


Figure 8. Comparison of development dynode process results with production process results.

first dynode conversion efficiency for the cesium ion. Still, the development process shows nearly a six fold gain improvement at this voltage.

#### Conclusion

The equipment and methods used to evaluate electron multiplier performance and process consistency have proved worthwhile since they provide a means to qualify electron multipliers prior to installing the multipliers in tubes. Test results continue to provide us with a high confidence level in dynode process reliability and in multiplier fabrication standards as well as handling and storage methods.

The production data are useful in establishing meaningful reference points for determining environmental effects and for determining the effects of process variations.

#### Acknowledgements

The author extends sincerest appreciation to Jerry Amaral, Adelaide Hamilton and Troy L. Payne for the support they provided for this work.

#### Bibliography

1. P. Wargo, B.V. Haxby and W.G. Shepherd,  
"Preparation and Properties of Thin Film MgO  
Secondary Emitters," J. Appl. Phys. 27, 11,  
(Nov. 1956) P.1311-1316.

A CESIUM BEAM FREQUENCY STANDARD  
WITH MICROPROCESSOR CONTROL

R. Michael Garvey

FREQUENCY & TIME SYSTEMS, INC.  
34 Tozer Road  
Beverly, MA 01915

ABSTRACT

The use of microprocessor based instrumentation in support of a cesium beam frequency standard is explored. Specific advantages and approaches are examined with the design goals of improved performance, enhanced system flexibility and increased reliability.

Introduction

The use of computers in the evolution of time and frequency technology has evolved primarily from their use in the laboratory for data acquisition and reduction. More recently computers have found application in timing receivers depending upon LORAN, TRANSIT, GPS and similar systems for their operation. A host of microprocessor and computer based instrumentation now supports the scientist and engineer in the laboratory; the power of this technology can be applied to the cesium frequency standard. A more sophisticated system of interrogation of the atomic system, a more accurate servo process combine with other techniques to provide the capability for more accurate, stable and flexible clocks and clock systems.

Timing Receivers

As the capabilities of time transfers advanced beyond the limitations of VLF transmissions, the requirement for increased receiver sophistication became apparent. Satellite receivers have the task to extract precise information in real time from a complex message format under varying conditions of signal-to-noise. Realization of such an instrument would not be practical without computer assistance.

The T-200 satellite timing receiver, manufactured by Frequency & Time Systems, Inc., is such a system, depending upon the Navy Navigational Satellite System (NNSS) or TRANSIT for its operation.<sup>1,2</sup> TRANSIT consists of a system of five satellites and associated ground support stations. The satellites are in nearly circular polar orbits of approximately 7500 km radius.

The satellite message contains orbital parameter data and time marks from which the satellite ephemeris may be computed. The T-200 microprocessor decodes the incoming satellite data and enables the recording of the time marks which occur at two minute intervals. During a single satellite pass, up to nine messages and time marks may be recorded. Satellite range is calculated for each message and propagation delay corrections made to each time mark reading. Subsequent data reduction involves rejection of noisy data or of low angle data (to eliminate multipath effects). At the choice of the user, single satellite corrections are implemented as received or an average correction over a number of satellites is executed. An optional version of the T-200 uses measured satellite doppler frequency changes during a pass to provide an accurate measure of receiver location in addition to precise time.

The microprocessor implementation of the T-200 points up several general advantages of this technology. The feasibility of extended data manipulation and reduction becomes apparent: the data size and task complexity would be impractical in any system without the computational power afforded by use of a microprocessor. The overall instrument performance is enhanced through increased reliability resulting from self-diagnostic features; reliability is also increased from the lower parts count which may be achieved in microprocessor based systems. Instrument operational flexibility is increased in the sense that manufacturer updates or custom user modifications become easily implemented as software changes. A specific example in the case of the T-200 is the Position Determination Option.

Additionally, the user mode or environment may be more easily accommodated by an adaptive instrument operating system. The T-200 receiver may be user programmed to selectively ignore specific satellites or to implement filtered corrections, allowing the user to tailor system operation to the stability characteristics of the available local clock.

AD P001527

## Cesium Standards

### Background

The performance of any atomic frequency reference is limited fundamentally by spectral line Q and by the available signal-to-noise ratio. From the designer's point of view, servo performance and the sophistication of the atomic interrogation are equally relevant. The user values ease of operation and reliability.

Non-ideal atomic interrogation and inadequate servo performance result in sensitivity to environmental perturbation such as temperature changes. In principle, the cesium atomic system contains adequate information to compensate for even more subtle perturbations such as vibration and changes in ambient magnetic field. Ageing effects either in components or indirectly in changing signal characteristics can produce long term frequency instabilities as well. Techniques for reducing the above deficiencies in performance are discussed below, particularly using microprocessor technology to implement system level solutions.

### Microprocessor Applications

Digital implementation of the frequency control servo is an obvious starting point. Digital demodulation and integration of error signal form the basis for a servo with zero offset which is not limited by finite gain. Scaling of the demodulated signal allows the possibility of variable loop bandwidths. In addition to running the frequency lock servo, it becomes possible to time-multiplex other system servos. If the implementation of such a servo does not perturb the atomic interrogation, the tasks may be executed by the microprocessor on a time available basis. Within the constraints of desired system unity gain frequency and stable loop behavior, it is possible to briefly disable the main frequency lock servo while performing other tasks. In this way measurement of C-field through interrogation of the  $M_F = 0$  transitions could be used to stabilize or otherwise compensate for changes in ambient magnetic field. Disabling the main frequency lock servo eliminates the possibility of introducing a frequency offset through the C-field measurement. The requisite data rate for such a magnetic field servo is adequately low so as to produce minimal perturbation. A similar servo could be implemented for control of the interrogating power level.<sup>3</sup>

Examination of system parameters via analog voltage monitors may be straightforwardly implemented in a background routine. The routine provides a quasi-continuous evaluation of system

performance, alerting the user of potential malfunction or failure. Addition of environmental sensors creates the potential for realization of adaptive servos. The quartz oscillator performance under benign conditions determines an optimum loop bandwidth which yields optimum overall system performance. Under conditions of changing ambient temperature, mechanical perturbation, or shortly after turn-on, oscillator performance is quite different, resulting in a different optimum loop bandwidth. User interaction or alternatively interaction with user systems becomes an attractive feature of flexibility available with microprocessor technology.

More sophisticated frequency lock servos may be implemented if control of loop gain is possible. Figure 1 illustrates two servo responses to linear oscillator drift. Note the permanent residual offset in the type I servo. To insure overall loop stability, type II servos may be implemented only if loop gain can be maintained adequately high. Ageing phenomena can result in decay of cesium beam tube signal amplitude which, if not otherwise compensated for, can lead to instabilities in type II servos.

Use of a time-multiplexed servo to measure and control loop gain allows implementation of the type II servo. Control of loop gain has other benefits as well. Loop time constant and dynamic behavior remain constant. Although loop offsets are not eliminated by this technique, frequency changes induced by changing loop gain are nullified, resulting in improved long term frequency stability.

Figure 2 shows a conceptual block diagram of a microprocessor based cesium frequency standard. Control of the frequency and amplitude of the interrogating signal applied to the cesium beam tube are achieved by use of a programmable synthesizer and attenuator. Measurement of the  $M_F = +1$  transitions permit correction of C-field current; alternatively, with adequately high synthesizer resolution, C-field changes can be compensated for in the frequency servo loop.

System analog monitors are also shown in Figure 2. These signals may be multiplexed and read by the same analog-to-digital converter which digitizes the error signal from the cesium interrogation. This use of electronic hardware to perform multiple tasks is an example of how system capabilities may be increased without increase in parts count.

The desirability for long term uninterrupted operation in clock applications guides the designer in the choice of hardware implementation of the concepts discussed above. Low power dissipation and low parts count are two general

elements which lead to reliable designs. Microprocessor implementation of complex tasks can lead to dramatically reduced parts count. The use of CMOS circuitry satisfies the desire for low power dissipation.

#### Implementation

The 1802 microprocessor was chosen to implement the new cesium frequency standard design. The 1802 is an 8 bit CMOS microprocessor with an associated family of CMOS support devices. Additionally, direct interface with the 4000 CMOS family of devices is possible. System memory is a 2K X 8 EPROM.

At turn-on, a self test is initiated and system monitors are examined. As soon as the quartz oscillator oven and cesium oven servos have stabilized, a lock acquisition routine is initiated. A fast loop attack time is employed to reduce the effects of oscillator turn-on transient behavior.

User interaction is handled completely by the microprocessor. A diagnostic bus has been included to permit detailed operational monitoring and to assist in troubleshooting and repair. A hardware failsafe alarm circuit is activated by malfunction of the microprocessor.

The frequency lock servo is a 1 kHz interrupt-driven routine, while system monitors and other servos run in background routines. The interrupt routine digitizes the sampled error signal, scales the recovered value as required and integrates the result. Transfer of the integrated result to a digital-to-analog converter completes the routine.

#### Conclusion

The application of microprocessor technology to the cesium frequency standard offers the opportunity to realize improved clock performance through better servos, better control of the atomic interrogation process and through increased reliability. Increased flexibility of instrument operation becomes realizable. Instrument upgrades, modifications and repair become more practical. Fast warm-up and responsiveness to environmental changes are possible.

#### Reference

1. G.A. Hunt and R.E. Cashion, "A Transit Satellite Timing Receiver", 9th Annual Precise Time and Time Interval Applications and Planning Meeting, March 1978, pp 153-166.
2. R.E. Cashion, W.J. Klepczynski and K. Putkovich, "The Use of Transit for Time Distribution", Navigation: Journal of the Institute of Navigation, 26, pp 63-69 (1979).
3. D.W. Allan, H. Hellwig, S. Jarvis Jr., D.A. Howe, R.M. Garvey, "Some Causes and Cures of Frequency Instabilities (Drift and Noise) in Cesium Beam Frequency Standards", Proceedings of the 31st Annual Frequency Control Symposium, June 1977, pp 555-561.

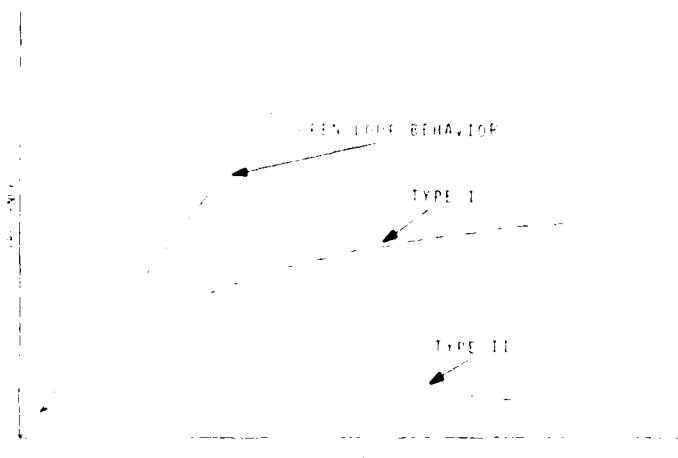


Figure 1: OPEN LOOP AND SERVO RESPONSE TO LINEAR FREQUENCY DRIFT

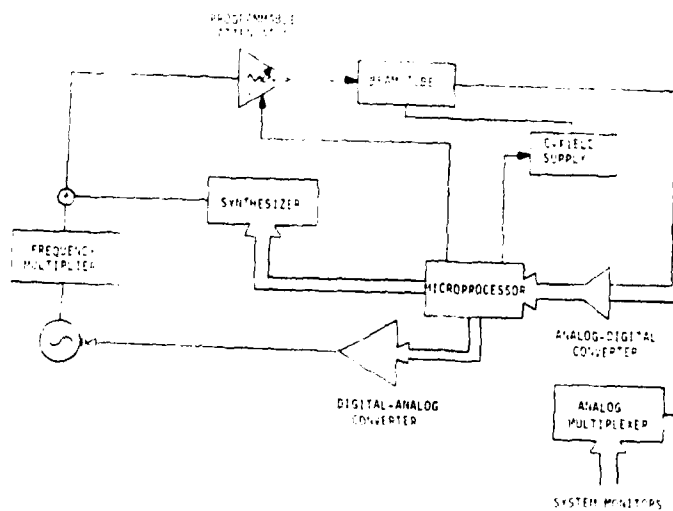


Figure 2: MICROPROCESSOR CONTROLLED CESIUM FREQUENCY STANDARD BLOCK DIAGRAM

EXPERIMENTAL RESULTS OF  
THE LIGHT-WEIGHT HYDROGEN  
MASER DEVELOPMENT PROGRAM

H. E. Peters

Sigma Tau Standards Corporation  
1014 Hackberry Lane  
Tuscaloosa, AL 35401

AD P001528

SUMMARY

A research and development program undertaken by Sigma Tau Standards Corporation with the support of the United States Air Force<sup>1</sup> entitled "Light-Weight Hydrogen Maser" has been completed. Starting from new concepts for a compact cavity maser, the work has progressed from experimental optimization of the bulb and cavity through testing of a breadboard maser to design, construction, and testing of a first operational prototype named the "Small Hydrogen Maser."

To achieve the program goals, several new developments or improvements in past practice were required. Some of these were: improved hydrogen supply, better beam optics, new state selectors, new techniques of cavity frequency control and Q enhancement, and more compact and efficient electronic systems. Recent experimental results with the Small Hydrogen Maser are presented in this paper, and the meaning of the improved technology in terms of further miniaturization of hydrogen masers and also in terms of improvements in large bulb masers will be discussed.

Key Words (for information retrieval)

Hydrogen Maser, Atomic Frequency Standard, Compact Maser.

INTRODUCTION

The light-weight hydrogen maser program was a three year project which involved development of a new compact hydrogen maser based upon design principles illustrated in the paper "Small, Very Small, and Extremely Small Hydrogen Masers," which was presented at the 32nd Annual Symposium on Frequency Control in 1978.<sup>2</sup>

During the first six months of the program experiments with cavities and storage bulbs with various electrode configurations were performed to determine the most promising configurations, and a breadboard test maser and associated electronics systems was designed. The next twelve months was spent constructing the breadboard maser and the associated subsystems and making the first operational tests of the maser.

At this point the design of a "deliverable prototype" hydrogen standard, which we have

named the "Small Hydrogen Maser" was finalized and the next twelve month period was occupied with construction and first operational test of this unit. Two papers,<sup>3,4</sup> presented at the 34th and 35th Annual Symposium on Frequency Control described, in part, the work up to this point.

During the next six month period, which ended in March 1982, further measurements and evaluations of the maser were made, and additional work towards developing a means to stabilize the maser cavity with an automatic servo system was undertaken.

In order to achieve the size, weight, power consumption, and performance goals of the light-weight hydrogen maser program it has been necessary to develop several new or improved maser subsystems, several of which are listed below.

- New Cavity and Bulb Configuration
- Miniature State Selectors
- Efficient Beam Optics
- Miniature, Low Pressure, Hydrogen Supply
- Hydrogen Purifier and Controls
- Active Cavity Gain Circuit
- Efficient, Compact, Electronics
- Convenient Instrumentation and Packaging
- A New Cavity Tuning Servo

The work on the light-weight hydrogen maser program has a significant impact on hydrogen maser technology in general. For example, the new cavity tuning servo is applicable to both large and small hydrogen masers, and its use can remove the requirement for a separate stable tuning reference which is needed to tune the maser by the usual spin-exchange auto-tuning method. In addition, new levels of long term cavity stability may be achieved without compromising the excellent short term frequency stability of the maser. Since this is the first

known publication of the new maser cavity tuning method, the system principles will be described in detail later in this paper.

The most important result of the program is the knowledge which has been obtained. Thus we have the design guide lines and practical skills which may make it possible to achieve much smaller hydrogen maser devices such as the "Extremely Small Hydrogen Maser" (which may be the ultimate portable clock) and in addition we know how to proceed to construct masers of conventional large bulb size which may achieve new levels of performance, have longer operational life, and be more economical to produce.

#### CAVITY AND BULB EVALUATIONS

To realize a hydrogen maser much smaller than those constructed in the past, the size of the cavity which confines the electromagnetic radiation emitted by the hydrogen atom must somehow be reduced below the size of an unloaded cavity resonant at the hydrogen frequency. In the present work inductive and capacitive structures in the form of metal electrodes are attached to and surround the quartz bulb which stores the state selected atoms of the hydrogen beam. In a cavity so loaded there are typically a great many resonant modes, some of which may be degenerate, and exact computational methods are impossible due to the complexity of the geometry. Thus, after first approximations are made as in reference (2), it is necessary to set up promising test configurations and make laboratory measurements of frequency, Q, mode geometry, and coupling by the use of RF magnetic and electric field probes and swept frequency techniques.

During the first six months of the program a large range of cavity sizes, bulb sizes, and electrode configurations were tested. Further measurements have more recently been made of extremely small structures. The required mode (analogous to the TE<sub>011</sub> mode in an unloaded cavity) has been identified and the parameters measured in cavity assemblies as small as 2.5 inches in diameter by 4.4 inches long up to 6.6 inches diameter by 11.0 inches long. It is clear that one may select most any cavity size up to that of the unloaded cavity, and with appropriate bulb size and placement of electrodes surrounding the bulb one may achieve the required resonant conditions for maser action. However, the measured quality factor for smaller size cavities falls a factor of two or more below the value required in an active maser oscillator. Thus to achieve oscillation conditions in a compact maser it is required that active cavity Q enhancement be used. As discussed later a new method of active cavity Q enhancement has been developed and is presently being used on the Small Hydrogen Maser.

From 13 experimental configurations using different combinations of cavity and bulb size and 1, 2, 3, 4, and 8 electrodes of various lengths, the most promising configurations

were as follows. Dimensions are in inches.

CAVITY SIZE		BULB SIZE		ELECTRODES		Q	
D	L	D	L	D	L	N	
6.6	11.0	3	7	3	5	8	16,800
6.0	10.0	2	7	2	5	4	12,000
5.0	8.5	2	7	2	5	4	11,200
2.5	4.4	1.5	3	1.5	1.9	2	4,100

The configuration chosen for the Small Hydrogen Maser used a 2 inch diameter by 7 inch long bulb with hemispherical ends. The cavity inside dimensions are 6.0 inches diameter and 9.0 inches long. Four copper foil electrodes 5.0 inches long with .14 inch gaps are cemented to the bulb with a thermosetting metal to glass adhesive (Palmer Products P-752) with heat, pressure, and vacuum. The bulb is coated internally with FEP-120 Teflon prior to attachment of the electrodes. The cavity Q measured for the completed assembly was 10,200. Tests of cavity frequency versus temperature under vacuum gave a temperature sensitivity of approximately 5 KHz per °C ( $3.5 \times 10^{-6}$  / °C fractionally.)

#### CAVITY Q ENHANCEMENT

To achieve oscillation an active cavity Q enhancement method was developed which could be located directly within the cavity and controlled by DC bias voltages. This system avoids the instabilities inherent in past attempts to use active gain to enhance the cavity Q, wherein two RF coupling loops are used to connect through coaxial cable to amplifiers, phase shifters, and band pass filters located external to the cavity environment. The present circuit uses a single low noise transistor connected to two small coupling loops inside the cavity top. One capacitor tunes one of the loops to limit the amplifier bandwidth and gain to be near the maser frequency and reject unwanted mode frequencies. The circuit Q is low in comparison to the cavity unenhanced Q and the frequency of the cavity with Q enhancement follows, to the extent presently determined, the frequency of the unenhanced cavity.

With the active Q enhancement circuit it has been possible to realize Q values from 10,000 (unenhanced) up to approximately 100,000. With two bias connections, it has also been found possible to smoothly vary the frequency over a range of approximately 150 KHz while simultaneously maintaining the Q at the desired value. The ability to change the frequency of the cavity, while maintaining constant cavity Q, is the basis for a new automatic cavity tuning method which was conceived and first applied to the Small Hydrogen Maser.

#### NEW CAVITY TUNING SERVO

Since the hydrogen maser was invented it has been a tantalizing dream to lock the cavity to the maser frequency in a simple way and so eliminate cavity pulling. Cavity pulling has been the most serious limitation to the stability of the maser for measuring times greater than approximately 1,000 seconds, and elimination of this effect would result in quite unprecedented frequency stability. Spin-exchange tuning has been used very successfully in the past,<sup>5</sup> but this requires a separate stable tuning reference, large variation in beam intensity, and long integration times. People working with both passive and active masers have used another cavity tuning scheme wherein a separate search signal is injected into the cavity with the frequency alternating between two values approximately at the half power points of the cavity resonance. The signal transmitted by the cavity is sampled, and amplitude variations are detected as a signal source for a servo system.<sup>6,7,8</sup> This system has the serious disadvantage of having relatively high power RF signals near the maser frequency which perturb the radiating hydrogen atoms, and additionally requires external RF components and at least two coaxial connections to the cavity; the problem of environmental isolation is severe and this system is extremely difficult to engineer in a manner which does not in itself disturb the cavity frequency.

To describe the physical basis of the present approach to cavity tuning, the interaction of the radiated beam power with the cavity impedance is illustrated in Figure 1. The signal output  $V$  appears as though it were coupled through a resonant impedance  $Z$  and fed by a constant current source. The constant current source derives from the oscillating magnetic moment of the assemblage of atoms within the maser storage bulb and it is effectively constant for times short compared to the relaxation time of the atoms.

In the new method of tuning, the cavity frequency is square wave modulated and a non-tuned condition is evidenced by a corresponding modulation of maser signal amplitude as observed at the maser receiver. This is illustrated in Figure 2. The cavity frequency is switched between  $f_1$  and  $f_2$  at a typical rate of a few hundred Hertz. If the average cavity frequency is not equal to the maser frequency, there is a modulation ( $V_2 - V_1$ ) produced on the output amplitude. By synchronously detecting variations in the received signal amplitude and feeding them back, after appropriate amplification and integration, as frequency corrections to the cavity, the average cavity frequency,  $f_c$ , is made equal to the maser frequency.

Since cavity pulling of the maser is linear with cavity offset frequency, the average pulling effect is that of a cavity maintained at the average of the two modulation frequencies. The

cavity pulling coefficient is therefore the usual relationship for an active hydrogen maser as given in Figure 2; when the cavity is tuned the average cavity frequency equals the maser frequency. Figure 3 is a block diagram of the overall servo system. There is a modulation generator which modulates the cavity frequency; the maser receiver IF amplitude is synchronously detected, amplified, averaged in a digital integrator, and fed back as a DC cavity correction voltage.

This somewhat simplified description requires elucidation well beyond the scope of the present paper to take into account second order effects such as possible inequality of cavity  $Q$ 's, differences in the modulation periods, spin-exchange pulling and the means to cancel it, random noise processes, systematic disturbances, and other potential problems or benefits. A brief discussion of the most important factors is contained in the next section. It should be emphasized that there is only one RF coupling to the cavity in this system - the usual receiver output coupling, and the tuning system itself requires only a few low frequency solid state circuits besides the means for varying the cavity frequency.

The above system is working at present on the Small Hydrogen Maser. While the servo system is not yet likely optimum, the statistical variations in the cavity correction voltage indicate that cavity drift is being effectively cancelled with an attack time short enough to eliminate systematic environmental disturbances.

It should be pointed out that the cavity servo described herein is eminently applicable to conventional large bulb hydrogen masers as well as compact masers. Two critical conditions are required for its successful application: one is that the maser be operated well above threshold so that a good signal to noise ratio of the maser output signal is obtained, the second is that a convenient means for rapidly modulating the cavity resonance frequency while maintaining constant quality factor is available. In the Small Hydrogen Maser the active gain circuit bias voltages provide the proper cavity control; in a large maser without active cavity gain, a reactive element such as varactor diode could also be used. It should be pointed out that the ability to modulate the cavity frequency or  $Q$  in a reproducible manner facilitates other approaches, in addition to the one described herein, to tuning the cavity so as to stabilize or eliminate cavity frequency offset. Thus if the cavity  $Q$  is modulated with the frequency held constant there is a phase modulation of the output signal when untuned which when nulled produces a null cavity frequency offset. This scheme has also been successfully tried on the Small Hydrogen Maser, but with the present receiver configuration it produces larger probable errors.

#### CAVITY SERVO NOISE PROCESSES

There are several potential noise sources or

systematic biases which need to be considered to determine the accuracy or stability of cavity tuning and the possible correction rate of the servo. The most obvious potential error source is inequality of the cavity Q's at the two modulation frequencies  $f_1$  and  $f_2$ . For stability, the Q's must only be relatively stable; this does not appear to be a serious problem because the frequency modulation is very small in comparison to the cavity center frequency.

For accuracy, the Q's may be calibrated upon initial operation of the maser so that the tuning point is located such that it just compensates for spin-exchange pulling. This is done by the usual spin-exchange tuning procedure. Thus in subsequent operation spin-exchange pulling of the maser is compensated by the cavity calibrated offset. Small variations of the cavity tuned position may also be achieved by creating small differences in the modulation periods. With the above procedure the only concern is higher order systematic drift effects. These should be small, but experimental confirmation of their magnitude will be required.

The cavity servo instability process of most concern is the effect of maser output random amplitude variations as seen at the receiver. The most prominent source of amplitude noise is the thermal noise power as increased by the noise factor of the cavity circuit and the maser receiver input stage. Letting N be the total noise factor and B the bandwidth of the servo system, the noise to signal ratio is given by

$$\frac{V_n}{V_s} = \sqrt{\frac{GKTNB}{2P}}$$

where P is the signal power coupled out of the cavity and G is the power gain of the cavity Q enhancement circuit. The bandwidth of the servo system is given by  $B = 1/(2\pi\tau)$  where  $\tau$  is the time constant of the servo system.

For a voltage signal of amplitude  $V_n$ , analysis of the cavity impedance function gives a corresponding offset in cavity frequency of

$$\Delta f_c = \frac{(1 + \Delta^2)^{\frac{1}{2}}}{4\Delta} f_{cw} \cdot \frac{V_n}{V_s}$$

where  $\Delta = (f_2 - f_1)/f_{cw}$  and  $f_{cw}$  is the cavity width at the half power points.

If the cavity is offset by an amount  $\Delta f_c$ , the maser is pulled by an amount

$$\frac{\Delta f}{f} = \frac{Q_c}{Q_1} \cdot \frac{\Delta f_c}{f}$$

From the above equations the maser fractional frequency instability induced by the servo is

$$\sigma_n(\tau) = \frac{K_c}{2Q_1} \sqrt{\frac{GKTN}{\pi P \tau}}$$

where

$$K_c = \frac{(1 + \Delta^2)^{\frac{1}{2}}}{4\Delta}$$

The minimum value of  $K_c$  occurs when  $\Delta = 1/\sqrt{2}$ , which gives  $f_2 - f_1 = f_{cw}/\sqrt{2}$ . However, in practice, it is better to operate with slightly smaller modulation since the received maser average power is also a function of the frequency modulation amplitude. Typical values used in the Small Hydrogen Maser are  $f_2 - f_1 = 6$  KHz,  $f_{cw} = 20$  KHz and  $K_c = .95$  (the minimum value of  $K_c$  would be .65.)

The servo time constant, or integration time, should be chosen so that corrections occur fast enough to remove systematic maser cavity perturbations. The largest effects which require correction in active hydrogen masers are temperature transients or long term creep or other dimensional changes in the cavity materials.<sup>9,10</sup> A servo time constant of 1000 seconds provides fast enough response to remove these effects. Using the foregoing information and typical parameters for 3 different maser designs (LHM = "Large Hydrogen Maser," SHM = "Small Hydrogen Maser," ESHM = "Extremely Small Hydrogen Maser") the following chart has been assembled.

	LHM	SHM	ESHM
$\tau$	1000s	1000s	1000s
$P_w$	$10^{-12}$	$7 \times 10^{-13}$	$5 \times 10^{-13}$
$T^{\circ}K$	320	320	320
G	1	6	12
N	2	4	4
$Q_1$	$2 \times 10^9$	$7 \times 10^8$	$3 \times 10^8$
$\sigma_n(\tau)$	$4 \times 10^{-16}$	$5 \times 10^{-15}$	$2 \times 10^{-14}$

From the above it is clear that the random cavity thermal noise perturbations of the servo system should be adequately small. There are, of course, potential error sources in the synchronous detector and amplifier and in the DC amplifier used subsequently in the servo system. Measurements on the presently operating system indicate that these error sources are small in a properly designed circuit, but careful signal processing considerations are required.

#### SMALL HYDROGEN MASER PHYSICAL ASSEMBLY

Figure 4 is an assembly drawing of the physics unit of the SHM which identifies the main parts and gives the basic dimensions. Figure 5 is a picture of the physical parts prior to final assembly. Figure 6 is a bottom view which shows the source bulb, RF dissociator components, pressure gauge and hydrogen supply. Figure 7 is a picture of the vacuum enclosure, source assembly and Ion Pump.

The weight of the assembled physics unit is approximately 50 pounds. One aspect of this assembly which will be changed in future designs is the use of two state selectors. A single state

selector with tapered pole tips will be used in future designs and this will reduce the maser weight and height and increase the hydrogen utilization efficiency. The reasons for the present configuration and the reasons for changing it in the future are discussed in the next section.

#### SHM STATE SELECTION

The original concept for the SHM design did not anticipate use of the active cavity Q enhancement circuit. Thus, to achieve oscillation conditions it was essential that spin-exchange broadening of the atomic resonance line be avoided. To do this it was planned to use a novel system, using two state selectors, which focussed only the  $F = 1, m = 0$  state into the storage bulb. A shielded region with magnetic coils was provided between the two state selectors wherein the  $F = 1, m = 1$  state was changed to an  $F = 1, m = -1$  state and was subsequently defocussed, while the  $F = 1, m = 0$  state remained unchanged. In tests with the breadboard hydrogen maser it appeared that this state selection system worked. However the overall efficiency was not very good and a very high source flux was required to get a reasonable signal. The beam was only detected by pulse stimulation and the maser would not oscillate. A contributing factor was that the achieved cavity Q was lower than anticipated.

With the realization of a practical circuit for cavity Q enhancement, two state selectors are not required. The SHM at present still uses the two state selectors as it was too late to change the spacings, however the coils and shielded region between the state selectors have been removed, and the second state selector has an aperture which is twice as large as the first one. Thus the effect is almost the same as use of a single unit.

The most efficient state selection system is one which uses a small tapered quadrupole configuration.<sup>11</sup> An example of a one inch long unit is shown in Figure 8. This unit is the same overall size as one of the state selectors used in the SHM, but the magnetic circuit has been designed so that the pole tip aperture, taper, and gaps may be adjusted after the state selector is assembled. While hydrogen flux utilization is not too large in the present SHM, typically .05 moles  $H_2$  per year, this should be improved by a factor of about 4 with the use of the new state selector.

#### HYDROGEN STORAGE AND SUPPLY

Hydrogen storage in a pressure vessel has been used very successfully in the past to contain an adequate supply for many years of hydrogen maser operation. Typically a one liter bottle with 1,000 PSI of hydrogen is used. The bottle contains about 3 moles ( $H_2$ ) and would last 60 years in the small maser. However, such a large size bottle at high pressure is not desirable in a compact maser, nor should it be required, since recent metal hydride research has resulted in the availability of many alloy combinations which store high densities of hydrogen at relatively

low pressure.

The hydrogen supply system of the small hydrogen maser uses a small stainless steel bottle with a volume of 34 cc which contains 1.25 moles of hydrogen absorbed in 180 gms of an alloy of cerium free mischmetal and nickel. The hydrogen is valved to the source by a palladium-silver purifier and the source pressure is controlled by a thermistor pirani gauge. The entire system is designed, constructed and assembled in house, and requires only about 5 watts of total D-C power to operate.

#### SHM PACKAGING, ELECTRONICS, AND CONTROLS

Figure 9 is a picture of the Small Hydrogen Maser within the mounting framework illustrating the electronics subsystems placement and controls arrangement.

The electronics subsystems have been packaged in functionally separate modules, each of which may be uncovered for operational testing without disconnection of power. They may also be removed, repaired, or replaced as units in case of malfunction. The modules on the front panel are: 1. Vac-Ion Pump supply; this is a DC-DC converter which provides 3,000 volts for the pump, 2. The source pressure control module which automatically regulates hydrogen flow, 3. The receiver synthesizer; this supplies the 405 KHz reference frequency for the receiver phase lock loop - there are 11 decades of control which give a resolution of  $\pm 5 \times 10^{-15}$  for the output frequency, 4. The receiver VCO and output buffer amplifiers, 5. The receiver local oscillator multiplier and IF amplifier module, 6. The module containing the magnetic field and cavity frequency controls, 7. The instrumentation read-out module. There are 16 read-out channels which are selected by 4 binary coded switches to provide visual indication of variables on a  $4 \frac{1}{2}$  decade digital panel meter.

The power supply has been placed in a module mounted at the rear of the frame. The cover may be removed for changing connections or trouble shooting without disconnecting the power. Batteries for uninterruptable standby operation are placed in a separate external battery pack. For long term operation without A-C power, a 45 A-H capacity battery is used which will last for twenty hours.

#### FUTURE WORK

There are two main goals which Sigma Tau Standards Corporation plans to pursue as a continuation of the present work. One is to undertake research and development of an "Extremely Small Hydrogen Maser" with the goal of providing the ultimate "portable clock." The goals for the "ESHM" are as follows:

#### EXTREMELY SMALL HYDROGEN MASER GOALS

CONFIGURATION: Active hydrogen maser with automatic cavity servo.

STABILITY: Better than  $1 \times 10^{-14}$  for  
 $\tau = 10^5$  to  $10^6$  seconds and active  
hydrogen maser performance for  
 $\tau < 10^5$  seconds.

SETTABILITY:  $\pm 5 \times 10^{-15}$  resolution.

SIZE: Physics Unit 5" diameter by 12" long  
plus 8 Liter/second Ion Pump.

WEIGHT: Physics unit and pump, 30 pounds.

POWER: 35 watts nominal, 45 watts maximum  
total main DC input.

The second goal is to produce the best  
ground based standard for fixed stations or basic  
time and frequency standards laboratories. To do  
this it is planned to construct hydrogen masers  
with a large storage bulb configuration. The goals  
for the "Large Hydrogen Maser" are as follows:

#### LARGE HYDROGEN MASER GOALS

CONFIGURATION: Active hydrogen maser with  
automatic cavity servo.

BULB SIZE: 5 liter atom storage bulb with  
total wall shift of  $3 \times 10^{-11}$ .

STABILITY: Additive Noise  
 $\sigma(t) = 2 \times 10^{-13}/\tau$  ( $\tau > 1$  sec)

Perturbing Noise  
 $\sigma(t) = 2 \times 10^{-14}/\sqrt{\tau}$  ( $\tau < 10^3$ )

Systematic Instability  
 $\sigma(t) < 5 \times 10^{-15}$  ( $\tau > 10^4$  to  $\tau > 10^6$ )

ACCURACY: (Reproducibility)  
Better than  $1 \times 10^{-13}$ .

SETTABILITY:  $\pm 5 \times 10^{-15}$  resolution.

POWER: 80 watts nominal, 100 watts maximum,  
total main DC input.

#### CONCLUSION

The present work illustrates that signifi-  
cant size, weight, and power reductions can be  
made in hydrogen masers and that stability, re-  
producibility, and operating life can be improved  
significantly, resulting in new levels of per-  
formance for future time and frequency  
applications.

#### REFERENCES

1. USAF, Deputy for Electronic Technology  
(RADC/ESD) Hanscom Air Force Base, MA 01931
2. H.E. Peters, "Small, Very Small, and  
Extremely Small Hydrogen Masers,"  
Proceedings, 32nd Annual Symposium on  
Frequency Control, USAERADCOM, Fort Monmouth,  
NJ, 1978.
3. H.E. Peters, "New Hydrogen Maser Designs,"  
Proceedings, 34th Annual Symposium on  
Frequency Control, USAERADCOM, Fort Monmouth,  
NJ, 1980.
4. H.E. Peters, "Feasibility of Extremely Small  
Hydrogen Masers," Proceedings, 35th Annual  
Symposium on Frequency Control, USAERADCOM,  
Fort Monmouth, NJ, 1981.
5. H.E. Peters, T.E. McGunigal, and  
E.H. Johnson, "Hydrogen Standard Work at  
Goddard Space Flight Center," Proceedings,  
22nd Symposium on Frequency Control, USAESC,  
Fort Monmouth, NJ, 1968.
6. D.A. Howe, F.L. Walls, H.E. Bell, and  
Helmut Helwig, "A Small, Passively Operated  
Hydrogen Maser," Proceedings, 33rd Annual  
Symposium on Frequency Control, USAERADCOM,  
Fort Monmouth, NJ, 1979.
7. P. Lesage, C. Audoin, and M. Tétu,  
"Amplitude Noise in Passively and Actively  
Operated Masers," Proceedings, 33rd Annual  
Symposium on Frequency Control, USAERADCOM,  
Fort Monmouth, NJ, 1979.
8. H.T.M. Wang, "An Oscillating Compact  
Hydrogen Maser," Proceedings, 34th Annual  
Symposium on Frequency Control, USAERADCOM,  
Fort Monmouth, NJ, 1980.
9. S. Jacobs, "Dimensional Stability Measure-  
ment of Low Thermal Expansion Materials  
Using an Iodine Stabilized Laser," Proceed-  
ings, 2nd Frequency Standards and Metrology  
Symposium, July 1976. (Available from  
Frequency and Time Standards Section, NBS,  
Boulder, CO 80302)
10. J. White and K. McDonald, "Long Term  
Performance of VLB-11 Masers," Proceedings,  
35th Annual Symposium on Frequency Control,  
USAERADCOM, Fort Monmouth, NJ, 1981.
11. H.E. Peters, "Magnetic State Selection in  
Atomic Frequency and Time Standards," Pro-  
ceedings, 13th Annual Precise Time and Time  
Interval Applications and Planning Meeting,  
Naval Research Laboratory, Washington,  
DC, 1981.

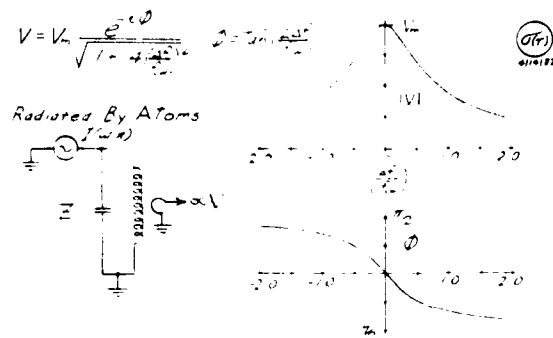


Figure 1. Interaction of Radiated Beam Power with Cavity Impedance

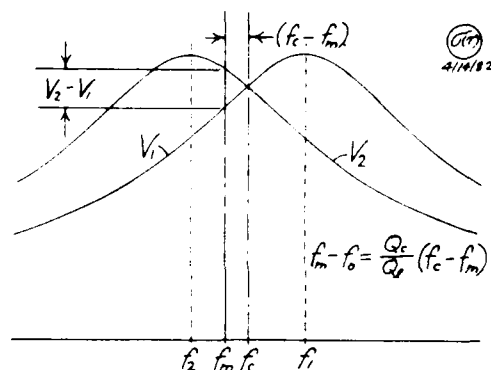


Figure 2. Signal Modulation Induced by Cavity Frequency Switching

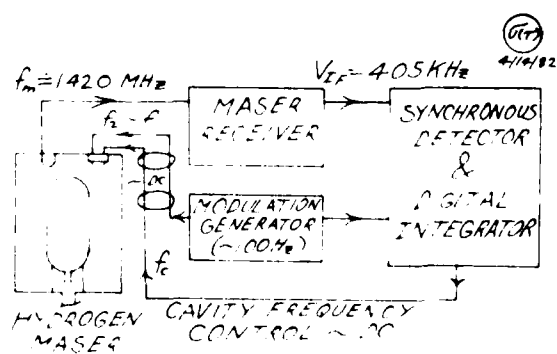


Figure 3. New Cavity Servo System

# EXTREMELY SMALL HYDROGEN MASER

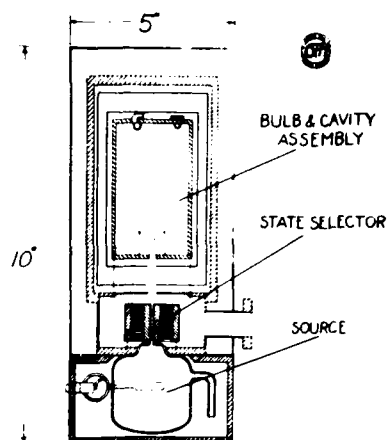


Figure 4. Small Hydrogen Maser Physics Unit



Figure 5. Small Hydrogen Maser Physical Parts Prior to Assembly



Figure 6. Bottom View of Source Assembly

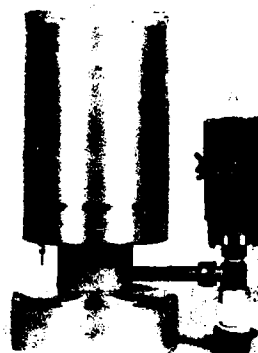


Figure 7. Vacuum Enclosure, Source Assembly, and Ion Pump

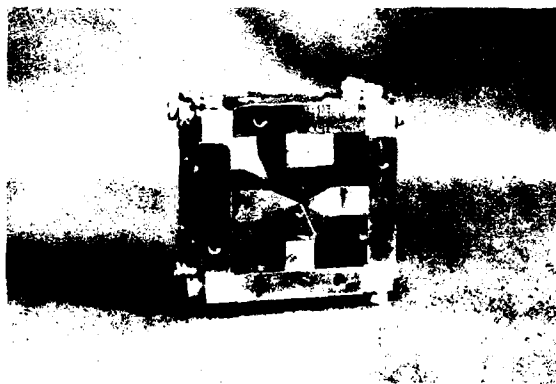


Figure 8. Miniature Quadrupole State Selector

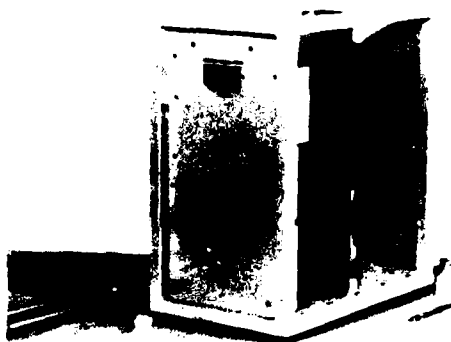
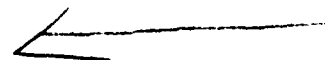


Figure 9. Small Hydrogen Maser Overall Assembly



## CHARACTERISTICS OF OSCILLATING COMPACT HYDROGEN MASERS\*

Harry T.M. Wang

Hughes Research Laboratories  
Malibu, CA 90265Summary

Oscillating compact hydrogen masers CHYMNS-I and II and their stability performance are described. Both masers have the same principle of operation, but are quite different in size and weight. This is made possible by the versatile compact cavity design. The expected sacrifice in performance as the size of the maser is reduced can be seen in the stability data. CHYMNS-I employs a cavity of 15 cm O.D. x 15 cm long and has a measured root Allan variance of  $\sigma_y(\tau) = 6.6 \times 10^{-14}$  for  $\tau = 100$  sec. For the smaller maser, CHYMNS-II, the corresponding values are: cavity, 11 cm O.D. x 15 cm long, and  $\sigma_y(\tau) = 1.3 \times 10^{-13}$  for  $\tau = 100$  sec. Of greater interest in considering device applications is the excellent long term stability of  $\sigma_y(\tau) = 4 \times 10^{-15}$  for  $\tau = 10^5$  sec that had been measured during a direct comparison between the two compact masers. This result illustrates the effectiveness of the electronic cavity stabilization technique used in overcoming environmental perturbations and, consequently, assuring a long term stable maser frequency output.

Introduction

The design, fabrication and test of the oscillating compact maser, CHYMNS-I, has been previously described.<sup>1</sup> The objective of CHYMNS-I was to demonstrate that a cavity Q-enhancement technique can be used to obtain sustained maser oscillation in a compact cavity. The superior signal-to-noise ratio of an oscillator and the simplified electronics would facilitate the development of a frequency standard of excellent performance. Obviously, an effective electronic cavity stabilization servo system would be essential to overcome the susceptibility of an external feedback system to environmental perturbations. On the other hand, such a system would provide improved long term maser performance compared to conventional masers where cavity stabilization is based on thermal

mechanical considerations. The objective of CHYMNS-I was successfully accomplished as described in Reference 1.

Even as the viability of the design was being demonstrated, an interesting problem arose: how the long term stability of the oscillating compact maser can be measured. The conventional maser design is known to have long term drifts. One solution is to build more units similar to CHYMNS-I. However, some interesting considerations suggest another approach. Since the compact cavity design<sup>2</sup> used in CHYMNS-I permits easy size scaling, the same basic design can be employed in a more compact maser. Also, a smaller package is more attractive for application. Although the increased wall collision rate and higher losses in a more compact cavity is expected to lead to some degradation, particularly in the short term regime, superior long term stability performance will be maintained. Thus, by building a second, much smaller maser, CHYMNS-II, we will provide further evidence of long term stability performance capability of oscillating compact masers. At the same time, we will also obtain experimental data on performance as a function of size. Design and fabrication of CHYMNS-II, a photograph of which is shown in Figure 1, was completed in 1981.

In this paper, we will briefly update developments in compact maser technology and discuss the stability data of these developmental masers.

Compact Maser Update

The parameters of the oscillating compact hydrogen masers, CHYMNS-I and II, are given in Table I. As mentioned earlier, the masers employ the same basic design and fabrication technique. Since these have been described in detail in Reference 1, they will not be repeated here. However, a few significant improvements or modifications are described below. It should be pointed out that these developmental masers are designed to facilitate experimentation where fast turn-around is a

\* This work has been supported by the Office of Naval Research under Contracts N00014-78-C-0139 and N00014-82-C-2016 administered by the Naval Research Laboratory.

AD P001529



Figure 1. A photograph of the physics unit of the oscillating compact hydrogen maser, CHYMNS-II.

Table 1. Parameters of CHYMNS Oscillating Compact Hydrogen Masers

	CHYMNS-I	CHYMNS-II
Cavity:		
Dimensions, cm	15 O.D. x 15 L	11 O.D. x 15 L
Loaded Q	9400	7000
Coupling Coeff (2 ports)	0.2	0.2
Enhanced Q	40600	49000
Temp Coeff, kHz/°C	16	22
Tuning Sensitivity, kHz/V	0.88	1.1
Storage Bulb		
Dimensions, cm	10 O.D. x 11.4 L	5.7 O.D. x 13 L
Atomic Line Q	$1 \times 10^9$	$9 \times 10^8$
Stability ( $10^{-11}$ sec)	$6.6 \times 10^{-13}/\sqrt{t}$	$1.3 \times 10^{-12}/\sqrt{t}$
Packaged Physics Unit (Est.)		
Dimensions, cm	28 O.D. x 60 L	22 O.D. x 40 L
Weight, kg	30	14

desirable feature. We have therefore not spent much effort on packaging. On the other hand, we believe that there is general interest, especially among system planners, in the size and weight of the device. The dimensions for a packaged physics unit shown in Table I represent our estimate of the capabilities of current technology based on a choice of the indicated cavity geometry.

As indicated in Reference 1, we suspected that a poor storage bulb coating in CHYMNS-I was responsible for the relatively poor line Q of  $6 \times 10^8$  obtained during earlier tests. Indeed, by recoating the bulb, an improved line Q of  $1 \times 10^9$  was obtained. In view of the measured line Q of  $9 \times 10^8$  obtained in CHYMNS-II in a storage bulb with a diameter almost a factor of two smaller, there is probably more room for improvement.

In addition to the smaller cavity and the resultant more compact size, the most significant difference between CHYMNS-I and II is in the hydrogen flow system. CHYMNS-II employs a quadrupole state selector magnet<sup>3</sup> instead of the conventional hexapole. The quadrupole magnet with a geometry of 3.8 cm diam x 3.2 cm long x 0.025 cm bore radius, and weighing 362 gm, is considerably smaller and lighter than the hexapole magnet used in CHYMNS-I. Furthermore, the small bore radius produces a higher field gradient, and consequently, a greater deflection force. This property permits the use of a shorter beam drift space, leading to a shorter overall maser length.

A new quartz dissociator design making use of the excellent thermal mechanical property of a sily-quartz transition also contributes to maser length reduction. Compared to the pyrex dissociator used on CHYMNS-I, the new design is about 3 cm shorter. The low rf loss property of fused quartz allows easy electrical tuning for self-ignition and efficient hydrogen atom production at low rf drive power levels. The single channel, 0.013 cm diam x 0.1 cm long, collimated output reduced considerably the hydrogen throughput of the system, relaxing vacuum pump speed and capacity requirements.

In view of the problems past maser designs have had with ion pumps, concerted efforts are being made, both in our laboratory and elsewhere,<sup>4</sup> to minimize reliance on ion pumps for maser vacuum maintenance. Both CHYMNS-I and II employ a combination getter and ion pump system. The idea is to let the getter pump handle most of the hydrogen gas load. A small ion pump is used to pump residual gases that are not gettered. Size and weight considerations lead us to select molded zirconium graphite (SI-171)<sup>5</sup> as the getter material. Ion pumps of 8./sec and 2./sec pumping speed are installed on CHYMNS-I and II, respectively. The 2./sec ion pump has operated continuously and adequately for several months. But a gradual rise in ion pump current indicating an increase in system pressure with time was observed. This is probably due to a drop in getter pumping speed, since the hydrogen flow rate was held fairly constant. We also believe that the elastomer seals in the maser are detrimental to getter pump operation. Separate experimental results have indicated that the getter hydrogen pumping speed degrades faster in the

presence of elastomer materials. The problem can be alleviated by eliminating elastomers from the maser vacuum system. If size and weight are not critical considerations, a different getter, zirconium aluminum (ST-101),<sup>5</sup> may be a superior getter material. The powdered getter is coated on pleated mechanical supports, resulting in a large gettering surface area, with a corresponding increase in size and weight. In addition to the high pumping speed, it seems to be more resistant to poisoning by residual gases. Much developmental effort remains to make getter pumps a reliable component of the maser. However, it looks much more promising than the ion pumps in contributing to significantly improved reliability of the maser.

#### Stability Performance

A schematic diagram of the set-up used to determine maser stability performance is shown in Figure 2. The system employs a dual-mixer-time-difference (DMTD)<sup>6</sup> technique, and the data provide both phase and frequency information. Timing reference for the system is provided by the reference maser. The common oscillator for the DMTD is a frequency synthesizer which can be set to give a convenient beat frequency. The measurement interval is given by the product of the beat period and the number of time interval counter readings to be averaged to give one data point. The computer controlled data acquisition, analysis and plotting programs greatly facilitate the measurement process.

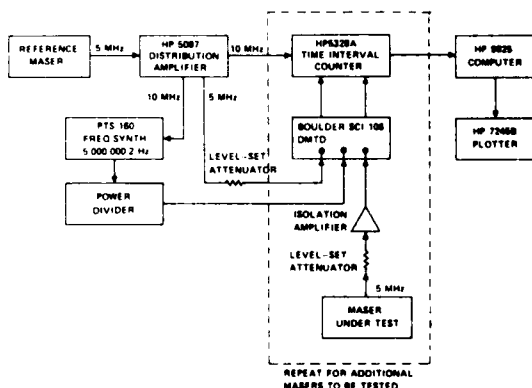


Figure 2. Schematic of stability measurement set-up.

Notice that the functions of the reference maser and the maser under test are easily interchanged. This flexibility is very useful since a conventional maser, the VLG-11, p 10,<sup>7</sup> is also available. The three masers make possible simultaneous comparison of more than one pair of masers. However, the interconnections of the three masers to the measurement system require care to prevent accidental interference. The addition of external isolation amplifiers to the already buffered outputs of the masers is such a precaution. There is also concern about possible frequency lock-up between masers operating at the same frequency and

physically located close together. However, the probability for this occurring in the three masers in our laboratory is small since the masers are very different in size, with correspondingly different storage bulbs. The different wall collision rates and the resultant proportional frequency shifts mean that the masers actually operate at three different frequencies. Although we have not made a systematic wall shift determination, the maser oscillating frequencies are easily deduced from the receiver synthesizer settings required to synchronize the 5 MHz standard outputs. Taking into account the Zeeman effect and making sure that the maser is spin exchange tuned so that there is no cavity induced frequency shift, the oscillating frequencies of CHYMNS-I and II are, respectively,  $-1.26 \times 10^{-11}$  and  $-2.63 \times 10^{-11}$ , offset from that of the VLG-11. It is not unreasonable to assume that these shifts are due to wall collisions. With such relatively large offsets and proper precautions exercised, the probability for frequency lock-up between the masers is greatly diminished.

Samples of stability data are shown in Figures 3 and 4. For each run, the phase data and the computed root Allan variance are plotted. The plot label indicates the masers used in the comparison and the date of the run. Near the bottom of the plot, other pertinent information, such as the computed average phase and frequency, their standard deviations, the number of data points, and the interval between measurements are also listed. In addition to the raw data plot an expanded display of the phase variations is obtained by plotting the residue of a linear least square fit of the phase data,  $X_i$ , to an equation of the form

$$X_i = A + BT_i \quad (1)$$

The fitted coefficients, A and B, give, respectively, the phase at time  $T = 0$  and the average beat frequency between the masers.

The analysis program also contains a drift removal routine. This consists of linear least square fitting the phase and the derived frequency data to equations of the form,

$$Y_i = C + DT_i \text{ and } X_i = X_0 + YT_i \quad (2)$$

Here the beat frequency is assumed to be a linear function of time, with a value C at time  $T = 0$ . The fitted drift coefficient, D, is another measure of the stability of the masers under comparison. It is rather sensitive to the data base, especially for runs of relatively short duration. From the fitted coefficients, the drift rate of the compact masers ranges from several parts in  $10^{15}$  per day or less.

From available stability data we see that the root Allan variance,  $\sigma_y(\tau)$ , for the oscillating compact masers can be expressed approximately by the expressions:

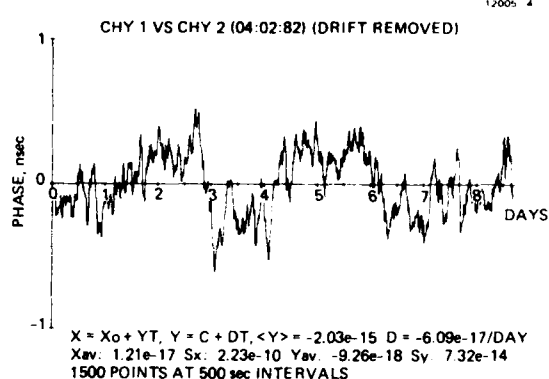
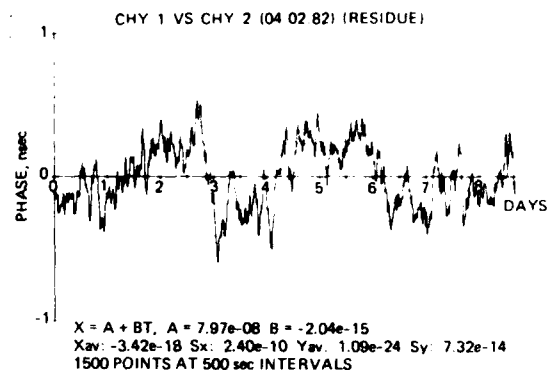
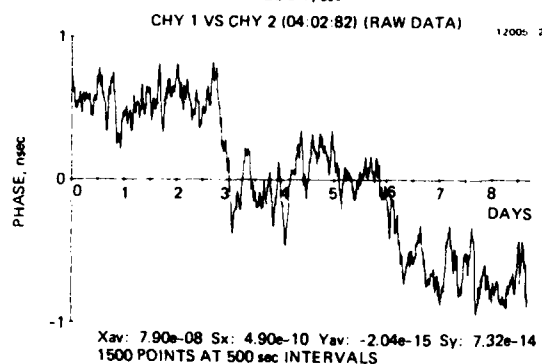
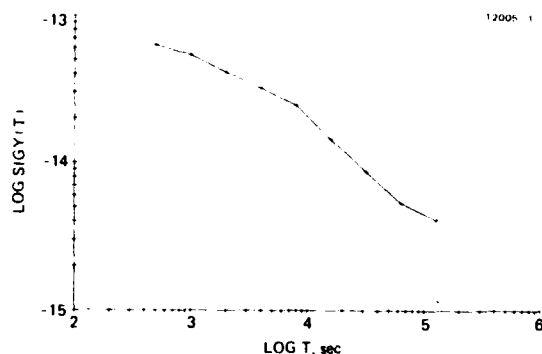


Figure 3. Stability data of CHYMNS-II measured against CHYMNS-I.

$$\text{For CHYMNS-I: } \frac{\dot{y}(t)}{y(t)} = \frac{6.6 \times 10^{-13}}{\sqrt{t}}; \quad (3)$$

$$10^2 \leq t \leq 10^5 \text{ sec}$$

$$\text{For CHYMNS-II: } \frac{\dot{y}(t)}{y(t)} = \frac{1.3 \times 10^{-12}}{\sqrt{t}}. \quad (4)$$

From the known performance of the VLG-11, which relies on thermal mechanical design for cavity stability, we see that beyond about  $5 \times 10^4$  sec, the compact maser begins to out perform it. This result demonstrates the effectiveness of the electronic cavity stabilization system employed in CHYMNS-I and II. Further evidence of the servo performance is shown in Figure 5 where CHYMNS-II cavity reactance tuner bias is plotted as a function of time. The tuner is, of course, the feedback part of the cavity stabilization servo system. The variations in the tuner bias reflect cavity frequency fluctuations due to whatever cause. Using the values of electronic cavity tuning sensitivity (1.1 kHz/volt), the atomic transition line,  $Q$  ( $9 \times 10^8$ ), and the enhanced cavity,  $Q$  (49,000), for the maser, the cavity fluctuations which gave rise to the variations in the tuner bias would have produced maser frequency fluctuations of several parts in  $10^{11}$  if the cavity had not been servo controlled. This is to be compared with the

actual stability data taken at the same time and shown in Figure 3. During the 9-day run, with data taken at 500 sec intervals, the average frequency offset was only  $-2.04 \times 10^{-15}$ , with a standard deviation of  $7.32 \times 10^{-14}$ . This is several orders of magnitude of improvement compared to a similar cavity, but without a servo control system. More significantly, since the servo uses a frequency derived from the atomic transition frequency as reference, it assures a stable long term maser output. We would like to point out that the servo system can be easily adapted for use in conventional maser oscillators, such as the VLG-11, to improve their long term performance.

An interesting question is how well do we expect the oscillating compact masers to perform. Lesage and Audoin<sup>8</sup> have given an analysis of the Q-enhanced maser oscillator where the stability of the cavity and other environmental factors were assumed to be ideal. Under these assumptions, the long term stability would be limited by noise over the atomic transition linewidth. The degree of Q-enhancement has a significant impact on the noise power density, and consequently, the stability performance. Without going into details here, we have calculated, using the expression for white noise frequency contribution to the maser stability derived by Lesage and Audoin, the following expected root Allan variances:

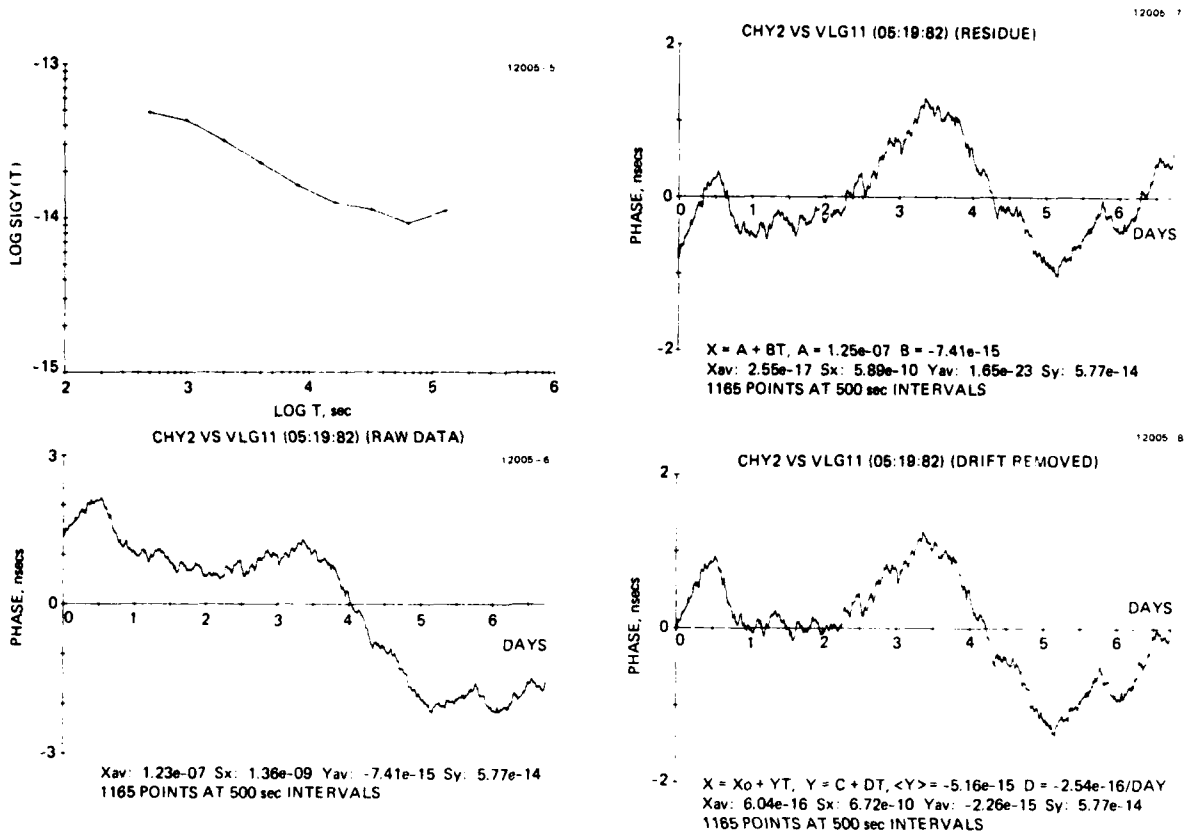


Figure 4. Stability data of CHYMNS-II measured against VLG-11, p10

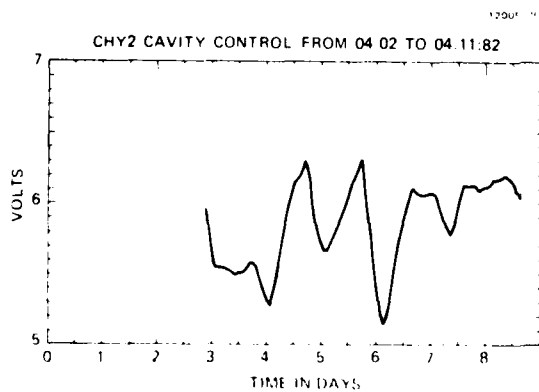


Figure 5. CHYMNS-II cavity reactance tuner bias as a function of time. Stability data taken concurrently is shown in Figure 3.

$$\text{For CHYMNS-I: } \tau_y(\tau)_{TH} = 3.7 \times 10^{-13} / \sqrt{\tau} \quad (5)$$

$$\tau > 10^2 \text{ sec}$$

$$\text{For CHYMNS-II: } \tau_y(\tau)_{TH} = 6.2 \times 10^{-13} / \sqrt{\tau} \quad (6)$$

We see that the experimental data are within a factor of two of theoretical expectations. This is rather remarkable for a pair of developmental masers. We expect that the performance will improve when the physics and electronic units are integrated and packaged.

#### Conclusions

We have shown the effectiveness of the cavity stabilization servo system in assuring long term cavity stability. The excellent performance of the oscillating compact masers should have dramatic impact on systems with critical dependence on frequency standard/clock performance. The drastically reduced size and weight will make it attractive even for spaceborne applications.

#### Acknowledgment

The enthusiastic and innovative contributions of T. Calderone, J. Lewis, L. McNulty, and J. Schmid in the design, fabrication and assembly of the CHYMNS compact masers are gratefully acknowledged.

#### References

1. H.T.M. Wang, "An Oscillating Compact Hydrogen Maser," Proc. 34th An. Symp. on Freq. Contr. p. 364 (1980).
2. H.T.M. Wang, J.B. Lewis, and S.B. Crampton, "Compact Cavity for Hydrogen Frequency Standard," Proc. 33rd An. Symp. on Freq. Contr. p. 543 (1979).
3. The quadrupole state selector magnet was furnished by Dr. J. White of NRL.
4. D.U. Gubser, S.A. Wolf, A.B. Jacob, and L.D. Jones, Proc. 13th Annual PTTI Appl. and Planning Mtg., p. 791 (1981).
5. ST-101 and ST-171 are trade marks of SAES Getters, Colorado Springs, CO 80906.
6. D. Allar, "Report on NBS Dual Mixer Time Difference System (DMTD)," NBSIR75-827, NBS, Boulder, CO (1976).
7. The VLG-11 p10 is the property of NRL. We are grateful to A. Bartholomew for making it available to us.
8. P. Lesage and C. Audoin, "Frequency Stability of an Oscillating Maser with External Feedback Loop," IEEE Trans. Instr. and Meas. IM-30, 182 (1981).

## THE DEVELOPMENT OF A MAGNETICALLY ENHANCED HYDROGEN GAS DISSOCIATOR

L. Maleki

Jet Propulsion Laboratory  
Pasadena, CaliforniaAbstract

A study of the processes which influence the efficiency of the rf hydrogen gas dissociator is made. Based on this study, a dissociator is developed by applying a dc magnetic field on the rf plasma. The influence of the magnetic field on the plasma is then evaluated. It is found that in this configuration the power consumption of the dissociator is decreased appreciably. Also, the application of the dc magnetic field allows the efficiency to be held at a constant level, while the hydrogen gas pressure is reduced. Based on these findings some approaches for the development of a dissociator low in gas and rf power consumption are presented.

I. Introduction

The development of an efficient hydrogen gas dissociator is part of an effort at JPL to develop techniques and components that enhance the performance and operational reliability of hydrogen masers. Since the operation of the hydrogen maser is based on the stimulated emission of radiation of hydrogen atoms in a particular hyperfine state<sup>(1)</sup>, the source of these atoms is naturally an important component of the maser. Specifically, the efficiency of the atom source directly determines the flux of the hydrogen beam, which in turn influences the power output and the stability performance of the maser.

The rf dissociator, as the source of the hydrogen atoms, has significant influence on the reliability of the maser operation, as well. Experience has shown that the degradation of the efficiency of atom production of the dissociator may directly cause maser breakdown. Furthermore, the dissociator efficiency influences the gas load of the vacuum pumps which generate the required high vacuum in the maser physics package. Since vacuum pump failures are the predominant mode of maser failures, the efficiency of the dissociator also indirectly influences this particular mode of maser breakdown.

In an effort to improve the performance of the dissociator we have studied the processes that take place within the rf plasma. Based on this study, we have developed a magnetically enhanced rf dissociator with improved atom production and lowered power consumption. Depending on the particular mode of operation, the magnetically enhanced dissociator may also reduce the gas load of the

vacuum pumps, thereby extending the operational life of the maser.

In this paper, we will briefly review some of the plasma processes, on the basis of which the development of the magnetically enhanced dissociator was motivated. We will then present the result of our investigation for the development of this source of hydrogen atoms.

II. Processes Influencing the Dissociator Efficiency

Figure 1 presents the picture of an rf dissociator (source) on the test assembly. The dissociator consists of a glass bulb with a stem through which hydrogen gas is introduced. The gas outlet consists of a glass multichannel array which causes the formation of a narrow beam of hydrogen out of this source. The rf power is coupled externally to the source by two probes or a coil, depending on whether a capacitive or an inductive coupling scheme is employed. In JPL masers rf power is coupled by an inductive coil, and so for the remainder of this discussion we will assume this coupling scheme; the major portion of the considerations presented here apply equally well to capacitance coupling.

When hydrogen gas is introduced in the dissociator glass bulb, and rf power turned on, electrons already present in the source (or generated by a high voltage pulse) oscillate in the rf field. During the course of oscillations, electrons collide with hydrogen molecules, resulting in the production of atoms, ions, and other electrons. The new electrons in turn participate in collisions, thereby producing a sustained plasma discharge.

The significance of any collisional process (between the electrons and other particles) in production of atoms is determined by the rate coefficient of the particular process<sup>(2)</sup>. The rate coefficient is given by  $\sigma V$  where  $\sigma$  is the cross section for the reaction and  $V$  is the relative velocity of the colliding electron and the particle (neutral or ion). In the case of the rf plasma in the dissociator, with typical average electron energy equivalent to 35,000 degrees Kelvin, the reaction which contributes most to atom production is simply electron impact dissociation  $e + H_2 \rightarrow H + H + e$ <sup>(2)</sup>. Dissociative excitation

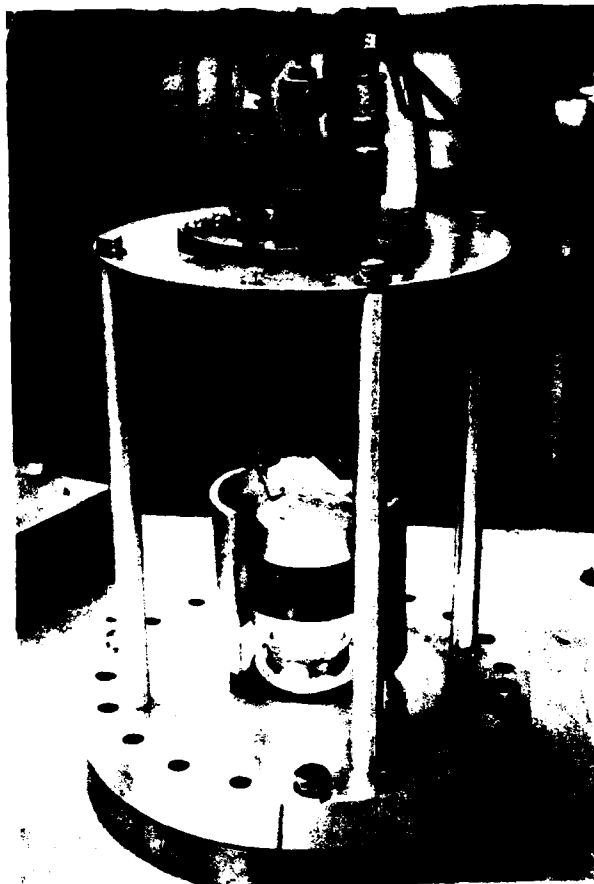


Figure 1. Dissociator on the Test Assembly

$e + H_2^+ \rightarrow H^+ + H + e$  and other reactions involving electron impact with ions contribute significantly less to atom production. In short, while plasma contains a number of ions such as  $H^+$ ,  $H_2^+$ , and  $H_3^+$ , electron impact with ions contributes little to production of atomic hydrogen due to corresponding lower reaction rates.

The efficiency of atom production in the rf dissociator is then determined by three factors: (1) an optimal reaction coefficient for the process of dissociation (i.e.,  $e + H_2 \rightarrow H + H + e$ ), as determined by an optimized electron energy through the relation  $\omega = \nu$ ; (2) the condition of the glass wall of the bulb, on which atoms recombine before they exit through the multichannel collimating array; and (3), the collision frequency of electrons with molecules.

While factors (1) and (2) above may appear unrelated at first glance, they are in fact interrelated through the influence of the plasma ions in the dissociator.

Ions, although of relatively low average velocity, eventually degrade the glass surface through collisions. This degradation consists of

production of macroscopic "pits" in the glass which amount to an increase of surface area. The extent of the degradation is a function of the number of impacts (and therefore time) as well as the energy of the ions. Figure [2] compares the scanning electron microscope picture of a fresh glass surface with the surface of a used dissociator bulb. The extent of the pitting in the dissociator glass is clearly visible.

It is clear then that the increase in the rf power input for the purpose of increasing electron energies to an optimal level will have a detrimental effect on the condition of the dissociator bulb, and therefore on the loss of atoms to the recombination processes. It would, however, be highly desirable to increase electron energies, and their collision frequency, without a corresponding increase in the energy of ions. As for the increase in the collision frequency of electrons with molecules, it should be pointed out that increase of the gas density in the bulb has the undesirable effect of increasing gas load to the vacuum pumps. With these considerations, we now evaluate the influence of an applied dc magnetic field on the efficiency of the dissociator.

### III. The Influence of An Applied dc Magnetic Field

Consider the motion of an electron in an rf plasma superimposed by a dc magnetic field. The electron will experience a force  $\vec{F} = e\vec{v} \times \vec{B}$ , where  $e$  is the charge and  $\vec{v}$  the velocity of the electron, and  $\vec{B}$  is the magnetic induction. According to this relation the path of the electron will be modified so that it will exhibit a helical path along the magnetic field line. The frequency of the circulating electron is given by Larmor relation  $f = eH/2\pi mc$ , where  $H$  is the magnetic field,  $m$  the mass of electron, and  $c$  the speed of light. This helical motion of the electron corresponds to an increase of its path length in the plasma, and therefore, an increase in its frequency of collision with particles in the plasma. Furthermore the circulating electron in the magnetic field can now absorb energy in resonance with the rf field as it moves in the direction of the field. The condition for this resonance absorption of energy is that the cyclotron frequency of the electron  $\omega_c = 2H/mc$  be equal to the oscillation frequency of the rf field. . .

In this manner, the effect of the applied magnetic field on the dissociation efficiency of the source is through the increase of the collision frequency of electrons with molecules, as well as the increase of electron energies. This may be accomplished without increasing the rf power and the gas pressure of the source.

It should be mentioned that a dc magnetic field of a 100 Gauss or less has negligible effect on the motion of the ions in the plasma, because of the relatively large mass of the ions. In this way the ion energies will remain essentially unchanged, while electron energies are modified.



fresh glass (X100 magnification)



fresh glass (X400 magnification)



used glass (X100 magnification)



used glass (X400 magnification)

Figure 2. Scanning Electron Microscope photos of the fresh and used surfaces of the glass wall. The fresh surface was acid washed and prepared through a procedure identical to that of dissociators used in JPL masers. The used surface belongs to a dissociator which was used continuously for about 6 months.

There are a number of examples of dc magnetic fields applied to rf ion sources used for generation of atomic and molecular ions.<sup>(5)</sup> The considerations for the influence of the magnetic field for ion generation, however, is quite different from those related to atom generation. Basically, magnetic fields influence the drift of ions in the plasma, which in turn enhances ion extraction from the ion source<sup>(3)</sup>. Furthermore, ion sources require relatively large electron energies because of the dependence of the cross section for ionization on electron energies. This latter effect is in fact undesirable for the case of hydrogen gas dissociator, and will be discussed further in the following section.

#### IV. The Magnetically Enhanced Source and Its Operation

Because the hydrogen gas dissociator assembly of JPL masers is inside the vacuum package and therefore not accessible without breaking of vacuum, a dissociator test bed was constructed. The test bed consists of a vacuum canister for connecting an ion pump to a source mating flange. A pyrex glass bulb was designed and constructed with dimensions identical to those of conventional sources used in JPL masers, but suitable modified for use in the test bed. The modification consists of a glass ring with an O-ring groove externally attached to the wall of the source containing the exit collimating holes. The source may then be positioned on the flange with the O-ring providing the necessary vacuum seal. The rf exciter coil assembly and hydrogen gas feed lines provide the necessary support for the glass bulb (see figure 1).

For the generation of the dc magnetic field a solenoid was constructed from an insulated copper wire wound on a copper cylinder with an inside diameter one inch larger than the diameter of the dissociator bulb. The solenoid was placed on the mating flange in a coaxial configuration with the source. This particular solenoid provided a maximum field of 145 gauss on its axis with a 2.0-A current input. The solenoid produced a field which was linearly dependent on current within the range of zero to 2.0-A, the maximum current which the power supply produced.

The dissociation efficiency of the source was determined by measuring the changes in the pressure observed when the plasma was on or off. The variation of the pressure was obtained by noting the current in the ion pump power supply. While method of efficiency determination for the dissociation lacks a high absolute accuracy, it does provide a satisfactory means for a relative determination of the dissociator efficiency.

The source was initially operated under the condition of power and pressure to those employed in the maser. A back pressure of hydrogen gas produced a pressure of 200 mtorr in the dissociator; an rf power input of 3 W produced an efficiency measured to be 5%. As the input power was decreased, the efficiency of the source deteriorated, and the plasma was not sustained if the power was reduced below 2 W. The source was left

to operate under normal operating conditions for a period of a few days to allow its performance to stabilize. After this period, the solenoid power supply was turned on and the solenoid current was varied between zero and 2 A. As the magnetic field was increased, the light intensity of the plasma increased significantly. Furthermore, for specific values of the field a change in the plasma mode was observed. A measurement of the efficiency of the source at this level of pressure and power was performed with the dc magnet on. The source exhibited an increase and a decrease in efficiency depending on the magnitude of the applied magnetic field. The amount of variation in the efficiency ranged from a 10% increase to a 10% decrease of the efficiency measured without the applied magnetic field.

The efficiency measurements were continued as the input rf power was decreased. First it was observed that the application of the magnetic field decreased the value of the minimum power required for maintaining a plasma, depending on the current in the solenoid. For a current of 0.4 A corresponding to a field of approximately 40 gauss, it was possible to reduce the power to about 0.3 W. With these parameters, the efficiency of the source was determined to be 5%, the same value as the efficiency of a conventional source operating with 3 W of input rf power. The dc magnetic field then resulted in a tenfold decrease in the power consumption.

The results obtained in our investigation are easily understood in the following way. For a given set of dissociator parameters such as size and gas pressure, a certain level of rf power yields maximum dissociation. A decrease in the rf power level decreases the efficiency of atom production through decreased electron energies. However, an increase in the rf power from the optimized level does not lead to increased dissociation efficiency. This is because electron impact dissociation of hydrogen molecules (with a threshold energy of 4.8 eV) is a competing process with electron impact ionization of molecules (with threshold energy of 15.8 eV). But the increase of the average electron energies, which have a Maxwellian distribution in the plasma, preferentially contributes to the ionization process; this is due to the dependence of the corresponding cross sections on the electron energies<sup>(4)</sup>. Finally, when the rf power is decreased from an optimal level, a dc magnetic field of suitable strength can compensate for the decreased electron energies by allowing the circulating electrons to absorb energy in resonance with the field. This analysis, then clearly explains our findings with the application of the dc magnetic field on the rf dissociator.

As a final step in our investigation we tried to determine the effect of an asymmetric field on the dissociator efficiency. This was based on the observation of the differences between the threshold energies for the competing dissociation and ionization processes. We reasoned that if energetic electrons in the tail of the Maxwellian distribution could be swept away from the plasma region close to the source exit, the ionization

process would be suppressed. A test of this reasoning was accomplished through positioning of the axis of the solenoid away from the source exit. When the solenoid axis was displaced by 1/2 inch, an increase in the dissociation efficiency was observed for a 200 m Torr pressure of hydrogen. With a decrease of pressure to 80 m Torr, the measured dissociation efficiency of the source increased from a 7% level to 12.8%, when a current of 0.75 A was applied to the solenoid; this is a 70% increase of the dissociation efficiency. The power level in both cases was 2.5 W.

While the configuration of this latter experiment with the dc magnetic field was somewhat arbitrary, and determined by the constraint of the existing setup, it clearly demonstrated the potential value of this approach in designing an efficient source. It is expected that a careful design of an inhomogeneous field would allow an appreciable suppression of the ionization process near the exit region of the source, resulting in an increase in the production of the atoms.

#### V. Summary and Conclusions

We have studied the processes that influence the performance of the rf hydrogen gas dissociator. Based on this study we have developed a magnetically enhanced dissociator through the application of a dc magnetic field on the rf plasma. With this configuration of the dissociator the following results were obtained:

- (1) For a specific value of the magnetic field, it is possible to maintain the efficiency of the source and yet decrease the rf power input by an order of magnitude. This conclusion is of significance to both spaceborne maser development and improved reliability of ground-based masers through the expected improvement in the source life.
- (2) It is possible to obtain good efficiency for the source and, at the same time, reduce the hydrogen pressure with an applied dc magnetic field. This finding implies a means for the reduction of the gas load to the maser vacuum pumps, thereby increasing their operational life, and reducing the frequency of maser breakdowns resulting from pump failures.
- (3) The results with the inhomogeneous field indicate that it is possible to design a magnetic field configuration to sweep energetic electrons away from the region near the source exit. This would increase the source efficiency by preferential dissociation of the molecules, as compared to the competing process of molecular ionization.
- (4) The application of a magnetic field on the rf plasma results in a significant increase of the light output from the plasma. While this effect is not of interest to maser application (except for

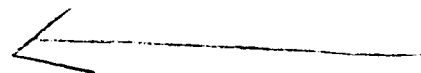
reaffirming that there is no direct relationship between the efficiency of the source and the intensity of the emitted plasma light) it may be of significance in other applications. In particular, certain light sources such as mercury ion light source, and rubidium light source, employ rf power for excitation. An application of a dc magnetic field can improve the performance of those sources and extend their operational life.

The investigation of the performance of the source was determined in a test bed and by obtaining the dissociation efficiency through the measurement of pressure variations. It is obvious that it would be highly desirable, and necessary, to perform the tests using a hydrogen maser. In this way, the extent of improvement obtained with the new source in relation to the maser vacuum system, power output, and line Q may be directly determined. Efforts are presently underway to design and construct a source unit which may be mounted externally to our existing maser test assembly. We intend to optimize the configuration and the strength of the magnetic field for a desirable mode of source and maser operation. Once this is accomplished, we will substitute equivalent permanent magnets for the solenoid, thereby eliminating the need for a solenoid power source. Finally, we intend to test the influence of the magnetic field on the light output of mercury lamps, which will be utilized in a trapped mercury ion frequency source. The results of this investigation will be reported in a later paper.

Acknowledgements. It is a pleasure to acknowledge the efforts of Mr. Thomas K. Tucker in the design and assembly of the Test Bed, and the dissociator. This paper presents the results of one phase of research carried out at the Jet Propulsion Laboratory, California Institute of Technology, under contract number NAS 7-100, sponsored by the National Aeronautics and Space Administration.

#### References

1. Kleppner, D., Berg, H. C., Crampton, S. B., and Ramsey, N. F. Phys. Rev., 138A, 972 (1965).
2. Maleki, L., "A Study of the Processes in the rf Hydrogen Gas Dissociator," in The TDA Progress Report 42-59: July and August 1980, Jet Propulsion Laboratory, Pasadena, Calif., (Oct. 15, 1980).
3. Francis, G., Ionization Phenomena in Gases, Chapter IV, Butterworths Scientific Publications, London, (1960).
4. Kieffer, L. J., and Dunn, G. H., Rev. Mod. Phys., 38, 1 (1966).
5. Vali, L., Atom and Ion Sources, Chapters II, III, and IV, John Wiley and Sons, New York (1977), and references therein.



PRELIMINARY MEASUREMENTS ON EFOS 1 H MASER

G. Busca, F. Addor, F. Hadorn, G. Nicolas, L. Prost,  
H. Brandenberger, P. Thomann

ASULAB S.A., Neuchâtel  
and

L. Johnson, OSCILLOQUARTZ S.A., Neuchâtel  
Switzerland

Abstract

*This paper is a progress report on development work of a full size active H maser (EFOS 1) presently in progress at ASULAB, NEUCHÂTEL, in view of an industrial production. The maser design philosophy, the physical package, the receiver and the measurement system are described and preliminary results on the frequency stability, measured by comparison with the prototype masers H1 and H2, are presented.*

Introduction

The EFOS 1 Maser has been conceived in order to obtain optimum frequency stability for averaging times between 100 and 10'000 secs. i.e. for the averaging times of interest to V.L.B.I. In addition to the stability requirement, the EFOS main design goals are those typical of an industrial product i.e.: reliability, easy maintenance and cost effectiveness. In view of these goals the option of high line Q, as opposed to the alternative option of high output power, has been adopted. In fact the fundamental limitation of the maser [1,2,3], which dominates the frequency stability for averaging times  $\tau > 100$  s is proportional to the parameter  $(PQ^2)^{-1/2}$ . From this point of view line Q is more important than the maser power. A high line Q has several advantages: it reduces cavity pulling effects and allows a smaller hydrogen flux to be used, with a corresponding decrease in spin exchange effects and increase in ion pump life. Finally an Aluminum microwave cavity has been preferred to the quartz cavity with the assumption that the higher temperature coefficient of the Aluminum cavity ( $1.5 \times 10^{-7}/^\circ\text{C}$ ) compared to the Quartz cavity ( $5 \times 10^{-7}/^\circ\text{C}$ ) could be balanced by several advantages of the Al cavity like the better mechanical stability, the absence of thermal gradients due to the high thermal conduc-

tivity of the Al and finally easy tunability by temperature changes. Furthermore the temperature sensitivity of the Al cavity can be effectively overcome by good thermal design using a vacuum envelope for thermal isolation.

Physical package

The physical package is inspired by the classical design of the full size Al cavity maser like for example the NASA NX [4] or the A.P.L. N.R. [5] Masers. Table 1 lists the most important characteristics of EFOS 1. A mechanical schematic diagram is shown in Fig. 1. All the elements of the physical package are well known; we focus the discussion on particular points of the EFOS 1 design.

Dissociator

The dissociator uses a pyrex bulb of approximately  $\frac{1}{4}$  of a liter, in order to minimize wall effects on the H plasma, and a single hole collimator. The H pressure is in the range of 0.1 to 0.2 torr. The R.F. oscillator has been studied in detail in order to present the best matching conditions to the plasma in the expected range of physical situations. It requires no more than 7 watts of total D.C. power for achieving the maximum molecular H dissociation efficiency. The discharge is self-starting and no regulation is needed after start-up for optimising the dissociation efficiency.

Quartz bulb

The quartz storage bulb is cylindrical in shape with hemispherical end cups and has 4.5 liters volume. It is coated with TEFLON FEP 120 with the usual technique and the exit hole is adjusted for a theoretical line Q, limited by the escape rate, of  $5 \times 10^{11}$ . In practice, we have measured line Q up to  $4 \times 10^{11}$  by cavity pulling measurements on an oscillating maser. This means that the teflon coating is good enough to ensure that the line Q

is not limited by wall relaxation. For normal operation the maser line  $Q$  ranges from 2 to  $3 \times 10^9$  for an output power in the range of -104 to -107 dbm.

#### Vacuum system

All the parts in contact with the H atoms are pumped by an independent 20 l/sec ion pump which produces a good vacuum ( $< 10^{-7}$  torr) essential for the proper maser operation. This "internal" vacuum system is completely separated from the "external" vacuum system which provides a thermal insulation for the Al microwave cavity and furthermore contains several parts like the C field solenoid, 3 thermal shields and 2 magnetic shields. The external vacuum system reduces, in addition, any barometric effect on the cavity frequency. Normal ion current in both pumps are of the order of 300  $\mu$  A for a voltage of 5 Kv. This ensures low power consumption and high pump life-time and reliability. A system of valves allows the replacement of the ion pumps without disrupting the vacuum in the maser.

#### The microwave cavity

The microwave cavity, operating on the TE<sub>111</sub> mode, has an elongated design. The cavity temperature coefficient ( $\frac{\Delta \nu_c}{\nu_c} / ^\circ\text{C}$ ) depends mostly on the diameter dimensional variations and is typically  $-2.5 \times 10^{-5} / ^\circ\text{C}$ . The cavity loaded  $Q$  ( $Q_c$ ) with a coupling factor ( $k$ ) of 0.15 is approximately 35000. From the cavity pulling equation:

$$\frac{\Delta \nu_m}{\nu_m} = \frac{Q_c}{Q_1} \frac{\Delta \nu_c}{\nu_c}$$

and actual measurements we obtained a typical value of  $\frac{Q_c}{Q_1}$  of  $1.25 \times 10^{-5}$  and a maser temperature coefficient of  $-3.2 \times 10^{-10}$  for  $+1^\circ\text{C}$  cavity temperature change. Using five proportional temperature controls in addition to the good thermal insulation around the cavity a thermal gain of the order of  $10^4$  is obtained resulting in a maser temperature coefficient due to the cavity, of  $-2.5 \times 10^{-14}$  for  $1^\circ\text{C}$  external temperature variation. The initial cavity tuning is made by temperature. The typical operating temperature is  $41 \pm 1^\circ\text{C}$ . The final tuning is realized by a varactor mounted inside the cavity. The varactor allows a fast cavity tuning which is especially useful for the start-up procedure and the spin-exchange cavity tuning.

#### Magnetic shields

Four magnetic field made of mu-permalloy and having a thickness of 0.1 mm, give a measured shielding factor of approximately 100 for external magnetic field and in the most critical axial direction. The magnetic homogeneity in the volume

of the Quartz bulb is good enough to allow operation at a "C" field value of 100  $\mu$  Oersted at full maser power, and limiting oscillation at substantially lower magnetic field; this shows that the magnetic inhomogeneity across the storage bulb practically does not contribute to the linewidth at the nominal operating magnetic field and that Crampton effects [6] are negligible. Finally, the measured maser magnetic coefficient is  $< 3 \times 10^{-13}$  gauss at a magnetic field of 300  $\mu$  gauss.

#### The Receiver

The block diagram of the receiver is shown in fig. 2. It is a conventional superheterodyne converter having 3 intermediate frequencies respectively at 19.6 MHz, 405 KHz and 5.7 KHz. A synthesizer at 5.7 KHz allows to extract the phase of the maser signal which is used, after filtering to phase-lock the 5 MHz VCXO to the maser signal. The noise figure of the receiver is practically that of the first RF amplifier i.e. 2.8 dB. The most critical parts, like the isolation amplifier and the multiplier, are housed in the maser head which is temperature stabilised with a minimum thermal gain of 100. Measurements of the receiver characteristics have been made. The phase noise of the multiplier, measured at 1.4 GHz and referred to 5 MHz is:  $\phi_n = 10^{-12.7} f^{-1} + 10^{-14.3} f^{-2}$ . Its phase-temperature coefficient is  $< 1 \text{ RAD}/^\circ\text{C}$  at 1.4 GHz. The 5 MHz isolation amplifier's phase-temperature coefficient referred to 1.4 GHz is  $< 0.1 \text{ RAD}/^\circ\text{C}$ . The previous figures need no improvement since the receiver is housed in the temperature stabilized maser head. The limitation on the maser frequency stability as imposed by the receiver noise has been measured directly in the time domain. (See the measurement system below). The receiver noise contribution for a maser signal at -105 dBm in a 1 Hz bandwidth is:

$\nu$ (Hz)	$\nu$ (GHz)
$1.4 \times 10^{-13}$	1.4
$6.5 \times 10^{-14}$	11.6
$4.1 \times 10^{-11}$	10
$6 \times 10^{-10}$	100

As usual, the receiver noise eliminates the frequency stability for averaging time  $t$  up to approximately  $1/t$  and does not hinder the maser frequency stability for longer averaging times since the maser frequency stability is lower.

#### Measurement system

Fig. 3 shows a block diagram of the frequency stability measurement system. The 5 MHz reference signal from maser I is multiplied up to 144 GHz and mixed with the signal of maser II in the receiver II. The 5.7 KHz beat from the receiver

contains now the noise of the two masers and is mixed with the output of the synthesizer of maser II in order to produce a beat of approximately 1 Hz selected by setting the synthesizer. The period of the beat after low pass filtering and shaping is counted by a counter used in the period average mode and programmed by a calculator which computes the Allan Variance.

For measurement of the receiver characteristics, independent of the maser, the same measuring system of Fig. 3 is used except that the signal from maser II is replaced by the output signal of maser I at 1.430 GHz derived from a power divider at the maser I output and taking care to maintain the same power level.

#### Frequency stability

The theoretical equation for the maser frequency stability is given by:

$$\sigma_y(\tau) = \left[ \frac{1}{2\pi\nu_0} \frac{4kT}{P_{IN}} \left(1 + \frac{F-1}{\beta}\right) 3f_c \tau + \frac{kT}{2P_{IN}Q^2} \tau^{-1} \right]^{\frac{1}{2}} \quad (2)$$

where:

$\sigma_y(\tau)$  : Two sample Allan Variance corrected for load time of the measuring system

	EFOS I Parameters
$\nu_0$ : H frequency	
$F$ : $1.0 \times 10^{-13}$ Ws <sup>1/2</sup> /K	
$T$ : Absolute bulb and cavity temperature	415° K
$P_{IN}$ : Power present inside the cavity	$2.1 \times 10^{-13}$ W
$\beta$ : Coupling factor	0.15
$3f_c$ : $P_{out}$	-100 dBm = $3.16 \times 10^{-14}$ W
$F$ : Noise figure of the RF amplifier	2.8 dB
$f_c$ : Cut-off frequency of the measuring system	1 Hz
$Q$ : H line Q	$2 \times 10^9$

The first two terms are present in the first term of the bracket, which are independent of the noise figure of the receiver and the additive white noise of the receiver. For the EFOS maser the parameter  $\frac{4kT}{P_{IN}}$  is 1. A perfect receiver would add only the dead time stability by a factor of 1.414. The first term of equation (2) dominates for averaging times  $\tau > 100$  sec. It must be noted that the Allan Variance for this

type of noise depends on the cut-off frequency of the filter used in the measuring system and must be corrected for the dead time of the counter.

The second term represents a white frequency noise and is the fundamental limitation of the frequency stability of the maser. The relevant parameter is the product of power and the square of the line Q. From this point of view the line Q is more important than the output power. The design of EFOS I maser is oriented towards obtaining a relatively low output power but high line Q. Fig. 3 shows the frequency stability obtained in a normal laboratory environment and the theoretical evaluation from the previously given maser parameters. The same results have been obtained from the comparison of H<sub>2</sub> and EFOS I masers. The frequency stability for longer averaging times ( $\tau > 1000$  sec.) depends mostly on the room temperature variations. The temperature coefficient of maser EFOS I has been measured as  $< 3 \times 10^{-14}/1^\circ\text{C}$ . The temperature coefficient is measured by making a step in the room temperature of 5°C, and measuring the maser frequency change after approximately 12 hrs i.e. when the maser frequency has reached its new equilibrium value.

There is evidence from these measurements that frequency stability for the longer averaging times ( $\tau > 10^4$  sec) will depend strongly on the ambient temperatures fluctuations which should be kept at the level necessary for the desired frequency stability.

TABLE 1  
CHARACTERISTICS OF EFOS MASER

#### Overall characteristics

Size	500 x 500 x 1150 mm
Weight	70 kg
Power Supply	22-30 Volt FROM EXTERNAL BATTERIES
Power Consumption	< 100 Watts

#### Construction details

- Dual chamber vacuum system
- Quatrupole state selector
- Quartz bulb for H storage: 4.5 liters
- Aluminum cavity
- 3 thermal shields
- 4 magnetic shields
- 5 thermal controls
- Receiver in the maser head

#### Physical characteristics

Line Q	$2 \times 10^9$
Output power	< -105 dBm
Loaded cavity Q	< 35'000
CAVITY PULLING FACTOR	$< 1.25 \times 10^{-5}$
Cavity tuning:	by temperature and varactor
Maser temperature coefficient	$< 3 \times 10^{-14}/^\circ\text{C}$
Maser magnetic coefficient	$< 3 \times 10^{-13}/\text{GAUSS}$

# References

- [1] L.S. Cutler and C.L. Seatie, "Some Aspects of the Theory and Measurement of Frequency Fluctuations in Frequency Standards", Proc. of the IEEE, 54, pp 136-154 (1966).
- [2] R.F.C. Vessot, M.W. Levine and E.M. Mattison, "Comparison of Theoretical and Observed Hydrogen Maser Stability Limitation due to Thermal Noise and the Prospect for Improvement by low-temperature Operation", Proc. 3th Annual Precise Time and Time Interval (PTTI) Conference, pp 549-559, (1977).
- [3] C. Undoin, J. Viennet and P. Lesage, "Hydrogen Maser: Active or Passive?", 3rd Symp. on Frq. Stds and Metrology, Journ. de Physique, Coll. C 8, suppl. au No 12, 42, pp 159-179, (1981).
- [4] V.S. Reinhardt, D.C. Kaufmann, W.H. Adams, J.J. Deluca and J.L. Soucy "NASA Atomic Hydrogen Standards Program - An Update -", Proc. 30th Ann. Symp. on Frq. Control, pp 481-488, (1976).
- [5] L.J. Rueger, A. Bates, L. Stillman and V.S. Reinhardt, "NASA NR Hydrogen Masers", Proc. 32nd Ann. Symp. on Frq. Control, pp 480-491, (1978).
- [6] S.B. Champton, E.C. Fiery and H.T.M. Wang, "Effects of Atomic Resonance Broadening Mechanisms on Atomic Hydrogen Maser Long-Term Frequency Stability", Metrologia 13, No 3, pp 181-185 (1977).

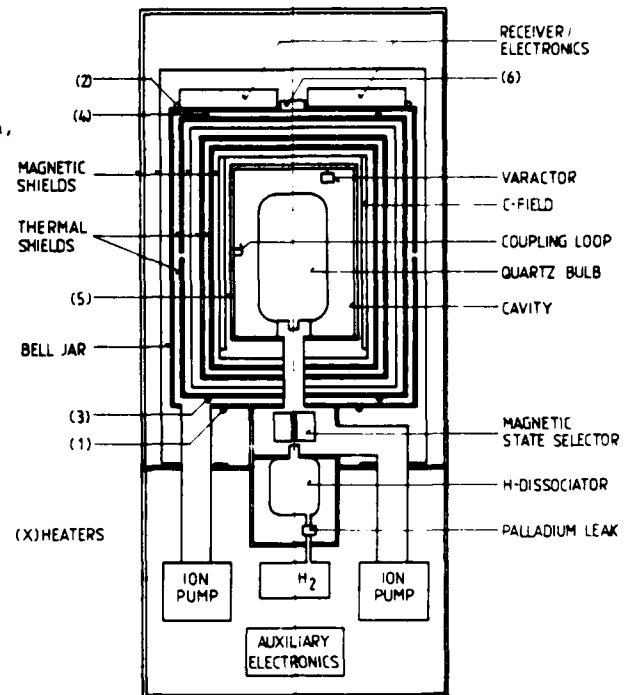


Figure 1. Hydrogen Maser Mechanical Schematic

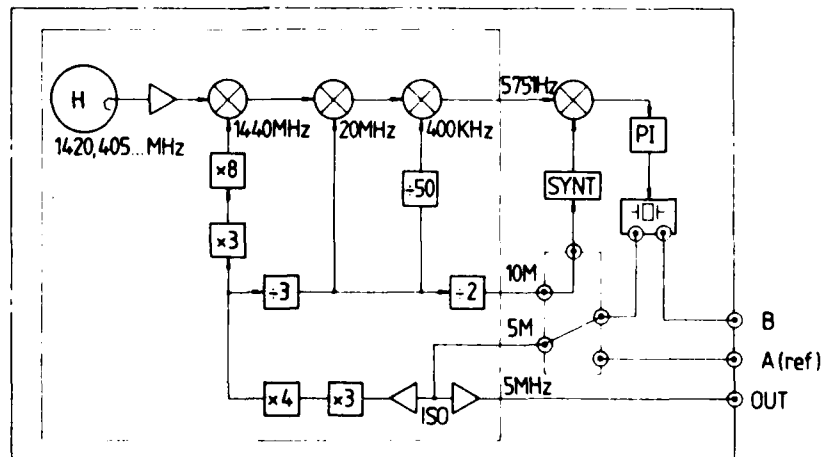


Figure 2. Receiver Block Diagram

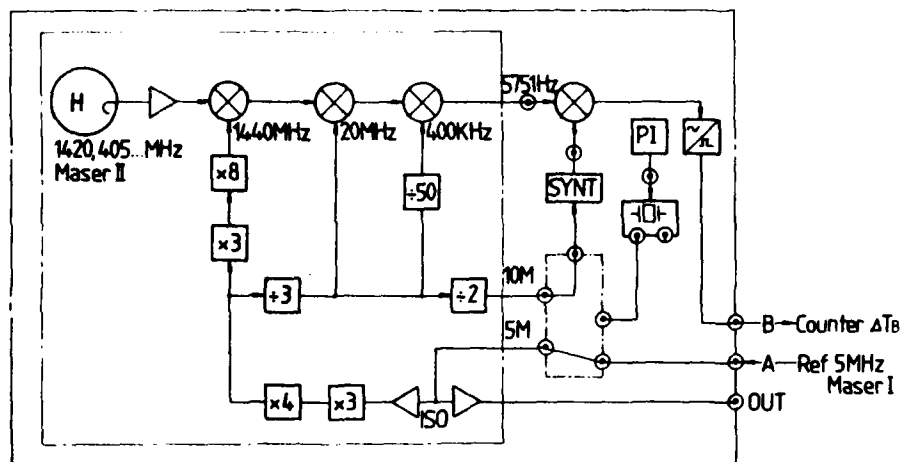


Figure 3. Frequency Stability Measuring System

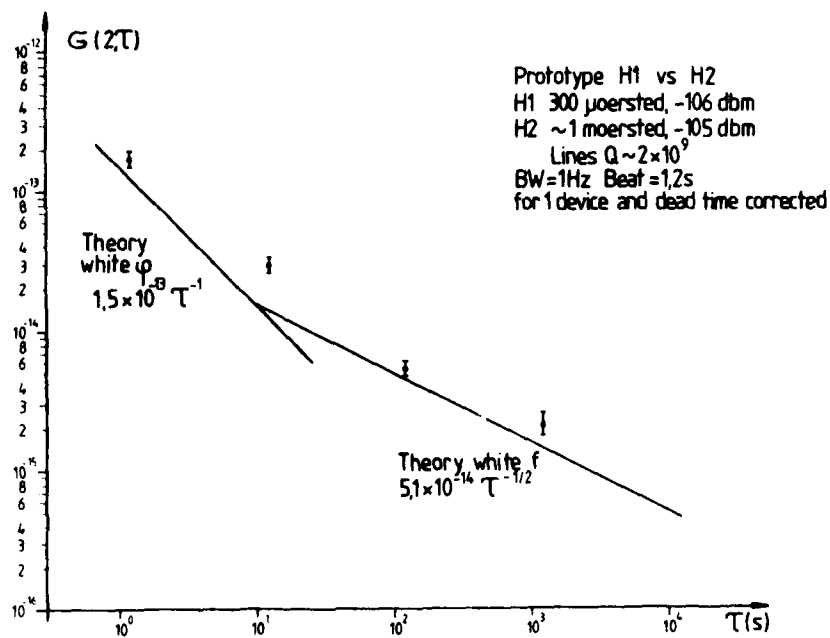


Figure 4. Hydrogen Maser Frequency Stability

AD P001532

## THE TORSIONAL TUNING FORK AS A TEMPERATURE SENSOR

R.J. Dinger

ASULAB S.A., Neuchâtel, Switzerland

Summary

A resonant temperature sensor has been developed using a torsionally vibrating quartz tuning fork. The unit has a linear temperature coefficient of 35 ppm / °C, operates at 262 kHz and is packaged in wrist watch tuning fork capsules of 1,5 mm diameter and 5,3 mm overall length.

**Key words:** Quartz crystal resonator, temperature sensor.

Introduction

Torsionally vibrating quartz crystals have been used for a long time as transducers or sensors for physical parameters. Mason [1] already in 1947 published a paper proposing the use of a torsion-bar crystal to measure the viscosity of liquids and his idea has been improved recently [2]. Torsionally vibrating tuning forks were investigated in 1976 by J. Hermann of the CHN [3] and independently by S.S. Chung of Stark Corp. in 1977 [4]. These authors were looking for a medium or low-frequency crystal with a better frequency-temperature characteristic than the usual x - y flexure tuning fork. The projects were dropped mainly due to the low piezoelectric coupling of a torsional crystal which makes difficult the use at a time base.

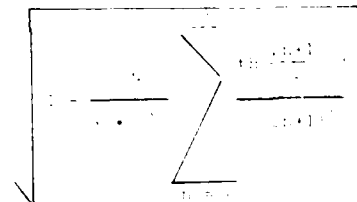
This work has been continued at ASULAB [5] in view of the development of a quartz temperature sensor. The frequency-temperature behaviour of a quartz resonator has been of continuing interest for the engineers and this quartz temperature sensor have been developed and commercialized for a long time, probably the first known being the 100 cut crystal D1 of Hewlett-Packard. - We felt that the existing devices are too bulky, too expensive and for some applications too high in frequency. The ever increasing use of microprocessors for control of equipment creates a large market for digital sensors that need not necessarily have the performance of laboratory instruments but where the main requirements are size, size and power consumption.

As shown earlier [3], linear frequency-temperature orientations exist for torsionally vibrating quartz crystals and a small tuning fork encapsulated in wrist-watch resonator cans of 1,5 mm diameter seems to us a good answer to the above mentioned market requirements.

Thermal parameters of the sensor

In order to calculate the frequency-temperature behaviour of a torsional tuning fork a three-dimensional finite element method or equivalent technique must be used. It has been found experimentally however that the differences between the calculated values and the experimental results are mainly due to the errors of the fundamental constants used. We therefore simplified the model and calculated a free-free bar. In addition the investigation was limited to crystal cans having their length parallel to the crystal longitudinal x-axis to avoid a second cut mode and to utilize the relatively high piezoelectric coupling that can be obtained in this orientation. With these simplifications the frequency may be calculated analytically [7], [8]

$$f = \frac{1}{L \sqrt{\rho \cdot G}} \cdot \frac{1}{\sqrt{1 - \frac{G}{E} \cdot \frac{L^2}{\pi \cdot r^2}}}$$



where  $t$ ,  $w$  and  $\rho$  are the crystal thickness, width and length,  $\rho$  its density and the parameter  $\beta$  is defined as:

$$\beta = \frac{w}{t} \sqrt{\frac{S_{11} - 2S_{12}}{S_{11} + S_{12}}}$$

$S_{11}$  and  $S_{12}$  are the rotated compliance moduli of quartz.

The frequency-temperature behaviour of a quartz torsion bar has been calculated according to eq. (1) using Bachmann's constants [9]. As usual the frequency has been fitted to a third order polynomial

$$f(T) = f_0(T_0) \left[ 1 + \alpha(T-T_0) + \beta(T-T_0)^2 + \gamma(T-T_0)^3 \right] \quad (2)$$

using 20°C as the reference temperature  $T_0$ . The loci of the thickness to width ratio  $t/w$  with vanishing second order temperature coefficient  $\beta$  are plotted in fig. 1 as a function of the cut angle  $\theta$ , defined as shown in the insert.

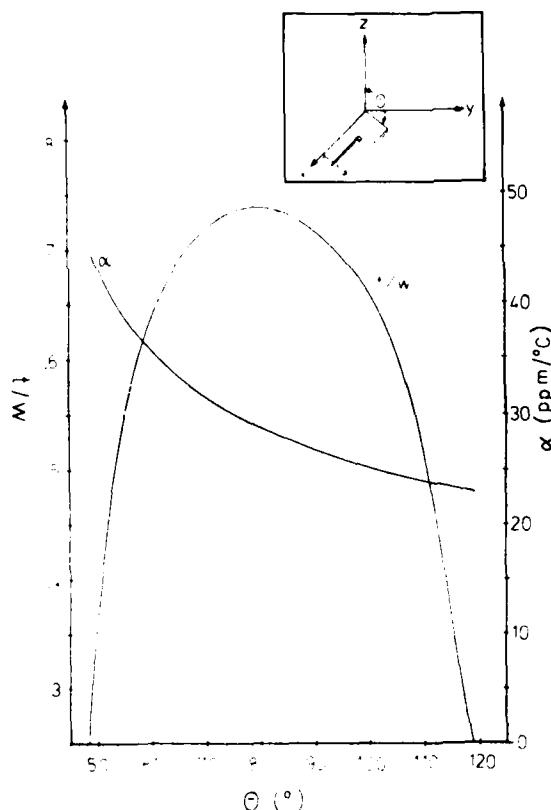


Fig. 1: Loci of vanishing second order coefficient  $\beta$  as a function of cut-angle for the thickness to width ratio  $t/w$  and the first order temperature coefficient  $\alpha$ .

The figure also shows the first order temperature coefficient  $\alpha$  associated with this  $t/w$ -ratio. It may be seen that a linear frequency-temperature characteristic will be obtained for cut-angles between 50° and 115° and that the strongest linear temperature coefficients are found around 50°. The large slope of the  $\alpha$  and  $t/w$  curve in this region requires tight cut-angle control and the small thickness to width ratio would yield small  $Q$ -values (cf. fig. 5). For these and technological reasons cut-angles around 90° ("z-cut") have been preferred and this paper describes tuning forks made from 92° material, which is the usual cut for x-y flexure tuning forks for wrist-watch applications. The thermal parameters for a cut-angle of 92° have been investigated experimentally and the result is plotted in fig. 2.

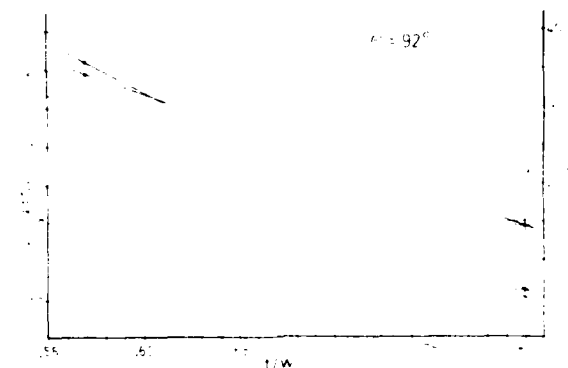


Fig. 2: First order ( $\alpha$ ) and second order ( $\beta$ ) temperature coefficient as a function of the thickness to width ratio  $t/w$ .  
broken lines : calculated  
solid lines : experimental results

The broken lines are calculated curves and the solid lines give the experimental results. The calculated curves show that the coefficients  $\alpha$  and  $\beta$  vary linearly with the thickness to width ratio justifying the straight lines through the measured values. There is a considerable difference between the experimental and theoretical curves. The experimental results have been measured with a large number of tuning forks made in different series from different crystals. The results agree with the parameters measured on samples made more recently in the production line. For these reasons the experimental curves are considered reliable and the error is thought to be in the calculated ones. In fact it has been found that the theoretical result is very sensitive to the elastic parameters and their temperature coefficients.

Fig. 2 shows that it is possible to make a linear device (in the sense of a device with vanishing second order temperature coefficient  $\beta$ ). Using a cut-angle of 92°, this would be the case for a thickness to width ratio of about 0.73. The cor-

responding linear temperature coefficient  $\alpha$  is about 20 ppm/°C.

For most of the applications of this temperature sensor it is preferable to have a larger linear coefficient  $\alpha$  even if this means that a second order coefficient  $\beta$  is present. An analysis of the overall error of the device quickly shows that within the limited temperature range (e.g. - 55°C to + 125°C) where most applications are found, the absolute calibration error and the deviation of the linear temperature coefficient from its nominal value are sufficiently large to allow for a small  $\beta$  without a significant increase of the overall error. For these reasons the first product developed uses a thickness to width ratio of 0.57. This ratio gives the following thermal parameters

$$\begin{aligned}\alpha &= 34 \text{ ppm/}^\circ\text{C} \\ \beta &= 20 \text{ ppb/}^\circ\text{C}^2\end{aligned}$$

The third order coefficient  $\gamma$  cannot be predicted by the calculation mentioned above due again mainly to the errors in the basic constants of quartz. Experimentally it has been found that the coefficient  $\gamma$  does not contribute to the overall error of the device. A fit according to eq. 2 of the experimental results yields values of the coefficient  $\gamma$  of the order of  $10^{-11}/^\circ\text{C}^3$ . Since the experimental accuracy influences the value of  $\gamma$  very much it is difficult to measure its value accurately. The probable best value is obtained by measuring the sensors at cryogenic temperatures (liquid nitrogen) thus enabling a fit from - 200°C to + 150°C. Doing this we obtain for the third order temperature coefficient  $\gamma$ :

$$\gamma = 9 \times 10^{-12}/^\circ\text{C}^3$$

Fig. 3 shows the frequency vs. temperature diagram of a typical unit made from 92° cut material and having a thickness to width ratio of 0.57.

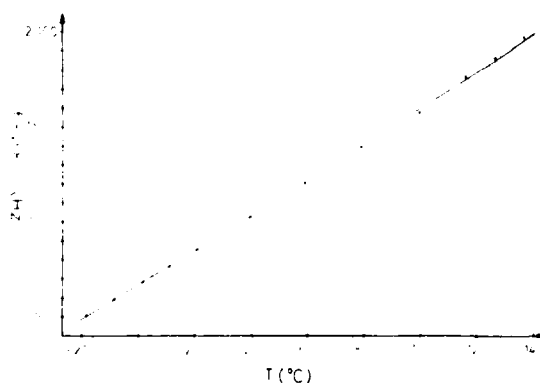


Fig. 3: Frequency-temperature characteristic of a tuning fork with  $\theta = 92^\circ$  and  $t/w = 0.57$ .

### Electrode pattern

The electrode arrangement used for a torsionally vibrating bar or tuning fork uses the x - y shear stress produced by an electric field parallel to the y-axis, originally proposed by Giebe and Scheibe [10]. Depending on the cut-angle the actual electrode pattern is different. Fig. 4 shows the cross section through one tine of the tuning fork with the metallization.

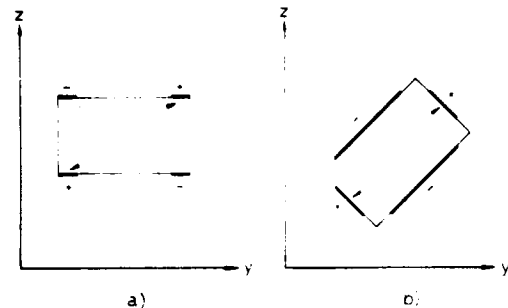


Fig. 4: Cross section through one tine of the tuning fork with electrodes. The arrows give the electric field used for driving the crystal.

For cut-angles close to the "z-cut" the electrode arrangement a) is used while for cut-angles around 45° (135°) the pattern shown in fig. 4b is more favourable. The latter is identical to the metallization pattern of an x-y flexure tuning fork (but the x-y flexure tuning fork has its length parallel to the y-axis). For the 92° cut-angles considered in this paper - almost a pure "z-cut" - the arrangement according to fig. 4a was chosen and fig. 5 shows the piezoelectric coupling obtained with this electrode system. The figure gives the measured motional capacitance  $C_1$  per unit length of the electrodes for both tines of a tuning fork.

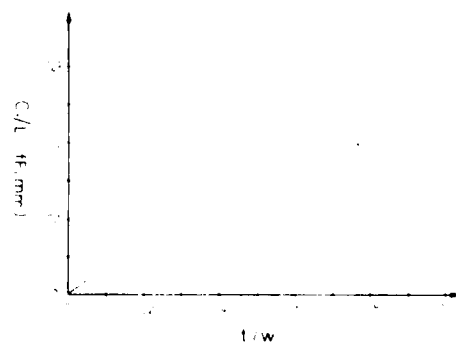


Fig. 5: Motional capacitance per unit length of the electrodes as a function of the thickness to width ratio for the arrangement according to fig. 4a and  $\theta = 92^\circ$ .

With an electrode length of 1.5 to 2 mm a state of the art device gives a motional capacitance of 0.2 to 0.4 fF, one order of magnitude less than the usual x-y flexure tuning forks. This low motional capacitance seems to be a serious disadvantage of the sensor mainly because fine frequency adjustment using a trimmer-capacitor is practically impossible. If the problem associated with the design of a trimmer-capacitor in a thermometer probe (that may be immersed in a liquid) are considered one concludes immediately that a trimmer-capacitor should not be used even if the resonators  $C_1$  would allow it.

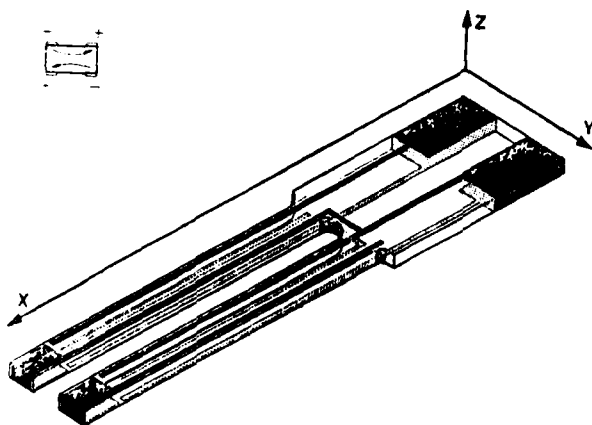


Fig. 6: The torsional tuning fork with electrodes.

Fig. 6 shows an overall view of the torsional tuning fork with the electrode pattern. Comparison with the metallization pattern of x-y flexure tuning forks [11] shows that the metallization pattern for the torsional tuning fork is much simpler and easier for a production technique based on photolithographic methods and chemical milling. In particular there are no parallel electrodes of opposite sign that are close together and the side metallization only serves to contact the upper and lower main surfaces.

#### Parameters of the unit

Eq. 1 shows that the frequency is given by the length of the tines of the tuning fork once the thermal parameters and the thickness to width ratio are fixed. For this development an overall size of the sensor of 1.5 mm diameter and a length of about 5 mm were required together with the thermal parameters mentioned above and a binary frequency. Analysis of the problem leads to the following dimensions and parameters.

#### Tuning fork

Overall length	4.5 mm
Overall width	0.7 mm
Thickness	0.125 mm
Frequency	262 144 Hz = $2^{18}$ Hz
Motional Capacitance	0.3 fF
Equivalent Resistance	15 k $\Omega$ typ.

#### Encapsulated sensor

Overall length	5.3 mm
Diameter	1.5 mm

#### Aging

A temperature sensor must be able to operate constantly at the upper limit of its specified temperature range. Therefore, the aging characteristic of the crystal is a very important parameter and can strongly influence the overall accuracy.

Accelerated aging experiments have been performed in order to estimate the long term frequency stability. Fig. 7 shows the result of a 1000 hour test at 150°C. The curves show the frequency drift of the best sample (curve ①) and the worst sample (curve ②) from a lot of 10 pieces. (The aging curves of the other samples are between curve ① and curve ②). No preaging of these devices has been made prior to this test.

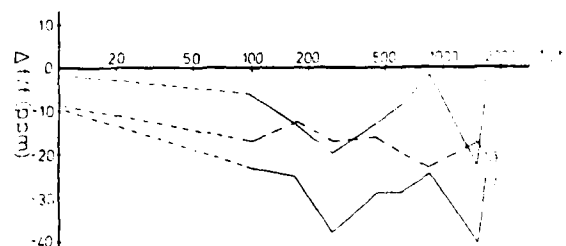


Fig. 7: Aging characteristics of the temperature sensor (for explanation see text).

The almost parallel behaviour of curves ① and ② suggests that the temperature control of the measurement fixture was not sufficient. In fact, for the measurement, the resonators were taken out of the 150°C oven, cooled down to room temperature and placed in a small measurement fixture, temperature stabilized by a Peltier element to 25°C. The influence of the ambient temperature on the fixture temperature was found to be 0.1°C per degree Celsius of room temperature change. With a linear temperature coefficient  $\alpha$  of 35 ppm/°C this means that an apparent frequency drift of 3.5 ppm is observed for every degree Celsius of variation of

INERTIAL GUIDANCE AND UNDERWATER SOUND DETECTION USING SAW SENSORS\*

E.J. Staples, J. Wise and A.P. Andrews

Rockwell International Microelectronics Research and Development Center  
1049 Camino Dos Rios  
Thousand Oaks, California 91360

Summary

This paper examines the use of SAW sensors for inertial guidance and underwater sound detection. In the detection of underwater sound, dynamic rather than static loading of the SAW crystal takes place resulting in information carrying sidebands in the SAW oscillator spectrum. Studies have shown that the sensitivity of prototype sensors in terms of signal-to-noise is at least equal to that of conventional hydrophones.

As an accelerometer, the SAW sensor provides high accuracy, a large dynamic range ( $10^6$ ), and a digital output without using analog-to-digital conversion. Using relatively simple digital processing techniques, the accelerometer output can provide inertial information such as velocity and displacement. Studies of the integrated error rates for SAW accelerometers have shown that they can consistently provide error rates less than a nautical mile per hour. The SAW oscillator sensor is a promising candidate for high performance, moderate cost sensor applications.

Introduction

The application of SAW sensors to underwater sound detection and inertial guidance is described in this paper. Several previous papers<sup>1-3</sup> have described the performance of SAW crystal oscillators when used to detect stress or strain as experienced in sensing the pressure applied to a quartz crystal. In the detection of underwater sound the pressure is dynamic rather than static and this results in information carrying sidebands in the SAW oscillator output spectrum. Studies<sup>4</sup> have shown that the sensitivity of SAW sensors is at least equal to conventional hydrophones with respect to signal-to-noise ratios in the low audio spectrum (0-1000 Hz).

Another useful application of SAW sensors is the detection of acceleration. In this application the SAW crystal has the advantage that it can be tailored to any shape without affecting the

resonant frequency of the resonators because the SAW frequency is independent of the bulk crystal shape. Likewise the attachment of the proof mass for fixing the scale factor of the sensor does not affect the resonant frequency of the sensor crystal.

SAW accelerometer sensors can also provide inertial information. This is accomplished by integrating the sensor output twice, once to generate velocity information, and a second time to generate displacement information. Because the SAW sensor output is a frequency proportional to acceleration, it can easily interface with digital processors without using A-to-D conversion circuitry.

SAW Sensor Fabrication

SAW resonators were photolithographically produced on polished ST-cut quartz blanks the size of which had been determined by the particular application. For underwater sound sensors the blanks were disks  $0.020 \times 0.550$  in. in diameter and for accelerometers, bars  $0.010 \times 0.200 \times 1.050$  in. were used. The resonator electrode pattern consisted of two reflective gratings symmetrically placed on either side of a 40 finger-pair, cosine weighted interdigital transducer. The reflective gratings were fabricated using a reactive ion etch technique in a freon plasma.<sup>5</sup>

SAW sensor crystals for underwater sound detection operated at a frequency of 62 MHz, had a Q of nominally 25,000 and a series resistance of 30 ohms. SAW accelerometer sensor crystals operated at a frequency of 400 MHz, nominally had a Q of 15,000 and a series resistance of 50 ohms. Oscillator circuitry was fabricated using all hybrid chip components.<sup>6</sup> Because a single-port/single-pole resonator crystal design was used, oscillator circuitry typically required only a one transistor amplifier with nominally 3 dB of gain. This resulted in a minimum number of components, high stability, and low cost.

Static Loading Characteristics

SAW crystals operate as sensors by converting an applied strain to a frequency deviation. Application of strain by loading the crystal mechanically results in a static frequency change which is a function of the geometry of the loading fixture and the direction of applied force with

\*Work supported by Defense Advance Research Projects Agency and the Naval Air Development Center.

AD P001533

the room temperature. This easily explains the form of these curves. In order to overcome this effect the difference between curve ② and ① was plotted (curve labeled ③).

This curve (③) is considered reliable enough to allow an estimate of the aging. A logarithmic aging according to

$$\Delta f/f = a \log \frac{t}{t_0} \quad (3)$$

fits the data well and leads to a constant  $a$  of  $-3$  ppm if  $t_0$  is 1 hour.

From similar experiments with series showing a stronger aging, permitting tests at different temperatures it has been found that the constant  $a$  doubles for every  $10^\circ\text{C}$  of temperature increase. Extrapolating this behaviour to resonators with typical aging performance one finds that the absolute value of the constant  $a$  is certainly below 1 ppm at the maximum specified operating and storage temperature of  $+125^\circ\text{C}$ .

### Conclusions

A torsional tuning fork with its length parallel to the x-axis has been developed for temperature sensor applications. Depending on the cut-angle and dimensional ratio used a linear or the series of vanishing second order temperature coefficients quartz thermometer can be made having a first order temperature coefficient of more than  $4$  ppm/ $^\circ\text{C}$ .

Compared to existing quartz temperature sensors the torsional tuning fork has the advantage of being a small and low cost device. Its main drawbacks with respect to the known quartz thermometers come from the fact that the temperature behaviour not only depends on the cut-angle but on the dimensional ratio as well thus leading to large dispersion in the thermal parameters and limiting its use to applications requiring low medium precision. With respect to other temperature sensors of comparable price and size the torsional tuning fork offers a better linearity and long term stability.

Our work with quartz fork manufacturing and particularly temperature sensitive non-linear sensor of constant length and constant mass for high precision open loop thermometry is intended for quartz temperature measurement elements replacing the metal expansion elements and the applied to initial development of the day.

### Acknowledgements

The author would like to thank J. Michel for encouraging discussions, J. Labourey for technical assistance and T. Gladden for assistance in the preparation of the manuscript.

### References

- [1] W.P. Mason, Measurement of the viscosity and shear elasticity of liquids by means of a torsionally vibrating crystal. Trans. A S M E 69 (1947), p. 359 - 370
- [2] G.J. Beukema and J. Mellema, Measuring System for complex shear modulus of liquids using torsionally vibrating quartz crystals. J. Phys. E : Sci. Instrum. Vol 14 (1981), p. 418 - 420
- [3] J. Hermann, CEH Report nr 168 (classified)
- [4] S.S. Chuang, private communication.
- [5] J. Michel, C.E. Leuenberger and R. Dinger "Thermomètre à quartz", European Patent Application Nr 0 048 689.  
See for instance :  
[6] D.L. Hammond and A. Benjaminsen, IEEE Spectrum April 1969, p. 53 - 58
- [7] E. Giebe, E. Blechschmidt, Ueber Drallschwingungen von Quarzstäben und ihre Benutzung für Frequenznormale, Hochfrequenztechnik und Elektroakustik 56, 3, (1940), p. 65 - 87
- [8] P.G. Pozdnyakov, "Quartz Crystals Resonators in Tension", Soviet Physics Crystallography 15, 1, (1970), p. 63 - 67.
- [9] R. Bachmann, A. Ballate and T.J. Lukaszek, "Higher Order Temperature Coefficients of Elastic Stiffnesses and Compliance of Aligned Quartz". Proc. of I.R.E., August 1967, p. 1812 - 1821
- [10] E. Giebe and A. Schenke, Z. Physik 41, (1928), p. 607
- [11] K. Oguchi and E. Matsuoka, "A Quartz Micro-thermometer by Lithographic process". Proc. of the 3rd Annual Symposium on Frequency Control, (1978), p. 177.

respect to the crystal axes. A test fixture to measure the stress sensitivity about any axis of a SAW resonator was fabricated and used to measure frequency deviation vs loading characteristics. Three types of loading, depicted in Fig. 1, were performed, (a) cantilever bending, (b) simple tension and (c) uniform diaphragm loading. The results are shown in Table I as coefficients obtained from least-squares fitting experimental data. Bending the Y'-axis of a SAW crystal produces a positive frequency shift as opposed to a negative frequency shift for bending about the X-axis. Both effects occur during uniform diaphragm loading.

Table I

Test	Measured Result
1. Cantilever, x-axis	-112 Hz/gram
2. X-axis tension	-14.8 Hz/gram
3. Cantilever, Y'-axis	+34.9 Hz/gram
4. Y'-axis tension	+ 0.3 Hz/gram
5. Pressure Diaphragm (compression)	+13.4 Hz/mm Hg

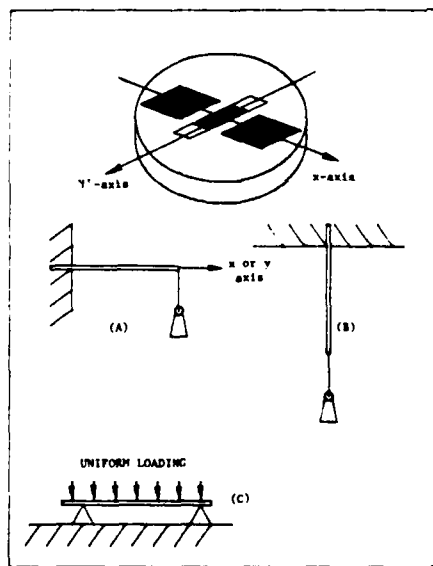


Fig. 1 Static loads applied to SAW sensor crystals; (a) cantilever bending, (b) tension, and (c) uniformly loaded diaphragm.

#### Bias Stability

Because SAW sensors operate by converting applied strain to frequency, frequency stability becomes equivalent to what is commonly termed bias stability. Bias stability, together with the full scale frequency deviation, determines the noise floor and dynamic range. Frequency stability in SAW oscillators can be expressed as a fractional

frequency distribution vs observation time (Allan variance) or as a spectral distribution (phase noise) as a function of frequency offset from the carrier. Previous studies<sup>7</sup> on many types of SAW oscillator crystals have shown that the best stability is achieved by high Q SAW resonators as opposed to SAW delay line controlled oscillators which have lower Q than resonators. Typically these oscillators have an Allan variance of  $1 \times 10^{-10}$  over measurement times 0.01 to 10 sec. Alternatively, the phase noise for a 400 MHz resonator controlled SAW oscillator is -70 dB/Hz at 10 Hz from the carrier and less than -120 dB/Hz at 1000 Hz from the carrier. For a SAW sensor with a full scale frequency deviation of 200 ppm, and a noise floor of  $1 \times 10^{-10}$ , the instantaneous dynamic range is  $2 \times 10^6$ .

In SAW sensors, bias stability is predominately controlled by long term aging and temperature stability. In practically all SAW sensor designs dual resonator crystals are used. The sensor output is the difference frequency of the two SAW oscillators which is invariant to aging and temperature to first order. Shown in Fig. 2 is the long term aging of two SAW resonators fabricated as a dual crystal. Shown in Fig. 3 is the differential aging of the two resonators. Although the absolute aging amounts to several ppm, the differential aging is practically zero because the two resonators age together with time. In order to achieve good long term bias stability in SAW sensors,<sup>8</sup> crystal processing and packaging must be closely controlled.

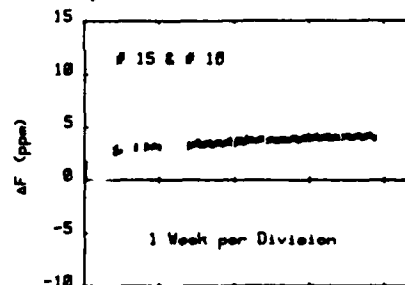


Fig. 2 Long term aging (absolute) of two SAW resonators fabricated as a dual resonator sensor crystal.

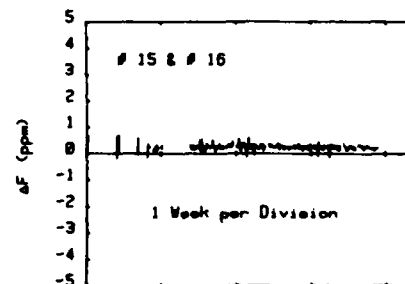


Fig. 3 Differential aging for Dual resonator sensing crystal showing long term bias stability.

Sensor bias instability due to temperature can also be reduced by using dual resonator crystals. In the sensor described in this paper dual resonators fabricated on the same quartz substrate were used to control two oscillator circuits. To first order any temperature variations influenced both oscillators identically making the difference frequency invariant to temperature. Shown in Fig. 4 are histograms obtained when the temperature was varied at a constant rate from 25°C to 85°C. Because the frequency scale is in ppm both oscillators start out equal at 0 ppm, however, as the temperature rises the frequency change is not equal. The primary cause of this bias instability was found to be variations in the metallization thickness of the resonators. This in turn caused the resonators to have slightly different parabolic turning points. The same data plotted as a differential frequency is shown in Fig. 5 and shows the bias stability to be linear over the 60°C range. These results show that to compensate against temperature perfectly, closely matched pairs of resonators must be fabricated.

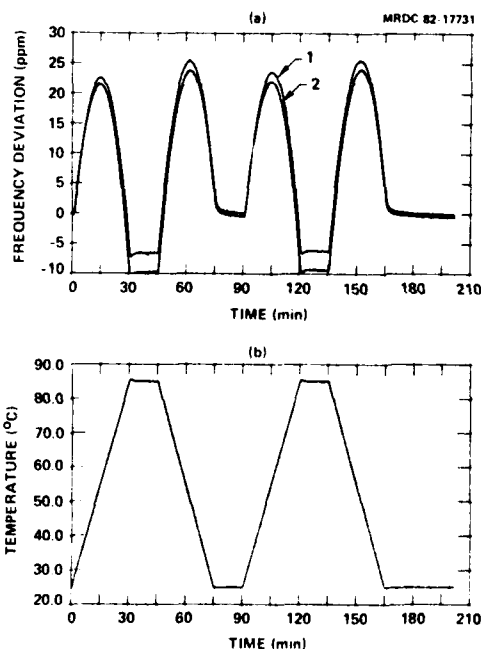


Fig. 4 Histograms showing (a) dual crystal oscillator frequencies and (b) temperature as a function of time.

#### Underwater Sound Detection

A prototype underwater sound wave detector was constructed using a cantilever beam SAW sensor. Each hydrophone contained two independent crystal oscillators and difference frequencies of 10 kHz and 125 kHz were used. Sound waves in the water were transmitted from a thin sensing diaphragm to the SAW crystal by means of a steel shaft and the sensing crystal was mounted as a cantilever beam with the bending axis perpendicular to the sagittal plane.

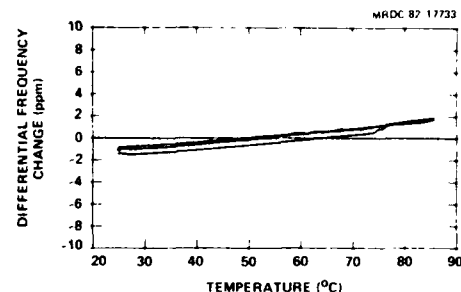


Fig. 5 Differential frequency stability or bias stability as a function of temperature, 25°C to 85°C.

Frequency modulation of the SAW oscillator produces an instantaneous frequency which is proportional to the modulating signal at frequency,  $\omega_m$ .

$$\omega_i(t) = \omega_c + \Delta\omega \cos(\omega_m t)$$

where  $\Delta\omega$  is the amplitude of the frequency deviation. Since the instantaneous frequency is defined to be the derivative of the phase, the output waveform will be given by,

$$V_o(t) = A_c \cos \left[ \omega_c t + \frac{\Delta\omega}{\omega_m} \sin \omega_m t \right]$$

The peak frequency deviation  $\Delta\omega$  is independent of  $\omega_m$ , while the peak phase deviation,  $\Delta\theta = \Delta\omega/\omega_m$ , is inversely proportional to the modulation frequency.  $\Delta\theta$  is commonly referred to as the modulation index.

The amplitude of the FM sidebands relative to the carrier can be represented by a Bessel function expansion of the signal waveform

$$V_o(t) = A_c \sum_{n=-\infty}^{\infty} J_n(\Delta\theta) \cos(\omega_c + n\omega_m)t$$

SAW hydrophones were fabricated and tested by comparing with a calibrated Naval G-19 hydrophone which had a sensitivity of -205.5 dB re 1 V/μPa. In these tests the frequency spectrum or sidebands of the SAW oscillator were measured under differing conditions of irradiation by ultrasound in a water column.

An example of the data taken is shown in Fig. 6 and consists of two spectrum plots. Figure 6a is a baseband spectrum of the calibrated Navy hydrophone indicating the presence of a 100 Hz tone with an intensity level of -68.873 dBV (7 pascals). The corresponding SAW hydrophone output spectrum is shown in Fig. 6b. The SAW sensor IF was set to 10 kHz and the spectrum analysis performed about this frequency as shown.

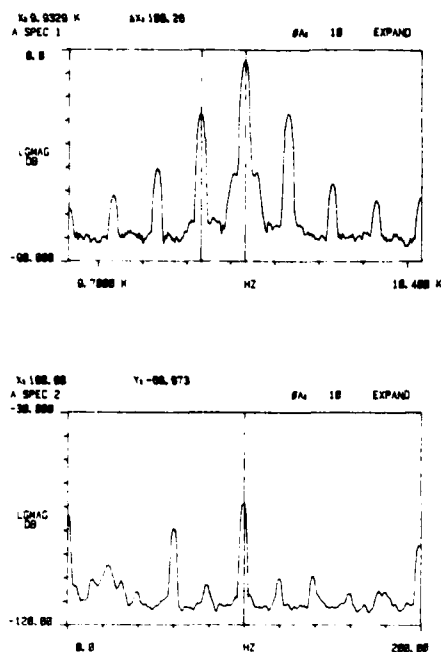


Fig. 6 SAW hydrophone output (a) compared with conventional baseband hydrophone response (b).

Sideband signal levels were measured at different frequencies by holding the intensity fixed at a level of 2 pascals. The frequency range covered was 50 to 1000 Hz. The ratio of sideband-to-carrier signal level at each modulating frequency provided a measure of the modulation index at that particular frequency. Frequency deviation was obtained by multiplying the modulation index by the modulating frequency. A plot of experimental frequency deviation vs modulating frequency is shown in Fig. 7 and a peak in the deviation occurs at approximately 500 Hz due to the mechanical resonance of the diaphragm post linkage and the sensor mounting structure. The observed frequency deviation is consistent with the device geometry and static cantilever loading.

In order to compare the sensitivity of SAW hydrophones to conventional (baseband) hydrophones the signal-to-noise ratio as a function of modulation frequency was measured under a 1 pascal irradiation. The results are listed in Table II. The SAW sensor S/N reached a high of 60 dB for low modulation frequencies and became equal to that of the calibrated phone at approximately 1000 Hz. At low modulation frequencies, < 500 Hz, the SAW hydrophone is comparable to a baseband hydrophone with a sensitivity of -180 dB re 1 V/μPa. The high sensitivity is a result of low phase noise in the SAW oscillator and increasing modulation index at low modulation frequencies.

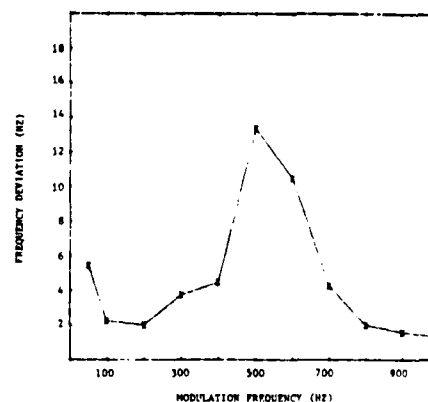


Fig. 7 Experimentally measured frequency deviation vs modulation frequency.

Table II

Modulation Frequency (Hz)	Sideband To Carrier (dB)	Modulation Index	Frequency Deviation (Hz)
50	-25.3	0.1089	5.45
100	-39.0	0.0224	2.24
200	-46.0	0.0100	2.00
300	-44.0	0.0125	3.75
400	-45.0	0.0112	4.48
500	-37.5	0.0267	13.35
600	-41.1	0.0175	10.50
700	-50.3	0.0061	4.27
800	-58.2	0.0025	2.00
900	-61.1	0.00175	1.57
1000	-63.8	0.00129	1.29

#### SAW Accelerometer - Inertial Guidance

Accelerometers are an important sensing element in many guidance systems. Modern signal processing methods dictate that the sensor be capable of interfacing with digital circuitry such as microprocessors. The SAW sensor output frequency is inherently a digital bit stream. The dual crystal SAW sensor provides a low frequency output with good bias stability. Digital interfacing in this case can be implemented with a high degree of accuracy using simple counting circuitry. For example, a 60 kHz SAW sensor output tone can be measured with 16 bit precision using two simple 8 bit counter chips in series.

A dual crystal SAW accelerometer was built and tested using quartz cantilever beams and SAW resonators operating at 400 MHz. One end was rigidly clamped and the other free with a proof mass attached. The proof mass was varied to achieve the full scale output sensitivity of 20 ppm/g. Each resonator of the dual resonator crystal was used to control the frequency of oscillator circuitry with ample shielding to prevent lock-up of the oscillators to a common frequency. The out-

puts were then mixed and the difference frequency input to an HP 5345 counter whose output was digitally processed using an HP9825 calculator.

In SAW accelerometer system applications the ability to use signal processing techniques without resort to A-to-D conversion is unique. For SAW accelerometer crystals operating at 400 MHz with a 20 ppm/g sensitivity, the digital output quantization is approximately 0.004 fps/bit. The acceleration expressed as a function of frequency deviation is

$$A = K \cdot \Delta F(t)$$

where the scale factor  $K = 2.6 \times 10^{-3}$  meter/Hz  $\cdot$  sec<sup>2</sup>. Digitally integrating the difference frequency yields velocity information,

$$V(t) = K \int \Delta F(t) dt$$

Performing a second integration reduces the data to the required displacement or inertial information,

$$X(t) = K \int \int \Delta F(t) dt$$

Shown in Fig. 8 is the actual count output of a SAW accelerometer when measured with a 1 sec gate time. The difference frequency was 60 kHz which has been subtracted out and only the deviation in the difference frequency ( $\pm 1$  Hz) is shown. Summing the counts results in the velocity count ( $\pm 10$  Hz\*sec) as a function of time shown. This curve represents the area under the acceleration-frequency curve. Performing another summation as a function of time results in the curve for displacement ( $\pm 4000$  Hz\*sec<sup>2</sup>). The scale factor was 20 ppm/g or 769 Hz/m/sec<sup>2</sup>. The integrated velocity error for the 1000 sec time period shown was typically less than 0.013 m/sec and the displacement error less than 5.2 meters. As expected the integrated error is closely related to the integration time and this is dependent upon the actual mission time or time for which no other inertial guidance data is available.

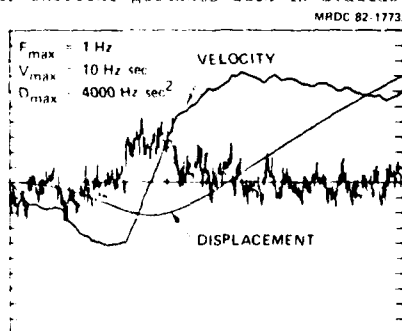


Fig. 8 Frequency output (a) from a SAW accelerometer and digitally processed velocity (b) and displacement (c) data information. (Time span = 30 min)

## Conclusions

An experimental SAW underwater sound sensor was constructed and evaluated in terms of static and dynamic loading. The results of static loading indicates that mounting of the crystal is important in order to achieve maximum sensitivity to applied loading. A SAW oscillator-sensor was configured as a hydrophone and compared in a water tank with a calibrated hydrophone. The SAW sensor was found to be comparable in sensitivity to conventional hydrophones over the frequency range 0-1000 Hz. The frequency deviation in a SAW sensor is constant and this causes an increase in the signal-to-noise ratio as the modulation frequency decreases. As a hydrophone, the SAW sensor is well suited when the frequencies of interest are in the low audio range.

SAW sensors were also tested as accelerometers for inertial guidance. Tests were performed on integrated noise levels for simulated guidance mission times. For times up to 1 hour, cumulative displacement error rates less than 20 meters/hour were achieved. This data is to be compared with typical error rates for moderately accurate accelerometers of 1 nautical mile per hour or 1851 meters per hour.

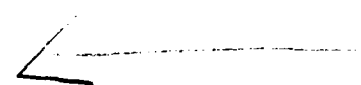
These results are encouraging and future studies will no doubt improve on the performance already demonstrated.

## References

1. T.M. Reeder, D.E. Culler and M. Gilden, "SAW Oscillator Pressure Sensors," IEEE Ultrasonics Symposium Proceedings, pp. 264-268 (1975).
2. J.F. Dias, H.E. Karrer, J.A. Kusters and C.A. Adams, "Frequency/Stress Sensitivity of SAW Resonators," Electronics Letters, 12, No. 22, pp. 580-582 (1976).
3. D.F. Weirauch, R.J. Schwartz and R.C. Bennett, "SAW Resonator Frit-Bonded Pressure Transducer," IEEE Ultrasonics Symposium Proceedings, pp. 874-877 (1979).
4. E.J. Staples, J. Wise, J.S. Schoenwald and T.C. Lim, "Surface Acoustic Wave Underwater Sound Sensors," IEEE Ultrasonics Symposium Proceedings, pp. 870-873 (1979).
5. C. Adams and J.A. Kusters, "Deeply Etched SAW Resonators," Proceedings of the 31st Annual Frequency Control Symposium, U.S. Army Electronic Command, Ft. Monmouth, New Jersey, pp. 24-250, June 1977.
6. S.J. Dolochycki, E.J. Staples, J. Wise, J.S. Schoenwald and T.C. Lim, "Hybrid SAW Oscillator Fabrication and Packaging," Proceedings of the 33rd Annual Frequency Control Symposium, U.S. Army Electronic Command, Ft. Monmouth, New Jersey, pp. 374-378, June 1979.

7. E.J. Staples and T.C. Lim, "300 MHz Oscillators Using SAW Resonators and Delay Lines," Proceedings of the 31st Annual Frequency Control Symposium, U.S. Army Electronic Command, New Jersey, pp. 371-373, June 1977.

8. J.S. Schoenwald, J. Wine and E.J. Staples, "Absolute and Differential Aging of SAW Resonator Pairs," Proceedings of the 35th Annual Frequency Control Symposium, U.S. Army Electronic Command, New Jersey.



## A SURFACE ACOUSTIC WAVE GAS DETECTOR\*

A. Bryant, M. Poirier, D.L. Lee and J.F. Vetelino  
 Department of Electrical Engineering and Laboratory for Surface  
 Science and Technology, University of Maine, Orono, Maine 04469

## Summary

Experimental results are presented on a new type of gas detector employing surface acoustic waves (SAW's). The SAW piezoelectric gas detector (SAWPG) consists of twin SAW delay lines fabricated on a single piezoelectric substrate each connected in an oscillator configuration. The propagation path of one delay line oscillator is coated with a selectively sorbent film, while the other is uncoated and used as a stable reference. Changes in phase delay resulting from mass loading or stress effects induced by gases sorbed on the delay line containing the film result in corresponding frequency shifts relative to the reference oscillator that are proportional to gas concentration. Since SAW energy is concentrated near the film, the detector is found to be highly sensitive. Further, the SAWPG offers the means to detect any gas given the corresponding selectively sorbent film.

For demonstration purposes, a detector has been realized for measuring sulfur dioxide ( $\text{SO}_2$ ) in air using a triethanolamine film and it has been shown that it is possible to detect  $\text{SO}_2$  at a concentration level of 10 parts per billion. The sensitivity, linearity, reproducibility, selectivity and reliability have been investigated and have been found, in many cases, to be superior to that found in other types of gas detectors. Primary limitations in device performance such as film selectivity and stability with time are discussed as well as potential means for improvement and directions for further research.

## Introduction

There is a need in both the commercial and military markets for a highly sensitive and selective means of detecting gases. Potential applications for such a device include monitoring of industrial processes, testing of pollution emission levels, and detection of very toxic gases in battlefield environments. To meet the requirements of such a wide range of applications, the detector should not only be highly sensitive and selective, but also small, rugged and inexpensive.

Some of the more common approaches which have been taken to realize such detection include the monitoring of (1) the V-I characteristics of solid state devices,<sup>1</sup> (2) the electrical conductance of thin films,<sup>1</sup> (3) the ionic conductivity of electrochemical gas sensors,<sup>1</sup> (4) the frequency of oscillation of piezoelectric bulk wave gas sensors,<sup>2</sup> and (5) the frequency of oscillation of piezoelectric surface acoustic wave gas sensors.<sup>3,4</sup>

The above-mentioned approaches can be divided into two general categories. Under one category are included those approaches in which the electrical properties of devices are monitored to detect the presence of a gas. The other category includes the bulk wave and surface acoustic wave gas sensors which signal the presence of gases by changes in their frequency of oscillation. It is this latter approach that is of concern in this work.

The use of a piezoelectric bulk wave oscillator as a gas sensor was first introduced by King.<sup>2</sup> The bulk wave piezoelectric gas detector (BWPG) is a simple piezoelectric device consisting of a bulk wave resonator coated with a selectively sorbent film. Detection occurs when mass loading, due to the selective sorption of a particular gas, produces a shift in the resonant frequency of the device. The BWPG detector can be used to detect many gases providing that a corresponding selectively sorbent film can be found. The BWPG detector has been used to detect microconcentrations of gases such as hydrogen sulfide, ammonia, hydrogen chloride and sulfur dioxide.<sup>5</sup> When coated with the same partitioning liquids used in gas chromatography columns, the BWPGD can also be used as the detector in a gas chromatograph.<sup>5</sup> In this application, the coating used is not necessarily selectively sorbent, since selectivity is provided by separation of gases in the chromatograph column.

Wohltjen and Dessy<sup>6</sup> extended the principle of the bulk wave chromatograph detector to surface acoustic wave (SAW) devices. They coated the delay path of a single SAW oscillator with partitioning films and attached the oscillator to the outlet of a gas chromatograph column. As separated gases passed through the outlet of the column, they were sorbed by the partitioning film. Detection of the separated gases occurred when their sorption by the partitioning film changed the SAW properties of the delay line path and, as a result, caused a shift in the oscillation frequency.

Recently, a surface acoustic wave piezoelectric gas detector (SAWPG) was introduced. The detector utilizes two SAW delay lines fabricated on the same substrate, each configured as an oscillator, to detect toxic and non-toxic gases. One delay line is coated with a film which selectively sorbs a particular gas while the other is uncoated and acts as a reference. Gas sorbed by the film alters the SAW characteristics which in turn causes the oscillating frequency to change. The relative change in the frequency of the two oscillators is monitored to measure the concentration of the gas.

\*This work was supported in part by NSF Grant No. SPI-8026415.

†Patent application has been prepared and filed in the U.S. Patent and Trademark Office.

AD P001534

The device geometry is shown in Figure 1. The relative shift in frequency between the two oscillators is obtained by mixing to obtain the difference frequency, passing the resulting signal through a low pass filter and a frequency to voltage converter.

#### Fundamental Limitations on Device Resolution

In many gas sensor applications, it may be desirable to detect as small a gas concentration as possible. The smallest detectable concentration which can be measured is a function of two important parameters: (1) the detector's frequency stability over time and (2) the sensitivity, that is the change in frequency,  $\Delta f$ , with change in gas concentration,  $\Delta c$ . The influence of these two factors is demonstrated in Figure 2 for two devices exhibiting the same random frequency fluctuation levels,  $\Delta f_{\min}$ , over some time period but with two different sensitivities.

It is apparent that those parameters which increase sensitivity without a corresponding increase in frequency fluctuations improve device resolution. For any given sensor, the magnitude of the frequency fluctuations,  $\Delta f_{\min}$ , depends on the time frame over which gas measurements are made. Typically SAW oscillator frequency stability is governed by either 1/f flicker phase noise, thermal drift, or aging depending on whether frequency measurement time intervals are short term (< seconds), medium term (< minutes or hours), or long term (> weeks, years). Thus gas sensor resolution must be defined within the context of the measurement time involved. While typical frequency stability over these three time scales is well documented for single SAW delay line oscillators placed in a sealed package, little is known about their behavior when exposed to the environment. Further, the influence of both the dual delay line configuration as well as the sorptive film on stability has apparently not been studied.

#### Detector Frequency Stability

To investigate the baseline frequency stability with time, a dual delay line was fabricated on Y-Z cut lithium niobate ( $\text{LiNbO}_3$ ). This material was chosen primarily due to its high coupling coefficient. This allowed low insertion loss IDTs having few finger pairs to be fabricated, thus maximizing the propagation path length on the substrate for film coating. An undesirable property of  $\text{LiNbO}_3$  SAW oscillators is high temperature instability. However, the frequency of the coated delay line oscillator is measured relative to that of the uncoated delay line on the same substrate; hence, the effect of this temperature instability is minimized. Further, the relatively large TCD of  $\text{LiNbO}_3$  facilitated investigation of the extent to which such temperature compensation was effective.

The delay lines fabricated on the  $\text{LiNbO}_3$  substrate had a 60 MHz center frequency with 30 finger pairs per IDT and a beam width of 3.49mm. The distance between IDT pairs was 2.62cm. Configured as oscillators, the frequencies of oscillation of the

two devices differed by 90 KHz. The delay line having the highest frequency of oscillation was used as the delay line to be coated.

In order to demonstrate the SAWPG detector, the delay line was coated with triethanolamine (TEA) which is an organic liquid selectively sorbent to  $\text{SO}_2$ .  $\text{SO}_2$  was chosen as a candidate gas since it is a very common gas effluent in industrial stacks and in the exhaust of automobiles. It is also often used as an index for air pollution. The use of  $\text{SO}_2$  as a candidate gas also offers the opportunity to compare the SAWPG sensor to the BWPG detector since the latter has previously been used to measure  $\text{SO}_2$  in conjunction with TEA.

The TEA films were applied using a small brush with a 2% solution of TEA in chloroform. Upon application, the chloroform would evaporate quickly, leaving a thin film of TEA on the surface of the delay line path. The TEA films not only produced downward shifts in the frequency of oscillation of the coated delay line, but also attenuated the SAW signal.

To accurately characterize films in terms of film uniformity and thickness is difficult, especially since the films form island structures when applied to the substrate surface. In order to obtain a rough measure of the film uniformity and thickness, the SAW device was used as a monitoring mechanism. It was found that films producing an initial downward shift in the difference frequency of about 60 KHz and an increase in SAW attenuation of approximately 8dB upon application were the most reproducible. Hence, in this work, only TEA films producing the aforementioned difference frequency and SAW attenuation were used.

Baseline frequency stability for gas detection was taken under ambient conditions over a period of 12 hours, measured from the time of application of the TEA film, and is compared with the response of the same sensor in absence of the film. The results are shown in Figure 3. It is observed that the TEA film stabilizes in a roughly exponential fashion over this period. This stabilization is likely due to the evaporation of the volatile solvent (chloroform) with which the film was mixed. Figures 4 and 5 show a comparison of the stability between coated and uncoated devices during one hour and five minute intervals, measured 12 hours after the film had been placed on the delay line. There appears to be no statistically significant difference in response between coated and uncoated substrates. The observed small fluctuations of the order of a part per million in these figures did not appear to be due to thermal factors. This was determined by placing the uncoated sensor in an environmental test chamber stabilized to  $\pm 0.1^\circ\text{C}$ . The measured frequency stability is shown in Figure 6, which shows no significant improvement. A first order measure of insensitivity to temperature was obtained by cycling the uncoated sensor slowly over a nominal 20°C range. The substrate temperature variation as well as sensor difference frequency is shown in Figure 7. It is apparent that the sensor was extremely sensitive to thermal gradients resulting from dynamic cycling but had excellent temper-

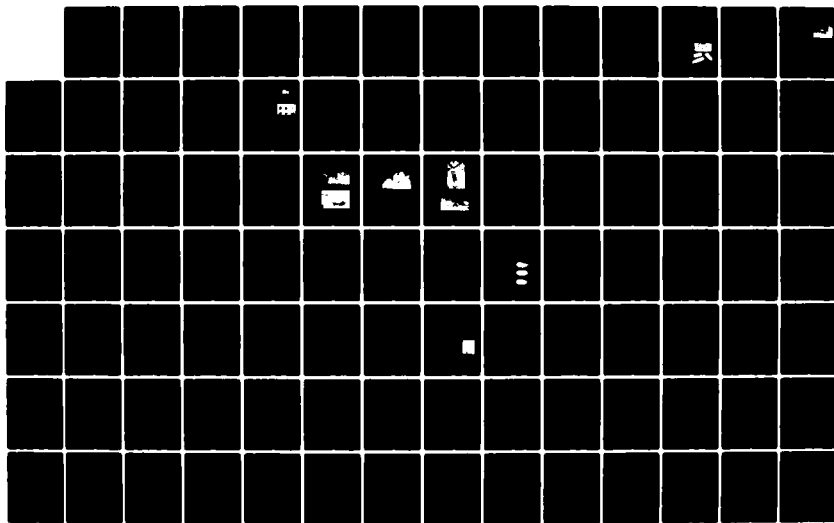
AD-A130 811 PROCEEDINGS OF THE SYMPOSIUM ON FREQUENCY CONTROL (36TH ANNUAL) 2-4 JUNE 1..(U) ARMY ELECTRONICS RESEARCH AND DEVELOPMENT COMMAND FORT MONMOUTH. E PAIGE ET AL. 1982

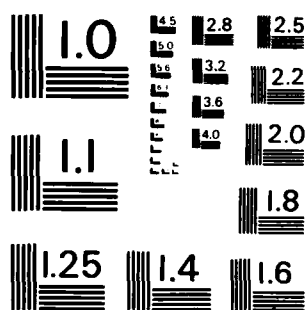
AD-A130 811 PROCEEDINGS OF THE SYMPOSIUM ON FREQUENCY CONTROL (36TH ANNUAL) 2-4 JUNE 1..(U) ARMY ELECTRONICS RESEARCH AND DEVELOPMENT COMMAND FORT MONMOUTH. E PAIGE ET AL. 1982

UNCLASSIFIED F/G 20/14

F/G 20/14

NL





MICROCOPY RESOLUTION TEST CHART  
NATIONAL BUREAU OF STANDARDS - 1963 - A

ature cancellation properties under static conditions. Once thermal equilibrium was achieved, overall device TCD was less than 0.1 ppm/°C, approximately a 1,000-fold improvement over single delay line performance. Two possible causes of the observed fluctuations are mechanical vibration or air currents. The first alternative is reasonably likely due to the fact that the SAW RF amplifiers were connected to the SAW sensor probe by fairly long cables. It is further considered unlikely that the fluctuations are due to flicker noise because the observed fluctuations are several orders in magnitude larger than those generally reported. However it should be noted that flicker noise data in the literature is generally available for quartz rather than  $\text{LiNbO}_3$ , so that a definitive comparison cannot be made. It can be concluded based upon these stability measurements that after the TEA film has stabilized, random frequency fluctuations,  $\Delta f_{\text{min}}$ , of from several ppm to several tenths of a ppm can be expected over measurement times in the second to hour range.

#### Repeatability

Repeatability of the SAWPGD was obtained by measurement of frequency changes due to repeated exposure to the same  $\text{SO}_2$  concentration in air. The coated sensor, was placed on the 144 ml air-filled test chamber shown in Figure 8.

$\text{SO}_2$  was injected in 1 ml samples into the test cell through a rubber septum. The pressure relief bellows shown were used to insure that no pressure changes were induced as a result of the gas injection. The dilutions of  $\text{SO}_2$  in air were attained using the syringe dilution method described by Karmarkar and Guilbault.<sup>7</sup> Figure 9 shows the typical frequency shifts with time resulting from device exposure to 7 ppm of  $\text{SO}_2$  in air. In each of these curves the beginning of the detector response was usually 10 to 15 seconds after the infusion of the  $\text{SO}_2$  gas into the test cell. The drift in the difference frequency was accounted for in Figure 9 by extrapolating the drift rate observed in the minute before the injection of  $\text{SO}_2$  into the test cell and subtracting it from the measured SAWPG detector response. The changes shown in the difference frequency correspond to decreases in the frequency of oscillation of the coated delay line. These responses appear to be exponentially asymptotic. The observed time constant may be a function of both the TEA film sorption properties as well as the gas diffusion mechanism inside the test chamber.

After each of the indicated five tests the SAW device was removed from the test cell and exposed to the laboratory air for 20 minutes to allow the TEA film to desorb the  $\text{SO}_2$ .

In order to quantify the detector repeatability as well as provide a measure of device response to any given concentration, the change in the difference frequency after a three minute interval was chosen to represent the response,  $\Delta F$ , of the SAWPG detector. Such a choice was required because, particularly for low gas concentration levels, it was impossible to estimate the asymptotic value of the frequency shift because of device frequency drift.

Using such a criterion, the average three minute response,  $\langle \Delta F \rangle$ , of the curves illustrated in Figure 9 is 1.220 KHz with standard deviation of 8%.

- The previously described experiment was then repeated for two other TEA films. The observed values of  $\langle \Delta F \rangle$  for these two films were 1.200 KHz and 1.150 KHz. This results in an average frequency shift of 1.190 KHz for the three different films with a standard deviation of 2%.

#### Sensitivity, Linearity and Range

The measured response of the SAWPG detector at room temperature to differing gas concentrations ranging between 70 ppb and 7 ppm is shown in Figure 10 along with a comparison of a bulk wave sensor response reported by Karmarkar and Guilbault for the same film and pollutant.<sup>7</sup> The SAWPG detector was found to be linear down to about 1 ppm. The apparent decrease in sensitivity below 1 ppm is likely to be due to the longer time required for film saturation at lower concentrations. If it is assumed that the saturation value of  $\text{SO}_2$  sorbed by the film is proportional to the gas concentration, then for high concentration values the film is saturated by the end of the three minute measurement interval and therefore faithfully reflects the true gas concentration; for lower concentration levels, saturation does not occur over this time period yielding a smaller effective value for gas concentration.

It was found that the lowest concentration of  $\text{SO}_2$  producing a repeatable and definite response was 70 ppb. Detector responses to concentrations below 70 ppb were not repeatable and approached the same order of magnitude as changes in the drift of the difference frequency due to film instability. Hence, the resolution of the SAWPG detector using this exposure method is determined by the stability of the sorbent film used.<sup>5</sup> The upper limit on concentration was determined by an increase in TEA film attenuation causing the coated delay line to cease oscillation. This upper limit can easily be varied by either changing film path length or amplifier gain.

#### Comparison to Bulk Wave Gas Sensors

While it is apparent from Figure 10 that the sensitivity of the SAWPG detector is superior to that reported on a BWPG sensor,<sup>7</sup> the latter has been reported to have a resolution of better than 10 ppb for  $\text{SO}_2$  when used in a flow system arrangement. To facilitate a meaningful comparison, tests of the SAWPG detector and a BWPG sensor were performed using an air gas flow arrangement similar to that reported in [8]. The arrangement is shown in Figure 11. Air is continually pumped through tubing leading to the test chamber at a rate of between 25 and 50 ml per minute and passes into a 40 ml glass test cell containing either the SAWPG or BWPG detector. When a small  $\text{SO}_2$  sample is injected into the tubing it is carried by the stream onto the detector surface and is subsequently exhausted out of the test cell into the atmosphere. This system therefore provides a short "pulse" of  $\text{SO}_2$  to the sensor. The two detectors used in the

measurements are shown mounted in their identical test cells in Figure 12. The bulk wave sensor consists of two 11 MHz AT-cut quartz bulk wave crystals one of which has been coated on both sides with the TEA film. The other uncoated crystal acts as a reference. Each crystal is connected in an oscillator configuration and mixed to obtain a difference frequency in the same fashion as with the SAWPG sensor. Frequency stability under ambient conditions for the BWPG detector measured over 12 hours with and without a TEA film was observed to be very similar in nature to that of the SAWPG shown in Figure 3. The two devices show similar aging characteristics for the film in both rate and in magnitude of change of  $\Delta f/f$  with time.

The response of the SAWPG detector in the flow system was measured for a number of different  $\text{SO}_2$  concentrations injected into the line. The exact concentration incident upon the SAW surface is not known due to possible diffusion during travel along the tubing. Thus the injected gas levels represent an upper concentration limit. Figure 13 shows the response to a 5 ml injection of 100 ppb of  $\text{SO}_2$  (upper curve) a 5 ml injection of air (lower curve). The sample was injected at the three minute mark on the figure. The small precursor prior to the response to  $\text{SO}_2$  followed immediately after injection and is believed to result from pressure fluctuations due to the injection. The time constant of the response fluctuations was comparable to the travel time required for the injected  $\text{SO}_2$  to reach the detector. Using this technique responses to gas concentrations as low as 10 ppb were obtained. The lower limit was determined not by frequency drift but by the inability to time resolve responses due to  $\text{SO}_2$  from pressure induced frequency fluctuations resulting from the injection.

Figure 14 shows a typical response from the BWPG sensor to both air and a concentration of 10 ppm of  $\text{SO}_2$  injected at the one minute mark. The fractional frequency change resulting from the  $\text{SO}_2$  is observed to be less than that for the SAWPG detector even though the  $\text{SO}_2$  gas concentration is two orders of magnitude higher. The minimum resolvable  $\text{SO}_2$  concentration which could be detected with the bulk wave sensor using the flow system was about 1 ppm, limited again by the inability to distinguish between injection of  $\text{SO}_2$  and pressure fluctuations.

#### Selectivity

An ideal  $\text{SO}_2$  gas detector should respond to  $\text{SO}_2$  only. However, TEA has been found to sorb gases other than  $\text{SO}_2$ , though not to the same extent. The selectivity of the TEA coated BWPG detector with respect to pollutants has been investigated, and the one gas other than  $\text{SO}_2$  found to produce an appreciable response is  $\text{NO}_2$ .<sup>7,8</sup> Similar results were observed with the SAWPG detector. This is to be expected, since the selectivity is a property of the TEA film. It should be added that the sorption of  $\text{NO}_2$  by TEA is an irreversible process decreasing the sensitivity of a TEA film. However, Cheney and Homolya<sup>9</sup> have reported that once a TEA film is treated with a sufficiently high concentration of  $\text{NO}_2$  so that it becomes insensitive to further  $\text{NO}_2$ , it still remains sensitive to  $\text{SO}_2$ . In a situation

where selectivity is a problem, use of a separate detector for the interfering gas would offer a potential solution to this problem.

#### Discussion and Conclusions

The SAWPG detector has been demonstrated to be extremely sensitive, capable of resolving gas concentrations of  $\text{SO}_2$  as low as 10 ppb. The minimum detectable  $\text{SO}_2$  level has been shown to be a function of the time period over which the gas measurement is made, being limited by the magnitude of the frequency fluctuations within this time interval resulting from film drift and small environmental perturbations such as mechanical vibration and air currents. Use of a flow system to inject transient "pulses" of  $\text{SO}_2$  has provided a mechanism for shortening the required measuring time resulting in improved resolution. For the SAWPG device tested, sensitivity and resolution are two orders of magnitude higher than a comparable bulk wave sensor. Improvements in the gas feed technique to eliminate pressure fluctuations upon injection which perturb the sensor may allow improvement in resolution to closer to the theoretical flicker noise limit.

Limitations on device performance are presently primarily a function of the film being used. It is anticipated that appropriate solid films will provide higher stability, longevity, and improved aging characteristics making the SAWPG gas detector a viable means for sensitive gas measurements. Further, if SAW delay line and RF electronics are integrated onto a single chip, the potential exists for small, rugged, low power and inexpensive gas sensor for laboratory and field applications.

#### References

1. Proceedings of Materials Research Conference, Section K, Gas Sensors, Boston, Mass. Nov. 15-19, 1981, (in press).
2. William H. King, Jr., "Piezoelectric sorption detectors," *Anal. Chem.*, Vol. 36, pp. 1735-1739, 1964.
3. A. Bryant, D. L. Lee, J. F. Vetelino, "A surface acoustic wave gas detector," *Proc. IEEE 1981 Ultrasonics Symp.*, pp. 171-174.
4. C. T. Chuang, R. M. White, "Sensors utilizing thin-membrance SAW oscillators," *Proc. IEEE 1981 Ultrasonics Symp.*, pp. 159-162.
5. J. Hlavay, G. G. Guilbault, "Applications of the piezoelectric crystal detector in analytical chemistry," *Anal. Chem.*, Vol. 49, pp. 1890-1898, 1977.
6. H. Wohltjen, R. Dessy, "Surface acoustic wave probe for chemical analysis," *Anal. Chem.*, Vol. 51, pp. 1458-1475, 1979.
7. K. H. Karmarkar, G. G. Guilbault, "A new design and coatings for piezoelectric crystals in measurement of trace amounts of sulfur dioxide," *Anal. Chem. Acta*, Vol. 71, pp. 419-424, 1974.
8. K. H. Karmarkar, G. G. Guilbault, "Detection and measurement of aromatic hydrocarbons in the air by a coated piezoelectric detector," *Envir. Lett.*, Vol. 10, pp. 237-246, 1975.
9. J. L. Cheney, J. B. Homolya, "A systematic approach for the evaluation of the triethanolamine as a possible sulfur dioxide sorption detector

coating," Anal. Lett., Vol. 8, pp. 175-193, 1975.

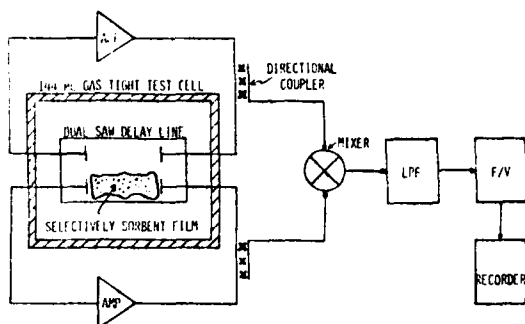


Figure 1. SAW piezoelectric gas (SAWPG) detector system.

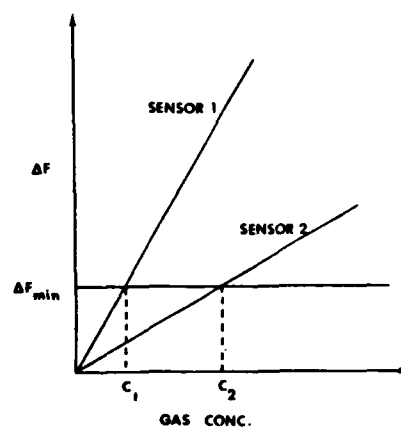


Figure 2. Comparison of minimum detectable gas concentration for two sensors having the same frequency stability,  $\Delta f_{\min}$ , but with different sensitivities.

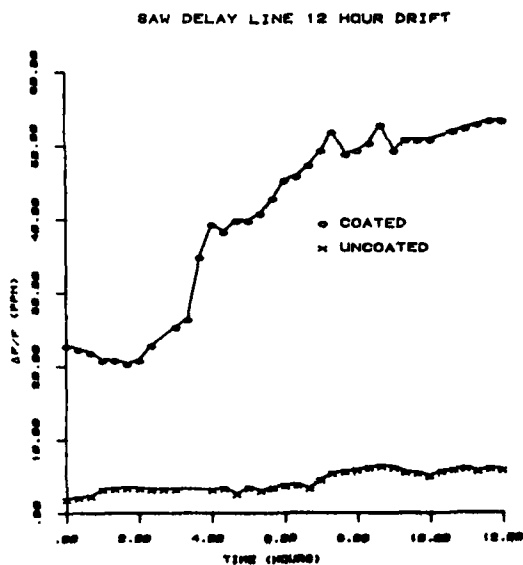


Figure 3. Comparison of frequency stability for SAWPG sensor under ambient conditions for first 12 hrs. after application of TEA film, and in absence of TEA film.

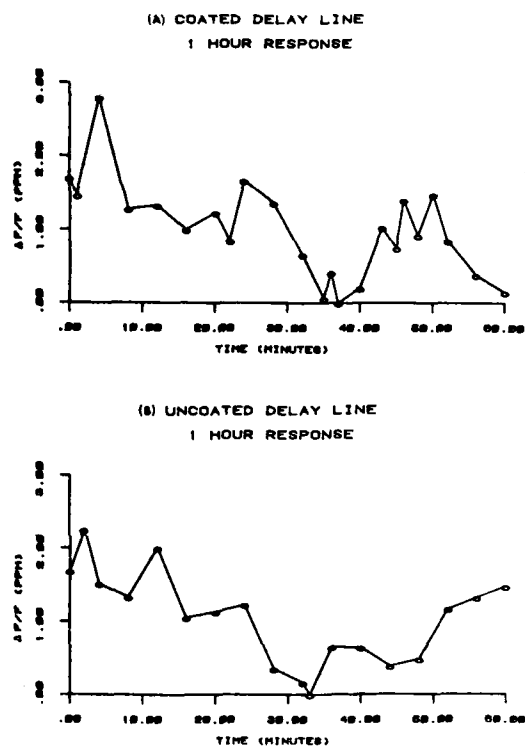
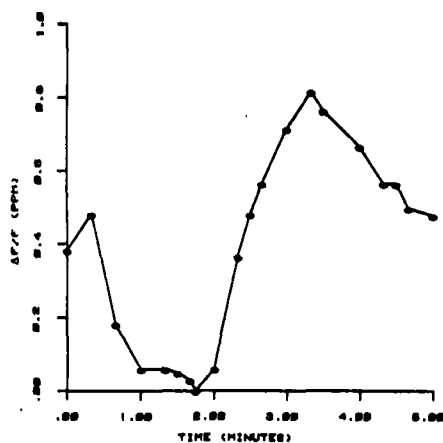
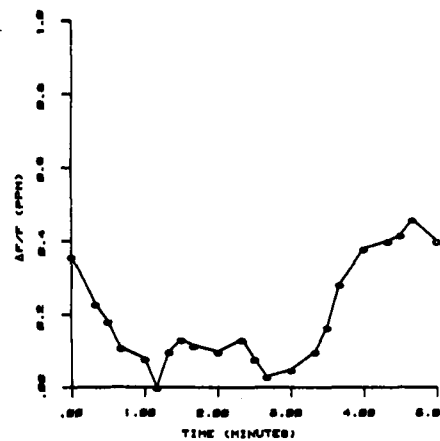


Figure 4. Frequency stability for SAWPG sensor over 1 hr. period (a) 12 hrs. after application of film (b) uncoated.

(A) COATED DELAY LINE  
5 MINUTE RESPONSE



(B) UNCOATED DELAY LINE  
5 MINUTE RESPONSE



UNCOATED SAW RESPONSE  
AT CONSTANT TEMPERATURE (23.5°C)

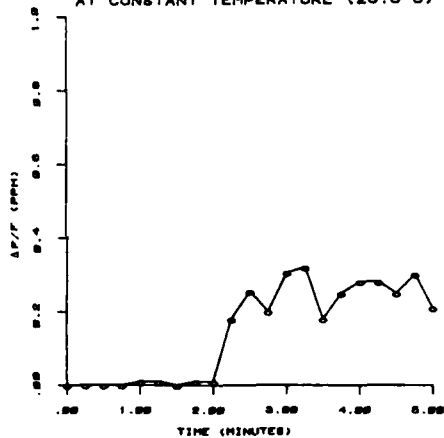


Figure 5. Frequency stability for SAWPG sensor over 5 minute period (a) 12 hrs. after application of film (b) uncoated.

Figure 6. Frequency stability for uncoated SAWPG sensor over 5 minute period in oven stabilized to  $\pm 0.1^\circ\text{C}$ .

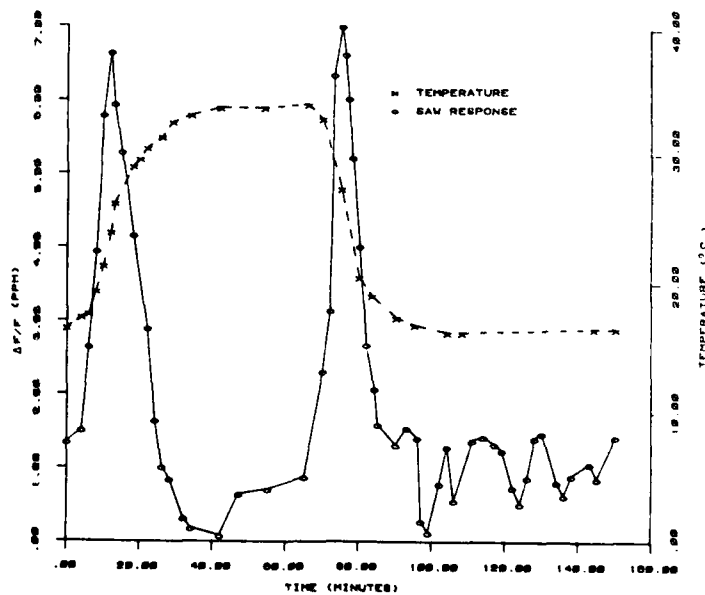


Figure 7. Frequency stability as a function of temperature for dual delay line SAWPG sensor configuration (uncoated).

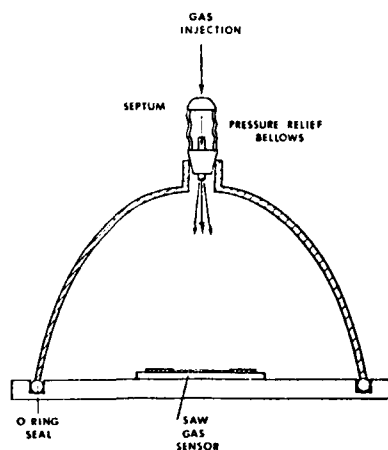


Figure 8. Test chamber for static gas measurements.

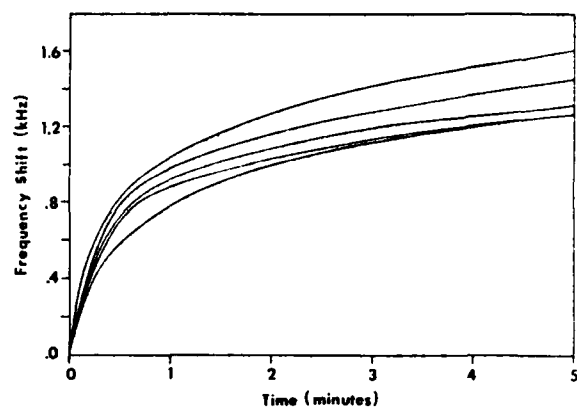


Figure 9. Repeatability of SAWPG sensor frequency shift with time for 5 separate trials with 7 ppm of  $\text{SO}_2$ .

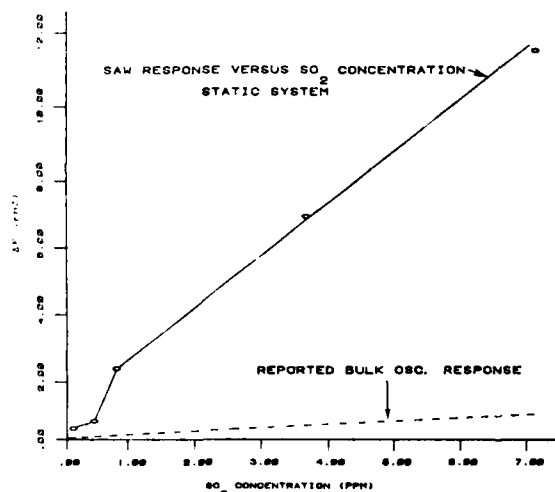


Figure 10. Linearity of SAWPG sensor response for various  $\text{SO}_2$  gas concentrations and comparison with reported results for bulk wave gas sensor.

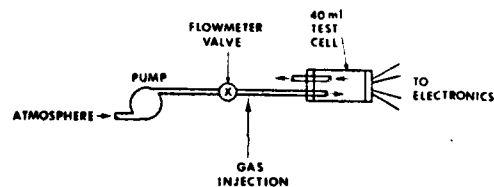
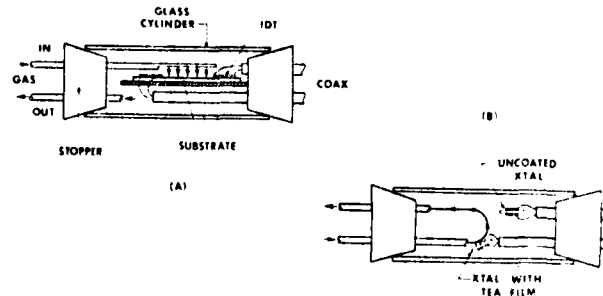


Figure 11. Apparatus for gas flow injection test system.

Figure 12. 40 ml. test cell containing (a) SAWPG and (b) BWPG sensor.



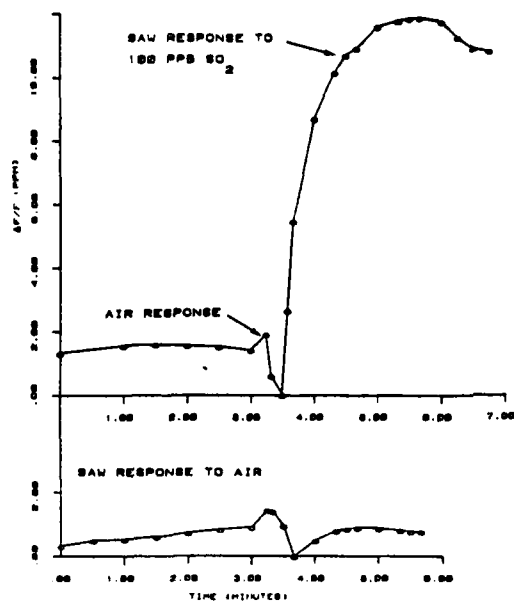


Figure 13. SAWPG sensor response to 100 ppb of  $\text{SO}_2$  using gas flow system.

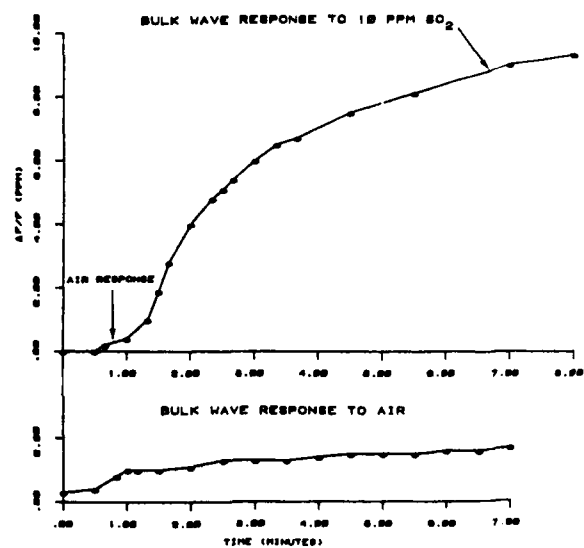


Figure 14. BWPG sensor response to 10 ppm of  $\text{SO}_2$  using gas flow system.

## PRESSURE AND TEMPERATURE MEASUREMENTS WITH SAW SENSORS

D. Hauden, S. Rousseau, G. Jafflet, E. Coquerel

Laboratoire de Physique et Métrologie des Oscillateurs du C.N.R.S.  
associé à l'Université de Franche-Comté-Besançon  
32, avenue de l'Observatoire - 25000 Besançon - France

Summary

Two different SAW-sensors are presented : a pressure-sensor for weak pressure and a SAW-temperature sensor.

The pressure sensor is built with a thin diaphragm of quartz-crystal on which two surface elastic waves are propagating in the same direction but at two different lateral positions. Pressure variations applied on the lower surface induce a strong bending which modifies both wave velocities. A differential detection enables to measure wave velocity variations (or corresponding oscillator frequency shifts) and also enables to eliminate in a large scale spurious velocity (or frequency) variations due to temperature fluctuations. Calculations of strain distribution and then of corresponding frequency shifts give both positions of SAW delay lines on the thin diaphragm to have a maximal pressure sensitivity and to minimize temperature effects at the same time. Theoretical results of Y-cut are compared with measurements performed at 105 MHz.

Temperature sensors built with quartz plates having LST and JCL crystallographical orientations have been tested in sensitivity (28 ppm/K), linearity, response time (0.1 s) and resolution (0.1 K). Temperature measurements obtained with SAW temperature sensor are compared with that one measured with a PAW temperature sensor (LC-cut). A new type of quartz thermometer using SAW temperature probes is proposed.

Introduction

The characteristics of surface acoustic waves are modified by external effects as temperature and mechanical perturbations (forces, pressures, ...). It has been shown that sensitivity is due to the nonlinear elastic properties of the crystal. These phenomena are advantageously used for sensor applications if the SAW is made selectively sensitive to a given physical quantity. Measurements are transposed into frequency measurement and high resolutions are obtained.

Under pressure variations, stress and strain fields are induced, which are function of the applied static forces. The static bias and

the wave are coupled by the nonlinear properties of the crystal which in the problem here considered are the third order elastic terms. The static deformation is calculated by using Mindlin's polynomial expansion and the corresponding velocity and/or frequency shifts are obtained by means of a perturbation method<sup>1,4</sup>. Following this method, the study of a pressure sensor is presented in this paper.

A new type of piezoelectric temperature sensor, presented here, uses thermal properties of SAW propagating on quartz crystal substrat<sup>5</sup>. From values obtained theoretically a temperature probe was built and tested to determinate its sensitivity and its linearity<sup>6</sup>. Different methods of response time measurements are performed and compared with values measured with B.W. temperature probe. Summarized results are given here with performances of a new SAW quartz thermometer.

Frequency shifts due to mechanical perturbations

The elastic equations of a finite amplitude wave propagating on a medium of specific mass  $\rho_0$ , submitted to a mechanical bias can be written with respect to the natural state  $a_1$

$$\rho_0 \ddot{u}_i = (\overline{A}_{ikjm} u_{j,m})_{,k} \quad (1)$$

Boundary conditions corresponding to a stress free surface are :

$$\overline{A}_{ikjm} u_{j,m} = 0 \quad \text{for } a_2 = 0 \quad (2)$$

$\overline{A}_{ikjm}$ -coefficients represent the nonlinear coupling between the static deformation and the high frequency wave. Consequently they are related to the static components (stresses, strains, displacements) and they can be presented as modified elastic constants following :

$$\overline{A}_{ikjm} = C_{ikjm} + H_{ikjm} \quad (3)$$

where the nonlinear coupling terms  $H_{ikjm}$  are function of space variables  $a_1$ .

AD P0015351

Calculations of  $\overline{H}_{ikjm}$ -terms have to take into account the functional dependance along the plate thickness by using a polynomial expansion

$$\overline{H}_{ikjm} = \sum_n \overline{a}_{ikjm}^{(n)} a_2^n \quad (4)$$

These coefficients are considered as small terms with respect to the second elastic constants  $C_{ikjm}$ . Thus, a perturbation method is directly applied and leads to the relative frequency shifts

$$\frac{\Delta f}{f_0} = \frac{\sum_n \sum_{p,q} \left[ \frac{A_p \overline{u}_p^{(p)}(p) A_q \overline{u}_q^{(q)}(q) u_m^{(p)} u_k^{(q)} u_l^{(n)} \overline{a}_{ikjm}^{(n)}}{(q_p - q_q) \left[ i \frac{v_0}{v_0} (q_p - q_q) \right]^n} \right]}{2 v_0 v_0 \sum_{p,q} \frac{A_p \overline{u}_p^{(p)}(p) A_q \overline{u}_q^{(q)}(q)}{q_p - q_q}} \quad (5)$$

This equation is general and can be used whatever the perturbation is. For each particular problem the static stress and strain distribution will be calculated.

Following Mindlin<sup>3</sup>, if thin plates of thickness  $2h$  are considered, the mechanical displacements  $U_i$  are written

$$\overline{U}_i = \sum_n \overline{U}_i^{(n)} a_2^n \quad (6)$$

The corresponding strains and stresses are developed the same way

$$\overline{S}_{ij}^{(n)} = \frac{1}{2} \left[ \overline{U}_{i,j}^{(n)} + \overline{U}_{j,i}^{(n)} + (n+1) (\delta_{2j} \overline{U}_i^{(n+1)} + \delta_{2i} \overline{U}_j^{(n+1)}) \right] \quad (7)$$

where  $\delta_{ij}$  is the Kronecker symbol.

Then strain-stress relations become

$$\overline{T}_{ij}^{(n)} = C_{ijkl} \sum_m K_{mn} \overline{S}_k^{(m)} \quad (8)$$

where  $K_{mn}$  is a constant equal to zero if  $m+n$  is odd and equal to  $2h^{m+n+1}$  if  $m+n$  is even.

#### S.A.W. pressure sensor

The sensitivity of SAW delay line to hydrostatic pressure is generally small, about 3 Hz/kPa at 105 MHz.

The sensitivity can be increased by using a thin circular diaphragm<sup>7,8</sup>. Those is built with a thin anisotropic plate clamped at its edges and submitted to a pressure on its lower surface (fig. 1).

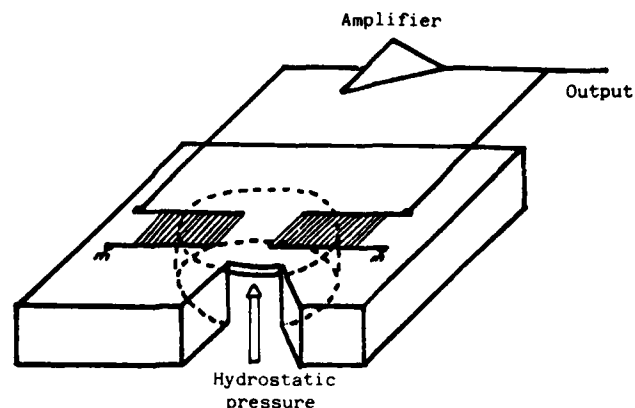


Fig. 1  
Thin circular diaphragm used as pressure sensor

For describing such an anisotropic diaphragm stiffly clamped all around a three-dimensional model is necessary. In account of the difficulty to solve it directly, the problem was split into two parts :

- a cross section in the  $a_1 a_2$  plane, normal to the main surfaces of the diaphragm, is first considered, with the boundary conditions  $T_{22} = 0$  at  $a_2 = 0$ ,  $T_{22} = P$  at  $a_2 = -2h$  and the edge conditions  $U_1 = U_2 = U_{2,1} = 0$  at  $a_2 = 0$  and  $a_1 = R$ . The stress and strain distribution are analytically calculated in this bi-dimensional model by using the polynomial method.

- then the solutions are transposed to any cross-section normal to the main surfaces (fig. 2). The stress and strain distributions are calculated at a point M whatever its position is in the cross section. By superposing at the point M the solutions corresponding to the all possible cross sections (this is equivalent to performing an integration over  $360^\circ$ ) the total stresses and strains are obtained at the point M.

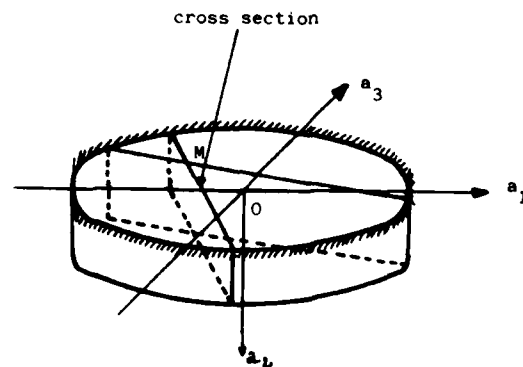


Fig. 2 : Cross sections used in the calculation of stress and strain distributions at a point M

The perturbation method gives the corresponding pressure-sensitivity at a point of the surface. The mean (and true) sensitivity is obtained by averaging over the path length ( $\delta$ ) and over the beam width ( $w$ ) given by the transducer location and geometry (fig. 3).

Fig. 4 gives the pressure-sensitivity for a Y-cut of quartz as a function of the mean position of the transducers on the  $a_3$  axis. The diaphragm thickness is 246  $\mu\text{m}$  and its diameter is 10 mm. The nominal oscillator frequency is 105 MHz.

For  $w = 1$  mm, three experimental points have been obtained and the calculation is in good agreement with them. At the center of the diaphragm ( $a_3 = 0$ ), the sensitivity is 170 Hz/kPa and is almost the opposite of that one at  $a_3 = 4$  mm.

Using this property, dual channel sensor with a sensitivity twice as large has been built (360 Hz/kPa at 105 MHz) (photo 1).

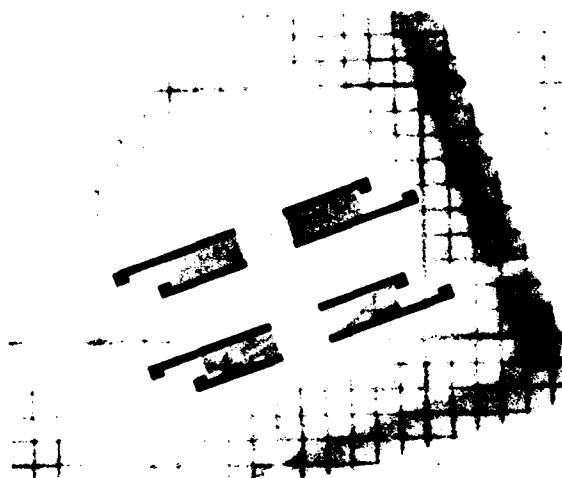


Photo 1  
Monolithic thin diaphragm for SAW-pressure sensor

The differential device also enables to decrease largely the temperature influence by compensating effect. Also the two channels pressure sensor reduces the spurious frequency temperature shifts within 400 Hz over a temperature range from  $-40^\circ\text{C}$  to  $80^\circ\text{C}$  (fig. 5). This is corresponding to an accuracy better than 1.5% over the total temperature range and over the total pressure dynamic of 100 kPa.

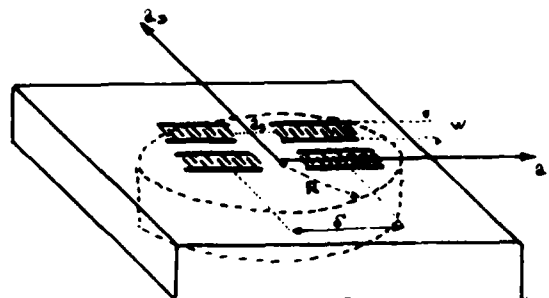


Fig. 3 : Position of the transducers

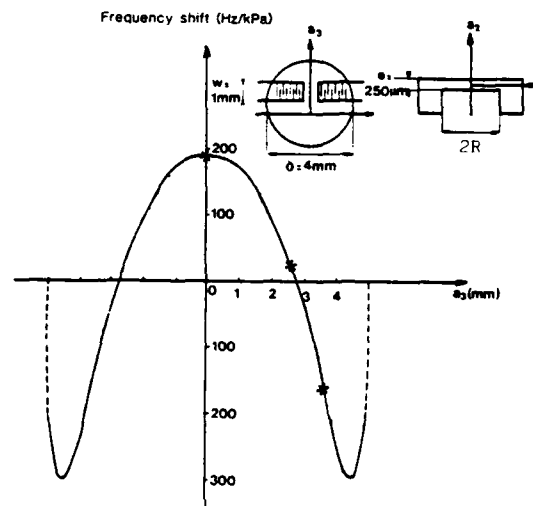


Fig. 4 : Pressure sensor sensitivity as a function of the transducer positions

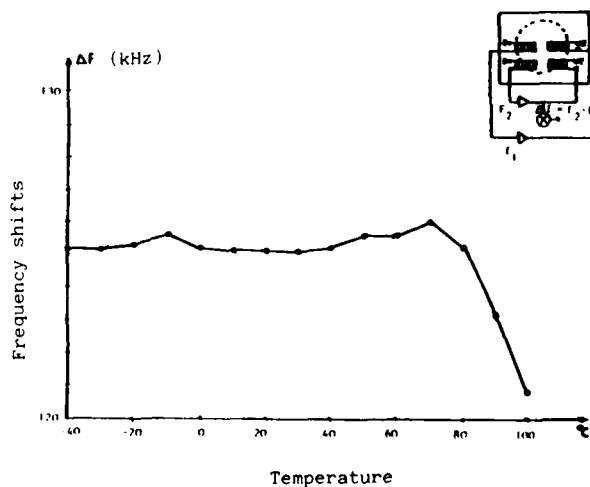


Fig. 5 : Temperature compensation of the SAW pressure sensor

### S.A.W. temperature sensor

Frequency shifts of SAW oscillator follow a law of polynomial expansion as a function of temperature :

$$\Delta f(T) = f(T_0) [a_0(T-T_0) + b_0(T-T_0)^2 + \dots] \quad (9)$$

where  $a_0$  and  $b_0$  are temperature coefficients (T.C.'s) of the first and second order of the frequency at reference temperature  $T_0$  (25°C).

A temperature sensor must have a large sensitivity and a good linearity, then  $a_0$  will be as large as possible and  $b_0$  null by choosing the cut and the propagation direction<sup>6,10</sup>

Table I shows theoretical values of propagation velocity, electromechanical coupling factor and T.C.'s of first and second order of two cuts with linear F-T characteristic, called JCL-cut and LST-cut.

cuts	cut angles		$\psi$	V m/s	k $\times 10^{-2}$	$a_0$ ppm/K	$b_0$ $\times 10^{-9}/K^2$
	$\phi$	$\theta$					
JCL	0	42.1	39	3275	0.21	22	-0.06
FST	11.4	59.4	35	3360	0.11	33	-0.04

Table I  
Theoretical characteristics of linear quartz crystal cuts

The temperature probe is a SAW delay line on quartz crystal substrat (JCL or LST-cuts). It is 10 mm long, 5 mm wide and 1 mm thick.

Two aluminium interdigital transducers are metallized on the quartz plate. One has 100 finger pairs and the other 150 finger pairs. Beam aperture is equal to  $75 \lambda$  and corresponding time delay is 1.45  $\mu s$  for JCL-cut and 1.41  $\mu s$  for LST-cut.

The delay line is bound in a metallic copper box with good thermal contact between the bottom of the box and the lower surface of the substrat. Elastic glue is used because it introduces very weak stresses. A cylindrical cover is bound on the top of the box within there is air or helium gaz (photo 2).

Insertion losses are respectively 20 dB for JCL-sensor and 25 dB for LST-sensor without impedance matching.

A rigid coaxial line carries electric signal from the delay line to the amplifier to build the sensitive SAW oscillator.

Oscillation frequencies are respectively 98.6 MHz for LST-cut and 95 MHz for JCL-cut. Characterizations of oscillators are made in temporal domain and measured relative stability of frequency is about  $10^{-9}$  from 1 to 10 seconds. Measurements are performed at 25°C.

Experimental F-T characteristics are shown on fig. 6 where frequency shifts are given in relative values with frequency at 25°C as reference for the temperature range from -30°C to 110°C.

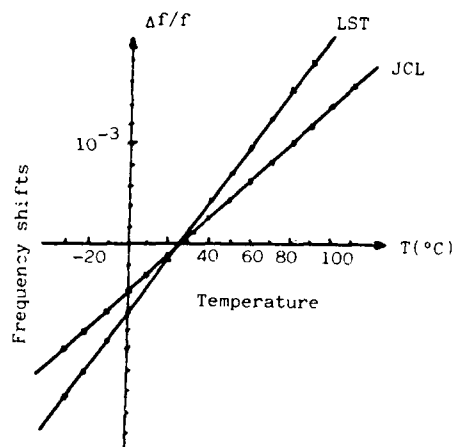


Fig. 6  
Experimental frequency-temperature characteristics of JCL and LST quartz crystal cuts

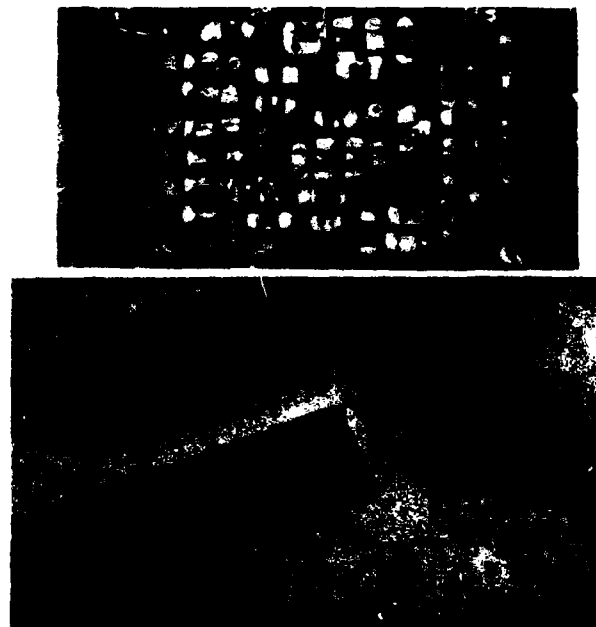


Photo 2  
SAW Temperature probe

### Sensitivity - Linearity

Sensitivity of JCL-cut is  $1.800 \text{ Hz/K}$ , then  $5.10^{-4} \text{ K/Hz}$  and sensitivity of LST-cut is  $2.800 \text{ Hz/K}$  then  $3.3.10^{-4} \text{ K/Hz}$ . Taken into account the temperature range, linearity deviation is better than  $.1 \text{ K}$  over the total range.

### Resolution

The limit resolution of the probe is obtained by considering sensitivity and frequency stability of the oscillator. When temperatures are measured over 1 second, the limit resolution of SAW temperature probe is better than  $100 \text{ } \mu\text{K}$ . ( $50 \text{ } \mu\text{K}$  for JCL-cut and  $34 \text{ } \mu\text{K}$  for LST-cut).

### Time constants

When the probe is submitted to temperature steps, its response can be more or less faster according to the technology used for the probe and mainly according to the physical thermal transient. One distinguishes three different cases which have respectively a peculiar time constant. Time constant value is given here at 90% of the final temperature. If a temperature step is applied on the probe box by a pulsed power laser beam at a point of the external surface, thermal energy diffuses from this point to the total volume. A great time constant corresponds to this phenomenon. Measured value of SAW temperature sensor is  $55 \text{ s}$ .

Thermal convection is simulated by chopped hot air flow in a pipe with a constant debit. In this case, measured values of time constant is about  $75 \text{ s}$ .

Generally, temperature measurements are performed in the case of thermal conduction. Time constant measurements are made with a pulsed water flow.

Fig. 7 shows that time constant value of SAW temperature probe measured at 90% of the final temperature is  $0.3 \text{ s}$ .

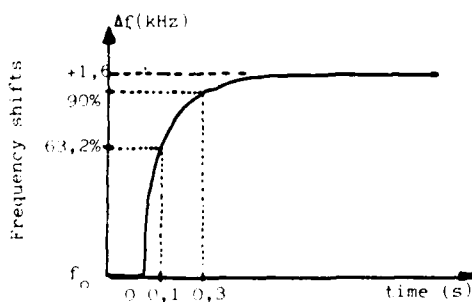


Fig. 7

Response time of SAW temperature sensor (JCL-cut)  
 $f_0 = 98.041 \text{ MHz}$   $\Delta f = 1.6 \text{ kHz}$

Time constants are summarized in Table II and compared with these ones of BW probe obtained in the same measurement conditions. For each case, SAW temperature probe is faster than BW sensor because its structure where the crystal plate is almost directly in contact with external medium.

sensors	diffusion	convection	conduction
	$\tau_1$ (s)	$\tau_2$ (s)	$\tau_3$ (s)
BW	1 000	91	6
SAW	550	75	0.3

Table II  
 Time constants ( $\tau$ ) of BW and SAW temperature sensors (measured at 90%)

### S.A.W. thermometer

Using SAW temperature probes, a new type of quartz thermometer was built. Fig. 8 shows the quartz thermometer scheme. SAW temperature probes are connected with an oscillator in a hybrid circuit at the end of rigid coaxial lines. Temperature values are measured by accounting oscillator frequencies about  $98.0 \text{ MHz}$ .

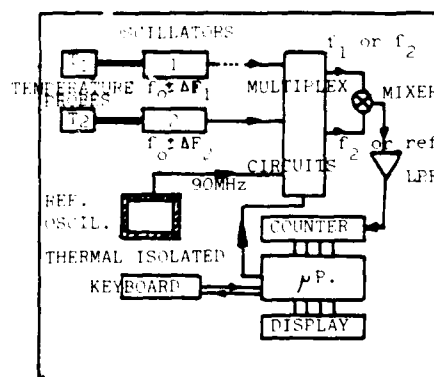


Fig. 8

SAW quartz thermometer scheme  
 $f_0 = 98.0 \text{ MHz}$

Multiplexing circuits driven from a microprocessor enable to choose one of both SAW oscillators or the reference oscillator. Mixed frequency is accounted after passing through a low pass filter (LPF). The microprocessing program drives also the display device after correcting linearity deviations.

Temperature calibrations (0°C and 100°C) are available from processing program. All possibilities of the program are selected from a keyboard. (photo 3).

The SAW thermometer enables to measure temperature in large temperature range from -100°C to 200°C with an accuracy of about  $10^{-4}$  K by using internal frequency counter over 1 s and with ten times better accuracy by accounting frequency over 10 s.

#### Conclusion

Those SAW quartz-sensors are high performances transducers for measurements in laboratories or aerospace applications. However, Thomson-CSF Company made a complementary study to adapt the pressure sensor for automobile market. Likewise, temperature sensor will be developed by an other french company (CGE) to have a larger diffusion.

#### Acknowledgements

The authors wish to thank Dr. P. Hartemann of "Thomson-CSF" company for collaboration on studies of pressure sensors and "Quartz et Electronique" company for technology help for temperature sensor.

#### References

1. D. Hauden, M. Planat, J.J. Gagnepain, "Nonlinear properties of surface acoustic waves : applications to oscillators and sensors", IEEE Trans. on Sonics and Ultrasonics, vol. SU-28, n° 5, p. 342, sept. 1981.
2. J.C. Baumhauer, H.F. Tiersten, "Nonlinear electroelastic equations for small fields superposed on a bias", J. Acoust. Soc. Am., 54, n° 4, p. 2018, (1973).
3. R.D. Mindlin, "An introduction to the mathematical theory of vibrations of elastic plates", Monograph USASCEL, Fort Monmouth N.J., 1955.
4. H.F. Tiersten, B.K. Sinha, "A perturbation analysis of the attenuation and dispersion of surface waves", J. Appl. Phys., 49, jan. 1978.
5. D. Hauden, M. Michel, J.J. Gagnepain, "Higher order temperature coefficients of quartz oscillators", Proc. of the 32nd A.F.C.S., p. 77, (1978).
6. D. Hauden, G. Jaillet, R. Coquerel, "Temperature sensor using SAW delay lines", IEEE Ultrasonics Symposium Proc., cat. 81CH.
7. J.F. Dias, H.E. Karrer, "Stress effects in acoustic surface wave circuits and applications to pressure and force transducers", IEEE Intern. Solid State Circuits Conference, 1974.
8. T.M. Reeder, D.E. Cullen, M. Gilden, "SAW oscillator pressure sensors", IEEE Ultrasonics Symposium Proc., cat. 75CH0994-4SU.
9. D. Hauden, S. Rousseau, J.J. Gagnepain, "Sensitivities of SAW oscillators to temperature, forces and pressure : applications to sensors", Proc. of the 34th A.F.C.S., (1980).
10. G. Jaillet, "Ondes de surface sur substrats piézoélectriques. Etude et réalisation d'un capteur de température", Thèse, Paris, (1981).

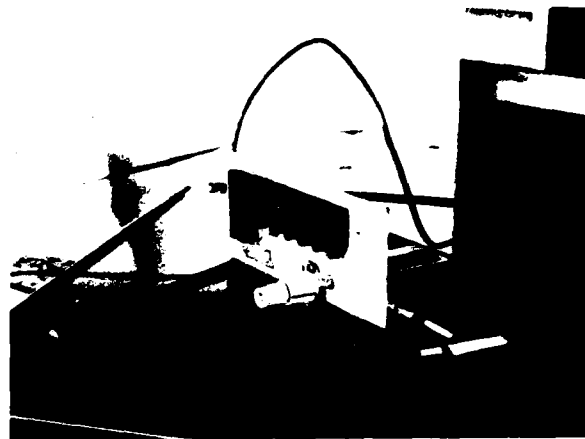


Photo 3  
SAW Thermometer

# NEW QUARTZ RESONATORS WITH PRECISION FREQUENCY LINEARITY OVER A WIDE TEMPERATURE RANGE

Mitsuo Nakazawa, Hideaki Ito and Atsushi Usui  
Shinshu University, Nagano 380, Japan

Arthur Ballato and Theodore Lukaszek  
Electronics Technology and Devices Laboratory  
Fort Monmouth, New Jersey 07703

AD P001536

## Abstract

It is well known that quartz crystal resonators have been employed in a number of thermometer applications. We have recently discovered two new thermometric cuts; one exhibits a high degree of linearity over a wide temperature range; the other is located in the vicinity of the stress compensated locus. These doubly rotated cuts were found by calculations based on the thickness - vibration theory for ideal plates.

This paper presents theoretical and experimental results concerning the frequency-temperature characteristics of these quartz resonators.

One of the quartz resonators is made by using a (YXw1)  $\phi=5^\circ/\psi=5^\circ$  cut and is formed as a rectangular plate. The measured physical features are as follows. The resonator operates at about 11 MHz, 3rd overtone, vibrating in the thickness-shear mode (c mode), and it exhibits excellent frequency linearity in the  $-196^\circ\text{C}$  to  $+160^\circ\text{C}$  range. The frequency sensitivity to temperature change is  $688\text{ Hz}/^\circ\text{C}$  and the first order frequency-temperature coefficient is  $62.6 \times 10^{-6} [^\circ\text{C}]^{-1}$ . The second and third order frequency temperature coefficients are  $-18.1 \times 10^{-9} [^\circ\text{C}]^{-2}$  and  $-35.9 \times 10^{-12} [^\circ\text{C}]^{-3}$ , respectively. The frequency constant is about  $1.85\text{ MHz}\cdot\text{mm}$ . The coupling coefficient is approximately 11.74 percent.

**Key Words:** Quartz resonators, quartz crystal thermometers, precision frequency linearity, doubly rotated cut, c mode, thickness-shear vibration.

## Introduction

Recently, there have been many advanced studies on highly stable quartz crystal resonators which have been applied to frequency control, communications, watches and so on. Most of these resonators are obtained by using the non-linear effects of the frequency to offset temperature variation, force change, and aging, etc.

On the other hand, if we can find resonators which have linear frequency effects over a wide temperature range, we can make use of these

resonators as excellent digital temperature-sensing elements such as the LC-cut exhibits [1,2].

In this paper, two new resonator cuts which show linear frequency - temperature characteristics are proposed. We shall call them the NL-cut series. The cuts are found by the calculation based on the thickness-vibration theory [3-10] and are made by double rotation. In these resonators, there are a longitudinal wave which is called an "a mode" and two transverse waves which are called "b mode" and "c mode". All these modes are excited piezoelectrically. The c mode shows excellent linearity of frequency over a wide temperature range. The experimental results coincide well with our theory. The frequency-temperature characteristics of these new cut resonators are compared with those of the LC-cut [2].

## Calculations

The right-handed rectangular Cartesian coordinate system ( $0-x_1, x_2, x_3$ ) in relation to the crystal axes will be assumed, as shown in Fig. 1. Fig. 1 shows a thin quartz crystal plate in relation to the crystal axes, where  $m$  and  $k$  are the unit vectors normal to the crystal main surface and the wave vector parallel to it, respectively. As in Fig. 1, if a point  $p(x_1, x_2, x_3)$  in a thin quartz plate is described in the spherical coordinate system ( $0-s, \theta_0, \phi_0$ ), we have

$$\begin{aligned} x_1 &= s \sin \theta_0 \cos \phi_0, \\ x_2 &= s \sin \theta_0 \sin \phi_0, \\ x_3 &= s \cos \theta_0. \end{aligned} \quad (1)$$

As we know, in thin quartz crystal plates, the frequency equation for the thickness-vibration modes is given by

$$f = \frac{n}{2 Y_0} \sqrt{\frac{c}{\rho}} \quad (n=1,3, \dots), \quad (2)$$

in which  $\rho$  and  $Y_0$  are the density and thickness of the crystal plate, respectively, and  $c$  represents eigenvalues and solutions of the following equation:

$$|C_{ijkl} m_j m_k - c_{11}^2| = 0, \quad (3)$$

and

$$C_{ijkl} = C_{ijkl}^E + (m_q \epsilon_{qj}^S m_j)^{-1} (e_{hij} m_h) \times (m_h e_{hkl}) \quad (4)$$

$C_{ijkl}^E$  = the elastic stiffness constants at constant electric field,

$e_{hij}$  = the piezoelectric constants,

$\epsilon_{qj}^S$  = the dielectric constants at constant strain.

The frequency of any cut can be expanded in a Taylor series with respect to temperature  $T$ . By using Equation (2), we have approximately

$$f(T) \approx f(T_0) \{1 + \alpha(T-T_0) + \frac{\beta}{2}(T-T_0)^2 + \frac{\gamma}{6}(T-T_0)^3\}, \quad \dots (5)$$

in which  $T_0$  is the reference temperature, and the coefficients are defined by

$$\begin{aligned} \alpha &= \left( \frac{1}{f(T)} \cdot \frac{\partial f(T)}{\partial T} \right)_{T_0} \\ \beta &= \left( \frac{1}{f(T)} \cdot \frac{\partial^2 f(T)}{\partial T^2} \right)_{T_0} \\ \gamma &= \left( \frac{1}{f(T)} \cdot \frac{\partial^3 f(T)}{\partial T^3} \right)_{T_0} \end{aligned} \quad (6)$$

The  $a$  mode is essentially a thickness-extensional vibration, while the  $b$  and  $c$  modes are thickness-shear vibrations. By using the Equations (2)-(6), and the values for  $C_{ijkl}$ , the linear expansion coefficients, the density, and these temperature coefficients, we find new cuts which have linear frequency-temperature characteristics. These new cuts are  $(YXWl)\phi=5^\circ/\psi=5^\circ$  and  $(YXWl)\phi=20^\circ/\psi=20^\circ$  plates, respectively. These will be named the  $NL_1$ - and  $NL_2$ -cuts, respectively. Here are some calculated properties of the  $NL_1$ -cuts. They are compared to values of some other quartz crystal cuts [3-6] (See Tables (1) - (3)).

Fig. 2 shows the orientation of the  $NL_1$ -cut plate defined by the angles  $\phi$  and  $\psi$ :  $(YXWl)\phi/\psi$ .

Fig. 3 shows the loci of  $\alpha=0$  and  $\beta=0$  for the  $c$  mode in thin quartz plates as functions of the polar angles  $\phi$  and  $\theta$ . Also shown is the locus of zero coefficient of stress (CS). This coefficient was originally calculated for a limited range around the SC cut by E. P. Eer Nisse [11], and recently expanded in angular range by B. Sinha [12]. As can be seen, the proximity of the  $NL_2$  cut to this zero locus suggests the possibility of achieving stress compensated behavior in linear temperature coefficient cuts making them suitable candidates for harsh-environments applications [3].

## Experiments

Figs. 4 and 5 are photographs of the  $NL_1$ -cut resonators used in the experiments. These sample units were kindly furnished by the Miyota Precision Co. and the Toyo Communication Equipment Co., Japan. The  $NL_1$ -cuts are displayed in Fig. 4 and samples Nos. 1 and 2 are rectangular and circular resonators, respectively. The  $NL_2$ -cuts are shown in Fig. 5 and samples Nos. 1 and 2 are rectangular resonators with the same dimensions, but their electrode diameters are somewhat different. Sample No. 3 in Fig. 5 is a pentagon-shaped resonator. The electrodes on these samples are gold-sputtered.

Fig. 6 shows the frequency-thickness characteristics of the  $c$  mode in thin  $NL_2$ -cuts. From Fig. 6 it is seen that the  $c$  mode in thin  $NL$ -cuts is surely the thickness vibration mode. Further, Table 4 shows the measured mean values of frequency constants for samples Nos. 1, 2, and 3 in Fig. 5. From Tables 1 and 4 it is seen that the experimental results coincide well with the theoretical ones.

Next, to measure the frequency-temperature coefficients of the crystal resonators, the experiments are carried out in the oven by using a copper-constantan thermocouple. Measurements were performed over a wide temperature range.

Fig. 7 shows the frequency-temperature characteristics for the  $NL_1$ -cut resonator operating on the fundamental  $c$  mode. The resonance frequency is 3.691275 MHz at 25°C. The first-order frequency temperature coefficient  $\alpha$  was measured and found to be 55.54 ppm/°C by using a least-squares method. Similarly, the second order frequency temperature coefficient was found to be  $\beta/2=65.68 \times 10^{-4}$  ppm/(°C)<sup>2</sup>. This result corresponds to a 0.012 percent departure from linear dependence. It is felt that resonance frequency fluctuations seen in the vicinity of -180°C and 100°C are due to the coupling of unwanted responses. The solid line shows the theoretical values.

Figs. 8 and 9 show the frequency-temperature characteristics for the same  $NL_1$ -cut resonator operating on the 3rd and 5th harmonic  $c$  mode, respectively. The resonance frequency is 11.021416 MHz at 25°C. The frequency sensitivity to temperature change is 688 Hz/°C and the frequency temperature coefficients were found to be  $\alpha=62.63$  ppm/°C,  $\beta/2=-18.11 \times 10^{-3}$  ppm/(°C)<sup>2</sup> and  $\gamma/6=35.93 \times 10^{-5}$  ppm/(°C)<sup>3</sup>, respectively. This result corresponds to a 0.029 percent departure from linear dependence. Similarly, in Fig. 9 the resonance frequency is 18.370302 MHz at 25°C. We find that  $\alpha=63.53$  ppm/°C,  $\beta/2=23.48 \times 10^{-4}$  ppm/(°C)<sup>2</sup> and  $\gamma/6=-16.60 \times 10^{-5}$  ppm/(°C)<sup>3</sup>, respectively. This corresponds to a 0.0037 percent departure from linear dependence.

Fig. 10 shows the linear frequency-temperature characteristics for the  $b$  mode in a  $NL_2$ -cut resonator. The frequency temperature sensitivities for the fundamental and 3rd harmonic modes are the negative values, -18.80 ppm/°C and -21.19 ppm/°C,

respectively. These values are somewhat different from one another. On the other hand, the dashed line is the theoretical value  $-16.43 \text{ ppm}/^\circ\text{C}$ . It is also felt that the resonance frequency fluctuation seen in the  $-40^\circ\text{C}$  to  $-20^\circ\text{C}$  temperature range is due to errors in measuring.

Similarly, Fig. 11 shows the frequency-temperature effects for the  $\text{NL}_2$ -cut resonator operating on the c mode. The  $\alpha$  for the 3rd and 5th harmonic represents the positive values, i.e.,  $17.20 \text{ ppm}/^\circ\text{C}$  and  $15.0 \text{ ppm}/^\circ\text{C}$ , respectively. The dashed line is the theoretical value for the 3rd harmonic mode. It is seen that these experimental results coincide well with the theory.

Now, in order to compare the frequency-temperature effects of another cut with the  $\text{NL}_1$ -cuts, the LC-cut was chosen. The circular LC-cut resonator used in the experiments is  $0.173 \text{ mm}$  in thickness,  $13.436 \text{ mm}$  in diameter, and the electrodes are  $6.807 \text{ mm}$  in diameter. The electrodes are gold-sputtered. Fig. 12 shows the frequency-temperature characteristics for the LC-cut operating on the a, b, and c modes in thin LC-cut resonator over the temperature range  $-40^\circ\text{C}$  to  $+100^\circ\text{C}$ . The first-order frequency temperature coefficients for the b and c modes were found to be  $-39.70 \text{ ppm}/^\circ\text{C}$  and  $38.40 \text{ ppm}/^\circ\text{C}$ , respectively. These results coincide well with the theoretical values as shown in the figure (Also Table 3). Similarly, the frequency effects of the same LC-cut resonator versus temperature over the range from  $-19^\circ\text{C}$  to  $+15^\circ\text{C}$  are shown in Fig. 13. The open circles represent the experimental values and the solid line represents the theory. Within the experimental error range, the  $\alpha$  and  $\beta/2$  of this c mode were found to be  $39.50 \text{ ppm}/^\circ\text{C}$  and  $126 \times 10^{-8} \text{ ppm}/^\circ\text{C}^2$ , respectively. These values correspond to 0.032 percent departure from linear dependence.

To obtain a small and clean response resonator, we made an another  $\text{NL}_1$ -cut (No. 2) as shown in Fig. 4. This is a bi-convex circular resonator,  $3 \text{ mm}$  in diameter and  $0.5 \text{ mm}$  thick. The resonance frequency is found to be  $4.025092 \text{ MHz}$  at  $25^\circ\text{C}$ . The  $Q$  value is of the order 55,000 in nitrogen gas at  $25^\circ\text{C}$ . The response time of this resonator to small temperature changes is fast. The  $\alpha$  is found to be  $65.26 \text{ ppm}/^\circ\text{C}$ .

#### Conclusion

From the theory and the experimental results it is found that the  $\text{NL}_1$ -cut resonator has frequency linearity over a wide temperature range, and that the frequency sensitivity to temperature is about 1.5 times that of the LC-cut resonator.

On the other hand, appears promising for thermometric sensing applications where high resolution with extremely low sensitivity transients that usually produce transient and/or induced frequency offsets are required.

#### Acknowledgments

The portion of the work performed at Shinshu University was supported by donations from the Miyota Precision Co. The authors wish to thank Professor P. C. Y. Lee, Princeton University, for his help and encouragement, and wish to thank Messrs. N. Asanuma and K. Yamazaki, Toyo Communication Equipment Co., for making the crystal samples.

#### References

1. W. L. Smith and W. J. Spencer: Quartz crystal thermometer for measuring temperature deviations in the  $10^{-3}$  to  $10^{-6}^\circ\text{C}$  range, Rev. Sci. Instrum., Vol. 34, 1963, pp. 268-270.
2. D. L. Hammond, C. A. Adams and P. Schmidt: A linear, quartz-crystal, temperature-sensing elements, ISA Trans, Vol. 4, 1965, pp. 349-354.
3. I. Koga, M. Aruga, and Y. Yoshinaka: Theory of plane elastic waves in a piezoelectric crystalline medium and determination of elastic and piezoelectric constants of quartz, Phys. Rev., Vol. 109, 1958, pp. 1467-1473.
4. R. Bechmann, A. Ballato, and T. J. Lukaszek: Frequency-temperature characteristics of quartz resonators derived from the temperature behavior of the elastic constants, Proc. 16th Annual Freq. Control Symp; U. S. Army Electronics R&D Command, Fort Monmouth, NJ 07703, April 1962, pp. 77-109.
5. A. Ballato: Physical Acoustics, (W. P. Mason and R. N. Thurston, editors), Academic Press, Inc., N. Y., London, Vol. 13, Chapter 5, 1977, pp. 115-181.
6. M. Nakazawa: Specific directions of plane elastic waves in thin quartz crystal plates, Int. J. Electronics, Vol. 48, 1980, pp. 275-282.
7. M. Nakazawa and H. Matsuzaka: Dependence of frequency-temperature characteristics upon cutting angles of quartz crystal oscillator, Journal of the Faculty of Engineering, Shinshu University, 1971, p. 67-73 (in Japanese).
8. H. Matsuzaka: A theoretical study on the temperature of quartz crystal resonators vibrating in thickness mode, MS paper, Shinshu University, 1971, pp. 1-40 (in Japanese).
9. H. Fukuyo: Researches in modes of vibrations of quartz crystal resonators by means of the probe method, Bulletin of Tokyo Institute of Technology, A-1, 1955, pp. 28-67 (in Japanese).
10. M. Onoe: General equivalent circuit of a piezoelectric transducer vibrating in thickness modes, Trans. I.E.C.J., Vol. 55-A, 1972, pp. 239 - 244, (in Japanese).

11. E. P. Eer Nisse: Calculations on the stress compensated (SC-cut) quartz resonator, Proc. 30th Annual Freq. Control Symposium, U. S. Army Electronics R&D Command, Fort Monmouth, NJ 07703, June 1976, pp. 8-11.

12. B. Sinha: Stress compensated orientation for thickness-shear quartz resonators, Proc. 35th Annual Freq. Control Symposium, U. S. Army Electronics R&D Command, Fort Monmouth, NJ 07703, May 1981, pp. 213-221.

Table 1  
Frequency constants  $N_m$  (m=mode number: a,b, or c). Values are in MHz-mm.

Cut	NL <sub>1</sub>	NL <sub>2</sub>	LC	AT	BT	Y	X
N <sub>a</sub>	3.11	3.27	3.17	3.50	3.09	3.01	2.87
N <sub>b</sub>	2.11	2.09	2.14	1.90	2.54	2.16	1.56
N <sub>c</sub>	1.84	1.70	1.73	1.66	1.88	1.96	1.66

Table 2  
Piezoelectric coupling coefficients  $|k_m|$ . Values are percentages (%).

$ k_a $	≈ 2	4.35	3.21	0	0	0	9.14
$ k_b $	≈ 6	7.48	7.64	0	5.62	0	0
$ k_c $	≈ 11	4.10	9.21	8.80	0	13.42	0

Table 3  
First order frequency temperature coefficients,  $\alpha_m$ . Values are in  $10^{-6}/^{\circ}\text{C}$ .

$\alpha_a$	-21.5	-37.4	-26.1	-48.9	-95.6	-16.3	-19.3
$\alpha_b$	-65.2	-16.4	-39.7	-51.3	0	-97.8	-23.0
$\alpha_c$	+62.0	+17.1	+39.8	0	-30.9	+85.7	+12.7

Table 4  
Measured mean values of the frequency constants for the NL<sub>2</sub>-cuts Nos.1, 2, and 3. Values are in MHz-mm.

$N_i$ (m)	No.1	No.2	No.3
N <sub>a</sub> (1)	3.30	3.28	3.27
N <sub>b</sub> (2)	2.12	2.10	2.10
N <sub>c</sub> (3)	1.71	1.71	1.71

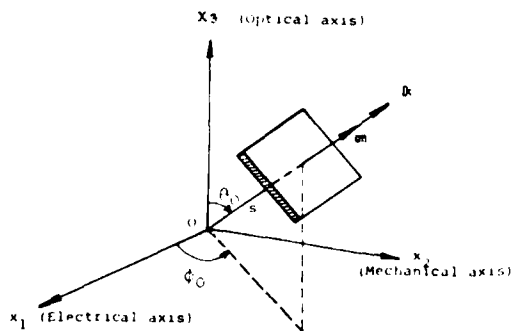


Figure 1. A Thin Quartz Crystal Plate in Relation to the Crystallographic Axes.

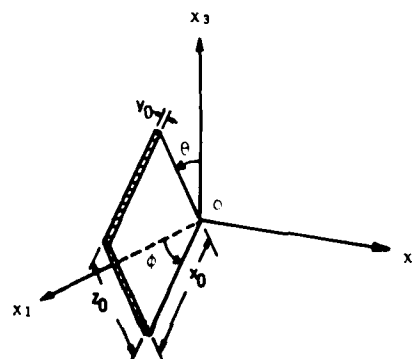


Figure 2. An NL-Cut Plate (YX w1)  $\phi/\theta$ .

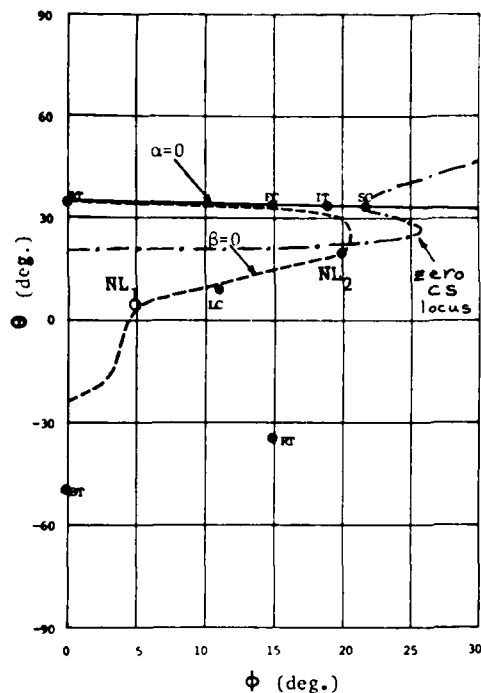


Figure 3. Loci of  $\alpha = 0$  and  $\beta = 0$  for the Thickness  $c$  Mode of Quartz Plates as a Function of the Polar Angles  $\phi$  and  $\theta$  in Figure 2, Where BT-Cut Belongs to the  $b$ -mode. Sinha's Locus of Zero Stress Coefficient is Also Shown.

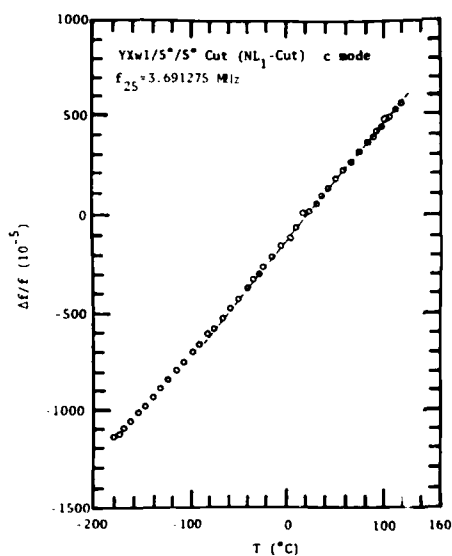


Figure 7. Frequency-Temperature Characteristics for the  $NL_1$  Cut Resonator Operating on the Fundamental Mode



Figure 4. The Large and Small  $NL_1$  - Cut Resonators

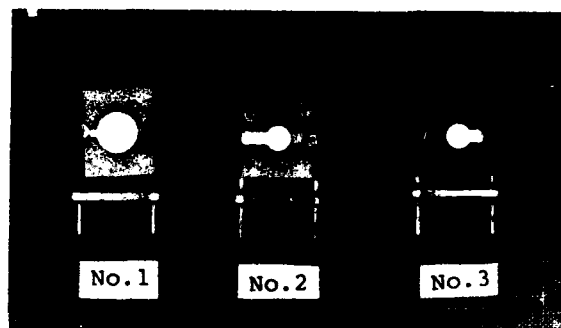


Figure 5.  $NL_2$  - Cut Resonators. The Dimensions of Nos. 1 and 2:  $X = 12.000$  mm,  $Y_0 = 0.500$  mm, and  $Z_0 = 14.729$  mm. The Dimensions of No. 3: Contour Dimensions  $6 \times 5 \times 7 \times 5 \times 8$  mm Clockwise from the Left Side to the Right Side

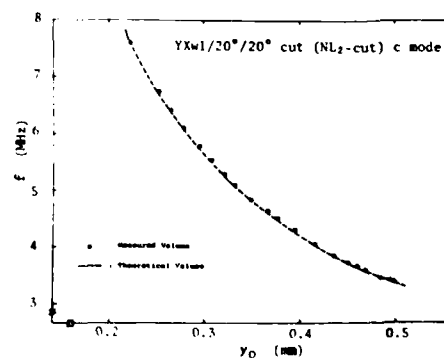


Figure 6. Frequency-Thickness Characteristic for the  $NL_2$  Cut Operating on the Fundamental  $c$  Mode.

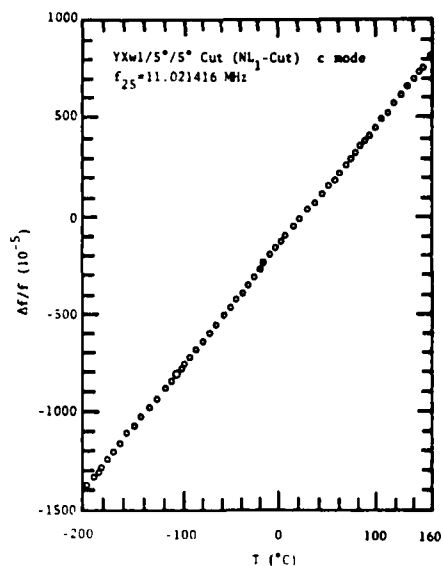


Figure 8. Frequency - Temperature Characteristics for the  $NL_1$  - Cut Resonator Operating on the 3rd Harmonic Mode

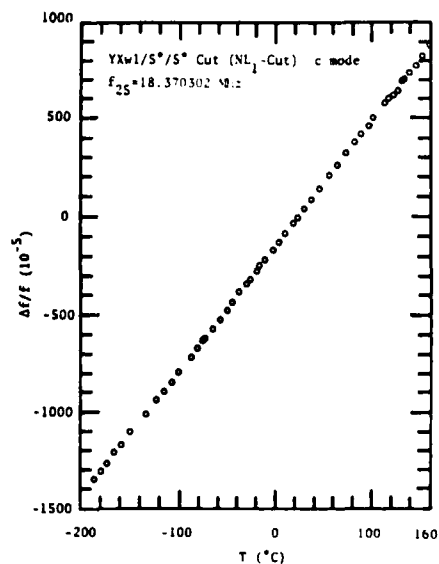


Figure 9. Frequency - Temperature Characteristics for the  $NL_1$  - Cut Resonator Operating on the 5th Harmonic Mode

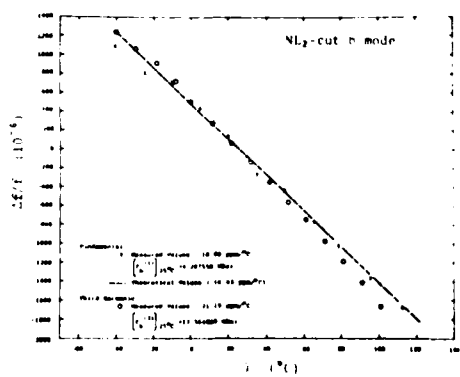


Figure 10. Frequency - Temperature Characteristics for the  $NL_2$  - Cut Resonator Operating on the b Mode

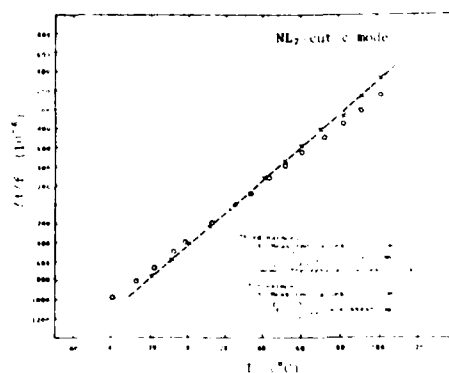


Figure 11. Frequency - Temperature Characteristics for the  $NL_2$  - Cut Resonator Operating on the c Mode

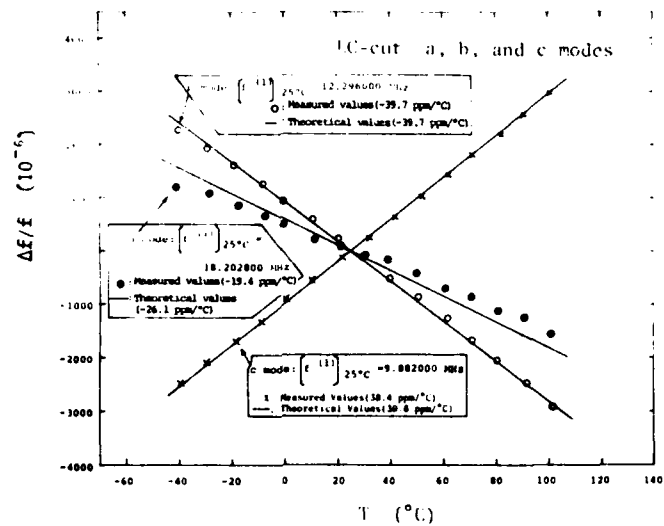


Figure 12. Frequency - Temperature Characteristics for the LC - Cut Resonator Operating on the a, b, and c Modes

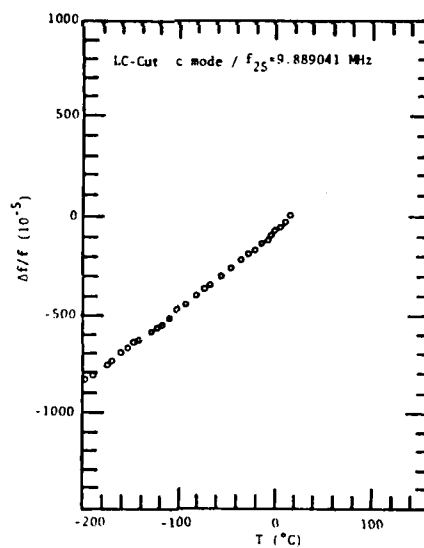


Figure 13. Frequency - Temperature Characteristics for the LC - Cut Resonator Operating on the Fundamental Mode

## NEW METHOD FOR THE MEASUREMENT OF QUARTZ CRYSTAL RESONATOR PARAMETERS

R C Peach, A J Dyer, A J Byrne and S P Doherty

The General Electric Company, p.l.c., Hirst Research Centre  
Wembley, HA9 7PP, EnglandAbstract

A network analyser based system has been established which characterises the crystal response over the region of the resonant and anti-resonant frequencies by a set of typically several hundred  $S_{12}$  measurements. A new software system has been developed which determines the equivalent circuit parameters by an iterative algorithm which fits the theoretical response to the measured values in an optimal way. This method is therefore virtually operator independent, and provides excellent resistance to random errors; reproducibility of motional inductance values are of the order of 1 in  $10^3$ .

The general philosophy of this approach is to use simple, well defined, RF hardware to provide a precise characterisation of the crystal, and then to use advanced software to resolve the problems of interpretation. The technique is quite practicable with desktop calculators. Measurements may be based on a wide range of different measured parameters, for instance magnitude data alone. It is therefore possible to use scalar measuring equipment, although this does reduce calibration accuracy, as vector error correction is no longer possible.

Key words : Network analyser, crystal resonator, least squares fit

1. Introduction

The measurements of crystal resonator parameters is a topic which has occupied many people over the years, and numerous methods have been proposed, including crystal impedance meters,  $\pi$ -network and T network transmission systems, impedance bridges, and network analyser s parameter systems. However the extent to which the crystal industry can justify the development of specialised measurement apparatus has always been limited, and the preferred choice of method must therefore be conditioned by the types of equipment commercially available. The ability to perform traceable high precision measurements on crystal resonators is essential, both as a research and development tool, and as a means of judging the wide range of methods commonly employed.

Automatic network analyser systems are becoming increasingly widely used, and, for a number of reasons, appear to offer the best avail-

able approach to the problem of performing standardised crystal measurements<sup>1</sup>. In particular, it is possible to use well developed automatic error correction routines, which rely on calibration with a suitably chosen set of coaxial standards, to provide a high degree of accuracy and traceability over a very wide frequency range. Normally a network analyser can provide amplitude and phase measurements of all four s parameters of a two port device, and this offers a wide range of possible methods for crystal parameter determination. A method which has achieved a degree of general acceptance is the IEC  $\pi$ -network/vector voltmeter method<sup>2</sup>, which relies on zero phase transmission measurements, and resistance substitution and capacitor loading techniques. However with the advent of calculator controlled equipment it is much more attractive to evaluate crystal parameters indirectly from simple s parameter measurements, and to avoid systems such as the  $\pi$ -network, with its separate set of calibration components which have proved so difficult to standardise in the past.

The first use of a network analyser in this way appears to have been by Pustarfi and Smith<sup>1</sup> who performed error corrected transmission measurements on quartz crystal resonators. The admittance of the crystal was calculated and the equivalent circuit parameters deduced directly from this. Once the use of computation to resolve calibration and interpretation problems is accepted, then it is always worth considering the use of more sophisticated software to reduce the complexity and refinement required in the hardware. Most s parameter methods to date, rely on knowledge of both amplitude and phase, but often there is a greater uncertainty in the phase measurements, and it may be desirable (and cheaper) to use scalar analysers. Provided that the measured information is sufficient to characterise the crystal completely then in principle it is possible to determine the equivalent circuit parameters by a numerical method. This opens the interesting possibility of implementing a non-linear fitting routine on the system controller, and thus making such a procedure an integral part of the measurement system. It will be demonstrated that such an approach is quite practicable with commonly used desktop calculators, and by such means it is possible to determine circuit parameters in an optimal way from a wide variety of measured data. Excellent resistance to random errors can be obtained as the final results are based on a large number of individual measure-

ments, and there is no reliance on the skill or judgment of the operator.

### 2. The measurement system

For most of this work measurements have been performed using an HP8507B network analyser, phase locked to an Admet 7100 frequency synthesiser and controlled by an HP9825 desktop calculator. The use of this equipment was dictated by availability, and it is certainly more complex and expensive than this application warrants; at present work is being transferred to a Rohde and Schwarz ZPV vector analyser.

For the highest levels of precision and traceability it is necessary to employ vector error correction techniques<sup>1,3</sup>, this involves the use of a linear model to characterise the RF system, the parameters of which are determined by measurements on standard calibration components. With this information it is possible to remove most hardware errors by computation, having only non-linear effects and problems such as connector and switch reproducibility unaccounted for. The standard twelve term error model which has been employed is very well documented in numerous references<sup>4,5</sup> (Figure 1), and a detailed description is not required, but some general observations are useful. When characterising a general two port device the connected value of any one  $s$  parameter is a function of all four measured  $s$  parameters, so the time required for measurement is considerably increased. For a simple reflection measurement on a one port device only three error parameters and one set of measurements are needed. The error correction procedures only account for errors up to the calibration reference plane, and any additional effects produced by a measurement jig must be accounted for by a separate model.

There are in general two techniques for crystal measurements which can be employed, reflection (return loss)<sup>6</sup>, and transmission. In the first method the crystal is treated as a one port, two terminal device with one terminal and the can grounded (Figure 2). In the second method it is regarded as a two port, three terminal, device with the can, which is grounded, constituting the third terminal (Figure 3). Both of these methods have advantages and disadvantages. The transmission approach furnishes a more complete characterisation of the crystal resonator, but whether or not this is useful depends on the actual application. In addition it tends to be more sensitive when measuring low  $Q$  resonators, and it gives a very precise value for the static capacitance due to the presence of the anti-resonant frequency. The great advantage of the reflection approach is simplicity and speed of measurement, for as noted earlier the error correction procedure is enormously simplified in this case. For the transmission method the main error correction required is for port impedance, effects such as tracking and directivity being negligible, and so in a simplified system automatic error correction could be dispensed with and port impedances improved by the use of attenuators.

Therefore with a slight loss in accuracy it is possible to use transmission measurements without correction, but this is not really so for reflection, where the finite directivity of most test systems can lead to severe errors for components with impedances close to 50  $\Omega$ .

For this paper we will describe in detail a system based on the transmission method, but most of the principles are applicable to the reflection approach, and both techniques certainly have definite roles to play.

### 3. The evaluation of the motional parameters

The ideal transmission measurement circuit shown in Figure 4 includes the capacitors,  $C_1$  and  $C_2$ , which represent the electrode to crystal can capacitances, and any other strays at the test ports. Due to the small values of  $C_1$  and  $C_2$  (~1 pF) the measurements are extraordinarily insensitive to their presence, and it is not possible to determine them with any high degree of accuracy anyway. In principle the effects of these capacitances may be removed by performing measurements away from resonance to determine  $C_1$  and  $C_2$  as accurately as possible; they may then be incorporated into the error parameters, and removed from the final measurements along with other system errors. This is a very small refinement, but we may now assume that we have true measurements of  $S_{12}$  for the LCRC<sub>0</sub> circuit in series between a 50  $\Omega$  source and load (Figure 5).

We will now describe a procedure by which 'optimal' values for the four major parameters may be deduced. It must be remembered that 'optimal' means minimising some measure of the error between the theoretical and experimental values. Numerous different error criteria can be adopted, and these can and will give slightly different values for the circuit parameters. It is perfectly reasonable to ask about the reproducibility of a particular procedure, but if two different procedures give slightly different answers it is meaningless to ask which are 'true'. To illustrate the non-linear fitting programme which forms an essential part of the proposed method, we will use a criterion which consists of minimising:

$$E = \sum_n A_n \left( 1 - \frac{|S_n|}{A_n} \right)^2 \quad (1)$$

The  $A_n$  are the measured transmission amplitudes after error correction, measured over a certain set of discrete frequencies. The  $S_n$  are the theoretical values of  $S_{12}$  for the circuit of Figure 5, evaluated over the same set of frequencies. The procedure therefore minimises the sum of the squares of the fractional errors with respect to the four parameters  $L, R, C$  and  $C_0$ . Each term in the summation is weighted by a factor  $A_n$ . This has two purposes: first, the dynamic accuracy of the equipment falls off with amplitude, and points with small amplitudes are therefore less significant; second, the range of frequency points is usually chosen to include the resonant and anti-

resonant frequencies, and it is required to give more emphasis to the characteristic in the region of the resonance. This criterion uses only amplitude information, and the procedure could therefore be used equally well with a scalar detection system.

If we choose parameters  $\alpha_1 = C_0$ ,  $\alpha_2 = R$ ,  $\alpha_3 = L$ ,  $\alpha_4 = C^{-1}$ , then the condition for a minimum of  $E$  may be written:

$$\frac{\partial E}{\partial \alpha_i} = 0, \quad i = 1 \text{ to } 4 \quad (2)$$

It is not possible to find an analytic solution to such a problem, and an iterative approach must be adopted. In the classical Newton method, to find the required increments  $\Delta \alpha_j$  we use the approximation:

$$0 = \frac{\partial E(\alpha + \Delta \alpha)}{\partial \alpha_i} \approx \frac{\partial E}{\partial \alpha_i} + \sum_j \frac{\partial^2 E}{\partial \alpha_i \partial \alpha_j} \cdot \Delta \alpha_j \quad (3)$$

and this provides a simple set of four linear equations to determine the four increments at each iteration. Despite the good convergence of this method in the vicinity of the solution, the problem of computing the second derivatives often prevents its use; fortunately in this case they are quite easily calculated, and it has been shown that Equation (3) provides a very satisfactory approach. For the circuit of Figure 5 it is easily shown that:

$$S_{12} \equiv S = (1 + Z/2R_0)^{-1} \quad (R_0 = 50 \Omega)$$

$$= \frac{2R_0 Y}{1 + 2R_0 Y} = 1 - \frac{1}{1 + 2R_0 Y} \quad (4)$$

as the parameters  $R, L$  and  $C^{-1}$  enter the formula for  $S$  on essentially the same footing we may use the equivalences:

$$\frac{\partial}{\partial \alpha_3} \equiv j\omega \frac{\partial}{\partial L} \quad \text{i.e.} \quad \frac{\partial}{\partial L} \equiv j\omega \frac{\partial}{\partial \alpha_3}$$

$$\frac{\partial}{\partial \alpha_4} \equiv (j\omega)^{-1} \frac{\partial}{\partial C^{-1}} \quad \text{i.e.} \quad \frac{\partial}{\partial C^{-1}} \equiv (j\omega)^{-1} \frac{\partial}{\partial \alpha_4} \quad (5)$$

and it is sufficient to compute:

$$\frac{\partial S}{\partial \alpha_1}, \frac{\partial S}{\partial \alpha_2}, \frac{\partial^2 S}{\partial \alpha_1^2}, \frac{\partial^2 S}{\partial \alpha_1 \partial \alpha_2}, \text{ and } \frac{\partial^2 S}{\partial \alpha_2^2}, \text{ the other}$$

two derivatives and seven second derivatives then being obtained by trivial application of Equation (5). Having done this the derivatives of  $E$  may be computed using the following formulae:

$$E = \sum_n e_n \text{ where } e_n = \left( A_n - \frac{1}{S_n} \right)^2 \quad (6)$$

$$\frac{\partial e_n}{\partial \alpha_i} = \left( \frac{1}{A_n} - \frac{1}{S_n} \right) \cdot \frac{\partial |S_n|^2}{\partial \alpha_i} \quad (7)$$

$$\frac{\partial^2 e_n}{\partial \alpha_i \partial \alpha_j} = \left( \frac{1}{A_n} - \frac{1}{S_n} \right) \frac{\partial^2 |S_n|^2}{\partial \alpha_i \partial \alpha_j} + \frac{1}{2|S_n|^3} \cdot \frac{\partial |S_n|^2}{\partial \alpha_i} \cdot \frac{\partial |S_n|^2}{\partial \alpha_j} \quad (8)$$

$$\frac{\partial |S_n|^2}{\partial \alpha_i} = S_n^* \frac{\partial S_n}{\partial \alpha_i} + S_n \frac{\partial S_n^*}{\partial \alpha_i} = 2 \operatorname{Re} \left( S_n^* \frac{\partial S_n}{\partial \alpha_i} \right) \quad (9)$$

$$\begin{aligned} \frac{\partial |S_n|^2}{\partial \alpha_i \partial \alpha_j} &= \frac{\partial S_n^*}{\partial \alpha_i} \cdot \frac{\partial S_n}{\partial \alpha_j} + \frac{\partial S_n}{\partial \alpha_i} \cdot \frac{\partial S_n^*}{\partial \alpha_j} \\ &+ S_n^* \frac{\partial^2 S_n}{\partial \alpha_i \partial \alpha_j} + S_n \frac{\partial^2 S_n^*}{\partial \alpha_i \partial \alpha_j} \\ &= 2 \operatorname{Re} \left( \frac{\partial S_n}{\partial \alpha_i} \cdot \frac{\partial S_n^*}{\partial \alpha_j} + S_n^* \frac{\partial^2 S_n}{\partial \alpha_i \partial \alpha_j} \right) \quad (10) \end{aligned}$$

Obviously for the evaluation of the derivatives of  $E$  it is necessary to go through the whole set of measurement frequencies and evaluate the derivatives for each one. For this reason the computation time required is directly proportional to the number of points used.

For the system in use at the moment it is normal to characterise the crystal by a set of measurements at equal frequency increments, over a range containing the resonant and anti-resonant frequencies. This data is scanned very crudely to find the points of maximum and minimum transmission, and from this, approximate starting values for the circuit parameters are obtained. These values are then refined by iteration, using Equation (3) to calculate each set of increments. The process is terminated when the values of  $R, L$ , and resonant frequency agree to within the stringent limits:

$$|R_n - R_{n-1}| < 0.001 R_{n-1}$$

$$|L_n - L_{n-1}| < 0.001 L_{n-1}$$

$$|\omega_n - \omega_{n-1}| < 0.001 \omega_{n-1} / Q_{n-1}$$

between successive iterations. Typically two to three iterations are required, and the time taken is approximately 500 ms per point per iteration using the HP9825. For machines with assembly language capability the critical part of the programme could be coded in assembler with a considerable increase in speed, but even so a typical 20 point fit takes a total of only 30 s. It should also be noted that there is no need to locate the resonant frequency exactly during measurement, and for this reason very high resolution synthesisers are not necessary.

#### 4 Experimental results

Ideally error parameters would be determined

for each measurement point, but this is impracticable, as recalibration would be necessary for virtually every measurement, and storage requirements could be prohibitive. The alternative method of calibrating at certain fixed points and using interpolation has therefore been used; crystals were all measured using a General Radio T05 transistor test mount. The frequency range of the equipment meant that crystals of almost any frequency could be measured, and the system has been successfully used up to 200 MHz.

Table 1 gives values of the parameters of a 10 MHz crystal as determined in a sequence of repeated measurements. The frequency range used was 9.99 MHz to 10.027 MHz in 250 Hz steps, so the evaluation was based on 149 individual measurements. The incident power level was approximately -12 dBm. The test system was housed in a temperature controlled room, and the crystal was surrounded by insulating foam to reduce thermal transients.

Table 1

Series resonant frequency (Hz)	L(mH)	ESR( $\Omega$ )	C <sub>0</sub> (pF)
1. 9998186.5	22.08	16.8	2.65
2. 9998185.9	22.09	16.8	2.65
3. 9998184.0	22.04	16.3	2.65
4. 9998185.6	22.05	16.6	2.65
5. 9998185.9	22.04	16.5	2.65
6. 9998184.7	22.06	16.4	2.65
7. 9998183.9	22.04	16.3	2.65
8. 9998186.1	22.04	16.5	2.65
9. 9998186.6	22.05	16.6	2.65
10. 9998186.0	22.04	16.5	2.65
11. 9998186.2	22.06	16.6	2.65
12. 9998185.5	22.03	16.5	2.65

Tables 2 and 3 show similar results for 90 MHz and 150 MHz crystals using frequency ranges of 90 MHz to 90.009 MHz in 50 Hz steps, and 149.999 MHz to 150.009 MHz in 100 Hz steps respectively. The other measurement conditions were similar.

Table 2

Series resonant frequency (Hz)	L(mH)	ESR( $\Omega$ )	C <sub>0</sub> (pF)
1. 90002095	8.915	51.6	2.85
2. 90002097	8.909	51.5	2.85
3. 90002099	8.909	51.5	2.85
4. 90002100	8.912	51.5	2.85
5. 90002101	8.914	51.6	2.85
6. 90002101	8.916	51.6	2.85
7. 90002101	8.910	51.6	2.85
8. 90002101	8.909	51.6	2.85

Table 3

Series resonant frequency (Hz)	L(mH)	ESR( $\Omega$ )	C <sub>0</sub> (pF)
1. 150002111	10.25	142.0	2.70
2. 150002115	10.24	142.0	2.70
3. 150002117	10.25	142.1	2.70
4. 150002116	10.25	142.1	2.70
5. 150002113	10.25	142.0	2.70
6. 150002116	10.24	142.0	2.70
7. 150002120	10.26	142.1	2.70
8. 150002121	10.26	142.1	2.70
9. 150002122	10.27	142.2	2.70
10. 150002115	10.25	142.1	2.70

These crystals had been measured some time previously by Salford Electrical Instruments Ltd using their standard IEC  $\pi$ -network, with additional C<sub>0</sub> cancellation for the 90 and 150 MHz crystals. The values of ESR obtained in this way agreed well with the above results even for the 150 MHz crystal. However for the motional inductance, values of 8.4 and 8.9 mH were obtained for the 90 and 150 MHz crystals, compared to the above values of 8.9 and 10.3 mH.

The above results are slightly idealised in that the crystals were not removed from the jig between measurements, but they show the excellent reproducibility of the basic system, with values of motional inductance consistent to 1 in 10<sup>3</sup> and ESR to within 1 in 10<sup>2</sup>. Equivalent series resistance is the parameter subject to the greatest fluctuations, and altering the number or distribution of the measurement points used in the fitting procedure can produce changes of several percent. It is therefore questionable whether ESR can be truly defined with more precision than this.

## 5 Conclusions

A network analyser system has been established for the measurements of crystal parameters, differing from previous systems in that the interpretation of the data is performed by a general non-linear fitting procedure which is implemented on the system controller and is an integral part of the method. Network analysers offer the advantages of excellent accuracy and frequency range, and are readily calibrated using traceable standards. A straightforward, but very reliable method for analysing the data using 'optimal' least squares fits has been demonstrated, and has been shown to provide excellent reproducibility, as the results are based on a large number of separate measurements, and all operator dependence is removed. It has been found that different fitting procedures produce noticeably different values for certain crystal parameters, particularly ESR, and this provides a limit to how meaningful these parameters are, independent of the method of measurement. The method has already been used, very successfully, for the selection of filter crystals, where tight matching for motional inductance was required.

### References

- 1 Pustarfi, H S and Smith, W L, "An automatic crystal measurement system", Proc 27th AFCS, p 63-72, 1973
- 2 IEC Publication 444 (1973), "Basic method for the measurement of resonance frequency and equivalent series resistance of quartz crystal units by zero phase technique in a  $\pi$ -network"
- 3 Hackborn, P A, "An automatic network analyser system", Microwave Journal, p 45-52, May 1968
- 4 Rehnmark, S, "On the calibration process of automatic network analyser systems", IEEE Trans, MTT-22, 4, p 457-458, 1974
- 5 Adam, S F, "Automatic microwave network measurements", Proc IEEE, 66, 4, p 384-391, 1978
- 6 Smythe, R C, "An automated resonator measurement system using a reflection coefficient bridge", Proc 35th AFCS, p 290-285, 1981

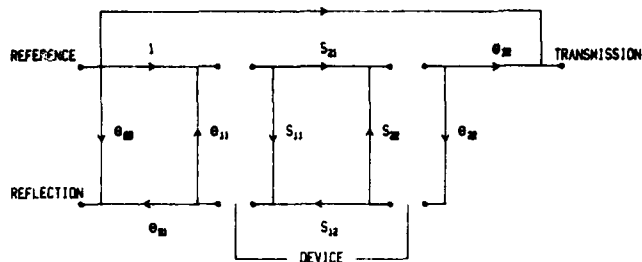


Figure 1. Network Analyser Error Model-One Direction

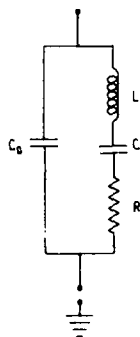


Figure 2. Crystal Equivalent Circuit with Can and One Terminal Grounded

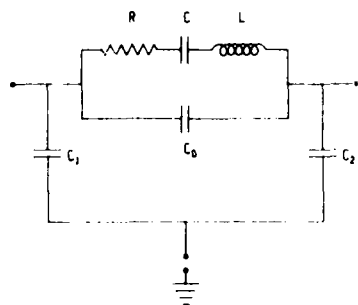


Figure 3. Equivalent Circuit with Can Grounded

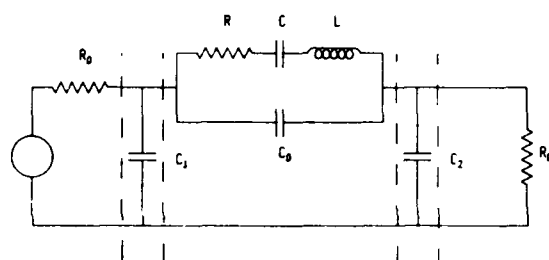


Figure 4. Measurement Circuit

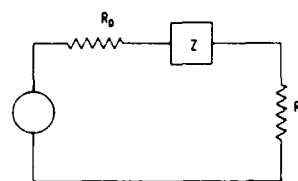


Figure 5. Ideal Circuit After Removal of Shunt Capacitances

# AN INSTRUMENT FOR AUTOMATED MEASUREMENT OF THE ANGLES OF CUT OF DOUBLY ROTATED QUARTZ CRYSTALS

John L. Chambers

Advanced Research and Applications Corporation  
1223 East Arques Avenue  
Sunnyvale, CA 94086

## Summary

The development of an automated x-ray orientation system for accurate measurement of the angles of cut of doubly rotated quartz crystal plates is described. Our goal is to develop a prototype instrument capable of determining the conventional phi and theta angles to 4 arc-seconds reproducibility and 10 arc-seconds absolute accuracy for the SC-cut, and capable of measuring the general orientation of any cut on the bulk-wave zero-temperature-coefficient locus. Blanks are assumed to be pre-cut to within 15 minutes of the desired angles of cut.

A prototype laser-assisted Laue diffractometer has been fabricated, and we are currently at the stage of evaluating and refining its performance. Currently the performance of the x-ray subsystem is as good as 2 arc-seconds. Recent improvements to the laser subsystem have brought its performance in line with that of the x-ray subsystem. When blanks are remounted between measurements, a precision of 3-4 arc-seconds standard deviation in phi and theta is observed for blanks with 3-5 micron surface finish.

## Introduction

In this paper we report progress made in the development of a laser-assisted Laue diffractometer for accurate and automated measurement of the angles of cut of quartz crystals, including doubly rotated cuts -- in particular the SC cut. Earlier work on this instrument has been described in the Proceedings from last year's Symposium<sup>1</sup> and elsewhere.<sup>2,3</sup> This instrument utilizes a continuous x-ray spectrum rather than a monochromatic one as in conventional diffraction instruments, permitting use of a sample mount with only one degree of freedom in motion of the blank.

The major objective of the instrument is, given a blank cut to within about 15 arc-minutes of the desired angles, the conventional phi, theta, and psi, to bring the angles of cut to a few arc-seconds accuracy in order to determine the orientation required to yield the desired angles. These measurements will be made with respect to a reference standard crystal for each type of cut

to be measured. The design goals we wish to meet include:

- 1) Types of Cuts. The system must be capable of measuring blanks of general orientation, in particular those on the bulk-wave zero-temperature-coefficient locus. It must be possible to measure round blanks, and to accommodate a variety of blank sizes and thicknesses.
- 2) Reproducibility and Accuracy. For SC cut blanks the goals are given as standard deviation from the mean in the conventional phi/theta angles of cut. The goal for reproducibility (i.e., for repeated measurements of the same blank) is plus-or-minus 4 arc-seconds, and the goal for absolute accuracy is plus-or-minus 10 arc-seconds.
- 3) Rate of Measurement. Measurements of doubly rotated cuts are to proceed at a rate of 50 or more plates per hour.

Thus, the design goals specify an instrument with greater flexibility and accuracy than commonly found in conventional x-ray orientation equipment. As described below we are very close to achieving the first two goals set forth above. While the time per measurement is currently about three times the design goal, the instrument at this stage has been developed with accuracy rather than speed as the prime consideration, and significant improvement is possible in the determination times. Although these determination times appear long compared with those for current production measurements of singly rotated cuts, the measurement of a general three-dimensional orientation is inherently a longer process than determination of one angle-of-cut, and longer measurement times would thus be expected regardless of the choice of x-ray method.

## The Laue Method

The differences between the Laue method and conventional diffraction techniques as they apply to this system have been described earlier.<sup>1-4</sup> An excellent general text on the theory and application of the Laue method is available.<sup>5</sup> The Laue method has long been used for orientation of

AD P001538

crystals to about 0.25 degrees, usually employing visual analysis of a diffraction pattern on film or on a fluorescent screen. Higher-precision Laue work (35 arc-seconds in favorable cases) has been previously performed where the desired crystal orientation places a crystallographic symmetry axis exactly along the incident x-ray beam, by matching the intensities of symmetry-equivalent reflections,<sup>6</sup> but that method is less useful for an instrument which must measure a variety of general orientations.

Because the Laue method uses a continuous incident x-ray spectrum, small changes in crystal orientation do not in general move the crystal in and out of the diffracting condition. This is in contrast to the case of conventional Bragg diffraction, where a small change in the orientation of a diffracting crystal in general causes the diffraction maximum to disappear entirely. Three degrees of freedom in motion of the sample are thus required to search for a diffraction peak when performing general orientation of a crystal by the Bragg method. In the Laue case, since the peak is visible over a wide range of orientations, only a single degree of freedom in sample motion, a rotation about the  $\psi$  axis, is required when the orientation in  $\phi$  and  $\theta$  is known to better than the separation of the prominent peaks in the Laue diffraction pattern. If it were not necessary to measure round blanks; i.e., if  $\psi$  were also known to 0.25 degrees at the outset, no motion of the blank would be required at all. Determination of the locations of two diffraction peaks, enabling the three-dimensional orientation of any two non-colinear normals to crystallographic planes to be computed, is sufficient to completely specify the three-dimensional orientation of a crystal.

The major advantage of the Laue method is thus the fact that peaks are much more readily located, leading to a mount with only one rotational degree of freedom, and therefore to a design which provides a great deal of accessibility to the sample. The major disadvantage lies in the lower counting rates obtained. Careful choice of instrument geometry and x-ray reflections is required to maximize the counting rates.

#### Laue Instrument Concept

Given a Laue diffraction peak, as the orientation of the crystal is changed by a small amount the position of the peak changes just as if the reflection were occurring from a mirror parallel to the diffracting lattice planes, slightly changing the peak energy of the diffraction. At a 400 mm crystal-to-detector distance, as in the system to be described, the x-ray spot moves about 4 microns for an arc-second change in crystal orientation in the plane of reflection. Figure 1 shows the concept employed in the Laue diffractometer for completely determining the crystal lattice orientation. A minimum of two x-ray detectors is required, although a larger number can be used (three are available on our system). The blank is mounted on a rotating stage with the axis

of rotation approximately parallel to the  $\psi$ -axis of the blank. The x-ray detectors, with apertures large enough (plus-or-minus 1 degree in this case) to accommodate any mounting errors as well as errors in the angles of cut, are positioned so that only at some unique stage rotation angle will x-ray reflections enter all counters simultaneously. The exact position of each reflection within its counter aperture is then determined. These measurements permit the normals to two or more sets of diffracting planes and, thus, the crystal orientation, to be computed.

Assuming that the blank has been mounted so that the normal to its face is exactly parallel to the rotator axis, this information is sufficient to determine the angles of cut. However, mounting errors are typically in the one-minute range, as described below, and a correction must be made. The method used is shown in Figure 2, and employs a He/Ne laser and linear position-sensitive detector to measure the precession of a laser beam reflected from the face of the blank as it rotates, to yield both the height and orientation of the face. Determination of the severity of errors arising from sample mounting and the method of laser-assisted diffractometry have been described previously by Vig.<sup>7</sup>

#### Description of the Laue Diffractometer

An overall view of the prototype Laue diffractometer is shown in Figure 3. Although the He/Ne laser itself is not visible from this angle, the other major features of the instrument can be seen. A steel table serves as the base of the instrument. Mounted in the center of this table is a high-precision rotating stage which, like the other moving parts of the instrument, is under computer control. Just to the left of the rotary stage is the x-ray source collimator, attached to the x-ray source itself. The diffracted x rays are detected by three x-ray detectors mounted on the three arch supports which can be seen at the right of the rotary stage. The He/Ne laser (not visible here) is mounted near the central arch support, and the reflected laser beam is detected by an optical system including a position-sensitive diode detector, shown at the far left. Each of the major components is described in more detail below.

#### Sample Mount

Figure 4 is a closer view of the rotary stage on which the sample is mounted. The stage was chosen for its low run-out normal to the rotational plane (under 2 arc-seconds). It is driven by a stepping motor at .01 degree/step and up to 2000 steps/second, giving a slew rate of about 20 degrees/second. On top of the stage is a three-point vacuum chuck, on which the blank is mounted. The collar around the sample mount is threaded to permit adjustment of the sample height, while keeping the orientation of the sample approximately the same (currently to 1-2 minutes). The viewing angle in this figure is approximately the same as in Figure 3. The x-ray source collimator

can be seen at the left, and the direction of the incoming He/Ne laser beam can be seen at the right.

#### X-ray Subsystem

The x-ray source is a standard sealed-tube 1800 watt x-ray diffraction tube, which is excited below the characteristic K-line potential in order to produce a relatively smooth "white-radiation" spectrum. The incident x-ray beam approaches the sample at a glancing angle of 20 degrees. The x-ray source collimator is approximately 20 cm in length and has a 1 mm aperture at each end. The x-ray tube mount permits fine translational and rotational adjustments of the source for alignment purposes. At the exit port of the x-ray tube housing is the x-ray shutter, which is also under computer control and has both "open" and "closed" fail-safe sensors for operator safety.

Figure 3 is a view from what we have been calling the "left" of the instrument, looking from the x-ray source toward the x-ray detectors. From this angle the three detector arch supports can be better resolved. Each of the arch supports permits its detector to be placed at any inclination angle between 15 and 65 degrees from horizontal, maintaining a fixed sample-to-detector distance of 400 mm. The center of the sample serves as the center of all detector motions. The central arch is fixed at zero azimuth (i.e., the angle in the horizontal plane), whereas each of the two outside detector arches can be varied in azimuth between 20 and 90 degrees from the central arch, again maintaining a fixed sample-to-detector distance. This detector mobility permits the instrument to be readily adapted to a wide variety of cuts, and a repositioning of the detectors is the only change in the instrument required to change from one type of cut to another. This method of measurement and reconfiguration makes no distinction between singly and doubly rotated cuts; i.e., every blank is measured in terms of its general three-dimensional orientation. While speed and accuracy therefore do not improve for a singly rotated cut, both angles of cut are obtained, and the instrument should be uniquely useful, for example, in measurement of planar Al-cut crystals.

The x-ray detectors are standard NaI scintillator photomultiplier detectors, with 6 mm aperture subtending approximately 1 degree at the sample, at a sample-to-detector distance of 400 mm. This configuration leads to a dynamic range of about  $\pm 0.4$  degree combined error in angles of cut and crystal mounting, while maintaining apertures sufficiently narrow to avoid positioning ambiguities in the initial search for x-ray reflections. During this initial search the x-ray counts in all detectors are monitored as the stage is rotated at slow speed. The search requires 30 seconds.

In front of each detector is a translating stage, which scans a pair of 1.0 mm slits over its aperture, in order to measure the spatial x-ray intensity distribution within the aperture. The

resulting x-ray peak profiles are then fit by least squares to a Gaussian to determine the position of the x-ray spot within the detector to 10-40 microns. Figure 6 is a close-up view of one of the outside translating stages, taken from the far "right" of the instrument. The stage has a 7.0 cm total travel and a 0.1 mm step size, leading to a 2 cm/sec slew rate. The nature of the slits used to determine the x-ray spot position can also be seen in Figure 6. The two slits are at 90 degrees to one another and each is at 45 degrees with respect to the direction of stage travel. This arrangement allows the X-Y coordinates of the x-ray spot within the detector to be determined with a single translational motion. Scans are performed on all three detectors simultaneously, first with the "upper" slit, then with the "lower." Scan times vary with the speed and accuracy requirements. The counting rates are typically a few thousand per second with the counter apertures unobstructed, and several hundred to one thousand at the highest point in a translator scan. These rates dictate counting times in the range of 15 seconds to 2 minutes per scan. Reproducibility in the measured spot positions varies with the scan times and the strength of the x-ray reflection being measured, but ranges from 40 microns for the shorter scans to better than 10 microns for longer scans of strong reflections. Careful choice of the particular x-ray reflections used is thus required, and their strength, accessibility, and sensitivity to the orientation angles must be taken into account, as well as the fact that they must result in an unambiguous initial positioning of the blank in psi. At present the reflections used for SC cuts are  $[0,-1,1]$ ,  $[2,-1,-1]$ , and  $[1,-2,-4]$ .

#### Laser Subsystem

In Figure 5 the laser subsystem source, a 2 mW He/Ne laser, can be seen mounted just to the left of the central x-ray detector arch support. Both the laser source and the laser detector are inclined at 15 degrees from horizontal with respect to the sample. One of the most important criteria in the choice of the laser was low angular drift, since significant drift with variation in the ambient temperature was observed with the first laser tried. The laser mounted on the prototype instrument (Spectra-Physics Model 145) is specified at less than 0.02 mrad (about 4 arc-seconds) drift and in practice no drift has been observed. The beam diameter is 0.5 mm and the divergence is 1.7 mrad.

The detector for the reflected laser beam can be seen in the foreground in Figure 5 and at the far left in Figure 3. It consists of a lens system to magnify the motion of the reflected laser beam, a bellows to decrease the amount of ambient light entering the system, and an electronics package consisting of a linear position-sensitive photodiode mounted with the position-sensitive axis vertical and circuitry to convert the diode output into a voltage proportional to spot position. This system enables the position of the reflected laser beam to be monitored by

the computer in real-time during the initial rotational search for x-ray reflections. The drawback of such a system is that the detector diode integrates the intensity over its entire active area, and is thus susceptible to problems caused by scatter, as described later.

As the initial search for x-ray reflections proceeds and the sample is rotated 360 degrees, the reflected laser beam traces out a pattern which is very close to an ellipse for small deviation of the normal to the face from the axis of rotation, as shown in Figure 2. The vertical component of the ellipse, which is measured by the laser detector, in the ideal case traces out a sine wave when plotted against rotator position. The amplitude of the sine wave yields the magnitude of crystal tilt, the phase yields the direction of tilt, and the DC offset yields the crystal height. Over the course of the real-time laser data acquisition, up to 300 individual stage position and laser spot position readings are taken and stored. The current method of analysis is a least-squares fit of the data to a sine curve.

#### Instrument Alignment

Although the measurements are made relative to a reference standard crystal, the high degree of accuracy needed requires that the instrument be very accurately aligned. For example, a 0.1 degree rotation of the translator slits within their frame is sufficient to produce a 10 arc-second systematic error component in the measured angles of cut.

The initial assembly and alignment of the instrument was accomplished with the use of an autocollimator and several special-purpose alignment fixtures. The equatorial plane of the instrument is defined by the plane in which the outside x-ray detectors move when their azimuth is varied. With aid of the autocollimator, the rotating stage axis was made normal to the equatorial plane within 0.1 minute. The meridional plane of the instrument, defined by the inclination motion of the central detector, and the 20-degree incident direction of the x-ray source collimator were also established to within a fraction of a minute. Fiducial marks were established for the x-ray detector motions to permit placement of angular scales for direct setting and readout of the detector angles, although the actual detector positions employed for measurement of each type of cut will eventually be set by means of locating pins.

With the instrument aligned, it became possible for the first time to set the x-ray detectors to computer-predicted positions and directly find the reflections sought, without the tedious procedure of first finding the reflections on film and adjusting the detector positions accordingly.

#### Control Subsystem and Software

The control subsystem, shown in Figure 7, is based on a Digital Equipment Corp. LSI-11/23

microcomputer. The computer is interfaced to the instrument through a CAMAC crate, which is a highly flexible standardized digital interfacing system. The CAMAC crate accepts standardized plug-in modules which in this case include four stepping-motor controllers, a digital I/O port (for control of the x-ray shutter, etc.), an A/D convertor for the laser detector, and a six-channel scaler which counts the pulses received by the x-ray detectors. Also present are a NIM bin containing the high-voltage power supply and pulse-height discrimination circuitry for the x-ray detectors, and a power supply for the x-ray shutter and stepping motors. The computer peripherals include dual floppy disk drives and, shown at the very top, a 5 Mbyte hard-surface disk drive. The hard disk is present for development purposes, and the instrument can normally be run with just the floppy disk. A CRT terminal for operator input and a 30-cps keyboard/printer for a hard-copy record of measurement results are also shown.

The primary function of the control subsystem software is to perform the automatic measurement sequence, first for a reference standard crystal, then for the blanks to be measured. The program outputs a hard-copy record of the measurement results for each crystal, and keeps track of the overall measurement statistics for each batch of crystals. The operator is prompted when any intervention, such as mounting the next blank, is required.

Since we are dealing with low-level signals compared to those commonly observed in conventional orientation equipment, and we require very high accuracy, the computer is essential in extracting as much information from the signal as possible. Reference has already been made above to the areas where least-squares curve fitting techniques are employed to extract this information. Another area where statistically weighted least-squares techniques are used to achieve the optimal result is in the determination of crystal orientation from the computed diffraction vectors. The set of vectors obtained from the measured blank is treated as a rigid body, which is rotated to achieve the best match (in a least-squares sense) with the set of vectors measured from the reference standard crystal. The three rotation angles determined from this procedure correspond to the changes in the angles of cut ( $\phi$ ,  $\theta$ , and  $\psi$ ) between the measured crystal and the reference standard.

Because of the developmental nature of the project, a great deal of flexibility has been designed into the control software. First, the scan parameters, counting times, sampling intervals, and machine calibration parameters (such as the exact incident x-ray beam angle, angle of each translator axis from its nominal value, etc.) can all be changed without any modification of the software. This permits a wide variety of scan types and conditions to be investigated in order to arrive at the optimal parameters. Second, the software is constructed in a highly modular

fashion, such that not only the fully automated measurement sequence, but also any individual operation within the automatic sequence, such as the initial search for x-ray reflections, the determination of laser scan results, the performance of the translator scans, etc., can be performed by issuing a single command. This feature greatly reduces the time required to change the configuration of or optimize the results from any individual subsystem. Third, there are a number of commands available to access the instrument at machine level; that is, to drive any stage to a specified position, to accumulate x-ray counts for a specified interval, to open or close the x-ray shutter, etc. Fourth, the program is capable of combining the data gathered from repeated measurements of the same blank, relating any inconsistencies to possible errors in the instrument calibration parameters. While the software envisioned for a production instrument would require only a subset of these features, they have proven to be invaluable to date in the development of the prototype.

#### Performance

Although the development is not complete, full automated measurements have been made on a number of Si-cut blanks. These measurements permit evaluation of the individual x-ray and laser subsystems, and of the instrument as a whole. In these cases where only two x-ray reflections were used, the  $\{0,-1,0\}$  and  $\{0,-1,-1\}$  reflections were the ones measured.

#### X-ray Subsystem

X-ray subsystem performance was evaluated by repeated measurements of the same blank without any remounting of the blank in between measurements. A number of blanks was tested in this manner. The crystal under test was used as both the reference standard and the blank to be measured; thus, a change of zero in theta and phi between the reference crystal and the test crystal would correspond to a perfect measurement. This x-ray-only reproducibility was excellent, with the actual values dependent as expected on the counting times. The values were computed as standard deviation from the mean over a series of measurements (usually between 20 and 40), and are shown in Figure 8. The reproducibility ranged from  $\pm 12$  arc-seconds in theta and phi for determinations requiring a total time of 1.7 minutes with 2 x-ray detectors, to  $\pm 2$  arc-seconds for determination times of 4 minutes or more with 4 detectors. Since each measurement was begun with a full initial search for x-ray reflections, the measurements within each series covered a range of psi values, typically  $\pm 0.25$  degrees. Since the measured orientation relative to the reference includes the change in psi as well as that in phi and theta, and we know the positional change in phi for these tests, we can compare the x-ray psi value as an additional indicator of x-ray subsystem performance. The agreement is found to be within one standard deviation in psi, which because of the geometry involved is about

twice that of phi or theta, given above. The x-ray subsystem results thus reflect not only the reproducibility of the translator scans, but also the overall linearity and accuracy of the x-ray subsystem. Moreover, a full set of laser data was recorded for each of these measurements, and a new mounting error correction computed and applied. Thus, these values also reflect the reproducibility (but not the accuracy) of the laser subsystem.

As Figure 8 shows, the x-ray reproducibility depends on the total measurement time, as expected from counting statistics. The relationship between the total determination time shown in Figure 8 and the x-ray counting times in determination of the x-ray spot positions is  $T = 90 + X$ , where T is the total determination time in seconds and X is the total x-ray counting time in seconds. The 90-second overhead includes the initial search for x-ray reflections, centering the reflections within the apertures as well as possible with the rotator, establishment of scan limits for the translator scans, and computation of the results. Since the algorithms and procedures have to date been optimized for accuracy rather than speed, it is felt that this overhead can be reduced considerably; e.g., by more than half. The x-ray counting times on the other hand cannot be reduced without a loss of accuracy, although location of a stronger x-ray source or use of additional detectors would enable shorter times to be employed.

The x-ray subsystem reproducibility of 2 arc-seconds for long counting times is excellent and is consistent with our initial goals. It indicates that the Laue method need not be limited to coarse alignment, but is suitable for high-precision work as well.

#### Laser Subsystem

The laser subsystem used to correct for small sample mounting errors is equally as important as the x-ray subsystem in the functioning of the instrument. The importance of correcting for mounting errors of this sort has been determined by Vig,<sup>7</sup> who found that these errors typically cause 1 arc-minute variations in orientation measurements. Our results are very similar, with a standard deviation from the mean of 30 seconds to 1 minute in repeated measurements of the orientation of the face of a blank remounted before each measurement. The x-ray-only reproducibility measurements included a new laser measurement in each determination. Since the blank was not remounted in between measurements, the results of these tests are indicative of the laser subsystem reproducibility (but not its absolute accuracy). This reproducibility was excellent, with a standard deviation from the mean of 0.5 arc-second in the orientation of the face and of 2 microns in the height of the blank, for series of 10-20 measurements.

Since the reproducibility of both the x-ray and laser subsystems was excellent, good results were expected for the first measurements in which

the same blank was repeatedly measured, but remounted after each determination. The results were, however, considerably worse than expected, with standard deviations in  $\phi$  and  $\theta$  of 10-15 arc-seconds for the two-detector case, as shown in Figure 8. After further experimentation, the absolute accuracy of the laser subsystem was the most likely source of error, in light of the following considerations:

The reflected laser beam was not clean. It was surrounded by scatter which was readily observable in normal room light. This scatter, or speckle, rotated around the primary beam as the crystal was rotated, and appeared non-uniform enough to produce problems in determination of the center position of the primary beam (remembering that the detector integrates the intensity over its entire active area).

Both the amount of scatter visible, and the magnitude of the errors in  $\phi$  and  $\theta$ , depended on the surface finish of the blank. More highly polished blanks (3-micron lapped, chemically polished) gave better performance than less highly polished blanks (5-micron lapped). For the roughest blanks tried (12.5-micron lapped), the primary reflected laser beam could not be visually or electronically differentiated from the speckle. Figure 9 is a plot of the laser data for a 5-micron lapped blank, along with the best-fit sine curve. The deviations from the curve caused by the scatter are readily apparent.

While the ability to accurately measure the change in  $\psi$  of a blank with the x-ray subsystem indicated a high degree of accuracy as well as precision, we had no such handle on the absolute accuracy of the laser subsystem.

These considerations led to an experiment designed to test whether improvement in the ratio of the primary reflected laser beam intensity to that of the speckle would improve our overall measurement statistics. Five SC-cut blanks (5-micron lapped) were subjected to deposition of a 500 Angstrom layer of aluminum on one surface. Visual inspection of the laser beam reflected from these blanks indicated a substantial improvement in the primary beam:scatter ratio. The x-ray intensities were not measurably affected by the presence of the aluminum on the surface. Repeated measurements of these blanks, dismounting and remounting the blank after each measurement gave a standard deviation from the mean of 5 arc-seconds in  $\phi$ , and 5 arc-seconds in  $\theta$ , for determinations requiring 4 minutes each with two x-ray detectors. Figure 10 is a plot similar to that in Figure 9 for one of the aluminized blanks, and it can be seen that the noise in the curve is considerably reduced. This result is also shown in Figure 8.

Thus, while the precision of the laser subsystem is excellent, its absolute accuracy

is currently the limiting factor in the accuracy of the instrument, contrary to expectations at the outset. Unlike the x-ray subsystem, where the performance can be increased with longer counting times, the laser subsystem performance is more rigidly fixed. Its accuracy currently limits the overall accuracy of the instrument to 10-15 arc-seconds, as shown in Figure 8. Since the initial writing, focusing optics between the laser source and the sample, and a lowering of the incident laser angle to  $7.5^\circ$  have reduced these overall standard deviations to 3-4 arc seconds in  $\phi$  and  $\theta$  for approximately 100 measurements of .550" diameter, .05" thick SC-cut plates with 3-5 micron surface finish, requiring 2.5 minutes time per measurement.

### Conclusions

The results obtained to date suggest that the instrument discussed in this paper can provide automated measurements of the full three-dimensional orientation required for doubly rotated quartz crystals to an accuracy and at a throughput that is unmatched by any other current system.

This study has demonstrated that it is possible to obtain very high accuracy in measurement of the orientation of crystals by the Laue method, and the method need not be restricted to low-precision work. The prototype instrument is capable of 3-4 arc-second precision on blanks with a surface finish in the 3-5 micron range.

The instrument is very versatile, since it can be readily changed by repositioning the x-ray detectors to accommodate different types of cuts of quartz, or even other crystalline materials. Moreover, measurements are made automatically, enabling the instrument to be integrated with automatic handling equipment.

Although fully suitable for measurement of singly rotated cuts, the lower x-ray counting rates obtained with the Laue technique compared to monochromatic techniques leads to longer determination times. Hence, the throughput of measured crystals is lower than for conventional x-ray orientation instruments designed for singly rotated crystal measurements. Improvements in throughput for this instrument would result from the use of a more intense x-ray source or more x-ray detectors.

### Acknowledgements

This work was supported by the US Army Electronics Research and Development Command, Fort Monmouth, NJ. P. R. Hoffman Co., Carlisle, PA, is the prime contractor and has been responsible for the mechanical elements of the prototype instrument. Advanced Research and Applications (ARACOR) is a subcontractor to P.R. Hoffman Co.

I wish to thank my colleagues at ARACOR, S.T. Workman, M. Pugh, L. Palkuti and J. Stanley, who have contributed substantially to this work, and am also grateful to John Vig for his support and valuable suggestions throughout the course of the program. I also wish to thank Roger Ward, who first suggested the Laue method to us for this application, and Jack Kusters and Charles Adams of Hewlett-Packard for kindly providing an SC-cut reference standard crystal.

#### References

1. J. L. Chambers, M. A. Pugh, S. T. Workman, R. W. Birrell, and R. J. Valihura, "An Instrument for Automated Measurement of the Angles of Cut of Doubly Rotated Quartz Crystals," Proc. 35th Annual Symp. on Frequency Control, pp. 60-70, 1981.
2. R. W. Birrell, R. J. Valihura, J. L. Chambers, M. A. Pugh, and S. T. Workman, Research and Development Technical Report DELET-TR-79-0254-1, USAERADCOM, Fort Monmouth, NJ, 1980.
3. R. W. Birrell, R. J. Valihura, J. L. Chambers, M. A. Pugh, and S. T. Workman, Research and Development Technical Report DELET-TR-79-0254-2, USAERADCOM, Fort Monmouth, NJ, 1981.
4. R. W. Birrell, R. J. Valihura, J. L. Chambers, M. A. Pugh, and S. T. Workman, Research and Development Technical Report DELET-TR-79-0254-3, USAERADCOM, Fort Monmouth, NJ, 1981.
5. J. I. Amoros, M. J. Buerger, and M. Canut de Amoros, "The Laue Method," Academic, New York, 1975, 375 pages.
6. G. Christiansen, L. Gerward, and I. Alstrup, Acta Cryst. A31, 142-145, 1975.
7. I. R. Vig, "A High Precision Laser Assisted X-Ray Goniometer for Circular Plates," Proc. 29th Annual Symp. on Frequency Control, pp. 240-247, 1975.

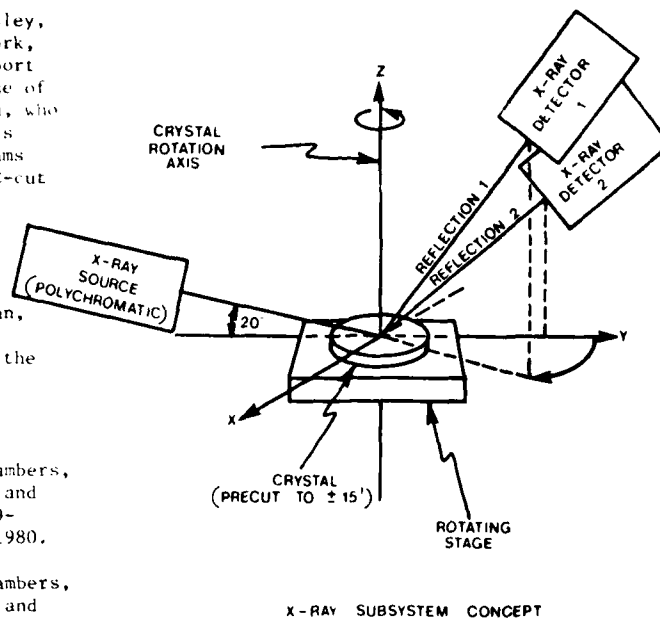


Figure 1. Concept for the X-Ray Portion of the Measurement Apparatus. A Minimum of Two Detectors is Required, Three are Available on the Prototype Instrument

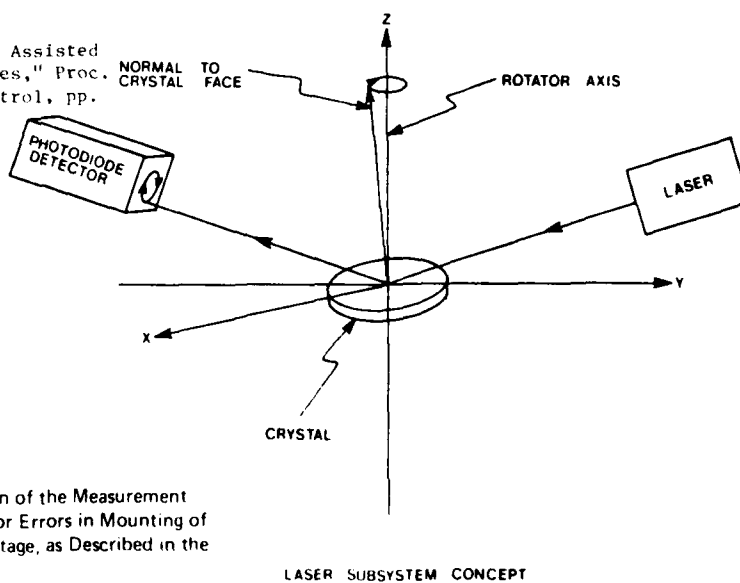


Figure 2. Concept for the Laser Portion of the Measurement Apparatus, Which Corrects for Errors in Mounting of the Crystal to the Rotating Stage, as Described in the Text



Figure 3. Full View of the Prototype Instrument



Figure 4. Closeup of the Rotating Stage. Angle of View is About the Same as in Figure 3.

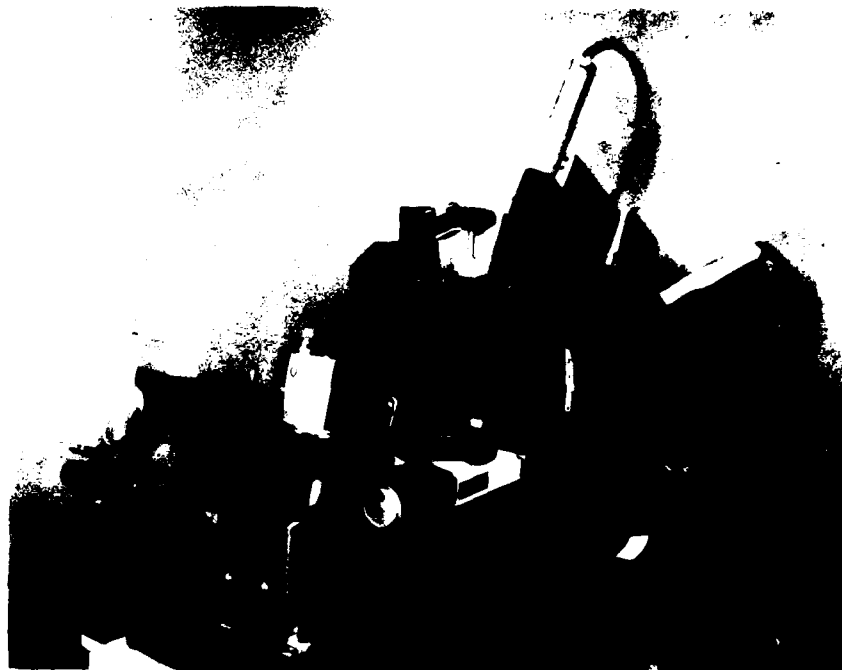


Figure 5. View of the Prototype Instrument from X-Ray Source  
Toward Detectors. The Laser Can Be Seen Just to the  
Left of the Central Arch



Figure 6. Closeup of One of the Outside Translators. The Pair of 1.5 mm Slits Used in the X-Ray Scans Can Be Seen



Figure 7. Control Subsystem for the Prototype Instrument, with Computer, Computer Peripherals, X-Ray Counting Circuitry, and CAMAC Digital Control Interface.

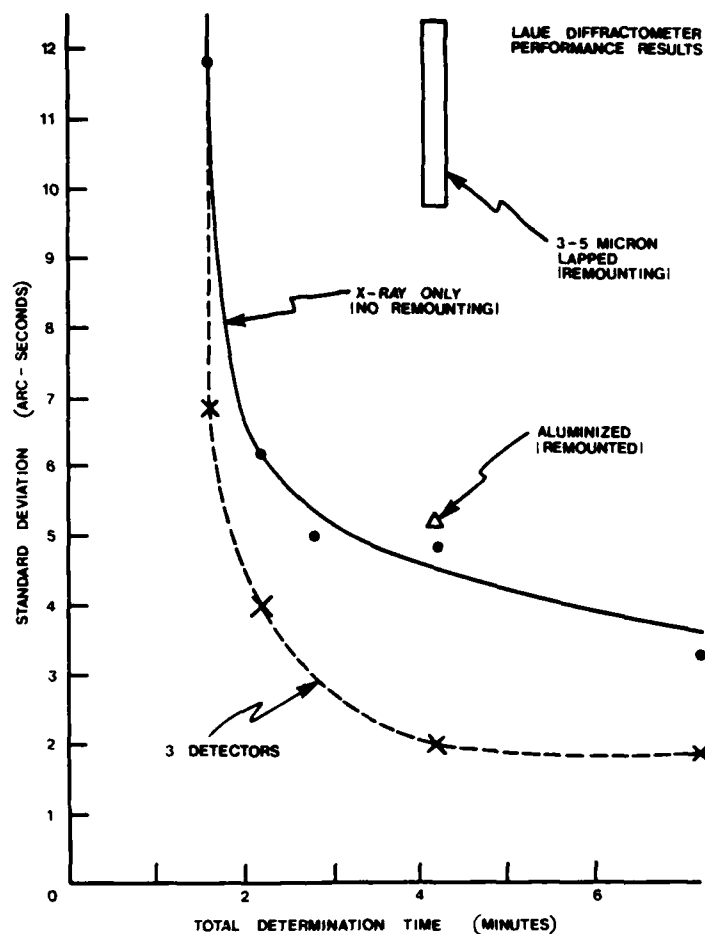


Figure 8. Performance of the Instrument. The Solid Curve Represents the X-Ray-Only Performance with 2 X-Ray Detectors for Repeated Measurements of a Typical Blank with a 5-Micron Surface Finish. Each Point on the Curve was Computed from Between 20 and 65 Measurements. The Dashed Curve Represents the Improvement Obtained When All Three Detectors Are Used. The Large Rectangle Represents the Results When Blanks With 3-5-Micron Surface Finish were Remounted Between Each Measurement. The Triangle Represents the Results for Aluminized Blanks.

LASER DATA, PRH XSTAL, 2ND 00 DEG CW ROTATION

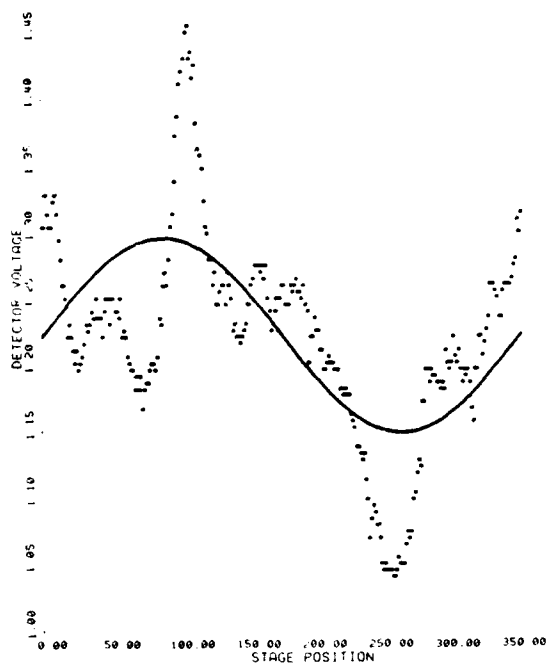


Figure 9. Laser Detector Data for a Full Rotation of an SC-Cut Plate with 5-Micron Surface Finish. The Best Least-Squares Sine Curve Fit to the Data is Also Shown.

LASER DATA, ALUMINIZED XSTAL #3.

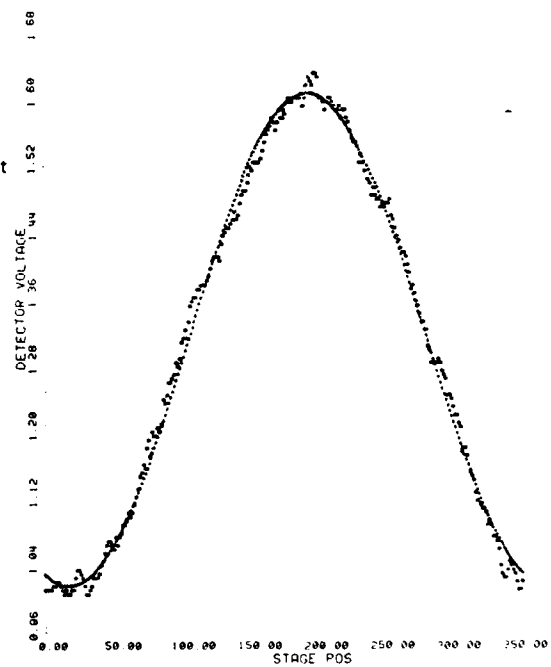


Figure 10. Laser Detector Data for a Full Rotation of an Aluminized SC-Cut Plate. The Data Follow the Expected Sine Curve to a Much Greater Degree than the Data in Figure 9.

AD P001539

PERFORMANCE OF AN AUTOMATED HIGH ACCURACY  
PHASE MEASUREMENT SYSTEMS. Stein, D. Glaze, J. Levine, J. Gray, D. Hilliard, D. Howe  
Time and Frequency Division  
National Bureau of Standards  
Boulder, Colorado 80303

and

L. Erb  
ERBTEC Engineering Inc.  
Boulder, ColoradoSummary

A fully automated measurement system has been developed that combines many properties previously realized with separate techniques. This system is an extension of the dual mixer time difference technique, and maintains its important features: zero dead time, absolute phase difference measurement, very high precision, the ability to measure oscillators of equal frequency and the ability to make measurements at the time of the operator's choice. For one set of design parameters, the theoretical resolution is 0.2 ps, the measurement noise is 2 ps rms and measurements may be made within 0.1 s of any selected time. The dual mixer technique has been extended by adding scalars which remove the cycle ambiguity experienced in previous realizations. In this respect, the system functions like a divider plus clock, storing the epoch of each device under test in hardware.

The automation is based on the ANSI/IEEE-583 (CAMAC) interface standard.<sup>2</sup> Each measurement channel consists of a mixer, zero-crossing detector, scalar and time interval counter. Four channels fit in a double width CAMAC module which in turn is installed in a standard CAMAC crate. Controllers are available to interface with a wide variety of computers as well as any IEEE-488 compatible device. Two systems have been in operation for several months. One operates 24 hours a day, taking data from 15 clocks for the NBS time scale, and the other is used for short duration laboratory experiments.

Review of the Dual Mixer  
Time Difference Technique

It is advantageous to measure time directly rather than time fluctuations, frequency or frequency fluctuations. These measurements constitute a hierarchy in which the subsequently listed quantities may always be calculated from the previous ones. However, the reverse is not true when there are gaps in the measurements. In the past, frequency was usually not derived from time measurements for short sample times because time interval measurements could not be performed with adequate precision. The dual

mixer technique, illustrated in Figure 1, made it possible to realize the precision of the beat frequency technique in time interval measurements.

The signals from two oscillators (clocks) are applied to two ports of a pair of double balanced mixers. Another signal synthesized from one of the oscillators is applied to the remaining two ports of the mixer pair. The input signals may be represented in the usual fashion

$$V_1(t) = V_{10} \sin [2\pi\nu_{10}t + \phi_1(t)],$$

$$V_2(t) = V_{20} \sin [2\pi\nu_{20}t + \phi_2(t)] \text{ and}$$

$$V_s(t) = V_{s0} \cos [2\pi\nu_{s0}t + \phi_s(t)]$$

where  $\nu_{s0} = \nu_{10}(1-1/R)$  and  $R$  is a constant usually called the heterodyne factor.

The low passed outputs of the two mixers are

$$V_{B1} = V_{B10} \sin [\phi_1(t) - \phi_s(t)] \text{ and}$$

$$V_{B2} = V_{B20} \sin [\phi_2(t) - \phi_s(t)] \text{ where}$$

$$\phi(t) = 2\pi\nu_0 t + \phi(t).$$

The time interval counter starts at time  $t_M$  when  $V_{B1}$  crosses zero in the positive direction and stops at time  $t_N$ , the time of the very next positive zero crossing of  $V_{B2}$ . Thus

$$\phi_1(t_M) - \phi_s(t_M) = 2M\pi \text{ and}$$

$$\phi_2(t_N) - \phi_s(t_N) = 2N\pi \text{ where}$$

$N$  and  $M$  are integers.

Subtracting the two equations in order to compare the phases of oscillators 1 and 2, one obtains

$$\phi_2(t_N) - \phi_1(t_M) = \phi_s(t_N) - \phi_s(t_M) + 2(N-M)\pi.$$

The phase of an oscillator at time  $t_N$  may be written in terms of its phase at  $t_M$  and its

average frequency over the interval  $t_M < t_N$ .

$$\phi(t_N) = \phi(t_M) + 2\pi[\bar{\nu}(t_M; t_N)](t_N - t_M) \text{ and}$$

when we apply this equation to both  $\phi_2$  and  $\phi_5$  we find

$$\begin{aligned} \phi_2(t_M) - \phi_1(t_M) &= 2(N-M)\pi \\ &\quad - 2\pi[\bar{\nu}_{B2}(t_M; t_N)](t_N - t_M) \end{aligned}$$

where  $\nu_{B2} = \nu_2 - \nu_5$ .

Since M and N are not measureable with the equipment in Figure 1, the dual mixer technique has heretofore only been used to measure the phase difference between two oscillators modulo  $2\pi$ . We denote the period of the time interval counter time base by  $\tau_c$  and the number of counts recorded in a measurement by P. Then the phase difference between the two oscillators is given by

$$[\phi_2(t_M) - \phi_1(t_M)] \bmod 2\pi = -2\pi[\bar{\nu}_{B2}(t_M; t_N)]\tau_c P$$

Figure 2 illustrates the output of the measurement system over a period of time. If a measurement begins and ends without the time interval counter making a transition between zero and its maximum value, e.g.,  $t_c < t_M < t_N < t_b$ , then the phase difference can be calculated from the data. If  $t_c < t_M < t_b < t_N < t_c$ , then the data must be corrected by  $2\pi$  to calculate the phase difference. Experience has shown that there are many measurement situations for which the number of transitions of the time interval counter which occur between  $t_M$  and  $t_N$  cannot be known. For this reason, a modification has been developed which removes the ambiguity by measuring M and N.

#### Extended Dual Mixer Time Difference Measurement Technique

In order to configure the system to acquire complete phase information, two scalars are added to count the zero crossings of each mixer. Figure 3 is the block diagram of a two channel system. It is constructed from identical circuit modules and therefore contains an unused time interval counter. However, this design permits very straightforward and inexpensive extension to the comparison of an arbitrarily large number of oscillators with no need for switching any signals.

The counter outputs are combined to form the phase difference between oscillators.

$$\begin{aligned} \phi_2(t_M) - \phi_1(t_M) &= 2(N_0 - M_0)\pi + 2(N-M)\pi \\ &\quad - 2\pi[\bar{\nu}_{B2}(t_M; t_N)]\tau_c P \end{aligned}$$

The first term is a constant which represents the choice of the time origin and can be ignored. The last two terms and their sum are plotted in Figure 4.

The average beat frequency  $\bar{\nu}_{B2}(t_M; t_N)$  cannot be known exactly. However,  $\bar{\nu}_{B2}$  may be estimated with sufficient precision from the previous pair of measurements designated ' and ". The average frequency is approximately

$$\bar{\nu}_{B2}(t_M; t_N) \approx (N'' - N') / [R(M'' - M') / \nu_{10} + \tau_c(P'' - P')]$$

provided that it changes sufficiently slowly compared to the interval  $t_M < t_N$ . A typical value for this error will be given in the following section.

#### Hardware Implementation

All measurement channels consist of a mixer, zero-crossing detector, scaler and time interval counter. Four such circuits can be built in a double width CAMAC module. The system is easily expanded to compare many oscillators and a complete system for making phase comparisons among four clocks is shown in Figure 5. We have chosen parameters which are reasonable for comparing state-of-the-art atomic standards. Thus, the synthesizer is offset 10Hz below oscillator #1 and  $R = 5 \times 10^3$ . The outputs from both mixers are approximately 10Hz. The noise bandwidth is 100 Hz. The time interval counter is twice the frequency of oscillator #1 or approximately 10 MHz. The quantization error is  $1/2R = 10^{-6}$  cycle or 0.2ps which is a factor of ten smaller than the measurement noise. As stated earlier, an error will result from frequency changes which violate the constancy assumption used to estimate  $\nu_{B2}$ . A change in  $\nu_2$  by  $10^{-10}$  during the interval between two measurements will result in a time deviation error of 10ps. Thus, one must make more closely spaced measurements for oscillators which have large dynamic frequency changes than for more stable devices. Two other sources of inaccuracy are the sensitivities to the amplitude and phase of the common oscillator. Figure 6 shows the measured value of  $x = \phi/2\pi\nu_0$  as a function of the amplitude of the input signal and the phase of the synthesizer.

The new measurement system has many desirable features and properties:

- (1) It has very high resolution, limited by the internal counters to 0.2 ps and by noise to approximately 2 ps.
- (2) It has much lower noise than divider based measurement systems. However compromises made to achieve low cost, low power, small size and automatic operation degrade the performance compared to state-of-the-art systems for comparing 2 oscillators.
- (3) The operation is fully automatic.
- (4) NBS has developed a detailed operating manual for the equipment and software.

- (5) All oscillators in the range of  $5 \text{ MHz} \pm 5 \text{ Hz}$  may be compared. Other carrier frequencies such as 1 MHz, 5.115 MHz, 10 MHz and 10.23 MHz are also usable. However, different carrier frequencies may not be mixed on the same system. The system has been successfully tested with an oscillator offset 4.6 Hz from nominal 5 MHz. Measurements were made at intervals of 2 hours between which the system had to accumulate approximately  $2 \times 10^6 \pi$ . The system has also been tested with an oscillator offset  $4 \times 10^{-5}$ , and no errors were detected during a period of 40 days.
- (6) All sampling times in the range of 1 second to 15 days with a resolution of 0.1 second are possible. Measurements may be made on command or in a preprogrammed sequence.
- (7) Measurements are synchronized precisely, i.e. at the picosecond level, with the reference clock. They may therefore be synchronized with important user system events, such as the switching times of a FSK or PSK system.
- (8) All oscillators are compared synchronously and all measurements are performed within a maximum interval of 0.1 second. As a result, the phase of any oscillator needs to be interpolated to the chosen measurement time for an interval of 0.1 second maximum. This capability, which is not present in either single heterodyne measurement systems or switched measurement systems eliminates a source of "measurement" error which is generally much larger than the noise induced errors. For example, interpolation of the phase of a high performance Cs clock ( $\sigma_y = 10^{-11}/\tau^2$ ) over a period of 3 hours would produce approximately 1.5 ns phase uncertainty. To maintain 4 ps accuracy requires measurements simultaneous to 0.1s.
- (9) There are no phase errors due to the switching of rf signals since there is no switching anywhere in the analog measurement system.
- (10) No appreciable phase errors are introduced when it is necessary to change the reference clock since, as shown in Figure 6, the peak error due to changes in synthesizer phase is 20 ps.
- (11) The measurement system is capable of measuring its own phase noise when the same signal is applied to two input ports. Figure 7 shows the phase deviations between two such channels over a period of 75,000 seconds and Figure 8 is the corresponding Allan variance plot. Figure 9 shows the phase deviations between 2 input channels over a period of 40 days.
- (12) Since the IEEE-583 (CAMAC) interface standard has been followed for all the custom

hardware, the system may be easily interfaced to almost any instrument controller. NBS has already tested the system using a large minicomputer, a small minicomputer and a desk top calculator. Interfaces between IEEE-583 and IEEE-488 controllers are available and have been used successfully.

- (13) The system is capable of comparing a very large number of oscillators at a reasonable cost per device.

There are also disadvantages to this measurement system. The most important are:

- (1) The complexity of the hardware is greater than for some systems. It is possible that this will reduce reliability.
- (2) A high level of redundancy is difficult to achieve. The system design stresses size, power, convenience and cost, resulting in an increase in the number of possible single point failure mechanisms compared to some other techniques. For example, a CAMAC power supply failure will result in a loss of data for all devices being measured.
- (3) A substantial commitment is required in both specialized hardware and software.
- (4) If an oscillator under test experiences a phase jump which exceeds 1 cycle, the measurement system records a jump with incorrect absolute magnitude. As a result, it may not be applicable to signals which are frequency modulated with discontinuous phase steps larger than  $2\pi$ .

#### Conclusions

We have demonstrated a new phase measurement system with very desirable properties: All oscillators in the range of  $5 \text{ MHz} \pm 5 \text{ Hz}$  may be measured directly. The sampling times are only restricted by the requirement that they exceed one second. The noise floor is  $\sigma_y(2, \tau) = 3 \times 10^{-12}/\tau$  in short term and the time deviations are less than 100 ps. All circuitry is designed as modules which allows expansion at modest cost. Compatibility with a variety of computers is insured through the use of the IEEE-583 interface and adapters are available to permit use with an IEEE-488 controller. The system makes it feasible to make completely automated phase measurements at predetermined times on large numbers of atomic clocks. Its own noise is one-hundred times less than the state-of-the-art in clock performance. It will be used in the near future to make all measurement needed to compute NBS atomic time, but it will also be very valuable for any laboratory which uses three or more atomic clocks.

#### References

- 1 D. W. Allan, "The measurement of frequency

and frequency stability of precision oscillators," NBS Tech. Note 669 (1975).

2. "CAMAC instrumentation and interface standards," Institute of Electrical and Electronic Engineers, Inc., 345 E. 47th St. New York, NY 10017.
3. D. J. Glaze and S. R. Stein, "Picosecond time difference measurements utilizing CAMAC based ANSI/IEEE -488 data acquisition hardware", NBS Tech Note 1056 (in preparation).

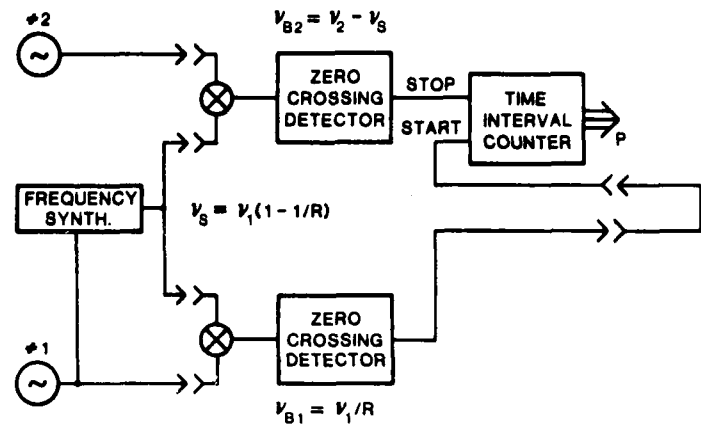


Figure 1. Dual Mixer Time Difference Measurement System

$$[\phi_2(t_H) - \phi_1(t_H)] \bmod 2\pi = -2\pi[\tilde{\nu}_{B2}(t_H; t_H)]t_c P$$

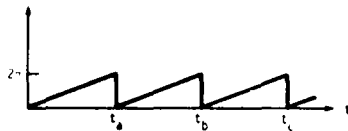


Figure 2. Dual Mixer Data

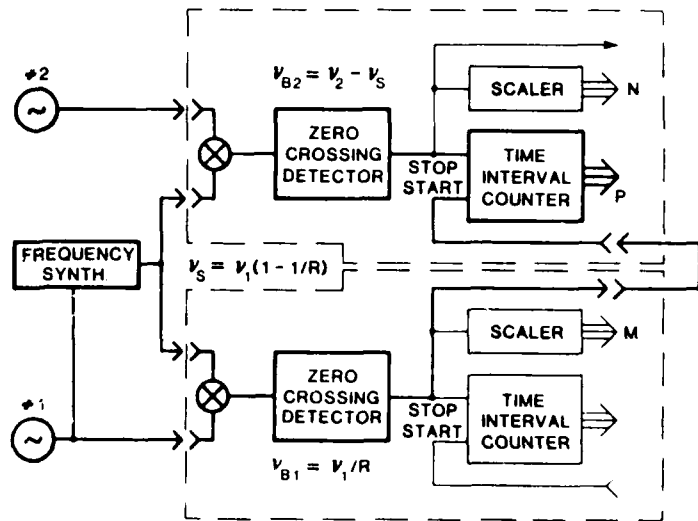


Figure 3. Extended Dual Mixer Time Difference Measurement System

$$\phi_2(t_M) - \phi_1(t_M) = 2(M_0 - M_0)n + 2(M - M)n - 2\pi[\nu_{B2}(t_M, t_N)]t_C P$$

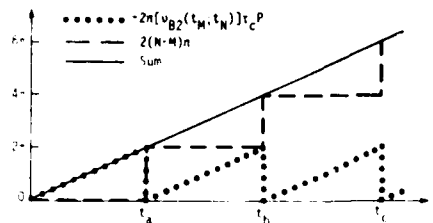


Figure 4. Extended Dual Mixer Data

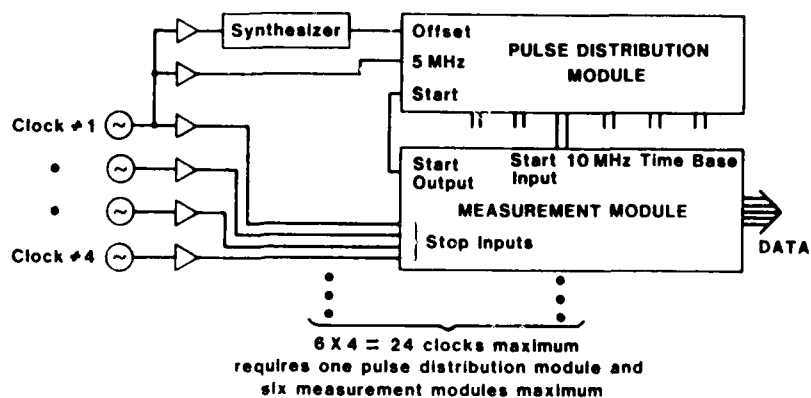


Figure 5. System Block Diagram

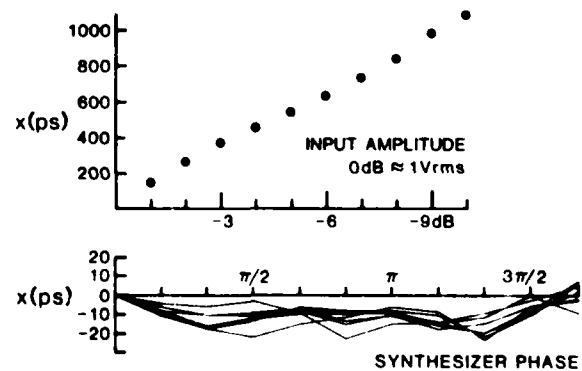
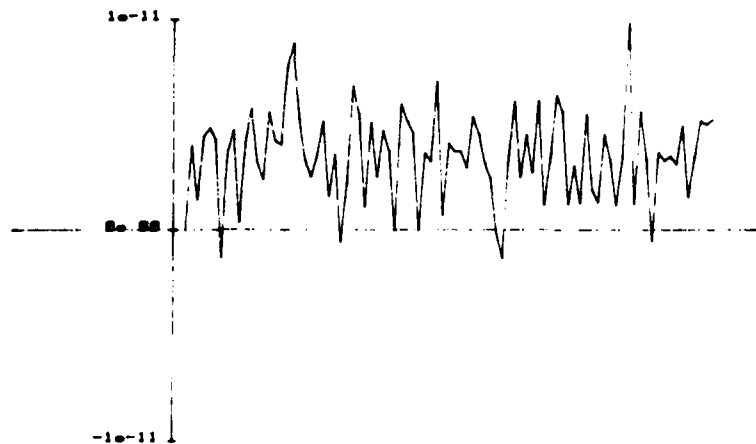


Figure 6. Measured Time Difference vs. Input Amplitude and Synthesizer Phase

PHASE PLOT Clock No. 4-8  
 Let Sqr Slope of -1.050200e-17/S Removed

nbe4a ~nbe4b  
 E)W 05 May 02



T = 74700 SECONDS

Figure 7. Raw Phase Data for Two Channels Driven from the Same Source

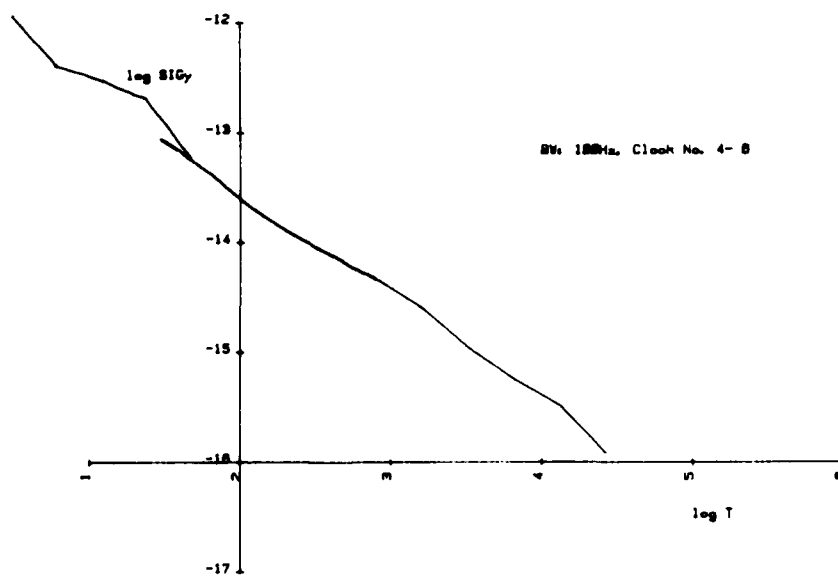


Figure 8. Noise Floor of Measurement System

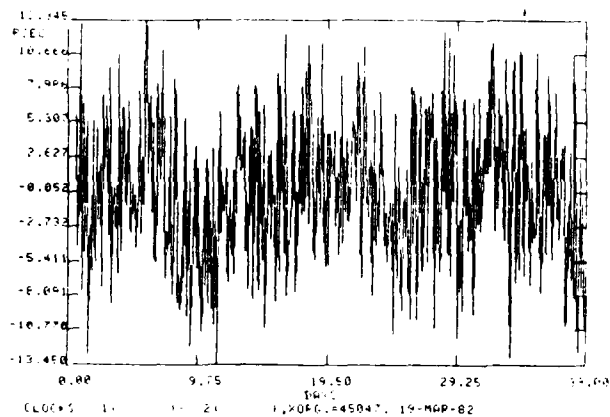
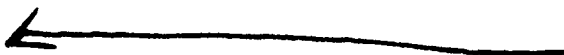


Figure 9. Raw Phase Data for Two Channels Driven from the Same Source



# A FREQUENCY DOMAIN REFLECTOMETER FOR QUARTZ

## RESONATOR INVESTIGATIONS

Charles S. Stone  
Brightline Corporation  
Austin, Texas

and

O. J. Baltzer  
Tracor, Inc.  
Austin, Texas

### Abstract

This paper presents the concept and operating principles of a phase modulated, frequency-domain reflectometer system for accurate and precise measurements of the resonant frequency characteristics of quartz crystals. The reflectometer method enables the crystal resonator under test to be remotely located in an environmental test chamber; furthermore, the system permits simultaneous, independent frequency measurements of the various resonant modes that can occur in any given crystal (i.e., the b-mode and c-mode resonances in SC-cut crystals). This reflectometer technique has major applicability in basic resonator research: in investigations of frequency-temperature characteristics; hysteresis and thermal shock effects; amplitude-frequency factor and multimode excitation behavior; effects of nuclear radiation; etc. The instrumentation also has applications in crystal manufacturing processes involving automated production, testing, and quality control.

### Introduction

A new technique for accurate measurement of the resonant frequency characteristics of precision quartz crystals is presented. An external, independent oscillator generates a carrier frequency in the vicinity of the anticipated resonant frequency of the crystal under test. A small phase modulation is applied and the resultant phase modulated signal is used to interrogate the crystal resonator. An error signal, derived from the reflected resonator signal, is used to servo control the oscillator, thereby providing a means for automatic tracking of changes in resonator frequency.

All tests to date indicate that this phase modulated reflectometer technique for measuring the resonant frequency of quartz crystals yields high sensitivity (to 1 part in  $10^6$  or better) and excellent long-term stability and repeatability.

The resonator under test may be remotely located away from the balance of the instrumentation. A single interconnecting coaxial cable, used jointly for the incident and reflected signals from the resonator, is adequate. The resonator units under test may therefore be temperature cycled

within a remote environmental chamber while the rest of the instrumentation is operated in a favorable laboratory environment. Reliable measurements may be obtained in the presence of wide variations in the resonator's resistance (in response, for example, to extremely high temperatures).

The phase modulated reflectometer technique described here also enables simultaneous, independent measurements of the various resonant modes that can occur naturally in a single crystal. As an example, the system could be used to interrogate concurrently the fundamental, third, and fifth overtone modes of both the c-mode and b-mode frequencies of an SC-cut crystal (a total of six separate resonances); these individual measurements, with no significant interaction between channels, could be made with any reasonable length of coaxial transmission line interconnecting the crystal resonator to the instrumentation.

### Historical Background

In 1980 Tracor engineers initiated an in-house R&D investigation to determine the performance potential of a frequency-compensated crystal oscillator (ECXC) for clock use in a spread spectrum communications system. The objective of the program was an ovenless oscillator having an absolute accuracy of  $\pm 1$  millisecc/day over the full military range of  $-55^\circ\text{C}$  to  $+85^\circ\text{C}$ ; this timing accuracy roughly corresponds to an average frequency error of  $\pm 1$  part in  $10^8$ .

Fig. 1 shows a plot of the measured frequency-temperature performance, over a limited temperature range, of the experimental ECXC developed in that program. Temperature compensation of the c-mode "clock" frequency of the doubly-rotated SC-cut crystal was obtained by using the accompanying b-mode frequency as a highly sensitive quartz "thermometer"; the b-mode frequency has a temperature coefficient of approximately  $-25$  ppm/ $^\circ\text{C}$  over a wide temperature region. The measured b-mode frequency is thus employed, together with a simple microprocessor, to select an appropriate digital compensation value from a stored FREQ table. With the ECXC concept, no attempt is made to "pull" the frequency of the c-mode oscillator to the correct clock frequency; instead, phase/time corrections

AD P001540

and a 100-MHz oscillator/frequency divider stage connected to the oscillator. This ICXO approach permits a ultimate clock/time-keeper accuracy that is at least 10-fold better than that possible with a conventional TCXO (in which "internal" frequency compensation of the oscillator is obtained by means of a varactor). The data shown in Fig. 1 indicate a maximum timing error of perhaps  $\pm 1$  millisecond over a 24-hour test run; temperature cycling over the range  $-20^{\circ}\text{C}$  to  $+60^{\circ}\text{C}$  was performed three times each day.

The question was raised whether the observed residual errors, although admittedly small, were due to the quartz resonator itself, to the associated oscillator circuit, or to the specific compensation technique used in the ICXO. A follow-up program was therefore initiated, under Air Force Contract F41633-81-C-0087 with NADCO/NSF, to collect data on the behavior and interrelationship of the dual b-mode and c-mode frequencies of 30-MHz crystals under various conditions of temperature, power application, and time (aging); however, suitable measuring instrumentation was recognized to be prerequisite to the planned data collection program.

#### Instrumentation Requirements

Certain functional requirements and performance capabilities for the measuring system were established:

1. Capability for the test resonators to be remotely located in a controlled environmental chamber (with balance of the instrumentation operating under normal laboratory conditions).
2. Simultaneous measurements of c-mode and b-mode frequencies.
3. Absolute frequency accuracy:  $\pm 1 \times 10^{-8}$ .
4. Resolution/precision:  $\pm 2 \times 10^{-7}$ .
5. Independent adjustment of b-mode and c-mode crystal excitation levels (each variable from fractional microwatts to many milliwatts).
6. Wide frequency range (e.g., adaptable to 5, 10, and 10.23 MHz crystals; also, sufficient dynamic range to handle b-mode frequency-temperature dependence).
7. Automated data logging.
8. System alignment and calibration procedure.
9. Low cost.

#### Frequency Domain Reflectometer

##### Basic Concept

In a traditional approach, the crystal is simply placed in an oscillator circuit and the resultant output frequency is accurately measured. Unfortunately, other circuit components in the active feedback type of oscillator can influence and perturb the output frequency. Accordingly, the active approach is not really suitable for the determination of aging or hysteresis characteristics of the resonator itself. Some other method must be utilized.

After a review of various alternative measurement methods, a system employing a frequency domain

reflectometer was selected. Fig. 2 shows the basic reflectometer concept. The quartz resonator under test is interrogated by a tunable frequency signal. The signal reflected from the resonator is displayed on an oscilloscope or voltmeter. A minimum (or null under special conditions) will be observed as the tunable oscillator passes through the resonant frequency of the test crystal.

It will be noted that a directional coupler (a four-port hybrid bridge) is used for input coupling the tunable oscillator to the resonator and for output coupling of the reflected signal to the oscilloscope. The resistor  $R_1$  provides proper termination for the hybrid bridge; if the resonator is remotely located at the end of a long coaxial cable,  $R_1$  should be selected to match the cable impedance; if no cable is required,  $R_1$  can be selected to match the nominal value of the crystal's equivalent series resistance (ESR).

This rudimentary reflectometer, using an unmodulated carrier signal, possesses several deficiencies: lack of polarity sensing for the sign of the frequency error, and a relatively low sensitivity (a broad minimum) if  $R_1$  does not provide a good match to the crystal's resistive component.

#### Phase Modulated Reflectometer

Fig. 3 shows a simplified block diagram of a phase modulation scheme for overcoming these limitations of a simple reflectometer. An external, independent RF oscillator generates a carrier frequency,  $f_c$ , in the vicinity of the anticipated crystal resonant frequency,  $f_r$ . A small phase modulation,  $\pm \Delta\phi/2$  is applied, and the resultant phase modulated signal is used to interrogate the resonator under test. The reflected signal from the crystal resonator, after passing through an isolation amplifier (not shown), is amplitude detected by a diode. An amplitude modulation, at the modulation oscillator frequency rate, will be observed in the detector output whenever the carrier frequency differs from the resonant frequency,  $f_r$ , of the quartz resonator. The sense and magnitude of this amplitude modulation depends upon the frequency deviation of the external oscillator from the center of crystal resonance. A phase sensitive demodulator can therefore be used to provide a d-c error signal proportional to the frequency offset of the external oscillator. This error signal, after loop filtering, is used to servo control the oscillator, thereby enabling automatic tracking of the crystal's resonant frequency in response to changes in crystal temperature, input power level, aging, etc. A high resolution counter, preferably under microprocessor control and with a digital output for automatic data logging purposes, can be used for measurement of the locked oscillator frequency.

Some understanding of the operating principles of the modulated system can perhaps be obtained from the vector diagrams of Fig. 4.  $S_1$  and  $R_1$  represent the successive vectors associated with the incident signal as the result of the square wave phase modulation process;  $S_2$ ,  $S_3$  and C represent the equivalent sidebands and carrier components for this

phase modulated signal. The corresponding reflected components are shown on the right. The crystal resonator unit appears as a very high impedance (highly reactive) for all frequency components even slightly removed from resonance; accordingly, the reflected sideband components,  $S'_1$  and  $S'_2$ , are virtually equal to the incident components,  $S_1$  and  $S_2$ , and maintain the same  $180^\circ$  relationship to each other. It is the carrier component that changes in magnitude and phase as the crystal resonant frequency is approached. At resonance, there is likely to be a residual reflected component,  $C'$  (as the result of any nominal mismatch between the ESR of the crystal and the hybrid termination resistance  $R_T$ ). However, this  $C'$  component (at resonance) is orthogonal to the sideband component vectors so that the resultant vectors,  $R'_1$  and  $R'_2$ , are equal in magnitude. Away from resonance, the reflected carrier component ( $C'$  or  $C''$ ) increases in magnitude and undergoes a large phase shift; accordingly, the two vectors,  $R'_1$  and  $R'_2$ , are no longer equal in magnitude and, consequently, an error signal is generated in the synchronous demodulation process.

This phase modulated reflectometer technique can be extended to multimode measurements (e.g., simultaneous measurement of b-mode and c-mode resonant frequencies of SC-cut crystals) by the addition of the components shown in Fig. 5. Independent operation at b-mode and c-mode frequencies simply requires the use of separate modulation frequencies,  $f_{m1}$  and  $f_{m2}$ , chosen so they have no harmonic relationship.

#### Experimental Results

Recent tests on the dual mode reflectometer (Fig. 5) indicate that the system satisfies all of the specifications listed under Instrumentation Requirements.

The oscilloscope photographs of Fig. 6 illustrate the sensitivity inherent within the phase modulated reflectometer technique. Each photo shows the raw reflected r-f signal (prior to the diode detector) for the c-mode signal of a 5 MHz SC-cut resonator; the phase modulation comprised a 1 kHz square wave signal modulating the r-f carrier signal by approximately  $\pm 15^\circ$ . The upper photo shows the reflected signal at resonance. The middle and lower photo show the effect of deliberately offsetting the oscillator from the crystal's resonant frequency by  $+1 \times 10^{-2}$  and  $-1 \times 10^{-2}$ , respectively. A large amplitude at the modulation frequency is clearly evident.

The effect of varying the modulation frequency and the magnitude of the phase angle has also been explored. For modulation frequencies ranging from 30 Hz to more than 3 kHz, the observed change in apparent resonant frequency was less than  $\pm 4 \times 10^{-10}$ . Similarly, for values of  $\Delta\phi$  ranging from approximately  $\pm 1.5^\circ$  to  $\pm 45^\circ$ , the deviation in measured resonant frequency was less than  $\pm 5 \times 10^{-9}$  (this test was not performed under ideal conditions so that actual performance may be better than this value). In summary, the instrumentation appears to be nearly

independent of the particular modulation frequency and phase angle offset that is employed.

The measured resonant frequency will be perturbed by any residual second harmonic component in the phase modulation. Such a component would exist if the square wave modulation did not have a precise 50% duty cycle; however, by conventional digital division techniques, it is possible to obtain a highly accurate 1:1 ratio in the switched phase modulated signal.

The length of the interconnecting cable between the quartz resonator and the balance of the instrumentation does not materially influence the measured resonance frequency if the hybrid bridge is properly terminated to match the cable impedance. An ideal, non-dispersive cable would affect the carrier and sideband frequency components in an identical manner, thereby producing no change in the relative magnitude or phase of the detected vector components. Furthermore, for moderate lengths of commonly available transmission cables, the dispersion effect is quite small and can generally be neglected. This has been confirmed in simple tests wherein an additional 50 feet of RG-58/CU cable has been inserted between the resonator and the reflectometer bridge; a deviation of less than  $\pm 5 \times 10^{-9}$  has been observed, and without using extreme care in adjusting the hybrid termination.

#### Application Areas

It is believed that the frequency domain reflectometer outlined here will facilitate frequency measurements of quartz resonators that would otherwise be expensive and difficult to perform by self-oscillator, vector voltmeter, impedance bridge,  $\pi$  network, or other methods. It can therefore have important application in basic investigations of resonator behavior, including: frequency-temperature dependence (static); effects of thermal shock; hysteresis and "retrace"; aging phenomena; direct and indirect amplitude-frequency effects; multimode excitation behavior; activity dips and bandbreaks; radiation and extreme environment effects; and measurement with non-contacting electrodes (e.g., BVA resonators).

The method should also have applicability in various monitor and control functions during crystal fabrication: plate-to-frequency control; turning point determination; EXXO/TCXO calibration; product burn-in and quality assurance; and measurement with non-contacting electrodes.

#### Bibliography

- <sup>1</sup>F. L. Walls and S. R. Stein, "A frequency-lock system for improved quartz crystal oscillator performance", IEEE Transactions on Instrumentation and Measurement, vol. IM-27, pp. 249-252, September 1978.

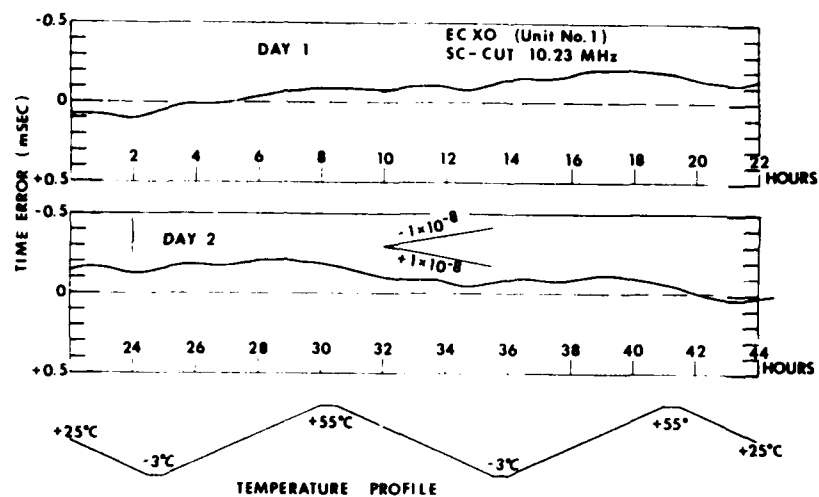


Figure 1.

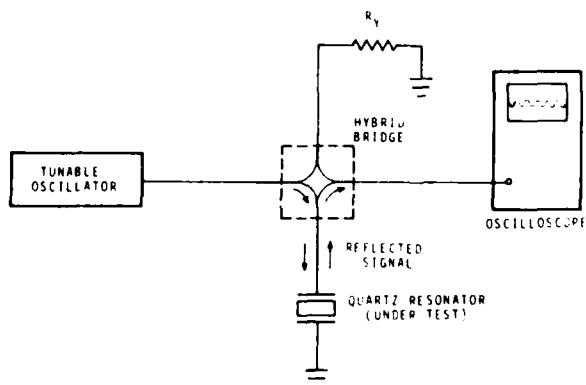


Figure 2. Basic Reflectometer

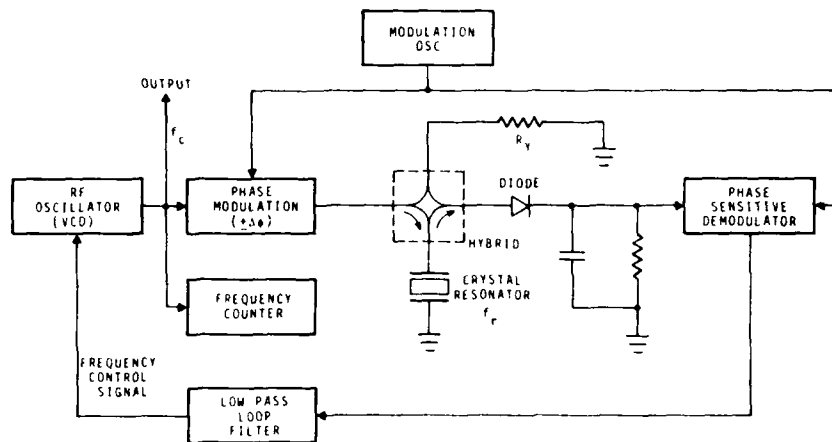


Figure 3. Phase-Modulated Reflectometer System (For Frequency-Locking an Oscillator to a Passive Quartz Resonator)

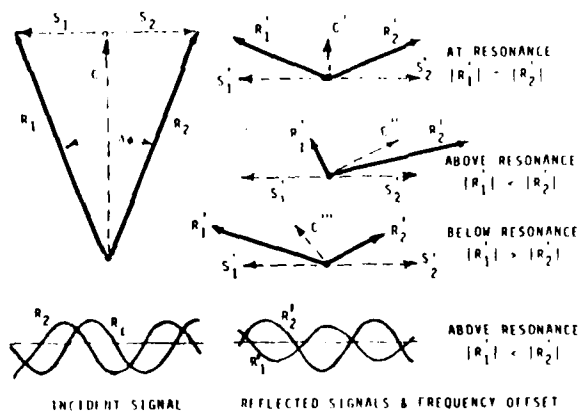


Figure 4.

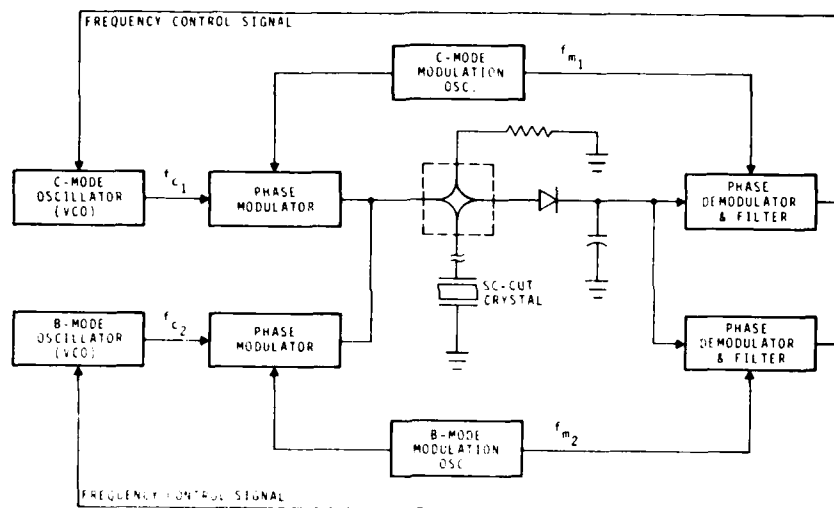


Figure 5. Dual Mode Frequency-Domain Reflectometer

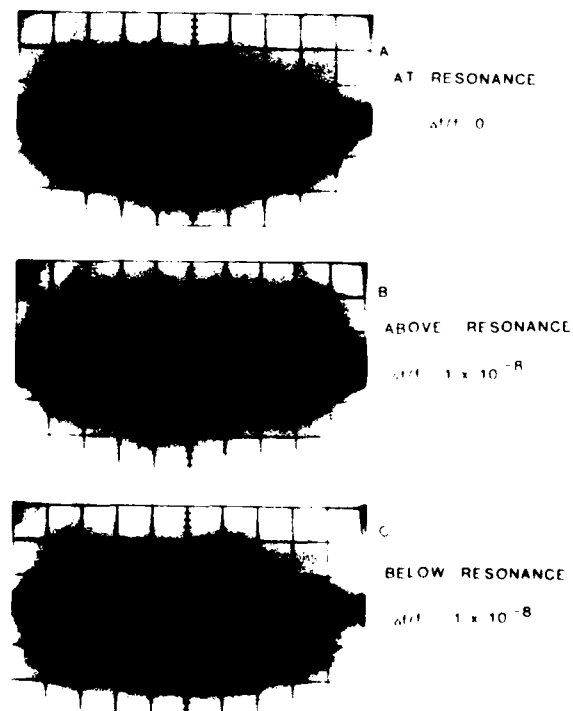


Figure 6.

## FREQUENCY STABILIZATION OF AlGaAs LASERS

Motoichi Ohtsu\*, Hidemi Tsuchida\*\* and Toshiharu Tako\*\*,

\* International Cooperation Center for Science and Technology,  
 \*\* Research Laboratory of Precision Machinery and Electronics,  
 Tokyo Institute of Technology,  
 2-12-1 O-okayama, Meguro-ku, Tokyo 152, Japan

## SUMMARY

Spectral width measurements and frequency stabilizations of AlGaAs lasers were carried out, and their applications were demonstrated. It was shown that the spectral width can be reduced as narrow as 1MHz. A stabilized Fabry-Perot interferometer, absorption spectra in  $H_2O$  and  $^{85}Rb$  were used as frequency references to improve the long-term ( $\tau \geq 1s$ ) frequency stability. The minimum of the square root of the Allan variance  $\sigma_y$  in these experiments were  $2.0 \times 10^{-11}$ ,  $1.1 \times 10^{-11}$ , and  $1.4 \times 10^{-12}$  (at  $\tau = 100s$ ), respectively. For the laser with an external grating, the minimum of  $\sigma_y$  obtained was  $3.2 \times 10^{-12}$  (at  $\tau = 100s$ ). Several experiments were carried out to improve the short-term ( $\tau < 1s$ ) frequency stability, and power spectral density for frequency fluctuations was reduced to less than  $10^{-12}$  of that of free running lasers for the Fourier frequency range lower than 200kHz.

An Allan variance real-time processing system (ARPS) was developed for frequency stability measurements, and optimal frequency control was carried out by using this apparatus.

As an application of frequency stabilized lasers, the precise wavelength measurements of the  $H_2O$  absorption spectra were demonstrated, in which the preliminary results of  $8164.8737 \pm 0.0003A^\circ$  for  $R(4_{-3})$  line was obtained. Furthermore, a brief comment on the preparation of optical pumping experiments for Rb and Cs was given.

## 1. INTRODUCTION

Performances of semiconductor lasers have been remarkably improved by the demand of the optical communications industry. Recently a single longitudinal mode, CW oscillation at room temperature has been realized. The price of each laser has been reduced as low as \$250. These lasers are mostly oscillated in the near-infrared, and the coherent lights of 0.83 $\mu m$  and 1.3-1.5 $\mu m$  in wavelengths are obtained by AlGaAs lasers and InGaAsP lasers, respectively. Since few number of other kind of lasers oscillate in these wavelength regions, these semiconductor lasers could be conveniently used not only in optical communications but in many fields of application, e.g., laser spectroscopy, optical pumping, frequency and length standards, laser radar, air-borne gyroscopes, etc. For these applications, however, CW oscillation

performances such as spectral width, mode structures, FM and AM noise, etc. have to be understood. If these performances are not sufficient enough for these applications, they must be improved by external optical components and electronic circuits, or by manufacturing thoroughly new type of semiconductor lasers. For example, long-term frequency stabilities of these lasers have to be improved for high resolution laser spectroscopy and short-term frequency stabilities have to be considerably improved for heterodyne-type optical communications. For these applications, the stabilities of semiconductor lasers are still considerably low.

In this paper, recent results on frequency stabilization of AlGaAs lasers, with the main purpose of looking for new possibilities for applications, will be discussed.

## 2. NOISE AND SPECTRAL WIDTH

In the present study, mainly  $1.3\mu m$  distributed planar (DSP) type AlGaAs lasers were mostly used. As an initial check for the present work, the intensity fluctuations, frequency fluctuations, and spectral width were measured. The temperature at the heat sink for the laser was kept at the room temperature with the fluctuations of  $\pm 0.1^\circ C$  and the laser was driven by a current-regulator. The temperature coefficient of the current from the regulator was 30ppm. The power spectral density of the intensity fluctuations was lower than  $10^{-11} (Hz^{-1})$ . The frequency fluctuations were measured by a stable Fabry-Perot interferometer, and the results are shown in Fig. 1. In this figure, it is seen that power spectral density falls between  $10^{-12}$  and  $10^{-11} (Hz^{-1})$  for the wide range of Fourier frequencies.

Figure 2 shows the spectral width of the laser measured by a long Fabry-Perot interferometer (1mb). The value of the spectral width  $\Delta\nu$  is decreased with increasing the injection current  $I$  and it can be seen that it gradually approaches the theoretically estimated value, which is expressed as

$$\Delta\nu = \frac{1}{4\pi} \left( \frac{c}{L} \right)^2$$

where  $\Delta\nu$  is the spectral width of the cavity,  $h\nu$  is the photon energy, and  $P$  is the laser power, respectively. In this figure,  $\Delta\nu$  is reduced as narrow as 1MHz, which means that this laser can be

and even for sub-Doppler spectroscopy.

### 3. METHOD OF FREQUENCY FINING AND STABILIZATION

The relative frequency shift  $\Delta f/f$  can be expressed as

$$\frac{\Delta f}{f} = -\frac{1}{n} \left( \Delta n + \frac{1}{\alpha} \frac{\Delta \alpha}{\alpha} \right) \left( \frac{\Delta T_1}{T_1} + \frac{\Delta T_2}{T_2} \right), \quad (2)$$

where  $\Delta = 4 \times 10^{-28} \text{ (m}^3\text{)}^{-1}$ ,  $n$  is the refractive index of the cavity,  $\Delta n$  is the variation of the refractive index by the injection current,  $\alpha$  and  $\Delta \alpha$  are the temperature coefficients of the cavity length and refractive index, respectively,  $\Delta T_1$  and  $\Delta T_2$  are the temperature variations at p-n junction by the injection current and ambient temperature variation, respectively. Here,  $\alpha + \Delta \alpha = 2.0 \times 10^{-6} \text{ } ^\circ\text{C}^{-1}$  at 633nm, which corresponds to 0.6nm/ $^\circ\text{C}$ . Both  $\Delta n$  and  $\Delta T_1$  depend on the injection current, however, their response speeds are widely different, i.e., the response of  $\Delta n$  to the injection current is fast and that of  $\Delta T_1$  is slow. On the other hand, the magnitude of the first term in eq. (2) is about ten times smaller than that of the second term. Therefore, when the laser is driven by a low frequency current, the frequency shift depends almost entirely on  $\Delta T_1$ , and it induces the red shift. On the other hand, when the laser is driven by a high frequency current, the shift depends only on  $\Delta n$ , which induces the blue shift. However, however frequency of the current exceeds the relaxation time of the current, an around 1 MHz.<sup>(6)</sup> When the laser was driven by a d.c. current, the following value of the frequency shift, i.e., the red shift through  $\Delta T_1$ , was measured for the  $\text{Al}^{3+}$  laser at 633nm.

$$\frac{\Delta f}{f} = -1.7 \times 10^{-6} \Delta T_1. \quad (3)$$

Following the discussions described above, both of the injection current control ( $\Delta T_1$ ) and ambient temperature control ( $\Delta T_2$ ) can be employed to improve the long-term frequency stability. When the ambient temperature control ( $\Delta T_2$ ) method is employed, the temperature at the p-n junction has to be varied, for example, by using a Peltier electric cooler to compensate for the frequency fluctuations.<sup>(6)</sup> In this case, the accuracy of the temperature control should be better than  $10^{-3} \text{ } ^\circ\text{C}$  to get the frequency stability higher than  $10^{-11}$ , which looks very difficult to realize and must need a sophisticated technique for temperature control. From this point of view, in the present work, the authors employed the injection current control method. The ambient temperature was roughly fixed at around room temperature with fluctuation of  $\pm 0.1 \text{ } ^\circ\text{C}$ , and the injection current was accurately controlled by a feedback servo controller. By this method, the frequency stability higher than  $10^{-11}$  can be expected.

The first of the injection current control was to stabilize the frequency of the free running laser. The relative frequency shift  $\Delta f/f$  of the free running laser is expressed as

$$\frac{\Delta f}{f} = -\frac{1}{n} \left( \Delta n + \frac{1}{\alpha} \frac{\Delta \alpha}{\alpha} \right) \left( \frac{\Delta T_1}{T_1} + \frac{\Delta T_2}{T_2} \right). \quad (4)$$

Since the temperature variation  $\Delta T_2$  is much smaller than  $\Delta T_1$ , the frequency shift is dominated by  $\Delta T_1$ .

When the laser is driven by a high frequency current, the frequency shift is dominated by  $\Delta n$ .

Therefore, the frequency shift of the free running laser is expressed as

$$\frac{\Delta f}{f} = -\frac{1}{n} \left( \Delta n + \frac{1}{\alpha} \frac{\Delta \alpha}{\alpha} \right) \left( \frac{\Delta T_1}{T_1} + \frac{\Delta T_2}{T_2} \right). \quad (5)$$

When the laser is driven by a low frequency current, the frequency shift is dominated by  $\Delta T_1$ .

by controlling the current,  $\Delta I$  is determined so that  $\Delta T_1$  is cancelled by  $\Delta T_2$  ( $\Delta T_1 + \Delta T_2 = 0$ ), but as a result of this cancellation, the term of  $\Delta I$  remains in eq. (5), i.e., the power drift of  $P_0 \Delta I$  is induced.

Figure 3 shows this phenomenon. In this figure, the time dependence of the power are shown for the frequency stabilized laser and for the free running laser. In this figure, power drift can be clearly seen for the stabilized laser, as discussed above. Therefore, if one needs to stabilize the frequency and power simultaneously, one has to suppress the power drift by controlling the temperature while controlling the frequency by the current.

Mode hopping phenomenon also gives a trouble in the present study, which is due to the temperature dependence of the energy gap of the semiconductor. The red shift of about 50-100 MHz (0.005-0.01 nm at 633nm) is induced by the mode hopping when the temperature is increased, which limits the continuous frequency tuning range of the laser. Furthermore, even if the lasers are made from the same material and using the same processes, the lasers have their own individual wavelength. To some extent, they can be compensated for by adjusting the temperature or current. However, a complete compensation can not be obtained because the working range of the temperature and current should be limited to  $10^{-3} \text{ } ^\circ\text{C}$  and  $10^{-4} \text{ A}$  to keep the life time of lasers long enough, which would also limit the continuous frequency tuning range.

To overcome these difficulties, it would be necessary to use other type of laser with high wavelength sensitivity, e.g., IBA lasers developed by Schmatz's school.<sup>(7)</sup>

### 4. IMPROVEMENTS IN LONG-TERM FREQUENCY STABILITY

It would be necessary to improve the long-term frequency stability, specially for I & L, for such applications as spectroscopy, frequency standard, etc.. In this case, a stable Fabry-Perot interferometer and absorption spectra of several atoms or molecules can be used as frequency references. Figure 4 shows the apparatus for frequency stabilization by using a Fabry-Perot interferometer as a reference, which is also stabilized by a low frequency-stabilized He-Ne laser (SP110).<sup>(8)</sup> In this figure, the amplifier (A) for current control are composed of an integrator (I), a proportional amplifier (P), and a differentiator (D). The frequency characteristics of these units are shown in Fig. 5. Their gains and cut-off frequencies are manually adjusted to find the optimal control conditions in each experiment. These amplifier were always used in the present work. Figure 6 shows the frequency stability obtained. The curve 1 represents the stability of the free running laser, and the minimum of the curve 2 at the frequency variation of 0 on this curve is

$$\frac{\Delta f}{f} = 1.1 \times 10^{-11} \text{ at } 633 \text{ nm}. \quad (6)$$

The curve 3 is for the free running laser.

For the experiment, the apparatus is rather complicated because the Fabry-Perot interferometer is stabilized by the stable He-Ne laser to reduce the thermal drift. Furthermore, the stabilized laser must be  $10^{-11}$  cannot be expected

because the stability of the interferometer is limited by that of the Lamb dip of the Ne transition in the discharge tube of the He-Ne laser. If some absorption lines of stable atoms or molecules are used as references, the apparatus may become simpler and higher stability can be expected. The authors started this stabilization scheme by employing H<sub>2</sub>O molecules as the reference. It has been well known that H<sub>2</sub>O has a combination tone of the vibration spectra ( $\nu_1, \nu_2, \nu_3$ ) = (2, 1, 1) around 0.6  $\mu$ m.<sup>11)</sup> Though the absorption by the combination tone is weak in general, that of this band is exceptionally strong because it is coupled with (0, 1, 3) band by Darling-Dennison resonance.<sup>12)</sup> A great number of rotation structures can be found within this band, and they have been assigned by Baumann and Mecke.<sup>13)</sup> Figure 7 shows some of these lines around the wavelength of AlGaAs lasers. It can be said from this figure that each laser can be tuned at least to one of those spectra even though the wavelengths of the lasers are individually distributed. It is expected that almost all of the lasers can be stabilized by using these spectra as references. Figure 8 shows the first and second derivatives of the linear absorption spectra observed. The H<sub>2</sub>O absorption cell of 10cm in length was used at room temperature, which means the H<sub>2</sub>O vapor pressure of about 20Torr. Figure 9(a) shows the simple experimental apparatus for stabilization and, as an example, in Fig. 9(b), the third derivative of the spectra of P(0-1<sub>1</sub>) line used as a reference, is shown. Figure 10 shows the frequency stability obtained, in which the curve A represents the result of stabilization. The minimum of  $\sigma$  on this curve is

$$\sigma = 1.1 \times 10^{-11} \text{ at } \tau = 100\text{s.} \quad (7)$$

The curve B represents the result of the previous experiment (the curve D in Fig. 6). Comparison between these curves shows that higher stability was obtained in the present method by a simpler apparatus.

In the stabilization method employing atomic or molecular spectra as references, the stability would depend on the S/N value of the signals, i.e., higher stability is expected by using a stronger absorption line. For such a strong absorption line, <sup>85</sup>Rb-D<sub>2</sub> line at 780nm was employed to improve the stability. Though it is not so easy to tune the laser frequency to the D<sub>2</sub> line because of the mode hopping, it can be highly stabilized if such a wavelength coincidence can be obtained. Fortunately, the authors found such a laser among their several CSP lasers, and wavelength coincidence was obtained with the temperature of 24.6°C at the heat sink. Figure 11 shows the linear absorption spectra and their first derivative line shapes. It can be seen that they have higher S/N values than those of H<sub>2</sub>O spectra in Figs. 8 and 9. The quantum numbers F in this figure are for the lower level (5S<sub>1/2</sub>). The lines for different values of F in the upper level (5P<sub>3/2</sub>) are not resolved in this figure. The <sup>85</sup>Rb absorption cell of 6cm was used at room temperature.<sup>\*)</sup> The corresponding vapor pressure is about 10<sup>-5</sup> Torr, and any buffer gas is not contained in it. Figure 12 shows the frequency stability obtained by locking the frequency at the center of the first derivative of

\*) This cell has been used for Rb atomic standard.

the D<sub>2</sub> line. The minimum of  $\sigma$  in this figure is

$$\sigma = 1.4 \times 10^{-12} \text{ at } \tau = 100\text{s.} \quad (8)$$

By comparing it to that by H<sub>2</sub>O spectra, it can be said that higher stability was obtained, as expected. The authors are now preparing to use the saturated absorption spectra in D<sub>2</sub> line as references to improve the stability. Figure 13 shows the saturated absorption spectra. The spectral width in this figure is 52.7MHz, which is consistent with the value estimated from the radiative life time of 5P<sub>3/2</sub> level (27.0ns).<sup>15)</sup> Six saturated absorption lines and six cross-resonance lines should be seen on the Doppler broadened profile in this figure because the upper and lower levels for D<sub>2</sub> line have four and two sublevels, respectively. However, only two lines can be seen in this figure. The cause of this discrepancy is still now under investigation. It is expected that the <sup>85</sup>Rb-stabilized lasers with such a high stability can be used as powerful tools for Rb atomic standards.<sup>16)</sup>

The frequency tunable range of the laser used above was limited by the mode hopping phenomenon, as mentioned before. One way of overcoming this phenomenon is to use an external grating.<sup>17)</sup> The authors just followed this method and have obtained preliminary experimental results. Figure 14 shows the experimental apparatus. All of the experiments described in this paper, the authors used CSP lasers, however, in this particular experiment, a transverse junction stripe (TJS) laser was used.<sup>18)</sup> One of the cleaved facet of this laser was AR coated and its reflectivity was reduced as low as 14%. A grating was placed at 6cm away from the facet to pick out one of the longitudinal modes. Seventeen longitudinal modes were separately picked out by rotating the grating. The frequency of each mode was tuned for 1-3GHz by translating the position of the grating, and was stabilized by using a stable Fabry-Perot interferometer as a frequency reference. Figure 15 shows the result. Comparison between the curves A and B tells us that the stability of the free running laser is improved by using the external grating, which is because the longitudinal mode competition is suppressed and the cavity -Q value is increased. The curve C represents the result of stabilization, and the minimum of  $\sigma$  on this curve is

$$\sigma = 3.2 \times 10^{-12} \text{ at } \tau = 100\text{s.} \quad (9)$$

The stabilities of other longitudinal modes were almost the same as that shown by the curve C.

## 5. IMPROVEMENTS IN SHORT-TERM FREQUENCY STABILITY

In 4., several experiments were carried out to improve the long-term frequency stability, i.e., the stability for  $\tau \geq 1\text{s}$ . For applications in heterodyne-type communications, high speed optical measurements, etc., the short-term stabilities ( $\tau < 1\text{s}$ ) of the lasers have also to be improved. In this case, even a simple Fabry-Perot interferometer made of a rigid fused quartz block can be satisfactorily used as a frequency reference. However, it is essentially necessary to expand the bandwidth of the servo controller as much as possible.

The stability for  $1\text{ms} \leq \tau \leq 1\text{s}$  was easily improved by increasing the cutoff frequency  $f_c$  of the proportional amplifier in Fig. 5. The dependence of the stability on  $f_c$  is shown in Fig. 16.<sup>19)</sup>

In this figure, the highest stability was obtained at  $f_c = 7.23 \text{ kHz}$ , and the minimum of  $\sigma$  was  $\sigma = 2.1 \times 10^{-12}$  at  $t = 100 \text{ ms}$ . (10)

To improve short-term stability for  $t < 1 \text{ ms}$ , one needs to use different type of servo controller. Figure 17 shows the frequency characteristics of the gain of such a controller developed by the authors. The bandwidth was increased as high as 500 kHz by connecting two differentiators ( $D_1$  and  $D_2$ ) in parallel with the proportional amplifier (P), which were constructed by using faster operational amplifiers than those in Fig. 5. Figure 18 shows the power spectral densities  $S$  of frequency fluctuations of the stabilized laser obtained by this circuit. It can be seen that the value of  $S$  for the stabilized laser is about  $10^{-2}$  of that of free running laser for Fourier frequency up to 500 kHz, and that this circuit is effective to improve the short-term frequency stability. This work is now in progress and faster servo controller is being designed by using faster video amplifiers.

As described in this and previous chapters, improvements of long and short term stabilities have been carried out separately until now. As the next step, several experiments are now in progress to improve the stability for a wide range of  $t$  by combining both of these techniques.

#### APPLICATION OF MICRO COMPUTERS

It is quite favorable if the real-time measurement of frequency stability can be done when the laser is stabilized. Such a real-time measurement system can be inexpensively made by using microprocessors. Figure 19 shows the block diagram of an Allan variance real-time processing system (ARPS) which have been developed by the authors for this purpose.<sup>20)</sup>

It is then possible to find the condition of optimal control for frequency stabilization by using the ARPS. The appropriate gains and cutoff frequencies of the amplifiers in Fig. 5 are found by a micro computer so that the value of  $\sigma$ , measured by the ARPS, will ensure the minimum value. Figure 20 and 21 show the experimental apparatus for optimal control and the result obtained by this apparatus, respectively. It can be seen that the stability obtained by this method is higher than the method in which the gains and cutoff frequencies of the controller are manually adjusted. By using this method, the conditions for optimal control can be kept so that the highest frequency stability is maintained even if the working conditions of the laser may change in time.

This system can be widely used not only for the present study, but for other frequency standards.

#### ALL-DIODE MODE FREQUENCY STABILIZED SEMICONDUCTOR LASERS

Frequency stabilized semiconductor lasers can be used in many fields of applications. As an example, the authors are preparing the precise wavelength measurements of absorption spectra in order to find more accurate values of the molecular constants of  $\text{RbH}$ . These wavelengths can be measured by comparing the wavelength of  $\text{H}_2\text{O}$ -stabilized

laser with that of a frequency stabilized He-Ne laser by using a pressure-scanned Fabry-Perot interferometer. As a preliminary result, the wavelength of  $\text{R}(4_2-3_1)$  line has been measured to be  $8164.8737 \pm 0.0003 \text{ \AA}$ .

As another example, the vibration-rotation spectra in several molecules can also be measured by InGaAsP lasers at 1.3 or 1.6  $\mu\text{m}$ , which may be used for pollutant gas monitoring system.

It has been proposed that AlGaAs lasers can be used for optical pumping of Rb and  $\text{Cs}$  beam atomic standards, and several experiments have already been carried out.<sup>21)</sup> For this particular study, it is very difficult to use commercially available lasers due to the mode hopping phenomenon. A specially designed semiconductor laser has to be made for this purpose. The authors are now preparing facilities for crystal growing to make DBR lasers<sup>22)</sup> with good wavelength selectivity for the optical pumping study. It is expected that these new lasers can be used also for the spectroscopy of the Rydberg states in alkali atoms.

#### 8. CONCLUSIONS

Recent results on spectral width measurements and frequency stabilization of AlGaAs lasers were described. It was demonstrated that the spectral width can be decreased as narrow as 1 MHz. A stabilized Fabry-Perot interferometer, absorption spectra in  $\text{H}_2\text{O}$  and  $^{85}\text{Rb}$  were used as frequency references to improve the long-term frequency stability. The minimum of the square root of the Allan variance in these experiments were  $2.0 \times 10^{-11}$ ,  $1.1 \times 10^{-11}$ , and  $1.4 \times 10^{-12}$  (at  $t = 100 \text{ s}$ ), respectively. For the laser with an external grating, the stability obtained was  $3.2 \times 10^{-12}$  at  $t = 100 \text{ s}$ . Several experiments were carried out to improve the short-term stability, and the power spectral density of frequency fluctuations was reduced to less than  $10^{-2}$  of that of free running lasers for the Fourier frequency range lower than 200 kHz.

An Allan variance real-time processing system (ARPS) was developed for frequency stability measurements, and optimal frequency control was carried out by using this apparatus.

As an application of the frequency stabilized lasers, the precise wavelength measurements of the absorption spectra in  $\text{H}_2\text{O}$  are prepared, and preliminary result of  $8164.8737 \pm 0.0003 \text{ \AA}$  for  $\text{R}(4_2-3_1)$  line was obtained. Finally, a brief comment on the preparation of optical pumping experiments for Rb and  $\text{Cs}$  was given.

#### ACKNOWLEDGEMENTS

The authors would like to express their thanks to Dr. M. Nakamura of Hitachi, Ltd. and Dr. W. Susaki of Mitsubishi, Ltd. for their support to the experiments. They also wish to thank Profs. Y. Suematsu and K. Iga of their institute for their valuable discussions, and to Prof. N. Oura and Dr. N. Kuramochi for offering a  $^{85}\text{Rb}$  cell.

This work was partially supported by a Grant-in-Aid for Scientific Research from the Ministry of Education, Science and Culture.

# REFERENCES

1. A. Aiki, M. Nakamura, T. Kuroda, and J. Umeda, Appl. Phys. Lett., 30, 649(1977).
2. T. Takakura, K. Iga and T. Tako, Japan. J. Appl. Phys., 19, L725(1980).
3. A. L. Schawlow and C. H. Townes, Phys. Rev., 112, 1940(1958).
4. M. Ito and T. Kimura, IEEE J. Quantum Electron., QE-16, 910(1980).
5. S. Kobayashi et. al., IEEE J. Quantum Electron., QE-18, (1982).
6. H. Tsuchida, S. Sampei, M. Ohtsu and T. Tako, Japan. J. Appl. Phys., 19 L721(1980).
7. C. L. Tang, "Method of Experimental Physics, vol 15, Quantum Electronics", Part A, p224, Academic Press, New York, (1979).
8. K. Utaka, K. Kobayashi, K. Kishino and Y. Suematsu, Electron. Lett., 16, 455(1980).
9. H. Tsuchida, M. Ohtsu and T. Tako, Japan. J. Appl. Phys., 20, L403(1981).
10. M. Ohtsu, S. Katsuragi and T. Tako, IEEE J. Quantum Electron., QE-17, 1100(1981).
11. G. Herzberg, "Infrared and Raman Spectra", 1st ed., Van Nostrand, Princeton, (1945).
12. R. T. Darling and D. M. Dennison, Phys. Rev., 57, 128(1940).
13. W. Baumann and R. Mecke, Zeits. Physik, 81, 445(1933).
14. H. Tsuchida, M. Ohtsu and T. Tako, Japan. J. Appl. Phys., 21, L1(1982).
15. J. K. Link, J. Opt. Soc. America, 56, 1195 (1966).
16. L. L. Lewis and M. Feldman, Proc. 35th Ann. Freq. Symposium, p-12(1981).
17. M. W. Fleming and A. Mooradian, IEEE J. Quantum Electron., QE-17, 44(1981).
18. H. Namizaki, IEEE J. Quantum Electron., QE-11, 427(1975).
19. H. Tsuchida, M. Ohtsu and T. Tako, Trans. IEEE Japan, E-65, 65(1982).
20. I. Sato, M. Ohtsu and T. Tako, Bull. P. M. E. (T. I. T.), 48, 47(1981).
21. V. Arditi and J.-L. Pique, J. Phys. B. Atom. Mol. Phys., 8, L331(1975).

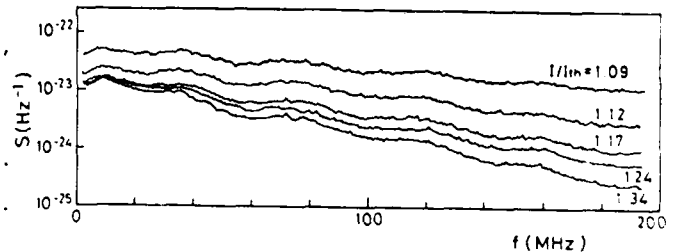


Fig.1. Power spectral density of the frequency fluctuations.  $I/I_{th}$  represents the injection current normalized to its threshold value.

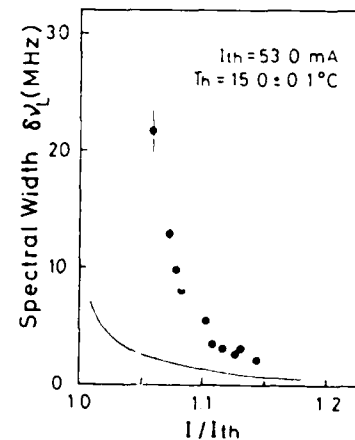


Fig.2. Relation between spectral linewidth  $\Delta\nu_L$  (FWHM) and injection current. The solid curve represents the theoretical value.

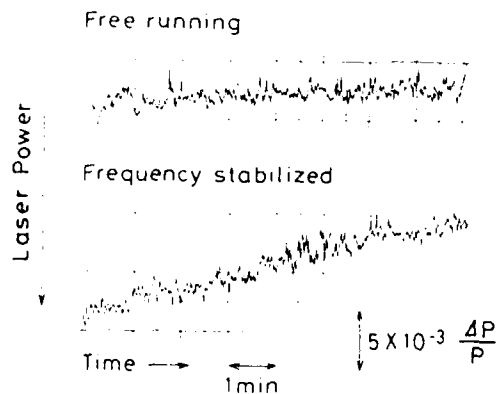


Fig.3. Time dependence of the laser power.

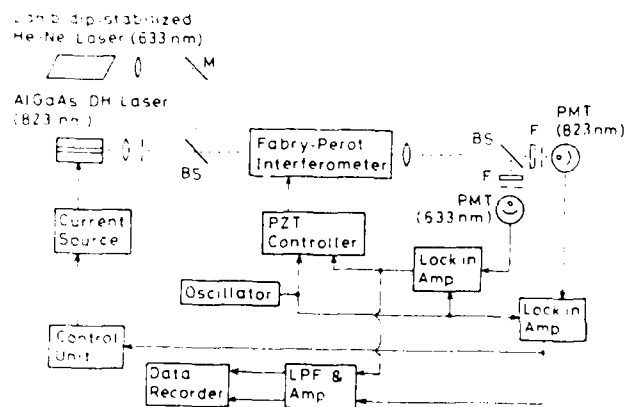
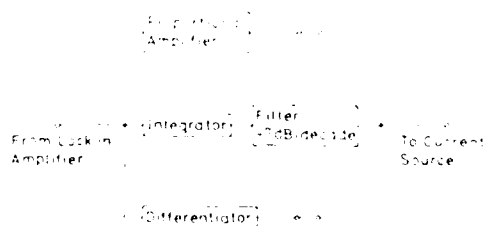
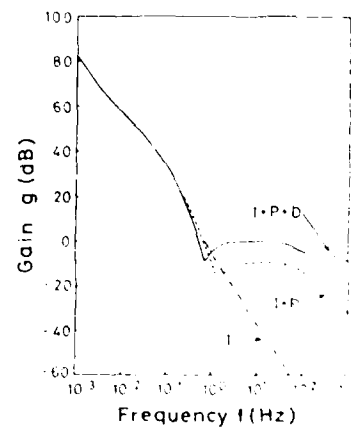


Fig.4. The experimental apparatus for frequency stabilization using the stabilized Fabry-Perot interferometer as a reference.



(a)

Fig.5. (a) The block diagram of the amplifiers used for the servo-controller.  
(b) Frequency characteristics of the gains of the amplifiers in (a).



(b)

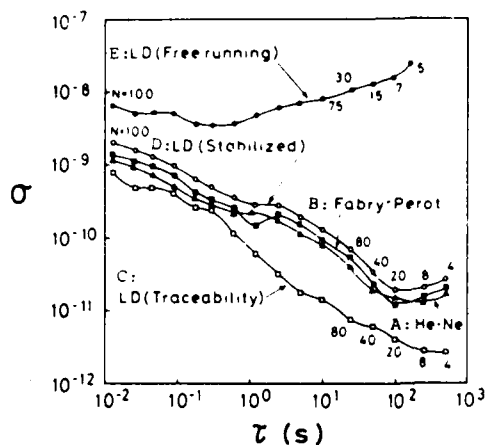


Fig.6. Experimental results. A: The frequency stability of the Lamb dip-stabilized He-Ne laser. B: The frequency traceability of the Fabry-Perot interferometer to the He-Ne laser. C: The frequency traceability of the semiconductor laser to the interferometer. D: The frequency stability of the stabilized semiconductor lasers estimated by the curves A, B, and C. E: The frequency stability of the free running semiconductor laser

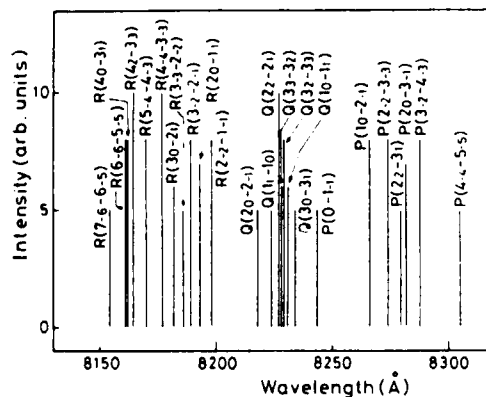


Fig.7. The assignment and relative intensities of the principal lines in the (2, 1, 1) band of  $H_2O$  spectra.

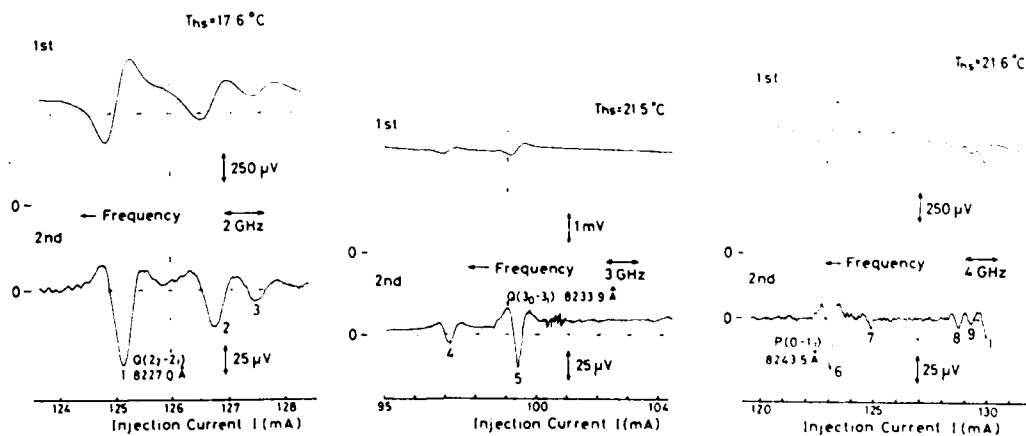
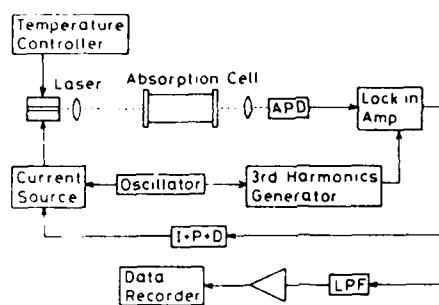
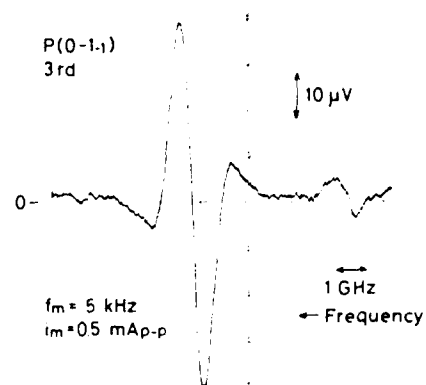


Fig.8. The first and second derivative signals of the absorption spectra in  $H_2O$ .



(a)



(b)

Fig.9. (a) Experimental apparatus for frequency stabilization by using H<sub>2</sub>O spectra as a frequency reference. (b) The third derivative of the absorption spectrum in H<sub>2</sub>O used as a frequency reference.

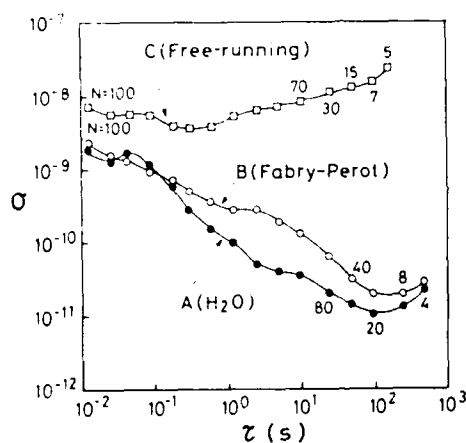


Fig.10. Frequency stability. The curves A and C represent the stability for H<sub>2</sub>O-stabilized and free-running lasers, respectively. The curve B is for the result of the previous work (The curve B is Fig.6.)

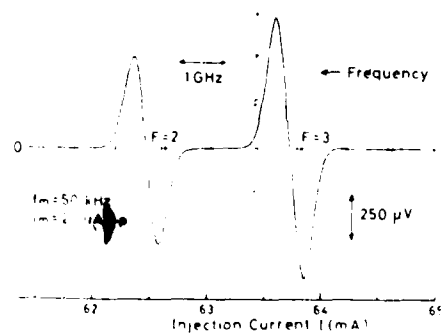
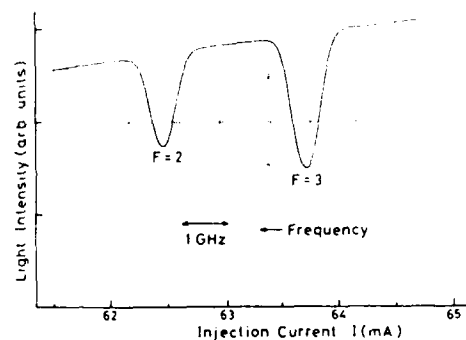


Fig.11. The linear absorption spectra of <sup>85</sup>Rb-D<sub>2</sub> line, and their first derivatives.

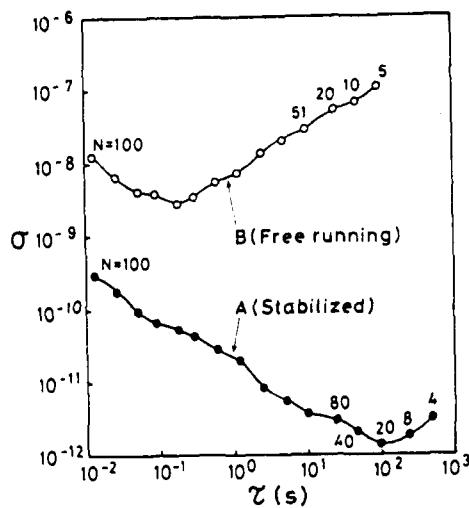


Fig.12. Frequency stabilities of the  $^{85}\text{Rb}$ -stabilized (A) and free running (B) lasers, respectively.

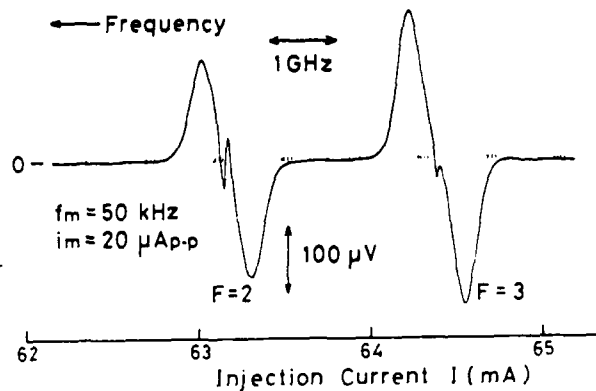


Fig.13. The first derivative signals of the saturated absorption spectra of  $^{85}\text{Rb-D}_2$  line.

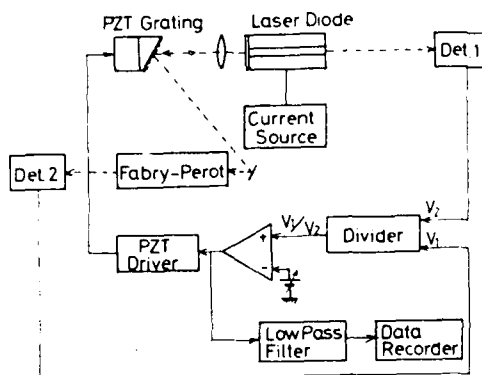


Fig.14. Experimental apparatus for frequency stabilization of a TJS laser with an external grating.

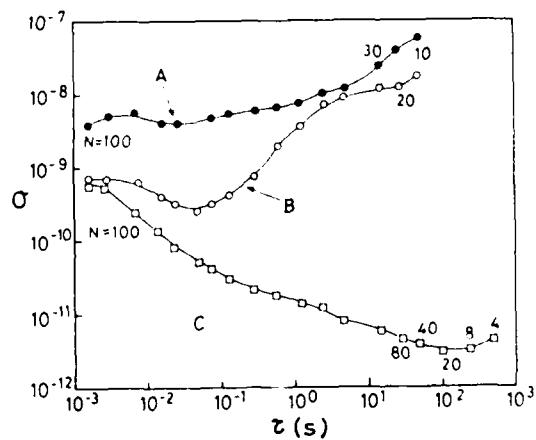


Fig.15. Frequency stability of the free running laser without an external grating (A), with an external grating (B), and of the stabilized laser with an external grating, respectively.

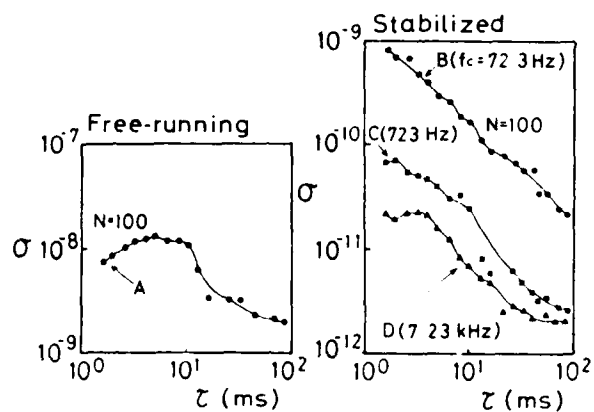


Fig. 16. The dependence of the short-term frequency stability (time  $\tau = 1$ ) on the center frequency  $f_c$  of the signal generator used in the study.

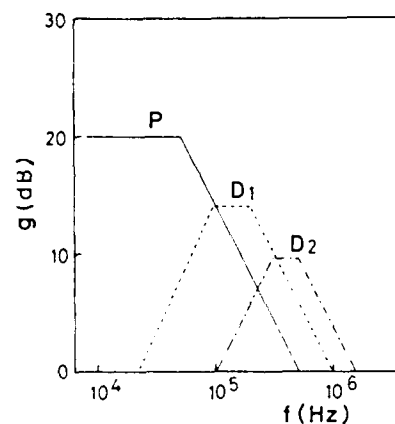


Fig. 17. Frequency characteristics of the gain of the amplifiers used to improve the short-term frequency stability ( $\tau < 1$  ms).

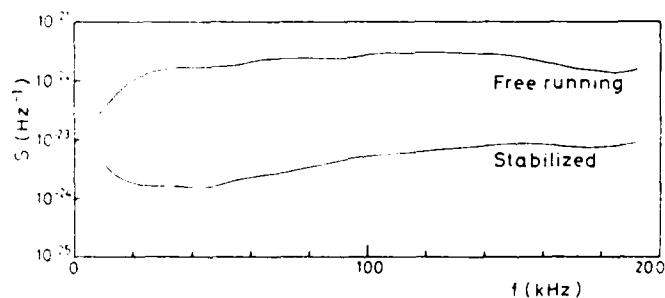
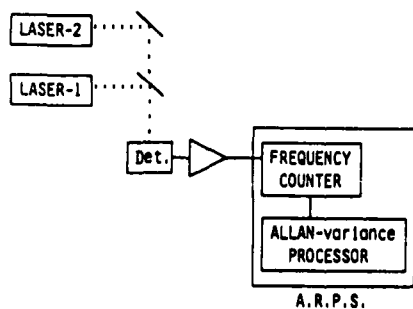
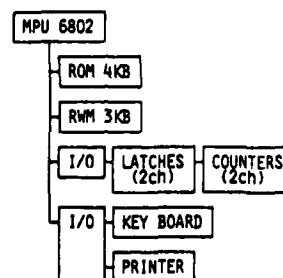


Fig. 18. Power spectral density of the frequency fluctuations. The amplifiers in Fig. 17 were used for stabilization.



(a)



(b)

Fig.19. (a) The measurement system of the laser frequency stability. (b) The block diagram of the Allan variance real-time processing system.

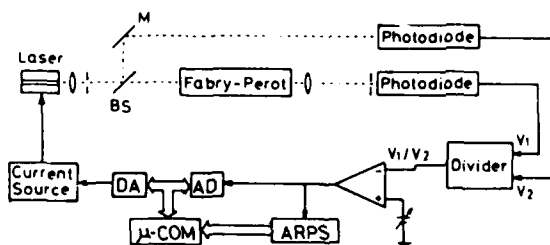


Fig.20. Experimental apparatus for optimal control for frequency stabilization by micro-computers.

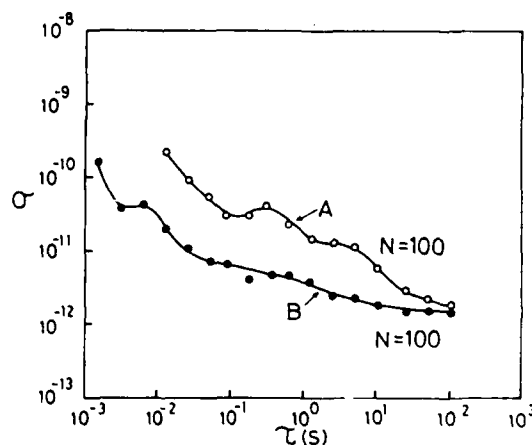


Fig.21. Frequency stability obtained by manual control (A) and by optimal control (B).

## FREQUENCY STABILITY AND CONTROL CHARACTERISTICS OF

## (GaAl)As SEMICONDUCTOR LASERS\*

A. Mooradian and D. Welford

Lincoln Laboratory, Massachusetts Institute of Technology  
Lexington, Massachusetts 02173Summary

A study of fundamental linewidth broadening mechanisms in cw (GaAl)As diode lasers is presented. The linewidths were observed to increase linearly with increased reciprocal output power which can be explained using a modified Schawlow-Townes theory. A power-independent broadening of the linewidth was also observed and has been explained as due to refractive index fluctuations resulting from statistical fluctuations in the number of conduction electrons in the small active volume of the devices studied. The range of linewidths for these devices can severely limit the utility of semiconductor lasers in various applications such as frequency standards, heterodyne communications, and fiber optical sensors. Significant performance improvements have been made by operating these devices in a stable external cavity.

The use of semiconductor diode lasers as high resolution spectral sources requires an understanding of the linewidth characteristics of these devices. Reported here is a study of the fundamental mechanisms which account for the spectral linewidth of cw single-frequency (GaAl)As diode lasers. The experiments were carried out on a number of Mitsubishi transverse-junction-stripe (TJS) and Hitachi channel-substrate-planar (CSP) lasers at 273, 195 and 77 K. The linewidths shown in Fig. 1 were observed to increase linearly with reciprocal output power<sup>1</sup> at all temperatures. However, a power-independent contribution<sup>2</sup> to the laser linewidth was also observed which increased in magnitude with decreasing temperature.

The experimental arrangement has been described elsewhere.<sup>3</sup> The devices were thermally isolated in a Dewar to reduce temperature fluctuations to an insignificant level. Each data point for a particular power and temperature was the result of the integration of many Fabry-Perot interferometer scans using a computer. The output power was measured using a calibrated silicon photodiode, and a dual-grating (12,000 lines/mm) 3/4-meter spectrometer was used to verify single-frequency operation of the laser diode. Precautions against optical feedback were taken to avoid

affecting the output of the devices. Injection current noise in the diodes was minimized by using a shielded lead-acid battery based passive component power supply incorporating a 500 kHz bandwidth filter network. Linewidth measurements were made using a scanning Fabry-Perot interferometer with a resolution of 3.5 MHz. The experimental data presented is for one particular TJS laser at 273, 195 and 77 K, and is representative of the typical performance of fifteen such diodes. The single-ended output power versus injection current characteristics for the diode lasers at each of the three temperatures was quite linear over the entire operating range.

The power-independent contribution to the laser linewidth is attributed to statistical fluctuations in the number of electrons in the small active volume of the devices which cause a refractive index fluctuation and hence a cavity frequency fluctuation. The output frequency fluctuation can be shown to be given by

$$\delta\nu = \frac{M\nu}{n} \left( \frac{dn}{dN} \right)_{N_t, \nu} \left( \frac{\Gamma_g}{c + \frac{\Gamma_g}{g}} \right) \delta N \quad (1)$$

where  $\delta N$  is the mean square fluctuation in the number  $N$  of electrons in the gain volume and  $dn/dN$  is evaluated at the laser frequency and at  $N$  equal to the number of electrons at laser threshold,  $N_t$ ,  $M$  is the mode filling factor, and  $\Gamma_g$  and  $\Gamma_c$  are the gain and cavity linewidths, respectively. The mean square fluctuation in electron number is assumed to be  $\sqrt{N_t}$ . By substitution of experimentally determined parameter values into Eq. (1), we get power-independent contributions of 2.2, 6.5 and 11.5 MHz at 273, 195 and 77 K, respectively, compared to observed values of 1.9, 5.2 and 8.4 MHz. The conventional theory of laser linewidth does not appear to include this power-independent limitation.

The power-dependent contributions to the laser linewidth are shown to be in agreement with a mechanism recently presented by Henry<sup>3</sup> which is similar to the problem treated by Lax<sup>4</sup> that occurs in detuned gas lasers, where the cavity resonance and optical transition frequencies do not coincide. In addition to the usual broadening caused by phase fluctuations arising from spontaneous emission events, there is an additional broadening which comes from a phase change associated with the laser field intensity change induced by spontaneous

\*This work was sponsored by the Department of the Air Force.

AD P001542

emission. The carrier density and hence gain will fluctuate to restore the laser field amplitude to the steady state value. The change in the gain or imaginary part of the refractive index arising from this carrier density change is accompanied by a change in the real part of the refractive index. The power-dependent contribution to the laser linewidth is then expressed as

$$2\Gamma = (h\nu/8\pi P_0)(c/nL)^2(\ln R - \alpha L)(\ln R)n_{sp}(1+\beta^2) \quad (2)$$

where  $\beta$  is the ratio of change in the real part of refractive index to the change in the imaginary part of refractive index due to spontaneous emission events over the same period of time,  $2\Gamma$  is the full width of the emission line at frequency  $\nu$  for single ended output power  $P_0$ ,  $n$  is an effective refractive index including dispersion,  $\alpha$  is the mode loss coefficient,  $L$  is the cavity length,  $R$  is the facet reflectivity and  $n_{sp}$  is the spontaneous emission factor. The spontaneous emission factor is the ratio of spontaneous emission rate per mode to the stimulated emission rate per laser photon. By substitution of experimentally determined parameter values into Eq. (2), we get slopes of 67.2, 43.7 and 8.2 MHz mW at 273, 195 and 77 K, respectively, compared to observed values of 74.7, 36.7, and 9.28 MHz mW.

The broad range of linewidths for these lasers is fundamental and can severely limit their utility in various applications such as frequency standards, heterodyne communications and fiber optical sensors. External cavity operation of a semiconductor injection laser is attractive for a number of applications requiring greater spectral purity and frequency stability than can be obtained from a solitary laser diode, while offering tunability of the emission frequency through the use of dispersive cavity elements. Operating these lasers in an external cavity can substantially reduce the linewidth because of a higher cavity Q. A stable grating tuned external cavity without feedback stabilization has been operated<sup>5</sup> with an RMS frequency jitter of 300 kHz in one second and a linewidth of less than 15 kHz for output powers of a few milliwatts and a 10 nm tuning range. An instrument limited 15 kHz heterodyne beat spectrum of two external cavity devices is shown in Fig. 2; the expected linewidth at 0.4 mW output power is about 400 Hz. This linewidth was limited by acoustic fluctuations of the external cavity structure. The measured amplitude noise spectrum was flat and down more than 40 dB in the range from 10 Hz to 2 GHz.

A new generation of external cavity devices incorporating feedback stabilization should have usable linewidths of less than 10 kHz and could tune continuously over the range 650-900 nm using GaAlAs and from 1100-1700 nm using GaInAsP.

#### References

1. D. Welford and A. Mooradian, Appl. Phys. Lett. **40**, 865 (1982).
2. D. Welford and A. Mooradian, Appl. Phys. Lett. **40**, 560 (1982).
3. C. H. Henry, IEEE J. Quantum Electron. **QE-18**, 259 (1982).

4. M. Lax, Phys. Rev. **160**, 290 (1967) and **157**, 213 (1967).
5. M. W. Fleming and A. Mooradian, IEEE J. Quantum Electron. **QE-17**, 44 (1981).

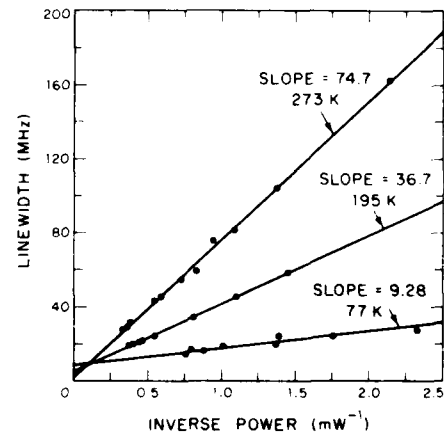


Fig. 1. Linewidth vs reciprocal output power for Mitsubishi (TJS) single-frequency (GaAl)As diode laser.

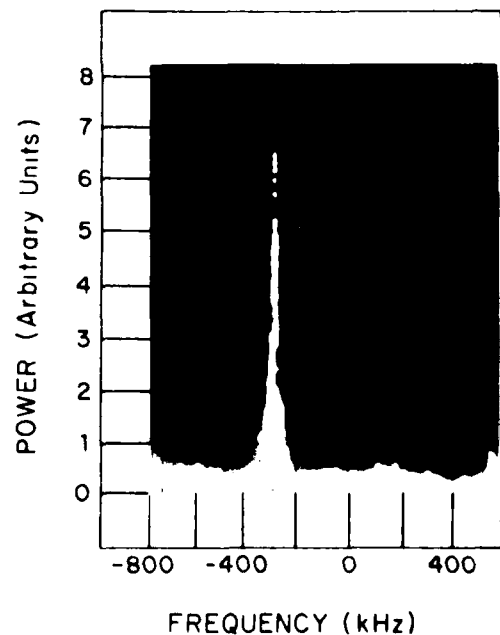


Fig. 2. Heterodyne beat spectrum between two external cavity (GaAl)As CW diode lasers with output power of 0.4 and 0.34 mW, respectively.

SHORT-TERM FREQUENCY STABILITY AND SYSTEMATIC EFFECTS ON THE RUBIDIUM 87  
MASER OSCILLATOR FREQUENCYMichel Têtu, Pierre Tremblay, Deni Bonnier  
and Jacques VanierDépartement de Génie Electrique  
Université Laval, Québec, Canada, G1K 7P4Summary

This paper presents an evaluation of the frequency stability achievable with a rubidium maser oscillator. The study takes into account the effect of the optical pumping rate, the bulb temperature, the coupling loop coefficient and the receiver noise. Systematic effects on the maser frequency are also considered. Experimental results show that their variations govern the frequency stability for averaging times longer than one second. Permitted excursions of the main maser parameters to achieve frequency stability better than  $1 \times 10^{-14}$  are determined.

**Key words:** Rubidium, Maser, Allan variance, Buffer gas, Light shift, Cavity pulling, Frequency stability.

Introduction

The rubidium maser frequency stability has been measured previously in the time domain for short averaging times<sup>1</sup> and for long averaging times<sup>2</sup> and in the frequency domain<sup>3</sup>. We present in this paper a theoretical evaluation of the possible performance of this type of oscillator taking into account the fact that the maser line is inhomogeneously broadened. Optimum conditions are established on the main maser parameters and the theoretical expression for the short term frequency stability is calculated according to realizable configurations. The systematic effects on the maser frequency were also considered in previous works<sup>4,5,6</sup>. We review here these effects adding to their contribution some undiscussed sources.

Short-Term Frequency StabilityTwo-sample variance (Allan variance)

The short-term frequency stability of a maser oscillator, expressed in the time domain by the two-sample variance (Allan variance) is given by:

$$\sigma^2(\tau) = K_{-2}\tau^{-2} + K_{-1}\tau^{-1} \quad (1)$$

with

$$K_{-2} = \frac{4kT}{P_0} \left\{ \frac{3f_c}{8\pi\nu_m^2} \left[ 1 + (F_r - 1) \frac{290}{T} \frac{(1 + \beta)}{\beta} \right] \right\} \quad (2)$$

and

$$K_{-1} = \frac{4kT}{P_0} \frac{1}{8} \frac{1}{Q^2} \quad (3)$$

The first term is a white phase noise and the second term is a white frequency noise. In these relations:  $P_0$  is the atomic power,  $\nu_m$  and  $Q$  are the maser frequency and the atomic line Q,  $\beta$  is the output loop coupling coefficient,  $F_r$  is the receiver noise figure,  $f_c$  is the measurement system cut-off frequency,  $T$  is the maser temperature,  $k$  is Boltzmann constant and  $\tau$  is the averaging time. The frequency stability relation shows that in order to improve the maser performances, one has to increase the atomic power, to couple-out more power and to increase the atomic line Q.

Atomic power

The rubidium maser has an inhomogeneously broadened line since the atoms are confined, by a buffer gas, to a restricted volume and they experience interactions that depend on their location in the active medium. One can show that the power delivered by the atoms to the microwave cavity containing the medium is given by<sup>8,1</sup>.

$$P_0 = \int \frac{2\pi \hbar \omega b^2 \Gamma A(\Gamma) dv}{\gamma_1 (\frac{1}{2}\Gamma + \gamma_2) + \gamma_1 (\omega_a - \omega)^2 / (\frac{1}{2}\Gamma + \gamma_2) + 4b^2 (1 - \Gamma B(\Gamma))} \quad (4)$$

where  $\hbar$  is Planck constant divided by  $2\pi$ ,  $\Gamma$  is the optical pumping rate,  $\gamma_1$  and  $\gamma_2$  are the population and coherence relaxation rates respectively,  $b$  is proportional to the stimulating field value and  $\omega$  its angular frequency,  $\omega_a$  is the angular frequency of each atom and  $n_0$  is the atomic density.  $A(\Gamma)$  and  $B(\Gamma)$  are two functions of the optical pumping rate and relaxation rates as defined in reference 1.

Oscillation occurs when the atomic power compensates the power dissipated in the cavity and the power coupled out. To evaluate the oscillation power one has to solve equation 4. This equation is an integral equation since the stimulating field and the optical pumping rate are functions of the atomic power. Numerical solutions are obtained by standard method<sup>8</sup> and we give in figure 1 the atomic power as a function of the optical pumping rate at the entrance of the bulb,  $P_0$ , for three cavity temperatures (45°C, 55°C and 65°C) and two different coupling coefficients (0.1 and 0.5). We see that the maser oscillates over a limited range of optical pumping rates when all the other parameters are kept constant and that an optimum can be reached. Also noted, the power could increase with the temperature of the cavity (or the atomic density) but more pumping (light intensity) would be required.

Our actual set up limits the value of  $P_0$  to 3000  $\text{s}^{-1}$  or less so the maximum operable cavity temperature is around 60°C and the delivered power is in the order of  $10^{-10}$  W. The maser behavior shown in figure 1 has been observed with corresponding devices<sup>9</sup> and gives great confidence on the mathematical model used.

In figure 2, we evaluate the atomic power and the received power as a function of the coupling coefficient; the two powers being related as:

$$P_r = \frac{\beta}{\beta + 1} P_0(\beta) \quad (5)$$

We see that the atomic power decreases steadily when the coupling coefficient is increased from zero while the received power (coupled out power) increases at low  $\beta$  values, reaches a maximum and decreases for high  $\beta$  values. This fact implies that the value of  $\beta$  should be adjusted to a value that minimizes the white phase noise contribution,  $K_{-2}$  (equation 2), without increasing too much the white frequency noise contribution,  $K_{-1}$  (equation 3).

#### Noise contributions

The white phase noise and the white frequency noise contributions can be deduced from equations 2 and 3 when the maser power is known. Figure 3 shows the square root of each term as function of the optical pumping rate for two values of the coupling coefficient (0.1 and 0.5). We indicate the square roots because they represent the asymptotical value of the published frequency stability (see next section). We observed that minima are reached. These minima are not too critical on the value of  $P_0$  when a small coupling coefficient is chosen but the corresponding values differ for the two types of noise. These contributions were evaluated with the following parameters:

$$F_p = 2.24 \text{ (3.5 dB)}, f_c = 50 \text{ Hz}, \nu_m = 6.835 \text{ GHz};$$

they are around  $1 \times 10^{-14}$  and  $2 \times 10^{-14}$  respectively.

#### Overall short-term frequency stability

The overall short-term frequency stability is calculated while considering the two noise contributions together. Since the published data for the stability, in the time domain, is the two sample standard deviation, we must consider the relation:

$$\sigma(\tau) = \sqrt{K_{-2}\tau^{-2} + K_{-1}\tau^{-1}} \quad (6)$$

Computation of this relation gives the values indicated in figure 4 for three values of the cavity temperature (318 K, 328 K and 338 K). The values  $P_{0,\text{opt}}$  indicated are mean value of the two  $P_0$  that minimize  $\sqrt{K_{-2}}$  and  $\sqrt{K_{-1}}$  respectively. The coupling coefficient is set at 0.1. The curves show that the white frequency noise dominated the white phase noise contribution for averaging time longer than one second. The frequency stability is of the order of  $10^{-13}$  at 1 second. It is important to notice here that these results are obtained without normalization factor. They are predicted values deduced from the maser model evaluated with typical parameters.

The data shown of figure 4 are typical results: the crosses are from recent measurements and the circles are data taken from reference 2. We see that the very short term frequency stability is close to the predicted value but for long averaging times, the discrepancy is significant. Although the existence of the white frequency noise has been observed on this type of maser<sup>10</sup>, another source of frequency instabilities dominates and the theoretical model has to be modified in order to explain the observation.

#### Systematic Effects on the Maser Frequency

##### Maser frequency

The frequency of a Rb maser depends on the resonant frequency of the atomic system and the tuning of the microwave cavity that confines the electromagnetic field. We can estimate that each atomic interaction will shift the resonant frequency and broaden the line<sup>11</sup>. The atomic frequency,  $\nu_a$ , can be written

$$\nu_a = \nu_0 + \sum \Delta\nu_i \quad (7)$$

where  $\nu_0 = 6,834,682,612.8 \pm 0.5 \text{ Hz}^{12}$  is the unperturbed hyperfine frequency and  $\Delta\nu_i$  represents the frequency shift associated with each interaction.

The full linewidth can be defined as a sum:

$$\delta\nu_a = \delta\nu_0 + \sum \delta\nu_i \quad (8)$$

where  $\delta\nu_i$  is the contribution from each interaction and  $\delta\nu_0$  includes the natural linewidth and the contribution from non-explicitly considered interactions. In terms of the coherence relaxation rate, the full-width can be written:

$$\delta\nu_a = \frac{1}{\pi} (\gamma_{2,0} + \sum \gamma_{2,i}) \quad (9)$$

where  $\gamma_{2,0}$  and  $\gamma_{2,i}$  correspond respectively to  $\delta\nu_0$  and  $\delta\nu_i$ .

$\gamma_{2,0}$  and  $\delta\nu_a$  are functions of the position in the active medium and, since the atoms are not allowed to move freely, only local averages over a small volume can be considered. To find the exact maser frequency one has to find the frequency at which the power is maximum taking into account the line inhomogeneity and the cavity pulling effect,  $\Delta\nu_{cp}$ , to be specified in the next section.

#### Frequency shifts

The main frequency shifts encountered come from the static magnetic field, the buffer gas, the pumping light, the spin exchange and the cavity pulling. For each, we evaluate the nominal value under usual operating conditions, specify the possible sources of variation and evaluate the required changes to produce a relative frequency shift of  $1 \times 10^{-14}$ .

**Magnetic field:** A static magnetic field is used to establish a quantum axis. The field independent transition is shifted, at low field level, by an amount:

$$\nu_B = 5.74 \times 10^{10} B^2 \quad (10)$$

where  $B$  is the magnetic induction given in Tesla. The usual field value is  $10^{-5}$  T and the corresponding shift is 5.7 Hz or  $8.3 \times 10^{-10}$  in relative value.

Variations of this shift are expressed by:

$$d\nu_B = 11.48 \times 10^{10} B dB. \quad (11)$$

At this field level, a variation of  $6 \times 10^{-11}$  T on the B-field is required to produce a relative shift of  $10^{-10}$ . Such a variation may result from

a change in the d.c. current producing the field or a change in the residual field from the ambient. For example, a shielding factor<sup>12</sup> of 67,000 is required to bring to this level a change of 10% of the natural magnetic field.

**Buffer gas:** A buffer gas is used to reduce the Doppler width of the transition and to improve the pumping efficiency by quenching the scattered light. The frequency shift associated with the interaction of rubidium atoms and buffer gas atoms can be expressed, to the first order in temperature<sup>13</sup>:

$$\Delta\nu_{bg} = (\beta' + \delta \Delta T) P_s \quad (12)$$

where  $P_s$  is the buffer gas pressure at the time of sealing,  $\beta'$  is the pressure coefficient,  $\delta$  is the temperature coefficient and  $\Delta T$  is the cavity temperature offset from a reference temperature:  $\Delta T = T_c - T_0$ . Usually, 11 torr of pure nitrogen has been used in order to maximize the maser gain<sup>14</sup>. For this gas pressure, the coefficients are  $\beta' = 538$  Hz/torr and  $\delta = 0.53$  Hz/°C - torr<sup>13</sup> and the resulting shift is  $(5918 + 5.83 \Delta T)$  Hz. When the operating temperature is set at the reference value, the frequency variation due to the buffer gas becomes:

$$d\Delta\nu_{bg} = \beta' dP_s + \delta P_s d\Delta T. \quad (13)$$

In our actual operating conditions, a variation of  $1 \times 10^{-5}$  °C on  $T_c$  or  $1.3 \times 10^{-7}$  torr on  $P_s$  gives a relative variation of  $10^{-14}$  on  $\nu_m$ . Such a variation on  $P_s$  can result from a change of the bulb volume occurring, for example, because of a barometric pressure change.

**Pumping light:** Population inversion is achieved through optical pumping. A frequency shift exists when the frequency of the incident photons does not coincide with the frequency of the absorbing atoms. A phenomenological way to express this shift is:

$$\Delta\nu_{op} = \alpha I_{00} \quad (14)$$

where  $I_{00}$  is the maximum intensity of the light spectrum and  $\alpha$  is the light shift coefficient. The latter takes into account the spectral distribution of the pumping light and the spectral distribution of the absorption coefficient. Nominal values are:  $I_{00} \approx 10^4$  photons/s-Hz-cm<sup>2</sup> and  $\alpha \approx -0.1$  Hz/1<sup>15</sup> of  $I_{00}$  consequently,  $\Delta\nu_{op} \approx -30$  Hz.

Variation of this shift is expressed simply by:

$$d\Delta\nu_{op} = \alpha dI_{00} + I_{00} d\alpha. \quad (15)$$

The value of  $I_{00}$  can vary under a change in the transmission of the isotopic filter (change of temperature, deposit of a Rb film) or a change in the emitted power (lamp temperature, excitation power). Variations of  $\alpha$  are mainly due to the temperature of the isotopic filter (shape of the spectrum, frequencies of the pumping light) and the transmission conditions through the active cell (atomic density, atomic power). Although the evaluation of this frequency shift and its variations is fairly complex, we can specify, from previous studies<sup>15,16</sup>, that  $I_{00} \partial \alpha / \partial T_f \approx 0.23 \text{ Hz/}^\circ\text{C}$  and  $\partial I_{00} / \partial T_f \approx .5 \text{ Hz/}^\circ\text{C}$  which indicate that a variation of  $10^{-6}^\circ\text{C}$  on the isotopic filter temperature will shift the maser frequency relatively by  $1 \times 10^{-14}$ .

**Spin exchange:** The spin exchange shift is proportional to the population difference between the two maser levels. Under steady state conditions, it turns out to be approximately:

$$\Delta \nu_{se} = -\frac{1}{2\pi} C \gamma_2 \quad (16)$$

where  $C$  is the spin exchange shift constant<sup>2</sup> and  $\gamma_2$  is the atomic full-width. The nominal value of this shift has not been measured yet, but is estimated to 1 Hz according to H-maser value. A variation of this shift should be attributed to a change in the atomic linewidth. It will be disregarded in this study.

**Cavity pulling:** The cavity pulling arises from an off-tuning,  $\Delta \nu_c$ , of the microwave cavity; its contribution can be written:

$$\Delta \nu_{cp} = \frac{Q_{cl}}{Q_l} \Delta \nu_c \quad (17)$$

where  $Q_{cl}$  is the loaded cavity  $Q$ , and  $Q_l$  is the atomic line  $Q$ . In terms of the coherence relaxation rate, equation 17 becomes:

$$\Delta \nu_{cp} = \frac{\pi Q_{cl}}{\nu_a} \Delta \nu_c \gamma_2 \quad (18)$$

This shift is proportional to the full linewidth and a certain compensation can be realized with the spin exchange shift (eq. 16). In usual conditions:  $Q_{cl} \approx 3 \times 10^4$ ,  $Q_l \approx 5 \times 10^7$ , so for  $\Delta \nu_c = 500 \text{ Hz}$ ,  $\Delta \nu_{cp} = 0.3 \text{ Hz}$ .

Variations of the cavity pulling effect are evaluated from the relation:

$$d \Delta \nu_{cp} = \frac{\Delta \nu_c}{Q_l} dQ_{cl} - \frac{Q_{cl} \Delta \nu_c}{Q_l^2} dQ_l + \frac{Q_{cl}}{Q_l} d\Delta \nu_c \quad (19)$$

The first two terms can be made small by a proper tuning of the cavity<sup>17</sup>. A change in  $Q_{cl}$  can be

associated with a deposit of Rb film on the bulb surface and depends on the cavity temperature. The cavity offset will vary with the temperature and a coefficient of  $-3 \text{ kHz/}^\circ\text{C}$  is typical. Also, the stability of the mechanical tuner and of the temperature of the output loop have to be considered. Finally the line  $Q$  changes if the width or the coherence relaxation rate,  $\gamma_2$ , changes. The value of this rate is approximately  $300 \text{ s}^{-1}$  and results mainly from spin exchange, pumping light and buffer gas and a change in these contributions will affect the line  $Q$ . After substitution in equation 19 of the known perturbation, we deduced that a relative frequency shift of  $1 \times 10^{-14}$  can be produced by a change of  $4 \times 10^{-5}^\circ\text{C}$  on  $T_c$  or 0.1% on  $I_{00}$ .

From this study on the systematic effects on the frequency of the actual maser, we retain that the temperature of the cavity has to be regulated to  $10^{-5}^\circ\text{C}$ , the isotopic filter temperature to  $10^{-4}^\circ\text{C}$ , the magnetic field to  $10^{-10} \text{ T}$ , the light intensity to .01% and the bulb volume should not changed more than  $10^{-5} \text{ cc}$  if the fractional frequency variations are to be less than  $1 \times 10^{-14}$ .

#### Possible Improvements

The systematic effect most difficult to overcome is the maser frequency dependency on the cavity temperature. Fortunately, a partial compensation between the cavity detuning effect and the buffer gas shift is possible<sup>5</sup> and the absolute value of the buffer gas shift coefficients can be adjusted using a mixture<sup>18</sup>. Methane and nitrogen in the ratio  $P_{CH_4}/P_{N_2} = 0.475$  at a total pressure of 12 torrs should give the right compensation and leave a high maser gain<sup>19</sup>.

A relative frequency shift of  $9 \times 10^{-11}/\text{kPa}$  has been correlated to barometric pressure changes. The maser has then to be placed in a rigid, sealed, enclosure.

A four-layer magnetic shield and a two-even regulator should be sufficient to reduce, to proper levels, the magnetic field and temperature variations of the ambient.

Finally, the light shift effect is not believed to be a limiting factor in the actual design but it may become so after improvements. It will be possible to limit its contribution by a proper choice of temperature at the sites of the lamp bulb, the filter cell and the active cell. Also, a light intensity automatic control system has shown to be effective<sup>2</sup>.

We show in figure 5 a lay-out of a small Rb maser that will incorporate the conclusions of this study.

### Acknowledgements

The authors would like to thank the "Natural Sciences and Engineering Research Council of Canada (CRSNG)" and "Le fond FCAC" of the Province of Quebec for their financial support.

### References

1. M. Têtu, G. Busca, J. Vanier, IEEE Trans. Inst. Meas., Vol. IM-22, No 3, pp. 250-257, 1973.
2. G. Busca, R. Brousseau, J. Vanier, IEEE Trans. Inst. Meas., Vol. IM-24, No 4, pp. 291-296, 1975.
3. M. Têtu, R. Brousseau, J. Vanier, IEEE Trans. Inst. Meas., Vol. IM-29, No 2, pp. 94-97, 1980.
4. N. Bazarov, V.P. Gubin, Radio Eng. Electr. Physics, Vol. 15, No 10, pp. 1860-1867, 1970.
5. G. Busca, M. Têtu, J. Vanier, Can. J. Phys., Vol. 51, No 13, pp. 1379-1387, 1973.
6. J. Vanier, D.H. Nguyen, G. Busca, M. Têtu, Can. J. Phys., Vol. 57, No 9, pp. 1380-1387, 1979.
7. P. Lesage, C. Audoin, M. Têtu, IEEE Trans. Inst. Meas., Vol. IM-29, No 4, pp. 311-315, 1980.
8. M. Tessier, J. Vanier, Can. J. Phys., Vol. 49, No 21, pp. 2680-2689, 1971.
9. M. Têtu, D.Sc. thesis, Laval University, Quebec, Canada, unpublished.
10. M. Têtu, P. Tremblay, P. Lesage, P. Petit, C. Audoin, 13th PTI, Washington, D.C., 1981.
11. J. Vanier: "Basic Theory of Lasers and Masers" (Gordon and Breach Science Publishers, N.Y.).
12. J. Vanier, G. Racine, R. Kinski, M. Picard, 12th PTI, Washington, D.C., 1980.
13. J. Vanier, R. Kinski, N. Cyr, J.Y. Savard, M. Têtu, Journ. Appl. Phys., 1982, accepted.
14. P. Davidovits, R. Novick, Proc. IEEE, Vol. 54, No 2, 1966.
15. G. Busca, M. Têtu, J. Vanier, Appl. Phys. Lett., Vol. 23, No 7, 1973.
16. G. Busca, M. Têtu, J. Vanier, 27th Annual Symposium on Frequency Control, Atlantic City, 1973.
17. M. Têtu, G. Busca, J. Vanier, 26th Annual Symposium on Frequency Control, Atlantic City, 1972.
18. V.A. Pankratov, Sov. J. Quant. Electr., Vol. 4, No 4, 1974.
19. W.A. Stern, R. Novick, 26th Annual Symposium on Frequency Control, Atlantic City, 1972.

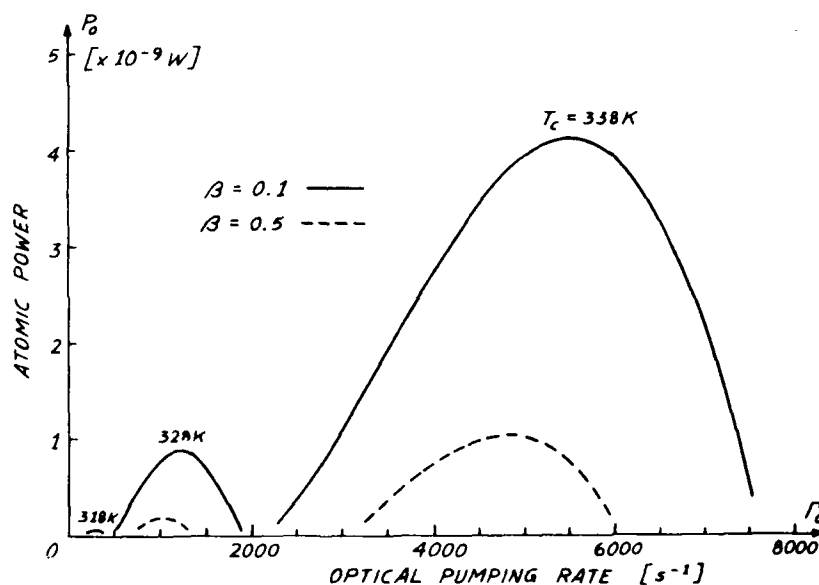


Figure 1 Variation of the Atomic Power as a Function of the Optical Pumping Rate at the Entrance of the Bulb. Computation is Done for Three Cavity Temperatures ( $T_c = 318\text{ K}$ ,  $328\text{ K}$  and  $338\text{ K}$ ) and Two Output Coupling Coefficients ( $\beta = 0.1$  and  $0.5$ )

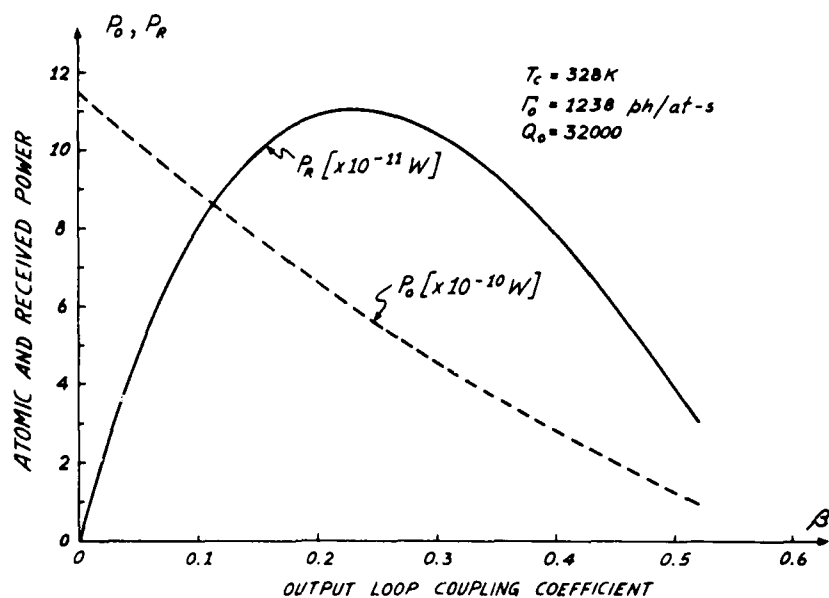


Figure 2. Variation of the Atomic Power,  $P_o$  and the Received Power,  $P_r$  As a Function of the Coupling Coefficient,  $\beta$ . The Temperature of the Cavity is Set at 328 K, the Optical Pumping Rate at the Entrance is 1238 Photons/S/Atom and the Unloaded Cavity Q is 32 000

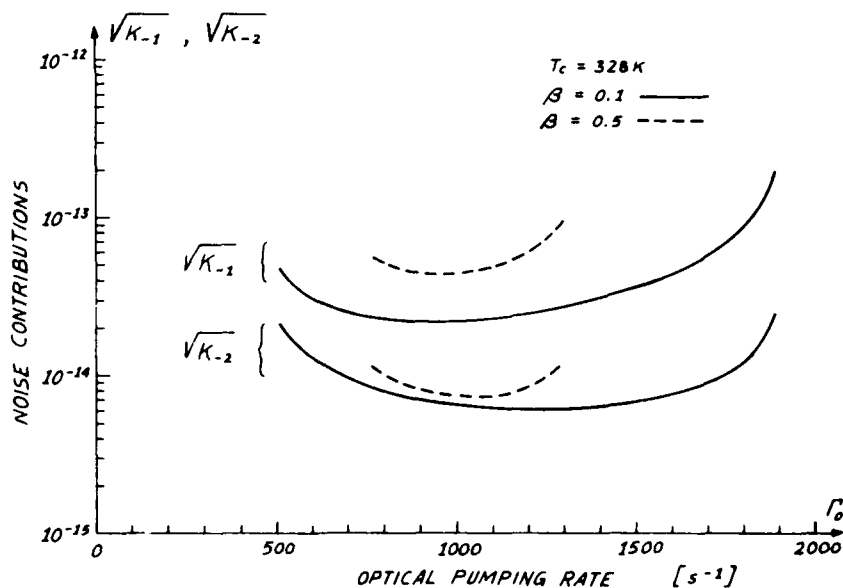


Figure 3. Variation of the White Phase Noise Contribution,  $K_2$  and the White Frequency Noise Contribution,  $K_1$  to the Frequency Instabilities as Functions of the Optical Pumping Rate at the Entrance of the Bulb for Two Coupling Coefficients (0.1 and 0.5). The Temperature of the Cavity is Set at 328 K

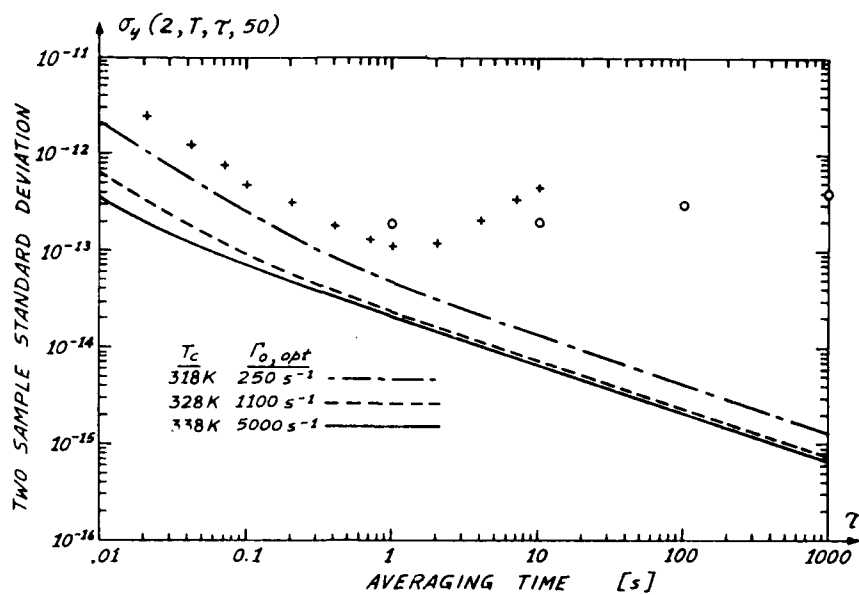


Figure 4. The Rubidium 87 Maser Oscillator Short-Term Frequency Stability as a Function of the Averaging Time,  $\tau$ , For Three Cavity Temperatures (318 K, 328 K and 338 K). For Each Temperature Setting, the Optical Pumping Rate was Fixed to a Value that Optimizes Both Noise Contributions. The Points are Typical Experimental Data, the Crosses are From Recent Measurements and the Circles are from Reference 2.

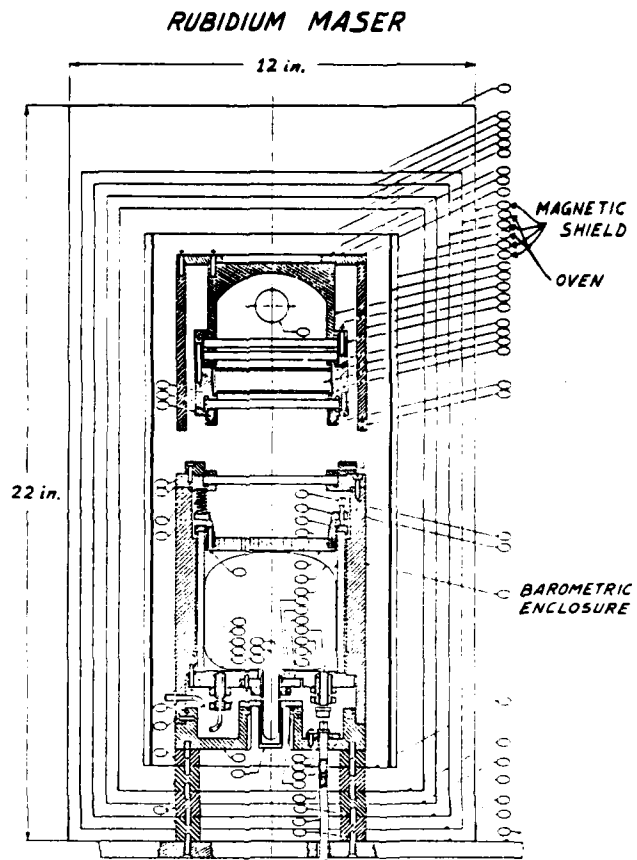


Figure 5. Layout of a Small Size Rubidium 87 Maser. The Main Features Are a Four-Layer Magnetic Shield, a Two-Oven Thermal Regulator and a Barometric Pressure Enclosure. The Unit is of the Shape of a Right Cylinder of 0.3 m O.D. and 0.56 m Long.

## ON THE LIGHT SHIFT AND BUFFER GAS SHIFT IN PASSIVE RUBIDIUM FREQUENCY STANDARDS

Folmer, R. Kunski, P. Paulin, J.Y. Savard, M. Têtu and N. Cyr

Laboratoire de Recherche sur les Oscillateurs et Systèmes  
 Département de génie électrique  
 Université Laval, Québec G1K 7P4 - Canada

Abstract

Results of calculation and measurements on the light shift and buffer gas shift in passive rubidium frequency standards are reported. The light shift was measured for two configurations: the separated filter and the integrated filter approaches. A phenomenological analysis, which describes well the results obtained, is presented. Measurements of the frequency shifts created by various buffer gases-pure or mixture- are reported. A non-linear dependence of frequency versus temperature is observed. The results are compared to already published data and a simple analysis using an equation quadratic in temperature is used to explain these results.

Introduction

In optically pumped passive rubidium frequency standards, among others, two important systematic effects take place. 1) The light shift. This effect is caused by the optical pumping itself used to invert the population of the ground state of the rubidium atom. The frequency shift produced depends on the setting of many parameters such as lamp temperature, hyperfine filter temperature, if used, and resonance cell temperature. Since the light intensity may change with time, this effect may be a cause of frequency instability. 2) The buffer gas shift. The buffer gas is required to inhibit wall relaxation and Doppler broadening. However, collisions between buffer gas and rubidium atoms cause a shift in the hyperfine frequency of the rubidium atoms.

We would like to report briefly on some recent theoretical and experimental results relative to these two topics.

Light Shift

Two approaches have been used extensively in the optical pumping of rubidium frequency standards [1,2].

a) Separated filter approach. In that case a rubidium 85 hyperfine filter is inserted between the lamp and the resonance cell. The primary function of the filter cell is to create an asymmetry in the pumping spectral lines and consequently to make the optical pumping more efficient. However,

that filter produces also a strong distortion of the spectral line profiles. The resulting effect is a frequency shift in the ground state hyperfine transition used for frequency control in the standard. The light shift is proportional to the light intensity:

$$\Delta\nu_{LS} = \alpha_1 I_0 \quad (1)$$

where  $\alpha_1$  is the light shift coefficient and  $I_0$  is the light intensity at the resonance cell. The coefficient  $\alpha_1$  is essentially a parameter which is a function of the coincidence between the pumping lines and the resonance cell lines. As a first approximation we may take it as a linear function of the filter cell temperature over the narrow range of temperature studied [3]. On the other hand, we assume that the light intensity  $I_0$ , at the resonance cell, is a decreasing linear function of the filter cell temperature. We thus write:

$$\alpha_1(t_F) = \theta_F(t_F - t_0) \quad (2)$$

$$I_0(t_F) = I_0(t_0)[1 - K_F(t_F - t_0)] \quad (3)$$

where  $t_0$  is the temperature for which the light shift,  $\Delta\nu_{LS}$ , is zero and  $K_F$  is a constant giving the fractional change in the intensity  $I_0$ , with the filter temperature. The light shift can thus be written as:

$$\Delta\nu_{LS} = (H)_{F0}[(t_F - t_0) - K_F(t_F - t_0)^2] \quad (4)$$

where

$$(H)_{F0} = \theta_F I_0(t_0) \quad (5)$$

$(H)_{F0}$  is the filter cell temperature coefficient at  $t_F = t_0$  where the light shift is zero. Figure 1 illustrates the effect for a filter cell containing 40 Torr of argon. The points are experimental while the solid line is a computer fit of equation (4) to the data. It is observed that the agreement between the theory and the experimental data is quite good and that the simple phenomenological theory outlined above explains quite well the experimental data. Similar results were obtained with filter cells containing argon at higher pressures. The results are summarized in table 1. It is observed that a reduction of the temperature coefficient is observed in filters filled with buffer gas at higher pressures.

AD P001544

b) Integrated filter approach. In that approach, the hyperfine filtering is done directly in the resonance cell. This is accomplished by using, in the resonance cell, natural rubidium which contains approximately 70% of rubidium 85. A typical result obtained with a resonance cell filled with nitrogen at a pressure of 9.5 Torr, is shown in figure 2. In that case the lamp contained a mixture of 50% rubidium 87 and 50% of natural rubidium. It is observed that there exist a light intensity for which the hyperfine frequency is essentially independent of the resonance cell temperature. These results can be explained as follows. The filtering effect that takes place in the absorption cell has associated with it a negative temperature coefficient of the same nature as the one observed in the case of the separated hyperfine filter technique. At 75 °C we expect this coefficient to be of the order of several parts in  $10^{10}$  (negative) per °C, depending on light intensity. On the other hand, the buffer gas in the resonance cell creates a temperature coefficient which, in the case of nitrogen at a pressure of 9.5 Torr, is  $+7 \times 10^{-10}$  per °C. These two coefficients are thus expected to cancel each other at least partly, and this is what is observed experimentally. However, we cannot go too far in this type of analysis because the light intensity is a function of the position in the cell. Consequently the integrated filter temperature coefficient is also a function of position and it cannot be cancelled completely by the buffer gas temperature coefficient which is homogeneous throughout the resonance cell. This appears to be the reason why, in figure 2, the lines do not cross at a single point.

#### Buffer gas shift

The buffer gases used to inhibit wall relaxation produce a frequency shift. This shift is temperature dependent. In the past, an equation, linear with temperature was used to explain the data [4,5]. We have found that an expression of the second degree in temperature was required if a better fit to the experimental data was desired. A typical result is shown in figure (3) for a cell containing nitrogen at a pressure of 40 Torr. The points are experimental while the solid line is a computer fit of the following expression to the experimental data:

$$\nu = \nu_0 + P_r(\beta_{or} + \delta_{or}\Delta T + \gamma_{or}\Delta T^2) \quad (6)$$

$P_r$  is the pressure at time of seal off;  $\Delta T$  stands for  $(t_c - t_{co})$ , where  $t_c$  is the cell temperature and  $t_{co}$  is a reference temperature normally set equal to 60 °C. The coefficients  $\beta_{or}$ ,  $\delta_{or}$  and  $\gamma_{or}$  are respectively the zero, first and second order temperature coefficients measured at temperature  $t_{co}$ . Table 2 gives the most probable values of the coefficients for the buffer gases most often used. The values were obtained by making averages of published data [5,6,7]. The quadratic effect with temperature has also been measured in the case of mixtures of buffer gases with opposite temperature coefficients. A typical result is shown in figure 4, for

a mixture of nitrogen and argon. The points are experimental while the solid line is a computer fit to the experimental data, of equation (6) applied to the mixture. It is quite clear that in such mixtures a zero temperature coefficient is possible only at a given temperature.

It is important to point out that in the case of buffer gas mixtures, systematic effects such as those introduced by the light shift described above, may become visible if great care is not taken to adjust the hyperfine filter temperature such as to make  $\alpha_1 = 0$ . Furthermore it is possible that in some cases, the residual rubidium 85 isotope, in the resonance cell has an effect on the light shift. In our sample of purified rubidium 87, the isotope 85 had a concentration of about 1%. It may then act as an integrated hyperfine filter. We have observed that our cells behave as if that effect was taking place. However, it is possible that inhomogeneous light shifts which are present at high temperatures may be responsible for the effects observed.

#### Summary and conclusions

In this article we have examined briefly two phenomena which take place in passive rubidium frequency standards: the light shift and the buffer gas shift. We have shown that regarding the light shift two approaches can be used: the separated and the integrated hyperfine filter approaches. It appears that in the integrated filter technique, both the temperature coefficient of the cell and the light shift can be made equal to zero if the proper buffer gas pressure is used. This, however, fixes the cell frequency. On the other hand more freedom relative to buffer gas mixtures and frequency setting exists in the separated filter approach. However, one is left with a strong temperature coefficient in the filter cell.

Concerning the buffer gas shift, we have shown that in the case of a mixture of buffer gases, the second order temperature coefficient cannot be neglected. Much care must be used in the filling of cells, otherwise a temperature coefficient different from the one desired may result.

#### Acknowledgment

The work reported above was sponsored by the "Natural Science and Engineering Research Council" of Canada and the "Fonds FCAC", Province de Québec.

#### References

- [1] R.J. Carpenter, E.G. Beaty, P.L. Bender, S. Saito and R.O. Stone, IRE Trans. Instrum. 1-9, 132, 1960.
- [2] H. Fruehauf and W. Weidemann, Proc. of the Twelfth Annual Precise Time and Time Interval (PTTI) Application and Planning Meeting, p. 719, December 1980.
- [3] G. Busca, M. Têtu and J. Vanier, Can. J. Phys., 51, 1379, 1973.
- [4] P.L. Bender, E.C. Beaty and A.R. Chi, Phys. Rev., Letters 1, 311, 1958.

- [5] G. Missout and J. Vanier, IEEE Trans. on Instr. and Meas., 24, 180, 1975.
- [6] B.L. Bean and R.H. Lambert, Phys. Rev., A-13, 492, (1976).
- [7] W.J. Riley and H. Stratemeyer (private communication).

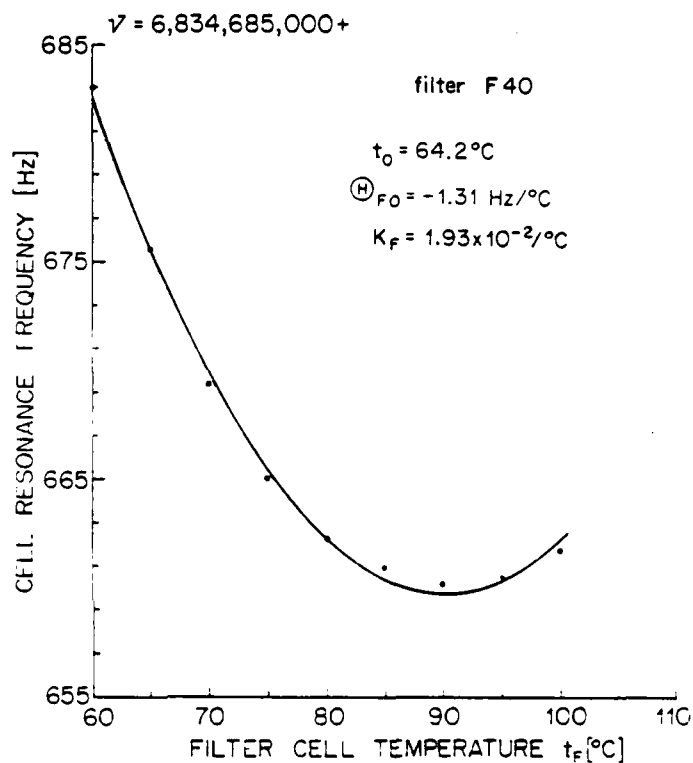


Figure 1. Variation of the Rubidium Resonance Frequency  $\nu_r$  As a Function of the Filter Cell Temperature  $t_F$ . The Points are Experimental While the Solid Line is a Computer Fit of Equation (4) to the Experimental Data.

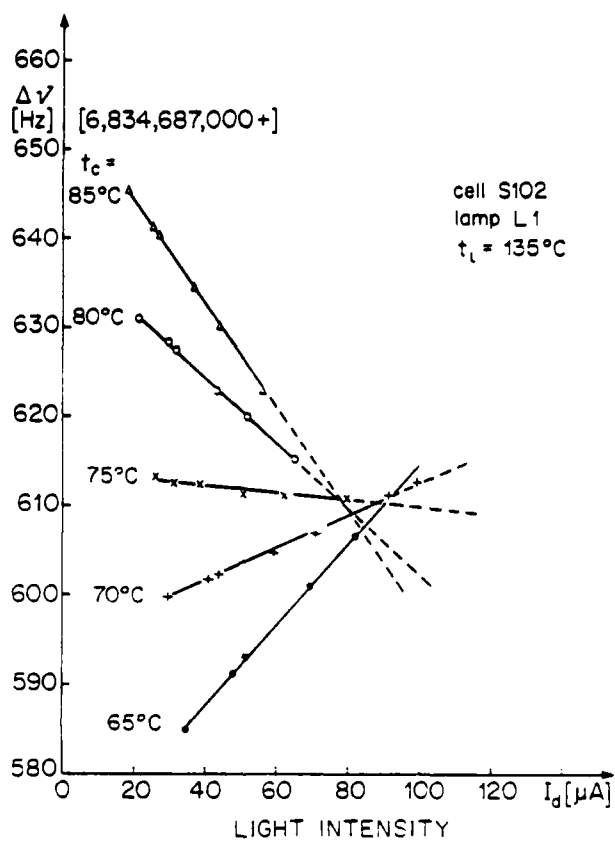


Figure 2. Integrated Filter Approach. Variation of the Rubidium Resonance Frequency with the Light Intensity. The Absorption Cell Temperature  $t_c$  is the Parameter.

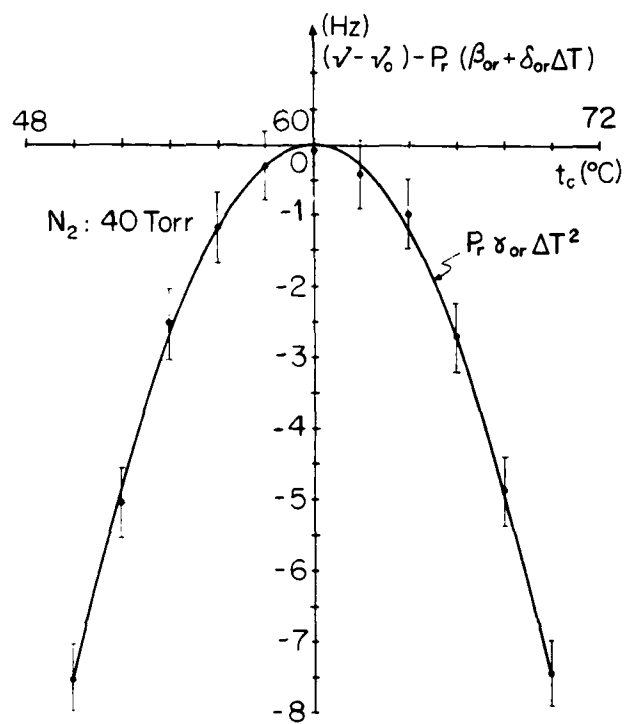


Figure 3. Variation of the Frequency of a Rubidium Cell Containing Nitrogen at a Pressure of 40 Torr. The Constant and Linear Terms have been Subtracted from the Data. The Points are Experimental While the Solid Line is a Computer Fit of Equation (6) to the Data.

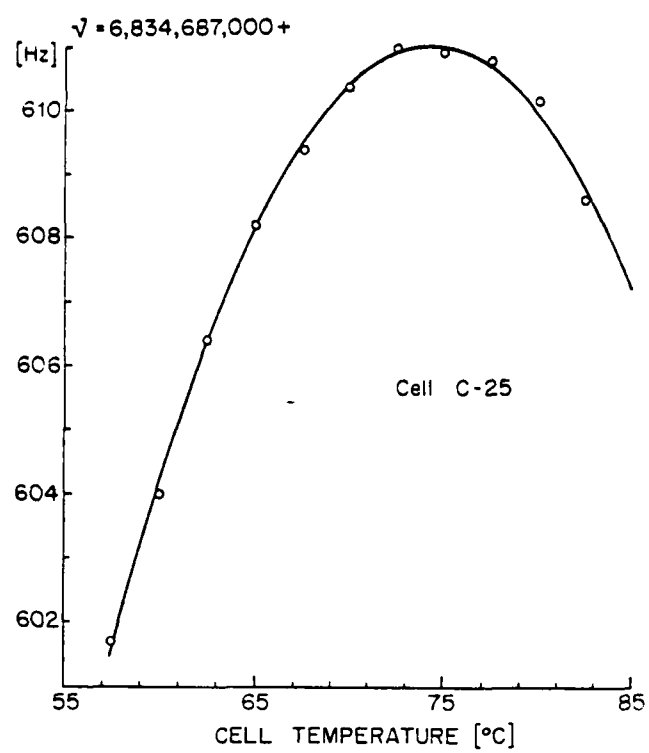


Figure 4. Resonance Frequency of a Cell, Containing a Mixture of Nitrogen and Argon, as a Function of Temperature.

Table 1  
Characteristics of the Three Separated Hyperfine Filters  
Used as Determined by Means of a Computer Fit to the  
Experimental Data. In this Table,  $T_m$  is the Temperature  
at Which the Minimum of the Curves Appears. Argon and  
Rubidium 85 were used in the Hyperfine Filter Cells.

	P [torr]	$t_o$ [°C]	$\textcircled{H}_{FO}$ [Hz/°C]	$K_F$ [°C] <sup>-1</sup>	$t_m$ [°C]
F-40	40	64.2	- 1.31	1.93 $10^{-2}$	90.1
F-80	79.5	67.0	- 1.27	2.1 $10^{-2}$	90.8
F-120	123.6	70.8	- 1.08	2.4 $10^{-2}$	91.6

Table 2  
Average Value of the Buffer Gas Coefficients  
Reported in the Literature, Including Measurements  
Made During the Cause of the Present Study.

	$\beta_{os}$ [Hz/torr] $T_o = 333$ K	$\delta_{os}$ [Hz/°C/torr]	$\gamma_{os}$ [Hz/°C <sup>2</sup> /torr]
Argon	- 59.7	- 0.32	- 0.00035
Krypton	- 593.5	- 0.57	
Nitrogen	547.9	0.52	- 0.0013

L

## SPECTRAL CHARACTERISTICS OF SINGLE MODE GaAlAs SEMICONDUCTOR LASERS

R. O. Miles

U.S. Naval Research Laboratory

Summary

Single mode semiconductor lasers are available with free-running noise characteristics comparable to single mode gas lasers but demonstrate a  $(1/f)^{1/2}$  dependence. The free running laser diode emission is spread over several MHz with significant frequency instability. Small amounts of feedback on the order of  $10^{-7}$  to  $10^{-5}$  enhance laser emission as the line is observed to narrow to approximately 100 kHz accompanied with a substantial increase in frequency stability. Greater amounts of feedback causes rapid deterioration of the emission characteristics.

We have investigated single mode GaAlAs semiconductor lasers emitting at 830 nm for use as possible sources in fiber optic sensor systems. These lasers have been characterized in terms of spectral quality, intensity noise and frequency stability. A list of the various lasers including laser structure and special features is shown in Table I.

Table I Lasers tested including laser structure and special features.

Laser	Type	Special Features
1. General Optonics TB47	PBBH	Tellurium Mask, Low Spontaneous Emission, Current Confinement Window, Index Guided
2. Laser Diode SCW 21	GSP	Gaussian Profile Gain and Index Guided
3. MITSUBISHI ML 4307	TJS	Strong Lateral Index Guided Weak Gain Confinement
4. HITACHI HLP 1400	CSP	Gain and Index Guided
5. HITACHI HIP 2400U	BH	Index Guided Low Threshold
6. HITACHI HIP 3400	BH	Index Guided Higher Current Density Capability

While each laser is limited to a single longitudinal mode each type of laser structure has unique spectral characteristics. These lasers can be separated into two broad categories. Those in which the light beam is guided strictly by the

waveguide refractive index, called index guided lasers, and those in which the light beam is formed by the distribution of the gain in the active medium. All of the above lasers, except the Buried Heterostructures (BH), fall into the latter category. The channel substrate planar (CSP), the gaussian substrate planar (GSP), the transverse junction-stripe (TJS), and the proton bombarded buried stripe (PBBS) all use index guiding transverse to the plane of the junction to eliminate all but the fundamental transverse mode and allow the pumping medium, such as electron flow, to determine the lateral beam dimensions. This kind of design allows higher output power with less waveguide material damage. The primary difference between these two categories of lasers, as far as will be discussed in this paper, is the emission characteristics in the presence of optical feedback. In general, however, in the free running mode (no optical feedback) all of these lasers show similar characteristics in emission linewidth, intensity noise, and frequency stability.

The intensity stability of the lasers was measured by radiating a photodiode with the laser. The noise voltage developed across the load resistor  $R$  of the photodetector (running photoconductively) by the current is given by

$$dV = dI' R \sqrt{B} \quad (1)$$

where  $I'$  is an rms broadband noise source normalized to a 1 Hz bandwidth. Since the photodetector is a square-law device, the voltage is proportional to the intensity or square of the light amplitude

$$V = I = |A|^2 \quad (2)$$

If this is treated as an optical power, the noise or intensity stability may be written in dB as:<sup>2</sup>

$$\frac{dV}{V} \text{ (dB)} = 10 \log \left( \frac{dV}{V} \right) \quad (3)$$

All of the work reported here, unless otherwise stated, was done with a 10 k $\Omega$  load and normalized to a 1 Hz bandwidth.

Shown in Fig. 1 is a plot of the intensity stability of several types of semiconductor lasers

AD P001545

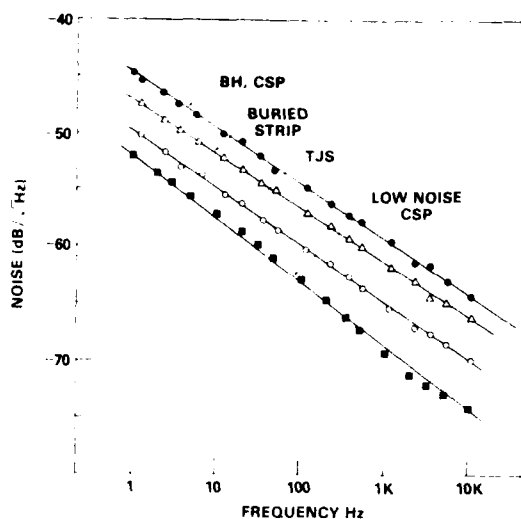


Fig. 1 Free running diode laser intensity noise in terms of optical power as a function of frequency.

Characteristic of all semiconductor intensity noise is the quasi  $(1/f)^{1/2}$  frequency dependence<sup>3,4</sup> in the low frequency regimes ( $f < 1$  MHz). The laser exhibiting the lowest intensity noise is a CSP device specially developed by Hitachi for low noise operation. When compared to the data for earlier CSP devices in the top trace, the progress in development of these devices can be seen.

Figure 2 is a plot of the laser intensity noise as a function of forward driving current.

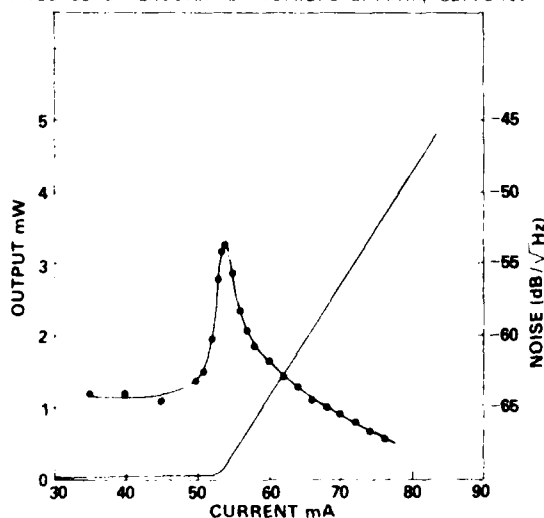


Fig. 2 Laser output characteristics as a function of forward driving current, showing intensity noise.

Shown as a solid line is the light output characteristics of the laser clearly demonstrating the laser threshold.<sup>5</sup> Figure 2 shows data taken for the low noise CSP laser demonstrating the decrease of intensity noise with forward driving current above threshold.

The emission linewidth of the lasers varied widely, but all was on the order of 10 to 100 MHz.<sup>6</sup> The frequency stability of these devices was measured by means of an unbalanced Michelson interferometer. Frequency jitter in the laser source is observed as an amplitude noise at the output of an unbalanced Michelson interferometer. Data showing the frequency fluctuations in a typical CSP laser is shown in Fig. 3, where the frequency fluctuations were observed with a 2 cm optical pathlength difference. All measurements are normalized to a 1 Hz bandwidth.

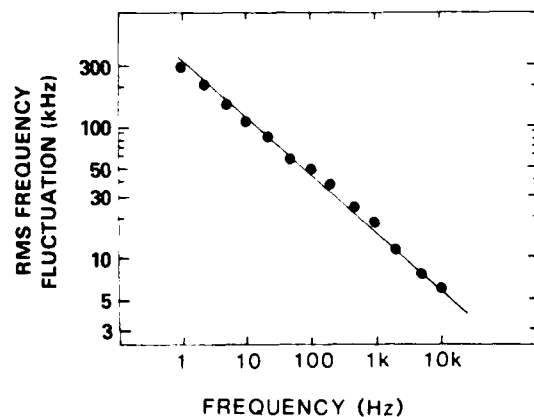


Fig. 3 Frequency fluctuations for a CSP laser as a function of frequency with a 1 Hz bandwidth. Measurements made with an unbalanced Michelson interferometer with a 2 cm optical path difference.

While the data shown in Fig. 3 represents only one laser, all lasers exhibited similar characteristics.<sup>7</sup> For the six lasers tested at 2 kHz, the frequency fluctuations were between 9-20 kHz. Interestingly, while both the intensity noise and frequency fluctuations all exhibit a  $(1/f)^{1/2}$  frequency dependence, the two noise sources are only partially correlated.<sup>8,9</sup> Figure 4 shows the dependence of phase noise on the forward driving current. This data shows that with increased driving current frequency fluctuations tend to remain constant. The significance of this characteristic will be discussed later in conjunction with emission linewidth narrowing.

Optical feedback from external reflectors induce changes in the spectral emission characteristics of the laser. Feedback on the order of  $10^{-7}$  to  $10^{-4}$  in some diode lasers has been observed

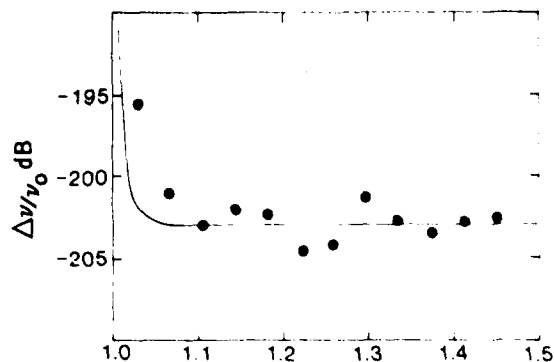


Fig. 4 Dependence of the relative frequency fluctuations with forward driving current.

to cause a reduction in emission linewidth on the order of  $10^3$  Hz.<sup>10,11</sup> In the emission linewidth data presented in Fig. 5, several CSP lasers and a BH laser were measured as a function of optical feedback into the laser cavity. A detailed description of the experiment can be found in Ref. 10. A 60 cm external cavity was used to

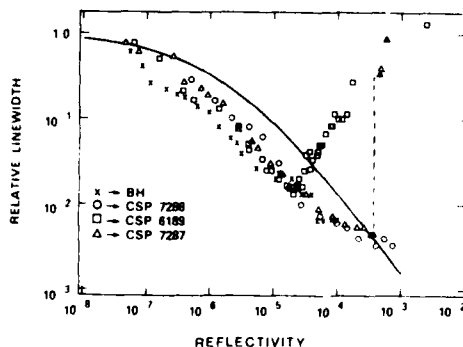


Fig. 5 Optical feedback induced line narrowing using a 60 cm external cavity.

provide feedback. The emission linewidth was measured using a delayed self-heterodyne technique,<sup>11</sup>

with a time delay of 4  $\mu$ sec corresponding to a frequency resolution of approximately 100 kHz. The direct optical signal was divided by a 3 dB beam splitter with one arm frequency shifted by means of an acousto-optic modulator operating at 90 MHz. The two beams were fed into a single mode fiber with the frequency shifted light traveling in a short piece of fiber while the other arm provided a 4  $\mu$ sec delay. When the output of these two fibers were recombined at the avalanche photodetector a frequency resolution of about 100 kHz was possible. Measured data shown in Fig. 5 are normalized to the free running (no feedback) laser linewidth. In all cases, the feedback phase angle was adjusted to obtain a minimum linewidth. Linewidth was found to vary with both amplitude and phase of the feedback. The line-width reduction assuming maximum phase coupling, can be calculated by using a model developed in Goldberg et al.<sup>10</sup> where the full width half max linewidth is given by

$$\Delta\nu_{1/2} = \frac{\Delta\nu_0}{(1+\gamma)^2} \quad (4)$$

and

$$\gamma = \frac{(1-R_1) \cdot \Gamma L}{R_1 n \lambda}$$

where  $\lambda_0$  is the free running linewidth, and  $R_1$  the laser facet reflectance,  $r$  is the external reflectance, and  $L$  the external cavity length with  $\lambda$  the diode laser cavity length. The solid line in Fig. 5 is the calculated linewidth using eqs. 4 and 5.

Accompanying the reduction in linewidth for feedback in this region is an increase in frequency stability. Figure 6 shows data taken for two different laser structures, CSP and BH, respectively. The frequency instability (exhibited as an amplitude fluctuation in an interferometer) was measured using a Fabry-Perot interferometer (FPI)

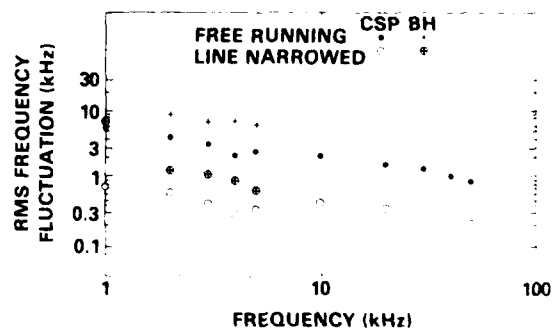


Fig. 6 Optical feedback reduction of frequency fluctuations.

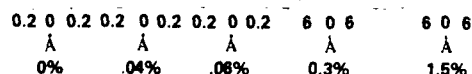
in a non-scanning mode. The FPI mirror separation was controlled piezoelectrically and held at about 0.70 of the resonance peak. In this configuration, wavelength fluctuations of the laser source are observed as relatively large fluctuations in the FPI transmission intensity. In Fig. 6, the upper curve for each laser was taken with no feedback while the lower trace was taken with a feedback of  $4 \times 10^{-5}$ . The FPI free spectral range is 8.8 GHz with a finesse of 50. A reduction by a factor of approximately 10 was seen for each laser.

Although linewidth has been observed to decrease with forward drive current in external cavity diode lasers,<sup>12</sup> frequency stability does not seem to improve as was seen in the data presented in Fig. 4.

As feedback is increased beyond  $10^{-4}$  linewidth is observed to increase in nearly all lasers.<sup>6</sup> Accompanying this is a rapid deterioration of the spectral characteristics including an increase in intensity noise as the light fed back from the external cavity causes the laser to switch longitudinal modes.<sup>9</sup> This kind of performance was observed to be quite pronounced for gain guided lasers as small increases in feedback caused self pulsation to occur. The self pulsation creates satellite modes spaced on the order of 3 to 5 GHz from the fundamental as seen in Fig. 7 for a CSP laser. As the amount of feedback is increased the amplitude of the satellite modes grow and higher order harmonics begin to appear. The frequency spacing of these modes are observed to be current dependent, but vary between 2 to 5 GHz. For feedback greater than  $10^{-3}$  the laser goes multimode and the linewidth quickly broadens from the free running linewidth of a few MHz to over 10 GHz.<sup>6</sup> The data presented in the lower portion of Fig. 7 shows the maximum obtainable intensity fluctuations in dB as a function of feedback. Each data point represents the maximum noise obtainable by varying the phase and holding the amount of feedback constant. Both the minimum and maximum obtainable noise is plotted. This data indicates that as the spectral qualities of the laser deteriorates, with a substantially broadened emission line, and with more output spread into higher order longitudinal modes, interaction between the laser output and the light fed back decreases and the maximum amount of noise obtainable begins to decrease. However, the minimum noise increases to a point where the two become equal and decrease together to the value of the free running laser (no feedback case) as the feedback increases beyond  $10^{-1}$ .

A second method for reducing frequency fluctuations makes use of a current feedback scheme.<sup>13</sup> Using this method, a reduction in frequency fluctuations by three orders of magnitude has been achieved at low frequencies ( $< 5$  Hz) and by a factor of 30 at 250 Hz. A schematic diagram of the experiment is shown in Fig. 8. Light output from the laser is collimated and split two beams. One beam is directly monitored by a large area photodiode and analyzed by a spectrum analyzer which is used to determine the amplitude noise. The other beam passes through a Fabry-Perot interferometer.

## (a) SPECTRAL PROPERTIES



## (b) FEEDBACK INDUCED NOISE

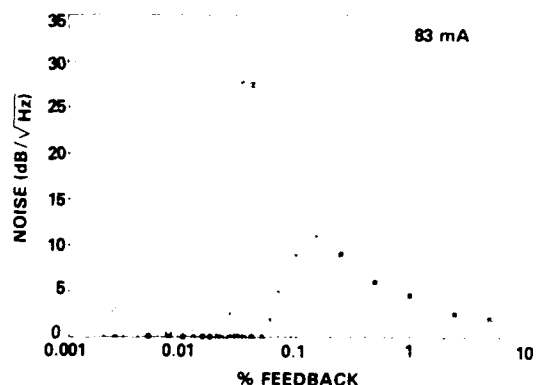
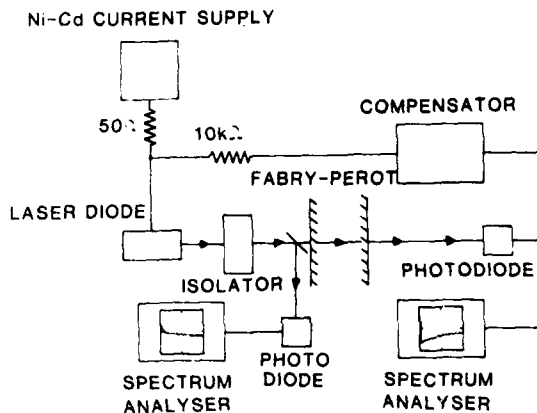
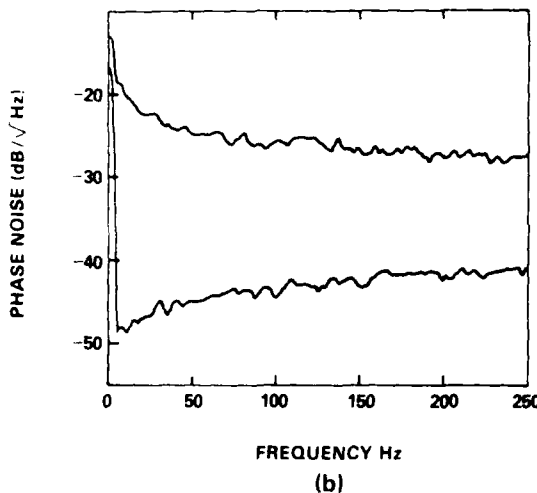


Fig. 7 Optical feedback induced effects on spectral properties of CSP laser for feedback greater than  $10^{-4}$ .

In this experiment the Fabry-Perot had a free spectral range of 7.5 GHz and a finesse of 55. A small area photodiode was used to detect this output. This output was also monitored with a spectrum analyzer which is used to monitor the phase noise. The output of this photodiode was also directed into a current feedback compensator, which in turn perturbs the current supply with a correction voltage. The circuit works such that when the voltage output of the photodiode corresponds to the maximum slope of the Fabry-Perot response, the error signal applied to the laser current supply is zero. However, when the laser shifts frequency, the voltage change on the output detector of the Fabry-Perot creates a voltage which is applied to the laser current supply as a correcting perturbation proportional to the frequency shift. The reduction in frequency fluctuation noise is shown in Fig. 8b. The free running laser frequency noise is shown in the upper trace. It should be noted that this noise contribution is 2.5 orders of magnitude greater than the intensity fluctuations of the free



(a)



(b)

Fig. 8 Electronic suppression of frequency fluctuations.

running laser. The lower trace shows the reduction in frequency fluctuation when the compensating circuitry is switched on.

In summary, the free running lasers that are reported here have shown intensity fluctuation on the order of -60 dB at 10 kHz, and for some low noise devices on the order of -70 dB at 10 kHz. Emission linewidths are typically between 1 and 100 MHz and varies from laser to laser. These lasers show frequency instabilities on the order of 10 kHz/√Hz. It has been shown that these characteristics can be altered significantly by small amounts of feedback. Feedback from large external cavities on the order of  $10^{-8}$  to  $10^{-11}$

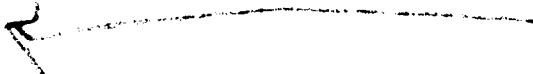
have caused the emission linewidth to narrow by a factor of  $10^{-3}$  to on the order of 100 kHz. This spectral narrowing is accompanied by a reduction in frequency fluctuations by a factor of 10. For greater amounts of feedback, self pulsations can be initiated in gain guided devices, causing side bands to appear in the emission characteristics. The side bands are spaced in frequency 1 to 5 GHz from the fundamental and this frequency spacing is seen to be dependent upon forward driving current values. With this amount of feedback, the laser has been observed to have increased modal noise as well as eventual multi longitudinal mode emission. A method of reducing frequency fluctuations on the order of 2.5 orders of magnitude at low frequencies ( $f < .5$  kHz), was described and the results shown for low frequencies.

#### Acknowledgements

I would like to acknowledge that this work is the contribution of several colleagues which have been referenced throughout the paper, some of whom are Anthony Dandridge, Allan B. Tveten, Lewis Goldberg, Joseph F. Weller, Thomas G. Giallorenzi and Henry F. Taylor.

#### References

1. T.G. Giallorenzi, J.A. Bucaro, A. Dandridge, G.H. Siegel, J.H. Cole, S.C. Rashleigh, and R.G. Priest, "Optical Fiber Technology" - IEEE, JOE; QE-18, 4, pp. 626-664 April (1982).
  2. It should be noted that in all papers referenced from the sensor community the noise measurements are regarded simply as an ac voltage referenced to a normalized 1 volt dc output, therefore Eq. 3 is written:
- $$\frac{dV}{V} \text{ (in dBV)} = 20 \log \left( \frac{dV}{V} \right) \quad (R1)$$
3. When the intensity noise is calculated as a noise voltage from Eq. R1 the intensity noise is observed to have a  $1/f$  dependence.
  4. A. Dandridge, A.B. Tveten, R.O. Miles, and T.G. Giallorenzi, "Laser Noise in Fiber Optic Interferometer Systems" - Appl. Phys. Lett., 37(6), 15 Sept. 1980, pp. 526-528.
  5. R.O. Miles, A. Dandridge, A.B. Tveten, T.G. Giallorenzi, and H.F. Taylor, "Low Frequency Noise Characteristics of Channel Substrate Planar GaAlAs Laser Diodes" - Appl. Phys. Lett. 38(11), 1 June 1981, p. 840.
  6. R.O. Miles, A. Dandridge, A.B. Tveten, H.F. Taylor, and T.G. Giallorenzi, "Feedback-Induced Line Broadening in CW Channel Substrate Planar Laser Diodes" - Appl. Phys. Lett. 37(11), 1 Dec. 1980, pp. 990-992.
  7. A. Dandridge and A. B. Tveten, "Phase Noise of Single-Mode Diode Lasers in Interferometer Systems" - Appl. Phys. Lett. 39(7), 1 Oct. 1981, pp. 530-531.

8. A. Dandridge and H.F. Taylor, "Correlation of Intensity and Frequency Fluctuations in GaAlAs Lasers" - 12th International Quantum Electronics Conference, 1982, Munich, Germany, Paper WE9.
  9. A. Dandridge and H.F. Taylor, "Correlation of Low-Frequency Intensity and Frequency Fluctuations in GaAlAs Lasers" - to be published IEEE JQE, Sept. 1982.
  10. L. Goldberg, H.F. Taylor, A. Dandridge, J.F. Weller, and R.O. Miles, "Spectral Characteristics of Semi-Conductor Lasers with Optical Feedback" - IEEE JQE, QE-18 (4), April 1982, pp. 555-567.
  11. S. Saito and Y. Yamamoto, "Direct Observations of Lorentzian Lineshape of Semiconductor Laser and Linewidth Reduction with External Grating Feedback" - Electron Lett., Vol. 17, pp. 325-327, April 1981.
  12. A. Mooradian and D. Welford, "Frequency Stability and Control Characteristics of (GaAlO as Semiconductor Lasers" - 36th Annual Symposium on Frequency Control, Philadelphia, June 1982.
  13. A. Dandridge, A.B. Tveten, "Electronic Phase Noise Suppression in Diode Lasers" - Electron. Lett., Vol. 17 (25) 10 Dec 1981, pp. 937-938.
- 

## ULTRA-STABLE LASER CLOCK

Lieutenant Roger Facklam  
AFWAL/AAAN-1  
Wright-Patterson AFB, Ohio

Summary

The Air Force has requirements for both high accuracy timing sources and precision inertial navigation systems for advanced fighter aircraft. The author has devised a method of using a multi-frequency ring laser gyro (RLG) simultaneously as a gyro and as a clock. This device uses a multi-frequency RLG with an auxiliary detector to sense a 583 MHz beat frequency, and necessary electronics to produce a 5 MHz clock signal.

Testing was accomplished on two RLGs. The first RLG was not operational as a gyro at low rotation rates. The stability data was good between 1 msec and 200 msec, but started to degrade at longer integration times. The second RLG tested was an operational gyro, although not tested as such in the experiment. The frequency stability data was  $4.6 \times 10^{-10}$  for 1 msec,  $3.4 \times 10^{-10}$  for 10 msec,  $8.706 \times 10^{-11}$  for 0.1 sec,  $1.6 \times 10^{-10}$  for 1 sec,  $4.5 \times 10^{-10}$  for 10 sec, and  $4.8 \times 10^{-9}$  for 100 sec. The data is quantum limited from 1 msec to 200 msec. The long-term degradation was apparently caused by temperature drift in the Faraday rotator. A method of compensation to improve accuracy is suggested.

The RLG clock is a transfer frequency standard which must be set to a reference before use. Setting could be accomplished by using the Global Positioning System (GPS), the Joint Tactical Information Distribution System (JTIDS), radar techniques, or physically connecting a time standard to the RLG clock.

**Key words.** Helium-Neon, Laser, Ring Laser, Clock, Frequency standard, Transfer Frequency standard.

Introduction

The objective of this paper is to demonstrate the feasibility of using a multi-frequency ring laser to simultaneously provide gyro and clock outputs. The clock output is a 583 MHz beat frequency between two optical modes of the laser. The output can also be counted down to near 5 MHz. Some application of precision timing sources are bi-static radar, secure/anti-jam communication, and aircraft identification systems. Precision navigation is needed to support fighter aircraft missions.

TheoryBackground

Clock accuracy is characterized by the standard deviation of the frequency fluctuations and may be written as

$$\sigma_y(\tau) = \sqrt{\frac{\sum_{k=1}^m (\bar{y}_{k+1} - \bar{y}_k)^2}{2m}} \quad (1a)$$

where 
$$\bar{y}_k = \frac{1}{\tau} \int_{t_k}^{t_k + \tau} \frac{f(t)}{2\nu_0} dt \quad (1b)$$

and  $\nu_0$  is the nominal frequency,  $m$  is the number of measurements,  $\tau$  is the integration time,  $f$  is time rate of change of the instantaneous phase fluctuations and  $\sigma_y^2(\tau)$  is the Allan variance.

The multi-frequency RLG produces four laser frequencies. The cavity, shown in Figure 1, which is non-planar, allows only circularly polarized light. The cavity also produced a frequency difference between the right and left hand circularly polarized (RHCP & LHCP) modes. The average beat frequency between RHCP and LHCP is given by

$$\bar{\nu}_{\text{beat}} = \frac{c}{2\bar{n}l} \quad (2)$$

where  $c$  is the speed of light in a vacuum and  $\bar{n}l$  is the average optical path length.

Figure 2 shows the gain curve for RLG #18. Here  $\nu_1$  is the frequency of the clockwise LHCP mode,  $\nu_2$  is the frequency of the counterclockwise LHCP mode,  $\nu_3$  is the frequency of the counterclockwise RHCP mode, and  $\nu_4$  is the frequency of the clockwise RHCP mode. This configuration does not work as a gyro because the clockwise (CW) and counterclockwise (CCW) frequencies are the same frequency. This is because of the frequency lock-in phenomenon at low rotation rates.

Figure 3 shows the gain curve for RLG #68. This configuration contains a Faraday rotator, which is a non-reciprocal optical device that uses the Faraday effect to split the CW mode from the CCW mode.

### Gyro Operation

RLG #68 operates as a gyro and the output is obtained by optically beating the LHCP modes and the RHCP modes. The difference between two beat frequencies is shown in Figure 4. The gyro output is given by

$$\text{gyro} = (\nu_4 - \nu_3) - (\nu_2 - \nu_1) = \Omega S \quad (3)$$

where  $\Omega$  is the angular input rate and  $S^{-1}$  is the scale factor of the gyro.

### Clock Only Operation

Laser #18 produces a clock frequency  $\nu_{\text{clock}}$  given by

$$\nu_{\text{clock}} = \nu_4 - \nu_1 \quad (\text{CW}) \quad (4a)$$

$$= \nu_3 - \nu_2 \quad (\text{CCW}) \quad (4b)$$

where the CW beat is the same as the CCW beat.

### Clock/Gyro Operation

Laser #68 produces a clock frequency  $\nu_{\text{clock}}$  given by

$$\nu_{\text{clock}} (\text{CW}) = \nu_4 - \nu_1 \quad (5a)$$

$$\nu_{\text{clock}} (\text{CCW}) = \nu_3 - \nu_2 \quad (5b)$$

where the  $\nu_{\text{clock}}$  (CW) is about 800 KHz higher than  $\nu_{\text{clock}}$  (CCW). The clock processing electronics is shown in Figure 5. The two optical frequencies are focused on an avalanche photo diode. The signal is amplified and filtered. The output can then be taken directly or counted down by 120. The output was tested in both configurations.

### Recommended Clock/Gyro Operation

The clock frequency drift is due to temperature effects in the Faraday rotator. The Faraday frequency drift  $\Delta \nu_F$  is given by

$$\frac{\Delta \nu_F}{\nu_F} = \frac{\Delta T}{T} = (\alpha_i + \alpha_e (n-1)) \Delta T \quad (6)$$

where  $\nu_F$  is the Faraday frequency,  $\Delta T$  is the change in temperature,  $T$  is the temperature,  $\alpha_i$  is the temperature coefficient of the index of refraction and  $\alpha_e$  is the coefficient of expansion ( $K^{-1}$ ) of the Faraday rotator. The Faraday rotator temperature sensitivity has to be corrected. This is accomplished by use of dual detectors as shown in Figure 6.

The Faraday stabilized clock frequency is given by

$$\text{clock} = (\nu_4 - \nu_1) + (\nu_3 - \nu_2) \quad (7)$$

So when the Faraday effect increases,  $(\nu_4 - \nu_1)$  is increased by the same amount that  $(\nu_3 - \nu_2)$  decreases,

thus holding a constant sum. This should allow the clock to reach the quantum limit at longer times. The quantum limited laser linewidth  $\Delta \nu_Q$  is given by

$$\Delta \nu_Q(\tau) = \frac{\nu_0}{Q} \sqrt{\frac{h\nu_0}{2P\tau}} \quad (8a)$$

where

$$Q = \frac{\nu_0 E}{2 - P} \quad (8b)$$

and  $\nu_0$  is the laser frequency,  $h$  is Planck's constant,  $P$  is the circulating power,  $\tau_4$  is the measuring time, and  $E$  is the stored energy. The quantum limit for the clock, the ratio of the quantum limited linewidth to the clock frequency, is then given as

$$\text{QUANTUM LIMIT}(\tau) = \left( \frac{\nu_0}{Q\nu_{\text{clock}}} \sqrt{\frac{h\nu_0}{2P}} \right) \sqrt{\frac{1}{\tau}} \quad (9)$$

For the device to work over the temperature range, a path length control (PLC) algorithm might be necessary. However, this need has not yet been shown.

### Experiment

The original plans were to test a dual detector system on an operating gyro as shown in Figure 6. This approach would avoid errors due to the Faraday rotator sensitivity. However, this approach proved to be too costly, so an approach using a gyro without a Faraday rotator was considered. Laser #18 was available without a Faraday rotator and, although it would not work as a gyro for low rotation rate, a design was developed to provide a clock output as shown in Figure 5. This approach minimized the electronics to be developed and the associated cost.

The experimental setup shown in Figure 7 was used. The basic frequency measurement system used the Hewlett Packard 5390A. The laser clock output was fed to the mixer (HP 10830A), as was the HP 8660C frequency synthesizer output. The reference for the HP 8660C and the HP 5345A counter was the Loran C Cesium based system. The output of the mixer was fed into the counter which was controlled by the HP 9825B calculator. The calculator outputs were produced using the HP 9871 printer/plotter.

Data from the test of Laser #18 is shown in Figure 8. This shows improved performance as the experiment proceeded. This was due to efforts that reduced noise, which were affecting the ring laser. The best short-term data was good for 1 msec, 10 msec, and 100 msec. However, the longer-term data showed increased instability. After using a Fabry-Perot analyzer to observe the modes, it was discovered that the PLC was drifting, thus causing the problem in the long-term stability data. Laser #18 PLC was an older experimental design with too small a bandwidth. The PLC drift was the reason that additional testing was done using a

state-of-the-art operational ring laser gyro #68. Laser #68 had a Faraday rotator which could not be temperature compensated since another set of electronics was not available to implement the approach in Figure 6. It was believed that even though Laser #68 was temperature sensitive, laser temperature drift could be minimized using a temperature controlled oven and better clock data obtained.

The test clock data for Laser #68 is shown in Figures 9 and 10. Figure 9 shows the data sets containing the best data points for 1 msec, 10 msec, and 100 msec. Figure 10 shows the data sets containing the best data points for 1 sec, 10 sec, and 100 sec. The data for the times from 1 to 100 msec is quantum limited. The Faraday drift starts affecting the data at 0.1 sec and the value of  $\sigma_y(t)$  increased. Figure 11 shows a comparison of the frequency stability of an HP 10811 quartz oscillator (Q), an HP 5065A rubidium atomic clock (R), and an HP 5062C cesium atomic clock (C). The best laser clock data falls between data for the cesium and rubidium standards from 1 msec to .3 sec. The Faraday drift then starts to decrease the laser clock stability. The long-term drift shown in Figure 12 is 30.5 mHz/sec. Figure 12 shows that the narrowest linewidth measured is 50 mHz. There was also a higher frequency fluctuation in the temperature shown in Figure 13. The short-term data was affected by the Faraday rotator but by picking the best data, this effect was minimized. The long-term data always has the Faraday induced drift present; that is to say, even the best data shows the drift. The single error bar in Figure 12 shows a factor of two deviations.

#### Conclusions

In conclusion, good short-term stability has been obtained, but long-term stability needs to be improved. The device is a transfer frequency standard. A transfer frequency standard used with GPS, JTIDS, and radar techniques will meet high performance fighter application requirements so that an absolute frequency standard is not required. If implemented in conjunction with existing RLG systems, the additional cost of the clock function would be one to three thousand dollars depending upon the level of integration. This could also help reduce life cycle cost compared to having a separate clock and gyro. Careful packaging could also yield a reduced volume when compared to separate devices.

#### Recommendations

The Faraday rotator temperature sensitivity must be corrected. The method outlined in the theory section of this paper would eliminate the drift. The estimated quantum limited performance window of the laser clock is shown in Figure 14.

#### Acknowledgments

The experimental part of this effort could not have been completed without the help of the Raytheon Company. The experiment was conducted at their plant in Sudbury, Massachusetts. I wish to

thank Jim Matthews, Al Zampello, Bill Nelson, Iri Smith, Terry Dorschner, Ed Perdue, Bob Gauthier, Dennis Day, and the Raytheon staff.

At RADC/ESE, Hanscom AFB, I wish to thank Nick Yannoni and Ferdinand Euler for background material on clocks and timing.

At Wright-Patterson AFB (AFWAL/AAAN) I wish to thank Ron Ringo, Reference Systems Branch Chief, for supporting my effort; Bob Witters, Reference Systems Technology Group Leader, for his continuing support; and Jerry Covert for many discussions on clock applications and listening to laser physics discussions.

At the AF Institute of Technology, I wish to thank Dr Leno Pedrotti, Head of the Physics Department AFIT, for his discussions on laser physics and academic support; Major M. R. Stamm and Dr W. B. Roh for serving on the thesis committee.

Finally, I wish to thank Colonel Hugo Weichel for chairing the thesis committee and providing technical support.

The work described was performed in partial fulfillment for a Master of Science degree in Engineering Physics, AF Institute of Technology. The thesis should be available through DTIC later in 1982.

#### Bibliography

1. Barnes, et al "Characterization of Frequency Stability," IEEE Transactions on Instrumentation and Measurements, IM-20 (2) : 105-120 (May 71).
2. Smith, I. W. and T. A. Dorschner, "Electromagnetic Wave Ring Resonator," U.S. Patent #4,110,045, 29 Aug 78.
3. Smith, I. W. and T. A. Dorschner, "Biasing the Raytheon Four-Frequency Ring Laser Gyroscope," SPIE, 157 : 21-29 (1978).
4. Dorschner, T. A., et al, "Laser Gyro at Quantum Limit," IEEE Journal of Quantum Electronics, 16 (12) : 1376 - 1379 (Dec 80).

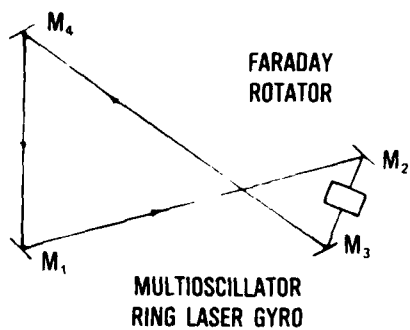


Figure 1. Multioscillator Ring Laser Gyro

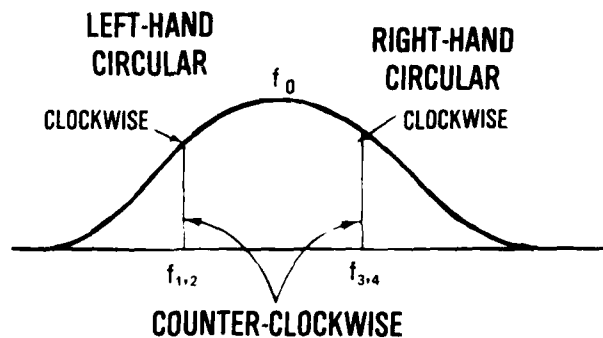


Figure 2. Four Modes on Gain Curve (No Faraday Rotator)

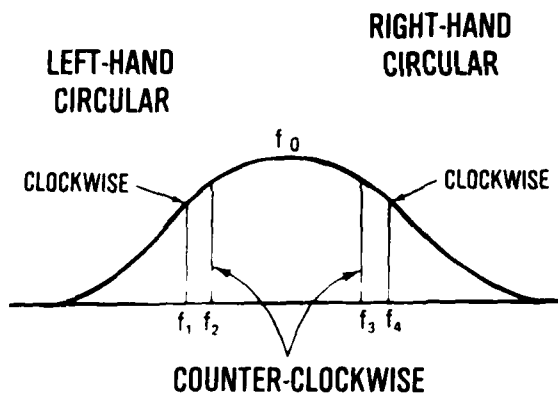


Figure 3. Four Modes on Gain Curve (With Faraday Rotator)

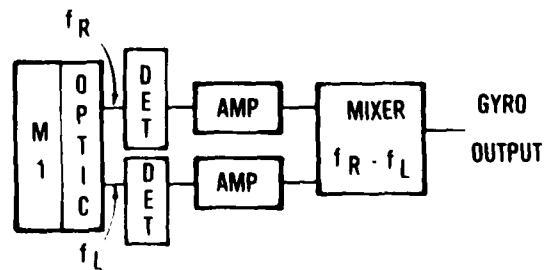
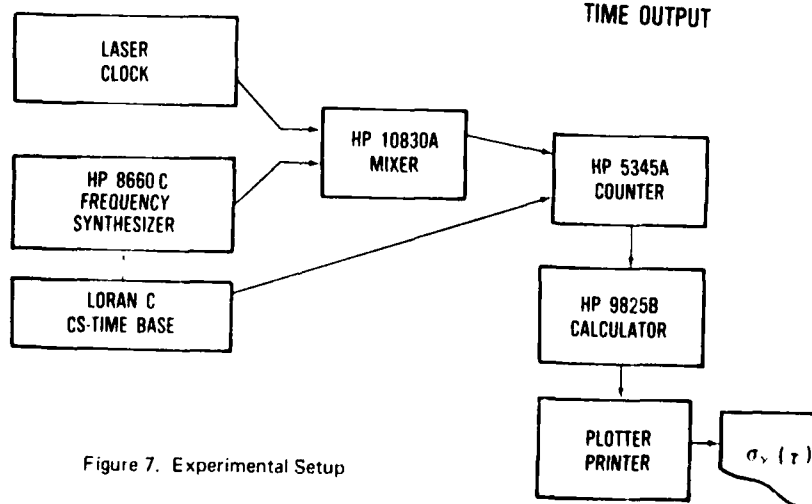
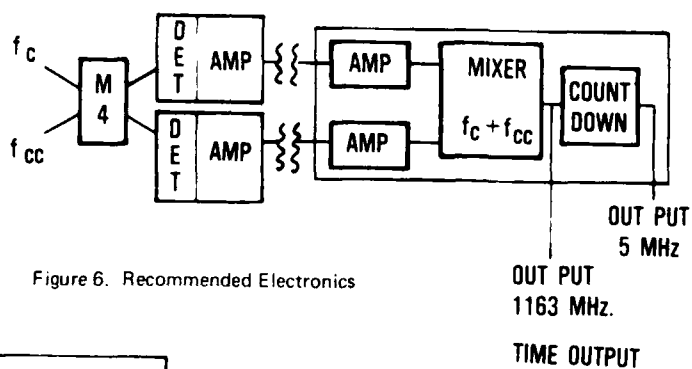
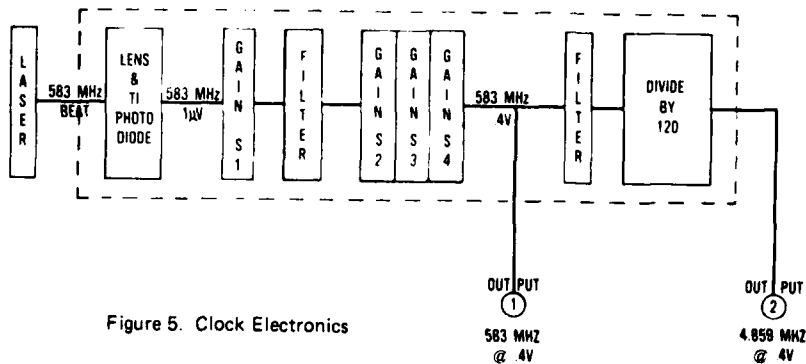


Figure 4. Possible Gyro Electronics



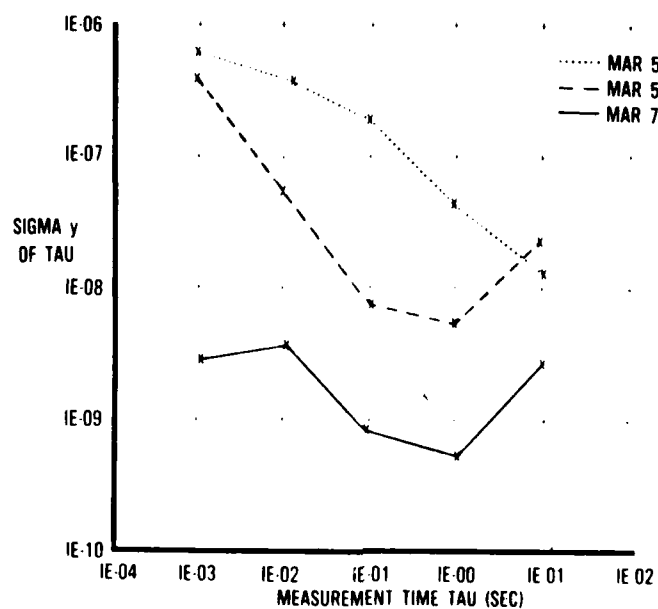


Figure 8. Laser No. 18 Stability Data

RUN	MAR 82
1 --- 1	10
2 --- 2	9
3 --- 3	10

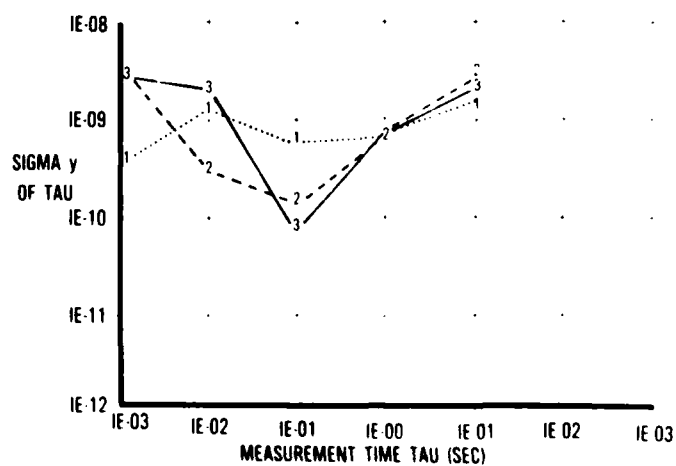


Figure 9. Laser No. 68 Data (1,2,3 Best Points for 1 msec, 10 msec, 100 msec)

RUN		MAR 82
4	..... 4	10
5	--- 5	10
6	— 6	9

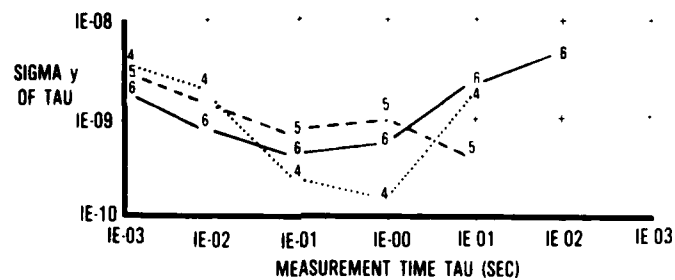


Figure 10. Laser No. 68 Data (4,5,6 Best Points for 1 sec, 10 sec, 100 sec)

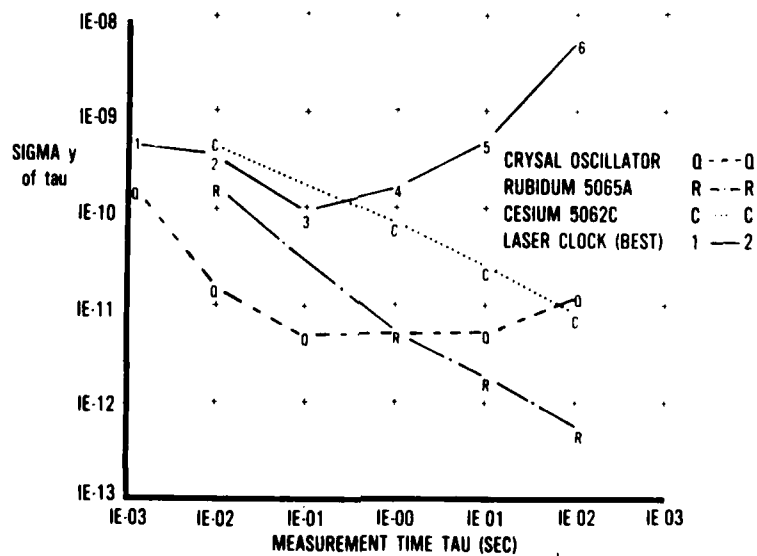


Figure 11. Stability Comparison

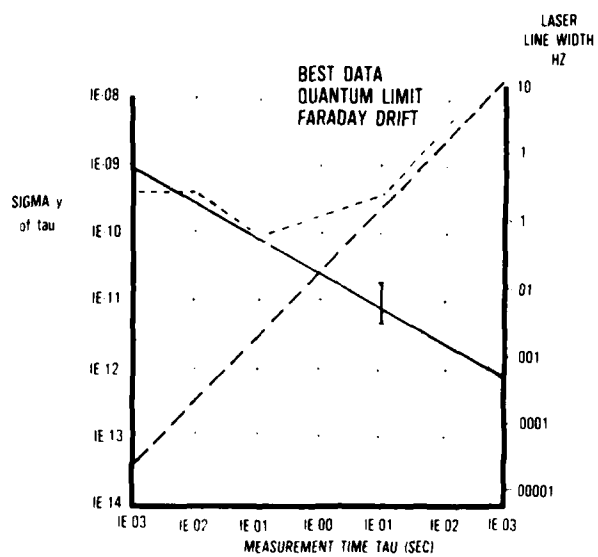


Figure 12. Error Analysis (—quantum limit, -- Faraday Drift  
--- Laser Clock Data)

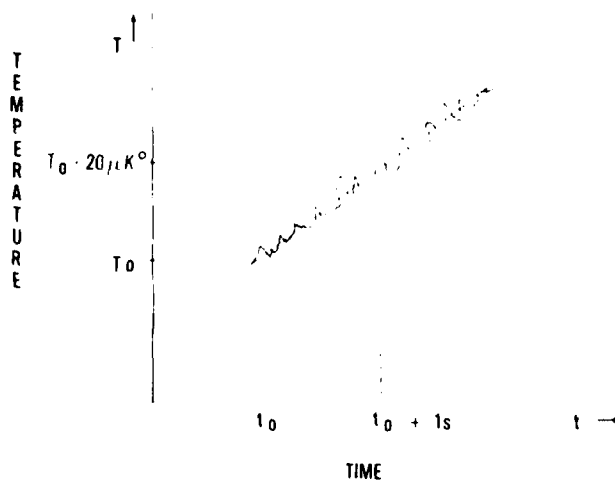


Figure 13. Temperature Drift (~~~~ Typical Profile,  
—— Averaged Profile)

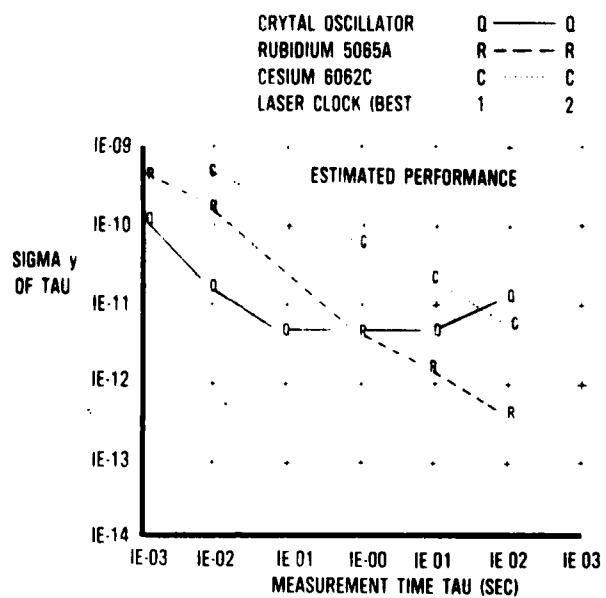


Figure 14. Estimated Performance (Cross Hatched Area)

## A LASER ATOMIC BEAM STANDARD

C. C. Leiby, Jr., and R. H. Picard  
Rome Air Development Center, Solid State Division,  
Hanscom AFB, MA 01731

and

J. E. Thomas, P. R. Hemmer and S. Ezekiel  
Research Laboratory of Electronics  
Massachusetts Institute of Technology, Cambridge, MA 02139

### Abstract

Ramsey fringes have been produced by stimulated resonance Raman scattering between ground-state hyperfine levels at two separated points along a sodium atomic beam. Observed transit time broadening was 1.3 kHz (FWHM), as expected for the 30 cm separation of the two regions. The requisite two copropagating laser fields,  $\omega_p$  (pump) and  $\omega_s$  (stokes), were obtained by frequency shifting a portion of our tunable dye laser output using an acousto optical modulator (AOM) such that  $\omega_p - \omega_s$  equaled the hyperfine transition frequency. The linear polarizations of  $\omega_p$  and  $\omega_s$  were perpendicular to each other. The initial and final states were the  $F = 1$  and  $F = 2$  hyperfine levels of the  $3^2S_{1/2}$  ground state. The resonant intermediate level was the  $3^2P_{1/2}$  ( $F' = 2$ ) state. A magnetic holding field ( $\sim 300$  mG), parallel to the laser beams, was used to separate the magnetic sublevels, enabling us to detect  $m' = 0 \rightarrow m'' = 0$  transitions.

The microwave oscillator used to drive the AOM was locked to the central Ramsey fringe. Preliminary precision frequency counter measurements indicated a stability  $\sim 0.5$  Hz (rms), for a 1 sec integration time, over a period of a few hours. This is the same order of magnitude as the stability of our counter. Initial measurements of the effects of various phenomena upon stability will be discussed.

In principle, techniques can be devised to enable the development of stimulated resonant Raman frequency standards capable of operating at millimeter and possibly far infrared wavelengths. Owing to the limitations of present laser frequency shifting technologies, however, to do so will require the use of two independent stabilized tunable lasers phase locked together to minimize relative jitter.

VIBRATION AND ACCELERATION-INDUCED TIMING  
ERRORS OF CLOCKS AND CLOCK SYSTEMS

F. L. WALLS

Time and Frequency Division  
National Bureau of Standards  
Boulder, Colorado 80303

Summary

There is an increasing interest in using precision atomic clocks in field applications where the frequency stability is usually dominated by environmental parameters such as vibration, acceleration, temperature variations, magnetic field changes, etc., instead of by the intrinsic noise processes. For highly mobile platforms, the acceleration sensitivity often contributes the largest timing errors for short measurement intervals. Local oscillator frequency modulation may be reduced somewhat by the frequency lock to the atomic resonance. It may also result in a dc offset through non-linear interaction with the atomic resonator modulation.

The vibration/acceleration sensitivity of atomic clocks is shown to be intrinsically very small, but not zero. The observed sensitivity has two major components; the first is due to the quartz crystal controlled local oscillator, and the second is due to the physical displacement of the platform. The first component causes a phase

modulation of the clock output at low vibration/acceleration levels, while at high levels the output frequency and time become decoupled from the atomic resonance, thereby losing precision. The second component is present even with a perfect clock and is due to the first order Doppler effect coming from the instantaneous velocity of the platform. A high platform vibration level precludes accurate velocity measurements unless one averages for a long time and/or uses a compensation scheme. A three-dimensional acceleration sensor plus a compensation network can accommodate and correct for both the oscillator and platform sensitivities at low vibration levels. On the other hand, high vibration levels call for a new approach.

Since clock frequency and timing depend on the sum of all environmental and noise processes, some care is needed in specifying worst case timing. The usual case of adding these clock errors in quadrature is examined.

THE U.S. NAVY'S STANDARDIZED PRECISE TIME AND TIME INTERVAL (PTTI)  
PLATFORM DISTRIBUTION SYSTEM (PDS)

Ralph T. Allen

Naval Electronic Systems Command  
Washington, D.C.

ABSTRACT

The U.S. Navy's Precise Time and Time Interval (PTTI) Program is a worldwide effort to provide all Navy surface, subsurface, air and shore platforms and their communications, navigation and weapon systems with time and frequency references traceable to the U.S. Naval Observatory's (NAVOBSY) Master Clock System (MCS).

The PTTI System Concept is comprised of three elements; i.e., the NAVOBSY MCS, the PTTI Dissemination System and the Standardized PTTI Platform Distribution System (PDS).

While undergoing continuous change and upgrade, two of these elements, the NAVOBSY MCS and the PTTI Dissemination System, do in fact exist today. This paper therefore describes very briefly the PTTI System Concept, the NAVOBSY MCS and the PTTI Dissemination System. The majority of the paper is devoted, however, to an overview of the Navy's Standardized PTTI PDS.

The United States Navy's Precise Time and Time Interval (PTTI) Program is a worldwide effort to provide Navy surface, subsurface, air and shore platforms and their onboard communications, navigation and weapon systems with time and frequency references traceable to the U.S. Naval Observatory's (NAVOBSY) Master Clock System (MCS).

In keeping with that mission statement, the Chief of Naval Operations (CNO) issued a draft Operational Requirement (OR) in 1975 which stated that the Navy had an operational requirement for:

a. The worldwide dissemination of precise time and time interval traceable to the NAVOBSY.

b. Cost effective distribution systems for the various platforms to support their designated missions.

Accordingly, one of the Navy PTTI Program's primary objectives is to satisfy Navy surface, subsurface, air and shore platform communications, navigation and weapon systems requirements for time and frequency in a cost effective manner subject to technical and operational constraints.

The PTTI System Concept, which constitutes the Navy's approach to attaining that objective, was first presented in the Navy's PTTI Program Master Plan in 1976 and is currently being enlarged upon in the proposed DoD-STD-1399 (NAVY) SECTION 441 PRECISE TIME AND TIME INTERVAL (PTTI). As depicted in Figure 1, the PTTI System consists of three major elements; i.e., the NAVOBSY MCS, the PTTI Dissemination System, and the Standardized PTTI Platform Distribution System (PDS).

While undergoing nearly continuous change and upgrade, two of these elements, the NAVOBSY MCS and the PTTI Dissemination System, do in fact exist today. The third element, the Standardized PTTI PDS, is currently undergoing a preliminary design and life cycle cost analysis.

In addressing the first element, the NAVOBSY MCS, the Department of Defense (DoD) and the CNO tasked the NAVOBSY with deriving and maintaining the standards of time and frequency for all DoD and Navy components; e.g., the U.S. Army, the U.S. Air Force, the National Security Agency, Naval Research Laboratories, Naval Calibration Laboratories and the Fleet. To provide accurate time and frequency to the DoD and Navy communities, the NAVOBSY maintains a MCS which is referenced to the Coordinated Universal Time (UTC) scale.

The NAVOBSY MCS constitutes the master reference and the start point for the entire Navy PTTI System. Currently, the MCS is based on a bank of approximately thirty to thirty-five cesium beam frequency standards. It provides accurate time to within one nanosecond per day, an exceedingly good long-term stability of two parts in  $10^{14}$ , and is extremely reliable.

While the MCS can meet the vast majority of present day DoD and Navy time and frequency requirements which are generally in the 100 nanosecond to 100 microsecond range, it will not be able to support projected requirements which will be in the ten nanosecond or better region.

The MCS is therefore being upgraded to incorporate the latest state-of-the-art technology including improved reference standards, distributed data processors and environmentally controlled chambers. Figure 2 is a depiction of the updated MCS.

The updated MCS will provide near-real-time accurate to within 1 nanosecond per ten days and a

AD P001546

frequency stability of 1 part in  $10^{15}$  or better.

The standard time and frequency references provided by the NAVOBSY MCS are then transmitted to Navy platforms around the world via the second element of the PTTI System, the PTTI Dissemination System.

The current PTTI Dissemination System employs portable clocks and numerous communications and navigation systems presently in use within the DoD community which have an inherent capability to disseminate time, frequency or time and frequency signals on a noninterference basis with the systems' primary missions. Figure 3 is a representation of the worldwide PTTI Dissemination System.

On each Navy platform, a primary PTTI Dissemination System, e.g., the Defense Satellite Communications System (DSCS) or the Global Positioning System (GPS), and an alternate or backup PTTI Dissemination System, e.g., TRANSIT or LORAN C, has been or will be identified to provide the platform with a link to an external reference traceable to the NAVOBSY MCS. This external reference will be used to monitor, update or calibrate the platform's onboard reference standards. The primary and alternate dissemination systems for each platform are selected according to that platform's time and frequency requirements, its mission scenario and its operational constraints.

In all cases, existing dissemination techniques and systems will be used to the maximum extent practical. Consideration is currently being given, however, to the possible need to develop new and perhaps even dedicated dissemination systems to meet future requirements.

The third and final element of the PTTI System is the Standardized PTTI PDS. While numerous PTTI equipments and a few PTTI systems do exist within the Navy and are currently installed in some Navy platforms, there is no Standardized PTTI PDS. The basic purpose of the Standardized PTTI PDS is to receive the time and frequency references from the PTTI Dissemination System; compare and update the on-board clocks and standards; calibrate those received references; generate standardized time and frequency reference signals; and distribute those standardized reference signals to on-board communications, navigation and weapon systems throughout the platform.

Taking into account the fact that the Standardized PTTI PDS is in the preliminary design phase, there still appear to be some general statements which can be made regarding its configuration and the benefits to be derived.

Figure 4 is a depiction of the Standardized PTTI PDS Concept.

A basic principle of this concept is that the PTTI PDS will be comprised of "standardized" component equipments, e.g., frequency standards, time code generators and distribution amplifiers, which can be configured to meet the time and frequency requirements of a particular platform; e.g., a

cesium beam frequency standard for a submarine platform, a rubidium standard for an aircraft platform and a quartz crystal oscillator for an auxiliary ship platform, all of which provide the same standard signal formats, e.g., 5 MHz, a standard time code and perhaps one pulse per second, at various degrees of accuracy, stability, spectral purity, etc.

Additionally, the Standardized PTTI PDS will:

a. Probably employ a combination of three onboard frequency standards or clocks to provide a back up capability and to allow for comparison of the onboard standards with each other in the absence of an external reference from the dissemination system to identify a standard which is drifting out of tolerance.

b. Make maximum use of decentralized system concepts to enhance survivability; e.g., the physical isolation of the onboard clocks and standards from each other to minimize system vulnerability to fire, battle damage, etc.

c. Provide for underway comparisons and updates of the onboard standards to an external reference from the dissemination system and, as stated above, comparisons of the onboard standards with each other in the absence of that external reference.

d. Possibly use an algorithm or algorithms with a very long time constant on the order of days or weeks to suppress noise and to remove systematic, error producing mechanisms such as frequency drift.

e. Provide an alarm when one of the onboard standards drifts beyond a preset limit and employ a, possibly manual, switch to remove a standard operating outside of acceptable limits from the system.

f. Reduce the number of reference signals being distributed around Navy platforms from the three basic frequency signals of 5 MHz, 1 MHz and 100 KHz, the two timing pulses of one pulse-per-second (1 PPS) and one pulse-per-minute (1 PPM) and an untold number of time codes to perhaps a single, standardized frequency and time code and a single timing pulse, if necessary.

g. Provide the amplification, distribution, and termination necessary to furnish onboard communications, navigation and weapon systems with their required time and frequency reference inputs.

h. Possibly use optical fibers in the distribution of the reference signals to reduce weight and EMI problems and to improve timing services to the user.

The Standardized PTTI PDS appears to offer numerous, significant technological, operational and economical benefits; e.g., the Standardized PTTI PDS will:

a. Provide Navy platforms with an integrated

AD-A130 811

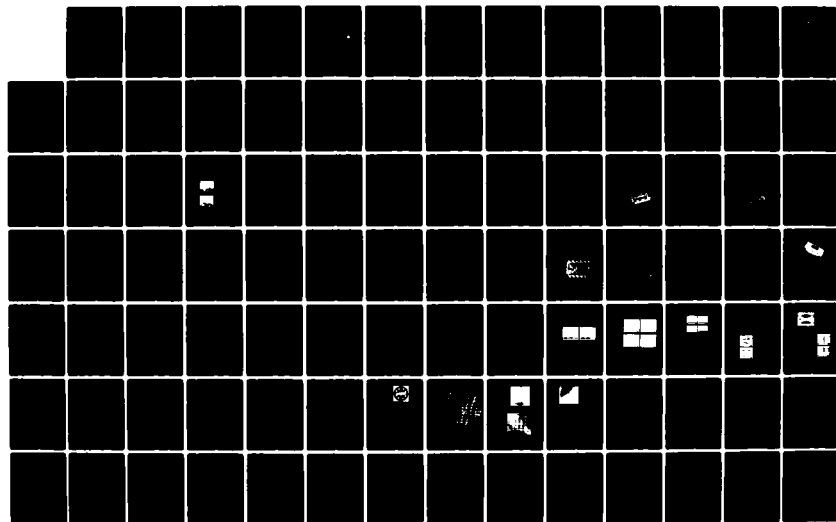
PROCEEDINGS OF THE SYMPOSIUM ON FREQUENCY CONTROL (36TH  
ANNUAL) 2-4 JUNE 1..(U) ARMY ELECTRONICS RESEARCH AND  
DEVELOPMENT COMMAND FORT MONMOUTH. E PAIGE ET AL. 1982

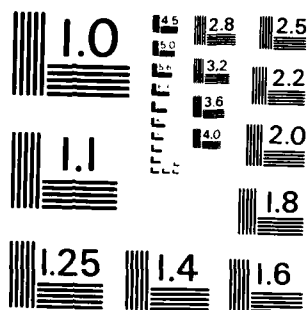
UNCLASSIFIED

F/G 20/14

NL

58





MICROCOPY RESOLUTION TEST CHART  
NATIONAL BUREAU OF STANDARDS - 1963 - A

PTTI PDS capable of meeting all current and projected onboard user system time and frequency requirements efficiently and effectively. While the Navy has today a few "standardized" PTTI equipments, e.g., the 0-1695A/U Cesium Beam Frequency Standard (CBFS), the AN/URQ-23 Frequency-Time Standard, and the AM-2123A(V)/U Frequency Distribution Amplifier, and a few, limited PTTI distribution systems, no Navy platform has a fully integrated, survivable, reliable PTTI PDS capable of supporting those current and projected onboard user systems with accurate, redundant time and frequency references. For example, many current Navy platforms have only one onboard frequency standard. Other platforms have two or more standards but in many instances those standards are dedicated to separate systems and are isolated from each other with no ability to be compared or switched in the event of a failure. Additionally, the current, onboard standards in many instances will simply not support the projected timing requirements of a platform.

b. In accordance with CNO guidance, reduce the proliferation of both types and quantities of time and frequency equipments in the Fleet. Currently, some platforms have as many as six, eight, ten or more onboard standards and as many as three or four different types of standards which are dedicated to one system and cannot be compared to or backed up by another onboard standard; e.g., one surface platform was recently observed to have onboard three AN/URQ-10 Frequency Standards, three 0-1107/SRC-16 Frequency Standards, two FE 1050A Disciplined Time/Frequency Standards, one HP 5062C CBFS and one HP 5061A CBFS all operating essentially independently.

c. Allow Navy platforms to operate independently over longer periods of time. As stated earlier, many Navy platforms do not have three onboard, integrated standards and most Navy platforms do not have access to an external reference while underway. With these capabilities onboard, a platform would after several weeks at sea and the loss of its external reference still be able to proceed with its mission based on the last underway update of its onboard standards from the external reference and continued comparisons of its onboard standards with each other.

d. Allow for future expansion and the relatively easy integration of new systems requiring increased accuracy and performance. This is feasible because the Standardized PTTI PDS will be modular and will be comprised of standardized component equipments which provide reference signals employing standardized formats with varying degrees of accuracy, stability, spectral purity, etc. as required. The installation of an additional distribution amplifier or the replacement of for example a quartz crystal standard with a CBFS to meet new requirements would be a relatively simple and inexpensive matter with a modularized, Standardized PTTI PDS.

e. Via "standardization", improve Navy personnel's familiarity with and efficiency in

maintaining and operating a sophisticated, worldwide PTTI System. Currently, the lack of standardization and the biennial transfer of Navy personnel can result in a high degree of unfamiliarity with time and frequency systems, equipments and procedures. The introduction of a modular PTTI PDS comprised of "standardized" component equipments will result in an increased similarity of equipments and procedures between platforms and hence an increase in personnel familiarity with those equipments and procedures when transferring from one platform to another.

f. Probably reduce the life cycle cost of providing Fleet user systems with time and frequency references. While the initial procurement and installation cost of a Standardized PTTI PDS may actually be higher for a particular platform, especially if it is being converted from one to three onboard standards or from quartz to atomic standards, the employment of a Standardized PTTI PDS which allows for example electronic update and calibration vice portable clock trips, fewer stocking requirements and fewer support system requirements in general based on fewer "standardized" component equipments in Navy inventories should yield an overall reduction in life cycle cost.

g. Probably encourage major "breakthroughs" in future onboard communications, navigation and weapon systems performance. The assured availability of high accuracy, low noise, survivable, reliable, onboard time and frequency references will allow design engineers and scientists to develop new systems with nearly instantaneous acquisition times, improved immunity to jamming environments, improved targeting, improved global coordination, etc.

In summary, Figure 5 is an exemplary illustration of a future application of an integrated PTTI System. The NAVOBSY MCS element and the PTTI Dissemination System element of the PTTI System are in essence already in place. The installation of the final element, the Standardized PTTI PDS, will assure as far as humanly possible the satisfaction of all current, projected and even unforeseen Navy surface, sub-surface, air and shore platform communications, navigation and weapon systems requirements for time and frequency references in a cost effective manner. It will also provide the basis for breakthroughs in the design of future communications, navigation and weapon systems and the performance of those systems in the hostile environment of a Navy platform.

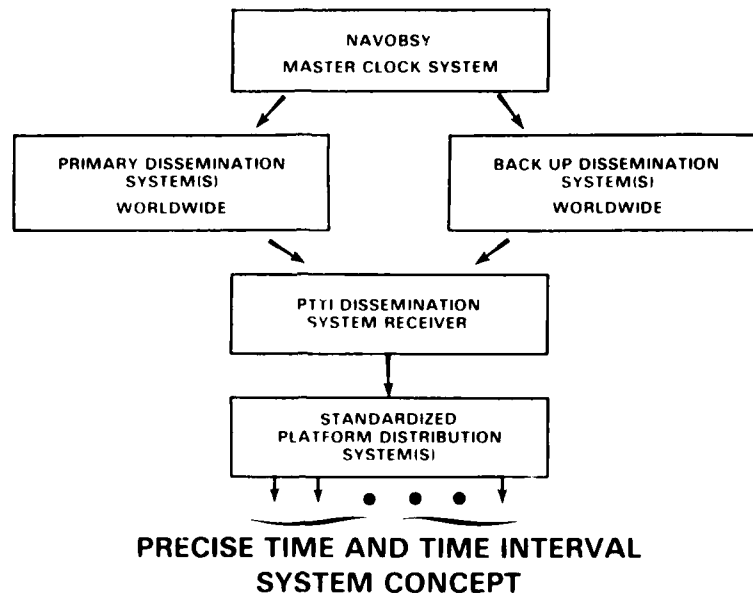


FIGURE 1

### U.S. NAVAL OBSERVATORY MASTER CLOCK SYSTEM

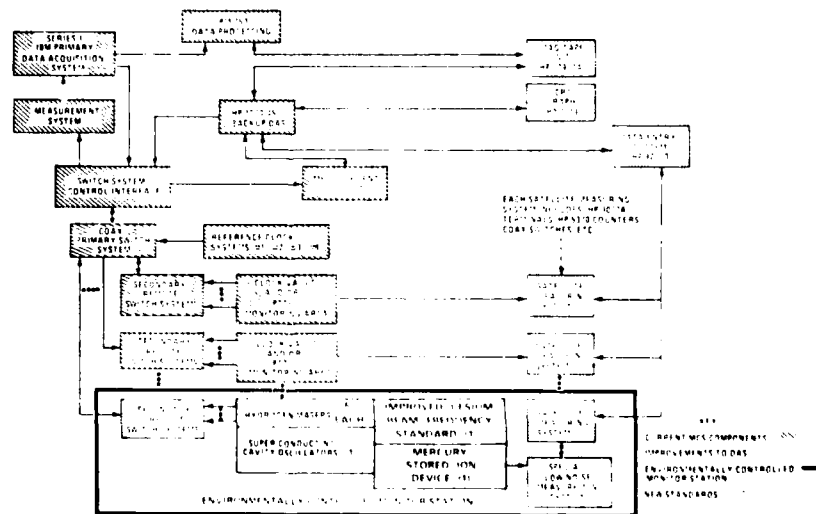
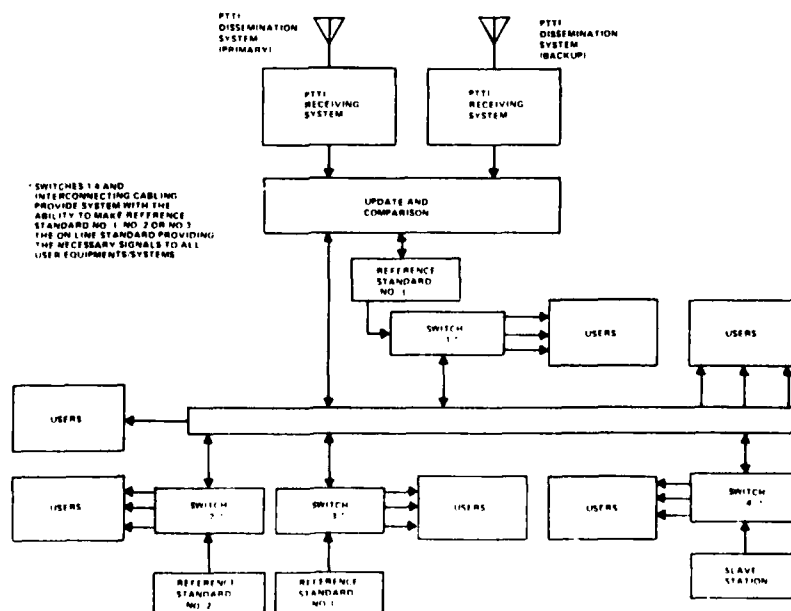


FIGURE 2

[illegible]

**FIGURE 3**



### STANDARDIZED PTI PLATFORM DISTRIBUTION SYSTEM CONCEPT

**FIGURE 4**

# EXAMPLE OF AN INTEGRATED PTTI SYSTEM

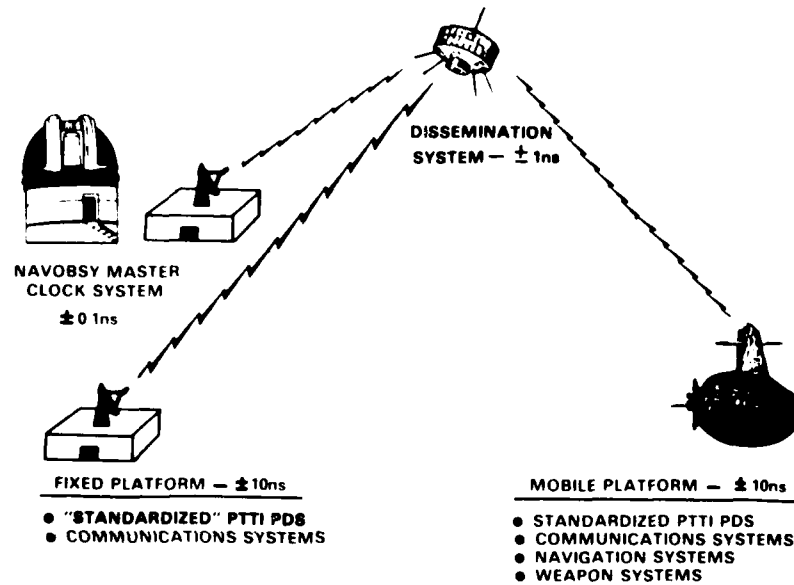
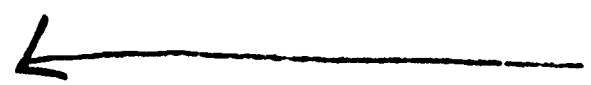


FIGURE 5



# OPTIMAL TIME AND FREQUENCY TRANSFER USING GPS SIGNALS

David W. Allan and James A. Barnes  
Time and Frequency Division  
National Bureau of Standards  
Boulder, Colorado 80303

## Introduction

The advent of the GPS Satellite constellation makes atomic clocks available to any one who has a receiver. Proper characterization of both the clocks and the user links is essential for optimal extraction of time and frequency (T&F) information. In this paper we will consider both optimum T&F extraction from a set of GPS data, and also some near optimum and simple data processing techniques.

We consider three simple cases: case A is what we call the "common-view" approach; case B is the direct viewing of a single satellite for sample times ranging from a few seconds to a few hours; and case C is viewing a single satellite for a few minutes each day for several successive days. The common-view approach has been studied elsewhere (1-3), and the results will be reviewed as they relate to the common-mode cancellation of errors which occur when two user sites view the same satellite for the same several minutes each day, and then subtract their results to get the time difference between the two receiving sites. If one of the two receiving sites is a primary T&F reference standard, then state-of-the-art calibrations are possible. Case B allows one to use the GPS signals as a short-term T&F reference to UTC(NBS) or UTC (USNO)--thus allowing one to calibrate against a primary reference standard.

After characterizing the real data for the above three cases, we develop models from which we can design a Kalman filter. We then test this filter on simulated data, and on some real data. As we proceed it is useful to review some definitions of terms so that the language is clear. Accuracy is defined as the degree to which one can relate a measurement to some absolute reference. Stability, on the other hand, is defined as a measure of constancy--typically over selected sampling periods. We consider both the accuracy and the stability of time and frequency as well as the Fourier frequency ( $f$ ) components of the instabilities of the GPS links and clocks involved. These instabilities or noise fluctuations are characterized in the time-domain by  $\sigma_y(\tau)$  and "modified"  $\sigma_y(\tau)$  diagrams (4,5). These noise fluctuations appear to be well characterized by power-law spectral densities(4). The "Modified Allan variance" is associated with a measurement bandwidth proportional to the reciprocal of the sample time for which

the data is taken. This sample time (denoted  $\tau_h$ ) results in a high-frequency cut-off for the data.

We use typical performance for the models except in those instances where there is a wide range of performance. In which case we use both the worst and best case situations. We do not deal in any detail with error detection and data rejection for this could be the text of a paper all by itself. Rather we have chosen reasonable rejection and interpolation criteria in order to minimize deleterious effects on a proper characterization. The resulting filters are, therefore, appropriate for well behaved data. However, intrinsic to their optimum or near optimum nature is the ability to do error detection and data rejection.

## GPS LINK AND CLOCK CHARACTERIZATION

A. Case A: GPS in common-view of two receiving sites.

The results of a previous study are reviewed in Figure 1 showing the GPS measurement limit using this common-view approach averaged across four satellites and over the approximately 3000 km baseline between NBS-Boulder and USNO. The  $\tau^{3/2}$  performance of MOD  $\sigma_y(\tau)$  indicates white noise phase modulation(PM). The level of the noise is such that MOD  $\sigma_y(\tau=1 \text{ day})=1 \times 10^{-13}$  for  $\tau_h=600\text{s}$ . The resulting RMS time fluctuations are about 5ns. Figure 1 compares these results with a "Range of performance of state-of-the-art standards", with the NBS + USNO instabilities, and with the historical Loran-C comparison method.

The data indicate that this white noise PM model is applicable over the range from about  $\tau=1$  day to about  $\tau=1$  to 2 weeks. This noise level allows one to measure at or beyond state-of-the-art limitations imposed by the standard.

B. Case B: Direct viewing of a single satellite for few minutes  $< \tau < \text{few hours}$ .

The stability data shown in Figure 2 is a typical example using an NBS/GPS receiver with an omni-antenna. In this case the level of the white noise PM is such that MOD  $\sigma_y(\tau=15\text{s})=$

AD P 001547

$5.8 \times 10^{-10}$  with  $\tau_h = 15$ s. Coincidentally the RMS time fluctuations resulting from this configuration are also 5ns. Because  $\tau_h$  is significantly different in case A and case B these noise levels are also quite different and arise from different mechanisms (a topic that could occupy another paper). One notices that for  $\tau > 1000$ s the fluctuations appear to be better modeled by the spectral density of the phase or time fluctuations going as  $f^{-3}$  (flicker noise frequency modulation, FM).

We conclude that averaging for longer than 1000s provides little or no improvement. The low frequency fluctuations generating the flicker noise FM spectra are probably caused by ionospheric and/or tropospheric delay fluctuations.

C. Case C: Viewing a single satellite for a few minutes each day for several successive days.

The data were taken from the USNO Series 4 publication for NAVSTAR 4, NAVSTAR 5, and NAVSTAR 6 (Space Vehicle 8, 5, & 9 respectively). One hundred and eighty four days of data were analyzed starting with 10 Nov. '81. As much as 23% of the days were missing from the published values. Interpolated values were filled in to avoid the problem of missing data in the analysis. Three obvious bad points were rejected over the first 100 days. The raw values with the interpolations are shown in Figure 3. There was obviously a rate change in the GPS clock at data point no. 109 of about 100 ns/day.

If one looks at the residuals, after fitting linear trends to the data some interesting results are seen. Using the last 74 days (since no bad data points had to be rejected from this set) we subtracted a linear least squares line from the UTC(USNO-MC) - GPS via NAVSTAR 4, 5, & 6. The mean slope removed by the linear least squares fit and the residuals are shown in Figure 4. Notice that the peak-to-peak deviation in the mean slopes removed was only about  $4 \times 10^{-15}$ . Also notice the high correlation in the long term (as it should be) since each satellite is being used to deduce the time difference between the same pair of clocks, UTC(USNO-MC) - GPS. That is, in long-term the relative clock noise predominates. In the day to day fluctuations, however, these uncorrelated processes probably arise from measurements made at varying times of day, through different parts of the ionosphere, and/or errors in satellites' ephemeris and up-load values. We can use the "three corner hat" routine to deduce the individual variances for each of the three satellites and their links. Figure 5 is such a stability diagram. The noise level is higher and not as well modeled as the common-view case, but still for sample times of a few days the white noise PM model seems to be reasonable, but breaks down for  $\tau$  of the order of  $1 \times 10^6$ s and longer. The RMS time or phase fluctuations range from about 6ns to 11ns for these data. Figure 6 shows the

UTC(USNO-MC) vs. GPS via NAVSTAR 5. Taking the difference between these variances will give the sum of the variances for the UTC(USNO-MC) and the GPS clock plus the variance for the correlated portion of the noise, which is then an upper limit on the clock's noise. Since we have reasonable confidence of the estimates for 1, 2, & 4 days we have calculated  $\text{MOD } \sigma_y(\tau)$  for these sample times:

$$12.2 \times 10^{-14}, \quad 7.0 \times 10^{-14}, \quad 4.0 \times 10^{-14}$$

respectively. This technique gives a nice way to compare the stabilities of two remote standards at the parts in 10 to the 14th level.

#### SIMULATION AND KALMAN FILTERS FOR GPS

##### A. Simulations

Over the past 15 years, scientists have developed reliable stochastic models of clocks and oscillators. Of course, these models cannot replace actual data, however, they can be used to predict performance of complex systems in advance of construction. Further, so much reliance on these models has developed, that if a model should actually fail, then the opportunity to refine the models would be quite significant.

The complexity of many systems poses problems for analytic solutions for system performance. Often one can become so greatly enmeshed in the mathematics of analytic solutions that the real problems become lost in a forest of equations. Of course, even the analytic solutions depend on model assumptions as much as the simulations. The advantage of analytic solutions is that often their extension to new parameter values is very simple and an "exact" solution is provided. In contrast, simulations using Monte Carlo trials can use much computer time and provide only an approximate value. Clearly, both simulations and analytic solutions have their advantages.

There is another potential problem with computer simulations and Monte Carlo trials. By virtue of the random character of the data, one could use strong selection criteria and influence the findings by presenting non-representative results. In this paper, seed numbers were chosen initially, and used throughout all simulations. As a further safe-guard, the simulation algorithm is included in the Appendix. Thus a critical reader can verify the results, and test the "representativeness" of the conclusions.

##### B. Stochastic Model

For times longer than a few seconds, commercial cesium beam clocks typically display frequency fluctuations which can be modeled well with three elements:

- 1) White noise FM.
- 2) Random walk noise FM, and
- 3) Linear frequency drift.

It should be mentioned that the linear frequency drift model tends to be more difficult in practice. Although one could add various failure modes to this model, they will be ignored here. Further, the present paper is concerned with sufficiently short durations that the third element, drift, will also be ignored. Thus, we are left with a two-element model for the clock: white FM, and random walk FM. Mathematically, this can be represented as the sum of two processes:

$$\Delta x'_n = \varepsilon_n \text{ and}$$

$$\Delta^2 x''_n = \eta_{n-1}$$

where  $\varepsilon_n$  and  $\eta_n$  are random, independent variables with zero mean, normal distributions, and variances of  $\sigma_\varepsilon^2$  and  $\sigma_\eta^2$  respectively; and  $\Delta$  and  $\Delta^2$  are the first and second difference operators, respectively. The clock model is totally represented by the sum of these processes given by

$$x_n = x'_n + x''_n, \text{ or} \\ \Delta^2 x_n = \eta_{n-1} + \Delta \varepsilon_n \quad (1)$$

The parameters,  $\sigma_\varepsilon$  and  $\sigma_\eta$ , along with the time interval between data samples,  $\tau_0$ , are taken to have the following values:

Clock type	$\sigma_\varepsilon$	$\sigma_\eta$	$\tau_0$
Conventional cesium beam	10 ns	3 ns	1 day
Option 004	3 ns	1 ns	1 day

(Note, the numerical values of  $\sigma_\varepsilon$  and  $\sigma_\eta$  are dependent on the sample interval,  $\tau_0$ .)

The Allan variance can be expressed as a function of these parameters with the following equation:

$$\sigma_y^2(N\tau_0) = \frac{\sigma_\varepsilon^2}{N\tau_0^2} + \frac{\sigma_\eta^2(2N^2 + 1)}{6N\tau_0^2} \quad (2)$$

where  $N$  may take on any value.

Figure 7 is a plot of the square root of the Allan Variance deduced from Eq. 2 and the parameters given in the above table. This model for the slave clock (relative to whatever master clock is being referenced), can be expressed in the familiar terms of Kalman Filters (6).

$$\begin{bmatrix} x \\ y \end{bmatrix}_n = \begin{bmatrix} 1 & 1 \\ 0 & 1 \end{bmatrix} \begin{bmatrix} x \\ y \end{bmatrix}_{n-1} + \begin{bmatrix} \varepsilon \\ \eta \end{bmatrix}_n \\ H = \begin{bmatrix} 1 & 0 \end{bmatrix} \\ Q = \begin{bmatrix} \sigma_\varepsilon^2 & 0 \\ 0 & \sigma_\eta^2 \end{bmatrix}$$

A little algebra can quickly show that this Kalman model is exactly equivalent to the clock model presented in Eq. (1). In addition to the clock model, the noise of the comparison link must be modeled also. The link noise appears to be random, uncorrelated (i.e., white) as has been found in the measurements reported above. Future experiments with different baselines and additional data may well refine this model of the comparison link, but for now the white phase model is in accord with observations. Thus the Kalman model is completed by introducing the variance of the measurement noise,  $R$ , according to the table below:

Comparison Mode	Value	$R$	range	$\tau_h$
Common View (4 satellites)	5 ns		$\geq 1$ day	600 s
One Satellite (short term)	5 ns		15 s to 900s	15 s
One Satellite ( $\tau \geq 1$ day)	6-20 ns		$\geq 1$ day	600 s

where  $\tau_h$  is the reciprocal software bandwidth (5).

The computer program used in the simulations can be found in the Appendix.

## RESULTS AND COMPARISONS

In section II we characterized the noise performance of the GPS link for the three cases under consideration. Along with the models developed from these characterizations we use as typical clock models those shown in Figure 7 for a standard commercial cesium and for a high performance option 004 cesium. Which clock model one uses, of course, depends on the actual measurement configuration. We simulated the three cases being studied in this paper, but the theory developed is applicable to a much broader set of cases and clocks.

In case A we simulated the common-view link noise. The stability of the resulting simulated link noise processed by the Kalman filter is shown in Figure 8, which is better than state-of-the-art clocks for sample times of a few days and longer. Thus, for a few days and longer, the oscillator noise predominates. For comparison purposes the calculated stability from real data using a 10 day simple mean is indicated by the solid square. The excellent agreement is not surprising when one realizes that the optimum estimate of a constant buried in a white process is the simple mean. In practice what is done is to calculate the least square fit to the time differences over a 10 day period, and the slope then gives a nearly optimum estimate of the frequency difference between the clocks in the presence of white noise PM. The advantage

of the Kalman output is that it gives in real time a daily optimum estimate of both the time and the frequency differences between the two remote clocks.

For the same level of link noise (5ns RMS), Figures 9 and 10 show the simulated time errors before and after the Kalman update as well as just after the Kalman update for a standard cesium and for an option 004 cesium respectively. Figure 11 graphically illustrates for a standard cesium the effects of looking at the clock just before update and just after update as indicated by the light and dark open squares respectively. The Kalman update stability values would, of course, be much closer together for the option 004 cesium.

For case B we simulated a standard cesium (comparable to those aboard the GPS satellites) and the 5ns link noise. The purpose was to test the improvement gained by the Kalman filter. Figures 12 and 13 are the results of that simulation. One sees about a 40dB improvement in stability for the Kalman output at  $\tau=15s$ . In fact except for a small turn-on transient (not shown) the Kalman filter output tracks nearly perfectly the on board clock's time, and stability levels of a few in 10 to the 12 seem reasonably achievable.

For case C we use the Kalman filter to process the actual data. Figure 14 is a plot of the residual time differences between UTC(USNO-MC) - GPS via NAVSTAR 5 both with and without the Kalman filter. It is obvious that it acts like a low pass filter and one could design a simple recursive (exponential) filter to approach the Optimum. However, the number of lines of code are so few for the Kalman filter (as shown in the Appendix) that little would be gained. Figure 15 nicely illustrates this improvement in stability for sample times shorter than 10 days. At  $\tau=1$  day there is an 11 dB improvement in stability using the Kalman filter over the stability of the raw data.

From the data studied in this paper, there are clear advantages in proper filtering. Despite the fact that the data studied is not comprehensive and that the GPS receivers used were a limited set, one can still draw some reasonable and impressive conclusions. Table 1 is a summary of the stability and accuracy ranges of F&T calibrations available using GPS for remote clocks within about 3000 km of a primary reference.

#### CONCLUSIONS AND FUTURE WORK

The advent of GPS has produced a significant step forward in the accuracies and stabilities with which time and frequency can be compared at remote sites. With appropriate filtering of GPS data as outlined in this paper one can compare and calibrate remote clocks at state-

of-the-art accuracies for sample times of the order of a few days and longer; e.g., a few parts in 10 to the 15 are achievable for averaging times of 10 days, and time accuracies of better than 10ns have been verified. The cesium standards on board GPS satellites may be used as accurate frequency references at the part in 10 to the 12 level. Even for short-term measurements of about 10 minutes duration nearly the full accuracy of these on-board cesiums can be transferred using appropriate data filtering as outlined above.

Future work will involve studies of world wide baselines leading to better understanding of the propagation medium's effects on GPS T&F measurements. Because the common-view approach appears to work even better than initially calculated, we have started some special studies. Some of the data indicates that there may be significant amounts of common-mode cancellation of errors due to a breathing effect working simultaneously across the ionosphere. This should be studied further. Steerable high gain antennas would lead to better time stabilities and perhaps better accuracies as multipath problems are reduced significantly. More accurate time transfers will result as people take advantage of the two frequencies radiated from the GPS satellites --giving a real time calibration of the ionosphere. The results of these research efforts suggest that the GPS system can support world-wide time and frequency comparison accuracies approaching a nanosecond and 1 part in 10 to the 15 respectively. The key questions, of course are regarding the availability of reasonably priced commercial receivers and continued access to the GPS constellation at full accuracy.

#### Acknowledgements

We are deeply appreciative of the support of the research staff at NBS including Dick Davis, Marc Weiss, Al Clements, Jim Jespersen and Trudi Pepler. The cooperation of the USNO staff has also been excellent and is much appreciated. Without the support of Air Force Space Division, Jet Propulsion Laboratories, Navy Metrology Engineering Center and Naval Air Logistics Center this work would not have been possible, and we express to them also our deep appreciation.

#### References

- 1) D. Allan and M. Weiss, "Accurate Time and Frequency Transfer During Common-View of a GPS Satellite", Proc. 34th Annual Symposium on Frequency Control, 334 (1980).
- 2) D. Davis, M. Weiss, A. Clements, and D. Allan, "Construction and Performance Characteristics of a Prototype NBS/GPA Receiver". Annual Symposium on Frequency Control, 1981.
- 3) D. Davis, M. Weiss, A. Clements, and D. Allan, "Unprecedented Syntonization and Synchronization Accuracy Via Simultaneous Viewing with GPS Receivers: Construction Characteristics of an NBS/

GPS Receiver" 13th Annual PTTI, 1-3 Dec. 1981.

- 4) J. Barnes, (A. Chi, L. Culter, D. Healey, D. Leeson, T. McGunigal, J. Mullen, W. Smith R. Sydnor, R. Vessot, and G. Winkler), "Characterization of Frequency Stability", NBS Technical Note 394 (Oct. 1970).
- 5) Allan and Barnes, "A Modified Allan Variance" with Increased Oscillator Characterization Ability, Proc. 35th Annual Symposium on Frequency Control 1981.
- 6) Gelb, Arthur, "Applied Optimal Estimation" The M.I.T. Press; Copyright 1974 by the Analytic Science Corporation.

#### APPENDIX

Attached are two copies of a computer program (in "BASIC") designed to (1) simulate the performance of typical cesium beam clocks, (2) simulate the comparison noise, and (3) operate on the simulated measurements with a Kalman Filter to obtain an optimum estimate of the clock's time. The constants listed in the program are chosen to simulate an average commercial cesium clock. The units are in nano-seconds and the time interval is one day. Other values of the sampling interval require different numerical values for the sigmas.

The data used for the Kalman Filter corresponds to the data which might actually be available in a real situation. Within the program, however, the "true" time is known. Thus it is possible to evaluate the absolute performance of the Filter operating on the simulated data. A slight modification of this program was used with real data as reported in the text.

The first copy of the program has numerous remarks (prefaced by "REM") to aid in the understanding of the program. These "REMARKS" are ignored by the operating program. The second version of the program is identical to the first, except that all remarks have been deleted and the steps renumbered. The second version was included to demonstrate how simple the Kalman Filter (which is only a part of the program) can really be.

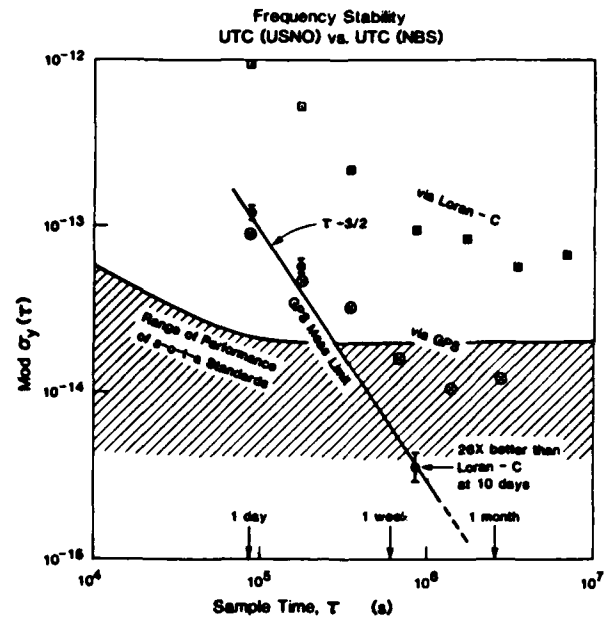


Figure 1

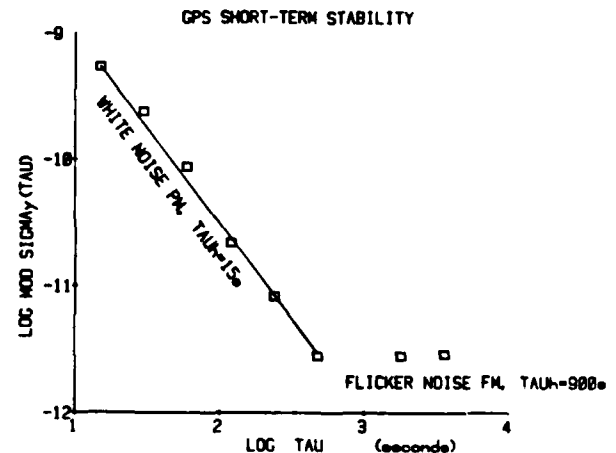
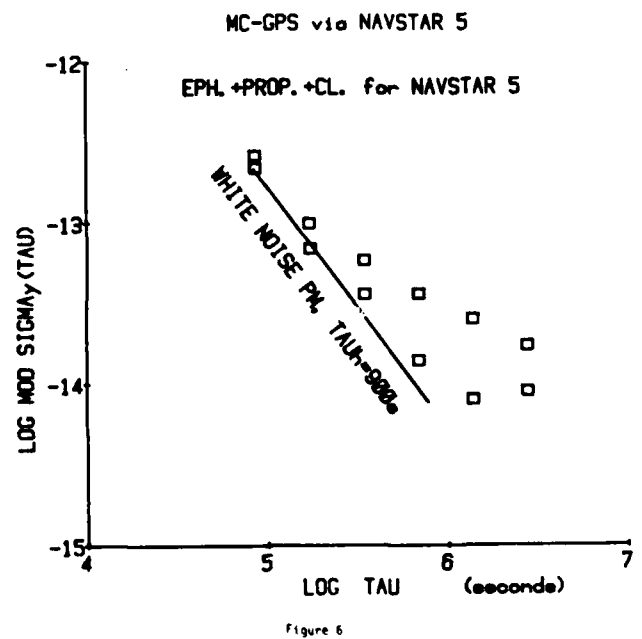
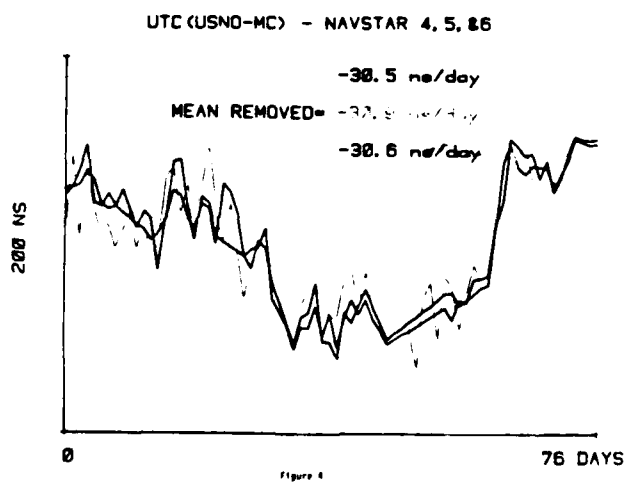
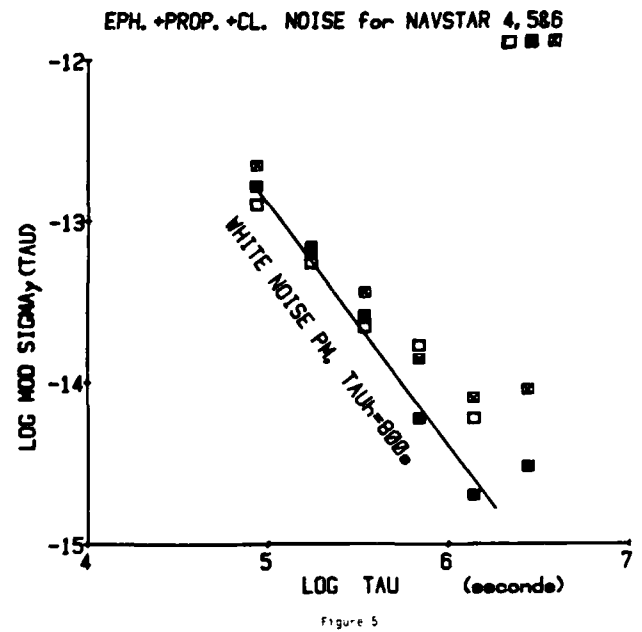
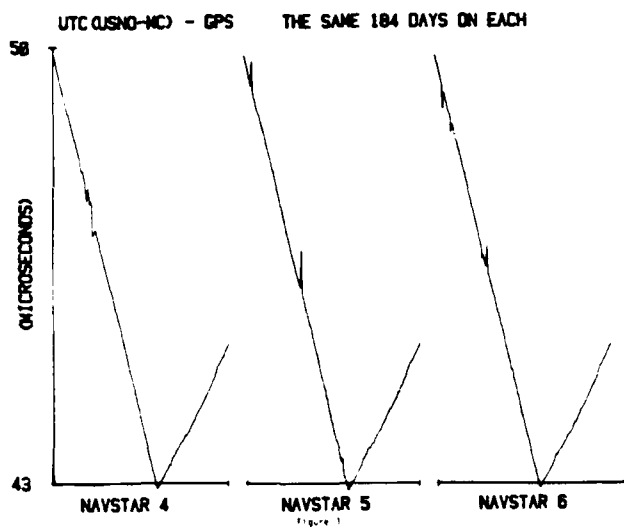


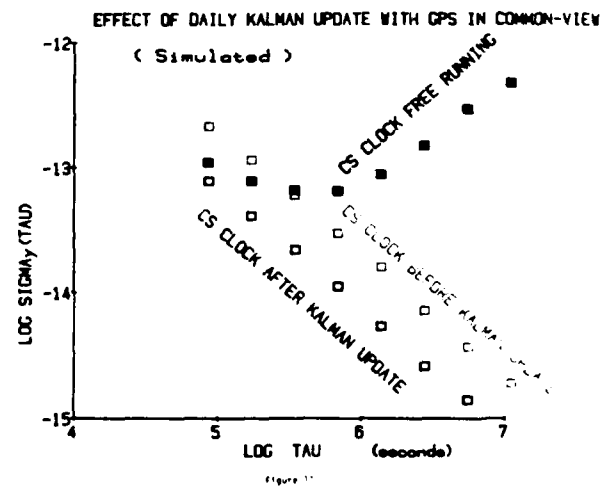
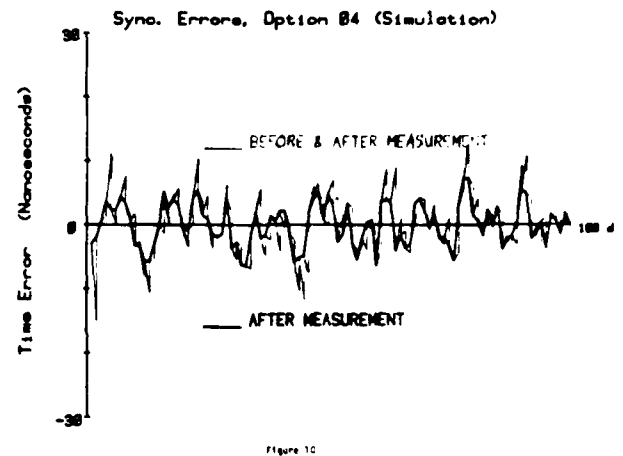
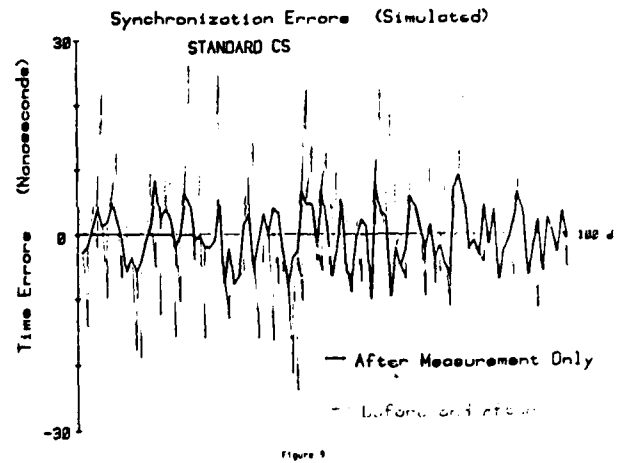
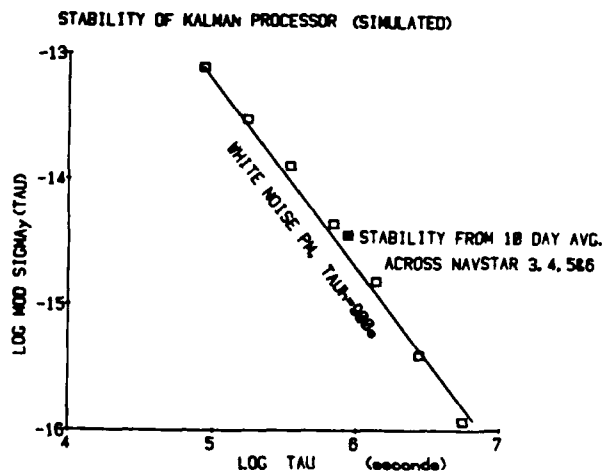
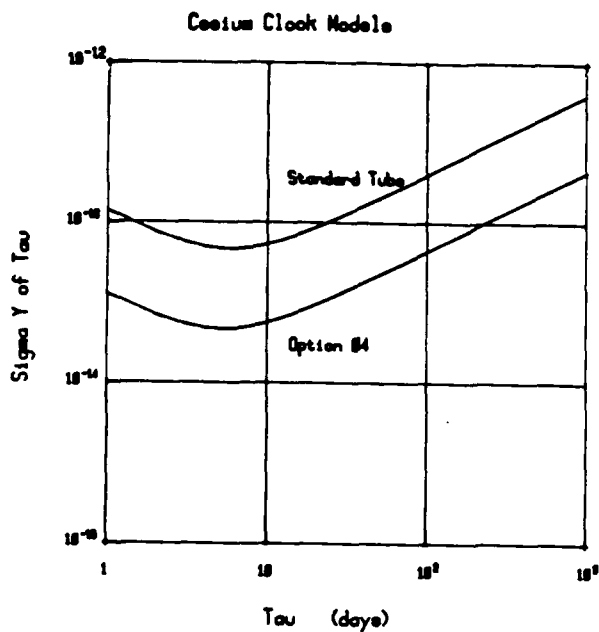
Figure 2

Table 1

For Kalman Filtered Data

CASE	Synchronization Accuracy	Time Stability	Synchronization Accuracy	Frequency Stability
A: Common-view	<10ns	~3.6ns $\tau_0=1$ day	<1x10 <sup>-14</sup>	<3.5x10 <sup>-15</sup> $\tau=10$ days
B: Single Satellite Short-term	<50ns	~0.7ns $\tau_0=15s$	~2x10 <sup>-12</sup>	~2x10 <sup>-12</sup> $\tau=1000s$
C: Single Satellite $\tau \geq 1$ day	<20ns	~4.4ns $\tau_0=1$ day	<2x10 <sup>-14</sup>	~1x10 <sup>-14</sup> $\tau=10$ days





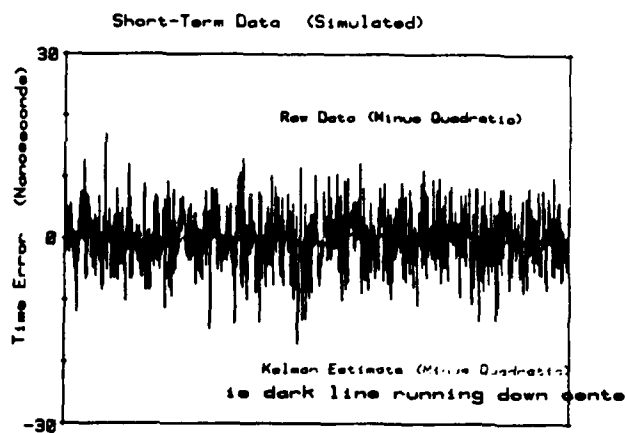


Figure 12

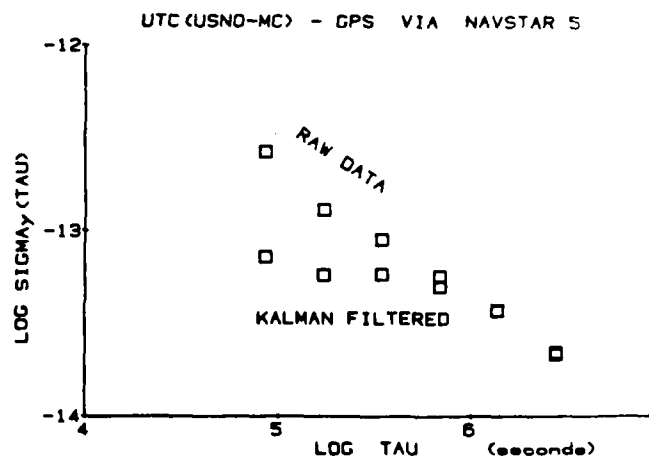


Figure 15

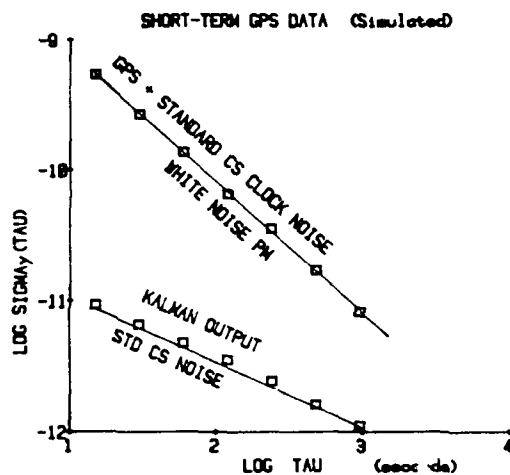


Figure 13

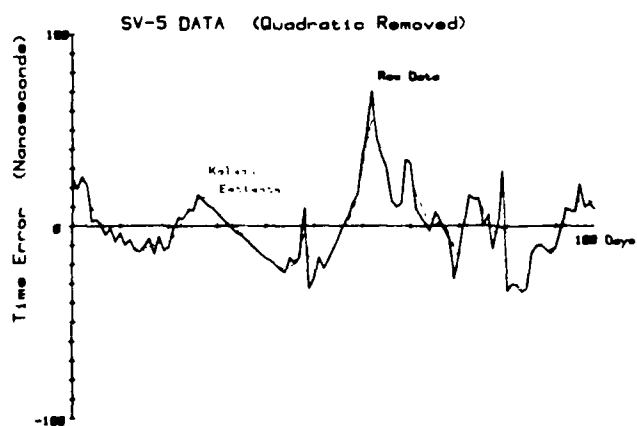


Figure 14

# COMPUTER PROGRAM

LIST 1,489

```

100 REM THIS PROGRAM SIMULATES
105 REM THE GPS SATELLITES,
110 REM PROPAGATION NOISE, AND
115 REM THE SLAVE CLOCK.
120 REM THE SLAVE CLOCK IS
125 REM CORRECTED BY THE USE
130 REM OF A KALMAN FILTER.
135 REM
140 REM
150 REM SET CONSTANTS
160 REM UNITS: NANOSEC & DAYS
170 P = RND (1 - 17.7771)
180 REM SEED FOR RAND NO.
190 SE = 10: REM WHITE FM
200 SN = 3: REM RANDOM WALK FM
210 S = 5: REM WHITE PHASE
220 REM INITIAL CONDITIONS
230 X = 5000: REM TIME ERROR
240 Y = 10: REM FREQ BIAS
250 A = 1E-7: REM TIME VARIANCE
260 C = 1E-9: REM FREQ VARIANCE
270 REM
280 REM
290 FOR N = 1 TO 200
300 REM SIMULATE 100 DAYS
310 REM
315 REM
320 REM SIMULATE CESIUM BEAM
330 GOSUB 1000: REM RANDOM NO.
340 IN P
350 X = X + Y + SE * P: GOSUB 100
360
370 Y = Y + SN * P: GOSUB 1000
380 Z = S * P: REM LINK NOISE
390 REM
400 REM
410 REM CALCULATE COVAR MATRIX-
420 REM
430 REM
440 REM
450 REM
460 REM
470 A = A + 1 * B + C + SE / 2
480 B = B + 2 * C + E + SN / 2
490 REM FORECAST X1+, AND Y1+
500 X1 = X + Y1 * Y1
510 REM
520 REM

```

```

500 REM COMPUTE MEASUREMENT
505 E = X + Z - X1: REM CLOCK +
510 REM LINK - FORECAST
515 REM
520 REM THE QUANTITY X-X1
525 REM IS THE FORECAST ERROR.
530 REM IT IS ALSO THE ERROR
535 REM JUST BEFORE CORRECTION
540 REM
550 REM
560 REM UPDATE COVAR MATRIX+
565 U1 = A:U2 = B:R = A + S * S
570 REM KALMAN GAIN K
575 K1 = U1 / R:K2 = U2 / R
580 A = A - U1 * K1
585 B = B - U1 * K2
590 C = C - U2 * K2
595 REM
600 REM
605 REM
610 REM
615 REM
620 REM
625 REM
630 REM
635 REM
640 REM
645 REM
650 REM
655 REM
660 REM
665 REM
670 REM
675 REM
680 REM
685 REM
690 REM
695 REM
700 REM THE TIME ERROR
705 REM IS THE DIFFERENCE
710 REM BETWEEN ACTUAL
715 REM CLOCK, X, AND
720 REM THE KALMAN ESTIMATE X1
725 PRINT N,X - X1
730 NEXT N
740 REM
750 REM RANDOM NUMBER GEN
755 REM ZERO MEAN, UNIT VAR
760 P = 0
765 FOR J = 1 TO 6
770 P = P + RND (1) - RND (1)
775 NEXT J
780 RETURN

```

# SIMPLE PROGRAM

LIST

```

100 P = RND ( - 13.3371)
110 SE = 10
120 SN = 3
130 S = 5
140 X = 5000
150 Y = - 10
160 A = 2E7
170 C = 1E4
180 FOR N = 1 TO 300
190   GOSUB 360
200 X = X + Y + SE * P: GOSUB 360

210 Y = Y + SN * P: GOSUB 360
220 Z = S * P
230 A = A + 2 * B + C + SE * 2
240 B = B + C: C = C + SN * 2
250 X1 = X1 + Y1: Y1 = Y1
260 E = X + Z - X1
270 U1 = A: U2 = B: R = A + S * S
280 F1 = U1 / R: K2 = U2 / R
290 A = A - U1 * F1
300 B = B - U1 * K2
310 C = C - U2 * K2
320 X1 = X1 + K1 * E
330 Y1 = Y1 + K2 * E
340 PRINT N, X - X1
350 NEXT N
360 P = 0
370 FOR J = 1 TO 6
380 P = P + RND (1) - RND (1)
390 NEXT J
400 RETURN

```

TEST RESULTS OF THE STI GPS TIME TRANSFER RECEIVER \*\*\*

DAVID L. HALL\*  
AND  
KENNETH PUTKOVICH\*\*

Global time transfer, or synchronization, between a user clock and USNO UTC time can be performed using the Global Positioning System (GPS), and commercially available time transfer receivers. This paper presents the test results of time transfer using the GPS system and a Stanford Telecommunications Inc. (STI) Time Transfer System (TTS) Model 502. Tests at the GPS Master Control Site (MCS) in Vandenberg, California and at the United States Naval Observatory (USNO) in Washington, D.C. are described. An overview of GPS, and the STI TTS 502 is presented. A discussion of the time transfer process and test concepts is included.

\* HRB-SINGER, INC., STATE COLLEGE, PA

\*\* UNITED STATES NAVAL OBSERVATORY (USNO)  
WASHINGTON, D.C.

\*\*\* This work was sponsored by the United States Government. The views and conclusions contained in this document are those of the authors and should not be interpreted as necessarily representing the official policies, either expressed or implied, of the United States Government.

AD P 001548

## INTERMEDIATE BANDWIDTH QUARTZ CRYSTAL FILTERS - A SIMPLE APPROACH TO PREDISTORTION

R C Peach, A J Dyer, A J Byrne, E Read and \*J K Stevenson

The General Electric Company, p.l.c., Hirst Research Centre,  
Wembley, HA9 7PP, England  
\*Polytechnic of the South Bank, London, England

Abstract

Intermediate band crystal filters can realize fractional bandwidths of more than 1%, but design and construction difficulties have severely limited their general use, despite the considerable number of practical applications. These filters rely on coils to broadband the response, and the effect of coil losses increases in proportion to the filter bandwidth.

This paper describes the development of a 15 MHz crystal filter with a 1% fractional bandwidth. An eighth order elliptic characteristic was chosen (COR25b 48), using a two crystal lattice configuration. The bandwidth of the filter was severely narrowbanded by coil losses, and it was found to be necessary to use optimization techniques to meet the required specification. As a result a special computer programme was developed which would provide a near optimal design allowing for an arbitrary distribution of coil losses in the chosen circuit configuration, but which only required minimal computational effort and was almost fool-proof in use.

Key words: <sup>1</sup>Crystal filter, Optimization

1 Introduction

In many respects a quartz crystal resonator is a near ideal circuit element, but for filter applications the small distance between the resonant and antiresonant frequencies limits the bandwidth achievable using crystals and capacitors alone to a few tenths of a percent. With the use of coils it is possible to increase bandwidths to several percent, and filters using this approach are generally classified into intermediate and wideband types. In an intermediate band filter the inductors act as constant reactances as far as the passband shape is concerned, and the poles which they introduce are assumed to lie well into the stopband and to produce no significant effects. Wideband filters have both crystals and coils contributing to the passband characteristic, and due to the enormous differences in the behaviour of these two types of component, this class of design is rarely practicable; it will be assumed that all discussions from now on are limited to intermediate band filters.

For filters of this type a lattice configuration is almost invariably employed, as it provides a flexible structure capable of realizing any of the common minimum phase characteristics, while being especially suited to the incorporation of crystal resonators. The basic lattice element permits the static capacitances of the crystals to be balanced at the terminals, and crystal losses tend to round the passband rather than introduce skewing. This is not necessarily true of coil losses which may, in certain configurations, introduce gross asymmetries into the passband.

Extensive tables of low pass filter designs are available, and these may be transformed into structures suitable for crystal realizations by a number of methods. These techniques however presuppose an implementation by ideal lossless components, and if a very tight specification, or a specification calling for a fractional bandwidth of more than a few tenths of a percent, is attempted, then such a design is unlikely to prove satisfactory. The obvious answer to this problem is to employ iterative optimization techniques to correct the passband characteristics for component losses, using the ideal circuit as a starting point. Despite the apparent merit of this technique it has not achieved wide acceptance among practical filter designers, probably because of the considerable amount of computer effort required, and the difficulties in locating the optimal solution for a high order crystal filter.

The purpose of the present work is to develop a simple optimization procedure which will be applicable to normal intermediate band crystal filter designs, will accommodate an arbitrarily specified distribution of coil losses, and will be quick and reliable to use.

2 General filter configuration

It will be assumed that a low pass realization of the filter characteristic is available in the form given in Figure 1, where each coil is ideal and has a coupling coefficient of unity. This is quite a generalized form and can realize almost any even order minimum phase filter characteristic with or without finite transmission zeros, and even includes cases with finite transmission at infinite

frequency, such as elliptic type 'a' responses. The transformation to lattice form is then accomplished by the widely used Holt-Gray transformation<sup>1,2</sup> (Fig 2), which includes techniques based on Bartlett's bisection theorem as a special case, when all attenuation poles are at infinity. This transformation uses the device of constant reactances, which are represented in Figure 2 by rectangular boxes; an equivalent circuit for the impedance inverter is given in Figure 3.

Having transformed each section of the ladder circuit to a lattice configuration, a considerable number of further transformations are possible. One of these consists of using impedance transformation to equalize the impedance of the inverters and to equalize the terminations. The inverters are then realized in T form and the series elements absorbed into adjacent lattice<sup>2</sup>; on transformation to bandpass form this gives the coil minimizing circuit illustrated in Figure 4 for an eighth pole filter. A second variation uses impedance transformation to equalize the motional inductances between lattices, the inverters are then realized in  $\pi$  form, and on conversion to a bandpass configuration it gives a circuit of the form shown in Figure 5 for an eighth order filter. At first sight it might appear that all the advantages lay with the coil minimizing version; however for finite attenuation pole designs such as elliptic, which are especially useful at wider bandwidths, this is by no means true. The finite attenuation poles require different motional inductances within each lattice for the circuit of Figure 4, and since the design will in general lack the special symmetries of Butterworth and Chebyshev responses, each lattice will be different also. In addition the normal implementation of the coil minimizing circuit displaces all crystal frequencies down, making it more difficult to exclude unwanted responses from the passband. For small quantities it is highly inconvenient to provide a separate crystal design for each resonator to allow for the specified motional parameters, and the use of tapped coils or capacitor transformation in the final circuit is extremely awkward. Due to the different characteristic impedances of the two types of circuit the effects of coil losses in the equal motional inductance design are not by any means double those in the coil minimizing structure. In fact in many cases, including the specific example to be discussed in this paper, the equal motional inductance circuit, without optimization, gives an intrinsically more satisfactory response.

For these reasons we will restrict specific consideration to the equal  $L_m$  circuit of Figure 5. In addition the coil losses and crystal losses for this type of structure only produce a symmetrical distortion, and this considerably reduces the number of variables in the optimization problem.

### 3. The optimization procedure

Having chosen the circuit structure, in this case adjusted to equalize motional inductances, the overall configuration, prior to conversion to

bandpass form, may be represented as a cascade of lattice sections and impedance inverters (Fig 6). Shunt resistances are shown on each side of each inverter; in the final circuit the shunt reactances of the inverters will be simulated by inductors, and a parallel resistance provides a simple but quite realistic model of the loss even for a centre tapped coil. It is assumed that the ESRs of the crystals within each lattice are equal, crystal losses are a small effect in this case, and this assumption is a 'priori' as probable as any. The motional inductance is generally specified at the outset by the resonator design, it is therefore desirable to impose the constraint that the motional inductances within the circuit should remain equal and at their specified value. The ESRs of the crystals move the transmission zeros a small distance off the imaginary axis in the complex  $s$  plane, but this is a minute effect and is not easily corrected by optimization. For this reason a second constraint is imposed on each lattice to fix the positions of the transmission zeros as close to their ideal locations as possible. This has no perceptible effect on the passband characteristic, and can at most cause some smearing of the zeros in the stopband. Also insisting that the constant reactances in the shunt and series arms of each lattice retain their equality of magnitude but difference of sign, ensures that the response remains symmetric.

Given these constraints there is in effect one adjustable parameter per lattice available, in addition to the impedance of each inverter and each termination. So for the eighth order filter illustrated there would be a total of nine circuit parameters which could be varied in the optimization procedure. For such a filter the response is now totally specified by the eighth order polynomial in  $s$  which gives the transmission poles in the complex  $s$  plane. As the response is constrained to be symmetric the nine polynomial coefficients are necessarily real, and these nine 'characteristic parameters' directly determine both passband shape and insertion loss. Therefore specifying the desired loss and passband shape fixes the ideal values for the nine 'characteristic parameters', and the problem is to determine the nine values of the circuit parameters which will provide these ideal values. It will be noted that all this manipulation is being done prior to the bandpass transformation; this produces slight simplification without any significant loss of generality.

Continuing with an eighth order filter as an example, we may suppose that the ideal values for the polynomial coefficients are given by  $(a_1^0, a_2^0 \dots a_9^0)$ , therefore defining a parameter

$$J = \sum_{i=1}^9 w_i (a_i - a_i^0)^2 \geq 0, \quad w_i > 0 \quad (1)$$

where the quantities  $(a_1, a_2, \dots a_9)$  are the actual coefficients; the problem is to find the global minimum of  $J$ , at which point its value will hopefully be zero. In general each  $a_i$  will be a function of all nine circuit variables, and as we are seeking a point where  $J = 0$ , all  $a_i = a_i^0$  and

the precise values of the weights  $w_i$  are not very important though they may affect the conditioning of the problem.

There are many algorithms available for this type of problem<sup>3,4</sup>, one of the simplest is the steepest descents method, which consists of choosing iterative increments

$$\Delta p_i = - \frac{\partial J}{\partial p_i} \quad (2)$$

where  $p_i$  are the circuit parameters. This method is guaranteed to converge, but convergence is only linear, and it is therefore very slow in the neighbourhood of the minimum. If second derivatives of  $J$  are known then much faster iterations may be employed, giving quadratic convergence.

$$J(p_i + \Delta p_i) = J(p_i) + \sum \frac{\partial J}{\partial p_i} \Delta p_i + \frac{1}{2} \sum \frac{\partial^2 J}{\partial p_i \partial p_j} \Delta p_i \Delta p_j + \dots \quad (3)$$

For a minimum we require

$$\frac{\partial J(p_i + \Delta p_i)}{\partial p_i} = 0$$

$$= \frac{\partial J}{\partial p_i} + \sum_j \frac{\partial^2 J}{\partial p_i \partial p_j} \Delta p_j \quad (4)$$

which provides a set of simultaneous equations for the  $\Delta p_j$ . Unfortunately the set of second derivatives is prohibitively large and it is advisable to avoid calculating them if at all possible. One method for doing this is to write  $J$  in the form  $\sum e_i^2$ , where  $e_i = w_i^{1/2}(a_i - a_i^0)$ , and to note that

$$\frac{\partial^2 J}{\partial p_j \partial p_k} = 2 \sum_i \frac{\partial e_i}{\partial p_j} \cdot \frac{\partial e_i}{\partial p_k} + 2 \sum_i e_i \frac{\partial^2 e_i}{\partial p_j \partial p_k} \quad (5)$$

then if the minimum of  $J$  corresponds to a point where all  $e_i = 0$ , as we require, then it is permissible to neglect the second term in Eq (5). With this modification we obtain

$$\sum_i \frac{\partial e_i}{\partial p_j} + \sum_k \frac{\partial e_i}{\partial p_j} \cdot \frac{\partial e_i}{\partial p_k} \cdot \Delta p_k = 0 \quad (6)$$

If the matrix  $\partial e_i / \partial p_j$  possesses an inverse, as it does in our case, then this reduces to

$$e_i + \sum_k \frac{\partial e_i}{\partial p_k} \Delta p_k = 0 \quad (7)$$

which is obviously the Newton-Raphson formula. This iteration converges quadratically but it is likely to diverge unless a good starting point is available. A serious problem is created by the presence of local minima in the function  $J$ , which will stall any of the common search routines, for this reason it is rarely profitable to attempt a direct optimization. However as the exact solution for the lossless case is known, it is possible to adopt a simple but effective expedient. If the losses are 'turned on' in a number of small increments, and a few iterations using the

Newton-Raphson formula are performed at each step, then the solution will track the target closely as the final configuration is approach. By these means the problem of being diverted on to subsidiary minima is avoided, and a good starting point is always available for the iteration, permitting the use of the more efficient Newton-Raphson method.

In the actual computer program the filter response was analysed by multiplying the chain matrices of successive stages, as shown in Figure 6. From this the coefficients of the polynomial determining the location of the transmission poles were evaluated. As each adjustable circuit parameter appears in just one of these sections, the parameters  $\partial e_i / \partial p_j$  could also be determined by the same method.

#### 4 Experimental results

The test vehicle for the method described in the previous sections was a filter with a centre frequency of 15 MHz, a 1% fractional bandwidth, and a shape factor to 70 dB of 1.33. The basic design chosen was an elliptic characteristic, C0825b 4805, which in principle permitted a fairly easy realization with eight crystals.

A trial filter was constructed using the ideal equal motional inductance design with no pre-distortion, and the experimental result is shown in Figure 7. As expected this filter possessed an essentially symmetric characteristic, but the pass-band was considerably rounded, and the loss in 1 dB bandwidth was between 30 and 40 kHz.

Using the same elliptic characteristic an optimized design was then developed. It was found that a full correction for the specified coil losses was only possible if the design insertion loss was above a certain critical value; in this case it was necessary to specify an insertion loss of over 12 dB. It is also normally necessary to start the optimization from an ideal design with a loss close to the final value required. Therefore, crudely speaking, it is only possible to correct a rounded filter response by pushing down the centre of the passband, not by pulling up the corners. In practice the insertion loss is always higher than this design figure because losses in the end coils are not taken into account; as far as the filter is concerned these losses appear as part of the terminations and do not affect passband shape. Responses of the fully optimized filter are shown in Figures 8 and 9. The predistortion successfully restored the 1 dB bandwidth to its ideal design value, and there was no degradation in shape factor. The crystals used in the filter were designed so that no unwanted responses would appear in the passband, and careful selection was employed to minimize their effects in the stopband. The main discrepancy with the ideal design was the passband ripple, which was 0.8 dB rather than 0.3 dB. Extensive circuit analysis failed to locate a specific cause for this, and it was attributed to accumulated tolerancing errors throughout the

filter. It was found that careful matching of the motional inductances of crystals within each lattice produced a significant improvement in passband ripple. Matching between lattices is unnecessary as any differences are automatically corrected during filter alignment. All the coils employed were of carefully selected dust-iron type, and were matched with NTC capacitors to provide temperature stability.

## 5 Conclusions

It has been demonstrated that for certain types of crystal filter, simple optimization techniques, practicable even on a desk top computer, can yield excellent results. The method was tested experimentally with a 15 MHz 1% fractional bandwidth design. Due to circuit tolerances some discrepancies still remained, but certain possible trade-offs were observed. In the filter which was constructed the motional inductances of the crystals were of the order of 23 mH, and this high value was a direct consequence of ensuring that no unwanted crystal responses could appear in the passband. However, the effect of allowing some small spurious responses into the passband can be made quite negligible, and if this is permitted a very worthwhile reduction in filter impedance can be made. The effect of losses is to round the passband and also to reduce passband ripple, so if any reduction in bandwidth is permissible, it is probably wise not to optimize for the full losses, but to seek a compromise where some of the losses are used to suppress ripple.

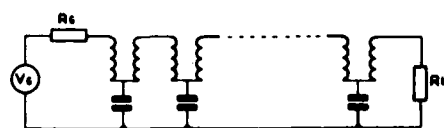
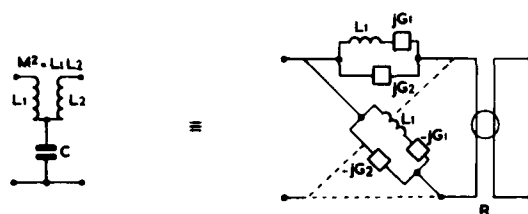


Figure 1. Generalized Low-Pass Filter

## 6 References

- 1 Holt A G J and Gray R L : Bandpass crystal filters by transformation of a low-pass ladder: IEEE Trans Circuit Theory, CT-15, 4, p 492-494 1968
- 2 Stevenson J K : Simple design formulae for third order crystal lattice filters with finite attenuation poles : Int J Electron., 38, 6, p 697-710, 1975
- 3 Temes G C and La Patra J W : Circuit synthesis and design : McGraw-Hill 1977
- 4 Ralston A and Rabinowitz P : A first course in numerical analysis : 2nd Ed., McGraw-Hill 1978
- 5 Saal R : Handbook of Filter Design : AEG-Telefunken, 1979.



$$G_1 = \sqrt{\frac{C}{L_1}}, G_2 = G_1 / (\sqrt{\frac{L_1}{L_2}} - 1)$$

$$R = \sqrt{\frac{L_1}{C}} - \sqrt{\frac{L_2}{C}}$$

Figure 2. Holt-Gray Transformation

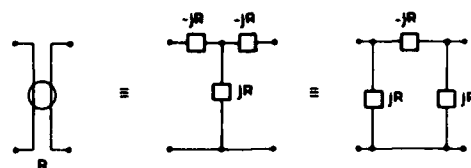


Figure 3. Inverter Equivalences

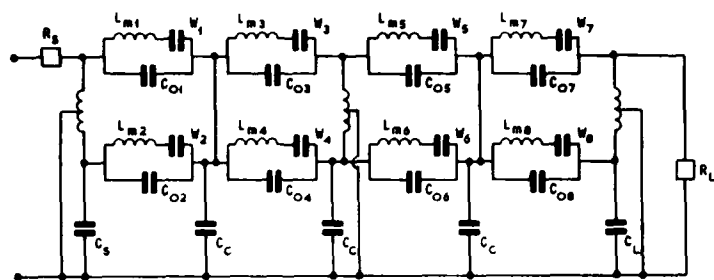


Figure 4. Coil Minimizing Circuit Configuration

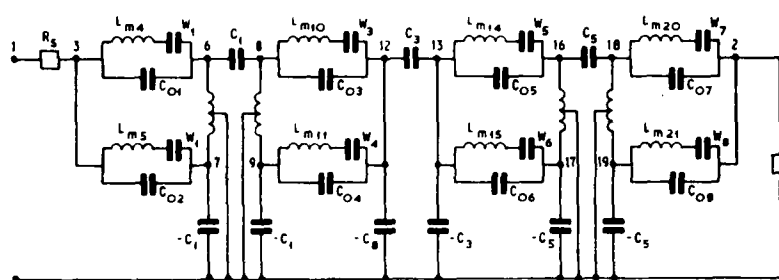


Figure 5. Equal Motional Inductance Circuit Configuration

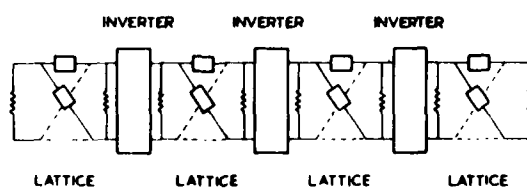


Figure 6. Generalized Lattice Filter with Losses

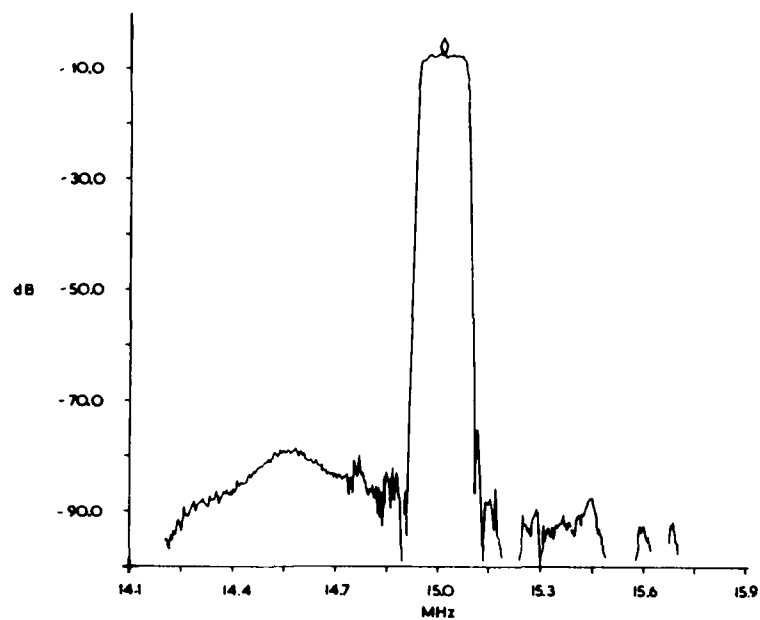


Figure 7. Filter Without Predistortion

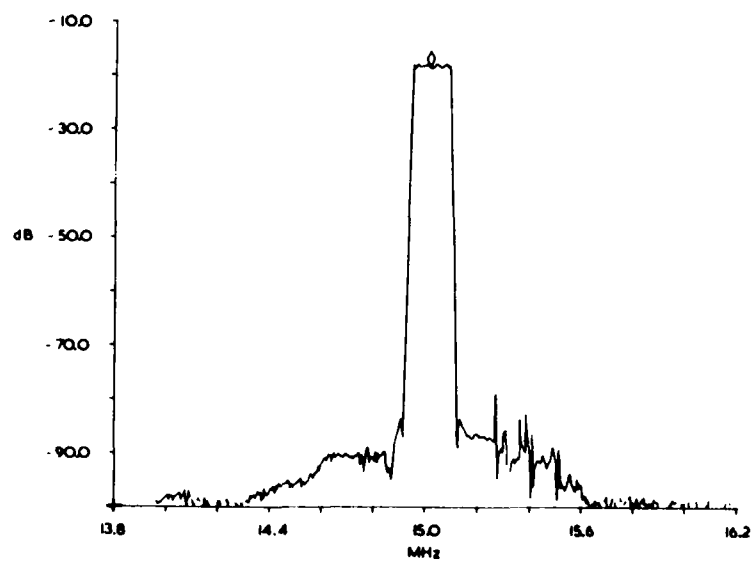


Figure 8. Predistorted Filter

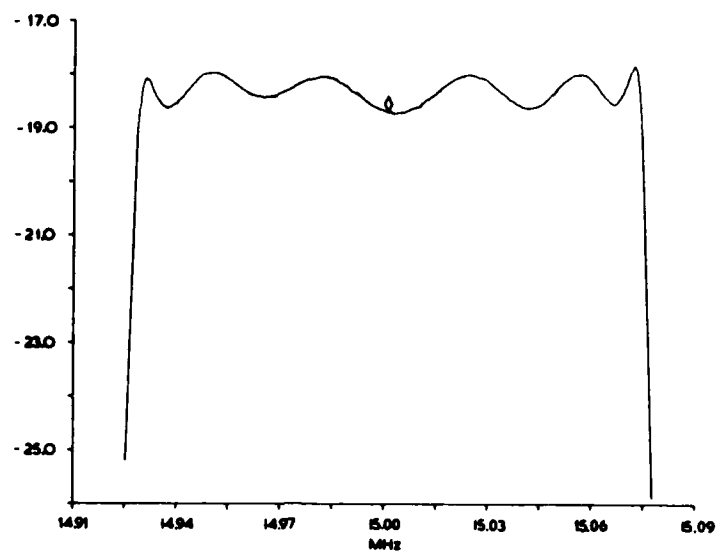


Figure 9. Predistorted Filter

## DEVELOPMENTS IN LOW LOSS, LOW RIPPLE SAW FILTERS

K. H. Yen, K. F. Lau, R. B. Stokes,  
A. M. Kong and R. S. Kagiwada

TRW Electronic Systems Group  
Redondo Beach, California

AD P001549

Abstract

SAW filters are often required by systems to possess low loss, low passband ripple and high out-of-band rejection properties simultaneously. This paper describes two recent developments in the design of such low loss filters.

In the first approach, three bidirectional transducers are arranged colinearly to eliminate half of the 6 dB bidirectional loss. The unique feature of this design lies in the use of centrosymmetric transducers for broadband triple transit suppression. Two design examples are reported. The filter fractional bandwidths range from 1.8% to 10.5%.

For the second approach, a new type of connecting and matching the group type unidirectional transducer (UDT) is described for narrowband filters. In this method, one of the two groups in the UDT is inductively matched to serve as acoustic reflector. Triple transit level of better than -50 dB is achieved for a device of 8 dB loss. The in-band peak-to-peak (p-p) amplitude ripple is less than 0.05 dB.

Introduction

Many systems require surface acoustic wave (SAW) filters which have low insertion loss ( $\leq 8$  dB), low ripple ( $\leq 0.5$  dB) and high out-of-band rejection ( $\geq 35$  dB). Several techniques have been employed to construct filters with these desired properties.<sup>1-4</sup> One approach is to use three bidirectional transducers arranged colinearly to eliminate half of the 6 dB bidirectional losses. With the center transducer receiving equal wave fronts from both directions, the total incident power may be extracted and triple transit echo eliminated.<sup>1</sup> This design offers simplicity and flexibility in device weighting, matching and fabrication, but often suffers from poor performance. The other approach eliminates bidirectional loss altogether by employing unidirectional transducers (UDT).<sup>2-4</sup> These UDT designs require more sophisticated design, fabrication and matching techniques, and have been reported in the literature.

In this paper, new types of filters based on these two basic approaches are reported. For the first approach, the filter is designed with symmetric and antisymmetric transducers for broadband

triple transit cancellation. For the second approach, a hitherto unreported way of connecting group type UDT is employed to achieve maximum triple transit cancellation. Both techniques offer advantages for specific applications.

Centrosymmetric Transducer Design

The design with three bidirectional transducers is the simplest in design and fabrication. As mentioned in the introduction, the design ideally achieves a minimum loss of 3 dB with no triple transit echoes. In reality, the center transducer cannot be perfectly matched over the bandwidth, and triple transit echoes produce passband ripple, which when enhanced by low insertion loss, causes unacceptable filter performance. To achieve broadband triple transit cancellation, the outer transducers can be designed to be identical except that one has symmetric and the other antisymmetric finger configuration with respect to the transducer center line. Such filters retain the advantages of the three-transducer approach while achieving good performances.

The filter configuration is shown schematically in Figure 1. This centrosymmetric transducer design is based on the principle that if the center-to-center separations between the center transducer to outside transducers are equal, the signal received at the symmetric outer transducer will have a 90° phase difference from that received at the antisymmetric transducer. This 90° phase relation is also maintained at all frequencies if the transducers are truly equal but have different symmetry.<sup>5</sup> Triple transit echoes from the transducer pairs therefore differ by 180° and are effectively suppressed.

One narrowband and one wideband filter were designed with the centrosymmetric configuration. Figure 2 shows the frequency response of a narrowband device fabricated on 128° rotated Y-cut LiNbO<sub>3</sub>. In this example, the two outer transducers are source withdrawal Hamming weighted. One has an antisymmetric finger configuration while the other is symmetric. The center transducer is symmetric and apodized, also with Hamming function. The performance of this filter is summarized in Table 1. For this device, only the center transducer is matched. Of the 5.2 dB insertion loss, 3 dB is bidirectional loss. 0.8 dB is due to apodization

loss of the center transducer. The rest is due to mismatch and resistivity losses.

The second example is a wideband device whose response is shown in Figure 3. Table 2 summarizes the device performances. For this device, the outer two transducers were apodized with  $\sin x/x$  function. Again, one has an antisymmetric finger configuration, while the other is symmetric. The center transducer is source withdrawal weighted, also with  $\sin x/x$  function. The slightly higher p-p amplitude ripple of this device is partly due to bulk wave interference. Better results could be obtained if multistrip couplers were incorporated.

To further demonstrate the versatility of the centrosymmetric design, the narrow band filter design was implemented with split finger configuration. Strong third harmonic response is observed. Figure 4 shows the third harmonic response of the narrowband filter fabricated on MDC LiTaO<sub>3</sub>. This response was obtained without any matching elements. The insertion loss is about 9 dB and the passband ripple is only 0.25 dB p-p. The out-of-band rejection of this filter is greater than 55 dB.

#### Group-Type Unidirectional Transducers

The group-type unidirectional transducer is ideal for narrowband filter applications. It can be fabricated with one step photolithographic process similar to conventional bidirectional devices. The matching technique of group-type unidirectional transducer has been discussed in the literature.<sup>6</sup> It requires either a 90° phase shifter or carefully chosen networks. Both transducers in each group-type UDT receive signals at a 90° phase difference.

In a new approach shown schematically in Figure 5, only one-half of the group-type UDT is connected to the electrical source. The other is inductively tuned to serve as resonant acoustic reflector. This concept is similar to that reported by Smith, et al., in one of the earlier papers<sup>7</sup> dealing with resonated acoustic reflectors. The difference is that in the previous case two transducers, each with only one group, are employed. As will be shown by the two examples, excellent triple transit cancellation and unidirectional operation can be achieved with such matching techniques. The matching elements required consist of inductors and capacitors. Size and complexity of the filter are greatly reduced.

Two filters with fractional bandwidth ranging from 0.2 to 0.5 were designed and constructed. Figure 6 shows the response of a filter with center frequency of 97.29 MHz and 3 dB bandwidth of 0.24 MHz. The overall feature of the response of the 0.5 MHz in-band characteristic is shown in Figure 7 at a 1 dB/div scale. The design and performance curves of the two filters are summarized in Tables 3 through 5. Three transducers were used in these designs so that weighting can be easily implemented with the center transducer, while the outside group-type UDT's can be optimized for insertion loss and triple transit suppression.

The long transducers required to weight these narrowband filters also required the use of finger withdrawal weighting instead of apodization to minimize diffraction effects.

#### Conclusion

The centrosymmetric transducer design offers simplicity and flexibility in implementing low loss, low ripple SAW filters. Because of its simplicity in fabrication, higher operating frequency can be achieved compared to the unidirectional approach. With harmonic operation, low loss, low ripple filters above 2 GHz can be constructed. When a high coupling substrate is used, the multistrip coupler UDT approach can also be combined with the centrosymmetric design to further reduce loss while retaining the one step fabrication advantage.

The simplified matching technique for the group-type UDT reduces matching complexity while maintaining excellent performance. This results in potential reduction in filter size, weight, and costs.

#### References

1. M. F. Lewis, "Triple Transit Suppression in Surface Acoustic Wave Devices," *Electronics Letters*, p. 553, 1972.
2. R. C. Rosenfeld, C. S. Hartmann and R. B. Brown, "Low-Loss Unidirectional Acoustic Surface Wave Filters," *Ann. Symp. on Freq. Control*, p. 299, 1974.
3. F. G. Marshall, E. G. S. Paige and A. S. Yoon, "New Unidirectional Transducer and Broadband Reflector of Acoustic Surface Waves," *Electronics Letters*, Vol. 7, p. 638, 1970.
4. K. Yamanouchi, F. M. Nyffeler and K. Shibayama, "Low Insertion Loss Acoustic Surface Wave Filter Using Group-Type Unidirectional Transducers," *IEEE Ultrasonics Symposium Proceedings*, p. 317, 1975.
5. R. I. Murray, R. C. Peach and S. Neylon, "True Quadrature Taps for SAW Delay Lines," *Electron. Letters*, p. 631, 1978.
6. W. S. Ishak, W. R. Shreve, "Low-Loss, Low Ripple SAW Filters Using Group-Type Unidirectional Transducers," *IEEE Ultrasonics Symposium Proceedings*, p. 7, 1981.
7. W. R. Smith, H. M. Gerard, G. H. Collins, T. M. Reeder and H. J. Shaw, "Design of Surface Wave Delay Lines with Interdigital Transducers," *IEEE Trans. MTT-17*, p. 865, 1969.

Table 1. Performance of narrowband filter with centrosymmetric transducer design

Center Frequency	92 MHz
3 dB Bandwidth	1.7 MHz
Substrate	128° Rotated Y-Cut $\text{LiNbO}_3$ , X-Propagation
Insertion Loss	5.2 dB
In-Band Ripple (p-p)	0.3 dB
Out-of-Band Rejection	55 dB
Triple Transit Level	- 35 dB

Table 2. Performance of wideband filter with centrosymmetric transducer design

Center Frequency	162 MHz
3 dB Bandwidth	17 MHz
Substrate	128° Rotated Y-Cut $\text{LiNbO}_3$ , X-Propagation
Insertion Loss	6.5 dB
In-Band Ripple (p-p)	0.8 dB
Out-of-Band Rejection	40 dB
Triple Transit Level	- 30 dB

Table 3. Group-Type UDT Design

Center Frequency (MHz)	97.3	92.8
3 dB Bandwidth (MHz)	0.24	0.5
Substrate Orientation	ST Quartz, X-Propagation	
Substrate Dimension (in.)	$3.1 \times 0.25 \times 0.025$	$1.7 \times 0.2 \times 0.025$
Finger Configuration	Split 4-Fingers Per Period	
Center Transducer Weighting	Source Withdrawal, $\sin^2 x/x$ Function	
Group-Type Transducer		
No. of Finger Pairs Per Section	2+3	3+2
No. of Sections	20	17

Table 4. Performance of the 0.24 MHz bandwidth filter

Center Frequency	97.29 MHz
Fractional Bandwidth	0.25
Insertion Loss	9 dB
Amplitude Ripple (p-p)	0.05 dB
Shape Factor (40 dB/3 dB)	2:1
Sidelobe Rejection	> 35 dB
Triple Transit Level	- 50 dB

Table 5. Performance of the 0.5 MHz bandwidth filter

Center Frequency	92.8 MHz
Fractional Bandwidth	0.54
Insertion Loss	8 dB
Amplitude Ripple (p-p)	< 0.05 dB
Shape Factor (40 dB/3 dB)	1.6:1
Sidelobe Rejection	> 30 dB
Triple Transit Level	< - 50 dB

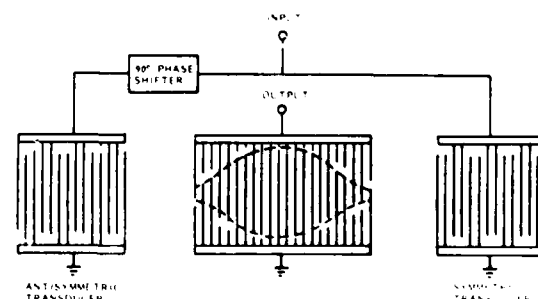


Figure 1. Schematic configuration of the centrosymmetric transducer design

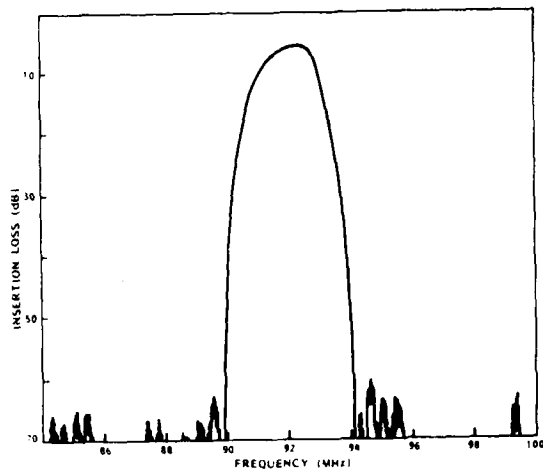


Figure 2. Performance of low loss SAW filter on  $128^\circ$  rotated Y-cut, X-propagating  $\text{LiNbO}_3$

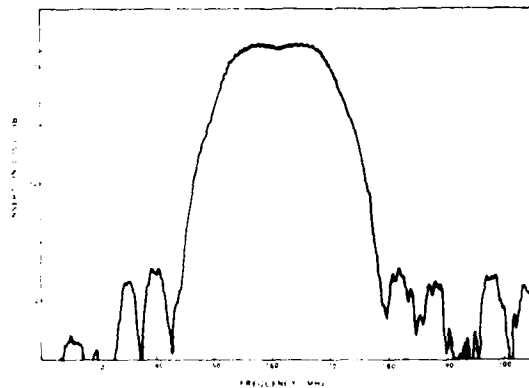


Figure 3. Performance of wideband filter on  $128^\circ$  rotated Y-cut  $\text{LiNbO}_3$

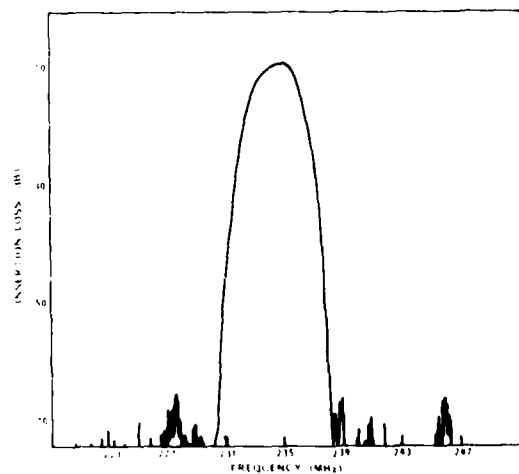


Figure 4. Third harmonic response of low loss SAW filter on MDC  $\text{LiTaO}_3$

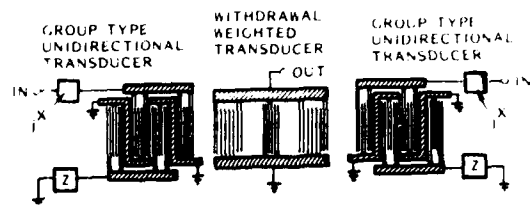


Figure 5. Group-type unidirectional transducers with simplified matching network

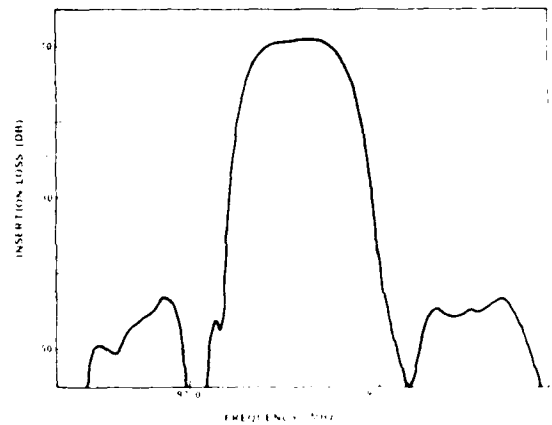


Figure 6. Frequency response of 0.24 MHz bandwidth SAW filter employing group type UDT

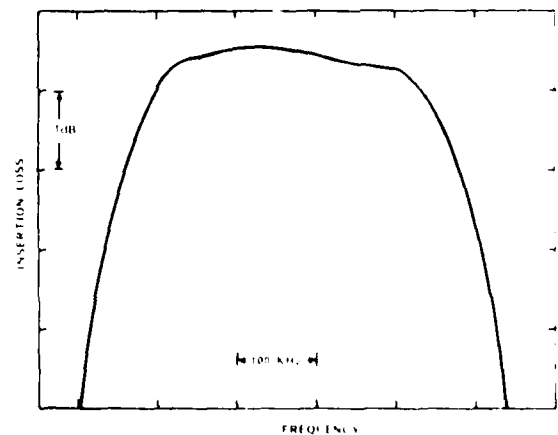


Figure 7. In-band ripple characteristic of 0.5 MHz bandwidth filter employing group-type UDT

AD P001550

## MULTIPOLE SAW RESONATOR FILTERS \*

William J. Tanski \*\*

Sperry Research Center  
Sudbury MA 01776

## ABSTRACT

We are engaged in the development of VHF multipole SAW resonator filters which are required to have high rejection levels ( $> 60$  dB), filter  $Q$  values in the range of 4000, and low shape factors ( $< 4:1$ ). Here we present the salient aspects of filter design and fabrication, and discuss experimental results. Our procedure utilizes the synthesis techniques developed by Matthaei plus detailed equivalent circuit analysis calculations to finalize each design. Inter-cavity coupling is by transducers or reflectors and the filter design is synchronous, that is; each cavity is set to resonate at the same frequency when coupled. Theoretical and experimental results are presented for several multipole configurations demonstrating the efficacy of the design and fabrication techniques. For example, six-pole filters have been produced with 7 dB loss, 55 dB rejection, and an acceptable passband shape.

## Introduction

The purpose of this work has been to produce high performance multipole SAW resonator filters requiring up to six resonant cavities (or poles) to attain the required shape factors. The filter requirements are listed in Table I, and reference to standard filter texts<sup>1,2</sup> shows that a minimum of three poles is required for the Type I design and five for the Type II filter. Since three- and five-pole designs only barely meet the filter requirements, we have implemented four- and six-pole designs, respectively. Single-pole SAW resonators are well developed<sup>3,4</sup> and two multiple-pole SAW resonator synthesis techniques<sup>5,6</sup> have been proposed. In our work we have developed additional techniques for cavity and coupler trimming, the use of unloaded reflection coefficient measurements, and the implementation of analysis techniques to realize synchronously tuned multipole SAW filters. These techniques and the results attained are discussed.

\* This work is supported by the U.S. Naval Research Laboratory under Contract No. N00014-81-C-2066.

Table I

## Required Frequency Response Characteristics

	Type I	Type II
Center Frequency ( $F_0$ )	150 MHz	217 MHz
3 dB Filter Bandwidth ( $\Delta F_3$ )	37 kHz (min)	40 kHz
3:60 dB Shape Factor Response	1:8.1	1:4
Insertion Loss - Max	6 dB	10 dB
Out-of-Band Rejection	60 dB min	60 dB
Minimum No. of Poles	3	5

## Filter Design

We are currently using the filter synthesis technique developed by Matthaei<sup>5</sup> as we have found that his procedures permit rapid and reasonably accurate designs. Matthaei's<sup>5</sup> use of a low-pass (infinite-loss) low-pass prototype results in some rounding of the filter passband edges when applied to the finite-loss structures we must work with. The finite-loss decreases the accuracy of the design somewhat, but we have not found this to be a significant limitation in the VHF range. Following synthesis we use an equivalent circuit model, based on the closed form computational techniques discussed by Chen,<sup>7</sup> to check the accuracy of the design parameters and to make the small adjustments which we find are normally required to yield the passband response desired. Further, our analysis technique allows us to compute the frequencies to which each cavity must be tuned, in isolation, such that synchronous operation is achieved when all cavities are coupled. For two-port, single-pole structures we calculate the transmission resonance frequency and, for two-port, two-pole acoustically-coupled sections, we calculate the electrical reflection coefficient resonance frequency for each cavity with the opposite cavity unloaded.

\*\* Present address: Schlumberger-Dell Research Center, Ridgefield CT 06877.

During fabrication we then set each cavity to the calculated frequency. The transmission response of each two-pole acoustically-coupled pair is also calculated to ascertain the shape of this response. This shape is then reproduced as accurately as possible during fabrication by trimming the cavity resonance frequencies<sup>8</sup> and by adjusting the reflector coupling strength using a selective etching technique.

Our designs utilize transducer and reflector coupling only since these allow us to achieve the range of coupling values required while suppressing unwanted responses. Further the technology for producing the devices with these coupling techniques is available and these techniques have no adverse thermal or aging effects. In Fig. 1 we show the design of a four-pole Type I filter where we note the use of split-symmetric transducers in the single-pole sections. These transducers were used to allow for larger transducers to attain larger coupling values without causing additional longitudinal mode responses. Two sets of transducer coupled stages were required to theoretically attain the required 60 dB rejection though two sets of acoustically coupled pair would have been more efficient spacewise. We note further that the transducer couplers were purposely made larger than required to allow us to use variable de-coupling capacitors ( $C_{12}$  and  $C_{34}$  on Fig. 1) to compensate for various errors. The computed response for the design of Fig. 1 is shown in Fig. 2 where we note that the theoretical rejection of 60 dB just meets the required value. Also, the passband response of Fig. 2 is not a Tchebyscheff since there is only one (0.5 dB) dip. The theoretical loss is only 2.1 dB (in vacuum), however, and the shape factor is lower than required.

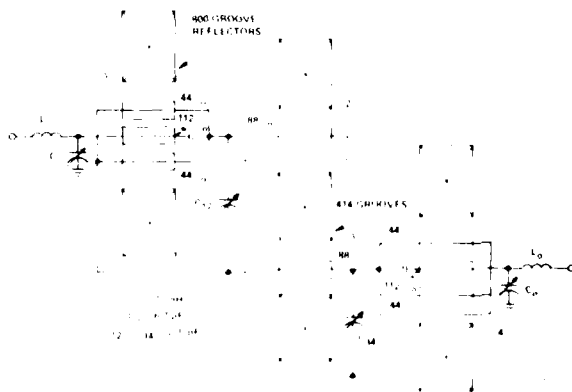


Fig. 1. Schematic showing the four-pole configuration with component values given for a Type I filter design.

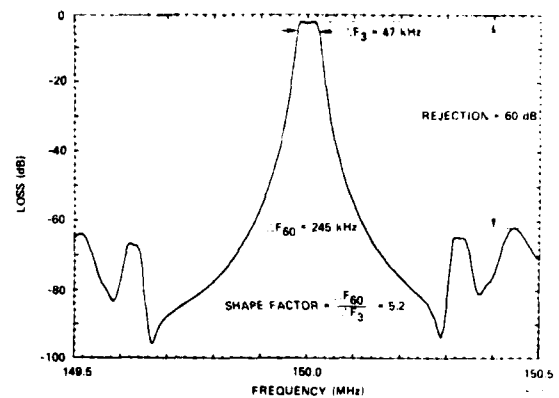


Fig. 2. Computed frequency response for the Type I filter design of Fig. 1. The minimum loss is 2.1 dB.

The design of a six-pole filter is shown in Fig. 3 where we utilize three acoustically coupled sections coupled together using transducer couplers, and the variable de-coupling capacitors. The computed response is shown in Fig. 4 where we note the rejection level of 74 dB and an approximate Butterworth passband. The 3 dB bandwidth for Fig. 4 is 48 kHz, with a loss of 4.3 dB and a shape factor of 3.5, all well within specification.

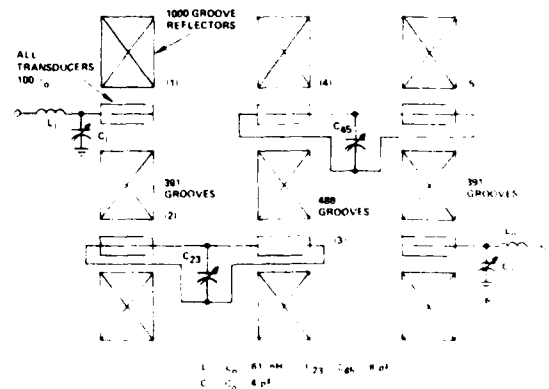


Fig. 3. Schematic showing the six-pole configuration with component values given for a Type II filter design.

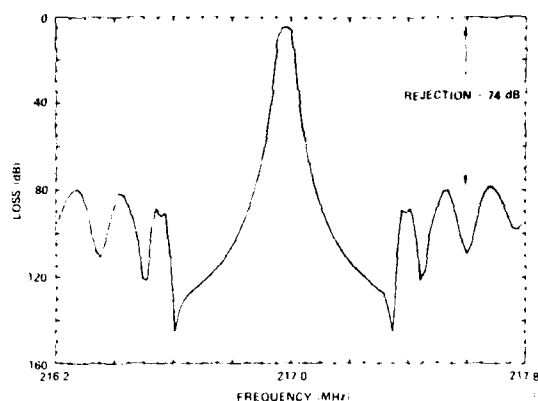


Fig. 4. Computed frequency response for the Type II filter design of Fig. 3. The minimum loss is 4.3 dB and the 3 dB bandwidth is 48 kHz with a 3/60 dB shape factor of 1:3.5.

#### Fabrication

We are using the recessed-aluminum-transducer/etched-groove-reflector configuration for these filters and the basic fabrication procedures are as discussed previously.<sup>3</sup> Important new aspects of this work are the use of a selective etching technique<sup>8</sup> to trim the cavity resonance frequency of each cavity to the required calculated value, the use of selective etching to adjust the coupling reflectors, and the techniques for measuring, using probes, the transducer electrical parameters. Most of our devices have been fabricated monolithically; that is, all filter sections (defined to be a two-port, single-pole or a two-port, two-pole resonant system) are placed on the same quartz substrate. Each substrate was then mounted on a cold weld sealable header and sealed in vacuum. However, we have found that it is very difficult to reduce the leakage (electromagnetic feedthrough) to acceptable levels using the monolithic scheme, so we have also placed each section in a separate header and assembled the transducers on a board. The board also has the matching networks and coupling components mounted so as to be easily changed to achieve the optimum values.

#### Experimental Results

The response of a four-pole Type I filter, fabricated monolithically, is shown in Fig. 5. The insertion loss of 6 dB just meets specification but is significantly larger than the computed value of 2.1 dB. The 3 dB bandwidth of 45 kHz is quite close to the design value of 47 kHz, but the rejection is only 40 dB compared to 60 dB computed. The passband has a ripple of about 1 dB peak-to-peak compared to an expected value of 0.5 dB. Several other devices of this type were fabricated and the

results are similar: i.e., the desired bandwidths and center frequency were generally attained but the rejection level and passband shape were not. For these four-pole devices the rejection was generally 15 to 20 dB poorer than predicted, the losses were greater and the passband did not conform to the Tchebyscheff type response.

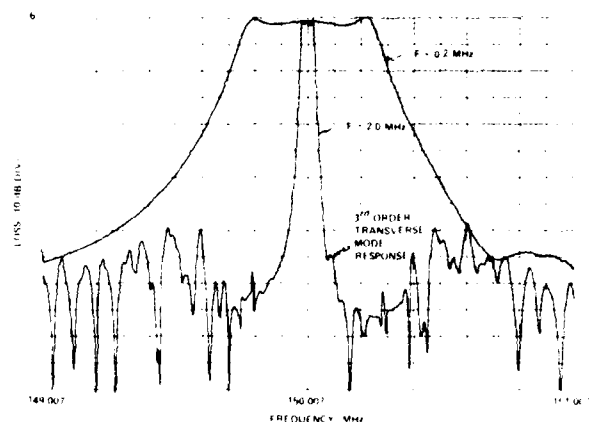


Fig. 5. Frequency response of a Type I filter approximately per the design of Fig. 1. The 3 dB bandwidth is 45 kHz and the filter was monolithic.

The response of a six-pole Type II filter, also fabricated monolithically is given in Fig. 6. For this device the rejection level is close to 50 dB which is also the approximate leakage level. The passband is not a Butterworth, but the loss level of 5.7 dB is not significantly greater than the computed value of 4.3 dB. The response of another six-pole filter, which was not fabricated monolithically, is given in Fig. 7 and we see a significant reduction in leakage, an improvement in rejection to about 56 dB, and a smoother passband shape. For this filter we were able to optimize the coupling elements, which were inductors due to an increase in parasitic coupling capacitance, something which is much more difficult to do in the monolithic configuration.

The results shown above are very encouraging in that, to our knowledge, we have produced the first six-pole SAW resonator filter made anywhere, and that the performance of these devices comes relatively close to meeting difficult specifications. However, a significant amount of work remains to be done to produce system-quality devices meeting all the specifications. First we must learn to accurately shape the passband. For most applications, however, a shape which only approximates the theoretical passband is acceptable so the problem here becomes one of

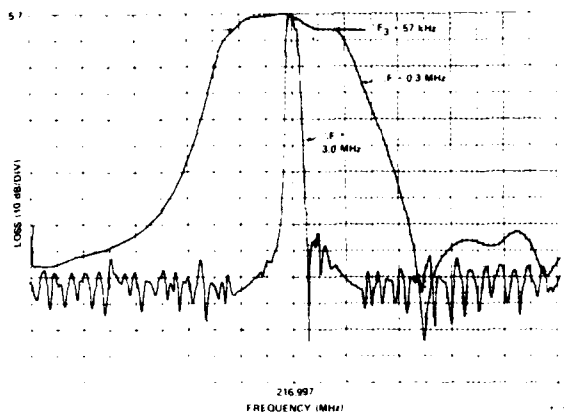


Fig. 6. Frequency response of a Type II filter fabricated in monolithic form approximately per the design of Fig. 3.

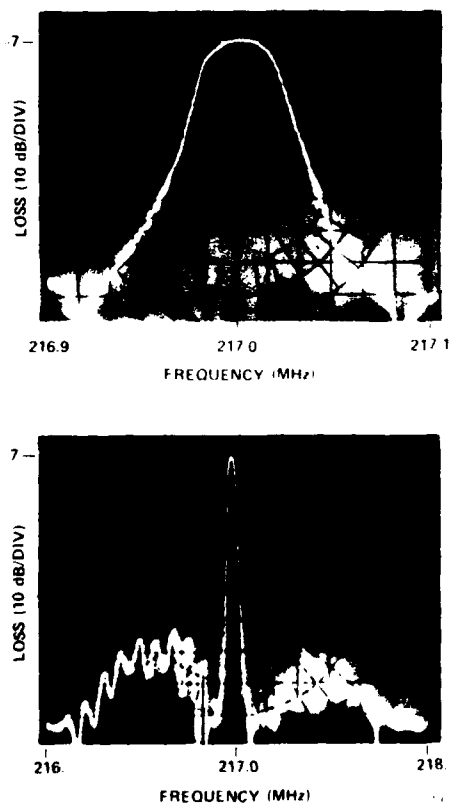


Fig. 7. Frequency response of a Type II filter. The fabrication was non-monolithic; that is, each filter section was in a separate header. Also coupling inductors ( $\approx 200$  nH) were used to couple cavities 2-3 and 4-5.

consistently attaining an acceptable approximation. Increasing the rejection level is very important and we believe that variations in loss and symmetry within the various filter sections contribute to the increase in sidelobe levels. Improvement in the fabrication procedures may be of benefit here. Another approach may be to design for a rejection level of something like 25 dB greater than desired to allow for the degradation we experience. We are investigating the use of weighted reflectors<sup>9</sup> to aid in reducing the sidelobe levels. Weighted reflectors have been of considerable value in reducing sidelobes in single-pole resonators, but this type reflector has not been utilized in multipole reflector-coupled devices thus far. We expect that a combination of fabrication and design changes will allow us to consistently exceed 60 dB rejection. The leakage level is largely a function of the arrangement of the various components, and the experimental results shown above demonstrate that the non-monolithic scheme is most successful in this regard. The non-monolithic scheme also allows one to carefully select the sections to be assembled into a filter. Thus only those sections with low loss, good rejection, and exactly the required resonance frequencies might be assembled to yield the very best possible performance. This is not possible with the monolithic approach since all sections are made at the same time on the substrate and we must accept whatever we get or discard the entire device.

#### Summary and Conclusions

We have shown that we can accurately synthesize multipole SAW resonator filter designs and, through analysis, obtain all the information required to fabricate synchronously tuned filters. Experimental results have been presented for four- and six-pole filters demonstrating the effectiveness of our procedures. Problems remain in accurately shaping the passband response, reducing the leakage level, and improving the out-of-band rejection. We have discussed approaches to solving these problems which are basically due to second order effects. These approaches include use of the non-monolithic scheme, design for higher rejection levels including the use of weighted reflectors, and more stringent fabrication procedures.

#### Acknowledgments

The author wishes to thank Mr. Doan Gunes for his helpful discussions in the course of this work and Ms. Jo Ann Columbus for fabricating the devices discussed herein.

#### References

1. A. I. Zvrev, "Handbook of Filter Synthesis." J. Wiley and Sons, New York (1967).

2. G. L. Matthaei, L. Young, and E. Jones, "Microwave Filters, Impedance Matching Networks, and Coupling Structures," McGraw Hill, New York (1964).
3. W. J. Tanski, "Surface acoustic wave resonators on quartz," IEEE Trans. Sonics and Ultrasonics, Vol. SU-26, pp. 93-104, March 1979.
4. W. J. Tanski, "UHF SAW resonators and applications," Proc. 34th Annual Frequency Control Symposium, U.S. Army Electronics Command, Ft. Monmouth, NJ, pp. 278-285. Copies available from Electronic Ind. Assoc., 2001 Eye St., N.W., Washington, DC 20006.
5. G. L. Matthaei, E. B. Savage, and F. Barman, "Synthesis of acoustic-surface-wave-resonator filters using any of various coupling mechanisms," IEEE Trans. Sonics and Ultrasonics, Vol. SU-25, pp. 72-84, March 1978.
6. R. L. Rosenberg and L. A. Coldren, "Scattering analysis and design of SAW resonator filters," IEEE Trans. Sonics and Ultrasonics, Vol. SU-26, pp. 205-230, May 1979.
7. M. E. Field, R. C. Ho, and C. L. Chen, "Surface acoustic wave grating reflectors," Proc. 1975 Ultrasonics Symposium, pp. 430-433 (1975).
8. W. J. Tanski, "Surface acoustic wave frequency trimming of resonant and traveling wave devices on quartz," Appl. Phys. Letters, Vol. 39, pp. 40-42, July 1981.
9. W. J. Tanski, "S.A.W. device reflectors weighted by a combination of withdrawn and segmented lines," Electronics Letters, Vol. 16, pp. 793-794, 1980.

AD P001551

# 36th Annual Frequency Control Symposium - 1982

## RECENT ADVANCES IN UHF CRYSTAL FILTERS

Bertrand d'Albaret and Pascal Siffert

Compagnie d'Electronique et de Piézo-Electricité  
95100 - ARGENTEUIL - FRANCE -

### Summary

Due to the new etching technology, the Argon Ion beam technique, CEPE is now able to provide piezoelectric devices with an enlarged useful bandwidth by the use of resonators operating either in the fundamental mode or in a low overtone mode ( i.e. 600 MHz 3rd overtone ).

The results issued from several applications, already used in new-generation Telecommunication systems, exhibit behaviour similar to that observed at lower frequencies ( i.e. 30 MHz to 50 MHz ) with conventional resonator lapping technologies.

### Introduction

During long period traditional lapping technologies allowed the production of piezoelectric resonators oscillating in the fundamental mode up to 30 MHz. Improvements on the grinding machines enabled frequencies up to 50 MHz.

The ion-etching technology introduced by M. BERTE in 1977, (31st Symposium on Frequency Control) has pushed back the fundamental frequency limit to about 500 MHz for AT cut quartz. Little has been published in this domain due to intensive laboratory work on prototypes.

At the occasion of the 35th Symposium L. BIDART and J. CHAUVIN presented a paper devoted to the application of ion-etched resonators to oscillators.

In this paper we present new products concerning filters composed of quartz resonators as well as using novel piezoelectric materials such as Lithium Tantalate.

### State of the Art

A piezoelectric resonator is commonly represented under its simplified scheme ( Fig.1 ) where L, C, R, are motional elements i.e. they transcribe mechanical vibrations of the crystal into the electrical domain.

$C_0$  is a physical capacitor related to the inter-electrode dielectric. The resonator has 2 noteworthy frequencies ;

$$F_s = \frac{1}{2\pi\sqrt{LC}}$$

$$F_p = \frac{1}{2\pi\sqrt{L\frac{C_0}{C_0+C}}}$$

( the transmission and impedance response curves are represented in Fig. 2, Fig. 3 ).

One usually calls the useful bandwidth of a resonator :  $\Delta F$ , the difference between the resonant and anti-resonant frequencies.

An approximation leads to an expression for the useful relative bandwidth :

$$\frac{\Delta F}{F_s} = \frac{C}{2C_0}$$

In fact  $\Delta F$  has the order of magnitude of the maximum bandwidth able to be produced in a filter and this value is close to the maximum tuning range of a VCXO.

When used in an overtone mode the maximum relative bandwidth is divided by the square of the overtone rank. One easily notices that wideband piezoelectric devices are limited by the maximum frequency achievable in the fundamental mode.

### Ion-Etching

The ion-etching technology is based on the use of a 50  $\mu$ m thick blank.

The wafer is eroded in its center by an Argon ion beam. If the attack angle is correct the tub bottom preserves a flatness parallelism and a surface state close to the one it had before etching. The principle is explained on Fig. 4.

Electrodes are deposited on the resonator. The resonator behaves as if the wafer thickness were that of the central part, i.e. rigidity and solidity are of the order of magnitude of the resonator having the thickness of the periphery ( Fig. 5 ).

#### Offered possibilities to Filters designed with ion-etched resonators

Let us refer to the well known chart representing the useful relative bandwidth versus the frequency but limited to piezoelectric devices (Fig. 10).

With conventional technology as concerns lithium tantalate we have a limit of 10% relative bandwidth at 50 MHz.

On the other hand, quartz that is used in fundamental and overtone modes exhibits a definite number of steps which we shall explain :

1% up to 50 MHz maximum of fundamental mode  
1.0% up to 150 MHz maximum of 3rd overtone  
 $3 \times 10^{-2}$  up to 200 MHz maximum of 5th overtone

Introduction of ion-etched resonators enables the extension of the chart up to :

300 MHz for lithium tantalate (fundamental only)  
400 MHz for quartz in fundamental  
Above 300 MHz in 3rd overtone mode operation.

It is clear that above 200 MHz the other components of the filter have to be specially designed with technologies similar to those employed in MHE (i.e. strip line...).

As an example, we shall give in table 7 some figures of motional elements characterising the resonator at different frequencies in the fundamental mode.

One may notice that these figures are compatible with those produced at lower frequencies.

We propose to analyse some filters produced either with quartz resonators or with lithium tantalate resonators operating in bulkwave.

#### Quartz Filters

##### e.g. 1. Switchable I.F. 70 MHz Filter

The specification implies the design of 2 switchable filters operable for 30 or 50 KHz channel transmission.

30 KHz channel spacing :  $F_0 = 70$  MHz  
6 dB PBW  $\pm 12$  KHz  
55 dB ABW  $\pm 30$  KHz

50 KHz channel spacing :  $F_0 = 70$  MHz  
6 dB PBW  $\pm 24$  KHz  
55 dB ABW  $\pm 50$  KHz

These 2 filters are encapsulated in the same package. Their response curves are given in Fig. 9, Fig. 10 b).

It is interesting to notice the low insertion loss of the order of magnitude of 1.4 and 3 dB and the absence of spurious resonances.

In addition, the characteristic impedance level inside the filter is about 10 ohms per KHz of BW. This confers a relatively low sensitivity to coil variations in the temperature range.

##### e.g. 2. 93 MHz 1 pole Filter

This filter is used for the recuperation of the rhythm frequency in a digital telephone repeater (speed 140 Mbit). The coding implies the center frequency at 93.944 MHz.

3 dB PBW  $\geq \pm 20$  KHz  
30 dB ABW  $\leq \pm 1$  MHz

If the filter had been designed with 3rd overtone resonators, 2 of them would have been necessary.

Only 1 resonator operating in the fundamental mode is sufficient to meet the specification.

Furthermore, the characteristic impedance level in the filter is low and as a consequence, the influence of the differential transformer is decreased. The spurious resonances are rejected to about 1 Mhz off the central frequency.

In addition, in order to preserve the phase coherence of all the repeaters, all the filter phases at the central frequency must be trimmed with a precision of  $10^\circ$  and a maximum drift of  $\pm 5^\circ$  is tolerated in the temperature range  $+10, +50$  (Fig. 11, Fig. 12).

##### e.g. 3. 102.5 MHz 4 pole Filter

A picture of this filter is represented Fig. 12b.

This filter is designed to be placed in the 1st I.F. of a receiver.

$F_0$  central frequency 102.5 MHz  
3 dB PBW  $\geq \pm 60$  KHz  
50 dB ABW  $\leq \pm 120$  KHz

This 4th order filter has been synthesized using effective parameter theory. It is a Tchebyshev polynomial filter with a 0.1 dB ripple.

One may notice that the actual response curve is very close to the theoretical one and that the insertion loss is very low : 2.5 dB (Fig. 13, Fig. 14).

##### e.g. 4. 169 MHz 2 pole Filter

This filter is proposed to recuperate the rhythm frequency in fibre optic transmission. Typical values are given below :

$F_0$  central frequency 169 MHz  
3 dB PBW  $\geq \pm 50$  KHz  
50 dB ABW  $\leq \pm 1$  MHz  
out of band rejection : 40 dB over  $\pm 150$  MHz

This filter has been designed in the fundamental mode so that a third overtone resonance occurs out of the attenuation bandwidth. ( Response curves are shown in Fig. 15, Fig. 16 ).

e.g. 5. 243 Filter

This filter is proposed for direct detection of the distress channel in air band transmissions.

$F_0$  Central frequency 243 MHz  
 3 dB PBW  $\geq \pm 25$  KHz  
 50 dB ABW  $\leq \pm 150$  KHz

This filter is produced with 4 resonators oscillating in the 3rd overtone. Each resonator has a quality factor superior to 20.000.

The order of magnitude of the motional inductance is 6 mH which confers to the filter characteristic impedance 1.5 Kohm. One can see on the response curves, ( Fig. 17, Fig. 18 ) that the insertion loss is 4.2 dB and that the filter presents an out of band rejection of about 55 dB which is quite correct for a 4 poles transfer function.

It is interesting to notice that coils have been advantageously replaced by striplines deposited on the printed circuit board.

e.g. 6. 3rd overtone 670 MHz Filter

This filter is proposed for the frequency recuperation in telephone repeaters for high speed data transmission.

The filter characteristics are as follows :

$F_0$  Central frequency 670 MHz  
 3 dB PBW  $\geq \pm 100$  KHz  
 30 dB ABW  $\leq \pm 2.5$  MHz

Only one pole is sufficient to achieve the specification ; nevertheless, a phase stability is demanded and the user tolerates a drift of  $\pm 10^\circ$  in the temperature range  $+ 10^\circ\text{C}$ ,  $+ 50^\circ\text{C}$ .

One must realize that at such frequencies the greatest difficulty lies not in the design of the resonator itself, but in the definition and design of the other components.

A high sensitivity to the proximity of conductive material provides a delicate adjustment and of course all the coils are made in stripline technology. ( Fig. 19, Fig. 20 ).

Let us now draw our attention to lithium tantalate filters.

The ion-etching technique can be applied to any piezoelectric material and some results obtained from filters employing lithium tantalate resonators will be proposed.

e.g. 1. 60 MHz 6 pole Bessel Filter

This filter is designed for I.F.F. ( Identification friend or foe ) receiver.

The specifications are as follows :

$F_0$  Central frequency 60 MHz  
 3 dB PBW  $\geq \pm 500$  KHz  
 72 dB ABW  $\leq \pm 4$  MHz

The response curve is remarkably close to the Bessel function filter synthesized with the effective parameter theory. The group delay is constant within  $\pm 5\%$  over 80% of the 3 dB pass-bandwidth. ( Both curves in-band and out-of-band attenuation are represented by Fig. 21, Fig. 22 ).

e.g. 2. 240 MHz 4 pole Lithium tantalate Filter

This filter is to be employed as a 1st I.F.

Characteristics are as follows :

$F_0$  Central frequency 240 MHz  
 3 dB PBW  $\geq \pm 1.5$  MHz  
 40 dB ABW  $\leq \pm 5$  MHz  
 Insertion loss 6 dB.

( Response curves of this filter are shown in Fig. 23, Fig. 24 ).

It seems that a limitation in the fundamental frequency of a lithium tantalate bulk wave resonator occurs just below 300 MHz.

In fact, we encounter some difficulties in the deposition of the electrodes whose diameters are about some ten's of micrometers.

Conclusion

The frequency limit of fundamental AT cut quartz resonators is today approximately 500 MHz.

If, as concerns oscillators, we are able to use overtone mode resonators up to 2 GHz as far as filters are concerned a limit occurs at 600 MHz.

This limit is not due to the resonator itself but to the other components of the filter especially the coils.

The filters that have been produced are used in systems operating under severe environmental conditions.

Resonators manufactured according to this technology have a certain number of advantages, the main ones being :

- low sensitivity to vibrations
- low sensitivity to shock
- the temperature characteristic is that of the original wafer
- low intrinsic characteristic impedance level
- possibility of using low overtone modes.

This technology had nevertheless a great disadvantage : manufacturing cost.

But improvements in the industrial method enable us to achieve lower costs.

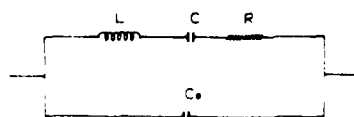
With this technology we can offer the telecommunication engineer a solution to his filtering problems in U.H.F.

CEPE is now engaged in industrial production of filters using fundamental high frequency bulk-wave resonators.

#### Bibliography

- 1 - M. Berté " Acoustic-Bulk-Wave resonators and Filters operating in the fundamental mode at frequencies greater than 100 MHz " Electronics Letters, Vol. 13, 1977, pp.248.
- 2 - L. Bidart and J. Chauvin " Direct Frequency crystal Oscillators " 35th Annual Frequency Control Symposium, May 1981, pp. 365.

SCHEME OF XTAL RESONATOR



$$F_0 = \frac{1}{2\pi\sqrt{LC}}$$

$$F_s = \frac{1}{2\pi\sqrt{L\frac{CC_0}{C+C_0}}}$$

$$F_s - F_0 = \Delta F$$

$$K = \sqrt{\frac{2\Delta F}{F_s}} = \sqrt{\frac{C}{C_0}}$$

$$\text{Relative Bw} = \frac{\Delta F}{F_s} = \frac{C}{2C_0}$$

Figure 1.

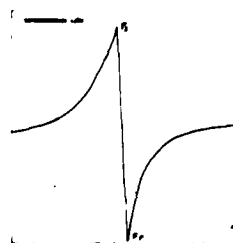


Figure 2.

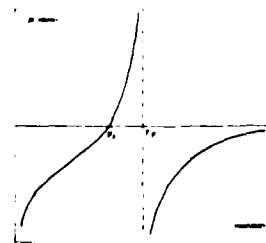


Figure 3.

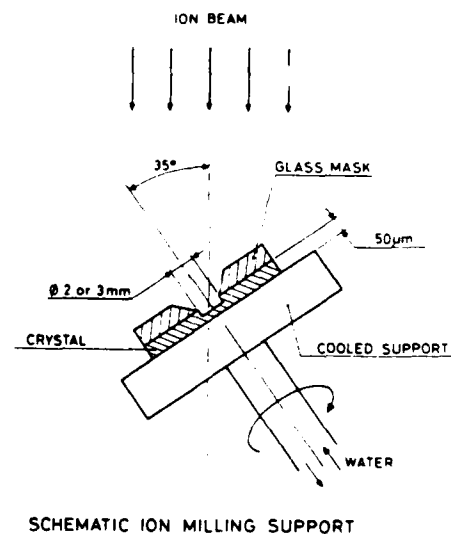


Figure 4.

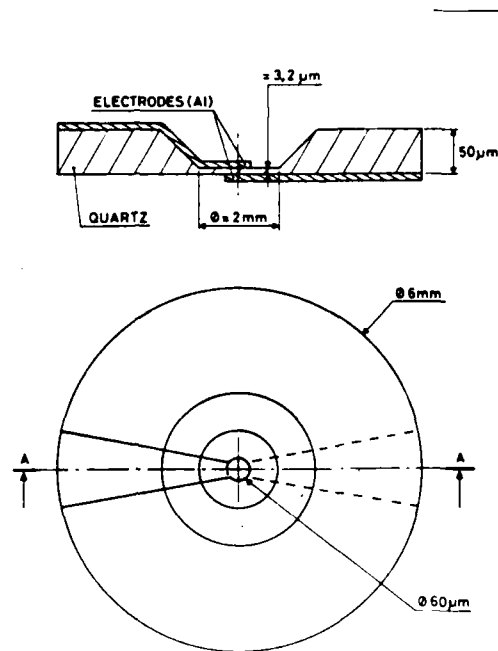


Figure 5.

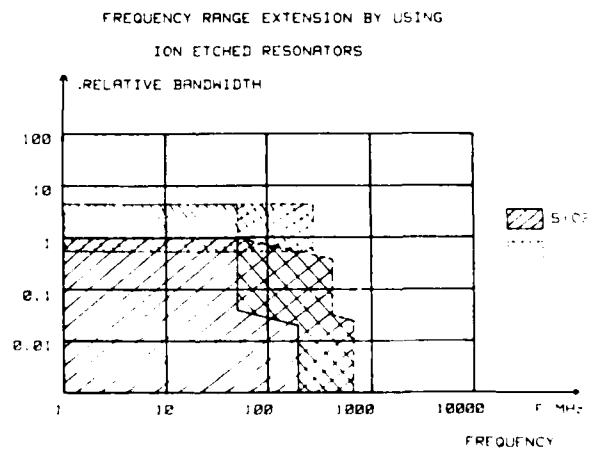


Figure 6.

- MOTIONAL ELEMENTS  
ORDER OF MAGNITUDE -

FREQ.	75 Mhz		100 Mhz		200 Mhz		400 Mhz	
MAT.	QUARTZ	LiTaO3	QUARTZ	LiTaO3	QUARTZ	LiTaO3	QUARTZ	LiTaO3
L	3 mH	60 uH	2 mH	40 uH	1.5 mH	20 uH	.8 mH	
Q	25000	1200	20000	1000	10000	500	5000	

Figure 7.

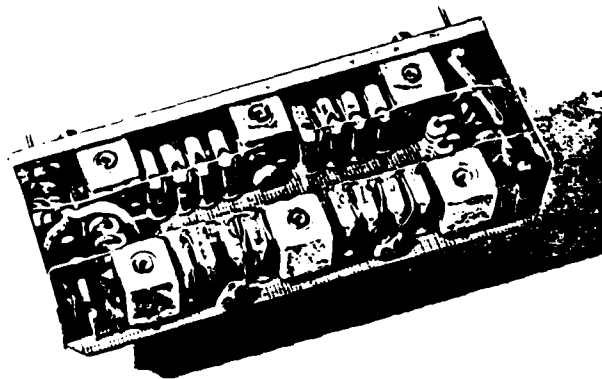


Figure 8.

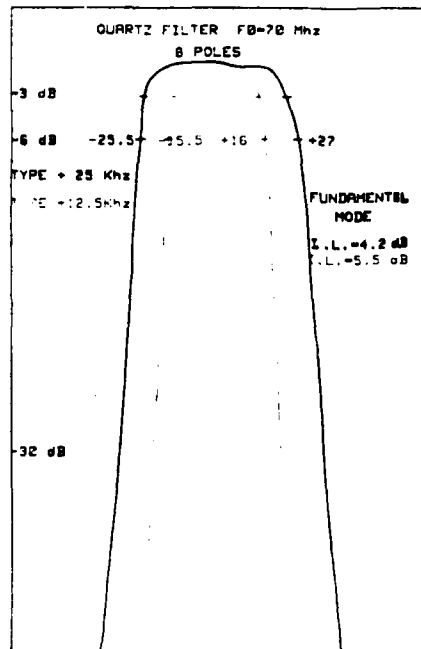


Figure 9.

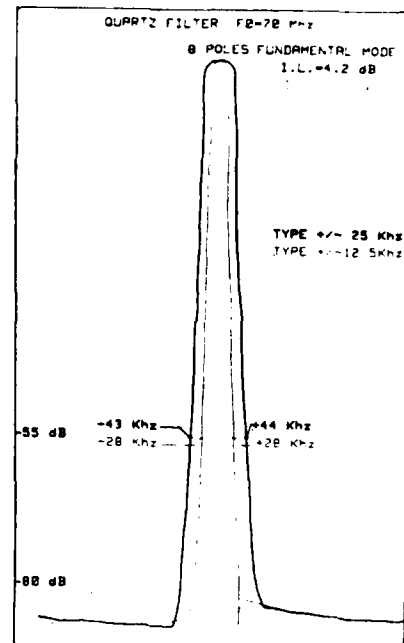


Figure 10.

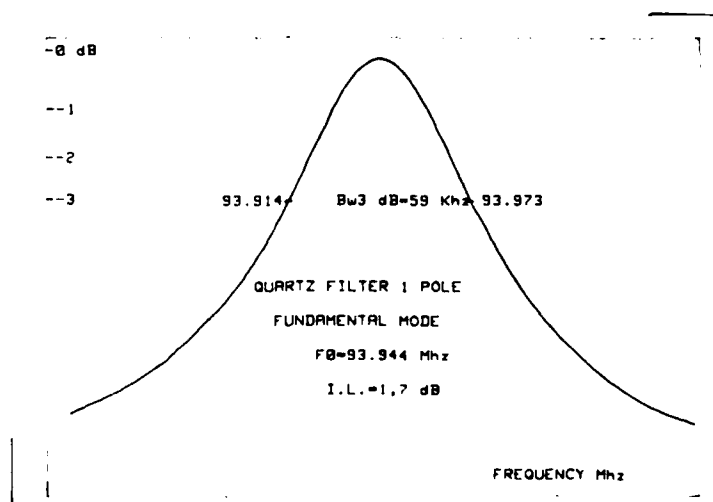


Figure 11.

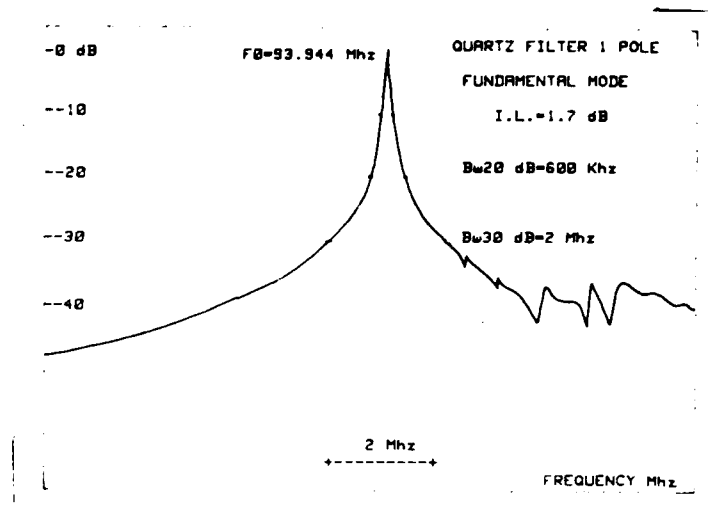


Figure 12.

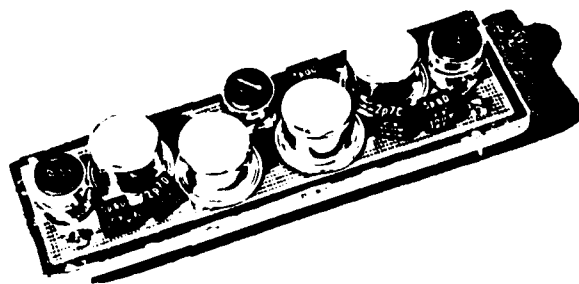


Figure 12 b.

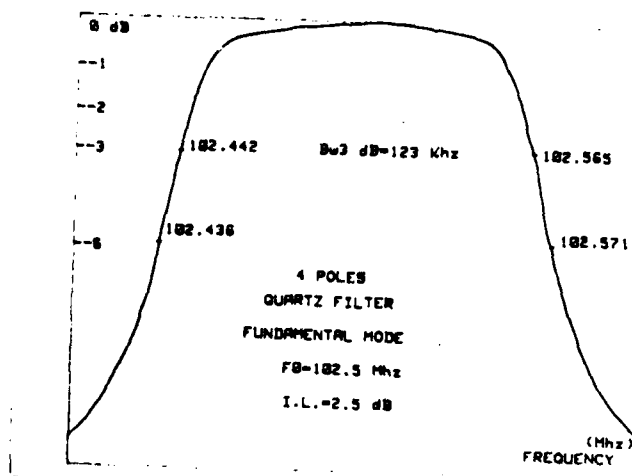


Figure 13.

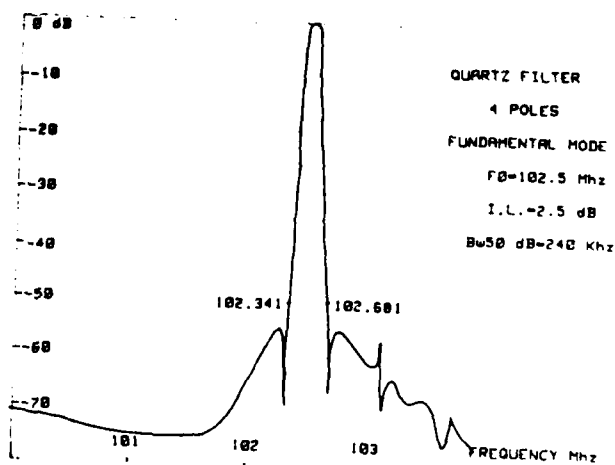


Figure 14.

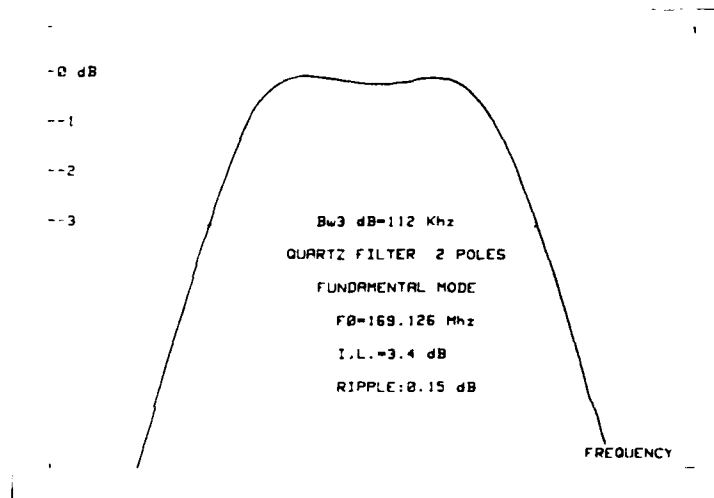


Figure 15.

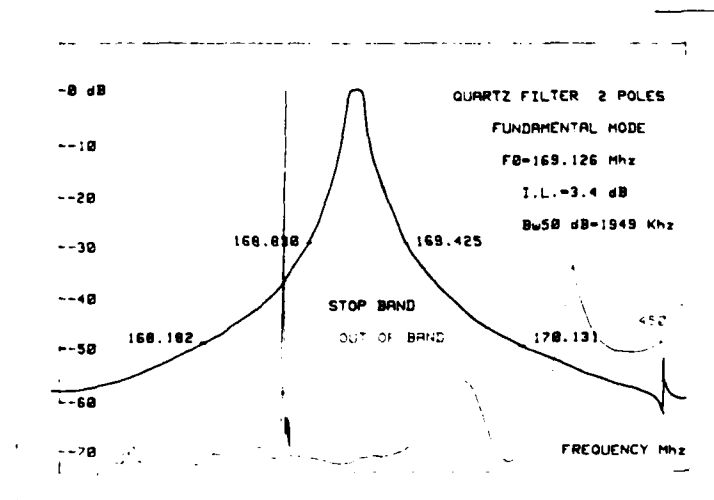


Figure 16.

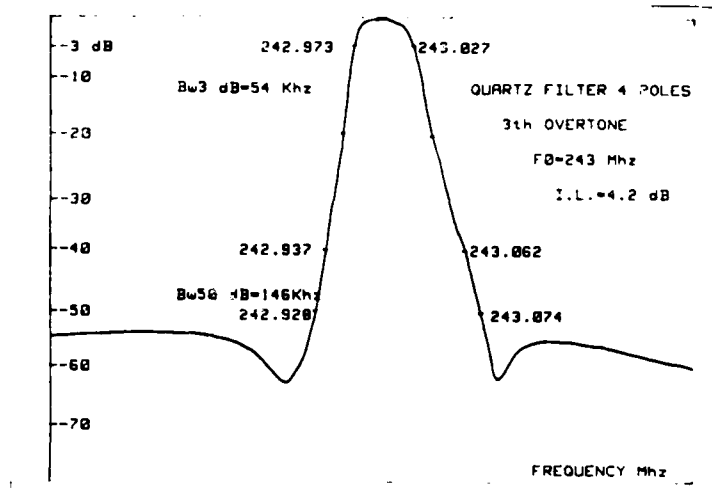


Figure 17.

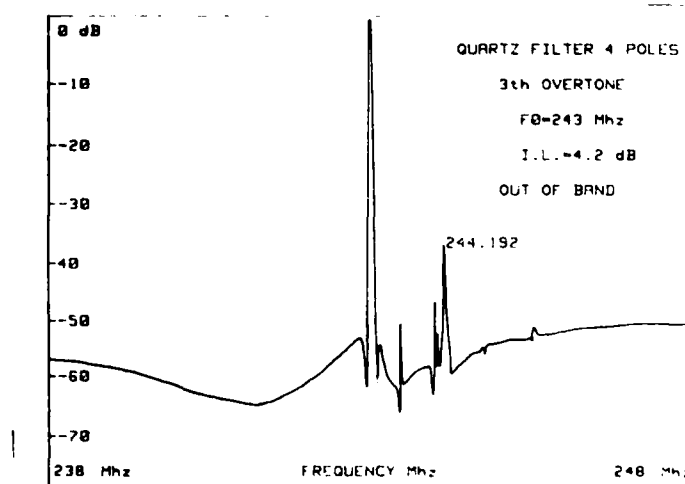


Figure 18.

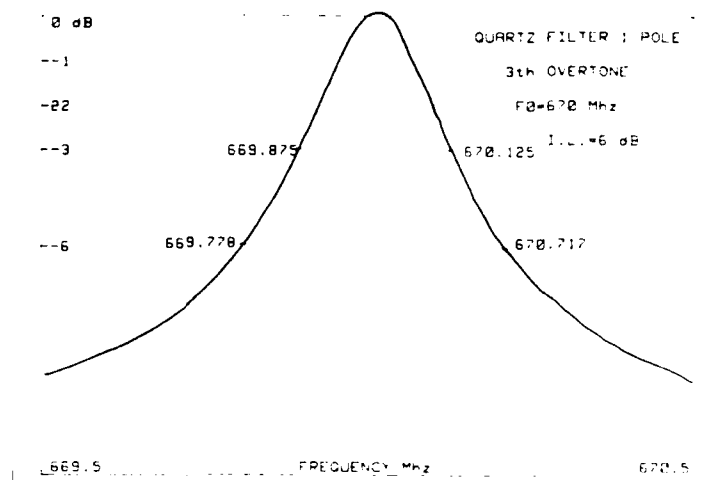


Figure 19.

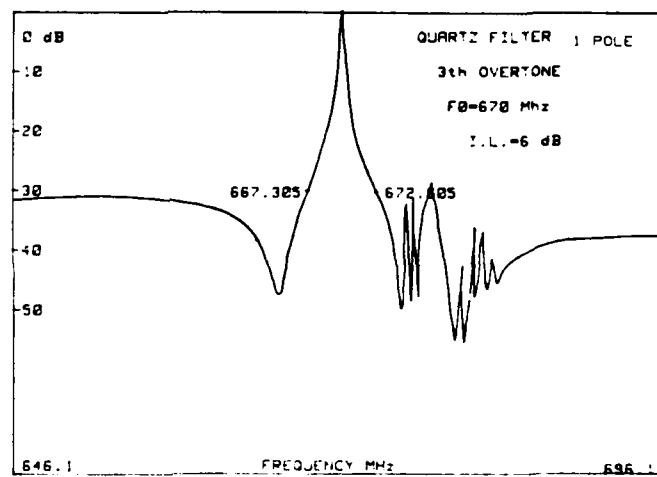


Figure 20.

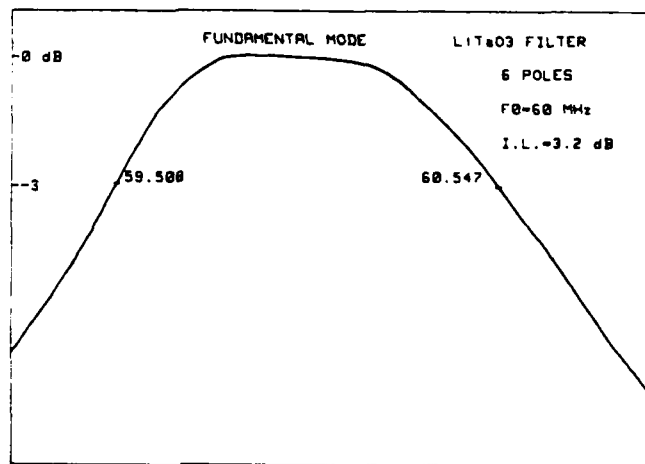


Figure 21.

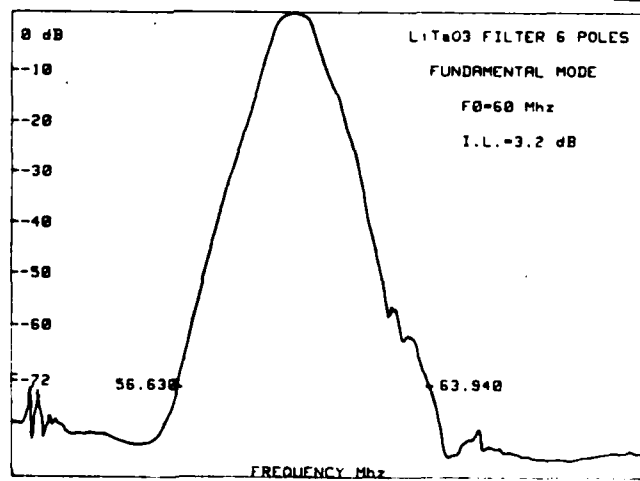


Figure 22.

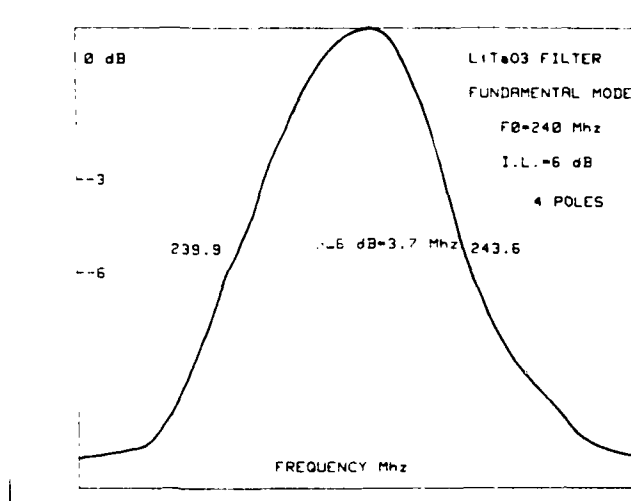


Figure 23.

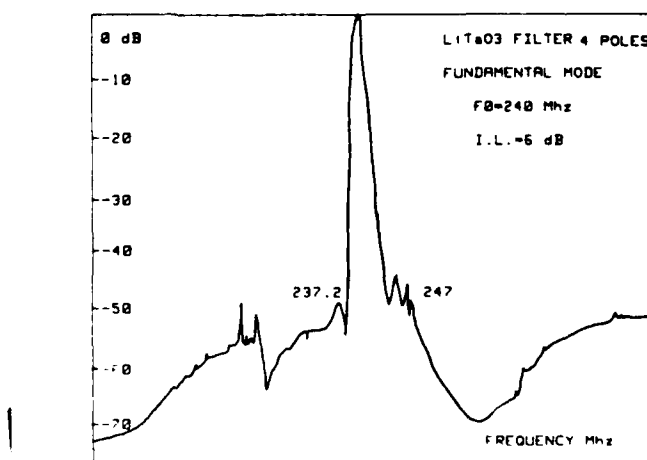


Figure 24.

AD P001552

## MAGNETOSTATIC WAVE MULTI-CHANNEL FILTERS

J. D. Adam

Westinghouse R&D Center  
Pittsburgh, Pennsylvania 15235Summary

The construction and operation of a 10-channel filter bank, operating at X-band and relying on magnetostatic wave (MSW) propagation in epitaxial yttrium iron garnet (YIG) films is described. Two filter techniques were investigated. First, reflective arrays were examined for their use in this application, but it was concluded that this technique was insufficiently developed at this time. The second technique used ten stagger-tuned narrow band magnetostatic forward volume wave (MFVW) delay lines fed from a common input transducer with separate outputs. This approach yielded characteristics which approximated the device objectives.

Introduction

The aim of the work described here was to design, fabricate, and test a 10-channel multiplexed filter bank using magnetostatic waves (MSW) propagating in epitaxial yttrium iron garnet (YIG) films.<sup>1</sup> The performance goals<sup>2</sup> for the filter bank are given in Table I.

Table I  
Performance Goals for 10-Channel Filter Bank

Center Frequency	9.0 GHz
Number of Channels	10
Channel 3 dB Bandwidth	50 MHz
Out-of-Band Rejection	55 dB
50 dB Bandwidth	100 MHz
Multiplexed Insertion Loss	20 dB $\pm$ 1 dB per channel
Bandpass Ripple	1 dB

Compact surface acoustic wave (SAW) devices have been developed for use at UHF, but filter banks operating at microwave frequencies have been restricted to waveguide, stripline or dielectric resonator techniques which become bulky if multipole circuits are necessary. Because the fields of propagating MSW are accessible at the surface of the YIG film, it was tempting to investigate approaches based on analogs to SAW filters using reflective arrays.<sup>3</sup> Experiments on single channels showed the potential of the SAW approach

but emphasized a lack of understanding of the interactions involved. An alternate approach based on narrow (1 mm) strips of YIG was also investigated, and it was found that suitable filter characteristics approximating those in Table I could be obtained.

Reflective Array Filters

The initial concept was to propagate magnetostatic forward volume waves (MFVW) through a series of reflective arrays. The elements in the reflective arrays were to be at 45° to the direction of propagation and have a different periodicity so that each array would select a narrow band of frequencies from the propagating wave. Arrays of metal strips were chosen since the alternative etched grooves which had already been demonstrated with surface waves<sup>4</sup> caused coupling of the MFVW to other modes in the YIG film.<sup>5</sup>

Experiments were performed to investigate the reflectivity of metal arrays for MFVW at a 45° angle of incidence using the arrangement shown in Figure 1. The transducers and reflecting array were defined in gold on 0.25 mm thick alumina. Thin aluminum was deposited in other areas to absorb unwanted MFVW and prevent reflections. Typically, the array consisted of 49 strips, each 50  $\mu$ m wide with a center-to-center spacing of 152  $\mu$ m. A 25 mm diameter YIG film could be laid down on the structure shown in Figure 1.

Figure 2 shows the variation, with frequency, of transmission loss to output ports 3 and 2 for an input at port 1. The YIG film used was 35.7  $\mu$ m thick and a bias field of 2.5 kOe was applied normal to the film surface. These results were obtained between 2 GHz and 4 GHz where e.m. feed-through levels in the structure were low. MFVW reflection occurs when the Bragg condition is satisfied and the stop bands in the direct transmission between ports 1 and 3 can be seen in Figure 2. These correspond to pass bands in the reflected signal between ports 1 and 2. Comparing transmission between ports 1 to 3 and 1 to 2, it is seen that the reflection is an efficient process. However, there is significant undesired low k transmission between ports 1 and 2, but this could be reduced by use of IDT's at the input and outputs.

As a result of the experience gained in the course of these experiments, it became clear that the reflective array approach to the 10-channel filter would only be feasible after a complete model for the interaction of MFVW's with currents in metal strips was available, i.e., an extension of transducer theory.<sup>6</sup> This approach was, thus, terminated in favor of an alternative simpler approach which is described in the next section. This is not intended to imply that the reflective array approach cannot be successful if sufficient time and effort can be devoted to the problems.

#### Multiplexed Delay Lines

Efficient transduction of magnetostatic waves requires that the delay line be located at an r.f. current maximum in the microstrip transducer. Thus, several delay lines could be placed on current maxima  $\lambda_m/2$  apart, along a long microstrip line whose end is either open or short circuit. If the center frequency of each delay line is different, e.g., by having different values of bias field, then the delay lines would have little effect on each other. Figure 3 shows a photograph of a multi-channel filter using open circuited transducers. Alternatively, if the long microstrip was terminated in a 50  $\Omega$  load, then the delay lines could be placed at arbitrary positions along the microstrip, but this results in a slightly reduced transduction efficiency. The bandwidth of a MFVW delay line is a function of the spacing of the YIG film from the single microstrip transducer and the width of the transducer. These parameters were used to control the pass band shape of the 10-channel filter described here which was constructed using ten narrow band delay lines, with separate output transducers, fed from a common input transducer as shown in Figure 3. The different center frequency of each delay line was achieved by a linear field gradient along the length of the device.

#### Single Channel Filter

Calculation and measurements<sup>2</sup> showed that wide microstrip transducers produce narrow band characteristics. Here alumina microstrip substrates 0.635 mm thick were used so that microstrip lines of 0.635 mm result in a characteristic impedance of 50  $\Omega$ , which was convenient to use where multiple transducers are effectively cascaded. The harmonic wave number or sidelobe responses of the microstrip transducer were suppressed by spacing the transducer away from the YIG film. Since the width of the transducer was fixed at 0.635 mm, the YIG film thickness was selected to give the required filter bandwidth and a thickness of approximately 20  $\mu$ m was found to be appropriate.

Transmission loss measurements were performed using YIG films approximately 20  $\mu$ m thick and 2 or 3 mm wide on transducers 5 mm long, 0.635 mm wide and spaced apart by 1 cm. The ends of the films were bevelled at an  $1^\circ$  angle to prevent reflections. These experiments showed that an approximation to the required filter response could be obtained but that severe amplitude ripple, due to the higher order width modes was

superimposed. Width modes<sup>7</sup> are characterized by a sinusoidal variation ( $\sin n\pi/W$ ) in r.f. magnetic field across the width (W) of the YIG strip. The lowest order mode corresponds to  $n=1$ , while higher order modes have  $n=2, 3, 4$ , etc. The width modes become degenerate at high wave numbers, but the frequency where the wave number  $k=0$  is different for each mode.  $k=0$  for the lowest order mode ( $n=1$ ) occurs at the lowest frequency and the frequency spacing between it, and  $k=0$  for the higher order modes is inversely proportional to the YIG strip width. Thus, narrow strips give a wide frequency separation of modes at  $k=0$ .

Measurements with 1 mm wide samples showed that good coupling was obtained at low wave numbers. Additional measurements on 1 mm wide samples showed that a film to transducer spacing of 160  $\mu$ m was close to optimum and at this spacing transmissions due to the  $n=3, 5$ , etc., width modes were outside the response of the  $n=1$  mode. Present transducer theory is inadequate for width modes so that the design of these filters was determined experimentally. Transmission loss measurements for a YIG film 18.5  $\mu$ m thick and 1 mm wide using input and output transducers each 5 mm long and 0.635 mm wide are shown in Figure 4. The YIG was spaced from the transducers by a glass slide 160  $\mu$ m thick. Apart from the responses due to the  $n=3$  and 5 modes, the out-of-band rejection is good.

Techniques to suppress or attenuate higher order width modes were investigated and included tapering the edges of the film which was effective in wider samples but difficult to implement in 1 mm wide films. The suppression method which was used in the completed device relied on an array of resistive aluminum strips deposited on the YIG film between the input and output transducer. The MFVW attenuation produced by a resistive film in contact with the YIG has been shown to increase with wave number of the MFVW.<sup>4</sup> The aluminum strips have an infinite resistivity in the direction of propagation and, hence, do not introduce attenuation through the component of wave number parallel to the axis of the YIG strip, i.e., normal to the axis of the aluminum strips. However, the aluminum strips have a finite resistivity transverse to its direction of propagation. Thus, since width modes have a transverse wave number  $k_t = n\pi/W$ , they will experience an attenuation which increases with mode number  $n$ .

The dependence of minimum transmission loss for the  $n=1, 3$  and 5 modes on the thickness of the aluminum strips is shown in Figure 5(a) for an 18.5  $\mu$ m thick YIG film with a 160  $\mu$ m spacer. The grating had 18 strips each 0.14 mm wide and separated by 0.13 mm. Viewed as a reflecting array, the strips would have a stop band at  $k \approx 150 \text{ cm}^{-1}$  which is well outside the desired pass band. Similar measurements for a continuous aluminum film of 2.5 mm length deposited on the YIG film are shown in Figure 5(b). Comparing Figures 5(a) and 5(b), the strips do indeed provide better discrimination in attenuation between the  $n=1$  and the higher order width modes. An aluminum thickness

of 200-300 Å results in adequate suppression of >50 dB for the  $n=3$  mode compared to the  $n=1$  mode at the expense of an additional 4 dB attenuation on the  $n=1$  mode. The transmission loss and return loss of a delay line with 18 aluminum strips of thickness 364 Å is shown in Figure 6. Other parameters are the same as in Figure 4. Note that the  $n=3$  mode is just visible and is ~50 dB below the  $n=1$  transmission peak.

Most MSW devices<sup>1</sup> described previously have used some technique to absorb MSFW incident on the ends of the YIG sample and, thus, prevent ripple due to reflections. A method for reducing the delay line insertion loss which was investigated involved the use of square, highly reflecting ends on the YIG film as seen in Figure 3. In this case, the amplitude of the MSFW travelling towards the output transducer has the form  $A \cos ki$ , where  $k$  is the wave number along the axis of the YIG strip and  $i$  is the distance between the reflecting end of the YIG strip and the center of the transducer.

Measurements of transmission loss were performed using a YIG film 18.5  $\mu$ m thick, 1 mm wide, and 1.19 cm long with square ends. Evaporated aluminum strips were used to attenuate the higher order width modes, and a 160  $\mu$ m glass slide spaced the YIG from the transducers. The position of the transducers and the ends of the YIG could be set. Figure 8 shows the transmission loss measured as a function of frequency for the optimum condition when  $i$  was 0.31 mm. In addition to a reduced insertion loss of 13 dB, the pass band shape is more symmetrical than in Figure 6. The notch on the low frequency side of the pass band may be due to the first zero of  $\cos ki$  when  $ki = \pi/2$ . These techniques were used in the delay lines for the 10-channel filter bank in order to achieve reduced insertion loss and an improved pass band shape. Return loss measurements are also shown in Figure 8. The maximum return loss for the  $n=1$  modes is 7.5 dB and return loss peaks due to  $n=3$ , 5, and 7 modes are clearly seen.

#### Bias Magnet

The magnet for the 10-channel filter was designed to produce a different bias field for each channel. A step type change between each channel would be ideal but as an approximation to this, a linear variation was used. In the assembled device, the center-to-center spacing between the delay lines for channels 10 and 1 was 1.95 in. and with a 50 MHz frequency spacing between channels, the linear bias field variation required was 161 Oe. Figure 8 is a drawing of the bias magnet. Soft iron pole caps were used on the SmCo pole pieces, both 2.25 in. x 1 in. x 0.25 in., and magnetized parallel to the 0.25 in. direction.

A typical variation in magnetic field along the center of the magnet gap (x direction) is shown in Figure 9 for a 9.5 mil taper in gap along the length of the pole pieces. Additional soft iron pieces 2 mil thick were attached to the ends of one

of the pole caps, to produce the peaks at both ends of the gap. In the absence of these thin pieces, the magnetic field rolled off too rapidly at the ends of the gap. The field measured along the y direction was symmetrical about the center of the gap and varied by less than 2 Oe over the 0.25 in. length of the delay lines on either side of the center.

#### Construction and Test

The assembled 10-channel filter minus magnet and lid is shown in Figure 3. The center section of the brass box, mainly comprising the L-shaped walls between adjacent delay lines, was 2.54 mm thick with a 0.25 mm thick brass base and lid. The center-to-center spacing between adjacent delay lines was 5.5 mm. The transducers were defined in gold, 16  $\mu$ m thick, on 0.635 mm thick alumina. Glass 160  $\mu$ m thick separated the YIG from the transducers. The YIG delay lines were each 1 mm wide and length approximately 6.7 mm cut from a 23  $\mu$ m thick film. The delay lines were accurately positioned relative to the transducer by glass blocks which can be seen in Figure 3.

The completed filter bank is shown in Figure 10. Measurements of transmission loss for each of the channels and return loss from the input as a function of frequency are shown in Figure 11. The pass band shapes are close to Figure 7. The lowest minimum insertion loss was 12 dB for channel 3, and the highest was 16 dB for channel 6. Owing to the 11 dB peak-to-peak ripple on the pass band, the 3 dB bandwidth is difficult to estimate precisely but is in the range 30 MHz, for channel 8 to 45 MHz for channel 4. The variable frequency spacings of the channels are due to the nonconstant field gradient in the bias magnet. The principal out-of-band spurious is due to the  $m=3$  width mode, which was not sufficiently attenuated because of the reduction in the number of strips from 18 to 15 with no compensating change in aluminum thickness. Such a reduction was necessary because in this case there was a shorter delay line path length (5.5 mm) compared to the longer (1 cm) path length used in the test samples. The performance goals for the 10-channel filter and the measured parameters of the delivered device are shown in Table II.

The main source of discrepancy between the goals and the achieved results are due to a) incorrect spacing between the delay lines in the box resulting in the higher center frequency, b) improper attenuation of the  $n=3$  mode probably caused by aluminum depositions which were too thin resulting in low out-of-band rejection, and c) variation in the spacing of the ends of the YIG from the transducers resulting in changes in the pass band shape, i.e., 3 dB and 50 dB bandwidths. In addition, although not shown in Table II, the nonuniform gradient on the bias field resulted in the nonuniform frequency spacings between the channels. In spite of these discrepancies, which are all potentially correctable, a general technique for obtaining multichannel filter operation has been demonstrated. In addition, it has been shown

that a degree of control over the filter pass band shape can be obtained with simple single element microstrip transducers. Further control may be possible with relatively simple multi-element transducers. For example, an IDT or parallel bar transducer could be used as the output.

Table II  
Comparison of Performance Goals with Measured  
Results on Delivered 10-Channel Filter

Property	Goal	Achieved
Center Frequency	9.0 GHz	9.45 GHz
Number of Channels	10	10
Channel 3 dB Bandwidth	50 MHz	30-45 MHz
Out-of-Band Rejection	55 dB	30 dB, 55 dB if m=3 mode suppressed
50 dB Bandwidth	100 MHz	120 MHz-150 MHz
Multiplexed Insertion Loss	20±1 dB	12 dB - 16 dB
Band Pass Ripple	1 dB	~ 1 dB

#### Acknowledgment

This work was supported in part by the U.S.  
Air Force Avionics Laboratory under Contract  
No. F33615-77-C-1068.

#### References

1. "The Status of Magnetostatic Devices," J. D. Adam and M. R. Daniel, IEEE Trans. *MAG-17*, 2951, 1981.
2. "Magnetic Surface Wave Device Technology," Final Report for Contract F33615-77-C-1068, USAF, AFSC Aeronautical Systems Division, Wright-Patterson AFB, OH 45433.
3. "Surface Wave Filters," H. Matthews (Ed.), Wiley-Interscience, New York, 1977.
4. "Magnetostatic Wave Propagation in a Periodic Structure," C. G. Sykes, J. D. Adam, and J. H. Collins, Appl. Phys. Lett. *29*, 388, 1976.
5. "Magnetostatic Forward Volume Wave-Spin Wave Conversion by Etched Gratings in LPE-YIG," R. L. Canter, C. V. Smith, Jr., and J. M. Owens, IEEE Trans. *MAG-16*, 1159, 1980.
6. "Interaction of Magnetostatic Waves with a Current," P. R. Emtage, J. Appl. Phys. *49*, 4476, 1978.
7. "The Effects of Width Modes in Magnetostatic Forward Volume Wave Propagation," J. D. Adam, presented at the Microwave Magnetic Workshop, Hanscom AFB, June 10-11, 1981.

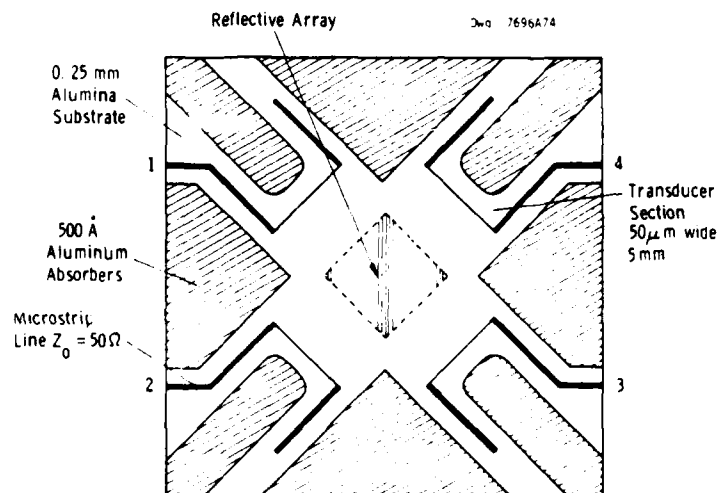


Figure 1. Experimental Arrangement for Measurement of Transmission and Reflection of MSFW Incident on an Array of Metal Strips at 45°. The Transducers are 5 mm long, 50  $\mu$ m wide. Opposite Transducers are 12.5 mm Apart. The Reflective Array is Comprised of 49 Strips Each 50  $\mu$ m Wide and Separated by 152  $\mu$ m Center to Center.

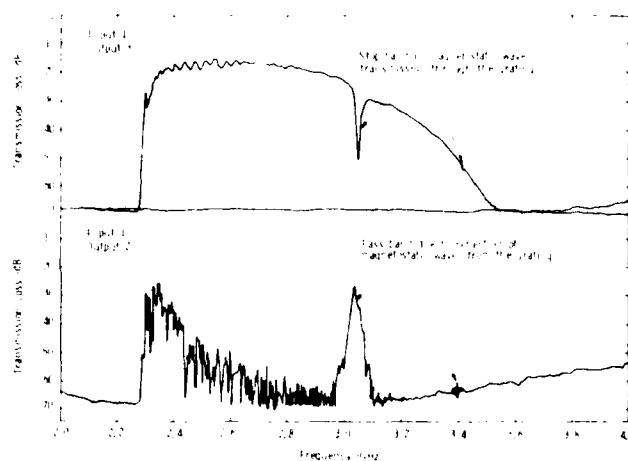


Figure 2. Measured MSFW Insertion Loss Between Ports 1 and 3 (Transmission) and Ports 1 and 2 (Reflection). The YIG Film was  $35.7\text{ }\mu\text{m}$  Thick and the Bias Field of  $2.5\text{ kOe}$  was Applied Normal to the Film Plane. The Transducers and Reflective Array are Shown in Figure 1.

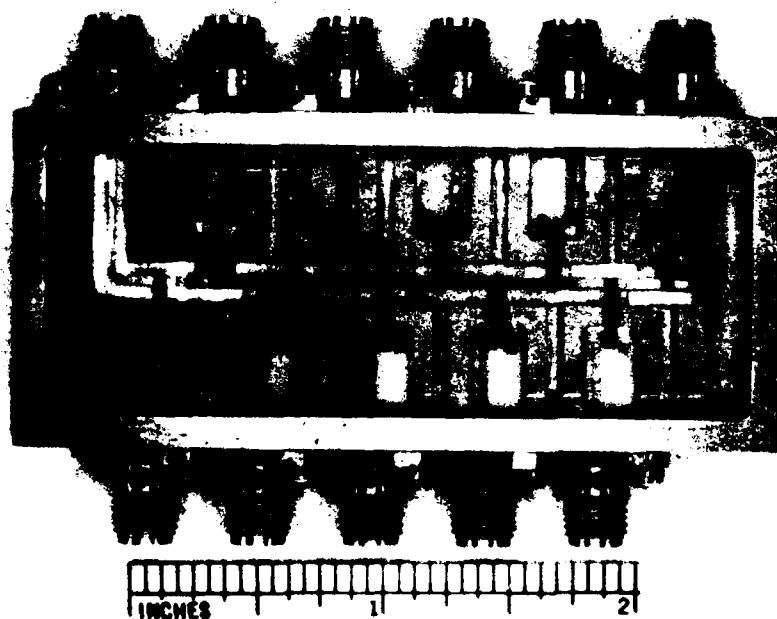


Figure 3. Assembled 10-Channel Filter Without Lid or Magnet

Curve 723722-A

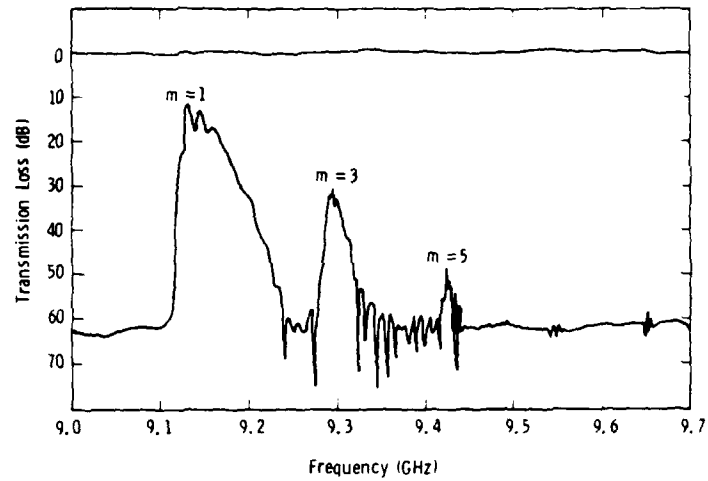


Figure 4. Measured Transmission Loss as a Function of Frequency for an 18.6  $\mu\text{m}$  Thick YIG Film, 1 mm wide. The Transducers were 5 mm Long, 0.635 mm Wide on 0.635 mm Thick Alumina. The YIG Film was Spaced from the Transducers by 160  $\mu\text{m}$  and the Bias Field was 4880 Oe.

Curve 723725-A

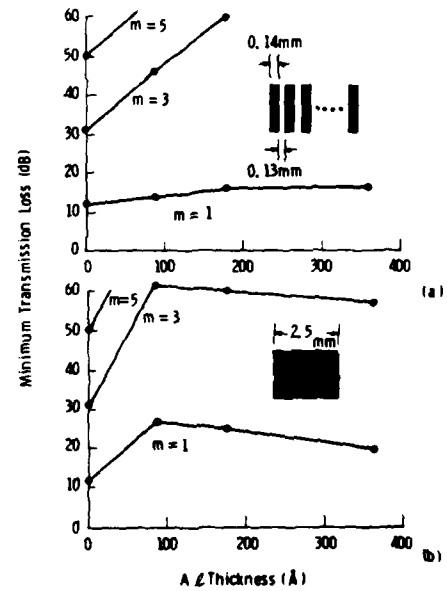


Figure 5. Attenuation of Higher Order Width Modes as a Function of Aluminum Thickness. Measured on an 18.5  $\mu\text{m}$  Thick YIG Film Spaced from 0.635 mm wide transducers by 160  $\mu\text{m}$ . (a) 18 Strips; (b) Continuous Film of Length Equivalent to the Strips.

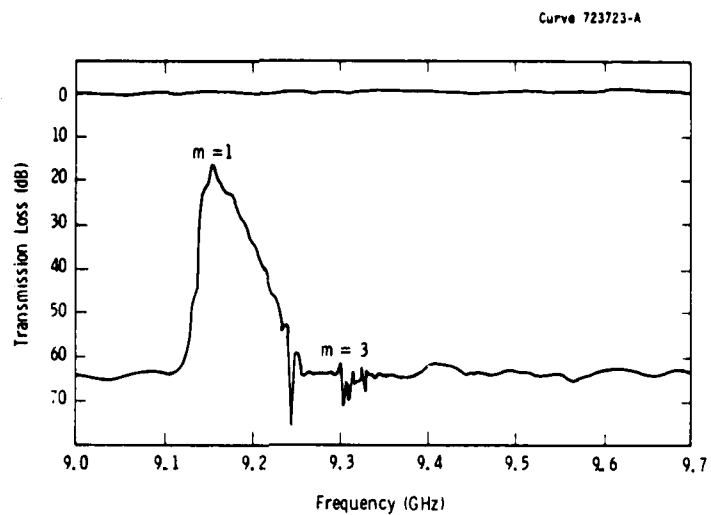


Figure 6. Measured Transmission Loss as a Function of Frequency for an  $18.5\text{ }\mu\text{m}$  Thick YIG Film with the Same Parameters as in Figure 4 but with 18 Aluminum Strips  $364\text{ }\text{\AA}$  Thick Evaporated onto the Surface.

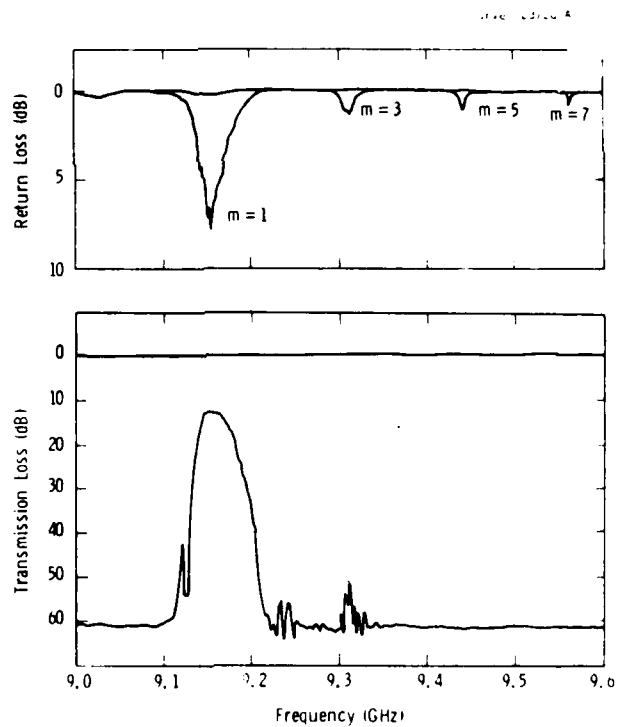


Figure 7. Measured Transmission Loss and Return Loss as a Function of Frequency for an  $18.5\text{ }\mu\text{m}$  thick YIG Film with Reflecting ends. The Spacing ( $l$ ) From the Ends of the Film to the Edge of the Transducer was  $0.31\text{ mm}$ . All Other Parameters were as in Figure 6.

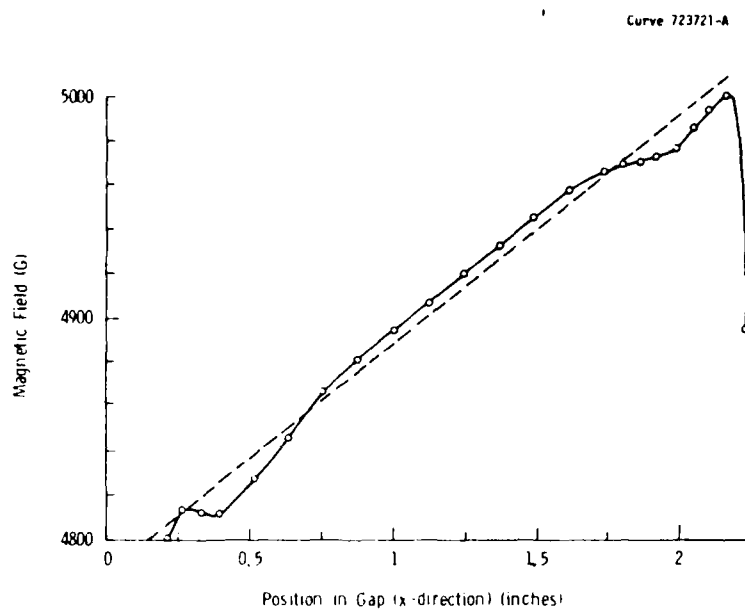


Figure 8 Bias Magnet for the 10-Channel Filter.

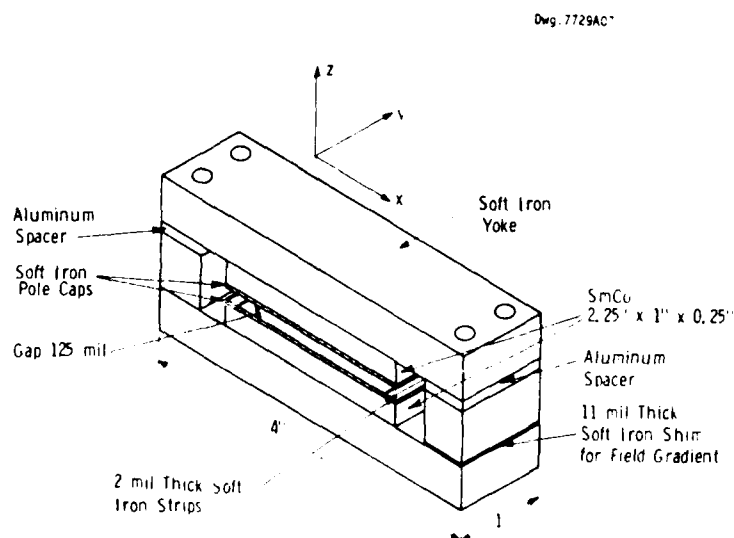


Figure 9 Variation in Magnetic Field ( $H_z$ ) Along the Center of the Gap (x Direction) in the Bias Magnet for the 10-Channel Filter.

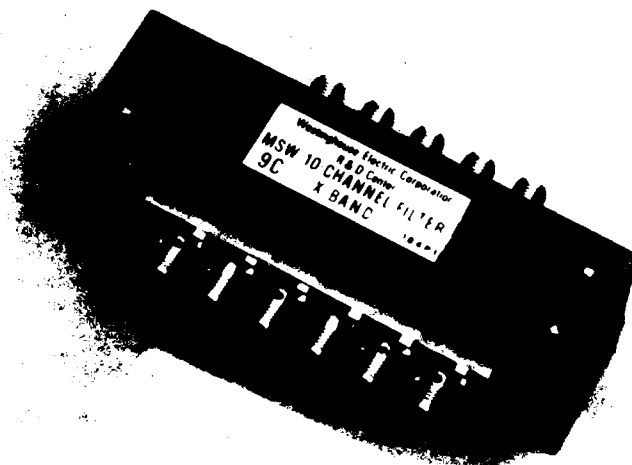


Figure 10. 10-Channel Filter.

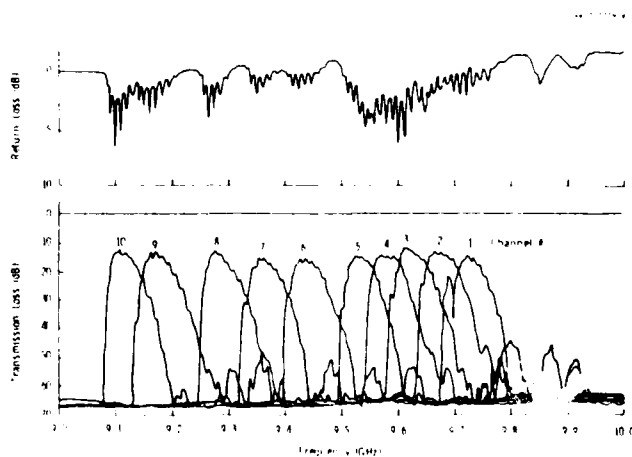


Figure 11. Measured Transmission Loss and Return Loss from Input for 10-Channel Filter.

## APPLICATION OF SAW CONVOLVERS AND CORRELATORS\*

H. GAUTIER

THOMSON-CSF A.S.M. DIVISION

Chemin des travaux - BP 53 - 06801 Cagnes/Mer Cedex - France

AD P001553

Whereas convolvers perform the convolution product of any two signals with limited duration and bandwidth, correlators are transversal filters with an impulse response which can be stored and modified at will.

The piezoelectric convolver is today the most advanced technology ; signals with 10 to 20  $\mu$ s duration and bandwidth up to 100 MHz can be processed over a dynamic range of more than 60 dB.

Such performances can be reached by no other means and they are well suited for a number of modern signal processing systems of which we wish to describe two :

- the detection and demodulation of spread spectrum signals
- the correlation of synthetic aperture radar signals.

## Introduction

A number of Surface Acoustic Wave (SAW) devices are directly applicable to signal processing : are to be found among them the fixed finite impulse response filters, the spectrum (or Fourier) analyzers and the convolvers/correlators. These last devices can also be viewed as programmable filters and the presentation will only deal with this family of devices.

We shall first briefly describe the major technologies available to build these devices, discuss their present status of development and compare their performances. This review will show that the piezoelectric convolver technology has reached the highest level. And two typical examples of application of this device will next be presented : they related to spread spectrum systems and radar mapping. In the former the analog processing capabilities of the convolver are directly employed ; and in the latter example coupling to digital circuits is performed to extend the field of applications of the device and make hybrid processors.

## SAW Convolvers and Correlators

One makes a distinction between convolvers which perform the convolution product of any two signals with limited duration and bandwidth and which may be built on a simple piezoelectric

\* Some of the work described here was done under DRET contracts.

substrate, and correlators which are transversal filters with an impulse response which can be stored and modified : serial or parallel injection can be obtained by various means but in all cases acoustic (piezoelectric) and electron (semiconductor) phenomena must be coupled.

## Elastic and acoustoelectric convolvers

Any acoustic convolver is made of an acoustic substrate, a nonlinear medium sensitive to at least one of the physical characteristics of the waves and a summing device. The simplest solution consists in using a single piezoelectric substrate as the propagation and the nonlinear medium, and depositing on it the electrodes capable of generating the waves, picking up and summing the convolution product.

This is in fact the oldest solution ; bulk waves<sup>1</sup> and surface waves<sup>2,3</sup> have been used. The geometry of the structure is then schematized in fig.1a. Signals to be convolved are carried by two contra-directive waves with identical frequencies, launched from the two end transducers. Due to second order nonlinear mixing in the substrate, spatially uniform charges are generated at the double frequency, and are summed up by the output electrode. Due to propagation effect, one easily shows that the output signal is the convolution of the input signals with a 2 : 1 time scale compression, provided the incoming signals cross under the interaction plate.

Very early, it appeared that the nonlinear phenomenon was weak and the efficiency of such parametric devices was proportional to the incoming wave power densities. This led to the introduction of beamwidth compressors and of an acoustic guiding structure. Multistrip<sup>4-7</sup> and parabolic horn<sup>8-12</sup> type compressors have been used and more recently narrow aperture chirp transducers have been proposed<sup>13,14</sup>.

We have chosen to use multistrip structure for a long time and the geometry of the convolver is shown in fig. 2.

Other techniques to build convolvers make use of the highly nonlinear admittance characteristic of semiconductor MOS or junction diodes to mix the acoustic fields. These convolvers are called acoustoelectric because of the electron-phonon interaction. Of the many geometries experimented, the highest performances, in terms of signal bandwidth

and duration capabilities, were obtained with the structure shown in fig. 1b. A carefully passivated semiconductor (generally Silicon) plate is located in close vicinity to the piezoelectric substrate; the necessary airgap which prevents acoustic mass-loading must be a few thousand angstroms high to ensure high acoustoelectric coupling and hence high efficiency. This structure can be made mechanically stable<sup>15</sup> and it has exhibited the best performances for several years. But elastic convolvers now show almost identical characteristics and their technology proves to be much simpler, more reliable and able to be produced at low cost: so that they are now considered as the only candidate for wideband convolution systems. "Wideband" means greater than 5 to 10 MHz for, below this figure, CCD or digital techniques may be applicable.

Table 1 shows typical and limit performances of elastic waveguide convolvers built on  $\text{LiNbO}_3$  substrate and employing beamwidth compressors.

Characteristics	Limit	Typical
Input Center frequency (MHz)	400	100-300
Input bandwidth, B (MHz)	120	30-80
Plate duration, T (ns)	40	10-20
T x B product	3000	500-1000
Max. Bilin. Factor, F ( $\text{dBm}^{-1}$ )	- 60	- 70
CW Self Convolution R (dB)	- 43	- 35
Max. input power (dBm)	30	- 25
Max. output S/N (dB)	80	60
Processing Uniformity :		
Time - amplitude (dB) p/p	1	
rms	0.2	
phase (deg) p/p	20	
rms	3	
Frequency-Phase (deg. p/p.)	60	

Table 1 - Performances of elastic convolvers

Maximum efficiency is when two CW signals at center frequency are fed-in. We then define the bilinearity factor F ( $\text{dBm}^{-1}$ ) as the ratio  $P_{\text{out}}/P_{\text{in1}} \cdot P_{\text{in2}}$  when all powers are expressed in mW.

Each CW input also generates a spurious self convolution due to reflexion off the end transducers. And one can similarly write

$$P_{\text{self.conv}} = R \cdot F \cdot P_{\text{in1}}^2$$

when R represents the maximum spurious level as referred to the max. convolution.

It follows that convolvers are capable of processing up to 100 MHz bandwidth, 10-20 ns duration signals with output signal-to-noise ratio of 60 dB and spurious rejection of 35 dB. In addition such devices are commercially available from several

suppliers; and they can be produced to military standards.

#### Memory Correlators

Convolution is a nice mathematical tool but in practice, correlation is much more useful for it corresponds to filtering. To employ convolvers, one input signal must be fed time inverted and, to turn a convolver into a matched filter, continuous recirculation of the time inverted reference is required. All this may be uneasy and power consuming. A better suited device is the memory correlator; it is capable of storing a given signal and correlating it with any later incoming signal. The memory element is generally made of an array of semiconductor diodes, which also acts as the nonlinear mixing element. The airgap coupling technique described previously can be used again, as shown in fig. 3.

The signal  $r$  to be stored is converted into a SAW; when it is fully underneath the array, a narrow high amplitude current pulse strongly forward biases the diodes. These charge up almost instantaneously if they are of the Schottky type: the stored charge pattern contains a uniform component and a periodic component corresponding to the acoustic signal. After the write-in, the stored charge reverse biases the diodes and the information can be kept for long times depending on the reverse current characteristic of the diode. Any subsequent signal  $f$  applied to the input transducer will mix with the stored pattern and the true correlation  $f \star r$  is generated.

The airgap coupled structure today shows the widest bandwidth (60 MHz) for an interaction length of some 5  $\mu\text{s}$ <sup>16,17</sup>. But the efficiency is weaker than the corresponding convolvers because of non-ideal operation, and the dynamic range is limited (see table II). This structure being also difficult to industrialize for the reasons discussed earlier, much work has been conducted to develop monolithic structures. The most advanced devices employ a piezoelectric  $\text{ZnO}$  layer deposited on Si diodes<sup>18-21</sup> as shown in fig. 4. Efficiency is somewhat higher but bandwidth does not exceed some 30-40 MHz and plate length will be limited by propagation losses. It is expected that devices with Time x Bandwidth products of no more than a few hundred will be feasible.

Although research has been going on for 10 years in this field, no really satisfying device today exists outside the laboratories. Other types of devices not making use of layered geometries are now being studied and GaAs is one interesting material<sup>22</sup>.

Characteristics	Si/LiNbO <sub>3</sub> (airgap)	ZnO/Si 20 (monolithic)
Center frequency (MHz)	300	150
bandwidth (MHz)	60	30-40
Plate duration (ns)	5	4
Memory time (ms)	50-100	1-10
Spurious level (dB)	- 30	- 35 - 40
Max. O/P S/N (dB) (30 dBm input)	> 50	> 60

Table II - Demonstrated Performances of Schottky diode memory correlators

#### Applications of Convolvers

As we wish to present experimental systems which are representative of actual needs and which can be developed and ready for industrialization within the next few years, the applications described next employ only elastic convolvers.

#### Detection and demodulation in spread spectrum systems

**Generals** - In these systems the bandwidth of the information to be sent is spread by means of wideband codes. The most common technique consists in replacing each bit of information (bit rate  $1/T$ ) by a PN code composed of  $N$  chips of duration  $T/N$ . Modulation of the carrier wave is generally of the PSK or MSK type<sup>23</sup>. The receiver must incorporate a filter matched to the expected encoded signals to recover the information. Bandwidth spreading yields processing gain which results in improved secrecy and protection.

To extend the performances, codes may vary from bit to bit and a programmable matched filter is required. At the same time encrypting and error correcting techniques can be employed.

Some of the actual spread spectrum systems being designed employ bit rates of 50-200 KHz ( $T = 1 - 20 \mu s$ ) and spreading chip rates of 50 to 200 MHz ( $T = 5-20 ns$ ). The elastic convolver is therefore a good candidate, but let us first present the operations to be performed.

Operations to perform - consider two major applications, that of Identification Friend-Foe (IFF) and that of Telecommunications.

In the IFF mode, one station interrogates another by sending out a signal composed of one (set of) codes. The receiving station must detect and recognize this signal and then send a reply message back to the interrogator, which will also have to recognize whether the answer is correct.

In a telecommunication system the signals are generally composed of a preamble followed by the message to be transmitted. The receiver knows the format and the codes making the preamble; it should detect its arrival and measure its time of arrival to synchronize itself and be able to demodulate the message which follows. Some systems may not require synchronization but data transmission is then done with time and localization (through TOA) being possible.

There exist therefore two different modes of operation: asynchronous and synchronous.

**Synchronous mode of operation** - This is by far the simplest mode. The two signals to be convolved are fed in the device at the same time. A convolver with plate duration  $T$  can process signals with max. duration  $T$ . A message made of continuous symbols can be demodulated by feeding a reference signal composed of the time reversed codes. The block diagram of a system applying this scheme is shown in fig. 5. We assume that information bit "1" and "0" are spread with orthogonal (uncorrelated) codes  $C_1$  and  $C_0$ ; the received IF signal is fed into two similar convolvers matched to  $C_1$  and  $C_0$  by continuously circulating the time reversed code  $C_1^*$  and  $C_0^*$  respectively. The correlation output peaks (whose positions in time are known) then correspond to the bit 1 and bit 0 contents of the message. In practice the spreading codes may evolve with time (to improve secrecy) according to a known law: the receiver has simply to generate the corresponding correct reference waveform to remain matched. Since one reference code (duration  $T$ ) only serves once, spreading codes can change every bit.

The above example corresponds to simple binary encoding of the information, higher order encoding is possible using more than two convolvers<sup>23</sup>, or using split plate convolvers<sup>24</sup>.

**Asynchronous mode of operation** - In general the time of arrival (TOA) of the expected signal is unknown. To be able to intercept (correlate) fully any incoming signal of duration  $T$ , it is easy to show that the convolver interaction length must correspond to a minimum delay time  $2T$ . One generally chooses  $2T$  for obvious reason of economy, the reference waveform are then made of the repetition of the time inverted code every  $2T$  (see fig. 6). The correlation output time scale being compressed one expects extra invalid signals to be generated. Indeed in fact in general three output correlations appears when one signal comes in, two being partial and only one being correct. Expressed in another way, one may show that 50 % of the output must be gated off; this corresponds to times when no reference signal is fully in the convolver, and it is easy to generate the gating signal from the bit-rate clock.

A convolver with a repetitive reference and a gated output is exactly equivalent to a matched filter except for the output time compression.

Detection of signals is then performed as in the synchronous mode. One can also measure the time of detection (TOD) and it is a simple matter to relate it to the TOA: there exists an injective relationship between TOD and TOA as plotted in fig. 6. In practice a simple binary counter allows for the calculation of the TOA from TOD and the reference clock, and correct enabling of this counter avoids analog gating of the convolver output.

**Demonstration of the asynchronous mode** - As an example of wideband signals we used 512 chip gold codes with a 12.5 ns chip duration, biphasic (PSK) modulating a 405 Mhz carrier. A special convolver was designed featuring the characteristics given in table III. And an active module including input/output amplifiers and filters was built around it.

Its F-factor measured with wideband signals was  $17.5 \text{ dBm}^{-1}$ . Matched Gold sequence generators and modulators generate the repetitive  $12.8 \mu\text{s}$  period reference and simulate received  $6.4 \mu\text{s}$  wideband symbols.

Input Center Frequency (MHz)	405
Input Bandwidth (MHz)	80
Plate Duration ( $\mu\text{s}$ )	12.8
F( $\text{dBm}^{-1}$ ) max CW	- 66
PSK 80 MHz	- 69
Processing Uniformity	
Amplitude (dB) p.top.	< 1
rms	0.2
Phase (deg.) p.top.	15
rms	< 5
CW Self Convolution (dB)	- 35
Implementation Loss (PSK-80 MHz) (dB)	- $0.4 \pm 0.5$

Table III - Characteristics of the multistrip beamwidth Convolver built to process 80 MHz chip rate,  $6.4 \mu\text{s}$  duration PSK signals

Input Center Frequency (MHz)	405
Processing Uniformity (as a function of TOA) (dB)	< 0.2
CW Self Convolution (dB)	- 36
Implementation loss (PSK-80 MHz) (dB)	- $0.4 \pm 0.5$
Max. Output S/Noise and Spurious (dB)	60
Power Dissipation (W)	11.5

Table IV - Performance of convolution module when employed as a filter matched to  $512 \times 12.5 \text{ ns}$  chip PSK modulated signals. Power level is 24 dBm at convolver reference input port. Maximum Power level at convolver signal input port is 24 dBm.

Typical output waveforms are represented in fig. 7. Three correlation signals appear in general (see fig. 7a), of which the middle one is only meaningful and useful; and two full correlations may appear when the reference is synchronized with the received signal (see fig. 7b). Details of the correlation figures are shown in fig. 8: the main lobe to side lobe level varies with the code used. It is generally around 18.5 dB and may reach 23.5 dB in some instance (with code n° 0 as shown in fig. 8a). This is in agreement with calculation taking into account the bandwidth limitations of the RF signals.

Dynamic range and implementation loss are two other major characteristics to be considered when designing such a correlation sub-system.

In absence of received signals the presence of the recirculating reference generates a noise-like output (due to self convolution) which adds to the output amplifier thermal noise. On the other hand the maximum input signal level should be so that no saturation effects take place and anti-jam protection is not degraded: this means that the CW filtering characteristics should not be degraded by the presence of CW self convolution. For example the present module can be operated up to input level of - 1 dBm (24 dBm at convolver port) and the maximum output signal-to-noise ratio is 60 dB. This may be called the dynamic range of the module.

The implementation loss characterizes how close to an ideal matched filter the correlation module behaves. This can also be viewed as the degradation in processing gain (in presence of white noise) from ideal. The detail of how this loss is measured are given elsewhere<sup>15</sup>. The measured value is here  $- 0.4 \pm 0.5 \text{ dB}$ . The oscillograms of fig. 9 pictorially suggest this result.

#### Processing of sidelooking synthetic aperture Radar (SAR) Signals

Digital processors using SAW Convolvers - The convolver can be considered as an analog calculator and as such it is interesting to express its performances using digital equivalents: it can be estimated<sup>25,26</sup> that its processing speed varies between 1 and 10 G.FLOPS (floating point operations per second) its accuracy corresponds to some 6 bits (floating complex) and its dynamic range to 8-12 bits.

Such high speeds together with reasonable accuracy and dynamic range make them very attractive for application to modern signal processing systems to be designed in the radar and sonar fields where either fast response or large quantity of information are required. These systems very often necessitate the use of digital memories to process non simultaneous signals, to acquire a large number of signals and perform multiplexing, or to vary the time scale by changing the memory readout speed. In addition post processing (decision making, display...) is generally digital. It is therefore necessary to make the convolver digitally compatible if one wishes to use it in such systems. A typical example is described next.

Principle of sidelooking SAR correlation processing - An airborne sidelooking SAR is meant to image a ground strip parallel to the plane's route (see fig. 10). Standard pulse compression techniques are employed to yield good sideways resolution. The plane progression is used to perform scanning in the other direction and to synthesize a large dimension antenna. Enhanced resolution ("refining") along the plane's route is achieved through correlation of the received signals from each range cell with the ideal point echo of the range cell. This turns out to be a linear chirp.

In practice they may be  $10^3$  to  $10^4$  range cells and the refining ratio (correlation gain TxB) may vary from 50 to 500. For each range cell a memory stores as many words on they are received responses

of an echo during its illumination by the radar. This number is at least equal to  $TxB$ .

Often it is interesting to process signals in real time and on-board for operational reasons (speed) or for technical reasons (to reduce the quantity of information to transmit, as in a satellite). The amount of information is then very large. If correlation is computed one point at a time, the required speed is extremely high (in the 1 GFLOPS range). It is more advantageous to compute several points at a time (computation by part) and the convolver is well fitted for such an operation.

Assuming 1000 range cells,  $TxB = 120$  and a radar repetition frequency of 500 Hz, one may for instance compute 10 points at a time and the required time for this calculation must be less than 20  $\mu$ s. A convolver with a  $TxB$  of some 120 and plate duration of less than 20  $\mu$ s is adequate. This is how the sub-assembly built was designed.

Correlation sub-assembly - A schematic of the digital input-output correlator built is represented in fig. 11. Its major characteristics are given in the figure.

The present stage of development of this prototype processor is that of a feasibility model. Yet it only fills a volume of 2.1  $\ell$  and dissipates 11.5 W. Simple integration should yield a 2 : 1 reduction of these figures.

By comparison, a specialized digital processor was also built. It computes the correlation point by point. For a 4-bit coding, the overall volume and dissipated power of the prototype are 15  $\ell$  and 600 W (not including the memories which are present in all configuration).

The gain in volume x power brought by the hybrid SAW-digital solution is of some 100. It would be far greater in they were more range cells and more samples to process since the present hybrid operator is not utilized at its full power yet.

Example of operation - To test the operation of the processor, we simulated the ideal echo from a point source (i.e. a linear chirp) and correlated it with the actual reference waveform (i.e. the matched linear chirp, with weighting for sidelobe suppression). The digital test signals are made of 256 complex samples coded over  $2 \times (5 + \text{Sgn})$  bits with sampling speed 22.2 MHz, providing two 11.5  $\mu$ s x 11 MHz ramps (see fig. 12). The resulting input RF signals are shown in fig. 13. And oscillograms of the correlation output are given in fig. 14. The design sidelobe suppression and main lobe 3 dB width are 28 dB and 54 ns respectively. In practice the shape of the main lobe is respected to within a few % and the max. sidelobe level is around - 25 dB. Spurious rejection is close to 28-30 dB meaning that an overall 6 bit accuracy has been achieved.

## Conclusion

Two families of SAW devices have been presented : the convolver and the memory correlator. Whereas the former can be built on a mere piezoelectric substrate using a simple and reliable technology and providing wide bandwidth and large dynamic range, the latter requires a semiconductor memory element in the form of a diode array and their performances are still somewhat limited for practical use. This type of device yet being in principle far superior to convolvers, research continues to be very active in this field and various concepts are being experimented.

As for now, all practical implementations have to rely on convolvers. Two main applications exist.

Wideband analog programmable matched filtering is one. The convolver is equipped with a reference generator (and an output gate to suppress invalid correlation products). Synchronous and asynchronous modes are possible. Wide dynamic range and near ideal operation have been demonstrated over bandwidth as high as 100 MHz. Alternate techniques (digital or CCD) are not viable beyond 5 to 10 MHz bandwidth and the convolver will remain the only solutions for several more years.

Fast calculation is the second application. Convolvers like other SAW devices<sup>26</sup> are well fitted to coupling to digital circuits. They allow for compact and very high speed digitally compatible processors. These multipurpose correlation processors can be used today in radar systems whenever real time processing of fast signals or of large quantities of information is needed ; this is the case of the application to synthetic aperture radar mapping described here. Modules are able to handle 200-500 digital samples coded over 6 to 8 complex bits at input rate of 20-30 MHz. The Development of faster modules will follow that of faster digital and interfacing circuits. And we know that progress in this field is steady.

## Acknowledgment

The author wishes to thank P. ANTHOUARD and M. DESBOIS (both from the AVS/RCM division of TH-CSF) for the detailed information they supplied on the correlation processors built for the side-looking SAR.

## References

- [1] C.F. QUATE, R.B. THOMPSON - "Convolution and Correlation in real Time with nonlinear Acoustics" Appl.Phys. Lett. 16, 494-496 (1970)
- [2] L.O. SVAASAND - "Interaction between Elastic Surface Waves in Piezoelectric Materials" Appl.Phys. Lett. 15, 300-302 (1969)
- [3] M.V. LUTKALA, G.S. KINO - "Convolution and Time Inversion using Parametric Interaction of Acoustic Surface Waves" - Appl. Phys. Lett. 18, 393-394 (1971)

- [4] Ph. DEFRANCOULD, C. MAERFELD - "A SAW Planar Piezoelectric Convolver" - Proc. IEEE, 64, 5, 748-751 (1976)
- [5] P.A. DUFILIE - "Low Cost SAW Convolver with high Spurious Suppression" - Proc. 1980 IEEE Ultrasonics Symp. 43-47
- [6] H. ENGAN, K.A. INGEBRIGTSEN, A. RØNNEKLEIV - "Design of SAW Convolver for Processing MSK Modulated waveform" - Elec. lett. 16, 908-909 (1980)
- [7] H. GAUTIER, C. MAERFELD - "Wideband Elastic Convolvers" - Proc. 1980 IEEE Ultrasonics Symp. 30-36.
- [8] N.K. BATANI, E.L. ADLER - "Acoustic Convolvers using Ribbon Waveguide Beamwidth Compressors" Proc. 1974 IEEE Ultrasonics Symp. 114-116
- [9] R.A. BECKER, D.H. HURLBURT - "Wideband LiNbO<sub>3</sub> Elastic Convolver with Parabolic Horns" - Proc. 1979 IEEE Ultrasonics Symp. 729-731
- [10] B.J. DARBY, D.J. GUNTON, M.F. LEWIS, C.O. NEWTON - "Efficient Miniature SAW Convolver" Elec. Lett. 16, 726-728 (1980)
- [11] J. YAO - "High Performance Elastic Convolvers with extended T.B. Product" - Proc. 1981 IEEE Ultrasonics Symp. 181-185
- [12] M.F. LEWIS, C.L. WELT, - "High Performances SAW Convolvers" - Proc. 1981 IEEE Ultrasonics Symp. 175-180
- [13] W.R. SMITH - Proc. 1980 IEEE Ultrasonics Symp. 59-64.
- [14] D.P. MORGAN, D.H. WARNE, P.N. NASH, D.R. SELVISH - "Monolithic SAW Convolver using Chirp Transducers" - Proc. 1981 IEEE Ultrasonics Symp. 186-191
- [15] S.A. REIBLE - "Acoustoelectric Convolver Technology for Spread Spectrum Communications" - IEEE Trans. Microw. Theory Tech. MTT-29, 463-473 (1981)
- [16] R.W. RALSTON, J.H. CAFARELLA, S.A. REIBLE and E. STERN - "Improved Acoustoelectric Schottky Diode/LiNbO<sub>3</sub> Memory Correlator" - Proc. 1977 IEEE Ultrasonics Symp. 472-477
- [17] D.H. HURLBURT, R.W. RALSTON, R.P. BAKER and E. STERN - "Anacoustoelectric Schottky Diode Memory Correlator Subsystem" - Proc. 1978 IEEE Ultrasonics Symp. 33-37
- [18] G.S. KINO - "Zinc Oxide on Silicon Acoustoelectric Devices" - Proc. 1979 IEEE Ultrasonics Symp. 900-910
- [19] R.L. THORNTON and G.S. KINO - "Monolithic ZnO on Si Schottky Diode Storage Correlator" - Proc. 1980 IEEE Ultrasonics Symp. 124-128
- [20] J.E. BOWERS, B.T. KHURI-YAKUB and G.S. KINO - "Monolithic Surface Wave Storage Correlators and Convolvers" - Proc. 1980 IEEE Ultrasonics Symp. 118-123
- [21] R.L. THORNTON, J.E. BOWERS and J.R. GREEN - "Recent development in the ZnO on Si Storage Correlator" Proc. 1981 IEEE Ultrasonics Symp. 774-779
- [22] T.W. GRUDKOWSKI, G.K. MONTRESS, M. GILDEN and J.F. BLACK - "GaAs Monolithic SAW Devices for Signal Processing and Frequency Control" - Proc. 1980 - Ultrasonics Symp. 88-97
- [23] R.C. DIXON - "Spread Spectrum System" - Wiley 1976
- [24] D. BROTKORB and J.E. LAYNOR - "Fast Synchronization in a Spread Spectrum System based on Acoustoelectric Convolvers" - Proc. 1978 IEEE Ultrasonics Symp. 561-566
- [25] H. GAUTIER and P. TOURNOIS - "Very fast Signal Processors as a Result of the Coupling of SAW and Digital Technologies" - IEEE Trans. Microwave Th. and Tech., MTT-29, 404-409 (1981)
- [26] H. GAUTIER - "Digital Processors using SAW Devices" - Proc. 1981 IEEE Ultrasonics Symp. 206-219

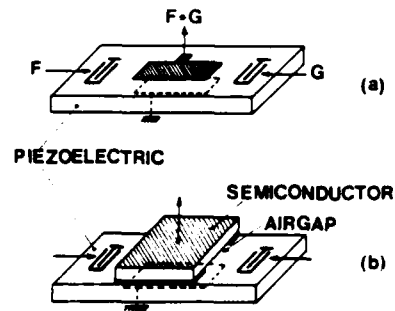


Figure 1. Basic Geometry of an Elastic (a) and an Acousto-electric (b) Convolver

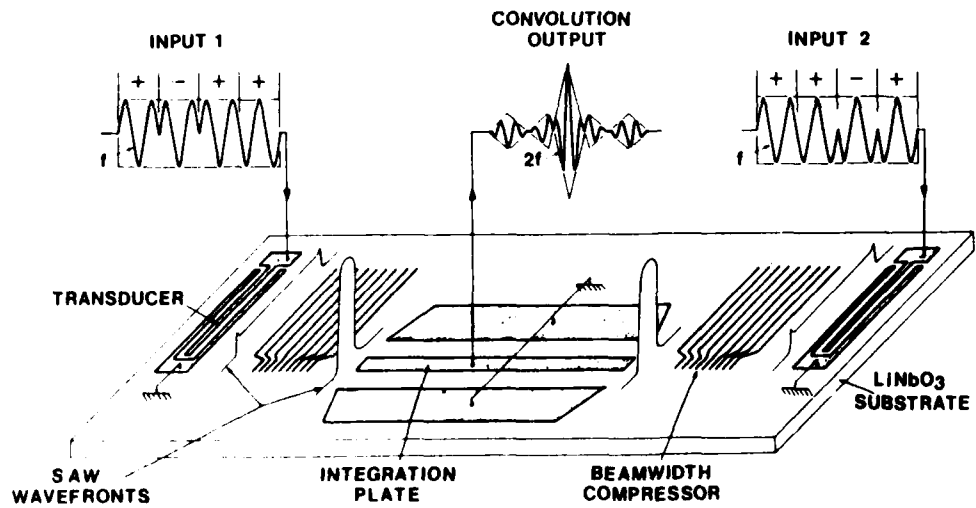


Figure 2. Piezoelectric Multistrip Beamwidth Compressor Waveguide Convolver (Elastic Type)

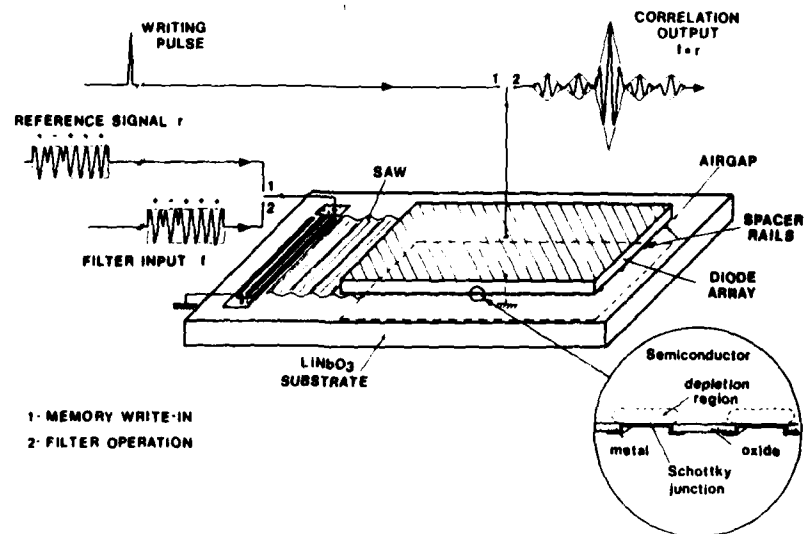


Figure 3. Schottky Diode/Airgap/LiNbO<sub>3</sub> Memory Correlator

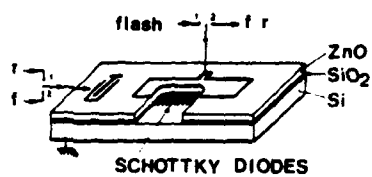
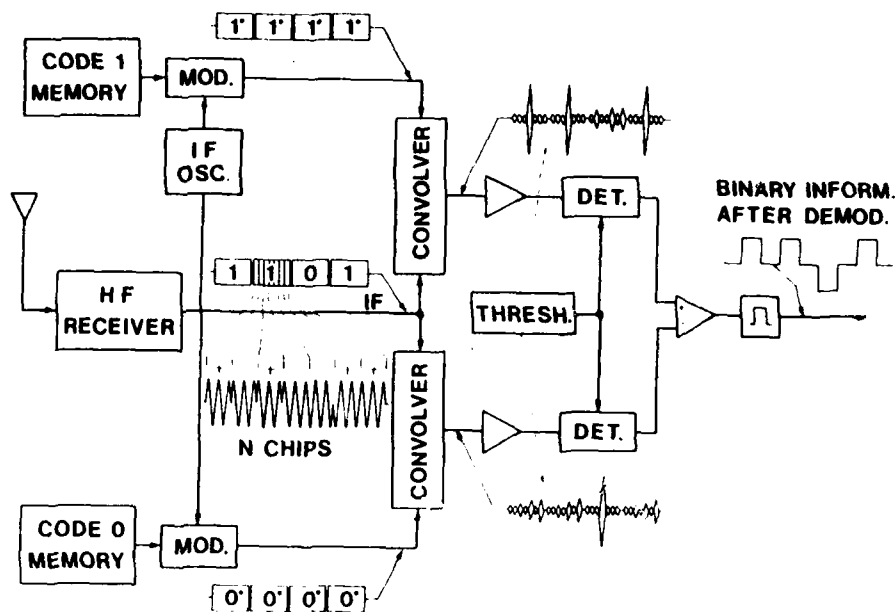


Figure 4. Schematic of a ZnO/Si Diode Array Memory Correlator



• Time Inverted Figure 5. Block Diagram of a Spread Spectrum Telecommunication System Employing Two Convolvers Operating in a Synchronous Mode to Demodulate Received Messages

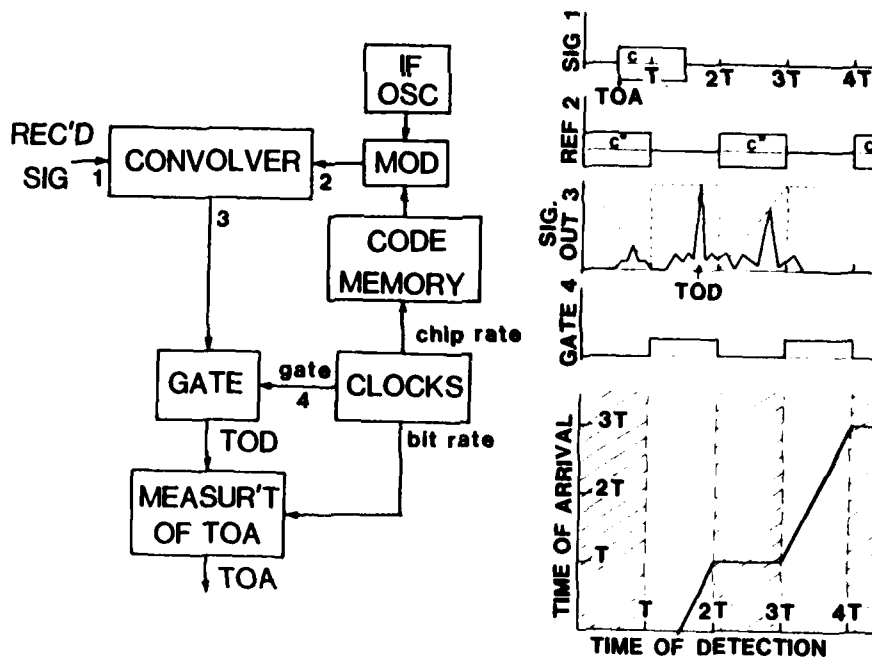
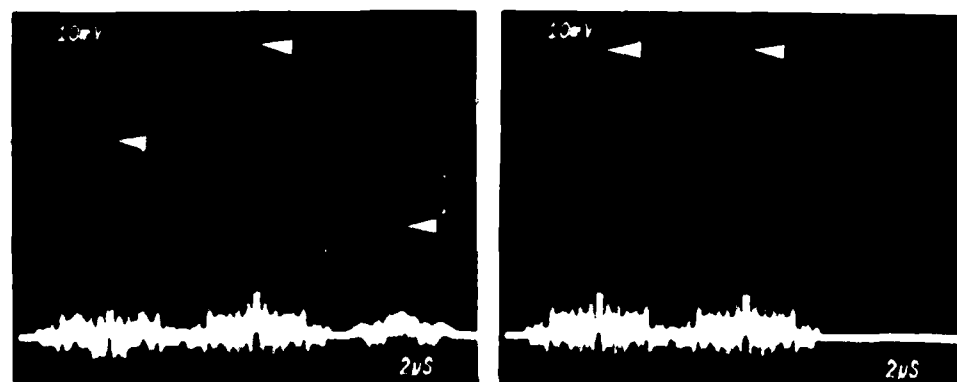


Figure 6. Simplified Block Diagram of a Spread Spectrum System Employing One Convolver to Operating in an Asynchronous Mode to Detect and Measure T.O.A. of Incoming Signals

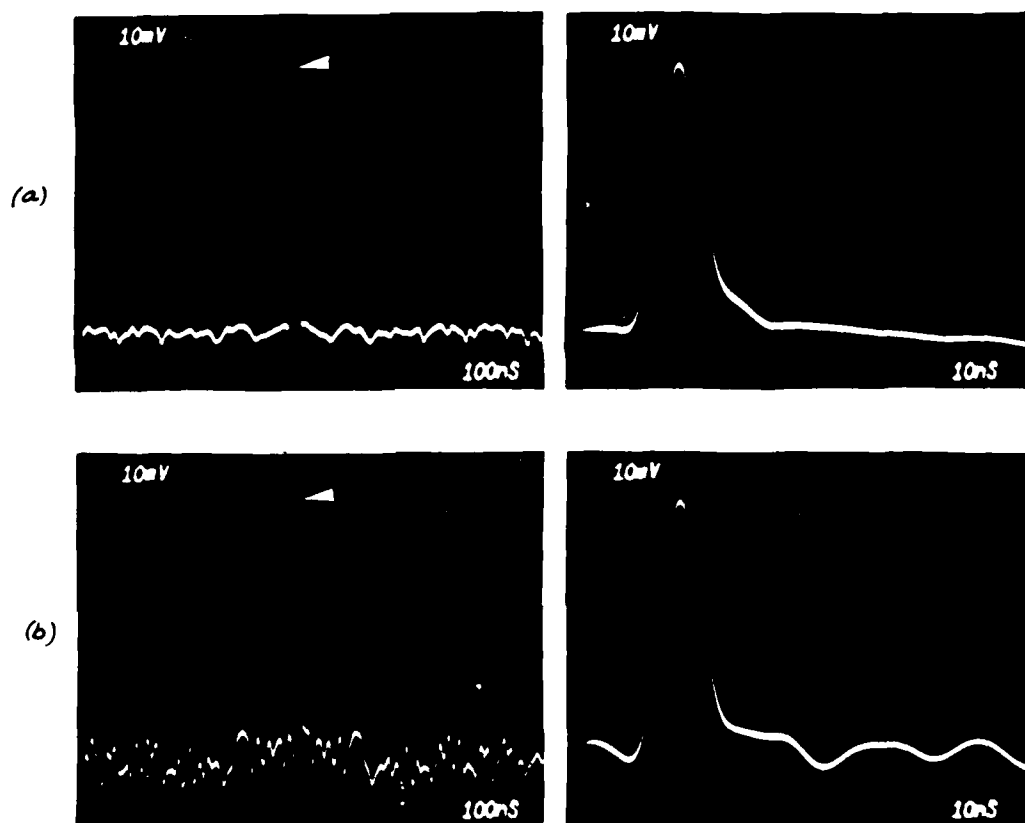
MCV-004B  
Coder de Gold 512 x 12.5ns



*Autocorrelation code 256  
avec référence répétitive (T = 12.8 μs)*

Figure 7. Typical Correlation Output Before Gating. (a) Reference Unsynchronized, (b) Reference Synchronized

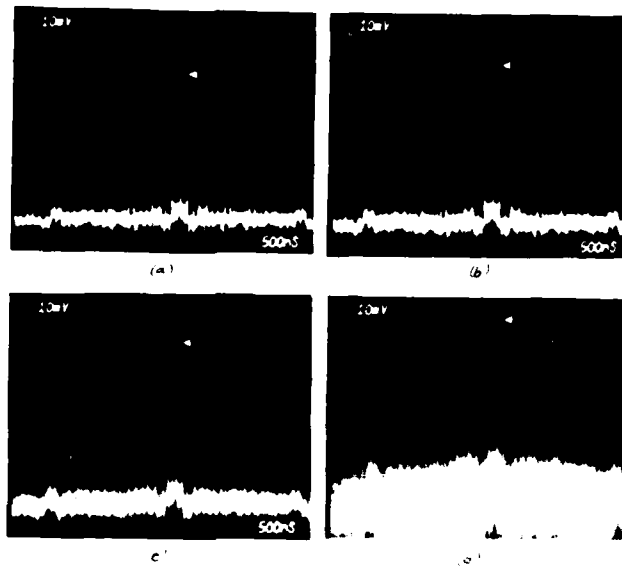
MCV-004B  
Code de Gold 512 x 12,5ns



Autocorrélation (a) code 0  
(b) code 256

Figure 8 Matched Filtering of Two 512 x 12.5 ns Chip Gold Codes (PSK Modulation) Using a Convolver Module

MCV 0048  
Code de Gold 512 x 12.5 ns



Autocorrelation code 256 en présence  
de bruit blanc additif sur signal  
(5/8)enher, 10 dB (a)  
0 dB (b)  
-10 dB (c)  
-20 dB (d)

Figure 9. Matched Filtering of a 512 x 12.5 ns Chip Gold Code in Presence of Additive White Noise. The Input Signal-to-Noise Ratio Varies from +10 to -20 dB by 10 dB Step

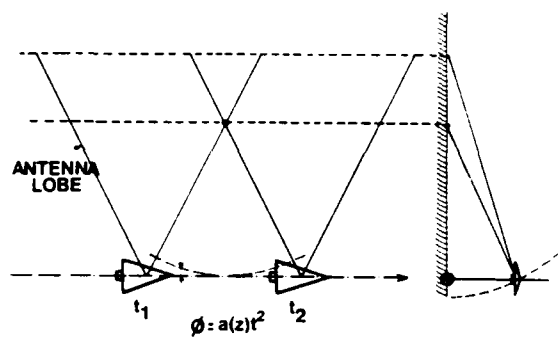
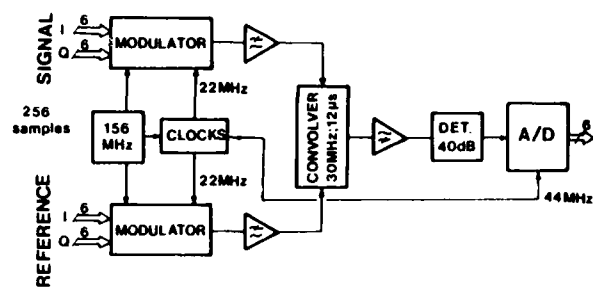


Figure 10. Principle of Operation of a Side Looking Synthetic Aperture Radar



#### CORRELATION PROCESSOR

Figure 11. Correlation Subsystem for SAR Processing

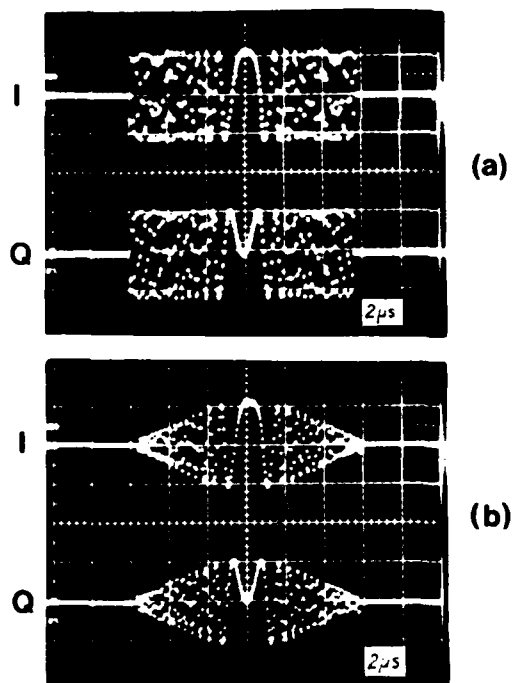


Figure 12. Input Test Signal (Unweighted) and Reference (Weighted) Linear Chirp Waveform (After D-to-A Conversion)

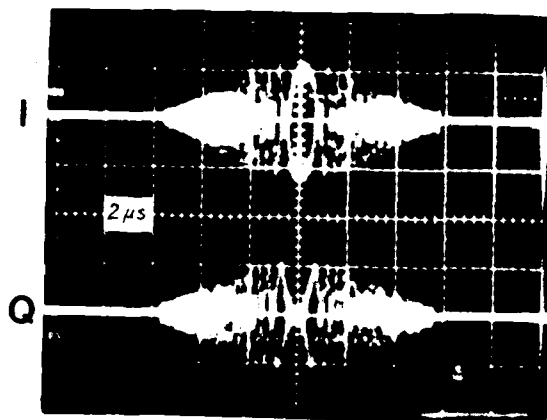


Figure 13. 155 MHz Carrier Wave Modulation by I and Q Digital Components of a Reference Weighted Chirp

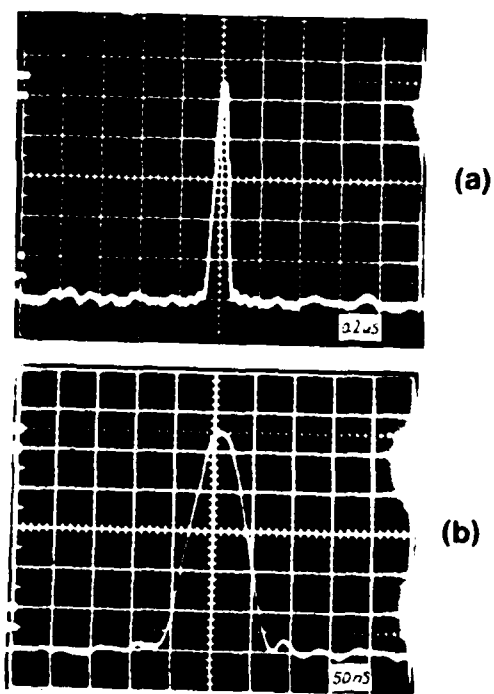


Figure 14. Correlation of Test Signal and Reference Digital Chirp Waveforms (After Linear Detection)

## ULTRAREPRODUCIBLE SAW RESONATOR PRODUCTION

W.E. Bulst, E. Willibald

Siemens AG, Research Laboratories, Munich, West Germany

Summary

A fabrication process for 300 MHz and 461 MHz SAW resonators with unloaded Q factors of 15000 and 12000 has been developed which yields a frequency reproducibility of  $\pm 15$  ppm within one substrate without individual frequency trimming for each chip. This was achieved by i) x-ray topographical preselection of natural-grown quartz substrates, ii) by the use of metallic grating reflectors fabricated by direct step on the wafer with a 1:10 optical projection printing and lift-off technique, and iii) by careful mounting. With typically 68 chips per substrate, 90% yield has been regularly achieved. The frequency deviation from substrate to substrate for selected natural quartz material is about  $\pm 0$  ppm. Therefore for most applications the post-fabrication frequency adjustment (trimming) of each individual resonator can now be omitted. The measurement of accelerated (high temperature) aging indicates that aging rates are obtained which are comparable to those for precision bulk wave crystals.

1. Introduction

A new technology such as that of surface acoustic waves (SAW) normally finds rapid initial application only in those sectors in which there are no practical alternatives. Examples of such applications are SAW pulse-compression filters for radar equipment<sup>1</sup>, wideband SAW delay lines for special receivers<sup>2</sup> and miniaturized oscillators with SAW resonators<sup>3</sup> as well as delay lines<sup>4</sup> in on-board equipments.

As against this, however, the unfamiliarity of SAW technology to the user leads to its reluctant acceptance in sectors in which well-established conventional techniques find wide application. In such cases the SAW component must offer a whole range of benefits, such as low cost, miniaturization, low power consumption etc. to start a change over to the new technology. Thus the TV-IF-filter, which is currently produced by the millions, offers the TV manufacturer a number of advantages in comparison with the conventional 6-pole LC filter,

such as greater design flexibility, small size, ruggedness and above all by obviating the considerable effort involved in individual tuning.

Advantages of SAW oscillators which have hitherto been realized, such as higher basic frequency and simple circuitry are however insufficient to persuade users to give up the familiar and optimally-established bulk wave crystal technology and thus bring about a wider application of SAW resonators and narrow band delay lines for oscillators in the VHF and UHF range in the sectors of TV, mobile radio, optical communications, measuring instruments etc. The user will switch to this technology only if there is severe pressure from the cost side and if such a switchover does not involve any performance degradation.

An essential cost factor in bulk wave resonator technology is the unavoidable frequency trimming of each individual crystal. In comparison with this, SAW technology involves planar techniques and thus promises greatly improved reproducibility. However, reported values for frequency reproducibility in SAW resonators currently are in the range of  $\pm 300 \dots \pm 500$  ppm<sup>5,6</sup> and thus still exceed the typical requirement of less than  $\pm 70$  ppm deviation from target frequency.

The purpose of this work therefore was to increase the reproducibility of SAW resonator fabrication to such a degree that individual resonator trimming can be completely omitted and to improve SAW resonator aging to achieve aging rates that are comparable to those of precision bulk wave crystals.

2. Design Considerations

SAW resonators were designed to be compatible with a simple single layer fabrication process. A two-port configuration was used consisting of two 24 finger pair Hamming weighted transducers with  $\pm 1/4$  fingers and two gratings with 500 shorted  $\pm 1/4$  metal strips. Transducers and gratings have an aperture of 100  $\mu$ . Using this design resonators with center frequencies of 300 MHz and 461 MHz were realized with

AD P001554

100 nm and 65 nm aluminium metallization thickness.

The metallization of the piezoelectric substrate leads to velocity changes in the metallized regions and thus to frequency shifts of the resonators. At least five factors must be considered in order to allow this velocity change to be anticipated in the design at least as an approximation. These are velocity changes resulting from

- short-circuiting of the piezoelectric tangential fields under the metallized layer

$$\frac{\Delta v}{v} \sim \frac{v_s - v_\infty}{v_\infty}$$

$v$  : SAW velocity

$v_s$  : SAW velocity on the electrically shorted substrate surface

$v_\infty$  : SAW velocity on the free substrate surface

- the mass loading of the surface acoustic waves by the metallized layer

$$\frac{\Delta v}{v} \sim h/\lambda$$

$h$  : thickness of metallic layer

$\lambda$  : SAW wavelength

- the storage energy effect<sup>7</sup> at the metal edges

$$\frac{\Delta v}{v} \sim (h/\lambda)^2$$

- the degree of coverage

$$B = \frac{F}{d} = \frac{F}{F + G} = \frac{1}{1 + \frac{G}{F}}$$

$d$  : finger period

$F$  : finger width

$G$  : finger gap

- the transducer thinning

$$T = \frac{\text{no. of metallized periods in transducer}}{\text{no. of all periods in transducer}}$$

The frequency change can be estimated by the empirically found formula:

$$\frac{\Delta f}{f} = \frac{\Delta v}{v} = T \cdot \left( B \cdot \left( \frac{v_s - v_\infty}{v_\infty} + A \cdot \frac{h}{\lambda} \right) + C \cdot \left( \frac{h}{\lambda} \right)^2 \right)$$

For

$$\frac{v_s - v_\infty}{v_\infty} = -0,58 \cdot 10^{-3}$$

an actual measurement on aluminium transducers on ST quartz, measured at 50 ohms, gave the results:  $A = -0.2$ ,  $C = -34$ .

Applied to 300 MHz SAW resonators with aluminium gratings ( $T \approx 1$ ) this formula yields a frequency deviation of about  $\pm 60$  ppm per 1 nm aluminium thickness variation and about  $\pm 4$  ppm per 10 nm line-width variation.

### 3. Fabrication

In order to attain the desired resonator frequency and high reproducibility in production four points have been considered carefully:

- quartz material
- mask pattern
- photolithography
- mounting.

The tolerances for the cut angle of the quartz substrates were specified at a maximum of  $\pm 1$  angular minute for the surface normal (37.5 deg.) and for the direction of wave propagation (X). The adjustment of our exposure equipment is accurate to  $\pm 1 \mu\text{m}/1 \text{ mm}$  or to 3.4 angular minutes, so that with this material relative frequency fluctuations of up to  $\pm 6$  ppm can be obtained<sup>8</sup>. Quartz material specified to such a precise degree is currently unobtainable on the market and is thus manufactured in-house. The wafers, having dimensions of 33 mm x 36 mm x 0.5 mm, are manufactured from natural quartz with maximum tapers of  $\pm 1 \mu\text{m}$ . A substrate etching subsequent to polishing, e.g. with ammonium bifluoride, to remove the damaged layer was not carried out.

Resonators were fabricated using direct step on the wafer with 1:10 optical projection printing. Reticles were manufactured by use of an ELECTROMASK pattern generator EM 220. It has been proven that machine tolerances in positional precision (effect on finger period) and in aperture resolution (effect on finger width) may result in fairly large frequency shifts ( $\approx \pm 20$  ppm... $\pm 60$  ppm for 300 MHz...900 MHz) for the SAW resonators. However, these frequency shifts can be compensated for by choosing an appropriate metallization thickness as will be shown later.

The photolithographic process consist of the following single steps:

- substrate cleaning
- evaporation of a 2 nm thick aluminium adhesive layer
- photoresist coating
- predevelopment
- exposure (D. MANN Photorepeater 3696)
- development
- aluminium evaporation
- lift-off.

Using this process the incidental fluctuations in line width (standard deviation) within one substrate are typically  $\delta \leq \pm 0.02 \mu\text{m}$  as measured with the "Latimet Automatic" by Leitz Ltd. This value is 10 times as accurate as that assumed in ref. 9 ( $\delta = \pm 0.2 \mu\text{m}$ ) and leads to a significant improvement in the reproducibility of both

the Q factor and the center frequency<sup>9</sup> (Fig. 6) of the resonators. A typical photolithographic yield for SAW resonators on quartz substrates is 98% for chip numbers between 50 and 100. The assessment criteria in this case are: no short-circuits or breaks in the transducers and a maximum of 5 defects (short-circuits and breaks) in the gratings. Yields of 95% are obtained in the individual chip handling process (cleaning, mounting, bonding).

After the optical check the 0.5 mm thick quartz substrates are cut into to a length of 0.45 mm and then broken. The mounting procedure is designed to avoid distortions by not clamping the chips in the direction of wave propagation. The result is the chip bonding mode (with Ablestik 611) shown in Fig. 1. Given workmanlike distortion-free mounting of the SAW chips in their packaging, microprobe measurements made directly on the wafer revealed no frequency shift as may result from sawing, breaking or bonding. After bonding, headers and lids are both subjected to intensive UV irradiation for 2 hours, then tempered for 24 hours in a vacuum oven at 180 deg. C, and finally welded in a nitrogen atmosphere (5% helium).

Taking into account the estimation in section 2, in most cases our first design provides us with an accuracy of  $\pm 100$  ppm in attaining the desired center frequency. Such frequency deviations may still be corrected in the prototype status simply by modifying the thickness of the metallic layer, without causing any significant distortions in the frequency response of the SAW resonators. Frequency deviations larger than  $\pm 100$  ppm may be corrected in a second reticle simply by scaling the finger periodicity and the desired center frequency is finally attained with an accuracy of  $\pm 30$  ppm.

#### 4. Electrical Testing

The resonators were electrically tested by using an automatic measurement system. This system consists basically of a network analyzer (HP 8505A), a synthesizer (HP 8662A), a quartz thermometer (HP 1804A) and a desk top computer HP 9835A, connected by the HP interface bus. In every run measurements were taken of temperature and minimum insertion loss as well as of the group delay time as a derivation of the phase response, and of the frequencies at minimum insertion loss and maximum group delay time. The uncertainty in the center frequency due to the limited resolution of amplitude (0.01 dB) and phase (0.1 deg.) measurement is  $\pm 1.5$  ppm.

## 5. Results

### 5.1 Resonator Frequency Response

Fig. 2 and 3 show the measured frequency response of typical 300 MHz and 461 MHz SAW resonators. One of the fundamental results of this investigation was to show that SAW resonators with aluminium gratings attain Q factors comparably to those of grooved resonators under the same conditions (air loading, non-recessed transducers with  $\lambda/4$  fingers). Their values range from about 50% to 60% of the material Q factor and can certainly be further improved by using more metal strips per grating, by making the strips thinner and by welding them under a vacuum. It should be noted in this regard that these Q factors were obtained by using a simple standard single layer process having optimal production conditions.

### 5.2 Reproducibility

The reproducibility of resonator frequency was first tested by fabricating 300 MHz resonators on a synthetic ST cut 3" quartz wafer (Fig. 4). Comparing resonator frequency and resonator location on the wafer (mapping) strong frequency shifts are observed also between adjacent chips which cannot be due to photolithography. Therefore the substrate material was investigated by x-ray topography in order to visualize defects and distortions in the crystal. At the center of the wafer shown in the topogram the small rectangular seed crystal can be seen, around which the quartz material grew in the autoclave under hydrothermal conditions. Growth lines run radially from the edges of the seed to the wafer edge, and these lines divide the wafer into sectors of varying crystal quality<sup>10</sup>. As was to be expected, the reproducibility in the more uniform grown Z sectors is higher than that in the X sectors. The resonators were exposed in pairs, i.e. each pair was exposed once only in a step-and-repeat process by the repeater, directly on the wafer. Thus the frequency variations within a pair result predominantly from local material irregularities. Probably the regular frequency increase in the direction of the flat occurs as a result of a gradual reduction of the aluminium layer thickness, but layer thickness measurements by an "Alphastep" by Tencor Ltd. provided no useful information since the measurements made by this instrument were reproducible only to  $\pm 2.5$  nm. In the future we hope to obtain an increase in reproducibility from wafers with pure Z areas (Fig. 5). Such wafers are currently being subjected to the same investigations.

X-ray topographs of natural quartz substrates (Fig. 6) with 461 MHz SAW resonators also show growth defects to some

extent and pronounced frequency scattering. After modification of our evaporation system to get better thickness uniformity we now regularly attain frequency reproducibility of  $\pm 50$  ppm on substrates of this kind. Typically the Q factor in these cases varies by  $\pm 5\%$  and the insertion loss by  $\pm 1$  dB.

Finally defect free natural quartz wafers were selected by x-ray topography (Fig. 7). Using these perfectly grown quartz wafers a frequency reproducibility of  $\pm 5$  ppm has been obtained.

### 5.3 Temperature response of aluminium grating resonators

The Q factor and insertion loss of aluminium grating resonators manifest a relatively high temperature dependence (Fig. 8 and 9). It is due probably to the increasing ductility of the aluminium with increasing temperature that the attenuation and hence the insertion loss in the resonator increase whereas the Q factor drops. In the case of ion milled grooved resonators (272 MHz,  $Q_{01} = 16000$ ) with only four finger pairs per transducer, the insertion loss and the Q factor remain almost unchanged in the temperature range  $-50$  to  $+130$  deg. C.

### 5.4 Aging investigations on aluminium grating resonators

It is intuitively assumed that the use of metal reflectors in place of grooved resonators, which are metallized only in the transducer area, must necessarily lead to an inferior aging response due to the high proportion of metallization in the active volume of the SAW resonator. With these factors in mind, active aging trials were carried out at room temperature. The effects of accelerated aging at  $150$  deg. C and of electrical drive level on the frequency response of the aluminium grating resonators were investigated. The results obtained indicate that the type of photolithographic fabrication process used is of decisive significance for the aging response of SAW resonators.

#### 5.4.1 Active Aging at Room Temperature

An unused 461 MHz resonator was connected together with a wideband amplifier (UTO 521, Avantek) in a simple, coaxial laboratory setup to form an oscillator circuit. The frequency and the power output were then measured with a counter (HP 5342A, aging rate of time base  $\approx 5 \cdot 10^{-10}$ /day), and the temperature with a quartz thermometer (HP 2804A). The initial aging rate was found to be  $\approx 1 \cdot 10^{-8}$ /day on the logarithmically fitted curve after 30 days warmup period (Fig. 10). The experiment was curtailed after 30 days when it became clear that the measurement would have to be repeated under much more closely controlled environmental conditions.

5.4.2 Accelerated Aging We subjected 35 300 MHz resonators (Fig. 1) to accelerated aging at  $150$  deg. C. The initial aging period in the oven was set at 2 hours and the time intervals were continually doubled. In the meantime the resonators were - after cooling down - successively connected into the same oscillator circuit as in section 6.4.1 and after a warmup period of 5 minutes and a temperature compensation to  $28$  deg. C, the oscillator frequency and output power were measured.

For 25 resonators the oscillator power was reduced by less than 2% in the course of the 44 days of accelerated aging at  $150$  deg. C, for a further 8 resonators it was reduced by less than 5%, and 2 resonators failed completely. The latter could be attributed to bonding failures, since subsequent bonding returned both these components to fully-functional condition.

The results of these aging measurements are shown for a typical case with logarithmic fitting in Fig. 11 and for all 35 resonators in Fig. 12. All the resonators age at fairly regular rate and apparently logarithmically towards higher frequencies. These results suggest a clean process and a good microclimate in the housing and indicate that aging is predominantly caused by oxidation and chemisorption processes<sup>11</sup>.

On the basis of van't Hoff's rule, according to which the reaction velocities of chemical processes approximately double at intervals of 10 Kelvin we estimated an acceleration factor of 512 for an conversion from  $150$  deg. C to  $60$  deg. C. Thus the logarithmically fitted curve (Fig. 13) of the mean value of 33 resonators, yields an aging rate at  $60$  deg. C of  $5 \cdot 10^{-6}$  ( $512 \cdot 22$  days)  $= 4.4 \cdot 10^{-10}$ /day  $= 1.6 \cdot 10^{-7}$ /year after 22 days of accelerated preaging.

Mention should be made in this connection of the relatively rough handling of our SAW resonators in comparison with that of the ultra-precise bulk wave crystals (no polyimide adhesive, no high-temperature process in an ultra-high vacuum prior to welding) and the high drive level of  $10$  mW for our SAW resonators in comparison with typical  $100$   $\mu$ W for precision bulk wave crystals<sup>12</sup>.

5.4.3 Aging as a Function of Electric drive level The effect of drive level on the properties of the resonators has already been described in <sup>13,14</sup>. The passive measurements showed reversible changes of the center frequency of the resonators to be a function of the magnitude of the drive level, this probably being due to thermal effects.

Of particular interest to the oscillator user is the aging rate of the oscillator frequency as a function of drive level<sup>15</sup>. For this purpose, a 461 MHz SAW resonator was connected together with a power amplifier (ZHL 2-8, Mini Circuits Lab.)

to form an oscillator loop, and the drive level was increased every 24 hours by means of the amplifier supply voltage. After one hour's warmup time, the oscillator frequency, resonator drive level and resonator temperature were measured, and then measured again 24 hours later at the same conditions. The measured frequency variation over a 24 hour period is plotted in Fig. 14 as a function of drive level and indicates increasing irreversible frequency shifts (aging) at drive levels  $> 15$  dBm.

#### 5.4.4 Discussion of the Aging Results

Our aging measurements indicate, that

- the measured accelerated aging rates of SAW resonators with aluminium gratings are clearly more reproducible than those previously published for grooved resonators<sup>16,17</sup>.
- SAW resonators with aluminium gratings can attain the aging rates of very good bulk wave crystals when their measured accelerated aging values are extrapolated down to normal temperatures.

To our understanding there are three possible explanations for these results:

- We do not evaporate a chrome adhesive layer before aluminium evaporation. Bulk wave crystals with chrome/gold electrodes manifest significantly higher aging rates than those with nickel/gold electrodes<sup>11</sup>.
- We use a lift-off technique instead of wet etching technique and therefore only mild organic solutions in contrast to extremely corrosive agents.
- We do not use ion- or plasma-etching and therefore the polished quartz surface remains in perfect condition.

It could even be, that the active region of SAW resonators, being only a few  $\mu\text{m}$  thin and close to the surface, may well attain its equilibrium condition more rapidly than a bulk wave crystal, typically more than  $0.1 \mu\text{m}$  thick, and can thus attain lower aging rates more rapidly.

#### Conclusion

The following conclusions can be drawn from the methods and results presented in this paper: SAW resonators with aluminium gratings are mature for large-scale application and, in technological terms, are ready for mass production in the frequency range from about 200 MHz to 800 MHz. The production process described here guarantees high yields, high reproducibility (individual trimming is obviated) and thus low expenditures. In addition, a substantially improved long-term resonator aging in comparison with previously known values is recorded. The use of SAW resonators could therefore represent a superior alternative in certain application areas which were

previously the exclusive domain of precision bulk wave crystals. With respect to yield, reproducibility and aging, the results of this investigation are fully transferable to narrow-band SAW and surface skimming bulk wave (SSBW) delay lines for oscillators in the frequency range 200 MHz to 1.5 GHz.

#### Acknowledgement

The authors would like to thank Gertrud Lindemann, Bernhard Kamp and Peter Keinath for the careful and workman-like fabrication of the resonators.

#### References

1. Stocker, H., Veith, R., Willibald, E., Riha, G., "Surface Wave Pulse Compression Filters with Long Chirp Time", Proc. Ultrasonics Symposium (1981), pp. 78-82
2. Stocker, H., Bulst, W., Eberharter, G., Veith, R., "Octave Bandwidth High Performance SAW Delay Lines", Proc. Ultrasonics Symposium (1980), pp. 386-390
3. Tanski, W., Cyr, R., Dragonetti, P., Kosco, E., "A Radar System Application of an 840 MHz SAW Resonator Stabilized Oscillator", IEEE Trans. Sonics Ultrasonics, Vol. SU-28, No. 3, May 1981, pp. 146-150
4. Lau, K., Yen, K., Kagiwada, R., Kong, A., "High Frequency Temperature Stable SBAW Oscillators", Proc. Ultrasonics Symposium (1980), pp. 240-244
5. Ebata, Y., Sato, K., Morishita, S., "LiTaO<sub>3</sub> SAW Resonator and its Application to Video Cassette Recorder", Proc. Ultrasonics Symposium (1981), pp. 111-116
6. Mierzewski, M., Terrien, M., "280 MHz Production SAWR", Hewlett Packard Journal, December 1981, pp. 15-16
7. Li, R., Melngailis, J., "Second-Order Effects in Surface Wave Devices due to Storage Energy at Step Discontinuities", Proc. Ultrasonics Symposium (1973), pp. 503-505
8. Bell, D.Jr., "Phase Errors in Long Surface Wave Devices", Proc. Ultrasonics Symposium (1972), pp. 420-423

9. Field, M., Chen, C., "Investigation of Statistical Variations of the Characteristics of SAW Devices due to Random Fabrication Errors", IEEE. Trans. Sonics Ultrasonics, Vol. SU-29, No. 1, January 1982, pp. 42-49
10. Prospects of Sawyer Research Products, Inc., Eastlake, Ohio
11. Landsberg, P., "On the Logarithmic Rate Law in Chemisorption and Oxidation, The Journal of Chemical Physics, Vol. 23, No. 6, June 1953, pp. 1079-1087
12. Privat Communication to W. Mattuschka, Quartz Specialist, Siemens AG
13. Schoenwald, J., Wise, J., Staples, E., "Absolute and Differential Aging of SAW Resonator Pairs", Proc. 35th AFCS (1981), pp. 383-387
14. Tanski, W., "Elements of SAW-Resonator Fabrication and Performance", Proc. 35th AFCS (1981), pp. 388-394
15. Shreve, W., Bray, R., Elliott, S., Chu, Y., "Power Dependence of Aging in SAW Resonators", Proc. Ultrasonics Symposium (1981), pp. 94-99
16. Bell, D.Jr., Miller, S., "Aging Effects in Plasma Etched SAW Resonators", Proc. 35th AFCS (1976), pp. 358-362
17. Shreve, W., "Aging in Quartz SAW Resonators", Proc. Ultrasonics Symposium (1977), pp. 857-861

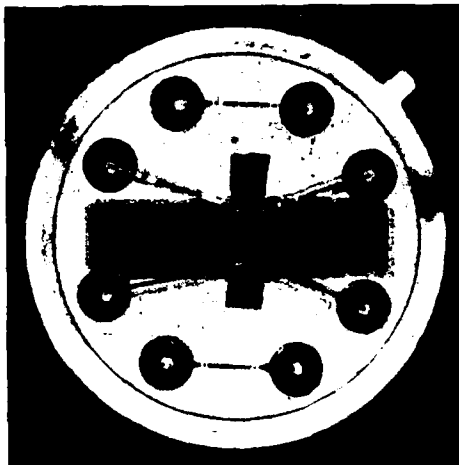


Fig. 1: 300 MHz SAW test resonator with aluminium grating mounted in a T08 header.

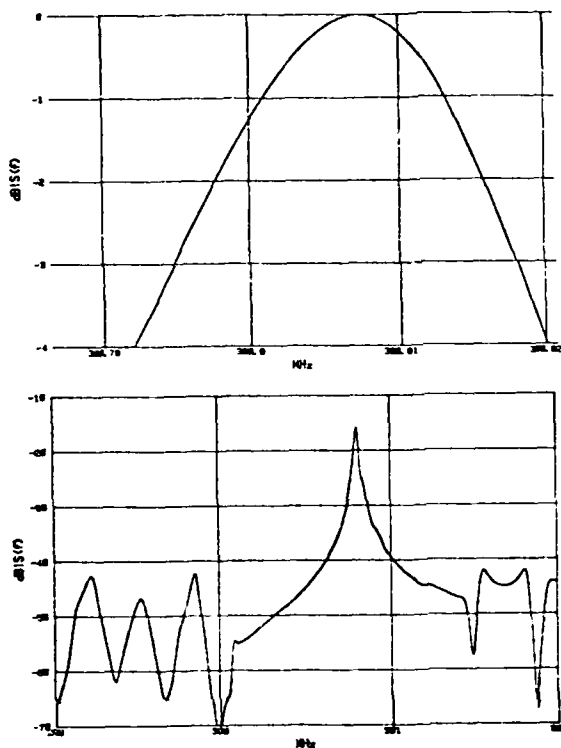


Fig. 2: Typical frequency response measurement of 300 MHz SAW resonators with aluminium gratings, showing an unloaded Q of 15,700.

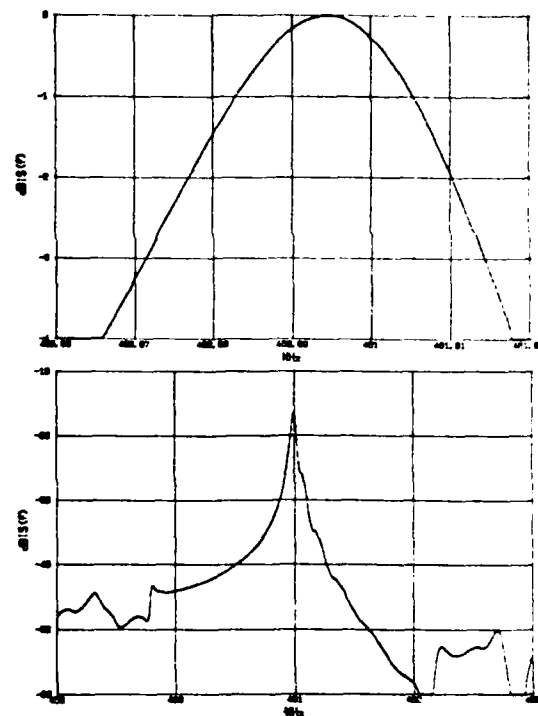


Fig. 3: Typical response of 461 MHz SAW resonators with aluminium gratings, showing an unloaded Q of 12,800.

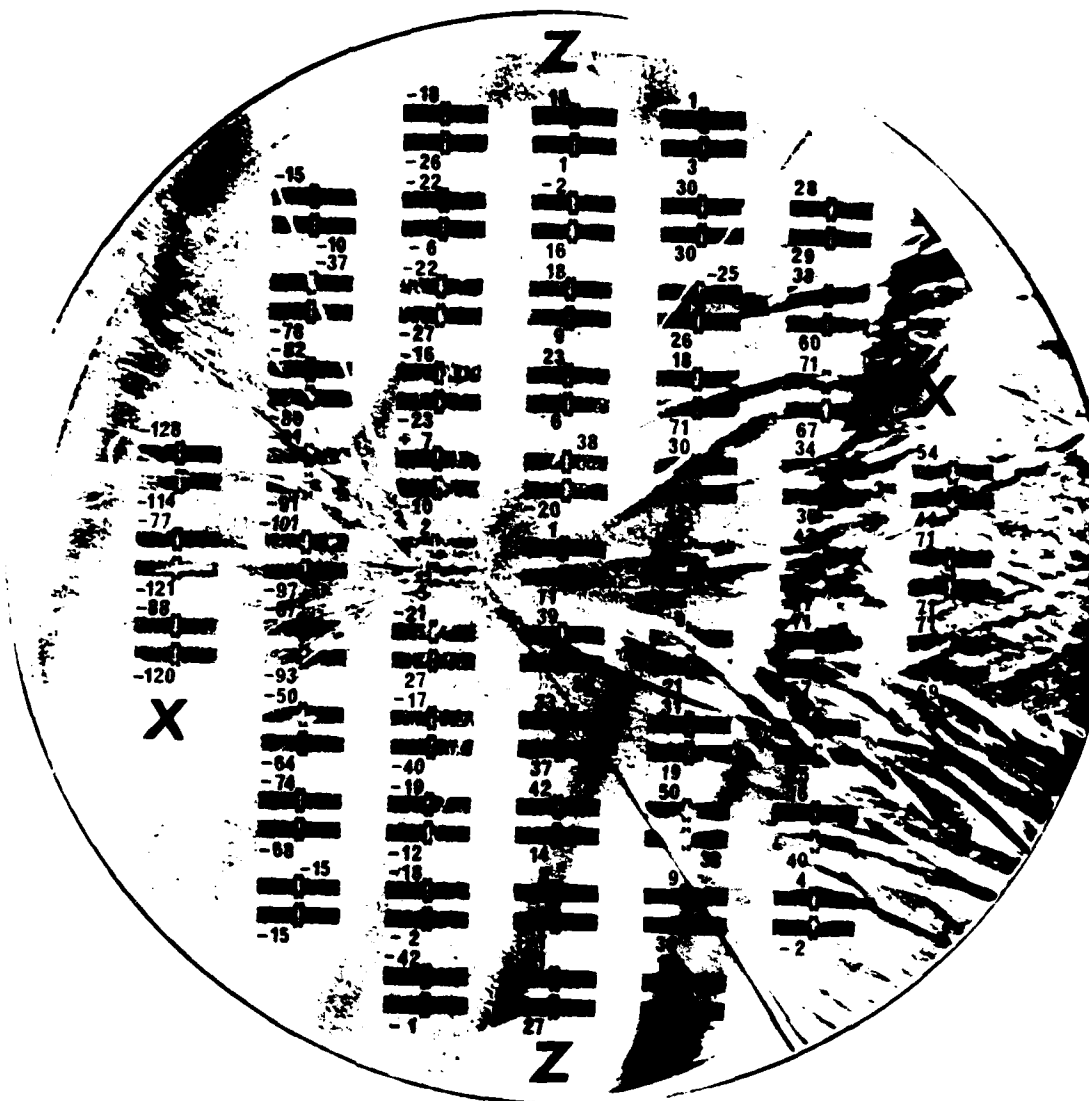


Fig. 4: SAW resonator reproducibility investigation on a 3" wafer of synthetic quartz with small seed and small low-defect Z areas. The wafer was x-ray topographed to obtain a correlation between resonator characteristic and material features. The figures indicate the relative frequency deviations in ppm from the mean value for all the resonators.

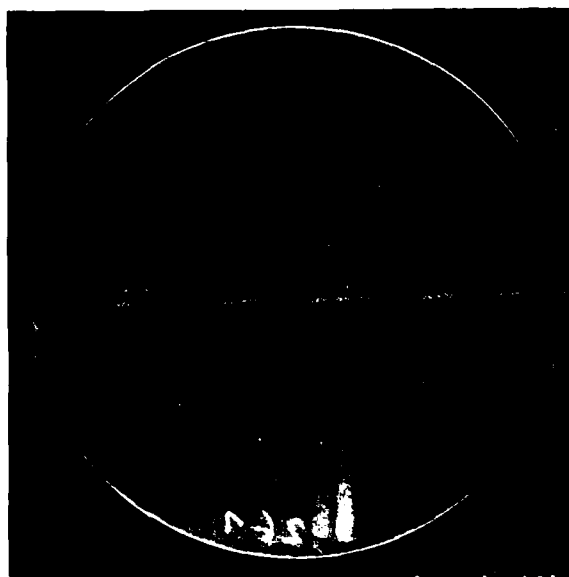


Fig. 5: X-ray topograph of a recent ST cut 3" wafer of synthetic quartz with a long, narrow seed and pure low defect Z growth.

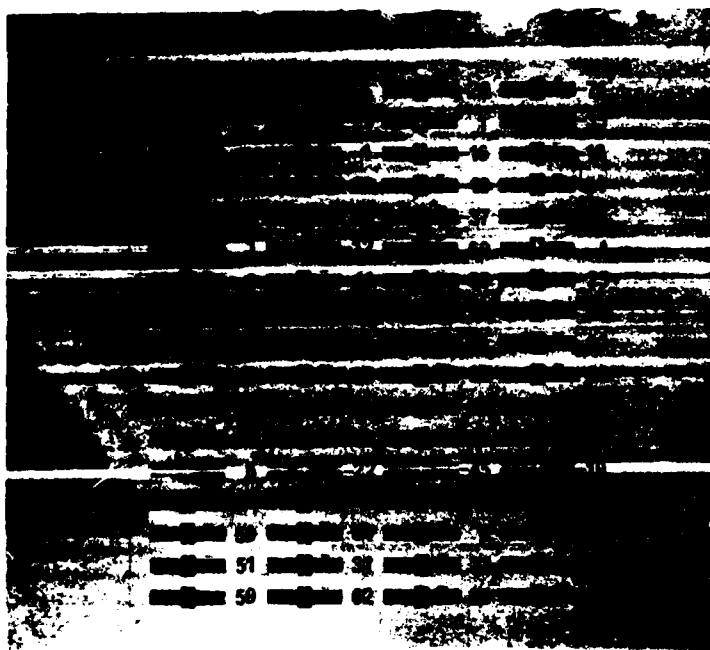


Fig. 6: As Fig. 4, but with rectangular wafer of natural quartz.

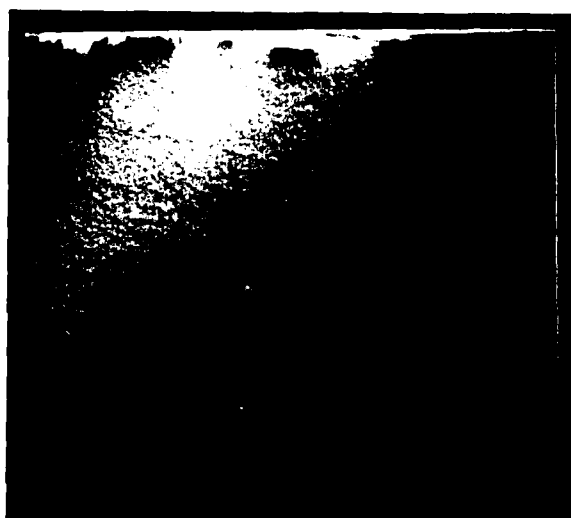


Fig. 7: X-ray topograph of a natural quartz wafer with perfect crystal structure.

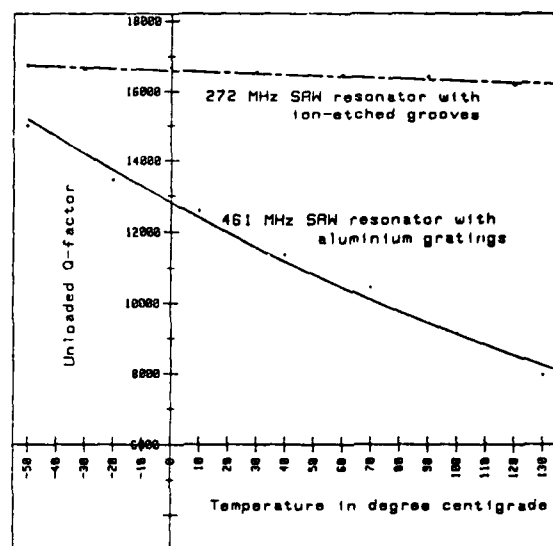


Fig. 8: Measured temperature dependence of Q factor for SAW resonators. Lines: exponentially fitted to measured data.

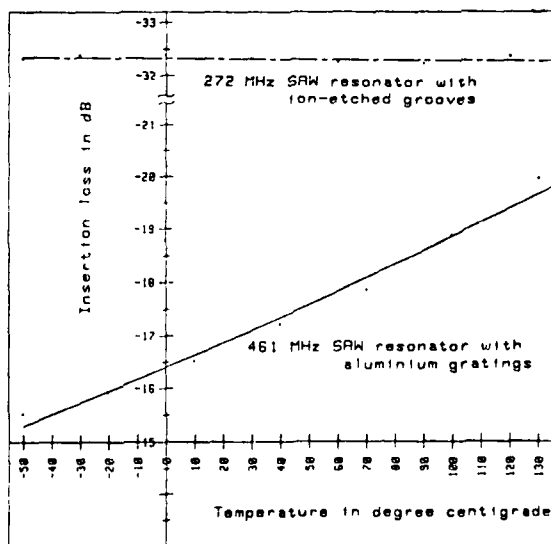


Fig. 9: Measured temperature dependence of insertion loss for SAW resonators. Lines: exponentially fitted to measured data.

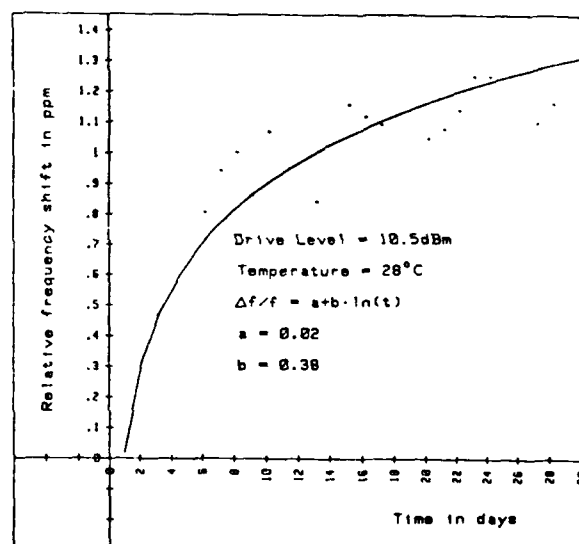


Fig. 10: Initial aging of a 461 MHz SAW resonator with aluminium gratings. Solid line: logarithmically fitted to measured data.

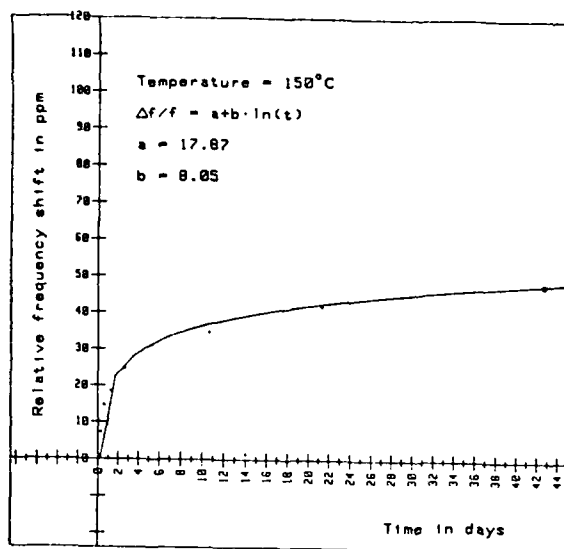


Fig. 11: Typical accelerated aging of a 300 MHz SAW resonator with aluminium gratings, solid line: logarithmically fitted to measured data.

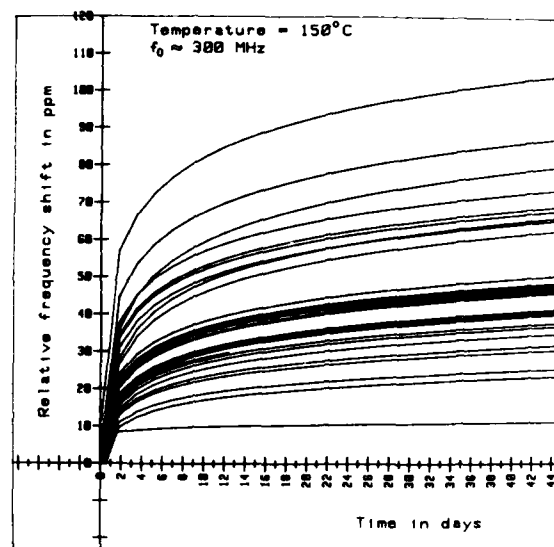


Fig. 12: Accelerated aging of 35 SAW resonators with aluminium gratings, logarithmically fitted curves to measured data shown only.

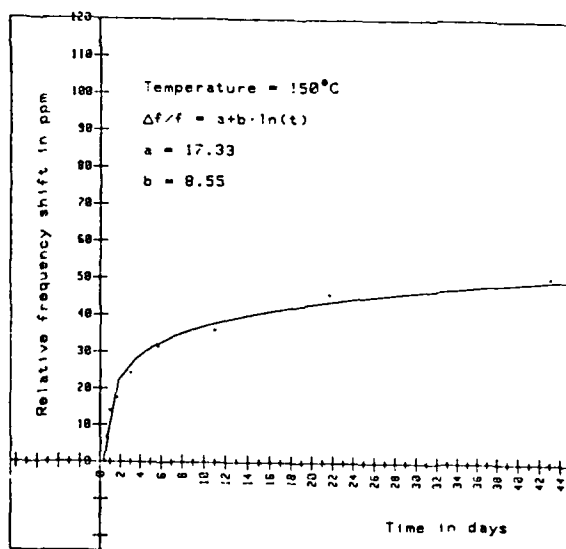


Fig. 13: Accelerated aging of 300 MHz SAW resonators with aluminium gratings, showing the mean value for 33 resonators.

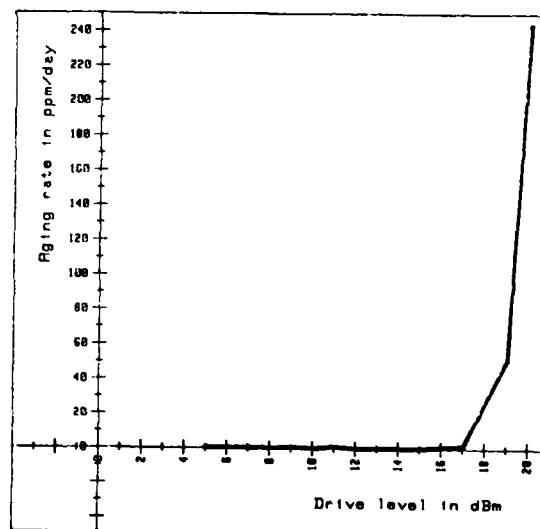


Fig. 14: Aging rate vs. drive level for a 461 MHz SAW resonator with aluminium gratings (active measurement).

AD P001555

## DEVELOPMENT OF PRECISION SAW OSCILLATORS FOR MILITARY APPLICATIONS

T. E. Parker  
Raytheon Research Division  
131 Spring Street  
Lexington, Massachusetts 02173  
(617) 863-5300, ext. 3084

Abstract

For the past few years Raytheon has had a program to develop, for potential military applications, SAW oscillators in the 300-600 MHz range which exhibit simultaneously state-of-the-art performance in frequency settability and stability. Though specific applications will not be discussed, the requirements are, in general: (1) The noise floor must be at least -160 dBc/Hz; (2) Vibration sensitivity should be at least as good as that of AT-cut bulk-wave devices; (3) The oscillator frequency must be set in, and stay in, a window of approximately  $\pm 10$  ppm. In some cases, a warm-up time of less than 3 minutes may be required. Significant progress has been made in meeting these requirements and will be discussed in this paper.

In the area of spectral purity, two topics are discussed. The first is a low-noise amplifier which has demonstrated a -176 dBc/Hz noise floor when used with a 310-MHz SAW resonator. Second, the effects of external vibration on noise sidebands are briefly reviewed. One of the most important areas of SAW oscillator development has been that of frequency settability. A trimming technique using gold phase pads has been demonstrated on both delay lines and resonators. Experimental results are presented. One complication that is discussed is the occurrence of a frequency shift during sealing that is on the order of 100 ppm. However, external pulling techniques have been developed to re-adjust the frequency. Many applications require the use of ovens to maintain a constant temperature. Fast warm-up may then become a requirement, and data is presented to show the frequency stability for a 3-minute warm-up period. Finally, in addition to all of the above requirements, a SAW oscillator must maintain a long-term stability of  $\pm 1$  ppm per year. Data is presented to establish baseline aging rates for devices cold weld sealed in TO-8 packages and also to show rates for trimmed devices, and devices mounted for low vibration sensitivity.

Introduction

Surface acoustic wave (SAW) controlled oscillators have been successfully used in a number of military and commercial applications where high frequency and/or low noise were important considerations. However, these applications have generally had rather loose requirements on frequency settability and stability. A typical frequency window

has been  $\pm 500$  ppm. There remain, however, a large number of other applications with significantly tighter requirements that would be ideal for SAW oscillators if they could meet the performance criteria. A number of problem areas, such as long-term stability, frequency trimming, and vibration sensitivity, have been under investigation, and in many cases acceptable performance has been obtained. However, it still remains to be demonstrated that all of these desirable improvements can be obtained simultaneously in a single device.

For the past few years Raytheon has had just such a development program on 300-600 MHz devices aimed at several potential military applications. Though specific applications will not be discussed, the requirements are, in general: (1) The noise floor must be at least -160 dBc/Hz and in some cases greater than -170 dBc/Hz; (2) Vibration sensitivity should be at least as good as that of AT-cut bulk-wave devices; (3) The oscillator frequency must be set in, and stay in, a window of approximately  $\pm 10$  ppm. In some cases, a warm-up time of less than 3 minutes may be required. Significant progress has been made in meeting these requirements and is discussed in this paper.

Spectral PurityLow Noise Floor

The performance of an oscillator using a custom-designed amplifier\* will be discussed to illustrate the low noise floor obtainable with a SAW oscillator and how this may interact with other areas of frequency stability. Figure 1 shows the oscillator circuit. The heart of the amplifier is a cascode arrangement of two HP HXTR 5104 bipolar transistors and a separate limiter stage. The two transistors provide 14 dB of gain with an output power of +20 dB. One-tenth of this power is coupled to the oscillator output through a directional coupler. The coupler, phase shifter, and limiter have about 6 dB loss (including 3.0 dB due to limiting), which results in a power level of +14 dBm incident on a two-port 310-MHz resonator. The resonator has 8 dB insertion loss (10 dB in a 50  $\Omega$  system), a loaded Q of 12,000, and dissipates 9 mW. With an amplifier noise figure of approximately 4 dB, this results in a noise floor on the order of -176 dBc/Hz. Figure 2 shows the measured RMS FM noise in the range from 10 KHz to 200 KHz. The solid line

\* See acknowledgements.

indicates a level corresponding to  $-176$  dBc/Hz, and the oscillator FM noise is clearly below this level down to about 20 KHz off the carrier.

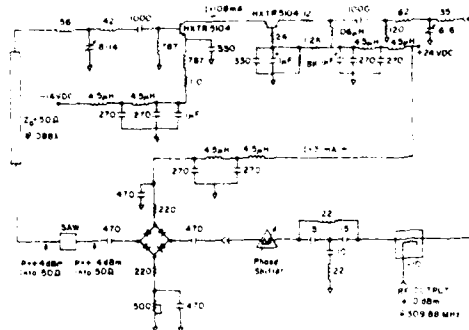


Fig. 1 Circuit diagram of a 310 MHz SAW oscillator which produces a noise floor of  $-176$  dBc/Hz. Unless otherwise stated, all values are pF, nH, or  $\Omega$ .

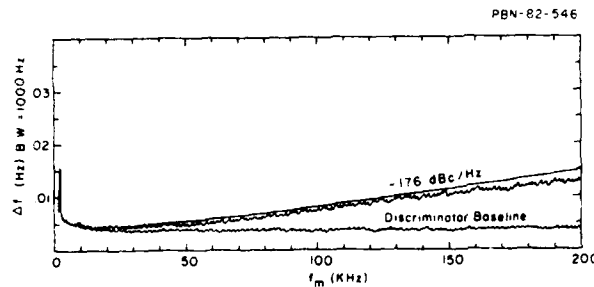


Fig. 2 Measured RMS FM noise for the SAW oscillator in Figure 1. Solid line shows the level corresponding to  $-176$  dBc/Hz.

The key to achieving this low noise floor is the high power level in the oscillator loop. Caution must be exercised in setting this level, however, since it has been shown that high power levels can lead to high aging rates in SAW resonators.<sup>(1,2)</sup> To minimize the stress level in the SAW device, a very large cavity area has been used. The 310 MHz resonator has an effective cavity length of 370 wavelengths and an acoustic aperture of 148 wavelengths. This results in a peak stress level of  $3.4 \times 10^7$  N/m<sup>2</sup>, which is safely below the high aging threshold of  $6 \times 10^7$  N/m<sup>2</sup> for pure aluminum transducers.<sup>(1)</sup> Further lowering of the noise floor is possible through the use of copper doping<sup>(1)</sup> in the aluminum, since this increases the high aging threshold and therefore permits higher power levels. Also, a device with lower insertion loss would help to decrease the noise floor even further.

#### Vibration Sensitivity

Catastrophic failure of SAW devices under vibration has not been a problem, but the effect of vibration on spectral purity is of considerable

importance. In severe military environments, high vibration levels may significantly degrade close-in noise performance of low-noise oscillators by creating sidebands at the vibration frequency. The sensitivity of SAW devices to vibration has been discussed in detail elsewhere,<sup>(3)</sup> but some aspects relating to interaction with long-term frequency stability will be reviewed here. As discussed in reference 3, ST-cut SAW devices exhibit a vibration sensitivity similar to that of AT-cut bulk-wave devices if proper mounting techniques are used. One technique which gives a vibration sensitivity of less than  $1 \times 10^{-9}$  per g uses double-sided tape to hold the SAW substrate against the SAW package. This technique is, however, unsatisfactory for good long-term frequency stability because of outgassing from the tape. A more practical approach is a four-point support which uses L-shaped steel clips and polyimide adhesive. This mounting technique gives a vibration sensitivity in the low  $10^{-9}$  per g range, and, as is shown later in this paper, does not cause high aging rates.

Figure 3 shows some recent data for the vibration sensitivity of an entire X-band source.\* This source was made up of a  $\times 24$  multiplier and six delay lines in the 400-MHz range mounted with the "L" clip and polyimide technique. Each of the six lines could be switched into the oscillator loop electronically to provide frequency agility. The whole source occupied a volume of only 24 cubic inches. Relatively large SAW substrates resulted in some increase in vibration sensitivity of the SAW itself, but vibration isolation at the board and module levels counteracted most of this. For a 5-g RMS random noise level (10 Hz to 3 KHz), a 23-dB rise was observed at 1 KHz. By 4 KHz, all evidence of a rise had disappeared.

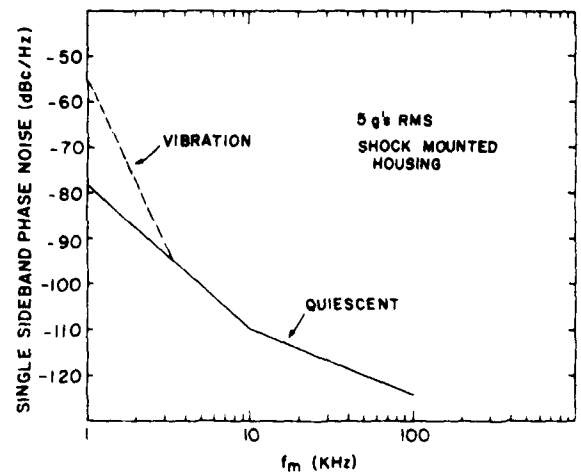


Fig. 3 Single sideband phase noise measured on X-band source when subjected to a random vibration level of 5 g's RMS. Two levels of shock mounting were used.

\* See acknowledgements.

## Frequency Settability

### Trimming

While spectral purity has been an important feature which has resulted in some applications for SAW oscillators, many more potential applications additionally require operation in a very narrow frequency range. Since the pulling range of resonators is limited, and in some cases circuit parameters limit the pulling of delay lines, the SAW devices must be fabricated to within a narrow frequency range. In practice, fabrication variables usually result in a frequency spread of  $\pm 500$  ppm, though careful process control can result in a much smaller spread.<sup>(4)</sup> An alternative technique for obtaining tighter frequency control is frequency trimming. This involves adjusting the frequency of the devices after the basic fabrication is finished. Trimming of resonators using reactive ion etching has been discussed in the literature<sup>(5,6)</sup> but here we will discuss results obtained by controlling the thickness of gold pads.

Figure 4 shows the basic geometry of frequency trimming with gold pads. For either a delay line or a resonator, a gold pad is placed between the input and output transducers. The surface wave propagates at a slower velocity under the gold and, hence, lowers the frequency of the oscillator. The actual trimming can be accomplished by controlling the pad thickness in either of two ways. One, as shown in Figure 4, requires that the gold pad be deposited photolithographically first, and then the thickness can be reduced by ion-beam etching. The etching is done while the SAW device is operating so that the trimming is accomplished in real time. The alternative technique is to deposit the gold through a metal mask onto an operating device and, therefore, adjust the frequency by depositing increasingly thicker pads. Both techniques proceed at very controllable rates and allow the frequency to be adjusted to well within 1 KHz. Typical pad dimensions are 0.1 mm width and 50 to 500 Å thickness.

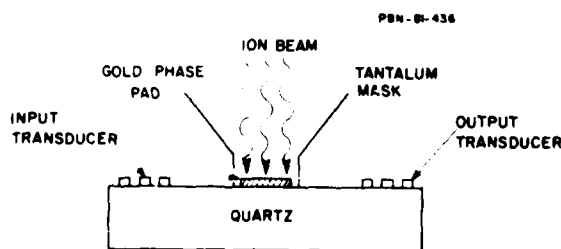


Fig. 4 - Geometry of frequency trimming with gold pads.

The main disadvantage of trimming with gold pads is that the gold increases the acoustic loss slightly. For delay lines, this has a negligible effect, but for resonators it causes a noticeable decrease in Q. The ion-beam etching technique has a further disadvantage in that some of the

gold removed by the ion beam redeposits elsewhere on the substrate. This has on occasion led to cessation of oscillation.

Though SAW oscillators can be trimmed to within 1 KHz of a desired frequency, this does not mean that the final operating frequency will be this well controlled. After trimming, the SAW devices undergo a high-temperature bake and sealing, and significant frequency shifts have been observed during this process. Frequency shifts have been measured on 37 devices (both delay lines and resonators) for both cold-weld sealing in high vacuum and resistance-weld sealing in dry nitrogen. The results of these measurements are summarized in Table I. For all devices, the trimming was done in a vacuum chamber different from that used for sealing. In the case of the cold-weld devices, the trimming and sealing equipment was in the same laboratory, and hence, the time spent in transporting from one system to the other was minimal. The resistance-weld sealing, however, was done in a different facility, and the transportation time was on the order of hours. Therefore, the vacuum bake-out on these devices was performed at the facility where the resistance welding equipment was located.

Table I

Frequency Shifts from Bakeout and Sealing

Packaging Parameters	Frequency Shift	No. of Devices
Cold Weld TO 8 in High Vacuum		
Baseline	$+117 \pm 47$ ppm	1
Trimmed	$+195 \pm 57$ ppm	5
"L" clips, polyimide	$+20 \pm 37$ ppm	4
Resistance Weld in Nitrogen		
(all trimmed and mounted with "L" clips and polyimide)		
TC 8	$74 \pm 65$ ppm	8
Flatpack	$63 \pm 12$ ppm	14 (3 separate packages)

As can be seen in Table I, the frequency shifts are on the order of 100 ppm and have a different sign for cold-weld and resistance-weld sealing. The devices in the cold-weld TO-8's, which are labeled as "baseline," are untrimmed and mounted with gold wire straps. The "trimmed" devices are mounted with gold wire straps and were trimmed with either ion-beam etching or direct evaporation. The "L clips, polyimide" devices were untrimmed and mounted as indicated. All resistance-weld devices were trimmed (either ion-beam etching or direct evaporation) and mounted with "L" clips and polyimide.

By anticipating the observed shifts, the initial frequency trimming can be done either high or low, depending on the type of sealing to be used. This still leaves, however, a frequency uncertainty of approximately  $\pm 50$  ppm. This is an order of magnitude smaller than the initial fabrication uncertainty, but it means that some sort of electronic pulling is still required to reach the desired range of  $\pm 10$  ppm.

## Electronic Pulling

SAW resonators in the 300-600 MHz range typically have loaded Q's from 5000 to 15,000, which makes them very narrow-band devices. Frequency tuning by a simple phase shift network may only provide a range of about  $\pm 20$  ppm, which is insufficient to cover the frequency uncertainty after sealing. Thus, a technique which actually pulls the resonant frequency must be used. Figure 5a shows the equivalent circuit for a two-port SAW resonator. By tuning out  $C_0$  at both ports with inductors  $L_S$ , series elements ( $C_T$  or  $L_T$ ) can be added to tune the resonant frequency. Figure 5b shows the resonator response for various values of tuning elements. The data shows that the frequency can be pulled over a range of about 60 KHz ( $\sim 200$  ppm) with not more than 1 dB increase in insertion loss and little decrease in Q. This is more than enough range to correct for frequency errors after sealing.

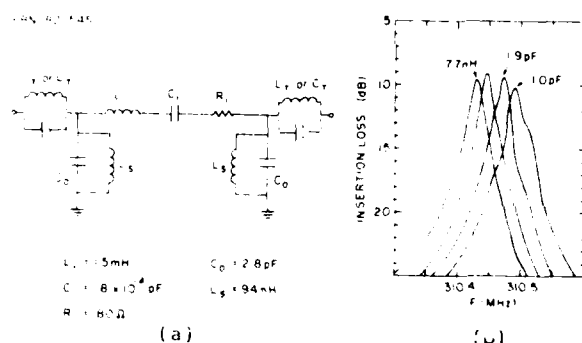


Fig. 5 (a) Equivalent circuit for a two-port SAW resonator and the necessary components for pulling the resonant frequency. (b) Resonator responses for tuning elements at both ports of (1) 7.7 nH, (2) nothing, (3) 1.9 pF, and (4) 1.0 pF.

Delay lines for SAW oscillators generally have much larger bandwidths than resonators and for most designs it is possible to electronically adjust the frequency over a large enough range to eliminate the need for a trimming step. However, this may require more than  $300^\circ$  of phase shift, which at 300 MHz corresponds to about 20 inches of coax. In some cases, circuit constraints may make it impractical to allow for such a large phase adjustment. By trimming the SAW device, the necessary phase shift can be reduced to about  $20^\circ$ .

## Frequency Stability

### Warm-Up Time

Once the oscillator frequency has been set within the desired frequency window, it is then necessary to keep it there. For SAW oscillators, this requires either ovenizing or temperature compensation. The latter will not be discussed in this paper, but one aspect of ovenizing that is particularly important for military applications will be addressed. This is the question of fast warm up. In many military situations a limited amount of time (approximately 3 minutes) may be available for an oscillator

to settle into the desired frequency range. This must be accomplished even if the oscillator is initially at a very low temperature at the time of turn-on. To evaluate the effect of rapid warm-up on the frequency stability of SAW oscillators, two experiments were performed. The first involved heating of just the SAW device, while the electronics were maintained at room temperature. The results are shown in Figure 6. With the SAW device at  $-48^\circ\text{C}$ , the heater was turned on with 18 watts of power at  $T = 0$ . At  $T = 70$  seconds, the heater power was decreased to 9.6 W, and by  $T = 160$  seconds, the SAW device had reached an equilibrium temperature of  $80^\circ\text{C}$ , which was the turnover point of this particular device. During this period of 160 seconds, the frequency increased by 430 ppm. The inset in Figure 6 shows the frequency drift from  $T = 3$  minutes to  $T = 90$  minutes. As can be clearly seen, the frequency stayed well within  $\pm 1$  ppm.

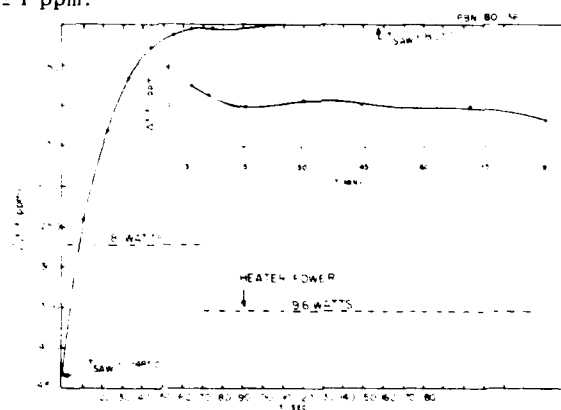


Fig. 6 Fast warm-up when only SAW device is heated.

Figure 7 shows the warm-up characteristics when an entire oscillator circuit board is heated by elements located directly on the circuit board.\* The data shows the frequency drift from  $T = 3$  minutes to  $T = 15$  minutes for two different soak temperatures.

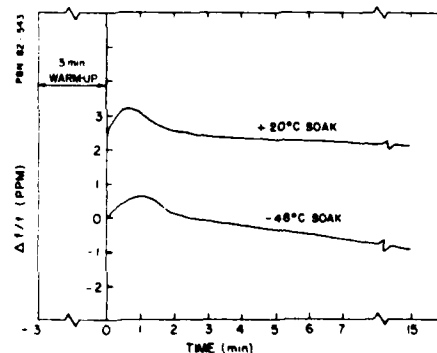


Fig. 7 Fast warm up when entire oscillator board is heated.

\*See acknowledgements.

In both cases, the drift after 3 minutes is less than  $\pm 1$  ppm, but the frequency is somewhat different for the two soak temperatures. This difference is probably due to different temperature gradients across the circuit board for the two soak temperatures. Nevertheless, the frequency for either soak temperature is well within the  $\pm 10$  ppm window that is required.

#### Aging

As a final step in maintaining a  $\pm 10$  ppm frequency window, good long-term frequency stability of SAW oscillators must be demonstrated. To accomplish this, aging studies are being conducted on devices cold-weld-sealed in TO-8 packages<sup>(7,8)</sup>. Data is presented on twenty-six 400-MHz delay lines which were all subjected to a 300°C bake-out and then sealed in high vacuum. Figure 8 shows some typical data for a few devices mounted with gold wire straps. Drift rates range from well under 1 ppm at one year to greater than 2 ppm at one year. Also, the scatter seen in this data is typical. Some devices show week-to-week fluctuations of several tenths of a ppm, which occur even when temperature control is sufficiently tight to rule out temperature-induced frequency fluctuations. In addition, some devices show fluctuations with periods up to ten or twenty weeks.

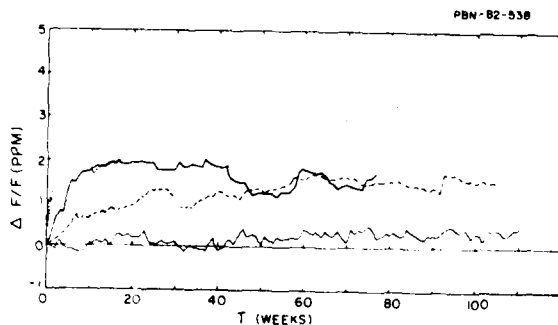


Fig. 8 Typical aging data for 400 MHz delay lines subjected to 300°C bake and cold weld sealed in TO-8 packages. Devices were mounted with gold wire straps.

To show more clearly the drift rates of the entire population of twenty-six devices, the data is presented in bar graph form in Figure 9. Each block represents an oscillator, and the distribution is shown at four points in time: 12, 25, 50, and 100 weeks. The horizontal scale is divided into increments of 0.5 ppm in the range from -7 to +7 ppm. Obviously, at  $T = 0$  weeks, all the devices are located at 0.0 ppm. However, by 12 weeks, the population begins to show some drift. Most devices drift up in frequency (to the right), but some also drift down. At 25, 50, and 100 weeks, the number of oscillators in the population decreases because not all oscillators have been operating for that length of time. None of the oscillators has failed. As one would expect, the distribution tends to spread with time.

Seventeen of the twenty-six oscillators are untrimmed and mounted with gold wire straps. These

devices constitute a base line for these tests and are indicated by empty boxes in Figure 9. All devices that have reached 100 weeks are baseline devices. To evaluate the effect of trimming with gold pads, four trimmed devices were included in the test. These are indicated by the boxes marked with plusses (+). Also, five devices (untrimmed) mounted with "L" clips and polyimide were included. These are indicated by boxes with open circles (o). At this point in the tests, neither of these variables appears to result in a statistically significant deviation from the general population.

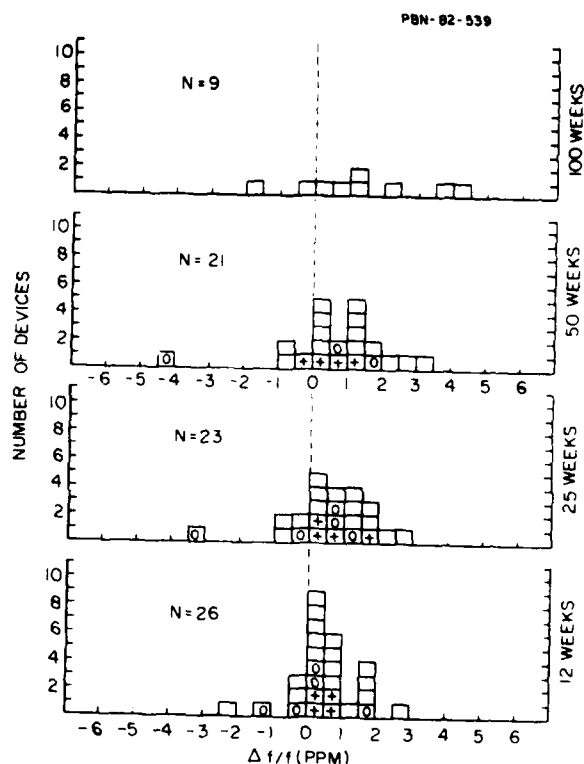


Fig. 9 Distribution of long term frequency drift for SAW devices sealed in cold weld TO-8 packages. Boxes marked with plusses (+) represent devices trimmed with gold pads. Boxes marked with open circles (o) represent devices mounted with "L" clips and polyimide. All other empty boxes represent untrimmed devices mounted with gold wire straps.

In terms of staying within the required  $\pm 10$  ppm window, the results of these tests have been very encouraging. At 50 weeks, 80 percent of the devices are still within 2 ppm of their start frequencies, and at 100 weeks 78 percent are within 3 ppm. Furthermore, the trimming and vibration-resistant mounting techniques which are needed to meet the overall requirements do not appear to degrade the long-term stability of the cold-weld-sealed devices.

### Conclusions

The requirements presented in the introduction of this paper represent a large number of typical military applications. When SAW oscillators which meet these requirements are available in production quantities, there will be a significant increase in the number of applications where they are used. Our program to develop SAW oscillators has made significant progress in meeting these goals and results are very encouraging. However, several tasks still need to be performed. A very important one is the demonstration of low aging in devices operating in a non-laboratory environment. Also, further improvement in device settability would be very useful. A reduction in frequency shift during bake-out and sealing would greatly increase the accuracy of frequency trimming and the use of reactive ion etching for trimming resonators may very well be more desirable than using gold pads. Finally, there were some packaging differences between the devices used for the aging tests and those which were used to demonstrate vibration sensitivity and fast warm-up. These differences must be removed before it can be conclusively demonstrated that all of the above requirements can be obtained simultaneously with SAW oscillators.

### Acknowledgements

The author would like to thank John Loan and Paul Pedi of Raytheon's Missile Systems Division for providing the data on vibration sensitivity and fast warm up for the X-band source, and also to thank Richard Kessler and Mark Koehnke of Raytheon's Equipment Division for providing the data on the low-noise floor oscillator. Thanks are also extended to Donald Lee, formerly of Raytheon's Research Division, for carrying out the experiment on the fast warm-up of a SAW device. Finally, the considerable help of John Lang and Merton Bennett in fabricating and testing many of the devices, and the helpful discussions with Joseph Callera and John Day are acknowledged.

### References

1. W. R. Shreve, R. C. Bray, S. Elliott, and Y. C. Chu, "Power dependence of aging in SAW resonators," 1981 IEEE Ultrasonics Symposium, 94 (1981).
2. J. I. Latham, W. R. Shreve, N. J. Tolar, and P. B. Ghate, "Improved metallization for surface acoustic wave devices," Thin Solid Films 64, pp. 9-15 (1979).
3. T. E. Parker and J. Callera, "Sensitivity of SAW delay lines and resonators to vibration," 1981 IEEE Ultrasonics Symposium, 129 (1981).
4. W. E. Bulst and E. Willibald, "Ultra-reproducible SAW resonator production," (in this Proceedings).
5. W. J. Tanski, "Surface acoustic wave frequency trimming of resonant and traveling wave devices on quartz," Appl. Phys. Lett. 39, 1, pp. 40-42 (July 1981).
6. S. Elliott, M. Mierzewski, and P. Planting, "The production of surface acoustic wave resonators," 1981 IEEE Ultrasonics Symposium, 89 (1981).
7. T. E. Parker, "Analysis of aging data on SAW oscillators," Proc. 34th Annual Symp. on Frequency Control, 292 (1980).
8. W. R. Shreve, J. A. Kusters, and C. A. Adams, "Fabrication of SAW resonators for improved long-term aging," 1978 IEEE Ultrasonics Symposium, 573 (1978).

AD P001556

## 36th Annual Frequency Control Symposium - 1982

EFFECTS OF RIE TUNING ON THE ELECTRICAL AND  
TEMPERATURE CHARACTERISTICS OF QUARTZ SAW RESONATORS

Carl Kotecki

Motorola, Inc.  
Schaumburg, ILSUMMARY

In recent years, Surface Acoustic Wave Resonators have been developed to the point of being useful in oscillator circuits used in the VHF and UHF ranges. The advantages of operating an oscillator at final frequency, as opposed to using a low frequency bulk crystal with multiplier circuits, are well known. If it is desired to cover an entire band with custom frequency sources, a multitude of masks (since each mask produces a single frequency resonator) or an effective tuning procedure is required. To minimize the number of masks required, the tuning procedure should have a wide tuning range with minimal effect on the other characteristics of the device. Reactive Ion Etching of the quartz meets these criteria.

Others<sup>1,2</sup> have reported on using this technique to tune resonators with buried or surface transducers and groove reflectors. Our devices are made with surface aluminum transducers and reflectors. Etching in a planar reactor using a  $CF_4$  and  $O_2$  plasma results in grooves being etched in the quartz with minimal effect on the aluminum pattern which acts as a mask. The grooves result in a lower surface wave velocity in both the transducer and reflector arrays, shifting the frequency downward. This simultaneous shift in velocities allows for a very large tuning range before device degradation becomes intolerable. The etching affects the electrical characteristics of the device as well as the turnover temperature. The effects on both these device characteristics have been investigated for resonators in the VHF band. Data is presented on resonators operating at 194 MHz.

INTRODUCTION

Surface Acoustic Wave resonators have been developed to the point of being useful in oscillator circuits used in the VHF and UHF ranges. These devices are made in batch form using standard photolithographic fabrication techniques. Variations of up to +200 ppm in center frequency,  $F_0$ , are observed for devices built on a single 2 inch square wafer. The center frequency of these devices can be trimmed by etching the aluminum metalization;

this reduces the mass loading of the surface resulting in two effects: the first effect is that the surface wave velocity increases causing the frequency to increase. The second effect is an increase in the turnover temperature,  $T_0$ .

Because of the large excursion of frequency over the temperature range of interest, (113.4 ppm from -30 to +85°C for 36° Y-rotated Quartz) the turnover temperature is important. A shift in  $T_0$  of 3°C from 27.5°C (center of the range) will result in an additional 12.1 ppm excursion, for a total of 125.5 ppm, (see figure 1.) Temperature compensating a 113 ppm drift is difficult; a 125 ppm drift only compounds the difficulty. For our devices we have found a  $T_0$  sensitivity to metal thickness of 1°C/93A° and a resonant frequency,  $F_0$ , sensitivity of 1.76 ppm/A°. To raise the  $F_0$  of a device 400 ppm (the lowest frequency device on a wafer) requires removing 227A° of aluminum. This would result in a  $T_0$  shift of 2.44°C; barely acceptable. Thus a very narrow range of frequencies (60 kHz at 150 MHz, 80 kHz at 200 MHz) can be covered by a single mask and wafer angle combination while maintaining  $T_0$  at 27.5 ± 3°C. If it is desired to cover the entire VHF range of 150-200 MHz, 715 masks are required. Since high resolution masks are both necessary and expensive, this is an impractical situation.

Reactive Ion etching of the quartz has proved to be a better solution. Frequency shifts of 330 ppm/degree centigrade change in  $T_0$  have been observed. This is better than a 2 to 1 improvement over metal removal. Under the conditions used, an  $F_0$  shift of -4200 ppm was obtained after 5 minutes of etching; a rate of 14 ppm/second. The process is very clean since it is carried out in a high vacuum chamber and no rinsing or cleaning afterwards is required. It is also possible to monitor the frequency directly while etching, although this was not done in this experiment. Since the process takes place in vacuum, the devices could be transferred to a sealing chamber through a load lock and sealed immediately after tuning.

#### EXPERIMENTAL PROCEDURE

The devices used in this experiment were fabricated on 36° Y-rotated quartz with 4300Å of aluminum. The interdigital transducer, IDT, is 50 Å wide and 120 Å long, and the reflectors contained 350 elements. The transducer is apodized to reduce transverse modes. Split fingers were used to minimize internal reflections in the IDT. To etch grooves in the surface of the quartz, a planar plasma sputtering machine was used in the reactive ion etch mode. Figure 2 is a schematic illustration of the reactor setup. The system was a Perkin Elmer rapid cycle system designed for sputtering applications. The glass bell jar was replaced with a stainless steel one and a cryo pump substituted for the ion pump. A Leybold-Heraeus mechanical pump was used for roughing down the system.

Twelve devices were loaded into a slot running diametrically across the cathode. The slot was required to allow the resonators to lie flat while mounted to HC-18 crystal holders. The chamber was roughed to 10 microns or less and the poppet valve opened for crossover to the cryopump. After opening the poppet valve completely the system pressure was reduced to  $5 \times 10^{-7}$  torr. The poppet valve was then closed and then reopened slightly to throttle the large pumping speed of the cryopump. With this procedure, a flow of 16.8 sccm of  $CF_4$  (78%) and 4.8 sccm of  $O_2$  (22%) was sufficient to maintain system pressure at 12 microns. The  $O_2$  flow controller was a slave to the  $CF_4$  flow controller to assure a constant gas ratio. The pressure in the chamber was monitored using a baratron gauge. The pressure signal was fed to the  $CF_4$  flow controller which adjusted the flow to maintain the system at 12 microns. The devices were etched in 30 second increments at 50 watts input power (0.274 watts/cm<sup>2</sup>). Figure 3 shows the effect of the etching on the device topography.

Before etching and after each 30 second etch period, the devices were characterized electrically and the turnover temperature was determined. The devices were characterized electrically by using an HP9825 calculator driving an HP8660 synthesizer phase locked to an HP8505 network analyzer to obtain reflection coefficient and phase data. Twenty seven data points were taken +27 kHz about the resonant frequency and 14 points were taken from 50-700 MHz. Figure 4 shows a Smith chart plot of the resonator response from 50-700 MHz. The data are fit to the model shown in figure 5 using an optimization routine to calculate the equivalent circuit parameters. The reproducibility of measuring and determining  $R_m$ ,  $L_m$ ,  $C_m$ , and  $C_0$  is better than 1%. The values determined for the parasitic elements,  $L_p$  and  $R_p$ , vary quite a bit more due to changes in the lead length and contact resistance in the test fixture. To determine the turnover temperature, the devices were

placed in oscillators in a temperature chamber and the frequency read at -2°C increments from 50°C to 4°C. Because the devices were not in sealed cans, the temperature was kept above 0°C to avoid condensation or frost forming on the devices. The data were fit to a parabola and the turnover temperature,  $T_0$ , determined by the temperature of maximum frequency. (Figure 1.)

#### EXPERIMENTAL RESULTS

Of the 12 devices etched, one device immediately jumped 60% in  $R_m$  value after the first 30 seconds of etching. Since this did not agree with the behavior of the other devices, the data for this device were excluded from the analysis. All results presented are the average for the remaining 11 devices. Figure 6 shows the frequency variation with etch time. The frequency shifts were normalized by calculating in ppm. Presenting the data in terms of percentage change from the original values effectively normalizes the data, eliminating fabrication variations and allows for direct comparison of the devices.

Figure 7 presents the change in  $C_0$  as a function of frequency shift. Since frequency shift is a linear function of etch time, as shown in figure 6, the abscissa is essentially etch time. The value of  $C_0$  was reduced by 9.3%, from 4.37 pF to 3.96 pF. The changes in the resonant arm parameters,  $R_m$ ,  $L_m$  and  $C_m$ , are shown in figures 8, 9 and 10, respectively.  $R_m$  increased 58% from 19.6 Ω to 31 Ω.  $L_m$  increased 25% from 353 microHenries to 441 microHenries.  $C_m$ , calculated from the measured values of  $L_m$  and  $F_0$ , decreased 19% from 1.93 mpF to 1.56 mpF. The  $Q$  was adversely affected as shown in figure 11. A reduction of 21%, from 22,000 to 17,400, was observed. The  $C_0/C_m$  ratio increased linearly from 2270 to 2550, as displayed in figure 12; a 12% increase. Figure 13 shows that  $T_0$  was reduced 11°C after a frequency shift of 4200 ppm.

#### DISCUSSION OF RESULTS

As shown in figure 6 the frequency shift was linear with etch time. If we consider the bottom of the grooves as a new surface, the etching makes the device pattern effectively thicker; this increases the effective mass loading, lowering the surface wave velocity and the frequency. The total step height increased 2200Å from the original 4300Å aluminum thickness. This increase was a result of a 1600Å groove in the quartz and a 600Å increase in the finger thickness. This increase in finger thickness was due to  $O^+$  ions reacting with the aluminum which was biased several hundred volts negative. (The leads of the crystal bases actually touch the cathode during etching.) Since the density of quartz and aluminum are almost identical, the

quartz step of 1600Å should cause a frequency shift of 2816 ppm and the 600Å  $\text{Al}_2\text{O}_3$  layer with a density of  $3.5\text{g/cm}^3$  should cause a 1369 ppm shift for a total of 4185 ppm; virtually the 4178 ppm actually observed.

As seen in figure 7, the static capacitance of the IDT was reduced.  $C_0$  was expected to decrease since the quartz between the fingers, with a dielectric constant of 4.52, is being replaced by air, with a dielectric constant of 1.00. Eventually further removal of quartz will cause no further change in  $C_0$  since the bottom of the groove will be outside the region of the concentration of the electric field. The data were curve fit to a parabola since this is the expected shape of the curve and provided a good fit to the data.

The motional resistance,  $R_m$ , of the devices increased dramatically as evidenced in figure 8.  $R_m$  is defined in table 1<sup>4</sup>, where  $R_0$  is the radiation resistance of the IDT and  $|\Gamma|$  is the overall reflection coefficient of the gratings.  $R_0$  is also defined in table 1, where  $k$  is the electromechanical coupling constant,  $F_0$  is the resonant frequency of the device,  $N_{\text{eff}}$  is the effective number of fingers in the apodized IDT and  $C_s$  is the capacitance per finger pair.  $R_0$  was measured on devices not etched, but adjacent to the devices used on the same wafer.  $R_0$  was measured by covering the reflectors with an acoustic absorber, negating the reflection properties of the gratings. (This effectively ruins the device, so devices other than those actually etched had to be used.) The average  $R_0$  measured was  $1175\Omega$  compared to a calculated value of  $1200\Omega$ , using  $k^2 = 0.0016$ .  $R_0$  measured on devices etched 5 minutes averaged  $1625\Omega$ . Using the measured  $F_0$  and  $C_0$  values, this indicated a reduction in  $k^2$  to 0.00131. Therefore,  $k$  was reduced from 0.04 to 0.0362, a 9.50% reduction, virtually matching the 9.32% reduction in  $C_0$ . This is not coincidental since both are electric field phenomena related to how the electric field lines permeate the air-dielectric combination. Assuming the reduction in  $k$  follows the reduction in  $C_0$ , new  $k$  values were calculated using the curve fit to the  $C_0$  data.

Knowing  $R_m$  and  $R_0$  at the end points,  $|\Gamma|$  can be calculated at these points. The initial value was 0.968 and the value after etching was 0.962. This decrease in  $|\Gamma|$  was unexpected because the step height is increasing, thereby increasing the impedance discontinuity. This should result in a larger reflection coefficient.<sup>3</sup> This was not observed because the resonance of the cavity is skewed from the center of the reflection stopband, resulting in a lower  $|\Gamma|$  than expected. As the devices were tuned they became even more skewed because the resonance of the cavity was shifted more than the reflector

stopband. This results in a lower  $|\Gamma|$ . Away from the center frequency of the reflector stopband, the curve has a  $\sin NX/\sin x$  type shape,<sup>3</sup> but the exact shape of the curve and the location on the curve is not known. The shape of the curve is critical since  $1-|\Gamma|/1+|\Gamma|$  is a rapidly varying function of  $|\Gamma|$ . Assuming a linear approximation for the change in  $|\Gamma|$  gave a poor fit even though going from a value of 0.968 to 0.962 is less than a 1% change. Making the reduction in  $|\Gamma|$  a second order function (proportional to etch time squared) and using the calculated  $k$  values and measured  $F_0$  and  $C_0$  values, new  $R_m$  values were calculated. This theoretical curve is shown in figure 8 and provides a good fit.

The change in  $L_m$  is shown in figure 9. The data fall on a straight line. Table 1 shows that  $L_m$  is determined by  $R_0$ ,  $|\Gamma|$ ,  $F_0$  and  $m$ , the number of halfwavelengths between reflection centers. Since  $R_0$  and  $|\Gamma|$  have been calculated and  $F_0$  measured, a set of  $m$  values was calculated from the line fit to the  $L_m$  data. The value of  $m$  drops quickly from 455.6 and levels out to a value of 423.8. The value of  $m$  is expected to decrease in this manner<sup>4</sup> since the impedance discontinuity is increasing with increased step height.

The linear change in  $C_m$  shown in figure 10 inversely follows the  $L_m$  change since  $C_m$  was calculated in the optimization program using the determined  $L_m$  and  $F_0$  values.

The quality factor of the resonators,  $Q$ , decreased due to the etching as shown in figure 11. The  $Q$ , defined in table 1, depends on  $R_m$  and  $L_m$ . Since  $R_m$  increases faster than  $L_m$ , a decrease in  $Q$  results, as shown (The data were fit to a straight line since higher order curves provided no improvement in the fit.)  $Q$  is also defined in terms of  $m$  and  $|\Gamma|$ . Since both quantities decreased and both appear in the numerator, the  $Q$  followed accordingly.  $|\Gamma|$  also appears in the denominator and the reduction in  $|\Gamma|$  caused the denominator to increase, also lowering the  $Q$ . Using the values for  $m$  and  $|\Gamma|$  calculated from the measured values of  $R_0$ ,  $R_m$  and  $L_m$  at the end points, resulted in values of 22,000 and 17,180 compared to the measured values of 21,980 and 17,400. This is quite good an agreement. Using the remaining theoretically calculated  $m$  and  $|\Gamma|$  values,  $Q$  was calculated for the rest of the points between and appears as the theoretical curve in figure 11.

The  $C_0/C_m$  ratio is important in oscillator applications. As shown in figure 12, it follows a linear increase. As seen in table 1,  $C_0/C_m$  depends on  $|\Gamma|$ ,  $m$  and  $k$ . Using the theoretically calculated values for these parameters,  $C_0/C_m$  was calculated for the range investigated. As can be seen in figure 12 the two curves virtually overlap.

The turnover temperature is expected to be reduced due to the apparent increase in mass loading resulting from the grooves being etched into the surface. As discussed under the change in frequency, the total step height increased 2200Å. Using the previously mentioned sensitivity in turnover temperature of 1°C/93Å, the 2200Å increase should result in a  $T_0$  reduction of 23.7°C. The observed value was approximately 11°C. Assuming a linear change in  $T_0$  versus the step height increase, the data were fit to a straight line in figure 13. The combination of aluminum oxide, aluminum and quartz for the steps is quite a bit better with respect to temperature characteristics than pure aluminum. The reason for this behavior is an anomaly.

#### CONCLUSIONS

As opposed to other reported techniques, Reactive Ion Etch Tuning has been shown to be an improved method for tuning Quartz SAW Resonators. The large tuning range and the lower shift in  $T_0$  are its major benefits. The drawback of the technique is the large increase in  $R_m$  and  $L_m$ ; the limit of the process is defined by the maximum permissible change in these parameters.

The assumptions that the change in the electromechanical coupling constant,  $k$ , follows the change in  $C_0$  exactly and that the reduction in  $|\Gamma|$  over the range investigated is parabolic were both proved to be correct by the good to excellent agreement between the theoretical curves and the data curves.

#### REFERENCES

- 1) W.J. Tanski, "Elements of SAW Resonator Fabrication and Performance", 35th Ann. Frequency Control Symposium (1981) pp 388-390.
- 2) S. Elliot, M. Mierzwinski and P. Planting, "The Production of Surface Acoustic Wave Resonators", 1981 Ultrasonics Symposium, pp 89-93.
- 3) E.K. Sittig and G.A. Coquin, "Filters and Delay lines Using Repetitively Mismatched Ultrasonic Delay Lines", IEEE Transactions on Sonics and Ultrasonics, Vol SU-15, no. 2 April 1968, pp 111-119.
- 4) E.J. Staples, J.S. Schoenwald, R.C. Rosenfeld and C.S. Hartmann, "UHF Surface Acoustic Wave Resonators", 1974 Ultrasonics Symposium, pp 245-252.

Table 1.  
Summary of Equivalent Circuit Parameters

$$R_m = R_0 \frac{1-|\Gamma|}{1+|\Gamma|}$$

$$R_0 = \frac{1}{8k^2 F_0 C_0 N_{eff}^2}$$

$$L_m = \frac{R_0 |\Gamma| m}{2(1+|\Gamma|)^2 F_0}$$

$$C_m = \frac{1}{\omega_0^2 L_m}$$

$$C_0 = C_{stiff}$$

$$Q = \frac{\omega_0 L_m}{R_m} = \frac{\pi m |\Gamma|}{1-|\Gamma|^2}$$

$$C_0 C_m = \frac{\pi^2 |\Gamma| m}{4k^2 (1+|\Gamma|)^2 N_{eff}^2}$$

$$L_{cal} = m \frac{\lambda_g}{2}$$

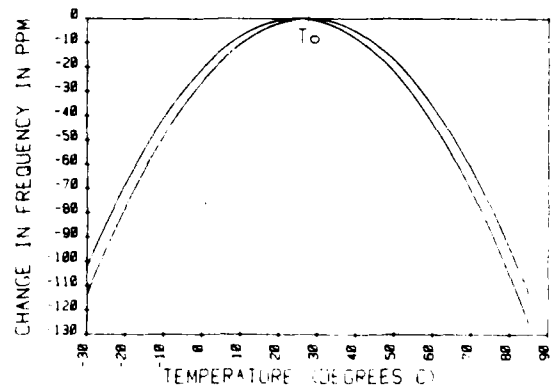


Figure 1. Frequency Shift vs. Temperature for 36 Deg Y-Cut

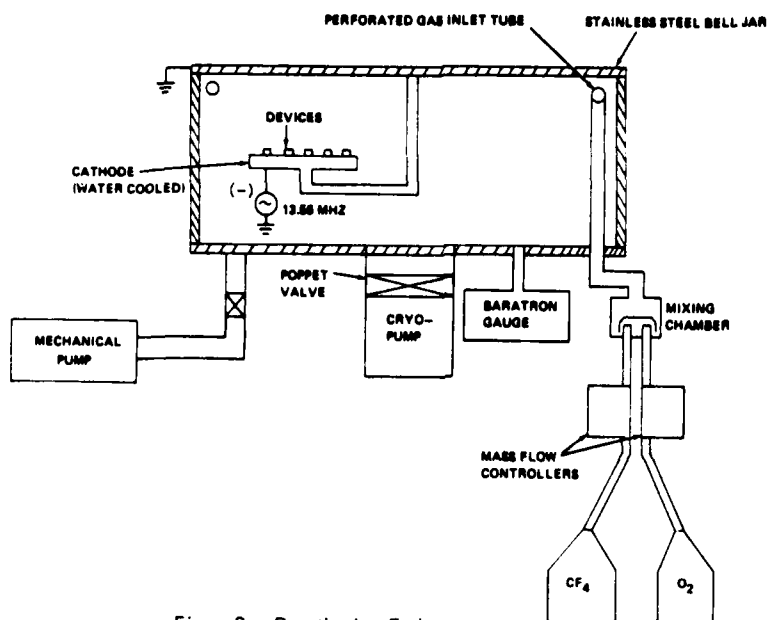


Figure 2. Reactive Ion Etcher

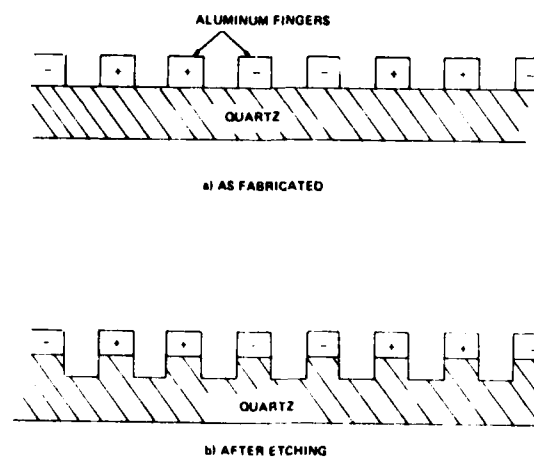


Figure 3. Device Topography

IMPEDANCE COORDINATES—50-OHM CHARACTERISTIC IMPEDANCE

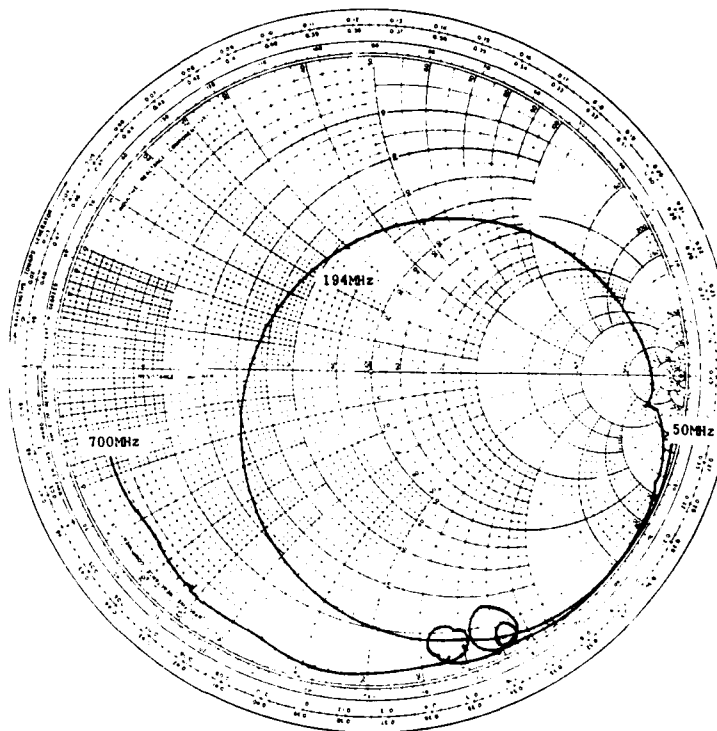
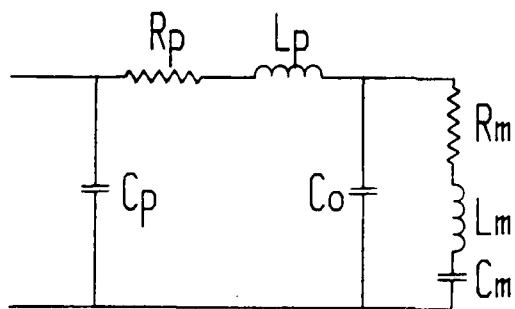


Figure 4. Smith Chart Plot of Resonator Response



- $C_p$  AVERAGE MEASURED PACKAGE CAPACITANCE [43pF]  
 $L_p$  LEAD INDUCTANCE  
 $R_p$  LEAD, CONTACT AND FILM RESISTANCE  
 $C_o$  STATIC TRANSDUCER CAPACITANCE  
 $R_m$  MOTIONAL RESISTANCE  
 $L_m$  MOTIONAL INDUCTANCE  
 $C_m$  MOTIONAL CAPACITANCE

Figure 5. Resonator Equivalent Circuit

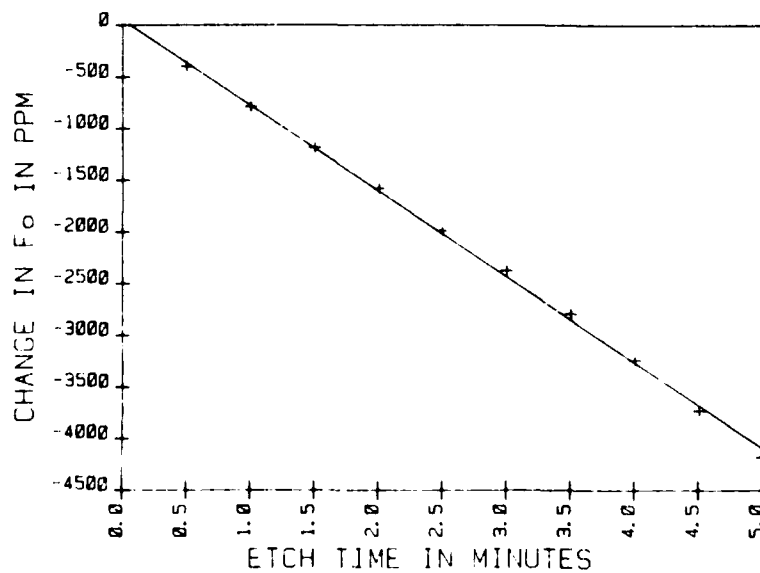


Figure 6. Change in  $F_o$  vs Etch Time

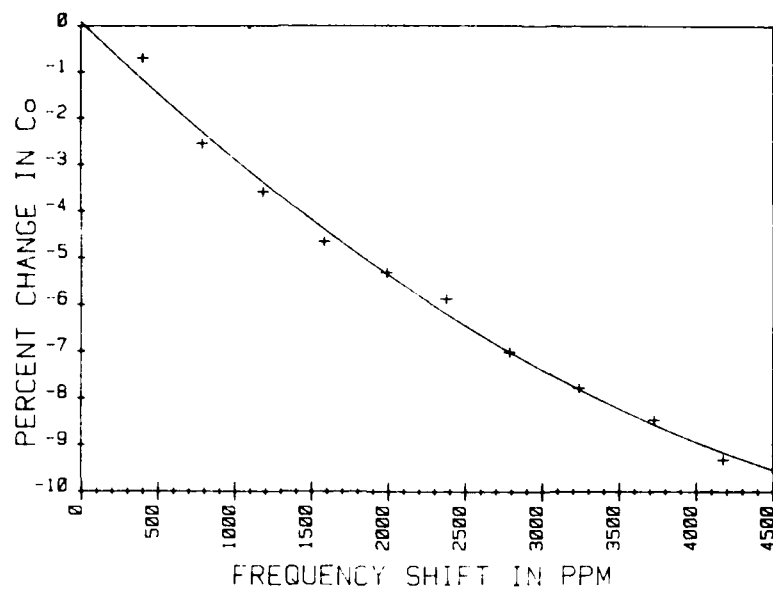


Figure 7. Change in  $C_o$  vs Frequency Shift

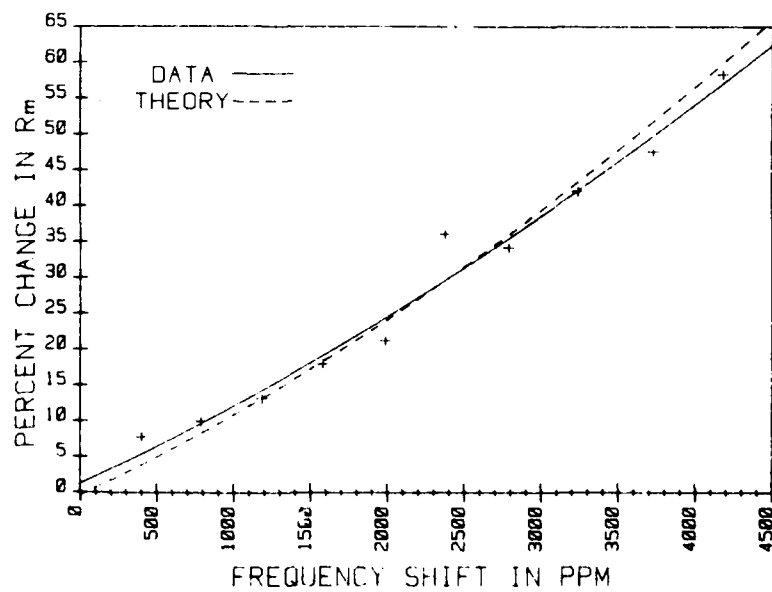


Figure 8. Change in  $R_m$  vs Frequency Shift

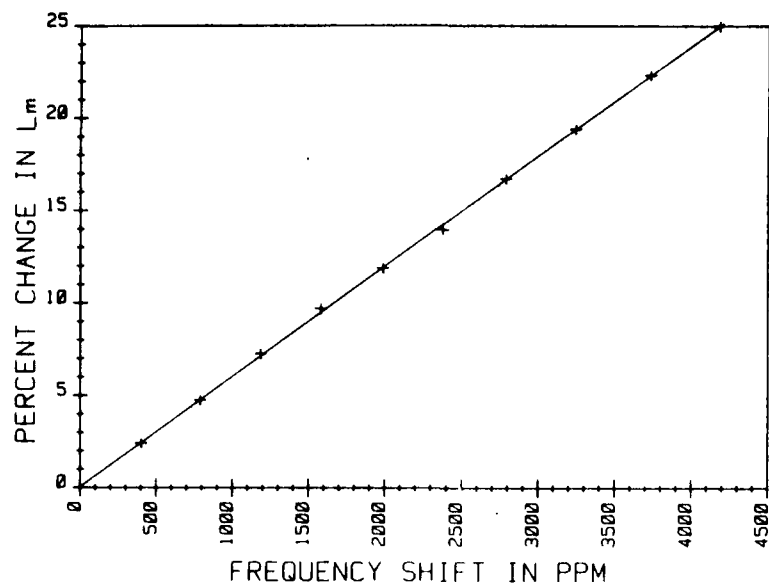


Figure 9. Change in  $L_m$  vs Frequency Shift

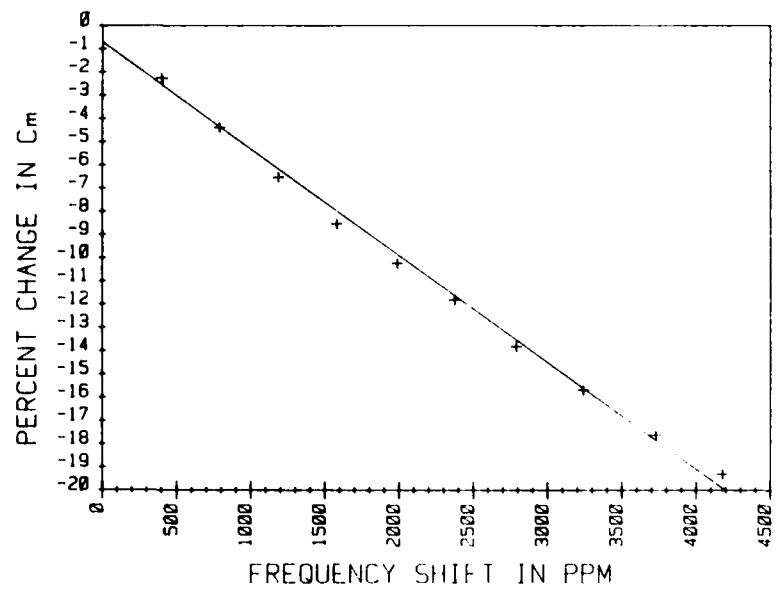


Figure 10. Change in  $C_m$  vs Frequency Shift

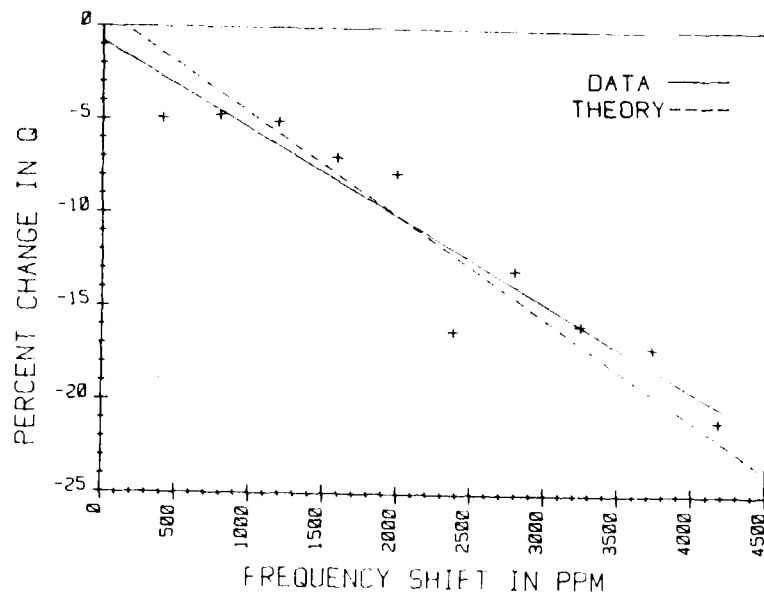


Figure 11. Change in Q vs Frequency Shift

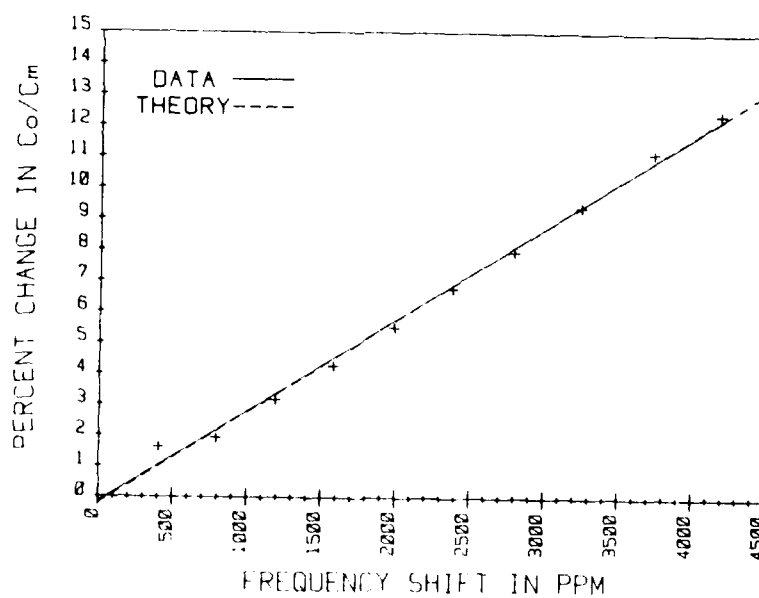


Figure 12. Change in Co/Cm vs Frequency Shift

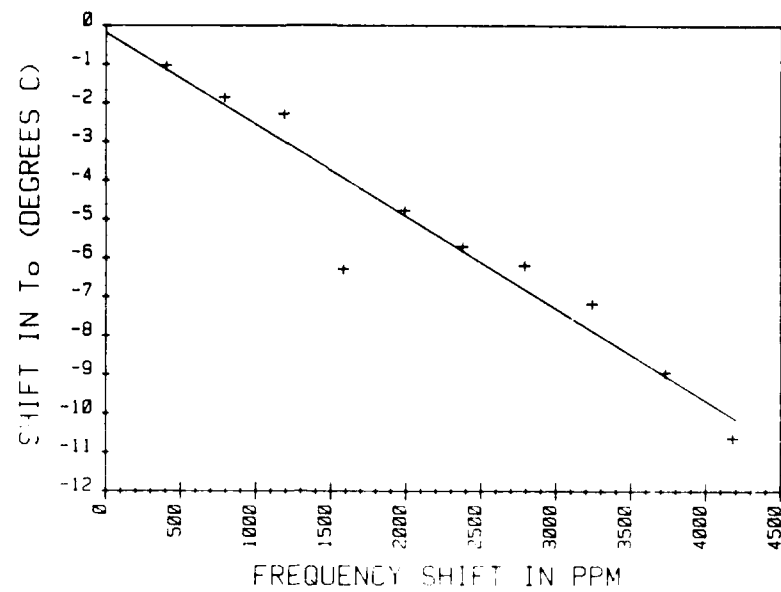


Figure 13. Change in  $T_0$  vs Frequency Shift

AD-A130 811

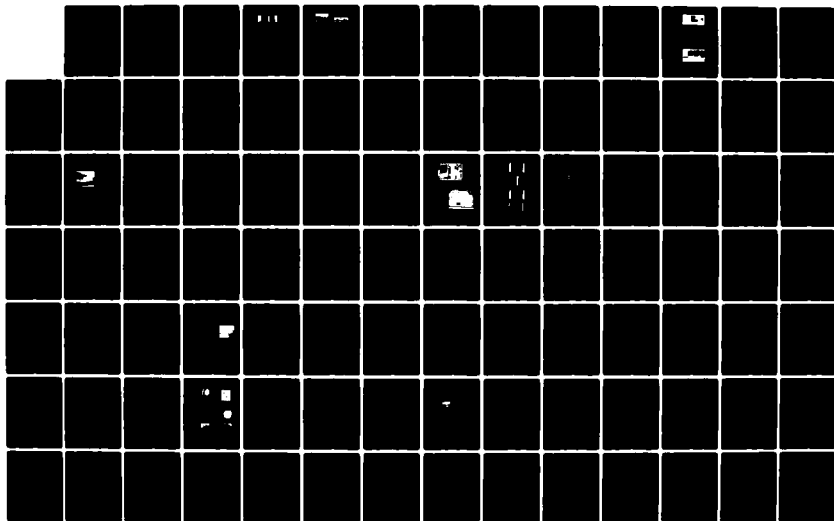
PROCEEDINGS OF THE SYMPOSIUM ON FREQUENCY CONTROL (36TH  
ANNUAL) 2-4 JUNE 1..(U) ARMY ELECTRONICS RESEARCH AND  
DEVELOPMENT COMMAND FORT MONMOUTH, E PAIGE ET AL. 1982

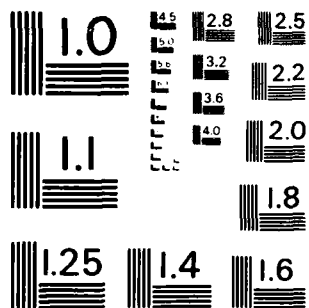
F/G 20/14

NL

UNCLASSIFIED

68





MICROCOPY RESOLUTION TEST CHART  
NATIONAL BUREAU OF STANDARDS - 1963 - A

# FREQUENCY FINE TUNING OF RELIABLE SAW TRANSDUCERS USING ANODIZATION TECHNIQUE

F.Y. Cho, T.B. Chatham and R. Ponce de Leon

Motorola Government Electronics Group  
Scottsdale, Arizona 85252

## SUMMARY

The reliability of SAW transducers is greatly improved by anodization process obtained with Oxygen plasma. The corrosive protection against acid etchant improved up to an order of magnitude has been achieved.

The frequency fine tuning of an anodized resonator and phase versus frequency of an anodized delay line will be presented.

## Introduction

The anodization process used to fine tune bulk resonator and filters has been reported by different authors (1-5). In this study the use of RF oxygen plasma has proved to be very effective in the fine tuning of narrow band SAW devices and increased resistance from corrosion caused by chemical reactions. Aging characteristics are improved due to the protection of the anodized layer which is formed on an aluminum transducer when the RF oxygen plasma combines with it and forms a layer of aluminum oxide. Experiments were conducted by controlling the operation parameters of the RF oxygen plasma, including various anodization duration, with a given oxygen gas pressure and RF power.

The relative anodization thickness was determined by measuring corrosion resistivity change on thin film aluminum. Accumulated data proved to be predictable in our results.

## Corrosion Protection

Recent experiments indicate that oxygen plasma anodization of a thin film aluminum pattern provides additional corrosion protection against chemical etchants. Figure 1 shows the result of placing two aluminum transducer patterns in an acid etchant. The aluminum pattern on the left was not anodized, whereas the pattern on the right was anodized prior to the etching process. The results indicate the corrosive protection of the oxygen plasma anodization process for aluminum patterns.

Numerous SAW devices were anodized for different time intervals after which they were put in an Al (acid) etch that consists of 10 ml of Nitric acid, 180 ml Phosphoric acid and 10 ml Di-H<sub>2</sub>O. They were timed while they were etched and then plotted on a graph (see Fig. 2). The etch time in this figure is defined as the time needed to etch-off the thin Al film transistor (600 Å) after the corresponding anodization time. The same test was performed with an Alkaline etch which consisted of 10 gm. of Potassium ferricyanide, 10 gm. of Potassium hydroxide and 1000 cc of Di H<sub>2</sub>O. The results are plotted on the graph of Figure 3. The etch time increased consistently with increased anodization time, which shows protection against corrosion in both acid and alkaline environments has not been reached after 52 hours of anodization under the described parameters of paragraph 2.3. The experimental results demonstrated that over fifty times improvement was obtained in the protection against acid corrosion after 34 hours of the anodization process.

Anodization is applicable to all thin film Al devices such as integrated circuits and other semiconductor devices. A test was conducted with an IC chip half covered with AZ 1350B photoresist and anodized for 2½ hours in 30 minute rotations. After every rotation the photoresist was taken off with acetone and a new coat was applied to prevent the resist from being baked on. After the anodization was completed, half of the chip was anodized and the other half that had the resist was not anodized. This provided a side by side comparison. The chip was then placed in an acid environment for 8 min. (see Fig. 4). The experiments indicate the additional protection from the anodization process particularly with respect to the aluminum bonding wires.

## Performance of SAW Devices Before and After Anodization

The effect of aluminum oxide forming on the aluminum transducers creates an added weight to the transducer. This

AD P001557

oxidation process causes a mass loading effect on the crystal substrate which in turn changes the velocity of that crystal. Therefore, by the equation  $V = f\lambda$ , where  $\lambda$  is a constant, it is possible to directly change the frequency of the SAW device by changing the velocity of the crystal substrate. This is beneficial in the fine tuning of SAW devices since fine tuning has to take place after device fabrication.

Figure 5 shows the passband of a resonator before and after 110 minutes of anodization. The process parameters are described in Figure 6. The shape of the passband shows no apparent change; the center frequency of passband is shifted by 340 PPM as a result of the mass loading of the mass loading effect, which provides an excellent process for frequency fine tuning.

#### Phase-vs-Frequency

An experiment was conducted using a stable frequency source, a vector voltmeter and a frequency counter for determining the phase-vs-frequency relation. Figure 6 shows a graph of this relation plotted for a SAW device. The device was then anodized for a period of 19 hours with the Tegal Plasmaline (Model No. 200) at 150 watts RF, and 1 torr of oxygen pressure. Another plot of phase-vs-frequency was taken; the results are also shown in Figure 6. The linear relation of the plots indicate no significant dispersion change caused by the anodization process; therefore, the desired performance of the device was maintained.

#### Frequency Fine Tuning of SAW Resonators

Fine tuning of narrow band SAW devices has been a success. The anodization of aluminum transducers causes a mass loading effect and leads to a decrease in the center frequency of a SAW device. Four resonators were used for this test; the device that had the lowest frequency was the reference (193.962). The other three devices were anodized for various time intervals according to their frequencies. All devices ended up within 2ppm of the reference. (The results are shown in Table 1.) The test equipment was checked periodically by taking a non-anodized resonator and checking the frequency every time the frequency of the anodized resonator was measured.

#### Aging of Anodized SAW Devices

The anodized SAW devices have demonstrated superior frequency stability compared to the unanodized devices. The accelerated life test equivalent to a five years' test time has shown a total change of less than  $\pm 2$ ppm in center frequency for

the anodized SAW frequency source, versus a  $\pm 200$ ppm shift of the non-anodized device.

#### Conclusion

The use of RF oxygen plasma has proved to be very beneficial in the corrosive protection of aluminum transducers on SAW devices due to the protective layer of aluminum oxide on the exposed aluminum. The non-anodized crystal etched off in 1 min. 50 sec. in comparison to 96 min. etch time in Al etch after 34 hours of anodization which provides a 50 times improvement. Fine tuning of SAW resonators up to 300-400 ppm has been demonstrated. Four resonators used for the fine tuning experiment were fine tuned from 124 ppm to within 2 ppm of each other, which improved the accuracy tolerance by 60 times. These

SAW devices were anodized under the same conditions as the corrosion test. The anodized resonators also have good aging characteristics. After an accelerated life test, equivalent to 5 years' aging, the resonators and the unanodized SAW's center frequency changed as much as 200 ppm but the anodized SAW changed less than 2 ppm. The results indicate that anodized SAW resonators are much more stable and reliable than the un-anodized SAW devices; better than 100 fold improvement was demonstrated in the experiment.

#### References

- 1 Bottom, Virgil E., "A novel method for adjusting the frequency of aluminum plated quartz crystal resonators," Proceedings of the 50th Annual Symposium on Frequency Control, 1976.
- 2 Ang, Dick, "A microprocessor assisted anodizing apparatus for frequency adjustment," Proceedings of the 53rd Annual Symposium on Frequency Control, to be published.
- 3 Reche, J.J.H., "Frequency tuning of quartz resonators by plasma anodization" Proceedings of the 52nd Annual Symposium on Frequency Control, 1978.
- 4 Shanley, Chip, "Plasma anodization for final Frequency," Motorola Report, 1979.
- 5 O'Hanlon, John E., "Plasma anodization of metals and semiconductors," Journal of Vacuum Science and Technology V7, no. 2, 1979.

AA

# PASSIVATION OF AL - SAW TRANSDUCER ON ST QUARTZ

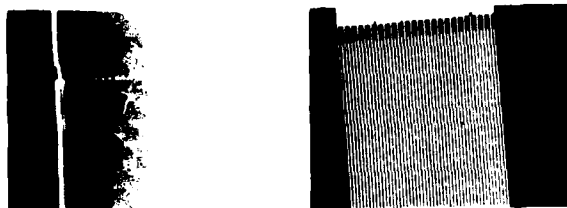


Figure 1. Corrosive Protection of Anodized Transducers

AA

## PHOSPHORIC ACID SAW ETCH

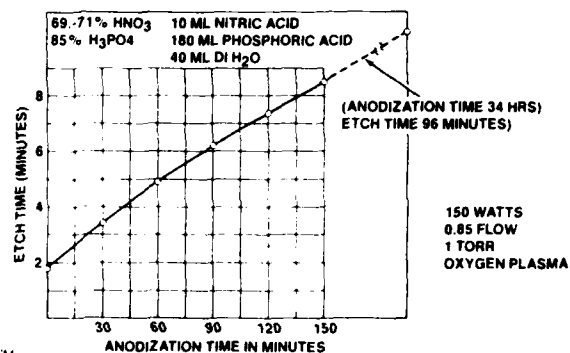


Figure 2. Time Required to Etch off A1 Transducer with Typical Acid Etchant After Anodization Process

AA

## KOH - ALKALINE ETCH

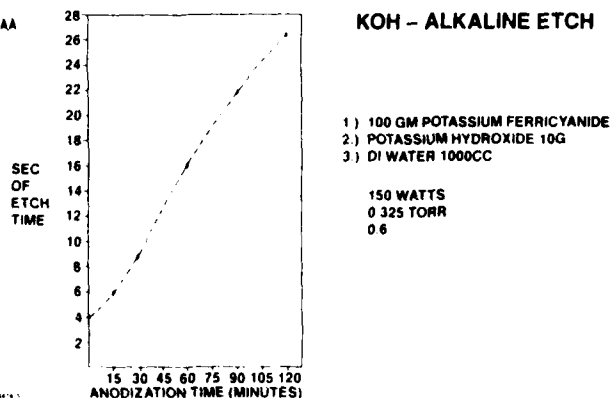


Figure 3. Time Required to Etch off A1 Transducer with Alkaline Etchant after Anodization Process



Figure 4. Anodization Protection on IC Chips

AA

### PASSBAND OF RESONATOR 500 KHz/DIV

NONANODIZED

ANODIZED 110 MIN



$F_c$  194 041 MHz



$F_c$  193 975 MHz

ANODIZED 110 MINUTES  
150 W POWER  
1 TORR OXYGEN  
GROUND LEADS FOLDED  
UNDER  
HOT LEADS FLOATING  
 $\Delta F = 340$  PPM  
F  
NO CHANGE IN BAND SHAPE

Figure 5. Frequency Response of a Resonator Before and After Anodization

AA

### PHASE VS FREQUENCY

150 WATTS  
1 TORR OXYGEN  
18 HRS

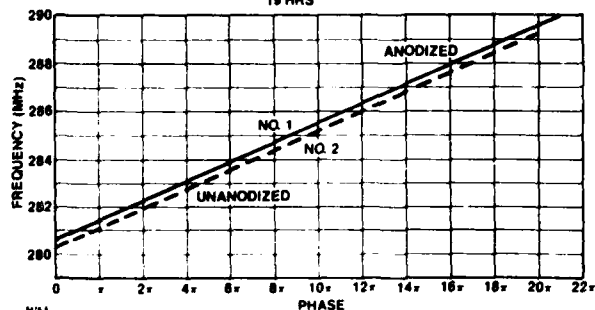


Figure 6. Linear Phase Versus Frequency of a SAW Device Before and After Anodization

Table 1  
Frequency Fine Tuning of SAW Resonators by  
Anodization Process

AA

### FREQUENCY FINE TUNING

DEVICE NUMBER	I	II	III	IV
CENTER FREQ BEFORE ANODIZATION (MHz)	193.982	193.986	193.986	193.982
	( $\Delta = 103$ PPM)	( $\Delta = 20$ PPM)	( $\Delta = 124$ PPM)	( $\Delta = \pm 2$ PPM)
CENTER FREQ AFTER ANODIZATION	193.982	193.982	193.982	193.982
DEVIATION FROM TARGET (PPM)	$\pm 2$ PPM	$\pm 2$ PPM	$\pm 2$ PPM	$\pm 2$ PPM

# A DIGITALLY COMPENSATED HYBRID CRYSTAL OSCILLATOR

G. B. Pollard

Hughes Aircraft Company  
Newport Beach, California

AD P001558

## Abstract

A thin film hybrid temperature compensated crystal oscillator has been developed which utilizes digital compensation techniques to maintain a stable output frequency with respect to changes in temperature. The digitally compensated crystal oscillator (DCXO) described has been designed to be compatible with automated manufacturing techniques in large volume production, a problem with conventional compensated oscillator designs. A look-up table, where each temperature increment corresponds to a particular compensation value, is maintained in an electrically erasable read only memory (EEPROM). This memory, together with an on-board I/O port, allows programming and reprogramming after the oscillator has been sealed. Thus, software can compensate for any subsequent changes in the frequency of the oscillator. Also, the I/O port and EEPROM memory permit automation of the programming and testing for multiple units simultaneously.

## Introduction

As the sophistication of radio communications and radar systems increases, high stability oscillators will, of necessity, be designed into lower levels of hardware. This trend creates the demand that oscillator performance be improved while package volume is reduced. More importantly, a greater number of oscillators will be required at a lower cost. To meet these requirements, extensive use must be made of automated manufacturing and testing capabilities which exist in the hybrid microcircuit industry. For this reason, the Digitally Compensated Hybrid Crystal Oscillator (DCXO) was developed. The DCXO is designed to provide precision frequency control over a broad temperature range in a small, rugged package suitable for use in such systems as man-pack radios and other applications where size is critical. Notable features include the

absence of mechanical adjustments and the ability to be electrically reprogrammed to synchronize multiple units or to correct errors due to aging of components affecting both the nominal frequency and the temperature compensation. These features have been achieved through the complete elimination of the traditional thermistor/resistor network, commonly used in Temperature Compensated Crystal Oscillators (TCXO's), and its replacement with a digitally synthesized bias voltage for the varactor<sup>1</sup>. A significant advantage of this approach is the ability to fully automate the compensation and test portions of the manufacturing process, ultimately decreasing costs and increasing throughput capability.

## Basic Concepts

A traditional TCXO maintains a constant output frequency by changing the reactance of the oscillator loop to offset variations in the crystal frequency due to temperature changes. This is accomplished using a varactor diode, biased with a network of thermistors and resistors, such that the crystal frequency variations with temperature are exactly cancelled by the changes in the oscillator loop capacitance due to the varactor diode. The difficulty with this approach is the realization of the voltage/temperature response required of the bias network which typically resembles Figure 1. This problem is further complicated by the fact that each crystal is unique and may exhibit one or more local perturbations about the expected response. The DCXO approach eliminates these problems through the use of software, rather than individually tailored hardware, to provide the appropriate bias for the varactor diode. A block diagram of a DCXO is shown in Figure 2. During each clock cycle, the voltage across the single thermistor is digitized by the analog to digital converter (ADC). This provides a word whose magnitude is proportional to the temperature of the oscillator. This value is used to

address the programmable CMOS memory. The data from the addressed memory location is input to a digital to analog converter (DAC), which generates the varactor bias voltage. The benefit of this scheme is that any shape response can be realized with equal ease, limited only by the resolution of the ADC and DAC. Localized slope reversals and peaks required to compensate some crystals can be created without additional components or increases in circuit complexity required by a TCXO.

Since all of the peculiarities of the compensation requirements can be realized by merely storing them in the memory, it is no longer necessary to use select value components. Additionally, the components used do not need to be particularly linear, even in the case of the ADC and DAC. As long as the nonlinearities do not degrade the resolution, and the ADC is monotonic, the software can make appropriate compensations. As a result, less costly components may be used without adverse effects.

A fundamental difference between the DCXO and the TCXO is the discontinuous transition from one frequency to another when the digital compensation changes value. This is to be contrasted with the slowly varying (with respect to temperature), continuous frequency variation of a TCXO. These rapid frequency shifts in the DCXO, although very small in magnitude, appear as noise on the oscillator output. The frequency of the system clock controls the rate at which the DCXO updates the compensation information, and thus the frequency at which these frequency transitions occur. Although there are components available which would allow the system to operate at speeds of hundreds of kilohertz, the system performance is improved by updating the compensation only as fast as is required to resolve the greatest thermal transient that is contemplated in the applicable oscillator specification. Slowing the clock down tends to avoid limit cycle types of oscillation in the compensation. Additionally, a low clock frequency allows the low pass filter on the DAC output to more effectively limit the output noise induced by the compensation.

The DCXO uses a single temperature sensor, a thermistor, to determine the compensation; a TCXO can have three to five temperature sensitive elements. To the extent that thermal gradients exist within the oscillator package, the DCXO is less susceptible to compensation errors caused by the sensor(s) being at different

temperatures than the crystal or from each other. This is particularly significant to the performance during a thermal transient. Since the quartz crystal, in its evacuated package, and the thermistors have differing thermal masses, a finite time will be required for them to reach the same temperature after a change in ambient temperature. In the case of a continuously varying temperature, the thermistor(s) may develop a temperature offset from the crystal that depends to some extent upon the rate of change of temperature. This offset will result in a compensation error and thus a frequency error. By using only one thermistor in the DCXO, and placing it in close proximity to the crystal package, the problem is minimized. Ideally, the thermistor should be mounted within the crystal package itself; this was tried with a DCXO prototype in which a thermistor was deposited onto the periphery of the crystal blank. Although this tended to eliminate the problems of thermal gradients between the sensor and crystal, it did not prove practical in large volume production at the time. More development in this area is required.

The accuracy of the compensation with respect to temperature is a function of the crystal's frequency variation with respect to temperature. This, in turn, establishes the minimum acceptable resolution of the ADC and DAC. These requirements are independent of each other. The number of discrete temperatures  $N$  that the ADC must be able to resolve is:

$$N = (S/A) \times T \quad (1)$$

where:  $A$  = the accuracy desired in ppm  
 $S$  = the maximum slope of the crystal response to temperature expressed in ppm/deg C  
 $T$  = the temperature range to be compensated

While the ADC resolution is determined by the worst case slope of the temperature response, the DAC resolution  $V$  is determined by the peak-to-peak frequency deviation of the crystal over the temperature range of interest:

$$V = D/A \quad (2)$$

where:  $D$  = the total frequency shift of the crystal expressed in ppm

A computer program has been developed to model the digital compensation network. This permitted the relative contributions of the ADC and DAC resolution to the overall compensation accuracy to be assessed with respect to changes in temperature range and changes in crystal responses

(angle changes). The error envelope for a DCXO using 8 bits of ADC and DAC resolution is shown in Figure 3. Note that the areas of minimum error correspond to the turning point temperatures of an AT cut resonator and that the maximum error occurs at the lower temperatures where the slope of the temperature response is a maximum.

The DCXO is provided with a serial I/O port which permits external modification of the memory contents after the package has been sealed. This feature permits the DCXO to be adjusted for output frequency after burn-in and aging are completed without the use of external mechanical adjustments or substantial labor inputs. Also, any changes produced in the output of the oscillator from sealing will be compensated for during testing. Sealing will also allow low temperature testing without the problems created by frost formation on critical components. Unlike the TCXO, in which the compensation is adjusted by changing components, no physical intervention is required with the DCXO. This means that the entire test, compensation and performance verification operations can be fully automated and combined so that the parts need not be touched until the cycle is completed.

All of the compensation and frequency adjustment data are stored in an Electrically Erasable Programmable Read Only Memory (EEPROM) developed by Hughes Aircraft Company. This CMOS device may be programmed, erased and reprogrammed many times without degradation of performance and without the use of ultraviolet light. Use of the EEPROM with an externally accessible I/O port allows the entire compensation to be altered. This permits the nominal frequency to be adjusted digitally which has application to remotely located equipment requiring periodic adjustment or synchronization. Additionally, with the passage of time, if the aging of the crystal or other components should degrade the accuracy of the compensation beyond the point where a simple linear shift will be sufficient to restore it, the DCXO can be retested and entirely new compensation data loaded. The device is then ready for continued use. This capability is limited by the capacitance range of the varactor diode and the DAC resolution. Both of these parameters may be specified so as to extend the useful life as required.

#### Construction Features

The DCXO was constructed using hybrid microcircuit packaging techniques

to conserve package volume. Thin film technology was employed to take advantage of the greater stability of the resistors as compared to thick film circuits. The prototype as developed occupied 1.05 cubic inches, although it was placed in a somewhat larger package initially. As shown in Figure 4, the circuit is partitioned into two substrates. The smaller substrate contains the complete oscillator and output gate. The larger substrate contains the compensation circuitry and power supply regulation. This arrangement permits oscillators to be developed over a wide range of frequencies with changes required only on the smaller substrate. The compensation network is not affected by changes in oscillator design so that the time and expense of a new layout and substrate are avoided. A possibility here is the creation of a series of compensation networks with varying resolution. Custom DCXO's could then be produced on relatively short notice, and at relatively low cost by combining appropriate substrates for oscillator frequency, output compatibility and compensation precision.

The temperature range over which the compensation network operates is determined by the trimming of two resistors on the large substrate. This permits the independent adjustment of the upper and lower temperature bounds, over a broad range, after the substrate has been assembled. Through the use of precision laser trimming techniques, these temperature bounds may be set very precisely. This is very important since any safety factor used to account for trim errors results in a degradation in apparent ADC resolution and thus compensation accuracy.

Temperature compensation accuracy is shown in Figure 5. Over the range -45°C to 85°C the DCXO exhibits a maximum frequency deviation of 0.8ppm. The nominal oscillator frequency is 5.0 MHz using an AT cut resonator operating on the fundamental mode. The power consumption is approximately 250mW. This performance was obtained using commonly available components. Significant reductions in size and power consumption are possible using custom semiconductor devices.

#### Automatic Compensation and Test

A significant advantage of the DCXO approach to temperature compensated oscillators is the ability to automate the compensation and test operations. The test equipment involved, shown in Figure 6, is relatively simple and inexpensive. An interface is required to transfer data through the internal DCXO I/O port. The

DCXO can output the temperature code from its ADC and its DAC can receive input from the internal memory or an external data source. Also, the memory contents can be output and new data can be loaded at specified addresses.

In operation, the test chamber temperature is set and the DCXO stabilized at a series of temperatures. At each temperature, the test equipment adjusts the DAC input until the frequency output is within pre-specified limits. The DAC input is stored on disc along with the ADC code. When the temperature test is complete, the controller calculates any missing entries in the look-up table through an interpolation scheme. The memory is loaded through the I/O port and the DCXO is fully functional. Appropriate acceptance tests are performed prior to removal from the test chamber.

The structure of the I/O port lends itself to bus structured networks. This will permit multiple DCXO's to be tested in a single run. The upper limit on the number of DCXO's tested simultaneously is controlled by the capacity of the temperature chamber and related fixturing. Automated testing, coupled with automated assembly technology currently available in the hybrid industry, can make volume production of precision oscillators a realizable goal.

#### Future Development

Much of the technology used in the DCXO, particularly the ADC and EEPROM, is relatively new and rapidly evolving. It is reasonable to expect this rapid evolution to continue which should result in increased accuracy and lower power consumption at lower cost. At present, although the DCXO uses 8 bit ADC's and DAC's, 12 and 14 bit monolithic devices are available. This will place the compensation accuracy inside the limits of aging and thermally induced frequency hysteresis present in conventional AT cut resonators. It is in this area that development is required in the future. A small, precision crystal with low aging and thermal hysteresis is needed if the crystal technology is to keep up with the semiconductor technology that encompasses the balance of the oscillator. With the appropriate investment in custom MOS devices, the entire DCXO, less the crystal, can be realized on two chips. It is the crystal that will ultimately limit both the stability and the size of future oscillators.

#### References

1. Scott, P. J., Design Considerations for a Digitally Temperature Compensated Crystal Oscillator, Proceedings of the 31st Annual Symposium on Frequency Control sponsored by the U.S. Army Electronics Command, pp 407-411, 1977.
2. Frerking, M. E., The Application of Microprocessors to Communications Equipment Design, Proceedings of the 33rd Annual Symposium on Frequency Control sponsored by the U.S. Army Electronics Command, pp 431-435, 1979.
3. Onoe, M., Yamagishi, I., Narai, H., Temperature Compensation of Crystal Oscillator by Microprocessor, Proceedings of the 32nd Annual Symposium on Frequency Control sponsored by the U.S. Army Electronics Command, pp 398-402, 1978.
4. Buroker, G. E., Frerking, M. E., A Digitally Compensated TCXO, Proceedings of the 27th Annual Symposium on Frequency Control sponsored by the U.S. Army Electronics Command, pp 191-198, 1973.

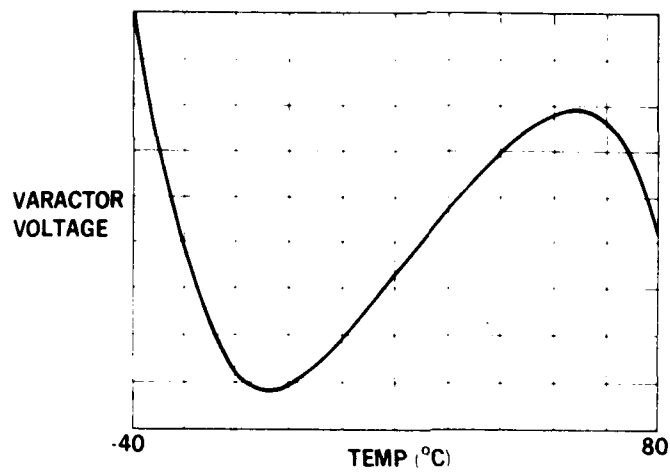


Figure 1. Typical Varactor Bias Voltage for an AT-Cut Crystal

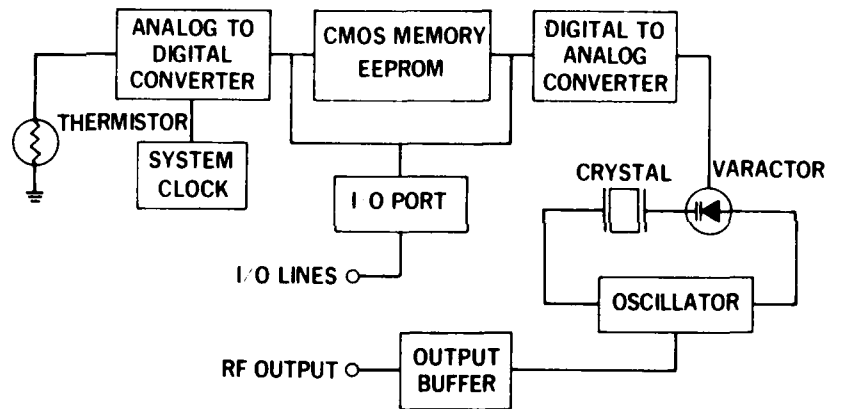


Figure 2. Block Diagram for a Digitally Compensated Crystal Oscillator

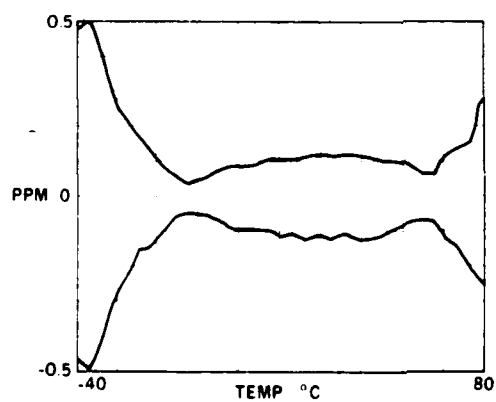


Figure 3. Computer Model of Error Envelope for 8-Bit DCXO with an AT-Cut Crystal

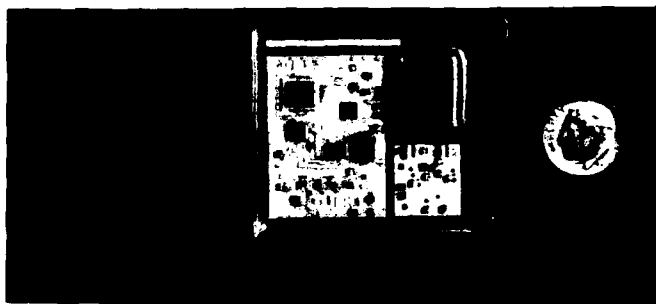


Figure 4. Hybrid DCXO Showing Circuit Partitioning into Oscillator and Compensation Substrates

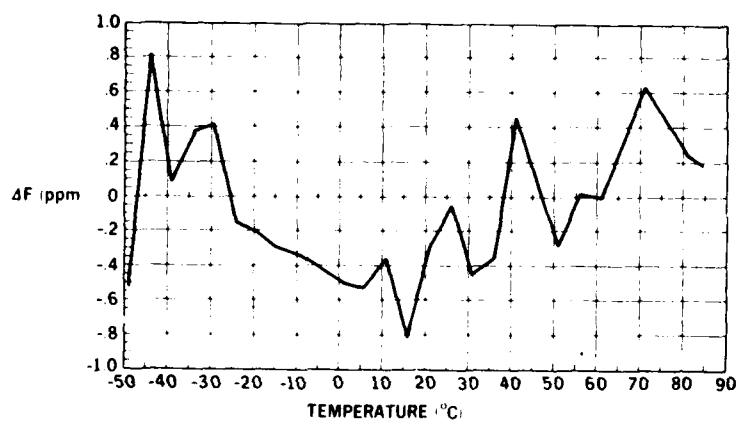


Figure 5. Typical DCXO Frequency Stability with Respect to Temperature

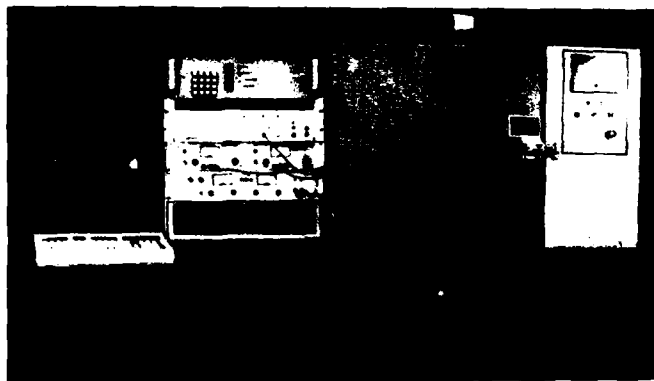


Figure 6. Automated Compensation and Test Position

# THEORETICAL AND PRACTICAL EFFECTS OF THE RESONATOR SPECIFICATIONS AND CHARACTERISTICS UPON PRECISION CRYSTAL OSCILLATOR DESIGN AND PERFORMANCE

Benjamin Parzen\*

Frequency Electronics, Inc.

AD P001559

## Summary

The heart of the crystal oscillator is the resonator, as the performance of the oscillator is always worse than that of the resonator. An important goal of good oscillator design is to minimize the difference between the resonator and oscillator performances. In order to achieve this goal, it is necessary to have full knowledge of the resonator performance. This knowledge is gained from the resonator specifications and from calculations based upon the resonator and oscillator specifications and oscillator circuit parameters.

This tutorial paper clarifies the existing resonator specifications and presents additional resonator and circuit concepts which relate the oscillator and resonator performances. The subject matter is particularly relevant to precision oscillators using low  $C_1$  crystals such as the fifth overtone SC cut.

## Introduction

With the growing popularity of the SC cut, low  $C_1$  crystals, some of the ideas associated with crystal characteristics, specifications and application merit closer reexamination. This reexamination should include the considerations involved in the practical interfacing of the crystal into the oscillator circuitry so that the correct operating frequency is obtained. This paper is intended to assist in this reexamination.

The paper is primarily tutorial, but it introduces some concepts useful in crystal specification and application, and it clarifies some of the implications in the present crystal specifications.

## Crystal Resonator Equivalent Circuits

Let us start with a review of the crystal resonator equivalent circuits.

Fig. 1(a) shows the symbol for the crystal resonator. Note the resonator housing marked as "c" and shown in dashed lines.

Fig. 1(b) shows the complete equivalent circuit, including the housing, which is rarely used except at the highest frequencies.

Fig. 2 is the very familiar circuit normally used, and around which the crystal specifications are written.  $C_1$ ,  $L_1$ ,  $R_1$  are well defined and can be measured with the desired degree of precision. However, as will be shown later, the magnitude of  $C_0$  is somewhat vague and depends upon the circuit in which the crystal is used.

Fig. 3 is a simplification of Fig. 2 assuming  $C_0$  is well defined.

The approximate relationships between the parameters of Fig. 2 and those of Fig. 3 are:

$$R_e \approx \frac{R_1}{\left(1 - 2 \frac{C_0}{C_1} \frac{f}{f}\right)^2} \quad (1)$$

$$X_e \approx \frac{\frac{2}{C_1} \frac{f}{f}}{1 - 2 \frac{C_0}{C_1} \frac{f}{f}} \quad (2)$$

\*Mr. Parzen is a consultant for Frequency Electronics, Inc.

$$\text{where } f = f - f_s \quad (3a)$$

$$\text{and } f_s = \frac{1}{2\sqrt{L_1 C_1}} \quad (3b)$$

#### Crystal Resonator Specifications

The parameters normally specified are  $C_1$ ,  $C_0$ ,  $f_L$ ,  $R_L$ , and  $C_L$ . Often  $C_1$  is not included in the specifications for many of the more popular crystals.

$C_1$  and  $C_0$  have been discussed above.  $f_L$  is the frequency at which ( $X_e = X_L$ ) in Eq. (2) is the negative of the reactance  $X_{C_L}$  of a capacitor  $C_L$ ; i.e.,

the frequency at which the network consisting of the crystal and  $C_L$  in series become series resonant.  $R_L$  is the value of  $R_e$  of Eq. (1) at  $f_L$ .

$C_L$  represents the reactance contribution of the oscillator circuitry to the oscillator frequency,  $f$ , which ideally should be  $f_L$ . It should be noted that  $C_L$  is not an intrinsic parameter of the crystal, since the crystal behavior is completely described by Eqs. (1) and (2), which do not include  $C_L$ . However, the specification of  $C_L$ , for a given crystal, fixes the crystal frequency,  $f_L$ , which ideally is equal to  $f$ , the desired oscillator frequency. There is much confusion regarding this point, and attempts have been made to change the given crystal properties by changing  $C_L$  which only changes specification but not the actual crystal parameters.

Defining

$$\Delta f_{LS} = f_L - f_s \quad (4)$$

$$\text{Then } \frac{\Delta f_{LS}}{f} = \frac{C_1}{2(C_0 + C_L)} \quad (5)$$

Of course,  $R_L$  is also a function of  $C_L$  and from Eqs. (1) and (5) is obtained

$$R_L = R_1 \left[ 1 + \frac{C_0}{C_L} \right]^2 \quad (6)$$

#### Interfacing the Crystal in the Ideal Oscillator

Fig. 4 shows the crystal connected into the ideal oscillator, using the negative resistance oscillator model. By ideal oscillator is meant that the operating frequency is  $f_L$  and that the oscillator does not contribute to the  $C_0$ , so that  $R_e$  of the crystal is  $R_L$  and  $X_e$  of the crystal is  $-X_{C_L}$ . The oscillator consists of the crystal in series with  $X_L$  and  $Z_{LL}$ .  $Z_{LL}$  is the negative resistance generator and has associated with it the negative resistance  $R_{LLg}$ , positive resistance  $R_{LLp}$ , which represents the power out and circuit losses, and  $X_{LL}$  the reactance in the generator.

In general,  $R_{LLg}$  is a strong function of the current  $I_X$  and provides the required limiting action.  $X_{LL}$  and  $R_{LLp}$  are usually weak functions of  $I_X$ . All the  $Z_{LL}$  parameters are weak functions of the frequency over the crystal frequency operating range. However,  $X_{LL}$  may vary substantially over large frequency excursions.

The purpose of  $X'_L$  is to transform  $X_{LL}$  so that the crystal sees the rated  $C_L$ . It usually includes an adjustable component for fine tuning the operating frequency.  $X'_L$  may be inductive or capacitive depending upon  $X_{LL}$ . From Fig. 4

$$X'_L = X_{C_L} - X_{LL} \quad (7)$$

Usually  $X_{LL}$  is optimized for the type of circuitry, frequency stability, and the necessary crystal drive and oscillator output powers, and is rarely equivalent to  $C_L$ . Fig. 4 shows the most popular means of transforming  $Z_{LL}$  to  $X_{C_L}$  and other means are available.

#### The Real Crystal Resonator

The model of the previous section is adequate for fixed frequency, moderate precision, high  $C_1$  crystal oscillators wherein variations in crystal cutting accuracy and in the magnitude of  $C_0$  do not produce intolerable oscillator frequency errors. However, it is unsatisfactory for precision oscillators using low  $C_1$  crystals such as the SC cut for two main reasons.

One reason is the insufficient precision in cutting the crystal so that  $f$  is not equal to  $f_L$ . For example, a 5 MHz 5th overtone SC crystal should be cut to within 1 Hz to make the model reasonably applicable. This results in excessive cost and a very high reject ratio for the crystal production.

The second reason is the vagueness of the value of  $C_0$  due to poorly defined and conflicting measurement techniques, as described in Refs. 1, 2 and 3, and the effect of the physical layout and the circuit type upon the effective value of  $C_0$ . For example, the leads to the crystal in temperature-controlled oscillators may add 2 to 7 pf to the value of  $C_0$ , depending upon the physical layout.

Fig. 5 shows the equivalent circuit of the crystal showing the components making up  $C_0$ . It is evident that the contributions of the different components are a function of the circuit type and whether the crystal housing is connected to the oscillator circuit. For example, in the Pierce oscillator, when the case is connected to the oscillator ground point,  $C_0$  consists of  $C_{10}$  and the remaining  $C_{d1}$  and  $C_{d2}$  are lumped into the oscillator circuit capacitances. However, often, even when the distribution of the components is taken into account, the value of the resulting  $C_0$  does not agree with that obtained from oscillator performance, as pointed out in Ref. 4. It is therefore recommended that the effective value of  $C_0$ , which we shall call the motional static capacitance,  $C_0'$ , be measured using the oscillator as the measuring vehicle. This measurement takes into account all the factors so far mentioned and any other unknown factors. This measurement is performed by inserting a known increment of  $X_e = X_e$  and noting the resulting change in the oscillator operating frequency ( $f = f + \Delta f$ ).  $C_0'$  is then calculated as a function of  $\Delta f$  from the following equation

$$C_0' = \frac{C_1}{2 \frac{\Delta f}{f}} \left( 1 - \sqrt{\frac{2}{\pi C_1} \frac{\Delta f}{f X_e}} \right) \quad (8)$$

A slightly different value of  $C_0'$  will be obtained for each practical value of  $\Delta f$ . It is therefore recommended that the geometric mean of these values be used in all calculations involving  $C_0$ .

Now assume that a crystal, of characteristics  $C_1$ ,  $R_L$ ,  $f_L$  and  $C_L$ , is available. It is desired to operate the crystal with an effective motional static capacitance,  $C_0'$ , at frequency  $f = f_L + \Delta f$ .

The following relationships are applicable:

$$R_1 = R_L \left( \frac{C_L}{C_L + C_0} \right)^2 \quad (9)$$

In terms of  $f = f_L + \Delta f$ ,

$$R_e = R_1 \left[ \frac{1}{1 - 2 \frac{C_0'}{C_1} \frac{\Delta f}{f}} \right]^2 \quad (10)$$

$$X_e = \frac{\frac{2}{\pi C_1} \frac{\Delta f}{f}}{1 - 2 \frac{C_0'}{C_1} \frac{\Delta f}{f}} \quad (11)$$

In terms of  $f = f_L + \Delta f$ ,

$R_{df}$  = the crystal resistance,  $R_e$ , at  $f$

$$= \frac{R_1}{\left[ 1 - \frac{C_0'}{C_L + C_0} - 2 \frac{C_0'}{C_1} \frac{\Delta f}{f} \right]^2} \quad (12)$$

$C_{Ldf}$  = the necessary  $C_L$  at  $f$ ,

$$= \left[ \frac{1}{C_L + C_0} + \frac{2 \Delta f}{C_1 f} \right]^{-1} - C_0' \quad (13)$$

Table 1 gives the characteristics of a high-performance SC cut crystal as a function of  $C_0'$  and  $\Delta f$ .

### Interfacing the Crystal in the Real Oscillator

Fig. 6 shows the complete oscillator in a circuit similar to that of Fig. 4. The major differences between the two oscillators are the contribution,  $C'_0 - C_0$ , of the oscillator circuitry and the fact that  $f = f_L + df$ . The figure shows  $X'_{Ldf}$  connected after  $(C'_0 - C_0)$  but it would be more desirable to connect it adjacent to the crystal, as that would result in a smaller  $R_{df}$ .

### Q Considerations

The Q of the motional arm of the crystal is

$$Q_x = \frac{X}{R} = \frac{1}{\omega C_1 R_1} \quad (14)$$

The Q of the above equation does not include the effect of  $C'_0$ , since it is the usual expression for the Q of a single mesh circuit.

However, a type of Q may be defined as

$$Q = \frac{\frac{\delta X_e}{\delta f}}{2 f R_e} \quad (15)$$

which surprisingly turns out, from Eqs (9), (10), and (13) to be equal to  $Q_x$  and independent of  $C'_0$  and  $\Delta f$ . This is because  $R_e$  varies at the same rate as  $\frac{\delta X_e}{\delta f}$ .

In Fig. 6, the oscillator operating Q

$$Q_{op} = \frac{Q_x R_{df}}{R_{df} + R_{LLp}} \quad (16)$$

Table 1- Example of Characteristics of SC Cut Crystal as a Function of  $C'_0$  and  $df$ , 5 MHz, 5th Overtone

Specifications:

$$C_1 = 40 \text{ aF}, C_0 = 2 \text{ pF}, C_L = 24 \text{ pF}$$

$$R_L = 350 \text{ Ohms}, f_L = 5 \text{ MHz}$$

Calculated Data:

$$Q_x = 2.67 (10)^6, R_1 = 297 \text{ ohms}$$

$$\Delta f_{Ls} = 3.84 \text{ Hz}$$

$(C'_0 - C_0) \text{ pF}$	$C'_0 \text{ pF}$	$df \text{ Hz}$	$R_{df} \text{ ohms}$	$C_{Ldf} \text{ pF}$
0	2	0	350	24
		2	381	15.1
		4	418	10.7
		6	464	8.2
2	4	0	415	22
		2	506	13.1
		4	632	8.7
		6	809	6.2
3	5	0	455	21
		2	593	12.1
		4	804	7.8
		6	1100	5.8
5	7	0	557	19
		2	853	10.1
		4	1466	5.7

## REFERENCES

1. Military Specification MIL-C-3098, Crystal Units, Quartz, General Specification Latest Issue
2. IEEE Standard on Piezoelectricity, IEEE Std. 176-1978.
3. Hafner, E., "The Piezoelectric Crystal Unit - Definitions and Methods of Measurements." Proc. IEEE, 57, Feb., 1969.
4. Healey, D. J., III, "SC-Cut Quartz Crystal Unit in Low-Noise Application at VHF." Proc. Annual Symposium on Frequency Control, U. S. Army Electronics Command, Fort Monmouth, N. J., pp. 440-454 (1981).

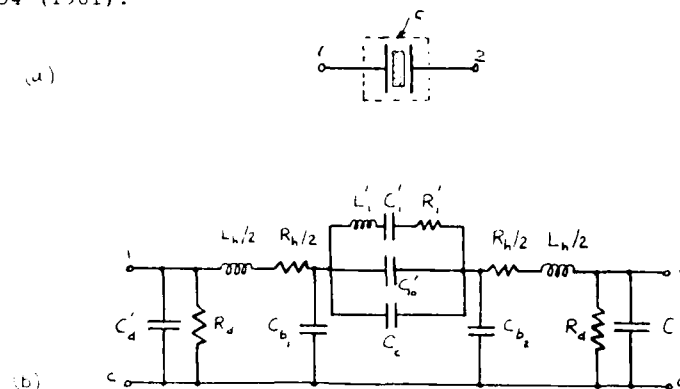


Figure 1. Crystal Resonator. (a) Circuit Symbol, (b) Complete Equivalent Circuit Including the Effects of Holder and Mounting Supports. A Single Crystal Resonance is Represented by the  $L_1', C_1', R_1'$  Arm. This Circuit is Valid in the Vicinity of a Single Resonance up to UHF Frequencies.

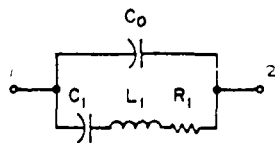


Figure 2. Simplified Equivalent Network of a Crystal Resonator. The Element Values are Measured Effective Quantities that Include Various Stray and Parasitic Effects, and are Constant in the Frequency Regions Centered About the Resonance Under Consideration.

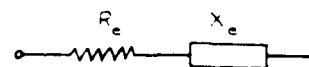


Figure 3. Resistive ( $R_e$ ) and Reactive ( $X_e$ ) Parts of the Impedance Represented by the Network of Figure 2. The Quantities  $R_e$  and  $X_e$  are Sensitive Functions of Frequency in the Region of Resonance.

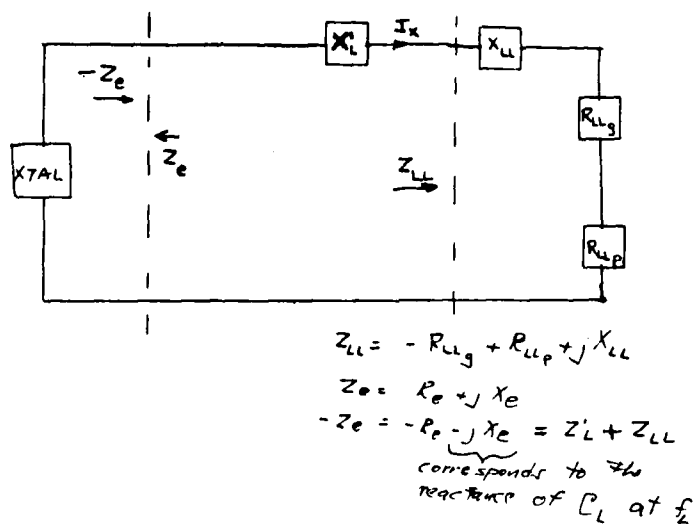


Figure 4. Negative Resistance Model of Oscillator (Idealized)

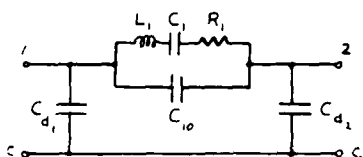


Figure 5. Equivalent Electrical Circuit of Crystal Resonator and Enclosure. Below VHF Frequencies the Element Values are Constant; at Higher Frequencies the Values are Very Weakly Dependent on Frequency, Following from the Constant Values of Figure 1.

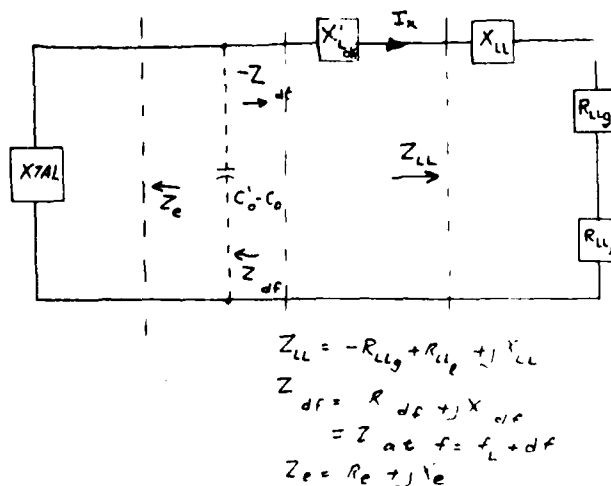


Figure 6. Negative Resistance Model of Oscillator (Real Case)

## REDUCING SAW OSCILLATOR TEMPERATURE SENSITIVITY WITH DIGITAL COMPENSATION

A. J. Slobodnik, Jr., R. D. Colvin, G.A. Roberts, J.H. Silva

Rome Air Development Center  
Electromagnetic Sciences Division  
Hanscom AFB, MA 01731Summary

A method of using digital compensation to reduce surface acoustic wave oscillator temperature sensitivity is described. Initial results with an AT quartz SAW oscillator show a reduction in frequency variation from 191.7 parts-per-million to 5.2 parts-per-million over the temperature range -13 to +97 °C. The key feature is the use of two delay paths on the same substrate. The first path is aligned with a SAW orientation having low temperature sensitivity. By means of oscillation around a feedback loop, it provides the more precise frequency or clock. The second delay path is aligned with a SAW orientation having high temperature sensitivity and acts, through its frequency of oscillation, as a thermometer or temperature measuring device. By using a thermometer placed directly on the substrate, thermal contact and time constant problems are minimized and accurate temperature sensing results. The thermometer frequency (a direct measure of temperature) is counted down to provide an address to a precalibrated read only memory. At each temperature the phase shifter control word necessary to maintain a stable clock frequency is generated on the data lines of the ROM and applied to the electronically variable phase shifter.

Introduction

Generation of precise frequencies by means of crystal oscillators is an important electronics function. Recently, surface acoustic wave (SAW) oscillators<sup>1</sup> such as the one illustrated in Figure 1, have shown themselves to be a particularly cost effective implementation of this function<sup>2</sup>. However, a problem exists in maintaining frequency stability over a wide temperature range; a problem shared to a lesser degree by bulk oscillators. A number of techniques have been proposed to compensate for this temperature sensitivity for bulk<sup>3-6</sup> and surface acoustic wave<sup>6-11</sup> oscillators. It is the purpose of this paper to describe a simple and effective means for digitally compensating for the temperature sensitivity of a SAW oscillator.

Description of the Concept

An overall description of the current concept is illustrated in Figure 2. The key feature is the use of two delay paths on the same SAW substrate. The first path is aligned with a SAW orientation having traditional low temperature sensitivity properties.

By means of oscillation around a feedback loop, it provides the more precise frequency or clock. The second delay path is aligned with a SAW orientation having high temperature sensitivity and acts, through its frequency of oscillation, as a thermometer or temperature measuring device. By using a thermometer placed directly on the substrate, thermal contact and time constant problems are minimized and accurate temperature sensing results. An advantage of the SAW device over the analogous bulk technique<sup>4</sup> is that the two paths are both electrically and spatially separate.

The thermometer frequency (a direct measure of temperature) is counted down to provide an address to a precalibrated erasable programmable read only memory (EPROM). At each temperature the phase shifter control word necessary to maintain a stable clock frequency is generated on the data lines of the EPROM and applied to the electronically variable phase shifter. System convergence is assured due to the intentional difference in temperature coefficients of the two delay paths. Note the simplicity of the system. The clock frequency itself is directly available as an output; no further manipulation or frequency synthesis is required.

Experimental Results

A SAW device having dual criss-cross delay paths as sketched in Figure 3 was fabricated on AT (34.25° rotated Y-cut) quartz. The clock propagation path was along the X-axis with the thermometer path at an angle of 34.8°. The properties of this and other digitally compensated SAW oscillator (DCSO) substrates are listed<sup>12-15</sup> in Table 1. Also listed<sup>16-20</sup> for comparison are several other popular SAW temperature compensated substrates. By choosing the angle between the clock and thermometer paths (last column in Table 1), one can trade off accuracy in sensing the clock path temperature (best with smaller angles) for additional electromagnetic leakage suppression (see Figure 3). Orientations in Table 1 are given in both Euler angle<sup>21</sup> and IRE/IEEE standard notation<sup>22</sup>. If those preferring IEEE notation could adopt ZXltt rather than YXwt rotations, direct commonality<sup>23</sup> of notation would result.

The frequency of operation of the experimental device was approximately 100 MHz. Erasable programmable read only memory chips were calibrated and the complete DCSO illustrated in Figure 2 was implemented. The SAW device was ovenized and the temperature

AD P001560

varied with results as shown in Figure 4. A significant improvement in frequency stability over the comparable uncompensated case is evident. Further improvement can be expected from the use of sealed packages with better thermal characteristics which increase reproducibility of conditions between calibration and operational runs.

#### Intelligent DCSO

A more advanced version of a digitally compensated SAW oscillator is shown in Figure 5. Here, intelligence in the form of a microprocessor or computer is incorporated. In addition to the previously described DCSO advantages of optimum temperature sensing, fast warmup and low cost; several other important features now become possible. (1) Based on starting temperature and direction and rate of change of temperature, hysteresis<sup>24</sup> can be compensated. (2) Compensation for aging<sup>16</sup> becomes possible. (3) Rapid temperature changes can be handled by outputting interpolated control words between available thermometer counts. (4) Frequency tuning while continuing to maintain low temperature sensitivity becomes possible. This latter property suggests use as a frequency synthesizer. Indeed, combining the fine frequency capability of a DCSO device with the broad bandwidth of a switched SAW filterbank synthesizer results in the wide-bandwidth, narrow-tone-spacing synthesizer shown in Figure 6.

#### Conclusions

Digital compensation promises to significantly improve the temperature stability of both bulk and SAW oscillators.<sup>16</sup> In the present paper we have described a technique which takes advantage of some of the unique properties of SAW devices.

#### Acknowledgement

Helpful discussions with R. T. Webster of RADC are much appreciated.

#### References

1. S.K. Salmon, "Practical Aspects of Surface-Acoustic-Wave Oscillators", IEEE Trans. Microwave Theory and Techniques, 27 pp 1012-1018, 1979.
2. S. C. Gratzke, "SAW Oscillators-Their Current Status", Microwave Journal, 20, pp 45-57, December 1977.
3. M. E. Frerking, Crystal Oscillator Design and Temperature Compensation, Van Nostrand, New York 1978.
4. J. A. Kusters, M.C. Fischer and J. G. Leach, "Dual Mode Operation of Temperature and Stress Compensated Crystals", Proc. 32nd Frequency Control Symposium, pp. 389-397, 1978.
5. G. A. Warwick, A. J. Prescott and W. Gosling, "The Frequency Shifting Synthesizer", The Radio and Electronic Engineer, 50, pp 122-126, 1980.
6. R. G. Kinsman, "Temperature Compensation of Crystals with Parabolic Temperature Coefficients", Proc. 32nd Frequency Control Symposium, pp. 102-107, 1978.
7. R. F. Mitchell, "Temperature Compensated Acoustic Surface Wave Oscillator", U.S. Patent No. 3,889,205, 1975.
8. T. I. Browning and M. F. Lewis, "Novel Technique for Improving the Temperature Stability of SAW/SSW Devices", Ultrasonics Symposium Proceedings, pp 474-477, 1978.
9. T. E. Parker, D. L. Lee and I. Leja, "Surface Acoustic Wave Stabilized Oscillators", Raytheon Research, Waltham, MA 1979.
10. M. F. Lewis, "Temperature Compensation Techniques for SAW Devices", Ultrasonics Symposium Proceedings, pp 612-622, 1979.
11. J. Henaff and M. Feldmann, "A SAW Temperature Compensated Oscillator Using The Difference Between Metallized and Free Delay Temperature Coefficients on LITA03", Ultrasonics Symposium Proceedings, pp. 448-451, 1978.
12. F. R. Lack, G. W. Willard, and I.E. Fair, "Some Improvements in Quartz Crystal Circuit Elements", Bell System Technical Journal, 13, pp 453-463, 1934.
13. M. B. Schulz, B. J. Matsinger, and M. G. Holland, "Temperature Dependence of Surface Acoustic Wave Velocity in a Quartz", Journal of Applied Physics, 41 pp 2755-2765, 1970.
14. A. Ballato, T. Lukaszek, D. F. Williams, and F. Y. Cho, "Power Flow Angle and Pressure Dependence of SAW Propagation Characteristics in Quartz", Ultrasonics Symposium Proceedings, pp 346-349, 1981.
15. D. F. Williams and F. Y. Cho, Doubly Rotated Cut SAW Devices, DELET-TR-79-0275-1, Motorola CED, Scottsdale, AZ 85252, 1982.
16. T. Lukaszek and A. Ballato, "What SAW Can Learn from BAW: Implications for Future Frequency Control, Selection, and Signal Processing", Ultrasonics Symposium pp 173-183, 1980.
17. B. K. Sinha and H. F. Tiersten, "Zero Temperature Coefficient of Delay for Surface Waves in Quartz", Applied Physics Letts. 34, pp 817-819, 1979.
18. R. M. O'Connell, "A New Surface-Acoustic-Wave Cut of Quartz With Orthogonal Temperature-Compensated Propagation Directions", Applied Physics Letts., 35 pp 217-219, 1979.
19. D. E. Oates, "A New Cut of Quartz for Temperature-Stable SAW Dispersive Delay Lines", IEEE Trans. Sonics Ultrasonics, 26, pp 428-430, 1979.

20. C. O. Newton, "A Study of the Propagation Characteristics of the Complete Set of SAW Paths on Quartz with Zero Temperature Coefficient of Delay", Ultrasonics Symposium Proceedings, pp 632-636, 1979.

21. J. J. Campbell and W. R. Jones, "A Method for Estimating Optimal Crystal Cuts and Propagation Directions for Excitation of Piezoelectric Surface Waves", IEEE Trans. Sonics Ultrasonics, 15, pp 209-217, 1968.

22. "Standards on Piezoelectric Crystals, 1949", Proc. IRE, 37, pp 1378-1395, 1949.

23. A. J. Slobodnik, Jr., and R. T. Webster, "Comparison of SAW Substrate Orientation Notations", Unpublished, 1982.

24. D. Hammond, C. Adams and A. Benjaminson, "Hysteresis Effects in Quartz Resonators", Proc 30th Frequency Control Symposium, pp 55-60, 1968.

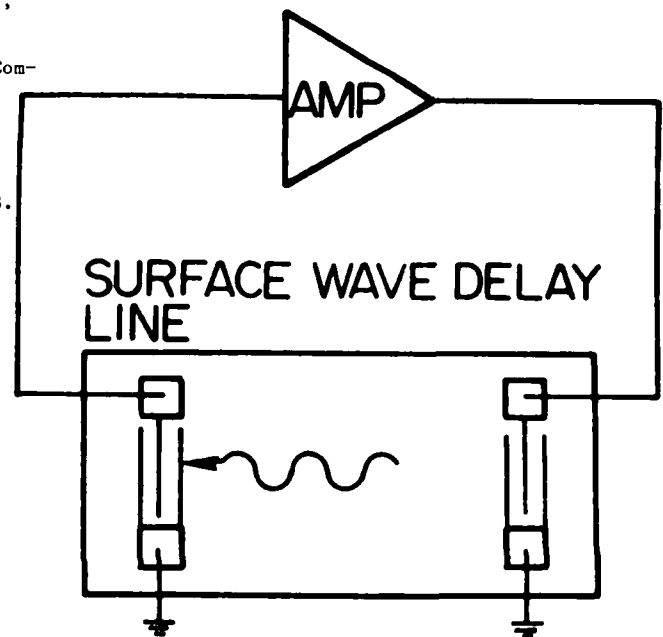
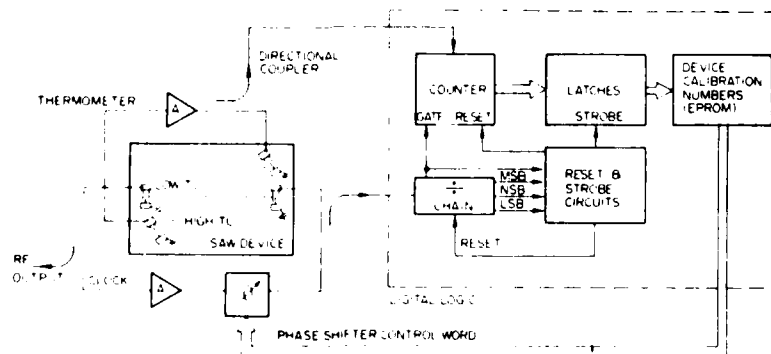


Figure 1. SAW Delay Line Oscillator



#### DIGITALLY COMPENSATED SAW OSCILLATOR - OPERATING MODE

Figure 2. Block Diagram of a Digitally Compensated SAW Oscillator (DCSO) in the Operating Mode

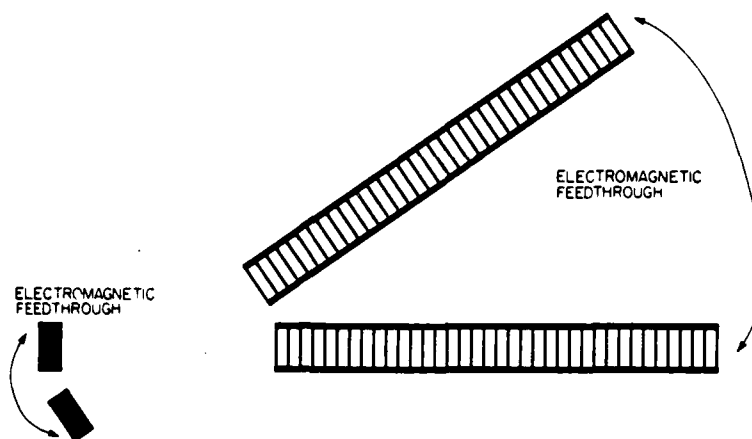


Figure 3. Transducers Used for Experimental Device, in Addition to Input-Output Leakage, Electromagnetic Feedthrough can Occur as Shown.

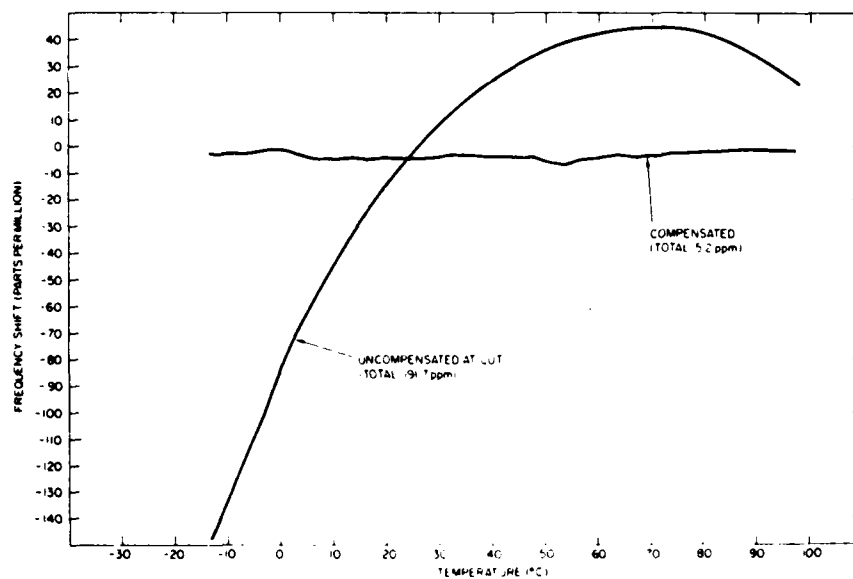
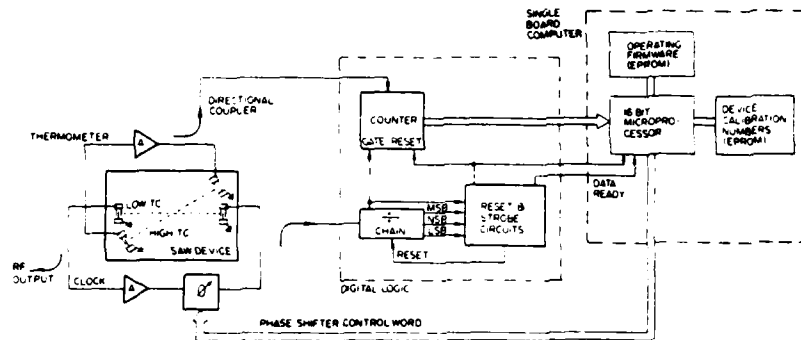


Figure 4. Experimental Temperature Sensitivity of a Digitally Compensated SAW Oscillator Compared to an Uncompensated AT-Cut Quartz SAW Oscillator. All Data at ~100 MHz.



INTELLIGENT DCSO - OPERATING MODE

Figure 5. Block Diagram of an Intelligent Digitally Compensated SAW Oscillator in the Operating Mode

### WIDE-BANDWIDTH, NARROW-TONE-SPACING FREQUENCY SYNTHESIZER

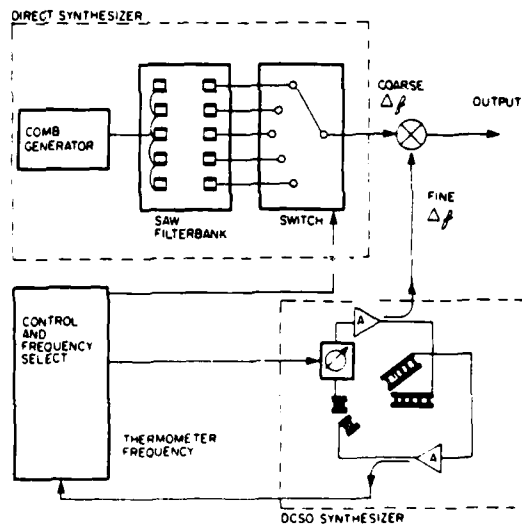


Figure 6. Wide-Bandwidth, Narrow-Tone-Spacing, Frequency Synthesizer

Table 1  
Properties of DCSO and Other SAW Orientations

TYPE OF SAW PATH	CRYSTAL CUT	ORIENTATION		TEMPERATURE DEFICIENT OF DELAY (ppm/°C)	VELOCITY (m/sec)	$\frac{\Delta v}{v}$	POWER FLOW ANGLE (DEGREES)	ANGULAR SEPARATION (DEGREES)
		Euler Angles (°)	Turnover (°C)					
CLOCK THERMOMETER	AT	0 0 0 25 0 0 0 0 0 25 0 0	0 0 0 25 0 0 0 0 0 25 0 0	36 8	352 3465	0.00064 0.00075	—	34.8
CLOCK THERMOMETER	AO	25 25 0 49.95 25 25 0 55.26	25 25 0 30.46 25 25 0 24.74	0 -26.8	35.5 34.98	0.0005 0.0009	12.5 <sup>2</sup>	74.3
CLOCK THERMOMETER	AO	5 5 2 3 4.80 5 5 2 3 5.98	5 5 3 3 30.2 5 5 3 3 22.0	0 -27.6	32.5 32.48	0.00049 0.00095	4.9	16.2
CLOCK THERMOMETER	SA	0 0 0 32.75 0 0 0 0 0 32.75 35	0 0 0 42.75 0 0 0 0 0 42.75 35	0 -2	35.9 32.79	0.00058 0.00075	—	35
CLOCK	RAK <sup>3</sup>	0 0 0 25.07 45 0 0 0 0 25.07 45 0	0 0 0 35.07 45 0 0 0 0 35.07 45 0	—	326.7	0.0005	3.46	—
CLOCK	SS <sup>1</sup>	0 0 0 4.8 23.46 0 0 0 4.8 23.46	0 0 0 49.2 23.46 0 0 0 49.2 23.46	—	364.9	0.00068	—	—
CLOCK	NEW <sup>1</sup>	0 0 0 0 0 0 0 0 0 0 0 0	0 0 0 0 0 0 0 0 0 0 0 0	—	364.9	0.0006	—	—

- Notes: (1) For AT Quartz Turnover Occurs Away from 25°C.  
(2) Euler Angles of 12.5, 125.0, 49.95 Yield Zero Power Flow Angle.  
(3) Values from Reference 18. (All Other Cuts Recomputed for this Paper).

UPDATE ON THE TACTICAL  
MINIATURE CRYSTAL OSCILLATOR PROGRAM

Harold W. Jackson

The Bendix Corporation  
Communications Division  
1300 E. Joppa Rd. Baltimore, Md. 21204

AD P001561

Summary

The Tactical Miniature Crystal Oscillator (TMXO) and its more significant design features have been described previously. In this paper, the performance characteristics of the early TMXO models will be presented. In addition, performance results representative of more recent units which use SC-cut crystals are included and mechanical changes to improve the internal structural characteristics are discussed. Finally, a test oscillator useful in evaluating crystals is described.

In general, the results of the evaluation of the initial TMXO models indicate that the major performance goals were realized. In those areas where performance was less than expected, modifications have been introduced to enhance performance. Later models having these modifications incorporated verify the effectiveness of the changes.

Key Words (for information retrieval) Miniature quartz oscillator, thermal control, hybrid microelectronics, vacuum techniques.

Introduction

The TMXO is a miniature, low power, fast warmup, thermally controlled quartz oscillator intended for use in tactical communications, navigation, and identification applications. Power consumption at  $-54^{\circ}$  Celcius is typically 250 mW and frequency accuracy over the temperature range of  $-54^{\circ}$  to  $+75^{\circ}$  Celcius is within  $1 \times 10^{-8}$  of the nominal frequency. Design goals for warmup time and vibration sensitivity are 3 minutes and  $1 \times 10^{-7}$  per g respectively. The volume of the TMXO is approximately 16 cm<sup>3</sup>.

The low power consumption of the TMXO results from the use of hybrid microelectronic techniques which reduce the volume of the thermally controlled parts, and a double walled construction in which the space between the walls is evacuated. An inner enclosure containing the crystal and electronics is supported within the evacuated space by a system of wires which also provide electrical connections. This support structure provides a thermal resistance from the electronics and crystal assembly to the ambient of approximately 500<sup>o</sup> C/W. Typical power consumption of the oscillator as a function of ambient temperature is shown in figure 1. A simplified illustration of the construction of the TMXO is seen in figure 2.

Another important feature of the TMXO is the use of a ceramic flatpack crystal enclosure which has been developed by the Army in a parallel program. This package is very compatible with the TMXO structural concept and it promises to provide significant improvements in a number of crystal related performance parameters.

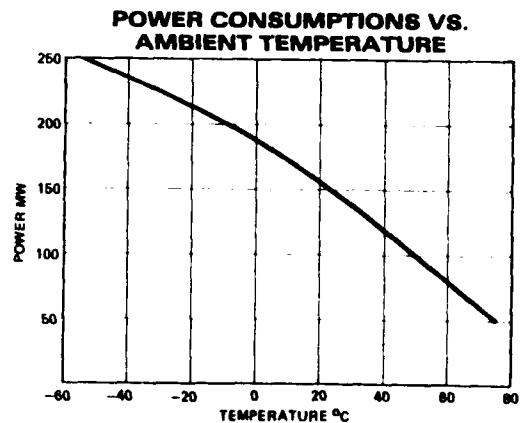


Figure 1

## TMXO STRUCTURE

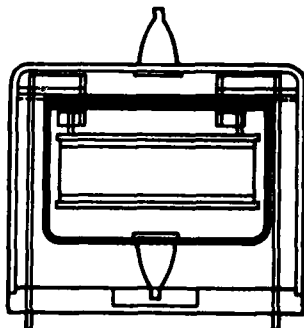


Figure 2

## Frequency Stability

The design of the crystal is an important factor in determining the frequency stability of the oscillator. Fundamental crystals were used in the early TMXO models because it was thought that this would decrease warmup time. Subsequent investigation has shown that warmup time for the fundamental crystal is only slightly less than that for overtone units. In the early models, which used fundamental AT-cut crystals, aging rate ranged from about  $1 \times 10^{-10}$  /day to  $1 \times 10^{-9}$  /day after two weeks of continuous operation. Aging data for four of these units is shown in figure 3.

Short term stability is also a crystal dependent parameter. Typical performance in this area is shown in figures 4 and 5. Figure 4 shows the Allen variance as a function of averaging period, and figure 5 shows the phase noise density as a function of frequency offset from the carrier.

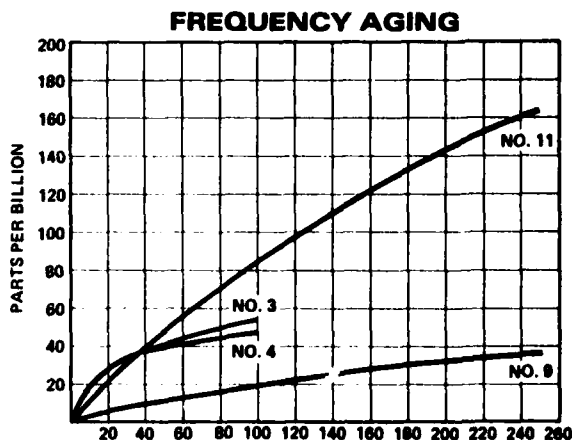


Figure 3

The crystals used in the first TMXO models were early developmental units processed in the 1978-79 time frame and are therefore not representative of current crystal performance. In general, recent crystals are considerably improved in both long and short term stability.

Frequency stability with respect to temperature is a function of the crystal frequency/temperature characteristic and also the thermal gain of the temperature control system. Frequency stability vs. temperature for a recent model which uses an SC-cut crystal is shown in figure 6.

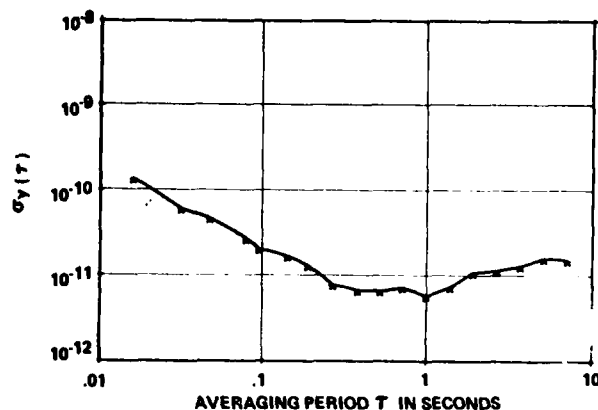


Figure 4

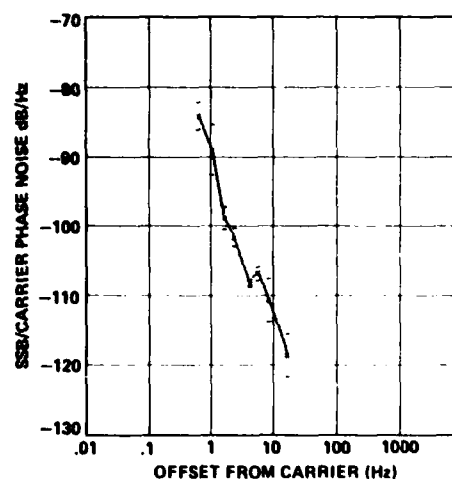


Figure 5

# **FREQUENCY VS. AMBIENT TEMPERATURE TMXO NO. 23 (10 MHz THIRD O.T. SC)**

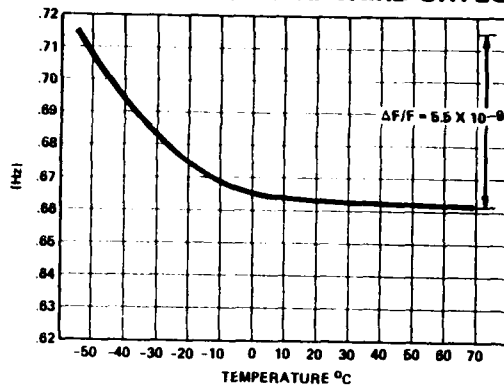


Figure 6

## Warmup Time

Fast warmup was a major performance objective of the TMXO development, and the construction of the internal assembly was designed to enhance this parameter. However, actual warmup performance for the first TMXO was much longer than expected. Since the effects which resulted in this poor warmup characteristic may be of general interest, the techniques used to isolate and resolve this problem are discussed here.

The design goal for warmup time to within an accuracy of  $1 \times 10^{-8}$  is 3 minutes. The warmup time for TMXO #1 is shown in the curve of figure 7. It is seen that the time required to reach the desired accuracy is approximately 14 minutes. In searching for an explanation for this behavior, it was observed that the frequency offset during warmup almost exactly paralleled the decay in warmup power as shown in figure 8. This relationship of frequency offset to heater power was also confirmed by static frequency vs. ambient temperature measurements.

A series of carefully designed experiments were performed to determine the cause of the unexpectedly slow warmup. The crystal and associated heater elements were physically separated from the substrates which contain the remaining active circuitry. Power was then applied to the crystal and heat spreaders to bring the resonator temperature to the upper turn point where the resonator frequency was measured. The ambient temperature was then increased so as to require less power to hold the crystal at the turn point, and the resonator frequency was again measured. Proceeding in this fashion, a

curve of resonator frequency offset vs. heater power was constructed. The results of this experiment indicated that to within experimental uncertainty, the frequency offset during warmup and much of the variation in frequency with ambient temperature was attributable to the effect of heater power on the resonator frequency.

It was found that the frequency-power relationship was different depending on the side of the crystal to which power was applied. The bottom cover (nearest to the resonator supports) was found to be the least sensitive and produced a deflection opposite in sign to that of the top cover. This discovery suggested the possibility of finding a configuration for heating the resonator which would minimize the effect.

## **WARM-UP TIME FOR TMXO NO. 1**

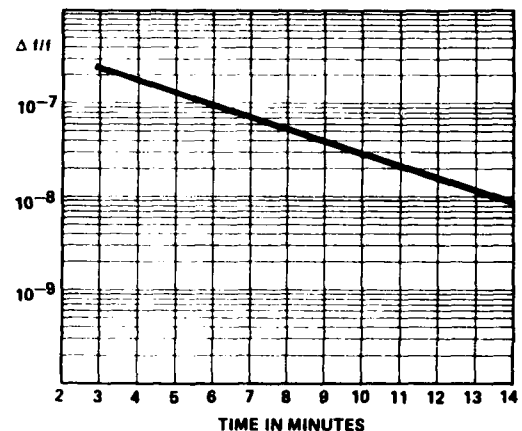


Figure 7

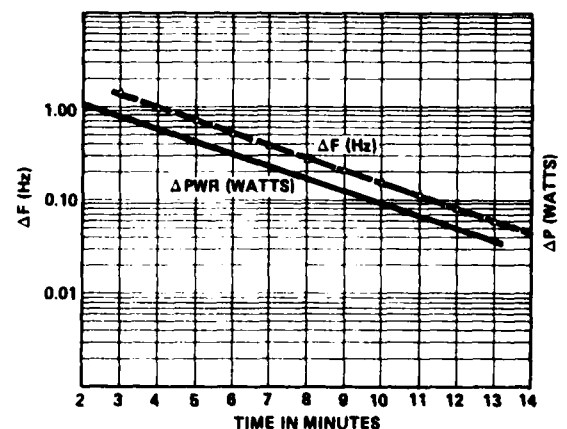


Figure 8

It was reasoned that there should be less effect if the heat flow through the covers were minimized. To accomplish this, the crystal covers were separated from the heat spreaders by a thin copper washer which provided thermal contact near the periphery of the covers. It was found that the copper washer did indeed modify the effect, and in the case of the bottom cover the effect could be minimized by varying the size of the hole in the washer. This is shown in figure 9 where the offset is plotted against heater power for different spacer configurations.

With these results, the design of the electronics assembly was modified to incorporate the copper spacer on one side of the crystal and to remove the heating elements from the other side altogether. Also, in order to reduce the time required for the complete internal package to reach thermal equilibrium, a heating element was added to the internal header so that the inner enclosure would warm up at about the same rate as the electronics assembly. This would cause the heater power to decay much faster following turn on and any residual effects of heater power would thus be minimized.

#### TMXO #2 FREQUENCY/POWER DEFLECTION

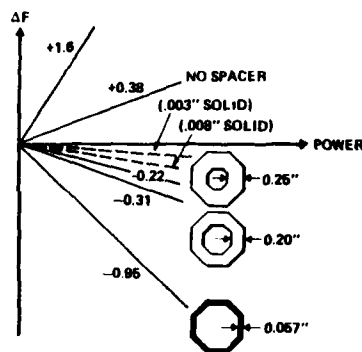


Figure 9

With these modifications, a substantial improvement in warmup time was achieved. The curve for TMXO #7 in figure 10 is representative of the warmup characteristics of 5.115 MHz fundamental AT-cut units. However, the compensation technique which works well for a particular crystal design will not, in general, be satisfactory for other designs, and for some crystals, compensation for this effect is not possible at all. It will therefore be necessary to characterize new crystal designs for this frequency-power effect before use in TMXO applications. SC-cut crystals which were used in more recent units do not exhibit this effect to any significant degree.

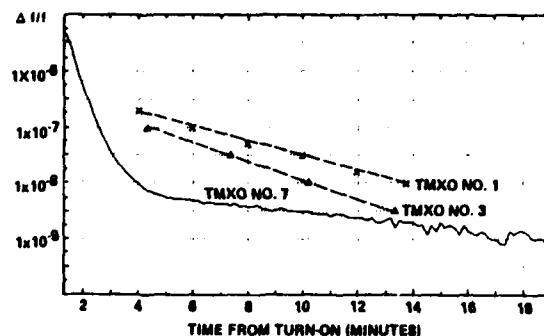


Figure 10

#### Vibration Effects

In the initial design of the TMXO, a great deal of emphasis was placed on reducing power consumption and enhancing the reliability of the vacuum. The objective of the mechanical design was to make the support structure as rigid as possible while maintaining a thermal resistance through the support structure of approximately 500° C/W.

In testing the frequency stability of the TMXO under vibration, a strong resonance at approximately 450 hertz was observed. This is seen in the curve of figure 11 where the amplification of the applied acceleration at resonance is about 16 times. Since this represents a significant degradation in stability relative to the acceleration sensitivity of the crystal, corrective steps were taken to improve the structural characteristics of the oscillator.

The principal resonance mode of the support structure is along the vertical axis. The resonance can be modeled by considering the inner enclosure to be a lumped inertial mass supported by a

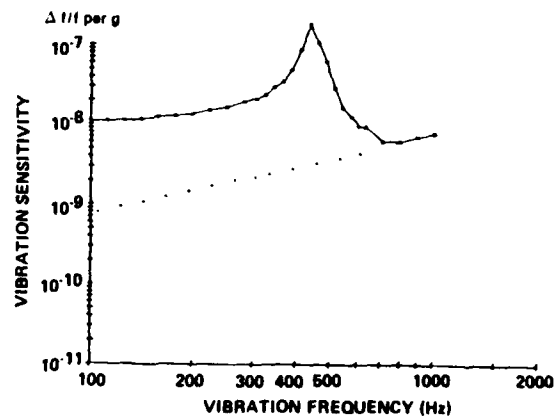


Figure 11

spring. If the spring constant is measured by observing the static displacement of the inner enclosure resulting from a constant force, and using the known weight of the inner enclosure, the calculated natural frequency agrees closely with the observed resonant frequency. Therefore, the static deflection resulting from a constant force is useful in predicting the structural resonant frequency.

When examining the distortion of the structure under constant force, a rotation of the horizontal straps connecting the vertical support wires to the inner header feedthrough pins (about an axis normal to the straps at each end) is observed. This rotation is greatest at the end connected to the inner header pin. It is clear that this strap rotation is the primary cause of the reduced structural rigidity.

As an interim technique to increase the rigidity of the structure, a second strap has been added in parallel with each existing strap on the side of the wires opposite from the existing strap. This increases the resonant frequency of the structure approximately 50% and also seems to reduce the amplification at resonance.

A more substantial solution to this problem, which is now being implemented, is the elimination of the straps altogether. A new ceramic header has been developed for the inner enclosure which will extend radially beyond the circle of the inner cover to provide electrical and mechanical connection to the vertical support wires. The electrical connections from the header feedthroughs to the vertical support wires are made by a metalization pattern on the outside of the header.

Vibration testing of a mechanical model of this new configuration indicates that there are no significant resonance modes below 2 kHz. This is quite an improvement over the earlier design, and it should be adequate for most applications.

#### Warmup Performance with SC Crystals

SC-cut crystals have been used in the most recent models of the TMXO and, as expected, warmup time and acceleration sensitivity have been improved substantially. In addition, the use of the copper spacer to compensate for the effects of heater power is not required for the SC crystals. Figure 12 and figure 13 show the warmup from room ambient and  $-40^{\circ}$  degrees Celsius respectively for a 10 MHz third overtone SC crystal. The curves are similar except that the warmup from  $-40^{\circ}$  is slower by the amount of time for the

temperature to make the transition from  $-40^{\circ}$  to  $25^{\circ}$ . This corresponds to a rate of change of temperature during warmup of  $1.7^{\circ}$  C/sec.

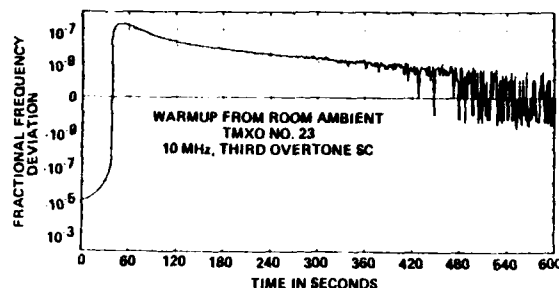


Figure 12

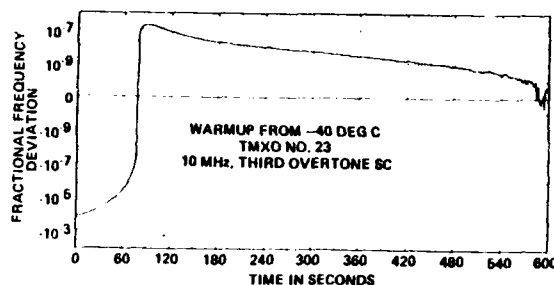


Figure 13

#### Crystal Test Oscillator

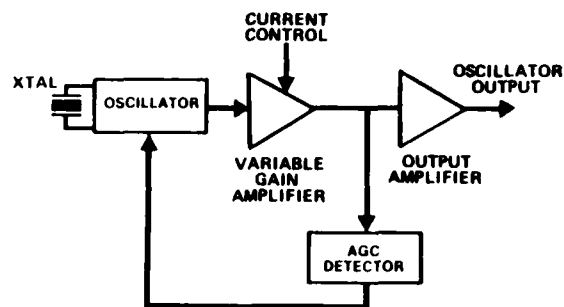
In the course of the TMXO development it was necessary to evaluate crystals independently of the TMXO in order to derive the necessary design parameters and, also, to determine the contribution of the electronics to such performance characteristics as aging and short term stability.

In order to facilitate this evaluation, a test oscillator was developed with a mechanical construction designed to allow convenient replacement of the crystal under test. Provision was also made for temperature monitoring and control. The original design of the test oscillator was optimized for the evaluation of fundamental AT-cut crystals operating at frequencies of 10 MHz and below. In the current design, the operating frequency has been extended to 20 MHz and additional features such as crystal current control have been added. A photograph of the test oscillator is shown in figure 14.

The electronics and crystal are mounted on four circular printed wiring boards supported coaxially inside a cylindrical aluminum shell. The shell is heated by resistance wire close wound

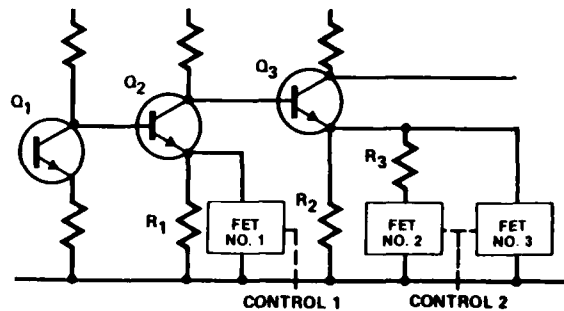
This entire assembly consisting of the heater shell, electronics, and crystal are housed inside a Dewar flask which is closed at the top by a plug having low thermal conductivity. Interconnecting wiring through the mouth of the flask is provided by a special ribbon cable also designed to minimize heat conduction.

### TEST OSCILLATOR BLOCK DIAGRAM



A simplified schematic diagram of the variable gain amplifier is shown in figure 16. The gain of the amplifier can be adjusted in 10 dB steps over a 40 dB range by controlling the bias on the three high conductance Field Effect Transistors (FET) switches in the emitter circuits of amplifier stages  $Q_2$  and  $Q_3$ . The bias of FET #2 and FET #3 is designed so that a single wire can be used to control the switches independently. The 40 dB crystal current control range can be adjusted to start at a minimum of 20  $\mu$ A and can be increased to end at a maximum of 5 mA.

### SIMPLIFIED SCHEMATIC VARIABLE GAIN AMPLIFIER



497

Crystal operating temperature can be adjusted coarsely by orienting the shell to select one of two control thermistors which correspond to high and low ranges of operation. Fine control to a resolution of a few millidegrees K is provided by a precision multi-turn potentiometer. Calibration accuracy of the potentiometer is about  $.1^{\circ}\text{K}$ .

Average short term stability for a number of oscillators is shown in the curves of figure 17 and 18. Figure 17 shows the Allen variance as a function of averaging time with constant crystal current. Figure 18 shows the Allen variance as a function of crystal current with the averaging time held constant. These results were obtained using a fundamental AT-cut resonator which is more susceptible to perturbations from the electronics than overtone resonators.

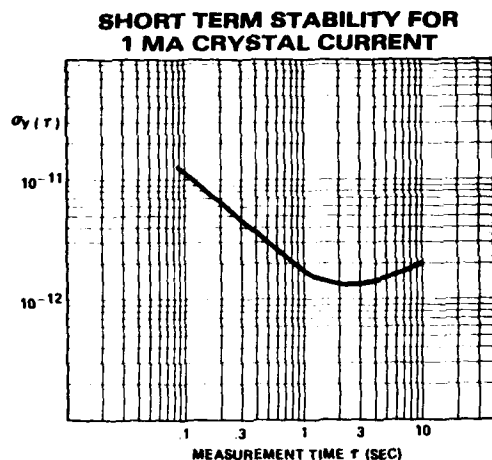


Figure 17

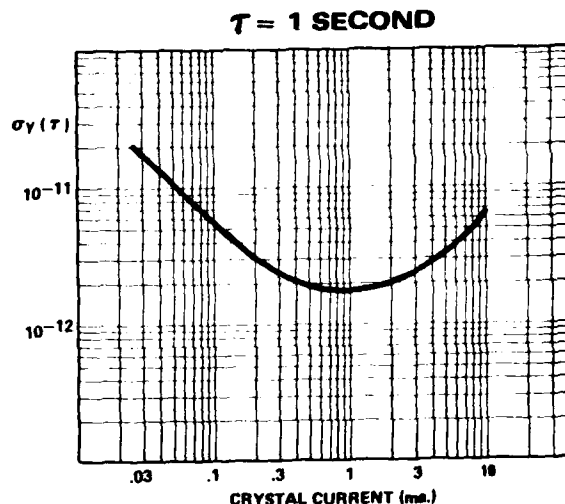


Figure 18

#### Acknowledgements

The author wishes to acknowledge the contribution of Dr. Raymond Filler of ERADCOM and Dwight Brown of Bendix in supplying much of the experimental data.

#### References

1. H. W. Jackson, "Tactical Miniature Crystal Oscillator," Proc. 34th AFCS, May 1980, pp. 449-456.
2. S. D. Wood, et. al., "An Investigation of the Stability of Thermistors," Journal of Research of the National Bureau of Standards, Vol. 83, No. 3, May - June 1978.

AD P001562

# ARGOS SYSTEM QUARTZ DEVICE PERFORMANCE AND ORBITAL DATA

M. Geesen, EMD; M. Brunet, CNES; M. Meirs, A. Strauss, J. Ho, and M. Rosenfeld

Frequency Electronics, Inc.  
Mitchel Field, New York 11553

## Introduction

This paper presents data on precision Quartz Oscillators, VCXO's, and Crystal Filters, with a detailed comparison of the data accumulated on these devices over a six-month period prior to launch, and the data that has been accumulated in up to two years in orbit on the TIROS N Platform. In correlating the data, we are trying to establish baseline ground testing to more accurately predict performance of critical quartz devices in an orbital environment.

Orbital data is available for the Ultra Stable Quartz Oscillator as it is possible to reconstruct this frequency data from the information received from the satellites.

## System Description

The operational Argos System is used for the collection of meteorological data, and the location of transmitting beacons. These beacons continuously sample meteorological information.

It is a random access system, which means that each beacon broadcasts at regular intervals. This message includes both a pure carrier and a modulated carrier.

Independent of other beacons, the system detects the beacon location and collects information from several thousand beacons dispersed around the world. The system capacity is as follows:

- 4000 with data collector and beacon location determination
- 16000 with data collection only

Figure 1 shows the physical configuration of the Argos system. Figure 2 shows the location of ten (10) permanent beacons.

The Argos system was conceived and built in France. It is installed aboard the American Meteorological Satellite of the TIROS N series.

- TIROS N launched in October, 1978, had a life of 29 months
- NOAA6 launched in June, 1979, is still operating

- NOAA7 launched in May, 1980, is still operating

A computer center situated in Toulouse (France) processes all the information from the Argos system and transmits the results to the users.

A block diagram of the Argos system is shown in Figure 3. The received signals from the beacons are distributed through various channels to be decoded through the logic circuitry and to determine location and meteorological information for retransmission back to the earth.

Figure 4 is a more detailed block diagram of the receiver section. The Ultra Stable Oscillator (OUS), Voltage Controlled Crystal Oscillator (VCXO), and Crystal Filters are shown in this block diagram. As can be seen, the VCXO and OUS are operated in an open loop configuration, and therefore require precise frequency stability in order to maintain system performance.

## Frequency Calculation of the Orbiting OUS

### Orbiter Beacons

The Argos System includes ten reference beacons for the orbit calculation of the TIROS N satellite series.

One of the beacons situated in Toulouse is also used as a time and frequency reference. This beacon is driven by a Cesium Standard from the CNES Meteorological Laboratory. C.N.E.S. is the French Space Agency, Centre National Etudes Spatiales. This broadcast frequency is  $F = 401,650,000$  MHz.

### OUS Frequency

The frequency of the onboard OUS is tracked every day for each satellite during the orbit calculation. An orbit calculation provides a simultaneous estimation for the orbit parameters from one satellite, and for the frequency offsets of the reference beacons. A classical method of Root means square is used. In this method, all the frequency data points collected by the satellite from all the reference beacons during the

last three days, are used. (Thus 3000 to 4000 data points provide a good geometric mean.

All frequency data is measured with the same multiplication factor which is the ratio between the true value of the OUS Frequency (unknown) and the last frequency estimation recorded on the ground. Knowing the broadcast frequency, a frequency offset  $\Delta F$  is estimated for the Toulouse beacon. This enables us to determine the multiplication factor.

The accuracy of this estimation is better than  $2.5 \times 10^{-10}$  at 2%. This precision is correlated to the global quality of the orbit calculation.

#### Quartz Devices

Both quartz oscillators and crystal filters were manufactured for the Argos system. Figure 5 defines each of the quartz crystal devices and some of the pertinent operational parameters.

Figure 6 shows a drawer of the TIROS N Transponder into which the OUS, one of the VCXO's, and a 59 MHz crystal filter are installed.

Figure 7 is another PC card in which another VCXO and 59 MHz crystal filter are also installed.

#### Performance Test

Comparisons were made of the data taken during acceptance testing, during installation into the satellite, and during actual orbit conditions to determine the consistence of these characteristics.

Figure 8 shows aging data for OUS Model PF1 which went through acceptance testing in February-March, 1976, and was put into orbit in October, 1978. Aging data through 1979 and 1980 shows that the initial aging of  $-7.7 \times 10^{-11}/\text{day}$  which was achieved during acceptance testing correlates well to the  $-4.2 \times 10^{-11}/\text{day}$  achieved in orbit.

Figure 9 which shows the aging on OUS PF3 shows that during acceptance testing in October of 1976, the aging was  $-8.7 \times 10^{-11}/\text{day}$ . This system was launched into orbit in July, 1979 and through 1980 and 1981 exhibited an aging of  $-5.5 \times 10^{-11}/\text{day}$ .

Figure 10 which is for OUS F7 shows a positive aging of  $+8.4 \times 10^{-11}/\text{day}$  during ATP in September, 1977. It was launched into orbit in June, 1981, and shows an aging rate that has flattened to  $1 \times 10^{-11}/\text{day}$ .

A series of additional oscillators which have not yet been launched have been kept in storage and periodically turned on after 2, 4, or 6 months for a period of five days to obtain frequency measurements. The data for these oscillators is shown in Figure 11, and shows aging rates from  $1.5 \times 10^{-12}/\text{day}$  to  $1.8 \times 10^{-11}/\text{day}$ .

Aging data on the VCXO's cannot be determined when the systems are in orbit. However, from the continued successful operation, it can be determined that they are operating within their specification limits.

Figures 12 and 13 show aging data on the ARGOS MV6 and MV7 systems which were taken on these VCXO's prior to their launch. These show aging characteristics well within their specification requirements.

#### Summary

The testing that has been performed on the quartz devices for the ARGOS System, and in particular on the Ultra Stable Quartz Crystal Oscillator has indicated that precise frequency aging characteristics can be determined with the appropriate type of acceptance testing. In particular, three Ultra Stable Crystal Oscillators which we have received adequate long-term data in orbit have shown that the aging magnitude and polarity agree with those determined many years prior during acceptance testing, and this testing can be used to model frequency drift characteristics.

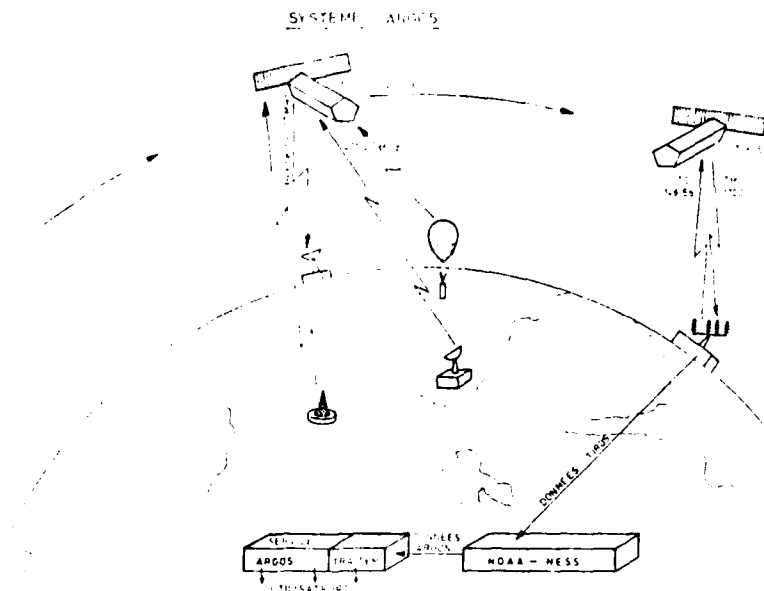


Figure 1. ARGOS System Configuration

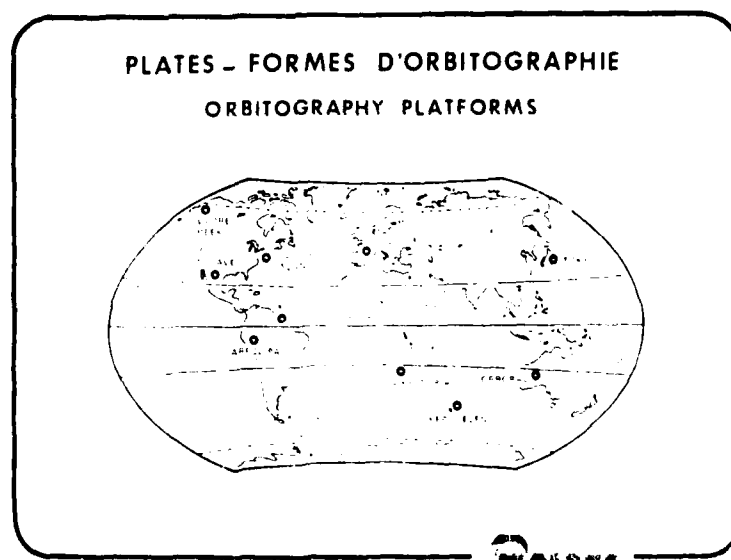


Figure 2. ARGOS System, Beacon Locations

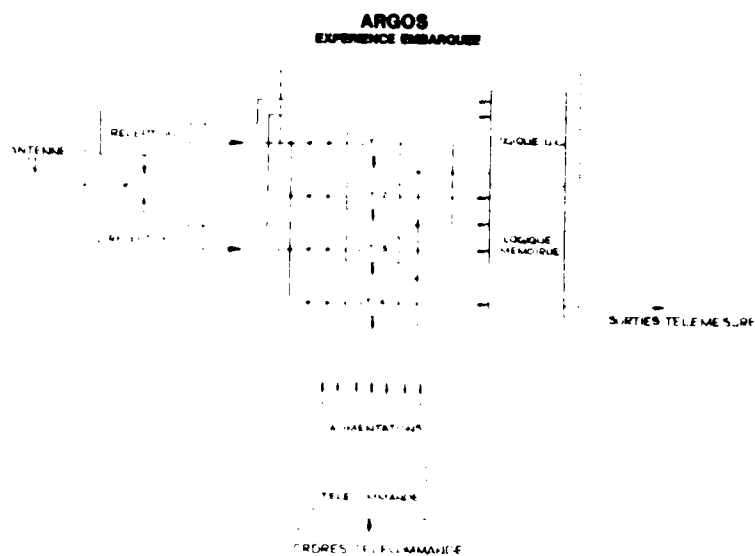


Figure 3. ARGOS System Block Diagram

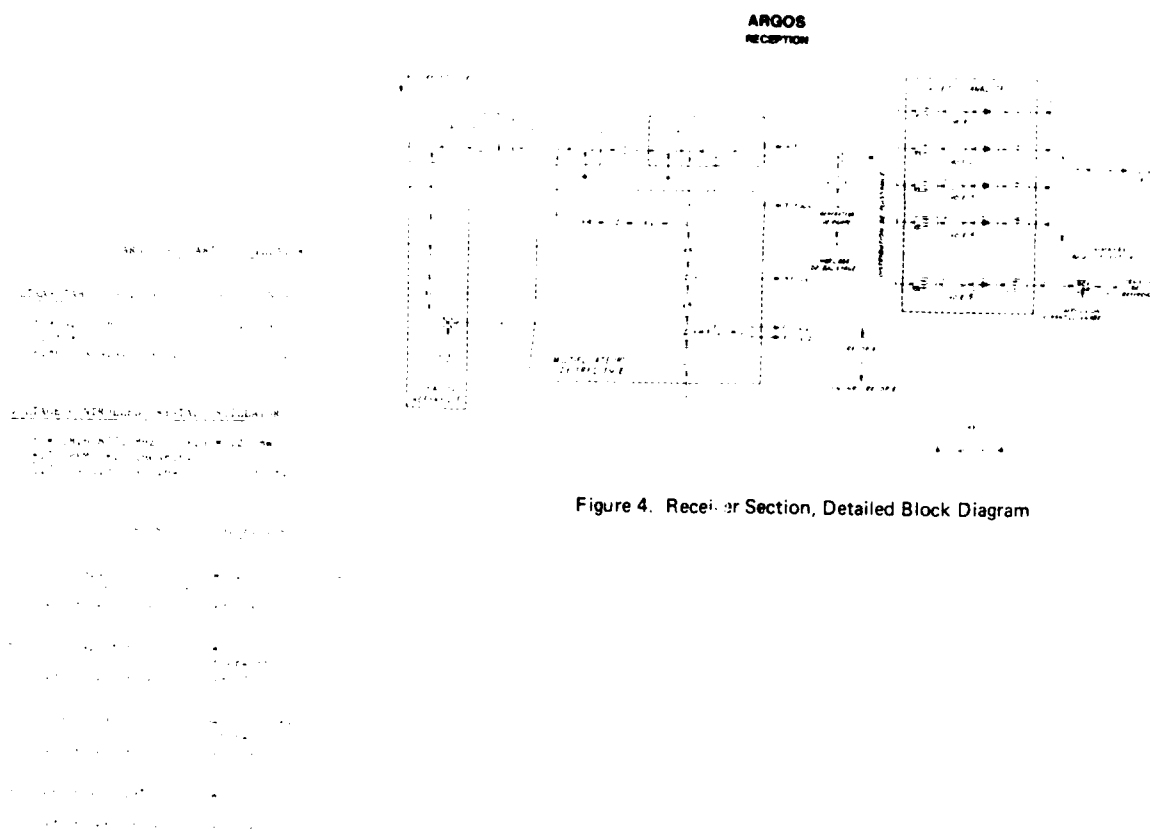
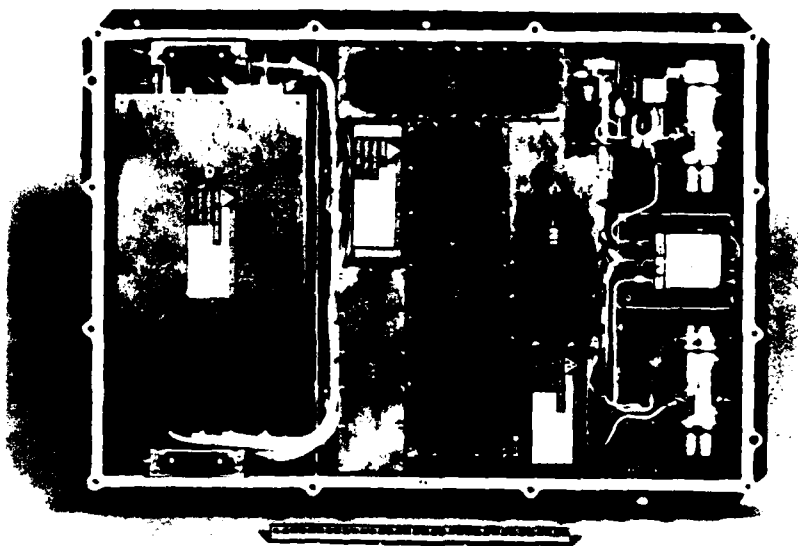


Figure 4. Receiver Section, Detailed Block Diagram

Figure 5. Quartz Crystal Device Parameters



ELECTRONIQUE MARCEL DASSAULT

Figure 6. TIROS-N Transponder, Typical Drawer

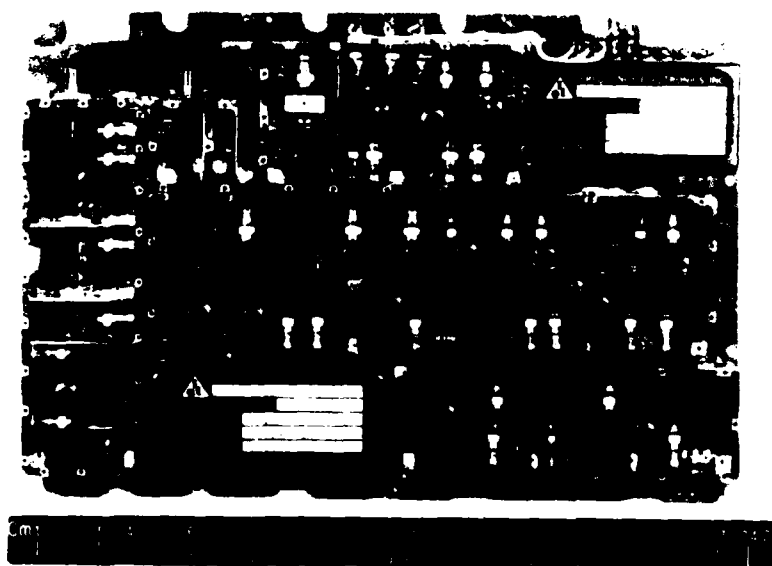
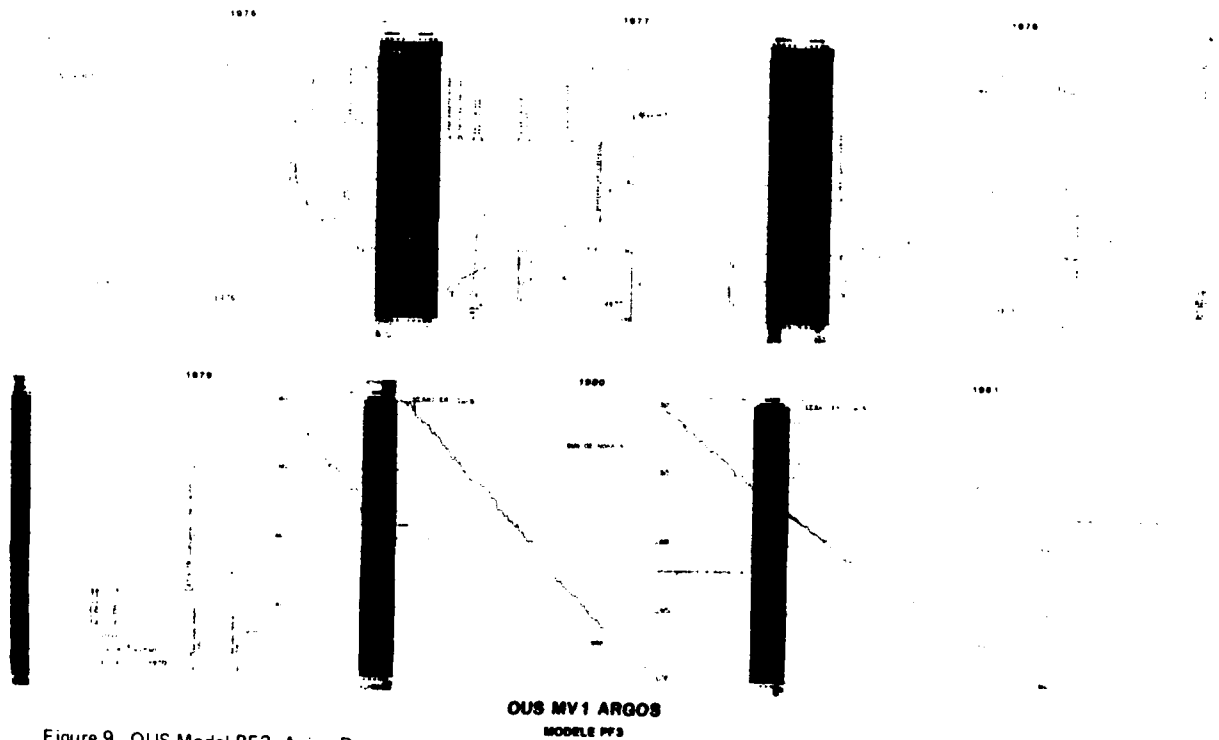
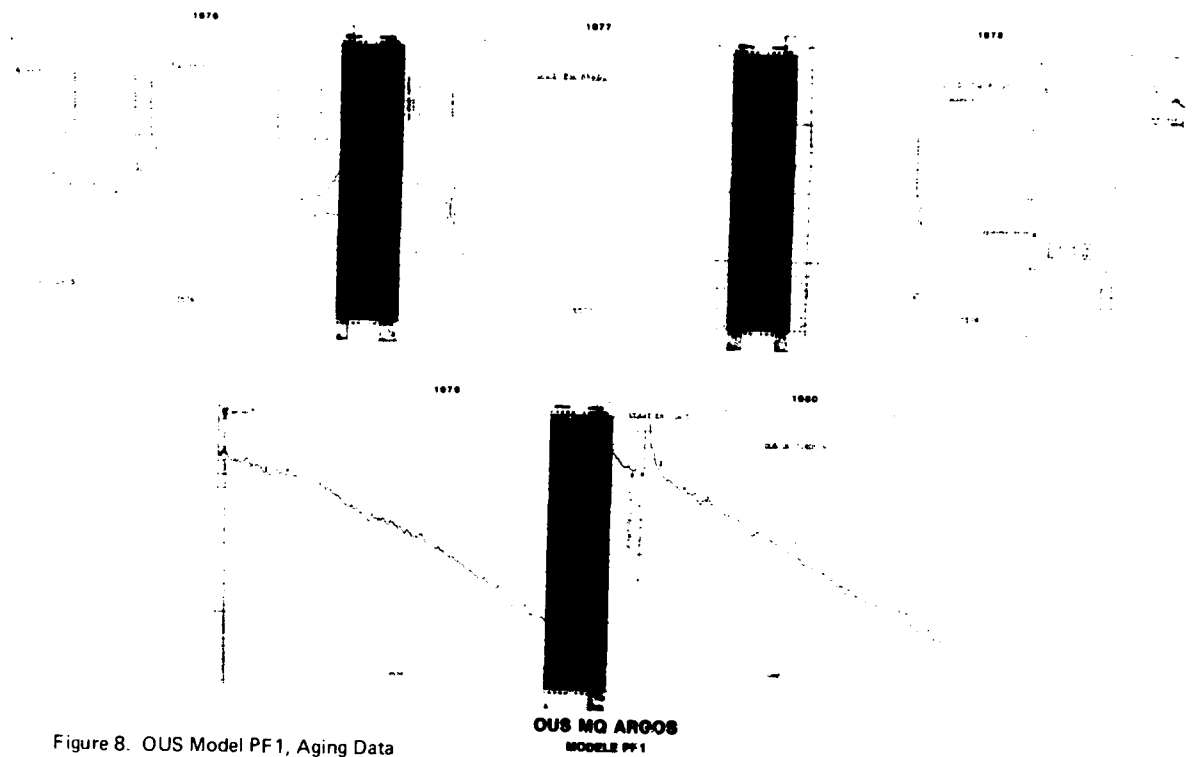


Figure 7. TIROS N Transponder, PC Card



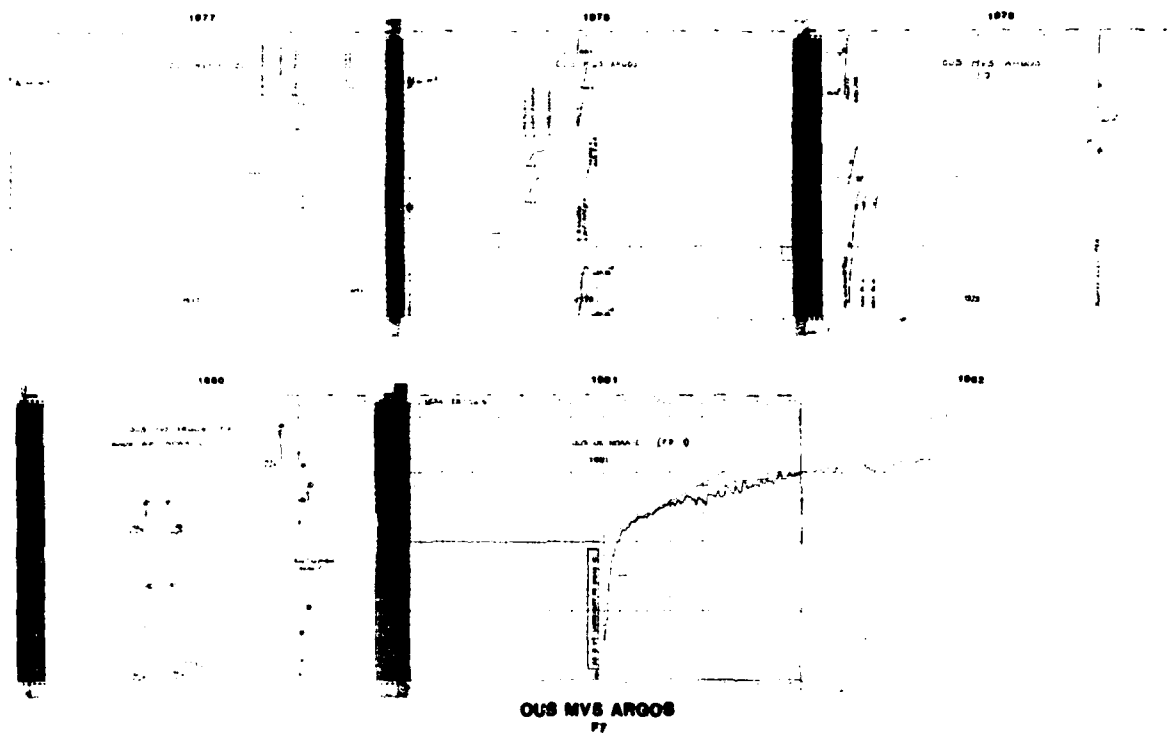


Figure 10. OUS Model F7, Aging Data

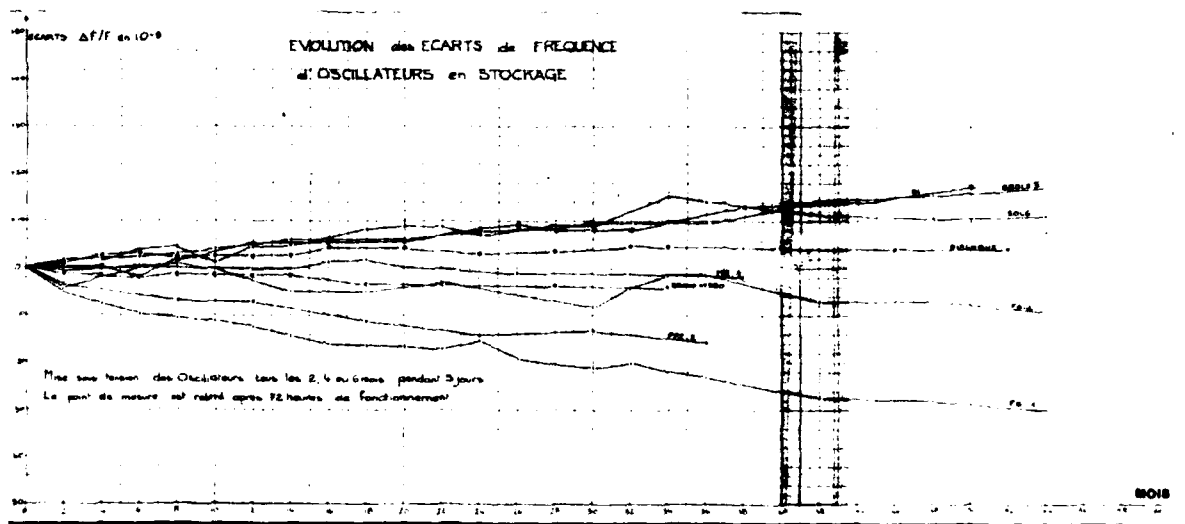


Figure 11. Oscillators in Storage, Aging Data

# VCXO MV6 ARGOS

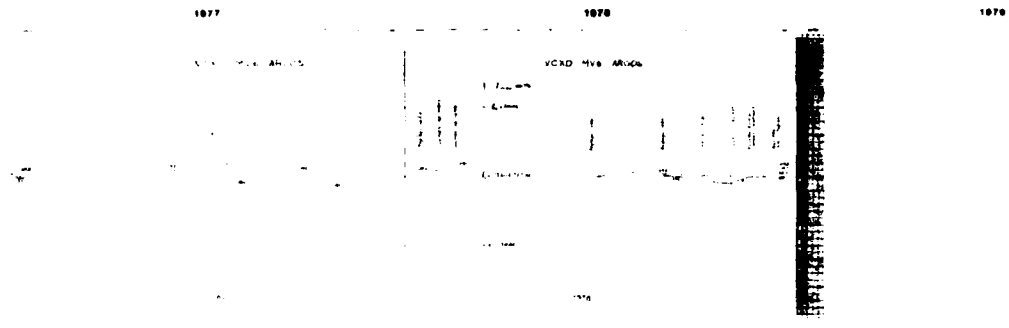


Figure 12. ARGOS MV6 VCXO, Aging Data

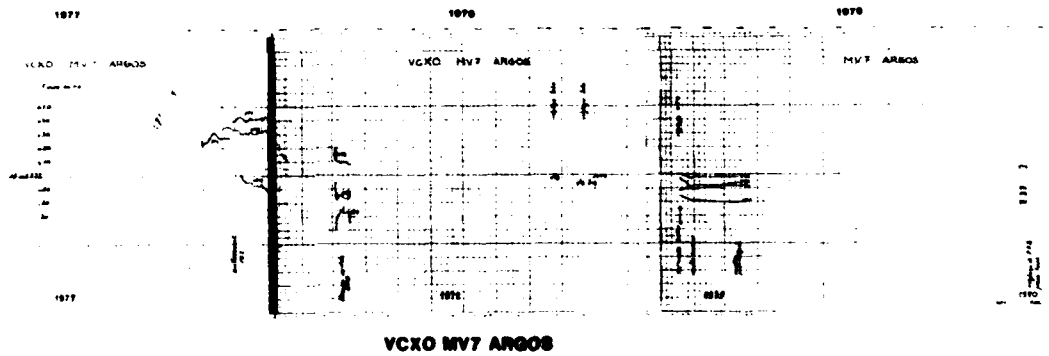


Figure 13. ARGOS MV7 VCXO, Aging Data

AD P001563

COMPUTER AIDED DESIGN AND ASSEMBLY  
OF OSCILLATORS

T. M. Hall

Bell Telephone Laboratories, Inc.  
555 Union Boulevard, Allentown, PA 18103Abstract

This paper provides an overview of Bell Lab's experience in applying computers to modeling and design; to data acquisition; to data analysis; to component selection; and to other miscellaneous tasks.

In the past, quartz crystal oscillators could be modeled most easily using linear circuits models. Although non-linear models exist (e.g., SPICE, CAPITOL, etc.), they could not be used to make a closed loop analysis of crystal oscillators because of the high  $Q$  involved. Recently, however, the WATAND program developed by the University of Waterloo has become available and allows closed-loop non-linear analysis of quartz crystal oscillators. Both linear and non-linear analysis programs are being used at Bell Labs to evaluate new designs with particular attention being paid to the effect of component variations on manufacturability.

The primary data acquisition task performed by the computers is taking frequency temperature measurements on TCXOs. An additional application is the final room temperature checkout of oscillators to determine waveform characteristics, power consumption, power supply sensitivity, and pulling range (for VCXOs). Real time component selection is used to aid in selecting resistor combinations to match the values determined from the analysis of the temperature-run data. In VCXOs and TCVCXOs, real time component selection is used to set varactor operating points to optimize frequency-voltage pulling characteristics.

Other uses include statistical analysis of performance data to project manufacturing yields; simulation of digital compensation schemes using A/D and D/A converters interfaced to a microprocessor based computer; and simulation of the

temperature performance of doubly rotated crystal cuts.

I. Introduction

Computer aids are being used increasingly in the design and assembly of oscillators for the Bell System. At present, the oscillator design and development organization uses 5 desktop computers, 1 mini computer, and 2 timeshared systems. Computers have been applied to modeling and design, to data acquisition, to data analysis, to component selection, and to other miscellaneous tasks. This paper will provide an overview of our experience in applying computers in these areas.

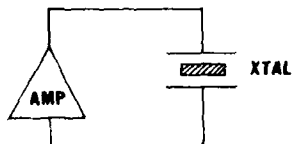
II. Modeling and Design

In the past, quartz crystal oscillators could be modeled most easily using linear circuits models. Although non-linear models exist (e.g., SPICE, CAPITOL, etc.), they could not be used to make a closed loop analysis of crystal oscillators because of the high  $Q$  involved. The top part of Figure 1 shows schematically a basic crystal oscillator with an amplifier and a crystal in the feedback loop. Recall that in a real oscillator the amplifier must be non-linear or else the oscillators would grow to infinite size. Therefore, a realistic model of the oscillator should include non-linearities.

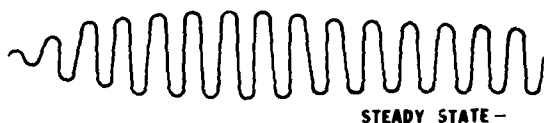
A conceptually simple way to model this oscillator is to model each individual component in the amplifier as realistically as possible and then connect these individual components in a circuit modeling program such as SPICE or CAPITOL. The oscillator can be started in the model by turning the power on, by closing the loop instantaneously, at  $t=0$ , or by exciting it with a sine wave that is removed at  $t=0$ . The oscillators will then build up through some initial transient period and finally settle down to a steady

state as shown in the lower part of the figure.

## COMPUTER MODELLING OF OSCILLATORS



### A NON-LINEAR MODEL : E.G. SPICE



### B. OPEN-LOOP LINEAR MODEL: E.G. LINCAD CANNOT MODEL NON-LINEAR ELEMENTS SUCH AS TRANSISTOR AND VARACTOR

Fig. 1 Computer Modeling of Oscillators. Shown in the upper part of the figure is a simplified schematic of an oscillator including the amplifier and quartz crystal. The lower middle part of the figure shows how a non-linear model such as SPICE can model the startup of an oscillator containing non-linear circuit elements. An open loop linear model such as LINCAD cannot model non-linear elements such as the transistor and varactor.

The only problem is that for a quartz crystal oscillator with a  $Q$  in the thousands, the approach to steady state can take many cycles.

The traditional solution, is to linearize the circuit model in some way and then apply the gain and phase criteria namely that the gain be greater than 1 at some point where the phase is  $0^\circ$ . But then we cannot model the effects of the non-linear elements such as the transistor and the varactor, at least not in a straight forward way.

After examining a number of different possible solutions to this problem, we discover the WATAND program which stands for the Waterloo Analysis and Design Program.<sup>1,2</sup> This was developed by the University of Waterloo in Waterloo, Ontario, Canada and is available on a dial-up time-shared system.

The basic features of the system are that it allows non-linear elements much like SPICE or any other non-linear analysis program; and that it uses iterative extrapolation to find the steady state solution to periodically varying waveforms.

The way it does this is shown schematically in the lower part of Figure 2. Basically it starts up either by building up from zero or by starting from some guess as to the initial state. The program integrates the waveform through several cycles until it detects a pattern and then it extrapolates to where it expects the waveform is headed. It again integrates through several cycles and extrapolates again.

## WATAND

### (WATERLOO ANALYSIS AND DESIGN)

#### A. ALLOWS NON-LINEAR ELEMENTS

#### B. USES ITERATIVE EXTRAPOLATION TO FIND STEADY STATE

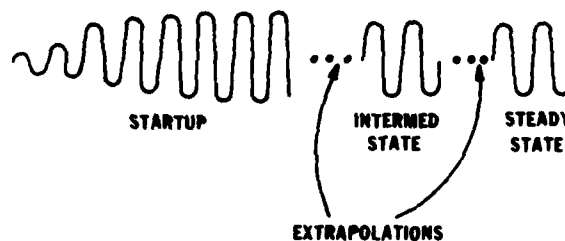


Fig. 2 The WATAND (Waterloo Analysis and Design) computer model allows non-linear circuit elements and uses iterative extrapolation to find the steady state solution. The lower part of the figure illustrates the extrapolation process.

It keeps extrapolating until no further changes are detected, that is, until the voltage and current on one cycle are exactly the same as the voltage and current one cycle later.

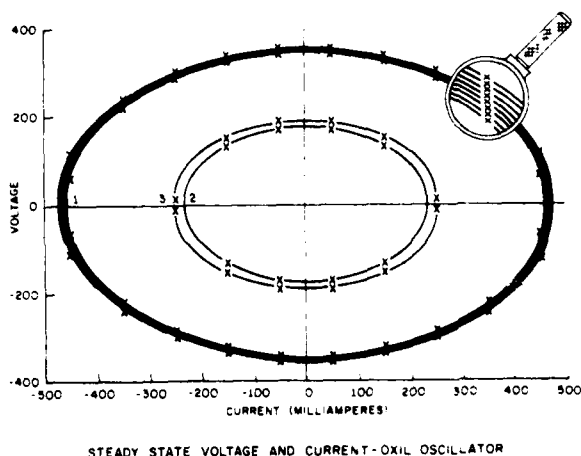


Fig. 3 Output of WATAND showing the voltage on the crystal capacitance,  $C_1$ , as a function of the current in the crystal inductance,  $L_1$ . The program integrates around the ellipses labeled 1, until it has established a pattern that allows it to extrapolate to the ellipses labeled 2. The final steady state solution is given by the ellipses labeled 3.

Figure 3 shows a plot of the voltage on  $C_1$ , the crystal's series capacitance, as a function of the current in  $L_1$ , the crystal's series inductance. The program starts at the extreme left of the outer ellipse with some initial guess for the current and integrates around several cycles. The program then extrapolates to curve 2 and again integrates for several cycles. In this case, it has overshoot slightly and needs to correct back to curve 3. While integrating around curve 3, the program finds (in this example) that the steady state criteria have been satisfied, and it is, therefore, done.

Figure 4 shows the final state waveform for the oscillator at the output of the oscillator stage. It should be pointed out that this modeling was done on an integrated circuit oscillator chip that has not yet been fabricated, and that to be able to view the final steady state waveform anywhere in the circuit before committing to silicon is very valuable to the integrated circuit designer.

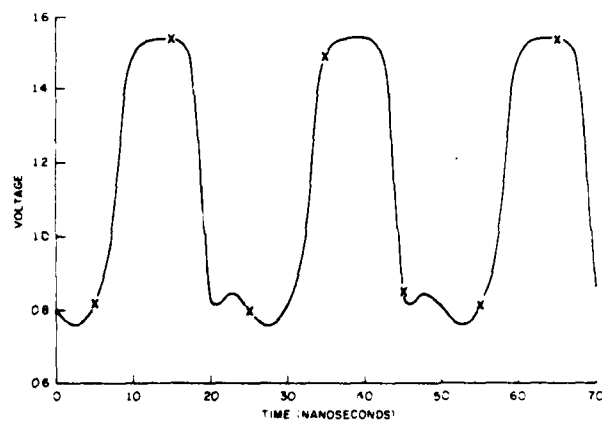


Fig. 4 Final state waveform for the oscillator stage output in an integrated circuit oscillator. This waveform was obtained before the design was committed to silicon and was, therefore, extremely valuable to the circuit designers.

### III. Data Acquisition

The primary data acquisition task performed by the computers is taking frequency temperature measurements on TCXOs. This involves both an uncompensated temperature run to obtain data for selecting the resistor-thermistor network and a final temperature run to confirm the actual performance. Miniature and ovenized oscillators are also temperature tested under computer control. An additional application is the final room temperature checkout of oscillators to determine waveform characteristics, power consumption, power supply sensitivity, and pulling range (for VCXOs).

### IV. Data Analysis and Component Selection, TCXOs

The primary data analysis task performed by the computers is analysis of the uncompensated TCXO data to determine the optimum resistor-thermistor network.

Real time component selection is used to aid in selecting resistor combinations to match the values determined from the analysis of the temperature-run data.

## V. Real Time Component Selection in TCVCXOs

In VCXOs and TCVCXOs, real time component selection is used to set varactor operating points to optimize frequency-voltage pulling characteristics.

The top part of Figure 5 shows a typical circuit configuration for a TCVCXO with one varactor. The temperature compensation voltage is derived from a network of resistors and thermistors to approximately cancel out the temperature dependence of the crystal and other oscillator components. The control voltage for adjusting the oscillator frequency is fed to the other side of the varactor and is derived from an external control voltage by attenuating it and offsetting it with a resistor network. Thus, the net voltage across the varactor is the difference between the temperature compensating voltage and the control voltage.

### TCVCXO WITH 1 VARACTOR

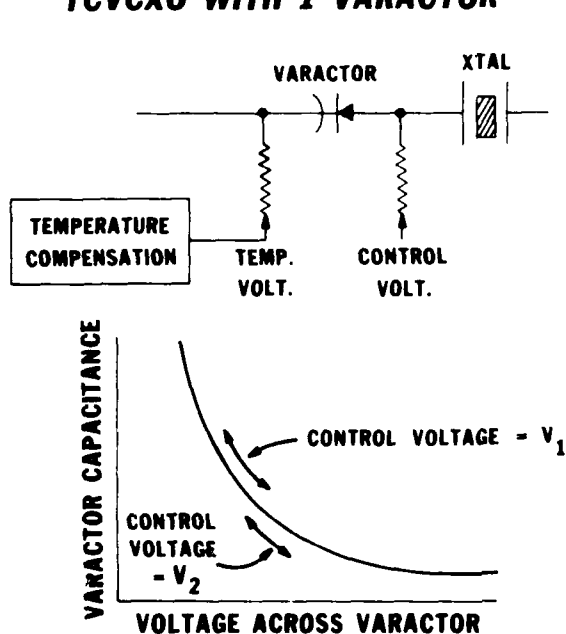


Fig. 5 TCVCXO with 1 varactor. The top part of the figure shows a common configuration for a TCVCXO with one varactor. The lower part of the figure shows schematically how the temperature compensation voltage and control voltage interact to limit precision (see text).

This scheme works well for moderate precision TCVCXOs, but there is a problem if high precision and/or a wide pulling range are needed. The cause of this problem is shown in the lower part of Figure 5. The vertical axis is varactor capacitance, and the horizontal axis is the net voltage across the varactor. What is indicated schematically by the arrows is that for one setting of the control voltage,  $V_1$ , variations in the temperature voltage moves the varactor capacitance along one part of the curve. For another setting of the control voltage,  $V_2$ , it moves along a different part of the curve. It is possible to optimize the temperature compensation for one or the other, but not both, and in the end, it is necessary to make some sort of compromise.

Figure 6 shows one way of improving the performance of TCVCXOs. That is, to use two varactors so that instead of adding voltages (which translates into frequency change in a non-linear way), the circuit is adding reactances which translate more linearly.

### TCVCXO WITH 2 VARACTORS

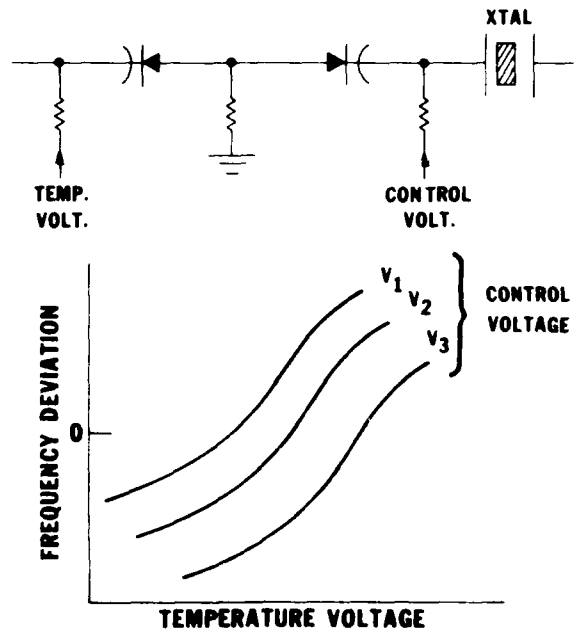


Fig. 6 TCVCXO with 2 varactors. An improved configuration for TCVCXOs uses 2 varactors so that reactance rather than voltage is being added. The lower part of the figure shows how the frequency criterion can be satisfied for an infinite combination of control voltages and temperature compensation voltages (see text).

The problem with this scheme is that it produces an added degree of freedom. Namely the capacitance of one of the varactors can be made smaller as long as the capacitance of the other varactor is made larger in a compensating way. Thus, there is an infinite number of equivalent solutions to setting the frequency on target. The lower part of the figure shows schematically how the frequency varies as a function of the temperature voltage for a series of 3 control voltage settings. We can see that for putting the oscillator on frequency all three of the points that correspond to  $f=0$  are on frequency.

What is needed is an additional criteria to select among the possible choices. In fact, there are two other properties that we would like to optimize: These are that the frequency-temperature voltage pulling curve should be such that it will give us the best possible curve for temperature compensation and that the changes in frequency with control voltage should be as linear as possible over the pulling range.

Our experience with laboratory models indicated that searching out the frequency voltage space manually and trying various combinations of temperature voltage and control voltage could take several hours of an engineer's time per oscillator.

To improve the throughput, the process was computerized using a Hewlett Packard 9825 desktop computer. The computer first measures the frequency voltage characteristics for both the temperature and control voltages. It then uses an algorithm to search for the optimum operating point for both voltages, and finally it computes the resistor values for the control voltage network to place it where desired. After these resistors are installed, the initial (uncompensated) heat run of the oscillator is made.

Using the computer for selecting the operating point has 3 main advantages:

1. It's faster: a few minutes vs. a few hours by hand.
2. It can be done by a relatively unskilled operator under manufacturing conditions.
3. It produces a more uniform product.

#### VI. Other Applications

VI.A. In design, we have been using a linear computer model to study the

temperature effects and how individual components affect the oscillators stability. In our work so far, we have found that inductors and varactors can have an effect, but capacitors and transistors so far appear to be ok.

VI.B. A second design category is the traditional one of determining component sensitivity. For this we have been using both linear and non-linear models. for the components studies so far, both methods are in agreement and agree fairly well with experimental measurements.

VI.C. Another application is simulation of digital compensation where our main interest has been developing algorithms for TCVCXOs which will compensate for the interaction between the temperature voltage and the control voltage.

VI.D. We have developed a program for simulating the temperature performance of doubly rotated cuts so that we can optimize the angles for a given temperature range and so that we can study the effect of angle tolerances on temperature stability.

VI.E. Finally, we use our computers for statistical analysis of data. As with the final checkout data, most of our data is stored on tape or disk for later analysis of overall performance to provide a data base for future designs and to provide estimates of manufacturing yields.

#### VII. Conclusion

We have been using computers increasingly in oscillator design and assembly and find that computers help greatly in meeting today's tighter performance requirements and needs for increased productivity.

#### Acknowledgements

The material presented in this paper includes work by E. K. Plomster, N. L. Fernandez, A. A. Manalio, I. P. Mantz, J. J. Royer, R. E. Paradysz, and F. J. Wagner.

#### References

- [1] P. R. Bryant, S. Fingerote, I. N. Hajj, S. Skelboe, and M. Vlach, WATAND Primer, Tech. Report No. UW EE 80-6 Part I, University of Waterloo, Waterloo, Ontario, November 1980.

- [2] P. R. Bryant, S. Fingerote, I. N. Hajj, S. Skelboe, and M. Vlach, Figures for WATAND PRIMER, Tech. Report No. UW EE 80-6 Part II, University of Waterloo, Waterloo, Ontario, November 1980.
- [3] M. Vlach, WATAND User's Manual Version 1.07, Tech. Report No. UW EE 80-3, March 1980.

## IMPROVED RING-SUPPORTED RESONATORS

Mitsuo Nakazawa and Hideaki Ito

Shinshu University, Nagano 380, Japan

Theodore Lukaszek and Arthur Ballato  
Electronics Technology and Devices Laboratory  
Fort Monmouth, New Jersey 07703Abstract

We have investigated some improved ring-supported (r-s) resonators. These resonators show promise of providing high precision frequencies for a wide temperature range and static and dynamic forces encountered in the field.

In this paper, we report the experimental results of the temperature and force effects for the improved ring-supported resonators.

These resonators are ring-supported and made from bi-convex quartz and from concavo-convex quartz in a suitable contour form. The frequency-temperature characteristics of these resonators are measured over a wide temperature range,  $-196^{\circ}\text{C}$  to  $+160^{\circ}\text{C}$ . Fortunately, it is seen that the results of the improved r-s concavo-convex quartz show excellent frequency stability.

We also discuss how the quality factors depend on the contour forms of the improved r-s resonators.

Through these optimum designs of the improved r-s resonators, we can further predict the form of stable and precise resonators.

**Key Words:** Precision frequency, frequency-temperature characteristic, force-frequency effect, improved r-s bi-convex quartz, improved r-s concavo-convex quartz.

Introduction

It has long been known that the resonance frequency of a crystal vibrator shifts when it is subjected to an externally applied force. The effects seem to be responsible for deformation of the crystal and thermal shock due to the static and dynamic forces encountered in field use. Insensitivity to these static and dynamic forces is one of the main problems encountered when attempting to make practical resonators. In order to solve it we have investigated some crystal resonator configurations that are referred to as grooved and r-s resonators. These resonators are provided with the high precision frequencies needed for the static and dynamic forces in severe environments. To obtain the best quality factors in these resonators it is clearly desirable to improve them. In order to improve the quality factors, certain configurations of the resonators are proposed. The

configurations are the r-s bi-convex quartz or the r-s concavo-convex quartz in a suitable contour form, as shown in Fig.1. In these experiments, frequency-temperature effects of these resonators are measured over a wide temperature range,  $-196^{\circ}\text{C}$  to  $+160^{\circ}\text{C}$ . Further, the force-frequency effects are described. The experimental results indicate that excellent frequency-temperature and force-frequency effects should be able to be obtained in the near future.

Geometrical Forms Of The Resonators

In order to improve the quality factors of the conventional r-s resonators, new configurations of the resonators are proposed. Fig.1 shows a conventional r-s bi-convex resonator Bi-1 and a conventional r-s concavo-convex resonator CC-1. The latter in particular is very useful for applications having acceleration directed toward the center of the curve. Fig.2 shows the improved r-s concavo-convex resonator. In Fig.2 the two cut sides are ground parallel to the  $z'$ -axis. The wings of the improved r-s resonators make both the frequency-temperature and the force-frequency characteristics more stable. These geometrical forms will provide the best physical properties in r-s resonators.

Force-Frequency Effects

Fig.3 shows the experimental results of the force-frequency effects in a r-s bi-convex resonator (AT-cut Bi-1). The horizontal axis shows the force azimuth angle  $\alpha$ , and it is measured from the X axis. The vertical axis represents the stress sensitivity of the resonance frequency. The dimensions of the resonator are shown in Fig.1. The force applied is 224 grams. The resonance frequency is the 3rd harmonic mode and is 7.419411 MHz at  $25^{\circ}\text{C}$ . From Fig.3, it is seen that the maximum frequency shift is about one third that of the reference AT-cut plate and that the points of zero pressure effect are about  $\alpha=58^{\circ}$  and  $\alpha=122^{\circ}$ .

Similarly, Fig.4 shows the experimental results of the force-frequency effects in the r-s concavo-convex resonator (AT-cut CC-1). The dimensions of this resonator are shown on Fig.2. The force applied is 360 grams. The resonance frequency is the 3rd harmonic mode and is 12.315671 MHz at  $25^{\circ}\text{C}$ . In Fig.4 the solid line shows the measured values and the dashed line shows the estimated curve. The zero pressure effect appears at about

0.60° and 0.140°.

From Figs. 5 and 6 it is expected that the positive point of the maximum frequency shift coincides with the X axis and the negative point of the maximum frequency shift is on the Z' axis. These results are similar to those for the conventional reference AT-cut resonators. As we know, the zero effects for diametric pressures depend on the cut angles of crystals. In these resonators, however, it is found that the zero effects for diametric pressures are almost independent of the form of the main surfaces.

#### Frequency Spectra

Fig. 6 shows the CC-1 crystal resonator and its frequency spectra at 25°C. The frequency mode is thickness vibration c mode. The tails of the electrode films are set at about 25° from Z' axis. These represent positions near the zero effect of pressure.

Fig. 7 shows the improved CC-1' crystal resonator and its frequency spectra at 25°C. The sides of the frame toward the X axis are ground parallel to the Z' axis as shown in the figure. It is seen that the intensity of response for the fundamental mode is considerably stronger than the CC-1 crystal, but the response in the case of the 3rd harmonic mode is the same.

Similarly, Fig. 7 shows the improved CC-1' crystal and its frequency spectra at 25°C. Both sides of the frame toward X axis are ground parallel to the Z' axis as shown in the figure. The Q-value for the fundamental mode is very low, but the one for the 3rd harmonic is somewhat higher. The 3rd harmonic mode is a clean response. From these facts it is found that the cutting toward the X axis shown in Fig. 7 is effective in increasing the Q-value of the CC-1 crystal.

#### Frequency-Temperature Characteristics

To measure the frequency-temperature characteristics, an oven filled with liquid N<sub>2</sub> is used. The temperature of the oven is exactly controlled with a voltage type regulator on the heater over a wide range -126°C to +100°C.

Fig. 8 shows the frequency-temperature characteristics of the r-s Bi-1 crystal. The horizontal axis represents the temperature scale, and the vertical axis represents the normalized change in frequency. The radii of curvature were measured and both were found to be 60 mm. The thickness of the frame and that of the center have been referred to as  $t_1 = 0.70$  and  $0.71$ , the 3rd harmonic resonant frequencies were measured and found to be  $f_3 = 7.418100$  MHz and  $f_3 = 7.417809$  MHz at 25°C, respectively. In Fig. 8, the frequency-temperature variation shows an ideal cubic curve and in particular it represents promising signs in the vicinity of room temperature.

Similarly, Figs. 9 and 10 show the frequency-temperature characteristics for the r-s Bi-2 and

Bi-7 crystals operating on the thickness c mode, respectively. In Fig. 9 the resonance frequencies were found to be  $f_3 = 5.48571$  MHz at  $t_1/t_2 = 0.50$  and  $f_3 = 5.449629$  MHz at  $t_1/t_2 = 0.51$ , respectively. In Fig. 10, the response is the 3rd harmonic mode and the frequency was found to be  $f_3 = 5.86735$  MHz at  $t_1/t_2 = 0.70$ . The results of these Bi crystals show that it is reasonable to design the optimum ratio  $t_1/t_2$  of the r-s Bi-convey crystal to be near 0.70.

Figs. 11 and 12 show the frequency-temperature characteristics of the improved CC-1 crystal and the CC-2 crystal, respectively. In Fig. 11 the crystal is operating on the 3rd harmonic c mode. The resonance frequency is  $f_3 = 1.21571$  MHz at 25°C. The results of our experiments show that both in the CC-1 and the CC-2 crystals are about 10 ppm over a wide temperature range -25°C to +120°C. On the other hand, in the improved CC-1 crystal we see that it is about 10 ppm over a wide temperature range -30°C to +90°C. Upon applying the grinding techniques to the frame as shown in Fig. 7, it is seen that the frequency-temperature characteristics of the r-s CC-1 crystal are considerably improved and that the turning point of the cubic curves shift as the frame is ground. These effects slowly diverge throughout the resonator volume and the resonators are gradually improved for temperature changes.

#### Conclusion

It is concluded that the improved resonators described herein are highly insensitive to the frequency perturbations produced in crystal resonators vibrating in thickness modes, by thermal changes and static and dynamic forces acting on the bodies of the resonators.

#### Acknowledgements

The authors wish to thank Professor P.C.Y. Lee, Princeton University, Miyota Precision Co., Fujikoshi Machinery Co., Saneyoshi Fund, Mr. H. Imai, and Mr. N. Asai, for their help and encouragement.

#### References

1. A. Ballato; Crystal Resonators with Increased Immunity to Acceleration Fields, IEEE Trans. Sonics Ultrason., Vol. SU-27, pp. 195-201, 1980.
2. M. Nakazawa, T. Iukaszek, and A. Ballato; Force- and Acceleration-Frequency Effects in Grooved and Ring-Supported Resonators, Proc. 35th AFCS, pp. 71-91, 1981.
3. P.C.Y. Lee and C.S. Li; Nonlinear Effect of Transverse Acceleration on the Resonances of Doubly Rotated, Rectangular Crystal Plates, Proc. 35th AFCS, pp. 193-204, 1981.

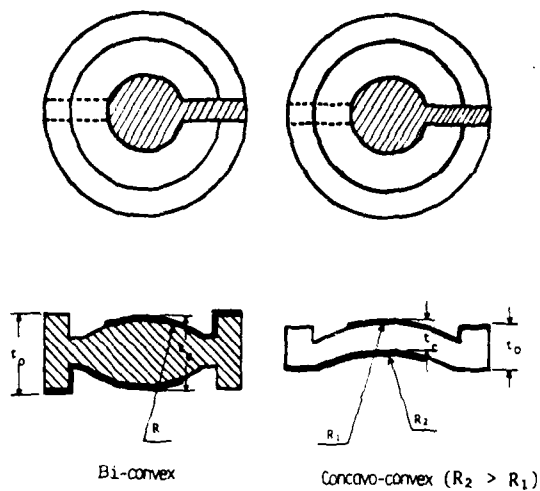


Fig. 1 Conventional Ring-Supported Resonators.

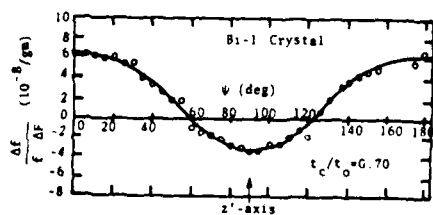


Fig. 3 Force-frequency effects for the r-s bi-convex crystal (AT-cut Bi-1) operating on the 3rd harmonic mode at 7.418406 MHz.

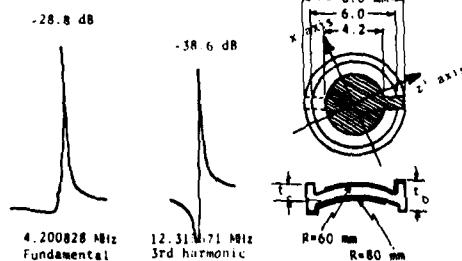


Fig. 5 Geometrical Configuration and Frequency Spectra for the CC-1 Crystal.

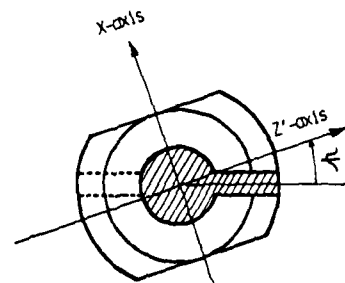


Fig. 2 Improved Ring-Supported

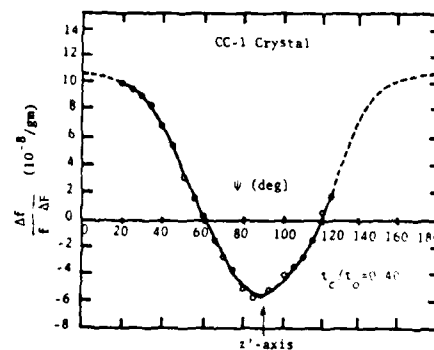


Fig. 4 Force-frequency effects for the concavo-convex crystal (AT-cut CC-1) operating on the 3rd harmonic mode at 12.315671 MHz.

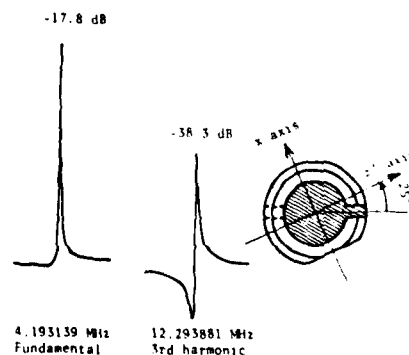


Fig. 6 Geometrical Configuration and Frequency Spectra for the Improved CC-1 Crystal

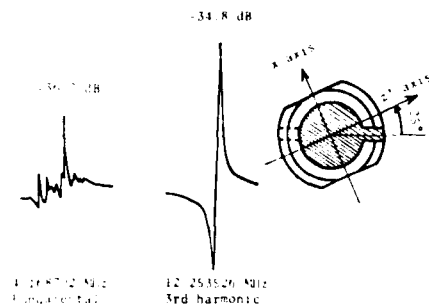


Fig. 7 Geometrical Configuration and Frequency Spectra for the Improved CC-1 Crystal.

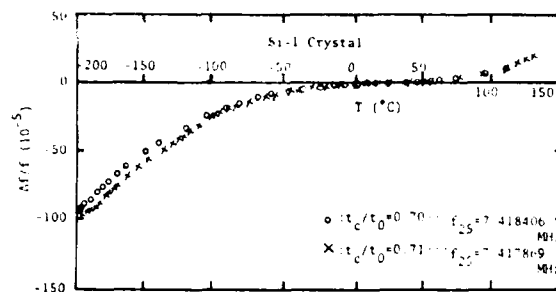


Fig. 8 Frequency-Temperature Characteristics for the Bi-1 Crystal Operating on the Harmonic Mode vs.  $t_c/t_0$  Ratio.

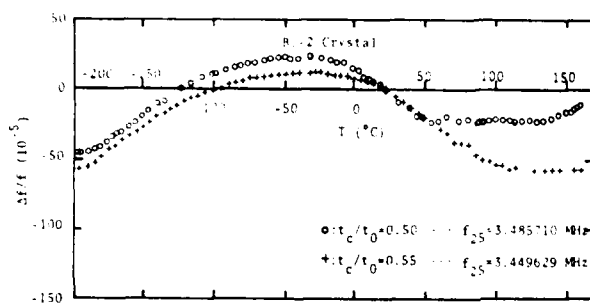


Fig. 9 Frequency-Temperature Characteristics for the Bi-2 Crystal Operating on the Fundamental Mode vs.  $t_c/t_0$  Ratio.

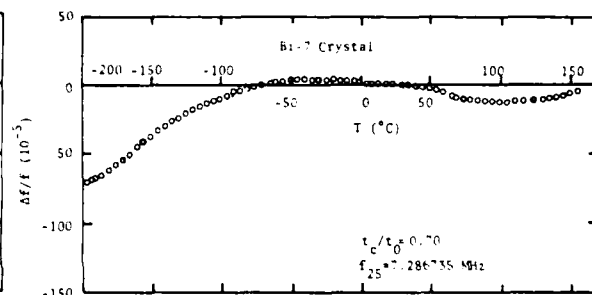


Fig. 10 Frequency-Temperature Characteristics for the Bi-7 Crystal Operating on the 3rd Harmonic Mode.

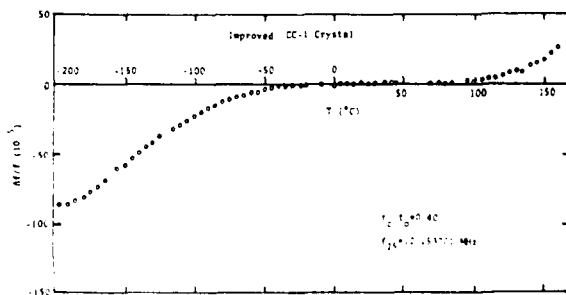


Fig. 11 Frequency-Temperature Characteristics for the Improved CC-1 Crystal Operating on the 3rd Harmonic Mode.

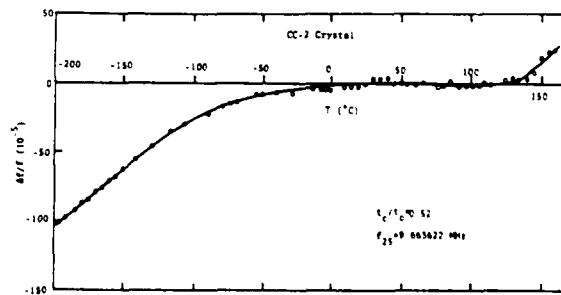


Fig. 12 Frequency-Temperature Characteristics for the CC-2 Crystal Operating on the 3rd Harmonic Mode.

ALUMINUM NITRIDE THIN FILM AND COMPOSITE  
BULK WAVE RESONATORS

K. M. Lakin, J. S. Wang and A. R. Landin  
Microelectronics Research Center and Ames Laboratory-USDOE  
Iowa State University  
Ames, IA 50011

## ABSTRACT

The fundamental material and device properties of miniature bulk wave resonators have been investigated for fundamental mode oscillator control and filter applications in the UHF range. The properties of aluminum nitride in the composite resonator geometry and in an edge-only supported plate configuration are reported.

The AlN films were grown in a DC planar magnetron sputtering system using the plasma reaction between sputtered Al from the target and  $N_2$  in the plasma. The general sputtering conditions were as follows: substrate temperature = 200°C, atmospheric gas = 99.99% Nitrogen, sputtering pressure:  $1 \times 10^{-3}$  torr, DC power = 225 watts and deposition rate = 1.2  $\mu\text{m/hr}$ . The films were evaluated by SEM, x-ray diffraction, and Auger electron spectroscopy. These results showed that the sputtered AlN films have a highly oriented structure with the c-axis normal to the surface of the Si substrate.

For a resonator composed of 1.7 micron of AlN and 8 microns of Si, the resonant responses were measured at fundamental frequencies of 328.53 MHz for series resonance and 328.61 MHz for parallel resonance. The electrical Q for this resonator was about 7500. Its measured temperature coefficient was about -4ppm/°C from -20°C to 120°C. For resonator having 1.7 micron of AlN and 6 microns of Si, the temperature coefficient was -6 ppm/°C. This resonator, with electrical Q about 5000, had a fundamental series resonance at 524.11 MHz and parallel resonance at 524.45 MHz.

Edge-only supported AlN plates have been fabricated using microelectronic semiconductor processing techniques. Plates of thickness from 1.0 to 7  $\mu\text{m}$  thickness, having areas up to 300  $\mu\text{m}^2$  square, are supported only at their edge in contrast to the membrane supported films reported previously.

A typical AlN plate of 6.5  $\mu\text{m}$  thickness had fundamental mode resonances near 790 MHz with a coupling coefficient of 10.3%. The temperature coefficient, measured over the range -20°C to 200°C, was found to be -20.5 ppm/°C.

Recently, c-axis in-plane ZnO plates have been fabricated with epitaxial character. These plates exhibit a shear wave resonance which implies higher Q resonance and a simpler mode structure.

## I. INTRODUCTION

This paper describes recent results on temperature compensated composite bulk wave resonators<sup>1,2</sup> and edge-only supported thin film resonators using aluminum nitride as the piezoelectric material. The composite resonator structures are similar to those reported previously using ZnO films on Si membranes<sup>1,3-6</sup>. Highly overmoded resonators using piezoelectric films have also been reported<sup>7,8</sup> with some performing at microwave frequencies.<sup>9</sup>

Those devices that employ semiconductor substrates allow established selective etching processing to be used in forming precision membranes and associated mechanical structures. Silicon is a particularly attractive substrate for its mechanical structural properties<sup>10</sup> as well as offering the eventual integration of passive resonators with active integrated circuits. We are also actively investigating GaAs as a substrate and have obtained edge-only supported AlN plates similar to those on silicon.

In the work reported here, aluminum nitride films are used for the piezoelectric region rather than zinc oxide due to its mechanical strength and wider range of chemical compatibility. The AlN/Si composite structure also exhibits a favorable temperature coefficient compared to traditional AT-cut quartz. This geometry is described in more depth in Section III.

The conventional resonator configuration consists of a thin piezoelectric plate that has been cut from a crystal and mechanically reduced to the desired thickness. Recently, thinner plates and higher resonant frequencies have been obtained by etching or ion machining techniques.<sup>11-13</sup> The approach reported in Section IV results in a thin (1-10 micron) piezoelectric plate which is supported only at its edges. The plate is formed by direct growth and electrochemical processing rather than by mechanical means. In this study AlN and ZnO c-axis perpendicular and ZnO c-axis in-plane piezoelectric plates have been formed.

## II. AlN FILM GROWTH AND CHARACTERIZATION

The AlN films were grown in a DC planar magnetron sputtering system using the plasma reaction between sputtered Al from the target and  $N_2$  in the plasma. This growth system, Fig. 1, was chosen for its simplicity of operation and flexibility in allowing the deposition of an Al film before or

after AlN growth as a step in device fabrication. In order to prevent electron bombardment of the dielectric film and subsequent arcing, an anode structure is used to collect the electron current. The general sputtering conditions were as follows:

Target	: 99.999 pure aluminum, 5" diameter
Substrate	: (100) Si, GaAs
Target-Substrate Spacing	: 3-5 cm
Atmosphere Gas	: low oxygen (0.5 ppm); nitrogen
Deposition Pressure	: $10^{-3}$ Torr
Substrate Temperature	: 200 C
Cathode Voltage	: -300 volts DC
Cathode Current	: 600 milliamperes
Anode Voltage	: +20 volts DC
Deposition Rate	: 1.2 microns/hr

Cathode and anode voltages are measured relative to the substrate with the anode voltage adjusted to reduce the substrate current to a small value.

In general, the sputtering rate was found to be proportional to the DC power with a value of 1.2 microns/hr at 140 watts.

Evaluation of the films involved optical and scanning electron microscopy,  $\theta$  and  $2\theta$  x-ray diffraction analysis, Auger microprobe impurity depth profiling and acoustical parameter characterization. A SEM examination of a cross section of an AlN/Si film revealed the columnar structure of a C-axis normal film indicating a high degree of film orientation and coherence. SEM viewing of the film top surface did not reveal the microcrystalline faceting found in some earlier work on CVD growth of AlN on sapphire.<sup>14</sup> Optical microscopy was used to examine the films for microcracking and other surface defects. Microcracking was absent in films of low oxygen content grown in the sputtering system having the anode separate from the substrate. The oxygen content was found to be less than 0.5% as determined by Auger microprobe analysis.

In this study, mainly x-ray diffraction was used for the quantitative characterization of the crystal structure of the film. Figure 2 shows an x-ray diffraction pattern of a 0.8 micron thick AlN film sputtered on (100) Si. The film is clear and only the (0001) orientation is revealed. An x-ray rocking curve was also taken for a further quantitative analysis of the orientation of the film.

It is apparent from the x-ray results that the sputtered AlN films have a highly oriented structure with the C-axis normal to the surface of the substrate. The quality of these films was also found not critically dependent on sputtering

deposition pressure for the range 0.4 to 4 millitorr or substrate heater temperature from 200 to 500 C. More highly oriented films ( $c = 0.55$ ) have been obtained on basal plane sapphire.

Electrical characterization of the material is done in the resonator configurations described in following sections and detailed in previous publications. Essentially, the resonator reflection coefficient was measured as a function of frequency and recorded by a data acquisition system. From the complex reflection coefficient the equivalent two-terminal impedance of the resonator was obtained from the equation,

$$Z = 50 \frac{1+r}{1-r}$$

where  $r$  is the reflection coefficient. From the computed phase of  $Z$ ,  $Z_0$ , the resonator  $Q$  was obtained near the resonant frequencies using

$$Q = \frac{f_r}{2} \frac{dZ_0}{df} \bigg|_{f_r}$$

where  $f_r$  is the resonant frequency (this definition of  $Q$  follows directly from parallel or series RLC circuits). Because impedance is a property of the resonator alone and not determined by the external circuit,  $Q$  determined in this manner is the unloaded or device  $Q$ .

Using reflection measurements allows the resonator to be placed at the end of a coaxial cable in an environmental chamber for temperature coefficient determinations.

### 111. TEMPERATURE COMPENSATED COMPOSITE RESONATORS

The temperature compensated composite resonator<sup>2</sup>, (TCCR), is shown schematically in Fig. 3. The TCCR is composed of a born diffused  $P^+$  layer formed into a membrane by selective etching to remove the n-type material from the desired region. The AlN piezoelectric film is sputtered directly onto the  $P^+$  region without any deliberate intermediate film structures.

For a resonator composed of 1.7 microns of AlN and 8 microns Si the following values were obtained from the measured data: 7600 for parallel  $Q$ , 7300 for series  $Q$ , 333 ohms parallel resistance, 35 ohms series resistance. This device was found to have 6.5 ohms series conduction resistance and 2 pf shunt capacitance. After subtracting these parasitic parameters from the resonator, the phase and absolute value of the impedance around fundamental resonant frequencies were computed and plotted as shown in Fig. 4. The resonant responses were detected at fundamental frequencies of 328.53 MHz for series resonance and 328.61 MHz for parallel resonance. The resonator coupling coefficient was found to be 2.5%. The third overtone impedance response is shown in Fig. 5. Here the  $Q$  was determined to be 1500 and the coupling coefficient 6%. Note that the overtone coupling is higher than the fundamental in accordance with the composite resonator theory described

previously.<sup>3,4</sup> The high frequency side of resonance shows some response due to spurious modes.

The temperature coefficient of the AlN/Si composite has been found to be nearly compensated. In Fig. 6 the fundamental mode temperature coefficient, TC, was measured from -20 to 120°C and compared with AT-cut quartz and ZnO/Si composite resonators. The ZnO/Si resonator was composed of 1 micron of ZnO on a 6 micron P<sup>+</sup> silicon membrane and exhibited a Q of approximately 9000 at 500 MHz. The second overtones TC of the AlN/Si resonator was -8.9 ppm/°C at 820 MHz and the third overtone TC was -27 ppm/°C near 1200 MHz.

In order to study the temperature compensation mechanism the TC was measured near room temperature for different Si to AlN thickness ratios and plotted in Fig. 7. For AlN only (zero thickness ratio) a TC of -20 ppm/°C is obtained and for very large thickness ratios we would expect the -30 ppm/°C calculated for Si. Our results show a TC as low as -0.6 ppm/°C for a thickness ratio of 4.5. The TC behavior exhibited for these devices would not be expected from linear elastic theory. Since there is evidence of finite strain in the structure we are making attempts to elucidate the effect and determine if finite strain is the controlling factor in the temperature compensation mechanism. We have found the TCCR devices to be reproducible and of obvious technological importance.

#### IV. THIN FILM EDGE-SUPPORTED RESONATORS

In the composite resonator structures described above thin films and microelectronic device processing play important roles. The desire for higher frequencies, thinner structures, and simpler modes has led to the more conventional piezoelectric plate implemented in thin film form. In Fig. 8 is shown the edge supported piezoelectric plate structure that has been implemented using AlN and ZnO C-axis normal and ZnO c-axis in-plane films. Both Si and GaAs have been used for the substrate along with chemical etching to remove the substrate from under the piezoelectric plate. Plate thicknesses have been fabricated with 1 to 10 microns thickness for AlN and ZnO. The thin AlN plates have been found to be mechanically rugged and able to withstand photolithographic processing operations without breaking.

The impedance plot for a 6.5 micron thick AlN plate resonator is shown in Fig. 9. The resonator Q of 1200 was somewhat lower than expected due to a parasitic transducer effect caused by the overlap of the bonding pad onto the substrate region. The transducer formed by the piezoelectric film on the P<sup>+</sup> counter electrode radiates into the substrate bulk. The transducer looks like an additional loss mechanism which lowers the overall device Q. For actual device applications the parasitic transducer can be eliminated. The resonator coupling coefficient was found to be 10.5% or approximately twice that for composite structures.

Temperature coefficient of the AlN plate was measured from -20 to +120°C and found to be approximately -20.5 ppm/°C, Fig. 10. From thermal

expansion data the AlN film should be under tension and again finite strain effects cannot be ruled out in determining the TC behavior. Optical normarski examination of the surface suggests that the plate is planar with no bowing evident. Some bowing has been found in ZnO plates suggesting that these plates are put in compression by the substrate.

#### V. SUMMARY

Temperature compensated composite resonators, TCCR, have been obtained in the configuration of AlN film on P<sup>+</sup> silicon single crystal membrane. A resonator having a Si-to-AlN thickness ratio of 4.5 has shown a TC of less than 1 ppm/°C at room temperature.

Edge-only supported AlN plates have been fabricated for plate thicknesses from 1 to 10 microns corresponding to resonant frequencies from 5 GHz to 500 MHz, respectively. Resonator Q's over 1000 have been obtained for frequencies above 1 GHz. Similar resonators have been constructed using C-axis normal ZnO plates and more recently C-axis in-plane shear wave resonators have been obtained.

Problems associated with aging finite strain, and spurious modes are still under investigation.

#### VI. ACKNOWLEDGEMENTS

The authors wish to acknowledge the technical contributions of G. Kline, M. Chen, and J. Hunt during the course of this work. This research was supported by the Air Force Office of Scientific Research.

#### REFERENCES

1. J. S. Wang and K. M. Lakin, IEEE 1981 Ultrasonics Sym. Proc. Vol. 1, 502 (1981).
2. J. S. Wang and K. M. Lakin, Appl. Phys. Lett. 40, 308 (1982).
3. K. M. Lakin and J. S. Wang, Appl. Phys. Lett. 38, 125 (1981).
4. K. M. Lakin and J. S. Wang, IEEE 1980 Ultrasonics Symp. Proc., 834 (1980).
5. T. W. Grudkowski, J. F. Black, T. M. Reeder, D. D. Cullen and R. A. Wagner, IEEE 1980 Ultrasonics Symp. Proc., 829 (1980).
6. K. Nakamura, H. Sasaki, and H. Shimizu, Japan. J. Appl. Phys. (to be published).
7. D. J. Page, Proc. IEEE, Oct. 1968.
8. T. R. Sliker and D. A. Roberts, J. Appl. Phys. 38, 2350 (1967).
9. R. A. Moore, J. T. Haynes and B. R. McAvoy, IEEE 1981 Ultrasonics Symp. Proc., 414 (1981).
10. K. E. Peterson, Proc. IEEE 70, 420 (1982).

11. G. K. Guttwein, A. D. Ballato, and T. J. Lukaszek, United States Patent 3 694 677, 26 Sept. 1972.
12. G. C. Coussot, Proc. IEEE 62, 590 (1974).
13. M. Berté, Electron. Lett. 13, 248 (1977).
14. K. M. Lakin, J. Liu, and K. L. Wang, Proc. IEEE 1974 Ultrasonic Symp. 302 (1974).

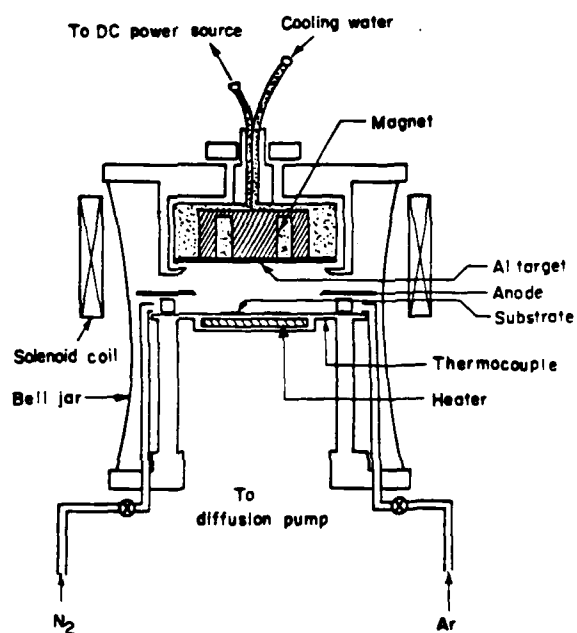


Figure 1. DC Planar Magnetron Reactive Sputtering System. Anode Ring is Biased Positive Relative to the Substrate in Order to Collect the Electron Current.

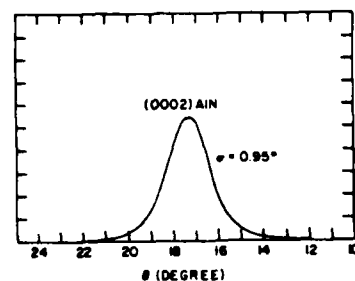
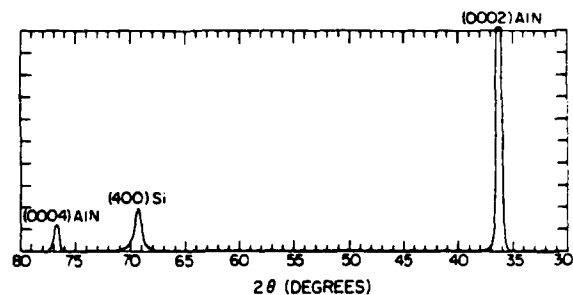


Figure 2. X-Ray Diffraction Scans for AlN/Si Piezoelectric Films. The Results Give a Quantitative Measure of C-Axis Orientation Perpendicular to the Substrate Surface.

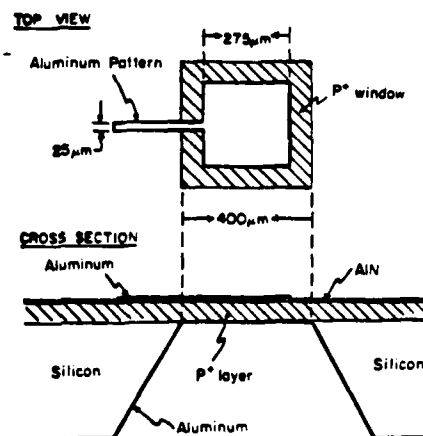


Figure 3. Configuration of the Temperature Compensated Composite Resonator, TCCR. The P<sup>+</sup> Layer is Formed by a Boron Diffusion. The AlN is Sputter Deposited Directly onto the Silicon Membrane.

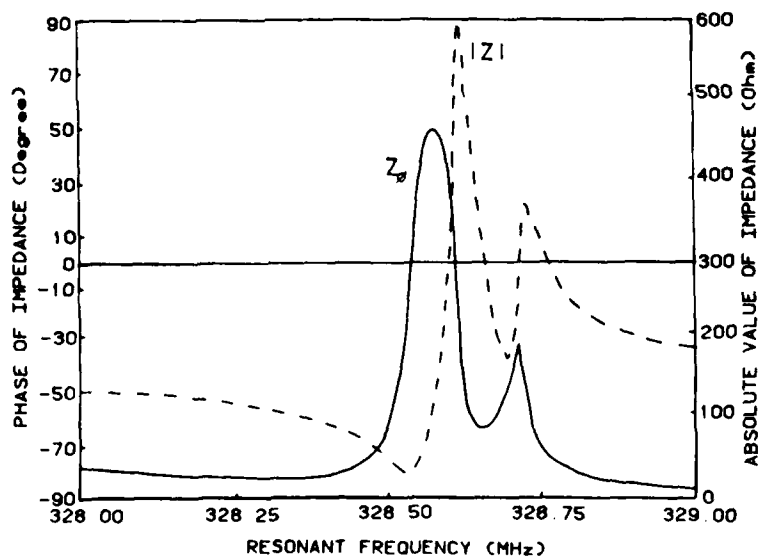


Figure 4. Impedance Plot of a TCCR Composed of 1.7 Microns of AlN on 8 Micron Silicon P<sup>+</sup> Membrane. From the Series Resonance Phase Slope the Q was Found to be 7500. Temperature Coefficient Measurements were Determined by Tracking the Series Resonance in Order to Avoid the Spurious Resonance on the High Frequency Side.

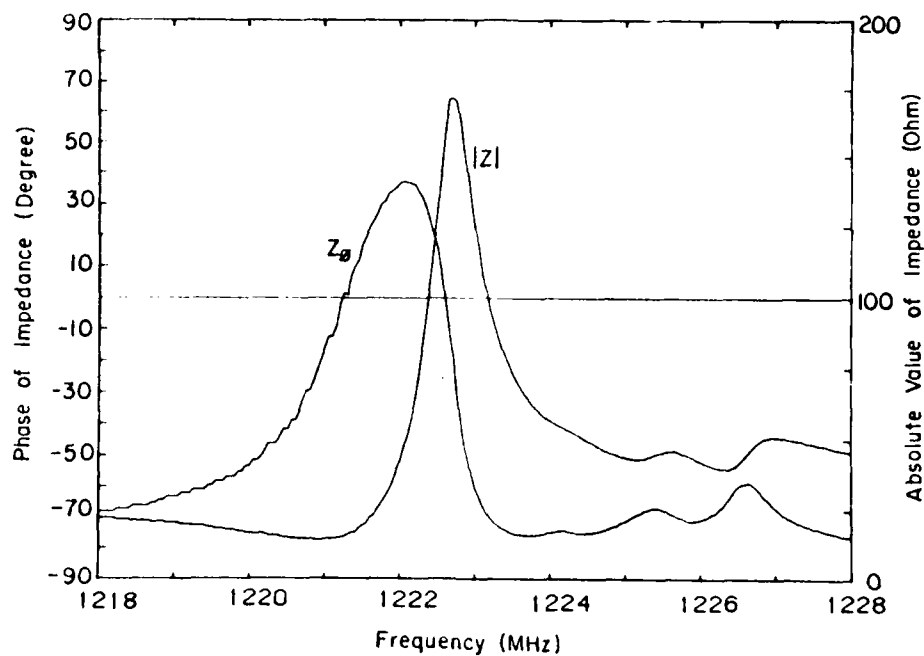


Figure 5. Impedance of the Third Overtone Response of the Resonator of Figure 4. The Q is Greater than 1500. The Coupling Coefficient is 6% and Higher, as Expected, Than the Fundamental Mode.

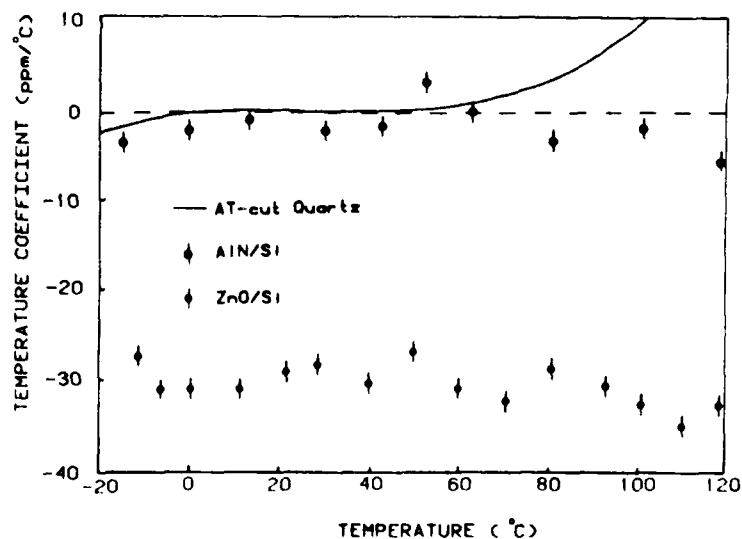


Figure 6. Temperature Coefficient for TCCR, At Quartz and ZnO/Si Composite Resonator. The AlN/Si Device was the Resonator of Figure 4. The ZnO/Si Resonator Consisted of 1 Micron of ZnO on 6 Microns of  $P^+$  Si having a Q of Approximately 9000 Near 500 MHz.

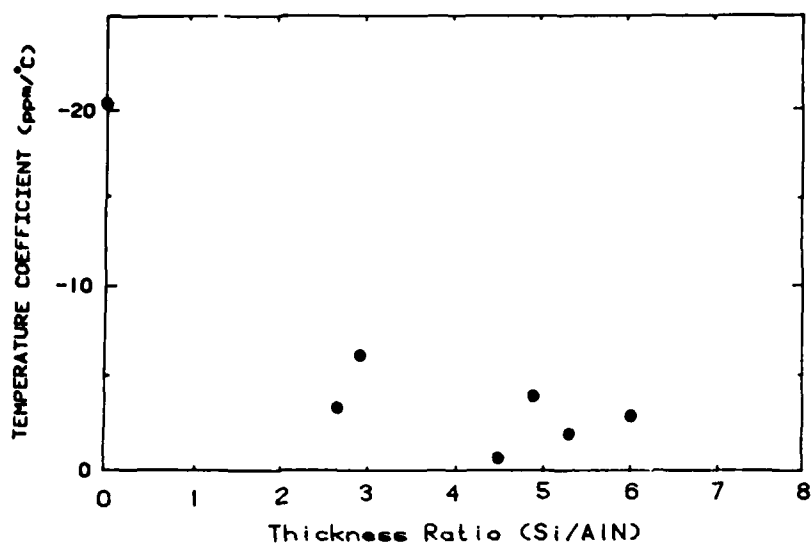


Figure 7. Temperature Coefficient Near Room Temperature Versus Si-to-AlN Thickness Ratio. At Zero Silicon Thickness the TC is -20 ppm and at Zero AlN Thickness the Calculated TC is -30 ppm. All Data Points Represent Different Devices.

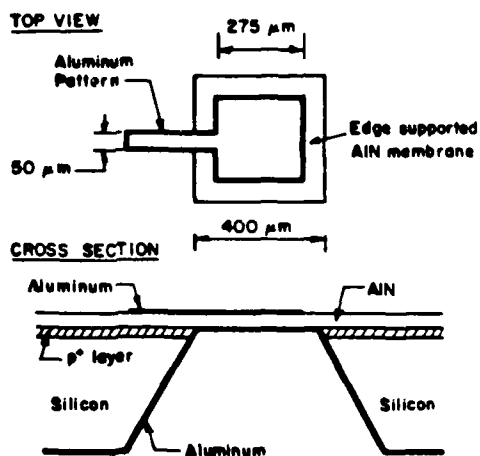


Figure 8. Edge-Only Supported Piezoelectric Plates. Plates of 1 to 10 Microns Thickness Have Been Fabricated on Si and GaAs Substrates. Plates of AlN and ZnO Having C-Axis Perpendicular and ZnO C-axis In-Plane Have Been Fabricated and Evaluated.

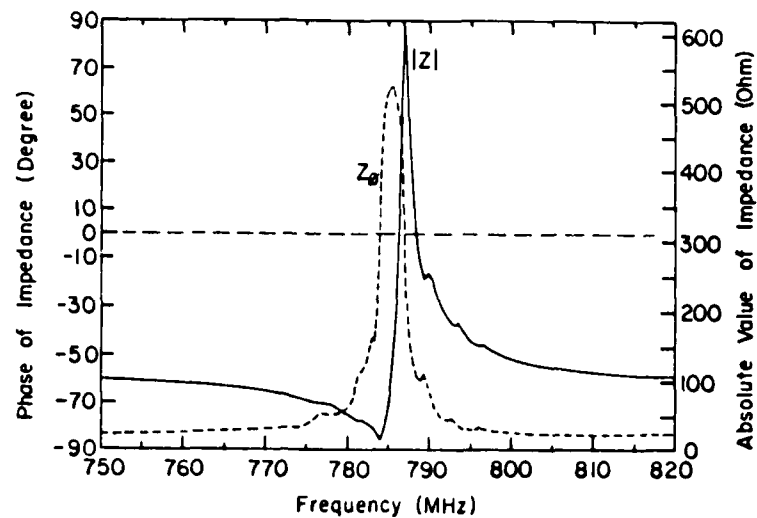


Figure 9. Impedance Plot for A1N Edge Supported Plate. The Plate Thickness was 6.5 Microns,  $Q > 1200$ , and Coupling Coefficient 10.5%. This Coupling Coefficient is Approximately Twice that of a Fundamental Mode Composite Resonator.

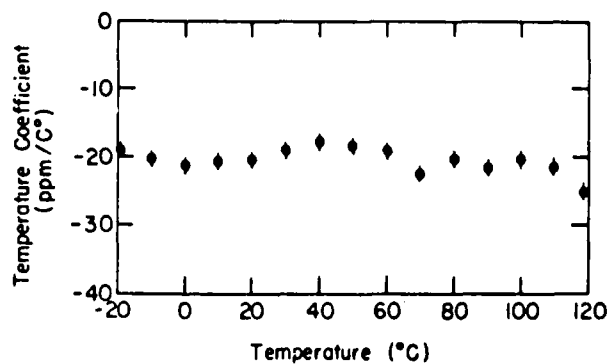


Figure 10. Temperature Coefficient of A1N Edge Supported Plate Resonator. The Plate was 6.5 Microns Thick.

## SAW AND SSBW PROPAGATION IN INDIUM PHOSPHIDE

Jeannine Hénaff and Michel Feldmann

Centre National d'Etudes des Télécommunications  
38-40 rue du Général Leclerc, 92131 Issy-les-Moulineaux, FranceAbstract

In view of combined use of piezoelectric and semiconducting properties of Indium Phosphide, new surface (SAW) and surface skimming bulk waves (SSBW) are described. The properties of semi-insulating InP crystals are investigated in terms of piezoelectric coupling demonstrating that the SSBW branches may be more useful than the SAW branches. Two Rayleigh modes and one Bleustein-Gulyaev branch have been experimentally investigated in the 200-300 MHz range and good agreement between theory and experiment is reported.

Introduction

Monolithic integration of surface acoustic wave (SAW) or surface skimming bulk wave (SSBW) devices and active electronic circuits, on the same substrate, allows the realization of high-frequency subsystems for signal processing and frequency control. These new developments take advantage of the inherent piezoelectric properties of III-V materials joined to their well-known semiconducting properties - high mobility and large bandgap as compared to silicon - and of recent improvements in the technology. By using n-type epitaxial semiconducting layers on semi-insulating substrates, one may combine the piezoelectric and semiconducting properties [1-3].

This paper presents the variations of both the surface and pseudo-surface wave velocities and electromechanical coupling coefficients for several crystallographic orientations in Indium Phosphide.

Principle of the calculation

The velocity and the electromechanical coupling coefficient for a given configuration (cut and direction of propagation) are obtained by the use of computer programs previously developed [4] by the authors following the same algorithm as Campbell and Jones [5] for lithium niobate.

Starting from the material data, one first has to compute the relevant tensors in the orientation of interest (cut, direction of propagation). The dynamic, electrostatic, and constitutive equations are solved in this orientation assuming a plane wave propagating in the x-direction on the z-plane. The solution consists of 8 z-dependent partial waves. From these partial waves, those with exponentially

increasing amplitude in the z-direction are combined to form the Rayleigh-wave. For the leaky waves it is necessary also to accept partial waves which have a group velocity component in the (-z) direction. The boundary conditions are the additional constraints which determine the propagation velocity in the x-direction. The mechanical boundary conditions are normally for a free surface, i.e. cancellations of the surface stress.

Since various electrical boundary conditions are of interest, we may follow Ingebrigtsen [6] to express these conditions as :

$$\frac{D_z}{E_x} = -\epsilon_s(v)$$

where  $v$  is the phase velocity component in the x direction,  
 $D_z$  is the dielectric displacement component  
 $E_x$  is the electric field component.

The equation defines a function of the velocity, called the surface permittivity of the actual configuration. If the medium, outside of the crystal ( $z > 0$ ) has a dielectric constant equal to  $\epsilon_e$ , the electrical boundary condition will be

$$\epsilon_s(v) = -\epsilon_e.$$

This relation defines the actual velocity  $v$  as the root of an equation. For example, if the external medium is a metallized electrode with an inverse dielectric constant  $1/\epsilon_e = 0$ , the relevant root  $v_0$  will define the velocity with a short circuit on the surface. On the other hand, if one defines a fictitious medium with  $1/\epsilon_e = \infty$ , the root  $v_\infty$  will define the phase velocity with open circuit condition. Intermediate boundary conditions are of course possible, including vacuum ( $\epsilon_e = \epsilon_0$ ) or air, which most often are very close to open circuit.

Using this surface permittivity, a piezoelectric substrate may be completely described by a simple analytic function.

The singularities of this function are poles and branching points (due to feasibility conditions in the half-crystal). The theory has been first given by Ingebrigtsen [6,7] in terms of surface impedance, and applied later by Greebe et al [8] to a particular branch, the Bleustein-Gulyaev mode. Generally, in the vicinity of a particular branch,

the surface permittivity may be expanded for real velocity as<sup>1</sup>:

$$\frac{1}{\epsilon_s(v)} = \frac{1}{\epsilon_s(v_0)} \left[ 1 - \left( \frac{k^2}{(1 - v/v_0)(1 + v/v_0^*)} \right) \frac{1}{v} \right]$$

where  $\epsilon_s(v_0)$  ( $v_0$  in the rotated frame) is the high frequency dielectric constant,  $k^2$  is the electromechanical coupling coefficient, and  $v_0$  is the free (open circuit) surface velocity. This velocity may be complex for leaky surface waves and then  $v_0^*$  is the complex conjugate of  $v_0$ . The parameter  $v/v_0$  is unity for the Rayleigh-like modes. Other values of  $v/v_0$  are possible: for example the value  $v/v_0 = 1$  applies to Bleustein-Gulyaev branches [9]. The electromechanical coupling  $k^2$  is related to the residue of the function  $\epsilon_s(v)$  in the neighbourhood of  $v_0$ . For true surface waves, we have:

$$k^2 = (v_0^2 - v_0^2) / v_0^2 = 2 \Delta v / v_0$$

(where  $\Delta v = v_0 - v_0^*$ )

Since the branching points are generally out of the domain of interest, most of the branches have Rayleigh-like behaviour. This is of interest from a numerical point of view in order to select fast algorithms, consistent with the analytical form of the equation. On the contrary, when a branching point falls in the vicinity of  $v_0$  and  $v_0^*$ , the behaviour is more complicated and the branch is called a surface skimming bulk wave (SSBW) with the particular case of the Bleustein-Gulyaev (BG) mode.

#### Theoretical results

The variations of the SAW and first pseudo SAW velocities and  $k^2$  for the two standard crystallographic cuts  $\langle 101 \rangle$  and  $\langle 111 \rangle$  of InP are presented versus the direction of propagation in Figures 1 and 3. The constants of InP used in the computer program are listed in Table 1: the constant  $\epsilon_{14}$  has been evaluated in Ref. 3 for best fit between experimental and theoretical results.

Table 1: Constants of InP used in the computer program.

InP	$\mu$	$4.787 \times 10^3$
$\epsilon_{11}$	$1.1$	$1.022 \times 12$
$\epsilon_{12}$	$1.2$	$1.576 \times 11$
$\epsilon_{13}$	$4.4$	$1.460 \times 11$
$\epsilon_{14}$	$1.4$	$1.100 \times 00$
EPG	$1.1$	$1.255 \times 02$

In the plane  $\langle 001 \rangle$  (cf. Figure 1) we see that a Rayleigh configuration (direction of propagation  $\parallel$ ), similar to the well-known corresponding branch

\*The surface permittivity locally depends on  $v^2$ . However, due to branching points, this is consistent with a global  $v$ -dependence [similarly as  $v = (v_0^2 - v^2)^{1/2}$ ].

in GaAs, is found on the first pseudosurface shell with a coupling of 0.04%. With directions of propagation close to  $\langle 110 \rangle$  the mode is leaky, but the actual attenuation is very low (about 0.01 - 0.02 dB/ $\lambda$ ). The Rayleigh mode has a maximum electromechanical coupling coefficient equal to 0.035% at an angle of  $15^\circ$  from  $\langle 110 \rangle$ .

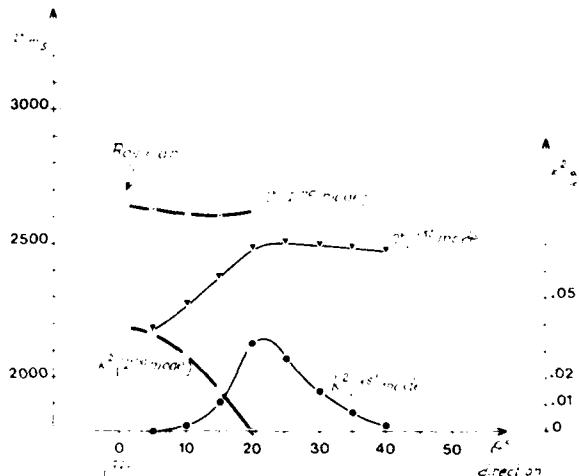


Figure 1: Variation of  $k^2$  and  $v$  for the first and second modes of InP as a function of the direction of propagation, for  $\langle 001 \rangle$  cut.

We have plotted in Figure 2 the surface permittivity versus velocity for a direction of propagation  $15^\circ$  apart from  $\langle 110 \rangle$ , always in the  $\langle 001 \rangle$  plane where the 2 first modes have about the same coupling coefficient. The first mode is a true generalized Rayleigh mode with a velocity of 2372 m/s and a coupling coefficient  $k^2$  equal to 0.0116%. The second one is a pseudo-Rayleigh mode with a velocity of 2602.5 m/s, a coupling factor of 0.0143% and a very low attenuation of 0.01 dB per wavelength. The pseudoresonance is soft due to the attenuation but the behaviour of the imaginary part of the permittivity is unambiguous.

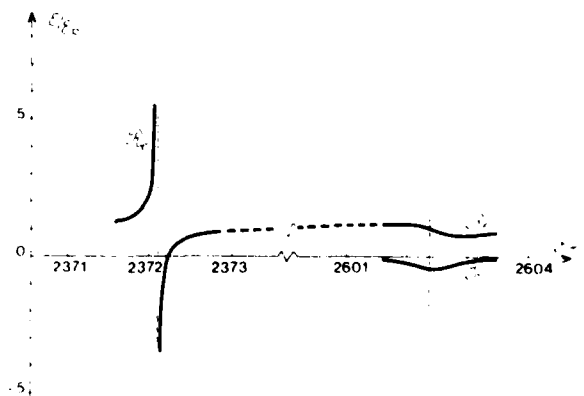


Figure 2: Surface permittivity versus velocity  $\langle 001 \rangle$  cut, direction of propagation  $15^\circ$  apart from  $\langle 110 \rangle$

In the plane  $\langle 111 \rangle$  (cf. Figure 3), whatever the propagation direction, the coupling coefficient is always very weak ( $k^2 \leq 0.01\%$ ) for the true surface wave, but the first pseudosurface shell is very interesting since a maximum coupling of 0.0568 % is obtained for the  $(\bar{1}10)$  direction of propagation with a velocity of 2992 m/s and a negligible attenuation ( $\alpha < 0.01$  dB/ $\lambda$ ). This behaviour is very similar to that of GaAs described in Ref. 2.

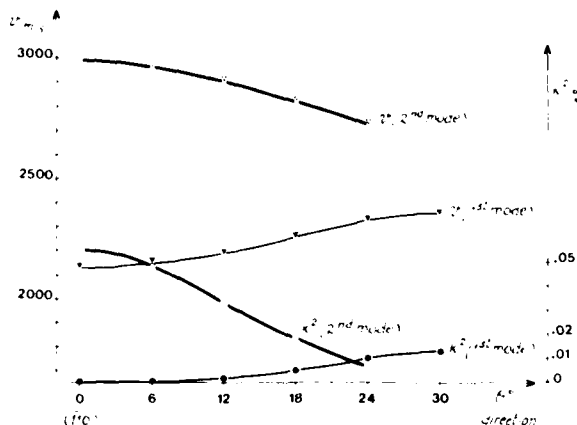


Figure 3 : Variation of  $k^2$  and  $v$  for the first and second modes of InP as a function of the direction of propagation, for  $\langle 111 \rangle$  cut.

Figure 4 shows the results obtained for different cuts with the same direction of propagation  $(\bar{1}10)$  starting from the  $\langle 001 \rangle$  cut with the 0.04 % coupling-Rayleigh mode. The coupling coefficient goes through a maximum at the previously established value of 0.0568 % of the pseudosurface mode for the  $\langle 111 \rangle$  cut, and this maximum is very flat:  $k^2$  remains larger than 0.05 % over  $20^\circ$  with a negligible attenuation.

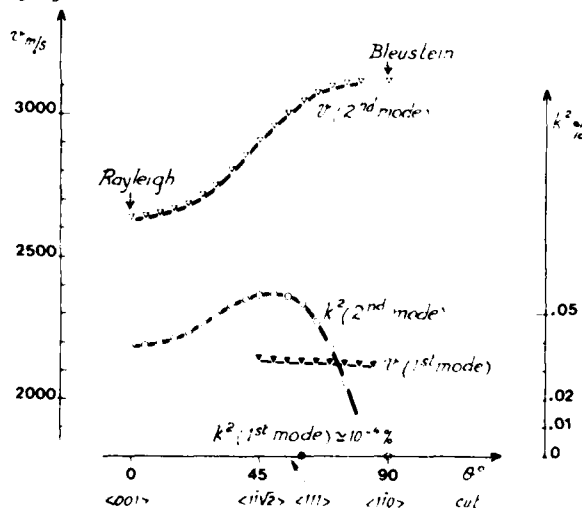


Figure 4 : Variation of  $k^2$  and  $v$  for the first and second modes of InP as a function of the cut, for  $\langle 110 \rangle$  propagation direction.

## Experimental results

We have experimented with three different configurations :

- i)  $\langle 001 \rangle$  cut,  $(\bar{1}10)$  propagation
- ii)  $\langle 110 \rangle$  cut,  $(110)$  propagation and
- iii)  $\langle 110 \rangle$  cut,  $\langle 001 \rangle$  propagation.

We have made a SAW delay-line with two transducers of 239 and 120 fingers of  $12.16 \mu\text{m}$  wavelength and 0.5 mm aperture. The distance between the centres of the two transducers is equal to  $119 \lambda$ . In a first experiment we used a conventional process with chemical etching of a 500 Å - thick thermally evaporated aluminum layer. Afterwards, better results were obtained using a lift-off process.

The frequency response of the configuration i) is shown in Figure 5 from 210 MHz to 222 MHz.

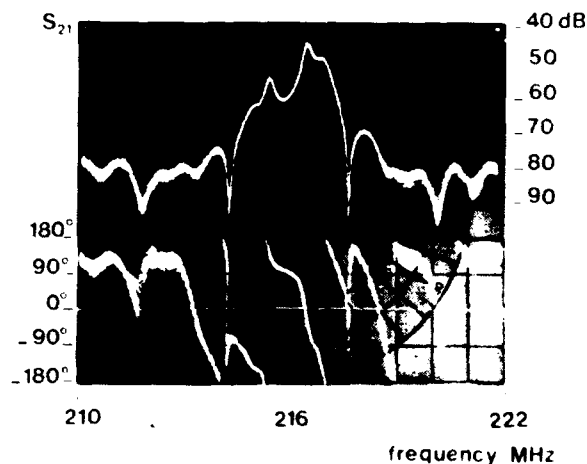


Figure 5 : Frequency response (amplitude : 10 dB/div. and phase :  $90^\circ$ /div.) of a  $\langle 001 \rangle$  cut,  $(\bar{1}10)$  propagation InP delay-line.

Due to mass loading, the response is not as smooth as generally obtained (for example on GaAs crystals), but the zeroes of the  $\sin x/x$  frequency response are clean and well-located as expected. From this curve, the velocity is found equal to 2627 m/s, i.e. slightly less than the theoretical value of 2639 m/s obtained from the computer program. In the same manner, the velocity values obtained experimentally for the ii) and iii) configurations are a little smaller than the computed values (cf. Table II), showing nevertheless good agreement between theory and experiments. Values of  $k^2$  obtained from impedance measurements are reported also in Table II, indicating that InP seems to be a weaker piezoelectric crystal than GaAs. Since InP is a very delicate material, some technological difficulties were encountered, and further experimental confirmations and theoretical investigations need to be done. The actual sensitivity to mass loading is understood in terms of lower stiffness of the InP substrate compared to the Al-layer. The electrodes increase periodically the surface velocity and then produce a corrugated cavity. This underlines the interest of SSBW which are not similarly disturbed.

Table II: Experimental and computed parameters of some cuts of InP (assuming  $\epsilon_{14} = 0.11$ )

	Angles			Cut	Prop	Velocity [m/s]		Coupl. Coeff. [%]	
	$\alpha$	$\theta$	$\phi$			Co	Ex	Co	Ex
A	90°	45°	0°	001	$\bar{1}\bar{1}0$	2639	2627	0.0384	0.02 R
B	0°	45°	54°7	111	$\bar{1}\bar{1}0$	2133	-	$5.6 \cdot 10^{-5}$	- -
B*	0°	45°	54°7	111	$\bar{1}\bar{1}0$	2992	-	0.056	- -
C	90°	45°	90°	110	001	2595	2576	0.013	0.012 R
D	0°	45°	90°	110	$\bar{1}\bar{1}0$	3113	3089	$2 \cdot 10^{-5}$	- B

Co = Computed  
Ex = Experimental

R = Rayleigh  
B = Bleustein-Gulyaev

### Conclusion

Owing to the properties of III-V semiconductors, micropiezoelectronic devices are likely to merge from the control of the technological process. Presently, the main applications are expected in signal processing for voltage controlled oscillators, adaptative filters and more complex signal processors in the VHF and UHF range. Other applications regarding optoelectronics, optical communications and solid state displays are also in the scope of these techniques. The present paper has investigated the properties of semi-insulating InP crystals in terms of piezoelectric coupling. We have emphasized the interest of SSBW rather than SAW branches because of their higher coupling. A more complete investigation of the leaky shell could induce significant results. However, the final advantages should be evaluated in the complete devices using semiconducting layers and mixing microelectronic and piezoelectric properties.

In conclusion, Indium Phosphide shows piezoelectric SAW properties very similar to Gallium Arsenide. From our present experiments, the coupling coefficient is roughly half of the GaAs coupling. This implies that while InP is useful in piezo-optics, GaAs has to be preferred for piezo-electronic devices.

Acknowledgement : The authors would like to thank Mme M. Feuillade, MM. M. Carel, R. Dubois and S. Sainson for technical assistance.

### References

- 1 - T.W. GRUDKOWSKI, G.K. GILDEN and J.F. BLACK : "GaAs monolithic SAW devices for signal processing and frequency control", 1980, Proc. Ultrasonics Symposium, pp. 88-97.
- 2 - J. HENAFF, M. FELDMANN, M. CAREL and R. DUBOIS : "New SSBW mode in GaAs" Electron. Lett., 1981, Vol. 12, pp. 427-429.
- 3 - J. HENAFF and M. FELDMANN : "New modes in III-V monolithic SAW devices", Proc. International Symposium on GaAs and related compounds, OISO, Japan, 20-23 sept 1981, Institute of Physics, London, pp. 455-460.
- 4 - M. FELDMANN and J. HENAFF : "Propagation des ondes élastiques de surface", Revue de Physique Appliquée, 1977, vol. 12, pp. 1775-1788.
- 5 - J.J. CAMPBELL and W.R. JONES : "A method for estimating optimal crystal cuts and propagation directions for excitation of piezoelectric surface waves", IEEE. Trans. Son. Ultrason, vol. SU-15, pp. 209-217, 1968.
- 6 - K.A. INGEBRIGTSEN : "Surface waves in piezoelectrics", J. Appl. Phys., vol. 40, n° 7, pp. 2681-2686, 1969.
- 7 - H. ENGAN, H. HANEBREKKE, K.A. INGEBRIGTSEN et al. : "Numerical calculations on surface waves in piezoelectrics", Appl. Phys. Lett., Vol. 15, n° 8, pp. 239-241, 1969.
- 8 - C.C.A. J. GREEBE, P.A. VAN DALEN et al : "Electric coupling properties of acoustic and electric surface waves", Phys. Rep. Vol. 1C, n° 5, pp. 235-268, 1971.
- 9 - J. HENAFF, M. FELDMANN and M. LE CONTELLEC : "Monolithic acoustoelectric amplifier using pseudosurface waves", Appl. Phys. Lett., vol. 24, n° 9, pp. 447-449, 1974.

AD P001567

# UNWANTED RESPONSES IN QUARTZ LOW FREQUENCY X-CUT BARS

J F Werner, H W Edwards\* and M Smith\*

The General Electric Company, p.l.c., Hirst Research Centre, Wembley,  
HA9 7PP, England  
\* Salford Electrical Instruments Ltd., Times Mill, Heywood  
OL10 4NE, England

## Abstract

The unwanted modes in quartz 5° X-cut low frequency resonator bars have been recorded and charted over the range of dimensional ratios  $l/w$  5 to 10 and  $l/t$  50 to 170. They have been found to occur at even multiples of the frequencies of coupled  $l$ - $t$  flexural and length torsional modes and a unified spectrum has been obtained by plotting  $flw/t$  against  $w/l$ . A simplified theory of these coupled modes is developed and is found to give good agreement with the observed spectrum.

Key words : quartz, length extensional, 5° X-cut, unwanted responses, flexural, torsional

## 1 Introduction

For many years the production of quartz low frequency bars has suffered from rejects due to unwanted responses within a few kilohertz of the main length extensional resonance. They give rise to disturbances in the transmission characteristics of the crystals and can cause troublesome spikes in the passband region of the filters. In many cases they have remained undetected until the crystals were assembled into a filter.

Records have been collected and attempts made to identify the interfering modes. It was suspected that some at least were due to the main response being close to a frequency multiple of a low order length-thickness flexural. Coincidence with the width-thickness flexure was also suspected in some cases. No such effects however have been reported in the literature.

We have therefore carried out a programme of recording and charting these responses in experimental 5° X-cut bars within the range of dimensional ratios  $l/w$  5 to 10 and  $l/t$  50 to 170, a total of about 800 crystals having been made and investigated. It has been found possible to plot the unwanted modes so as to show a unified spectrum, thus giving a means for choosing the best dimensional ratios to avoid them.

## 2 Experimental procedure

Crystals were made in batches of a chosen width and thickness and covering a range of lengths. After measuring the blank dimensions the crystals were fully plated with nichrome/gold electrodes and headed phosphor bronze wires were soldered to the nodal points. The crystals were mounted in standard wire cages in evacuated glass envelopes.

A search for unwanted modes was carried out on each crystal within  $\pm 10$  kHz of the main response using a Wandel and Goltermann swept frequency test set connected directly to the crystal. The suspected responses were all tested for the sign of their temperature coefficient of frequency and show a negative coefficient. This test also confirms that the charted responses are true effects due to the crystal.

Since the crystals are fully plated there is no direct piezoelectric drive to excite flexural vibrations. The offending disturbances are usually found within about  $\pm 5$  kHz of the main response and are stronger the closer they are to it in frequency. If the crystal is being examined in direct transmission or in a  $\pi$ -network then the unwanted modes are also stronger if close to anti-resonance. Since the responses have a negative temperature coefficient it is sometimes possible, on heating, to observe a response growing in strength as it approaches and passes through anti-resonance, then weakening and growing in strength again as it approaches and passes through the main resonance peak, as illustrated in Figure 1. This observation demonstrates that the coupling to the modes is mechanical in nature.

## 3 Charting the responses

Many of the responses were observed to be close in frequency to an even multiple of a length-thickness flexure, but with many divergencies. Close examination, including lycopodium powder studies in cases where the modes are strongly excited, suggested that the flexural modes were coupled to torsional modes. Since the length extensional frequency is closely proportional to  $1/l$ , the length-thickness flexural frequencies are proportional to  $t/l^2$  and the

length torsional frequencies are proportional to  $t/w$ , the responses from various crystals can be brought into a regular relationship with each other by plotting  $flw/t$  against  $w/l$ . When this is done a unified spectrum for the modes is revealed. In the resulting chart a pure length-thickness flexural would give a straight line through the origin and a purely torsional mode would show a horizontal straight line.

The main length extensional mode does not appear in the chart. Each crystal is defined by the independent ratios  $w/t$  and  $w/l$ , and, since  $fl = \text{constant}$  (approx 2.8 kHz m), a crystal can be designed to place the main mode at any required point (i.e.  $w/l$ , 2.8  $w/t$  kHz m). The results from about 450 crystals are shown as points in Figure 2, while Figure 3 shows the distribution of the crystal dimensional ratios for the experimental batches.

It can be seen from Figure 2 that the experimental points denoting the unwanted modes fall into distinct bands, so that the chart has an immediate application to crystal design. The main mode of a crystal of known dimensions gives a point on the chart which may fall in either a clear or a fouled region, and the minimum frequency separation from the nearest unwanted mode can then be estimated.

Most of the observed modes can be identified as even multiples of coupled length-thickness flexural and length torsional modes. A prominent feature of the chart, however, is a mode following a hyperbolic curve which is identified as the width-thickness flexure, for which frequency is proportional to  $t/w^2$ . Figure 4 illustrates the various vibrational modes of the bar which are discussed in this paper. The mode described as 'anharmonic overtone of width-thickness flexure' is included as a possibility for which there is some evidence (not all shown in Figure 2) as unwanted responses at about 2 kHz m above the modes identified as width-thickness flexure.

#### 4 Theory of coupled flexural and torsional modes

Simple equations governing the coupled length thickness flexural and the length torsional modes are formulated and their solutions show symmetric flexural modes coupling to antisymmetric torsional modes and vice versa.

##### 4.1 Simple torsional

Referring to Figure 5, length  $l$ , width  $w$  and thickness  $t$  are parallel to the  $Z'$ ,  $Y'$  and  $X$  axes respectively. The convention used in this paper is that the rotation is  $+85^\circ$  from length originally along  $Z$ . Figure 6 illustrates length torsion of the bar. For an angle of twist  $\phi$  about the  $Z'$  axis:

$$\text{Torque } T = \frac{wt^3 F}{3S_t} \frac{\partial \phi}{\partial z} \quad (1)$$

where  $S_t = (S_{55} + S_{44})/2$  is an approximate value for the torsional compliance.  $S_{55}$  and  $S_{44}$  are the appropriate rotated coefficients, the usual prime indications being omitted for convenience.  $F$  is a factor for rectangular bars given by  $F = 1 - 0.63(t/w)/(S_{44}/S_{33})$  for  $w > 3t$ . Since the moment of inertia  $I$  for a cross sectional slice is given by  $I = \rho wt(w^2 + t^2)/12$ , the equation of motion for the torsional mode is:

$$\ddot{\phi} = \frac{1}{I} \frac{\partial T}{\partial z} = \frac{4F}{\rho S_t} \frac{t^2}{w^2 + t^2} \frac{\partial^2 \phi}{\partial z^2} \quad (2)$$

##### 4.2 Simple flexural

In Figure 7  $\eta$  is the deflection from the rest position and  $M$  is the bending moment given by:

$$M = \frac{wt^3}{12S_{33}} \cdot \frac{1}{R} = \frac{wt^3}{12S_{33}} \frac{\partial^2 \eta}{\partial z^2} \quad (3)$$

The simple equation of motion for the flexural mode is therefore:

$$\ddot{\eta} = - \frac{1}{\rho wt} \frac{\partial^2 M}{\partial z^2} = - \frac{t^2}{12\rho S_{33}} \frac{\partial^4 \eta}{\partial z^4} \quad (4)$$

##### 4.3 Coupling between torsional and flexural modes

Flexing produces extension on one side of the neutral surface and compression on the other and, due to the cross coupling coefficients, a shearing stress pattern is produced which is equivalent to a torque  $T'$ . By analogy with Equation (1) the flexure produces a torque:

$$T' = \frac{wt^3 F}{3} \cdot \chi \cdot \frac{1}{S_{33}} \frac{\partial^2 \eta}{\partial z^2} \quad (5)$$

where  $\chi$  is a function of cross coupling compliances and  $T'$  is proportional to  $M$ . The equation of motion for the torsional mode becomes:

$$I \ddot{\phi} = \frac{\partial T}{\partial z} + \frac{\partial T'}{\partial z} \quad \text{i.e.} \quad \ddot{\phi} = \frac{4Ft^2}{\rho S_t(w^2 + t^2)} \frac{\partial^2 \phi}{\partial z^2} + \frac{4Ft^2 \chi}{\rho S_{33}(w^2 + t^2)} \frac{\partial^3 \eta}{\partial z^3} \quad (6)$$

Similarly it can be shown that a twist produces a bending moment:

$$M' = \frac{wt^3}{12S_t} \chi' \frac{\partial \phi}{\partial z} \quad (7)$$

and, by invoking the reciprocal theorem, it appears that  $\chi' = \chi$ . The equation of motion for the flexural mode thus becomes:

$$\rho wt \ddot{\eta} = - \frac{\partial^2 M}{\partial z^2} + \frac{\partial^2 M'}{\partial z^2}$$

$$\text{i.e. } \eta = -\frac{t^2}{12\rho S_{33}} \frac{\partial^4 \eta}{\partial z^4} + \frac{t^2}{12\rho S_t \chi} \frac{\partial^3 \phi}{\partial z^3} \quad (8)$$

Assuming sinusoidal motion with time at an angular frequency  $\omega$ , and normalising using the relations  $\bar{\omega} = \omega l / \omega_c$ ,  $\bar{z} = z/l$  and  $\bar{\eta} = \eta/l$ , Equations (6) and (8) lead to:

$$\begin{aligned} -\bar{\omega}^2 \phi &= \alpha \frac{\partial^2 \phi}{\partial \bar{z}^2} + \beta \frac{\partial^3 \bar{\eta}}{\partial \bar{z}^3} \\ -\bar{\omega}^2 \bar{\eta} &= \gamma \frac{\partial^4 \bar{\eta}}{\partial \bar{z}^4} + \epsilon \frac{\partial^3 \phi}{\partial \bar{z}^3} \end{aligned} \quad (9)$$

as the equations for the coupled flexural and torsional modes where:

$$\begin{aligned} \alpha &= \frac{4F}{\rho S_t \{1 + (t/w^2)\}} & \beta &= \frac{4F}{\rho S_{33} \{1 + (t/w^2)\}} \\ \gamma &= \frac{(w/l)^2}{12\rho S_{33}} & \epsilon &= \frac{(w/l)^2}{12\rho S_t \chi} \end{aligned}$$

In finding solutions to these equations the quantities  $\beta$  and  $\epsilon$  appear only as their product, so that  $\chi$  is eliminated. It is thus not necessary to find its precise form.

Normalised quantities are used henceforth, but the bar signs are omitted for typographical convenience.

#### 4.4 The dispersion equation

There are two series of solutions, one with  $\phi$  anti-symmetric and  $\eta$  symmetric and the other vice versa. Taking the former case as an example, the assumed solutions are:

$$\begin{aligned} \phi &= A_1 \sin \zeta_1 z \\ \eta &= B_1 \cos \zeta_1 z \end{aligned} \quad (10)$$

Substituting in Equations (9) gives:

$$\begin{aligned} A_1(\omega^2 - \alpha \zeta_1^2) + B_1 \beta \zeta_1^3 &= 0 \\ -A_1 \epsilon \zeta_1^3 + B_1(\omega^2 + \gamma \zeta_1^4) &= 0 \end{aligned} \quad (11)$$

which are true for all  $i$ . The condition for non-trivial solutions for  $A_i$  and  $B_i$  thus leads to a cubic equation in  $\zeta^2$ , which is the dispersion equation:

$$\text{i.e. } \zeta^6 + \zeta^4 \frac{\omega^2 \gamma}{\beta \epsilon - \alpha \gamma} - \zeta^2 \frac{\omega^2 \alpha}{\beta \epsilon - \alpha \gamma} + \frac{\omega^4}{\beta \epsilon - \alpha \gamma} = 0 \quad (12)$$

Below a critical value of  $\omega$ , say  $\omega_c$ , the equation gives real values of  $\zeta^2$ . Since  $\gamma$  is a negative

quantity there are two positive roots and one negative root i.e.  $\zeta_1^2$ ,  $\zeta_2^2$  and  $-\zeta_3^2$ . The full line in Figure 8 shows a typical example of computed values of  $\zeta$  plotted against  $\omega/2\pi$ . Equation (10) may thus be written:

$$\begin{aligned} \phi &= A_1 \sin \zeta_1 z + A_2 \sin \zeta_2 z + A_3 \sinh \zeta_3 z \\ \eta &= B_1 \cos \zeta_1 z + B_2 \cos \zeta_2 z + B_3 \cosh \zeta_3 z \end{aligned} \quad (13)$$

where  $\zeta_1$ ,  $\zeta_2$  and  $\zeta_3$  are all real.

#### 4.5 The frequency equation

From the first of Equations (11)  $A_1 = -B_1 \beta \zeta_1^3 / (\omega^2 - \alpha \zeta_1^2)$  so there are three independent variables  $B_1, B_2$  and  $B_3$ , and there are three boundary conditions to apply at  $z = \pm l/2$ .

$$\text{i.e. } \frac{\partial \phi}{\partial z} = 0, \quad \frac{\partial^2 \eta}{\partial z^2} = 0 \quad \text{and} \quad \frac{\partial^3 \eta}{\partial z^3} = 0 \quad (14)$$

By substituting from Equation (13) into Equations (14) a set of three homogenous equations in  $B_1, B_2$  and  $B_3$  is obtained. The condition for non-trivial solutions forms the frequency equation which is listed in the Appendix. The values of  $\omega$  for which this determinant becomes zero are the normalised frequencies of the coupled flexural/torsional modes.

#### 4.6 Complex solutions

Above  $\omega_c$  the dispersion equation has one real and two complex roots of the form  $-\zeta_3^2$ ,  $\zeta_1^2 = A - jB$ ,  $\zeta_2^2 = A + jB$ . It can be shown that  $\zeta_1$  and  $\zeta_2$  are complex i.e.  $\zeta_1 = \zeta'_1 - j\zeta''_1$  and  $\zeta_2 = \zeta'_1 + j\zeta''_1$  where real values for  $\zeta'_1$  and  $\zeta''_1$  can be computed. The solutions for  $+$  and  $-$  are:

$$\begin{aligned} \phi &= 2A_1 \sin \zeta'_1 z \cosh \zeta''_1 z + A_3 \sinh \zeta_3 z \\ \eta &= 2B_1 \cos \zeta'_1 z \cosh \zeta''_1 z + B_3 \cosh \zeta_3 z \end{aligned} \quad (15)$$

and the frequency equation can then be shown to have the form listed in the Appendix.

#### 4.7 Other forms of equations

Corresponding equations can be developed for solutions with symmetrical  $\phi$  and anti-symmetrical  $\eta$ . Account must also be taken of flexure coupling to either a positively or negatively travelling torsional wave which leads to an alternative form for the equations of motion:

$$\begin{aligned} -\omega^2 \phi &= -\alpha \frac{\partial^2 \phi}{\partial z^2} + \beta \frac{\partial^3 \eta}{\partial z^3} \\ -\omega^2 \eta &= \gamma \frac{\partial^4 \eta}{\partial z^4} - \epsilon \frac{\partial^3 \phi}{\partial z^3} \end{aligned} \quad (16)$$

(Compare Equations (9)). The roots are now  $-\zeta_1^2$ ,  $-\zeta_2^2$  and  $\zeta_3^2$  as illustrated by the broken line in Figure 8.

The Appendix lists the various forms of the equations.

### 5. Computed results

Computed values of  $f\omega/t$  plotted against  $w/t$  are shown in Figures 9 and 10. Four separate hunting procedures have been used:

- Hunt 1 : symmetric flexure,  $\tau_3^2$  positive
- Hunt 2 : symmetric flexure,  $\tau_3^2$  negative
- Hunt 3 : anti-symmetric flexure,  $\tau_3^2$  positive
- Hunt 4 : anti-symmetric flexure,  $\tau_3^2$  negative

A value of 0.005 has been used for the fractional mass loading, having the effect of multiplying  $\tau$  by 1.005, and a value of 15 has been used for the  $w/t$  ratio. Both of these factors have a very minor effect on the curves and their values have been chosen to represent averages for the experimental crystals. The spread of  $w/t$  among them was 7.1 to 22, corresponding to a variation in the terms  $\tau$  and  $\rho$  of less than 1.5%. Some small spread of the practical results may therefore be attributed to differences of these quantities between the crystals.

#### 5.1 Coupling to length extensional modes

The realisation that the flexural and torsional modes are coupled leads to some clarification of the mechanism whereby they become excited. Due to the twisting action, a mode with a torsional component displays a length variation at twice its frequency (say  $2\omega$ ). There is thus a direct means for it to be driven by a length extensional vibration at  $2\omega$ , such as would occur if the length extensional resonance was close to this frequency. Also since the expansion of  $\cos 2n\tau$  has a term in  $\cos^2 \tau$  for odd values of  $n$  (but not for even values) it may be expected that coupling will also occur at 6, 10, 14 etc times the frequency of the flexural/torsional mode.

In Figure 2 the curves of Figures 9 and 10 are displayed with multiplying factors of 2, 6, 10 or 14 as indicated. Arbitrary multiplication factors for the two significant compliances  $S_{33}$  and  $S_6$  have been used in the computations, values of 1.06 and 1.08 having been chosen to improve the fit with the experimental points. In view of the simplified nature of the theory these corrections (representing 3% and 4% in frequency terms) are not considered to be excessive.

### 6. Conclusions

In Figure 2 most of the experimental points correspond fairly closely to some theoretical line and there is good agreement between the slopes of the lines and the bands of points. The theory should therefore be useful for predicting the likely occurrence of coupled modes following changes in such quantities as crystal orientation,  $w/t$  ratio and fractional mass loading, and for making tentative extrapolations beyond the range of the experimental results. The prominent band

identified as the width-thickness flexure has not been brought into the coupling theory, and the mechanism whereby this mode is excited, other than via fortuitous asymmetry of the crystal, remains unexplained.

The principal value of the work lies in the assistance given to crystal design by the unified spectrum.

### References

- 1 W G Cady, 'Piezoelectricity' p 62, McGraw-Hill, 1946

### Appendix

#### Various forms of the equations

##### 1 Equations of motion (first sort)

$$-\omega^2 z = \tau \frac{\omega^2 z}{\tau z^2} + \rho \frac{\omega^3 z}{\tau z^3}$$

$$-\omega^2 z = \gamma \frac{\omega^4 z}{\tau z^4} + \rho \frac{\omega^3 z}{\tau z^3}$$

##### 1.1 Dispersion equation

$$\tau^2 6 + \tau^4 \frac{\omega^2 \gamma}{6\tau - \gamma} - \tau^2 \frac{\omega^2 \rho}{6\tau - \gamma} + \frac{\omega^4}{6\tau - \gamma} = 0$$

Since  $\gamma$  is negative, the roots are  $\tau_1^2$ ,  $-\tau_2^2$  and  $-\tau_3^2$

##### 1.2 Solutions symmetric in flexure

$$z = A_1 \sin \tau_1 z + A_2 \sin \tau_2 z + A_3 \sinh \tau_3 z$$

$$n = B_1 \cos \tau_1 z + B_2 \cos \tau_2 z + B_3 \cosh \tau_3 z$$

##### 1.2.1 The frequency equations (used in Hunt 2 of the program)

(a)  $\omega < \omega_c$  (i.e.  $\tau_1, \tau_2$  real)

$$\begin{vmatrix} \tau_1^2 \cos(\tau_1/2) & \tau_2^2 \cos(\tau_2/2) & \tau_3^2 \cosh(\tau_3/2) \\ \tau_1^2 \tau_1^2 & \tau_2^2 \tau_2^2 & \tau_3^2 \tau_3^2 \\ -\cos(\tau_1/2) & -\cos(\tau_2/2) & \cosh(\tau_3/2) \\ \tau_1 \sin(\tau_1/2) & \tau_2 \sin(\tau_2/2) & \tau_3 \sinh(\tau_3/2) \end{vmatrix} = 0$$

(b)  $\omega > \omega_c$  (i.e.  $\tau_1, \tau_2$  complex)

$$G \begin{vmatrix} 0 & \cosh(\tau_3/2) \\ E & \tau_3 \sinh(\tau_3/2) \end{vmatrix} = 0$$

$$G = \tau^2 \sin(\tau'/2) \sinh(\tau''/2) + \tau' \cos(\tau'/2) \cosh(\tau''/2)$$

$$D = (\zeta''^2 - \zeta'^2) \cos(\zeta'/2) \cosh(\zeta''/2)$$

$$-2\zeta''\zeta' \sin(\zeta'/2) \sinh(\zeta''/2)$$

$$E = \zeta''(\zeta''^2 - 3\zeta'^2) \cos(\zeta'/2) \sinh(\zeta''/2)$$

$$-\zeta'(\zeta''^2 + \zeta'^2) \sin(\zeta'/2) \cosh(\zeta''/2)$$

### 1.3 Solutions antisymmetric in flexure

$$\phi = A_1 \cos \zeta_1 z + A_2 \cos \zeta_2 z + A_3 \cosh \zeta_3 z$$

$$\eta = B_1 \sin \zeta_1 z + B_2 \sin \zeta_2 z + B_3 \sinh \zeta_3 z$$

#### 1.3.1 The frequency equations (used in Hunt 4 of the program)

(a)  $\omega < \omega_c$  (i.e.  $\zeta_1, \zeta_2$  real)

$$\begin{vmatrix} \frac{\zeta_1^2 \sin(\zeta_1/2)}{\omega^2 - \alpha \zeta_1^2} & \frac{\zeta_2^2 \sin(\zeta_2/2)}{\omega^2 - \alpha \zeta_2^2} & \frac{\zeta_3^2 \sinh(\zeta_3/2)}{\omega^2 + \alpha \zeta_3^2} \\ -\sin(\zeta_1/2) & -\sin(\zeta_2/2) & \sinh(\zeta_3/2) \\ -\zeta_1 \cos(\zeta_1/2) & -\zeta_2 \cos(\zeta_2/2) & \zeta_3 \cosh(\zeta_3/2) \end{vmatrix} = 0$$

(b)  $\omega > \omega_c$  (i.e.  $\zeta_1, \zeta_2$  complex)

$$G. \begin{vmatrix} D & \sinh(\zeta_3/2) \\ E & \zeta_3 \cosh(\zeta_3/2) \end{vmatrix} = 0$$

$$G = \zeta'' \cos(\zeta'/2) \sinh(\zeta''/2) - \zeta' \sin(\zeta'/2) \cosh(\zeta''/2)$$

$$D = (\zeta''^2 - \zeta'^2) \sin(\zeta'/2) \cosh(\zeta''/2)$$

$$+2\zeta' \zeta'' \cos(\zeta'/2) \sinh(\zeta''/2)$$

$$E = -\zeta'(\zeta''^2 + \zeta'^2) \cos(\zeta'/2) \cosh(\zeta''/2)$$

$$+\zeta''(\zeta''^2 - \zeta'^2) \sin(\zeta'/2) \sinh(\zeta''/2)$$

### 2 Equations of motion (second sort)

$$-\omega^2 \phi = -\alpha \frac{\partial^2 \phi}{\partial z^2} + \beta \frac{\partial^3 \eta}{\partial z^3}$$

$$-\omega^2 \eta = \gamma \frac{\partial^4 \eta}{\partial z^4} - \epsilon \frac{\partial^3 \phi}{\partial z^3}$$

#### 2.1 Dispersion equation

$$\zeta^6 - \zeta^4 \frac{\omega^2 \gamma}{\beta \epsilon - \alpha \gamma} - \zeta^2 \frac{\omega^2 \gamma}{\beta \epsilon - \alpha \gamma} - \frac{\omega^4}{\beta \epsilon - \alpha \gamma} = 0$$

Since  $\gamma$  is negative, the roots are  $-\zeta_1^2$ ,  $-\zeta_2^2$  and  $\zeta_3^2$ .

#### 2.2 Solutions symmetric in flexure

$$\phi = A_1 \sinh \zeta_1 z + A_2 \sinh \zeta_2 z + A_3 \sin \zeta_3 z$$

$$\eta = B_1 \cosh \zeta_1 z + B_2 \cosh \zeta_2 z + B_3 \cos \zeta_3 z$$

#### 2.2.1 The frequency equations (used in Hunt 1 of the program)

(a)  $\omega < \omega_c$  (i.e.  $\zeta_1, \zeta_2$  real)

$$\begin{vmatrix} \frac{\zeta_1^2 \cosh(\zeta_1/2)}{\omega^2 + \alpha \zeta_1^2} & \frac{\zeta_2^2 \cosh(\zeta_2/2)}{\omega^2 + \alpha \zeta_2^2} & \frac{\zeta_3^2 \cos(\zeta_3/2)}{\omega^2 - \alpha \zeta_3^2} \\ \cosh(\zeta_1/2) & \cosh(\zeta_2/2) & -\cos(\zeta_3/2) \\ \zeta_1 \sinh(\zeta_1/2) & \zeta_2 \sinh(\zeta_2/2) & \zeta_3 \sin(\zeta_3/2) \end{vmatrix} = 0$$

(b)  $\omega > \omega_c$  (i.e.  $\zeta_1, \zeta_2$  complex)

$$G. \begin{vmatrix} D & \cos(\zeta_3/2) \\ E & -\zeta_3 \sin(\zeta_3/2) \end{vmatrix} = 0$$

$$G = \zeta'' \sin(\zeta'/2) \sinh(\zeta''/2) + \zeta' \cos(\zeta'/2) \cosh(\zeta''/2)$$

$$D = (\zeta''^2 - \zeta'^2) \cos(\zeta'/2) \cosh(\zeta''/2)$$

$$-2\zeta' \zeta'' \sin(\zeta'/2) \sinh(\zeta''/2)$$

$$E = \zeta''(\zeta''^2 - 3\zeta'^2) \cos(\zeta'/2) \sinh(\zeta''/2)$$

$$-\zeta'(\zeta''^2 + \zeta'^2) \sin(\zeta'/2) \cosh(\zeta''/2)$$

### 2.3 Solutions antisymmetric in flexure

$$\phi = A_1 \cosh \zeta_1 z + A_2 \cosh \zeta_2 z + A_3 \cos \zeta_3 z$$

$$\eta = B_1 \sinh \zeta_1 z + B_2 \sinh \zeta_2 z + B_3 \sin \zeta_3 z$$

#### 2.3.1 The frequency equations (used in Hunt 3 of the program)

(a)  $\omega < \omega_c$  (i.e.  $\zeta_1, \zeta_2$  real)

$$\begin{vmatrix} \frac{\zeta_1^2 \sinh(\zeta_1/2)}{\omega^2 + \alpha \zeta_1^2} & \frac{\zeta_2^2 \sinh(\zeta_2/2)}{\omega^2 + \alpha \zeta_2^2} & \frac{\zeta_3^2 \sin(\zeta_3/2)}{\omega^2 - \alpha \zeta_3^2} \\ \sinh(\zeta_1/2) & \sinh(\zeta_2/2) & -\sin(\zeta_3/2) \\ \zeta_1 \cosh(\zeta_1/2) & \zeta_2 \cosh(\zeta_2/2) & -\zeta_3 \cos(\zeta_3/2) \end{vmatrix} = 0$$

(b)  $\omega > \omega_c$  (i.e.  $\zeta_1, \zeta_2$  complex)

$$G. \begin{vmatrix} D & \sin(\zeta_3/2) \\ E & \zeta_3 \cos(\zeta_3/2) \end{vmatrix} = 0$$

$$G = \zeta'' \cos(\zeta'/2) \sinh(\zeta''/2) - \zeta' \sin(\zeta'/2) \cosh(\zeta''/2)$$

$$D = (\zeta''^2 - \zeta'^2) \sin(\zeta'/2) \cosh(\zeta''/2)$$

$$+2\zeta' \zeta'' \cos(\zeta'/2) \sinh(\zeta''/2)$$

$$E = -\zeta'(\zeta''^2 + \zeta'^2) \cos(\zeta'/2) \cosh(\zeta''/2)$$

$$+\zeta''(\zeta''^2 - \zeta'^2) \sin(\zeta'/2) \sinh(\zeta''/2)$$

# ILLUSTRATIONS OF UNWANTED RESPONSES

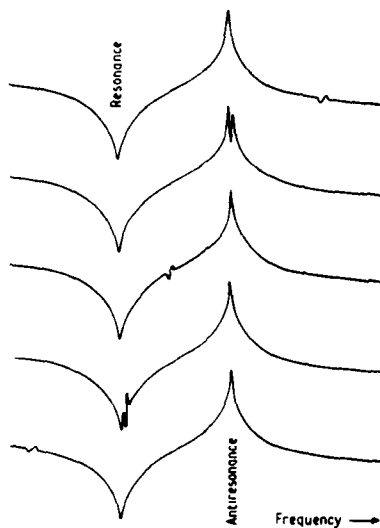


Figure 1. Illustrations of Unwanted Responses

# DIMENSIONAL RATIOS FOR THE CRYSTALS USED TO OBTAIN THE RESULTS OF FIG. 2

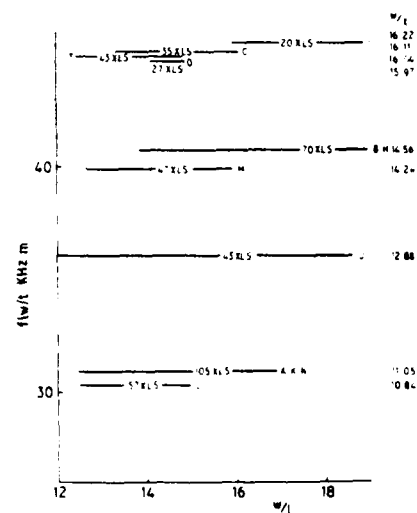


Figure 3. Dimensional Ratios for the Crystals Used to Obtain The Results of Figure 2.

# CHART OF OBSERVED UNWANTED MODES WITH COMPUTED CURVES

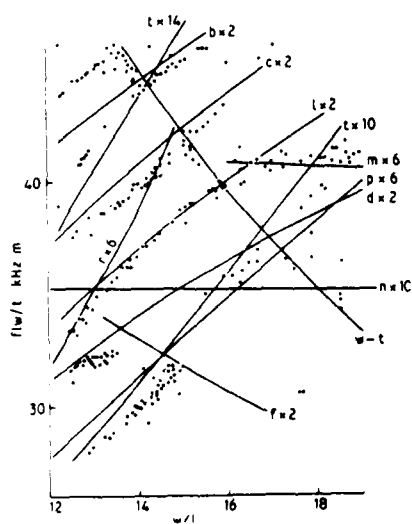


Figure 2. Chart of Observed Unwanted Mode with Computed Curves

# VARIOUS VIBRATIONAL MODES OF A BAR

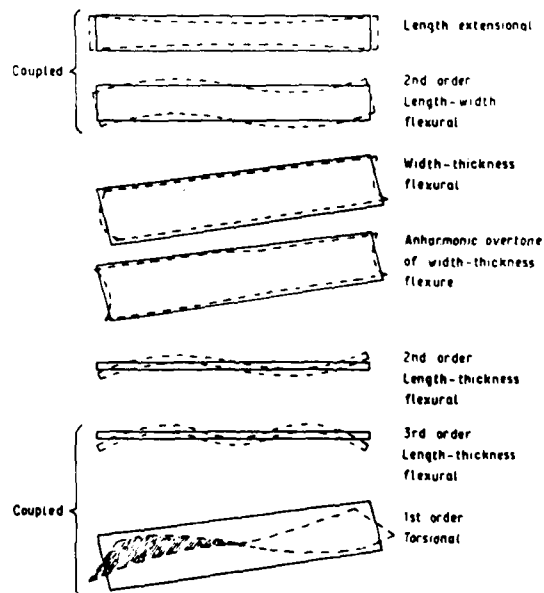


Figure 4. Various Vibrational Modes of a Bar

### X-CUT BAR

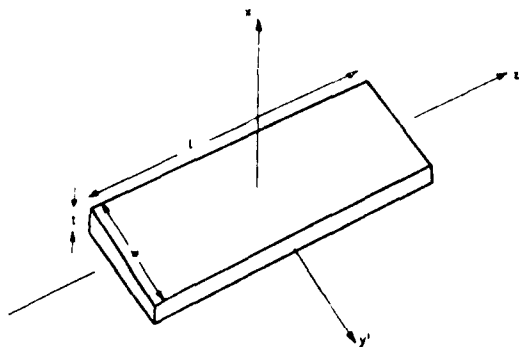


Figure 5. X-Cut Bar

### CURVATURE DUE TO FLEXURE

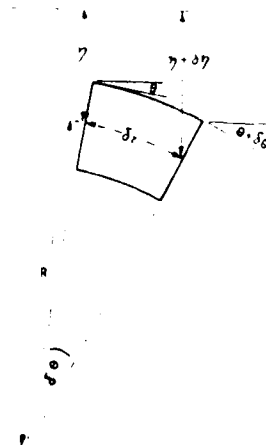
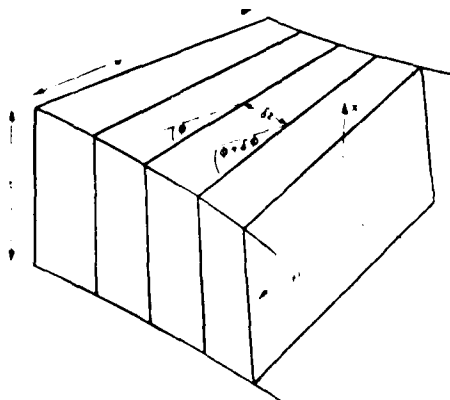


Figure 7. Curvature Due to Flexure

### TORSION OF A BAR



$$\text{Torque } T = \frac{w^2 b}{3 \eta} \frac{\partial \phi}{\partial z}$$

Figure 6. Torsion of a Bar

### COMPUTED VALUES OF S PLOTTED AGAINST $\omega/2\pi$ ( $= f$ in kHz)

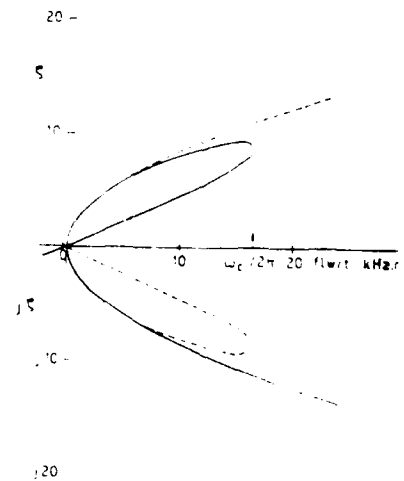


Figure 8. Computed Values of S Plotted against  $\omega/2\pi$  ( $= f$  in kHz)

COUPLED FLEXURAL AND TORSIONAL MODES  
FOR A 5° X-CUT BAR

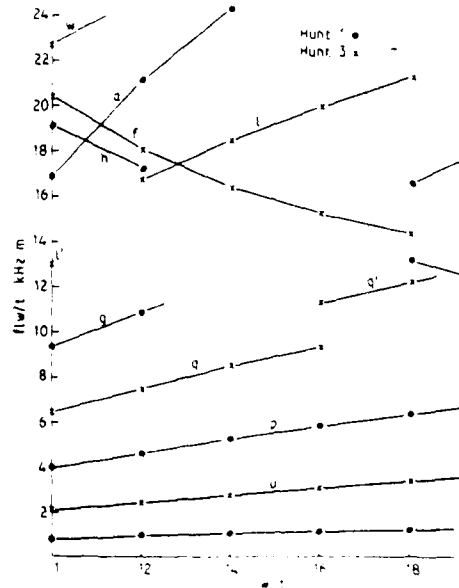


Figure 9. Coupled Flexural and Torsional Modes for a 5° X-Cut Bar

COUPLED FLEXURAL AND TORSIONAL MODES  
FOR A 5° X-CUT BAR

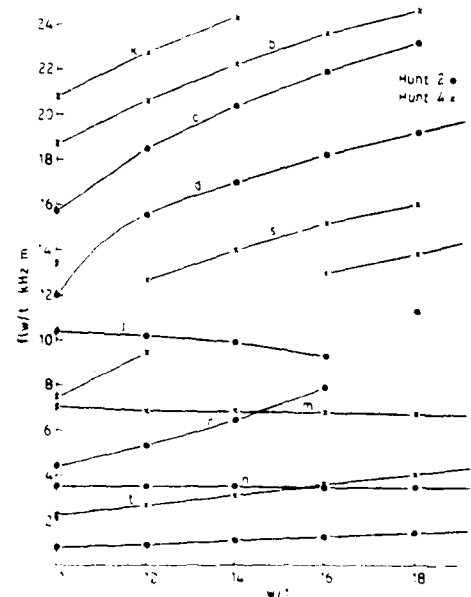


Figure 10. Coupled Flexural and Torsional Modes for a 5° X Cut Bar

## PROGRESS IN THE DEVELOPMENT OF MINIATURE THIN FILM BAW RESONATOR AND FILTER TECHNOLOGY

T. W. Grudkowski, J. F. Black, G. W. Drake, and D. E. Cullen

United Technologies Research Center  
East Hartford, Connecticut 06108Summary

Fundamental mode bulk acoustic wave resonators and filters have been fabricated from ZnO/Si composite thin films prepared by sputter depositing c-axis oriented polycrystalline ZnO onto single crystal silicon. Resonant frequencies of these devices, which are compatible with silicon IC technology, can be readily controlled in the 100 MHz to 1000 MHz range. Development of improved fabrication procedures is described, emphasizing the importance of smooth resonator surfaces and precise control of ZnO sputtering conditions. Chemical etch treatments of the ZnO is shown to markedly reduce spurious resonances. Device modeling theory is described and the good agreement between experimental data and theory is discussed.

Filter insertion loss as low as 4.1 dB and bandwidths between 0.1 and 5 percent have been achieved. Q values as high as 2700 were observed, and out of band rejection of 45 dB was realized.

**Key Words:** Bulk Acoustic Wave, Thin Films, Resonators and Filters, Fabrication, Theory, Device Measurements.

Introduction

Fundamental mode bulk acoustic wave (BAW) resonators and filters fabricated from thin films of piezoelectric materials have been the subject of considerable interest in the past few years.<sup>1-3</sup> The devices under development are intended to fill a gap which presently exists between silicon IC technology and frequency filtering technology for application in the 100 to 1000 MHz range. The centimeter lengths required of SAW filters near 100 MHz, and the ultrafine photolithographic resolution requirements, plus high propagation losses near 1000 MHz, limit the usefulness of a thin-film SAW approach for ultra miniature low loss resonators and filters.<sup>4-6</sup> While the fundamental mode operation of crystal quartz resonator filters have recently been extended above 100 MHz,<sup>7-9</sup> it is not clear that these devices can be combined with a silicon monolithic structure. The purpose of this paper is to describe a silicon integrated circuits compatible resonator/filter

based on a ZnO/Si diaphragm approach.<sup>1</sup> The very small size of ZnO/Si based BAW devices is illustrated in Figure 1. A SEM cross sectional view of the thin diaphragm and its supporting substrate is shown in Figure 2.

Fabrication Procedures

Fabrication begins with a (100) oriented silicon wafer on which a thin heavily boron doped epitaxial layer has been grown. Boron diffusion has also been used to create this layer but epitaxial growth is preferred for ease in simultaneous doping with elements other than B.

An oxide layer is formed on both the epi and substrate sides of the wafer. The oxide layer on the underside of the substrate is photolithographically processed to create an etch mask. The oxide on the epitaxial surface is kept intact to protect this surface (smoothness better than 500 Å) during subsequent etch processing. A square diaphragm is then produced by a selective chemical etchant, ethylenediamine-pyrocatechol-water (EDPW-typically 75 ml ED, 24 gm P, 24 ml W) which rapidly etches away the exposed undoped silicon substrate and leaves the highly boron doped silicon intact.<sup>10</sup> In order to act as a reliable etch stop it is essential that the boron doping be greater than  $7 \times 10^{19}/\text{cm}^3$ . In our experience,  $1 \times 10^{20}/\text{cm}^3$  was optimal. Rapid etching was found to be conducive to well defined, blemish-free diaphragms. The best results were obtained with additions of an etch catalyst, 1 gm quinoline per liter of ethylene diamine, using an etch temperature of 115°C, which produced an etch rate of 160-170 µm/hour.

With heavy boron doping, you must expect large numbers of misfit dislocations due to the lattice contractile effects of boron.<sup>11</sup> In (100) oriented wafers these dislocations form along both of the two orthogonal (110) directions on the (100) surface. During the final phases of chemical etching, when the thick substrate of undoped silicon is completely etched away to expose the etch stop layer, these misfit dislocations cause undesirable surface roughening of the underside of the diaphragm. This occurs because the dislocations are regions of enhanced chemical activity, where highly preferential

et hix; leads to a cross-hatched array of (110) oriented grooves that are sometimes as deep as 2000 Å. The diaphragm surface shown in Figure 3 had a roughness of about 1200 Å. Since this is one of the two surfaces forming the acoustic resonant cavity, it is important that it be as smooth as possible to assure a high cavity Q-factor. If, simultaneous with the boron doping we introduce impurities which expand the silicon lattice we should be able to prevent misfit dislocations from ever appearing and thus prepare diaphragms with highly smooth surfaces. Germanium was best suited for this purpose, with 6.8 times as much Ge as B required to compensate the lattice contractile effects of boron. As can be seen from Figure 4, germanium and boron co-doping resulted in diaphragms with greatly reduced misfit dislocation density and highly smooth surfaces. The surface shown in Figure 4 had a smoothness better than 500 Å.

Since silicon is not a piezoelectric material, a highly oriented (0001) polycrystalline ZnO film is required to allow electrical excitation (and detection) of longitudinal bulk acoustic waves. The formation of this c-axis oriented layer must be closely controlled to obtain good results and careful attention to detail is necessary. A 2000 Å thick SiO<sub>2</sub> layer is first sputtered onto the epitaxial surface to mask the orthogonal symmetry of the (100) surface. This SiO<sub>2</sub> film also serves to prevent undesired metallurgical interactions between the silicon and a following titanium-gold layer that is needed for an electrical ground plane. This titanium-gold layer is a composite of 600 Å Ti/1000 Å Au/1000 Å Ti that is sequentially sputter deposited in a 2-target system to form a low resistance electrical ground plane. The presence of the titanium layers promotes good adhesion of the gold and at the same time promotes the formation of a composite layer with trigonal symmetry conducive to growth of (0001) c-axis oriented ZnO. Precise control of the ZnO sputtering conditions is essential to consistently produce 1) films of high, piezoelectric quality and high resistivity, and 2) buckle-free diaphragms. Using a side mounted substrate holder in an RF-diode reactive sputtering system, a pre-mixed 8- Argen-20 Oxygen gas fill, and a pressure of  $8-9 \times 10^{-3}$  torr was found to give optimum results. At  $12 \times 10^{-3}$  torr, good piezoelectric quality was obtained but the film resistivity tended to be low. At  $5 \times 10^{-3}$  torr, serious diaphragm buckling was encountered and the piezoelectric quality was completely degraded, even though very high resistivity films were obtained. The very close control of sputtering pressure required was accomplished with a capacitive-type Baratron pressure sensor coupled to a Granville-Phillips control valve. Surface smoothness of the sputtered ZnO was typically better than 200 Å.

A lift-off process was used to produce the resonator filter electrode metallization pattern.

A 100 Å Cr/100 Å Al/200 Å Cr metallization was vacuum deposited to form the resonator top electrode. Next, a thicker low resistance 100 Å Cr/4000 Å Al/200 Å Cr bond pad lead metallization was deposited to connect the electrode to a bonding point well off of the thin diaphragm region. The lower Cr-layer promoted good adhesion, while the upper Cr-layer served to protect the Al from chemical attack during further processing that involved etching of the excess ZnO.

#### Device Properties and Analysis

A schematic cross sectional view of a prototype BAW single resonator is shown in Figure 5. When the round trip transit time of the bulk wave between top (ZnO) and bottom (Si) surfaces of the composite diaphragm is exactly equal to the inverse of the resonant frequency, the acoustic wave reflections add in phase, establishing a high Q fundamental mode resonance. Although the resonant waves are largely confined within the volume defined by the electrode area and the diaphragm thickness, some of the acoustic energy is present in the form of acoustic fringing fields just outside of this volume. This is the basis for one form of inter-resonator coupling where strong transmission from input to output ports of a two-pole resonator filter occurs at the resonant frequency. It is this kind of interresonator coupling that we are concerned with here.

In the resonator structure depicted in Figure 5, the ZnO film extends well outside of the electrode metallization. This excess ZnO was found to cause large spurious resonance content in the resonator characteristics. These spurious resonances could be largely eliminated by applying acoustic damping materials such as glycerine to the diaphragm edges, i.e., the regions where diaphragm and supporting substrate meet. Substantial improvement in resonator quality was also consistently observed when the excess ZnO was chemically etched away outside of the electrode periphery so that only the regions immediately beneath the electrode metallization and between the electrodes of a coupled resonator filter was piezoelectrically active. Figure 6 shows a typical example of a device before and after ZnO etching. We concluded that the spurious contributions were dramatically reduced by eliminating the effects of the acoustic discontinuity of the silicon diaphragm boundaries. The ZnO/Si thickness ratio was also found to affect the spurious resonances, with ZnO/Si ratio of 0.5 or less favoring lower spurious content. The device of Figure 6 had a ZnO/Si ratio of 0.44.

In order to understand the device characteristics in terms of the many interdependent fabrication and materials parameters, a one-dimensional analysis of the equations which describe

longitudinal thickness mode bulk wave propagation and resonance was performed. The analysis takes into account the physical, acoustic, and piezoelectric properties of the resonator structure such as wave velocities, mass densities, film thicknesses, electrode area, resonator dissipation, and the piezoelectric coupling coefficient of the ZnO.<sup>12</sup> When the electrical circuit elements such as series resistance of the lead metallization  $R_{C1}$ , series inductance of the bond wire  $L_{C1}$ , and bond pad capacitance  $C_p$ , are included; the equivalent circuit shown in Figure 7 results. In this model for a single resonator, which is based on the Mason equivalent circuit<sup>13</sup>,  $C_0$  represents the ZnO film capacitance defined by electrode area and film thickness. The parallel equivalent circuit resonator resistance  $R_a$  (where  $R_a = 1/G_a$ ) arises from resonator dissipation and diffraction losses. The acoustoelectrical susceptance ( $B_a$ ), is formulated in terms of the physical thickness, density, velocity and piezoelectric constants for the composite films. An example of the agreement between theory and experiment is shown in Figure 8. When the separate materials and circuit parameters for this device (given below) were entered into the theoretical expressions described above, the resulting fit between the data and the theory was excellent. Materials thicknesses, Cr/Al = 0.15  $\mu$ m, ZnO = 4.99  $\mu$ m, Au = 0.20  $\mu$ m, SiO<sub>2</sub> = 0.15  $\mu$ m, Si = 11.2  $\mu$ m,  $K_a^2 = 0.035$  for the ZnO. Circuit elements,  $C_{p1} = 0.1$  pf,  $R_{C1} = 28$  ohms,  $C_{01} = 4.85$  pf,  $L_{C1} = 10$  nH,  $R_a = 805$  ohms,  $G_a = 1220$ ,  $L_a = 0.49$  nH,  $C_a = 1141$  pf,  $B_a = 2 \times 10^{-4}$  S,  $R_a = 1220$ .

The thin film resonator-filter construction is shown in Figure 9. This illustration depicts a rectangular resonator geometry, but unless otherwise indicated all data described herein is for a semicircular resonator geometry. In addition, Figure 9 indicates a device with the excess ZnO etched away. The equivalent circuit model for describing transmission and impedance frequency response of two acoustically coupled resonators is comprised of the models for each resonator and for the interresonator coupling. As shown in Figure 10, the acoustic coupling between resonators is modeled as an inverter network, as has previously been found valid for low frequency filters.<sup>14</sup> By analysis of experimental filter transmission phase response, the inverter element was established to be capacitive for the fundamental " $\lambda/2$ " thickness mode and inductive for the " $\lambda$ " thickness mode. For low acoustic coupling between resonators, the magnitude of the inverter impedance  $Z_{12}$  is high, corresponding to weak electrical coupling. As the acoustic coupling increases, the  $Z_{12}$  decreases, resulting in high transmission efficiency. The parasitic circuit elements  $L_a$  and  $R_a$  which shunt the acoustically coupled resonator electrodes represents the interresonator stray capacitance and resistance, and predominates in the out-of-band transmission. In the ideal case,  $Z_{12}$  approaches zero, and  $R_a$

approaches infinity. In the equivalent circuit of Figure 10,  $V_s$  = source voltage,  $Z_s$  = source impedance,  $L_c$  = lead inductance,  $C_p$  = parasitic pad capacitance,  $R_c$  = lead resistance,  $R_s$  = shunt resistance,  $C_s$  = shunt capacitance,  $Z_a$  = acoustoelectric impedance,  $C_0$  = ZnO resonator capacitance,  $G_a = 1/R_a$  = resonator dissipative resistance,  $C_a$  = equivalent resonant inductance,  $Z_{12}$  = interresonator equivalent coupling impedance, and

$$Z_{12} = \begin{cases} \frac{1}{j\omega C_{12}} & (" \lambda/2 " \text{ Mode}) \\ j\omega L_{12} & (" \lambda " \text{ Mode}) \end{cases}$$

The above described models were implemented using a UNIVAC 1110 computer to provide rapid analysis of experimental data, and to provide an accurate assessment of the effects of various electrical and acoustic parameters. The comparison of experimental data and theory was accomplished by least mean square's fit of a data set. The data was inputted via a computer terminal and an x-y digitizer.

Figure 11a shows a photomicrograph of a filter M979-7C that was chosen to illustrate the capabilities of the computer fitting routine. Figure 11b shows the measured insertion loss, which was 12.4 dB at resonance for the fundamental " $\lambda/2$ " thickness mode frequency of 531 MHz. The x-y digitizing of experimental data ignored spurious response which, for this device, are on the low frequency side of the fundamental resonance. In general, it has been observed that for ZnO/Si thickness ratios near 0.35 to 0.45, the " $\lambda/2$ " mode spurious response was significantly reduced, especially on the high frequency side. In Figures 12, 13, and 14, the results of simultaneous computer fitting for insertion loss, input resistance and reactance, and output resistance and reactance are given. As may be seen, good fits are obtained for all sets of digitized data. The two-port phase delay data is seen to be accurately modeled for the capacitive inverter coupling model. The use of an inductive inverter coupling model resulted in a phase-offset by 180° relative to the plot shown in Figure 12b. The inductive inverter model was found to be correct for coupling at the full wavelength mode.

In order to decrease the insertion loss, the length of the acoustic coupling interface between resonators was increased. With a resonator filter electrode structure such as shown in Figure 15, the coupling interface was lengthened by a factor of 3.25, while the area of the electrodes was kept constant. Note that the ZnO was etched away between uncoupled finger edges of the electrode pattern to provide isolation. The increased length of the common interface was effective in decreasing insertion loss to as low as 4.1 dB to 8 dB for a number of devices on this initial wafer. As

illustrated in Figure 16, these filters have characteristics indicating that an overcoupled response was achieved. Equivalent circuit modeling indicates that for reduction in series resistance to 5 ohms, and a parallel resonance resistance,  $R_a$ , of 800 ohms, a 2 dB insertion loss can be achieved for a critically coupled or over coupled design.

Filters with fundamental  $\lambda/2$  mode resonances ranging from 200 MHz to 570 MHz have been fabricated with out-of-band rejection as great as 45 dB, and with bandwidth between 0.1 and 5 percent. Figure 17 contains several examples of these 2-port resonator filters. All of them had ZnO/Si thickness ratios between 0.44 and 0.52.

### Conclusions

A ZnO/silicon BAW resonator and filter structure which is small enough to be incorporated within silicon integrated circuits has been investigated. The fabrication technology for producing highly planar, smooth ZnO/silicon diaphragms has been developed and found to be critically dependent on the silicon doping, chemical etching conditions, and ZnO deposition parameters. Control of ZnO deposition pressure provided buckle free, highly piezoelectric films, smooth enough for subsequent photolithography. Elimination of the ZnO film outside of the resonator electrode area, except between electrodes of a coupled resonator filter, has significantly reduced unwanted spurious modes. Control of the ZnO to silicon ratio further reduced the unwanted sidelobe content of coupled resonator filters.

One dimensional equivalent circuit analysis has adequately described the response of these devices in the absence of spurious response. This analysis and supporting experimental data indicates that low loss, low spurious response filters can be achieved with this technology in a form compatible with silicon integrated circuits.

### References

1. Grudkowski, T. W., J. F. Black, T. M. Reeder, D. E. Cullen, and R. A. Wagner: Fundamental VHF/UHF Miniature Acoustic Resonators and Filters on Silicon. *Appl. Phys. Lett.*, **37**, pp. 993-995, December 1980.
2. Lakin, K. M. and J. S. Wang: Acoustic Bulk Wave Composite Resonators. *Appl. Phys. Lett.*, **38**, pp. 125-127, February 1981.
3. Nakamura, K., H. Sasaki, and H. Slumuzer: ZnO/SiO<sub>2</sub> Diaphragm Composite Resonator on a Silicon Wafer. *Electronics Letters*, **17**, pp. 507-509, July 1981.
4. Slobodnik, V. J., T. L. Szabo, and K. R. Laker: Miniature Surface Acoustic Wave Filters. *Proc. IEEE*, **26**, pp. 129-146, January 1979.
5. Gilden, M., et al.: Design of Stable SAW Oscillators Operating Above 1 GHz. *IEEE Ultrasonic Symposium Proceedings IEEE Cat. #78CH1344-1SU*, pp. 452-457, September 1978.
6. Shreve, W. R.: Surface Wave Resonators and Their Use in Narrow Band Filters. *IEEE Ultrasonic Symposium Proceedings, IEEE Cat. #76CH1120-SSU*, pp. 706-715, October 1976.
7. Guttwein, G. K., A. D. Ballato, and T. J. Lukaszek: U. S. Patent 2 694 677, 26 September 1972.
8. Berte, M.: Acoustic Bulk Wave Resonators and Filters Operating in the Fundamental Mode at Frequencies Greater than 100 MHz. *Electronics Lett.*, **13**, pp. 248-250, April 1977.
9. Berte, M. and P. Hartemann: Quartz Resonators at Fundamental Frequencies Greater than 100 MHz. *IEEE Ultrasonic Symposium, IEEE Cat. #78CH1344-1SU*, pp. 148-151, September 1978.
10. Reisman, A., et al.: The Controlled Etching of Silicon in Catalyzed Ethylenediamine-Pyrocatechol - Water Solutions. *J. Electrochem. Soc.*, **126**, pp. 1406-1415, August 1979.
11. Lee, Y. T., N. Miyamoto, and J. Nishizawa: The Lattice Misfit and Its Compensation in the Si-Epitaxial Layer by Doping with Germanium and Carbon. *J. Electrochem. Soc.*, **122**, pp. 530-535, April 1975.
12. Grudkowski, T. W., et al.: Fundamental Mode VHF/UHF Bulk Acoustic Wave Resonators and Filters on Silicon. *IEEE Ultrasonic Symposium Proceedings, IEEE Cat. #80CH1602-2*, pp. 829-833, November 1980.
13. Mason, W. R.: *Physical Acoustics*. Vol. 1A, pp. 335-415, Academic Press, 1964.
14. Dishal, M.: Alignment and Adjustment of Synchronously Attuned Multiple-Resonant Circuit Filters. *Proc. IRE*, **39**, pp. 1448-1450, November 1951.



Figure 1. Size of ZnO/Si BAW Resonators and Filters

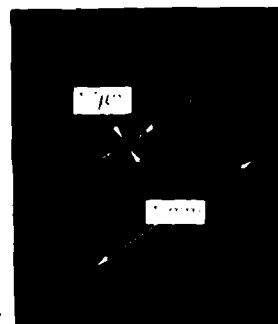


Figure 2. Cross Sectional SEM Photomicrograph of ZnO/Si Diaphragm

a) BRIGHT FIELD



b) INTERFERENCE FRINGE CONTRAST

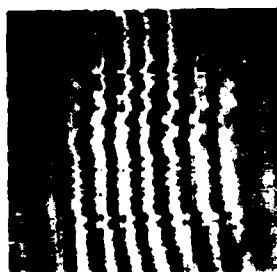


Figure 3. Substrate Surface of Etched Diaphragm, Made From Boron Doped Epitaxial Silicon

a) PHASE CONTRAST



b) INTERFERENCE FRINGE CONTRAST



Figure 4. Substrate Surface of Etched Diaphragm Made From Boron Plus Germanium Doped Epitaxial Silicon

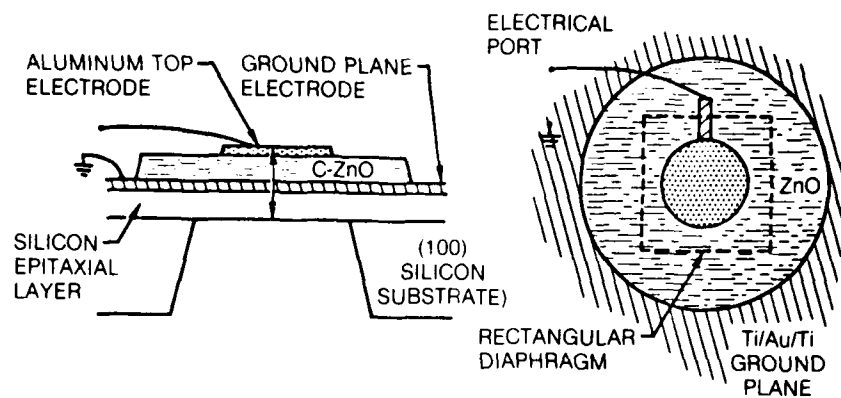


Figure 5. ZnO/Silicon Resonator Geometry

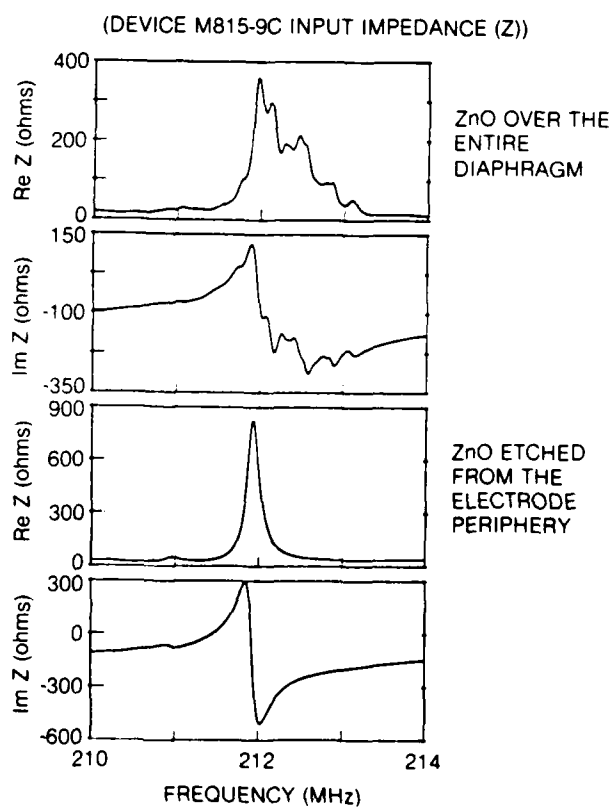
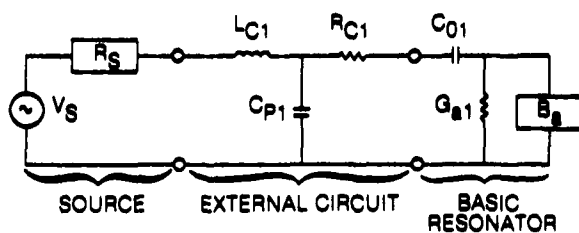
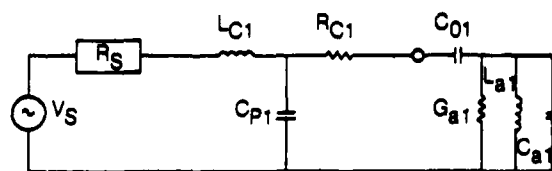


Figure 6. Effect of ZnO Removal at the Periphery of a Fundamental Mode ZnO/Si Resonator

a) ACOUSTOELECTRIC MODEL



b) LUMPED ELEMENT MODEL (VALID NEAR RESONANCE)



$$\text{RESONANT FREQUENCY, } f = \frac{1}{2\pi\sqrt{L_a C_a}}$$

$$Q = 2\pi f C_a R_a$$

Figure 7. Electrical Equivalent Circuit Models for a Single (1-Port) Resonator

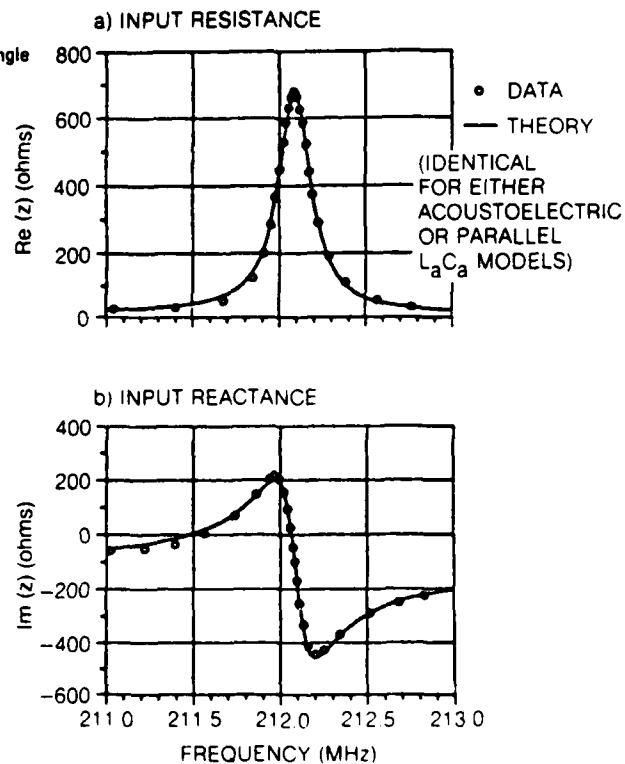
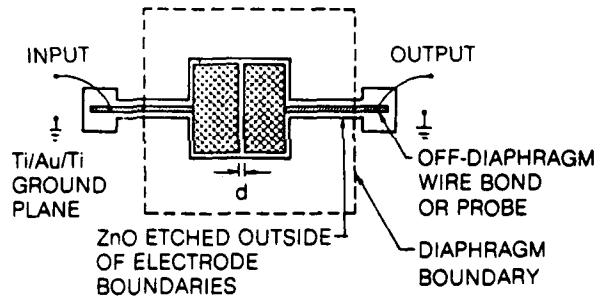


Figure 8. Computer Fit Single Resonator Impedance Response

a) TOP VIEW



b) CROSS SECTION

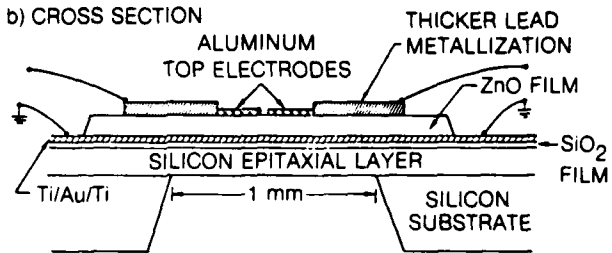


Figure 9. ZnO/Si BAW Resonator Filter Construction

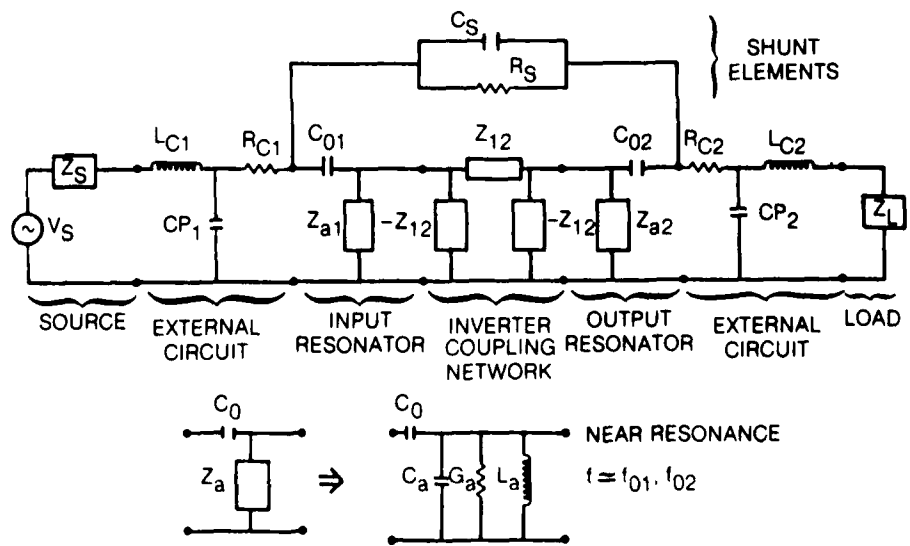
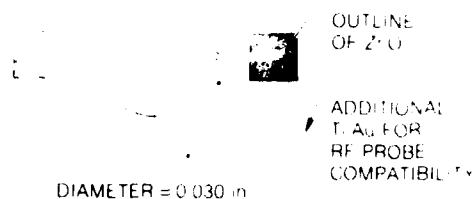


Figure 10. Equivalent Circuit for Two Acoustically Coupled BAW ZnO/Si Resonators

a) GEOMETRY



b) FUNDAMENTAL  $\lambda/2$  MODE TRANSMISSION RESPONSE

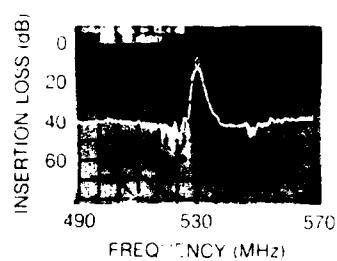
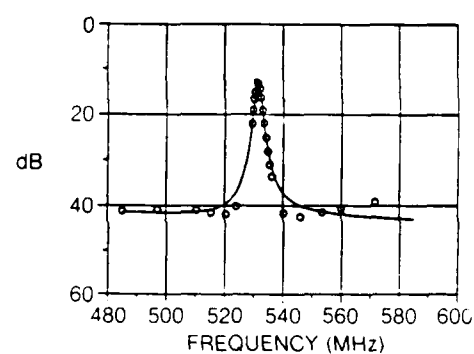


Figure 11. Filter M979-C Used for Computerized Data Fitting Example

a) INSERTION LOSS



b) TWO-PORT PHASE DELAY

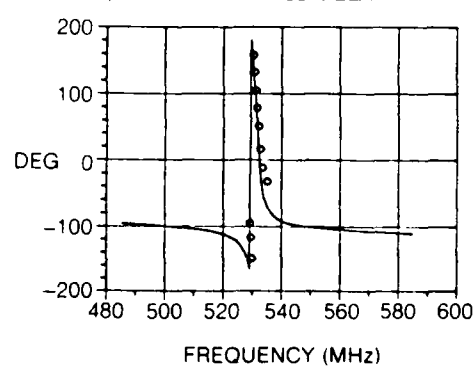


Figure 12. M979-C Computer Fitted Insertion Loss (a) and Two-Port Phase Delay (b)

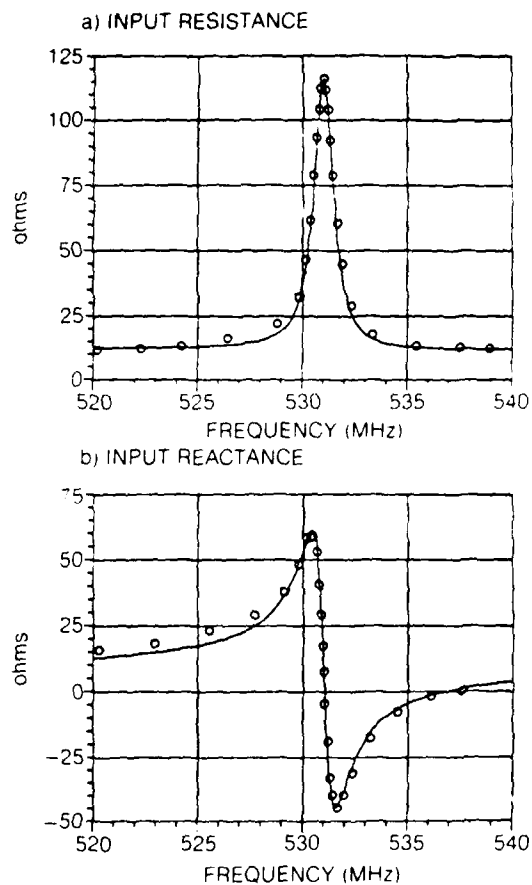


Figure 13. M979-C Computer Fitted Input Resistance (a) and Input Reactance (b)

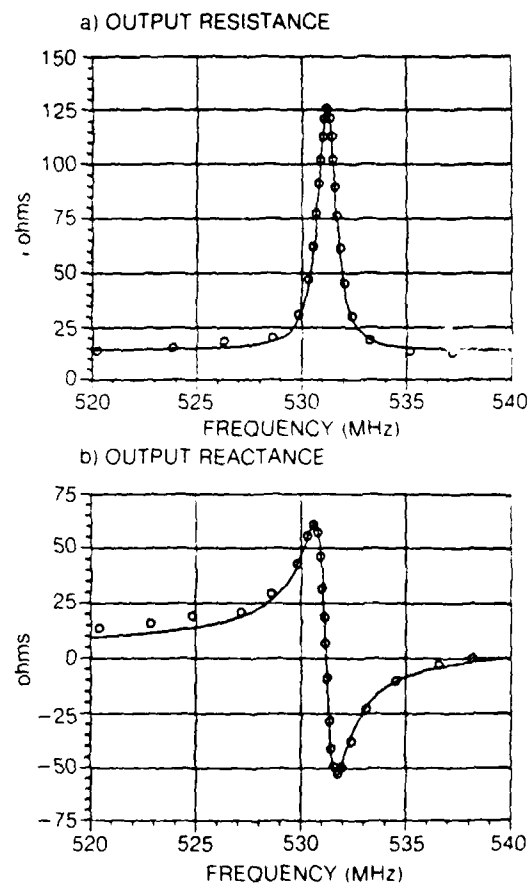
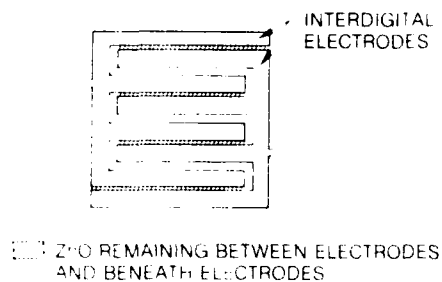


Figure 14. M979-C Computer Fitted Output Resistance (a) and Output Reactance (b)

FIG 15

1. SAWD INTERDIGITAL ELECTRODE STRUCTURE



2. CLOSE UP VIEW SHOWING LOCATION OF ZnO ETCHING

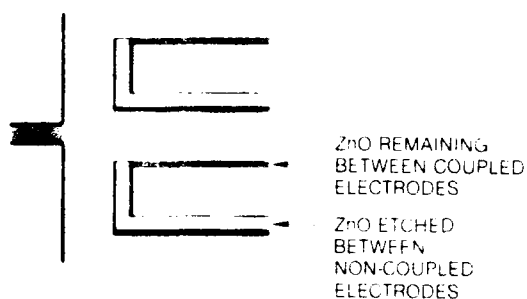


Figure 15. ZnO/Si BAW Resonator Filter Electrode Design for Increased Acoustic Coupling

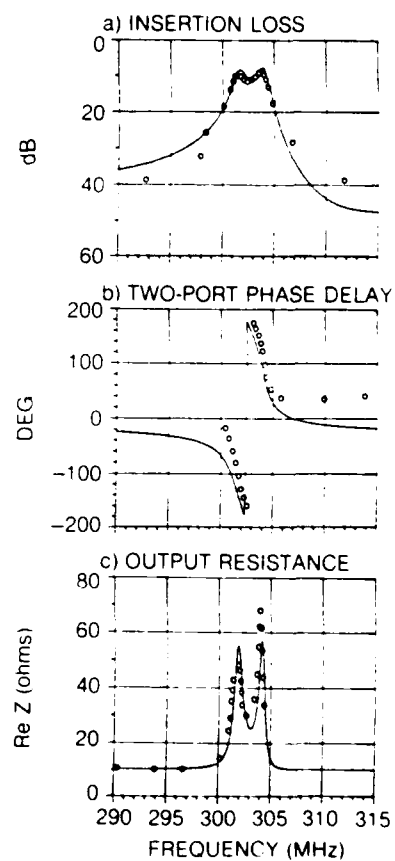


Figure 16. Overcoupled Filter Response

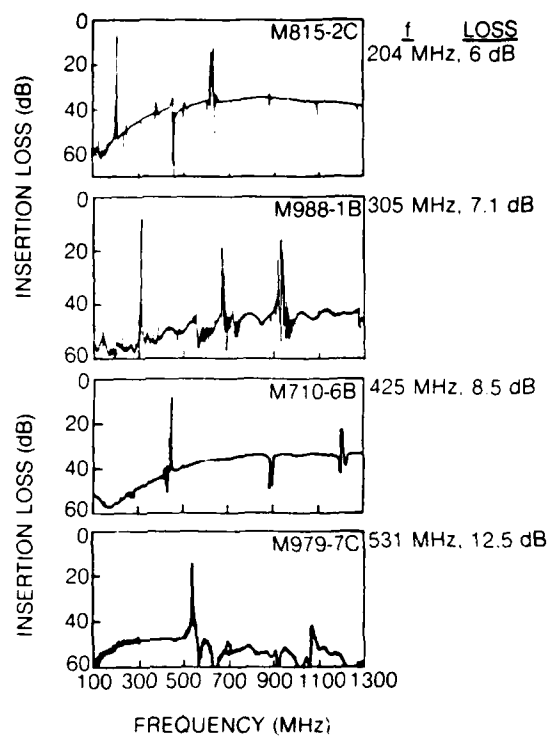


Figure 17. Transmission Response for Several 2-Port Resonator Filters

AD P001569

DEVELOPMENT AND TECHNOLOGY OF PIEZOELECTRIC BULK WAVE  
RESONATORS AND TRANSDUCERS \*

T. R. Meeker

Bell Telephone Laboratories, Inc.  
Allentown, Pennsylvania, 18103

Summary

The coupling of elastic and electrical parameters in a piezoelectric material has been widely used in a number of practical applications such as transducers for digital and analog ultrasonic delay lines and resonators for oscillators and filters.

Basic dispersion relations for elastic waves in piezoelectric plates are used to show how to understand some of the features of these devices that are of general interest to the device engineer. Some of the elementary characteristics of extensional, shear, and flexural resonators and transducers are discussed.

The concept of an exact equivalent electrical circuit for the piezoelectric plate will be reviewed and used to show how to understand some of the more important characteristics of a delay line transducer, an oscillator resonator, and a crystal filter resonator.

In order to simplify the discussion, this paper will only mention a few of the many possible device configurations. The thickness mode piezoelectric delay line transducer, the high precision quartz crystal and oscillator, the low cost wristwatch resonator, and the multiresonator monolithic crystal filter are considered as examples of applications of recent and current interest. Many other applications of crystal resonators, such as tone selection and band elimination, will not be considered in this paper.

\*Workshop on Application of Elastic Waves in Electrical Devices, Non-Destructive Testing, and Seismology, May 24-26, 1976, at Northwestern University, Evanston, Illinois; Editors - Y. H. Pao, H. E. Tiersten, and J. D. Achenbach.

Some recent reports on basic device design, fabrication techniques, and device characteristics such as temperature dependence and aging, are reviewed.

Introduction

In piezoelectric crystalline and ceramic materials electrical current and voltage are coupled to elastic displacement and stress. This coupling makes it possible to electrically excite elastic wave motions in these materials. The elastic motion can be used to launch elastic waves into other materials attached to the piezoelectric material (delay lines, ultrasonic testing, elastic wave velocity measurement, etc.) or elastic resonances can be excited by confining the elastic motion to a limited volume of the material (resonators, etc.). Resonators may be used in oscillators in frequency standards, transmission timing circuits, wrist watches, etc., or they may be coupled together electrically or elastically in frequency selective or amplitude or phase equalizing filters.

Figure 1 shows these three applications of the piezoelectric plate in schematic form. The resonator is shown at the top, the elastically coupled monolithic crystal filter is shown in the middle, and the ultrasonic delay line is shown at the bottom. In many applications the main reasons for using the piezoelectric devices are likely to be:

1. Size:

A piezoelectric resonator is about  $10^{-5}$  of the size of the electromagnetic waveguide or transmission line resonator at the same frequency.

2. Dependence of Frequency on Temperature:

Quartz resonators may have a few parts per million change in frequency for temperatures from 0° to 50°C, or thermometer crystals can be used to convert temperature changes into easily measured frequency changes.

3. Time Stability:

Quartz resonators may have frequency changes of a few parts in  $10^{11}$  per day or a few parts in  $10^6$  per 20 years.

4. Loss and Q:

Quartz resonators with Q's of  $5 \times 10^6$  at 5 MHz are used in precision oscillators.

Ultrasonic bulk wave delay lines have been used for high speed digital and analog storage in data processing systems. Other special requirements may often be satisfied best by using a piezoelectric device.

Basic Theory For Piezoelectric Plates

Most of the important properties of piezoelectric delay line transducers and crystal or ceramic resonators and monolithic crystal filters may be understood in terms of the fundamental dispersion relations for waves in piezoelectric plates. The dispersion relations express the conditions on frequency and propagation wavenumber so that waves are solutions to the appropriate differential and constitutive equations.

Figure 2 shows the basic differential, constitutive, and boundary equations for a quasi-static linear representation of a piezoelectric plate.<sup>1,2</sup> An exact solution for these equations for a three-dimensional system has not yet been found, except for some very limited conditions.<sup>3</sup> A particularly useful approximate solution for plates reduces the three-dimensional equations to a truncated set of two-dimensional equations by integrating through the thickness of the plate.

Dispersion relations and corresponding wave solutions for the lower order three basic kinds of modes included in this approximate theory of a piezoelectric plate are shown in Figure 3 and Figure 4. Figure 3 shows dispersion relations and wave solutions for quartz

plate modes varying along  $x_3$ . Figure 4 shows dispersion relations and wave solutions for quartz plate modes varying along  $x_1$ . In these two figures,  $Q$  is proportional to the product of the plate thickness and the frequency, and  $\phi$  is the wavenumber ( $2\pi$  divided by the wavelength) along the respective lateral direction.

Plate distortions or mode shapes or mode displacements are shown in Figure 5.<sup>4</sup> Higher order modes are not considered in this approximate theory. Figure 5 defines three kinds of shear distortions (thickness shear, thickness twist, and face shear), a flexural distortion, and an extensional distortion. All five of these distortions can vary along either  $x_1$  or  $x_3$ . Figure 3 and Figure 4 show that the lower order face shear, flexural, and extensional modes all have zero frequency for zero wavenumber. Thickness shear and thickness twist both have a finite frequency for zero wavenumber. The finite frequency at zero wavenumber is called a cutoff frequency, since energy propagation ceases for frequencies below this frequency. Since these features of the lower modes are also found for exact solutions of an infinite piezoelectric plate, the much simpler approximate theory can be used to develop an understanding of the role of many of the important design parameters of piezoelectric devices.

Application Of Basic Plate Theory To Resonator Design

Resonators may use either cutoff or non-cutoff modes. The non-cutoff modes (flexural, face shear, and extensional) have frequencies which are primarily determined by the lateral dimensions of the plate. Since the face shear and extensional modes have linear dispersion relations as shown in Figure 3 and Figure 4, the resonant frequencies of these kinds of resonators vary inversely with the lateral dimensions and the overtones are harmonically related. For high overtone numbers the flexural dispersion relation is also linear so that the resonant frequency varies inversely with the lateral dimensions, and the high order overtones are harmonically related. For low frequencies, however, the flexural mode dispersion relation is quite curved, and the low order flexural modes are not harmonically related. Exact design relations for these resonators are somewhat complicated, but the basic principles can be understood in terms of one lateral dimension as in Figure 3 or Figure 4. Since  $\phi = 2\pi/\lambda$ , the resonant frequency will occur when

the lateral dimension (plate length for example) is some number of half wavelengths. This means that  $L = m\lambda/2$  or  $\lambda = 2L/m$  and  $\omega_{\text{resonant}} = 2\pi/\lambda = \pi m/L$ . This relation and Figure 3 suggest that the flexural mode has the lowest frequency of the modes considered for the same overtones number and plate dimensions.<sup>9,10</sup> This small size is one of the reasons for the popularity of flexural mode resonators for small size crystal controlled oscillators such as those used in the new wrist watches.<sup>7,8</sup>

Resonators using modes with a cutoff frequency resonate at the cutoff frequency for very large lateral dimensions ( $\lambda = \pi m \rightarrow 0$ ). The cutoff frequency is inversely proportional to the plate thickness, and these modes are called thickness modes. A thin plate with large lateral dimensions may, therefore, have a high resonant frequency, so that these modes are popular for high frequency applications. Thickness overtones corresponding to various numbers of half wavelengths in the thickness are not harmonically related, especially for resonators made of material with a high piezoelectric coupling.

Figure 3 shows that as the resonant wavenumber increases, (or the appropriate lateral dimensions decrease) the resonant frequency rises. An infinite number of resonant frequencies occur on each thickness overtone branch. These frequencies are called the anharmonics of the thickness mode plate.<sup>4</sup> The thickness overtones and some of their various anharmonics are shown in Figure 6. For frequencies lower than the cutoff frequency, the wavenumber becomes imaginary, and the waves are evanescent, decaying exponentially along the lateral dimensions. For this condition, wave stress and strain become  $90^\circ$  out of phase, and the wave cannot propagate energy. This absence of energy propagation has important consequences in the design of high Q thickness mode resonators and monolithic crystal filters.

A plate with thick and thin regions has a separate dispersion relation for each region as shown in Figure 7. The resonant frequency of the thicker region is low when its lateral dimension is approximately some multiple of a half wavelength. In an actual case, both lateral dimensions and a phase shift at the resonator edge need to be considered. At the resonant frequencies of the thicker region, the allowed wavenumbers in the thinner regions are imaginary. Consequently, if the

edges of the plate are far enough away, no energy can leave the thicker region, and a very high Q results. Resonators of this kind are called trapped energy resonators.<sup>10</sup>

The thicker resonant region of the plate is commonly produced in two ways - by using a thick electrode or by contouring the plate.<sup>11</sup> The thick electrode resonator is commonly used for filter and low precision oscillator crystals, for which only moderate stability and Q are required. The contoured plate resonator with thin electrodes is commonly used for very high precision oscillator crystals, where very great stability and maximum Q are required. The contoured plate resonator is usually more expensive to make, and cost-performance tradeoffs must be examined carefully for any particular design.

The coupling between the elastic motion and the electrical current and voltage causes the resonant frequency of a piezoelectric plate resonator to depend on its electrical environment. Figure 8 shows the dispersion relation for the open circuited and short circuited thickness mode resonator. Short circuiting a resonator of this type produces effects similar to mass loading.<sup>12,13</sup> In oscillator circuits a variable series capacitor can be used to provide the necessary electrical changes, and the resonant frequency may be adjusted or "pulled" by the capacitor.<sup>14</sup> A second consequence of this effect is that careful attention to the electrical environment is necessary in the design of oscillator resonators and filter crystals.

If the lateral dimensions of the plate are very large (infinite), the equations in Figure 2 can be solved exactly. In this solution it is important to define a consistent set of definitions for the generalized stresses and flows at the system boundaries. For a simple electrical system, this consistent set of definitions involves the signs of the voltage and current flow at each electrical port of the system. For the piezoelectric transducer, the electrical port must be treated in the same way, but in addition, the stress and particle velocity at each of the plate surfaces must be defined. Figure 9 shows a set of convenient boundary definitions for the thickness mode piezoelectric transducer.<sup>7,15</sup> The boundary definitions defined in Figure 9 and solutions to the equations of Figure 2 can be expressed as the set of generalized impedance equations shown in Figure 10.<sup>16</sup> The impedance equations give the relationship

between the electrical current and voltage and the stresses and particle velocities on the two plate surfaces. All of the transducer and resonator properties of the large area plate may be derived from these impedance equations. An exact equivalent circuit (with the same impedance equations) for the piezoelectric plate is shown in Figure 11.<sup>2,15,16</sup> Some properties of the plate are easier to understand in terms of the equivalent circuit, although both representations (circuit or impedance equations) are complete in themselves.

When the surfaces of the large area plate are stress free, the exact electrical impedance is shown in Figure 12. This condition is quite accurate for a resonator so that Figure 12 is a good description of the impedance of a piezoelectric thickness mode resonator. In Figure 12 the frequencies of zero impedance are resonant frequencies (short circuit natural frequencies) and the frequencies of zero admittance are antiresonant frequencies (open circuit natural frequencies). The frequencies of zero impedance are at the value of  $X$  for which  $1/k^2 = \tan(x)/x$ . The first two resonant frequencies are at  $X = X_{1r}$  and  $X = X_{3r}$ . The frequencies of zero admittance or infinite impedance are at the infinite values of  $\tan(x)/x$ . The first two antiresonant frequencies are at  $X = X_{1a} = \frac{\pi}{2}$  and  $X = X_{3a} = \frac{3\pi}{2}$ . The shape of the  $\tan(x)/x$  curve causes anharmonic behavior in the resonant frequencies. The antiresonant frequencies are harmonically related. Boundary or material loss causes shifts in these frequencies. A discussion of the loss question is beyond the scope of this paper. Figure 13 shows the ratio of the first resonant frequency to the first antiresonant frequency versus the piezoelectric coupling.<sup>17</sup> The significance of these two frequencies is that a circuit composed of a resonator in series with a capacitor has a resonant frequency between  $\omega_1$  and  $\omega_0$ , depending on the value of the capacitor. Figure 12 shows how to understand the well known result that this effect is smaller for resonator overtone operation. In the design of crystal controlled oscillators, fundamental modes in plates made of materials with high piezoelectric coupling are used for applications in which a wider range of adjustment is desired and higher overtone modes in plates made of material with low piezoelectric coupling are used in applications in which relative insensitivity to circuit variation is desired.

#### Application Of The Basic Theory To The Design Of Piezoelectric Transducers

If a plate of material sustaining a mode with real wavenumber is attached to a material which can support a corresponding propagating mode, the plate may transfer energy into that mode as a transducer. The transducer may also be used as a detector to convert elastic waves into an electrical signal.

The impedance equations or the exact equivalent circuit in Figures 9, 10 and 11 have also been used to understand both the sending and the receiving properties of the piezoelectric transducer.<sup>2,15,16</sup> In the absence of transducer loss, it is possible to tune the two transducers for zero insertion loss with a bandwidth determined by the piezoelectric coupling. A compromise between insertion loss and bandwidth has been used in the design of digital delay lines.

#### Temperature Dependence And Time Stability Of Quartz Crystal Resonator Frequency

Two very important characteristics of the quartz crystal resonator are the temperature dependence and time stability of resonant frequency. Many other important resonator characteristics, such as the effects of changing to other materials, mounting and packaging, impedance level, and unwanted resonances are not discussed in this paper.

Early work on the temperature dependence of resonant frequency of quartz resonators operating in the modes shown in Figure 3 and Figure 4 (extensional, face shear, flexural, thickness-shear, and thickness-twist) showed either parabolic or cubic behavior, depending on the particular crystal cut used.<sup>6,18,19</sup>

Four useful properties of the crystal resonator, which depend on the crystal orientation, the resonator dimensional ratios, or the electric field distribution, have limited the design of resonators to a few crystal orientations and mode types. The four properties listed are not the only ones of importance, and each application has other criteria which will not be mentioned here.

1. The effective coupling to the mode of interest.
2. The suppression of other modes.

3. The temperature coefficient of the desired mode.
4. The complexity and resultant cost of manufacturing plates and bars of multiply rotated crystal cuts.

Figure 14 and Figure 15 show some of the resonator types which have been widely used. Figure 14 shows typical temperature characteristics for three common quartz flexural mode resonators. The turnover temperature (temperature of zero dependence of frequency on temperature) can be placed at various temperatures or the temperature coefficient may be made positive or negative.

Figure 15 shows temperature characteristics for an extensional mode (E), face shear modes (CT and DT), and thickness shear modes (BT, AT, and GT). The cubic temperature dependence of the AT and GT resonators gives a wide temperature range with very small frequency shifts. In Figure 15 the extensional and face shear modes are usually designed at lower frequencies than the thickness shear modes, so that the smaller frequency shift in parts per million does not imply a smaller shift in absolute frequency with temperature.

A second very useful property of the piezoelectric resonator is the inherent stability with time. This property, particularly for the quartz resonator, has not been matched by any other technology and a great deal of effort has been applied to its optimization. Many studies reported over the last forty years have led to an understanding of the role of resonator fabrication techniques and design in determining the time stability. The effects of plate preparation, premetallization cleaning, electrode metallization choice and thickness, mounting, and packaging have been studied in some detail. System demands for greater stability at lower cost make it necessary to continue to evaluate the capability of present fabrication techniques and of newer techniques. Some of the results of studies on time stability reported recently are listed in Figure 16 for various applications. Short term (pp10<sup>-11</sup>/day) and long term (pp 10<sup>-6</sup>/20 years) stabilities are shown.<sup>7,20,21,22,23</sup> Although these aging rates are nearly the same, some applications emphasize short term stability (precision oscillators), while other applications emphasize long term stability (crystal filters).

## Resonator Design And Fabrication Techniques

It is not within the scope of this paper to discuss design and fabrication techniques in detail, but it seems worthwhile to at least outline some of the important considerations. Figure 17 is an outline of some of the important factors in a typical resonator design. The plate, electrode, attachment, enclosure, and test requirements are included. Figure 18 shows some of the important fabrication techniques used in the manufacture of quartz resonators.<sup>11,19</sup>

Similar design and fabrication techniques are used for monolithic crystal filter production. For low cost resonator and monolithic crystal filter production the relationship between initial and end-of-life requirements, design, and fabrication techniques must be carefully optimized.

## The Piezoelectric Crystal Oscillator

The oscillator is one of the most important applications of the piezoelectric resonator.<sup>24</sup> The available impedance levels, time stability, and cost of the crystal resonator have been optimized for a wide variety of different kinds of applications, such as the precision crystal oscillator<sup>21</sup> and the recently developed wrist watch.<sup>8</sup> A very schematic representation of a crystal oscillator circuit, some properties of the oscillator, and some applications are shown in Figure 19.

## Piezoelectric Crystal Filter

Two kinds of crystal filters are in current use. One kind uses crystal resonators to replace the tuned LC tanks of the conventional filter circuit.<sup>16</sup> The higher Q of the crystal resonator is highly desirable in realizing higher frequency filters. The factors affecting the choice of a particular filter design will not be discussed here. In the last few years, techniques for putting several resonators on the same crystal plate and using the separation between the resonators to control the interresonator coupling have been developed.

These structures are true monolithic crystal filters in the sense that all elements of the filter are on one piece of material with no assembly other than mounting and packaging being necessary.<sup>10,25</sup> No external tuning is needed for some applications.

Various combinations of monolithic crystal multi-resonator devices and electrical components have been used to control stop band performance and optimize the filter cost.<sup>25</sup> A two resonator ladder filter design in electrical form is shown in Figure 20. This design is easily transformed to as monolithic crystal filter design. Some properties and applications of interest are shown in Figure 20.

#### Ultrasonic Delay Line Transducer

Ultrasonic bulk wave delay lines have been developed for high frequency storage of information.<sup>15</sup> Figure 21 shows some circuit considerations and application of the ultrasonic delay line and transducer.

#### Conclusions

The basic theory of the piezoelectric plate is reviewed, with special emphasis on the use of dispersion relations (conditions between wave number and frequency) to understand some of the properties of the trapped energy resonator and the monolithic crystal filter. An important approximate theory is mentioned and used to define the dispersion relation for flexural, extensional, face shear, thickness-shear, and thickness-twist modes.

The exact equivalent electrical circuit of the piezoelectric plate is used to show how to understand the effect of the electrical circuit on the frequency of a resonator. The temperature performance and the time stability of several kinds of quartz resonators are reviewed briefly. A list of resonator design and fabrication techniques are presented. Applications in oscillators, crystal filters, and delay line transducers are discussed.

No paper of this scope and length can possibly do full justice to the subject considered. The presentation of a very brief introduction to some basic principles is all that has been attempted.

#### References

- [1] H. F. Tiersten, Linear Piezoelectric Plate Vibrations, Plenum, New York, 1969.
- [2] T. R. Meeker, "Thickness Mode Piezoelectric Transducers", Ultrasonics, Vol. 10-1, 1972, pp 26-36.
- [3] P. C. Y. Lee and S. Syngellakis, "Waves and Vibrations in an Infinite Piezoelectric Plate", in: Proceedings of the 29th Annual Symposium on Frequency Control, U.S. Army Electronics Command, Fort Monmouth, New Jersey, 1975, pp 65-70.
- [4] R. D. Mindlin and W. J. Spencer, "Anharmonic Thickness-Twist Overtones of Thickness-Shear and Flexural Vibrations of Rectangular AT-Cut Quartz Plates", J. Acoust. Soc. Am. 42, 1967, pp 1268-1277.
- [5] J. H. Staudte, "Subminiature Quartz Tuning Fork Resonator", in: Proceedings of the 28th Annual Symposium on Frequency Control, U.S. Army Electronics Command, Fort Monmouth, New Jersey, 1973, pp 50-54.
- [6] N. J. Beane and R. C. Richards, "Flexure Mode Quartz Oscillators", The Marconi Review, No. 111, Vol. XVI, 1953, pp 141-168.
- [7] J. Engdahl and H. Matthew, "32 kHz Quartz Crystal Unit for High Precision Wrist Watch", in: Proceedings of the 29th Annual Symposium on Frequency Control, U.S. Army Electronics Command, Fort Monmouth, New Jersey, 1975, pp 19-87-194.
- [8] H. Yoda and N. Horie, "Technical Aspects of Crystal Wrist watches", in: Proceedings of the 28th Annual Symposium on Frequency Control, U.S. Army Electronics Command, Fort Monmouth, New Jersey, 1974, pp 57-66.
- [9] T. R. Meeker, "Plate Constants and Dispersion Relations for Width-Length Effects in Rotated Y-Cut Quartz Plates", in: Proceedings of the 29th Annual Symposium on Frequency Control, U.S. Army Electronics Command, Fort Monmouth, New Jersey, 1975, pp 54-64.
- [10] W. J. Spencer, "Monolithic Crystal Filters", in: Physical Acoustics, Vol. I, Principles and Methods (W. P. Mason and R. N. Thurston, ed.), Academic Press, New York, 1972, pp 167-220.
- [11] R. E. Bennett, "Quartz Resonator Handbook-Manufacturing Guide for AT Type Units", Union Thermoelectric Company, Mies, Illinois, Clearinghouse PB171839, 1960.

- [12] A. Ballato and T. Lukaszek, "Mass Effects on Crystal Resonators with Arbitrary Piezo-Coupling", in: Proceedings of the 27th Annual Symposium on Frequency Control, U.S. Army Electronics Command, Fort Monmouth, New Jersey, 1973, pp 20-29.
- [13] O. Lewis and C. Lu, "Relationship of Resonant Frequency of Quartz Crystal to Mass Loading", in: Proceedings of the 29th Annual Symposium on Frequency Control, U.S. Army Command, Fort Monmouth, New Jersey, 1975, pp 5-9.
- [14] W. G. Cady, Piezoelectricity, Vol. I, Rev. Ed., Dover Publications, New York, 1964, pp 365-366.
- [15] E. K. Sittig, "Design and Technology of Piezoelectric Transducers for Frequencies Above 100 MHz", in: Physical Acoustics, Vol. IX, Principles and Methods (W. P. Mason and R. N. Thurston, Ed.) Academic Press, New York, 1972, pp 221-275.
- [16] W. P. Mason, Electromechanical Transducers and Wave Filters, D. Van Nostrand Co., Princeton, 1948, p 403.
- [17] M. Onoe, H. F. Tiersten, and A. H. Meitzler, "Shift in the Location of Resonant Frequencies Caused by Large Electromechanical Coupling in Thickness-Mode Resonators", J. Acoust. Soc. Am., Vol 35, No. 1, 1963, pp 36-42.
- [18] W. P. Mason, Piezoelectric Crystals and Their Application to Ultrasonics, D. Van Nostrand Co., Princeton, New Jersey, 1950, pp 95-106.
- [19] R. A. Heising, Quartz Crystals for Electrical Circuits - Their Design and Manufacture, D. Van Nostrand Co., New York, 1946, pp 23-56.
- [20] S. H. Olster, I. R. Oak, G. T. Pearman, R. C. Rennick and T. R. Meeker, "A6 Monolithic Crystal Filter - Design for Manufacture and Device Quality", in: Proceedings of the 29th Annual Symposium on Frequency Control, U.S. Army Electronics Command, Fort Monmouth, New Jersey, 1975, pp 105-112.
- [21] M. B. Block and J. L. Denman, "Further Development on Precision Quartz Resonators", in: Proceedings of the 28th Annual Symposium on Frequency Control, U.S. Army Electronics Command, Fort Monmouth, New Jersey, 1974, pp 73-84.
- [22] G. Gilbert, J. S. Brousson, and J. Morel, "Quartz Crystal Units for Space Applications", in: Proceedings of the 27th Annual Symposium on Frequency Control, U.S. Army Electronics Command, Fort Monmouth, New Jersey, 1973, pp 39-41.
- [23] E. P. Err Nisse, "Quartz Resonator Frequency Shifts Arising from Electrode Stress", in: Proceedings of the 29th Annual Symposium on Frequency Control, U.S. Army Electronics Command, Fort Monmouth, New Jersey, 1975, pp 1-4.
- [24] W. A. Edson, Vacuum-Tube Oscillators, John Wiley and Sons, Inc., 1953, pp 111-120.
- [25] G. T. Pearman and R. C. Rennick, "Monolithic Crystal Filters", IEEE Transactions on Sonics and Ultrasonics, Vol. SU-21, No. 4, 1974, pp 238-243.

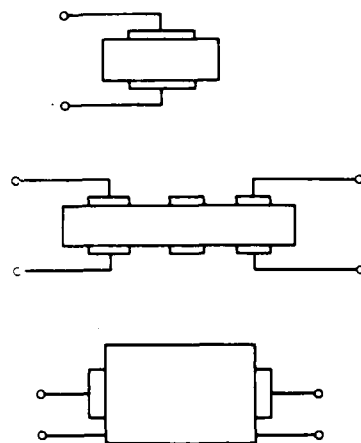


Figure 1. Three Applications of the Piezoelectric Plate:  
Resonator, Monolithic Crystal Filter, Ultrasonic  
Transducer

#### BASIC DESCRIPTION OF A PIEZOELECTRIC TRANSDUCER

##### POTENTIALS

ELASTIC DISPLACEMENT -  $\mu_i$

ELECTRIC POTENTIAL -  $\phi$

##### FIELDS

ELASTIC STRAIN -  $S_{ij} = \frac{1}{2} (\mu_{i,j} + \mu_{j,i})$

ELECTRIC FIELD -  $E_i = -\phi_{,i}$

##### CONSTITUTIVE RELATIONS

ELASTIC STRESS -  $T_{ij} = C_{ijkl}^E S_{kl} - e_{kij} E_k$

ELECTRIC DISPLACEMENT -  $D_j = e_{jkl} S_{kl} + \epsilon_{jk}^S E_k$

##### DIFFERENTIAL EQUATIONS

NEWTON'S LAW FOR CONTINUUM -  $T_{ij,i} = \rho \mu_{,j}$

MAXWELL'S EQUATION -  $D_{i,i} = 0$

##### BOUNDARY CONDITIONS ON PLATE SURFACES

ELECTRICAL -  $\phi$  &  $D_j$

MECHANICAL -  $T_{ij}$  &  $\mu_{,i}$

Figure 2. Basic Description of a Piezoelectric Transducer

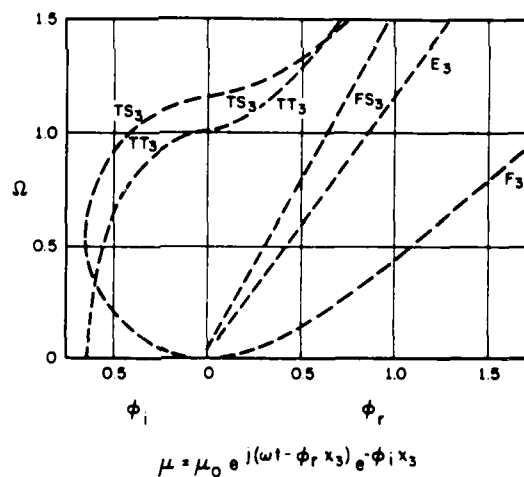


Figure 3 Dispersion Curves for  $X_3$  Propagation in an  $X_2$  Plate

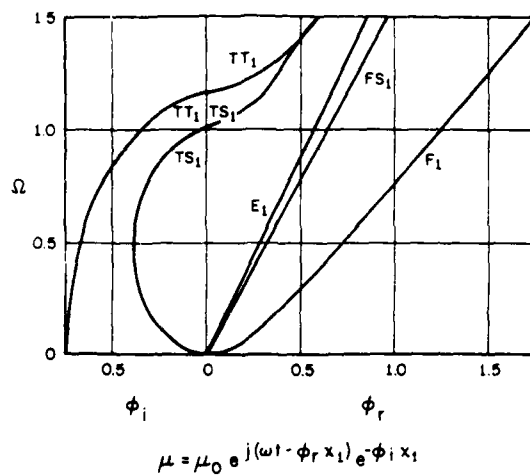


Figure 4. Dispersion Curves for  $X_1$  Propagation in an  $X_2$  Plate

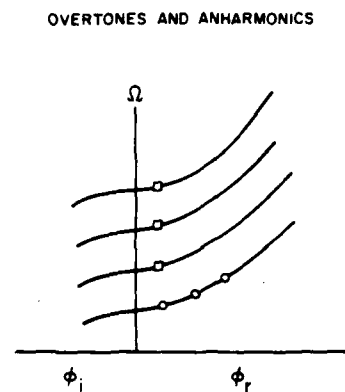


Figure 6. Overtones and Anharmonics

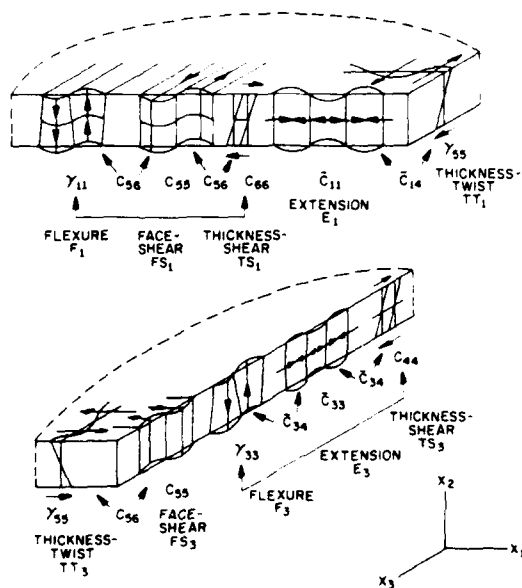


Figure 5. Basic Mode Types in an  $X_2$  Plate

#### MASS LOADING AND THICKNESS CONTOURING

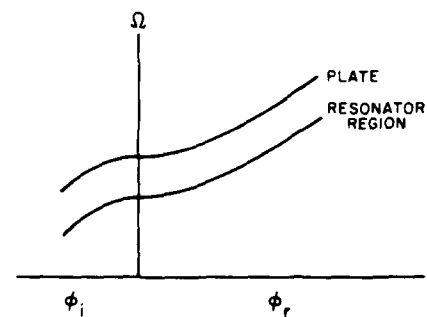


Figure 7. Mass Loading and Thickness Contouring

# PIEZOELECTRIC EFFECTS

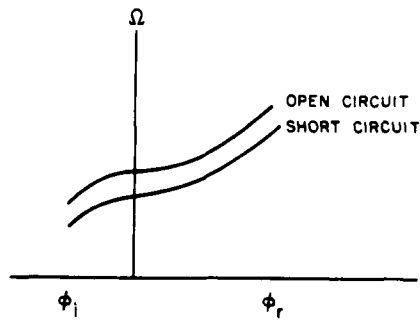


Figure 8. Piezoelectric Effects

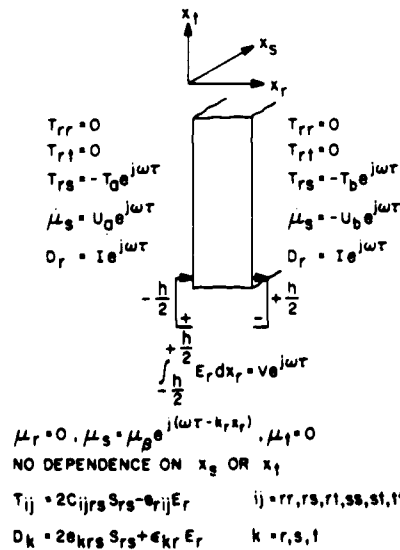


Figure 9. Boundary Conditions for a  $X_r$  Piezoelectric Plate

## IMPEDANCE EQUATIONS FOR THICKNESS MODE PIEZOELECTRIC TRANSDUCER

$$I \quad T_a = -jz_t \frac{C}{S} U_a - jz_t \frac{1}{S} U_b + \frac{\Phi A}{j\omega C_0} \frac{I}{A}$$

$$II \quad T_b = -jz_t \frac{1}{S} U_a - jz_t \frac{C}{S} U_b + \frac{\Phi A}{j\omega C_0} \frac{I}{A}$$

$$III \quad V = \frac{\Phi A}{j\omega C_0} U_a + \frac{\Phi A}{j\omega C_0} U_b + \frac{A}{j\omega C_0} \frac{I}{A}$$

$$C = \cos k_r h, \quad S = \sin k_r h,$$

$$k_r = \omega \sqrt{\frac{\rho}{C'_{rsrs}}}, \quad z_t = \sqrt{\rho C'_{rsrs}}$$

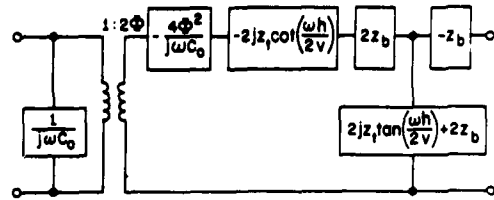
$$C_0 = \frac{\epsilon_{rr}^s A}{h}, \quad \frac{\Phi A}{C_0} = \frac{e_{rrs}}{\epsilon_{rr}^s}$$

$$\Phi = \frac{e_{rrs}}{h}$$

$$C'_{rsrs} = C_{rsrs}^E + \frac{e_{rrs} e_{rrs}}{\epsilon_{rr}^s}$$

Figure 10. Impedance Equations for Thickness Mode Piezoelectric Transducer

# EXACT EQUIVALENT ELECTRICAL CIRCUIT



$$\Phi = \frac{\theta rrs}{h} \quad z_1 = \sqrt{\rho C' rrs} \quad C_0 = \frac{\epsilon_{rr}}{h}$$

$$\frac{\omega h}{2v} = \frac{\omega h}{2} \sqrt{\frac{\rho}{C' rrs}} \quad 4\Phi^2 = \frac{4}{\pi} (\omega_0 C_0) z_1 k^2$$

$$k^2 = \frac{\theta rrs \theta rrs}{C' rrs \epsilon_{rr}} \quad \frac{\omega_0 h}{2v} = \frac{\pi}{2}$$

Figure 11. Exact Equivalent Electric Circuit

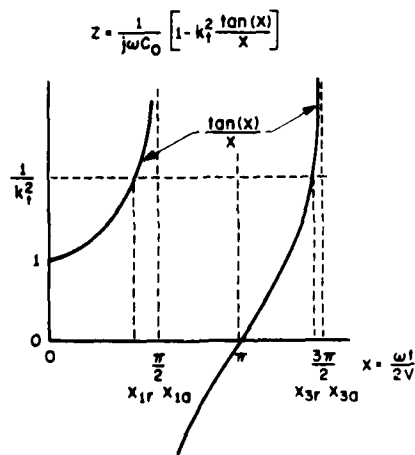


Figure 12. Electrical Impedance of Ideal Lossless Thickness Mode Resonator

# DEPENDENCE OF RATIO OF MECHANICAL SERIES FREQUENCY ( $\omega_1$ ) TO HALF WAVE FREQUENCY ( $\omega_0$ ) ON THE PIEZOELECTRIC COUPLING

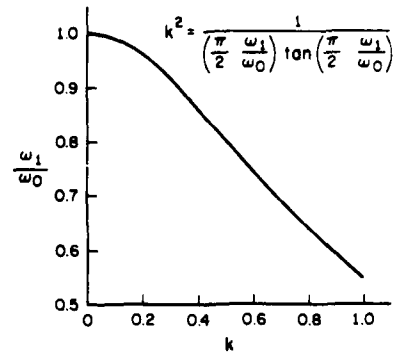


Figure 13. Dependence of Ratio of Mechanical Series Frequency to Half Wave Frequency on the Piezoelectric Coupling

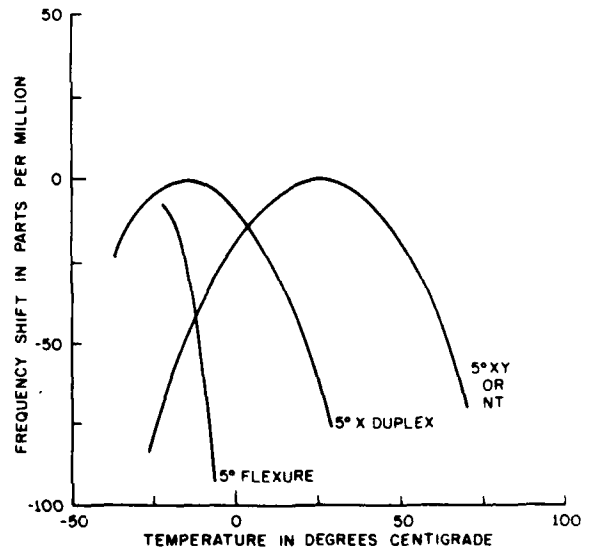


Figure 14. Temperature Coefficients

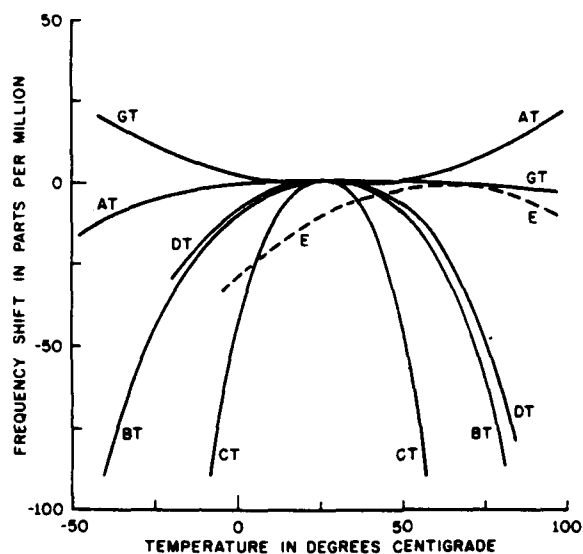


Figure 15. Temperature Coefficients

#### ELEMENTARY CRYSTAL RESONATOR DESIGN TECHNOLOGIES

##### PLATE

ANGLE  
SIZE  
SHAPE  
FINISH  
THICKNESS  
CONTOUR

##### ELECTRODE

METAL  
AREA  
SHAPE  
THICKNESS

##### ATTACHMENTS

TYPE  
MATERIAL

##### ENCLOSURE

SHAPE  
ENVIRONMENT

##### TEST REQUIREMENTS

Figure 17. Elementary Crystal Resonator Design Techniques

#### TIME STABILITY OF PIEZOELECTRIC RESONATORS

##### FILM STRESS

5 PPM TOTAL

##### 32 KHZ WATCH CRYSTAL

XY FLEXURE - RT

.5 MIN/YR.

1 PPM/YR.

##### 8 MHZ A6 MONOLITHIC CRYSTAL FILTER

1 TO 2 PPM/20 YR. AT 50°C

##### PRECISION OSCILLATOR

2 TO 7 PP10<sup>11</sup>/DAY

##### 38 MHZ - THIRD OVERTONE

2 PPM/YR. - RT

Figure 16. Time Stability of Piezoelectric Resonators

#### ELEMENTARY CRYSTAL RESONATOR FABRICATION TECHNIQUES

##### WAFERING

##### LAPPING

##### POLISHING

##### ETCHING

##### CLEANING

##### METALLIZING

##### ADJUSTING

##### BONDING

##### CLEANING

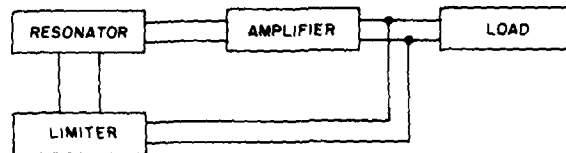
##### ENCLOSING

##### TESTING

Figure 18. Elementary Crystal Resonator Fabrication Techniques

## PIEZOELECTRIC CRYSTAL OSCILLATORS

### CIRCUIT CONSIDERATIONS



LOOP PHASE AND GAIN  
CRYSTAL PULLING  
CRYSTAL STABILITY  
COST

### APPLICATIONS

SIGNAL GENERATION  
PRECISION SYSTEM CLOCKING  
WRIST WATCH

Figure 19. Piezoelectric Crystal Oscillator

## ULTRASONIC DELAY LINE TRANSDUCERS

### CIRCUIT CONSIDERATIONS

EQUIVALENT ELECTRICAL CIRCUIT  
IMPEDANCE LEVEL  
BANDWIDTH  
TUNING  
MATCHING

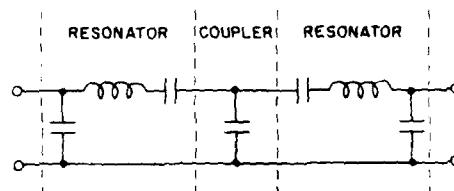
### APPLICATIONS

ULTRASONIC TESTING  
DIGITAL DELAY LINES  
ANALOG DISPERSIVE DELAY LINE  
ANALOG NONDISPERSIVE DELAY LINE

Figure 21. Ultrasonic Delay Line Transducer

## PIEZOELECTRIC CRYSTAL FILTERS

### EQUIVALENT CIRCUIT CONSIDERATIONS



### MONOLITHIC CRYSTAL FILTER

TRANSMISSION BAND CONTROL  
IMPEDANCE LEVEL  
STABILITY  
COST

### APPLICATIONS

SIGNAL SELECTION - PILOT TONES  
CHANNEL BANK SIDEBAND SELECTION  
TELEVISION, RADIO, CITIZENS BAND

Figure 20. Piezoelectric Crystal Filter

TEMPERATURE COMPENSATED CRYSTAL OSCILLATOR PANEL DISCUSSION

PANEL CHAIRMAN - Dr. D. E. NEWELL, NORTHERN ILLINOIS UNIVERSITY - PANEL MEMBERS - Dennis Marvin-Motorola; Kurt Bowen-CTS Corp; A.J. Slobodnik, Jr.-Rome Air Development Center; Jack Saunders-Saunders Associates; Marvin Freiking-Rockwell International; Walter Galla-McCoy Electronics

AD P001570

Q: At what stability-temperature range does the practicality of digital compensation exceed analog compensation and what is the future of digital compensation?

Digital compensation becomes practical for units with an overall frequency tolerance of less than 0.5 ppm. The future of digital compensation is very much dependent on the suitability of the crystals that are produced.

Q: What are some of the critical component requirements affecting the miniaturization of TCXO's?

The quality of thermistors is one of the most important factors in the miniaturization of TCXO's. Chip thermistors offer a reasonable alternative to conventional devices. Screened thermistors on the other hand, are lacking in beta and in the consistency of the resulting device.

Q: What trends will be seen in the area of data collection and compensation techniques?

Automated data collection is one of the easiest and surest ways to reduce the per oscillator labor cost. The demand for low cost units will make auto collection commonplace. Data collection of total oscillator performance parameters seems to be the easiest way to go for tighter tolerance oscillators, provided the compensation is done during the compensation run. Among the three common methods of accomplishing the voltage function, A) tweaking pot B) compensation based on crystal data C) pull data, there is a need to determine which is the most useful for a given accuracy. Because of the increasing availability of dedicated computational capabilities, analog compensation techniques will develop to point where the compensation operation will be done on the fly, not unlike digital compensation.

Several methods of compensation were reviewed during the course of the discussion. One method is implemented by varying the oscillating loop frequency. This approach is used for varactor modulator type systems. From this information, biasing resistors can be determined for a specific compensation network. The resistor value is determined by the data taken at several specific temperature points. A second approach involved the use piec-wise compensation segments controlled by switching networks. The segments are switched in and out according to preset temperature points.

After introductions by the panel chairman, Dr. Newell, the panel entered into a discussion of several prepared topic areas.

Q: What are the anticipated market trends in TCXO production?

The consensus of the panel is that the next few years will see a majority of the TCXO's made with specifications in the area of 1 to 2 ppm over an operational temperature range of -40°C to +95°C. Packaging requirements will dictate shape factors corresponding to the standard 14 pin DIP package or in some cases a double height DIP package. Output power for these devices is anticipated to be in the range of 0 dbm to 5 dbm. The trend of the market is for higher frequency units. This last is expected to continue to even higher frequency requirements in the future.

A: What are the cost as a function of performance considerations?

The per unit cost for units used in the 2-way radio market must come down. The oscillator is now a major factor in the cost of a 2-way radio. The 2 ppm unit of tomorrow must be produced for the same cost as today's 5 ppm unit.

Computerized compensation involves the combination of measured crystal data, table values of thermistors, and varactor data as the input for an iterative algorithm. A variation on this approach requires that the oscillator be subjected to a pull run. The results of the pull run are combined with other data in a computer program. In the most elaborate approach, the complete oscillator, including thermistors, is subjected to a pull run. Varactor pull data and thermistor values at specific temperatures are acquired. This data serves as the input data for a computer program.

Q: What are the effects of the accuracy of component data on the compensation approach?

At least one member of the panel indicated that the characterization of thermistors is so variable as to make it unuseable. The variability of thermistors was a common complaint among most panel members. However it was agreed that there are cases where the nominal thermistor data may be used. Varactors are generally specified according to nominal value and slope. There is enough variability among devices such that the entire compensation network may be affected. There was a general feeling that the quality of data for the crystal has improved during the past five years and because of this the hysteresis and coupled mode analysis will become easier.

Q: What are the effects of sealing on compensation changes?

There is little information available on this topic fundamentally because most manufacturers have avoided extensive sealing of units. The broader range of environmental specifications, including tighter humidity specifications, may require sealing of units in the future. It may be possible to accomplish this sealing with a low-temperature hermetic seal. Circuit boards and components that absorb moisture may become a problem at some point. The change in the stray capacitance of coils, due to a condensing humidity environment, is presently one of the most serious environmental considerations.

Q: What are some of the major problems that remain in TCXO production?

A common concern expressed by members of the panel was the question of crystal hysteresis. This phenomena may be the limit factor in the production of a 1 ppm oscillator. The question of how to minimize the hysteresis was put forth as a vital concern to all. Other problems mentioned included trim range, room offset and frequency stability problems. With regard to frequency adjustment requirements continuing improvement in the quality and characteristics of the basis crystal will lead to an almost total elimination for this operation. Today a range of  $\pm 10$  ppm is no longer necessary for some units.

Q: What are the testing and burn in requirements likely to be for the future?

Temperature runs will obviously continue to

be required for a long time. A ramp cycle is necessary for the design phase but logistical problems limit its usefulness in production. Discrete temperature runs are much easier to accomplish but must include enough points to truly characterize the unit under test. The trend for burn in is moving toward a 100% burn in of all units shipped. This probably the only effective way to eliminate the DOA and bad agers.

The following three papers were presented as further background material.

## METHODS OF TEMPERATURE COMPENSATION

M. E. Frerking

Collins Telecommunications Products Division  
 Defense Electronics Operations  
 Rockwell International Corporation

AD P001571

Temperature compensation of crystal oscillators has been successfully employed since the early 1960's and a large number of networks and techniques have been employed with varying degrees of success. This paper addresses several of the major methods which have been used for compensation of precision crystal oscillators. The methods which are considered are enumerated in Figure 1.

Before describing these methods, it may be desirable to review briefly the frequency vs temperature characteristics of AT and SC cut crystals. These are shown in Figure 2 for angles of cut which are nearly optimum for temperature compensation over the MIL temperature range. We note that the uncompensated AT cut crystal has a frequency deviation of about  $\pm 15$  ppm. It can be optimized for a deviation of about  $\pm 1$  ppm over the 0 to  $50^{\circ}\text{C}$  temperature range. The SC cut on the other hand has a deviation of about  $\pm 50$  ppm. Thus a greater degree of improvement is required for the SC cut crystal if it is to be used over a wide temperature range. The SC cut crystal promises to hold several advantages for TCXO applications. Among those reported are reduced frequency hysteresis, greatly improved

temperature transient performance, and lower aging rates. The AT cut crystal has been used with both analogue and digital temperature compensation techniques, while most of the investigation with SC cuts has involved one of the digital methods.

The basic analogue compensated TCXO is shown in the block diagram of Figure 3. In this diagram a varactor is placed in the oscillator, usually in series with the crystal, so that it can pull the frequency of the crystal by exactly the same amount but in the opposite direction that it has drifted due to temperature. This is shown in the graph in the lower portion of Figure 3. The solid curve represents the frequency change of the crystal over the temperature range, while the dotted curve shows the frequency pulling effect of the varactor. If the varactor bias is carefully generated as a function of temperature, a nearly zero temperature coefficient can be obtained over a wide temperature range. TCXO's of this type have been used to obtain a frequency stability of  $\pm 0.5$  ppm over a wide temperature range. Most of the units have employed fundamental mode crystals and have been in the 3 to 20 MHz frequency range. The AT cut fundamental crystal seems to be nearly optimum for temperature compensation in the 3 to 5 MHz frequency range. Third overtone crystals have also been extensively used, however, fifth overtone units are quite difficult to pull and have generally not been used in TCXO's to date. Many variations of the resistor thermistor network have been used, and some have advantages over others particularly in the upper temperature range. For the network shown, which will be discussed subsequently, it is desirable to use an AT cut fundamental mode crystal with a frequency deviation of 30 to 40 ppm between turning points. The crystal should have a motional arm capacitance of about .012 pf. The oscillator is designed to have a pullability of around 35 ppm for a voltage range of perhaps 1 to 3 V on the varactor. This usually results in a varactor in the 33 to 47 pf range.

The resistor thermistor network is shown in more detail in Figure 4. This network achieves a considerable degree of independence of adjustment over the temperature range because of the values chosen for the thermistors. The cold thermistor, TR1 has a nominal value of 2 to 4 K with a  $\beta$  of 4410. The room temperature thermistor has a resistance of 100 K with a  $\beta$  of 3900, and hot thermistor, RT3 has a resistance of 5 Meg with a  $\beta$  of 5850. Thus in the cold temperature range of the TCXO at  $-40^{\circ}\text{C}$  or  $-55^{\circ}\text{C}$ , the room temperature thermistor and the hot thermistor are for practi-

cal purposes open circuits. The output voltage  $V_1$  is then determined by the cold thermistor,  $RT1$ , and the cold resistor,  $R2$ . As the temperature increases, the output voltage decreases, pulling the oscillator frequency down to compensate for the positive slope of the crystal in the cold temperature region. As the temperature approaches the room temperature region, the cold thermistor resistance decreases until it becomes relatively negligible compared to  $R1$ . The network output is then most strongly influenced by  $R1$  and  $RT2$ . This results in a positive voltage slope with temperature to compensate for the negative slope of the crystal in this region. Finally in the upper temperature region both the cold thermistor and the room temperature thermistor have decreased in value to where they are only of secondary importance. The network input voltage,  $V_1$ , then appears on the left side of  $R3$ , and the performance is essentially determined by  $R3$  and  $RT3$ . This again results in a negative voltage slope to compensate the positive temperature coefficient of the crystal beyond the upper turning point.

Manual temperature compensation can be accomplished by replacing the  $R1$ ,  $R2$ , and  $R3$  by potentiometers or resistance decade boxes, and following a procedure similar to that described below.

Adjust  $R1$  for on frequency operation at  $25^\circ\text{C}$ . Cool the TCXO to the cold extreme and adjust  $R2$  for on frequency operation. If a large adjustment was required, the procedure must be repeated. The frequency is next checked in the vicinity of the lower turning point. If it is too high, the pullability must be increased. If too low, the pullability must be decreased. A change in pullability will unfortunately make it necessary to begin the compensation procedure again. After the cold temperature region has been compensated, the resistor  $R3$  is adjusted to put the unit on frequency at the highest temperature. A final confirming temperature run is then made. Failure to meet the specification at this point requires that some parameter be changed depending on where the excessive deviation is encountered. It has been found that the test operators become quite skilled with the procedure and a large number of TCXO's have been compensated to  $\pm 0.5$  ppm over the  $-55^\circ\text{C}$  to  $75^\circ\text{C}$  temperature range using this procedure. The procedure generally requires 3 to 5 temperature runs.

This experimental analogue method of temperature compensation has been used for over two decades, however, most recent designs have employed a computer program to assist in selection of the resistors and/or thermistors of the compensation network. Two methods of computer aided compensation are discussed. The first uses measured crystal parameters along with the nominal data for the thermistors and the varactor. This method has also been referred to as the "no pull" method.

A flow diagram for the computer program developed by the author is given in Figure 5. Nominal data for the TCXO type being compensated is read into the computer from a disc file. The three coefficients for the cubic equation of the

crystal are then inputted from the terminal. The operator is then given the opportunity to modify any parameters he desires and the program generates the resistor values using an iterative process. All values for the TCXO are then stored by serial number, and the test select values are printed for the operator who then installs the components. The major equations used by the program are shown in Figure 6. It is desirable to obtain the crystal coefficients  $A_1$ ,  $A_2$ , and  $A_3$  from measurements on the individual crystals, although for certain tolerance studies the formulas given, based on angle of cut, can be useful.

After finding the crystal temperature drift, the next formula can be used to determine the load capacitance necessary to pull the crystal back to frequency. Having found the load capacitance, the required varactor capacitance can be determined. From this capacitance, the required network voltage can be determined. This is done for temperatures spaced about  $10^\circ\text{C}$  over the temperature range. An iterative procedure is then used to determine the network resistor values and the pullability. The program is written in PASCAL and generally achieves a frequency stability of  $\pm 1$  ppm to  $\pm 2$  ppm with the calculated values. Provisions are also made to input frequency errors from the confirming temperature run. These errors are used by the program to generate corrected resistor values. With 1 or 2 correction runs, a frequency stability of  $\pm 1$  ppm can consistently be obtained.

The second method of computer compensation is shown on the flow diagram of Figure 7. With this method, the test station is equipped to measure the actual thermistor resistances and the required resistance values as well as the sensitivity of each resistor at several temperatures. Using this method, a frequency stability of  $\pm 0.5$  to  $\pm 1$  ppm can usually be obtained with the calculated resistors. With several correction runs, a stability of  $\pm 0.5$  can consistently be obtained.

Most TCXO's in production today use the method of analogue temperature compensation, however, as advances continue to be made with digital and integrated circuit technology, the use of digital temperature compensation is becoming more attractive. The block diagram of a digitally compensated crystal oscillator is shown in Figure 8. A reasonably linear temperature sensor is used to generate a voltage which is proportional to temperature. This voltage is converted to a digital word using the A/D converter. The digital output of the converter is used as the address for a PROM. The memory is preprogrammed so that the word being addressed at a specific temperature contains the correction value required at that temperature. The correction value is then applied to a D/A converter which converts it to a voltage which is applied to the varactor. This technique has been used to achieve frequency stabilities in the  $\pm 0.5$  ppm region over a wide temperature range or  $\pm 5 \times 10^{-8}$  over the 0 to  $50^\circ\text{C}$  range.

The digital system results in errors due to the use of finite arithmetic and the equations describing two of the major sources of error are

AD-A130 811

PROCEEDINGS OF THE SYMPOSIUM ON FREQUENCY CONTROL (36TH  
ANNUAL) 2-4 JUNE 1..(U) ARMY ELECTRONICS RESEARCH AND  
DEVELOPMENT COMMAND FORT MONMOUTH E PAIGE ET AL. 1982

7/8

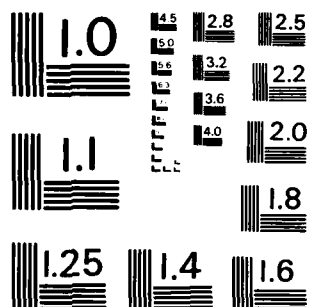
UNCLASSIFIED

F/G 20/14

NL

END  
X  
\*D  
07C

CONT



MICROCOPY RESOLUTION TEST CHART  
NATIONAL BUREAU OF STANDARDS-1963-A

given in Figure 9.\* The first equation gives the error due to an A/D converter with  $b_a$  bits, while the second describes the error due to a D/A converter with  $b_v$  bits. For a TCXO with a total temperature excursion,  $T$ , of  $140^\circ\text{C}$  and a crystal with a maximum slope,  $S$ , of  $1.4 \text{ ppm}/^\circ\text{C}$ , a 9 bit A/D converter results in an error of about 0.2 ppm. Additionally, an 8 bit D/A converter results in an error of  $6 \times 10^{-8}$  if the total frequency excursion of the crystal is 35 ppm.

An equation which can be used to optimize the memory size is given at the top of Figure 10.\* If this equation is satisfied, then the minimum number of memory locations required to achieve a frequency stability  $f/f$  is given by the lower equation. Using these equations it can be shown that, over the  $-55$  to  $+85^\circ\text{C}$  temperature range, a 0.1 ppm tolerance can theoretically be obtained with 1161 10 bit words. A tolerance of  $\pm 0.5$  ppm can be obtained with 224 8 bit words. Unfortunately, some of the errors which are present in analogue TCXO's are also present in digital TCXO's and the total tolerance cannot be allowed for the digital system. Among these errors are crystal hysteresis, voltage changes, load variations, temperature transient, aging adjustments and the like.

Crystal oscillators have also been temperature compensated using microcomputers. A block diagram of a microcomputer compensated oscillator is shown in Figure 11. Here the PROM of the digitally compensated crystal oscillator in Figure 8 has been replaced by a microcomputer and a PROM. The flow chart for the microcomputer program is shown in Figure 12. Basically the temperature in digital form is inputted to the microcomputer. The computer then searches out the closest stored correction values in the memory, interpolates between them and outputs the required correction to the D/A converter. The use of a microcomputer has several advantages over digital compensation because a smaller memory can be used. Additionally the microcomputer allows the use of a simpler A/D converter. For example, it can count the frequency of a thermistor controlled temperature sensor oscillator or determine the period of a thermistor controlled timer.

An equation which can be used for interpolation is shown at the top of Figure 13. In this equation  $V_1$  represents the correction required at temperature  $T_1$  below the present ambient temperature,  $T_2$  and  $V_2$  is the correction at  $T_2$  above the present ambient.

Errors, of course, result from the use of linear interpolation. For a typical AT cut crystal, this error is less than  $1 \times 10^{-7}$  for points stored at  $3^\circ\text{C}$  intervals.\* The error increases approximately as the square of the spacing.

A power series representation of the correction voltage can also be used by the microcomputer rather than the method of interpolation. This is

\*For additional details see Crystal Oscillator Design and Temperature Compensation, Marvin E. Frerking, Van Nostrand Reinhold Co., 1978, pp 154-157.

shown by the second equation of Figure 13. It should be noted, however, that if only 3 terms of the power series are used, errors of a few ppm can result, and it may be necessary to include higher order terms. Finally, the last equation gives the error resulting from the finite correction time required by the microcomputer. Here  $R$  is the rate of change of temperature of the TCXO, and  $t$  is the time required to determine the correction. For example if  $R = 2^\circ\text{C}/\text{minute}$  and  $t = 50 \text{ msec}$ , then if the crystal slope is  $1.4 \text{ ppm}/^\circ\text{C}$ , the error resulting is  $2.3 \times 10^{-9}$ .

The final method of temperature compensation listed in Figure 1 is external temperature compensation. With this method the crystal is not actually pulled to frequency by changing the varactor voltage. Rather the correction is applied in some other way which may be tailored to a specific application. For example if the oscillator is used as the time base for a frequency counter, the output reading of the counter can be digitally corrected for the known frequency error. If the oscillator drives a time of day clock, the time can be corrected periodically. This technique has been referred to as a Time Compensated Clock Oscillator. The clock can also be corrected by the addition or deletion of pulses from the oscillator.

This brief description of TCXO techniques is intended to give the reader an overall understanding of the principles involved in temperature compensation. Obviously a great deal of detailed knowledge and experience is required to achieve a high degree of frequency stability improvement. The reader is therefore advised to seek more specific information on any method contemplated for use prior to attempting precision temperature compensation.

FIGURE 1  
METHODS OF TEMPERATURE COMPENSATION

- Experimental Analogue
- Computer Aided Analogue
- Digital
- Microcomputer
- External Temperature Compensation

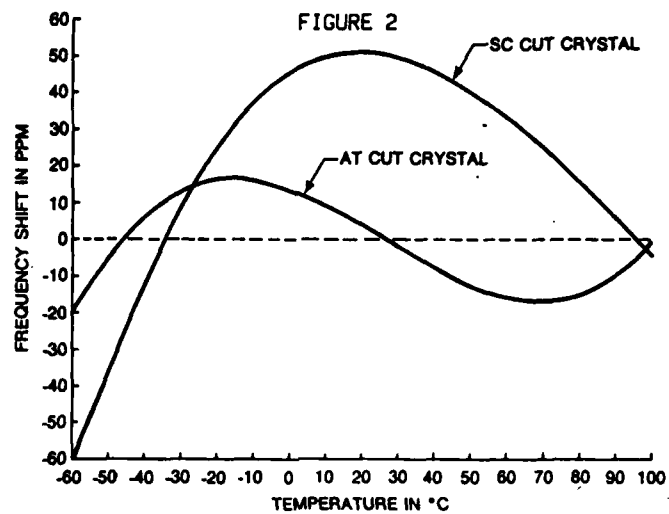


FIGURE 3  
BASIC TCXO

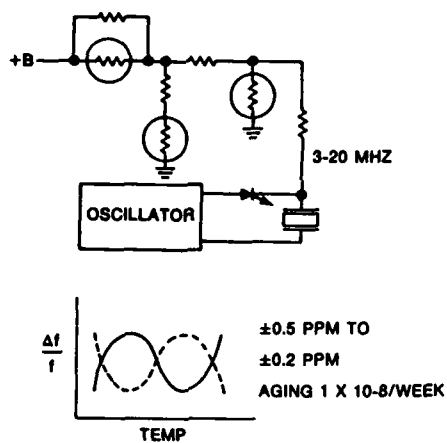


FIGURE 4  
EXPERIMENTAL TEMPERATURE COMPENSATION

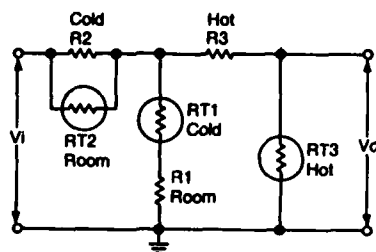


FIGURE 5  
COMPUTER COMPENSATION  
WITH CRYSTAL DATA

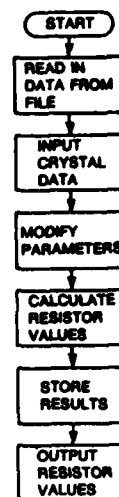


FIGURE 6  
COMPUTER COMPENSATION

$$\frac{\Delta f}{f} = A_1 (T - T_0) + A_2 (T - T_0)^2 + A_3 (T - T_0)^3$$

$$A_1 = \frac{-5.08 \times 10^{-6}}{60}$$

$$A_2 = -45 \times 10^{-9}$$

$$A_3 = 108.6 \times 10^{-12}$$

$$\frac{\Delta f}{f} = \frac{C_1}{2 (C_0 + C_1)}$$

$$C_v = \frac{K}{(V + V_0)^n}$$

$$R_T = R_{T0} \times P \left[ B \left( \frac{1}{T + 273} - \frac{1}{298} \right) \right]$$

FIGURE 7  
COMPUTER COMPENSATION WITH MEASURED DATA

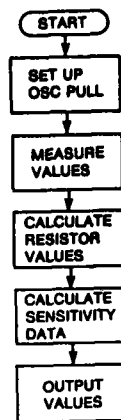


FIGURE 8  
DIGITAL TCXO

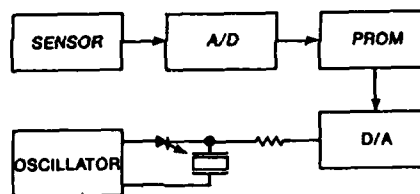


FIGURE 9  
DIGITAL TEMPERATURE COMPENSATION

$$\frac{\Delta f}{f} = \frac{S}{2} \left( \frac{T_m}{2^b} \right) \quad \text{Temp Error}$$

$$\frac{\Delta f}{f} = \frac{\left( \frac{\Delta f}{f} \right)_m}{2} \left( \frac{1}{2^{b_v}} \right) \quad \text{Voltage Error}$$

$T_m$  = Total Temp Excursion

$S$  = Max Crystal Slope

$b$  = No. BITS

$n$  = No. Words

FIGURE 10  
DIGITAL TEMPERATURE COMPENSATION

$$2^b = \frac{\left(\frac{\Delta f}{f}\right)_{\text{MAX}} (1 + b \ln 2)}{2 \left(\frac{\Delta f}{f}\right)}$$

$$n = \frac{S T_m}{2 \left(\frac{\Delta f}{f}\right) - \left(\frac{\Delta f}{f}\right)_{\text{MAX}} / 2^b}$$

FIGURE 11  
MICROCOMPUTER COMPENSATED  
CRYSTAL OSCILLATOR

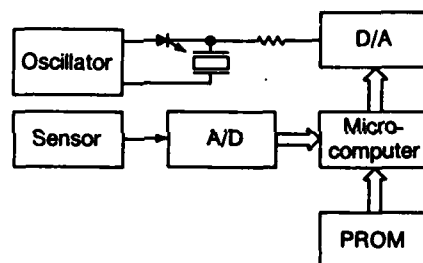


FIGURE 12

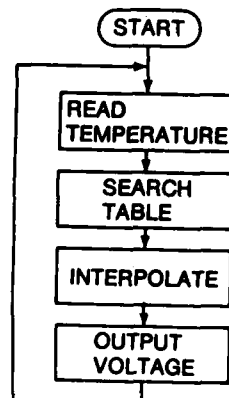


FIGURE 13

MICROCOMPUTER COMPENSATED  
CRYSTAL OSCILLATOR

$$V = V_1 + \frac{(V_2 - V_1)(T - T_1)}{(T_2 - T_1)}$$

$$V = aT + bT^2 + cT^3 + \dots$$

$$\frac{\Delta f}{f} = SR\Delta t$$

AD P001572

# DUAL MODE DIGITALLY TEMPERATURE COMPENSATED CRYSTAL OSCILLATOR

Robert Rubach

Midland - Ross Corporation/NEL Unit

This paper describes a method of utilizing a low frequency mode of vibration of an AT cut resonator to temperature compensate a second AT cut resonator to an accuracy of  $\pm 2 \text{ pp } 10^7$  over the temperature range  $0^\circ\text{C}$  to  $70^\circ\text{C}$ .

In the DMDTCXO (Dual Mode Digitally Temperature Compensated Crystal) a two loop oscillating scheme was developed to allow a 3.0 MHz AT cut resonator to vibrate in two modes of oscillation, approximately half the time each, as shown in Figure 1. The 810 kHz low frequency mode used was digitized to an eight bit address, and an eight bit correction word was used to compensate the 3.0 MHz mode of the resonator.

The second oscillating loop contains a second AT cut 3.0 MHz resonator that oscillates continuously. For one-half of the time the second resonator is phase-locked to the first resonator. During the remaining half cycle, the output is held at its previous value to present a continuous output from the system. If the frequency does not change too much before the loop is closed again, then the system can remain at a steady state frequency locked condition.

## System Timing

The system timing diagram is shown in Figure 2. CLK2 enables the temperature sensing low frequency mode, while CLK2 enables the AT mode of resonator X1. The system is phase-locked during the sample portion of S/H. and held at this locked value during HOLD. A temperature address is counted at the signal labeled COUNT, and latched onto the address buss by the two latching signals.

## Resonator

The resonators used had the following physical parameters: blank diameter 13.5 mm, electrode diameter 5.2 mm, plano-convex with 5.00 diopter contour.

The electrical parameters for the AT mode are shown in Figure 3. Some of the possible low frequency modes for the resonator are given in Figure 4, with the values in parentheses being calculated. The equivalent electrical parameters for the flexure mode used are given in Figure 5.

## Results

Frerking describes the maximum error in a

digitally compensated system such as this by the following relation:

$$f = \frac{S}{2} \frac{T}{n} + \frac{F}{2} \frac{1}{2^B}$$

Here S = the maximum frequency versus temperature slope in  $\text{ppm}/^\circ\text{C}$ ; T = the temperature range of the compensation in  $^\circ\text{C}$ ; n = number of words in the memory; F = the maximum peak to peak frequency deviation in ppm; B = the number of bits in a correction word; and f = total frequency error.<sup>2</sup> For the resonator used, S = .7  $\text{ppm}/^\circ\text{C}$ , T =  $70^\circ\text{C}$ , F = 25ppm, B = 8, and n = 140. The maximum frequency error should be  $2 \text{ pp } 10^7$ .

The compensated frequency vs. temperature curve is shown in Figures 6, and 7. An analysis of the data shows that the greatest error is  $\pm 2 \text{ pp } 10^7$ . This error occurs around room temperature where the contribution from the slope of the curve is a maximum.

The compensated resonator was run over the temperature range  $25^\circ\text{C}$  to  $50^\circ\text{C}$  at several temperature rates, shown in Figure 8. This is the expected temperature transient response of an AT cut resonator with a slight improvement over an uncompensated resonator.

To determine the degree of hysteresis in the system, each resonator was subject to the following test. After stabilizing for one hour at the address corresponding to  $20^\circ\text{C}$ , the system was cooled to  $0^\circ\text{C}$ , then heated to  $70^\circ\text{C}$ , and then cooled back to  $20^\circ\text{C}$ . Here each resonator was stabilized at the address corresponding to  $20^\circ\text{C}$  for one hour. The frequency difference between the resonator after the temperature run and before was noted and is recorded in Figure 9.

The data shows that only two of the ten resonators tested showed any hysteresis effects. The amount of hysteresis exhibited by these two resonators was .1 Hz ( $3.3 \text{ pp } 10^8$ ). This hysteresis could be attributed to round off error in the data taking technique, seeing that the frequency counter used was only accurate to  $\pm .1 \text{ Hz}$ . Further work must be done to determine what level of hysteresis actually exists in the system.

## Conclusion

The use of a temperature sensing mode of oscillation in digitally compensated systems using SC cut resonators has received much attention recently. This paper presented a method of using a temperature sensing mode in an AT cut resonator to achieve good results in the  $\pm 2 \text{ pp } 10^7$  range. Further areas of study might serve to

improve the spectral purity, reduce data taking requirements, and finally design a resonator that would have a temperature sensing mode that would compensate for the temperature transient response and hysteresis effects known to exist for the AT cut resonator.

<sup>1</sup>Raymond A. Heising, Quartz Crystals For Electrical Circuits (Washington, D.C.: Electronic Industries Association, 1978), p. 246

<sup>2</sup>Marvin E. Freiking, Crystal Oscillator Design and Temperature Compensation (New York, N.Y.: Van Nostrand Reinhold Co., 1978) p. 155

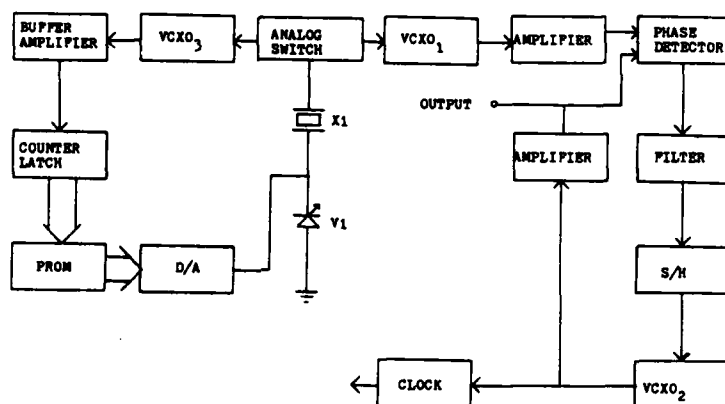


Figure 1 DMDFCXO System Block Diagram

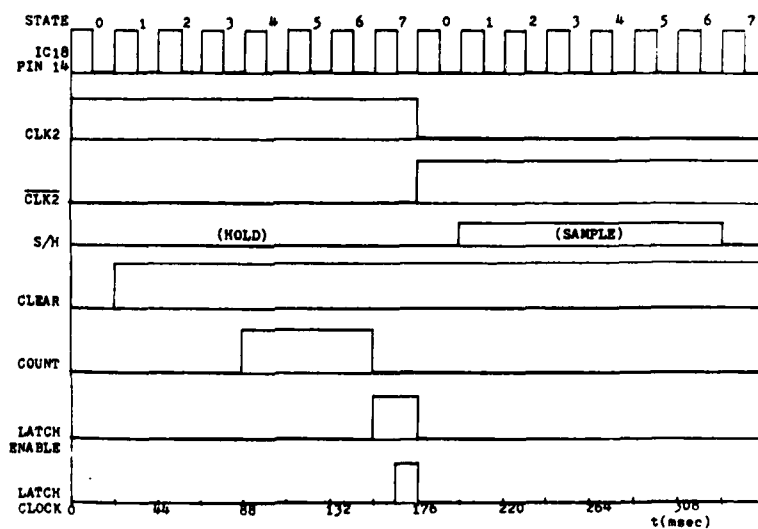
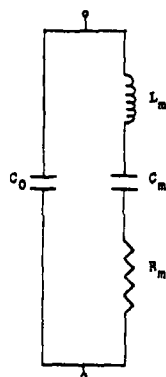


Figure 2 System Timing Diagram.



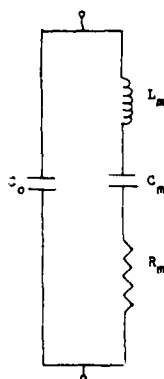
PARAMETERS	#82520	#82535
$C_0$	2.5 pf	2.5 pf
$R_m$	60 $\Omega$	60 $\Omega$
$f_B$	2999518 Hz	2999492 Hz
$f_A @ C_L = 20$ pf	3000004 Hz	2999991 Hz
$C_m$	7.3 mpf	7.5 mpf
$L_m$	381 mH	370 mH
Q	122,000	118,000

Figure 3 AT Mode Resonator Parameters.

Figure 4  
Low Frequency Modes of Resonator #82520

MODE	HARMONIC OVERTONE NUMBER							
	1	2	3	4	5	6	7	8
FLEXURE	99 (101)	198 (202)		397 (404)		596 (600)		795 (810)*
EXTENSION	181 (176)		543 (537)		905 (895)			
SHEAR	189 (187)		567 (547)		945 (915)			

\* Low Frequency Mode Used.  
(Values are in kHz)



PARAMETERS	#82520	#82535
$C_0$	2.5 pf	2.5 pf
$R_m$	12 k $\Omega$	7 k $\Omega$
$f_B$	810433 Hz	809328 Hz
$f_A @ C_L = 20$ pf	810472 Hz	809367 Hz
$C_m$	2.0 mpf	2.1 mpf
$L_m$	19.2 h	17.2 h
Q	7,700	12,950

Figure 5 Low Frequency Mode Parameters.

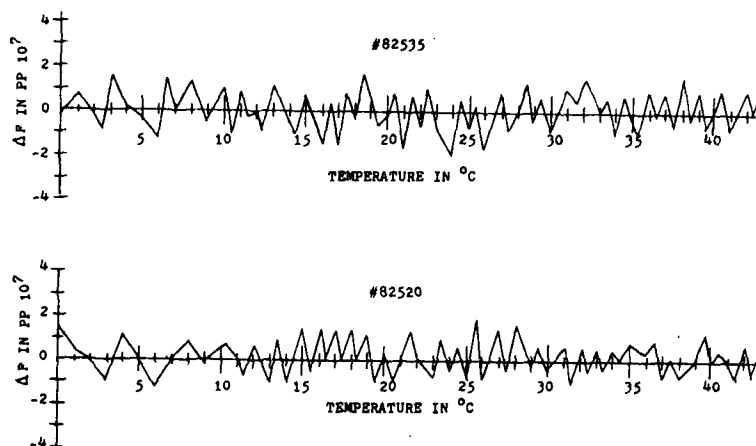


Figure 6 Temperature Compensation Curves for Resonators #82535 and #82520.

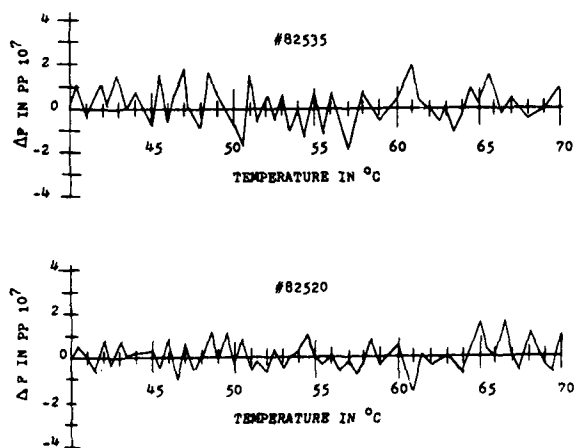


Figure 7

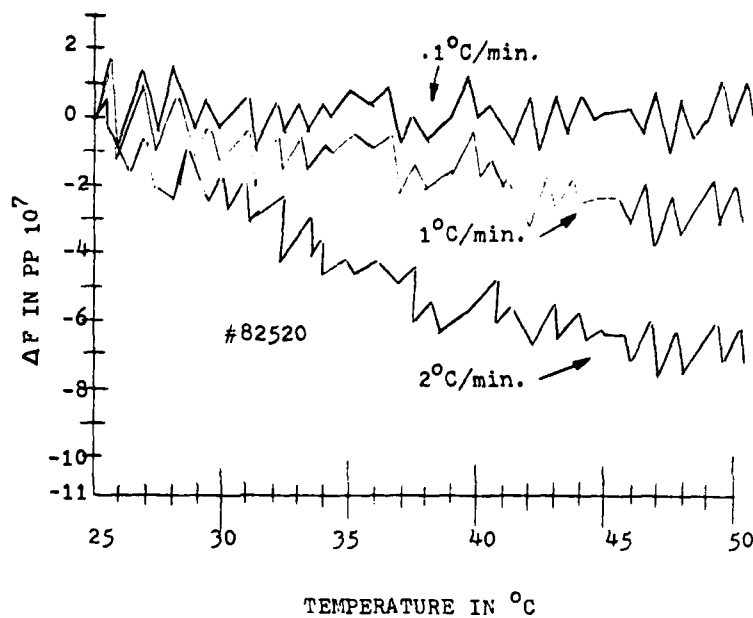


Figure 8 Temperature Transient Curve  
for #82520, Compensated.

RESONATOR	ADDRESS	DIFFERENCE FROM 3.0 Mhz INITIAL	DIFFERENCE FROM 3.0 Mhz FINAL	HYSTERESIS
#82524	\$69	+.5 hz	+.5 hz	0.0 hz
#82502	\$81	+.2 hz	+.3 hz	+0.1 hz
#82510	\$88	-.4 hz	-.3 hz	+0.1 hz
#82533	\$C5	+.4 hz	+.4 hz	0.0 hz
#82522	\$0E	-.1 hz	-.1 hz	0.0 hz
#82503	\$BD	-.2 hz	-.2 hz	0.0 hz
#82528	\$37	+.2 hz	+.2 hz	0.0 hz
#82538	\$74	+.3 hz	+.3 hz	0.0 hz
#82520	\$8E	+.1 hz	+.1 hz	0.0 hz
#82535	\$53	+.3 hz	+.3 hz	0.0 hz
MEAN HYSTERESIS				.02 hz

Figure 9 Hysteresis Data

## A Temperature Compensated SC Cut Quartz Crystal Oscillator

Edward K. Miguel

Northern Illinois University  
DeKalb, ILL.

A method of temperature compensating a pullable SC Cut quartz crystal is presented. The B and C modes of the SC Cut are resonated simultaneously. The B mode is used as a temperature sensor which has a linearity of  $-25$  ppm/ $^{\circ}\text{C}$ . The C mode is compensated using the temperature information from the B mode. A dual mode oscillator is developed which allows the frequency of the C mode to be controlled without affecting the B mode. A digital compensation method uses a RAM for on board information storage and programming. The address to the RAM is temperature generated and the output of the RAM is converted to a voltage to control the C mode oscillator. The compensation information is programmed automatically, during a temperature slew of  $1.5^{\circ}\text{C}/\text{min.}$ , using a phase-locked-loop, an up/down counter and a track-and-hold circuit all of which are connected to the oscillator only during the programming step. The system was compensated from  $-20^{\circ}\text{C}$  to  $+70^{\circ}\text{C}$  and accomplished an accuracy of  $\pm 0.5$  ppm during a fast temperature scan of  $5^{\circ}\text{C}/\text{min.}$

## INTRODUCTION

Up until very recently, temperature compensated crystal oscillators (known as TCXO's) have almost always used the AT Cut quartz crystal. They also incorporate a temperature sensing means located externally or outside of the crystal enclosure. This has led to two very characteristic traits of TCXO's and they are 1) large unpredictable frequency excursions during temperature shock conditions and 2) frequency errors due to the thermal lag between the crystal and the temperature sensing devices.

Within the last decade, a new quartz crystal orientation has been developed called the SC Cut. It retains most of the good qualities of the AT Cut such as a low frequency-temperature coefficient. Yet it eliminates some of the bad qualities like the AT Cut's temperature shock sensitivity.

The SC Cut is a doubly rotated quartz crystal. It has an orientation of  $(\theta, \phi) = (21.9^{\circ}, 33.9^{\circ})$  about the Z and X crystallographic axes. Its modal spectrum shown in Figure 1 is very rich and must be dealt with accordingly in oscillator designs. The main mode of interest is the C mode and this is because it is similar to the AT Cut fundamental except that the stress sensitivity of the C mode is 830 times less sensitive to stress. A graph comparing the

sensitivities of various cuts is shown in Figure 2.

Another mode of interest is the B mode which is located about 10% higher in frequency than the C mode. The B mode is worthy of mention because it has a linear frequency-temperature coefficient of approximately  $-25$  ppm/ $^{\circ}\text{C}$ . It has been shown that this mode can be a very accurate temperature sensor of the crystal blank.<sup>1</sup>

The SC Cut has not been easily applicable in TCXO's up to now because of its inherent stiffness characteristics due to a Co/Cl ratio which was almost three times that of AT Cuts. Its initial applications were in ovenized oscillators which do not consider stiffness or pullability in their temperature compensating schemes. However, SC Cuts now exist which offer limited but practical pullability ranges for use in TCXO's.

Two SC Cuts are used in this study. They are both 5.115 MHz fundamentals manufactured by Colorado Crystal Corporation of Loveland, Colorado. Their parameters and temperature characteristics are shown in Figure 3. With the parameters shown, the approximate pullability of each crystal is about 60 ppm. This somewhat limits the maximum compensatable temperature range to  $-40^{\circ}$  to  $+100^{\circ}\text{C}$  because the frequency excursion of the crystal at the low end of the temperature range exceeds the pullability of the crystal.

The purpose of this study is to investigate the possibility of an SC Cut TCXO which uses the B mode frequency as an on-blank temperature sensor to compensate the C mode over a temperature range of  $-20^{\circ}\text{C}$  to  $70^{\circ}\text{C}$  with an accuracy of  $\pm 0.4$  ppm which, as calculated using a formula for worst case frequency error by Frerking<sup>2</sup>, is all that is theoretically possible, given the crystal characteristics and some other digital constraints which will be mentioned later.

In order to accomplish this goal, a dual mode oscillator had to be developed which offered good isolation and independent control over each mode. A digital compensation system also had to be developed which could store and recall compensation information to stabilize the C mode over temperature. Due to the time constraints of the study an automatic compensation system had to be devised to speed up the manual compensation process.

## DUAL MODE OSCILLATOR

The dual mode oscillator consists of one 5.115 MHz SC Cut quartz crystal surrounded by two Pierce oscillators which are composed of two cascode amplifiers and two selective filters as shown in Figure 4. The cascode amplifier is required to

AD P001573

provide good input to output isolation and the necessary gain for startup and circuit losses during oscillation. One cascode stage is required for each mode. A selective filter is required at the input of each cascode amplifier in order to separate the desired mode with a certain degree of isolation from the other mode.

The filter passes only the desired mode to the input of the cascode amplifier. The other mode is trapped out. The tapping point for each mode is after the filter or on the input of the cascode amp.

The filters are a combination of a series pass and a parallel trap filter. Component values are calculated using the formulas in Table 1. Note that there are two different networks. One has a capacitance series element and the other has an inductive series element. This is due to the difference in the relationship of the frequencies illustrated in Figures 5 and 6. In one case the mode to be passed,  $f_s$ , is higher than the mode to be trapped,  $f_a$ , and vice-versa in the other case. The networks are still basically the same.

The location of certain capacitors, shown in Figure 4, is also very important. These capacitors (often referred to as "pi" capacitors) are necessary if the crystal is to run as an equivalent inductor and they fulfill the requirements for oscillation in such a case. Normally their location is on both sides of the crystal. However, for this application one of the capacitors is replaced by two capacitors and located after the filters. In this manner, the conditions for resonance in each oscillator are fulfilled only for those frequencies passed by the filters.

Overall the dual mode oscillator performed quite well. It has fair isolation (about 40db) which was less than desired but still practical. The A mode had the best isolation. The C mode oscillator had to tolerate the hyperabrupt varactor in its filter and this caused some loss of isolation at the extremes of the varactor voltage. Yet, pulling the C mode had no effect on the B mode frequency. The voltage coefficient worked out to be about  $3 \times 10^{-7}$  for a variation of  $\pm 1.5V$  about a nominal 9V.

The tuning of the oscillator required a little patience due to a seesaw effect of one mode on the other. For good isolation the tuning of the traps in the filters was critical. The isolation of the B mode however did not require as much isolation since it was only being counted internally so most of the tuning procedure concentrated on the C mode oscillator.

One problem did occur with activity dips in the B mode of both crystals. One crystal had a dip between 55-65°C. The other crystal also had one but it was above 80°C so this crystal was used for compensation.

#### DIGITAL COMPENSATION SYSTEM

The block diagram of the digital compensation system is shown in Figure 7. The principle of the system is to generate a correction voltage to be applied to the C mode voltage controlled oscillator. The correction voltage

will be generated by a digital-to-analog converter and a sample-and-hold circuit. The digital information to the DAC is from the output of a 126 x 8 CMOS random access memory. The address for the RAM is generated by an eight bit frequency counter which samples the B mode of the oscillator. The base for the counter is generated by a digital state machine which also generates the other required logic signals. The clock for the C mode output is a divided down version of the C mode.

The flow chart in Figure 8 shows the order of sequence for the logical operations. For the first three states the system is in a READ RAM state which means that the RAM is just outputting its stored contents. However, in the first state the address to the RAM is being setup by clearing the counter. In the next state the counter is enabled for a precise time interval allowing the B mode to be counted. At the end of this interval, the counter's output is latched which updates the addressing of the RAM. If the TCXO is to be programmed, the signal PGM to the digital state machine is pulled high externally so the fourth state is implemented whereby the R/W line of the RAM is pulled low to program the RAM. Hopefully the data input to the RAM at that time is correct.

The premise of this compensation system is that the frequency of the B mode represents an accurate linear temperature sensor which, if converted to digital information through a frequency counting scheme, could represent unique temperature increments. These increments, when applied to a RAM, could address the proper compensation information necessary to correct the crystal's frequency deviations over temperature. The actual value of the address of the compensation data is not important; it does not even have to be known because the RAM is programmed on-board. What is important is that each address is unique and repeatable for a given unique measurement of the B mode.

For programming, the information is input externally via a 24 pin DIP cable which is connected only during this phase. The data and address are also monitored for recording purposes. Programming is accomplished by holding the PGM line high and then adjusting the digital inputs so that the C mode is constantly at the desired frequency.

The temperature must be changing slowly but constantly at a slow rate of about 1°C/min.

Manual programming requires 5-8 hours of constant attention. If one address is missed, it is possible to poorly compensate one or two temperatures. This means finding and reprogramming these addresses.

One solution to this tedious task is to automatically compensate the oscillator. This can be done using a phase-locked loop as shown in Figure 9. The oscillator frequency is compared with a reference frequency in an MC 1441 phase detector. The phase difference generates a voltage which pulls the C mode oscillator in frequency and which is compared with the output of the DAC. The DAC is being swept by a 40193, eight bit up/down counter, in a direction dependent on the result of the comparison of the DAC output and the phase detector voltage. If the DAC output is lower than the phase detector's, the counter will count up.

otherwise it will count down. Or if the frequencies are as close as the resolution of the DAC will allow, the counter will toggle up and down. By gating certain signals from the digital state machine of the oscillator, shown in Figure 10, the RAM's R/W signal will be controlled in such a way so that data is programmed only when the DAC is toggling on the high side of the phase detector voltage. This is done for optimum compensation results.

### RESULTS

After a certain amount of time, dealing with poor results due to activity dips of the B mode and low frequency jitter in synthesizer used for the reference frequency, some favorable results occurred. The test runs were done very quickly because I was pressed for time. The programming of the compensation information was done at about 1.5°C/min. from cold to hot after allowing the oscillator to settle at the cold end for 15 minutes. No heat treating or other stabilizing procedures were performed. Also the oscillator had no enclosure other than a cardboard box to reduce drafts on the crystal.

Usually the final test was performed immediately after the compensating step. The compensation and monitoring equipment, outside of the oven, was equipped to switch over from compensation to final frequency testing without opening the oven.

Figure 11 is a typical result of a temperature run. The increased error at the cold end, due to the high slope of the crystals f-T curve, is a characteristic of digitally compensated systems with equally spaced temperature compensated points. If more temperature points (or addresses) could be assigned to the cold end this problem could be minimized.

For a slew rate of about 6°C/min. the results are within  $\pm .5$  ppm with most of the error at the cold end. On the second page of the figure, the chart shows what happens when the upper temperature limit is exceeded. Initially the frequency goes lower (towards the top of the chart) as the addresses start to repeat. The natural f-T curve of the crystal is taking control of the frequency. The chart also shows the oscillator coming back within the limits to the same frequency for which it was compensated. This indicates good address repeatability. Afterwards the oven is stepped to room temperature (by blasting CO<sub>2</sub>). While the temperature is changing, the frequency increases steadily to about 3 ppm above the compensated frequency. But once the CO<sub>2</sub> value stops, the frequency recovers very quickly.

In Figure 12, the temperature shock characteristics are repeated. Every two minutes the oven temperature is reduced by 10°C. The increase in frequency after each shock is about 1 ppm.

### CONCLUSION

This investigation, though far from exhausting all possibilities, has demonstrated a feasibility of an SC Cut TCXO with predictable

stability over temperature. It points out the need for more "pullable" SC Cuts as well as the need for pullable SC Cuts with an inflection temperature that is lower than room temperature so as to offset the high slope of frequency deviation at the cold end.

The problem with the B mode activity dips is not a good omen if this method is to be used. The B mode must be absolutely predictable if it is to be useful. Since little of the manufacturing process concerns itself with these, more attention may just eliminate them. Obviously this must occur for this compensation method to be in production.

More testing should be done on the temperature shock characteristics. It is unclear whether or not the results as shown are a result of the circuit or the crystal. There are other characteristics which should be tested in greater detail such as frequency-temperature hysteresis.

The dual mode oscillator may also be improved by trying a cascode hybrid amp, like the MC 1550 by Motorola, because this device offers AGC control.

There are also many ways to improve the digital compensation schemes. The most obvious is to increase the addressable locations which will reduce the  $\Delta T$  between the compensated temperature points. It would also help to have more compensation at the extremes of temperature where the f-T curve of the crystal is greatest. Of course a micro-processor could be applied to interpolate data between known temperatures thereby reducing memory requirements and most likely replacing some of the control hardware with software.

My thanks to Colorado Crystal Corporation, CTS Knights, Inc. and Northern Illinois University for their assistance in the development of this thesis.

### References:

1. John A. Kusters, et. al., "Dual Mode Operation of Temperature and Stress Compensated Crystals," Proceedings of the 32nd Annual Frequency Control Symposium (June, 1978), p. 389.
2. Marvin F. Frerking, Crystal Oscillator Design and Temperature Compensation (New York: Van Nostrand Reinold Co., 1978), pp. 146-152.

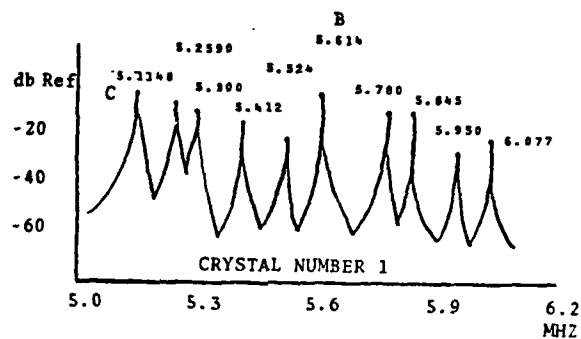
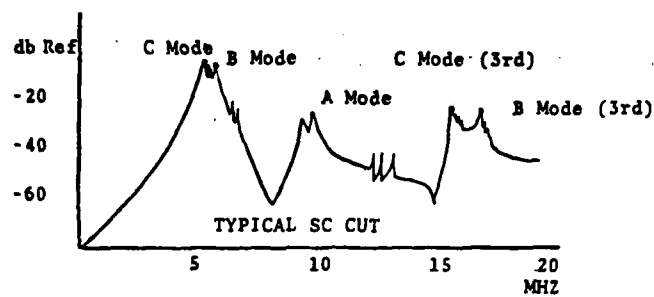


Figure 1. SC Cut Modal Spectrum Examples.

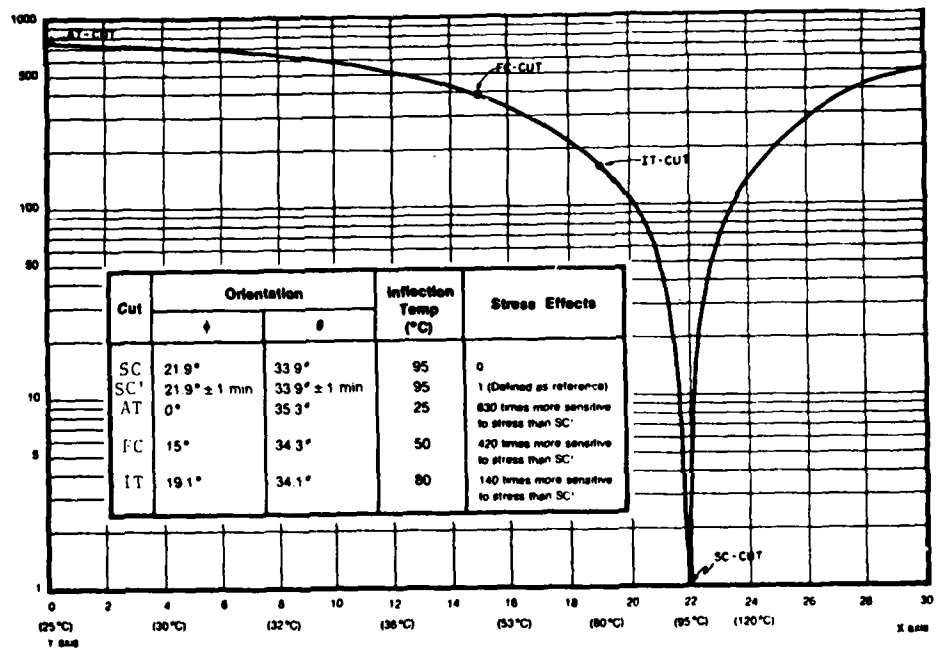


FIGURE 2. Relative Stress Sensitivity of Various Cuts.  
Source: Colorado Crystal Corp., Loveland, Colo.

CRYSTAL #1				CRYSTAL #7			
	MODE C	MODE B			MODE C	MODE B	
FS	5.114832	5.613102	MHZ	FS	5.114807	5.610250	MHZ
R1	6	20	$\Omega$	R1	9	9	$\Omega$
C $\emptyset$	6.8	6.7	pf	C $\emptyset$	6.6	6.6	pf
C1	4.377	4.013	mpf	C1	4.361	3.977	mpf
Q	1146.521	351.485	$10^3$	L1	222.033	202.342	mh
				Q	810.855	766.945	$10^3$

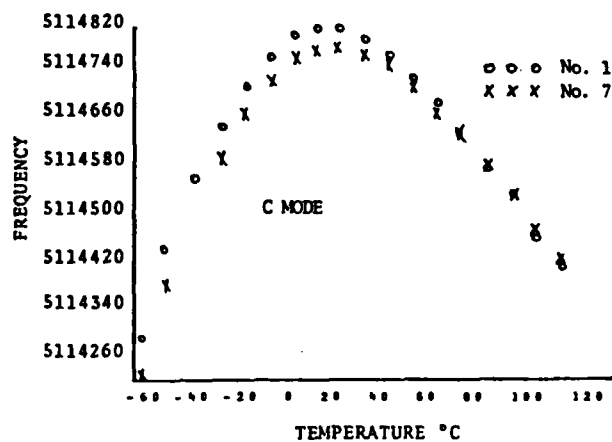
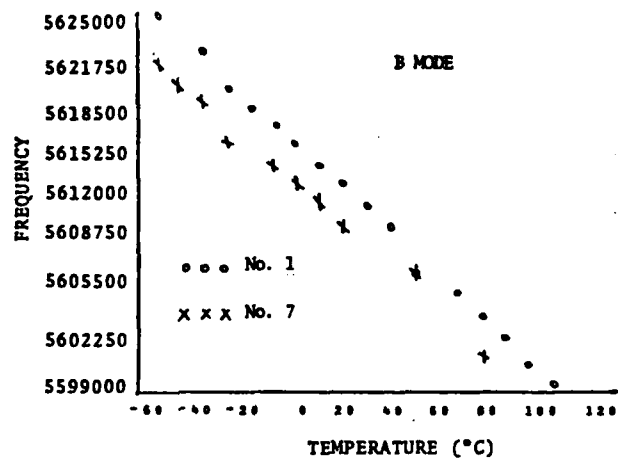


Figure 3. SC Cut Crystals Number 1 and Number 7



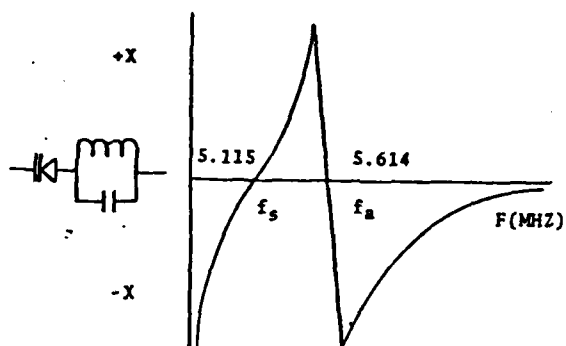


Figure 5. C Mode Filter.

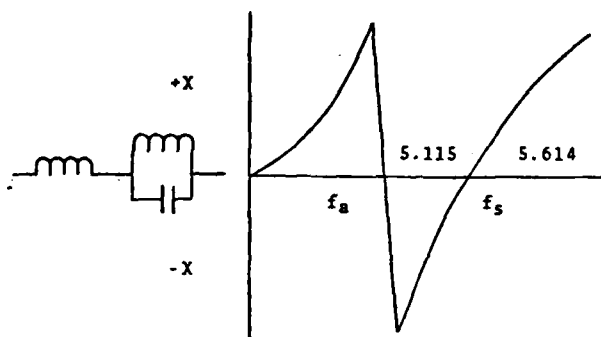


Figure 6. B Mode Filter.

	C MODE	B MODE
$w_s$	$\sqrt{\frac{1}{L(C_1 + C_2)}}$	$\sqrt{\frac{L_2 + L_1}{L_1 L_2 C}}$
$w_p$	$\sqrt{\frac{1}{LC_2}}$	$\sqrt{\frac{1}{L_2 C}}$
$C_1$	$\frac{\frac{1}{w_s^2} - LC_2}{L}$	
$L_1$		$\frac{L_2}{w_s^2 CL_2 - 1}$
TYPE		

Table 1. Formulas For B and C Mode Filters.

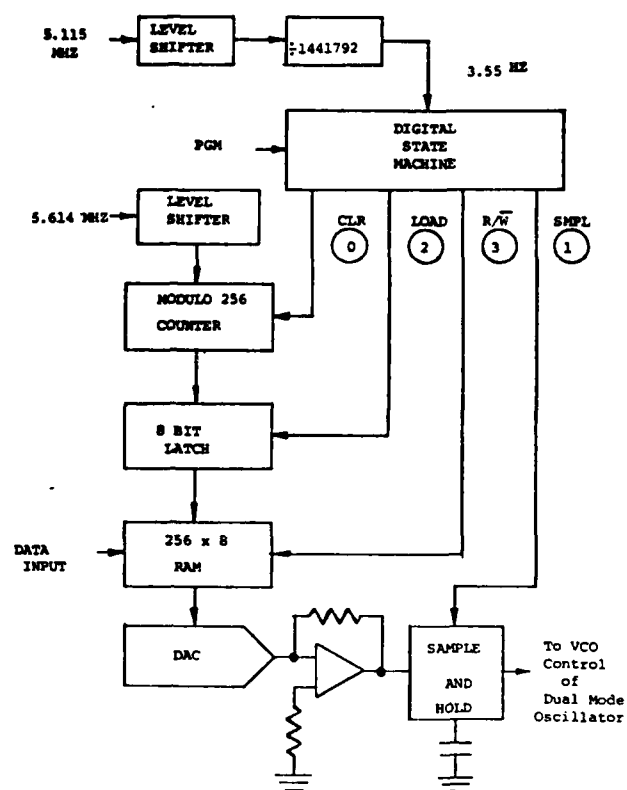


Figure 7. Block Diagram of Digital Compensation System.

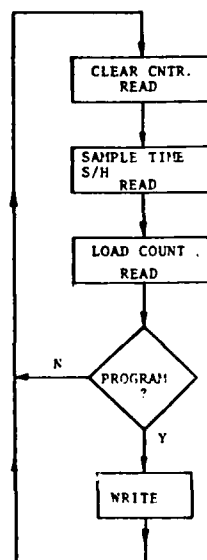


Figure 8. Digital State Machine Flow Chart.

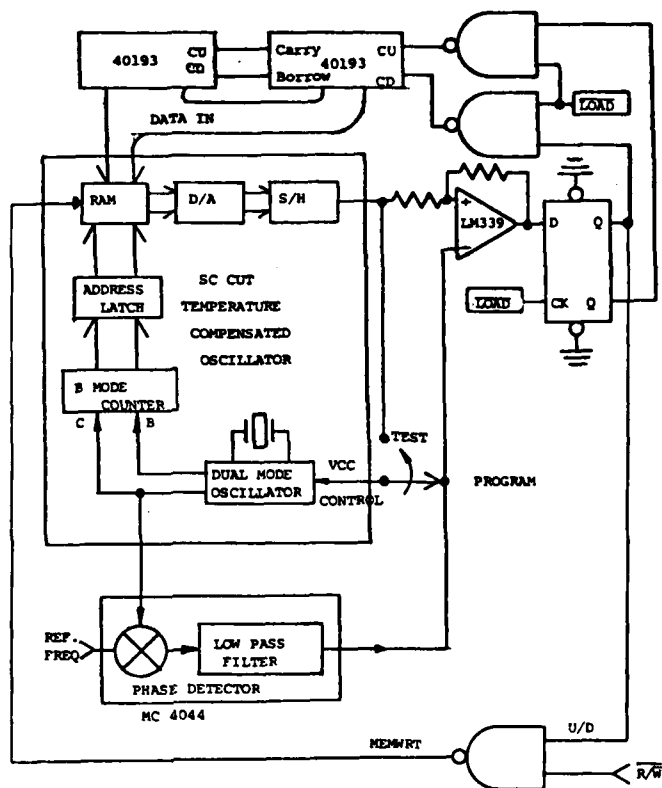


Figure 9. Phase Locked Loop Automatic Temperature Compensation.

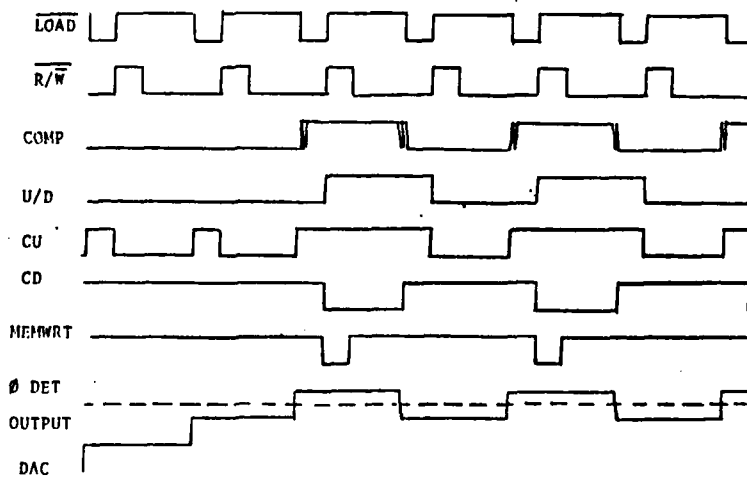


Figure 10. Timing Diagram for Synchronous Automatic Compensation.

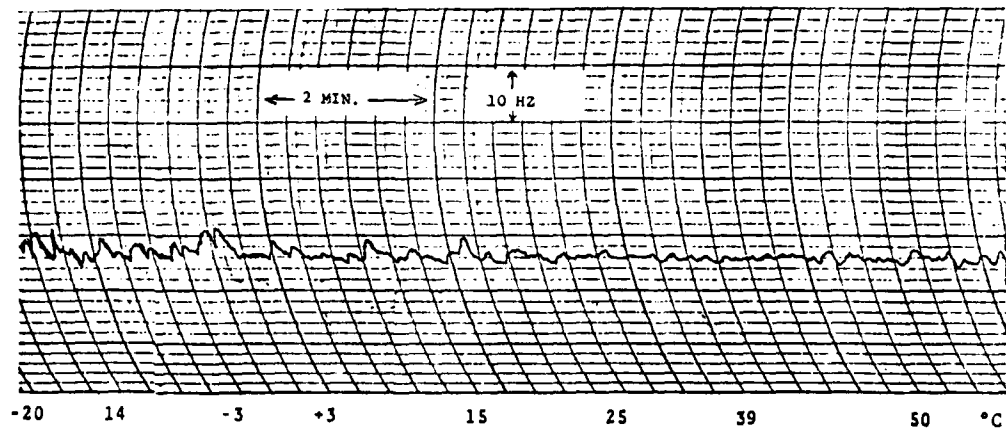


Figure 11. Dynamic F-T Behavior. (Continued on next page)

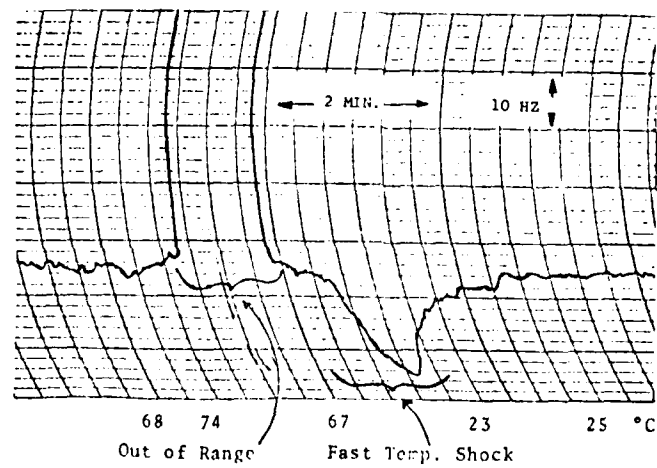


Figure 11. (Continued)

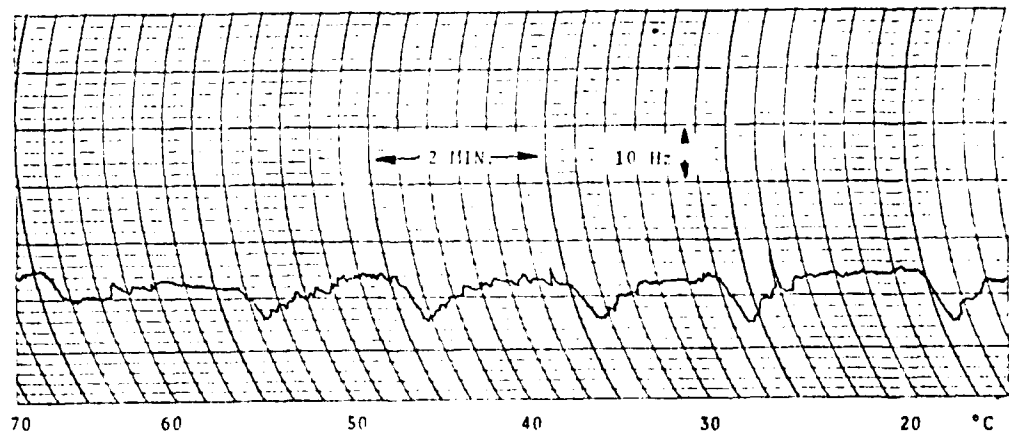


Figure 12. F-T Behavior During Successive Temperature Shocks.

## 36th Annual Frequency Control Symposium - 1982

## AUTHOR INDEX

AUTHOR	PAGE	AUTHOR	PAGE	AUTHOR	PAGE
Adam, J.D.	419	Hadorn, F.	260	Parker, T.E.	453
Addor, F.	260	Hall, D.L.	388	Parzen, B.	480
Allan, D.W.	378	Hall, T.M.	507	Paulin, P.	348
Allen, R.T.	372	Halliburton, L.	77	Peach, R.C.	22, 297, 389
Andle, J.C.	124	Halperin, A.	187, 193	Peters, H.E.	240
Andrews, A.P.	270	Hauden, D.	200, 284	Picard, R.H.	370
Andrews, D.C.	66	Hemmer, P.R.	370	Poirier, M.	276
Armington, A.F.	55, 77, 115	Hénaff, J.	525	Pollard, G.B.	474
Bailey, D.S.	124	Hilliard, D.	314	Ponce de Leon, R.	470
Ballato, A.	290, 513	Ho, J.	499	Prost, L.	260
Baltzer, O.J.	321	Holt, J.M.	62	Putkovich, K.	388
Barnes, J.A.	378	Horrigan, J.A.	55	Read, E.	389
Baughman, R.J.	82	Howe, D.	314	Roberts, G.A.	486
Black, J.F.	537	Isherwood, B.J.	62	Ronen, M.	187
Bonnier, D.	349	Ito, H.	290, 513	Rosenfeld, M.	499
Bossoli, R.B.	77	Jackson, H.W.	492	Rousseau, S.	284
Bourquin, R.	200	Jaillet, G.	284	Rubach, R.	571
Brandenberger, H.	260	Johnson, L.	260	Savard, J.Y.	348
Brendel, R.	97	Kagiwada, R.	396	Schieber, M.	193
Brunet, M.	499	Kahan, A.	115, 159, 170	Shanley, C.W.	108
Bryant, A.	276	Katz, S.	187, 193	Siffert, P.	405
Bulst, W.E.	442	Kawashima, H.	90	Silva, J.H.	486
Busca, G.	260	Koga, Y.	223	Stobodnik, Jr., A.	486
Byrne, A.J.	297, 389	Kong, A.	396	Smith, M.	529
Chai, B.	124	Kosinski, J.	181, 215	Soluch, W.	124
Chambers, J.L.	302	Kotecki, C.	459	Staples, E.J.	270
Chatham, T.B.	470	Kudo, A.	90	Stein, S.	314
Cho, F.Y.	470	Kunski, R.	348	Stevens, D.S.	37, 46
Christie, I.R.A.	62	Kuramochi, N.	133	Stevenson, J.K.	389
Colson, C.	197	Lakin, K.M.	517	Stokes, R.	396
Colvin, R.D.	486	Lam, C.S.	29	Stone, C.S.	321
Coquere, R.	284	Landin, A.R.	517	Straka, E.R.	230
Croxall, D.F.	62, 66	Larkin, J.J.	55	Strauss, A.	499
Cullen, D.E.	537	Lau, K.	396	Tako, T.	327
Cyr, N.	348	Lee, D.L.	124, 276	Tanski, W.J.	400
D'Albaret, B.	405	Lee, P.C.Y.	29	Tétu, M.	340, 348
Dinger, R.J.	265	Leiby, Jr., C.	370	Thomann, P.	260
Doherty, S.P.	66, 297	Levine, J.	314	Thomas, J.E.	370
Drake, G.W.	537	Lipson, H.G.	115	Tiersten, H.F.	37, 46
Dworsky, L.N.	108	Lukaszek, T.	290, 513	Todd, A.G.	62
Dyer, A.J.	297, 389	Maleki, L.	255	Trembley, P.	340
Edwards, H.W.	529	Martin, J.J.	77	Tsaclos, J.	208
Erb, L.	314	Meeker, T.	549	Tsuchida, H.	327
Euler, F.	115	Meirs, M.	499	Usui, A.	290
Ezekiel, S.	370	Migue, E.K.	576	Vanier, J.	340, 348
Facklam, R.L.	361	Miles, R.D.	355	Vetelino, J.F.	124, 276
Feldmann, M.	525	Mindlin, R.D.	3	Vig, J.	181, 215
Filler, R.	181, 215	Mooradian, A.	338	Walls, F.L.	371
Forman, P.	220	Morris, S.E.	66	Wang, H.T.M.	249
Förster, H.J.	140	Nakadan, Y.	223	Wang, J.S.	517
Frerking, M.E.	564	Nakajima, A.	90	Warner, A.W.	208
Gagnepain, J.J.	97	Nakamura, J.	133	Welford, D.	338
Garvey, R.M.	236	Nakazawa, M.	290, 513	Werner, J.F.	529
Gautier, H.	428	Nassour, D.	200	Willibald, E.	442
Geesen, M.	499	Newell, D.E.	562	Wise, J.	270
Glaze, D.	314	Nicolas, G.	260	Yen, K.	396
Goldfrank, B.	208	Ochiai, O.	90		
Gray, J.	314	Ohtsu, M.	327		
Grudkowski, T.W.	537	O'Connor, J.J.	55		
		Ogawa, T.	133		
		Oura, N.	133		

**36th Annual Frequency Control Symposium - 1982**  
**SPECIFICATIONS AND STANDARDS GERMANE TO FREQUENCY CONTROL**

**Institute of Electrical and Electronic Engineers**

Order through: IEEE Service Center  
 445 Hoes Lane  
 Piscataway, NJ 08854  
 (201)-981-0060

- 176-1978 Piezoelectricity \$ 9.00
- 177-1966 Piezoelectric Vibrators, Definitions and Methods of Measurements for (ANSI C83.17-1970) \$ 4.00
- 180-1962 Ferroelectric Crystal Terms, Definitions of \$ 3.00
- 319-1971 Piezomagnetic Nomenclature \$ 4.00

**Electronic Industries Association**

Order through: Electronic Industries Assn.  
 2001 Eye Street, N.W.  
 Washington, DC 20006  
 (202)-457-4900

(a) **Holders and Sockets**

- RS-192-A, Holder Outlines and Pin Connections for Quartz Crystal Units. (Standard Dimensions for older types.) \$ 6.80
- RS-367, Dimensional and Electrical Characteristics Defining Receiver Type Sockets. (Including crystal sockets.) \$20.20
- RS-417, Crystal Outlines (Standard dimensions and pin connections for current quartz crystal units - 1974.) \$ 7.80

(b) **Production Tests**

- RS-186-E, (All Sections), Standard Test Methods for Electronic Component Parts \$42.00

(c) **Application Information**

- Components Bulletin No. 6, Guide for the Use of Quartz Crystals for Frequency Control \$ 4.90

(d) **RS-477, Cultured Quartz (Apr. 81)** \$ 5.50

**International Electrotechnical Commission**

Order through: American National Standards Inst.  
 1430 Broadway  
 New York, New York 10018

\*ANSI can quote prices on specific IEC publication on a day to day basis only. All IEC and ISO standards have been removed from its Standards Catalog. Cal ANSI, NYC (212)-354-3300 for prices.

**IEC Publication 122-1 (1976)**

Quartz crystal units for frequency crystal and selection. Part 1: Standard values and test conditions. (Second edition)

**IEC Publication 122-2 (1962) Section 3:**

Guide to the use of Quartz Oscillator Crystals, including Amendment 1 (1969).

**IEC Publication 122-3 (1977) Part 3: Standard Outlines and Pin Connections. (Second edition)**

**IEC Publication 283 (1968) Methods for the Measurement of Frequency and Equivalent Resistance of Unwanted Resonances of Filter Crystal Units**

**IEC Publication 302 (1969) Standard Definitions and Methods of Measurement for Piezoelectric Vibrators Operating Over the Frequency Range up to 30 MHz**

**IEC Publication 314 (1970) Temperature Control Devices for Quartz Crystal Units, including Supplement 314A Contents: General Characteristics & Standards; Test Conditions; Pin Connections**

**IEC Publication 314A (1971) First Supplement to Publication 314 (1970) Contents: Guide to the Use of Temperature Control Devices for Quartz Crystal Units**

**IEC Publication 368 (1971) Piezoelectric Filters including Amendment 1, Amendment 2, and Supplement 368A and 368B Contents: General Information & Standards Values; Test Conditions**

**IEC Publication 368A (1973) First Supplement to Publication 368 (1971) Contents: Guide to the Use of Piezoelectric Filters**

**IEC Publication 368B (1975) Second Supplement to Publication 368 (1971) Contents: Piezoelectric Ceramic Filters**

**IEC Publication 444 (1973) Basic Method for the Measurement of Resonance Frequency and Equivalent Series Resistance Quartz Crystal Units by Zero Phase Technique in a  $\pi$  - Network**

**IEC Publication 483 (1976) Guide to Dynamic Measurements of Piezoelectric Ceramics with High Electromechanical Coupling**

**Department of Defense**

Order through: Naval Publication & Form Center  
 5801 Tabor Avenue  
 Philadelphia, PA 19120

**MIL-C-3098 Crystal Unit, Quartz, General Specification For**

**MIL-H-10056 Holders (Enclosures), Crystal, General Specifications For**

**MIL-STD-683 Crystal Units, Quartz/And Holders, Crystal**

**MIL-F-28734 Frequency Standards, Cesium Beam, General Specification For**

**MIL-O-55310 Oscillators, Crystal, General Specification For**

**MIL-F-18327 Filters, High Pass, Low Pass, Band Pass Suppression and Dual Functioning, General Specification For**

**MIL-O-39021 Oven Crystal, General Specification For**

**MIL-O-55240 Oscillators, Audio Frequency**

**MIL-F-28811 Frequency Standard, Cesium Beam Tube**

*36th Annual Frequency Control Symposium - 1982*

PROCEEDINGS

ANNUAL FREQUENCY CONTROL SYMPOSIA

<u>NO.</u>	<u>YEAR</u>	<u>DOCUMENT NO.</u>	<u>OBTAIN FROM*</u>	<u>COST</u>
10	1956	AD 298322	NTIS	\$28.00
11	1957	AD 298323	"	30.00
12	1958	AD 298324	"	31.00
13	1959	AD 298325	"	33.00
14	1960	AD 246500	"	22.00
15	1961	AD 265455	"	19.00
16	1962	PB 162343	"	24.00
17	1963	AD 423381	"	29.00
18	1964	AD 450341	"	29.00
19	1965	AD 471229	"	32.00
20	1966	AD 800523	"	32.00
21	1967	AD 659792	"	28.00
22	1968	AD 844911	"	30.00
23	1969	AD 746209	"	17.00
24	1970	AD 746210	"	19.00
25	1971	AD 746211	"	19.00
26	1972	AD 771043	"	18.00
27	1973	AD 771042	"	23.00
28	1974	AD A011113	"	21.00
29	1975	AD A017466	"	23.00
30	1976	AD A046089	"	27.00
31	1977	AD A088221	"	30.00
32	1978		EIA	20.00
33	1979		"	20.00
34	1980		"	20.00
35	1981		"	20.00
36	1982		SGC	25.00

\*NTIS - National Technical Information Service (NTIS prices are as of Sept 1980  
Sills Building and are subject to change.)  
5285 Port Royal Road  
Springfield, VA 22161

\* EIA - Annual Frequency Control Symposium  
c/o Electronic Industries Association  
2001 Eye Street  
Washington, DC 20006

\* SGC - Systematics General Corporation  
Airport Plaza Suite 902  
2711 Jefferson Davis Highway  
Arlington, VA 22202

Remittance must be enclosed with all orders. For orders placed with NTIS and SGC from outside the United States, double the domestic price list per copy for handling and mailing.

When referencing these Proceedings, please use the format shown in the following examples:

- (1) D. E. Newell and R. H. Bangert, "Temperature Compensation of Quartz Crystal Oscillators", Proceedings, 17th Annual Symposium on Frequency Control, US Army Electronics Command, Ft. Monmouth, NJ, pp 491-508, (1963). National Technical Information Service Accession No. AD 423381.
- (2) I. Pascaru and M. Meirs, "Development of a Light Weight, Military, Cesium Standard", Proceedings, 33rd Annual Symposium on Frequency Control, US Army Electronics Command, Ft. Monmouth, NJ, pp 484-489 (1979). Electronic Industries Association, 2001 Eye Street, NW, Washington, D.C. 20006.



62

AD-A130 811

PROCEEDINGS OF THE SYMPOSIUM ON FREQUENCY CONTROL (36TH  
ANNUAL) 2-4 JUNE 1..(U) ARMY ELECTRONICS RESEARCH AND  
DEVELOPMENT COMMAND FORT MONMOUTH. E PAIGE ET AL. 1982

8/4

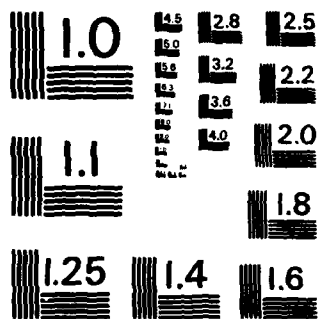
UNCLASSIFIED

F/G 20/14

NL



END  
DATE  
FILMED  
DTIC



MICROCOPY RESOLUTION TEST CHART  
NATIONAL BUREAU OF STANDARDS-1963-A

**SUPPLEMENTAR**

**INFORMATION**



DEPARTMENT OF THE ARMY  
US ARMY ELECTRONICS RESEARCH AND DEVELOPMENT COMMAND  
TECHNICAL SUPPORT ACTIVITY  
FORT MONMOUTH, NEW JERSEY 07703

REPLY TO  
ATTENTION OF

DELS-D-L-S

16 Sep 83

Defense Technical Information Center  
Document Acquisition  
(ATTN: Jim Cundiff)  
Cameron Station  
Alexandria, VA 22314

RE: All Rights Reserved

Pursuant to our conversation, this confirms Dr. Arthur Ballato's express information, this date, that DTIC and NTIS have permission to reproduce and sell "Proceedings of the 36th Annual Symposium on Frequency Control, 1982."

  
L. W. Goldberg  
STINFO Office

~~\_\_\_\_\_~~